

THE INTERNATIONAL ARCHIVES OF THE PHOTOGRAMMETRY, REMOTE SENSING AND SPATIAL INFORMATION SCIENCES
ARCHIVES INTERNATIONALES DE PHOTOGRAMMÉTRIE, DE TÉLÉDÉTECTION ET DE SCIENCES DE L'INFORMATION SPATIALE
INTERNATIONALES ARCHIV FÜR PHOTOGRAMMETRIE, FERNERKUNDUNG UND RAUMBEZOGENE INFORMATIONSWISSENSCHAFTEN

VOLUME
VOLUME
BAND

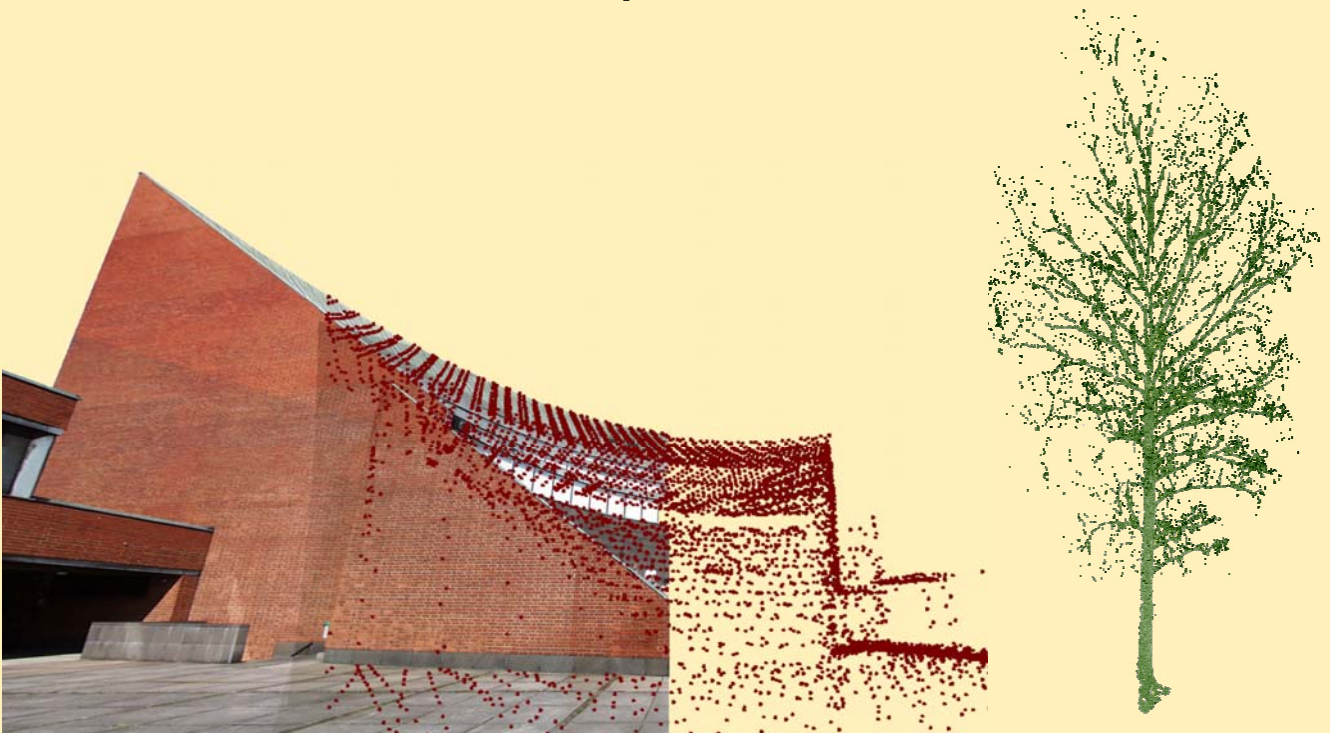
XXXVI

PART
TOME
TEIL

3 / W52

**Proceedings of the ISPRS Workshop
'Laser Scanning 2007 and SilviLaser 2007'**

**Espoo, Finland
12 – 14 September 2007**



Editors

P. Rönholm, H. Hyypä, J. Hyypä

Organisers

ISPRS WG III/3, III/4, V/3, VIII/11, ASPRS Lidar Committee
Finnish Geodetic Institute

Institute of Photogrammetry and Remote Sensing, Helsinki University of Technology (TKK)

THE INTERNATIONAL ARCHIVES OF THE PHOTOGRAMMETRY, REMOTE SENSING AND SPATIAL INFORMATION SCIENCES
ARCHIVES INTERNATIONALES DE PHOTOGRAMMÉTRIE, DE TÉLÉDÉTECTION ET DE SCIENCES DE L'INFORMATION SPATIALE
INTERNATIONALES ARCHIV FÜR PHOTOGRAMMETRIE, FERNERKUNDUNG UND RAUMBEZOGENE INFORMATIONSWISSENSCHAFTEN

VOLUME
VOLUME
BAND

XXXVI

PART
TOME
TEIL

3 / W52

Proceedings of the ISPRS Workshop

'Laser Scanning 2007 and SilviLaser 2007'

Espoo, Finland

12 – 14 September 2007

Editors

P. Rönholm, H. Hyypä, J. Hyypä

Organisers

ISPRS WG III/3, III/4, V/3, VIII/11, ASPRS Lidar Committee
Finnish Geodetic Institute

Institute of Photogrammetry and Remote Sensing, Helsinki University of Technology (TKK)

This compilation © 2007 by the International Society for Photogrammetry and Remote Sensing. Reproduction of this volume or any parts thereof (excluding short quotations for the use in the preparation of reviews and technical and scientific papers) may be made only after obtaining the specific approval of the publisher. The papers appearing in this volume reflect the authors' opinions. Their inclusion in this publication does not necessarily constitute endorsement by the editors or by the publisher. Author(s) retain all rights to individual papers.

Published by

ISPRS Working Groups

- WG III/3 - Processing of Point Clouds from Laser Scanners and Other Sensors
- WG III/4 - Automatic Image Interpretation for City-Modelling
- WG V/3 - Terrestrial Laserscanning
- VIII/11 - Sustainable Forest and Landscape Management

ASPRS Lidar Committee

Finnish Geodetic Institute

Institute of Photogrammetry and Remote Sensing, Helsinki University of Technology (TKK)

Cover Images © Petri Rönholm (left) and © Petri Rönholm / Juho Lumme (right)

ISPRS Headquarters 2004-2008

c/o ORHAN ALTAN, ISPRS Secretary General
Division of Photogrammetry, Faculty of Civil Engineering
Istanbul Technical University
Ayazaga, 34469 Istanbul, Turkey
Phone: +90 212 285 38 10
FAX: +90 212 285 65 87
Email: oaltan@itu.edu.tr

ISPRS WEB Homepage: <http://www.isprs.org>

Copies of the proceedings (only in CDROM) are available from

GITC bv
P.O.Box 112
8530 AC Lemmer
The Netherlands
Tel: +31 (0) 514 56 18 54
Fax: +31 (0) 514 56 38 98
E-mail: mailbox@gitc.nl
Website: www.gitc.nl

Preface

ISPRS Workshop on Laser Scanning and SilviLaser 2007, for which we use acronym LS SL 2007, is a continuation of ISPRS Workshops on Laser Scanning, held in Dresden 2003 and in Enschede 2005, and laser scanning workshops of forestry, held e.g. in Canada and Australia 2002, Umeå 2003, Freiburg 2004, Blacksburg 2005, Vienna 2006 and Matsuyama 2006. By putting together the technology-oriented laser scanning and the forestry-related silvilaser conference series we wanted to foster the development of methods and applications in both communities. Thus, the workshop is intended to bring together an interdisciplinary group of researchers, system developers, data providers, application developers, and end-users of airborne and terrestrial laser scanning on both disciplines.

The workshop is organized in co-operation with the Finnish Geodetic Institute (FGI) and Helsinki University of Technology (TKK). The workshop actually celebrates 10 years' research on laser scanning at TKK and FGI. The research was initiated in 1997 in co-operation with FM-Kartta Oy (today known as Blom Kartta Oy). At that time, Arttu Soinen from Terrasolid Oy has already implemented some first tools for ALS. Today, the co-operation with these companies is even stronger. Prior to the ALS research in Finland, there were already related research going on: laboratory measurements of lidar/laser, 3D video digitizing, waveform-based microwave radar development and data analysis and use of profiling radar for forest inventory, and thus the physics and background of ALS were already very familiar to the researchers. Today, both the forest community and public authorities (e.g. National land survey) are aiming at using laser scanning for operative forest inventory and DEM generation in Finland implying that the research has had some impacts.

The papers in the proceedings to be distributed at the workshop are peer reviewed by at least two (most of them by three) experts in the field. The names of the reviewers are mainly selected from the scientific board, which we even had to enlarge due to the need of so many reviews. Additionally, the editorial board read the papers. We hope that all our effort improved the quality of the papers.

In the LS SL 2007, there is also a collection of keynote presentations. We were very fortunate to have prof. Wolfgang Wagner to talk about waveform analysis techniques, software developer Arttu Soinen, father of TerraScan and other TerraSolid products, prof. Matti Maltamo giving summary of ALS-based experiences and possibilities in forestry, prof. Norbert Pfeifer focussing on geometrical aspects of ALS and TLS and Petri Rönholm talking about integrating LS and photogrammetry. The main findings of Wagner, Maltamo, Pfeifer and Rönholm can also be read from the proceedings.

Finally, we want to thank all contributing authors, scientific board, other reviewers, our sponsors, the companies in exhibition and local organizing committee. Their support was essential for realizing the workshop, which we hope to contribute to science and practice.

Juha Hyypä, Petri Rönholm and Hannu Hyypä
Otaniemi 24 August 2007

Organizing Committees

Scientific Program Committee

Claus Brenner (University of Hanover, Germany)
Naser El-Sheimy (University of Calgary, Canada)
Norbert Haala (University of Stuttgart, Germany)
Henrik Haggrén (Helsinki Univ. of Technology, Finland)
Ross Hill (Bournemouth University, UK)
Yasumasa Hirata (FFPRI, Japan)
Johan Holmgren (SLU, Umeå, Sweden)
Markus Holopainen (Helsinki University, Finland)
Juha Hyypä (Finnish Geodetic Institute, Finland)
Hannu Hyypä (Helsinki Univ. of Technology, Finland)
Sanna Kaasalainen (Finnish Geodetic Institute, Finland)
Barbara Koch (University of Freiburg, Germany)
Ilkka Korpela (Helsinki University, Finland)
Derek Lichti (Curtin University of Technology, Australia)

Hans-Gerd Maas (Dresden Univ. of Technology, Germany)
Matti Maltamo (University of Joensuu, Finland)
Ross Nelson (NASA, USA)
Erik Næsset (UMB, Norway)
Håkan Olsson (SLU, Sweden)
Norbert Pfeifer (TU Vienna, Austria)
Franz Rottensteiner (Univ. Melbourne, Australia)
Petri Rönnholm (Helsinki Univ. of Technology, Finland)
Andre Samberg (ASPRS Lidar Committee)
Marco Scaioni (Politecnico di Milano, Italy)
Tatsuo Sweda (Ehime University, Japan)
Ulf Söderman (Foran Remote Sensing, Sweden)
Wolfgang Wagner (TU Vienna, Austria)
George Vosselman (ITC, the Netherlands)
Randy Wynne (Virginia Tech, USA)
Xiaowei Yu (Finnish Geodetic Institute, Finland)

Local Organizing Committee

General Chair

Juha Hyypä, Finnish Geodetic Institute

Technical and Publicity Co-Chairs

Petri Rönnholm, TKK

Hannu Hyypä, TKK

Juha Hyypä, Finnish Geodetic Institute

Conference Coordinator

Marika Ahlavo, TKK

Secretary-General

Hannu Hyypä, TKK

Conference Secretary

Kirsti Filén, Finnish Geodetic Institute

Web Coordinator

Petri Rönnholm, TKK

Vice-Chair

Henrik Haggrén, TKK

Finance Chair

Hannu Hyypä, TKK

Finance Vice-Chair

Marika Ahlavo, TKK

Committee Members

Mika Karjalainen, Finnish Geodetic Institute

Harri Kaartinen, Finnish Geodetic Institute

Eero Ahokas, Finnish Geodetic Institute

Social Program Committee

Nina Heiska, TKK

Milka Nuikka, TKK

Anna Erving, TKK

Hanne Junnilainen, TKK

Table of Contents

Papers were accepted on the basis of peer-reviewed full manuscripts.

Generalized Least Squares Multiple 3D Surface Matching <i>D. Akca, A. Gruen</i>	1
Statistical Properties of Mean Stand Biomass Estimators in a Lidar-Based Double Sampling Forest Survey Design <i>H.-E. Andersen, J. Breidenbach</i>	8
On-Site Self-Calibration Using Planar Features for Terrestrial Laser Scanners <i>K.-H. Bae, D. Lichti</i>	14
Problems Related to the Generation of True-Orthophotos with Lidar DDSMs <i>L. Barazzetti, M. Brovelli, M. Scaioni</i>	20
Improving the Morphological Analysis for Tree Extraction: a Dynamic Approach to Lidar Data <i>A. Barilotti, F. Sepic, E. Abramo, F. Crosilla</i>	26
Registration of Terrestrial Laser Scans via Image Based Features <i>S. Barnea, S. Filin</i>	32
Towards the Estimation of Tree Structural Class in Northwest Coastal Forests Using Lidar Remote Sensing <i>C. W. Bater, N. C. Coops, S. E. Gergel, N. R. Goodwin</i>	38
Combined Feature Extraction for Façade Reconstruction <i>S. Becker, N. Haala</i>	44
Tree Detection and Diameter Estimations by Analysis of Forest Terrestrial Laserscanner Point Clouds <i>A. Bienert, S. Scheller, E. Keane, F. Mohan, C. Nugent</i>	50
Application of Terrestrial Laser Scanning for Shipbuilding <i>K. Biskup, P. Arias, H. Lorenzo, J. Armesto</i>	56
Using Airborne Small-Footprint Laser Scanner to Assess the Quantity of Seedlings in an Uneven-Aged Spruce Forest <i>O. M. Bollandsås, K. H. Hanssen, S. Marthiniussen, E. Næsset</i>	62
Automatic Segmentation of Building Facades Using Terrestrial Laser Data <i>H. Boulaassal, T. Landes, P. Grussenmeyer, F. Tarsha-Kurdi</i>	65
Validation of Airborne Lidar Intensity Values from a Forested Landscape Using HYMAP data: Preliminary Analyses <i>D. S. Boyd, R. A. Hill</i>	71

A Mixed Effects Model to Estimate Stand Volume by Means of Small Footprint Airborne Lidar Data for an American and German Study Site	77
<i>J. Breidenbach , R. McGaughey, H.-E. Andersen, G. Kändler, S. Reutebuch</i>	
Automatic Relative Orientation of Terrestrial Laser Scans Using Planar Structures and Angle Constraints	84
<i>C. Brenner, C. Dold</i>	
Supervised Classification of Water Regions from Lidar Data in the Wadden Sea Using a Fuzzy Logic Concept	90
<i>A. Brzank, C. Heipke</i>	
Using Airborne Lidar for the Assessment of Canopy Structure Influences on CO2 Fluxes	96
<i>L. Chasmer, A. Barr, A. Black, C. Hopkinson, N. Kljun, J. H. McCaughey, P. Treitz</i>	
Processing Full-Waveform Lidar Data: Modelling Raw signals	102
<i>A. Chauve, C. Mallet, F. Bretar, S. Durrieu, M. P. Deseilligny, W. Puech</i>	
Icesat Fullwaveform Altimetry Compared to Airborne Laser Altimetry over the Netherlands	108
<i>H. Duong, R. Lindenbergh, N. Pfeifer, G. Vosselman</i>	
Simulating Sampling Efficiency in Airborne Laser Scanning Based Forest Inventory	114
<i>L. Ene, E. Næsset, T. Gobakken</i>	
Detection and Reconstruction of Free Form Surfaces from Airborne Laser Scanning Data	119
<i>S. Filin, N. A. Akel, Y. Doytsher</i>	
Terrestrial Lidar Measurements for Analysing Canopy Structure in an Old-Growth Forest	125
<i>S. Fleck, N. Obertreiber, I. Schmidt, M. Brauns, H. Jungkunst, C. Leuschner</i>	
Adaptive Filtering of Aerial Laser Scanning Data	130
<i>G. Forlani, C. Nardinocchi</i>	
Lidar-Derived Site Index in the U.S. Pacific Northwest - Challenges and Opportunities	136
<i>D. Gatzliolis</i>	
Accuracy of Forest Parameters Derived from Medium Footprint Lidar under Operational Constraints	144
<i>C. Ginzler, J. Boehl, R. Boesch, L. T. Waser</i>	
Assessing Effects of Laser Point Density on Biophysical Stand Properties Derived from Airborne Laser Scanner Data in Mature Forest	150
<i>T. Gobakken, E. Næsset</i>	

Estimation of the Lidar Height Offset in Coastal Vegetated Areas	156
<i>J. Goepfert, U. Soerge</i>	
Automatic Co-Registration of Terrestrial Laser Scanner and Digital Camera for the Generation of Hybrids Models	162
<i>D. González Aguilera, P. Rodríguez González, J. Gómez Lahoz</i>	
Assessment of Sub-Canopy Structure in a Complex Coniferous Forest	169
<i>N. R. Goodwin, N. C. Coops, C. Bater, S. E. Gergel</i>	
Planar Feature Extraction in Terrestrial Laser Scans Using Gradient Based Range Image Segmentation	173
<i>B. Gorte</i>	
Registration of Agia Sanmarina Lidar Data Using Surface Elements	178
<i>W. von Hansen</i>	
Going Undercover: Mapping Woodland Understorey from Leaf-On and Leaf-Off Lidar Data	184
<i>R. A. Hill</i>	
Modelling Canopy Gap Fraction from Lidar Intensity	190
<i>C. Hopkinson, L. Chasmer</i>	
Glacier Surface Segmentation Using Airborne Laser Scanning Point Cloud and Intensity Data	195
<i>B. Höfle, T. Geist, M. Rutzinger, N. Pfeifer</i>	
Radiometric Calibration of ALS Intensity	201
<i>S. Kaasalainen, J. Hyyppä, P. Litkey, H. Hyyppä, E. Ahokas, A. Kukko, H. Kaartinen</i>	
Extending Generalized Hough Transform to Detect 3D Objects in Laser Range Data	206
<i>K. Khoshelham</i>	
Tree Height Estimation Methods for Terrestrial Laser Scanning in a Forest Reserve	211
<i>G. Király, G. Brolly</i>	
REIN Algorithm and the Influence of Point Cloud Density on nDSM and DTM Precision in a Submediterranean Forest	216
<i>A. Kobler, P. Ogrinc</i>	
Automatic Glacier Surface Analysis from Airborne Laser Scanning	221
<i>M. Kodde, N. Pfeifer, B. Gorte, T. Geist, B. Höfle</i>	
Single-Tree Forest Inventory Using Lidar and Aerial Images for 3D Treetop Positioning, Species Recognition, Height and Crown Width Estimation	227
<i>I. Korpela, B. Dahlin, H. Schäfer, E. Bruun, F. Haapaniemi, J. Honkasalo, S. Ilvesniemi, V. Kuutti, M. Linkosalmi, J. Mustonen, M. Salo, O. Suomi, H. Virtanen</i>	

Laser Scanner Simulator for System Analysis and Algorithm Development: a Case with Forest Measurements	234
<i>A. Kukko, J. Hyyppä</i>	
Road Environment Mapping System of the Finnish Geodetic Institute - FGI Roamer -	241
<i>A. Kukko, C.-O. Andrei, V.-M. Salminen, H. Kaartinen, Y. Chen, P. Rönholm, H. Hyyppä, J. Hyyppä, R. Chen, H. Haggrén, I. Kosonen, K. Čapek</i>	
Estimation of LAI Using LiDAR Remote Sensing in Forest	248
<i>D.-A. Kwak, W.-K. Lee, H.-K. Cho</i>	
Deciduous-Coniferous Tree Classification Using Difference between First and Last Pulse Laser Signatures	253
<i>X. Liang , J. Hyyppä, L. Matikainen</i>	
Waveform Features for Tree Identification	258
<i>P. Litkey, P. Rönholm, J. Lumme, X. Liang</i>	
Generating Lidar Data in Laboratory: Lidar Simulator	264
<i>B. Lohani, R. K. Mishra</i>	
Experiences and Possibilities of ALS Based Forest Inventory in Finland (Keynote)	270
<i>M. Maltamo, P. Packalén, J. Peuhkurinen, A. Suvanto, A. Pesonen, J. Hyyppä</i>	
Classification Tree Based Building Detection From Laser Scanner and Aerial Image Data	280
<i>L. Matikainen , H. Kaartinen, J. Hyyppä</i>	
Recovering Plot-Specific Diameter Distribution and Height-Diameter Curve Using ALS Based Stand Characteristics	288
<i>L. Mehtätalo, M. Maltamo, P. Packalen</i>	
Ray Tracing for Modeling of Small Footprint Airborne Laser Scanning Returns	294
<i>F. Morsdorf, O. Frey, B. Koetz, E. Meier</i>	
Utilizing Airborne Laser Intensity for Tree Species Classification	300
<i>H. O. Ørka, E. Næsset, O. M. Bollandsås</i>	
Quality Analysis of 3D Road Reconstruction	305
<i>S. Oude Elberink , G. Vosselman</i>	
Geometrical Aspects of Airborne and Terrestrial Laser Scanning (Keynote)	311
<i>N. Pfeifer, C. Briese</i>	
Extracting Windows from Terrestrial Laser Scanning	320
<i>S. Pu , G. Vosselman</i>	
Classification of Building Damages Based on Laser Scanning Data	326
<i>M. Rehor</i>	

Combined Tree Segmentation and Stem Detection Using Full Waveform Lidar Data	332
<i>J. Reitberger, P. Krzystek, U. Stilla</i>	
From Point Cloud to Surface: Modeling Structures in Laser Scanner Point Clouds	338
<i>P. Rodríguez González, D. González Aguilera, J. Gómez Lahoz</i>	
A Method of Directly Estimating Stemwood Volume from Glas Waveform Parameters	344
<i>J. Rosette, P. North, J. Suárez</i>	
Using Airborne Laser-Scanner-Data in Forestry Management: a Novel Approach to Single Tree Delineation	350
<i>J. Rossmann, M. Schluse, A. Bücken, P. Krahwinkler</i>	
Integration of Laser Scanning and Photogrammetry (Keynote)	355
<i>P. Rönholm, E. Honkavaara, P. Litkey, H. Hyyppä, J. Hyyppä</i>	
An Implementation of the ASPRS LAS Standard	363
<i>A. Samberg</i>	
Integrated Bundle Adjustment with Variance Component Estimation - Fusion of Terrestrial Laser Scanner Data, Panoramic and Central Perspective Image Data	373
<i>D. Schneider, H.-G. Maas</i>	
Mapping Defoliation with Lidar	379
<i>S. Solberg, E. Næsset</i>	
Hierarchical Clustered Outlier Detection in Laser Scanner Point Clouds	383
<i>S. Sotoodeh</i>	
Estimation of Carbon Stocks in New Zealand Planted Forests Using Airborne Scanning Lidar	389
<i>P. R. Stephens, P. J. Watt, D. Loubser, A. Haywood, M. O. Kimberley</i>	
Extracting Structural Characteristics of Dormant Herbaceous Floodplain Vegetation from Airborne Laser Scanner Data	395
<i>M. Straatsma, H. Middelkoop</i>	
Assessment of LiDAR-Derived Tree Heights Estimated from Different Flight Altitude Data in Mountainous Forests with Poor Laser Penetration Rates	401
<i>T. Takahashi, Y. Awaya, Y. Hirata, N. Furuya, T. Sakai, A. Sakai</i>	
Hough-Transform and Extended RANSAC Algorithms for Automatic Detection of 3D Building Roof Planes from Lidar Data	407
<i>F. Tarsha-Kurdi, T. Landes, P. Grussenmeyer</i>	
Waveform Analysis Techniques in Airborne Laser Scanning (Keynote)	413
<i>W. Wagner, A. Roncat, T. Melzer, A. Ullrich</i>	

Development of a Procedure for Vertical Structure Analysis and 3D Single Tree Extraction within Forests Based on Lidar Point Cloud	419
<i>Y. Wang, H. Weinacker, B. Koch</i>	
Terrestrial Laser Scanning Versus Traditional Forest Inventory First Results from the Polish Forests	424
<i>P. Wezyk, K. Koziol, M. Glista, M. Pierzchalski</i>	
Change Detection via Terrestrial Laser Scanning	430
<i>R. Zeibak, S. Filin</i>	
Hierarchical Watershed Segmentation of Canopy Height Model for Multi-Scale Forest Inventory	436
<i>K. Zhao, S. Popescu</i>	
Index of Authors	442
Index of Keywords	445

GENERALIZED LEAST SQUARES MULTIPLE 3D SURFACE MATCHING

Devrim Akca* and Armin Gruen

Institute of Geodesy and Photogrammetry, ETH Zurich, Wolfgang-Pauli-Str. 15, CH-8093 Zurich, Switzerland
(akca, agruen)@geod.baug.ethz.ch

Commission V, WG V/3

KEY WORDS: Surface matching, co-registration, multiple surfaces, 3D surface, pointcloud, georeferencing.

ABSTRACT:

A method for the simultaneous co-registration and georeferencing of multiple 3D pointclouds and associated intensity information is proposed. It is a generalization of the 3D surface matching problem. The simultaneous co-registration provides for a strict solution to the problem, as opposed to sequential pairwise registration. The problem is formulated as the Least Squares matching of overlapping 3D surfaces. The parameters of 3D transformations of multiple surfaces are simultaneously estimated, using the Generalized Gauss-Markoff model, minimizing the sum of squares of the Euclidean distances among the surfaces. An observation equation is written for each surface-to-surface correspondence. Each overlapping surface pair contributes a group of observation equations to the design matrix. The parameters are introduced into the system as stochastic variables, as a second type of (fictitious) observations. This extension allows to control the estimated parameters. Intensity information is introduced into the system in the form of quasisurfaces as the third type of observations. Reference points, defining an external (object) coordinate system, which are imaged in additional intensity images, or can be located in the pointcloud, serve as the fourth type of observations. They transform the whole block of "models" to a unique reference system. Furthermore, the given coordinate values of the control points are treated as observations. This gives the fifth type of observations. The total system is solved by applying the Least Squares technique, provided that sufficiently good initial values for the transformation parameters are given. This method can be applied to data sets generated from aerial as well as terrestrial laser scanning or other pointcloud generating methods.

1. INTRODUCTION

The early approach for the multiple pointclouds registration is to sequentially apply pairwise registrations until all views are combined. Chen and Medioni (1992) propose a method, which registers successive views incrementally with enough overlapping area. Each next view is registered and merged with the topological union of the former pairwise registrations. Later, this approach is equipped with a coarse-to-fine mesh hierarchy (Turk and Levoy, 1994), and the least median of squares (LMS or LMedS) estimator with random sampling (Masuda and Yokoya, 1995).

The shortcomings of the incremental solution were recognized early. The registration of a view does not change once it has been added to the integrated model. However, it is possible that a following view brings information that could have improved the registration of previously processed views (Bergevin et al., 1996; Pulli, 1999). Bergevin et al. (1996) propose a solution in which every view is sequentially matched with all other overlapping views. The procedure is iteratively executed over all views. The iteration is stopped when the registration converges. For each view a separate transformation is calculated, and they are applied simultaneously before the next run of iteration. Although it diffuses the registration errors evenly among all views, slow convergence is the main disadvantage. Benjemaa and Schmitt (1997) accelerate the method by applying the new transformation as soon as it is calculated (like the Gauss-Seidel method) and employ a multi-z-buffer technique which provides a 3D space partitioning. Pulli's (1999) solution performs pairwise registrations between

every overlapping view pairs. Subsequently, these pairwise registrations are incrementally treated as constraints in a global registration step. However, these constraints do not imply functional constraints in the optimization scheme. Rather, it is a set of virtual points that uniformly subsample the overlapping areas, called as virtual mate. This approach has the capability to handle large data sets, since using the virtual mates from pairwise alignments does not require loading the entire data set into memory. A concrete mate version of this method, in which a set of corresponding points themselves rather than the virtual points is used as constraint, is proposed for robot navigation (Lu and Milios, 1997). The subsequent global registration is achieved by employing a sequential estimation procedure.

Alternatively, some works carry out the multiview registration task in the sensor coordinate system. In Blais and Levine (1995) couples of images are incrementally registered. It is based on reversing the range finder calibration process, resulting in a set of equations which can be used to directly compute the location of a point in a range image corresponding to an arbitrary location in the three dimensional space. Another multiview registration method based on inverse calibration, developed independently, called Iterative Parametric Point (IPP), is given in Jokinen (1998). Differently, it simultaneously registers all views using the Levenberg-Marquardt non-linear optimization technique. Although the reverse calibration method, also called point-to-projection technique, provides fast access mechanisms for the point correspondence, it is performed on 2.5D range maps. It is not suitable for truly 3D applications.

* Corresponding author. www.photogrammetry.ethz.ch

Stoddart and Hilton (1996) first find the pairwise correspondences between all the overlapping views, and then iteratively solve the global registration using a gradient descent algorithm. Although this is a two steps procedure, the final transformations are simultaneously computed as one system in the global registration step. A similar approach, developed independently, is given in Eggert et al. (1998). Neugebauer (1997) reduces the problem to only a global registration step, and simultaneously registers all views using the Levenberg-Marquardt method. Correspondence search is performed on the range maps, which is a 2.5D approach. Williams et al. (1999) suggest a further simultaneous solution by including a priori covariance matrices for each individual point. The non-linear system is solved using the Lagrange multipliers method, or so called Gauss-Helmert estimation model.

Iterative linear (closed-form) solutions have become very attractive. Although they are straightforward to implement, their stochastic model is of limited value in comparison to non-linear optimization techniques. Williams and Bennamoun (2001) present a generalization of Arun et al.'s (1987) well known pairwise registration method, which uses the Singular Value Decomposition (SVD) to compute the optimal registration parameters in the presence of point correspondences. This method is a closed-form solution for 3D similarity transformation between two 3D point sets. Beinat and Crosilla (2001) propose the Generalized Procrustes Analysis as a solution for the multiple range image registration problem in the presence of point correspondence. The Procrustes Analysis is another kind of closed-form solution, which was introduced by Schoenemann and Carroll (1970). In fact, both of the methods use Gauss-Seidel or Jacobi type of iteration techniques. Further similar methods are given in Sharp et al. (2004) and in Krishnan et al. (2005).

Recently, Al-Manasir and Fraser (2006) propose an alternative technique, called image-based registration (IBR), for digital camera mounted/integrated terrestrial laserscanner systems, based on the photogrammetric image orientation procedure. The network of images is first oriented using the bundle block adjustment, and then the exterior orientations are transferred to the laserscanner stations provided that the camera calibration and spatial relationship between the camera and laserscanner coordinate systems are known. Since it exclusively uses the imagery, registration can be achieved even in the situations where there is no overlap between the point clouds. However, the method is only applicable for camera mounted laserscanner data.

Several review and comparison studies are available in the literature (Jokinen and Haggren, 1998; Williams et al., 1999; Cunningham and Stoddart, 1999; Campbell and Flynn, 2001).

In a previous work, we proposed an algorithm for the least squares matching of overlapping 3D surfaces, called least squares 3D surface matching (LS3D). The LS3D method estimates the transformation parameters of one or more fully 3D search surfaces with respect to a template one, using the Generalized Gauss-Markoff model, minimizing the sum of squares of the Euclidean distances between the surfaces (Gruen and Akca, 2005). The mathematical model is a generalization of the Least Squares image matching method, in particular the method given by Gruen (1985).

In order to optimize the run-time, a rapid method for searching the correspondence is added. It is a space partitioning method,

called 3D boxing (Akca and Gruen, 2005b). False correspondences with respect to outliers and occlusions are detected and eliminated using a weighting scheme adapted from Robust Estimation methods (Akca and Gruen, 2005c).

When the object surface lacks sufficient geometric information, i.e. homogeneity or isotropicity of curvatures, the basic algorithm will either fail or find a side minimum. We propose an extension of the basic algorithm in which available attribute information, e.g. intensity, color, temperature, etc., is used to form quasisurfaces in addition to the actual ones. The matching is performed by simultaneous use of surface geometry and attribute information under a combined estimation model (Akca and Gruen, 2005a).

When more than two pointclouds with multiple overlaps exist, we adopt a two step solution (Akca and Gruen, 2005b). First, pairwise LS3D matchings are run on every overlapping pairs and a subset of point correspondences are saved to separate files, similar to Lu and Miliotis's approach (1997). In the global registration step, all these files are passed to a block adjustment by independent models procedure (Ackermann et al., 1973), which is a well known orientation procedure in photogrammetry.

In some applications georeferencing is needed, which is the procedure to transform the spatial data from a local system to an external object coordinate system. We also provide for an integrated solution for this problem.

1.1 Our proposed method

Terrestrial laser scanning companies (e.g. Z+F, Leica, Riegler) commonly use special kind of targets for the registration of point clouds. However such a strategy has several deficiencies with respect to fieldwork time, personnel, equipment costs, and accuracy. In a recent study, Sternberg et al. (2004) reported that registration and geodetic measurement parts comprise 10-20% of the whole project time. In another study a collapsed 1000-car parking garage was documented in order to assess the damage and structural soundness of the structure. The scanning took 3 days, while the conventional survey of the control points required 2 days (Greaves, 2005). In a recent project conducted by our group at Pinchango Alto (Peru) two persons set the targets to the field and measured with Real-Time Kinematic GPS in 1½ days.

Not only fieldwork time but also accuracy is another important concern. The target-based registration methods cannot exploit the full accuracy potential of the data. The geodetic measurement naturally introduces some errors, which might exceed the internal error of the scanner instrument. In addition, the targets must be kept stable during the whole scanning campaign. This might be inconvenient with the scanning works stretching over more than one day. On the other hand, target-based registration techniques can provide immediate georeferencing to an object coordinate system.

Surface-based registration techniques stand as efficient and versatile alternative to the target-based techniques. They simply bring the strenuous additional fieldwork of the registration task to the computer in the office while optimizing the project cost and duration and achieving a better accuracy. However, they do not provide the georeferencing option.

This work proposes a method which combines the advantageous parts of both techniques based on the least squares matching framework. The proposed method is a (truly) simultaneous one step solution for the matching and georeferencing of multiple 3D surfaces with their intensity information. The mathematical model is a hybrid system which contains different type of observations. The proposed method is an algorithmic extension of our previous work given in Gruen and Akca (2005). It generalizes the 3D surface matching problem in the sense that multiple 3D surfaces with their intensity information are globally matched and simultaneously georeferenced. Multiple primitives, surface information (geometry and intensity) and the (reference) point features, are co-registered together.

The paper is structured as follow. The next chapter introduces the mathematical model with the execution aspects. The third chapter presents the experimental results.

2. MATHEMATICAL MODELLING

2.1 Least Squares Multiple 3D Surface Matching

Assume a set of n surfaces of an object: $g_1(x, y, z), \dots, g_n(x, y, z)$. The object is defined in a 3D Cartesian coordinate system, whereas the n surfaces are located in arbitrary local coordinate systems. The n surfaces are discrete 3D approximations of continuous functions of the object surface. They are digitized according to a sampling principle.

The surface representation is carried out in a piecewise form, individually for each surface. $g_i(x, y, z)$ stands for any element of the i -th surface in this representation.

There are m mutual spatial overlaps between the surfaces $g_i(x, y, z)$. Every overlap satisfies a pairwise matching:

$$g_i(x, y, z) - e_i(x, y, z) = g_j(x, y, z) \quad , \quad i, j = 1, \dots, n \quad , \quad i \neq j \quad (1)$$

where $e_i(x, y, z)$ is a true error vector. It is assumed that i -th surface's noise is independent of j -th one.

In order to prevent duplication, Equations (1) are written for every possible i - j pair with $i < j$.

Equations (1) are considered as nonlinear observation equations which model the observation vector $g_i(x, y, z)$ with functions $g_j(x, y, z)$. The Least Squares matching of the j -th surface to the i -th one is to be satisfied while the i -th surface is also subject to a 3D transformation (with respect to a predefined datum). This is the 3D analogy of the X - Y constraint version (i.e. grid sampling mode) of the multiphoto geometrically constrained matching (MPGC) (Gruen and Baltsavias, 1987) where both the template and the search image patches are transformed.

Both surfaces are transformed to an object coordinate system while minimizing a goal function, which measures the sum of the squares of the Euclidean distances between them. The geometric relationships are established via 7-parameter similarity transformations. They can be replaced by another type if needed.

Each surface is associated with a set of 3D similarity transformation parameters,

$$\begin{bmatrix} x \\ y \\ z \end{bmatrix}_i = \begin{bmatrix} t_x \\ t_y \\ t_z \end{bmatrix}_i + m_i \mathbf{R}_i \begin{bmatrix} x_0 \\ y_0 \\ z_0 \end{bmatrix}_i \quad (2)$$

where $\mathbf{R}_i = \mathbf{R}_i(\omega, \phi, \kappa)$ is the orthogonal rotation matrix, $[t_x \ t_y \ t_z]_i^T$ is the translation vector, m_i is the uniform scale factor, and $(x_0, y_0, z_0)_i$ stand for the initial location of the surface.

Because Equations (1) are nonlinear, they are linearized by Taylor series expansion.

$$\begin{aligned} -e_i(x, y, z) &= g_j^0(x, y, z) + \frac{\partial g_j^0(x, y, z)}{\partial x_j} dx_j + \frac{\partial g_j^0(x, y, z)}{\partial y_j} dy_j \\ &+ \frac{\partial g_j^0(x, y, z)}{\partial z_j} dz_j - g_i^0(x, y, z) - \frac{\partial g_i^0(x, y, z)}{\partial x_i} dx_i \\ &- \frac{\partial g_i^0(x, y, z)}{\partial y_i} dy_i - \frac{\partial g_i^0(x, y, z)}{\partial z_i} dz_i \end{aligned} \quad (3)$$

dx , dy and dz are the differentiations of the selected 3D transformation model in Equation (2):

$$\begin{aligned} dx &= dt_x + a_{10} dm + a_{11} d\omega + a_{12} d\phi + a_{13} d\kappa \\ dy &= dt_y + a_{20} dm + a_{21} d\omega + a_{22} d\phi + a_{23} d\kappa \\ dz &= dt_z + a_{30} dm + a_{31} d\omega + a_{32} d\phi + a_{33} d\kappa \end{aligned} \quad (4)$$

with a_{pq} as the coefficient terms.

Using the notation

$$g_x = \frac{\partial g^0(x, y, z)}{\partial x}, \quad g_y = \frac{\partial g^0(x, y, z)}{\partial y}, \quad g_z = \frac{\partial g^0(x, y, z)}{\partial z} \quad (5)$$

and substituting Equations (4), Equation (3) results in:

$$\begin{aligned} -e_i(x, y, z) &= g_{xj} dt_{xj} + g_{yj} dt_{yj} + g_{zj} dt_{zj} \\ &+ (g_{xj} a_{10} + g_{yj} a_{20} + g_{zj} a_{30}) dm_j \\ &+ (g_{xj} a_{11} + g_{yj} a_{21} + g_{zj} a_{31}) d\omega_j \\ &+ (g_{xj} a_{12} + g_{yj} a_{22} + g_{zj} a_{32}) d\phi_j \\ &+ (g_{xj} a_{13} + g_{yj} a_{23} + g_{zj} a_{33}) d\kappa_j \\ &- g_{xi} dt_{xi} - g_{yi} dt_{yi} - g_{zi} dt_{zi} \\ &- (g_{xi} b_{10} + g_{yi} b_{20} + g_{zi} b_{30}) dm_i \\ &- (g_{xi} b_{11} + g_{yi} b_{21} + g_{zi} b_{31}) d\omega_i \\ &- (g_{xi} b_{12} + g_{yi} b_{22} + g_{zi} b_{32}) d\phi_i \\ &- (g_{xi} b_{13} + g_{yi} b_{23} + g_{zi} b_{33}) d\kappa_i \\ &- (g_i^0(x, y, z) - g_j^0(x, y, z)) \end{aligned} \quad (6)$$

where a_{pq} and b_{pq} are the coefficient terms for the differentiation of the transformation equations of the i -th and j -th surface, respectively. The terms g_x , g_y and g_z are the numerical derivatives of the object surface function $g(x, y, z)$. They are defined as the elements of the local surface normal vectors at the exact surface correspondence locations (Gruen and Akca, 2005). The linearized observation Equations (6) are written for each element of the i -th surface.

Equations (6) result in the following linear systems in matrix/vector form

$$\begin{aligned} -\mathbf{e}_1 &= \mathbf{A}_1 \mathbf{x} - \mathbf{l}_1, & \mathbf{P}_1 \\ -\mathbf{e}_2 &= \mathbf{A}_2 \mathbf{x} - \mathbf{l}_2, & \mathbf{P}_2 \\ & \vdots & \vdots \\ -\mathbf{e}_m &= \mathbf{A}_m \mathbf{x} - \mathbf{l}_m, & \mathbf{P}_m \end{aligned} \quad (7)$$

Equations (7) consist of m groups of observation equations. They can be combined in one sub-system as

$$-\mathbf{e} = \mathbf{A} \mathbf{x} - \mathbf{l}, \quad \mathbf{P} \quad (8)$$

where \mathbf{A} is the design matrix, \mathbf{x} is the parameter vector which contains n sets of transformation parameters, $\mathbf{P} = \mathbf{P}_i$ is the a priori weight matrix, $\mathbf{l} = g_x^0(x, y, z) - g_x^0(x, y, z)$ is the discrepancies vector that consists of the Euclidean distances between the corresponding elements of the overlapping surfaces. The calculation of the discrepancy vector \mathbf{l} and the numerical derivative terms g_x , g_y and g_z requires an appropriate correspondence search procedure (Akca and Gruen, 2005b).

Provided that $m \geq n$ is satisfied, the sub-system (of the design matrix) consisting of m Equations (7) implicitly contains the multiple overlap conditions. The normal equation matrix explicitly shows all the spatial relationships by non-zero off-diagonal elements (see Chapter 2.3.1).

With the statistical expectation operator $E\{\cdot\}$, it is assumed that

$$E\{\mathbf{e}\} = 0, \quad E\{\mathbf{e}\mathbf{e}^T\} = \sigma_0^2 \mathbf{P}^{-1} \quad (9)$$

The parameters are introduced into the system as observables with the associated weight coefficient matrix \mathbf{P}_b as

$$-\mathbf{e}_b = \mathbf{I} \mathbf{x} - \mathbf{l}_b, \quad \mathbf{P}_b \quad (10)$$

where \mathbf{I} is the identity matrix and \mathbf{l}_b is the (fictitious) observation vector. The weight matrix \mathbf{P}_b has to be chosen appropriately, considering a priori information of the parameters.

2.2 The Generalized Model with Intensity Matching and Georeferencing

When some surfaces lack sufficient geometric information, their intensity information, if available, is introduced to the system. The intensity information is used to form quasisurfaces in addition to the actual ones. The formation of quasisurfaces is given in Akca and Gruen (2005a). The quasisurfaces are treated like actual surfaces in the estimation model. They contribute observation equations to the design matrix, joining the system by the same set of transformation parameters

$$-\mathbf{e}_c = \mathbf{A}_c \mathbf{x} - \mathbf{l}_c, \quad \mathbf{P}_c \quad (11)$$

where \mathbf{e}_c , \mathbf{A}_c and \mathbf{P}_c are the true error vector, the design matrix, and the associated weight coefficient matrix for the quasisurface observations, respectively, and \mathbf{l}_c is the constant vector that contains the Euclidean distances between the corresponding quasisurface elements.

Reference points whose coordinates are defined in an external (object) coordinate system, which are imaged in additional intensity images, or can be located in the pointclouds, serve as the fourth type of observations. They are formulated as 3D similarity transformations from local pointcloud systems to the object coordinate system in linearized matrix form

$$-\mathbf{e}_d = \mathbf{A}_d \mathbf{x} - \mathbf{l}_d, \quad \mathbf{P}_d \quad (12)$$

where \mathbf{A}_d is the design matrix, \mathbf{P}_d is the associated weight matrix, and \mathbf{l}_d is the discrepancies vector which contains the coordinate value differences of the reference points between the transformed local system and object coordinate system. At least 7 coordinate elements of 3 control points are needed for georeferencing.

Actually, the coordinates of the control points are not error-free quantities. In a strict model, they are treated as observations with their associated weight matrices as

$$-\mathbf{e}_e = \mathbf{A}_e \mathbf{x} - \mathbf{l}_e, \quad \mathbf{P}_e \quad (13)$$

where \mathbf{A}_e , \mathbf{x} , and \mathbf{P}_e are the design matrix, the parameter vector, and the associated weight coefficient matrix for the observations of the control point coordinates, respectively, and \mathbf{l}_e is the discrepancy vector that contains the differences between the observed and estimated coordinate values. Here, the vector \mathbf{x} is extended to include the x - y - z coordinate values of the control points in addition to the transformation parameters.

Equations (12) eliminate the datum deficiency existing in Equations (8). Alternatively, the datum constraints can be imposed by fixing the minimal number of parameters in Equations (10).

The hybrid system of Equations (8), (10), (11), (12) and (13) is of the combined adjustment type that allows simultaneous matching of geometry and intensity and additionally georeferencing of multiple 3D surfaces. The Least Squares solution of the system gives the solution vector as

$$\hat{\mathbf{x}} = (\mathbf{A}^T \mathbf{P} \mathbf{A} + \mathbf{P}_b + \mathbf{A}_c^T \mathbf{P}_c \mathbf{A}_c + \mathbf{A}_d^T \mathbf{P}_d \mathbf{A}_d + \mathbf{A}_e^T \mathbf{P}_e \mathbf{A}_e)^{-1} (\mathbf{A}^T \mathbf{P} \mathbf{l} + \mathbf{P}_b \mathbf{l}_b + \mathbf{A}_c^T \mathbf{P}_c \mathbf{l}_c + \mathbf{A}_d^T \mathbf{P}_d \mathbf{l}_d + \mathbf{A}_e^T \mathbf{P}_e \mathbf{l}_e) \quad (14)$$

and the variance factor as

$$\hat{\sigma}_0^2 = \frac{\mathbf{v}^T \mathbf{P} \mathbf{v} + \mathbf{v}_b^T \mathbf{P}_b \mathbf{v}_b + \mathbf{v}_c^T \mathbf{P}_c \mathbf{v}_c + \mathbf{v}_d^T \mathbf{P}_d \mathbf{v}_d + \mathbf{v}_e^T \mathbf{P}_e \mathbf{v}_e}{r} \quad (15)$$

where r is the system redundancy, \mathbf{v} , \mathbf{v}_b , \mathbf{v}_c , \mathbf{v}_d and \mathbf{v}_e are residual vectors for actual surface observations, parameter observations, quasisurface observations, reference point observations (for georeferencing) and control point coordinate observations, respectively.

The solution is iterative. At the end of each iteration all surfaces are transformed to their new states using the updated sets of transformation parameters, and the design matrices and discrepancy vectors are re-evaluated. The iteration stops if each element of the alteration vector in Equation (14) falls below a certain limit.

The estimation model is the Generalized Gauss-Markoff, which can accommodate any kind of functional constraint flexibly, e.g. concentric scans, certain rotational differences, parallel or perpendicular objects in the pointcloud data, etc.

2.3 Execution Aspects

2.3.1 Matrix Structures

Figure 1 shows the matrix structures of a hypothetical example of a data set with four pointclouds and three control points. For the sake of simplicity, the example does not cover the intensity matching case.

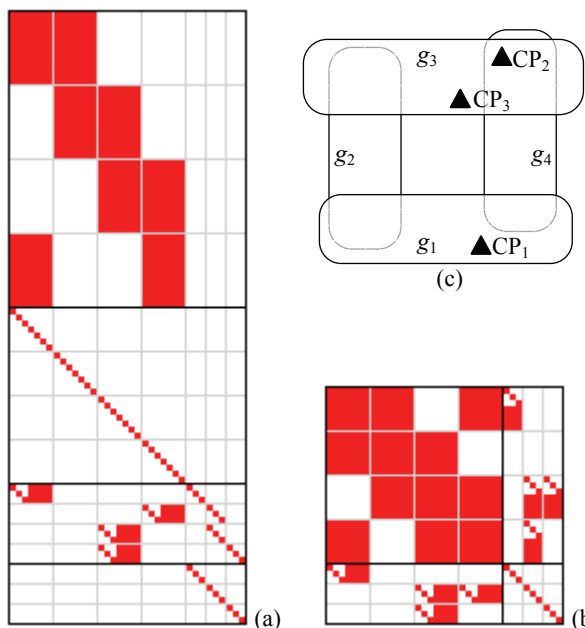


Figure 1. (a) The design matrix and (b) the corresponding normal equations matrix of a data configuration case (c) with four pointclouds and three control points.

The design matrix (Figure 1a) consists of 4 sub-systems. The first sub-system includes the observations of surface geometry. Each overlapping pointcloud, i.e. g_1 - g_2 , g_2 - g_3 , g_3 - g_4 and g_4 - g_1 , gives a group of observation equations. The second sub-system represents the fictitious observations of the unknown transformation parameters. The third sub-system contains the reference point observations for the georeferencing. The last sub-system consists of the x - y - z coordinate value observations of the control points. The columns stand for 4 sets of transformation parameters (28 elements) and the coordinates of 3 full control points (9 elements).

The normal equations matrix comprises 4 sets of unknown transformation parameters and 3 sets of control point coordinates. The non-zero 7×7 sub-parts show the spatial overlaps among the pointclouds.

2.3.2 Memory Efficiency

In a typical real-world example, the data set may contain 10-20, sometimes more than 100 pointclouds. It is not operable to load all pointclouds into the physical memory. This most probably exceeds the memory limit of the computer. Our software implementation loads at maximum two pointclouds into the memory at any instant of (processing) time. All the information, e.g. 3D coordinates, correspondences, elements of the 3D boxing for the space partitioning, etc. are kept in the files whose contents are loaded into memory only when needed.

3. EXPERIMENTAL RESULTS

Because of the 125 anniversary of the construction of the Gotthard Tunnel (Switzerland), Credit Suisse has decided to have an exhibition in Zurich about the life and person of Alfred Escher (1819-1882), Swiss politician, promoter of the Gotthard Tunnel, railroad entrepreneur, and founder of Credit Suisse as well as of ETH Zurich.

In Zurich, there is a monument of Alfred Escher, which is located in front of the main railway station and is approximately 5 meter in high (9.5 meter considering also the basement). The goal of the project is the production of ten physical replicas of the Escher monument, starting from a 3D computer model.

The digitization was done with a Faro LS880 HE80 laser scanner, placed on a cherry picker (Figure 2). Totally 36 scans were acquired during two nights of on-site work. The data set contains approximately 4.4 million points with an average point spacing of 5-10 millimetres.



Figure 2. Pointcloud acquisition by laser scanning of the Alfred Escher statue on a cherry picker.

The proposed algorithm was used for the co-registration of the point clouds. Only the surface geometry and parameter observations were used. The example does not include the georeferencing and intensity matching extensions.

At the first step, 3-5 tie points per pointcloud were interactively measured. Initial approximations were calculated by use of the tie point coordinates in a chained 3D similarity transformation. The first pointcloud was defined as the datum by fixing its parameters to a unit transformation with zero translation and rotation elements.

The transformation parameters of the all pointclouds were simultaneously calculated with $\sigma_{\text{naught}} = 2.7$ mm for the accuracy of the surface observations. Any surface correspondence whose Euclidean distance exceeds 6 times the current σ_{naught} value was excluded from the design matrix. The final iteration of the adjustment used 20,442,040 surface correspondences. A high noise level in the data slowed down the convergence to 16 iterations.

The computation lasted more than 18 hours processing time on a laptop computer with Intel dual-core 2.16 GHz CPU and 2 GB physical memory. The main reason is the file-access oriented design of our software implementation. The file access

for reading and writing is within a few milliseconds, while the memory access is within some nanoseconds. On the other hand, the memory request of the software has never exceeded 300 MB during the entire calculation.



Figure 3. The final 3D model of the Alfred Escher statue.



Figure 4. Still incomplete physical replica of the Alfred Escher monument (the missing parts are attached later).

After the co-registration step, all pointclouds were merged, filtered for noise reduction, sub-sampled and triangulated for surface generation. The 3D modelling operations were carried out using Geomagic Studio 9. Note that no editing has been made on the final model, except for the cropping of the area of interest (Figure 3). An edited version of the 3D model was used for the replica production. Ten replicas were produced at a scale 1:2 (Figure 4).

4. CONCLUSIONS

A method for the simultaneous co-registration of multiple 3D pointclouds is presented. It is capable of georeferencing as well as matching of the intensity information when some parts of the object surface lack sufficient geometry information. The estimation model is the Generalized Gauss-Markoff which allows any kind of object space conditions to be formulated as functional constraints, e.g. co-centric scans, perpendicular or parallel objects in the pointclouds, etc.

A practical experiment shows the capability of the method. A successful solution has been achieved. However, the computation time is the main burden. A more efficient software implementation and a multi-resolution approach during the iterations can accelerate the procedure substantially. The future work will also include experimentations with the georeferencing and intensity matching approaches.

5. REFERENCES

- Ackermann, F., Ebner, H., and Klein, H., 1973. Block triangulation with independent models. *Photogrammetric Engineering and Remote Sensing*, 39 (9), 967-981.
- Akca, D., Gruen, A., 2005a. A flexible mathematical model for matching of 3D surfaces and attributes. *Videometrics VIII, Proc. of SPIE-IS&T Electronic Imaging, San Jose (California), USA, January 18-20. Proc. of SPIE, vol. 5665, pp.184-195.*
- Akca, D., Gruen, A., 2005b. Fast correspondence search for 3D surface matching. *ISPRS Workshop Laser scanning 2005, Enschede, the Netherlands, September 12-14. International Archives of the Photogrammetry, Remote Sensing and Spatial Information Sciences, vol. XXXVI, part 3/W19, pp. 186-191.*
- Akca, D., Gruen, A., 2005c. Recent advances in least squares 3D surface matching. In: Gruen, A., Kahmen, H. (Eds.), *Optical 3-D Measurement Techniques VII, Vienna, Austria, October 3-5, vol. II, pp. 197-206.*
- Al-Manasir, K., and Fraser, C.S., 2006. Registration of terrestrial laser scanner data using imagery. *The Photogrammetric Record*, 21 (115), 255-268.
- Arun, K.S., Huang, T.S., Blostein, S.D., 1987. Least-squares fitting of two 3D point sets. *IEEE Transactions on Pattern Analysis and Machine Intelligence*, 9 (5), 698-700.
- Beinat, A., and Crosilla, F., 2001. Generalized Procrustes analysis for size and shape 3D object reconstructions. *Optical 3-D Measurement Techniques V, Vienna, October 1-4, pp. 345-353.*
- Benjemaa, R., and Schmitt, F., 1997. Fast global registration of 3D sampled surfaces using a multi-z-buffer technique. *IEEE International Conference on 3D Imaging and Modeling, Ottawa, May 12-15, pp. 113-120.*

- Bergevin, R., Soucy, M., Gagnon, H., and Laurendeau, D., 1996. Towards a general multi-view registration technique. *IEEE Transactions on Pattern Analysis and Machine Intelligence*, 18 (5), 540-547.
- Blais, G., and Levine, M.D., 1995. Registering multiview range data to create 3D computer objects. *IEEE Transactions on Pattern Analysis and Machine Intelligence*, 17 (8), 820-824.
- Campbell, R.J., and Flynn, P.J., 2001. A survey of free-form object representation and recognition techniques. *Computer Vision and Image Understanding*, 81(2), 166-210.
- Chen, Y., and Medioni, G., 1992. Object modelling by registration of multiple range images. *Image and Vision Computing*, 10 (3), 145-155.
- Cunnington, S.J., and Stoddart, A.J., 1999. N-view point set registration: a comparison. *British Machine Vision Conference*, Nottingham, September 13-16, pp. 234-244.
- Eggert, D.W., Fitzgibbon, A.W., and Fisher, R.B., 1998. Simultaneous registration of multiple range views for use in reverse engineering of CAD models. *Computer Vision and Image Understanding*, 69 (3), 253-272.
- Greaves, T., 2005. Laser scanning shaves weeks from failure analysis of parking garage collapse. *Spar ViewTM*, 3(14), <http://www.sparllc.com/archiveviewer.php?vol=03&num=14&file=vol03no14-01> (accessed August 2005).
- Gruen, A., 1985. Adaptive least squares correlation: a powerful image matching technique. *South African Journal of Photogrammetry, Remote Sensing and Cartography*, 14 (3), 175-187.
- Gruen, A., and Baltsavias, E., 1987. High-precision image matching for Digital Terrain Model generation. *Photogrammetria*, 42 (3), 97-112.
- Gruen, A., Akca, D., 2005. Least squares 3D surface and curve matching. *ISPRS Journal of Photogrammetry and Remote Sensing*, 59 (3), 151-174.
- Jokinen, O., and Haggren, H., 1998. Statistical analysis of two 3-D registration and modeling strategies. *ISPRS Journal of Photogrammetry and Remote Sensing*, 53 (6), 320-341.
- Jokinen, O., 1998. Area-based matching for simultaneous registration of multiple 3-D profile maps. *Computer Vision and Image Understanding*, 71 (3), 431-447.
- Krishnan, S., Lee, P.Y., Moore J.B., and Venkatasubramanian, S., 2005. Global registration of multiple 3D point sets via optimization-on-a-manifold. *Eurographics Symposium on Geometry Processing*, Vienna, July 4-6, pp. 187-197.
- Lu, F., and Milios, E., 1997. Globally consistent range scan alignment for environment mapping. *Autonomous Robots*, 4 (4), 333-349.
- Masuda, T., and Yokoya, N., 1995. A robust method for registration and segmentation of multiple range images. *Computer Vision and Image Understanding*, 61 (3), 295-307.
- Neugebauer, P.J., 1997. Reconstruction of real-world objects via simultaneous registration and robust combination of multiple range images. *International Journal of Shape Modeling*, 3 (1-2), 71-90.
- Pulli, K., 1999. Multiview registration for large data sets. *IEEE International Conference on 3D Imaging and Modeling*, Ottawa, October 4-8, pp. 160-168.
- Schoenemann, P.H., and Carroll, R.M., 1970. Fitting one matrix to another under choice of a central dilation and a rigid motion. *Psychometrika*, 35 (2), 245-255.
- Sharp, G.C., Lee, S.W., and Wehe, D.K., 2004. Multiview registration of 3D scenes by minimizing error between coordinate frames. *IEEE Transactions on Pattern Analysis and Machine Intelligence*, 26 (8), 1037-1050.
- Stoddart, A.J., and Hilton, A., 1996. Registration of multiple point sets. *IEEE International Conference on Pattern Recognition*, Vienna, pp. B40- 44.
- Sternberg, H., Kersten, Th., Jahn, I., and Kinzel, R., 2004. Terrestrial 3D laser scanning - data acquisition and object modeling for industrial as-built documentation and architectural applications. *International Archives of the Photogrammetry, Remote Sensing and Spatial Information Sciences*, 35(B7), 942-947, <http://www.isprs.org/istanbul2004/comm5/papers/183.pdf> (accessed August 2006).
- Turk, G., and Levoy, M., 1994. Zippered polygon meshes from range images. In: A. Glassner (ed.), *Proceedings of SIGGRAPH'94*, Florida, July 24-29, pp. 311-318.
- Williams, J.A., Bennamoun, M., Latham, S., 1999. Multiple view 3D registration: A review and a new technique. *IEEE International Conference on Systems, Man, and Cybernetics*, Tokyo, October 12-15, pp. 497-502.
- Williams, J., and Bennamoun, M., 2001. Simultaneous registration of multiple corresponding point sets. *Computer Vision and Image Understanding*, 81 (1), 117-142.

STATISTICAL PROPERTIES OF MEAN STAND BIOMASS ESTIMATORS IN A LIDAR-BASED DOUBLE SAMPLING FOREST SURVEY DESIGN

H.-E. Andersen^{a,*} and J. Breidenbach^b

^a USDA Forest Service, Pacific Northwest Research Station, Anchorage, Alaska, USA - handersen@fs.fed.us

^b Forstliche Versuchs- und Forschungsanstalt Baden-Württemberg Abteilung Biometrie und Informatik
Wonnhaldestr. 4, 79100 Freiburg, Germany - johannes.breidenbach@forst.bwl.de

KEY WORDS: Forestry, statistics, LIDAR, sampling, inventory, biomass

ABSTRACT:

Airborne laser scanning (lidar) can be a valuable tool in double-sampling forest survey designs. Lidar-derived forest structure metrics are often highly correlated with important forest inventory variables, such as mean stand biomass, and lidar-based *synthetic regression estimators* have the potential to be highly efficient compared to single-stage estimators, which could lead to increased precision for inventory estimates. However, when a limited sample is available to develop the regression model, an estimate based solely on the synthetic regression estimator can yield biased results for stands within a forest area where the regression model was unrepresentative. A number of *modified (approximately) design-unbiased regression estimators* have been proposed that serve to reduce this model-induced bias while also maintaining the efficient, variance-reducing properties of the synthetic regression estimator. In this study, we use a simulation approach to explore the statistical properties of several lidar-based regression estimators of mean stand biomass, using lidar and field plot data collected at a study site in a conifer forest in western Washington State, USA.

1. INTRODUCTION

1.1 Double-sampling in forest inventory

The use of covariate information obtained from remote sensing in a double-sampling design (e.g. with regression estimators) has been a well-established technique in forest survey for decades. A double-sampling design using a combination of remote sensing and field data is particularly cost-effective in the inventory of large, remote forest areas, where the cost of establishing field plots can be considerable, and the number of plots established is necessarily limited. In these cases, the use of remotely-sensed covariate information collected over a larger number of plots can greatly increase the precision and reliability of the inventory estimates for a given area. The use of aerial photos in forest mensuration, and particularly the use of aerial stand volume tables, has been used for many years to decrease forest inventory costs (Paine and Kiser, 2003). Although accurate forest measurements can be acquired from aerial photos through manual interpretation, automated extraction of three-dimensional information from stereo imagery is complex and error-prone, due to the inherently two-dimensional format of photographs, as well as shadows, layover, and the characteristically irregular shapes and surfaces of tree crowns. In addition, tree heights are difficult to measure accurately using aerial photographs, unless accurate terrain models are already available for the area. Because of these issues, the use of aerial photos for acquisition of detailed forest measurements in a double-sampling design has been limited in large-scale forest inventory programs in the United States.

1.2 Lidar for forest inventory applications

Airborne laser scanning (lidar) provides data on the full three-dimensional structure of the forest canopy, at a high resolution, and is readily amenable to automated processing and analysis. Due to the high demand for lidar-derived terrain information in forested areas, high-resolution, discrete-return lidar data is becoming increasingly available to forest managers all over the

world. Therefore, lidar has the potential to be a much more cost-effective sampling tool for operational forest inventory than aerial photography. In fact, the very strong correlations between lidar metrics and plot-level variables suggest that parameters such as stand biomass could be estimated with a high level of precision over a large area using a relatively small number of representative field plots.

The potential of lidar for forest measurement has already been well-established in numerous previous studies. In studies carried out across a wide variety of different forest types in North America, Japan, Europe, and Australia, lidar-derived canopy structure metrics have been shown to be highly correlated with forest inventory variables. Næsset (1997) reported that forest stand volume could be accurately estimated in 36 spruce (*Picea abies*) stands in Norway using a pool of various canopy height and canopy cover density metrics. Means *et al.* (2000) reported that a variety of stand inventory parameters in a Pacific Northwest forest could be accurately estimated using lidar-derived metrics.

1.3 Use of lidar in a double-sampling forest inventory

Although the utility of lidar as a predictive tool has been demonstrated in previous studies, the issues that arise in using lidar as sampling tool in an operational inventory sampling design have received less attention. Parker and Evans (2004) presented an approach to using lidar in a double-sampling forest inventory design in southern Idaho. In this study, lidar was collected along a strip of plots, where every 5th plot was measured on the ground. Lidar-derived individual tree-based estimates of height and stem density were used to estimate DBH, basal area, and volume for all plots. Næsset (2002) developed a two-stage lidar-based forest sampling procedure in a conifer forest in Norway. This approach used a pool of lidar-based structural metrics at the plot level, and then used stepwise regression techniques to select the best predictive model for the inventory variables. This study found that lidar-based stand-level estimates for all inventory parameters were more precise

that those obtained from conventional techniques. Although these authors found that stand-level estimates were unbiased in most cases (after correcting for the log-transformations), it is likely that regression models developed using fewer plots (e.g. 25-30 plots instead of 35 – 60 plots) will result in biased estimates for small stands within the coverage area. The models that are developed from lidar tend to draw from a large pool of structural metrics, and are often developed using an automated variable selection technique (such as stepwise regression), and therefore may not be representative of the full range of forest conditions within the entire lidar coverage area, potentially leading to bias in parameter estimates for the smaller stands in a given area.

In most forest surveys, the number of plots available for model development is constrained by accessibility and cost. Although efforts are sometimes made to obtain a representative sample, often the sample can be considered a random sample from the population. Although this is certainly a simplification of reality – managers often have previous knowledge of stand conditions and can use this to increase the sample size in more variable stands – for the purposes of this study we will assume that very little *a priori* information is available, beyond stand boundary information. If this sample is used in a double-sampling design with regression, the simple *synthetic* regression estimators for small domains, or stands, typically have low variance, but can have considerable bias due the use of an unrepresentative regression model. Approaches have been developed to reduce the bias in estimates for small domains within a double-sampling design (Särndal and Hidiroglou, 1989). In particular, these authors introduced a *modified* regression estimator that is (approximately) design-unbiased but with increased variance.

In this paper, we will present an investigation of the statistical properties of several lidar-based regression estimators for mean stand biomass, using simulation to estimate the sampling distribution (variance and mean) of these statistics. In particular, we will discuss the use of a synthetic regression estimator, a modified synthetic regression estimator, a

dampened regression estimator, and the possible effect of transformation bias on mean stand biomass estimates.

2. STUDY AREA

2.1 Capitol Forest study area

The study area for this project was a conifer forest within Capitol State Forest, in western Washington state, USA. This forest is composed primarily of Douglas-fir (*Pseudotsuga menziesii*), western hemlock (*Tsuga heterophylla*), and western redcedar (*Thuja plicata*). This area is the site for an ongoing silvicultural trial resulting in a wide variety of residual stand densities and structures, including patch cuts, group selection, heavy thinning, light thinning, clearcut, and control (see Figure 1). The stands used in this study varied in age from 35 to 70 years.

2.2 Field plot data

The USDA Forest Service and University of Washington have established 98 growth plots in each of these stands, as well some surrounding younger stands (Figure 1), with plot sizes ranging from 0.02 ha to 0.2 ha.

Species and diameter were recorded for each tree with diameter greater than 14.2 cm. Total height was measured using a handheld laser rangefinder on a representative subset of these trees, and regression-based height-diameter models were used to estimate height for all unmeasured trees within the plots. In addition, very accurate locations for the plots were acquired through a closed-traverse survey. More detailed information on the plot measurements can be found in Curtis *et al* (2004). Using the measured tree list data, biomass estimates (kg/ha) for each plot were generated using the BIOPAK software package (Means *et al.*, 1994).

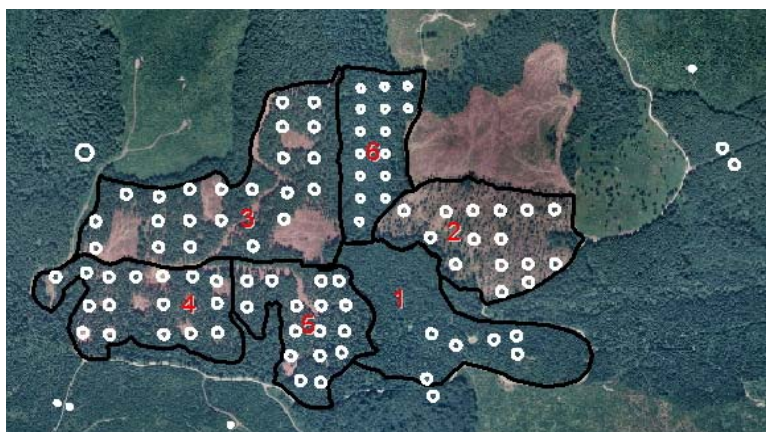


Figure 1. Capitol Forest study area, Washington State, USA. Stand numbers are shown in red, field plots are shown in white.

3. LIDAR DATA

Lidar data were collected over the study area in March, 1999 with a SAAB TopEye system mounted on a helicopter platform.

The details of the lidar acquisition are provided in Andersen *et al.* (2005). The nominal pulse density was 4 returns/m², and the

footprint diameter was approximately 0.4 m. The contractor provided raw lidar point data along with ground returns filtered using a proprietary algorithm.

4. METHODS

4.1 Background

Previous analyses of lidar-based double sampling techniques have used cross-validation (Næsset, 2002) and comparison to the field plot data used in the second stage of the survey (Parker and Evans, 2004) to validate their survey methods. Using a leave-one-out cross-validation procedure, Næsset (2002) assessed the predictive value of the models developed for three different stand types (young, mature(poor site), mature(good site)). This was essentially a test of the predictive quality of the regression models, as opposed to an assessment of the sampling distribution of the regression estimator, since all of the plots (except one) were used to develop the regression models. Parker and Evans (2004) implemented a traditional double-sampling design, where only a limited number of the lidar plots were measured on the ground. The relatively limited number of ground-measured field plots allowed for an assessment of bias, but limited their ability to assess the variance of the regression estimator.

In this study, we used a simulation approach to analyse the sampling distributions of several lidar-based regression estimators of mean stand biomass in the Capitol Forest study area. For the purposes of this study, we assumed that the complete set of 98 plots represented the population, and in each iteration of the simulation, 30 plots were randomly sampled from this population. Using the *R* statistical package, at each iteration a stepwise regression procedure was used to find the (presumed) best fit model relating a suite of lidar-derived, plot-level metrics (mean height (ht), maximum ht, coefficient of variation of heights, 10th percentile ht, 25th percentile ht, 50th percentile ht, 75th percentile ht, 90th percentile ht, and 2-dimensional canopy cover) to the square root of the biomass at the plot (*R*-Development-Core-Team, 2006). Previous analyses had indicated that the square-root transformation was appropriate in the estimation of biomass (Andersen *et al.*, 2006). The predictive model that was selected using the sample of 30 plots was then used to estimate the biomass for all 98 plots in the area. Various estimators of stand biomass (sample mean, synthetic regression estimator (*SY*), modified regression estimator (*MRE*), and dampened regression estimator (*DRE*)) were then generated from these predicted plot-level biomass values. This procedure was repeated for 50000 iterations to develop the sampling distribution of the various estimators. Although all of the plots were available in the model development stage of this study, only stands with multiple plots were used in the stand-wise analysis, giving a total of six stands (Stand 1: 35-yr Douglas-fir, Stand 2: 70-yr Douglas-fir (heavily thinned), Stand 3: 70-yr Douglas-fir (group selection), Stand 4: 70-yr Douglas-fir (patch-cut), Stand 5: 70-yr Douglas-fir (lightly thinned), and Stand 6: 70-yr Douglas-fir (uncut)). The variables selected in each iteration were also observed to assess the stability of the models. Canopy cover was selected as a significant predictor variable in every iteration, while the other selected variables tended to vary among the different height-based metrics (52% of models included 25th percentile ht, 48% of models included mean ht, 40% of models included 50th percentile ht, etc.). Interestingly, the least-used variable was maximum height, possibly due to the generally homogeneous nature of the stands used in this study, where height was much less variable than density, understory density, etc.

4.2 Estimators of mean stand biomass

4.2.1 Single-stage estimator

The single stage estimator of mean stand biomass is the arithmetic mean of plot-level biomass measurements from a given stand, or the sample mean. This estimator is unbiased, but can have a high variance, depending upon the number of plots sampled and the variability of a given stand. Following Särndal and Hidiroglou (1989), U denotes the population of plots $U = \{1, \dots, k, \dots, N\}$ that is divided into D domains (or stands), $U_1, \dots, U_d, \dots, U_D$. If the biomass for a given plot is denoted as y_k , U_d are the plots in U that fall in stand d , and N_d is the size of U_d , then we want to estimate the mean stand biomass

$$t_d = \sum_{k \in U_d} y_k / N_d \quad (1)$$

If s denotes a sample of size n that is drawn randomly from U with inclusion probabilities π_k , then s_d denotes the part of U that falls in stand d . The estimated mean biomass for stand d is then given by: $\hat{t}_d = \sum_{s_d} y_k / n_d$. The sampling distributions for the

single-stage estimate of mean stand biomass for each stand is show in Figure 2.

4.2.2 Lidar-based two-stage regression estimators

The use of auxiliary covariate information obtained over a larger number of plots, or in this case, every element within the population, has the potential to greatly increase the efficiency of an estimator. For example, a vector of lidar-based metrics generated at the plot level can be used to increase the precision of estimates of mean stand biomass. In the case of double-sampling with regression, and again following Särndal and Hidiroglou (1989), a linear regression model is used to relate the variables of interest, y , to x , a vector of correlated variables. If the coefficients of the population linear model of y on x can be denoted as B , then the estimated coefficients are \hat{B} . The predicted values are $\hat{y}_k = x'_k \hat{B}$, and the $e_k = y_k - \hat{y}_k$ are the residuals. The so-called *synthetic regression estimator (SY)* of the mean stand biomass is then given by: $\hat{t}_{dSY} = \sum_{U_d} \hat{y}_k / N_d$. In

cases where the regression model is not representative of the entire population, the synthetic regression estimator can yield estimates for small areas that are significantly biased. In order to reduce this bias, Särndal (1981, 1984) developed the (approximately) design-unbiased estimator:

$$\hat{t}_{dRE} = \frac{\left(\sum_{U_d} \hat{y}_k + \sum_{s_d} e_k / \pi_k \right)}{N_d} \quad (2)$$

This estimator consists of the synthetic regression estimator (the left term in the numerator) and an adjustment term (right term in the numerator) that will correct for bias due to use of an unrepresentative model. However, the variance of the design-unbiased estimator is typically higher than the synthetic estimator, because the adjustment term is, in effect, inflated by the expansion factor π_k . Hidiroglou and Särndal (1985) went on to develop a modified design-unbiased estimator:

$$\hat{t}_{dRE} = \frac{\left(\sum_{U_d} \hat{y}_k + N_d \frac{\sum_{s_d} e_k / \pi_k}{\hat{N}_d} \right)}{N_d} \quad (3)$$

where $\hat{N}_d = \sum_{s_d} 1/\pi_k$. As Särndal and Hidiroglou (1989) point out,

this estimator tends to have smaller variance than the unmodified version because the ratio term will give heavier weight to the adjustment term in cases where the model fit in a particular domain is poor. Unlike the unmodified version, the modified estimator has the additional property that, in the case of simple random sampling, it is consistent as the size of the sample approaches the size of the population, or $\hat{t}_d = t_d$ when $s_d = U_d$. However, these authors also note that in cases where the sample size for a domain is particularly small (e.g. $n_d < 5$), and the model fit is therefore particularly poor in this domain, the modified regression estimator can yield unacceptable results due to the heavy weight given to the adjustment term (for example, negative estimates in cases where the residuals are overwhelmingly negative). Särndal and Hidiroglou (1989) therefore suggest using a *dampened* version of the modified regression estimator:

$$\hat{t}_{dRE} = \frac{\left(\sum_{U_d} \hat{y}_k + \left(\hat{N}_d / N_d \right)^{H-1} \sum_{s_d} e_k / \pi_k \right)}{N_d} \quad (4)$$

where:

$$H = 0 \quad \text{if} \quad \hat{N}_d \geq N_d$$

$$= h \quad \text{if} \quad \hat{N}_d < N_d$$

Previous studies have found that using $h = 2$ provided a reasonable level of dampening. This has the effect of inverting the ratio term when a sample is disproportionately undersampled, giving less weight to the correction term.

4.3 Transformation bias

Typically in a double-sampling framework it is desirable to obtain estimates in the units of the original data. However, simply applying the reverse-transformation of the square-root, or logarithmic, transformation, can result in biased estimates (Næsset, 2002). In the case of the square-root transformation, it has been shown that adding the residual variance (σ^2) to the predicted values can correct for much of this bias (Miller, 1984).

5. RESULTS AND DISCUSSION

The summary statistics (mean, variance) of the simulated sampling distributions for each estimator, and for each stand, are shown in Table 1. It should be noted that the mean coefficient of determination (R^2) values for the 50000 regression models for *sqrt*(biomass) was 0.88, and the standard

deviation of the R^2 values was 0.04. The simulated sampling distributions for the various estimators, and the true mean stand biomass values, are shown in Figures 2-5. The possible influence of transformation bias in converting back to original data units (tons/ha for biomass) is shown in Table 2.

In general, the variance of the single stage estimator is quite high, especially in highly heterogeneous stands (e.g. 3, 4, and 6) (Figure 2). In contrast, in homogeneous stands (e.g. 1 and 2) the sampling error is quite low and even small samples can precisely characterize the population parameter. However, it should be noted that the single-stage mean stand biomass estimates shown here are based only on cases where at least one plot was available in the sample from a given stand, and therefore underestimates the variance of the single-stage estimator, especially in stands with few plots, such as Stand 1 (which was likely unsampled in many of the iterations). As expected, in general the application of the synthetic regression estimator dramatically reduces the variance of the estimator, especially in the more heterogeneous stands (Figure 3). For example, in stand 4, the variance decreased from 3494.8 to 192.7, and in stand 6, the variance decreased from 4569.6 to 892.2. However, as expected, the synthetic estimator's complete reliance on the sometimes ill-fitting regression model led to significant bias for most of the stands (Table 1). This is particularly striking in the case of stand 3, where use of the synthetic estimator led to an 82% reduction in the variance but also introduced a significant 5% bias. Application of the modified design unbiased regression estimator served to dramatically reduce this bias in almost all stands (Figure 4). However, the price of this reduction in bias was a consistent increase in the variance. In general, the variance was still well below that of the single stage estimator. For example, in stand 3, the bias was reduced to 0.5 %, while the variance was reduced to 65% of the variance of the single stage estimator. The form of the dampened estimator appears to moderate both the bias-inducing influence of the synthetic regression term and the variance-inflating effect of the adjustment term (Figure 5). The application of these modified regression estimators may be particularly useful in situations where unbiased estimates are desired for smaller stands within a lidar coverage area.

The results indicate that applying the reverse square-root transformation to recover the original data units does generally lead to a slight negative bias, as we would expect from the explanation in Miller (1984) (Table 2). In all but one stand, application of the bias correction as proposed by Miller (1984) does remove a portion, but not all, of this bias.

	Stand					
	1	2	3	4	5	6
Population mean stand biomass	583.9	311.3	625.7	562.6	620.9	668.2
Single-stage estimator	583.9 (149.8)	311.2 (648.6)	625.7 (894.8)	562.8 (3494.8)	620.7 (418.5)	667.6 (4569.6)
Synthetic regression estimator (SY)	575.0 (965.7)	334.5 (592.3)	594.4 (162.8)	561.9 (192.7)	628.5 (222.2)	692.3 (892.2)
Modified design unbiased regression estimator (MRE)	580.3 (755.5)	315.6 (680.9)	622.3 (315.9)	561.4 (759.5)	622.3 (340.8)	671.4 (2240.1)
Dampened design unbiased regression estimator (DRE)	578.6 (760.2)	321.1 (650.0)	616.4 (298.8)	561.3 (458.3)	623.8 (249.8)	677.1 (1636.9)

Table 1. Statistical properties of (square-root transformed) mean stand biomass estimators (mean (above) and variance (below) of simulated sampling distribution). The stand biomass for the population is shown in the top row.

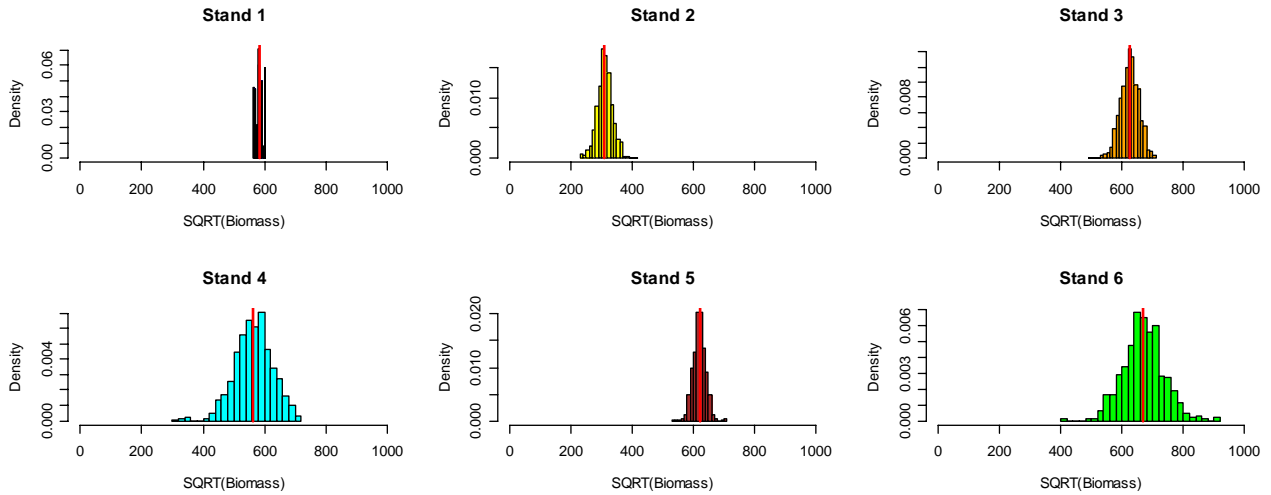


Figure 2. Simulated sampling distributions for the *single-stage estimator* for mean stand biomass. Vertical red line indicates the true mean stand biomass within the population.

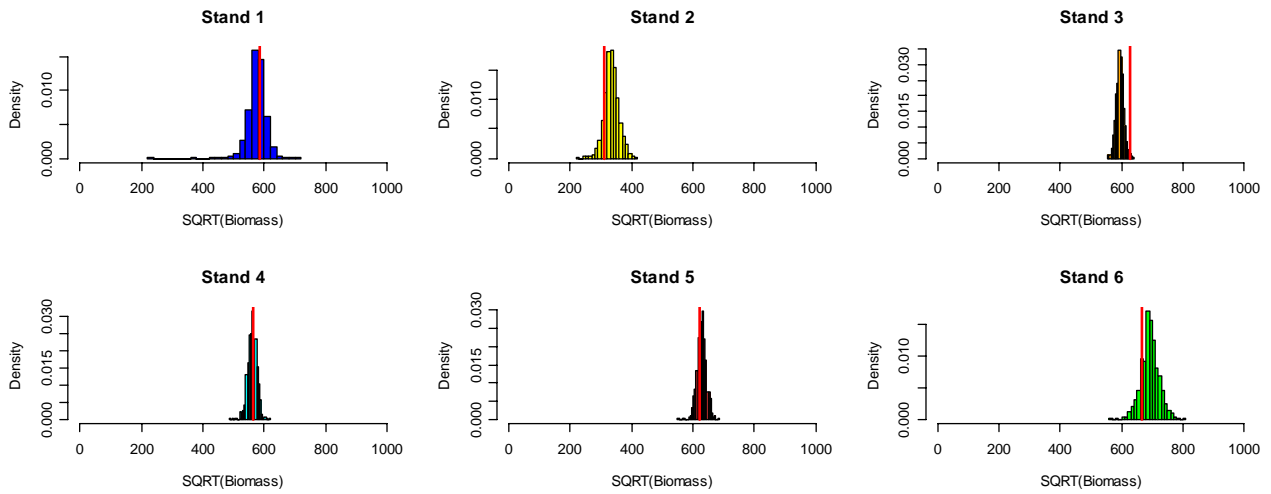


Figure 3. Simulated sampling distributions for the *synthetic regression estimator* for mean stand biomass. Vertical red line indicates the true mean stand biomass within the population.

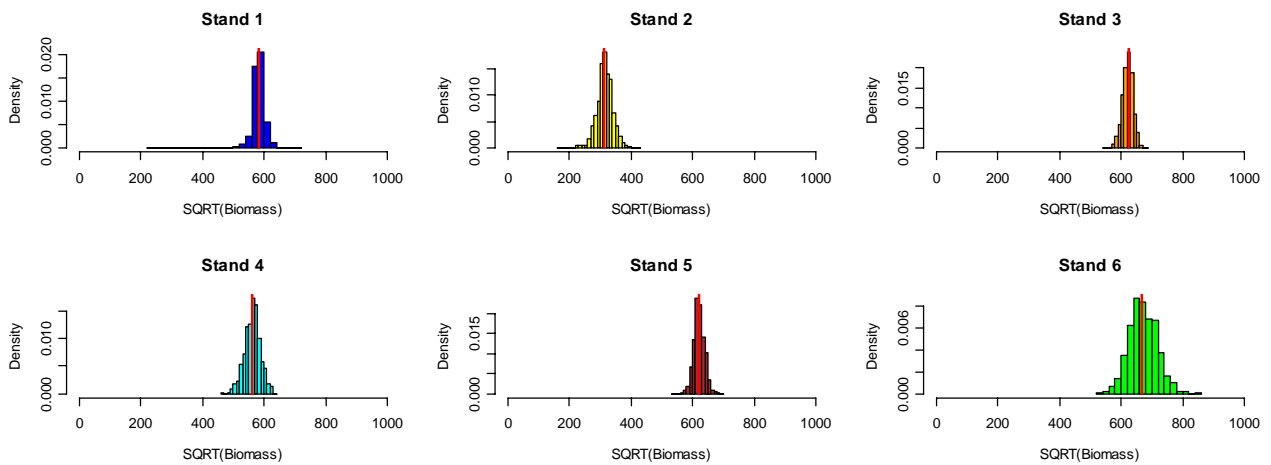


Figure 4. Simulated sampling distributions for the *modified design-unbiased regression estimator* for mean stand biomass. Vertical red line indicates the true mean stand biomass within the population.

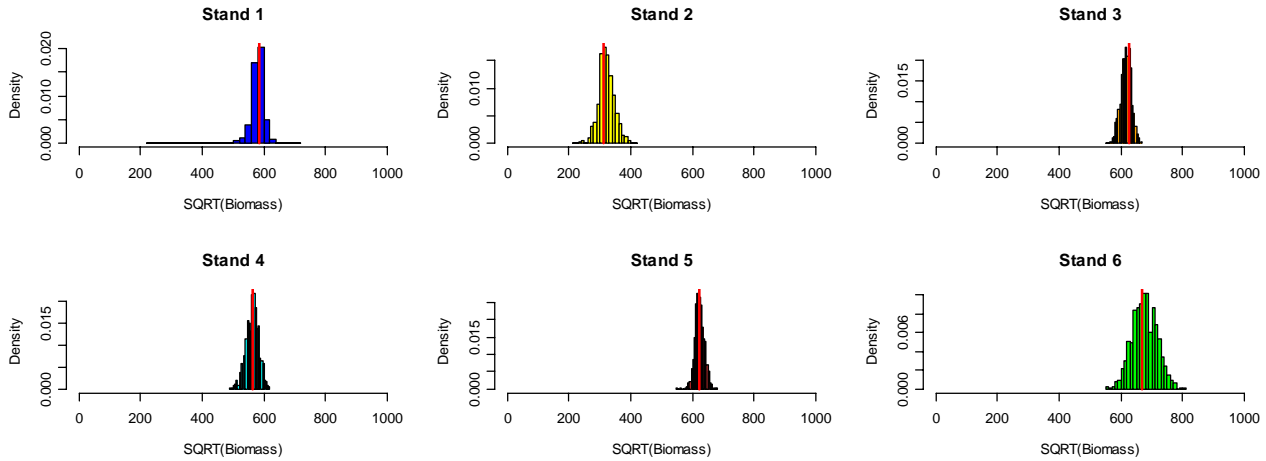


Figure 5. Simulated sampling distributions for the *dampened design-unbiased regression estimator* for mean stand biomass. Vertical red line indicates the true mean stand biomass within the population

	Stand					
	1	2	3	4	5	6
Population mean	341	100	399	335	388	465
Estimate w/o bias correction	336	104	380	316	389	460
Estimate with bias correction	340	107	384	320	392	463

Table 2. Effect of applying reverse square-root transformation to recover original data biomass units (tons/ha).

6. CONCLUSIONS

This investigation confirm the results of previous studies that use of lidar-based regression estimators can significantly increase the precision of estimates for important forest inventory variables, such as mean stand biomass. These results also indicate that use of simple synthetic regression estimators can lead to biased stand-level estimates. The application of a modified regression estimator can reduce the bias at the stand level and will incorporate both the variance-reducing properties of the synthetic regression term and the bias-reducing properties of the correction term.

7. REFERENCES

Andersen, H., R. McGaughey, and S. Reutebuch. 2005. Estimating forest canopy fuel parameters using LIDAR data. *Remote Sensing of Environment* 94, pp. 441-449.

Andersen, H., S. Reutebuch, and R. McGaughey. 2006. Active remote sensing. Chapter 3 in: Shao, G., and K. Reynolds, eds., *Computer Applications in Sustainable Forest Management*. Springer, Dordrecht.

Curtis, R., D. Marshall, D. DeBell, eds. 2004. *Silvicultural options for young-growth Douglas-fir forests: the Capitol Forest study—establishment and first results*. PNW-GTR-598. USDA Forest Service, Pacific Northwest Research Station, Portland, OR.

Hidiroglou, M. and C. Särndal. 1985. An empirical study of some regression estimators for small domains. *Survey Methodology* 11, pp. 65-77.

Means, J. H. Hansen, G. Koerper, P. Alaback, M. Klopsch. 1994. *Software for computing plant biomass--BIOPAK users guide*. PNW-GTR-340. USDA Forest Service, Pacific Northwest Research Station, Portland, OR.

Means, J. S. Acker, J. Fitt, M. Renslow, L. Emerson, and C. Hendrix. 2000. Predicting forest stand characteristics with airborne scanning lidar. *PE&RS* 66, pp. 1367-1371.

Miller, D. 1984. Reducing transformation bias in curve fitting. *The American Statistician* 38(2), pp. 124-126.

Næsset, E. 1997. Estimating timber volume of forest stands using airborne laser scanner data. *Remote Sensing of Environment* 61, pp. 246-253.

Næsset, E. 2002. Predicting forest stand characteristics with airborne scanning lidar using a practical two-stage procedure and field data. *Remote Sensing of Environment* 80, pp. 88-99.

Paine D. and J. Kiser, 2003. *Aerial photography and image interpretation. 2nd edition*. Wiley, Hoboken.

Parker, R. and D. Evans. 2004. An application of LiDAR in a double-sample forest inventory. *Western J. of Applied Forestry* 19(2), pp. 95-101.

R-Development-Core-Team. 2006. *R: A language and environment for statistical computing*. Technical Report, R Foundation for Statistical Computing, Vienna, Austria.

Särndal, C. 1981. Frameworks for inference in survey sampling with applications to small area estimation and adjustment for nonresponse *Bull.of the Int. Stat. Institute* 49, pp. 494-513.

Särndal, C. 1984. Design-consistent versus model-dependent estimators for small domains. *JASA*, 79, pp. 624-631.

Särndal, C., and M. Hidiroglou. 1989. Small domain estimation: A conditional analysis. *JASA*, 84(405), pp. 266-275.

ON-SITE SELF-CALIBRATION USING PLANAR FEATURES FOR TERRESTRIAL LASER SCANNERS

Kwang-Ho Bae and Derek D. Lichti

The Institute for Geoscience Research and Department of Spatial Sciences,
Curtin University of Technology, GPO Box U1987, Perth, WA 6845, Australia,
Cooperative Research Centre for Spatial Information (CRC-SI), Australia
k.h.bae@curtin.edu.au, d.lichti@curtin.edu.au

Commission V, WG 3

KEY WORDS: Calibration, Systematic error, Planar targets, Laser Scanning

ABSTRACT:

Terrestrial laser scanners provide a three-dimensional sampled representation (i.e. point cloud) of the surfaces of objects. They have great potential to improve the measurement and representation of remote and widespread objects for applications such as engineering metrology, cultural heritage recording and forestry, among others. Prior to performing measurement tasks such as these, proper error modelling and estimation is essential in order to remove the inherent systematic effects such as range finder offset, collimation axis error, etc.. A rigorous, point-based self-calibration method has been demonstrated to be effective, but it is very labour-intensive since it requires manual measurement of a large number of signalised targets. In this paper, we propose a planar-feature-based “on-site” self-calibration method that can reduce the manual labour needed in the point-based method. After outlining the principles and mathematical models of the proposed method, the subject of model identification is addressed. Tests with simulated datasets reveal that the residual patterns from the plane-based method are markedly different from those of the point-based method. The ramification of this outcome is that systematic error identification, an important process for new instrumentation such as terrestrial laser scanners, is not straightforward. In addition, the tests of the proposed method with real terrestrial laser scanner datasets are presented and analysed.

1. INTRODUCTION

Terrestrial laser scanners (TLSs) have emerged as new measurement instruments for surveying, photogrammetry and computer vision for their fast data acquisition time to measure a three-dimensional point cloud of objects in a matter of minutes. Consequently, the scientific and practical interest in developing calibration procedures to remove systematic errors inherent in terrestrial laser scanner datasets has expanded.

In photogrammetry, “on-site” or “on-the-job” calibration methods are often used as an alternative to laboratory calibration (Luhmann et al., 2007). This is particularly relevant when the temporal stability of the camera used is in doubt. This procedure is performed by imaging portable frames or targets positioned beside the object(s) of interest. Exterior orientation, object space points and camera calibration parameters are estimated simultaneously. In this paper, we propose an on-site calibration method for terrestrial laser scanners using planar features in the point cloud.

Much work has been done on point-based TLS calibration by exploiting their similarities with theodolites or total stations, (e.g. Lichti and Franke, 2005; Lichti and Licht, 2006; Lichti, 2007; Reshetyuk, 2006). Amiri Parian and Grün (2005) developed a point-based calibration method by based on a panoramic camera model for the Z+F Imager 5003. Gielsdorf et al. (2004), however, proposed error models and a calibration method using planar targets for their own low-cost laser scanner.

Though the point-based methods are rigorous and have been shown to be effective, their principal drawback is the need to

manually measure a large number of targets. The use of planar features is therefore favoured as their extraction from point clouds can be highly automated, though it is recognised that signalised target extraction and measurement could also be automated to a large extent. An on-site calibration method has been pursued due to the apparent instability of the calibration parameters (as reported in Lichti, 2007) of the instrument under investigation, the FARO 880 laser scanner. The idea is that calibration can be performed on-site using planar features that exist on many industrial and heritage recording sites, for example, with minimal manual labour.

After outlining the principles and mathematical models of the proposed method, the subject of model identification is addressed. Tests with simulated datasets are undertaken to explore the difference in the residual patterns from the plane-based and point-based methods. In addition, the precision of the proposed method with terrestrial laser scanner datasets is presented and analysed.

2. PLANE-BASED CALIBRATION

2.1 Observation equation

The spherical co-ordinate observations of the i^{th} object space point in the j^{th} scanner space are range, ρ_{ij} , horizontal direction, θ_{ij} , and elevation (vertical) angle, α_{ij} , which are parameterised in terms of scanner space Cartesian co-ordinates (x_{ij}, y_{ij}, z_{ij}) as follows:

$$\rho_{ij} = \sqrt{x_{ij}^2 + y_{ij}^2 + z_{ij}^2} + \Delta p \quad (1)$$

$$\theta_{ij} = \arctan\left(\frac{y_{ij}}{x_{ij}}\right) + \Delta\theta \quad (2)$$

$$\alpha_{ij} = \arctan\left(\frac{z_{ij}}{\sqrt{x_{ij}^2 + y_{ij}^2}}\right) + \Delta\alpha \quad (3)$$

The spherical observation correction terms are given by Lichti (2007) as follows:

$$\begin{aligned} \Delta\rho = & A_0 + A_2 \sin(\alpha_{ij}) + A_3 \sin\left(\frac{4\pi}{U_1} \rho_{ij}\right) \\ & + A_4 \cos\left(\frac{4\pi}{U_1} \rho_{ij}\right) + A_5 \sin\left(\frac{4\pi}{U_2} \rho_{ij}\right) \\ & + A_6 \cos\left(\frac{4\pi}{U_2} \rho_{ij}\right) + A_7 \sin(4\theta_{ij}) + A_8 \cos(4\theta_{ij}) \end{aligned} \quad (4)$$

$$\begin{aligned} \Delta\theta = & B_1 \sec(\alpha_{ij}) + B_2 \tan(\alpha_{ij}) + B_3 \sin(2\theta_{ij}) \\ & + B_4 \cos(2\theta_{ij}) + B_5 \theta_{ij} + B_6 \cos(3\alpha_{ij}) + B_7 \cos(4\alpha_{ij}) \end{aligned} \quad (5)$$

$$\Delta\alpha = C_0 + C_2 \sin(\alpha_{ij}) + C_3 \sin(3\theta_{ij}) + C_4 \cos(3\theta_{ij}) \quad (6)$$

where the sensor-driven additional parameters (APs) for terrestrial laser scanners for range, horizontal direction and elevation angle components of the observations are expressed as A, B and C, respectively. The term U_1 in Eq. 4 represents half the finest modulating wavelength, which is approximately equal to 0.6m. The term U_2 in Eq. 4 equals one-half the median unit length, which is approximately 4.8m. These terms need to be included since the FARO 880 scanner measures range on the basis of the phase-difference method. The aim of a plane-based calibration procedure is to accurately estimate these proposed additional parameters with low correlation among the exterior orientation and plane parameters and other APs.

The problem underlying terrestrial laser scanner calibration is that of model identification. Some systematic error sources, such as those common to total stations, are expected to be observed in the residuals from a registration-only least-squares adjustment. Investigation of these residual patterns has permitted us to develop a systematic error model for laser scanners.

The models can be categorised to two groups: the physical and empirical additional parameters. The physical interpretation of latter is not necessarily apparent, although their systematic trends may be observed in the residuals of a highly redundant and geometrically strong, minimally constrained least-squares adjustment. Detailed description of all the additional parameters and their residual plots can be found in Lichti and Licht (2006), Lichti and Franke (2005) and Lichti (2007).

2.2 Formulation of the proposed plane-based calibration

The proposed plane-based self-calibration method utilises the combined least-squares method that minimises the distance between points and their corresponding planes with a constraint condition. The exterior orientation, plane and the additional

parameters presented in Eqs. 4-6 can be simultaneously estimated. Since the observations and parameters of the point-on-plane condition equation are not separable and each condition includes more than one observation, the combined (or Gauss-Helmert) adjustment model is used.

Let $\mathbf{x} \in \mathbb{R}^u$ be the parameter vector and $\mathbf{l} \in \mathbb{R}^n$ be the observation vector, where u and n are the number of parameters and observations, respectively. Let $f_{ijk}(\mathbf{x}, \mathbf{l})$ be the distance function between the i^{th} point in the j^{th} scanner space (\mathbf{p}_{ij}) and the k^{th} plane target in the object space whose normal vector and orthogonal distance from the origin are $\mathbf{n}_k = (a_k, b_k, c_k)$ and d_k , respectively. The distance function is given as

$$f_{ijk}(\mathbf{x}, \mathbf{l}) = \mathbf{n}_k^T (\mathbf{M}_j^T \mathbf{p}_{ij} + \mathbf{Tr}_j) - d_k = 0 \quad (7)$$

where \mathbf{M}_j and \mathbf{Tr}_j are the rotation and translation parameters between the object and j^{th} scanner spaces, respectively. In other words, this is the condition function for the registration between multiple point clouds and one fixed scan, i.e. the object space. Then the linearised equation for the Gauss-Helmert model is given by

$$\mathbf{A} d\mathbf{x} + \mathbf{B} \mathbf{v} + \mathbf{w}_0 = 0 \quad (8)$$

where m is the total number of point observations, $\mathbf{A} \in \mathbb{R}^{m \times u}$ and $\mathbf{B} \in \mathbb{R}^{m \times n}$ are the Jacobians of $f_{ijk}(\mathbf{x}, \mathbf{l})$ with respect to \mathbf{x} and \mathbf{l} , respectively, \mathbf{v} is the residual vector, \mathbf{w}_0 is the misclosure vector and $d\mathbf{x}$ is the vector of corrections to the approximate parameter values. In its current form, the adjustment is minimally constrained since the inner constraint equations for plane parameters are still under development.

Note that u equals the sum of u_e , u_{ap} and u_p where u_e is the number of the transformation parameters, u_{ap} is the number of the additional parameters and u_p is the number of plane parameters, respectively. The unit length constraint on the direction cosines for each plane is given as

$$g_k(a_k, b_k, c_k, d_k) = \mathbf{n}_k^T \mathbf{n}_k - 1 = 0 \quad (9)$$

and the linearised constraint equation can be given as

$$\mathbf{A}_c d\mathbf{p} + \mathbf{w}_c = \mathbf{v}_c \quad (10)$$

where $\mathbf{A}_c \in \mathbb{R}^{c \times up}$ is the Jacobian of $g_k(a_k, b_k, c_k, d_k)$ with respect to the k^{th} plane target, $d\mathbf{p}$ is the vector of corrections to the approximate plane parameter values and c is the number of constraints. The cost function to be minimised with respect to

$$\begin{aligned} \varphi = & \mathbf{v}^T \mathbf{P} \mathbf{v} + \mathbf{v}_c^T \mathbf{P}_c \mathbf{v}_c + 2\mathbf{k}^T (\mathbf{A} d\mathbf{x} + \mathbf{B} \mathbf{v} + \mathbf{w}_0) \\ & + 2\mathbf{k}_c^T (\mathbf{A}_c d\mathbf{p} + \mathbf{w}_c - \mathbf{v}_c) \end{aligned} \quad (11)$$

where \mathbf{P} and \mathbf{P}_c are the weight matrices for point observations and the constraint for the plane parameters, respectively, and \mathbf{k} and \mathbf{k}_c are the Lagrange multiplier vectors. Minimisation of the cost function leads to the following system of normal equations

$$\mathbf{N} d\mathbf{x} + \mathbf{w} = 0 \quad (12)$$

where

$$\mathbf{N} = \mathbf{A}^T (\mathbf{B} \mathbf{P}^{-1} \mathbf{B}^T)^{-1} \mathbf{A} + \begin{bmatrix} \mathbf{0} & \mathbf{0} \\ \mathbf{0} & \mathbf{A}_c^T \mathbf{P}_c \mathbf{A}_c \end{bmatrix} \quad (13)$$

and

$$\mathbf{w} = \mathbf{A}^T (\mathbf{B} \mathbf{P}^{-1} \mathbf{B}^T)^{-1} \mathbf{w}_0 + \begin{bmatrix} \mathbf{0} \\ \mathbf{A}_c^T \mathbf{P}_c \mathbf{w}_c \end{bmatrix}. \quad (14)$$

2.3 Nonlinear least-squares

The Newton-Raphson solution method can be successfully utilised for point-based calibration (Amiri Parian and Grün, 2005; Lichti, 2007). In the case of plane-based calibration, the inclusion of the point-on-plane condition equations renders the cost function highly nonlinear and thus a nonlinear least-squares method is required in order for the solution to converge rapidly to a global minimum (Shewchuk, 1994; Golub and Van Loan, 1989; Teunissen, 1990).

The normal equations for the proposed method with the Gauss-Helmert model from Eq. 12 can be expressed as

$$\frac{\partial^2 \varphi}{\partial \mathbf{x}^2} d\mathbf{x} + \frac{\partial \varphi}{\partial \mathbf{x}} = \mathbf{0}. \quad (15)$$

When the cost function is either linear or can be linearised, the solution of Eq. 15 is given by

$$d\mathbf{x} = - \left(\frac{\partial^2 \varphi}{\partial \mathbf{x}^2} \right)^{-1} \frac{\partial \varphi}{\partial \mathbf{x}}, \quad (16)$$

which is a special case of the gradient-descent method (Shewchuk, 1994). In the case of the minimisation of nonlinear cost functions, the gradient of the cost function given in Eq. 10 may not be the optimal direction for searching the solution. Therefore, the conjugate gradient method proposes to search a solution in a direction calculated from $-\frac{\partial \varphi}{\partial \mathbf{x}}$ using Gram-Schmidt orthogonalisation (Shewchuk, 1994). Details of the conjugate gradient method and its implementation can be found in Shewchuk (1994) and Golub and Van Loan (1989).

2.4 Outlier detection

The reliability matrix, standardised residuals and variance component estimation (Baarda, 1968; Schaffrin, 1997; Cothren, 2005) are utilised for outlier detection in the proposed plane-based calibration method. For the linearised Gauss-Helmert model equations given (Eq. 12), the reliability matrix \mathbf{R} is given by

$$\mathbf{R} = \mathbf{P}^{-1} \mathbf{B}^T \bar{\mathbf{P}}^{-1} (\mathbf{I}_n - \mathbf{A} \mathbf{N}^{-1} \mathbf{A} \bar{\mathbf{P}}^{-1}) \mathbf{B} \quad (17)$$

where \mathbf{P} is the weight matrix, $\bar{\mathbf{P}} = \mathbf{B} \mathbf{P}^{-1} \mathbf{B}^T$, and \mathbf{I}_n is the identity matrix with rank of n . The i^{th} standardised residual r_i is calculated from its corresponding a priori observation precision, σ_i , the i^{th} component of the residual vector, v_i , and i^{th} diagonal element of \mathbf{R} , R_{ii} , as

$$r_i = \frac{v_i}{\sigma_i \sqrt{R_{ii}}}. \quad (18)$$

Assuming that a priori variance factor is known is conducted under the standard null hypothesis that the standardised residual follows a zero-mean, unit variance Gaussian density function (Schaffrin, 1997; Cothren 2005).

3. EXPERIMENTS

The subject of the self-calibration experiments described herein is the FARO 880 TLS. Two sets of experiments are described in the following sub-sections. The first used simulated data in order to learn how the various systematic errors manifest themselves in the residuals and to investigate the accuracy of AP estimation. The second use real data in which the results are compared to those from point-based calibration.

3.1 Model identification using residual patterns

Eight simulated point clouds of a room (dimensions 4.0m x 10m x 10m) were generated from two different scanner locations (4 orthogonal scans were captured at each position). The distance between two scanners was 8m and the height of the scanner was set to 2m. Six 1.5m x 1.5m planar targets on were simulated to lie in the centre of each wall, the floor and the ceiling of the room. The sampling was such that each target had 100 points—see Figure 3a. In short, the simulated dataset represents the point clouds captured by an ideal laser scanner in a test room with perfectly flat walls, floor and ceiling.

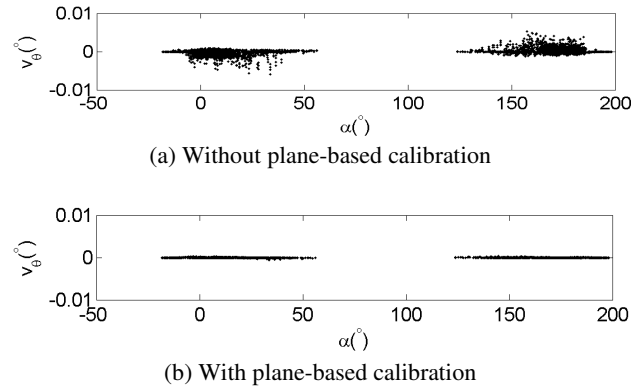


Figure 1. Residuals of the plane-based calibration method in the presence of a collimation axis error ($B_1=50''$) for the simulated dataset.

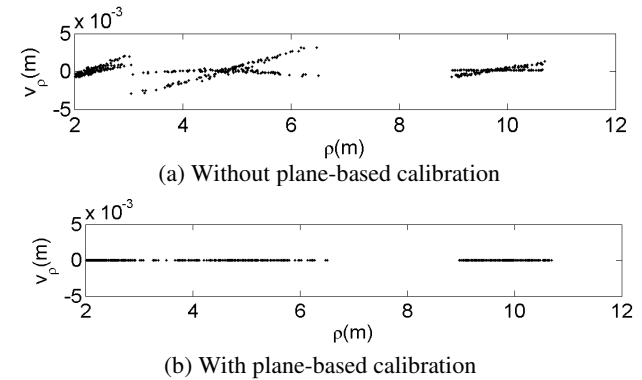


Figure 2. Residuals of the plane-based calibration method in the presence of a rangefinder additive constant ($A_0=1\text{mm}$) for the simulated dataset

The systematic errors of terrestrial laser scanners described in Eqs. 4-6 were first added one-by-one to the error-less, simulated point clouds. In a point-based method, most misclosure patterns appear very similar to functional form of the corresponding systematic error model (Lichti, 2007). For example, the vertical eccentricity error, C_2 in Eq. 6, can be observed as a sine function of the elevation angle in the residual pattern of the point-based method.

Figures 1 and 2 are plots of residual due to collimation axis error (B_1) and rangefinder additive constant (A_0), respectively. These residual patterns are quite different from those observed in the point-based calibration method (Lichti and Franke, 2005) in which the residuals appear as the expected secant function for collimation axis error and the effect of the rangefinder offset is manifest as a linear function of range due to correlation with the positional elements of exterior orientation. These differences make it difficult to identify the systematic errors in the residuals from plane-based self-calibration.

3.2 Optimal locations of laser scanners with simulated data

An empirical investigation into optimal laser scanner location for the plane-based self-calibration was also conducted under the previously-described conditions. This investigation with simulated datasets in Figure 3 was based on the ratio of the estimated additional parameter to the true value, i.e. artificially added systematic error to the simulated data. With one of the two scan locations fixed at location “101” shown in Figure 3b, point clouds for the second position were simulated from each of the 9 locations “102” to “110”. We found that the accuracy of the range and elevation angle additional parameters was as high as 99% for this test. On the other hand, the accuracy of the collimation axis error (B_1) varies in different laser scanner combinations.

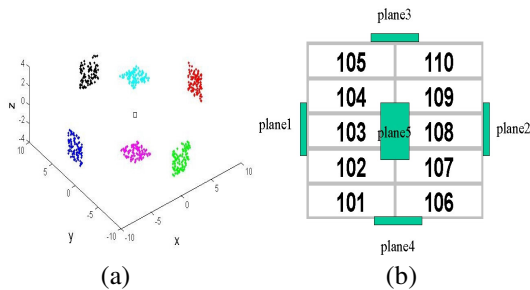


Figure 3. (a) Simulated point clouds for finding the optimal scanner locations. Square sign is the centre of the test room. (b) The scanner is located in the centre of each cell, e.g. 105. The height of the scanner is 2m.

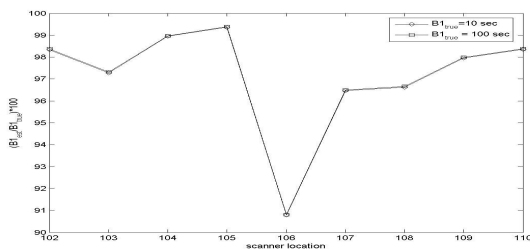


Figure 4. The ratio between the estimated and true B_1 for different laser scanner locations when the first location of the scanner is 101 in Figure 3(b).

For all combinations of scanner locations in Figure 3(b), the accuracy of the estimated APs was high except for the collimation axis error, B_1 . The ratio of its estimated to true value was found to be strongly dependent on the scanner location, as can be seen in Figure 4. This additional parameter is accurately estimated at all locations except for the combination of 101 and 106. For the collimation axis error, the best laser scanner combinations were 105 and 110 with the location 101 in the case of this test room.

3.3 Accuracy tests with simulated datasets

The plane-based self-calibration method was applied to the simulated data described in the previous section. Two systematic errors, A_0 and B_1 , were added to the error-less point clouds. The standard deviations of residuals for the range, horizontal direction and elevation angle without correction, with correction of A_0 only and with correction of A_0 and B_1 are given in Table 1. In addition, the residual patterns of these cases are presented in Figure 5. Clear improvements in all spherical observations were observed and, in particular, that of elevation angle is the largest. The difference between the standard deviations of range in the cases with A_0 correction only and with A_0 and B_1 correction is on the order of 10. This suggests that a priori knowledge of the existing systematic error, i.e. A_0 and B_1 , is required in order to achieve the maximum observational precision from calibration since, as already mentioned and can be seen in Figure 5a, model identification is difficult.

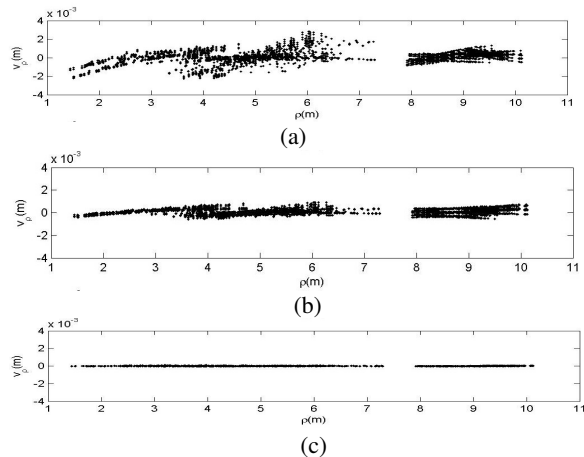


Figure 5. Residual plots in the presence of rangefinder additive constant (A_0) and the collimation axis error (B_1). (a) Without calibration (i.e. registration only) (b) with A_0 only (c) with A_0 and B_1

	No correction	A_0	A_0 and B_1
STD v_ρ (mm)	0.70	0.24	0.02
STD v_θ (")	1.00	0.42	0.03
STD v_α (")	1.50	0.03	0.04

Table 1. Residual statistics of the plane-based self-calibration method in three different cases: without correction (registration only), with A_0 correction only, and with A_0 and B_1 correction. STD is the standard deviation.

A further series of accuracy tests was conducted in which a range of possible AP values was added to the simulated dataset. The range for rangefinder additive constant (A_0) was 0.25mm to

10mm, 10" to 200" for the collimation axis error (B_1) and for the vertical circle index error (C_0) was 10" to 100". These values were chosen for consistency with other studies (e.g. Lichti and Licht, 2006). A maximum bias of 0.006% was observed for all three additional parameters, with larger values generally being estimated more accurately. Some difficulty in the estimation of collimation axis error is expected when the magnitude of the applied B_1 is increased as shown in Figure 5(b). For example, from Table 1, we observed a slight increase in v_α in

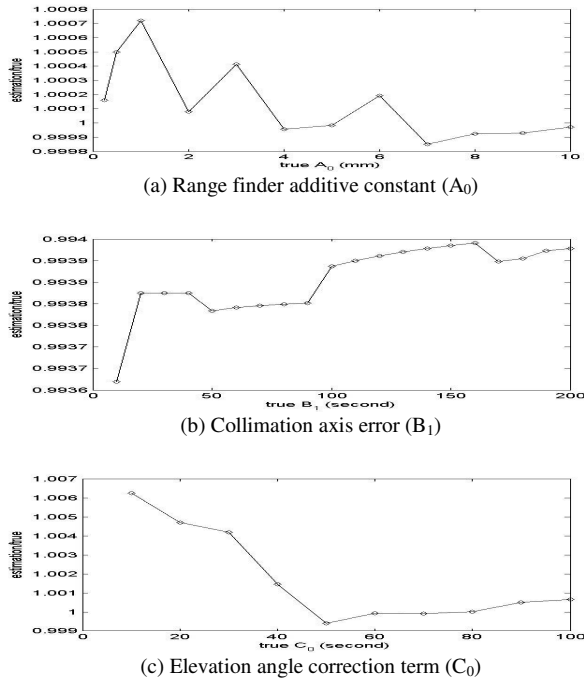


Figure 6. Accuracy of some additional parameters with simulated datasets, which defined as the ratio of the true and estimated parameters.

3.4 Estimation of the APs of the FARO 880 from real data

The FARO 880 terrestrial laser scanner offers a near spherical field of view made possible by a 320° vertical angle scanning range and a 180° horizontal field of view. The scanner features two orthogonal inclinometers that correct the captured data for instrument tilt. The manufacturer specifies 0.01° ($36''$) for the inclinometer accuracy and 3mm linearity error at 10m with 84% target reflectivity for the rangefinder. See Lichti (2007) for a description of its salient properties.

Two datasets, named here Data1 (28 October/2005) and Data2 (7 December/2005), captured with the FARO 880, were utilised for the test. A total of eight point clouds of a room were captured from two locations. The scanner was manually rotated on the tripod by 90° after each of the set of four scans was captured.

The dimension of the room in Data1 is (H, W, L) = (3m, 5m, 9m) with 18 planar targets. The nominal distance between the two scanner locations was 4m. The radial distance from the laser scanner to the object was approximately from 1.5m to 7.5m. The plane-based calibration adjustment (minimally constrained) had 5641 observations with 5538 degree of freedom. The dimension of the room Data2 is (H, W, L) = (3m, 9m, 12m) with 25 planar targets. The nominal distance between

the two scanner locations was 6.7m. The radial distance from the laser scanner to the object was approximately from 2m to 10m. The plane-based calibration adjustment (minimally constrained) had 8231 observations with 8107 degree of freedom.

Note that the planar targets for this on-site calibration were manually extracted from wall, ceiling and floors of the original point clouds and some obvious outliers were removed by investing the results of the first order plane fit. For the proposed plane calibration method, spherical coordinate observations were derived from the Cartesian coordinates exported using the commercial software, iQscene. Variance component estimation and the outlier detection method explained in Section 2.5 were used to optimise the contribution of each of the three groups of spherical observables.

For the point-based calibration with the room Data1, 134 planar, A4-size targets were mounted on all four walls, the floor and the ceiling. Target center measurement was conducted using the commercial software, iQscene. The point-based calibration method (with free-network) adjustment had 2469 observations with 2019 degrees of freedom. For the point-based calibration with the room Data2, 131 planar, A4-size targets were mounted on all four walls, the floor and the ceiling. The point-based calibration method (with free-network) adjustment had 2193 observations with 1738 degrees of freedom.

	Without self-calibration	With calibration	Improvement (%)
STD v_p (mm)	1.2	1.2	5.4
STD v_θ (")	67.9	18.6	72.6
STD v_α (")	24.3	19.9	18.4

Table 2. Residual statistics from plane-based calibration after outlier removal for Data1 (28 October/2005).

	Without self-calibration	With calibration	Improvement (%)
STD v_p (mm)	2.4	1.9	21.0
STD v_θ (")	86.3	35.2	59.2
STD v_α (")	51.8	46.5	10.3

Table 3. Residual statistics from point-based calibration after outlier removal for Data1 (28 October/2005).

	Without self-calibration	With calibration	Improvement (%)
STD v_p (mm)	1.0	0.8	21.4
STD v_θ (")	49.2	47.3	3.8
STD v_α (")	55.3	49.5	10.6

Table 4. Residual statistics from plane-based calibration after outlier removal for Data2 (7 December/2005).

	Without self-calibration	With calibration	Improvement (%)
STD v_p (mm)	2.3	1.7	26.1
STD v_θ (")	109.8	36.7	66.6
STD v_α (")	65.88	20.9	68.3

Table 5. Residual statistics from point-based calibration after outlier removal for Data2 (7 December/2005).

Only a reduced set of the additional parameters (A_0 , B_1 , B_2 , B_3 , B_4 , C_0 and C_2) was used for all calibrations. The standard

deviations of the residuals for the range, horizontal and elevation angle for both the plane- and point-based methods are given in Tables 2 and 4. Both datasets showed significant improvement in the precision of all spherical observations.

The plane-based calibration provided greater precision in the spherical observables than did the point-based method. In contrast, Lichti and Licht (2006) reported a similar level of point observational precision with all physical and empirical additional parameters of terrestrial laser scanners.

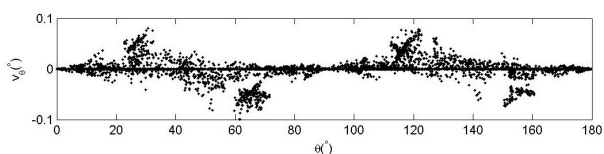


Figure 7. Horizontal direction residual vs horizontal direction without plane-based self-calibration (Data1).

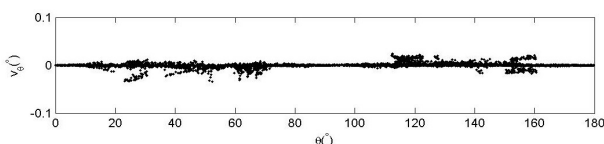


Figure 8. Horizontal direction residual vs horizontal direction with plane-based calibration (Data1).

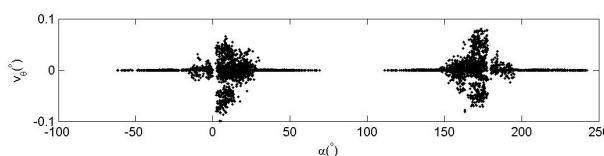


Figure 9. Horizontal angle residuals vs elevation angle without plane-based self-calibration (Data1).

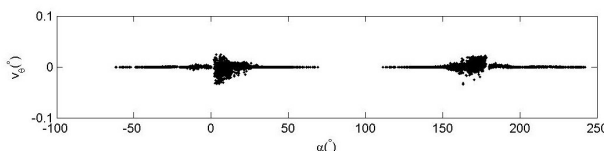


Figure 10. Horizontal angle residual vs elevation angle with plane-based self-calibration (Data1).

Plots of the residuals of horizontal direction angle both with and without, additional parameter correction from the plane-based case are presented in Figures 7-10. Although they clearly show an improvement in the precision of the observations, they also show residual systematic effects that are likely due to unmodelled errors since only a reduced-AP model has been implemented thus far.

4. CONCLUSIONS

A plane-based self-calibration method based on terrestrial laser scanner systematic error modelling has been presented and has been demonstrated to improve observational precision of the self-calibration residual standard deviation up to 72.6% with the help of outlier detection and variance component estimation.

The contributions of this paper can be summarised as follows: First, the residual patterns of the plane-based calibration method are shown to be different from the functional models of systematic errors. This could cause great difficulty in systematic

error model identification, not only for formulating error models but also for confirmation of the removal of the targeted systematic errors. Second, the results of the plane-based calibration are improved over those of the point-based method, although there are some difficulties in the accurate estimation of some known additional parameters.

5. ACKNOWLEDGEMENTS

This work has been supported by Curtin University of Technology and the Cooperative Research Centre for Spatial Information, whose activities are funded by the Australian Commonwealth's Cooperative Research Centres Programme.

REFERENCES

- Amiri Parian, J. and A. Grün, 2005. Integrated laser scanner and intensity image calibration and accuracy assessment. In: *The International Archives of the Photogrammetry, Remote Sensing and Spatial Information Sciences*, Vol. 36 (Part 3/W19), pp. 18-23.
- Baarda, W., 1968. A testing procedure for use in geodetic networks. In: *Publication on Geodesy*, Netherlands Geodetic Com., Delft, The Netherlands, 2(5)
- Cothren J., 2005. Reliability in constrained Gauss-Markov models: an analytical and differential approach with applications in Photogrammetry, In: Ph.D. dissertation, Department of Civil and Environmental Engineering and Geodetic Science, Ohio State University, Columbus, USA, 61 pages
- Gielsdorf, F., A. Rietdorf and L. Gruendig, 2004. A Concept for the calibration of terrestrial laser scanners. In: *Proceedings of the FIG Working Week*, Athens, Greece. [On CD-ROM].
- Golub G. H. and Van Loan C. F., 1989. *Matrix computations* (2nd ed.), Johns Hopkins University Press.
- Lichti, D.D. and J. Franke, 2005. Self-calibration of the iQsun 880 laser scanner. In: *Optical 3-D Measurement Techniques VII*, Vienna, Austria, Vol. I, pp. 112-121.
- Lichti, D.D. and M. G. Licht, 2006. Experience with terrestrial laser scanner modelling and accuracy assessment. In: *The International Archives of the Photogrammetry, Remote Sensing and Spatial Information Sciences*, Vol. 36 (Part 5), pp. 155-160.
- Lichti D. D., 2007. Error modelling, calibration and analysis of an AM-CW terrestrial laser scanner system, In: *ISPRS Journal of Photogrammetry and Remote Sensing*, 61 (5), pp. 307-324.
- Luhmann T., S. Robson, S. Kyle and I. Harley, 2007. *Close Range Photogrammetry*, Whittles Publishing
- Reshetyuk, Y., 2006. Calibration of terrestrial laser scanners Callidus 1.1, Leica HDS 3000 and Leica HDS 2500. In: *Survey Review* 38 (302), 703-713.
- Schaffrin B. 1997, Reliability measures for correlated observations. *Journal of Surveying Engineering*, 124 (3), pp. 126-133
- Shewchuk J. R., 1994. An Introduction to the Conjugate Gradient Method Without the Agonizing Pain, In: *Technical Report: CS-94-125*, Carnegie Mellon University, Pittsburgh, PA, USA, 64 pp.
- Teunissen P. J. G., 1990. Nonlinear least squares, In: *Manuscripta Geodaetica*, Vol. 15, pp. 137-150
- von Hansen, W., Michaelsen, E. and Thonnessen, U., 2006. Cluster analysis and priority sorting in huge point clouds for building reconstruction. In: *Proceedings of the 18th International Conference on Pattern Recognition (ICPR'06)*, pp. 23-26.

PROBLEMS RELATED TO THE GENERATION OF TRUE-ORTHOPHOTOS WITH LIDAR DDSMs

Luigi Barazzetti, Maria Brovelli, Marco Scaioni

Politecnico di Milano, DIAR, piazza L. da Vinci 32, 20133 Milano, Italy
luigi@geomatica.como.polimi.it, [maria.brovelli, marco.scaioni]@polimi.it

Commission III, WG III/4

KEY WORDS: Digital Terrain Model, Dense Digital Surface Model, LiDAR, Orthophoto, Spatial DB, True Orthophoto

ABSTRACT:

Nowadays orthophotos from satellite and aerial imagery are very requested products, considering their low cost motivated by the highly automated production chain. The generation of orthophotos requires a block of oriented images and a digital model of the ground (DTM or DSM). In case a DTM is adopted, the lackness of information about buildings results in distortions. The availability of a LiDAR DDSM allows to overcome this problem, even though if the spatial resolution is not very high, some problems in correspondence of building contour might arise. To solve for this drawback, a method based on thickening a LiDAR DDSM from an initial grid of 2x2 m² to a 0.2x0.2 m² one is proposed here. This method has been implemented by exploiting the availability of a spatial DB of the same area, which allows to classify all points of the thickened DDSM in two categories: those belonging to a building and those not. A test of the method has been carried out on a photogrammetric block taken over the town of Lecco (Northern Italy) by a RC30 Wild camera at 1:17,000 mean scale, and afterward digitized by scanning. The LiDAR DDSM adopted has been provided by Lombardia Region at a spatial resolution of 2x2 m². The thickening of the DSM has been performed using a building mask extracted from the new spatial DB of Lecco. Orthophotos created in this manner take advantage of the whole cartographic and spatial material already available at the Public Administration Department, and presents an improved accuracy than a classic orthophoto with a computation time approximately equal.

1. INTRODUCTION

In recent years, increasing demand for digital orthophotos has been pushing researchers to improve data quality and reduce production costs. Indeed, if in the past orthophotos were considered a cheap alternative to vector maps, or a by-product of the photogrammetric mapping process, today they have come to play an autonomous role. This is mainly motivated by two factors: the growing worldwide diffusion of *web location services* (see e.g. Heipke, 2005; Walter, 2005; Leberl, 2007) requiring geographical support, which might help on-line users to access information; the need of organizations to produce detailed and up-to-date geographical data describing land changes, a particularly important task when dealing with urban areas, where data of high resolution and accuracy are required. Furthermore, the availability at an operational level of new technologies, such as IMU sensors, airborne digital cameras and aerial laser scanners, has significantly contributed to the development of orthophoto production.

Not long ago, before the development of LiDAR technology, dense DTMs/DSMs could be generated at low cost only by means of aerial photogrammetry. However, especially in highly urbanized areas, due to perspective occlusions, a photogrammetric DTM/DSM may produce a higher error rate than LiDAR (Brovelli & Cannata, 2004).

Therefore, we would like to investigate how urban area orthophotos could be improved through the use of LiDAR DDSMs.

Currently, Italian government agencies and departments tend to buy gridded DTMs/DSMs with a resolution of 2x2 m or 1x1 m.

Therefore, we have looked into problems related to using such DSMs, and we have tried to understand somehow these

problems may be solved using other mapping products generally available at government agencies and departments. The results obtained should be considered as practical guidelines for institutions which would allow them to improve orthophoto quality by exploiting already available material (Dequal & Lingua, 2004).

The resulting orthophotos will not have perspective deformations and can therefore be directly superimposed onto spatial databases or vector maps, which are not affected by such deformations. The generation of accurate orthophotos based on the use of DSM to model ground geometry was first proposed by Amhar *et al.* (1998) under the term "True-Orthophoto[®]". It was then implemented in different photogrammetric packages. From a theoretical point of view, the generation of a true-orthophoto[®] does not significantly differ from that of classical orthophotos; however, it does introduce further problems, requiring suitable solutions (Schickler, 1998; Brown, 2003). For example, when a building is correctly represented, no information is obtained about the ground level area due to the occlusion produced by the building itself. If the generation of orthophotos is based on single images, there is no way to correctly fill in these empty areas. Consequently, the portions of orthophoto relative to these areas are usually generated by means of the DTM alone without the DSM, and this results in duplication of the image content ("ghost image"). The solution to this problem is to combine several images from different points of view (Rau *et al.*, 2002, Biasion *et al.*, 2004), so if there is an occlusion area on an image, information about this area can be extracted from another images.

A more complex issue to cope with is that of roof modeling. If the goal is the realization of a high resolution true-

orthophoto[®] and the DSM has a lower planimetric resolution, information about where the roof border of a building is located might be lacking, and here the algorithm does not know if a pixel of the image represents a piece of terrain or roof. The result is a rough roof border, without a straight line (Figures 7 and 9).

The aim of this paper is to present a solution which corrects this unwanted effect by exploiting a Dense Digital Surface Model (DDSM) using LiDAR data integrated into a spatial database which provides information about the building ground coverage. This solution may seem contradictory, given that the generation of an orthophoto is based on the availability of a higher quality product, such a Spatial DB.

However, given the occlusion issues discussed here, this practical solution results in improvements to the quality of spatial data which can be used by government institutions, especially if the following considerations are taken into account:

1. digital orthophotos can be generated and upgraded with a higher frequency and a lower cost with respect to existing vector maps;
2. upgraded orthophotos are a very useful tool for checking landscape content and detecting changes, especially in urban areas.

In addition to the presentation of the method implemented for deriving geometrically corrected orthophotos, and to the results of its application, in the following an analysis of cases in which corrections may or may not be truly necessary will be reported.

2. THE PROPOSED METHOD

As shown in Section 1, the problem focused in this paper has aimed to correct the border effects (see Fig. 7) due to the absence, which is very common, of break-lines in the DDSMs used to derive digital orthophotos. In urban areas this outcome is evident for buildings, specifically when they show large difference in height with respect to their surrounding terrain.

Break-lines can be obtained by three different strategies. The first one is based on the automatic extraction of the building contours from the DDSM itself (i). However, DDSMs have often resolution of about 1 m or less, which makes approximate the derived contours, especially when buildings do not have simple shapes, such as regular figures with sides much longer than the DSM resolution (Forlani *et al.*, 2005). The automatic detection of a detailed roof perimeter needs a resolution of a few tens of centimetres, which is rarely available.

Indeed, even though LiDAR data are usually acquired with a higher point density, they are usually delivered, after filtering, at a resolution of 1-2 m. The other possible strategies rely on the building contour availability from external data source (ii), e.g. vector maps, or on their manual digitization from imagery (iii); the last solution is generally of low practical interest because of its high cost. Both the two solutions (ii) and (iii) require also the knowledge of the height of each building, whose availability is not commonplace in all countries. However, also when building heights can be derived from maps, these are limited to mean values, which do not enable to correctly model the roof geometry.

The proposed method tries to exploit the high accuracy in describing the building height, which is typical to DDSM, coupled by the detailed description of building contours, which can be extracted from existing Spatial DB or digital vector maps, data that are generally available for the most urban areas.

Starting from the original LiDAR DDSM, a denser one at a few centimetres resolution is generated, according whether the new grid node lies on the roof or on the terrain. Considering the planimetric layout of all building contours (and possibly accounting for other objects which need to be corrected due to their relative height with respect to the surrounding terrain), two binary masks are generated (see Fig. 1):

1. the *building mask* (BM): the building raster map;
2. the *terrain mask* (TM): the raster map which is complementary to the BM.

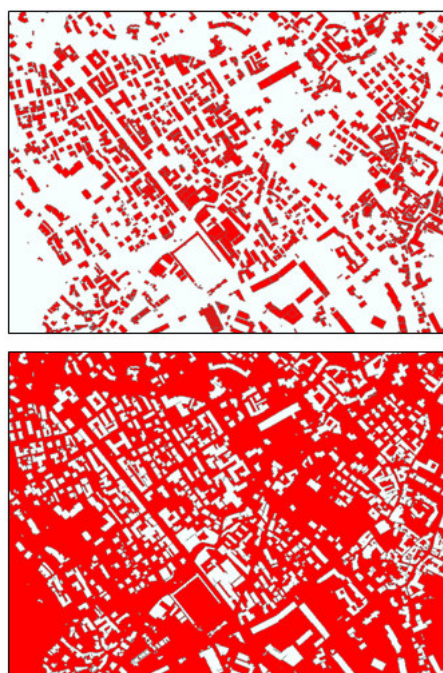


Figure 1. The *building mask* (on top) and the *terrain mask* (on bottom).

Obviously the sum of both masks gives the entire zone. From an original vector format the two masks are rasterized with a planimetric resolution higher than that of the DDSM (few centimetres). Then the original DDSM is resampled according to new denser regular grid. Every new node will have the height of the nearest cell of the original DDSM, considering if the point lies on the BM or on the TM (Fig. 2). The approach allows the roof to be determined with a precision equal to the raster masks.

The densification of the original DDSM is carried out at first on the zone covered by the BM, in such a way that the new node outside this mask is classified as a null value. The same operation is later performed with the TM. The sum of the two resulting DDSMs gives the whole DDSM useful for the generation of the geometrically corrected orthophoto.

The flow chart of the developed method is shown in Figure 3.

In the following sections some applications of the proposed method based on different data set covering the same area will be shown.

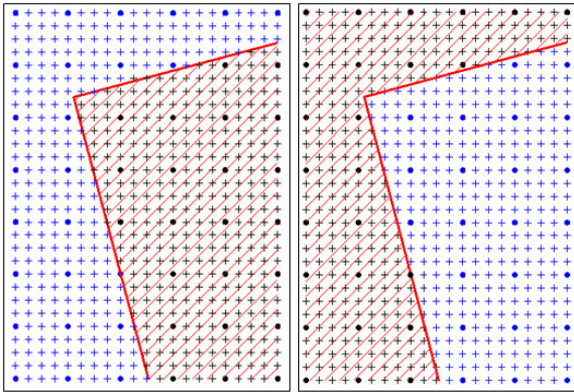


Figure 2. The creation of the Building and Terrain DDSMs
 Legend: ● node of the original DDSM
 + node of the new DDSM
 // mask

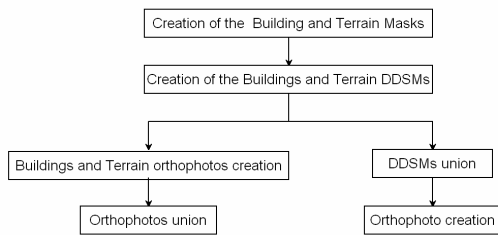


Figure 3. Flow chart of the proposed method

3. ORTHOPHOTO USING A GRID DTM

3.1 Data set description

The proposed method for the generation of orthophoto has been tested on a small aerial block (8 images) captured over the city of Lecco (Lombardia, Italy) by an analogue camera Wild RC30, equipped with a standard lens (150 mm). Images have been taken during 2003 and feature a mean scale of about 1:17000, covering an area of about 10,000 m². The transformation from analogue to digital has been accomplished by using a photogrammetric scanner at a geometric resolution of 14 μm pixel size, corresponding to a footprint on the terrain of about 20 cm.

The aerial triangulation and the ortho-rectification have been performed by Geomatica V10 Orthoengine, i.e. by using a standard commercial processing package. The advantage of the proposed technique relies in the fact that no special algorithms have to be implemented for the orthophoto generation, but only a pre-processing of the DSM is needed. This consists in the creation of both masks adopted to classify points on the terrain and on buildings, that are derived from a *spatial DB* of the study area. This has been created by a digital photogrammetric process on the basis of the same image block adopted for the generation of the orthophotos themselves. Indeed, either the *spatial DB* and the images represent the landscape exactly at the same time, and therefore they should not show differences. On the other

hand, discrepancies might arise concerning the DSMs and the DTM adopted for testing the procedure, which have been captured at different epochs.

In the next sub-sections, results using DTM and DSM with different resolution will be shown.

3.2 Results using a 20 m DTM

Initially orthophotos at two different image resolution (50 cm and 20 cm, respectively) have been created based on a DTM covering the whole Lombardia region, featuring a grid of 20 m resolution.

In figure 4 a patch of the resulting orthophoto at the resolution 20 cm is reported. The layer corresponding to buildings on the *spatial DB* has been super-imposed to orthophoto, in order to check the quality of the geometry correction. In reality, these tests have been performed on a wider area than that shown in figure 4. For the sake of picture clarity and readability, here we only show a detail of orthophotos generated by different data sets and methods over the area where a large commercial centre designed by Renzo Piano arises. This choice is motivated by the complex geometry of the roof and the height of this building (50 m), representing a very critical case study to check the effectiveness of the proposed approach.

In figure 5 a zoom on the central area of figure 4 is reported, showing that low buildings are correctly represented because the use of a DTM does not result in significant errors. On the contrary, the piece of orthophoto corresponding to the central building has not an adequate correspondence with the vector map, because a DTM in this area is not able to provide information to correct geometric distortions. The mean magnitude of this misalignment error results in the order of some meters. Very similar results have been obtained with both 20 cm and 50 cm resolution orthophotos.

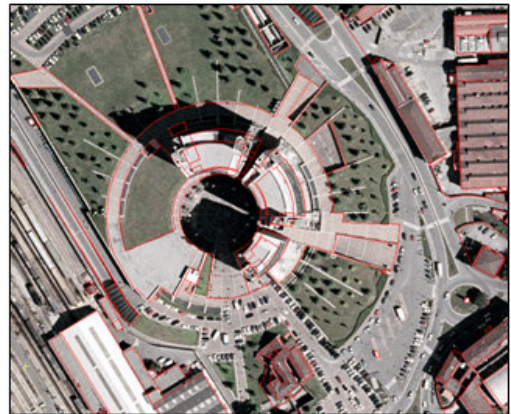


Figure 4. Orthophotos with resolution 20 cm generated by using a 20 m resolution DTM; the building layer (in red) has been super-imposed.

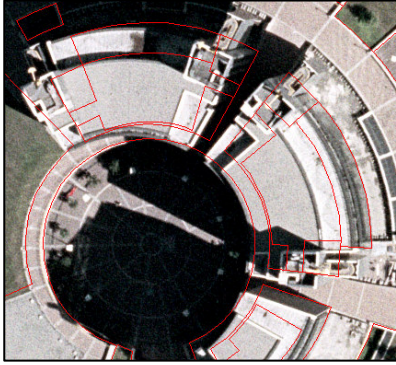


Figure 5. Detail on errors concerning the Renzo Piano building by using the DTM at 20 m resolution.

3.3 Results using a 2 m LiDAR DTM

LiDAR (*Light Detection and Ranging*) technology is able to provide a complete 3-D model (DSM) of the investigated surface. By filtering vegetation, buildings and other objects, a DTM can be derived with an accuracy in the order of decimetres.

In this test, a DTM at a resolution of 2 m has been provided by the Land Administration Dept. of Lombardia Region.

A detail of the orthophoto generated using a LiDAR DTM at 20 cm image resolutions is shown in Figure 6. Also in this case, like in Fig. 4, there is not a good correspondence to vector maps in case of tall buildings.

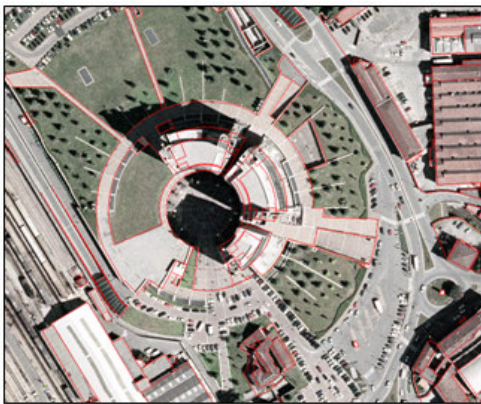


Figure 6. Orthophotos at an image resolution 20 cm according to a LiDAR DTM of 2 m resolution.

4. ORTHOPHOTO USING A GRID DSM

LiDAR allows also to derive a DSM of the interested area, that can be used to straighten up the position of each buildings, especially when the height is relevant. The adopted DSM was also provided by Lombardia Region at a 2 m spatial resolution.

Some tests have been performed at the original resolution of the DSM (2 m), and with other two reduced resolutions (4 m and 10 m). These last DSMs have been created with a thin out operation on the original DSM, up to 4 m (deletion of the 50% of the nodes), and 10 m (deletion of the 96% of the nodes). In Fig. 7 the orthophoto at image resolution of 20 cm according to a DSM of 2 m is shown.

Likewise the previous case when a DTM has been adopted, here the correspondence between orthophoto and vector data is satisfying not only for low buildings, but also for the tall constructions. Moreover, results achieved by using DSMs at different resolutions (2, 4 and 10 m) are quite similar, even though the results correspond to the use of the DSM at the higher resolution (2 m). After a more accurate analysis, it is possible to pick out a jagged gutter line on each orthophoto, generated by a lack of data along the roof edges (see Fig. 7). Indeed, here an interpolation of the grid DSM is needed, because the resolution of the orthophoto is higher than the resolution of the DSM, but the algorithm has not information about where the roof edge is really located. The interpolation is based on the height values of the points in a surrounding area, independently if a point is located on a terrain or on the roof building.

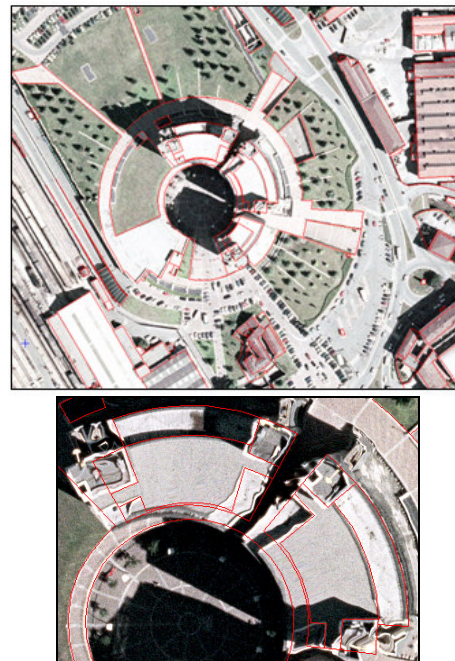


Figure 7. Orthophoto at image resolution of 20 cm, according to a DSM at resolution 2 m (on top); on the bottom a detail showing the jagged gutter line effect is reported.

5. ORTHOPHOTO USING THE PROPOSED METHOD

5.1 Generation of orthophotos

The method to generate orthoimages proposed in this paper has been developed to avoid the jagged gutter line effect due to the use of a coarse DSM.

As described in Section 2, the first step is to create the *buildings* and *terrain masks* of the considered area in raster format. Using a *spatial database* provided by the administration of the city of Lecco, we could extract only the zone relating to the surface covered by buildings, while the remaining part have been classified as terrain. From an original vector format, both masks have been rasterized with 40 cm and 20 cm pixel size resolution (see Figure 1). These resolutions allow to derive information about where a

building border line is really located with a largest error of 40 and 20 cm, respectively.

The following step is the thickening of the original 2 m LiDAR DSM to the same resolution of the masks. Initially, the portion covered by the BM has been thickened, by assigning the height value of the first nearest node (*nearest neighbour* method) to each new grid node of the derived DDSM, considering only the point inside the mask. To each point outside the mask a “nodata” value has been assigned. The same operation has been performed with the TM. These tasks have been implemented to be carried out in GRASS and ArcGIS GIS environments.

By using these two DDSMs it is now possible to generate of the corresponding orthophotos (Figure 8).

The last step is the fusion of both orthophotos, being one the complementary of the other. The same result could be achieved by the preliminary mosaicking of two DDSMs and the generation of the complete orthophoto in only one step.

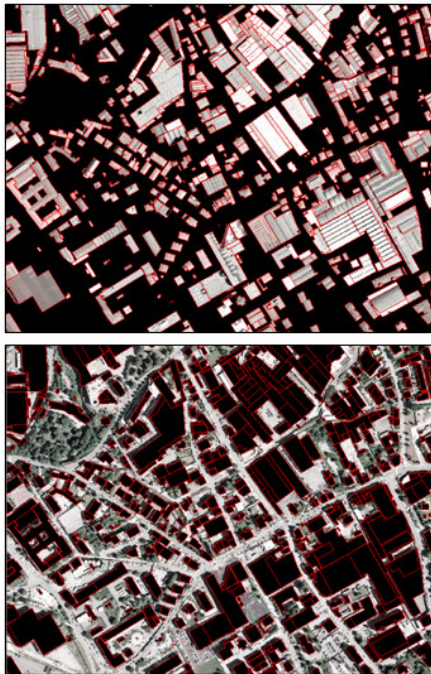


Figure 8. Orthophotos generated in correspondence of *buildings* and *terrain DDSMs*.

5.2 Results with the proposed method

In order to show the improvement in the orthophoto quality obtained by adopting the proposed method, we focus on the results achieved in correspondence of the building of Renzo Piano already used in the previous cases. In Fig. 9 the orthophotos generated on the basis of the *building DDSM* and the full orthophoto are reported. In this case the *building DDSM* has a resolution of 20 cm, exactly the same of the orthophoto. Results are very good, being the jagged gutter line effect fully removed. Figure 10 illustrates the results using the complete DDSM with the union of both *buildings* and *terrain DDSMs* to generate an orthophoto at the resolution of 20 cm. Here both DDSMs at resolutions of 20 and 40 cm have used.

In these cases the correspondence between the vector map and the corrected orthophoto is verified in zones with both low and tall buildings, therefore in every area of the picture.

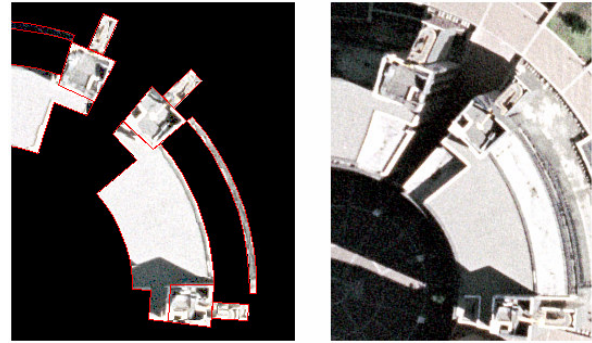


Figure 9. The orthophoto generated on the basis of the *buildings DDSM* and the complete orthophoto.



Figure 10. Orthophoto generated from a 20 cm DDSM.

5.3 Quantitative check of the results

A quantitative control of the results using a 20 m resolution DTM and a 2 m LiDAR DSM has been performed with the evaluation of the displacements between the spatial DB and the generated orthophotos. In particular, a sample of 100 buildings around the tall Renzo Piano building adopted a case study has been chosen for this control. The histograms in Figure 11 represent the measured displacements.

As it can be seen by analyzing the histograms, with a 20 m DTM the errors vary from a few centimetres up to 5-6 meters, the latter corresponding to the tallest buildings. Using a 2 m DSM, the error is always less than the DSM resolution but the jagged gutter line effect is present.

Finally the check with the proposed method has given errors in the range of few centimetres, because the orthoprojection of buildings has been corrected to coincide to the contours coming from the vector map.

Moreover, it was verified that the 40 cm DDSM resolution orthophotos have also a high quality, even though the best results can be obtained by fixing the resolution of the DDSM exactly equal to the resolution of the orthophoto, (in our case 20 cm).

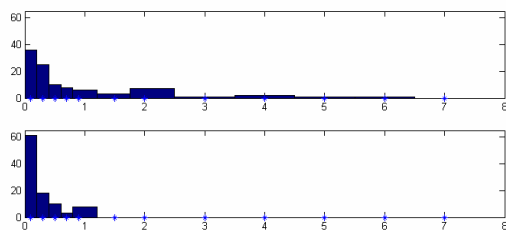


Figure 11. Displacement histograms (in m) measured using a 20 m DTM (on top) and 2 m LiDAR DDSM (on bottom)

5.4 Computational cost

It was verified that the computational cost depends mainly on the values of the output parameters, and specifically on the final orthophoto image resolution. In the test executed with the different DTMs, DSMs and DDSMs, the time necessary for the orthophoto production was about the same if the orthophoto resolution was kept constant. This is quite obvious, because with a low resolution DTMs or DSMs the software must execute a grid interpolation to get the height values needed for the rectification of each pixel of the original image. Instead, with a DDSM the interpolation is not necessary and this can increase the computation speed. In any case the file dimension is considerable (for example passing from 2 m up to 20 cm resolution, the dimension of the file has increased by about 96%) and therefore, considering the need to manage a so large file, the computational time remains about the same.

6. FINAL CONSIDERATIONS AND FURTHER IMPROVEMENTS

This paper proposes a method, which has been tested on real data, for generating orthophotos geometrically corrected to account for modelling of buildings. The implemented technique exploits a Dense Digital Surface Model (DDSM) acquired through LiDAR technology, coupled with a vector map describing the shape of the buildings. The method is useful when the goal is to create a high accuracy orthophoto in which every building is correctly rectified.

For this reason, it is particularly suitable for areas where there is a high density of tall buildings. When generating such orthophotos (also described in the literature as “True-orthophoto[®]”), the main problem to consider is the rectification of the gutter line of every building with a precision of the same order of the orthophoto’s geometric resolution. Tests carried out during this research have shown that this problem cannot be solved for by using DTM or DSM only.

In the paper, the orthophoto corresponding to the building roof is generated by deriving heights from the DSM through a simple interpolation method (nearest neighbour). This technique could be improved by better 3-D modelling of the roof structure (e.g. by using a parameterized model), or by a more refined interpolation technique. The decision about which portion of the ground is covered by buildings is currently taken by using existing vector maps of the same area. However, the vectorization of raster maps (Brovelli & Zamboni, 2006) would make available this kind of data as well.

ACKNOWLEDGEMENTS

We would like to thank the Land Administration Dept. of Lombardia Region to provide all digital surface and terrain models adopted for testing the developed technique. Moreover, acknowledgements go to the city administration of Lecco city for the availability of the Spatial DB.

REFERENCES

- Amhar F., Jansa J., Ries C., 1998. The Generation of the True-Orthophotos Using a 3D Building Model in Conjunction With a Conventional DTM. *IAPRSSIS*, Vol. 32(4), pp.16-22.
- Biason A., Dequal S., Lingua A., 2003. A New Procedure for the automatic production of true orthophotos. *IAPRSSIS*, Vol. 35, pp.538-543.
- Brovelli, M. A., and G. Zamboni, 2006, The usability of vectorization and a new point matching procedure as first step in conflating raster and vector maps. *IAPRSSIS*, Vol. 36(2/W40), pp.85-91.
- Brovelli M. A., Cannata M., 2004. Digital Terrain model reconstruction in urban areas from airborne laser scanning data: the method and an example for Pavia (Northern Italy). *Computers & Geosciences*, n. 30, pp.325-331.
- Brown, J., 2003. Aspects on True-Orthophoto Production. Proc. of *Phot. Week '03*, Fritsch, D., Hobbie, D. (ed.s), Wichmann, Stuttgart, Germany, pp.205-214.
- Dequal S., Lingua A., 2004. True orthophoto of the whole town of Turin. *IAPRSSIS*, Vol. 34(5/C15), pp. 263-268.
- Forlani G., Nardinocchi C., Scaioni M., Zingaretti P., 2005. Complete classification of raw LIDAR data and 3D reconstruction of buildings. *Pattern Analysis and Applications*, n. 4(8), pp. 357-374.
- Heipke, C., 2005. Web-Based Photogrammetric Image and Geospatial Services – An Overview. Proc. of *Phot. Week '05*, Fritsch, D. (ed.), Stuttgart, Germany, pp.157-164.
- Leberl F., 2007. Die automatische Photogrammetrie für das Microsoft Virtual Earth System. In Proc. of *14th Int. Geodätische Woche*, G. Chesi and T. Weinold (ed.s), Obergurgl, Austria, pp. 200-208.
- Rau J.Y., Chen N.Y., Chen L.C., 2002. True Orthophoto Generation of Built-Up Areas Using Multi-View Images. *PE&RS*, 68(6), pp. 581-588.
- Schickler W., 1998. Operational Procedure for Automatic True Orthophoto Generation. *IAPRSSIS*, Vol. 32(4), pp.527-532.
- Walter, V., 2005. Phoogle the Web – Google’s Approach of Spatial Data Visualization. Proc. of *Phot. Week '05*, Fritsch, D. (ed.), Stuttgart, Germany, pp.321-330.

IMPROVING THE MORPHOLOGICAL ANALYSIS FOR TREE EXTRACTION: A DYNAMIC APPROACH TO LIDAR DATA

A. Barilotti*, F. Sepic, E. Abramo, F. Crosilla

Dept. of Georesources and Territory, University of Udine, via del Cottonificio 114, 33100, Udine, Italy
(andrea.barilotti, fabio.crosilla)@uniud.it, sepic@dimi.uniud.it, abramo@dgt.uniud.it

Commission III/3, III/4, V/3, VIII/11

KEY WORDS: LiDAR, Tree extraction, Morphological analysis, Region Growing, Vegetation indexes, Dynamic approaches

ABSTRACT

The improvement of laser scanning as a proficient technology to better understand the complexity of the forest has recently allowed the detection of the forestry parameters at tree level. From a forest inventory point of view, however, a common use of such technology is related to the accuracy that can be obtained if vast and differently composed forestry surfaces are considered. In this paper, an improvement in the morphological analysis methods for tree extraction is presented. The method, developed in an open source environment, is based on the automatic determination of the forest structure by means of some LiDAR-extracted vegetation indexes. The study site is located in some mountainous parts of Friuli Venezia Giulia (N-E Italy) characterized by coniferous, mixed and broad-leaved forests with high variability in terms of population densities and composition. The results have been validated using topographic total station data surveyed in situ, in 13 forestry sample plots with a total of about 550 reference trees. Moreover, some further datasets have been studied by mean of photo-interpretation process on high resolution aerial images. The paper highlights the advantages of using this dynamic approach for tree extraction.

1. INTRODUCTION

Monitoring of the forestry ecosystem is a current topic in the context of quantification and sustainable management of wooded resources. To characterize the vegetation from an ecological state and biomass content point of view, an accurate knowledge of the population density is needed. The assessment of such parameters is critical in terms of field operations and time needed. In this context, Airborne Laser Scanning (ALS) is a promising survey technique for forestry inventories because of its capacity to directly assess the three dimensional structure of the forest due to the high point number of sampling per surface. Computer science plays a major role in the laser surveying field: the data processing and the developing of new algorithms for filtering, classifying and modelling of LiDAR data in the forestry field are research topics constantly being developed. Part of the research activities carried out within the Interreg IIIA Italy-Slovenia 2003-2006 project "Cadastral map updating and regional technical map integration for the Geographical Information Systems of the regional agencies by testing advanced and innovative survey techniques" at the University of Udine concerned the use of LiDAR data in the forestry field. In this context, attention has been focused on the development of informative methodologies and algorithms useful in the automatic extraction of the parameters characterizing the three-dimensional structure of the trees. The experiments were performed using an original software developed in the laboratory. The main components of the software allow the visualization of the laser scanning data, to draw sections, to calculate DTM and DSM and to overlap them with other cartographic maps (Beinat, Sepic, 2005). On this basis a specific tool were implemented in order to extract forestry parameters of interest like the cartographic position of the single trees, the tree height, the crown shape and the crown insertion depth.

From a tree-level inventory point of view, the extraction of tree position is the most important parameter to determine. The tree parameters (e.g. crown area, crown depth, volume) can be derived starting from the preliminary detected tree position, as many authors have already done (Hyypä et al, 2004; Morsdorf et al., 2003; Pitkänen et al, 2004; Weinacker et al., 2004). The results obtained for individual tree extraction have varied significantly from study to study. Many factors contribute to cause this variation: the methods applied and the forest characteristics are the principal ones. Concerning the methods, the first studies were related to the use of rasterized Crown Height Model (CHM) as input data to perform local analysis while, recently, a trend towards using the point cloud data directly has been noticed (Pyysalo and Hyypä, H., 2002; Tiede et al., 2005; Barilotti and Sepic, 2006). As far as the forest composition is concerned, some authors derive forest information using laser data in synergy with high resolution aerial images. The latter technique provides color information usable for classification (Leckie et al., 2003; Persson et al. 2004). In this paper, a new methodology for tree extraction is presented. The characteristic elements of the implemented procedure are based on the assessment of local forest structure which is carried out by a multivariate analysis on laser-derived vegetation indexes. This allows the application of mathematical morphology in an auto-adaptive way. The method, following an automatic approach, is able to dynamically fit the apex searching parameters on the basis of the dataset characteristics, increasing the efficiency of the tree extraction process.

2. MATERIALS

The study areas are located in some mountainous areas of Friuli Venezia Giulia Region (N-E Italy) essentially characterized by coniferous forests (spruce, spruce-fir), broad-leaved forests

* Corresponding author.

(beech) and mixed forests (spruce, fir, beech and Alpine Larch). Within these areas some sub-zones of interest have been located and geo-referenced using topographic total station and GPS. This has allowed the precise and accurate determination of the coordinates of 13 circular forestry plots (transects) with radius ranging between 12 and 25 meters. During a field measuring campaign, detailed information on the morphology and the structure of each tree were collected. Using a topographic total station the cartographic position of all trees (diameter at breast height more than 5 cm) and the crown extension (4 sampling points for each one) were measured (e. g. in Figure 1). The total data acquired in situ using topographic instruments covers approximately 550 tree points and 2200 crown points.

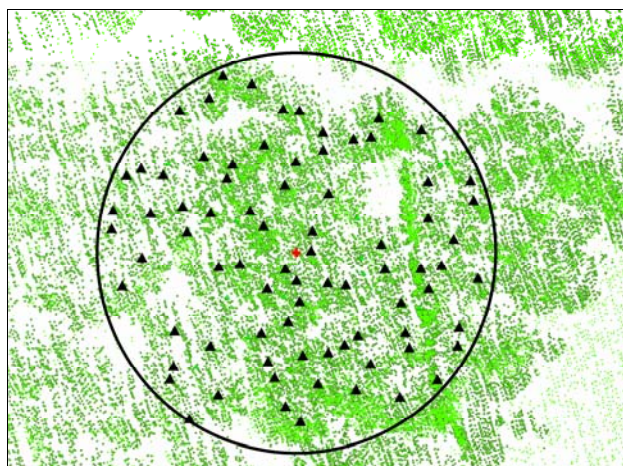


Figure 1 – Example of trees collected on site in MBD plot. The correspondent high vegetation laser points can be seen in the background of the image.

The forestry characteristics of the studied plots with the respective laser point densities are reported in Table 1.

Plot ID	n° of trees/h _a	Area (m ²)	Forest characteristics	LiDAR data characteristics
FOA	663	450	Mature - mixed	2 pt/m ² - F&L
FOB	531	450	Mature - mixed	2 pt/m ² - F&L
MBA	619	450	Mature - mixed	6 pt/m ² - Multi
MBB	1525	450	Juvenile - spruce	7 pt/m ² - Multi
MBC	575	450	Juvenile - spruce	8 pt/m ² - Multi
MBD	463	2000	Mature - spruce	10 pt/m ² - Multi
PRB	840	450	Juvenile/adult - spruce	1,5 pt/m ² - F&L
PRC	752	450	Juvenile/adult - spruce	1,5 pt/m ² - F&L
SAA	336	2000	Mature - beech	4 pt/m ² - F&L
TUA	538	700	Juvenile - beech	2 pt/m ² - F&L
TUB	862	450	Juvenile - beech	2 pt/m ² - F&L
TUC	553	450	Juvenile - beech	2 pt/m ² - F&L
VBA	1105	450	Juvenile - spruce	5 pt/m ² - Multi

Table 1 – Summary of the georeferenced plot characteristics. Considering the different age and composition of the 13 transects compared to the different laser densities, 8 different forestry situations can be found.

The height of crown insertion was measured using portable instruments (length and angle). The diameter at breast height was also measured. These values were used to localize the dominated vegetation. However, the individual trees whose apex did not reach the top of the canopy were objectively surveyed during the field operations. As far as the laser data is concerned, the main characteristics of the datasets are reported in column 5 (Table 1). Some datasets were detected using a multiple pulse laser scanner (Optech ALTM 3100). On one hand, such an instrument increases the capacity to sample the intermediate layers of the vegetation but, on the other, it does not substantially furnish extra information on the higher part of the canopy, when compared to the First and Last (F&L) data. However, in these cases we have plots with higher sampling points (5-10 pts/m²) than those surveyed with a F&L pulse laser scanner (low density, 1.5 – 2 pts/m²). The flight altitude was about 1000 m above ground and the laser beam divergence was 0.2 mrad (small footprint), according to the different datasets. It has to be specified that none of this laser data was specifically collected for forestry measurements.

Moreover, 4 further datasets have been studied using high resolution aerial photography (20 cm pixel) which allowed us to single out the position of the trees by a photo-interpretation procedure. The forest characteristics were also photo-interpreted. The corresponding LiDAR dataset was surveyed with a F&L instrument (Optech ALTM 3033) for an average density of about 3 point/m², as shown in Table 2.

Plot ID	n° of trees/ha	Area (m ²)	Forest characteristics	LiDAR data characteristics
PHA	1380	450	Juvenile - spruce	3.5 pts/m ² - F&L
PHB	410	2000	Adult - spruce	3 pts/m ² - F&L
PHC	385	2000	Mature - spruce	3 pts/m ² - F&L
PHD	185	2000	Mature - mixed	2.5 pts/m ² - F&L

Table 2 – Summary of 4 photo interpreted transect. The PHA transect, in particular, is composed of a very dense population of planted spruces.

Approximately 258 trees were photo-interpreted on the basis of the high resolution aerial photography.

3. METHODS

The methods presented here for tree extraction are related to the morphological mathematical approaches. The procedure is composed of a series of elaborations and transformations that can be schematized as follows:

- Pre-processing of the raw laser data (true DSM);
- Application of mathematical morphology algorithms, following a single tree approach, to extract the canopy apexes;
- Application of a dynamic search radius based on multivariate analysis of LiDAR-extracted indexes.

The last step is an important improvement in the method used for tree extraction because it makes it possible to automatically apply the morphological analysis in a local context. As will be shown later, such a dynamic and auto-adaptive procedure has been implemented in order to eliminate the need for a detailed knowledge of the dataset characteristics and the forest composition as well. A description of the implemented algorithms and the related steps of elaboration are reported below.

3.1 Pre-processing (true DSM)

The implemented step relating to the laser data pre-processing consists of an algorithm that eliminates from the dataset the points corresponding to the laser beam reflection under the canopy. The algorithm executes a first triangulation (Delunay) of all points, then analyzes the height (z) difference between the vertices of each triangle. Those vertices whose height difference is greater than a threshold value (according to the minimal height of the forest) are eliminated. This allows the creation of a Digital Surface Model (DSM) without any triangulation inside canopy (true DSM) and therefore introduces a higher degree of DSM adhesion to the external forest surface.

3.2 Morphological analysis

3.2.1 Mathematical morphology

The method proposed for the tree extraction is based on the morphologic analysis of the laser point distribution. Accordingly, the Top Hat algorithm, whose formulation is related to the image elaboration theory (Serra, 1982), was implemented. This mathematical function allows the extraction of the highest elements in the scale of the represented values, independently from the image typology (Andersen et al., 2001, Barilotti and Turco, 2006). If we considering $f(x)$ as the grey value of a generic pixel x of a point localized in u ; $f(X)$ as the corresponding value of the transformation of the matrix X ; λ as the structural geometric element to determine (or as the dimension of the explorative kernel centred in x), the Top Hat function is based on the *Opening* transformation (1) defined as follows:

$$O^\lambda f(X) = D^\lambda [E^\lambda f(X)] \quad (1)$$

Therefore, the following transformations of *Erosion* (2) and *Dilatation* (3) are applied:

$$E^\lambda f(X) = \inf \{f(u) : u \in \lambda_x\} \quad (2)$$

$$D^\lambda f(X) = \sup \{f(u) : u \in \lambda_x\} \quad (3)$$

The Erosion operator (2) associates to the centre of the kernel (λ_x) the inferior (inf) value among the surrounding pixels while the Dilatation operator (3) associates the superior (sup) value.

The extraction of the local maximums in the scale of the image values is carried out by using the function *Top* (4) that subtracts the primitive image (function) from the *Opening-transformed* function:

$$TOP = \{x: f(x) - O^\lambda f(X)\} \quad (4)$$

Extending the Top Hat concept directly to the pre-filtered point cloud, the method allows the detection of the set of points belonging to the top of the crown, avoiding the interpolation on raster images. A preliminary set of higher points (seed points) is obtained in this way, the number of which depends on the kernel used (e.g. $\lambda = 3 \times 3$ and cell value of 1 meter). It is assumed that these points are an over estimation of the real trees, particularly when a kernel smaller than 3 meters is used (e.g. $\lambda = 3 \times 3$ and cell value of 0.5 meters).

3.2.2 Fixed search radius

In order to diminish this kind of error, a checking algorithm that identifies and corrects the erroneously classified apexes (often localized in the crown edges) was introduced. The algorithm compares the height value of each extracted apex to the nearest

laser points, using an opportune (user defined) search radius. If a point with a greater height value is found inside the search window, it becomes the new apex. Normally, a search radius slightly bigger than the kernel (λ used in the morphological analysis) maintains the high level of the method efficiency but, on the other hand, the number of false positive trees remains high. Experimentally, it has been observed that the optimal radius ranges between 1.50 and 1.80 meters when a 3 m kernel is used. This average radius can be manually set up and optimized on the basis of the expected forest typology. However, different λ and radius should be used depending on the forestry species present and population density.

3.3 Pre-detection of forestry composition

When the study area is characterized by a very high variability of forest composition and structure, the working procedure should foresee a sub segmentation of the LiDAR dataset, applying different analysis parameters. To avoid this procedure, which is expensive in terms of time, a method to automatically assess the forest structure was introduced, performing a multi-variate analysis on two different LiDAR-extracted indexes:

- Laser Penetration Index (LPI) (Barilotti et al, 2006);
- Crown Height Model (CHM).

3.3.1 Laser Penetration Index (LPI)

The laser beam penetration through the canopy varies depending on to the macro-species composition, the tree density, the height of the forest. Concerning the broad-leaved forests, the season of survey plays an important role for the laser penetration capacity, which is reduced by the presence of the foliage cover. Moreover, geometric LiDAR parameters like the laser beam dimension, the flight altitude and the scan angle should be taken into consideration but, as constant flight setting, are not considered here. This specific capacity of the LiDAR measurements in penetrating the canopy can be studied in terms of ground point number variation through the dataset. On the basis of this assumption, a Laser Penetration Index (LPI) (5) was defined as follows:

$$LPI_{ij} = G_{ij} / (G_{ij} + V_{ij}) \quad (5)$$

Where

G_{ij} = Ground Point Density

V_{ij} = High Vegetation Point Density ($h > 1$ above the ground)

G_{ij} in the denominator allows the normalization of local sampling density due to LiDAR strips overlapping and variations in the helicopter speed. Because of the non-homogenous distribution of LiDAR sampling points in the studied areas, G_{ij} and V_{ij} are calculated on the basis of a neighbourhood analysis by means of an explorative radius which is determined using the initial point sampling density.

An example of LiDAR data elaboration is given below: Ground Point Density and High Vegetation Point Density are reported in Figure 2-Upper and 2-Center, respectively. In the sequence the values are represented using a yellow-blue coloured scale. As normalized index, LPI ranges between 0 and 1, as expected (yellow to blue respectively in Figure 2-Lower). LPI values close to 0 describe dense vegetation while values close to 1 are characteristic of an open stand or clear ground. Intermediate values of the LPI synthesize local variations of the forest in terms of structure and composition. An analysis of the LPI values leads us to the following conclusions:

- The denser the population the less the penetration (this is

particularly true when the same species is considered);

- The laser penetration is lower in the broad-leaved forests than in the coniferous forests if the dataset is surveyed in summer (the opposite is true in autumn, because of the absence of foliage cover);
- A multi-layered forest tends to reduce the LPI values;
- The penetration is generally lower when tall stand or very dense populations are considered.

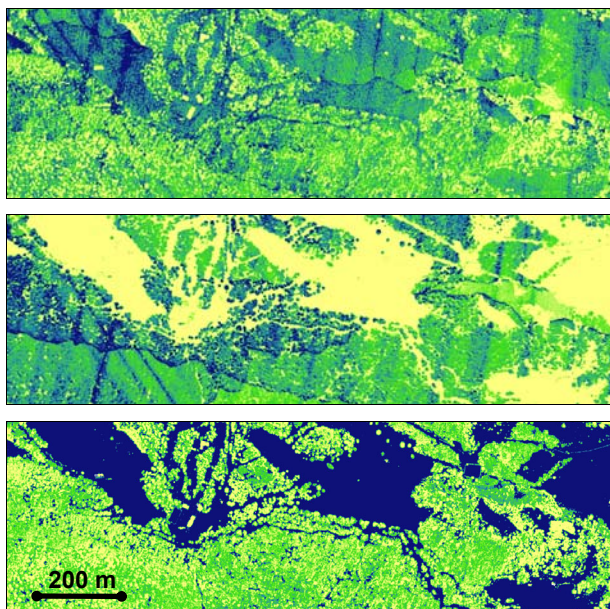


Figure 2 – Penetration index (LPI) elaboration in a mixed forest area. Upper: Ground Point Density map; Center: High Vegetation Point Density map; Lower: Laser Penetration Index.

3.3.2 Crown Height Model (CHM)

The Crown Height Model is a widely used vegetation index allowing the automatic estimation of the forest height, the forest cover and, in the case of multi-temporal surveyed data, the detection of the forestry cover changes. This index can be easily obtained by an algebraic subtraction between the rasterized Digital Surface Model and the Digital Terrain Model (Hyypä et al., 2001). Even though a tendency to underestimate the real heights has been highlighted (Patenaude, 2004), the information on the CHM can be used to interpret the age of the forest. In a natural ecosystem, if the same species is actually considered, the higher the average stand height, the more mature the population, therefore, the lower the density.

3.3.3 Multivariate analysis

Multivariate statistical analysis allows the exploration of the relationship between many different types of attributes. In an unsupervised classification, the features actually at any specified locations are unknown. The structure of the forest can be however derived in a relative way. Reading the spatial variability of the LPI and CHM values it is possible to aggregate each of the locations into one of a specified number of groups or clusters. The following examples (Figure 3) show 9 classes of variability in 3 different forested areas when multivariate analysis is performed using LPI and CHM. The sequence highlights the capacity of the method to separate differently composed areas. Each clustered area corresponds to a different forestry composition. Thus, the multivariate map can be used for an automatic sub-segmentation of the dataset.

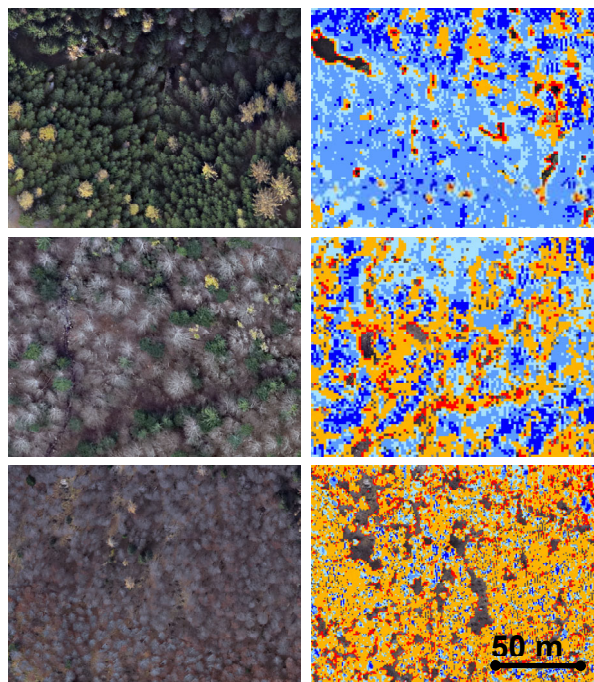


Figure 3 – Examples of multivariate map on three different forested areas. From top to bottom: coniferous forest (spruce with larch.), mixed forest (spruce and beech), broad-leaved forest (beech).

3.4 Dynamic morphological analysis

A dynamic process which considers the multivariate values was implemented allowing the local application of morphological methods previously described. On the basis of the classified index values, a double entrance table was implemented. The search radius is considered as the independent variable which value is empirically determined. Moreover, independently from the stand characteristics, the local density of laser points was taken into consideration for tree extraction processes. This further variable was introduced by performing a triple-entrance table. This means that, for each class of laser density, a double entrance table was implemented. Thus, each location (apex) can be visualized as a point in a multidimensional attribute space whose axes correspond to the represented variables. The method is applied to the preliminary apexes, extracted using the Top Hat algorithm. In this case, a 3×3 kernel (λ) with cell dimension of 0,5 m was used in order to guarantee the maximum degree of efficiency. For each seed apex, the average values of LPI, CHM and laser density are calculated within an explorative surrounding window. The combination of these values furnishes the best value to use as a search radius within each preliminary space location. Afterwards, the search radius procedure is iteratively applied, until the false apexes converge to the correct ones. The convergence procedure is performed until no greater height values are found inside the dynamic-defined search window.

4. RESULTS

The result of the comparison between field trees (see Table 1) and laser extracted trees is reported in Table 3 and Table 4. The former table is related to the fixed radius approach shown in paragraph 3.2.2. In this case, the analysis parameters (λ and radius) were manually determined and optimized according to the real tree locations. The latter table reports the results of the

correlation between field trees and LiDAR-extracted trees when the dynamic search radius method is performed (3.4 chapter).

Plot ID	LiDAR Extracted	Correct dominant	Correct dominated	False positives
FOA	70	85	0	13
FOB	92	100	0	25
MBA	86	68	0	39
MBB	29	63	0	0
MBC	65	81	0	0
MBD	86	88	0	9
PRB	84	82	0	13
PRC	85	76	0	21
SAA	95	83	0	17
TUA	118	100	33	50
TUB	79	85	0	21
TUC	80	71	0	12
VBA	60	83	0	0
PHA	61	61	0	2
PHB	68	68	0	0
PHC	79	79	0	0
PHD	84	81	0	3

Table 3 – Comparison between field tree number and LiDAR-extracted trees using the fixed search radius method. All values are reported in percentage.

Plot ID	LiDAR Extracted	Correct dominant	Correct dominated	False positives
FOA	60	90	0	0
FOB	88	100	12	17
MBA	89	84	0	32
MBB	29	63	0	0
MBC	81	100	0	0
MBD	95	99	0	8
PRB	71	79	0	3
PRC	68	69	0	9
SAA	97	89	0	12
TUA	116	100	38	45
TUB	79	89	0	18
TUC	120	83	0	40
VBA	60	83	0	0
PHA	82	82	0	2
PHB	86	85	0	1
PHC	85	85	0	0
PHD	111	95	0	16

Table 4 – Comparison between field tree number and LiDAR-extracted trees using the dynamic search radius method. All values are reported in percentage.

In the two tables, trees with a diameter which significantly inferior to the surrounding ones are considered “dominated”. Moreover, the apexes which are located 3 meters beyond field surveyed trees are considered “false positives”. In Figure 4, an example of the use of these approaches is given. The green

triangles represent the position of the trees surveyed on site. The red points identify the trees extracted using a fixed search radius, while the black ones, which are tagged with the corresponding radius used, derive from the application of dynamic radius. As can be seen in the image, three more apexes were detected while a false positive one was extracted in this transect.

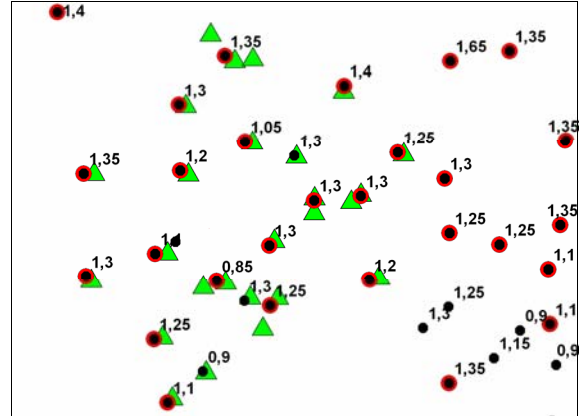


Figure 4 – Example of dynamic search radius application in the MBC transect. The green triangles are the real trees and the black points the extracted trees using a dynamic approach. The apexes, extracted using the fixed-radius method, are shown in red.

A summary of the percentage differences between the two approaches is given in Table 5.

Plot_ID	Diff. correct dominant (%)	Diff. correct dominated (%)	Diff. false positives (%)
FOA	5	0	-13
FOB	0	12	-8
MBA	16	0	-7
MBB	0	0	0
MBC	19	0	0
MBD	11	0	-1
PRB	-3	0	-11
PRC	-7	0	-12
SAA	6	0	-5
TUA	5	5	-5
TUB	4	0	-3
TUC	13	0	28
VBA	0	0	0
PHA	21	0	0
PHB	18	0	1
PHC	5	0	0
PHD	14	0	14

Table 5 – Comparison between percentage of extracted trees using fixed and dynamic search radius methods. The values reported in red show a decreased quality of the results obtained using the dynamic method.

The first column, showing positive values, implies that the dynamic method generally enhances the performance of the tree extraction process. This improvement reaches significant values especially in the case of juvenile forests, characterized by small

diameters, where the population density is very high. The results also seem to improve significantly when the forestry plot is mature and mono-layer structured (even-aged). In this case, the percentage of trees extracted correctly reaches high values, meaning that the most interesting part of the forest (from an above ground biomass content point of view) is extracted in coniferous forests as well in broad-leaved forests. Only two transect (PRB, PRC) show worse results. This is probably due to the insufficient density of the laser survey ($< 1.5 \text{ pts/m}^2$). However, the second column in table 5 is related to the differences regarding trees which were extracted but were in fact "false positive". In this case negative values indicate that the dynamic radius approach is able to maintain a lower level of local overestimations, due to the high variability of laser point distribution. However, this overestimation remains high in the case of juvenile converted broadleaved forests. Within these forestry categories, as the LPI tends to assume minimum values, the corresponding search radius become much small. Further experiments should be done, in order to consider whether the use of denser laser surveys could diminish this kind of error.

5. CONCLUSIONS

An innovative method of laser scanning data processing to automatically detect tree positions is proposed. The method, developed in an open source environment, is based on the automatic determination of the forest structure by means of some LiDAR-extracted vegetation indexes. This information is used to improve the quality and the accuracy of the tree extraction process based on mathematical morphology analysis. The main characteristic of the method is its high flexibility due to the multivariate approach implemented that not only considers the local forest composition but also adapts itself to the relative distribution of the laser sampling points. A field survey campaign in some mountainous geo-referenced plots highlighted the optimal performances of the method as far as the positioning and counting of the dominant trees (the main source of forestry biomass), in both coniferous and broad-leaved forests is concerned. The high percentage values of trees extracted prove the LiDAR to be an interesting and efficient technology in improving the knowledge of the forestry ecosystems and may be useful in the better management of natural resources.

REFERENCES

- Andersen, H.E., Reutebuch, S.E., Schreuder, G.F., 2001. Automated Individual Tree Measurement through Morphological Analysis of a LIDAR-based Canopy Surface Model. *Proceedings of the first International Precision Forestry Cooperative Symposium*, Seattle, Washington.
- Barilotti, A., Turco, S., Alberti, G., 2006. LAI determination in forestry ecosystem by LiDAR data analysis. *Proceedings International Workshop 3D Remote Sensing in Forestry*, pp. 248 - 252, Wien, 14-15 Feb. 2006.
- Barilotti, A., Turco, S., 2006. A 3-D GIS for the sustainable management of forest resources. *Proc. of the 4th Meeting of IUFRO Working Party 8.01.03, Pattern and Processes in Forest Landscapes - Consequences of human management*, pp. 349 - 354, Locorotondo (Italy), 26-29 Sept. 2006
- Barilotti, A., Sepic, F., 2006. Delineazione automatica delle chiome in diverse tipologie forestali attraverso analisi di dati LiDAR. *Atti della 10° Conferenza Nazionale ASITA*, Bolzano (Italy), 14-17 Nov. 2006
- Beinat, A., Sepic, F., 2005. Un programma per l'elaborazione di dati Lidar in ambiente Linux. *50° Convegno Nazionale della Società Italiana di Fotogrammetria e Topografia*, Mondello, (Italy), 29-30 Jun. 2005.
- Morsdorf, F., Meier, E., Koetz, B., Nüesch, D., Itten, K., Allgöwer, B., 2003. The potential of high resolution airborne laser scanning for deriving geometric properties of single trees. In *EGS - AGU - EUG Joint Assembly*, Nice, France. 2003.
- Hyypä, J., Mielonen, T., Hyypä, H., Maltamo, M., Yu, X., Honkavaara, E., Kaartinen, H., 2005. Using individual tree crown approach for forest volume extraction with aerial images and laser point clouds. *ISPRS WG IIIA, V/3 Workshop "Laser scanning 2005"*, Enschede, Sept. 12-14.
- Leckie, D., Gougeon, F., Hill, D., Quinn, R., Armstrong, L., Shreenan, R., 2003. Combined high-density lidar and multispectral imagery for individual tree crown analysis. *Canadian Journal of Remote Sensing* 29, No. 5, pp. 633-649.
- Patenaude, G., Milne, R., Dawson, T.P., 2005. Synthesis of remote sensing approaches for forest carbon estimation: reporting to the Kyoto Protocol. *Environmental Science & Policy*, 8, pp.161-178.
- Persson, Å., Holmgren, J., Söderman, U., Olsson, H., 2004. Tree species classification of individual trees in Sweden by combining high resolution laser data with high resolution near infrared digital images. *Proceedings of the Natscan Conference*, 4-6 Oct. 2004.
- Pitkänen, J., Maltamo, M., Hyypä, J., 2004. Adaptive methods for individual tree detection on airborne laser based canopy height model. *International Archives of Photogrammetry, remote Sensing and Spatial Information Sciences*, Vol. XXXVI - 8/W2.
- Pyysalo, U. and Hyypä, H., 2002. Reconstructing Tree Crowns from Laser Scanner Data for Feature Extraction. *ISPRS Commission III Symposium*, Graz, Austria.
- Serra, J., 1982. Image analysis and mathematical morphology 2. *Theoretical advances*, Academic press, London.
- Tiede, D., Hochleitner, G., Blaschke, T., 2005. A full GIS-based workflow for tree identification and tree crown delineation using laser scanning. *IAPRS, Vol XXXVI, Part 3/W24*, Vienna, 29-30 Aug. 2005.
- Weinacker, H., Kock, B., Heyder, U., Weinacker, R., 2004. Development of filtering, segmentation and modelling modules for LiDAR and multispectral data as a fundament of an automatic forest inventory system. *International Archives of Photogrammetry, remote Sensing and Spatial Information Sciences*, Vol. XXXVI - 8/W2, 2004.

ACKNOWLEDGEMENTS

This work was carried out as a part of the research activities supported by the extended INTERREG IIIA Italy-Slovenia 2003 - 2006 project "Cadastral map updating and regional technical map integration for the Geographical Information Systems of the regional agencies by testing advanced and innovative survey techniques".

REGISTRATION OF TERRESTRIAL LASER SCANS VIA IMAGE BASED FEATURES

Shahar Barnea, Sagi Filin

Dept. of Transportation and Geo-Information Eng., Technion – Israel Institute of Technology, Haifa 32000, Israel
{barneas, filin}@tx.technion.ac.il

Commission V, WG 3

KEY WORDS: Registration, Feature Extraction, Terrestrial Laser Scanner, Point Cloud, Algorithms

ABSTRACT:

The complexity of natural scenes and the amount of information acquired by terrestrial laser scanners turns the registration among scans into a complex problem. This problem becomes even more complex when considering the relatively low angular resolution of terrestrial scanner compared to images, the monotonicity of manmade surfaces that makes the detection of corresponding objects difficult, and the lack of structure of vegetated objects that makes the detection of meaningful features difficult. Since most modern scanners are accompanied with consumer cameras of relatively high quality, it stands to reason making use of the image content for the registration process. Such alternative will benefit from the large body of image based registration work that has been carried out for several decades and therefore has the potential of providing an alternative and simple approach for the registration of pairs and multiple scans simultaneously. In this paper, we study the registration of terrestrial scans via image-based information. For this purpose, we propose an efficient autonomous model that supports the registration of multiple scans. Following the presentation of the model, we analyze its application to outdoor, complex scenes, ones that are common to find in actual laser scanning projects.

1. INTRODUCTION

Terrestrial laser scanners are rapidly becoming a standard technology for 3D modeling in surveying and engineering projects. In most cases, the acquisition of several scans is needed to obtain full scene coverage, and therefore requires the registration of the individual scans into one global reference frame. For the registration, the common practice involves the deployment of artificial targets in the scene as tie objects, with typical targets having the form of spheres, which are easily distinguishable, or reflectors whose high-energy return eases their detection. Following the detection of the tie objects, the rigid body transformation between the coordinate systems can be solved. To avoid manual intervention in the registration process, a growing body of work addresses the problem of autonomous registration in relation to both range images and terrestrial laser scans. The commonly studied model usually involves variants of the Iterative Closest Point (ICP) algorithm family (Besl and McKay, 1992; Chen and Medioni, 1992) that differ in the features toward which distances are minimized (see e.g., Rusinkiewicz and Levoy, 2001), and the numerical framework that is being used (e.g., Mitra et al., 2004; Pottmann et al., 2006). Dalley and Flynn (2002) sort the iterative algorithms by their robustness to initial pose parameters, rate of convergence, and by their sensitivity to outliers. For reasons such as existence of local extrema in the solution space, existence of outliers, occlusions, and lack of information regarding the point distribution in the object space, no guaranty can be given that convergence to the actual solution is reached unless the iterations begin close enough.

As the iterative methods require good initial pose parameters, autonomous techniques for their approximation have been proposed for range images of relatively simple objects, with well-defined shape and structure, and high-level of connectivity (see e.g., Gelfand et al., 2005; Huber, 2002; Huang et al., 2006). A small number of works address the actual complexity of terrestrial laser scans. Bae and Lichti (2004) are using a variation in curvature as the matching criterion on local points. This requires the computation of the normal vector and the curvature itself. Dold and Brenner (2006) propose an

autonomous matching procedure that is based on planar patches. Following their extraction, patches from different scans are matched subject to geometric constraints. Gruen and Akca (2005) present a least squares matching based registration scheme. The reported algorithm is more stable than the classic ICP, but still requires an initial transformation.

The registration of terrestrial laser scans can be aided by the images that are usually acquired simultaneously with the range data. Images enjoy high spatial resolution, and record color content of the scene, which is usually very rich and diverse. The role of image content for realistic texture rendering suggests that the tight link between the two sensors is only due to increase. As such, it provides an alternative candidate to form the registration process of laser scans. Image based registration also benefits from the vast amount of research that has been devoted to the registration problem. Registration of laser scans supported by images received indeed some attention in recent years. Ulirsch et al. (2003) define a framework to integrate image information with scanning data. Kang et al. (2007) propose using the Moravec operator and cross correlation as a means to find point correspondence between images and use those for the registration phase. Al-Manasir and Fraser (2006) suggest using relative orientation between images for scans registration supported by the placement of artificial, signalized, targets. Seo et al. (2005) present an approach that uses image-matching schemes on relatively small scenes acquired by a table scanner. Finally, Liu et al. (2006) consider a more general framework with no rigid attachment between the camera and the scanner but with the imposition of some specific geometric constraints.

Since image-based content is only an integral part of most laser scanning systems, it stands to reason investigating the potential in the registration of laser scans using intensity information. Normally, such registration will be purely image based (e.g., via bundle adjustment), where images will be mutually matched and simultaneously solved. However, laser-scanning projects usually acquire data from a relatively wide base, and therefore, especially in open scenes, only a limited number of images overlap between scans, particularly for establishing a strong



Figure 1. Top: panoramic view of the scanned scene as acquired by a camera mounted on the scanner (for the original images see Figure 5), Bottom: Polar representation of terrestrial laser scans; the horizontal and vertical axes of the image represent the values of θ , φ respectively and intensity values as distances ρ (bright=far). "No-return" and "no-reflectance" pixels are marked in red.

photogrammetric image block. Additionally, image based registration will relate to object space by up to a scale factor. Therefore, establishing this link requires a subsequent registration, and if autonomous registration is of concern, such registration should relate to the laser point cloud.

The approach proposed here is based on using the direct relation between the acquired images and the laser data (see Fig. 1), but instead of solving a block of images it solves a set of rigid body transformations, which are more robust, efficient, and require a small subset of points. The model applies to the registration of pair of scans as well as multiple scans and assumes no support in the form of artificial targets or a priori scanning pose parameters. Essentially the assumption is that a digital camera is attached to the laser scanner equipment and is calibrated with respect to it. Our objective is to utilize both the relatively robust geometric models for the registration of 3D scans with the powerful techniques of keypoint image matching as a means to generate the initial set of correspondences. Our aim is to develop an algorithm that can handle the data volume and the expected complexity of the scanned scenes. To make the registration more reliable and robust we make use of the known calibration between the laser scanner and the imaging system to treat the problem in a dual manner – extracting features and matching them in 2D image space but computing the actual transformation between the scanners, in 3D space. With the proposed model, we test the applicability of the model to the registration of terrestrial laser scans. We analyze the advantages and disadvantages of image supported terrestrial laser scans registration. The results provide an insight into how these sources of information can be used jointly for the registration of terrestrial laser scans.

2. METHODOLOGY

Generally, there are two reference frames involved in the model – the image reference frame (and there are n images acquired per scan), and the scanner reference frame. Essentially, our objective is to recover the scanner pose parameters, using the

image content. Such problem can be approached in two ways: i) solving the image (relative) pose parameters and then computing the scanner pose parameters using a boresight transformation, see e.g., Al-Manasir and Fraser (2006), and ii) using the boresight computation between scanner and images to find the local 3D point coordinates and computed directly the scanner pose parameters using a rigid body transformation.

While the first approach offer slight advantages in terms of the quality of the matched entities (therefore, leading to better registration accuracy) it leads to a more complex framework involving the simultaneous orientation of multiple images. In contrast, the second approach that estimates a rigid body transformation, involves only a single transformation per scan, one that is relatively easier to compute.

2.1 Camera to scanner registration

The camera mounted on top of the scanner can be linked to the scanner body by finding the transformation between the two frames shown in Figure 2. Such relation involves three offset parameters and three angular parameters. This relation can also be formulated via the projection matrix P . With P a 3×4 matrix that represents the relation between world 3D point (X) and image 2D point (x) in homogeneous coordinates. Compared to the six standard boresighting pose parameters, the added parameters (five in all) will account to interior orientation parameters. The projection matrix can be formulated as follows:

$$x = KR[I \mid -t]X = PX \quad (1)$$

with

$$K = \begin{bmatrix} f_x & s & x_0 \\ & f_y & y_0 \\ & & 1 \end{bmatrix}$$

f_x and f_y are the focal lengths in the x and y directions respectively, s is the skew value, x_0 and y_0 are the perspective offset across the two image axes. R is the rotation matrix

between the scanner and the camera reference frames (the red and the blue coordinate systems in the figure respectively) and t the translation vector (Hartley and Zisserman, 2003).

For the estimation of the relative pose offset between the scanner and the camera image, points for which well-defined 3D laser points exist are selected. Using the laser points as control information allows computing the projection matrix directly and linearly. In this regard, we point that the calibration of the lens distortion parameters (radial and decentring) will provide an even better accuracy. At each scanning position, n images are acquired in predefined “stops” along the scan (e.g., every $360/n$ degrees). For each image, the projection matrix, P , represents the relation between the image and the scan. The proposed model assumes that, i) the camera is rigidly mounted to the scanner, ii) the interior camera parameter are fixed and known, and iii) the acquisition position is fixed across all scanning positions. These standard assumptions enable using the same projection matrices for all images in the same “stop” in different scans.

2.2 Detection of corresponding points

Finding an image points correspondence has been an active research for several decades. Mikolajczyk and Schmid (2004) present a comparative review of the modern methods, and note that they are composed of two fundamental steps: extraction, and matching. The goal of the extraction phase is to detect keypoints (sometimes terms interest points) in a repeatable manner. The challenge in this stage is to yield high repeatability rate even under extreme viewpoint, resolution, and exposure changes (e.g., brightness and contrast). The goal of the matching phase is to find correspondence among the keypoints that were extracted from the different images. For this purpose, descriptors that provide distinctive characterization of the keypoint are used. Following the generation of a descriptor for each detected keypoint, the matching is performed by searching for similar descriptors in different images and upon finding them, recording them as candidate tie-points. The challenge in the matching phase is to design a descriptor that offers unique and descriptive features while being insensitive to small detection errors and perspective deformation. Following the generation of proposed correspondences phase, some correct and some not, comes the computation of the transformation between the images. This will usually be driven by the Random Sampling Consensus (RANSAC) algorithm (Fishler and Bolles, 1981). An important aspect in the application of the RANSAC algorithm is the minimal number of points required to compute the hypothesis transformation in each iteration. This number affects the number of required iterations and thus, the chances to finally converge to the correct solution. In this regard, one should prefer a geometric model with a small set of points to calculate the hypothesis transformation.

For the extraction of keypoints and their descriptors, we make use of the Scale Invariant Feature Transform (SIFT) that was proposed in Lowe (2004), and was applied in photogrammetry in Shragai et al. (2005), and Läbe and Förster (2006).

2.3 Scale Invariant Feature Transform

The Scale Invariant Feature Transform - SIFT (Lowe, 2004) is a methodology for finding corresponding points in a set of images. The method designed to be invariant to scale, rotation, and illumination. The methodology consists of the following four steps:

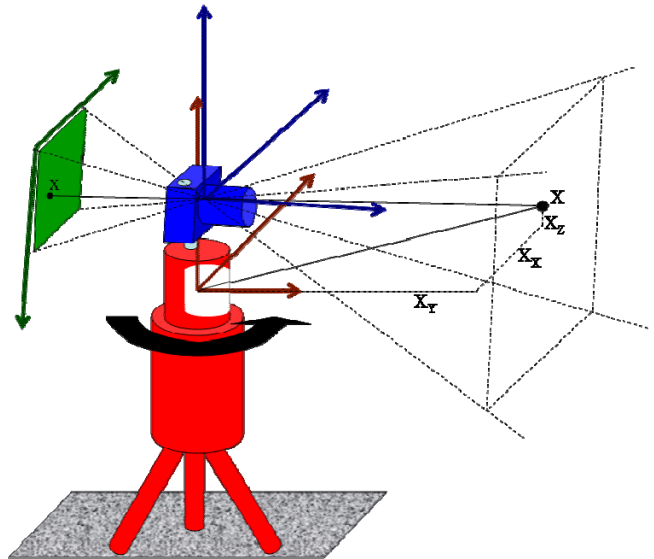


Figure 2. Reference frames of the scanning system with a mounted camera.

1. Scale-space extrema detection – using the difference of Gaussian (DoG), potential interest points are detected.
2. Localization – detected candidate points are being probed further. Keypoints are evaluated by fitting an analytical model (mostly in the form of parabola) to determine their location and scale, and are then tested by a set of conditions. Most of them aim guaranteeing the stability of the selected points.
3. Orientation assignment – orientation is assigned to each keypoint based on the image local gradient. To ensure scale and orientation invariance, a transformation (in the form of rotation and scale) is applied on the image keypoint area.
4. Keypoint descriptor – for each detected keypoint a descriptor, which is invariant to scale, rotation and changes in illumination, is generated. The descriptor is based on orientation histograms in the appropriate scale. Each descriptor consists of 128 values.

With the completion of the keypoint detection (in which descriptors are created), the matching process between images begins. Matching is carried out between the descriptors, so the original image content is not considered here. Generally, for a given keypoint, matching can be carried with respect to all the extracted keypoints from all images. A minimum Euclidian distance between descriptors will then lead to finding the correspondence. However, matching in this exhaustive manner can be computationally expensive (i.e., $O(N^2)$ with N the number of keypoints). Common indexing schemes cannot be applied to improve the search here because of the descriptors dimensionality. However, an indexing paradigm, called Best Bin First (BBF) can be applied (Lowe, 2004). The BBF algorithm reduces the search to a limited number of the most significant descriptors values and then tries locating the closest neighbor with high probability. Compared to the exhaustive matching, this approach improves the performance by up to two orders of magnitude, while difference between the amounts of matched points is small. Our proposed solution follows Brown and Lowe (2003) where all key points from all images are organized in one K-d tree. Once a set of matching points has been generated, another filtering process is applied.

Figure 3 shows the keypoints extracted in a scene that mixes structured and unstructured objects, the squares around each keypoint illustrates the scale in which it was detected and the small vector, its orientation.

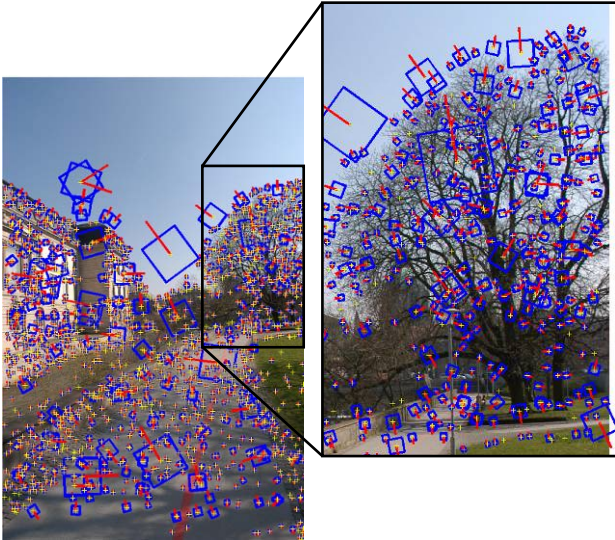


Figure 3. SIFT keypoints with orientation and scale.

2.4. Linking the laser scans and the image information

Since the registration scheme is based on a rigid body transformation, the extraction of keypoints in image space should now be transferred into the local 3D object space. Generally, this transfer requires tracing the ray into object space. However, we apply here a back projection of the 3D point cloud onto the image using the boresight parameters that were derived in the calibration phase (see Section 2.1). We then assign the 3D coordinates of the relevant laser point to the keypoints. The result of the back-projection of the laser point cloud into the imaging system reference-frame is demonstrated in Figure 4. Notice that vegetation expression in the range image compared to intensity one.

The 3D coordinate assignment is not immediate, however. Keypoints are defined by their position and scale (window size), therefore, for each keypoint, candidate 3D coordinates are collected from the scale dependent corresponding window (see Figure 3). Generally, the coordinate assignment problem can be partitioned into two cases the first is when the point falls on a solid object; the second is when the point falls between surfaces. In the first case, we assign the nearest 3D coordinate in terms of angular distance between the keypoint direction and laser point direction, while in the second we assign the 3D coordinates of the point closest to the imaging system. The motivation for this is as follows, for solid objects the keypoint location is well defined and, therefore, the nearest 3D point will have the smallest bias among all candidates (we note that some refinement to the ray direction can be applied, but this is negligible). For the other case, with lack of any other information we opt toward assigning the closest distance within the candidate 3D points under the realization that it is the foreground object, which is likeliest to do with the detection of the point as keypoint. Differentiation between the two cases is achieved by computing the *std.* of the 3D points' depth.

2.5 Registration between scans

With the candidate matches, the registration of the laser scan becomes an estimation problem of the rigid body transformation,

$$X = X_0 + (I + S)^{-1}(I - S)x \quad (2)$$

where I is a 3x3 identity matrix, and S is an skew-symmetric matrix, defined as:

$$S = \begin{bmatrix} 0 & c & -b \\ -c & 0 & a \\ b & -a & 0 \end{bmatrix}$$

The transformation can be estimated linearly using such methods as the one proposed in Horn et al. (1988). Since some of the proposed matches are outliers, a RANSAC solution guides the parameter estimation. One of the appealing properties of the registration based on the rigid body transformation is that only three points are needed to generate a hypothesis. Therefore, even if a small fraction of inliers is assumed, the number of trials will be controllable and very efficient. Choosing the relative orientation option and using, for example, the well-known eight-point algorithm to estimate the fundamental matrix (Hartley and Zisserman, 2003) will obviously have a much higher cost under a small fraction of inliers assumption.



Figure 4. Depth image calculated to fit the original image, left: the depth image, right: the original image. Because the spatial resolution of the laser point cloud is much sparser than the image resolution (0.12° compared to 0.03° here) filling of depth image was applied for demonstration purposes only.

3. RESULTS

To demonstrate our approach we test the proposed algorithm on three scans acquired in a row by Riegl 360. The image sequences of the three scans are presented in Figure 5. The distance between the scanners is 8.15, and 22.28 [m] respectively, and the maximal scanning range ~ 100 [m]. Six mega-pixel size images acquired by the Nikon-D100 were processed in full resolution. For each image SIFT keypoints were extracted with 4,000-11,000 keypoints per image evaluated for the matching. Figure 3 shows a typical set of keypoints (with some pruning for visual clarity). Matches are then evaluated between each image in a scan to all seven images in the counterpart scan (for multiple scans a similar procedure will apply). Tables 1, 2 list the number of matches (descriptor wise) between each image in one scan and the images in the other. Even though Table 1 has a dominant diagonal, the structure of the match matrix is arbitrary and depends on similarity between the images in the scans. Figure 5 clearly shows why the first set is diagonal dominant. Figures 6 (top and center) shows the matched keypoints between the pair of sixth images in set 1-2. Generally most matches are correct, but some outliers can be

seen, e.g., point 134 (encircled) that has no counterpart. Figure 6(bottom) shows the matched keypoints between image 7 of scan 2 and 3 of scan 3. One can see that the number and quality of the matches is relatively poor compared to the first pair. Overall, 1256 matched points (sum of all values in the table) were found all scans in set 1-2, and 123 points between 2 and 3. For each matched keypoint, 3D coordinates are assigned (see Section 2.3). Image pairs with less than four matched points are overlooked due to the realization that such a small number is most likely the result of lack of overlap between the images with only accidental matches found (this was also validated by manual inspection). This further pruning reduces the number of matched keypoints to 1219 and 68 matches respectively. Following the assignment of the 3D coordinates to the matched keypoint comes the RANSAC guided 3D rigid body transformation.

Table 1: number of matches, scans 1 & 2 –baseline 8.15 [m]

		scan 2						
		img #	1	2	3	4	5	6
scan 1	1	4	6	4	0	1	3	0
	2	4	1	11	3	4	3	3
	3	0	5	16	5	0	3	0
	4	0	1	2	35	36	2	4
	5	4	1	1	0	347	115	6
	6	2	3	4	0	55	414	38
	7	5	2	1	0	2	4	96

Table 2: number of matches, scans 2 & 3 –baseline 22.28 [m]

		scan 3						
		img #	1	2	3	4	5	6
scan 2	1	3	2	1	1	2	0	2
	2	0	2	1	1	2	2	2
	3	0	3	0	6	2	4	1
	4	3	5	0	0	3	5	0
	5	0	12	4	8	1	2	2
	6	1	6	7	4	0	2	0
	7	0	2	13	3	2	1	0

Out of 1219 proposed matches, 979 were found correct (amount to 80.3% of the proposed matches) for set 1-2. In contrast, out of the initial 68 candidates in the 2-3 scan, 18 proposed correspondences were found (amounts to 26.5%). The differences in correct correspondences reflects the change in the baseline between the scan pair (8 compared to 22 [m]). The comparison of the estimated parameters to manual calculation, considered as ground truth, shows that the translation error on the scanning position is on order of 0.65 [m] for the first pair and 1.15 [m] for the second one; the angular error was (0.12, 0.3, 0.01) [°] for ω, ϕ, κ angles respectively and (0.18, 0.07, 1.09) for the second. Those offsets can related to errors that are accumulated in the course of the process (calibration errors, image to range data conversion errors and matching accuracy errors). However, these values are good enough to launch an ICP procedure between the point clouds, which is advisable to perform for tuning the registration.

4. CONCLUSIONS

The registration results of the two scans show the great potential of registration via images. As the paper has demonstrated when considering the image-based registration problem between scans as a platform for an eventual rigid body transformation, the rich image-based information (extracted keypoints) allows using

homologous registration candidates which wouldn't have been naturally detected using any of the range data registration methods one finds. The rigid body transformation also allows using small subsets of points for the RANSAC hypothesis generation, thereby allowing greater flexibility in the feature extraction phase.

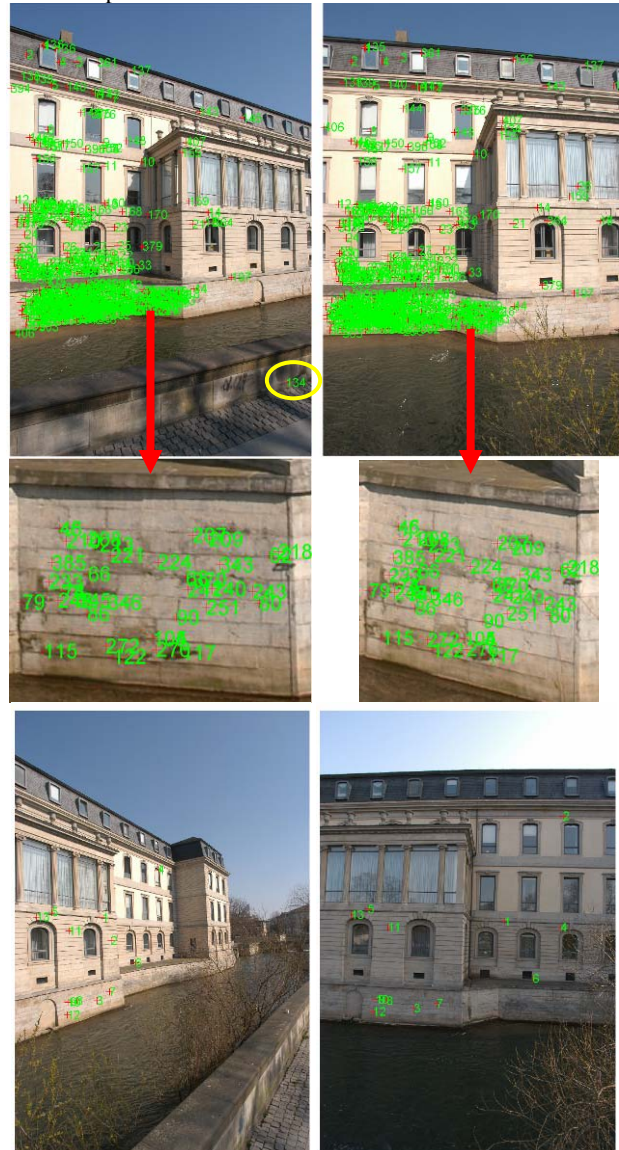


Figure 6. Matched keypoints between images pairs, up) from scans 1-2, center) blowup showing the quality of the matches, bottom) matches from scan 2-3 the different viewing geometry dropped the number of matches.

5. ACKNOWLEDGEMENT

The authors would like to thank Dr. Claus Brenner for making the data used for our tests available.

6. REFERENCES

- Al-Manasir K., Fraser C., 2006. Registration of terrestrial laser scanner data using imagery. *Photogr. Rec.* 21 (115), 255–268.
- Besl P., McKay N., 1992. A method for Registration of 3-D Shapes. *IEEE Transactions on Pattern Analysis and Machine Intelligence*, 14 (2), 239–256.
- Brown M., Lowe G. D., 2003. Recognising Panoramas. *International Conference on Computer Vision*. Nice, France, 1218-1227



Figure 5. Image sequences of the three scans

Chen Y., Medioni G., 1992. Object Modeling by Registration of Multiple Range Images. *Image Vision Comp.* 10(3), 145-155.

Dalley G., Flynn P., 2002. Pair-wise range image registration: a study in outlier classification. *Computer Vision and Image Understanding archive*, 87 (1-3), 104–115.

Dold C., Brenner C., 2006. Registration of Terrestrial Laser Scanning Data using Planar Patches and Image Data. *International Archives of Photogrammetry, Remote Sensing and Spatial Information Sciences* 36 (Part 5), 25–27.

Fischler M.A., Bolles R.C., 1981. Random Sample Consensus: A paradigm for model fitting with application to image analysis and Automated Cartography. *Communication Association and Computing Machine*, 24(6), 381-395.

Gelfand, N., Mitra, N. J., Guibas, L. J., Pottmann, H. 2005. Robust global registration. *Proceedings of the Third Eurographics Symposium on Geometry Processing*, Vienna, Austria 4-6 July, 2005, pp. 197-206.

Gruen A., Akca D., 2005. Least squares 3D surface and curve matching. *ISPRS J. of Phot. and Rem. Sens.*, 59(3), 151–174.

Hartley R., Zisserman A., 2003. *Multiple View Geometry in Computer Vision*. Cambridge University Press, Second Edition.

Horn B., Hilden H.M., Negahdaripour S., 1988. Closed-form solution of absolute orientation using orthonormal matrices. *Journal of the Optical Society of America* 5 (7), 1127–1638.

Huang Q.X., Flvry S., Gelfand N., Hofer M., Pottmann H. 2006. Reassembling Fractured Objects by Geometric Matching. *ACM Trans. on Graphics* 25 (3), 569–578.

Huber D., 2002. Automatic three-dimensional modeling from reality. PhD thesis, Carnegie Mellon University.

Kang Z., Zlatanova S., Gorte B., 2007. Automatic Registration of Terrestrial Scanning Data Based on Registered Imagery. *FIG Working Week 2007, Hong Kong SAR, China*, 13-17 May.

Läbe, T., Förstner, W., 2006. Automatic relative orientation of images. *Proceedings of the 5th Turkish-German Joint Geodetic Days*, March 29th - 31st, 2006, Berlin,

Liu L., Stamos I., Yu G., Wolberg G., Zokai S., (2006) *Multiview Geometry for Texture Mapping 2D Images Onto 3D Range Data*, IEEE Computer Society Conference on CVPR, New York, 17-22 June, Vol. 2 pp. 2293–2300.

Lowe D. G., 2004. Distinctive Image Features from Scale-Invariant Keypoints. *IJCV* 60(2), 91-110.

Mikolajczyk K., Schmid C., 2004. Scale & Affine Invariant Interest Point Detectors. *IJCV* 60 (1), 63–86.

Mitra N. J., Gelfand N., Pottmann H., and Guibas L., 2004. Registration of point cloud data from a geometric optimization perspective. *Proceedings of the 2004 Eurographics/ACM SIGGRAPH Symposium on Geometry Processing*, 23-32.

Pottmann H., Huang Q. X., Yang Y. L., Hu S. M., 2006. Geometry and convergence analysis of algorithms for registration of 3D shapes. *IJCV* 67 (3), 277–296.

Rusinkiewicz S., Levoy M., 2001. Efficient variants of the ICP algorithm. In: *Proceedings 3rd International Conference on 3D Digital Imaging and Modeling*, pp. 145–152.

Seo J. K., Sharp G. C., Lee S. W., (2005) *Range Data Registration Using Photometric Features* IEEE Computer Society Conference on CVPR, 20-25 June, Vol. 2. 1140–1145.

Shragai Z., Barnea S., Filin S., Zalmanson G., Doytsher Y., 2005. Automatic Image Sequence Registration Based on a Linear Solution and Scale Invariant Keypoint Matching. *International Archives of Photogrammetry and Remote Sensing*. 36(3/W36): 5-11.

Ullrich, A., Schwarz, R., H. Kager, 2003. Using Hybrid Multi-Station Adjustment for an Integrated Camera Laser-Scanner System. in *Proc. of Optical 3D Meas. Tech. VI*, Zurich, Switzerland, 298-304.

TOWARDS THE ESTIMATION OF TREE STRUCTURAL CLASS IN NORTHWEST COASTAL FORESTS USING LIDAR REMOTE SENSING

C.W. Bater^{a,*}, N.C. Coops^a, S.E. Gergel^b, N.R. Goodwin^a

^aIntegrated Remote Sensing Studio, Department of Forest Resources Management

^bDepartment of Forest Sciences and Centre for Applied Conservation Research

Faculty of Forestry, University of British Columbia, 2424 Main Mall, Vancouver, British Columbia, V6T 1Z4, Canada
nicholas.coops@ubc.ca, cbater@interchange.ubc.ca, sarah.gergel@ubc.ca, ngoodwin@forestry.ubc.ca

KEY WORDS: Lidar, Forest Structure, Forest Biodiversity, Wildlife Tree Class, Decay Class, Snags

ABSTRACT:

The amount and variability of dead wood in a forest stand is an important indicator of forest biodiversity, and relates to both the structural heterogeneity and the amount of habitat available for biota. In this study, we investigate the capacity of light detection and ranging (lidar) technology to estimate the percentage of dead trees in coastal forests on Vancouver Island, British Columbia, Canada. Twenty-two field plots were established from which the tree structural classes, or wildlife tree (WT) classes, of all stems (DBH > 10 cm) were estimated. For each plot, the frequency distributions of the WT classes were highly skewed, so lognormal distributions were fitted, and the means (μ) and standard deviations (σ) of the log-transformed data were extracted. The relationship between μ and the percentage of dead trees within the plots was highly significant ($r^2 = 0.77$, $p < 0.001$). A variety of metrics were extracted from the lidar vegetation returns and compared against μ , and results indicated that the natural logarithm of the coefficient of variation was the best predictor ($r^2 = 0.75$, $p < 0.001$), followed by the heights of the 20th percentile ($r^2 = 0.69$, $p < 0.001$). In general, results indicated that the lowest lidar height percentiles were more significant predictors of μ , which is likely based on the direct linkage between the number of dead trees in a stand and its canopy architecture.

1. INTRODUCTION

The Canadian province of British Columbia contains approximately half of the country's softwood lumber inventory, and in 2005 the forestry industry was responsible for 45% of the province's manufacturing shipments (BC Stats 2005). While forestry's economic benefits are significant, extraction must be performed in a sustainable manner. In response to this need, the Province of British Columbia has developed a suite of resource values to monitor forest health and sustainability, such as biodiversity, timber, and soil, amongst others.

Each resource value is assessed by monitoring a number of indicators, such as tree height, diameter at breast height (DBH), species richness, and wildlife tree (WT) class (or decay class), which are traditionally measured using field-based approaches in association with aerial photography. Field assessments, however, can be expensive, labour intensive, provide small sample sizes and intensity, and often cover only limited geographic areas, while aerial photography suffers from time and cost issues, is prone to operator bias and subjectivity, and is limited by a shortage of trained interpreters. As a result, there has been increased interest in augmenting ecosystem and timber inventory mapping initiatives using digital remote sensing technologies, including recent research into light detection and ranging (lidar).

Various measures of forest structure and biodiversity have previously been estimated within the context of coastal northwest forests using lidar (e.g. Lefsky et al., 1999; Hudack et al., 2002; Anderson et al., 2005; Lefsky et al., 2005a; Lefsky et al., 2005b; Coops et al., 2007). Seielstad and Queen (2003) discussed the ability of lidar to characterise fuel bed roughness

in forests in the western United States, and noted that the direct estimation of coarse woody debris loads may be achievable. One important variable that has not been examined, however, is the decay class or structural life stage of the tree, which captures the growth form of the current individual tree, from young vigorous trees, to older large live trees and veterans, to standing dead snags, to broken stems in various stages of decay. Within British Columbia the form classification is known as the wildlife tree class, which when accumulated over a stand provides an indication of the amount of dead trees and their state of decay. The amount and variability of dead wood is an important indicator of forest biodiversity (Noss, 1999). Snags are a critical component of coastal forests, increasing structural heterogeneity and providing habitat for forest biota (Clayoquot Sound Scientific Panel, 1995). The goal of this paper was to estimate the percentage of dead trees within plots in unmanaged forests by developing statistical relationships between plot-level distributions of WT class and lidar-derived vegetation metrics.

2. METHODS

2.1 Area of Investigation

Our investigation focused on the Kennedy Flats, Clayoquot Sound, Vancouver Island, British Columbia, Canada, (49°0'35" N, 125°37'21" W). Clayoquot Sound includes both mature first and second growth forest. The area is classified as Coastal Western Hemlock (CWH) zone, based on the Biogeoclimatic Ecosystem Classification (BEC) system (Meidinger and Pojar 1991), and has been mapped using the province's Terrestrial Ecosystem Mapping (TEM) classification system, which is derived from 1:20,000 to 1:50,000 aerial photography (Mitchell

* Corresponding author

et al., 1989; Demarchi et al., 1990). Based on the TEM classification system, the area encompasses the full range of forest structural stages from shrub and herb (14% of total area), pole and sapling (32%), young forest (4%), and old forest (46%).

2.2 Field Data Collection

Field data were collected in 2005 and 2006 from 22 forest plots ranging from pole/sapling to old forest based on the TEM classification (Table 1). Five of the old forest plots were located in variable retention harvest blocks. Data were collected from 625 m² or greater rectangular plots, with plot centres and corners mapped at a horizontal accuracy of approximately 1-5 m using a post-processed differentially corrected GPS (Trimble GeoXT). For each stem with a DBH > 10 cm, distance and bearing from plot centre, tree height, DBH, and species were recorded, with crown dimensions measured for every fifth tree. For conifers, the WT class was estimated using a field sheet showing growth and decay stages ranked 1 through 9: classes 1-2 were living trees; 3-5 were dead trees with hard wood; 6 represented dead trees with broken tops and spongy wood; 7 and 8 were dead trees with broken tops and soft wood; and class 9 represented dead and fallen trees.

Variable	Pole/Sapling n = 5 (mean/range)	Young Forest n = 3 (mean/range)	Old Forest n = 12 (mean/range)
Stems ha ⁻¹	1491 / 1544	1147 / 816	957 / 1391
Basal Area (m ² ha ⁻¹)	144.9 / 127.3	84.1 / 36.8	142.3 / 372.6
Mean Height (m)	19.3 / 5.3	18.3 / 3.9	12.6 / 12.6
Standard Deviation of Height (m)	6.1 / 2.0	5.1 / 1.3	6.33 / 12.1
Maximum Height (m)	32.5 / 18.0	25.8 / 4.7	27.0 / 30.4
Mean DBH (cm)	27.8 / 12.8	25.6 / 5.5	31.3 / 37.2
Maximum DBH (cm)	107.6 / 106.8	125.7 / 98.9	170.5 / 343.2
Standard Deviation of DBH (cm)	17.2 / 13.7	15.8 / 5.4	29.4 / 63.4
Dead Trees (WT Class 3+) (%)	12.0 / 18.1	13.1 / 9.0	19.6 / 12.1

Table 1. Summary statistics for sample plots by age class for stems with a DBH > 10 cm. Two outliers were excluded from this summary and all subsequent analyses.

Initial examination of the field data indicated that two plots were outliers and excluded from analysis. The first was composed of extremely dense overstocked conifer and

contained no lidar ground returns; the second was located in a stand which had experienced significant disturbance, possibly from insect infestation, resulting in a stand structure not replicated in the dataset.

2.3 Fitting Lognormal Probability Density Functions to WT Class Data

For all plots, the majority of the trees were living (WT classes 1 and 2), with the small remainder being dead and in various stages of decay (WT classes 3-9), resulting in skewed distributions. Lognormal distributions may be fitted to data that are highly skewed, which is a common problem across the biological sciences (Limpert et al., 2001). A random variable (x) has a lognormal distribution if log(x), usually the natural logarithm, is normally distributed. For each plot, lognormal probability density functions (PDFs) were then fit to the frequency distributions of WT classes using the following equation:

$$f(x) = \frac{1}{x\sigma\sqrt{2\pi}} * \exp\left(-\frac{(\ln(x) - \mu)^2}{2\sigma^2}\right) \tag{1}$$

where f(x) = the lognormally distributed variable
 μ = mean of x or scale parameter
 σ = standard deviation of x or shape parameter

The μ and σ parameters are related to the frequency distribution of WT class of a given plot in similar ways. Stands containing large numbers of healthy living trees (e.g. WT class 1) tend to have small values for μ and σ. Increases in the percentages of dead trees, however, particularly in the more advanced stages of decay, will cause increases in both parameters (Figure 1).

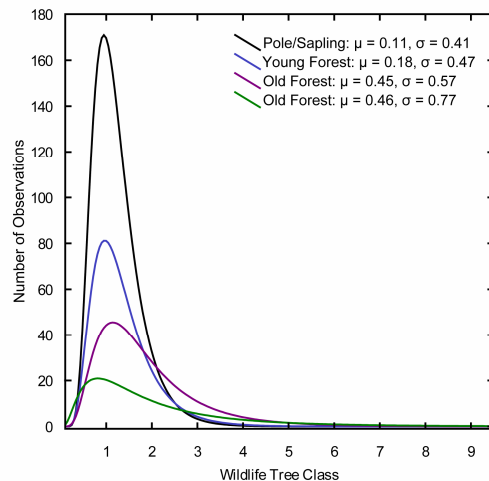


Figure 1. Examples of lognormal distributions fit to WT class frequencies in one pole/sapling, one young forest, and two old forest plots. Note increases μ and σ as stand age increases.

The lognormal μ and σ parameters were compared to the percentages of dead trees (WT classes 3-9) within each plot using linear regression techniques. These parameters were then

used as proxies to represent the percentage of dead trees within each plot.

2.4 Lidar Data Collection and Variable Extraction

Small footprint laser data were collected during July 2005 by Terra Remote Sensing (Sidney, British Columbia), using a TRSI Mark II two-return sensor onboard a fixed-wing platform. Flying at a mean height of 800 m above ground level, the survey was optimized to achieve a nominal point spacing of one laser pulse return every 1.5 m² (Table 2). Ground and non-ground returns were separated using Terrascan v 4.006 (Terrasolid, Helsinki, Finland).

Sensor and Survey Parameters	Value
Sensor Type	TRSI Mark II discrete return sensor
Number of Returns	Two, first and last
Beam Divergence Angle (mrad)	0.5
Wavelength (nm)	1064
Mean Flying Height Above Ground (m)	800
Pulse Frequency (kHz)	50
Mirror Scan Rate (Hz)	30
Scan Angle (degrees)	±23
Mean Footprint Diameter (m)	0.4

Table 2. Lidar sensor and survey parameters.

A 0.5 m spatial resolution digital elevation model (DEM) was created by applying a natural neighbour interpolation algorithm to the ground returns (Sibson, 1981; Sambridge et al., 1995). The heights of the vegetation returns above the ground were then computed by subtracting the DEM heights from the vegetation return heights. A large number of variables were extracted from the lidar vegetation data based on Gobakken and Næsset (2005), and Næsset (2002; 2004), but without removing returns below a height threshold. These variables attempt to capture vertical structure by classifying hits into percentiles based on their height distribution through the forest canopy, and included the 5, 10, 15... 95 percentiles, in addition to the means, maximums, standard deviations, and coefficients of variation of vegetation return heights within each plot. The natural logarithms of the cases of each variable were also computed.

2.5 Data Analysis

The lidar-derived variables were compared to the lognormal parameters for the WT class distributions using both correlation analyses and simple regression approaches to test the significance of these relationships.

3. RESULTS

3.1 Predicting the Percentages of Dead Trees with Lidar-Derived Variables.

The best lidar-derived variables for directly predicting the percentages of dead trees in the plots (where 0% indicates a stand contains no dead trees, and 100% is indicative of a stand where all trees are dead and showing some sign of decay) were the natural logarithm of the coefficients of variation ($r^2 = 0.42$, $r = 0.64$, $RMSE = 4.4\%$, $p = 0.0021$) and the heights of the 20th percentiles ($r^2 = 0.39$, $r = 0.62$, $RMSE = 4.5\%$, $p = 0.0033$).

3.2 Lognormal Distribution Parameters and Percentages of Dead Trees

Using the plot-based field observations, the relationship between the percentage of dead trees and the parameters derived from the fitted logarithmic distributions (i.e. μ and σ) were explored. Results indicated that μ (mean of the lognormally distributed variable, or scale) was the best predictor of the percentage of dead trees (Figure 2).

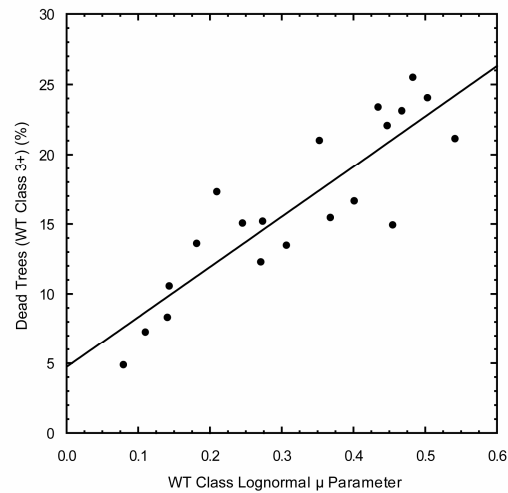


Figure 2. The best predictor of the percentage of dead trees in each plot was the lognormal μ parameter. Model: $r^2 = 0.77$, $r = 0.88$, $RMSE = 2.8\%$, $p < 0.001$; $y = 4.73 + 35.96 * x$

3.3 Predicting the Lognormal μ Parameter with Lidar-Derived Variables

The best predictors of the WT class lognormal μ parameter were the natural logarithm of the coefficients of variation (Figure 3) and heights of the 20th percentiles (Figure 4) The lowest height percentiles, from the 5th to the 35th, were each capable of explaining 60%-70% of the variance in μ , and all were negatively correlated with the parameter. This capacity diminished with increases in the percentiles (Figure 5).

Figure 6 shows the height of the 20th percentile and the percentage of dead trees by structural class. As forest stands increase in age, the percentage of dead trees and the number of canopy gaps increase, allowing lidar pulse returns to penetrate deeper through the forest canopy. The trend of the mean vegetation return height varies closely with that of the 20th

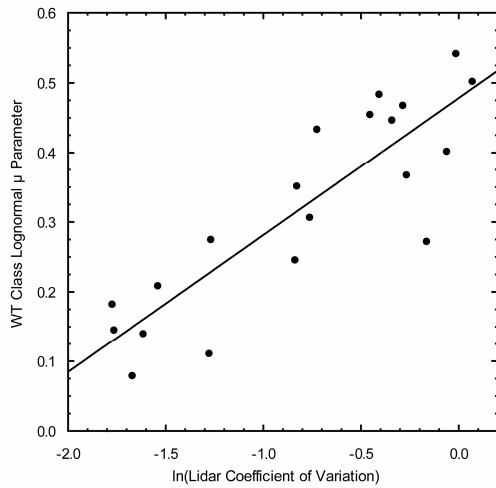


Figure 3. The best predictor of the WT class lognormal μ parameter was the natural logarithm of the lidar coefficient of variation. Model: $r^2 = 0.75$, $r = 0.87$, $RMSE = 0.070$, $p < 0.001$; $y = 0.48 + 0.20 * x$

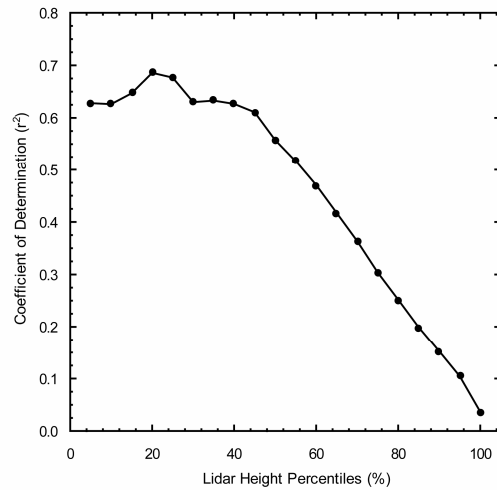


Figure 5. The lidar height percentiles, plotted against the coefficients of determination between the lognormal μ parameter and the heights of the percentiles. It is the lowest percentiles that account for most of the variance in μ . Note that all Pearson correlation coefficients were negative, indicating an inverse relationship between μ and the heights of the percentiles.

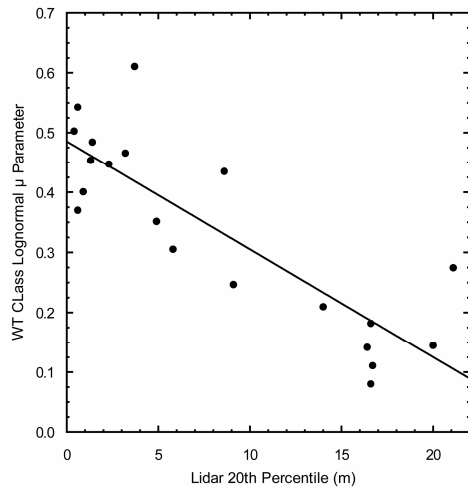


Figure 4. The WT class lognormal μ parameter estimated using the lidar 20th percentile. Model: $r^2 = 0.69$, $r = -0.83$, $RMSE = 0.079$, $p < 0.001$; $y = 0.45 - 0.16 * x$

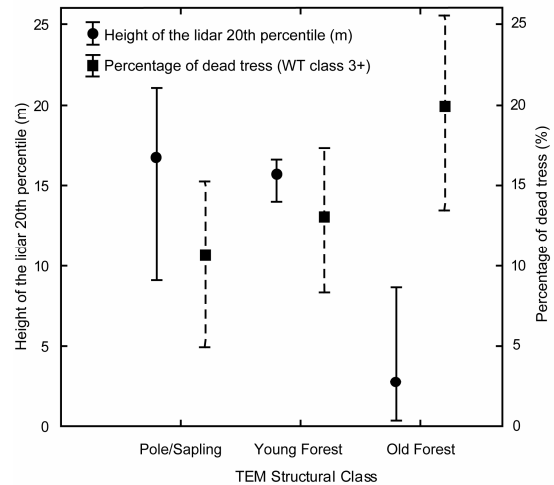


Figure 6. Means and ranges of (1) lidar-derived heights of the 20th percentile, and (2) the percentage of dead trees, grouped by TEM structural class.

percentile ($r = 0.88$). The standard deviation of the vegetation return heights, however, were relatively stable across the age classes, resulting in an increase in the coefficient of variation from approximately 0.15 to 0.3 for pole sapling and young forest, to 0.4-1.2 for old forest.

4. DISCUSSION

The distribution of WT classes, or tree structural classes, within a plot is an important variable to consider when developing an understanding of the current structure of a forest stand, as well as for managing the stand for wildlife and biodiversity values. Whilst the range of wildlife tree classes from 1 to 9 within a plot is highly variable, fitting distributions to the observed frequency of WT classes and correlating these parameters with a simplified index of the proportions of live and dead stems is, we believe, an important result. Once we have developed confidence in our capacity to understand how the distribution parameters vary over the landscape as a function of stand form, we then look to lidar technology to extrapolate over large areas.

The results presented here indicate the capacity of lidar to estimate lognormal parameters describing the percentage of dead trees within plots in unmanaged forests. The method was superior to simply attempting to predict the percentage of dead trees directly using lidar-derived variables. The natural logarithm of the coefficient of variation was the best predictor of μ , however, generally all of the lower percentiles were also strongly and negatively correlated with the parameter. We believe this is a result of the direct linkage noted by Clark et al. (2004) between tree mortality and overall stand structure.

Clayoquot Sound's old forests are characterized by heterogeneous canopies and patchy understories, with gaps where old trees have died and young ones are regenerating (Clayoquot Sound Scientific Panel, 1995). These gaps, at least partly the result of the presence of defoliated, often limbless snags with very different structures than living trees, increased the mean penetration depth of lidar returns into the forest canopy, and decreased the heights of the lower height percentiles. Critically, non-ground returns were not removed below a given height threshold, and though many may have actually intercepted the understorey, coarse woody debris, large stones, or the ground, their inclusion was nonetheless an important contribution to the analyses.

Increasing the number of plots across the full range of tree structural class distributions is a necessary next step to both adequately capture the heterogeneity within and between the structural classes (especially old forests) found in the study area. Additional field data will also enable the application of multivariate statistical techniques, where more than a single predictor variable can be employed. Furthermore, additional research is required to determine if these techniques can be extended to managed forests. We believe that distribution parameters can be robust proxies for plot-based indicators of forest structure and biodiversity, and can be useful to ecologists and forest managers interested in augmenting their current mapping initiatives using lidar remote sensing.

5. REFERENCES

Anderson, H.A., McGaughey, R.J., and Reutebuch, S.E., 2005. Estimating forest canopy fuel parameters using LIDAR data. *Remote Sensing of Environment*, 94, 441-449.

BC Stats, 2005. Fact sheet released by the British Columbia Ministry of Labour and Citizen's Services, "Quick facts about British Columbia," Victoria, Canada. <http://www.bcstats.gov.bc.ca/data/qf.pdf> (accessed 12 October 2006)

Clark, D.B., Castro, C.S., Alvarado, L.D.A., and Read, J.M., 2004. Quantifying mortality of tropical rain forest trees using high-spatial-resolution satellite data. *Ecology Letters*, 7, 52-59. DOI: 10.1046/j.1461-0248.2003.00547.x

Clayoquot Sound Scientific Panel, 1995. Sustainable Ecosystem Management in Clayoquot Sound. Report 5, Halfmoon Bay, British Columbia, Canada.

Coops, N.C., Hilker, T., Wulder, M.A., St-Onge, B., Newnham, G., Siggins, A., and Troymow, J.A., 2007. Estimating canopy structure of Douglas-fir forest stands from discrete-return LiDAR. *Trees*. DOI:10.1007/s00468-006-0119-6

Demarchi, D. A., Marsh, R. D., Harcombe, A. P. and Lea, E. C., 1990. The Environment (of British Columbia). In: R.W. Campbell, N.K. Dawe, I. McTaggart-Cowan, J. M. Cooper, G. W. Kaiser, and M. C. E. McNall (Eds.). *The Birds of British Columbia*. Royal British Columbia Museum, Environment Canada, and Canadian Wildlife Service, Victoria, British Columbia, Canada Victoria, pp. 55-142.

Gobakken, T., and Næsset, E., 2005. Weibull and percentile models for lidar-based estimation of basal area distribution. *Scandinavian Journal of Forest Research*, 20, 490-502.

Hudack, A.T., Lefsky, M.A., Cohen, W.B., Berterretche, M., 2002. Integration of lidar and Landsat ETM+ data for estimating and mapping forest canopy height. *Remote Sensing of Environment*, 82, 397-416.

Lefsky, M.A., Cohen, W.B., Acker, S.A., Parker, G.G., Spies, T.A. and Harding, D, 1999. LiDAR remote sensing of the canopy structure and biophysical properties of Douglas-fir western hemlock forests. *Remote Sensing of Environment*, 70, 339-361.

Lefsky, M.A., Hudack, A.T., Cohen, W., and Acker, S.A., 2005a. Geographic variability in lidar predictions of forest stand structure in the Pacific Northwest. *Remote Sensing of Environment*, 95, 532-548.

Lefsky, M.A., Turner, D.P., Guzy, M., and Cohen, W.B., 2005b. Combining lidar estimates of aboveground biomass and Landsat estimates of stand age for spatially extensive validation of modeled forest productivity. *Remote Sensing of Environment*, 95, 549-558.

Limpert, E., Stahel, W.A., Abbt, M., 2001. Log-normal distributions across the sciences: keys and clues. *BioScience*, 51(5), 341-352.

Meidinger, D. and Pojar, J., 1991. *Ecosystems of British Columbia*. BC Special Report Series No. 6. BC Ministry of Forests, Victoria, British Columbia, Canada.

Mitchell, W.R., Green, R.N., Hope, F.D. and Klinka, K., 1989. *Methods for Biogeoclimatic Ecosystem Mapping*. Rep.

RR89002-KL. BC Ministry of Forest Resources, Victoria, British Columbia, Canada.

Næsset, E., 2002. Predicting forest stand characteristics with airborne scanning laser using a practical two-stage procedure and field data. *Remote Sensing of Environment*, 80, 88-99.

Næsset, E., 2004. Practical large-scale forest stand inventory using a small-footprint airborne scanning laser. *Scandinavian Journal of Forest Research*, 19, 164-179.

Noss, R.F., 1999. Assessing and monitoring forest biodiversity: a suggested framework and indicators. *Forest Ecology and Management*, 115, 135-146.

Sambridge, M., Braun, J., and McQueen, H., 1995. Geophysical parameterisation and interpolation of irregular data using natural neighbours. *Geophysical Journal International*, 122, 837-857.

Seielstad, C.A, and Queen, L.P, 2003. Using airborne laser altimetry to determine fuel models for estimating fire behaviour. *Journal of Forestry*, 101(4), 10-15.

Sibson, R., 1981. A brief description of natural neighbour interpolation. In V. Barnett (Ed.), *Interpreting Multivariate Data*. Wiley, Chichester, pp. 21-36.

6. ACKNOWLEDGEMENTS

This research is partly support by the British Columbia Forest Science Program (Y07-1024), NSERC grants to Bater and Coops, and funds from the BC Ministry of Forests and Range. Dr. Denis Collins (BCMF&R) provided valuable discussion on methods and results. We thank Parks Canada and Interfor for providing access to the study area, and Clayoquot Biosphere Trust for the use of a field office in 2005. Yulia Stange, Kate Kirby, Andy Ackland, Yanny Barney, Selina Agbayani, Sam Coggins, Jessica Currie, Jamie Pascoe, Shanley Thompson, and Trevor (TG) Jones provided significant help with the field program.

COMBINED FEATURE EXTRACTION FOR FAÇADE RECONSTRUCTION

Susanne Becker, Norbert Haala

Institute for Photogrammetry, Universitaet Stuttgart
Geschwister-Scholl-Str. 24D, 70174 Stuttgart
Forename.Lastname@ifp.uni-stuttgart.de

KEY WORDS: Three-dimensional, Point Cloud, Urban, LIDAR, Modelling, Façade Interpretation

ABSTRACT:

Within the paper, the combined application of terrestrial image and LIDAR data for façade reconstruction is discussed. Existing 3D building models as they are available from airborne data collection are additionally integrated into the process. These given models provide a priori information, which efficiently supports both the georeferencing of the terrestrial data and the subsequent geometric refinement. Approximate orientation parameters for the terrestrial LIDAR measurements are provided by suitable low-cost components. Exact georeferencing is then realised by an automatic alignment to the building models, which are given in the required reference coordinate system. The automatic relative orientation of the terrestrial images is implemented by tie point matching. A modified version of this matching process is then used to align these images to the terrestrial LIDAR data, which were already georeferenced in the preceding step. After this fully automatic orientation process, the given 3D model is refined by the extraction of window structures from the LIDAR point clouds and façade images.

1. INTRODUCTION

Terrestrial LIDAR is frequently used for the collection of highly detailed 3D city models. Urban models are already available for a large number of cities from aerial data like stereo images or airborne LIDAR. However, while airborne data collection is especially suitable to provide the outline and roof shape of buildings, terrestrial data collection from ground based views is especially suitable for the refinement of building facades. Thus, terrestrial and aerial data provide complementary information during 3D city model generation. In our approach, this is realised by using given 3D building models from aerial data collection as a priori information during geocoding of the terrestrial data. This automatic alignment for both the terrestrial LIDAR and image data is one of the main focuses of this paper. In the second part of the paper, the combination of LIDAR and image data for façade modelling while using the given 3D models as reference surfaces will be discussed.

Spatially complex areas like urban environments can only be completely covered by terrestrial laser scanning (TLS) if data collection is realised from different viewpoints. Usually, scans from different viewpoints are aligned based on tie and control point information measured at specially designed targets. These targets are manually identified while a refined measurement is performed automatically. In contrast, our approach allows for fully automatic registration and georeferencing by matching the point clouds from terrestrial laser against the corresponding faces of the given 3D building model. This can be implemented by the standard iterative closest point algorithm introduced by (Besl & McKay 1992) since a coarse alignment of the scans is available. For this purpose, the position and orientation of the scanner is determined simultaneously to point measurement by integrated GPS and digital compass.

One of the main applications of 3D city models is the generation of realistic visualisations. This requires a suitable texture mapping for the respective building surfaces in addition

to geometric data collection. Thus, in order to simultaneously capture corresponding colour information, a digital camera is directly integrated in some commercial 3D systems. However, this limits the camera viewpoints to the laser scanning stations, which might not be optimal for the collection of high quality image texture. Additionally, laser scanning for the documentation of complex object structures and sites frequently has to be realised from multiple viewpoints. This can result in a relatively time consuming process. For these reasons, the acquisition of object geometry and texture by two independent sensors and processes to allow for an image collection at optimal positions and time for texturing will be advantageous. Even more important, images collected from multiple terrestrial viewpoints can considerably improve the geometric modelling based on the TLS data.

Captured images can be directly linked to the 3D point cloud if the camera is directly integrated to the laser scanner and a proper calibration of the complete system is available. In contrast, for independent viewpoints of camera and laser, the combined evaluation requires a suitable co-registration process for the respective range and image data sets. The automatic orientation of terrestrial images considerably benefits from the recent availability of feature operators, which are almost invariant against perspective distortions. One example is the affine invariant key point operator proposed by (Lowe 2004), which extracts points and suitable descriptions for the following matching based on histograms of gradient directions. By these means robust automatic tie point measurement is feasible even for larger baselines.

We use this operator to align both the terrestrial images and the terrestrial LIDAR data. First, a bundle block adjustment based on the matched key points between the digital images is realised. The resulting photogrammetric network is then transferred to object space by additional tie points which link the digital images and the TLS data that were georeferenced in the preceding step. For this purpose, the feature extraction and

matching is also realised using the reflectivity images as they are provided from the laser scanner. These reflectivity images, which are usually measured in addition to the run-time during scanning, represent the backscattered energy of the respective laser footprints. Thus, the intensities are exactly coregistered to the 3D point measurements. Despite the differences between these reflectivity images and the images captured by a standard digital camera with respect to spectral band width, resolution and imaging geometry they can be matched against each other automatically by the key point operator.

While the automatic georeferencing of the different data sets will be discussed in Section 2, their combined use for a refined 3D modelling will be presented in Section 3. The benefit of using both image based measurements and densely sampled point clouds from terrestrial laser scanning is demonstrated for automatic façade refinement by the extraction of window structures.

2. DATA PREPARATION AND ORIENTATION

Within our investigations, a standard digital camera NIKON 2Dx was used for image collection, while the Leica HDS 3000 scanner was used for LIDAR measurements. This scanner is based on a pulsed laser operating at a wavelength of 532 nm. It is able to acquire a scene with a field of view of up to 360° horizontal and 270° vertical in a single scan. The typical stand-off distance is 50 to 100 meters, but measurements of more than 200 meters are possible. The accuracy of a single point measurement is specified with 6 mm. Within our tests the façades of the historic buildings around the Schillerplatz were recorded. In order to be able to reconstruct the scene in detail, the resolution on the façades was chosen to about ten centimetres, which is typical for this type of application. To prevent holes in the point cloud i.e. due to occlusions by the monument placed in the centre of the square, the dataset is composed of three separate 360°-scans from varying stations.

For direct georeferencing of the terrestrial scans, a low-cost GPS and a digital compass were additionally mounted on top of the HDS 3000 laser scanner. Digital compasses such as the applied TCMVR-50 can in principle provide the azimuth at a standard deviation below 1°. However, these systems are vulnerable to distortion. Especially in build-up areas the Earth's magnetic field can be influenced by cars or electrical installations. These disturbances usually reduce the accuracy of digital compasses to approximately 6° (Hoff and Azuma, 2000). The used low cost GPS receiver mounted on top of the digital compass is based on the SIRF II chip. Since it was operated in differential mode, the EGNOS (European Geostationary Navigation Overlay Service) correction signal could be used. By these means the accuracy of GPS positioning can be improved from 5-25m to approximately 2m. The vertical component of the low-cost GPS measurement was discarded and substituted by height values from a Digital Terrain Model.

For our test area the geometry of the respective buildings is already available from a 3D city model, which is maintained by the City Surveying Office of Stuttgart. In the following this building geometry is used both for georeferencing and refined modelling. The quality and amount of detail of this data set is typical for such 3D models, like they are available area covering for a number of cities. For the applied city model the roof faces were collected semi-automatically by photogrammetric stereo measurement. In contrast, the outlines of the buildings were captured by terrestrial surveying. Thus, the horizontal position accuracy of façade segments, which were generated by extru-

sion of this ground plan, is relatively high, despite the fact that they are limited to planar polygons.

2.1 Georeferencing of LIDAR data

A global orientation of the laser scanner head in WGS 84 is measured by the low-cost GPS in combination with the digital compass. This approximate solution is further refined using the iterative closest point (ICP) algorithm introduced by (Besl & McKay 1992). The result of the direct georeferencing is used as an initial value for the iterative registration of the laser scans. Once the registration of the TLS data has converged, it is kept fixed. Then the complete dataset is registered with the city model using the same algorithm. Since the initial approximation of the direct georeferencing is within the convergence radius of the ICP algorithm, this approach allows for an automated georeferencing of TLS data (Schuhmacher & Böhm 2005).

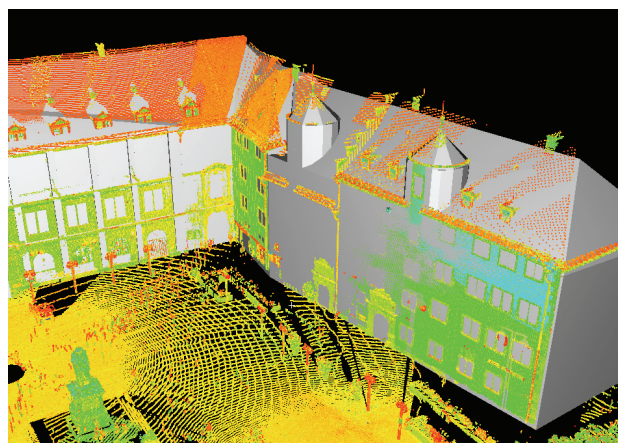


Figure 1: 3D point cloud from laser scanning aligned with a virtual city model.

As it is demonstrated in Figure 1, after this step the 3D point cloud is available in the reference system as provided by the 3D city model.

2.2 Alignment of image data

The integration of image data into the façade reconstruction requires image orientation in a first step. The images have to be aligned with each other and registered according to the already georeferenced laser point cloud. This is usually performed by means of a bundle block adjustment providing accurate estimates of the orientation parameters. While tie points are necessary for connecting the images, control point information is needed for the georeferencing. Aiming at a fully automatic reconstruction process, both tie points and control points are to be derived automatically.

2.2.1 Image to image registration

Image to image registration based on tie points is a prerequisite step for photogrammetric 3D modelling. In the recent past, much effort has been made to develop approaches that automatically extract such tie points from images of different types (short, long, and wide baseline images) (Remondino & Ressel 2006). While matching procedures based on cross-correlation are well suited for short baseline configurations, images with a more significant baseline are typically matched by means of interest points. However, these techniques would fail in case of wide baseline images acquired from considerably different viewpoints. The reason is large perspective effects that are caused by the large camera displacement. Points and corners cannot be reliably matched. Therefore, interest point operators

have to be replaced by region detectors and descriptors. As an example, the Lowe operator (Lowe 2004) has been proved to be a robust algorithm for wide baseline matching (Mikolajczyk & Schmid 2003).



Figure 2. Image data for photogrammetric modelling.

Figure 2 shows images from a calibrated camera (NIKON D2x Lens NIKKOR 20mm). For the automatic provision of tie points the SIFT (scale invariant feature transform) operator has been applied to extract and match key points. Wrong matches were removed by a RANSAC based estimation (Fischler & Bolles 1981) of the epipolar geometry using Nister's five point algorithm (Nister 2004). Finally, the image orientations were determined from 2079 automatically extracted tie points.

2.2.2 Image georeferencing

The provision of control point information, which is necessary for the determination of the orientation parameters, typically involves manual effort if no specially designed targets are used. The reason is that object points with known 3D coordinates have to be manually identified in the images by a human operator. The idea to automate this process is linking the images to the georeferenced LIDAR data by a matching process (Böhm & Becker 2007) which is similar to the automatic tie point matching as described in Section 2.2.1.

Common terrestrial laser scanners sample object surfaces in an approximately regular polar raster. Each sample provides 3D coordinates and an intensity value representing the reflectivity of the respective surface point. Based on the topological information inherent in data acquisition, the measured reflectivity data can be depicted in the form of an image. This allows for the application of image processing tools to connect the images captured by the photo camera to the LIDAR data.



Figure 3. Measured laser reflectivities as 3D point cloud (left) and 2D image representation (right).

Figure 3 (left) shows the laser point cloud of an already georeferenced scan. The position of the laser scanner is marked by the coordinate axes of the local scanner system. The image representation derived from the reflectivity values is given in Figure 3 (right). Each pixel with a valid laser reflectivity value refers to the 3D coordinates of the related sample point. Thus, obtained point correspondences between the laser image and the photos provide control point information which is necessary for the determination of the photos' orientation parameters.

However, images generated from laser reflectivities considerably differ from images that have been captured by photo cameras. On the one hand, the laser intensities represent the reflectivity of the measured surface only in a narrow wavelength range (for example 532 nm for the HDS 3000). Furthermore, the viewing direction and the direction of illumination are identical in case of laser scanning. By contrast, photo cameras usually work with ambient light sources which may cause shadow areas on the object and therefore lead to grey value edges in the photograph. On the other hand, the laser image is not based on central projection but on polar geometry. Thus, like it is visible in the right image of Figure 3, straight 3D lines appear curved in the reflectivity image. Another aspect is the sampling distance, which is often much higher for a laser scan compared to the spatial resolution of a photo captured by a camera. For these reasons, the determination of point correspondences between a laser reflectivity image and a photograph requires an algorithm which is insensitive to changes in illumination and scale and uses region descriptors instead of edge detectors.

Figure 4 depicts the laser reflectivity image (left) and one of the photographs captured by the NIKON camera (right) in real proportions. In order to have similar intensity values in both images, only the green channel of the photograph has been considered for the determination of corresponding points. The resulting key points were extracted and matched by means of the SIFT implementation provided by Vedaldi (2007). Using default settings 492 key points are detected in the laser reflectivity image and 5519 in the photograph. Of those 31 are matched to corresponding key points represented by the red dots and lines in Figure 4. Due to the decreasing reflectivity values in the right part of the laser image, correct matches could be found only on the left part of the building façade.

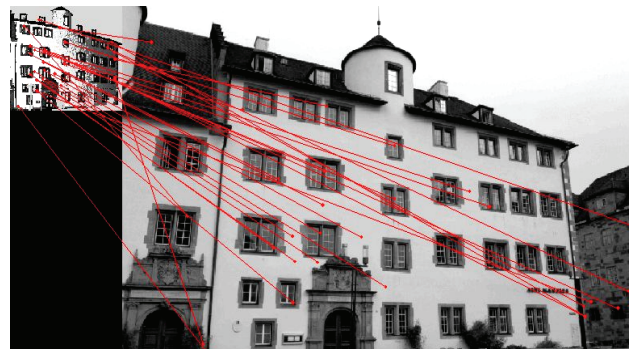


Figure 4. Key point correspondences for the laser reflectivity image (left) and one of the photographs (right).

In a next step, wrong matches are to be removed by a RANSAC based computation of a closed form space resection (Zeng & Wang 1992). For this purpose, the SIFT point correspondences are used as control point information. However, the accuracy of orientation parameters obtained from a minimal set of points strongly depends on the point configuration. If the points are close together, the solution of the space resection becomes unstable and the uncertainty of the SIFT point coordinates (Remondino & Ressel 2006) leads to significant variations in the orientation parameters. Therefore, it is difficult to find the correct solution within the RANSAC process. In order to improve the accuracy of the key point positions and the derived orientation parameters, the initial set of point correspondences is augmented: For each pair of key points, new point correspondences are generated by randomly shifting the key point in the photograph by a few pixels. Out of these additional point correspondences only the one is kept which contributes to

the best solution for the exterior orientation. Beyond that, for a further stabilisation of the RANSAC process, a priori information on the ground height is integrated. Assuming a smooth terrain in front of the building, only those solutions are considered, where the positions of the camera and the laser scanner differ less than 1m in height. In this way, about 22% of the key point matches are confirmed as valid correspondences.

The resulting approximate orientation parameters for the photographs are then refined in a final bundle adjustment. For this purpose the Australis software package was used. The average standard errors of the estimated orientation parameters are $\sigma_x = 7.6\text{cm}$, $\sigma_y = 5.6\text{cm}$, $\sigma_z = 8.1\text{cm}$, $\sigma_{az} = 0.167^\circ$, $\sigma_{el} = 0.164^\circ$, $\sigma_{roll} = 0.066^\circ$. The average precision of the computed object coordinates is $\sigma_x = 3.3\text{cm}$, $\sigma_y = 4.7\text{cm}$, $\sigma_z = 2.1\text{cm}$.

3. FAÇADE RECONSTRUCTION

After this georeferencing process, the collected terrestrial data sets are aligned to the existing building model, which is provided from the existing 3D city model. Thus, both the LIDAR point clouds and the images can be used to enhance this coarse model. In the following, this is demonstrated exemplarily for the geometric refinement of the building façade by a two-step approach. First, the LIDAR point clouds are used to decompose the given building model into 3D cells to additionally represent façade structures like windows and doors. This cell decomposition, which can be used very effectively to represent building models at multiple scales (Haala et al 2006), is then refined in a second step by photogrammetric analysis of the images. Thus, the amount of detail is further increased for the window frames while profiting from the higher resolution of the image data.

3.1 Façade Refinement by Terrestrial LIDAR

As a first step of the LIDAR based refinement of the building façade, suitable 3D point measurements are selected by a simple buffer operation. While assuming that the façade can be described sufficiently by a relief, the vertical distances between the measured 3D laser points and the given façade polygon can be used to generate a 2.5D representation, or can even be interpolated to a regular grid. Thus, further processing like the following segmentation is simplified considerably by such a mapping of the 3D points against the given façade plane.

3.1.1 Point cloud segmentation

The LIDAR measurement will be used to decompose the coarse 3D building with a flat front face into suitable façade cells. For this purpose, planar delimiters are derived by segmenting LIDAR points measured at the window borders.

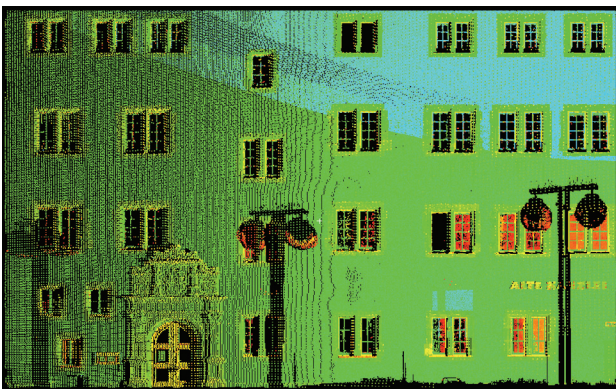


Figure 5. 3D point cloud as used for the geometric refinement of the corresponding building façade.

Figure 5 shows a point cloud, which was selected for a building façade based on the alignment to the virtual city model as depicted in Figure 1. This 2.5D representation clearly demonstrates that usually fewer points are measured at window areas than the façade of a building. This is due to specular reflections of the LIDAR pulses on the glass or points that refer to the inner part of the building and were therefore cut off in the pre-processing stage. If only the points are considered that lie on or in front of the façade, the windows will describe areas with no point measurements. Taking advantage thereof, our point cloud segmentation algorithm detects window edges, which are defined by these no data areas. In principle, such holes can also result from occlusions. This is avoided by using point clouds from different viewpoints, though. In that case, occluding objects only reduce the number of LIDAR points since a number of measurements are still available from the other viewpoints.

Our segmentation process differentiates four types of window borders: horizontal structures at the top and the bottom of the window, and two vertical structures that define the left and the right side. As an example, the edge points of a left window border are detected if no neighbour measurements to their right side can be found in a pre-defined search radius at the façade plane. We used a search radius a little higher than the scan point distance on the façade, otherwise, no edge points would be found at all.

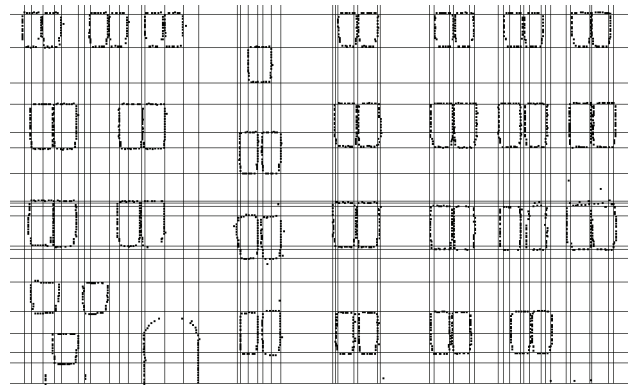


Figure 6. Detected horizontal and vertical window lines.

Based on the extracted edge points, which are depicted in Figure 6, the window borders can be determined in the following step.

3.1.2 Spatial-Partitioning of the building façade

Within this step, horizontal and vertical lines are estimated from non-isolated edge points. As it is also visible in Figure 6, these boundary lines are then used to decompose the building façade in suitable cells. Each of these cells represents either a homogeneous part of the façade or a window area. After a classification based on the availability of measured LIDAR points, window cells can be eliminated from the façade and the refined 3D building model is generated.

The separation of cells into building and window fragments is based on a 'point-availability-map'. This low resolution binary image provides pixels which either represent façade regions, where LIDAR points are available, or areas with no 3D point measurements. This image is then used to compute the ratio of façade to non-façade pixels for each façade cell as required for the following classification. A refined classification is implemented based on neighbourhood relationships and constraints concerning the simplicity of the resulting window objects. Uncertain cells are for example classified depending on

their neighbours in order to align and adapt proximate windows in horizontal and vertical direction. Within this step, convex window objects can additionally be guaranteed.

3.1.3 Model Refinement

Finally, the façade geometry is modelled by eliminating the classified window cells from the existing coarse building model. For this purpose, a plane parallel to the façade at window depth is determined from LIDAR points measured at the window crossbars.

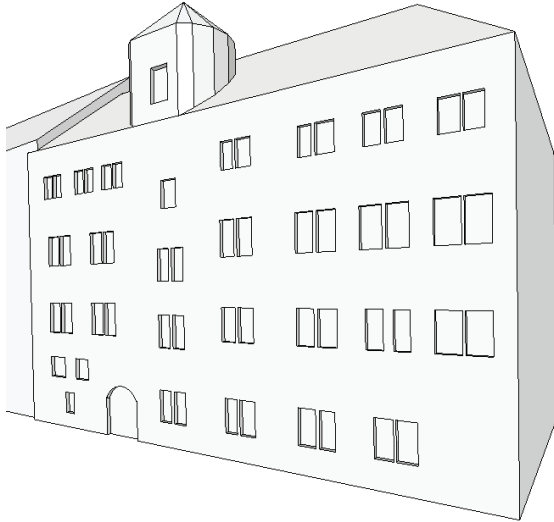


Figure 7. Refined façade of the given building model.

As depicted in Figure 7, the classified façade cells are then carved out from the building model at this window depth. While the windows are represented by polyhedral cells, also curved primitives can be integrated in the reconstruction process as demonstrated by the round-headed door of the building. Furthermore, our approach is not limited to the modelling of indentations like windows or doors. Details can also be added as protrusions to the façade.

3.2 Image based Façade Refinement

For our data set, the point sampling distance of terrestrial laser scanning was limited to approximately 10cm. Thus, smaller structures can not be detected. However, the amount of detail can be increased by integrating image data in the reconstruction process. This is exemplarily shown for the reconstruction of window crossbars.

3.2.1 Derivation of 3D edges

By matching corresponding primitives, the georeferenced image data is used to derive the required 3D information. In order to reconstruct linearly shaped façade detail such as crossbars, edge points are extracted from the images by a Sobel filter. These edge point candidates are thinned and split into straight segments. Afterwards, the resulting 2D edges of both images can be matched. However, frequently occurring façade structures, such as windows and crossbars, hinder the search for corresponding edges. Therefore, the boundaries of the already reconstructed windows are projected into both images. Only the 2D edges within these regions are further processed. Thus, possible mismatches are reduced, even though, they cannot be avoided completely. Figure 8 depicts the selected 2D edges for an exemplary window in both images.

Remaining false correspondences result in 3D edges outside the reconstructed window. Therefore, these wrong edges can be

easily identified and removed. In addition, only horizontal and vertical 3D edges are considered for the further reconstruction process. The reconstructed wrong (green) and correct (red) 3D edges are shown in local façade coordinates in Figure 9. The position of the window that has been derived from the LIDAR data is illustrated in black.

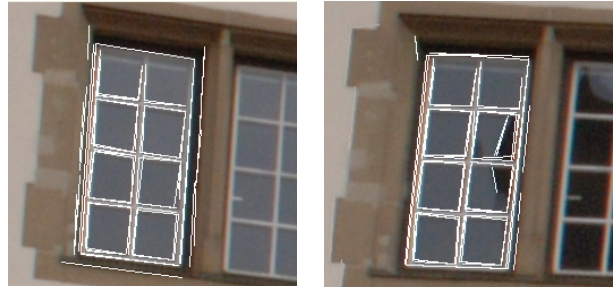


Figure 8. Selected 2D edges for a window in both images.

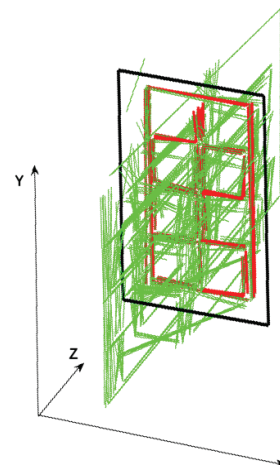


Figure 9. Wrong (green) and correct (red) 3D window edges.

3.2.2 Reconstruction of additional façade structures

Photogrammetric modelling allows the extraction of well-defined image features like edges and points with high accuracy. By contrast, points from terrestrial laser scanning are measured in a pre-defined sampling pattern, unaware of the scene to capture. That means that the laser scanner does not explicitly capture edge lines, but rather measures points at constant intervals. For this reason, the positional accuracy of window borders that are reconstructed from LIDAR points is limited compared to the photogrammetrically derived 3D edges at crossbars. As a consequence, the 3D reconstructions from laser points and images may be slightly shifted. Therefore, the reconstruction of the crossbars is done as follows:

For each window, hypotheses about the configuration of the crossbars are generated and tested against the 3D edges derived from the images. Possible shapes are dynamically generated as templates by recursively dividing the window area in two or three parts. Recursion stops when the produced glass panes are too small for a realistic generation of windows. The minimum width and height of the glass panes are restricted by the same threshold value. After each recursion step, the fitting of the template with the 3D edges is evaluated. The partition is accepted if 3D edges are available within a buffer area around the dividing line. In a final step, the crossbars and the window frame are modelled. For this purpose, new 3D cells with a pre-defined thickness are generated at the accepted horizontal and vertical division lines as well as at the window borders. The result is exemplarily shown for two windows in Figure 10.

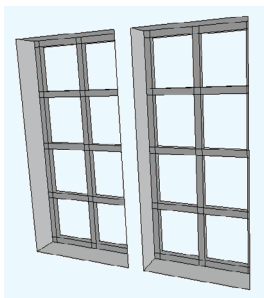


Figure 10. Reconstructed crossbars for two windows.

Most crossbars can be reconstructed reliably. However, problems may arise for windows that are captured under oblique views. This is due to perspective distortions or occlusions making it difficult to detect 2D edges at crossbars (Figure 11). Consequently, only a reduced number of 3D edges can be generated thereof in those areas.

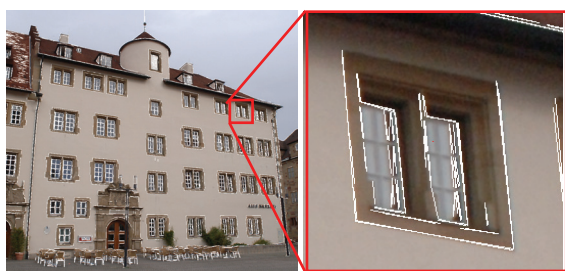


Figure 11. 2D edges for a window under an oblique view.

In order to stabilize the modelling process of crossbars, neighbourhood relationships are taken into account. The crossbar configuration is assumed to be equal for all windows of similar size which are located in the same row or column. Based on this assumption, similar windows can be simultaneously processed. Thus, the crossbar reconstruction leads to robust results even for windows that are partially occluded or feature strong perspective distortions in the respective image areas.

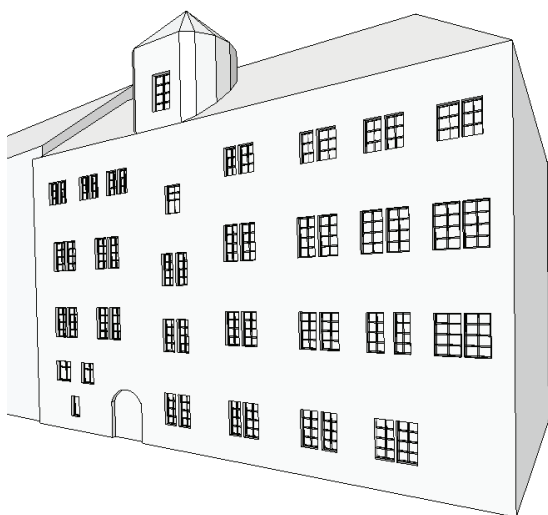


Figure 12. Refined facade with detailed window structures.

The final result of the building façade reconstruction from terrestrial LIDAR and photogrammetric modelling can be seen in Figure 12. This example demonstrates the successful detection of crossbars for windows of medium size. However, the dynamic generation of templates even allows for the modelling of large window areas as they often occur at facades of big office buildings.

4. CONCLUSION

Within the paper the combined use of terrestrial image and LIDAR data for the extraction of façade geometry was presented. For this purpose a fully automatic georeferencing of the collected data sets based on SIFT algorithm was realised in a first processing step. As presented, SIFT matching is a promising tool for the marker-free connection of photos and laser data. It is working well in standard scenarios for relative small baselines when the viewing direction of the laser scanner is approximately perpendicular to the dominating object surfaces. In this case, perspective distortions and decreasing reflectivity values in the laser image are negligible. However, problems may arise if the point density of the laser scans is low compared to the spatial resolution of the photograph leading to an instable matching and orientation process.

The refinement of 3D building models is based on a cell decomposition approach. As it was already proved for the automatic generation of topologically correct building models at different levels of detail (Haala et al 2006), this approach allows the simple integration and removal of geometric detail for given building models. Even more important, symmetry relations like coplanarity or alignment can be guaranteed even for larger distances between the respective building parts. Thus, despite of the limited extent of the window primitives, which were extracted from terrestrial LIDAR and images, structural information can be generated for the complete building.

5. REFERENCES

- Besl, P. J. & McKay, N. [1992] A method for Registration of 3-D Shapes. *IEEE PAMI* 14[2], pp. 239-256.
- Böhm, J. & Becker, S. [2007]. Automatic marker-free registration of terrestrial laser scans using reflectance features. To appear in *Optical 3D*, Zurich, Switzerland.
- Fischler, M. A. & Bolles, R. C. [1981]. Random Sample Consensus: A Paradigm for Model Fitting with Applications to Image Analysis and Automated Cartography. *Comm. Of the ACM*, Vol. 24, pp. 381-395.
- Haala, N., Becker, S. & Kada, M. [2006]. Cell Decomposition for the Generation of Building Models at Multiple Scales. *IAPRS Vol. 36 Part III, Symposium Photogrammetric Computer Vision*, pp. 19-24.
- Lowe, D. [2004]. Distinctive image features from scale-invariant keypoints. *IJCV*, Vol. 60(2), pp. 91-110.
- Mikolajczyk, K. & Schmid, C. [2003]. A performance evaluation of local descriptors. *Proc. Conf. Computer Vision and Pattern Recognition*, pp. 257-264.
- Nistér, D. [2004]. An efficient solution to the five-point relative pose problem. *IEEE PAMI*, 26(6), pp. 756-770.
- Remondino, F. & Ressel, C. [2006]. Overview and experiences in automated markerless image orientation. *IAPRS*, Vol. 36, Part 3, pp. 248-254.
- Schuhmacher, S. & Böhm, J. [2005]. Georeferencing of terrestrial laserscanner data for applications in architectural modeling. *IAPRS Vol. 36, PART 5/W17*.
- Vedaldi, A., [2007]. An Implementation of the Scale Invariant Feature Transform, *UCLA CSD Tech. Report N. 070012*, 2007.
- Zeng, Z. & Wang, X. [1992]. A general solution of a closed-form space resection. *PE&RS*, Vol. 58, No. 3, pp. 327-338.

TREE DETECTION AND DIAMETER ESTIMATIONS BY ANALYSIS OF FOREST TERRESTRIAL LASERSCANNER POINT CLOUDS

A. Bienert^{a,*}, S. Scheller^a, E. Keane^b, F. Mohan^b, C. Nugent^c

^aTechnical University of Dresden, Institute of Photogrammetry and Remote Sensing, D-01062 Dresden, Germany
anne.bienert@tu-dresden.de

^bTreeMetrics, The Rubicon Centre, CIT Campus, Bishopstown, Cork, Ireland

^cUniversity College Cork, Cork Constraint Computation Centre, Cork, Ireland

Commission V, WG V/3

KEYWORDS: Terrestrial laserscanning, point cloud, segmentation, automation, forest inventory, diameters along the stem

ABSTRACT:

Forest inventory schemes collect, besides tree species and some area parameters, geometric tree parameters such as diameter at breast height (DBH), tree height, stem profiles, azimuth and distance. For some years the use of a terrestrial laserscanner for this forestry inventory task has been discussed. Dense 3D point clouds recorded in forest stands may form the basis for automatic determination of forest inventory parameters.

The paper presents an algorithm to detect trees in a horizontal cross section through a point cloud. This algorithm is divided in two segmentation steps to minimise the probability of false detections. The first segmentation step is a point cluster search in a cross section of the point cloud. In a second step all clusters are verified or discarded by analysing the point density in neighbouring cross sections. A study with 547 trees shows a detection rate of 97.4 % in single scan laserscanner data. Two other plots with heavy branching show a detection rate of 100 % and 94 %. Besides the tree detection, a new parameter is introduced to eliminate miss-fitted stem diameters. By using this parameter a least squares polynomial model is generated to smooth the diameters along the stem. Finally some results are demonstrated.

1. INTRODUCTION

Almost 73% of the European forest areas are used as production forest (Food and Agriculture Organisation of the United Nations, 2007). In order for efficient cultivation and planning to take place the current timber volume of standing trees inside a forest holding needs to be carefully monitored. Therefore forest inventories are carried out at regular intervals. Besides other inventory parameters, the most important geometric tree parameters are diameter at breast height and tree height, which are typically measured manually. Measurements on standing trees to determine the timber present is a time-consuming and costly process. The boles are typically measured after felling. Terrestrial laserscanning is an important technique which enables a non-destructive determination of standing timber. In the last 5 years terrestrial laserscanning has become an interesting tool for forest application. For instance, Aschoff et al. (2006) have researched the forest hunting habitats of bats with the use of terrestrial laserscanner data.

Laserscanner point clouds have a very high point density, which enables an extensive analysis and an automation of several utilisation processes. Different studies have been published with the aim of automatically determining forest inventory parameters from point clouds (Simonse et al., 2003; Hopkinson et al., 2004; Watt and Donoghue, 2005; Henning and Radtke, 2006b).

Segmentation and tree identification is done in a horizontal cut of the point cloud, to reduce processing time. Scan points on stem surfaces are mapped as an arc within the layer. Hopkinson

et al. (2004) demonstrated tree detection by overlaying a manually surveyed tree map on the point cloud layer. Fully automatic segmentation and tree identification is presented in Aschoff et al. (2006). A horizontal cut from the scanned point cloud is mapped to a constant raster and after a layer segmentation a Hough-transformation is performed. Based on this work Thies and Spiecker (2004) present a detection rate of 22% in single scan and 52% in multiple scan setups.

The approach presented here was first suggested in Bienert et al. (2006). The goal was to develop a program to determine forest inventory parameters by analysing laserscanner point clouds. In the following section, the plot acquisition and different data sets, provided in several study areas, will be outlined. Previous work had shown that the tree identification in single scans still produce false detections (classified as type I and type II errors). Heavy branching or dense undergrowth influence the tree identification. Sometimes a detection rate was obtained of less than 15%. Thus, the tree detection method was enhanced to minimise the probability of false detections. Section 3 will present the automatic identification of forest trees scanned in single scan setups by using two different approaches of segmentations. Beyond the use of segmentation, section 4 will show the profile fitting at several heights along the stem. A parameter which eliminates miss-fitted diameters will be introduced. In section 5 a diameter smoothing technique using a least squares polynomial model along the stem is given. Finally, section 6 will present the segmentation results of study areas containing a total of 547 trees of different species. Additionally results of the profile fitting and smoothing will be presented.

2. DATA SETS

2.1 Data recording

All data sets presented in this paper were acquired with the terrestrial laserscanner FARO LS 800 HE80. This full spherical laserscanner with a field of view of 360° horizontal and 320° vertical has a range up to 80 m. With a distance accuracy of ± 3 mm and a data rate of 120 000 points per second, point clouds with more than a million accurate measured surface points can be obtained in a short time (a typical 30 million point scan can be performed in 8 minutes). The LS 800 HE80 uses the phase-shift principle for range determination where a mirror rotates and directs the laser pulses (Faro, 2005).

To ensure a levelled instrument a built-in spirit level was used. The start direction was aligned to north to calculate azimuths without an offset. All plots were scanned in the single scan mode, so the scanner was placed at the plot centre.

2.2 Study areas

In May 2006 (leaf-on), 21 plots were acquired in several stands in the Vienna Woods 25 km west of Vienna. 52% of all plots were mixed plots with coniferous and deciduous trees, 33% were beech (*Fagus sylvatica*) and 5% spruce (*Picea abies*) plots. The stands ages are between 65 and 140 years. Manual reference data like DBH, tree height, azimuth and distance were measured subsequently. The radius of each plot was 15 m and the used scan resolution was 0.045°.

Another test site was acquired in March 2007, close to Aberfoyle in Scotland. These plots (plot A and B) contained 34 year old spruce (*Picea abies*) and were located on hilly terrain with less undergrowth. Both were scanned with a scan resolution of 0.036° and had a plot radius of 10 m. Figure 1 shows an intensity image of plot A. In contradiction to the study area of the Austrian forest, heavy branching on the lower region of the stems is present.



Figure 1. Intensity image of plot A

Yet another plot (plot C) was scanned 2006 in a Sitka spruce (*Picea sitchensis*) plantation in North Tipperary near Roscrea, Ireland. This plot was located on flat terrain and had a stand age of 35 years. A scan resolution of 0.036° was used. Inside a plot radius of 12 m harvester data was available to compare the diameter along the stem obtained from the program. Harvesters equipped with the appropriate sensors are able to measure diameter and length of boles.

3. TREE DETECTION

After a terrain model reduction, as described in Bienert et al. (2006), tree detection was undertaken. The segmentation was subdivided into two different algorithms to minimise classification errors, which is helpful on data sets from plots with heavy branching. Initially a segmentation based on a point cluster search was done. Then all clusters were analysed in a second step, to determine their point density inside a raster. The outcome of the tree detection was the number of trees in the plot and the approximate position of each tree.

3.1 Segmentation based on point cluster search

As outlined in Bienert et al. (2006) and Scheller and Schneider (2006) the segmentation was done on a slice with a thickness of 10 cm cut through the point cloud 1.3 m above the terrain model. The whole slice was analysed by a 2D-quadratic structure element with a size s . This element moves over the slice in X/Y projection and searches for point clusters with more than $n > n_{min}$ points. One object will be separated into two objects if the distance between one point and the nearest one is bigger than $s/2$. To classify the objects as trees, a circle fitting with all points of an object was done. As exclusion criteria the error of unit weight and the fitted diameter of the circle fitting are used to classify objects.

This algorithm produces type I and type II errors. Points which belong to a branch produce an error of unit weight bigger than the present threshold value and so the object will be rejected. As a result of this segmentation an object list was generated with all classified trees (containing false objects – type II errors) and a rejected object list with point clusters which fail the classification (containing tree cluster points – type I errors).

3.2 Segmentation based on point density raster analysis

Scanning techniques are characterised by a regular point grid area on a surface. The number of points inside this defined raster area depends on the scan resolution used and the alignment of the object surface to the scanner. A cut with a thickness greater than (minimum two times) the vertical scan resolution through a point cloud produces different numbers of points inside this defined raster in X/Y projection.

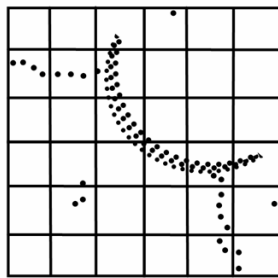
Subsequently the point density raster analysis of the object and rejected object list from the first segmentation step could be performed. The rejected object list was used to minimise type I errors, given that it contained stems which are not detected in the first segmentation phase. The 2D-bounding box for each cluster with x_{min} , x_{max} , y_{min} and y_{max} defined the object size and a raster with a cell size of 4 cm was overlaid (Figure 2a). Because of the distance from scanner to object and scan resolution are known, a maximum number of target points, which exist inside one raster (Figure 2c), can be calculated (equation 1 and 2). To get the number of redundant points a diagonal oriented vertical object surface (inside a raster element) was used. Because of the perpendicular stem direction, raster elements with a very high point number were produced (Figure 2b). Minimising the predicted target number by about 30% the minimum threshold for the raster analysis was defined. All scan points of a raster element above the threshold (Figure 2d) were copied to a new co-ordinate list, which includes only points of the stem surface. After analysing all rejected objects the new co-ordinate list was checked with the cluster search method mentioned in section 3.1.

$$n = \frac{\Delta z}{\Delta d} \cdot \frac{cell_{diag}}{\Delta d} \quad (1)$$

$$\Delta d = \sqrt{2 \cdot S^2 - 2 \cdot S^2 \cdot \cos \alpha} \quad (2)$$

where: n = number of points
 Δz = cut thickness
 $cell_{diag}$ = diagonal cell size
 Δd^* = average distance between object point
 S = distance from scanner to object
 α = scan resolution

* assumed that the scanner is on the same level like the object points



a)

0	0	4	1	0	0
4	3	15	0	0	0
0	0	16	1	0	0
0	1	2	14	16	9
0	2	0	0	4	1
0	0	0	0	2	2

b)

scan resolution: 0.1°
 distance to scanner: 10 m
 target number
 on a raster element: 19
 - 30%: 6
 threshold: 13

c)

0	0	4	1	0	0
4	3	15	0	0	0
0	0	16	1	0	0
0	1	2	14	16	9
0	2	0	0	4	1
0	0	0	0	2	2

d)

Figure 2. a) Rejected object with overlaid raster; b) number of points inside the raster; c) threshold value calculation with simulated scan parameters; d) raster elements which pass the threshold (yellow elements)

The object list, which contained type II errors, was examined, repeating the technique of point density analysis. Type II errors caused by branching or undergrowth were characterized by a lower point density. Raster elements with a point number beneath the threshold were detected and therefore deleted from the object list.

4. DIAMETER PROFILE FITTING

Stem profiles at different height intervals (Figure 3) can be determined with the knowledge of the approximate position and diameter returned by the tree detection process. Starting from the reference ground point (Bienert et al., 2006) the profile fitting was done, using a least square circle fitting algorithm (Bienert et al., 2006). This procedure minimises the mean square distance from the fitted circle to the data points, which is similar to the algorithm shown in Henning and Radtke (2006a).

Henning and Radtke (2006a) show that surface points caused by branching appear outside of the stem cross-section. An overestimated diameter will result. If only a short section of the stem profile is visible, it is not possible to determine reliable diameters.

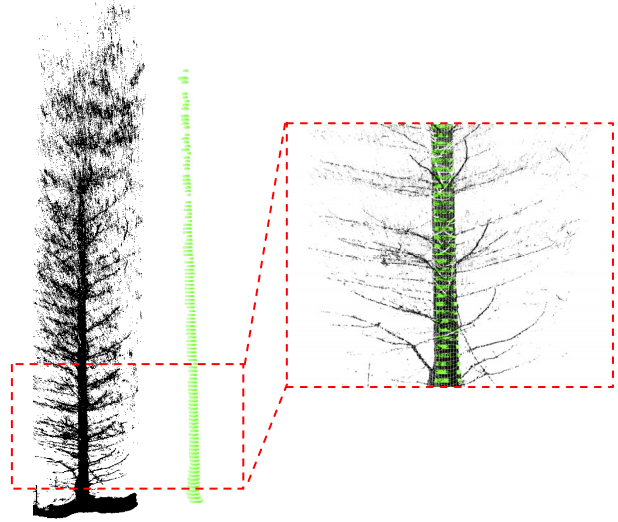


Figure 3. Point cloud of a spruce (left); generated profiles (middle); combined side view of a cut-out (right)

A new parameter, the “Reliability Factor”, was introduced to detect these over- and underestimated diameters as outlined in Bienert et al. (2007). Attributes of the circle fittings are used to evaluate the quality of the fit. The belonging to the universe is defined by the probability P_x of each parameter x . The following information are used:

- the error of unit weight of the circle fitting ($P_{\sigma 0}$),
- the standard deviation of the fitted diameter ($P_{\sigma \text{Diameter}}$),
- the visible stem section (angle of the visible circle section) (P_α),
- the ratio of the scanned point number and the calculated number of points (determined by scan resolution, distance to stem, cut thickness) ($P_\%$)
- a median filtering with 11 neighbour elements of the fitted diameters along the stem (P_{Median}).

The probability $P_{\sigma 0}$, $P_{\sigma \text{Diameter}}$ and P_α are determined by calculating the ratio of each value to a threshold ($P_x = x / TH_x$). To consider the median filtering the diameter is compared with the median of its five neighbour up- and downward diameters. If the difference between the diameter and the median diameter is smaller than 5% of the median diameter, P_{Median} is 1 otherwise 0. All five summands consist of values between 0 and 1. The reliability factor was calculated as an arithmetic mean (equation 3). In general, diameters with a factor greater than 0.7 are deemed as reliable.

$$ZP = (P_{\sigma 0} + P_{\sigma \text{Diameter}} + P_\alpha + P_\% + P_{\text{Median}}) / 5 \quad (3)$$

To predict the taper of standing trees taper equations and basic taper models are extant (Nieuwenhuis, 2002). A modified Kozak taper equation was used. Therefore a prediction of taper in non-observable stem heights can be done based on observed measurements.

5. UTILISING A POLYNOMIAL MODEL TO SMOOTH THE STEM

To improve the value recovery in forest stands, accurate stem shape and position of trees is essential. The efficiency of the harvesting operations can be greatly increased by determining the crop “profile”. Three important aims are to consider: maximising of (timber) volume, maximising of (timber) value and minimising of costs (Nieuwenhuis, 2006). Even just a few noisy values in the predicted stem profile can greatly impact on the processes used to determine the expected products extracted from a stem and its overall value. This in turn means that there are inaccuracies in the inventory data. In order to ensure the stem profile is as accurate as possible the effects of noisy values must be minimised as much as possible. In pursuit of this goal a weighted polynomial function is an invaluable technique to smoothen stem diameters.

In fitting a smoothing function, such as spline or polynomial model to the stem diameters, the important point to realise is that one can obtain a fit as close to the data as one wants, simply by adding more and more breakpoints. However, what one really wants is a smooth curve, flexible enough to capture the (unknown) functional relationship underlying the data, yet smooth enough not to follow the noise component in the data due to measurement errors. The problem of separating the noise from the underlying trend becomes more manageable if an indication of reliability can be determined. During the circle fitting process the reliability factor was determined as outlined in section 4.

This Reliability Factor was used to produce a set of weights for each point on which the polynomial model was to be built. This helps to ensure that unreliable data does not impact greatly on the fitted model. The inputted data to the model is the set of diameters from the circle fitting process and their corresponding reliability values as weighting factors. The polynomial model was fitted to the weighted set of inputs, using least squares regression. This minimised the residual sum of errors over the data (Hastie et al., 2001). A polynomial model was used instead of an interpolating spline, as the goal in fitting the model is to approximate the trend of the data and minimise the effects of noise. Approximating spline models exist and a smoothing spline was originally used for this purpose (De Boor, 1978). However, given the levels of noise and relatively simple shape of tree stems the least squared polynomial model was favoured. This simpler model was found to track the underlying trend adequately, given the noise and did not require the specification of a smoothing parameter.

6. RESULTS

6.1 Segmentation

The results shown here are derived from the 21 plots acquired in May 2006. Overall 533 of 547 trees could be detected correctly and therefore the detection rate was 97.4%. There were 14 type I errors, mainly caused by occlusions of trees and vegetation standing in the foreground. Therefore not enough laser points were landing on the stem surface within the horizontal data cut. 60 type II errors are produced. Figure 4 shows the number of errors caused in the different plots.

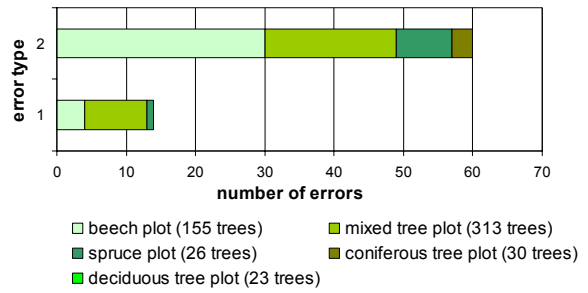


Figure 4. Detection errors

To assess the efficiency of both segmentations two plots (plot A and B) with heavy branching (Figure 5) were processed. Plot A and plot B consist of each 16 trees inside a plot radius of 10 m. By using the segmentation based on point cluster search only 2 (plot A) and 6 (plot B) stems could be found correctly. After the second segmentation using point density raster analysis all trees of plot A could be identified correctly and only one tree of plot B could not be found. The results of the segmentation of both plots are outlined in Table 1.

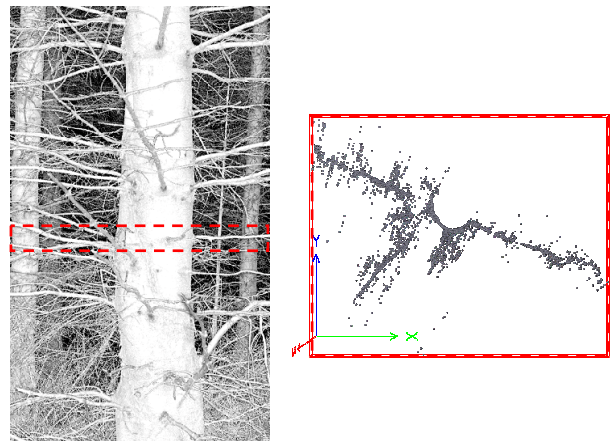


Figure 5. Spruce with heavy branching (left); top-view of a horizontal 10 cm cut

	Segmentation based on			
	point cluster search		point density raster analysis	
Data	Plot A	Plot B	Plot A	Plot B
Trees	16	16	16	16
Classified objects	23	21	16	21
Correct found stems	2	6	16	15
Detection rate	12.5%	37.5%	100%	93.75%
Type I error	14	10	0	1
Type II error	21	15	0	6

Table 1. Results of the segmentation

6.2 Diameter profile fitting

To assess the accuracy of profile fitting along the stem harvester stem file data was used. Figure 6 shows the comparison between the profile fitting and the diameters from the harvester along a Sitka spruce stem located 8.5 m from the laserscanner. The underestimation caused by too few survey points landing on a short stem segment, while the overestimation is caused by branching. The standard deviation of the profile differences of all fitted diameters (yellow rectangles in Figure 6) along the stem is 3.91 cm. Thus, all under- and overestimated diameters can be detected by using profiles with a “Reliability Factor” bigger than 0.69 (Figure 7). A standard deviation of 1.36 cm is obtained.

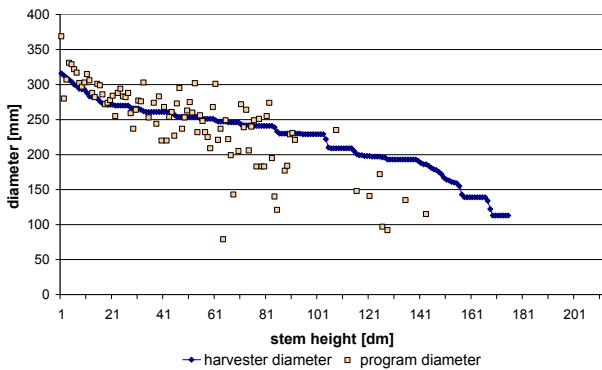


Figure 6. Derived diameters from the profile fitting of a Sitka spruce in comparison with the diameter obtained from the harvester

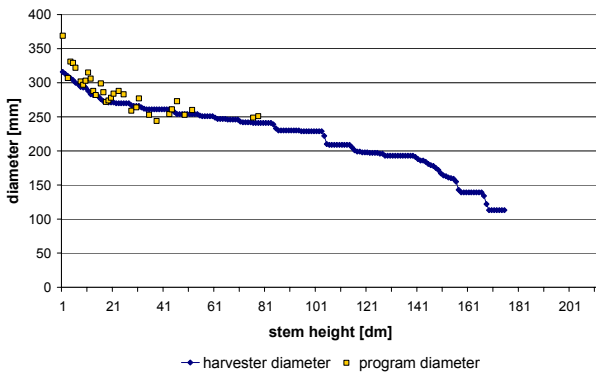


Figure 7. Derived diameters of a Sitka spruce with an “Reliability Factor” bigger than 0.69 in comparison with the diameter obtained from the harvester

The stem was smoothed up to a height of 7.8 m with a standard deviation of 0.64 cm by a polynomial model (Figure 8 - green triangles). As a height of 7.9 m a taper prediction based on the modified equation of Kozak, as outlined in section 4, was done (Figure 8 – red points). This equation was specific for spruce species with Ireland-Centric coefficients.

Table 2 summarises the accuracies of the profile fitting (all diameters, reliable diameters), the smoothing and the predicted taper for the tree from Figure 8. Finally the standard deviation of 22 trees inside a 12 m radius of the Sitka spruce plantation (plot C) are shown in Table 3.

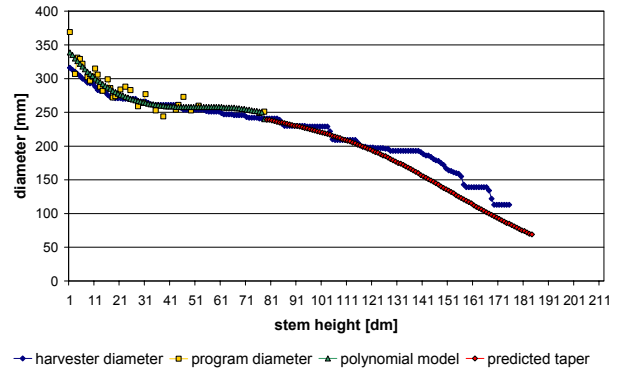


Figure 8. Reliable diameters, smoothed data and predicted taper compared with harvester data of one Sitka spruce

[cm]	Standard deviation	Arithmetic mean	Max. difference	Min. difference
All diameters	3.91	1.03	0.168	0
Reliable diameters	1.36	-0.94	-5.30	0
Polynomial model	0.64	-2.20	-2.30	0
Predicted taper	1.36	0.20	3.70	0

Table 2. Results of the profile fitting of one Sitka spruce located in plot C (compared with harvester data)

[cm]	Standard deviation	Arithmetic mean	Maximum difference	Minimum difference
Reliable diameters	2.48	-0.64	19.60	0

Table 3. Results of the profile fitting of plot C with 22 trees (compared with harvester data)

7. CONCLUSION

In collaboration with TreeMetrics (www.treemetrics.com), a computer program (*AutoStemTM*) was developed in the C++ programming language to automatically determine forest inventory parameters based on terrestrial laserscanner point clouds. Figure 9 shows the *AutoStemTM* user interface. By processing a point cloud (X, Y, Z), stem number ordered by azimuth, stem position, diameter at breast height (DBH - measured at a height of 1.3 m), tree height and profiles along the stem in user specific heights are displayed. Data sets recorded in natural or production forests from one position (single scan mode) or more positions (multiple scan mode) can be processed. Obstructions such as undergrowth, rocks and heavy branching do limit the effective range of a single scan. In these situations multiple scans are done to gather the necessary information.

By using two segmentation algorithms a slice of a point cloud was analysed. The rate of success was enhanced by using both algorithms for plots with heavy branching. Type I errors were minimised by the second segmentation process. Furthermore robust tree detection is possible, which the detection rate of 97.4% confirms. Nevertheless some type I and type II errors are present.

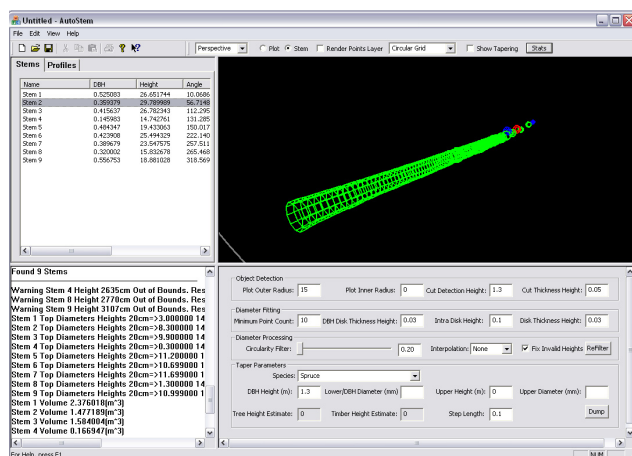


Figure 9. *AutoStem*TM user interface

The newly introduced reliability factor enables the detection of badly fitted diameters (Figure 7 vs. Figure 8) allowing a better determination of the stem shape to be made. An average standard deviation of 2.48 cm for 22 Sitka spruces was presented for profile fitting with a height interval of 10 cm, compared with harvester data. Henning and Radtke (2006a) present a standard deviation of nine loblolly pine trees of 2.1 cm estimated at every 1-m bole section. However, this was done using co-registered datasets of three separate scanner positions around each tree. By processing point clouds obtained in multiple scan setups, occlusions can be reduced and accuracy increased.

REFERENCES

- Aschoff, T., Spiecker, H., 2004. Algorithms for the automatic detection of trees in laser scanner data. In: Thies, M.; Koch, B.; Spiecker, H.; Weinacker, H. (eds.): *Laser-Scanners for Forest and Landscape Assessment, Proceedings of NATSCAN-Conference on Laser-Scanners for Forest- and Landscape Assessment, International Archives of Photogrammetry, Remote Sensing and Spatial Information Sciences Vol. XXXVI, Part 8/ W2: 66-70*
- Aschoff, T., Holdenried, M. W., Spiecker, H., 2006. Terrestrische Laserscanner zur Untersuchung von Wäldern als Jagdlebensräume für Fledermäuse. In: Luhmann, T. und Müller, C. (Hrsg.): *Photogrammetrie - Laserscanning - Optische 3D-Messtechnik, Beiträge der Oldenburger 3D-Tage 2006*, Herbert Wichmann Verlag, Heidelberg, pp. 280-287
- Bienert, A., Scheller, S., Keane, E., Mullooly, G., Mohan, F., 2006. Application of terrestrial laser scanners for the determination of forest inventory parameters. *International Archives of Photogrammetry, Remote Sensing and Spatial Information Sciences, Vol. 36, Part 5*
- Bienert, A., Scheller, S., Keane, E., Mullooly, G., Mohan, F., 2007. Automatische Erfassung forstinventur-relevanter Geometrieparameter von Waldbäumen aus terrestrischen Laserscannerdaten. In: Luhmann, T. und Müller, C. (Hrsg.): *Photogrammetrie - Laserscanning - Optische 3D-Messtechnik, Beiträge der Oldenburger 3D-Tage 2007*, Verlag Herbert Wichmann Verlag, Heidelberg
- de Boor, C., 1978. *A practical guide to splines*. Springer, New York
- Faro Europe GmbH & Co. KG, 2005. *Aufbruch in neue Dimensionen: der FARO Laser Scanner LS*. Laser Scanner Broschüre
- Food and Agriculture Organisation of the United Nations, 2007. *State of the World's Forests 2007*. Rome, Italy
- Hastie, T., Tibshirani, R., Friedman, J. H., 2001. *The elements of statistical learning*. Springer
- Henning, J. G., Radtke, P. J., 2006a. Detailed stem measurements of standing trees from ground-based scanning lidar. *Forest Science* 52(1), pp. 67-80
- Henning, J. G., Radtke P. J., 2006b. Ground-based laser imaging for assessing three-dimensional forest canopy structure. *Photogrammetric Engineering & Remote Sensing*, 72(12), pp. 1349-1358
- Hopkinson, C., Chasmer, L., Young-Pow, C., Treitz, P., 2004. Assessing forest metrics with a ground-based scanning lidar. *Canadian Journal of Forest Research*, 34, pp. 573-583
- Nieuwenhuis, M., 2002. The development and validation of pre-harvest inventory methodologies for timber procurement in Ireland. *Silva Fennica*, 36(2), pp. 535-547
- Scheller, S., Schneider, D., 2006. Extraktion von Primitiven aus Laserscannerpunktewolken zur Rekonstruktion von Tragwerken. In: Luhmann, T. und Müller, C. (Hrsg.): *Photogrammetrie - Laserscanning - Optische 3D-Messtechnik, Beiträge der Oldenburger 3D-Tage 2006*, Herbert Wichmann Verlag, Heidelberg, pp. 156-163
- Simonse, M., Aschoff, T., Spiecker, H., Thies, M., 2003. Automatic determination of forest inventory parameters using terrestrial laserscanning. *Proceedings of the ScandLaser Scientific Workshop on Airborne Laser Scanning of Forests, Umeå*, pp. 251-257.
- Thies, M., Spiecker, H., 2004. Evaluation and future prospects of terrestrial laser scanning for standardized forest inventories. In: Thies, M.; Koch, B.; Spiecker, H.; Weinacker, H. (eds.): *Laser-Scanners for Forest and Landscape Assessment. Proceedings of NATSCAN-Conference on Laser-Scanners for Forest- and Landscape Assessment. International Archives of Photogrammetry, Remote Sensing and Spatial Information Sciences Vol. XXXVI, Part 8/ W2: 192- 197*
- Watt, P. J., Donoghue, D. N. M., 2005. Measuring forest structure with terrestrial laser scanning. *International Journal of Remote Sensing*, 26(7), pp. 1437-1446

ACKNOWLEDGEMENTS

All data presented here were acquired by *TreeMetrics Ltd, Cork/ Ireland*. Their support is gratefully acknowledged. We also like to thank Bernhard Posch from *Österreichische Bundesforste AG* for providing the reference data for the Austrian plots.

APPLICATION OF TERRESTRIAL LASER SCANNING FOR SHIPBUILDING

K. Biskup^{a*}, P. Arias^a, H. Lorenzo^a, J. Armesto^a

^a Dep. of Natural Resources and Environmental Engineering, University of Vigo, C/ Campus Universitario As Lagoas-Marcosende s/n, C.P. 36200, Vigo, Spain – (biskupka, parias, hlorenzo, julia)@uvigo.es

KEY WORDS: laser scanning, terrestrial, point cloud, shipbuilding, underbody, 3D modelling

ABSTRACT:

Recently, a laser scanner technology has been receiving more attention. Nowadays use of terrestrial laser scanners (TLS) is continuously increasing. This technique offers the possibility of measuring millions of points within short period of time. Thus, it is possible to record complete 3D objects efficiently. In this communication the process followed to model the hull and the deck of the ship will be described. To perform this process, a point definition from a terrestrial laser – scanner Faro LS 880 was used as information source. From this data, the commercial package software Geomagic Studio 8 has been used, to obtain the three-dimensional model of two differentiated parts of the ship. The importance of this process lays on the fact that an inverse process has been followed: it is the model that has been obtained from the real ship. From these 3D models some series of analysis and verifications could be made, like diverse measurements, construction defects, determination of possible asymmetries, etc. even though these aren't presented in this communication. Another remarkable objective of this project is to calculate the volume of the underbody. The waterline which indicates the level at which the ship floats in the water (thus it's a line which separate underbody from dead works of the ship) helps us to obtain the 3D model of the underbody by means of Geomagic software and then to calculate its volume.

1. INTRODUCTION

The construction of sporting, pleasure and fishing craft has, in recent years, become an important source of revenues for the shipbuilding sector. Demand, moreover, is steadily growing, and this grow is expected to continue in the medium term. Consequently, an increasing number of businesses are entering into the sector which is made increasingly competitive.

The manufacturing process for this type of craft, which is largely manual, relies on the expertise of individual operatives, and results in products that are generally unique and different. Moreover, rigorous quality control programmes are rarely implemented and construction or assembly workflow diagrams are not generally used. Parts are on occasion wasted or re-worked due to production errors, for example, causing production delays and increased costs. This situation, combined with the urgent need to increase productivity and competitiveness, is putting pressure on shipbuilders to improve production processes with the incorporation of design and new manufacturing technologies, which - without increasing costs significantly - will define a priori the quality of the final product and ensure that the different parts of the finished craft contain no asymmetries or construction defects.

The construction of accurate three-dimensional models that use terrestrial laser scanning techniques, which permit millions of points to be measured in a question of minutes, offers particular promise in terms of the design and construction of boats (Thiyagarajan, 2003), replacing other traditional, slower and more inaccurate methods based on moulds subsequently adapted to the definitive boat shape.

Terrestrial laser scanner measurement techniques generate a large quantity of information, which requires substantial processing to arrive to the point where a definitive 3D model is obtained.

2. 3D LASER SCANNER TECHNOLOGY APPLICATIONS

Cultural heritage recording (Barber, 2005; Stenberg, 2006; Vistini, 2006), architectural modelling (Levoy, 2000; Akca, 2006), building reconstruction (Alshawabkeh, 2005), accident investigation (Pagounis, 2006) and structural engineering (Gordon, 2004) are just some of the subjects now benefiting from the use of terrestrial laser scanning.

The most important area of application of laser scanning to engineering is 3D modelling of existing structures and industrial equipment (Straiger, 2002). 3D plant models are needed as basic data for design, especially when modernising industrial plants. Plant models are also used in maintenance and facility management systems of industrial plants as a 3D virtual reality. The 3D virtual model gives dimensions for efficient maintenance.

The main infrastructure applications are for modelling of buildings, bridges, tunnels, underground facilities and for virtual city modelling (Kretschmer, 2004; Böhm, 2005; Arayici, 2005). Laser scanning is also used for mining industry and modelling in the shipbuilding (Gutiérrez, 2006; Arias, 2006).

3. AIMS OF THIS PROJECT

In this paper the investigations of the 3D modelling using the terrestrial laser scanning system are presented. It describes a project whose final aim was to establish overall conditions of a wooden boat, because of the future possibility to do up it. Other important aim of the project was to calculate a volume of the underbody. To reach this goal of the work we needed to mark a waterline on the hull. The waterline refers to an imaginary line marking the level at which the boat floats in the water, thus it's a line which separate underbody from dead works of the boat. The ship speed is determined by, amongst other things, the waterline length.

* Corresponding author

The boat is based on a structure consisting of two differentiated parts: the deck and the hull. From a mosaic of TLS point clouds we have constructed three-dimensional models of these two components using the commercial package software Geomagic Studio 8.

4. MEASURING OF THE SHIP

3.1. Instrumentation

The equipment used for the data collection is listed as follows:

- Three-dimensional terrestrial laser scanner FARO LS 880 (Figure 1). Each scan covers a 320° vertical and 360° horizontal field-of-view.
- Magnetic targets were implemented to increase the precision in assembling the different scans.
- Laptop computer. Terrestrial laser applications require the scanner to be connected to a computer in which the point clouds recorded by the laser are stored in real time.
- Tripod. A tripod provides the support necessary to ensure the terrestrial laser scanner during scanning operations.
- Software application for linking up the point clouds captured in each of the scans.
- Software for cleaning up, debugging and filtering the point clouds generated by the scans.
- Software for generating 3D surface models from the pre – processed point clouds.



Figure 1. The 3D laser scanner FARO LS 880

3.2. Data Acquisition

Preliminary steps. Prior to commencing the scanning tasks, the surroundings of the element to be modelled should be analysed in detail. The following points need to be taken under consideration:

- Suitable positions to capture data, using the laser that will minimise both the number of scan locations and information lost, must be identified.
- Elements that may prevent correct data capture or that may introduce information that could hinder subsequent processing, must be identified.

- Any possible sources of vibrations near the scanning area must be removed to avoid adverse effects on the quality of the scans.

Scanning procedure. Once these preliminary steps have been taken, the fieldwork stage can proceed. This phase is structured as follows:

- 1) Creation of sketches, indicating the position of elements of interest and of the scanner in each scanning session is extremely useful for subsequent information processing phases.
- 2) The scanner is positioned in the previously selected locations and scanning commences. The scanning procedure consisted of moving the 3D laser scanner around the ship, so that the studied object was surrounded completely. During the scanning process, the following guidelines should be followed:
 - a. Ensure overlaps of about 20% between adjacent areas of interest and avoid shadow areas where there is no information. This will ensure that all areas are fully covered so that when the different scans are finally put together, no essential elements will be excluded from the final model.
 - b. Once the data capture process commences, ensure that the objects to be scanned are not moved.
 - c. Avoid any movement or vibration, no matter how small, of the scanner.
 - d. It is recommended that targets that can be automatically recognised by the software are used as control points. In this way overlapping between scans can be minimised.

In our case this matter was essential. Every scan was made with 10 targets always ensuring overlaps of 5 targets between two following scans. It was especially important at the moment of assembly of the hull and the deck. During the scanning process of the hull at least one of the targets was placed on the deck, which helps us during assembly process.
- 3) Finally, it is recommended during this phase to assemble the successive scanned models prior to leaving the site. This will avoid any subsequent problems arising as a consequence of incomplete data, corrupted files, etc. The additional time required for this work is more than compensated for by the avoidance of possible subsequent complications that may be difficult to rectify.

The measurement procedure followed for the data collection took approximately 7 working hours, scanning both elements of the boat, the hull and the deck.

The waterline that refers to an imaginary line marking the level at which the boat floats in the water, was marked by some targets to help us to recognize it on the scans (showed by Fig.2). The waterline was the essential date to calculate the volume of the underbody in this case.



Figure 2. Waterline marked with black and white targets

Discussion. In general, our scanning procedure works quite smoothly.

Our biggest failure was the lack of calibration of the scanner before the scanning procedure that caused a standard deviation of registration accuracy of about 3-4 cm.

We have found some problems during the automatic recognition of white spherical targets by the software especially with the direct sun. It was needed to find the way to make a shadow in the place of the targets (i.e. to cover it with something dark, i.e. umbrella in our case) and repeat the scan. It takes up about one working hour in the course of our outside work. During the registration some difficulties were encountered as will be discussed in section 5.

In my opinion the registration accuracy could be improved changing direction of scanning procedure. Instead of moving the 3D laser scanner around the ship (the beginning point and the end point are the same), it could be moved from the beginning to the end along the left side of the ship and then from the beginning to the end along the right side of the ship. This procedure should be applied both to the hull and to the deck of the ship.

3.3. Data processing: 3D visualization

Data processing. Once the previous phase is completed, the next stage is data processing, which will result in the 3D surface models. This is a slow and laborious process performed using a computer and specialised software for pre-processing the 3D point clouds. This phase, in fact, represents the bulk of the work involved in the project. Therefore, the cost of this phase is largely dictated by the cost of labour for the information processing process in the laboratory.

The scans, registered in the global coordinate system, are analysed in order to locate points not relevant to the project. The scanner records measurements returned from all the elements within its field of view, many of which will not be parts of the boat (surrounding things, other boats, work tools and accessories, etc). These data are removed from the point cloud with the help of the photographs.

The “cleaning” process and data processing are made by the commercial package software Geomagic Studio 8. Our work consists of three main phases:

- Point Phase,
- Polygon Phase,
- and the last one – Shape Phase.

Point Phase. The first one is the phase of point elimination and noise reduction. In this phase redundant information is eliminated from the point cloud that is to be modelled with the intention of reducing the volume of data, thereby simplifying subsequent operations. We need to remove these stray point, known as disconnects or outliers that may exist around the object. These can be identified as points that are far away from the main point cloud and don’t represent any geometry that we want to keep. The filtering process requires a certain degree of skill and experience, as there is a risk of filtering out too much data - with the consequent loss of information – or too little data, which can cause subsequent problems due to excessive information and overly-large files.

Frequently, during the scanning process, an element of “noise” is introduced into the data. This “noisy data” is identified by a rough, uneven appearance in the surface object and is due to such factors as small vibrations in the scanning device, inaccurate scanner calibration, or the character of the surface on

the object being scanned. It’s need to minimize this noise. Finally we can use sampling to reduce the number of points in the object while maintaining an accurate representation of the part. With unordered data, we can use uniform sampling to reduce the number of points and leave points organized so they produce triangles roughly the same size when wrapped. The point cloud prepared like that (“clean point cloud”) is ready to go to the wrap phase.

Polygonal Phase. Once the point object has been cleaned and organized, it is time to wrap the object with a polygon mesh. Three-dimensional surface models comprising triangular facets are constructed for the hull and for the deck from the filtered point clouds. Correct triangulation is the basis for subsequent correct modelling of curves and surfaces, and the results will largely depend of how well the point clouds have been filtered. In regular areas with simple shapes, filtering may be more intense, resulting in a lower number of triangles with longer sides. In irregular areas with complex shapes, filtering should be less intense, resulting in a larger number of triangles with shorter sides.

The wrapping process shows us the first result of our work. Before the coming to the finish part of the project, it’s need to fill the missing data.

Shape Phase. Once the polygon model has been edited to fix any imperfections and holes, it is ready for the next phase. This would be the Shape Phase, which is the phase where it’s creating NURBS (Non-Uniform Rational B-Spline) surfaces over the polygon object using autosurfacing.

The figures 3 and 4 show the results of three main phases of the project of both parts of the ship.

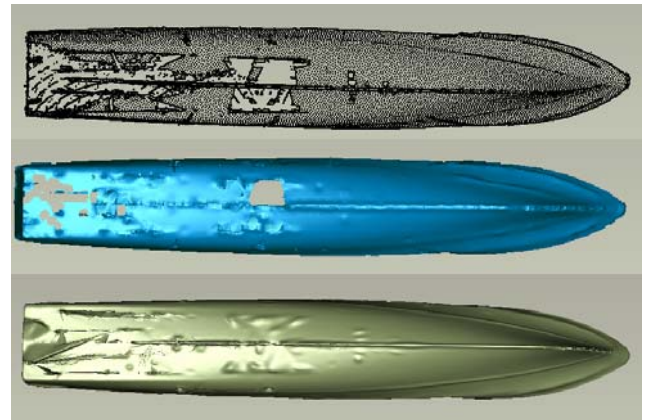


Figure 3. Results of Point Phase, Polygon Phase and Shape Phase of the hull

Discussion. How well our data processing flow works? In most cases, it works well. However, it was time-consuming because of the enormous quantity of points. Sometimes the computer works very slowly, especially in cases of surface extraction. In the worst cases the computer suspended after the long working hours and it was needed to repeat the Shape Phase, which was the most time-consuming task.

We were disappointed by the number of holes, some several centimeters in size, even with the results of the application of “fill holes” tool. The Shape Phase of the hull wasn’t very satisfactory because of the too much missing data. The deck was a more complex structure but personally we were quite more pleased with the results of the filling holes of the deck than of the hull.



Figure 4. Results of Point Phase, Polygon Phase and Shape Phase of the deck

5. RESULTS

Scanning procedure. Fieldwork lasting approximately 7 hours was performed by a team of 3 individuals, as follows:

- 1) A sketch was first created of the position of the elements to be modelled, as also of the position of the scanner and of the field of vision for each scan. The scanner was prepared to capture data within its 320° x 360° field of view. The 360° field of view was necessary because some targets were placed around the ship to obtain the best precision possible in every scan. It helps us during the assembly process then.
- 2) Magnetic targets, which are automatically recognised by the software, were used to mark a series of control points on the objects. About 7 hours' fieldwork was necessary for the measurements, and over 41 million points were measured.
- 3) Finally all the scans were registered to object space. During this operation some difficulties were encountered, for example variation of the sea level (flow and ebb) between start and final of the scanning process, difficulties of placing the laser scanner in some scans, etc.

There were 11 scans needed to scan the deck of the boat and 15 scans to scan the hull. 10 targets were used in every scan, always ensuring overlaps of 5 of them between two following scans. During the scanning process of the hull at least one target was placed on the deck and then during the scanning of the deck, one of the targets was placed in the same site. This method works perfectly and helps us to assembly the deck and the hull during the laboratory work. All the scans were registered in the computer using the software FARO SCENE and the results were quite satisfactory.

Data processing. The first step before start the 3D modelling was to apply the previous filtering to the point clouds of the hull and the deck. The results of this process were the point clouds with spaces between the neighbour points of 10 cm. The surface models were obtained as follows:

- 1) Point Phase. Areas of irrelevance to the project were eliminated from the scans aligned in the global coordinate system, mainly representing the

surrounding things, other boats, work tools and accessories, etc. The pre-processing of the point clouds was carried out separately for the hull and the deck, with 778,742 points obtained for the hull, and 332,213 points for the deck.

Redundant information on the point clouds and points falling outside the future model surface were eliminated to facilitate file handling. Given the simplicity of the hull surface, the noise reduction wasn't apply, only the filtering process and uniform sampling were performed, thereby reducing the number of points to a total of 139,446. Since the deck was a more complex structure, we applied the noise reduction, and then filtering process and uniform sampling were performed, resulting in a final total of 179,874 points.

The Figure 5 shows the standard deviation values along the deck of the ship after application of noise reduction. The mean value of standard deviation in shape after noise reduction was of 0.0221 m.

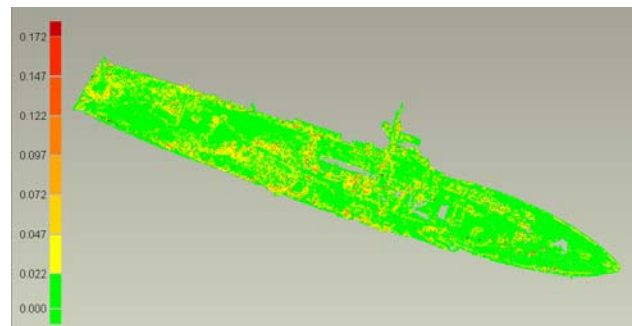


Figure 5. The standard deviation values along the deck of the ship after application of noise reduction

- 2) Polygonal Phase (the wrapping). The quality of this polygonal model depends directly on the filtering process. The hull, with relatively simple shapes, resulted in fewer triangles with longer sides compared to the deck (more complex shapes, therefore more triangles and shorter sides). Triangulation of the point clouds for the hull resulted with 211,794 current triangles, and for the deck, with 312,932 current triangles.

In the above Table 1 we find the results after the Polygonal Phase applied to the hull and the deck of the ship. The hull has no residuals in this case because we haven't applied the noise reduction.

The standard deviation gives the reference to deviation in shape between the point cloud data set and polygonal model.

Value [m]	The hull		The deck	
	Positive	Negative	Positive	Negative
Max. distance	0		0.008162	-0.008197
Average distance	0		0.000008	-0.005841
Standard deviation	0		0.000319	

Table 1. Values of standard deviation and the residuals after the Polygonal Phase

- 3) Fill Holes. Identification of missing data and manual completion. This task was mainly manual.
- 4) Shape Phase (autosurfacing). Using the triangles obtained, the next stage was definition of the surfaces that would form the models. This operation was again carried out separately for the deck and the hull.

The figure 6 shows the standard deviation values along the hull of the ship after application of autosurfacing. The full results after the Shape Phase applied to the hull and the deck of the ship are shown in Table 2.

The standard deviation gives the reference to deviation in shape between the point cloud data set and surface model.

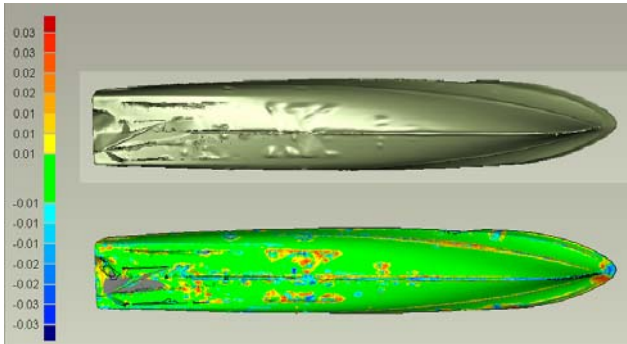


Figure 6. The standard deviation values along the hull of the ship after the autosurfacing

- 5) Assembly of the two main elements of the boat – the hull and the deck (first part of the Figure 7 shows the result of the assembly).

	The hull		The deck	
Value [m]	Positive	Negative	Positive	Negative
Max. distance	0.029997	-0.029840	0.059953	-0.059851
Average distance	0.004767	-0.003123	0.007784	-0.008039
Standard deviation	0.006847		0.012581	

Table 2. Values of standard deviation and the residuals after the Shape Phase

About 46 hours of laboratory work was required for above mentioned tasks. The results of the 3D modelling were quite satisfactory. The standard deviations of shape (between the point cloud data set and the surface model) for the 3D models resulted of 0.006847m for the hull and 0.012581m for the deck.

It's possible to apply three above mentioned phases to 3D point cloud of the whole boat.

We have started with 1,110,955 points and we applied the noise reduction. Then filtering process and uniform sampling were performed, resulting in a final total of 167,750 points in Point Phase.

Triangulation of the point cloud for the boat resulted with 323,862 current triangles, in Polygon Phase. Finally the Shape Phase resulted with 5342 patches obtained by applying the autosurfacing. The final results of every one of these phases are shown in Fig. 7.

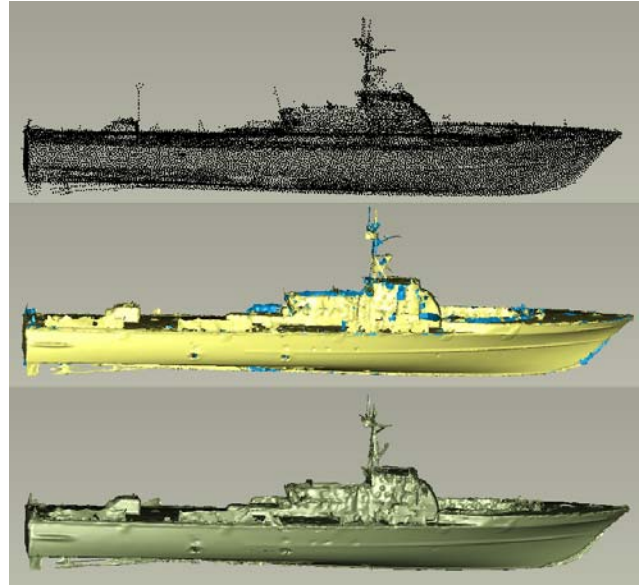


Figure 7. The results of Point Phase, Polygon Phase and Shape Phase of the ship

The standard deviation (deviation in shape between the point cloud data set and the surface model) resulted of 0.012161m for the 3D model of the whole boat.

The residuals are shown in Table 3.

Value [m]	Positive	Negative
Max. distance	0.059715	-0.059498
Average distance	0.008139	-0.006322
Standard deviation	0.012161	

Table 3. Values of standard deviation and the residuals of the whole ship after the Shape Phase

One of the most important matters when we speak about the speed of the boat it's surely the power of the engine.

The essential information to start calculating the power that we need for the boat is its length of waterline. So the length of waterline was the crucial date needed.

There exist diverse ways to obtain the power that we need in the propeller of the boat to reach the wished speed relating the length of waterline with the displacement of the boat. The length of waterline was obtained by means of marking it on the hull with black and white targets which were easily recognized on the scans.

The displacement of the boat is related with the submerged volume of underbody (in this case it was 145 m³) and with its form. These would be easily obtained by means of use of commercial package software Geomagic Studio 8.

The underbody point cloud is demonstrated in Fig. 8.

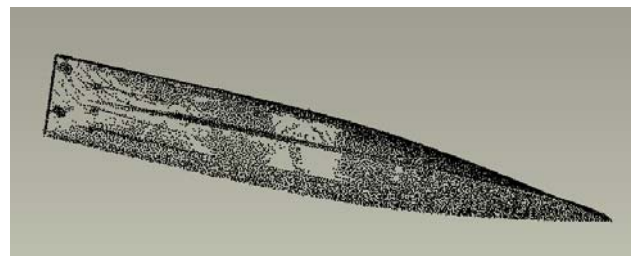


Figure 8. The form of the underbody of the ship (the point cloud)

Discussion. Our results were quite satisfactory because we obtained 6,8 mm of deviation of shape in the hull and 12,5 mm of deviation in shape in the deck case. Considering the size of the whole ship (about 40 m) the results obtained were really good. The residuals weren't so big so the stability of the laser scanner during the data acquisition was quite good.

The final results could be improved by previous calibration of the laser scanner.

Comparing the results of the whole boat with the results of the hull and the deck, which we obtained during the separate processing results of better values for the whole boat (we obtained 12,5 mm of deviation in shape for the whole model of the ship), but it can result little objective in this case because of different ways of pre – processing of the point clouds of the boat: separate handling and joint handling. The first one permits personal and separate processing of both parts of the boat and the second one requires applying of the same processing parameters to the hull and the deck what can provoke a loss of some information. Besides it's easier to work with separate parts of the boat because the point clouds contain less points and it facilitates the 3D modelling.

6. CONCLUSIONS

Nowadays, three-dimensional models can be rapidly and effectively created using laser scanning techniques, which can measure millions of points in a matter of minutes with millimetre-level precision. Moreover, they avoid the error propagation that is typical of classical topographic methods. Specific software is used to process the point clouds and to develop the final 3D surface models.

Although these techniques offer the potential for improving the working methods currently employed in most companies in the sector, they have some drawbacks. The two major disadvantages are: the cost of the equipment and the highly specialised, laborious and lengthy data processing work required to develop the 3D models. Nevertheless, it is likely that equipment costs fall, and the data processing and 3D model creation become less complex in the future.

References

- Akca D., Gruen A., Alkis Z., Demir N., Breuckmann B., Erduyan I., Nadir E., 2006. 3d Modeling of the Weary Herakles Statue with a Coded Structured Light System. *Archives of IAPRS Volume XXXVI*, Part 5, Dresden, Germany.
- Alshawabkeh Y., 2005. Using Terrestrial Laser Scanning for the 3D Reconstruction of Petra/Jordan. *Archives of 'Photogrammetric Week 05' Dieter Fritsch, Ed.*, Heidelberg, Germany.
- Arayici Y., Hamilton A., 2005. Modeling 3D Scanned Data to Visualize the Built Environment. *Proceedings of the Ninth International Conference on Information Visualisation (IV'05)*, London, United Kingdom.
- Arias P, Armesto J., Lorenzo H., Ordóñez C., 2007. Terrestrial Laser Technology in Sporting Craft 3D Modelling. *Proceedings book of the International Symposium CompIMAGE 2006. Computational Modelling of Objects Represented in Images: Fundamentals, Method and Applications*. ISBN 978-0-415-43349-5, Vol. 1, 63-69. 2007. Taylor & Francis Group. London, United Kingdom.
- Barber D. M., Mills J. P., Bryan P. G., 2005. Maintaining Momentum In Terrestrial Laser Scanning: A Uk Case Study. *Archives of ISPRS WG III/3, III/4, V/3 Workshop "Laser scanning 2005"*, Enschede, the Netherlands.
- Böhm J., Haala N., 2005. Efficient Integration Of Aerial And Terrestrial Laser Data for Virtual City Modeling Using Lasermaps. *Archives of ISPRS WG III/3, III/4, V/3 Workshop "Laser scanning 2005"*, Enschede, the Netherlands.
- Fernández Gutiérrez D., Berruelo García J., Leal H., Cercós Pita J., Souto Iglesias A., 2006. Modelado 3D de una carena, apéndices y propulsor de un arrastrero de 67 m de eslora. *Art. Tec. Model.*, pp. 100-106.
- Gordon S., Lichti D., Franke J., Stewart M., 2004. Measurement of Structural Deformation using Terrestrial Laser Scanners. *Archives of 1st FIG International Symposium on Engineering Surveys for Construction Works and Structural Engineering*, Nottingham, United Kingdom.
- Kretschmer U., Abmayr T., Thies M., Fröhlich C., 2004. Traffic Construction Analysis by Use of Terrestrial Laser Scanning. *Archives of Photogrammetry, Remote Sensing and Spatial Information Sciences*, Vol. XXXVI-8W2.
- Levoy M., Pulli K., Curless B., Rusinkiewicz Sz., Koller D., Pereira L., Ginzton M, Anderson S., Davis J., Ginsberg J., Shade J., Fulk D., 2000. The Digital Michelangelo Project: 3D Scanning of Large Statues. *SIGGRAPH*, New Orleans, LA USA.
- Pagounis V., Tsakiri M., Palaskas S., Biza B., Zaloumi E., 2006. 3D Laser Scanning for Road Safety and Accident Reconstruction. *Archives of XXIII FIG Congress*, Munich, Germany.
- Staiger R., 2002. Laser Scanning in an Industrial Environment. *Archives of FIG XXII International Congress*, Washington, D.C. USA.
- Sternberg H., 2006. Deformation Measurements at Historical Buildings with Terrestrial Laserscanners. *Archives of IAPRS Volume XXXVI*, Part 5, Dresden, Germany.
- Thiyagarajan, R., 2003. Use of 3D Laser Scanner and Close Range Photogrammetry for Shipbuilding. Ship Production. *Track of the World Maritime Conference*, October 17-20, San Francisco, EEUU.
- Visintini D., Crosilla F., Sepic F., 2006. Laser Scanning Survey of The Aquileia Basilica (Italy) and Automatic Modeling of the Volumetric Primitives. *Archives of IAPRS Volume XXXVI*, Part 5, Dresden, Germany.

USING AIRBORNE SMALL-FOOTPRINT LASER SCANNER TO ASSESS THE QUANTITY OF SEEDLINGS IN AN UNEVEN-AGED SPRUCE FOREST

O. M. Bollandsås^{a,*}, K. H. Hanssen^b, S. Marthiniussen^a, E. Næsset^a

^aDept. of Ecology and Natural Resource Management, Norwegian University of Life Sciences, P.O. Box 5003, N-1431 Ås. - (ole.martin.bollandsas, erik.naesset)@umb.no, solfrid.marthiniussen@student.umb.no

^b Norwegian Forest and Landscape Institute, P.O. Box 115, N-1431 Ås - kjersti.hanssen@skogoglandskap.no

KEY WORDS: Regeneration, uneven-aged forest, laser scanner data, canopy structure

ABSTRACT:

The relationships between measures of forest structure as derived from airborne laser scanner data and the variation in quantity of young trees established by natural regeneration in a size-diverse spruce forest were analyzed. A regeneration success rate (RSR) was regressed against 27 different laser-derived explanatory variables. The 27 different models were ranked according to their Akaike information criterion score. Each laser variable was then associated with two categories. These were return and type. Within the return and type categories, the variables were grouped according to if they originated from first or last return echoes and if they were canopy height or canopy density metrics. The results show that the laser variables strongest correlated to the quantity of small trees could be attributed to last return and density metrics.

1. INTRODUCTION

The number of seedlings in uneven-aged forest types is influenced by several factors. An essential requirement for regeneration is a source of seeds. Furthermore, the establishment of a seedling from a seed is dependent on the properties of the humus layer, competition from other plants, nutrient availability, and microclimate (moisture and light/heat) at the specific site. Many of these factors are directly or indirectly influenced by stand structure. For instance, stand structure will affect below canopy light levels, which not only determine energy input but also influence temperature, the composition of the bottom- and field layer species, humus layer processes and so on. Thus, under varying forest structure, the quantity and vitality of the young growth will be expected to vary accordingly.

Small footprint airborne laser scanning has shown to produce good data for reproducing forest structures. The laser depicts the canopy by transmissions of geo-referenced laser pulses, recording vegetation heights at the hit point of each pulse. Structural characteristics of the canopy have been modelled from discrete laser returns by several authors (e.g. Maltamo et al., 2004; Parker and Russ, 2004; Tickle et al., 2006). The results have been good because laser pulses can penetrate at least 40 % of maximum canopy height (Næsset, 2004a) and therefore account for much of the variation in canopy structure. However, the retrieval of small trees (say diameter less than five cm in breast height) under a dominating canopy by means of laser scanning is challenging. Still, even though there are several factors that influence establishment and growth that are not, or only partly, affected by the stand structure, it is likely that there exist some relationship between the laser-depicted canopy and the variation in young growth. We believe that utilization of laser data describing canopy structure to detect young growth could be a valuable contribution for improving

existing recruitment models or constructing new ones based solely on laser variables.

The objective of the present study was to analyze the relationship between measures of forest structure as derived from airborne laser scanner data and variation in the quantity of young trees in the height range of 0.1 to 3 m in a size-diverse spruce-dominated forest. The focus was on exploration and identification of laser-derived variables that have a potential for development of future prediction models that might be used in operational forest management.

2. MATERIALS AND METHODS

2.1 Field inventory

The data were collected on 72 circular field plots of 25 m² each. The plots were located in 18 clusters comprising four plots in a boreal forest reserve outside Oslo (59° 50' N, 11° 02' E, 190–370 m a.s.l.). Stand characteristics appear in Table 1. The forest area is further described by Bollandsås and Næsset (2007). From the centre of each cluster, one plot of 25 m² was located 12 meters from this centre in each cardinal direction. The position of each cluster centre was determined by differential GPS+GLONASS measurements. Each plot was split into four by two perpendicular lines through the plot centre in a north/south and east/west direction. In each of these resulting 6.25 m² quadrants, the number of seedlings between 0.1 and 3 m were recorded. A regeneration success rate (RSR) was computed from these records by first counting seedlings in each quadrant (n_i). However, we stopped counting if the number reached a limit considered sufficient on an area of 6.25 m² (n_{suf}). This limit was set to three seedlings. Then we summed n_i for the four quadrants and RSR was computed as this sum relative to a number of seedlings considered sufficient for the entire plot ($4n_{suf}$). The reasons for using RSR instead of the actual number

* Corresponding author.

are that above a certain number, the establishment is most likely dependent on growth factor variations on a very small spatial scale, for instance the occurrence of partly decomposed downed logs or bare mineral soil, but also that RSR will be more

representative of the number of seedlings needed for the regeneration to be successful.

Characteristic ^a	n	Mean	STD	Range	
Minimum diameter (cm)	18	3.2	0.3	3.0	- 4.0
Maximum diameter (cm)	18	47.0	7.3	33.3	- 60.6
Diameter range (cm)	18	43.8	7.3	30.3	- 57.1
Mean diameter by basal area (cm)	18	21.11	3.8	14.60	- 30.32
Lorey's mean height (m)	18	21.65	3.7	15.20	- 28.90
Dominant height (m)	18	26.27	3.3	19.80	- 32.00
Number of stems (ha ⁻¹)	18	1033	308	630	- 1780
Stand basal area (m ² ha ⁻¹)	18	34.2	5.7	21.6	- 45.5
Volume (m ³ ha ⁻¹)	18	360.7	110.4	171.9	- 634.8
Species distribution (%)					
Spruce	18	90		71	- 100
Pine	18	0		0	- 2
Deciduous	18	10		0	- 28

Table 1. Forest data by clusters.

2.2 Laser scanner data

A Hughes 500 helicopter carried the ALTM 1233 laser scanning system produced by Optech, Canada. The average footprint diameter was approximately 18 cm. The mean number of pulses transmitted was 5.0 m⁻². First and last returns echoes were recorded.

First and last pulse height distributions were created for a circle ($r=8.46$ m) around each sample plot centre from the laser echoes considered to be reflected from the tree canopy, i.e., echoes with height values of >3 m. The radius of 8.46 is the maximum radius that could be used without having overlap between laser data from adjacent plots. The tree canopy threshold value of 3 m was set to correspond to the maximum height of trees belonging to the understorey. From these distributions a total of 27 variables were derived. Three percentiles of 10%, 50%, and 90% of maximum height characterized both first and last return laser heights. We labelled these as the height variables. Accordingly, measures of canopy density were derived by dividing the range between the lowest laser canopy height (>3 m) and the maximum canopy height into four uniform fractions. Cumulative canopy densities, henceforth called density variables, were then computed as the proportions of first and last pulse laser hits between the lower limit of each fraction and maximum laser height to total number of pulses. Moreover, maximum and mean height values, standard deviations and coefficients of variation were derived. Further details are provided by Næsset (2004b).

2.3 Data analysis

Because the data originate from clustered plots, there exists spatial dependency between plots within clusters. Thus, data analysis was carried out by means of the PROC MIXED procedure of the SAS statistical software package (Anon., 1999), estimating random coefficient models. Each variable extracted from the laser data were regressed against RSR. Subsequently, each of the models was ranked by their Akaike information criterion (AIC) (Akaike, 1974) score. This yielded a rank of each laser variable according to the goodness of fit of each model.

Then, each laser variable was attributed to groups of first- or last return; and height- or density variable. The first- and last return groups constitute what we labelled the return category. Similarly, the height- and density groups constitute the type category.

3. RESULTS

Table 2 displays the results from the ranking of the laser variables according to the AIC values. The table shows the modus group (most frequent group of variables within the category) with the corresponding frequency for both variable categories. The best explanatory variables for RSR according to these rankings are attributed to last return echo and density metrics. Of the five highest AIC-ranked variables 80% were related to last return echo and 100% to density metrics.

# of ranked variables	Return ^a		Type ^b	
	Modus group	Freq. (%)	Modus group	Freq. (%)
5	Last	80	Density	100
10	Last	70	Density	100
15	Last	60	Density	100

Table 2. The most frequent group of variables (modus group) of the best AIC-ranked 5, 10, and 15 variables assigned to return and type categories.

^a First or last laser echo.

^b Type of laser variable (height or density variable).

4. DISCUSSION

Establishment – measured as regeneration success rate – was found to be best explained by density metrics and variables originated from last return data. While the first return data

describes the surface of the canopy, the last returns penetrate deeper into the canopy and thus account for more vertical canopy variation. Last return data are therefore better accounting for light conditions on the ground. This may also be the reason why density metrics are better than height metrics. Since they are greatly affected by the density and structure of the canopy, they also account for light conditions on the ground better than the height variables.

For germination and early establishment of spruce seedlings, soil temperature and humidity are the most important factors (Mork, 1938; Bjor, 1971). Light levels affect both temperature and the distribution of bottom and field layer vegetation, which can be important for water availability. Even though the nearest neighbour trees may have a large influence on light conditions, light levels below the canopy will be affected by trees on a large scale in this mature forest. In fact, the radius of 8.46 m that we used in this study was not very large, as light levels below the canopy are affected by trees or gaps up to at least twice the dominant stand height at northern latitudes (Flemming, 1962; Golser and Hasenauer, 1997). Our radius was set to avoid overlap between adjacent plots, but in further studies different and greater radii should be investigated.

Establishment may be influenced by many stochastic factors, of which weather conditions are the most important, having a strong influence on seed production, germination, and seedling mortality. Also non-stochastic factors like soil conditions, ground vegetation or micro-topography may influence establishment, regardless of stand structure. Our study was conducted in a multi-storied, natural spruce forest. In a managed spruce forest, the relationship between structure and regeneration may not be completely the same. One obvious difference may be the type and frequency of treefall gaps, which enhances regeneration by soil disturbance and woody debris and are important regeneration niches in a natural spruce forest (Kuuluvainen, 1994). Those elements are created mostly by the downfall of (over-) mature trees and related to stand structure. In the managed forest trees are removed at an economic maturity age, and the presence of treefall gaps and downed logs are lower and not related to stand structure in a similar way as in natural forests. Thus, a separate study should be conducted for managed forests.

5. CONCLUSION

Our study was a screening which aimed at identifying laser variables that might explain regeneration success. A full correlation between laser data variables derived from the canopy and regeneration will never be found, as factors not affected by canopy structure also strongly influence regeneration success. However, the study has shown that already existing data derived from laser scanning, for instance during a regular forest inventory, may give us surplus information on regeneration. Our data show that there is a relationship between canopy structure and seedling number, possibly strong enough for prediction of regeneration success in future prediction models.

6. REFERENCES

Akaike, H., 1974. A new look at the statistical model identification. *IEEE Transactions on Automatic Control* 19, pp. 716-723.

Anon., 1999. SAS OnlineDoc®, Version 8. SAS Institute Inc. Cary, NC.

Bjor, K., 1971. Forest meteorological, soil climatological and germination investigations. Meddelelser fra Det norske Skogforsøksvesen 28, pp. 429-526. (In Norwegian with English summary).

Bollandsås, O. M. & Næsset, E., 2007. Estimating percentile-based diameter distributions in uneven-sized Norway spruce stands using airborne laser scanner data. *Scand. J. For. Res.* 22, pp. 33-47.

Flemming, G., 1962. Strahlung und Wind an Bestandesrändern. *Archiv für Forstwesen* 11, pp. 647-656. (In German).

Golser, M. & Hasenauer, H., 1997. Predicting juvenile tree height growth in uneven-aged mixed species stands in Austria. *For. Ecol. Manage.* 97, pp. 133-146.

Kuuluvainen, T., 1994. Gap disturbance, ground microtopography, and the regeneration dynamics of boreal coniferous forests in Finland - a review. *Ann. Zool. Fennici* 31, pp. 35-51.

Maltamo, M., Eerikäinen, K., Pitkäinen, J., Hyyppä, J. & Vehmas M., 2004. Estimation of timber volume and stem density based on scanning laser altimetry and expected tree size distribution functions. *Remote Sens. Environ.* 90, pp. 319-331.

Mork, E., 1938. Gran- og furufrøets spirning ved forskjellig temperatur og fuktighet. Meddelelser fra Det norske Skogforsøksvesen 20, pp. 225-249. (In Norwegian).

Næsset, E., 2004a. Effects of different flying altitudes on biophysical stand properties estimated from canopy height and density measured with a small-footprint airborne scanning laser. *Remote Sens. Environ.* 91, pp. 243-255.

Næsset, E., 2004b. Practical large-scale forest stand inventory using small-footprint airborne scanning laser. *Scand. J. For. Res.* 19, pp. 164-179.

Parker, G.G., Russ, M.E., 2004. The canopy surface and stand development: assessing forest canopy structure and complexity with near-surface altimetry. *For. Ecol. Manage.* 189, pp. 307-315.

Tickle, P.K., Lee, A., Lucas, R.M., Austin, J., Witte, C., 2006. Quantifying Australian forest floristics and structure using small footprint LiDAR and large scale aerial photography. *For. Ecol. Manage.* 223, pp. 379-394.

7. ACKNOWLEDGEMENTS

This research was funded by the Research Council of Norway (research project no. 153185/110). We wish to thank Blom Geomatics AS for collection and processing of the laser scanner data.

AUTOMATIC SEGMENTATION OF BUILDING FACADES USING TERRESTRIAL LASER DATA

H. Boulaassal*, T. Landes, P. Grussenmeyer, F. Tarsha-Kurdi

Photogrammetry and Geomatics Group MAP-PAGE UMR 694, Graduate School of Science and Technology
INSA, 24 Boulevard de la Victoire, 67084 STRASBOURG, France.
(hakim.boulaassal|tania.landes|pierre.grussenmeyer|fayez.tarshakurdi@insa-strasbourg.fr)

Commission V, WG V/3

KEY WORDS: TLS, Point Cloud, Three-dimensional, Segmentation, Algorithm, Accuracy

ABSTRACT:

There is an increasing interest of the scientific community in the generation of 3D facade models from terrestrial laser scanner (TLS) data. The segmentation of building facades is one of the essential tasks to be carried out in a 3D modelling process. Since in reality, majority of facade components are planar, the detection and segmentation of geometric elements like planes respond to the previous task. The RANSAC paradigm is a robust estimator and probably the most widely used in the field of computer vision to compute model parameters from a dataset containing outliers. Indeed, RANSAC algorithm is usually successful for fitting geometric primitives to experimental data like for example, 3D point clouds resulting from image matching or from airborne laser scanning. The innovative idea of this study is the application of RANSAC algorithm to TLS data, characterized by a meaningful proportion of outliers. Therefore, this paper presents an approach allowing automatic segmentation and extraction of planar parts of facades scanned by TLS. Firstly, potential planes describing planar surfaces are detected and extracted using RANSAC algorithm. Then, a quality assessment based on manually extracted planes is carried out. The obtained results are evaluated and prove that the proposed method delivers qualitatively as well as quantitatively satisfactory planar facade segments.

1. INTRODUCTION

The reconstruction of geometric 3D models is one of the most important goals of 3D modelling in urban areas. In recent years, advances in resolution and accuracy have rendered airborne laser scanners (ALS) suitable for generating Digital Surface Models (DSM) and 3D models. These data alone do not provide complete 3D models since they do not cover building facades. In this context, generation of 3D city models with both high details at ground level, and complete coverage for bird's-eye view became more and more a challenging task. On the one hand, facades are acquired at ground level using Terrestrial Laser Scanners (TLS). On the other hand, roof shapes and terrain information are deduced from a DSM produced by ALS data (Tarsha-Kurdi *et al.*, 2006).

However, if numerous approaches have been developed over the past 10 years for airborne laser data, the situation is not so bright for terrestrial laser data. This is due, among others, to the gap between the architectural 3D range scanning and an efficient use of the data by professionals (Spinelli *et al.*, 2006).

According to (Barber *et al.*, 2001; Stephan *et al.*, 2002), the way in which point cloud modelling is performed depends strongly on the aim of the study. Generally, two modelling approaches can be distinguished: approaches fitting geometric primitives and approaches based on meshing methods. The latter allows fitting unspecified objects having irregular shapes and that cannot be approximated by simple geometric primitives.

The goal of this paper is to introduce an approach allowing automatic segmentation and extraction of planar parts from facades acquired by TLS. This approach is in line with fitting geometric primitives approaches. The step of segmentation

which aims to decompose facades into planar surfaces is carried out using RANSAC paradigm.

After introducing the RANSAC algorithm, the methodology used to segment and extract multiple planes describing planar surfaces is presented. Furthermore, each operation is illustrated and applied on a point cloud describing a multi-planar facade. Finally, the results are presented and evaluated in a qualitative as well as in a quantitative way.

2. RELATED WORKS

A variety of techniques applied to the classification and 3D segmentation of point clouds originally result from traditional photogrammetric, computer vision and signal processing fields (Belton and Lichti, 2006). Some of these include transformations from one space into a parameter space, like for example the Hough transform and the Gaussian sphere (Vosselman *et al.*, 2004). They try to gather common elements based on the surface parameters and surface normal information respectively. Techniques such as tensor voting (Tong *et al.*, 2004; Schuster, 2004) and region growing (Besl and Jain, 1988) have been applied to segmented data based on localised information. Morphological approaches such as medial axis and skeletonisation have also been used by introducing diffusion equations, radial basis function and grass-fire techniques (Gorte and Pfeifer, 2004; Ma *et al.*, 2003).

Related to facade segmentation collected by TLS, extended region growing algorithms are often used to extract planar surfaces (Pu and Vosselman, 2006; Stamos *et al.*, 2006; Dold and Brenner, 2004; Lerma and Biosca, 2005). It starts by determining a seed surface (a group of nearby points that fit to a plane), and then the seed surface grows according to specific

criteria. On the one hand, the proximity criterion means that only points within a certain distance to a seed surface can be added to this seed surface. On the other hand, the globally planar criterion means that a plane equation is determined after fitting a plane passing through all points located in this seed surface. Points can only be added if the perpendicular distance to the plane is below some threshold. Although it provides interesting results, the limitations of this algorithm come from the big number of thresholds needed. Also computing time is considerable when the algorithm is applied on 3D point clouds.

Another method is increasingly used to extract planar surfaces especially by fitting geometric primitives. It is the RANSAC (RANDOM SAMple Consensus) paradigm, which is applied to a wide range of problems dealing with model parameters estimation. Indeed, (Bauer *et al.*, 2005) use RANSAC method to detect and extract the main facade planes. Promising results are obtained for creating plane based models for buildings, even using dense 3D point clouds. However, the 3D point cloud was not acquired by TLS, but through image matching. According to (Durupt and Taillandier, 2006), RANSAC estimation algorithm can also be used to extract planar primitives directly from cadastral limits and from a DEM (Digital Elevation Model). Through their study, it is shown that an evaluation carried out on 620 buildings in a dense urban centre provides encouraging results. Nevertheless, the algorithm has only been tested on ALS data.

Often, when one wants to compute model parameters from a dataset containing a significant proportion of outliers, many computer vision algorithms - especially algorithms including robust estimation steps - are adopted. The RANSAC algorithm is probably the most widely used robust estimator in this field (Matas *et al.*, 2002). Nevertheless it has rarely been applied on TLS data for fitting models, although affected by noise and artefact errors. Hence, it is interesting to study the performance of this algorithm in estimating model parameters in a purpose of segmenting TLS data.

3. RANSAC PARADIGM

The RANSAC paradigm is an algorithm for robust fitting which has been introduced by (Fischler and Bolles, 1981). It is one of the probabilistic voting methods known to reduce the computing time. Indeed, it was developed in order to reduce the number of necessary trials of traditional voting techniques, like Hough Transform for example. In spite of the simple structure of RANSAC algorithm, it is known to be efficient.

Firstly, subsets are randomly selected from the input data and model parameters are computed so that they fit the sample. The size of the sample depends on the mathematical model (line, plane, cylinder, sphere...) one wants to find. Typically, the size of the sample is the "smallest" number of points sufficient to determine the model parameters. For example, to find a plane in the dataset, one has to select a set of three points, since three points are required to determine the parameters of a plane (normal vector and distance of plane to origin).

In a next step, the quality of the model will be evaluated. Typically, an error tolerance determines a volume around the geometric primitive within which all compatible points must fall in. Then, a cost function computes the quality of the model, the standard one being the number of inliers, i.e. points which agree with the model within an error tolerance. But other quality criteria could be used such as a standard deviation of distances

from points to model for example. Therefore, the plane containing more points is considered to be the best plane. The process terminates when the likelihood of finding a better model becomes low.

The minimum number (m) of trials needed to reach a probability (p) to find at least one good set of observations - assuming a certain percentage (w) of observations to be erroneous - is given by relation (1).

$$m = \frac{\log(1-p)}{\log(1-(1-w)^S)} \quad (1)$$

where (S) is the minimum number of points necessary to calculate the parameters of the model (in the case of a planar model, $S=3$). Demonstration of the equation mentioned above can be found in (Fischler and Bolles, 1981).

The next part explains the methodology used and refined in order to segment a 3D point cloud of a facade into multiple planes.

4. SEGMENTATION METHODOLOGY

The segmentation proposed in this work starts with the decomposition of a 3D point cloud into many planes. After data description, a facade segmentation algorithm based on RANSAC procedure is presented. Then the step of plane extraction is explained. It must be noted that in this context, a "segment" means a set of 3D points belonging to the same surface.

4.1 Data description

The point cloud used for testing the segmentation approach covers the facade of the Graduate School of Science and Technology (INSA) of Strasbourg. It is composed of many planar surfaces containing different elements (windows, planar wall, balconies) and characterized by different materials (concrete, pane, stone). A photograph of the facade is presented in Fig. 1.



Figure 1. Photograph of the building under study

The dataset used in this study is a point cloud acquired by a Trimble GX laser scanner. The technical specifications of this kind of TLS are depicted in Table 1. Generally, a cloud is composed of 3 dimensional points defined by their Cartesian coordinates. The point cloud used as sample contains 47710 points acquired with a horizontal and vertical resolution of 150 mm at 50 m. Other properties assigned to the points provided by

the laser scanner such as colour properties are voluntarily not used in this study.

Technical specifications	
Distance accuracy	7 mm at 100 m
Position accuracy	12 mm at 100 m
Angular accuracy	60 μ rad (Horizontal) 70 μ rad (Vertical)
Grid Resolution over 360°	3 mm at 100 m with no restriction on number of points in a scan
Spot size	3 mm at 50 m
Speed	up to 5000 points per second

Table 1. Technical specifications of Trimble GX laser scanner.

The points captured through glass and returned by parts located behind the facade have easily been manually removed using the RealWorks Survey software (Trimble). Fig. 2 shows the point cloud of the facade presented in Fig. 1, acquired by Trimble GX.

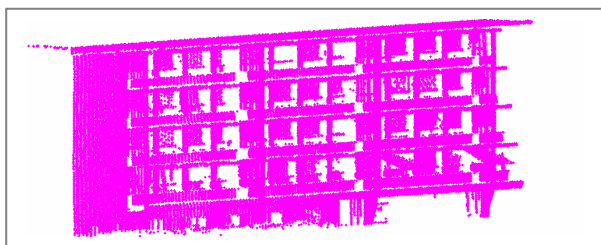


Figure 2. Point cloud describing the facade sample under study.

4.2 Facade segmentation using RANSAC algorithm

The RANSAC algorithm is used here in order to detect and extract planes describing planar parts of the facade. Practically, a plane is a row of four values [a b c d]. The first three define the unit normal vector ($a^2 + b^2 + c^2 = 1$); the fourth is the distance of the plane to the origin. Thus, all points (x, y, z) fulfilling the Equation 2 belong to the same plane.

$$a.x + b.y + c.z = d \quad (2)$$

The basic RANSAC approach is limited by the assumption that a unique model accounts for all of the data inliers. The term inliers means points which agree with the model according to an error tolerance.

However, one would like to extract all potential planes from the data. To do this, it is suggested to apply sequentially RANSAC algorithm and to remove the inliers from the original dataset every time one plane is detected. This constitutes the first adaptation of RANSAC algorithm in our context. The sequential process guaranties that each point belongs to one unique segment (plane) and that there is no intersection between two segments. Thus, a point contributes only to the fitting of the plane it belongs to.

To determine the points belonging within some tolerance to the given plane, the Euclidian distance between a point P (x,y,z) and a plane PL(a,b,c,d) is calculated (see Equation 3).

$$d(P, PL) = |a.x + b.y + c.z - d| \quad (3)$$

In reality, data acquired by terrestrial laser scanning are not immediately compatible with mathematical models. In other words, no planar walls, no straight edges, no right angles are directly provided in the digital model. Therefore, to obtain planes representing walls, one tolerance value describing the authorized thickness of a plane is imposed. Thus, the researched plane is considered to be a parallelepiped, but this is necessary at first to get meaningful segments.

In this process, different planes are detected one after the other. It is obvious that the number of planes detected depends strongly on the tolerance value chosen as input. The more this value is low, the more the number of detected planes is large. This is because each segment is a parallelepiped firstly, and tends to become a planar surface when tolerance value tends to zero. Therefore, the threshold value must be carefully chosen.

After many experiments, it turns out that the tolerance value used to get significant planes has to be set between $t = 20 \text{ mm}$ and $t = 40 \text{ mm}$. For instance, with threshold $t = 5 \text{ mm}$, the segments obtained are too numerous and not significant (Fig. 3). The main characteristic of these planes is to contain an insufficient number of points. It becomes clear that this kind of result is unusable for a later modelling process.



Figure 3. Detection of meaningless planes when data are segmented using $t = 5 \text{ mm}$. Each colour represents one plane.

On the other hand, the threshold should not overcome some tolerance (in our case $t \leq 40 \text{ mm}$). Over this value, two or more different planes are considered as one unique plane (Fig. 4).

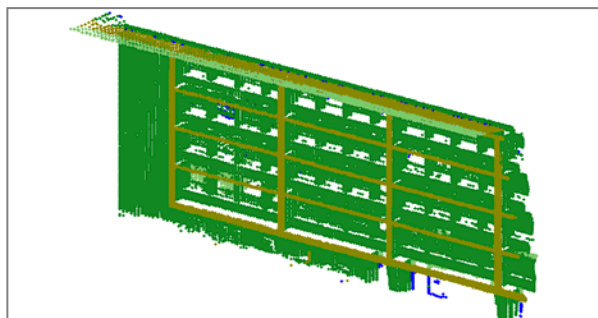


Figure 4. Detection of only two planes when data are segmented using $t = 350 \text{ mm}$.

Logically, the threshold value must be close to the thickness of the cloud. The thickness is usually generated by noise coming from the surface roughness, the object colours and the TLS resolution capacities. In the point cloud under study, it reaches about 2 to 4 cm. Thus, with $t = 40 \text{ mm}$, the expected planes are correctly detected and extracted (Fig. 5). However, it is necessary to underline that an optimal tolerance value can only be obtained in an empirical way depending heavily on the objects under investigation, on the data characteristics and the objective of the study.

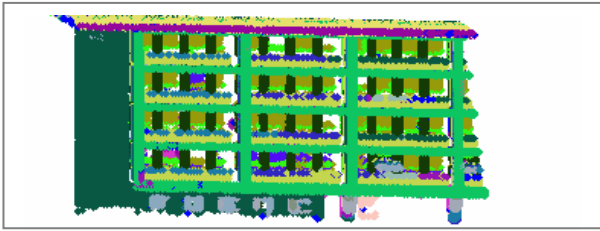


Figure 5. Successful segmentation with $t = 40$ mm.

The minimum number of trials needed to get the best plane is given by Equation (1). Considering a value of 0.2 for w , a probability of 99% should theoretically be reached after 1000 trials.

4.3 Planes extraction

Once the main planes are determined by automatic segmentation, each plane is extracted and displayed separately. Fig. 6 shows four different planes containing points belonging to the same planar facade. The first segment is composed of points belonging to windows (Fig.-6a); the second one describes horizontal and vertical beams (Fig.-6b); the third is composed by balconies (Fig.-6c). The last one is a principal planar wall (Fig.-6d).

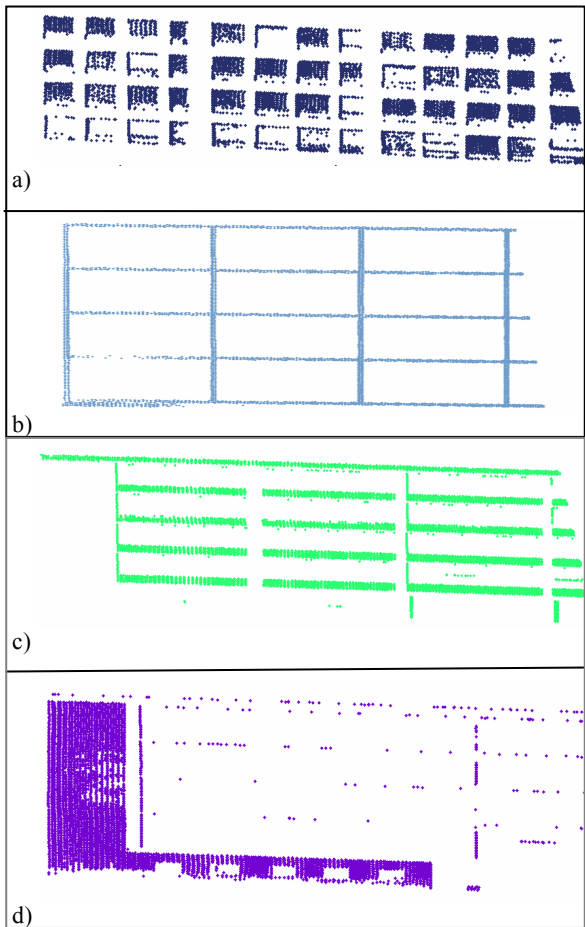


Figure 6. Four planes displayed separately; a) windows; b) beams; c) balconies; d) principal wall.

In the plane composed of windows, some windows are filled by points and others are empty. This is because either no return is

measured (due to specular reflectance), or the available points refer to curtains. In principle, such holes in a point cloud can also result from shadows generated by objects located between the laser and the facade. However, this phenomenon is avoided by using several point clouds acquired from different points of view.

It can be remarked, that the extracted planes are coherent and correspond to a specific planar part of the facade. Now the results must be evaluated in detail, regarding the geometric accuracy, as well as the semantic coherency.

5. RESULTS EVALUATION

In order to evaluate the accuracy of the plane detection obtained by the presented approach, a reference model is necessary. For this purpose, a manual segmentation has been performed on the same point cloud and provided the planar surfaces composing the facade under study. These planes are then compared to their homologous, extracted automatically in the previous part. Only the results of the evaluation performed on a successful extraction (plane of Fig.-6b) and a less successful extraction (Fig.-6d) are presented in this section.

Fig. 7 presents with two colours, the same plane extracted automatically (in blue) and manually (in red). This superimposition enables to compare the results of the proposed approach to the reference data.

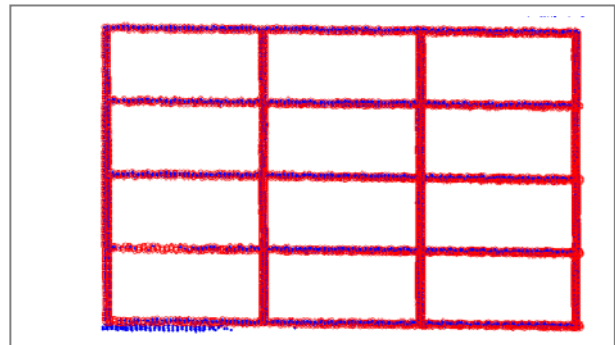


Figure 7. Superimposition of two layers: plane extracted manually (red points) and his homologous detected automatically (blue points).

A qualitative analysis of the superimpositions lead to the conclusion that both layers (automatically extracted plane against manually extracted plane) are similar. The planes extracted automatically are satisfactory, since their form and aspect are almost identical to those of the planes extracted manually.

The quantitative analysis consists in comparing two homologous planes. For this purpose, operators like intersection (\cap) and difference (\setminus) are applied on the two layers to be compared. Considering that each plane is composed of a set of points defined by their Cartesian coordinates, let's denote (A) as the set of points belonging to the automatically extracted plane and (M) the set of points belonging to the manually segmented plane.

Table 2 shows the results of the comparison of the automatically and manually segmented planes corresponding to Fig.7.

Plane	Number of points	Description
A	4658	Points extracted automatically
M	4888	Points extracted manually
$A \cap M$	4406	Points common to both A and M planes.
A/M	482	Points of (A), not present in (M).
M/A	252	Points of (M), not present in (A).

Table 2. Comparison between automatically (A) and manually (M) extracted planes.

In proportion, 4406 among 4658 points of the automatically extracted plane (A) are correctly detected. In terms of percentage, they represent 94.6 % of points. Indeed, only 252 points are lost by the proposed algorithm.

On the other hand, 482 points are in excess of the expected points. This can be explained by the fact that a plane determined by RANSAC algorithm is defined by its mathematical equation (Equation 2). Thus, all points fulfilling this equation are considered belonging to the plane, regardless of the architectural constraints describing a plane. Fig.8 shows the geometrical constraints characterizing the plane extracted in Fig.7.



Figure 8. Part of the facade corresponding to the detected plane in Fig.7 (contours digitized in red)

Actually, manually extracted planes correspond to well-defined walls. Moreover, the architectural or semantic constraints are quite present in the manual segmentation. On the other hand, an automatically detected plane is based only on the mathematical criterion of flatness. This explains the presence of points randomly dispersed outside the expected wall (Fig.9-b), which are absent in Fig.9-a. In consequence, the percentage of points common to both planes ((A) and (M)) does not overcome 87.8% ($A \cap M$).

This problem can be attenuated by adding constraints of topological and geometrical nature to the proposed algorithm. Indeed, from a topological point of view, a criterion of vicinity (characterized for example by a tolerated number of neighbours around each point within a given radius), enables to eliminate points lying outside the expected planar surface. From a geometrical point of view, a criterion of surface enables to keep only the significant objects. This can be done for example by converting the set of points into an image and applying image processing tools, like region growing algorithms in order to remove the meaningless points (points of (A) that are absent in (M)).

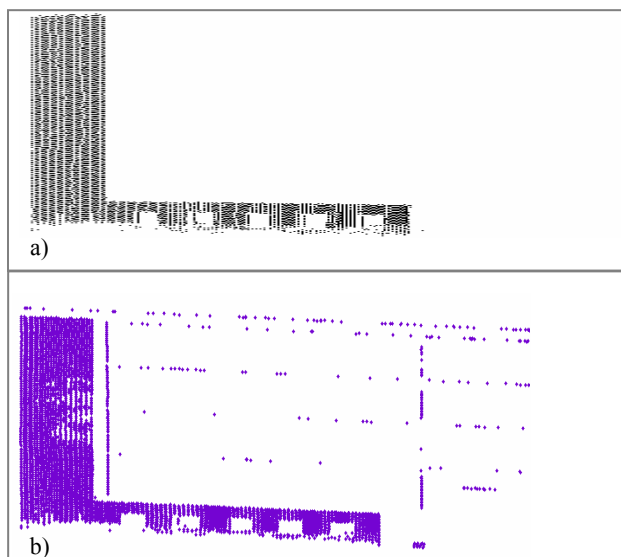


Figure 9. Representation of a planar wall, extracted in two ways; a) manual extraction; b) automatic extraction.

Moreover, the plane parameters estimated by RANSAC algorithm are not very accurate, since they are established based on three initial points only. They will be recomputed and adjusted, for example by a least-square fitting, to all points assigned to the detected plane.

Nevertheless, considering purely the segmentation and extraction approach proposed in this study, it can be concluded that the method is reliable. Indeed, 90% of the points composing the complete sample of the facade are correctly extracted.

6. CONCLUSION AND FUTURE WORK

The approach described in this paper aims to segment automatically and extract planar surfaces from a building facade captured by TLS. Firstly, the point cloud is segmented into several planes using sequential RANSAC algorithm. The results obtained are satisfactory, because they are produced based on the unique assertion that the best plane is the plane containing a maximum of points. Thus, considering that no additional constraint is needed, the global accuracy is better than expected. Therefore, the proposed methodology enables reliable facade segmentation with weak processing time, using TLS data. It constitutes a first and primordial step in the generation of complete 3D building models.

Future work will focus on the enhancement of segmentation operation. In order to avoid problems discussed above and increase the global and relative accuracy of the results, additional geometrical and topological constraints will be considered. Moreover, further investigations regarding the empirical parameters of RANSAC algorithm will be carried on.

REFERENCES

- Barber, D., Mills, J. and Bryan, P. G., 2001. Laser Scanning and Photogrammetry: 21st century metrology. *Proceedings of 18th International Symposium CIPA 2001*. Potsdam, Germany, September 18 – 21, pp. 360 – 366.

- Bauer, J., Karner, K., Schindler, K., Klaus, A. and Zach, C., 2005. Segmentation of building from dense 3D point-clouds. *Proceedings of the ISPRS. Workshop Laser scanning 2005*, Enschede, the Netherlands, September 12-14, 2005.
- Belton, D. and Lichti, D. D., 2006. Classification and segmentation of terrestrial laser scanner point clouds using local variance information. *IAPRS*. Volume XXXVI, Part 5, Dresden 25-27 September 2006.
- Besl, P. J. and Jain, R. C., 1988. Segmentation through variable-order surface fitting. *IEEE Transactions on Pattern Analysis and Machine Intelligence*. 10(2), 167–192.
- Dold, C. and Brenner, C., 2006. Registration of terrestrial laser scanning data using planar patches and image data. *IAPRS*. Volume XXXVI, Part 5, Dresden 25-27 September 2006.
- Durupt, M. and Taillandier, F., 2006. Reconstruction automatique de bâtiments à partir d'un MNE et de limites cadastrales : une approche opérationnelle. 15ème congrès francophone *AFRIF-AFIA* Reconnaissance des Formes et Intelligence Artificielle. 25 au 27 janvier 2006, à Tours.
- Fischler, M. A. and Bolles, R. C., 1981. Random Sample Consensus: A Paradigm for Model fitting with application to Image Analysis and Automated Cartography. *Communications of the ACM*, 24(6): 381-395.
- Gorte, B. and Pfeifer, N., 2004. Structuring laser-scanned trees using mathematical morphology. In Proc. 20th *ISPRS* Congress, Istanbul, Turkey, pp. 929–933.
- Lerma, J.L. and Biosca, J.M., 2005. Segmentation and filtering of laser scanner data for cultural heritage. *CIPA 2005 XX International Symposium*, 26 September – 01 October, 2005, Torino, Italy.
- Ma, W. C., Wu, F. C. and Ouhyoung, M., 2003. Skeleton extraction of 3d objects with radial basis functions. International Conference on Shape Modeling and Applications (SMI 2003), 12-16 May 2003, Seoul, Korea. *IEEE Computer Society* 2003
- Matas, J., Chum, O., Urban, M. and Pajdla, T., 2002. RobustWide Baseline Stereo from Maximally Stable Extremal Regions. *Proceedings of the British Machine Vision Conference*, volume 1, pages 384-393, 2002.
- Pu, S. and Vosselman, G., 2006. Automatic extraction of building features from terrestrial laser scanning. *IAPRS*, vol. 36, part 5, Dresden, Germany, September 25-27, 5 p. (on CD-ROM).
- Schuster, H.F., 2004. Segmentation of lidar data using the tensor voting framework. In Proc. 20th *ISPRS* Congress, Istanbul, Turkey, commission 3, pp. 1073–1078.
- Spinelli, A., Ganovelli, F., Montani, C. and Scopigno, R., 2006. Recovering 3D architectural information from dense digital models of buildings. *Fourth Eurographics Italian Chapter Conference*. University of Catania, Italy, pp. 177-182.
- Stamos, I., Yu, G., Wolberg, G., Zokai, S., 2006. 3D Modeling Using Planar Segments and Mesh Elements. 3rd International Symposium on 3D Data Processing, Visualization & Transmission, University of North Carolina, Chapel Hill, June 14-16 2006.
- Stephan, A., Heinz, I., Mettenleiter, M., Härtl, F., Frölich, C. and Hined, D., 2002. Interactive Modelling of 3D-Environments. In *Proc. of the 11th IEEE Int. Workshop on Robot and Human interactive Communication*, ROMAN2002. Berlin, Germany, September 25 – 27, pp. 530 – 535.
- Tarsha-Kurdi, F., Landes, T., Grussenmeyer, P. and Smigiel, E., 2006. New approach for automatic detection of buildings in airborne laser scanner data using first echo only. *IAPRS* Vol. 36, part. 3, pp. 25-30.
- Tong, W.S., Tang, C.K. and Mordohai, PH., 2004. First Order Augmentation to Tensor Voting for Boundary Inference and Multiscale Analysis in 3D. *IEEE transactions on pattern analysis and machine intelligence*, vol. 26, no. 5, may 2004.
- Vosselman, G., Gorte, B.G.H., Sithole, G. and Rabbani, T., 2004. Recognising structure in laser scanner point clouds. *IAPRS*, vol. 46, part 8/W2, Freiburg, Germany, October 4-6, pp. 33-38.

VALIDATION OF AIRBORNE LIDAR INTENSITY VALUES FROM A FORESTED LANDSCAPE USING HYMAP DATA: PRELIMINARY ANALYSES

D.S. Boyd^a, R.A. Hill^b

^a School of Geography, University of Nottingham, University Park, Nottingham, NG7 2RD, UK - Doreen.Boyd@nottingham.ac.uk

^b School of Conservation Sciences, Bournemouth University, Talbot Campus, Poole, BH12 5BB, UK - rhill@bournemouth.ac.uk

ISPRS WG III/3, III/4, V/3, VIII/11

KEY WORDS: Lidar intensity, interpolation, coniferous, deciduous, validation, HyMap, canopy height model

ABSTRACT:

There is a growing body of literature that points to the value of using the intensity measures of the backscattered laser light in addition to the pulse range measurements for studying a range of environments, including forests. However, there is a lack of literature that has validated the lidar intensity values captured in a campaign, and therefore limited understanding in the full utility of these data. This paper presents preliminary analyses of lidar intensity values captured over an area of woodland in the UK in comparison with concurrently acquired HyMap data, which measures the passive reflected radiation at the same wavelengths. The study concludes that lidar intensity values are broadly representative of the NIR radiation reflected from the forested landscape and therefore could be utilised. However, there is a real need for calibration of intensity data, particularly if flight lines are to be merged. Furthermore, if lidar intensity values are to be interpolated into a raster and used in a similar way to conventional image analysis, the selected interpolation technique significantly affects the resultant lidar values.

1. INTRODUCTION

1.1 Background

Airborne lidar systems are able to record the intensity of the backscattered laser light, with intensity measured either as the maximum of the returned pulse or signal integration over the returned pulse width. This is in addition to the pulse range measurements (Wehr and Lohr, 1999). Intensity data thus provide a record of the backscattered intensity of reflection for each laser pulse, supplying information about the reflecting surface or object at sampled points across the landscape. This ability to capture backscattered reflectance from returning pulses has proved useful for the identification of broad land cover types (e.g., Brennan et al., 2006) and as ancillary data for post-processing (e.g., Liu et al., 2007). This intensity information within lidar echos is a function of the wavelength of the source energy (often within the near infrared spectral region (NIR: 0.7 – 1.5µm) for terrestrial applications), path length and the composition and orientation of the surface or object which the pulse has hit. For any data capture project, the system specific factors are known (but may be unavailable), whilst those that are site specific are typically unknown. However, tabulated values of reflectances of materials are available through endeavours of spectroscopy (e.g., Clark et al., 2003 - <http://pubs.usgs.gov/of/2003/ofr-03-395/ofr-03-395.html>) and suggest that there is scope in using lidar intensity for applications common place in remote sensing.

The potential in the exploitation of lidar intensity has recently been realised and been demonstrated in a number of

application areas. These include the identification and mapping of the age of lava flows from active volcanoes (e.g., Mazzarini et al., 2007); glacial features (e.g., Arnold et al., 2006; Kaasalainen et al., 2006); features of archeological interest such as palaeochannels (e.g., Carey et al., 2007); and vegetation types (e.g., Farid et al., 2006). Within forestry, lidar intensity has been used to estimate forest volume and biomass in a temperate forest of coniferous, deciduous, and mixed stands (van Aardt et al., 2006); to filter lidar-height to estimate the basal area of northern hardwood forests (Lim et al., 2003). and as a predictor in tree species classification (Holmgren and Persson, 2004). Hudak et al. (2006) concluded that lidar intensity was more useful than the EO-1 Advanced Land Imager multispectral data acquired concurrently for predicting basal area and tree density of coniferous forests. All these studies illustrate that lidar intensity values are being utilized in ways beyond perhaps originally intended. The emergence of full-waveform laser scanners may well increase this trend.

1.2 Factors determining lidar intensity

There are a number of factors that determine the lidar intensity values captured by a system and can be conveniently grouped into system variables and target variables, with the effect of exhibiting co-dependency. The system variables include target-emitter distance, beam divergence (there is a loss of intensity with the diverging beam), the laser footprint size, angle of incidence, atmospheric attenuation and signal processing. Target variables include target reflectivity, surface roughness and bidirectional properties and the size of the target (Wagner et al., 2006). Within forests this is mainly a function of leaf

area, leaf inclination, species type, and tree density. Another factor to consider, if the data are converted from a point cloud into an interpolated 2-dimensional surface, is the post-processing procedure. Interpolation technique and selected output cell size will influence the nature of the resulting surfaces. All of these factors need to be considered and understood if lidar intensity values are to be used optimally.

Limitations in the effective use of lidar intensity values are the lack of calibration techniques (Kaasalainen et al., 2005) and the lack of validation of the lidar intensity values obtained over a particular environment. Much progress has been made to calibrate intensity both under laboratory and field conditions (e.g., Coren and Sterzai, 2006; Ahokas et al., 2006). Validation of lidar intensity by means of comparison with a similar product derived by more “conventional” means should lead to a better understanding of the parameters within which lidar intensity values can be employed. The challenge for validating lidar intensity data is the lack of reference data at appropriate spatial, spectral and temporal resolution to compare with lidar intensity values. In this study, HyMap data have been acquired concurrently with small-footprint lidar data over a woodland area in the UK, thus enabling an exploration of the lidar intensity across a landscape.

2. STUDY AREA

The study area focuses on two woodland sites, Monks Wood and Bevill’s Wood, and their immediate agricultural vicinity, in Cambridgeshire, UK (52° 24’ N, 0° 14’ W). Monks Wood, covers 157 hectares and is a National Nature Reserve comprising broadleaf forest. Monks Wood is divided up into 30 compartments for management purposes. It is a complex woodland environment and extremely heterogeneous in terms of the woody species comprising the canopy and understorey, their relative proportions in any area, canopy closure and density, tree height and stem density (Hill and Thomson, 2005). The dominant tree species are ash *Fraxinus excelsior* L., oak *Quercus robur* L., field maple *Acer campestre* L., elm *Ulmus carpiniifolia* Gleditsch. and aspen *Populus tremula* L., while the dominant shrub species are hawthorn *Crataegus monogyna* Jacq., hazel *Corylus avellana* L., blackthorn *Prunus spinosa* L., dogwood *Cornus sanguinea* L., and wild privet *Ligustrum vulgare* L. The majority of overstorey trees are 70–80 years old. The soils are gleyed brown calcareous and surface water gley resting on impervious clay. To the south of Monks Wood, separated by a minor road, is Bevill’s Wood, a 36-hectare site that was almost entirely clear-felled and replanted in the 1950s–1960s. Bevill’s Wood has stands dominated by beech *Fagus sylvatica* L., Scots pine *Pinus sylvestris* L. and Norway spruce *Picea abies* L.. These patches of woodland have a relatively homogeneous structure and tend to lack an understorey. There are, however, stands of pine and spruce that have areas of ash and scattered beech intermingled. The edges of stands inside Bevill’s Wood are ringed with ash or willow trees. Both Monks Wood and Bevill’s Wood have an outer fringe comprising ash, oak, field maple, hazel, hawthorn and blackthorn, and throughout both woods are open areas of herbaceous vegetation with scattered shrubs.

The woods are divided up into compartments. Within the compartments are stands and in July 2000, five contrasting stands in Monks Wood were surveyed. These covered the species composition and structure present within Monks Wood, providing a representative sample of the composition of the broadleaved woodland area. For further information on the stands refer to Table 1 in Patenaude et al., 2003 and Hill 2007.

3. REMOTELY SENSED DATA

3.1 Airborne Lidar data

An Airborne Laser Terrain Mapper (Optech ALTM 1210—see <http://www.optech.on.ca>) was flown over the study site in a east-west direction in June 2000. Laser pulses were emitted by the ALTM with a NIR wavelength of 1.047 μm . By scanning in sweeps perpendicular to the flight-line, the forward motion of the aircraft generated a saw-toothed pattern of point sample elevation and intensity recordings. A small scan angle range of $\pm 10^\circ$ was selected to minimize the influence of varying incidence angle on the penetration into the canopy of each laser pulse (Leckie, 1990) and thus the effect of incidence angle on intensity (Ahokas et al., 2006). The parallel flight lines had overlapping swaths of data acquisition, resulting in an irregular distribution of points. On average, one point was recorded every 4.83m² across the study site. Both first and last return range and intensity data were recorded for each laser pulse, which generated a circular footprint on the ground surface with a diameter of approximately 0.25m at nadir. Based on the instrument specifications supplied by the manufacturer and the flying altitude, the lidar data had a horizontal and vertical accuracy of approximately 0.6m and 0.15m respectively. The Lidar data acquired by the ALTM were supplied by the Environment Agency of England and Wales as an ASCII file of x-, y- and z- British National Grid co-ordinates for the first and last significant return of each laser pulse and the associated intensity values. The intensity values themselves are unitless as no method was applied to calibrate them. The individual flight lines of point sample data were supplied merged together into a single point cloud.

3.2 HyMap image data

The HyMap sensor records reflected radiation in 126 wavebands, for pixels with a 4-m spatial resolution (see <http://www.hyvista.com>). The HyMap provides a signal to noise ratio (>500:1) and image quality that is setting the industry standard and thus provides a reliable validation dataset for use in this study. Moreover, the sensor operates close to backscatter providing similarity to the laser scanner which operates practically at exact backscattering (Kaasalainen et al., 2005). This sensor was flown over the study site at a time coincident with the lidar and the acquired data were supplied as a 126-waveband raster image with DN values converted to radiance. The HyMap data were geo-registered to British National Grid co-ordinates with a 4-m spatial resolution using the aircraft telemetry from the time of data acquisition and a plug-in routine for ENVI software supplied by the HyVista Corporation. A subsequent comparison with the lidar data showed geometric accuracy to be within 1 pixel (i.e. 4-m) in the x- and y- directions. Here the reflected radiation in waveband 42 (band centre 1.0475 μm , width 0.0188 μm) were used as the validation data for the lidar intensity values.

4. DATA PROCESSING AND ANALYSIS

4.1 Data processing

Since comparisons were being made with the HyMap Band 42 data, only the first return intensity values were processed; over a wooded landscape it is most likely that the first returning pulse is from the top part of the canopy (leaves or branches), similar to that of the passive NIR radiation reflected from a canopy recorded by the HyMap sensor (Gaveau and Hill, 2003). The point-sample intensity data were interpolated into three sets of raster images, at 4-m and 1-m spatial resolution using three interpolation routines; Delaunay Triangulation (DT), Inverse Distance Weighting (IDW) and Ordinary Kriging (OK) for direct comparison with the HyMap data. Previous studies have used the lidar range data for Monks Wood to produce a digital terrain model (DTM) for the site which was then used to extract canopy height from the first-return lidar data as a grid-based digital canopy height model (DCHM). Both the DTM and DCHM have a 1-m spatial resolution (Patenaude et al., 2004). These were also available for use in the analyses.

4.2. Preliminary assessment of intensity rasters

A qualitative visual assessment of all the intensity images was undertaken. A grainy texture is evident in the intensity raster and this speckle is similar to that seen in radar images and a function of echo fading. Despite this, similar landscape features were visible in both the HyMap (Figure 1a) and lidar intensity data (Figure 1b), and this was most evident in the krigged intensity data. Particularly evident are the different crop types and management, the rides between compartments, clearings in the woodland, as well as areas of shrub. Also strongly evident in the interpolated lidar intensity data are the differences between individual flight lines. This demonstrates that lidar intensity data could be useful for visualisation purposes and developing an understanding of the area of interest, but that for more detailed analyses some form of calibration within each flight line is required prior to interpolation to a raster.



Figure 1a. HyMap sensor image of the study site (displayed in band 42).

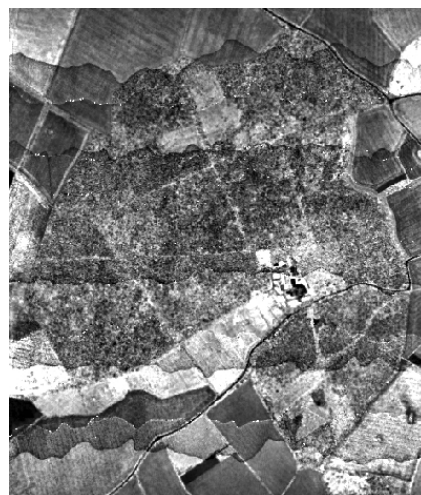


Figure 1b. First return lidar intensity image derived through ordinary kriging of the study site.

Landscape features such as deciduous and coniferous forest stands, shrubs, grassland and crops were examined for their intensity characteristics and compared with corresponding HyMap reflectances. Generally, intensity values are as expected (e.g., bare soil has low intensity and shrub a high intensity). These plots illustrate large variance in lidar intensity from each landscape feature in relation to the HyMap values. Additionally, lidar intensity from coniferous forests are high, such that there is no radiometric separability between this feature and deciduous forest and shrubs (Figure 2). This was not the case for HyMap reflectances illustrating that the mature forests have a complex returning echo causing a similar backscatter despite structural and physiological differences between them. These results illustrate the complexity of factors that influence the lidar intensity data, further work is required to fully understand the data prior to its optimal use.

4.3 Stand analysis of intensity values

Per pixel analysis was conducted that compared the intensity and HyMap data at 4-m spatial resolution for all three interpolation methods for the five sampled stands in Monks Wood. The focus on these five stands should provide a range of NIR values from both the HyMap and lidar sensors for a forest of this type. Table 1 documents the regression equations computed for each stand and for each interpolation method, while Figure 3 illustrates the plots obtained for stand 5, as an illustrative example. Both the table and plots of Figure 3 show that correlation coefficients are small (although in the case of stand 4 significant at $p < 0.01$) and that a large degree of scatter exists in the relationships between HyMap and lidar intensity data. This scatter may be a function of pixel mis-alignment where the geometric correction of the HyMap data was not absolute and the lack of calibration applied to the intensity data. Moreover, the intensity values for stands 1 to 3 were from areas where flightlines overlap and thus interpolated values were calculated from a double set of intensity data.

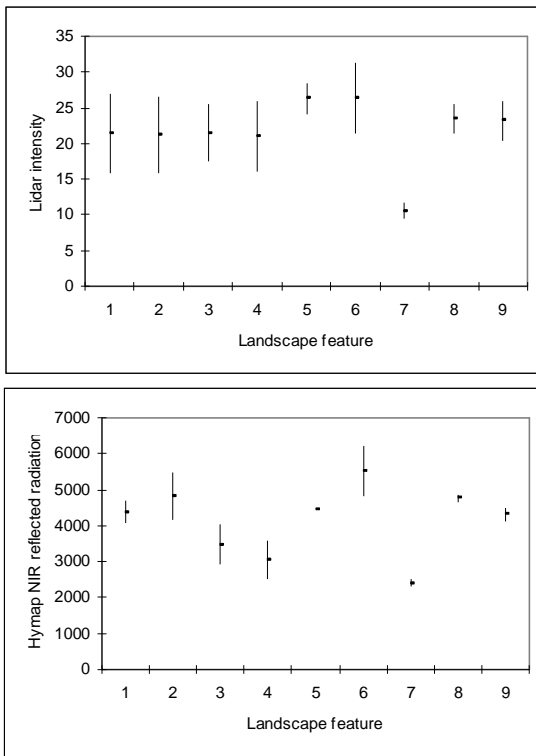


Figure 2. Characteristics (mean and ± 1 standard deviation) of lidar intensity and HyMap reflectances for landscape features (1) stand 4 (Ash dominated); (2) stand 5 (Elm dominated); (3) coniferous forest; (4) coniferous forest; (5) beech; (6) shrub; (7) bare soil; (8) crop and (9) grass.

	Stand 1 (N = 1747)
DT	$y = 0.0013x + 15.736; r^2 = 0.01$
IDW	$y = 0.001x + 16.169; r^2 = 0.01$
OK	$y = 0.0013x + 15.064; r^2 = 0.03$
	Stand 2 (N = 2088)
DT	$y = 0.0001x + 17.845; r^2 = 0.0001$
IDW	$y = 0.0004x + 16.963; r^2 = 0.002$
OK	$y = 0.0007x + 15.54; r^2 = 0.012$
	Stand 3 (N = 2010)
DT	$y = 0.0005x + 16.424; r^2 = 0.003$
IDW	$y = 0.003x + 17.729; r^2 = 0.002$
OK	$y = 0.0004x + 17.245; r^2 = 0.005$
	Stand 4 (N = 3131)
DT	$y = 0.0018x + 13.259; r^2 = 0.01$
IDW	$y = 0.0017x + 13.808; r^2 = 0.014$
OK	$y = 0.0017x + 14.003; r^2 = 0.032$
	Stand 5 (N = 430)
DT	$y = 0.0024x + 9.7862; r^2 = 0.09$
IDW	$y = 0.002x + 11.483; r^2 = 0.08$
OK	$y = 0.0021x + 10.832; r^2 = 0.19$

Table 1. Regression equations computed between HyMap data and lidar intensity data derived using each interpolation method for each of the five stands.

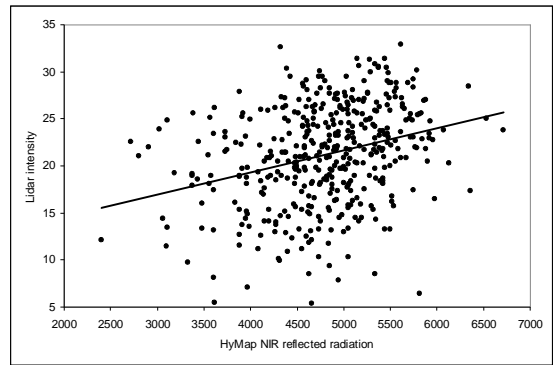


Figure 3a. Plot of HyMap NIR data against lidar intensity data derived using DT for stand 5

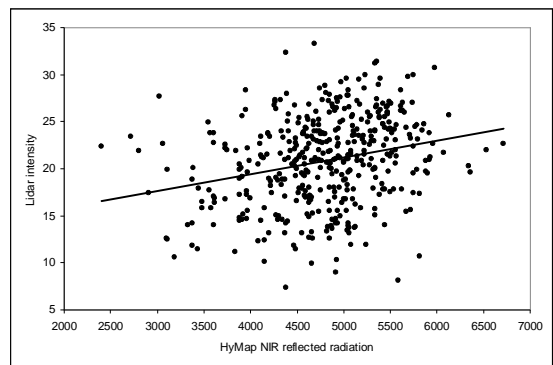


Figure 3b. Plot of HyMap NIR data against lidar intensity data derived using IDW for stand 5.

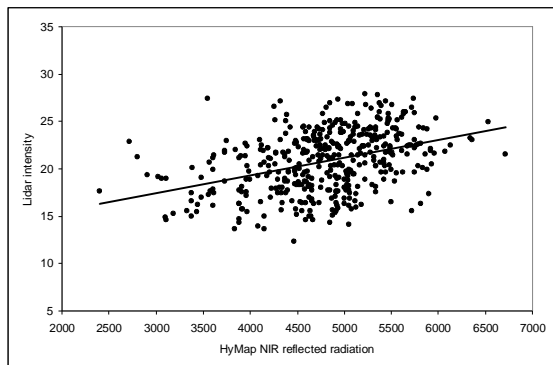


Figure 3c. Plot of HyMap NIR data against lidar intensity data derived using OK for stand 5.

Further examination of the per pixel stand data focused on the differences in the plots between HyMap and lidar intensity data apparent as a function of interpolation method. Figure 4 illustrates the histograms of intensity values derived using each interpolation method for stand 5 and the three plots between the three pairs of interpolation methods. It is evident that there are differences in the lidar intensity values, with Fisher's Z test calculations showing that each relationship is significantly different from the other ($p < 0.01$). This demonstrates the significance of the selected interpolation technique if lidar

intensity values are to be interpolated into a raster and used in a similar way to conventional image analysis. The full implications of this require further investigation and will be a function of point support characteristics. Similar findings can be found in the literature pertaining to the derivation of DSMs from lidar range values (e.g., Lloyd and Atkinson, 2002).

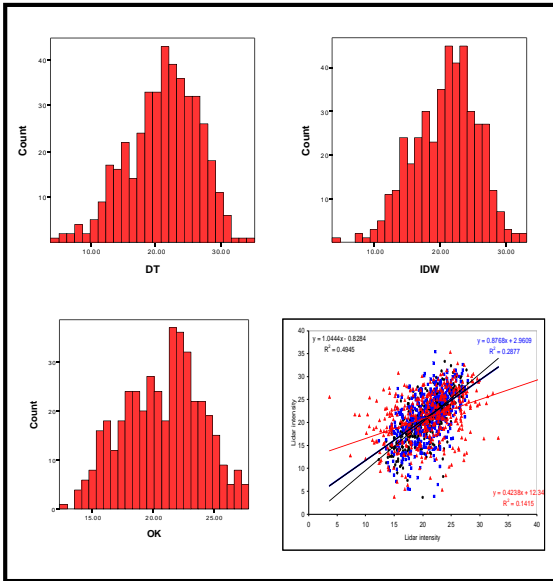


Figure 4. Illustrating the differences in lidar intensity values derived from three interpolation methods (stand 5 data): Histograms and plots of lidar intensity from OK against lidar intensity from IDW (●); lidar intensity from OK against lidar intensity from DT (■) and lidar intensity from IDW against lidar intensity from DT (▲).

4.4. Per parcel analysis of intensity values

To overcome the uncertainty in the per pixel analysis, further analysis focused on using parcels of pixels sampled from compartments within Monks Wood and Bevill’s Wood.. Here plots were drawn for the OK derived lidar intensity values against HyMap data for 28 broadleaved parcels and 11 coniferous parcels (Figure 5a and b respectively).

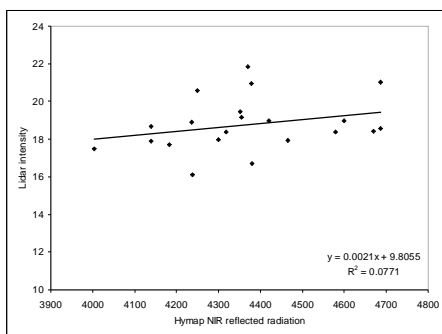


Figure 5a. Plot of HyMap NIR against lidar intensity values for broadleaved forest.

An initial examination of the plots in Figure 5, revealed insignificant relationships between HyMap data and lidar

intensity values. However, on further examination of Figure 5 there is evidence of an effect of different flight lines. Within a flight line plots exhibit strong relationships between HyMap data and lidar intensity values. This is illustrated using the broadleaved compartment data. Within a flight line strong (significant at 0.01 level; two tailed) relationships exist between HyMap data and lidar intensity values (Figure 6). This suggests a real need for calibration of intensity values of different flight lines of an area of interest, if they are to be used to produce one raster for subsequent analysis. In particular there is a need to correct for observation angle (Ahokas, 2006).

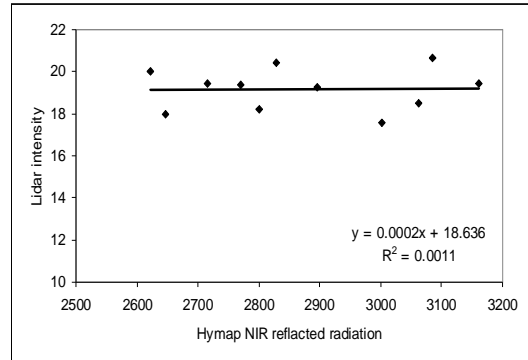


Figure 5b. Plot of HyMap NIR against lidar intensity values for coniferous forest.

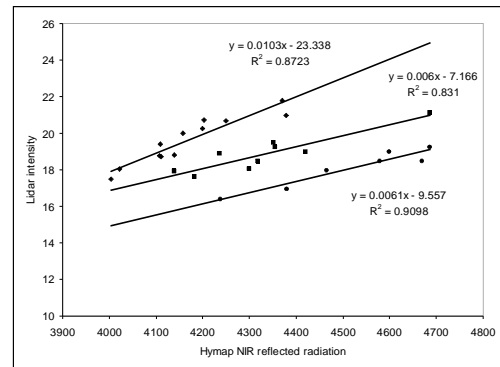


Figure 6. Plot of HyMap data against lidar intensity values for 28 compartments of broadleaved forest for each flight line.

5. DISCUSSION AND CONCLUSION

This paper reports on analyses into the validity and utility of lidar intensity values for a woodland environment. A number of factors influencing lidar intensity values have been explored, including interpolation methods to derive a two dimensional surface and the effect of merging flight lines on the resulting lidar intensity values to be used as an image in direct comparison with a “conventional” remotely sensed image (HyMap data). The results show that lidar intensity values correspond strongly with the HyMap data, however, there is a real need for calibration of the intensity values on an individual flight line basis so they can be used readily. The limiting factor here are a lack of calibration techniques that can be applied to a lidar dataset of this nature, in particular one that has been

provided with flight lines merged. Furthermore, the lessons learned in using the lidar range values via interpolation to a grid should be heeded when using the intensity values. There is potential in using lidar intensity values, but there is still much to do to explain some of the lidar intensity values obtained. One specific query relates to the intensity from coniferous forest. Once a full understanding of the lidar intensity values obtained is achieved, it may be that future lidar campaigns need to consider the specification for mapping classes of interest via intensity in addition to the specification for terrain mapping (Reutebuch et al., 2005).

Two main conclusions can be drawn from this study: (i) lidar intensity values are broadly representative of the NIR radiation reflected from the landscape, though there are some features, such as coniferous forest, that require further analysis to understand their backscatter (ii) there is a real need for calibration of intensity data, particularly if flight lines are to be merged and interpolated.

6. ACKNOWLEDGEMENTS

This work was carried out whilst the RAH was based at the Centre for Ecology & Hydrology (CEH), at Monks Wood. We are grateful to the Environment Agency of England and Wales for funding and acquiring the ALTM 1210 data used in this study. The HyMap data were acquired during the SAR and Hyper-spectral Airborne Campaign (SHAC 2000) and are courtesy of the Natural Environment Research Council (NERC) and the British National Space Centre (BNSC). HyMap data pre-processing was carried out by Laine Skinner, University of Wales Swansea.

7. REFERENCES

- Ahokas, E., Kaasalainen, S., Hyypää, J., and Suomalainen, J., 2006. Calibration of the Optech ALTM 3100 laser scanner intensity data using brightness targets. In: *The International Archives of the Photogrammetry, Remote Sensing and Spatial Information Sciences*, Marne-la-Vallée, France, Vol. 36, Part A1, CD-ROM.
- Arnold, N.S., Rees, W.G., Devereux, B.J., & Amable, G.S., 2006. Evaluating the potential of high-resolution airborne LiDAR data in glaciology. *International Journal of Remote Sensing*, 27, 1233-1251.
- Brennan, R., & Webster, T.L., 2006. Object-oriented land cover classification of lidar-derived surfaces. *Canadian Journal of Remote Sensing*, 32, pp.162-172.
- Carey, C.J., Brown, T.G., Challis, K.C., Howard, A.J., & Cooper, L., 2007. Predictive modeling of multiperiod geoarchaeological resources at a river confluence: a case study from the Trent-Soar, UK. *Archaeological Prospection*, 11, pp. 37-53.
- Coren, F., and Sterzai, P., 2006. Radiometric correction in laser scanning. *International Journal of Remote Sensing*, 27 (15-16), 3097-3104.
- Farid, A., Rautenkranz, D., Goodrich, D.C., Marsh, S.E., & Sorooshian, S., 2006. Riparian vegetation classification from airborne laser scanning data with an emphasis on cottonwood trees. *Canadian Journal of Remote Sensing*, 32, pp. 15-18.
- Gaveau, D.L.A., & Hill, R.A., 2003. Quantifying canopy height underestimation by laser pulse penetration in small-footprint airborne laser scanning data. *Canadian Journal of Remote Sensing*, 29, pp. 650-657.
- Hill, R.A., & Thomson, A.G., 2005. Mapping woodland species composition and structure using airborne spectral and LiDAR data. *International Journal of Remote Sensing*, 17, pp. 3763-3779.
- Holmgren, J., & Persson, Å., 2004. Identifying species of individual trees using airborne laser scanning. *Remote Sensing of Environment*, 90, pp. 415-423.
- Hudak, A.T., Crookston, N.L., Evans, J.S., Falkowski, M.J., Smith, A.M.S., Gessler, P.E., & Morgan, P., 2006. Regression modeling and mapping of coniferous forest basal area and tree density from discrete-return lidar and multispectral satellite data. *Canadian Journal of Remote Sensing*, 32, pp.126-138.
- Kaasalainen, S., Ahokas, E., Hyypää, J. & Suomalainen, J., 2005. Study of surface brightness from backscattered laser intensity: Calibration of laser data. *IEEE GeoScience and Remote Sensing Letters*, 2, pp. 255-259.
- Kaasalainen, S., Kaasalainen, M., Mielonen, T., Suomalainen, J., Peltoniemi, J.I. & Naranen, J., 2006. Optical properties of snow in backscatter. *Journal of Glaciology*, 52, pp. 574-584.
- Lim, K., Treitz, P., Baldwin, K., Morrison, I., & Green, J., 2003. Lidar remote sensing of biophysical properties of tolerant northern hardwood forests. *Canadian Journal of Remote Sensing*, 29, pp.658-678.
- Lloyd, C.D., & Atkinson, P.M., 2002. Deriving DSMs from LiDAR data with kriging. *International Journal of Remote Sensing*, 23, pp. 2519-2524.
- Mazzarini, F., Pareschi, M.T., Favalli, M., Isola, I., Tarquini, S. and Boschi, E., 2007. Lava flow identification and ageing by means of lidar intensity: Mount Etna case. *Journal of Geophysical Research-Solid Earth*, 112, B2.
- Patenaude, G.L., Briggs, B.D.J., Milne, R., Rowland, C.S., Dawson, T.P., & Pryor, S.N., 2003. The carbon pool in a British semi-natural woodland. *Forestry*, 76, pp. 109-119.
- Patenaude, G.L., Hill, R.A., Milne, R., Gaveau, D.L.A., Briggs, B.D.J., & Dawson, T.P., 2004. Quantifying forest above ground carbon content using LiDAR remote sensing. *Remote Sensing of Environment*, 93, pp. 368-380.
- Reutebuch, S.E., Andersen, H.E., & McGaughey, R.J., 2005. Light Detection and ranging (LiDAR): An emerging tool for multiple resource inventory. *Journal of Forestry*, 103, pp. 286-292.
- van Aardt, J.A.N., Wynne, R.H., & Oderwald, R.G., 2006. Forest volume and biomass estimation using small-footprint lidar-distributional parameters on a per-segment basis. *Forest Science*, 52, pp. 636-649.
- Wehr, U., & Lohr, U., 1999. Airborne laser scanning – an introduction and overview. *ISPRS Journal of Photogrammetry and Remote Sensing*, 54, pp. 68-82.
- Wagner, W., Ullrich, A., Ducic, V., Melzer, T., & Studnicka, N., 2006. Gaussian decomposition and calibration of a novel small-footprint full-waveform digitising airborne laser scanner. *ISPRS Journal of Photogrammetry and Remote Sensing*, 60, pp. 100-112.

A MIXED-EFFECTS MODEL TO ESTIMATE STAND VOLUME BY MEANS OF SMALL FOOTPRINT AIRBORNE LIDAR DATA FOR AN AMERICAN AND A GERMAN STUDY SITE

Johannes Breidenbach ^{a,*}, Robert J. McGaughey ^b, Hans-Erik Andersen ^c, Gerald Kändler ^a, Stephen E. Reutebuch ^b

^a Forstliche Versuchs- und Forschungsanstalt Baden-Württemberg, Abteilung Biometrie und Informatik
Wonnhaldestr. 4, 79100 Freiburg, Germany - johannes.breidenbach@forst.bwl.de

^b USDA Forest Service, Pacific Northwest Research Station
University of Washington, PO Box 352100, Seattle, WA 98195-2100, USA

^c USDA Forest Service, Pacific Northwest Research Station
Anchorage Forestry Sciences Laboratory, 3301 C Street, Suite 200, Anchorage, AK 99503, USA

KEY WORDS: Mixed-effects models, random effects, lidar, forest inventory, stand volume

ABSTRACT:

Similar datasets (inventory plots, stand maps and lidar data) were available for study sites in the USA and Germany. These datasets are grouped or hierarchical in that several sample plots are located within a stand and the stands are located within two study sites. Fixed-effects models and mixed-effects models with a random intercept on the stand level were fit to each dataset. Mean lidar raw data return height and its interaction term with canopy cover as well as its interaction term with the coniferous proportion were found to be the most influential predictor variables. The mixed-effects models significantly improved the estimates and especially reduced the bias which was present for numerous stands in the estimates of the fixed-effects models. This resulted in a slight increase of the variance within the stands. The RMSE for the German study site was higher (34.7% and 29.7% for fixed- and the mixed-effects model respectively) than on the US study site (19.2% and 16.8% for fixed- and the mixed-effects model respectively). A mixed-effects model with random effects on the study site and stand level was fit to the combined dataset. It showed almost the same errors as the local mixed-effects models (17.6% and 29.8% for the US and the German study site respectively). Hence a single model is sufficient to make estimates for both datasets. The study shows the potential of mixed-effects models in this context. It illustrates that the common practise of fitting different models for different strata may be unnecessary.

1 INTRODUCTION

Height and density metrics, derived from lidar (light detection and ranging) point clouds can be used as predictor variables in statistical models to estimate forest parameters at the stand or plot level (Næsset, 2004; Andersen et al., 2005, among others). Such models are usually fit using sample plots where both lidar (co-variables) and ground-truth information (response) are available. To map the variable of interest, the entire lidar dataset is gridded into tiles having the same size as a sample plot. Then the predictor variables are computed and the regression models are applied to every tile. Compared to plot-based inventories, estimation errors can be significantly decreased for the area of interest (e.g. a single forest stand), since the number of observations (i.e. the tiles) is usually much higher than the number of sample plots within a stand.

The predictor variables derived from lidar data are mainly related to the vegetation height and structure (e.g., height- and density metrics, crown cover). The vegetation cover can, under certain circumstances, also be classified into broadleaf and coniferous trees. However, information about the site quality or tree species cannot be derived without additional data. Therefore, predictions for stands with rare site index classes or tree species compositions might deviate from the mean model, resulting in a bias.

If the grouping structure (i.e., the stand boundaries) is known, the deviation from the mean model of plot estimates within a stand can be utilized to reduce the bias using mixed-effects models (mixed models). From the statistical point of view, the grouping structure has to be considered since the observations are not independent. In a mixed model, the effects of the variable that indicates the level of grouping (i.e. the stand-ID) are assumed to be a random sample of a larger population that vary randomly

around a population mean. This is referred to as random effects. Mixed models with forestry application were discussed by Lappi and Bailey (1988). An in-depth description of mixed models is given for example by Pinheiro and Bates (2002).

In a mixed model, the variance is split into within and between group variance. The coefficients and standard errors for predictor variables that vary less within than between the groups are therefore more accurate. Another advantage of a mixed model, compared to a fixed-effects model with the grouping level as a dummy variable, is that predictions can also be made for individuals with grouping levels that did not exist in the dataset used to fit the model (e.g., in our case those stands without sample plots). In a forest inventory context, a mixed model provides an additional advantage. A model can be fit to a large dataset (e.g., to a well inventoried public forest) and subsequently be calibrated with just a few sample plots for a new forest area (e.g., a small private forest). (A new model would need to be fit, if a fixed-effects model were used.)

Publications regarding the estimation of volume and biomass on the plot level include these of Næsset (2002) who created separate models for different ages and site qualities and achieved R^2 between 0.80 and 0.93 in a boreal forest and Means et al. (2000) for Douglas fir stands in the Cascade Mountains (Oregon, USA) who reported R^2 between 0.93 and 0.95. In a study by Packalén and Maltamo (2006) in a Finnish boreal forest, plot volume was assigned to tree species by using the k-MSN method. They report a RMSE of roughly 24% for estimates of total volume. Aardt et al. (2006) segmented homogeneous forest units first and used the lidar vegetation height distribution and the field data for the units to calibrate prediction models. They report R^2 between 0.58 and 0.79 for their study which was located in Virginia (temperate mixed forests).

The objective of this research was to develop a single statistical model for estimates on study sites located in the USA and Germany. Furthermore, we wanted to find out if information about the stand-level grouping of sample plots can be used to further improve the regression models. The datasets contain several levels of grouping or random effects: (i) The study sites are two random samples of all potentially existing study sites, (ii) the stands are grouped within the study site and are a random sample of the stands within each study site. Due to this structure, the resulting model is referred to as a multi-level or hierarchical model.

2 MATERIAL AND METHODS

2.1 American Dataset

The study site in the USA is part of Capitol State Forest and is managed by the Washington State Department of Natural Resources. The terrain is moderate with elevations varying from 300 to 425 meters and ground slopes up to 30°. The forest is composed primarily of Douglas-fir (*Pseudotsuga menziesii* (Mirb.) Franco; 81%) and western hemlock (*Tsuga heterophylla* (Raf.) Sarg.; 13%). Additional species present include western red cedar (*Thuja plicata* Donn ex D. Don; 2%) and few deciduous hardwoods such as red alder (*Alnus rubra* Bong.; 3%) and maple (*Acer spp.*; <1%). The height of dominant trees in the study area was approximately 50 meters (table 1). As part of a forest management study (Curtis et al., 2004), the canopy of the 70-year-old forest stand was partially harvested in 1998, resulting in four different residual canopy density classes.

A total of 98 fixed area field inventory plots were established over a range of stand conditions in 1999. Plot sizes ranged from 0.02 to 0.2 ha. Measurements acquired at each plot included species and diameter at breast height (DBH) for all trees greater than 14.2 cm in diameter. In addition, total height was measured on a representative selection of trees using a hand-held laser rangefinder. A detailed description of the plot measurement protocol can be found in Curtis et al. (2004). Inventory plot locations were surveyed with a Topcon ITS-1 total station and are accurate to within 1 m.

The Saab TopEye lidar system mounted on a helicopter was used to map approximately 5.25 km² of the study area in the spring of 1999 (before foliation). Table 2 summarizes the flight parameters and instrument settings for the data acquisition. Data for each return included the pulse number, return number for the pulse (up to four returns were recorded per pulse), X, Y, elevation, off-nadir angle and intensity.

2.2 German Dataset

The 49 km² study area is located approximately 60 km north of Freiburg. Elevations range between 400 and 1050 m above sea level. The average gradient across the site is approximately 12° with some slopes of up to 35°. The average forest stand is approximately 1.2 ha in size. Tree heights within the study area range from 5 to 47 m, with an average height of 23 m. Norway spruce (*Picea abies* (L.) Karst.; 65%), silver fir (*Abies alba*; 17%), beech (*Fagus sylvatica* L.; 9%) and Scotts pine (*Pinus sylvestris*; 6%) are the most common tree species. The forest is managed using a group selection system, where the regeneration phase may take several decades (clearcuts are not common in Germany).

A regular forest enterprise inventory was conducted in the second half of 2003 in the state forest of the study area, using plots positioned on the intersections of a 100 x 200 m sample grid. The horizontal accuracy of the inventory plot locations is estimated to

be better than 10 m. Forest characteristics were recorded within sample plots consisting of four concentric circle plots (i.e. they have the same centre) with radii of 2 m, 3 m, 6 m and 12 m. Trees with a diameter at breast height (DBH) greater than 7 cm, 10 cm, 15 cm and 30 cm, respectively, were recorded within the four circle plots. The heights of the two tallest trees per species were measured in each plot using a *Vertex* angle measurement instrument. The height of the remaining trees within a plot were estimated using forest stand height curves and the DBH. Single tree volumes were calculated using DBH and height as parameters for taper and volume functions of the Baden-Württemberg state forest service (Kon-Allan et al., 2004). Plots intersecting stand or forest borders were excluded for this study. A total of 1061 inventory plots, with an overall area of 48 ha, were used as terrestrial reference data for the remotely sensed data. Stand boundaries were digitized from orthophotos in 2003 and were adjusted to meet operational purposes during the field work. Additional information describing the stands that could be used as covariates were not available for this study.

Lidar data were acquired in spring 2003 (before foliation) using the Optech ALTM 1225 airborne laser scanner. Adjacent swaths overlapped about 50% (table 2). First and last return laser data were automatically classified into ground and vegetation hits by the data provider (TopScan).

2.3 Computation of predictor variables

A digital terrain model (DTM) and a digital surface model (DSM) was computed for both test sites using the software *TreesVis* (Weinacker et al., 2004) for the German and *Fusion 2.0* (McGaughey et al., 2004) for the American study site. An evaluation of the American DTM, presented in Reutebuch et al. (2003), found an average lidar elevation error of 22 cm. For the German study site, a DSM was derived from the first (DSM_F) and the last return (DSM_L) vegetation returns. Canopy height models (CHM, CHM_F, CHM_L) were computed by subtracting the DTM from the according DSMs. The lidar vegetation height was determined by calculating the difference between the elevation of the lidar vegetation data (raw data) and the corresponding DTM raster bin elevation.

Circular subsets of the same radius as the corresponding sample plot were created from the lidar raw data. The 0th, 25th, 50th, 75th and 100th percentiles and the mean of the lidar vegetation heights were calculated for each subset to characterize the vegetation height distribution. Vegetation density metrics were derived by dividing the range between the highest and lowest measurement into 10 classes and determining the proportion of measurements within each class. *Fusion 2.0* was used for the raw data manipulation.

Since broadleaf trees in leaf-off condition had only a few vegetation returns in the last return data, they do not show up in the CHM_L. Therefore, a classification of the pixels into those belonging either to coniferous or broadleaf trees was possible by subtracting the CHM_L from the CHM_F. The result was normalized with the CHM_F. By comparison with orthophotos, a threshold of 0.3 was found to separate coniferous and broadleaf pixels well (equation 1). It should be noted that Larches (*Larix spp.*) are a potential problem for this classification approach, since they are deciduous conifers. However, few Larches were present in the study area so we felt the classification approach was applicable.

$$P_i \begin{cases} 1 & (\text{CHM}_{F,i} - \text{CHM}_{L,i})/\text{CHM}_{F,i} \leq 0.3 \\ 0 & (\text{CHM}_{F,i} - \text{CHM}_{L,i})/\text{CHM}_{F,i} > 0.3 \end{cases} \quad (1)$$

Parameter	German study site		American study site	
	Mean	Max	Mean	Max
Trees per ha [ha ⁻¹]	411.10	2255.00	309.10	1093.00
Mean heights [m]	23.07	42.56	36.42	51.97
Volume [m ³ ha ⁻¹]	347.10	1265.00	567.90	1167.00

Table 1. Summary of forest attributes derived from sample plot data for the study sites.

Parameter	Characteristic	
	German study site	American study site
Laser pulse frequency	25,000 Hz	7,000 Hz
Scan angle	± 20°	± 10°
Swath width	500-600 m	70 m
Laser pulse density	0.51 m ⁻²	4 m ⁻²
Flying height	900 m AGL	200 m AGL
Flying speed	80 m sec. ⁻¹	25 m sec. ⁻¹
Beam divergence	0.25 mrad	2 mrad
Vertical accuracy	0.15 m	n.a.
Horizontal accuracy	0.45 m	n.a.

Table 2. Operating parameters of the Lidar sensors (n.a. = not available).

The i th pixel P will have a value of 1 if it is classified as coniferous and 0 if classified as coming from a broadleaf tree.

The proportion of coniferous trees (coniferous proportion = CP) at a plot, which is assumed to be equal to the proportion of pixels classified as coniferous, was calculated as the sum of coniferous pixels divided by the overall sum of pixels within a sample plot. For numerical reasons, this 0..1 distributed variable was then stretched between -infinity and infinity using the logit-transformation ($\log(\frac{p}{1-p})$). Since the lidar dataset of the US study site was not separated into first- and last return data, a computation of CP was not possible.

The percentage of canopy cover (CC) on a sample plot was computed as the number of pixels in the CHM (CHM_F for the German data set) greater than 1 m divided by the total number of pixels within the plot. As for CP , a logit transformation was applied to this variable.

2.4 Modeling

Modeling consisted of two steps: (i) Select adequate predictor variables, (ii) fit mixed models by adding random effects. To select predictor variables, scatter plots and correlations of the response variables over the height metrics were analyzed for the German study site. The mean vegetation height measured by lidar data ($mean.l$) was found to be the most influential predictor variable. Since the variance increases as the response variable increases (heteroscedasticity), $mean.l$ was also used as a predictor variable for the variance function. More precisely, a generalized-least-squares (GLS) regression was used with weights based on $mean.l^{2\delta}$ where δ was estimated during the fitting of the model (Pinheiro and Bates, 2002, p. 208).

Since the height metrics vary depending on the canopy structure, we wanted to know if the model improves as interaction terms between $mean.l$ and the canopy cover and between $mean.l$ and the crown shape (expressed as conifer proportion) are considered (equation 2). We also explored whether or not density metrics further improved the model. The selected model (fixed-effects model for the German study site) was then re-fit using data for the American study site and the coefficients were compared. As it was not possible to compute the coniferous proportion for the

US study site, this variable was not included in the fixed effect model for the US data.

The fixed-effects model can be written as

$$y_k = \beta_0 + \beta_1 mean.l_k + \beta_2 CC_k + \beta_3 CP_k + \beta_4 CC_k \cdot mean.l_k + \beta_5 CP_k \cdot mean.l_k + \epsilon_k, \quad (2)$$

$$k = 1, \dots, n, \quad \epsilon_k \sim N(0, \sigma^2 mean.l_k^{2\delta}),$$

where y_k is the response variable for the k th sample plot, $\beta_0.. \beta_5$ are the coefficients, ϵ_k is an independent error term with a variance model depending on $mean.l$ and δ and n is the number of sample plots.

In the second step, random effects for the intercept on the stand level were introduced for the local models (equation 3). Their results were compared to a global model with random effects for the intercept on the study site as well as on the stand level. For the global model, we checked if it was necessary to have a random effect for the coefficients. To do this, models with a random intercept on the study site and the stand level as well as a random effect for either one of the coefficients (equation 4) were compared with the global model with the random effect only for the intercept using a F-test.

The following equation is the general form of a local mixed model

$$y_{jk} = \beta_0 + b_{0,j} + \beta_1 x_{1,jk} + \dots + \beta_m x_{m,jk} + \epsilon_{jk}$$

$$k = 1, \dots, n_j, \quad b_j \sim N(0, \sigma_j^2), \quad (3)$$

$$\epsilon_{jk} \sim N(0, \sigma^2 mean.l_k^{2\delta}).$$

Here y_{jk} is the response variable for the k th sample plot in the j th stand, $x_{1,jk}..x_{m,jk}$ are the m fixed effects, $\beta_0.. \beta_m$ are the coefficients thereof and n_j is the number of sample plots within a stand. The stand random effects $b_{0,j}$ are assumed to be independent for different j and the within-group errors, ϵ_{jk} are assumed to be independent of different j and k and to be independent of the random effects.

If the response variable of the k th sample plot in the j th stand within the i th study site is denoted as y_{ijk} $i=1,2$; $j=1,..,l_i$; $k=1,..,n_j$, with l_i as the number of stands in the i th study site and $b_{0,i}$; $b_{0,i,j}$ are random effects for the intercept on the study

site and stand level respectively, an example for the global model including a random effect on the study site level for the coefficient of the first fixed effect ($b_{1,i}$) can be expressed as

$$y_{ijk} = \beta_0 + b_{0,i} + b_{0,ij} + (\beta_1 + b_{1,i})x_{1,ijk} + \dots + \beta_m x_{m,ijk} + \epsilon_{ijk}. \quad (4)$$

The random effects are, technically speaking, not parameters of the statistical model. Nevertheless, their values (Best Linear Unbiased Predictors, BLUPs) can be estimated. Details on the estimation of BLUPs can be found in Pinheiro and Bates (2002).

A leave-one-out cross-validation procedure was used to check for potential overfitting of the data. A close similarity of the RMSE and the RMSE of the cross-validation (RMSE.CV) indicates that the model is not overfitting the data (Andersen et al., 2005). All statistical analysis were carried out with the software package R (R-Development-Core-Team, 2006) including the library *nlme* (Pinheiro and Bates, 2002) for the fitting of mixed-effects models.

3 RESULTS

3.1 Selected models

Canopy closure and coniferous proportion as well as their interaction with *mean.l* significantly improved the linear model for the German study site. The addition of density metrics seemed to enhance the model fit significantly but improved the R^2 less than 1%. They were therefore not included in the model in order to keep the amount of predictor variables to a minimum. The selected model of the German study site explains about 70% of the variance and leads to an RMSE of ca. 35%.

The model including the same predictor variables as the model for the German study site showed better goodness-of-fit measures (R^2 of 0.86 and RMSE of ca. 17%) for the US study site. Nevertheless, it was also tested, if the model improves as other height metrics (e.g. the median or the 75th percentile) serve as predictor variables instead of *mean.l*. But none of the models including those variables was significantly different from the model including *mean.l*. We concluded that the same predictor variables can be used for the German and for the US study site. Additional model attributes and RMSE can be found in tables 3 and 4.

3.2 Mixed effect models

Random effects on the stand level improved the models for both study sites significantly. In general, it can be observed that the median residual per stand is closer to zero, while the variance slightly increases. This also means that the prediction for some observations gets better, while the opposite is true for others. In other words, the mixed models lead to a decreased bias with a trade-off of higher variance. This of course, is most present in stands where the bias of the fixed effect model was large. However, the variance within the stands is relatively high, especially for the German study site. Therefore, the bias will not be eliminated completely (figure 1 and table 5).

For the global model, besides the random effects on the stand level, only a random effect for the coefficient of the interaction between the canopy cover and *mean.l* significantly improved the model. This suggests, that the other coefficients do not differ significantly between the study sites. Interestingly, the RMSE does not increase very much, meaning that this model can be used for predictions at both study sites.

The global model can be expressed as

$$y_{ijk} = \beta_0 + b_{0,i} + b_{0,ij} + \beta_1 mean.l_{ijk} + \beta_2 CC_{ijk} + \beta_3 CP_{ijk} + (\beta_4 + b_{1,i}) CC_{ijk} \cdot mean.l_{ijk} + \beta_5 CP_{ijk} \cdot mean.l_{ijk} + \epsilon_{ijk}. \quad (5)$$

The other models can be written the same way without $b_{0,i}$ and $b_{1,i}$ for the local models with random effects, without $b_{0,i}$, $b_{1,i}$ and $b_{0,ij}$ for the local models with fixed effects only and without CP for the US models.

3.3 Characteristics of the regression models

The slope of *mean.l* is slightly higher for the US study site than for the German site. This is also true for the coefficient of canopy cover. The models will predict higher volumes with an increase of canopy cover or an increased number of coniferous trees per plot. The global model produces almost the same predictions for given *mean.l* but differs slightly more from the local models given canopy cover (figures 2 and 3).

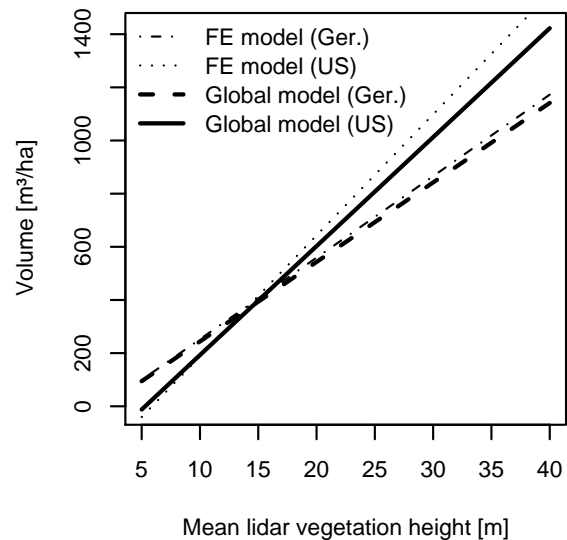


Figure 2. Comparison of predictions of local fixed-effects models (FE) with the global mixed model (Ger.=Germany). *mean.l* alters, *CC* and *CP* are fixed at 100%.

4 DISCUSSION

In this study, we compared fixed-effects models with mixed-effects models containing random effects on the stand level and on the study site level. The grouping information was used to calibrate the mixed models on the stand level using the variance information of sample plots located within a stand. A drawback of this method is that this information can only be used reliably for stands that contain several sample plots if the within stand variance is high as it was the case in this study.

Reasons for bias in some stands, besides rare tree species and site indices, might be uncommon taper shapes, varying density of small trees in the understory (i.e. two layers of trees, which probably does not change *mean.l* explicitly) or other incidents that change the canopy structure but are not reflected in the selected covariates.

Coefficients	FE model (Ger.)		FE model (US)		RE model (Ger.)		RE model (US)		Global model	
	Est.	p-val.	Est.	p-val.	Est.	p-val.	Est.	p-val.	Est.	p-val.
Intercept	-10.12	0.42	77.24	0.24	-3.93	0.74	57.47	0.39	-82.04	0.33
<i>mean.l</i>	15.44	<0.01	9.15	<0.01	14.98	<0.01	10.48	<0.01	14.48	<0.01
<i>CC</i>	-11.86	<0.01	-50.00	<0.01	-13.02	<0.01	-35.56	0.01	-13.69	<0.01
<i>CP</i>	5.45	0.14			3.52	0.24			5.86	0.06
<i>mean.l · CC</i>	1.64	<0.01	5.27	<0.01	1.74	<0.01	4.31	<0.01	2.68	<0.01
<i>mean.l · CP</i>	0.57	<0.01			0.59	<0.01			0.36	0.04
δ	0.46		0.34		0.58		0.44		0.46	

Table 3. Attributes of the fitted models (Est. = Estimate, p-val. = p-value).

	German models		American models		Both
	FE model	RE model	FE model	RE model	Global model
RMSE [m³ ha⁻¹]	120.33	103.12	108.96	95.51	103.00
German study site					
RMSE [%]	34.67	29.71			29.76
RMSE.CV [%]	34.90	34.40			34.43
American study site					
RMSE [%]			19.19	16.82	17.58
RMSE.CV [%]			19.95	18.49	18.69
Both					
RMSE [%]					28.16
RMSE.CV [%]					32.35
R ²	0.70	0.78	0.86	0.89	0.81

Table 4. RMSE, RMSE of the cross-validation (RMSE.CV) and R² for the fitted models (FE = fixed effect, RE = random effect).

Stand-ID	FE model		RE model		Global model	
	SD	Bias	SD	Bias	SD	Bias
9	117.59	96.24	126.85	95.13	110.91	95.61
8	46.82	49.75	48.97	31.25	50.17	32.24
6	145.39	115.49	128.37	98.74	127.78	96.67
5	90.34	82.60	94.41	75.50	96.20	77.60
4	105.32	86.24	119.01	96.46	120.77	99.31
3	117.69	102.09	123.99	100.16	123.83	98.40
2	50.51	94.66	50.45	40.64	51.27	58.44

Table 5. Standard deviations (SD) of the residuals and bias for the stands on the American study site.

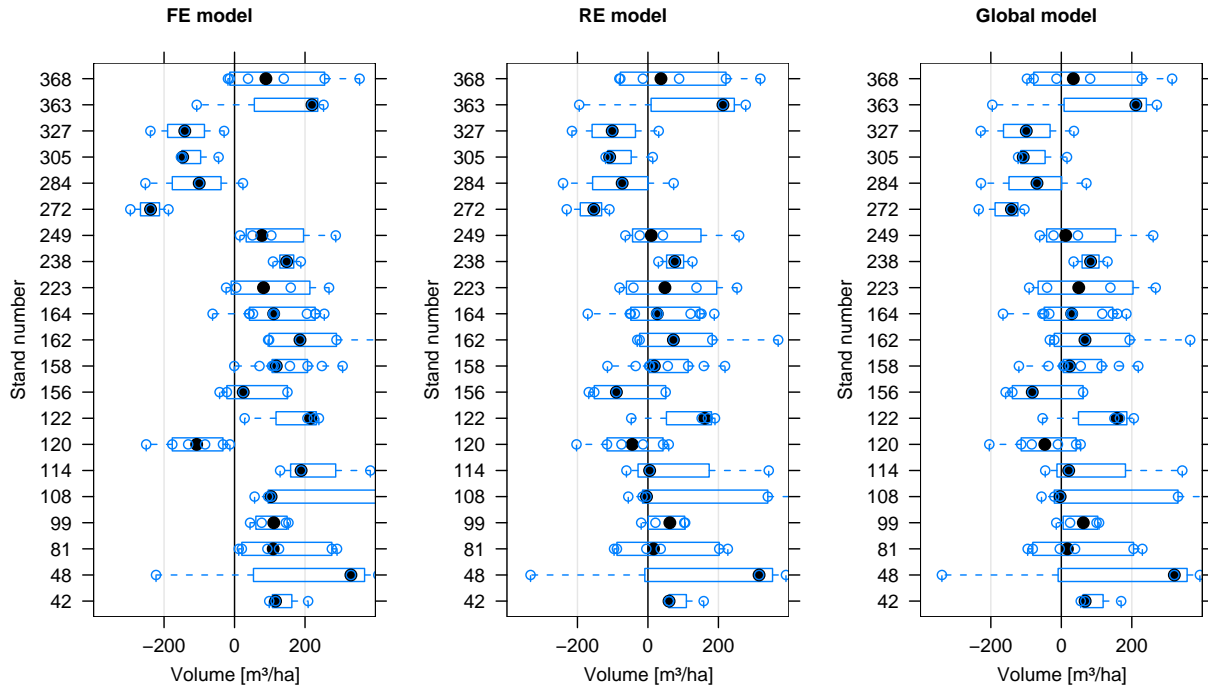


Figure 1. Residuals of a leave-one-out cross-validation for selected stands at the German study site. Stands with a mean residual > 100 and at least 3 observations were selected for this graph.

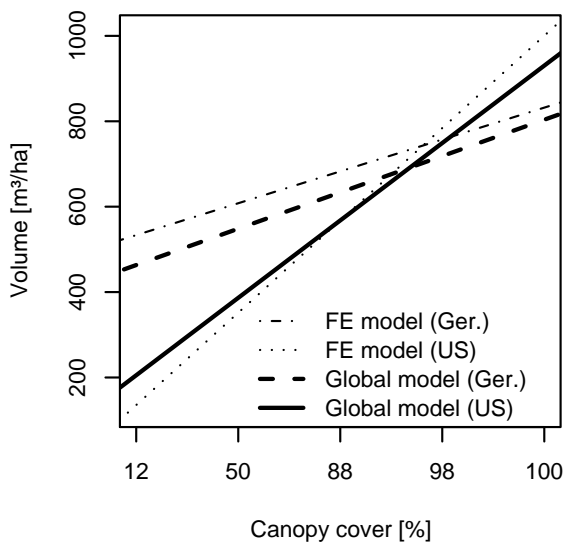


Figure 3. Comparison of predictions of local fixed-effects models (FE) with the global mixed model (Ger.=Germany). *CC* varies, *mean.l* is fixed at 30 m and *CP* at 100%.

We assume that differences in the model coefficients for the study sites can be attributed to variation in the vegetation cover and the lidar parameters:

1. The US study site is highly productive (high site index) and is stocked mainly by Douglas-fir, which is one of the fastest growing tree species in temperate forests. In comparison, the German study site encompasses a range of productivity classes, a broader range of elevations and a more diverse mix of tree species. In addition, the main coniferous tree species

(Norway spruce) does not accumulate as much volume as Douglas-fir.

2. Although both lidar systems produced small footprint data, return density, footprint size and flying platforms were significantly different. This could influence the penetration rates through the canopy, amount of shadowing, etc.

However, whether vegetation or lidar parameters have a larger influence in these study results could not be determined. The same is true for possible interactions between lidar parameters and vegetation.

Interestingly, the predictor variable canopy cover improved the model more on the American study site than on the German study site. This improvement is likely related to the extensive changes in the canopy structure resulting from the silvicultural treatments carried out on the American study site. These treatments resulted in a wider range of canopy densities than was present on the German dataset.

The coefficients of the coniferous proportion indicate that the volume increases with an increasing amount of coniferous trees on a plot. This is consistent, since *mean.l* tends to be smaller for conifer dominated plots compared to plots dominated by deciduous species but having the same mean tree height due to the conifer crown shape (Breidenbach et al., 2007). Another reason for this effect is probably that the amount of usable timber is higher for most coniferous species, since the ratio of stem to branch volume is higher for coniferous trees. Therefore, similar heights correspond to more volume for conifer dominated sample plots.

The observed errors for the US study site (~ 17%) are comparable to those reported by Næsset (2002), but somewhat higher than those reported by Means et al. (2000) (73 m³ ha⁻¹ opposed to ~ 95 m³ ha⁻¹). The errors for the German study site are much higher which is probably due to the wider range of tree species

and stand types. Another reason could be that the horizontal accuracy of the field plot positions for the German study site is worse than for the US study site. Aardt et al. (2006), whose study site is probably more similar to the German site, report smaller absolute RMSE ($\sim 40\text{--}68\text{ m}^3\text{ ha}^{-1}$) than we observed for the German site. However, since the range of stand volumes in their data is significantly smaller than in this study, the relative errors seem to be larger.

5 CONCLUSIONS AND FUTURE WORK

A mixed-effects model was fit to data from the USA and Germany. The goodness-of-fit metrics indicate, that the model fit to the combined data is almost as good as models fit to data for each site, although the stand conditions and lidar properties varied greatly between the study sites. It should be emphasized that the random effects at the stand level were able to significantly reduce the bias that was found at the stand level. The relatively expensive field data were consequently used twofold: (i) To fit prediction models, (ii) to reduce the bias by calibrating random effects and utilizing the information that they provide at the stand level. Therefore the effectiveness of the money spent to collect field data was increased using mixed models.

The results of this study indicate that other researchers that stratified their data and used different models for each stratum could potentially enhance their models with random effects on the level of these strata. An additional benefit would be that the amount of data for modeling is then larger.

Future work will strive to better understand the bias observed at the stand level. The stands, represented as polygons, on the German site were delineated based on operational considerations. Hence, small groups of trees were included with adjacent but different (in terms of species composition and age) stands to avoid creating small stands. We speculate that stand delineations that result in more homogeneous conditions within each stand will lead to lower within-stand variance and larger between-stand variance which could further improve the models. Furthermore it seems to be interesting to determine the contribution of the different lidar acquisition parameters (e.g. return density, foot print size) to the coefficients of the regression models. The use of mixed models can also reduce the number of sample plots needed for new study areas once a basic model exists. This issue will be discussed in an other study.

ACKNOWLEDGEMENTS

This paper is dedicated to Jürgen Bayer who died during the synthesis of this paper. He was a GIS-specialist at the Forstliche Versuchs- und Forschungsanstalt Baden-Württemberg and thus was involved in this research by consulting with questions regarding spatial data. We cannot express how much we miss him and his expertise.

We appreciate the comments of two unknown reviewers. We also would like to thank Dr. Edgar Kublin for his support regarding statistical analysis as well as Nick Vaughn and Nain Martinez for their general help. Special thanks go to Daniele Stöhr for the many years of good collaboration. Funds for this research were provided by the German Federal Ministry of Education and Research (0330616B). This document was typeset using \LaTeX .

References

Aardt, J. A. N. v., Wynne, R. H. and Oderwald, R. G., 2006. Forest volume and biomass estimation using small-footprint

lidar-distributional parameters on a per-segment basis. *Forest Science* 52(6), pp. 636–649.

Andersen, H. E., McGaughey, R. J. and Reutebuch, S. E., 2005. Estimating forest canopy fuel parameters using lidar data. *Remote Sensing of Environment* 94(4), pp. 441–449.

Breidenbach, J., Koch, B., Kändler, G. and Kleusberg, A., 2007. Quantifying the influence of slope, aspect, crown shape and stem density on the estimation of tree height at plot level using lidar and insar data. *International Journal of Remote Sensing* (in review).

Curtis, R. O., Marshall, D. D. and DeBell, D. S. (eds), 2004. Silvicultural options for young-growth Douglas-fir forests: the Capitol Forest study-establishment and first results. *Gen. Tech. Rep. PNW-GTR-598*. U.S. Department of Agriculture, Forest Service, Pacific Northwest Research Station, Portland, OR.

Kon-Allan, E., Goltz, v. H., Blust, M. and Nothdurft, A., 2004. *Manual for enterprise inventories*, version 1.1. Landesforstverwaltung Baden-Württemberg (German, title translated).

Lappi, J. and Bailey, R. L., 1988. A height prediction model with random stand and tree parameters: an alternative to traditional site index methods. *Forest Science* 34(4), pp. 907–927.

McGaughey, R., Carson, W., Reutebuch, S. and Andersen, H.-E., 2004. Direct measurement of individual tree characteristics from lidar data. In: *Annual ASPRS Conference*, American Society of Photogrammetry and Remote Sensing, Denver, USA.

Means, J. E., Acker, S. A., Fitt, B. J., Renslow, M., Emerson, L. and Hendrix, C. J., 2000. Predicting forest stand characteristics with airborne scanning lidar. *Photogrammetric Engineering & Remote Sensing* 66(11), pp. 1367–1371.

Næsset, E., 2002. Predicting forest stand characteristics with airborne scanning laser using a practical two-stage procedure and field data. *Remote Sensing of Environment* 80(1), pp. 88–99.

Næsset, E., 2004. Practical large-scale forest stand inventory using a small-footprint airborne scanning laser. *Scandinavian Journal of Forest Research* 19(2), pp. 164–179.

Packalén, P. and Maltamo, M., 2006. Predicting the plot volume by tree species using airborne laser scanning and aerial photographs. *Forest Science* 52(6), pp. 611–622.

Pinheiro, J. and Bates, D., 2002. *Mixed Effects Models in S and S-Plus*. Springer.

R-Development-Core-Team, 2006. *R: A language and environment for statistical computing*. Technical report, R Foundation for Statistical Computing.

Reutebuch, S. E., McGaughey, R. J., Andersen, H.-E. and Carson, Ward, W., 2003. Accuracy of a high resolution lidar terrain model under a conifer forest canopy. *Canadian Journal of Remote Sensing* 29(5), pp. 527–535.

Weinacker, H., Koch, B., Heyder, U. and Weinacker, R., 2004. Development of filtering, segmentation and modelling modules for lidar and multispectral data as a fundament of an automatic forest inventory system. In: *ISPRS Working Group VIII/2 'Laser-scanners for forest and landscape assessment'*, University of Freiburg, Freiburg, Germany.

AUTOMATIC RELATIVE ORIENTATION OF TERRESTRIAL LASER SCANS USING PLANAR STRUCTURES AND ANGLE CONSTRAINTS

Claus Brenner and Christoph Dold

Institute of Cartography and Geoinformatics
Leibniz Universität Hannover
Appelstr. 9A, 30167 Hannover, Germany
claus.brenner@ikg.uni-hannover.de, christoph.dold@ikg.uni-hannover.de

KEY WORDS: Relative orientation, registration, range images, terrestrial laser scanning

ABSTRACT:

The relative orientation of independently acquired terrestrial laser scan point clouds is an important task. If good starting values are available, well-known iterative algorithms exist to determine the required transformation. In this paper, we describe a method to obtain such starting values fully automatically, which is applicable to scenes containing planar elements. Our method first extracts planar patches in each scan individually and then assigns patch triples across scans in order to compute the rotation and translation component of the relative orientation. We assess the performance of our approach using a set of 20 terrestrial scans acquired systematically at increasing distance. For each scan, we automatically extract the 50 largest planar patches. We show that, although there are 1.15 billion possible patch triple assignments, we are able to compute efficiently a ranked list of possible transformations where the correct transformation is usually within the first few positions. For our test data and three test runs, it has been among the first 53 positions, even for scans with little overlap. Thus, instead of 1.15 billion candidate solutions, the score function needs only to evaluate on the order of 100 candidate solutions, which is an improvement by a factor of 10^7 .

1 INTRODUCTION

In terrestrial laser scanning, an important problem is to find the relative orientation of independently acquired datasets, also called range image registration. This is a very well-known problem dating back to the first investigations on range images. It can be divided into two subproblems, coarse registration, which assumes no previous knowledge about the relative orientation of the two scans, and fine registration, where the assumption is that an initial orientation is known and the goal is to refine this in order to find the most accurate transformation parameters. Fine registration can be achieved using iterative techniques, usually based on the *iterative closest point* (ICP) approach. There is extensive literature on this subject. Originally described by Chen and Medioni (1991) and Besl and McKay (1992), many variants were proposed in the sequel, differing in the selection, matching, weighting and rejection of correspondences, e.g. (Zhang, 1994; Kapoutsis et al., 1999; Greenspan and Godin, 2001; Jost and Hügli, 2002; Sharp et al., 2002). An overview is given by Rusinkiewicz and Levoy (2001) and Gruen and Akca (2005). The ICP algorithm is nowadays also widely available in commercial software.

Any relative orientation based on the data itself requires two steps, (i) finding corresponding features in both datasets, and (ii) determination of the relative orientation which aligns those features. Iterative schemes like the ICP solve the correspondence problem by assuming that, applying the known coarse transformation, any point in the first scene is already close to his counterpart in the second scene. This allows to define corresponding features solely based on vicinity, with no or only limited interpretation of the scenes.

As for the coarse registration, finding the relative orientation of two overlapping scans without previous knowledge of the transformation is a hard (and mainly combinatorial) problem. For practical purposes, it is often solved in software by letting the user define a number of corresponding point pairs manually, which allows to compute the 3D Euclidean transformation. Automation

of this step is not only interesting in terms of improvement of laser scan software. It also is related to fundamental problems such as object recognition (where one of the scans is replaced by a known model) and the problem of the ‘kidnapped robot’ in robotics (where the robot has to find its initial pose by determination of the relative orientation of its scan data and a known map).

Establishing correspondences between datasets without any previous knowledge requires features ‘stronger’ than points. Features should be stable with respect to partial occlusion, and should carry enough information to recover position and orientation (Faugeras and Hebert, 1986). In this paper, we investigate a coarse registration technique using correspondences of planar patches. We chose this feature since planar faces are often present in the vicinity of man-made structures. Furthermore, planar patches are relatively easy to extract from laser scanner data. We extend our previous work on that topic (Brenner et al., 2007) by an improved method to find patch correspondences.

This paper is organized as follows. In section 2, we present the mathematical background, in section 3 the basic problem and our approach are stated, and section 4 introduces our test data. Then, section 5 and 6 introduce and evaluate our solution for the determination of the rotation and the translation, respectively. Finally, section 7 draws conclusions and gives an outlook.

2 MATHEMATICAL FORMULATION OF THE PROBLEM

This section is based on the notation used in (Brenner et al., 2007), briefly repeated here to keep the paper self-contained. Two scenes (point clouds) S_1 and S_2 are given, each consisting of a set of points in 3D space. Any two corresponding points $\mathbf{x}_1, \mathbf{x}_2 \in \mathbf{R}^3$ with $\mathbf{x}_1 \in S_1, \mathbf{x}_2 \in S_2$, are related by an Euclidean (rigid) transformation

$$\mathbf{x}_1 = \mathbf{R}\mathbf{x}_2 + \mathbf{t}, \quad (1)$$

where \mathbf{R} is a 3×3 rotation matrix, and $\mathbf{t} \in \mathbf{R}^3$ is the translation vector. Usually, due to errors, the transformed point of \mathbf{x}_2 , denoted as \mathbf{x}'_2 (i.e., $\mathbf{x}'_2 = \mathbf{R}\mathbf{x}_2 + \mathbf{t}$), and its counterpart \mathbf{x}_1 from S_1 , do not exactly coincide. Then, the transformation parameters for \mathbf{R} and \mathbf{t} can e.g. be found by (least-squares) minimization of $\sum \|\mathbf{x}_1 - \mathbf{x}'_2\|^2$. Given three or more point correspondences, closed form solutions exist to compute \mathbf{R} and \mathbf{t} (Sansò, 1973; Horn, 1987).

If no previous information is available, point correspondences cannot be established easily, since single points do not carry enough information. One way to solve this problem is to define descriptors (Johnson and Hebert, 1999). In contrast, we use a feature based approach which relies on planar patches. We assume the patches are given by their plane equations

$$\langle \mathbf{n}_i, \mathbf{x} \rangle - d_i = 0 \quad (2)$$

$$\langle \mathbf{m}_i, \mathbf{x} \rangle - e_i = 0 \quad (3)$$

$$\langle \mathbf{p}_i, \mathbf{x} \rangle - f_i = 0 \quad (4)$$

where \mathbf{n}_i , \mathbf{m}_i , \mathbf{p}_i are normal vectors of unit length, d_i , e_i , f_i are the plane distances from the origin, and for each of the equations, $i = 1$ (plane in scene S_1) and $i = 2$ (plane in scene S_2) form a pair.

Three such plane pairs suffice to determine all six degrees of freedom of \mathbf{R} and \mathbf{t} in two steps. First, \mathbf{R} can be found in closed-form by eigenvector analysis (actually part of the solutions in (Sansò, 1973; Horn, 1987)). Then, assume that scene S_2 has already been rotated, so that only the translation component \mathbf{t} in Eq. 1 has to be determined. From Eq. 2,

$$\langle \mathbf{n}_1, \mathbf{x} \rangle - d_1 = 0$$

$$\langle \mathbf{n}'_2, \mathbf{x} - \mathbf{t} \rangle - d_2 = 0.$$

Since \mathbf{n}'_2 is already rotated, $\mathbf{n}_1 = \mathbf{n}'_2 = \mathbf{n}$, and \mathbf{x} can be eliminated to obtain $\langle \mathbf{n}, \mathbf{t} \rangle = d_1 - d_2$. Doing the same for Eqs. 3 and 4 and stacking the equations yields

$$\begin{bmatrix} \mathbf{n}^T \\ \mathbf{m}^T \\ \mathbf{p}^T \end{bmatrix} \mathbf{t} = \begin{bmatrix} d_1 - d_2 \\ e_1 - e_2 \\ f_1 - f_2 \end{bmatrix} \quad (5)$$

from which \mathbf{t} can be determined.

Note that the determination of the full transformation is done in two steps, first the rotation, then the translation. While at least three plane pairs are required to obtain the translation, only two plane pairs are sufficient to determine the rotation. This will be exploited below to reduce search space. In fact, a plane normal vector (of unit length) has two degrees of freedom, so that two plane pairs fix four degrees of freedom, one more than what is required to determine \mathbf{R} . As a result, given two corresponding normal vector pairs \mathbf{n}_1 , \mathbf{m}_1 from S_1 and \mathbf{n}_2 , \mathbf{m}_2 from S_2 , due to measurement errors, the angle $\angle(\mathbf{n}_1, \mathbf{m}_1)$ and $\angle(\mathbf{n}_2, \mathbf{m}_2)$ are usually slightly different. Then, one can choose to determine \mathbf{R} such that either \mathbf{n}_1 and \mathbf{n}_2 or \mathbf{m}_1 and \mathbf{m}_2 align perfectly. Using the eigenvector solution mentioned above, a preferable rotation \mathbf{R} is found, which distributes the angle error equally to both corresponding vectors.

Noting that the determination of the rotation is a time-critical operation, the following alternative can be used, which achieves the same result without the need for an eigenvector analysis (based on (Horn, 1987)). Using \mathbf{n}_1 and \mathbf{m}_1 , a Cartesian coordinate frame $\{\mathbf{u}_1, \mathbf{v}_1, \mathbf{w}_1\}$ is constructed by

$$\tilde{\mathbf{u}}_1 = \mathbf{n}_1 + \mathbf{m}_1, \quad \mathbf{u}_1 = \tilde{\mathbf{u}}_1 / \|\tilde{\mathbf{u}}_1\| \quad (6)$$

$$\tilde{\mathbf{v}}_1 = \mathbf{m}_1 - \langle \mathbf{m}_1, \mathbf{u}_1 \rangle \mathbf{u}_1, \quad \mathbf{v}_1 = \tilde{\mathbf{v}}_1 / \|\tilde{\mathbf{v}}_1\| \quad (7)$$

$$\mathbf{w}_1 = \mathbf{u}_1 \times \mathbf{v}_1,$$

where Eq. 7 uses standard Gram-Schmidt orthonormalization. Due to Eqs. 6 and 7, \mathbf{u}_1 and \mathbf{v}_1 span the same plane as \mathbf{n}_1 and \mathbf{m}_1 . Then, $\mathbf{M}_1 = [\mathbf{u}_1 \mathbf{v}_1 \mathbf{w}_1]$, writing \mathbf{u}_1 , \mathbf{v}_1 , \mathbf{w}_1 as column vectors, is an orthogonal matrix by construction. Doing the same for \mathbf{M}_2 , one can see that

$$\mathbf{R} = \mathbf{M}_1 \mathbf{M}_2^T \quad (8)$$

is orthogonal and in fact is the desired rotation matrix (since $\mathbf{M}_2^T \mathbf{n}_2$ gives the components of \mathbf{n}_2 along the axes $\{\mathbf{u}_2, \mathbf{v}_2, \mathbf{w}_2\}$ and \mathbf{M}_1 maps this back to the first coordinate frame). Adding \mathbf{n}_1 and \mathbf{m}_1 in Eq. 6 ensures that the angle error is equally distributed to both corresponding vectors.

3 FUNDAMENTAL PROBLEMS AND APPROACH OF THIS PAPER

The foremost problem of coarse registration is the combinatorial complexity. If p plane patches are extracted in S_1 and S_2 independently and then all possible transformations are evaluated based on plane triples ($k = 3$), as described above, there are

$$\binom{p}{3} \cdot \binom{p}{3} \cdot 3!/2 \quad (9)$$

possible combinations. The first two terms are due to picking three planes (the triple) out of p , while the last factor reflects the possible permutations when assigning the triple from S_1 to S_2 , reduced by a factor of two, since only triples of the same chirality need to be considered (i.e., a right-handed normal vector triple from S_1 can only match a triple in S_2 which is also right-handed). For $p = 50$ planes, which we use regularly, this yields 1.15 billion possible combinations which need to be tested.

Noting the positive effect of chirality in Eq. 9 (reduction by a factor of two), one may wonder if picking more planes may have a positive effect. If $k = 4$ planes are picked, the chirality can be computed for any sub-combination of 3 planes picked out of those four. That is, for $k = 4$ planes, four 'chirality numbers' ± 1 are obtained. Any pick of $k = 4$ planes in S_1 is thus one case in the set $\{(+1, +1, +1, +1), (+1, +1, +1, -1), \dots, (-1, -1, -1, -1)\}$ (all of which may occur). Instead of all $4! = 24$ permutations of a plane quadruple picked from S_2 , only those with the same four chirality numbers need to be considered. Depending on the actual sign combination, either 3 (8 cases), 4 (6 cases) or 12 (2 cases) permutations need to be considered, which yields an expectation of 1.5 cases on average (which is also obtained from $6!/2^4$). Thus, comparing the cases $k = 3$ and $k = 4$, one sees that $k = 4$ has an advantage only if the number of planes is relatively small ($p < 9$), in which case the computational cost is anyhow so low that one would not consider using the more complex approach. In summary, increasing k does not reduce the number of cases (for practical p), even if chirality is considered.

The second important problem is the rating of a solution. Ideally, a score function would be desirable which attains its maximum when the correct solution is found. If exhaustive search would be possible, the best solution would then be obtained by simply picking the transformation with the highest score. A candidate for this score function is the overlap of S_1 with the transformed S_2 , for example based on counting the points in S_1 with close neighbors in S_2 . While this works well when the scene contents of S_1 and S_2 are similar (e.g., scan positions are close together), it usually fails when they are very different (e.g., scan positions

far apart, occlusions, tilted scan). In the latter case, the score of the true transformation is low, and it may well be that a larger score can be achieved by using a wrong transformation.

Using additional criteria (such as point normals) to make the score function more selective is possible, however comes at an additional computational cost. While it is practicable to compute the score for hundreds of cases, it is usually not feasible to do so for 1.15 billion cases. Thus, the main idea is to build up a hierarchy of tests which cuts down search space and has the property that (i) the most inexpensive tests are applied first, (ii) the more expensive tests are only applied after a large number of false solutions has been ruled out already, and (iii) the tests, though simple, do not erroneously rule out the correct solution.

The goal of this paper is not to elaborate on the score function, but on this test hierarchy. Thus, we do not show that our algorithm finds *and indicates* the correct transformation (which requires a search *and* a score function which has a maximum at the correct transformation). Instead, we show that we are able to reduce the set of solution candidates substantially, while still retaining the correct solution in this set.

4 THE TEST DATA SET AND INITIAL PROCESSING

We selected an area called ‘Holzmarkt’ in the historic district of Hannover, Germany, for the evaluation of our algorithms. Twenty scans were acquired, of which 12 were taken (approximately) upright, another 8 with a tilted scan head. Throughout the text, the scan positions and datasets are denoted by ‘SP01’, ‘SP02’, etc. for the upright and ‘SP03a’, ‘SP05a’, etc. for the tilted scans. Fig. 1 shows all 12 scan locations in a cadastral map. The scan positions were chosen systematically along a trajectory with a spacing of approximately 5 meters. All scans were acquired using a Riegl LMS-Z360I scanner, which has a single shot measurement accuracy of 12 mm, field of view of $360^\circ \times 90^\circ$ and a range of about 200 m. Reference orientations for the scans were obtained by placing artificial targets in the scene, which were manually identified in the scans. The procedure yields errors in the range of a few millimeters, thus the reference is considered to be sufficiently accurate for our tests on coarse registration. We used the reference orientations to compute an approximate value for the overlap of scan pairs, ranging from 83.1% for scan pair SP01-02 down to 2.3% for SP01-12a, see (Brenner et al., 2007).

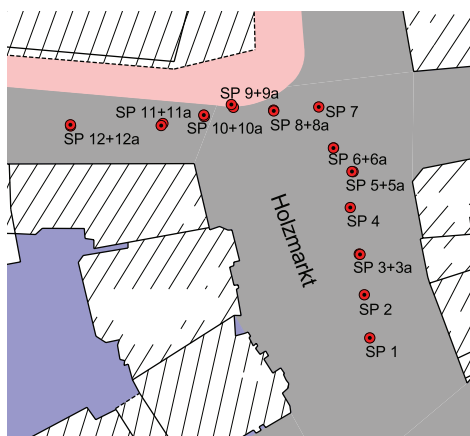


Figure 1: Placement of scan positions along a trajectory, shown in a cadastral map. Tilted scans are marked with an ‘a’ suffix.

For the extraction of planar patches, we used standard region growing, working on the regular raster of scan points. Region growing iterates the two steps of seed region selection and region

expansion. Seed regions are prioritized according to their local planarity, which is computed using the residuals of a local best-fit plane. Once a seed region is selected, scan points along the region border are added if they lie in the plane (within a threshold of 6 cm), and the plane equation is updated. Fig. 2 shows an example segmentation.

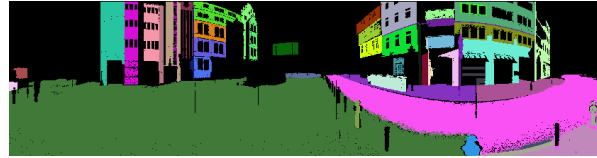


Figure 2: Planar segmentation of SP01, using random colors for the segments.

5 DETERMINATION OF THE ROTATION COMPONENT

5.1 The triple product and pairwise enclosed angles

For our test scene, we exhaustively computed all 1.15 billion plane triple combinations and the resulting transformations (this took several hours on a standard PC for each scan pair). Transformations were considered to be correct if the deviation from the reference is less than 5° in rotation and 1 m in translation. From table 1, one can see that at most, 0.212‰ of the triple combinations lead to a correct transformation, and this number even decreases rapidly with increasing distance between the scan standpoints.

	Triple assignments leading to correct transformation		Triples with compatible angles	Triples with compatible angles leading to correct transformation	
	#	‰		#	#
SP 01-02	244635	0.212	1022507	42945	42.00
SP 01-03	208970	0.181	1020667	38947	38.16
SP 01-03a	153111	0.133	684729	20283	29.62
SP 01-04	147045	0.128	1091474	19043	17.45
SP 01-05	55116	0.048	698353	9681	13.86
SP 01-05a	41353	0.036	557906	4955	8.88
SP 01-06	48721	0.042	949832	8361	8.80
SP 01-06a	47843	0.042	1041477	8562	8.22
SP 01-07	14776	0.013	880668	3034	3.45
SP 01-08	15576	0.014	791156	2609	3.30
SP 01-08a	11372	0.010	840829	1048	1.25
SP 01-09	6306	0.005	605209	1125	1.86
SP 01-09a	11545	0.010	513071	778	1.52
SP 01-10	13372	0.012	754447	1357	1.80
SP 01-10a	4584	0.004	438870	596	1.36
SP 01-11	4232	0.004	758084	593	0.78
SP 01-11a	11160	0.010	653320	1572	2.41
SP 01-12	0	0.000	552271	0	0.00
SP 01-12a	0	0.000	402779	0	0.00

Table 1: Triple assignments leading to the correct transformation, angle compatible triple assignments, and angle compatible triple assignments leading to the correct transformation (for all scan pairs).

In order to raise this percentage, we used in (Brenner et al., 2007) the triple product to only consider plane triples above a threshold. A large triple product is desirable, since it leads to a good matrix condition number on the left hand side of Eq. 5. However, it is also problematic, since the appropriate value depends on the scene contents. If the scene does not contain planes leading to triple products above the threshold, no candidates are found. In this case, the threshold has to be lowered, which however quickly increases the number of false combinations as well.

In order to form a more selective and scene independent criterion, we investigated the use of the three angles enclosed by the three normal vectors instead of their triple product. To evaluate how accurate the angles between any two pairs of plane normal vectors

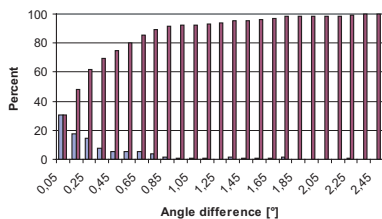


Figure 3: Histogram and cumulated histogram of the angle differences of manually selected plane pairs.

are, we manually identified a small set of corresponding planes between scans. For any possible plane pair in one scan S_1 , we computed the angle between the plane normal vectors. Knowing the corresponding vectors in S_2 , we computed the enclosed angle as well and derived the difference. In total, 328 pairs were considered. From Fig. 3, one can see that for more than 90% of the normal vector pairs from S_1 , the corresponding pairs in S_2 form the same angle within a 1° tolerance. This leads to the conclusion that tight bounds can be imposed on the angles when searching for corresponding plane triples. Table 1 shows that out of the 1.15 billion triple combinations, only between 400,000 and 1 million compatible combinations remain. The rate of triple combinations which lead to correct transformations is as high as 42%. Thus, for SP01-02, by using angle constraints, we can reduce the amount of search required by a factor of $42\%/0.212\% \approx 200$. This is also the average factor over all scans.

5.2 Searching for the correct orientation

As noted in section 2, the rotation is fully determined by two normal vector pairs, using Eq. 8. Thus, only p over 2 pairs need to be picked, and (c.f. Eq. 9 for $k = 2$) a total of $p^2(p-1)^2/2$ plane pair combinations exist. For $p = 50$, this yields 1,225 pairs in each scan, and 3 million combinations. If only vector pairs including the same angle (tolerance 1°) are regarded, this reduces to 140,000 compatible combinations, or 4.8%, on average. From table 2 one can see that the number of compatible normal vector pairs is relatively stable. However, if the rotation matrix is computed for each of the compatible combinations and compared to the (known) reference orientation (allowing a 2° tolerance), one can see that the number of those pairs leading to a correct orientation decreases with increasing scan numbers, from 8,034 (5.5%) down to almost zero. Thus, even scans far apart yield a large number of compatible normal vector pairs, but the percentage leading to the correct transformation decreases. Note that there is no need to test the 3 million cases by exhaustive enumeration. Instead, all 1,225 angles between pairs in S_2 can be sorted into angle bins (we used 1° bins for this purpose). Then, for each plane combination in S_1 , the subset of candidates in S_2 can be retrieved quickly.

In the next step, the goal is to pick a correct orientation from the approximately 140,000 candidates – or more precisely, to rank the candidates in such a way that the correct solution is among the first few proposals. Since the percentage of correct solutions can be around only 1% (for the cases we wish to be able to succeed), random picking would imply that we can expect only one correct solution among (the first) 100 picks.

In order to improve this rate, we computed the rotation matrix for all compatible combinations. Note that using Eq. 8, this does not require matrix inversion or eigenvalue analysis, so it is computationally inexpensive, even for 140,000 candidates. For each candidate rotation matrix, we recovered the three rotation angles ω , ϕ , κ . Fig. 4 shows a plot of all rotation candidates, in (ω, ϕ, κ)

Pair	Compatible	%	Correct	%
SP01-02	145202	4.84	8034	5.53
SP01-03	147944	4.93	7497	5.07
SP01-03a	115260	3.84	5566	4.83
SP01-04	164200	5.47	5852	3.56
SP01-05	145098	4.83	3496	2.41
SP01-05a	121400	4.04	2885	2.38
SP01-06	166238	5.54	4218	2.54
SP01-06a	165922	5.53	4414	2.66
SP01-07	173934	5.80	2513	1.44
SP01-08	167550	5.58	2639	1.58
SP01-08a	168050	5.60	2728	1.62
SP01-09	141868	4.73	1651	1.16
SP01-09a	140498	4.68	926	0.66
SP01-10	157464	5.25	2115	1.34
SP01-10a	113540	3.78	1007	0.89
SP01-11	138768	4.62	929	0.67
SP01-11a	147310	4.91	1642	1.11
SP01-12	105978	3.53	2	0.00
SP01-12a	94758	3.16	148	0.16

Table 2: Angle compatible normal vector pairs, percentage relative to total number of combinations (3 million), number of correct rotations computed from the pairs, and percentage relative to the compatible cases.

space, for the scan pair SP01-02. For the figure, the rotations were normalized using the known reference orientation, so that the correct rotation is at $(\omega, \phi, \kappa) = (0, 0, 0)$. At this point (center in Fig. 4), one can see a dense point cloud (according to table 2, 5.53% of the points should be located there). In order to test this, we sorted all candidate rotations (ω, ϕ, κ) into bins (using a bin size of 2°). After this, the bins are extracted highest count first. Similar (ω, ϕ, κ) values are merged during this step if they differ in all angles by less than 2° (this operation is similar to histogram smoothing considering neighboring cells).

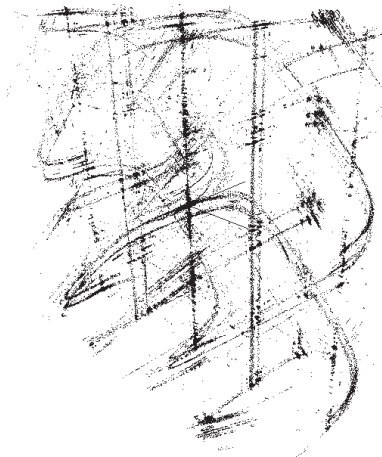


Figure 4: Plot of all rotation candidates for the scan pair SP01-02, in (ω, ϕ, κ) space. Each orientation is represented by a point. The correct orientation is at the center of the figure, where the ω and ϕ axes can be seen. The κ axis points upward.

As a result of this procedure, we obtain a list of orientations, sorted in descending order of bin hits. Fig. 5 shows the number of hits for the 20 bins with highest count, for the scan pair SP01-02 and SP01-09a. In the case SP01-02, the first bin (8,034 hits) has a much higher count as the second bin (1,752 hits). In fact, the first bin represents the correct orientation and the bin count is equal to the value in table 2. This situation is not always as clear. For example, in the case SP01-09a, the counts are generally lower and there is no clear peak at the first bin. In this case, the correct orientation corresponds to the 8th largest bin.

To give a better overview, Fig. 6 shows a plot of the 20 bins with

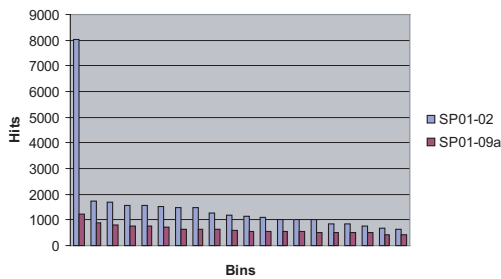


Figure 5: Histogram of the first 20 (orientation) bins with largest bin count for the scan pairs SP01-02 and SP01-09a.

highest count, for all scan combinations. As can be seen, for low scan numbers, there is a clear peak at bin 1, which is also the reference orientation. For SP01-04 and up, the peak gets wider, but still the correct orientation is at the first bin. The first exception to this is SP01-07 (which has 51% overlap), where the correct transformation is in the second bin (count 2,332). Closer examination reveals that the first bin (similar count of 2,362) represents a turn by $\kappa=180^\circ$ around the up- (Z-) axis with respect to the reference orientation. SP01-09a (29% overlap) is the first case where the correct orientation is not among the first two bins. SP01-11 is still worse, but note this pair has only 9.9% overlap. SP01-11a has 12.2% overlap and the correct solution is in bin 1. For SP01-12 and SP01-12a, the reference orientation was not part of the first 100 bins, however their overlap is only 4% and 2%, respectively.

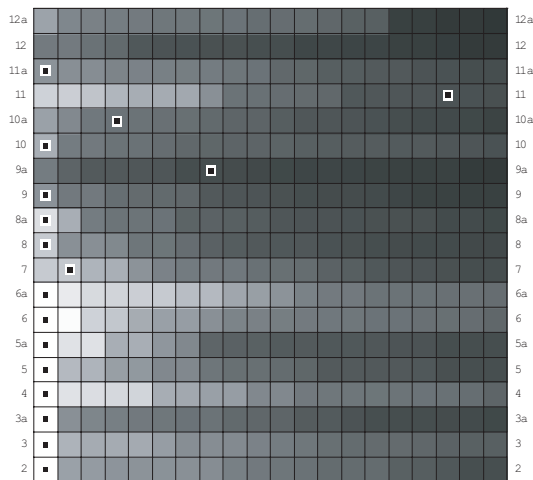


Figure 6: Bins with highest count for all scan combinations. White corresponds to a count of 3,000 or more, black is 0. The small rectangles indicate the bin which corresponds to the reference rotation. For example, the lowest line represents the first 20 bins for scan pair SP01-02 and is the equivalent of Figure 5. It has a clear peak (white) at the first (leftmost) bin, which also represents the true rotation (small rectangle).

6 DETERMINATION OF THE TRANSLATION COMPONENT

The translation is determined according to Eq. 5, using three plane pairs. Note that it is not necessary to actually rotate S_2 , because Eq. 5 requires only d_2 , e_2 , f_2 from S_2 , the plane distances from the origin, which are not affected by rotation. Also, instead of picking all triple pairs, one can work on the rotation

candidates one after the other, so that not only the rotation matrix is known, but also a set of combinations of two plane pairs which led to this rotation (i.e., a quadruple of plane indexes). For example, for SP01-02, the first rotation considered corresponds to a bin with 8,034 hits, meaning that 8,034 cases of assigned plane pairs are known already. This compares favorably to the 140,000 compatible (and the 3 million total) pairs.

Both pairs, of S_1 and of S_2 , need to be extended by a third plane, picked from the remaining $p - 2$ planes. For example, for the mentioned case, this would mean on the order of $8,034 \cdot 48 \cdot 48 = 18,510,336$ possible picks. However, when imposing angle constraints (of 1°) for the angles between the already picked pair and the newly picked plane, and considering chirality, a much smaller number remains. In the example, only 188,732 picks are left.

However, we chose a conceptually simpler approach. Instead of picking a third plane, we simply pick pairs of quadruples from the bin. Thus, for each pick, we have 4 plane pairs, and solve Eq. 5 for the translation in a least squares manner. Fig. 7 shows the translations corresponding to 100,000 of such picks, where each translation vector is represented by a point in 3D space. The correct translation vector is at the center of the figure, where several 'linear structures' intersect. There are many candidates along the Z axis, indicating a correct lateral position, but a varying height. Perpendicular to this, there are several linear structures which we believe are due to the arrangement of the facades in the 'Holzmarkt' scene: if one moves the point cloud SP02 further apart from SP01, the distance between the right and left building facades increases and there are two choices for the translation, either matching the 'right' or the 'left' facades.

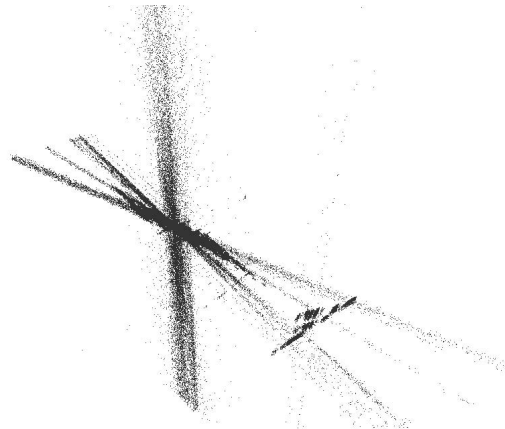


Figure 7: Plot of all translation candidates for the first orientation bin of the scan pair SP01-02. Z axis points upward.

Picking two quadruples from the bin yields $8,034 \cdot 8,033/2$ possible picks for the example bin (way too many). Instead, we apply the RANSAC principle at this point (Fischler and Bolles, 1981). We only pick a subset of m pairs of quadruples. For each pick, we compute the translation and then count the number of planes in S_1 for which a matching plane in S_2 exists. Planes were considered to match if their normal vectors agree within 1° and their distance from the origin agrees within 1 m. Note this comparison is computationally inexpensive, since it uses only the plane parameters, rather than original scan points.

To derive the necessary number of picks m , we picked 10,000 quadruple pairs and determined the percentage of picks which lead to the correct translation (within 1 m along each axis). We found that for close scan positions, such as SP01-02, this is around 20%, decreasing with increasing scan position distance, for a minimum of 3% (not considering SP01-12 and SP01-12a). Following Fischler and Bolles (1981), if we want to ensure

SP01-	02	03	03a	04	05	05a	06	06a	07	08	08a	09	09a	10	10a	11	11a	12	12a
Run 1	1	1	1	1	1	2	3	2	2	15	23	11	5	12	33	14	12	-	-
Run 2	1	1	1	1	1	2	6	5	12	4	20	53	6	35	15	13	12	-	-
Run 3	1	1	1	2	1	2	2	5	12	7	28	13	5	27	13	21	11	-	-

Table 3: Ranking of correct transformations. The value ‘1’ in row ‘Run 1’ and column ‘02’ means that for the scan pair SP01-02, and the first run, the first transformation returned by the algorithm also was the correct one.

with probability z to find at least one correct solution among m picks, where the probability to draw a correct solution is b , then $m = \log(1 - z) / \log(1 - b)$. For $z = 99\%$, $b = 3\%$, it follows that $m \approx 150$ picks are required.

The number of corresponding plane pairs is also used to rank the entire transformation (rotation and translation). Table 3 shows the results obtained for three separate runs of the algorithm. The rankings indicate at which position in the result list the algorithm returned a correct transformation (defined by as most 2° off in rotation and 1 m off in translation, for each axis). As one can see, for most of the close scan pairs, the algorithm returned the correct solution in the first place or within the first few ranks. For all runs except SP01-12 and SP01-12a, the solution was ranked among the first 53. For SP01-12 (overlap 3.6%) and SP01-12a (overlap 2.3%), we obtained no solution. However, for those cases, we were even unable to manually select suitable plane pairs.

7 CONCLUSIONS AND OUTLOOK

In this paper, we addressed the problem of finding good initial values for the relative orientation of two laser scans when no previous information is available. Our method is based on the automatic extraction and assignment of planar patches. For a set of terrestrial laser scans, with 50 extracted planar patches per scan, we showed that there is a large number of 1.15 billion possible assignments, however only 0.2% or less (one in 5000) of them lead to a correct transformation. Thus, it was our goal to devise an efficient method which cuts down search space and produces a ranked list of possible transformations, where the correct transformation is among the top entries. The general idea behind this is to build a hierarchy of tests, where the most elaborate test (the score function) needs only to be performed for very few cases.

We showed that the relative angles between patch normal vectors are a good (and scene independent) criterion to eliminate false assignments. For the determination of the rotation matrix, we started from the assignment of two patch pairs. Using a clustering of orientations by way of bins, we obtained a ranking, where the correct solution is at the top for the majority of scan pairs and ranked among the first 18 in all cases. As for the translation, we used a RANSAC based approach, where the sampling consists of picking two patch pairs, and the consensus set is the total number of compatible patch pairs. Overall, we obtained an efficient algorithm which computes a ranked list of transformation candidates, where the correct transformation is at rank one for scans with a high overlap, and ranked among the first 53 for all scan pairs with an overlap larger than 3.6%. We conclude that the number of candidates for which a more elaborate score function needs to be evaluated is on the order of 100, which is, compared to a total of 1.15 billion possible cases, a massive reduction by a factor of 10^7 .

In the future, we plan to test the algorithm on other scenes as well, and to work on an efficient yet selective score function.

ACKNOWLEDGEMENTS

This work has been supported by the VolkswagenStiftung, Germany.

References

- Besl, P. J. and McKay, N. D., 1992. A method for registration of 3-D shapes. *IEEE Transactions on Pattern Analysis and Machine Intelligence* 14(2), pp. 239–256.
- Brenner, C., Dold, C. and Ripperda, N., 2007. Coarse Orientation of Terrestrial Laser Scans. *ISPRS Journal of Photogrammetry and Remote Sensing* (in press, doi:10.1016/j.isprsjprs.2007.05.002).
- Chen, Y. and Medioni, G., 1991. Object modeling by registration of multiple range images. In: *International Conference on Robotics and Automation*, pp. 2724–2729.
- Faugeras, O. D. and Hebert, M., 1986. The representation, recognition, and locating of 3-D objects. *International Journal of Robotics Research* 5(3), pp. 27–52.
- Fischler, M. A. and Bolles, R. C., 1981. Random sample consensus: a paradigm for model fitting with applications to image analysis and automated cartography. *Comm. ACM* 24(6), pp. 381–395.
- Greenspan, M. and Godin, G., 2001. A nearest neighbor method for efficient ICP. In: *Proceedings of the Third International Conference on 3D Digital Imaging and Modeling*, Quebec City, Canada, pp. 161–168.
- Gruen, A. and Akca, D., 2005. Least squares 3D surface and curve matching. *ISPRS Journal of Photogrammetry and Remote Sensing* 59(3), pp. 151–174.
- Horn, B. K. P., 1987. Closed-form solution of absolute orientation using unit quaternions. *Optical Society of America* 4(4), pp. 629–642.
- Johnson, A. E. and Hebert, M., 1999. Using spin images for efficient object recognition in cluttered 3D scenes. *IEEE Transactions on Pattern Analysis and Machine Intelligence* 21(5), pp. 433–449.
- Jost, T. and Hügli, H., 2002. A multi-resolution scheme ICP algorithm for fast shape representation. In: *Proceedings of 1st International Symposium on 3D Data Processing, Visualization and Transmission*, pp. 540–543.
- Kapoutsis, C., Vavoulidis, C. and Pitas, I., 1999. Morphological iterative closest point algorithm. *IEEE Transactions on Image Processing* 8(11), pp. 1644–1646.
- Rusinkiewicz, S. and Levoy, M., 2001. Efficient variants of the ICP algorithm. In: *Proceedings of the Third Intl. Conf. on 3D Digital Imaging and Modeling*, pp. 142–152.
- Sansò, F., 1973. An exact solution of the roto-translation problem. *Photogrammetria* 29(6), pp. 203–216.
- Sharp, G., Lee, S. and Wehe, D., 2002. ICP registration using invariant features. In: *IEEE Transactions on Pattern Analysis and Machine Intelligence*, Vol. 24number 1, pp. 90–102.
- Zhang, Z., 1994. Iterative point matching for registration of free-form curves and surfaces. *International Journal of Computer Vision* 13(2), pp. 119–152.

Supervised classification of water regions from lidar data in the Wadden Sea using a fuzzy logic concept

A. Brzank, C. Heipke

Institute of Photogrammetry and GeoInformation
University of Hanover
(brzank, heipke)@ipi.uni-hannover.de

KEY WORDS: lidar, laser scanning, classification, fuzzy logic, water

ABSTRACT:

The Wadden Sea is an almost untouched area with a size of about 7300 km² along the German, Dutch and Danish coast. Because of tide the area is flooded two times a day, creating a very special and sensitive ecosystem. In order to protect the Wadden Sea up-to-date Digital Terrain Models (DTM) of high accuracy are needed to detect morphological changes. Lidar is an adequate method to obtain an accurate DTM. However Lidar is not able to penetrate water regions. Thus, raw Lidar data contain several water points, which do not belong to the terrain surface, leading to a wrong DTM.

In this paper we present a supervised classification method to detect water regions from Lidar data using a fuzzy logic concept. Starting with raw data points of one strip, the points are grouped into scan lines. Based on training areas for the classes *water* and *mudflat* the features height, intensity and 2D point density are analysed. The significance level of the assumption that each feature differs for both classes is determined. Then, individual weights are derived from this significance level for every feature taking into account systematic feature changes depending on the angle of incidence of each laser pulse. A fuzzy logic classification is used to distinguish all points into *water* and *mudflat* points. Several additional steps are performed in order to refine and improve the classification result. Two meaningful examples are presented, which show the capability of this supervised fuzzy classification.

1. INTRODUCTION

The Wadden Sea is a very special and sensitive ecosystem. Two times a day the area is flooded and falls dry afterwards. The area reaches from Esbjerg, Denmark to Den Helder, Netherlands. Almost 60 % of the 7300 km² is situated in Germany. The Wadden Sea represents a unique and protectable wildlife habitat. Many plants and animals have developed in accordance to the tidal influence and their future depends on the existence of the Wadden Sea.

In order to monitor morphologic changes of the Wadden Sea, Digital Terrain Models of high accuracy are needed. Lidar proved to deliver high accurate spatial data of mudflats (e.g. Brzank et al., 2005). However, Lidar is not able to penetrate water. Due to the fact that water still remains in tidal trenches and depressions even during low tide, water points are parts of the captured Lidar data. In order to calculate a DTM, which describes the mudflat surface accurately, water points have to be detected and removed, and additional correct height data have to be introduced.

Depending on the available data sources different approaches are possible. Two general cases can be distinguished. In the first case simultaneous acquisition of Lidar and multispectral image data is assumed. In this case, the images can be used to classify water with standard classification methods. Lecki et al. (2005) pointed out that high-resolution multispectral imagery and appropriate automatic classification techniques offer a viable tool for stream mapping. Within their analysis, especially water was classified accurately. Mundt et al. (2006) demonstrated that the accuracy of classification significantly increases by combining images and height data.

Considering the rapid change of water-covered region caused by a fast changing water level, Lidar and multispectral data has to be captured simultaneously. Taking into account that the flight has to be performed during low tide and the weather conditions must be adequate for multispectral data capturing,

available time windows are rather rare and small. This leads to much higher costs forcing many customers to order only Lidar data. Thus, in the second case, only the Lidar data is assumed to be available. Typically, Lidar data providers deliver irregularly spaced 3D points and intensity values, which correspond to the strength of the backscattered beam echo. Up to now, only a few approaches using exclusively the intensity of Lidar data for classification were published. Katzenbeisser and Kurz (2004) emphasized the fact that classification methods used for remote sensing images need to be adapted to intensity data. They pointed out that the intensity has only a useful information value within open areas where only one echo was detected. Hence, other criteria have to be considered in order to filter water points from Lidar data.

In this paper, we extend the previous approach of Brzank and Heipke (2006). First, we summarize important physical characteristics of Lidar data and previous approaches, which were carried out to separate water and land points in Lidar data. Then, a new supervised method is presented for classification of Lidar data into water and land points.

First, the raw data points are grouped into scan lines. Based on training areas for the classes *water* and *mudflat* the significance of the difference of the features height, intensity and 2D point density is calculated. Then, individual weights are calculated using the significance level for these three features, which also take into account systematic changes of intensity and 2D point density depending on the angle of incidence. Afterwards, a fuzzy classification is performed. All required parameters are obtained from training areas. Finally, the classification result is revised and improved by applying several tests. To illustrate the capability of the algorithm, two examples with different characteristics regarding Lidar scanner system, point density, point distribution etc. are presented. Finally, this paper concludes with a summary and an outlook on further development issues.

2. STATE OF THE ART

2.1 Physical characteristics of Lidar data within coastal areas

In order to develop a suitable algorithm, which is capable to classify Lidar data (raw 3D Lidar points and their intensity values), the physical characteristics of common Lidar systems as well as the reflection of water and land areas have to be considered. Generally, Lidar systems operate in the near infrared range. Wolfe and Zisis (1989) describe the absorption of infrared radiation depending on the illuminated surface material and the wavelength. They point out that the absorption for water is significantly higher than the absorption for soil. This leads to the fact that the intensity of water points is normally lower than the intensity of land points.

Additionally, as a result of the Rayleigh Criteria, calm water surfaces behave like a mirror. Thus, specular reflection occurs. Often, a distance measurement can not be accomplished successfully because the received radiation energy is not distinguishable from background noise. Hence, the point density of Lidar data within water areas is normally significantly lower than within land areas.

2.2 Systematic changes of intensity and point density depending on the angle of incidence

As pointed out in the previous chapter, intensity and point density depend on the characteristics of the illuminated area. The reflectance of water is lower in case of near infrared light than the reflectance of mudflat. However, also mudflat has quite a smooth surface yielding in similar specular reflection behaviour of the laser beam. Thus, intensity and 2D point density are systematically influenced depending on the angle between the laser beam and the surface normal.

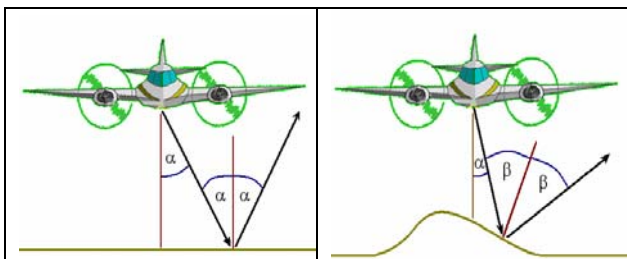


Figure 1. Specular reflection in case of (left) horizontal and (right) tilted area

Figure 1 illustrates how the laser beam is deflected depending on the angle of deflection (α) and the angle of incidence (β), if specular reflection occurs. Assuming that the area of interest is horizontal (which can be stated approximately for large parts of the Wadden Sea) α equals β . In case of tilted regions the surface orientation has to be taken into account in order to calculate β . Practically, the reflectance behaviour of the laser beam hitting water or mudflat is not exactly equal to specular reflection but similar. Hence, intensity values of points increase, if β decreases. Additionally, more points are measured correctly, if β decreases because the intensity is strong enough to trigger a correct measurement. In order to obtain accurate classification results using intensity and point density, the different reflectance properties of water and mudflat, but also the systematic changes depending on the angle of incidence, have to be taken into account.

2.3 Previous approaches to extract water areas from Lidar data

Brockmann and Mandlbürger (2001) developed a technique to extract the boundary between land and river water, and applied it to data from the German river “Oder”. Based on Lidar data, the planimetric location of the river centre line as well as bathymetric measurements of the riverbed, the boundary was obtained within a two-stage approach. First, the height level of the water area was derived by averaging the Lidar points in the vicinity of the river centre line. Afterwards, a DTM of all Lidar points (including also points of the water surface) was calculated. Then, the 0 m contour line of the difference model of the Lidar DTM and the water height level was derived. This contour line is called “preliminary borderline”. Within step two, the bathymetric points of the preliminary water area were combined with all Lidar points outside the preliminary water area. Then, a DTM representing the riverbeds instead of waterlevel was calculated. Afterwards, the final borderline was obtained by intersecting this DTM including the riverbeds and the height level of water area.

Mandlbürger (2006) proposed another method based on the same input data, which also detects the borderline of a river. First, the Lidar points are transformed into the river-axis system. Then, segments with a fixed length in flow direction are created. All points for each segment are used to create a profile across flow direction. After removing all outliers (vegetation and water points etc.), bank slopes of both sides are generated by an adjusted line. Then, one border point for each side is calculated by intersecting these lines with the prior known water height. Finally, all border points are transformed back into project coordinate system and linked.

Brzank and Lohmann (2004) (see also Brzank et al., 2005) developed another algorithm which separates water regions from non-water regions based on a DSM calculated from Lidar data. The main idea is to detect reliable water regions and expand those using height and intensity values. For that purpose, local height minima were extracted from the DSM, which represent potential seed zones of water areas. This step was followed by a region growing procedure using height and intensity data of the DSM grid points. In comparison to the previously mentioned algorithms, no additional information, such as water height or river axis is necessary. However, results were not satisfying, because systematic changes of intensity were not modelled.

2.4 Fuzzy classification concept

In order to classify water points from Lidar data in the Wadden Sea, the first two concepts described in section 2.3 are not sufficient. The algorithm of Brockmann and Mandlbürger (2001) as well as Mandlbürger (2006) require additional data, such as water height, approximate position of water and bathymetric data. However, these data are not available for the Wadden Sea. Moreover, the algorithms do not use further available information such as intensity and point distribution. The method of Brzank and Lohmann (2004) is also not sufficient, because systematic changes of intensity are not modelled. Furthermore, the method is not capable of dealing with different water heights within one water region. This remarkable effect occurs, because water height changes over time because of tide. Data of several flight strips are linked together in order to calculate a DSM. The time difference in capturing flight strips can lead to different height levels within one and the same water region.

Hence, Brzank and Heipke (2006) developed a new algorithm which focuses on classifying water points in Wadden Sea using only raw Lidar data. In contrast to previous approaches, classification is carried out for each flight strip separately in order to avoid different water heights within one region. The classification uses a fuzzy logic concept. A membership value for the class *water* $\mu_i(\underline{x})$ is calculated for every point based on its feature values and their weights. Six different features are used: height, intensity, slope, missed points, segment length and 1D point density. While height and intensity are measured directly for every point, all other features are defined based on points of the same scan line.

The classification is performed for each scan line using a hysteresis threshold method. After classification, several additional routines are performed in order to control and improve the classification result.

Brzank and Heipke (2006) proved that this method is capable to classify water regions. The algorithm has many advantages:

- All feature values can be obtained either directly from the measured point or in connection with other points of the same scan line.
- The classification is carried out for each scan line separately, making the classification very fast.
- The classification is done for every flight strip avoiding height changes due to time differences.
- The classification uses a certain weight for every feature taking into account the individual benefit of this feature for the classification.

However some facts are not taken into account:

- Systematic changes of intensity and point density across the flight direction are not be modelled.
- The needed classification parameters are not derived from data. The user has to set these values.
- The features missed points, segment length and 1D point density refer to one scan line, leading to a more noise depended classification result.
- The features missed points, segment length and 1D point density are correlated, which is not considered in the classification process.

3. CLASSIFICATION OF WATER POINTS WITH SUPERVISED FUZZY LOGIC CONCEPT

Based on the evaluation in chapter 2.4, fuzzy classification (Brzank and Heipke, 2006) was improved. First, the number of features was reduced to height, intensity and 2D point density. The features missed points, segment length and 1D point density were replaced by the new feature 2D point density. Thus, for every point the number of Lidar points inside a given polygon is determined. The centre of the polygon is given by the point of interest. Then, the number is divided by the size of the polygon. Furthermore, the feature slope was removed.

In order to tackle systematic changes of intensity and 2D point density their weights depend on the angle of deflection of the measured point. This leads to a new formula to calculate the entire membership value of class *water* (equation 1).

$$\mu(h, i, p, \alpha) = \frac{[\delta_H \mu_H(h) + \delta_I(\alpha) \mu_I(i, \alpha) + \delta_P(\alpha) \mu_P(p, \alpha)]}{[\delta_H + \delta_I(\alpha) + \delta_P(\alpha)]} \quad (1)$$

h, i, p, α	individual height, intensity, 2D point density and angle of deflection
$\delta_H, \delta_I(\alpha), \delta_P(\alpha)$	weight for features height, intensity, 2D point density
$\mu_H(h), \mu_I(i, \alpha), \mu_P(p, \alpha)$	membership value water of features height, intensity, 2D point density
$\mu(h, i, p, \alpha)$	entire membership of class water

3.1 Determination of classification parameters from training areas

In order to classify Lidar data into *water* and *mudflat* with the proposed fuzzy logic concept several classification parameters are needed. Table 1 shows these parameters and their function. As pointed out earlier, all parameter are to be derived automatically from training areas.

classification parameter	function
two thresholds to limit the application range of the membership function, (intensity and 2D point density)	transforms crisp height value into fuzzy membership value for height (intensity and 2D point density)
constant weight for height	describes how useful the feature height is evaluated for the selected data set
individual weight for intensity (2D point density)	describes how useful the feature intensity (2D point density) is evaluated for the selected point
water thresholds - low and high	classification of fuzzy membership value of every point into class <i>water</i> or <i>mudflat</i>

Table 1. Classification parameters and their function

First, training areas for the classes *water* and *mudflat* are determined. Typically, prior knowledge is used to define these areas. Then, all Lidar points inside these areas are extracted. Afterwards, the mean height and the corresponding standard deviation for all water and mudflat training areas are calculated. Due to a systematic dependency of intensity and 2D point density on their angle of incidence, the mean values and standard deviations are not significant. Hence, the mean intensity (2D point density respectively) must be referenced either with the angle of incidence β or the angle of deflection α . For reason of simplicity, we use in this paper only α . In order to calculate α , the flight trajectory must be available. Based on the actual position of the plane for each scan line α can be calculated for every point. If β should be used, the difference between the angle of deflection and the corresponding surface normal must be determined. For this purpose, the DTM is needed. Afterwards, the feature values of intensity and 2D point density of every point can be associated with the corresponding angle. These value pairs are used to fit a monotonically decreasing function for both classes. Generally, every function, which describes the systematic dependency correctly, can be used. We chose a function with 4 parameters (see equation 2), which was formerly used as weight function in linear prediction with robust filtering (Kraus and Pfeifer, 1998).

$$f(r) = \frac{c}{(1 + (ar)^b)} + d \quad (2)$$

Figure 2 shows a typical result of function fitting for intensity of both classes. It can be seen that intensity decreases, if the angle of deflection increases.

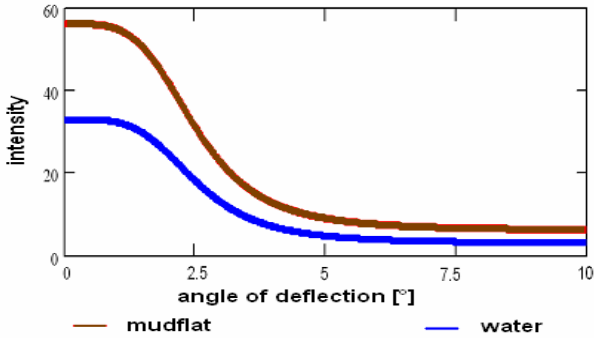


Figure 2. Intensity for both classes as a function of the angle of deflection α

3.1.1 Determination of membership function and their corresponding thresholds

In order to transform a crisp feature value into a fuzzy membership value, a membership function and two thresholds, which limit the application area of the membership function, are needed. We define a straight line as membership function. In case of the feature height the determined mean value of class *mudflat* is used as lower threshold with membership value 0, while the mean value of class *water* is used as upper threshold with membership value 1. In case of intensity and 2D point density, the adjusted functions are used. The individual threshold low (high) of every point equals the adjusted value of function *mudflat* (*water*) using the certain angle of the point of interest.

3.1.2 Determination of individual weights

In order to calculate the entire membership value of every point individual weights have to be determined. We define the weight to be in the range of 0 up to 1, where 0 means that the feature is not suited and 1 means that the feature is most useful for classification. For the feature height, only one constant weight is determined, because the height values do not depend on the angle of deflection. In case of intensity and 2D point density an individual weight depending on the angle at the point of interest is obtained. In order to calculate the constant weight of the feature height, all training areas for *water* are combined and the mean \bar{x} and standard deviation \bar{s} is computed. The training areas of *mudflat* are processed in the same way. Then, the values are used to create the Gaussian distribution of the probability density (Figure 3).

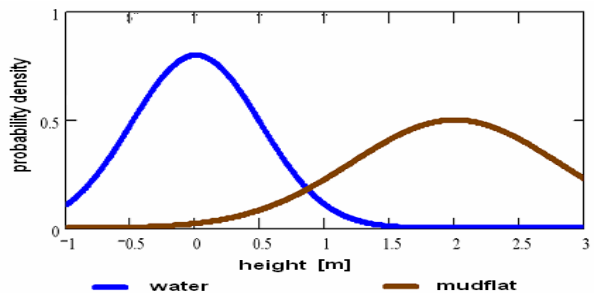


Figure 3. Probability density function of feature height for classes *water* and *mudflat*

It can be stated that the higher the overlapping rate of both distributions the less useful the feature height is to separate between *water* and *mudflat*. Based on this conclusion, the level of significance for the assumption that both distributions are different ($H_0: \bar{x}_{water} \neq \bar{x}_{mudflat}$) is calculated using a statistical test. Equation 3 displays the used test statistics t_f . Then, the corresponding weight is derived from the level of significance by linear interpolation. For that purpose, two constraints are set. If the level of significance is 50% the weight amounts to 0. In case of 100% the weight is 1.

$$t_f = \frac{\bar{x}_{mudflat} - \bar{x}_{water}}{\sqrt{s_{x_{mudflat}}^2 + s_{x_{water}}^2}} = \frac{d}{s_d} \quad (3)$$

For intensity and 2D point density the determination of the individual weight is very similar. The adjusted values for *mudflat* and *water* are calculated using the estimated features of equation 2. The residuals of all observations of one class are used to calculate the standard deviation. Again, both Gaussian distributions are derived and the level of significance is determined leading to the individual weight depending on the angle of deflection of the point of interest.

3.1.3 Determination of water thresholds

After determination of weights the entire membership value of every training point can be calculated using equation 1. Then, the mean of all entire membership values of class *water* and *mudflat* as well as the standard deviation are derived. Now, the two Gaussian distributions of the entire membership value are created. To find the low and high water thresholds the user defines two specific ratios (we normally use 1/10 and 10) of probability density *water* and probability density *mudflat*. The values that match these ratios are used as low and high thresholds.

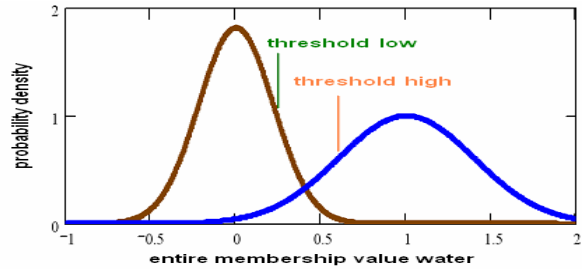


Figure 4. Determination of water threshold low and high

Remark: Generally, a membership value can only lie in the range of 0 to 1. For that reason (see chapter 3.1.1) two thresholds are used in order to limit the use of the membership function. In case of classification all points with feature value below threshold low get a membership value of 0, while all points with feature value above threshold high get a membership value of 1. However, in the analysis of training areas the use of the membership function is not limited leading to membership values below 0 and above 1. This is necessary in order to create normal distributions of the entire membership value *water* (see Figure 4).

4. EXAMPLES

In order to demonstrate the ability of the algorithm, two examples are presented in the section. The first example contains a part of a flight strip of the campaign “Friedrichskoog

2005”, which is situated at the coast of the North Sea next to the estuary of the river Elbe. The flight was carried out by the German company Toposys using their Lidar system Falcon II. The second example is a part of a flight strip of the campaign “Juist 2004”. The flight was carried out by German company Topscan using an ALTM2050 from Optech in order to capture Lidar data of the East Friesian island Juist and its surrounding.

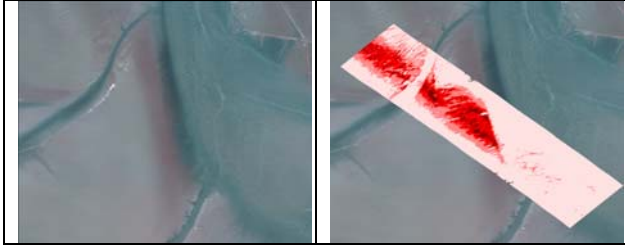


Figure 5. Orthoimage of Lidar campaign “Friedrichskoog 2005” (left) and Lidar points of a part of a flight strip – intensity coded (right)

Figure 5 (left) shows an orthoimage (size: 1.5km length, 1.3km width) of the campaign “Friedrichskoog”. In the image some tidal trenches filled with water as well as a huge water covered swale can be seen. Figure 5 (right) displays captured Lidar points of a part of a flight strip. The points are coded in relation to their intensity (low intensity – bright colour, high intensity – dark colour). It can be seen that the intensity values in the middle of the strip are significantly higher than at the border. Hence, a systematic dependency of the deflection angle exists.

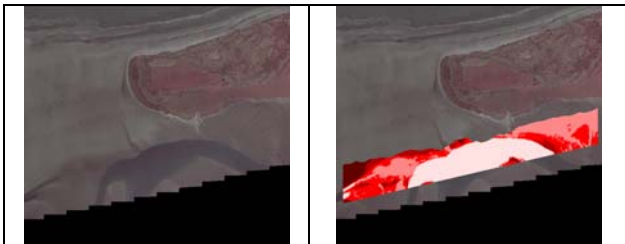


Figure 6. Orthoimage of Lidar campaign “Juist 2004” (left) and Lidar points of a part of a flight strip – intensity coded (right)

Figure 6 displays an orthoimage (size: 4km length, 2.6km width) of campaign “Juist”. There is a huge tidal trench situated south of the island. Again, intensity values are significantly smaller for water than for mudflat. However, a systematic dependency of intensity is not obvious.

Based on the orthoimage a training area for each class was manually selected. Afterwards, all classification parameter were derived from automatic analysis of the training areas. Figure 7 and 8 show the dependency of both classes from angle of deflection for features intensity and point density. The blue (pink) line marks the average feature value of class *water* (*mudflat*), while cyan (ochre) area indicates the single standard deviation of all residuals. As was already obvious from Figure 5, intensity of points from campaign “Friedrichskoog” is systematically influenced by the angle of deflection. Intensity of water and land differ strongly in case of a small angle of deflection. The more the angle increases, the more the intensities for both classes resemble each other. At the border of the flight strip the intensity of water and land do not differ significantly. Hence, the intensity weight within the classification has its maximum for $\alpha = 0$ and decreases, if α increases. At the border of the flight strip, intensity is not considered in the classification. In contrast to the intensity, the point density only differs marginally between classes *water* and

mudflat. The scan pattern has almost no holes for both training area. Hence, the individual weight of point density is always 0.

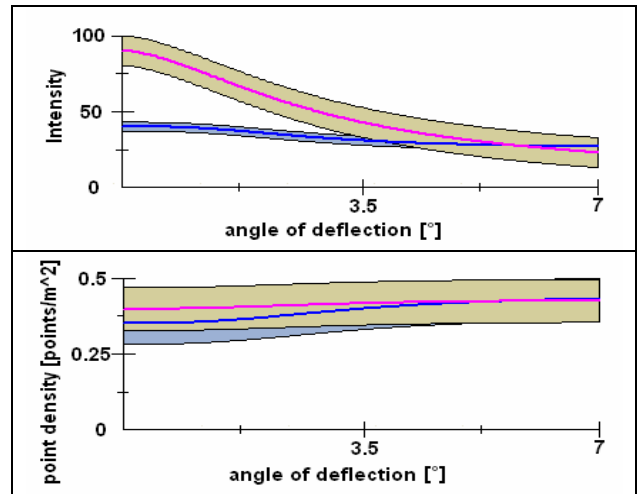


Figure 7. Determination of systematic changes of intensity (up) and point density (down) depending on the angle of deflection - Friedrichskoog

The intensity and point density of Lidar points from the campaign “Juist” only slightly depend on the individual angle of deflection. However, intensity and point density of both classes significantly differ from each other for all angle of deflection. Thus, both features are effective within classification.

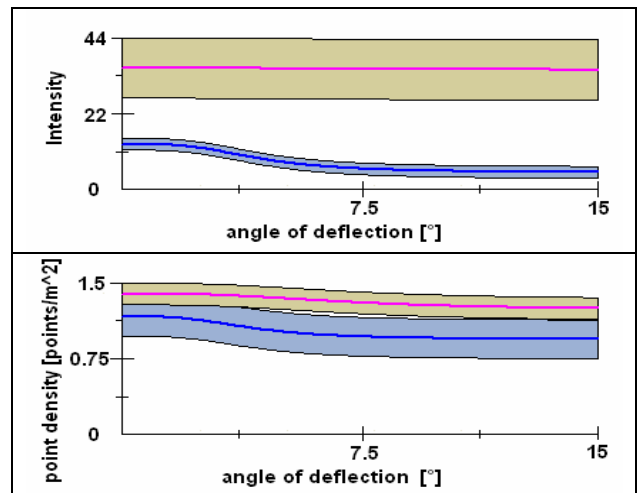


Figure 8. Determination of systematic changes of intensity (up) and point density (down) depending on the angle of deflection - Juist

Based on automatically determined classification parameters, the classification of both datasets was performed. Afterwards, classification discrepancies were detected and removed. Finally, every classification result was smoothed in order to suppress classification noise. Results are displayed in Figure 9 and 10. Figure 9 (left) shows the classification result of campaign “Friedrichskoog”. Based on a visual comparison of the classification result with the orthoimage it can be stated that the overall correctness is satisfying. However, some points within tidal trenches are misclassified due to waves and noisy intensity values. Most highly noisy misclassified points were suppressed by performing additional checks and smoothing leading to the result displayed in Figure 9 (right).

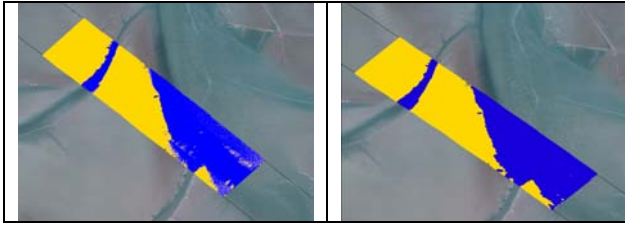


Figure 9. Water (blue) and mudflat (yellow) points after classification (left), additional checks and smoothing (right) - Friedrichskoog

The classification result of campaign “Juist” is visibly slightly better. There are only a few misclassified points due to waves and intensity noise.

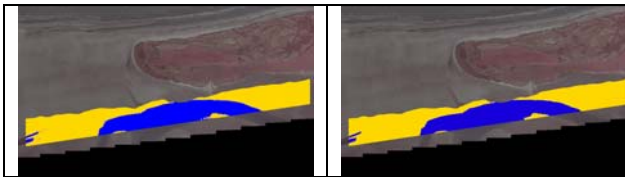


Figure 10. Water and mudflat points after classification (left), additional checks and smoothing (right) – Juist

In order to evaluate the overall correctness, *water* and *mudflat* areas were manually digitized from aerial images and the resulting areas were used as reference for the automatically derived classification. Table 2 lists the results. The correctness of campaign “Juist” is higher than for “Friedrichskoog”. Two reasons can be found. On one side, intensity does not differ significantly for all points while point density is not used for the classification “Friedrichskoog”. In case of “Juist”, all features differ significantly. Furthermore, height increases very slowly at the transition zone from *water* to *mudflat* in case of “Friedrichskoog” making it very difficult to derive correct results. For campaign “Juist” height changes are larger at the transition zone leading to a more accurate classification.

	Friedrichskoog 2005		Juist 2004	
Number of classified points	1.257.518		1.469.405	
Classified water points	592.577		517.858	
Classified land points	664.941		951.547	
	Water	Land	Water	Land
Classified water points	527.641	64.936	510.339	7.519
Classified land points	4.127	660.814	5.886	945.661
Correctness [%]	89.0	99.4	98.5	99.4

Table 2. Evaluated classification results

5. CONCLUSION AND OUTLOOK

A supervised fuzzy classification approach to separate Lidar points into the classes *water* and *mudflat* is introduced. The algorithm is based on the original Lidar data and classifies every flight strip. For the analysis the features height, intensity and 2D point density are used. The classification is based on the fuzzy logic concept. All necessary classification parameters are derived from training areas. Two different examples are presented to illustrate the capability of this algorithm. They demonstrate that the classification algorithm is able to deliver accurate results for different Lidar scanner types.

Future work will focus on the determination of highly precise DTMs for the whole investigated areas. For this purpose, bathymetric data has to be included in the calculation in order to fill areas, which are classified as water.

ACKNOWLEDGMENTS

This research has been financed by the Federal Ministry of Education and Research (BMBF) under project no. 03KIS050. We gratefully acknowledge the support of our project partners: Department of Rural Area Husum (ALR), Federal Waterways Directorate (WSD) and the Lower Saxony Water Management, Coastal Defence and Nature Conservation Agency Division Norden-Norderney (NLWKN).

REFERENCES

- Brockmann H., Mandlbürger G., 2001. Aufbau eines Digitalen Geländemodells vom Wasserlauf der Grenzoder. In *Publikationen der Deutschen Gesellschaft für Photogrammetrie, Fernerkundung und Geoinformationen*, Band 10, 2001, pp. 199 – 208.
- Brzank, A., Göpfert, J., Lohmann, P., 2005. Aspects of Lidar Processing in Coastal Areas. In *International Archives of Photogrammetry and Remote Sensing*, Hanover, Germany, Vol. XXXVI Part1/W3, CD , 6 p.
- Brzank, A., Lohmann, P., 2004. Steigerung der Genauigkeit von Digitalen Geländemodellen im Küstenbereich aus Laserscannermessungen. In: *Publikationen der Deutschen Gesellschaft für Photogrammetrie, Fernerkundung und Geoinformationen*, Band 13, 2004, pp. 203 – 210.
- Brzank, A., Heipke, C., 2006. Classification of Lidar Data into water and land points in coastal areas. In: *The International Archives of Photogrammetry and Remote Sensing*, Bonn, Germany, Vol. XXXVI/3, pp. 197-202.
- Katzenbeisser, R. and Kurz, S., 2004. Airborne Laser-Scanning, ein Vergleich mit terrestrischer Vermessung und Photogrammetrie. In: *Photogrammetrie Fernerkundung Geoinformation*, Heft 8, 2004, pp. 179-187.
- Kraus K., Pfeifer N., 1998. Determination of terrain models in wooded areas with airborne laser scanner data. In: *ISPRS Journal of Photogrammetry & Remote Sensing*, Volume 53, pp. 193 – 203.
- Leckie, D., Cloney, E., Jay, C. and Paradine, D., 2005. Automated Mapping of Stream Features with High-Resolution Multispectral Imagery: An Example of the Capabilities. In: *Photogrammetric Engineering & Remote Sensing*, Vol. 71, No. 2, February 2005, pp. 145 – 155.
- Mandlbürger, G., 2006. Topographische Modelle für Anwendungen in Hydraulik und Hydrologie. Dissertation, TU Wien. http://www.ipf.tuwien.ac.at/phdtheses/diss_gm_06.pdf (assessed March 29, 2007), 150 p.
- Mundt, J. T., Streutker, D. R., Glenn, N. F., 2006. Mapping Sagebrush Distribution Using Fusion of Hyperspectral and Lidar Classifications. In *Photogrammetric Engineering & Remote Sensing*, Vol. 72, No.1, January 2006, pp. 47 – 54.
- Wolfe, W. and Zissis, G.J. 1989. The infrared handbook. The Infrared Information Analysis Center. Environmental Research Institut of Michigan, Detroit, 1700 p.

USING AIRBORNE LIDAR FOR THE ASSESSMENT OF CANOPY STRUCTURE INFLUENCES ON CO₂ FLUXES

L. Chasmer^{a,*}, A. Barr^b, A. Black^c, C. Hopkinson^d, N. Kljun^e, J. H. McCaughey^a, and P. Treitz^a

^a Department of Geography, Queen's University, Kingston Ontario, K7L 3N6 - lechasme@yahoo.ca, mccaughe@post.queensu.ca; paul.treitz@queensu.ca

^b Climate Research Branch, Meteorological Service of Canada, Saskatoon SK

^c Faculty of Agricultural Sciences, University of British Columbia, Vancouver BC

^d Applied Geomatics Research Group, NSCC, Middleton NS

^e Institute for Atmospheric and Climate Science, ETH Zurich, Universitätsstrasse 16 ETH Zentrum, CHN CH-8092 Zurich

Commission VI, WG VI/4

KEY WORDS: airborne lidar, carbon dioxide, eddy covariance, flux footprint, canopy structure, photosynthesis, respiration.

ABSTRACT:

Fluxes of carbon dioxide (CO₂), water, and energy measured using the eddy covariance method (EC) will vary spatially and temporally within the catchment area of the EC system, especially if parts of the forest are structurally heterogeneous. This is important because within site vegetation structural and topographic heterogeneity may tip the balance between an ecosystem being a net sink or source of CO₂ within a given year. Further, if wind directions are non-varying, the EC method may possibly either over- or under-estimate energy and mass fluxes if source locations are not representative of the entire ecosystem. The following study will use airborne lidar assessments of canopy structure, a simple flux footprint parameterisation, and EC estimates of net ecosystem productivity (NEP), ecosystem respiration (Re), and gross ecosystem productivity (GEP) to test the hypothesis that vegetation structural heterogeneity has some influence on CO₂ fluxes within a mature jack pine forest in Saskatchewan, Canada. The results found in this study indicate that vegetation structural variability (canopy height, depth, and foliage amount) within the site have significant influences on the variability in CO₂ flux estimates of uptake and respiration made using the EC method. However structural heterogeneity is not more important than meteorological driving mechanisms. The influences of structure may therefore become more influential in more heterogeneous ecosystems. Variability in vegetation fractional cover (a proxy indicator for foliage amount) and height, observed from airborne lidar, have the greatest influences on NEP and GEP, where increased fractional cover is directly related to increased CO₂ uptake on most days studied.

1. INTRODUCTION

Fluxes of CO₂, water vapour, and energy vary spatially and temporally due to changes in solar radiation, soil and air temperature, soil type, the photosynthetic capacity of vegetation and foliage density (e.g. Baldocchi et al. 1997; Griffis et al. 2003). Therefore, it is likely that variability in the conditions required for the transfer of CO₂ into the ecosystem, via photosynthesis, and fluxes of CO₂ out of the ecosystem, via ecosystem respiration, may be manifested in the vegetation structural and topographic heterogeneity within the ecosystem. Canopy structural and ground surface topographic variability are important considerations when examining the annual carbon balance of forests, especially if these affect the differences between annual net CO₂ uptake and release. Ecosystem respiration (Re) plays an important role in the carbon balance of many climatically sensitive boreal forests (e.g. Lindroth et al. 1998) because Re may alter the ecosystem from being a sink for atmospheric CO₂ to a source. For example, Griffis et al. (2003) determined that 46% of net ecosystem productivity resulted in CO₂ loss through respiration at a mature jack pine site, indicating the importance of ecosystem Re to the carbon balance. At OJP, CO₂ uptake and respiration processes are often dependent on canopy foliage cover and solar heating of the ground surface, whereby interception of solar radiation by

greater numbers of leaves results in increased photosynthesis and CO₂ uptake as well as decreased warming of the soil surface, and possibly, decreased Re (Baldocchi et al. 1997). Further, within canopy radiation scattering during sunlit (direct radiation) and cloudy (diffuse radiation) periods will also affect the efficiency with which light is used for photosynthesis, especially when the canopy becomes isotropic (Baldocchi et al. 1997). If water stress is a limitation to vegetation growth, then a positive feedback may result whereby productivity (and leaf area) will decrease or remain low, and penetration of radiation through the canopy will increase causing soils to warm and the possibility of respiration increase (Baldocchi et al. 1997).

Airborne lidar, in combination with a spatially and temporally varying flux footprint model parameterisation and the eddy covariance method (EC) offer one method for which mass and energy exchanges can be assessed within complex vegetated ecosystems. Footprint parameterisations of the upwind distribution area can be used to examine the sources and sinks of fluxes such that the relative contributions of elements from different places within the ecosystem diffuse with atmospheric turbulence to the EC measurement system (Schmid, 1994). Particle diffusion is strongly dependent on wind direction, wind velocity, the height of the EC system, atmospheric stability, roughness length, and land surface heterogeneity (Kljun et al.

* Corresponding author.

2004). Flux footprints, therefore, plot the shape in x and y coordinates of the source/sink area as well as the probability density function (PDF), defined as the probability of the distribution of flux throughout the site by continuous sampling of that flux, via relative frequency. Airborne lidar can be used to determine the relative variability of vegetation structural characteristics and topography within an individual flux footprint or source/sink area per unit time. The combination of source/sink area defined by the footprint model parameterisation, flux exchanges measured using the EC method, and detailed structural and topographic information from lidar will continue to become important mechanisms for understanding some of the physical mechanisms associated with temporal and spatial variability in CO₂ uptake and respiration within vegetated environments.

In this study, we use airborne lidar to characterise vegetation structural heterogeneity within the contours of half-hourly flux footprint maximum area PDFs (approximately 80% of flux contribution area) in order to quantify the magnitude of influence that within-site canopy structural variability has on CO₂ uptake and respiration estimated using the EC method. A simple footprint climatology parameterisation of Kljun et al. (2004) is applied at a naturally regenerating, mature jack pine forest in Saskatchewan, Canada.

2. METHODOLOGY

2.1 Study Area

The study site consists of a fairly homogeneous mature jack pine (*Pinus banksiana* Lamb.) forest (OJP) located near the southern edge of the boreal forest in Saskatchewan (520230 E, 5974262 N, zone 13). The site is maintained by Environment Canada for the Fluxnet-Canada Research Network (www.fluxnet-canada.ca) and is part of the Boreal Ecosystem Research and Monitoring Sites (BERMS). BERMS contains multiple chronosequence, fire, and a fen sites for which flux, meteorological and mensuration data have been collected consecutively since 2005 (Table 1).

Plot #	Elevation (m)	DBH (cm)	Tree height (m)	Canopy depth (m)	LAI	Stem density (m ⁻¹)
1	494.3	15.9	14.9	6.3	1.36	0.12
2	495.1	14.6	13.6	6.1	1.54	0.08
3	494.1	11.7	13.0	5.9	1.06	0.17
4	492.5	12.9	13.3	5.2	1.26	0.15
5	489.5	17.5	15.7	8.8	1.35	0.09
6	491.9	16.1	14.9	8.1	1.44	0.1
7	487.0	11.8	11.4	6.2	1.00	0.14
8	492.4	23.6	13.4	11.2	1.76	0.04

Table 1. Average stand characteristics measured at eight plots. DBH = diameter at breast height, LAI = Leaf area index. Corrections for canopy clumping, woody-to-total area ratios and needle-to-shoot area ratios were used to adjust LAI according to Chen et al. (2006).

Elevation within the EC catchment area at OJP (1000 m radius) varies between 482 and 494 m, and cross-site variability in tree heights range from approximately 13 m and 18 m. Mensuration data were collected at eight plots during the growing season of 2005, coincident with the airborne lidar survey (Table 1). Mensuration plots (11.3 m diameter) were set up and georeferenced using survey-grade (differential, post-processed)

GPS such that four plots were located within 100 m of the flux measurement tower, and four plots were located within 500 m of the tower for spatial representivity. Understory vegetation consists of alder (*Alnus crispa* Ait.), reindeer lichen (*Cladina* spp.), and bearberry (*Arctostaphylos uva-ursi* L.). Soils within the site tend to be sandy and dry with little nitrogen content (Baldocchi et al. 1997).

2.2 EC Flux Estimates

Three, approximately one to two week periods of flux and meteorological data were examined during the dry growing season of 2002. CO₂ observations were excluded during periods of rainfall and low wind speed. Average tree height growth since 1996 was approximately 1 m, therefore growth between 2002 and 2005, when the lidar survey was performed, is minimal and within the range of error of the lidar system used. Vegetation growth likely has an insignificant influence on the results of the analysis.

Above canopy CO₂ fluxes were measured at approximately 30 m above the ground surface using the eddy covariance method at 10 Hz and aggregated to 30-minute periods. EC instrumentation and methodology are discussed in Barr et al. (2004). In this study, net ecosystem productivity (NEP) ($\mu\text{mol}\cdot\text{m}^{-2}\cdot\text{s}^{-1}$) is directly measured by the EC system where NEP = net ecosystem exchange (-NEE) ($\mu\text{mol}\cdot\text{m}^{-2}\cdot\text{s}^{-1}$). Therefore, a positive NEP indicates that the ecosystem uses more CO₂ for photosynthesis than it releases. Re ($\mu\text{mol}\cdot\text{m}^{-2}\cdot\text{s}^{-1}$) is modelled via the relationship between night-time respiration and soil temperature (Barr et al. 2004). Gross ecosystem productivity (GEP) ($\mu\text{mol}\cdot\text{m}^{-2}\cdot\text{s}^{-1}$), defined as the uptake of CO₂ by the ecosystem for photosynthesis, is calculated from NEP and Re whereby GEP = NEP + Re. It is important to note that NEP is the most direct estimate of CO₂ flux measured using the EC. GEP and Re, on the other hand, are modelled based on soil temperature relationships and may possibly be over- or underestimated. Fluxes have been averaged over coincident 30-minute periods during daylight conditions. Daytime is defined as the above-canopy incoming shortwave radiation >0.5 W·m⁻² to avoid errors in EC measurements, occasional condensation on radiation sensors, and footprint model parameterisation during generally stable nocturnal atmospheric conditions. Uncertainties in measuring carbon fluxes occur because, during calm and stable conditions, the transfer of carbon dioxide by non-turbulent exchanges is not detected by the EC system (Griffis et al. 2003). Further, early morning and late afternoon periods were not examined due to CO₂ storage and 'flushing' of CO₂ out of the ecosystem, not related to canopy structure.

Variability in CO₂ fluxes caused by meteorological influences such as soil moisture, soil temperature, air temperature, relative humidity, incoming photosynthetically active radiation (PAR), and vapour pressure deficit have been removed using residual analysis (not shown) (e.g. Chen et al. 2002). Therefore, influences of vegetation structure on CO₂ fluxes are examined after all meteorological driving mechanism influences have been removed. Average 24-hour energy balance closure for each day and each period studied was determined using the Energy Balance Ratio method (Wilson et al. 2002). Average energy balance closure during the first period of study was ~88% (standard deviation = ~10%), during the second period was ~83% (standard deviation = ~8%), and during the third period was ~85% (standard deviation = ~14%).

2.3 Lidar Data Collection and Processing

Lidar data were obtained at OJP using a small-footprint, discrete pulse return ALTM 3100 (Optech Inc., North York, Ontario), owned and operated by the Applied Geomatics Research Group, Nova Scotia on August 12, 2005. Up to four laser pulse returns were obtained per laser pulse emitted, at a rate of 71 kHz and at a flying height of 950 m a.g.l. The scan angle was set at $\pm 19^\circ$ with 50% overlap of adjacent flight lines. This enabled penetration of the laser pulses through to the base of the canopy, whilst also obtaining returns on all sides of individual tree canopies (Chasmer et al. 2006). Cross-track and down-track resolutions, with the 50 percent overlap of scans, are 35 cm (“post spacing”).

Percentile distributions, frequently used to estimate average tree canopy heights using lidar data (e.g. Magnussen and Boudewyn 1998) were used to approximate average tree heights and base of live crown height (used to determine live canopy depth, where depth = canopy height – canopy base height) at the plot level and also within-footprint probability density function (PDF) contours using a canopy height model (CHM). Height and live canopy base height percentile distributions were calculated on individual laser pulse returns greater than or equal to 2 m above the ground surface so that laser pulse returns from the ground surface would not influence and shift the percentiles downwards. Also, the 2 m threshold was used to receive pulses from the canopy only, as opposed to stems and understory. Percentile distributions were also compared at eight individual plots to determine the most accurate and descriptive percentiles to use. The 90th and 8th percentiles were most appropriate for determining average tree heights and base of live crown height at the plot level at OJP. Accuracy in predicting tree heights and base of live crown height were 0.94 and 0.77 (coefficients of determination) for the 90th (corresponding to canopy height) and 8th (corresponding to base of live crown height) percentiles, respectively. Differences between average measured canopy height, canopy height derived from airborne lidar (L90 = 90th percentile), and average canopy base height, canopy base height derived from airborne lidar (L8 = 8th percentile) are shown on a per plot basis in Table 2. These were then applied to laser pulse returns within the 30-minute footprint 80% PDF contour lines.

A proxy for plant area index (PAI) has been created from laser pulse returns within the canopy and the total number of laser pulse returns, following a simple methodology discussed in Morsdorf, et al. (2006) for gap fraction and fractional cover. Gap fraction increases when gaps within the canopy increase, thereby resulting in increased radiation passing through the open canopy without intercepting foliage. The inverse of this is “fractional coverage” or *fcover* whereby gaps are represented by a foliage cover of zero, and increased radiation interception results in increased fractional coverage of foliage. Laser pulses can exhibit similar properties to solar radiation as they pass through the canopy. Laser pulses that are returned from within the canopy have been effectively ‘blocked’ by the canopy from reaching the ground. Laser pulses that reflect from the ground surface likely passed through gaps within the canopy. Therefore, the ratio of the laser pulses returned from within the canopy to those returned from the ground surface is a reasonable proxy for the gaps within the canopy and the fractional coverage of leafy and woody material intercepting radiation.

To obtain spatial estimates of *fcover*, laser pulses have been classified using “canopy” and “non-canopy” pulse returns

within Terrascan (Terrasolid, Finland) such that all laser pulses located 1.3 m above ground level were classified as “canopy” and all pulses located below 1.3 m, including ground were classified as “low vegetation and ground”, coincident with the height of the digital camera, and photographs. Vegetation fractional coverage from lidar has been determined by counting the total number of “canopy” laser pulse returns and then, by counting the total number of “low vegetation and ground” laser pulse returns within corresponding 1 m x 1 m x 30 m columns. Counts were performed within Surfer (Golden Software Inc., Golden, Colorado) and *fcover* was determined for the entire area within the EC catchment using the SAS statistical package (SAS Institute Inc., Cary, North Carolina). *fcover* is calculated as:

$$fcover = \left(\frac{\sum P_{canopy}}{\sum (P_{canopy} + P_{ground})} \right) \quad [1]$$

where *Pcanopy* is the total frequency of laser pulse returns within the canopy, and *Pground* is the total frequency of laser pulse returns for low vegetation and ground within each 1 m x 1 m x 30 m column (Figure 1) throughout the catchment area of the EC (approximately 750 m radius). *Fcover* has been compared with estimates of gap fraction (*1-fcover*) and effective leaf area index (LAIe) for 9 of 10 analysis rings determined from digital hemispherical photography (DHP) ($r^2 = 0.68$) (Leblanc et al. 2005). This indicates that *fcover* is a reasonable estimate of leaf area at this site, when compared with DHP. In order to correct LAIe obtained from DHP, the needle-to-shoot area ratio, woody-to-total area ratio, and clumping index from Chen et al. (2006) were used.

Plot #	Ave. height (m)	L90 (m)	Diff. (m)	Ave. canopy base height (m)	L8 (m)	Diff. (m)
1	14.9	14.8	-0.1	6.3	6.1	-0.2
2	13.6	14.1	0.4	6.1	5.9	-0.2
3	13.0	13.0	0	5.9	6.1	0.2
4	13.3	13.7	0.4	5.2	5.3	0.1
5	15.7	14.7	-1.0	6.9	7.0	0.1
6	14.9	14.7	-0.2	6.8	6.5	-0.3
7	11.4	12.0	0.6	5.2	6.1	0.9
8	13.4	14.9	-1.5	5.2	6.0	0.8

Table 2. Average canopy height and canopy base height measured on a per tree basis within individual 11.3 m radius mensuration plots compared with lidar estimated canopy heights and canopy base height determined using percentile distributions (L90 and L8, respectively).

The amount of vegetation fractional cover (*fcover*) is illustrated at OJP in Figure 1. The site tends to be relatively homogeneous, with *fcover* ranging between 0.2 and 0.5. The area immediately surrounding the EC flux station tends to have the lowest *fcover*, on average. Areas to the north and south tend to have large gaps within the canopy and little foliage cover. Interestingly, low-lying areas, which often contain alders, tend to correspond with areas of higher *fcover* and tree height (not shown) due to the nitrogen fixing capabilities of alder and increased resources for jack pine growth (Vogel and Gower, 1998).

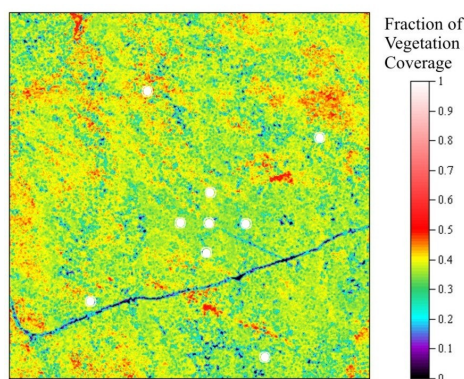


Figure 1. Vegetation fractional cover mapped at 1 m resolution at OJP. White circles represent field mensuration plot locations, and the central white circle represents the location of the EC flux station. All plots were located using survey-grade, post processed GPS with base and rover within 4 kms of each other at all times.

2.4 Footprint Parameterisation

The footprint parameterisation used in this study follows that discussed in Kljun et al. (2004). The parameterisation was chosen because a) the cross-wind integrated footprint is considered; b) it incorporates variables that are easy to derive from measurements obtained from EC; c) it is neither computationally difficult nor time-intensive; and d) it has been thoroughly applied and tested using a variety of meteorological (e.g. varying stability, roughness length, etc.) and technological (instrument measurement height) applications.

Briefly, the crosswind-integrated footprint ($\overline{f^x}$) as discussed in detail in Kljun et al. (2004), is scaled based on the along-wind distance from the receptor (x), the receptor height (z_m), roughness length (z_0), and the height of the planetary boundary layer (H). Directionality and origin of the flux is also determined from wind direction. Particle advection and diffusion is accounted for in the surface friction velocity (u_*), whereas buoyancy and the formation and size of eddies within the planetary boundary layer are described as the standard deviation of the vertical velocity (σ_w). These parameters create the non-dimensional form of the cross-wind integrated footprint F_* based on four dimensionless contributions and a function of the non-dimensional along-wind distance X_* (see Kljun et al. 2004). Dispersion in the y direction (the cross-wind distance from the centre-line) has been estimated using a Gaussian function (e.g. Amiro, 1999). Roughness length (z_0) at OJP has been calculated from Choudhury and Monteith, (1998) based on the height of the canopy, soil surface roughness, LAI, the height of the understory and zero-plane displacement. Therefore z_0 for OJP, using an average measured tree height of 14.16 m is 1.93 m and varies between 1.55 m and 2.23 m for averaged shortest and tallest trees within measured plots (11.4 and 16.4 m, respectively). The location of maximum flux varies between 200.2 m and 175.8 m from the flux tower for footprints containing shorter trees to footprints containing taller trees, respectively. The 80% origin of the flux area varies between 438 m (short trees) to 384 m (tall trees). Therefore the along wind distance (and subsequent error in footprint extent) may vary by as much as 50 m or approximately 10% of the total footprint ($\geq 80\%$) in the x direction. However, variable wind speed and boundary layer height will also alter the length of the footprint (not shown). Finally, Richardson number (Ri) is used to determine approximate stability of the atmosphere (Monteith

and Unsworth, 1990) using air temperature and windspeed at 30-minute periods during relatively unstable conditions when u_* is $>0.2 \text{ ms}^{-1}$. Ri can therefore be used to approximate the height of the planetary boundary layer (H). Measured boundary layer heights were found to sometimes exceed 1.75 km during the growing season at OJP. A flux footprint example with maximum and 80% contour lines is provided in Figure 3 overlaid onto a canopy height model at OJP on June 13, 2002 at 10:00 (LST). The 80% contour (outer) line is used to extract within footprint canopy structural information for each 30-minute period throughout the day.

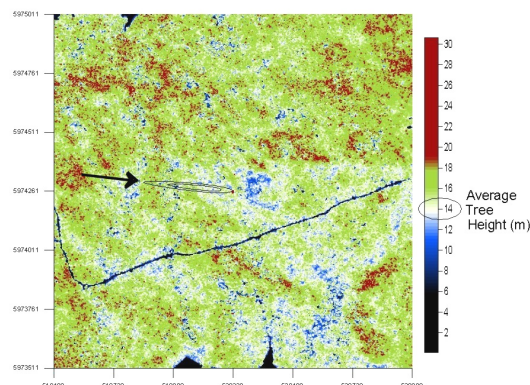


Figure 2. 30-minute flux source contour lines at 80% (outer contour) and maximum (inner contour) total integrated footprint on June 13, 2002 at 10:00 LST. The footprint has been overlain onto the lidar CHM at OJP. The arrow represents average wind direction during the 30-minute period.

3. RESULTS AND DISCUSSION

3.1 Vegetation Structural Influences on CO_2

In this study, the maximum part of the footprint is plotted such that a PDF of CO_2 flux $\geq 0.001 \text{ m}^{-1}$, and is within 500 m of the EC system (limited to the upwind areas only). The remaining parts of the footprint often extend up to and beyond the 1 km radius of the EC system, especially during stable conditions. Parts of the footprint that are outside of the 80% PDF tend to contribute relatively little compared to the maximum source of flux area. As such, canopy structural variability within the footprint (e.g. tree height, canopy depth, and f_{cover}), play an important role on the residual variability in CO_2 fluxes after accounting for meteorological influences. Topography also plays an important role, but is not examined here. Table 3 provides summary results on remaining (residual) variability in 30-minute fluxes due to structural variability after accounting for meteorological driving mechanisms.

NEP at OJP is significantly influenced by within site canopy structural heterogeneity (vegetation height, canopy depth, and f_{cover}) on 16 of 22 days examined ($p < 0.1$) (Table 3). Further, the magnitude of influence tends to vary on a daily basis, often with respect to variations in meteorological driving mechanisms and likely, resource use. On five days, average structural variability accounts for 25% of the total variability in NEP, but does not play a more significant role than meteorological driving mechanisms on any given day. Meteorological driving mechanisms account for 74%, 75% and 52% of the variability in NEP, on average, during the periods studied (June, July, and August, respectively). Throughout the three periods of study, structural variability accounts for $\sim 16\%$ of the total variability in NEP on average during 18 of 22 days or 81% of the time

period. In most cases, increased biomass associated with increased tree heights, base of canopy height, and increased $fcover$ were positively related to increased CO_2 uptake used for photosynthesis. However, during three of the days studied, the opposite was found to be true, especially in June, and one day in August, when the source was located within upland areas. This may be related to cooler air temperatures, lower incoming PAR and reduced carbon uptake on June 11, 2002, and increased air temperatures and respiration on June 13, and August 10 2002, leading to a reduction in NEP.

Date (2002)	Tree Height (r^2)	Canopy Depth (r^2)	$fcover$ (r^2)	% of total variability in NEP	# of days affected
June 10	0.03	0.06	0.07	4	4 of 6
June 11	-0.41	-0.36	-0.36	-29	
June 13	-0.05	-0.05	-0.2	-8	
June 14	0.08	0.05	0.03	4	
July 6	0.11	0.18	0.04	8	5 of 9
July 7	0.2	0.001	0.45	16	
July 8	0.06	0.09	0.22	9	
July 10	0.021	0.09	0.013	3	
July 12	0.7	0.57	0.43	43	
Aug. 7	0.26	0.1	0.18	26	7 of 7
Aug. 8	0.02	0.04	0.16	11	
Aug. 9	0.09	0.05	0.07	10	
Aug. 10	-0.09	-0.06	-0.02	-8	
Aug. 11	0.18	0.12	0.09	19	
Aug. 12	0.16	0.02	0.35	25	
Aug. 13	0.27	0.24	0.1	29	

Table 3. Coefficients of determination of the residual of NEP flux variability for individual canopy structural components, as well as the percent of the total variability in NEP accounted for by canopy structure. Negative signs indicate that NEP is negatively correlated with increases in biomass (e.g. via height, depth, or $fcover$) per day studied. Missing days indicate relationships that were not significant ($p < 0.1$).

In the case of GEP, estimated as the total CO_2 used for photosynthesis, it is expected that footprint areas containing taller trees and increased $fcover$, as well as greater depth of canopy will be positively related to increased CO_2 uptake for photosynthesis. During 14 of the 22 days studied, structural variability in vegetation characteristics have a significant influence on GEP ($p < 0.1$) (Table 4), but also does not have a greater influence than meteorological driving mechanisms, which account for 74.5%, 47.5%, and 82% of GEP variability during the three periods of study (June, July, and August, respectively). On average, ~12% of the total variability in GEP is influenced by vegetation structural characteristics. Positive and significant increases in GEP with increased $fcover$ tend to correspond during certain days with greater average incoming photosynthetically active radiation (PAR), especially in July and to a lesser extent, in August. Canopy height and $fcover$ have the most significant influence on NEP and GEP flux variability. Canopy depth, although correlated with vegetation height, tends to have a lower influence on CO_2 uptake.

Within footprint average structural heterogeneity has a lower influence on modelled Re because atmospheric and hydrological driving mechanisms play more of a key role in ecosystem respiration (Table 5). Meteorological driving mechanisms account for more than 80% of the variability in Re. On 13 of 22 days studied, structure has a significant influence on Re, and on 10 of these days, structural influences are $\geq 5\%$ of the total variability in Re. Average structural influences

throughout the 13 of 22 days studied account for ~9% of the total variability in Re. It is likely that ground surface topography also plays an important role in GEP, NEP, and Re, and will be examined in a future study.

Date (2002)	Tree Height (r^2)	Canopy Depth (r^2)	$fcover$ (r^2)	% of total variability in GEP	# of days affected
June 11	0.28	0.26	0.2	20	1 of 6
July 6	0.14	0.10	0.05	7	6 of 9
July 7	0.16	0.0002	0.35	13	
July 8	0.23	0.03	0.17	11	
July 10	0.02	0.12	0.007	4	
July 11	0.008	0.17	0.03	5	
July 12	0.7	0.6	0.014	33	
Aug. 7	0.24	0.08	0.23	14	7 of 7
Aug. 8	0.02	0.04	0.15	5	
Aug. 9	0.14	0.09	0.11	9	
Aug. 10	0.001	0.17	0.06	11	
Aug. 11	0.09	0.05	0.16	14	
Aug. 12	0.09	0.04	0.28	20	
Aug. 13	0.02	0.03	0.11	8	

Table 4. Coefficients of determination of the residual GEP flux variability due to within-footprint variations in canopy structure after the influence of meteorological driving mechanisms have been removed. Negative signs indicate that GEP is negatively correlated with increases in biomass. Missing days indicate relationships that were not significant within $p < 0.1$.

Date (2002)	Tree Height (r^2)	Canopy Depth (r^2)	$fcover$ (r^2)	% of total variability in Re	# of days affected
June 10	-0.34	-0.34	-0.025	-13	5 of 6 days
June 11	-0.15	-0.12	-0.014	-5	
June 13	0.46	0.42	0.53	25	
June 14	-0.12	-0.10	-0.11	-6	
June 15	-0.15	0.07	0.003	-4	
July 5	-0.35	-0.38	0.08	-13	4 of 9 days
July 7	-0.11	-0.0008	-0.26	-6	
July 8	-0.16	-0.19	-0.28	-10	
July 13	-0.26	-0.28	-0.29	-13	
Aug. 7	-0.38	-0.46	-0.17	-12	4 of 7 days
Aug. 8	0.001	0.008	0.15	2	
Aug. 12	-0.31	-0.26	-0.23	-10	
Aug. 13	0.07	0.05	-0.13	-3	

Table 5. Coefficients of determination of the residual Re flux variability due to canopy structural variability as well as the total variability in Re accounted for by canopy structure. Negative signs indicate that variability in Re is negatively correlated with canopy structure (e.g. increased Re is associated with locations with decreased biomass).

3.2 Potential Uncertainties and Future Research

The results from this study corroborate results from other studies, with respect to canopy structural influences on CO_2 fluxes, however, in this study, we have also quantified the magnitudes of influence that canopy structure has on CO_2 fluxes. Despite this, some potential uncertainties may slightly alter the results of the analysis and could be examined in the future. We will discuss each of these in turn.

Within footprint canopy height, depth and $fcover$ will likely depend on the configuration of the lidar survey, especially where the calculation of $fcover$ depends on a ratio of canopy to below canopy laser pulse returns. Changing lidar survey specifications will slightly alter the canopy structural

characteristics (e.g. Chasmer et al. 2006). Because a ratio is used, it is likely that lower densities of laser pulse returns will yield the same results as higher densities, so long as the probability of distribution of laser pulse returns between the canopy and the ground surface does not change. Tests on the influence of changing lidar survey specifications, etc. may be the focus of future research or a flux footprint sensitivity analysis.

In this study, we also assume that the canopy is non-varying throughout the growing season, and therefore ignore periods of needle flush in June, which will alter the photosynthetic capacity and uptake of CO₂ at this site.

The flux footprint parameterisation used in this study, like all models, is a simplification of the processes that are believed to be occurring within the EC catchment area. It therefore has assumptions that may alter the size and accuracy of the location of the footprint. By using 80% of the footprint probability density function, we have effectively reduced the error to the most probable location of the footprint, if wind directions are not highly variable within the period. Another source of error may be caused as a result of temporal lag effects of turbulent transfer of fluxes to the EC system. Further, variability in the spatial distribution of vegetation heights associated with roughness length, leaf area, photosynthetic capacity, and elevation will influence the extent and probability of flux in x and y directions. Geographic information systems are now able to include complex layers of data, as well as a variety of indices, such as topographic wetness index, vegetation indices, spectral characteristics, and so on. These can be integrated to form more complete and operational flux footprint parameterisations for individual sites.

4. CONCLUSIONS

The results of this analysis indicate that CO₂ fluxes within this relatively homogeneous ecosystem are frequently related to differences in vegetation structural heterogeneity within the site. Variability in structure and fluxes of CO₂ and H₂O throughout the EC catchment area will also have influences on spatial and temporal variability in light use efficiency (LUE) and water use efficiency (WUE) frequently used in ecosystem and remote sensing-based ecosystem models. CO₂ fluxes within heterogeneous forests may have increased dependency on canopy structure and topography (not examined), and these may be a deciding factor in whether the annual carbon balance of a vegetated ecosystem is a net sink or a net source.

5. REFERENCES

- Amiro, B. D., 1998. Footprint climatologies for evapotranspiration in a boreal catchment. *Agricultural and Forest Meteorology*. 90:195-201.
- Baldocchi, D. D., C. A. Vogel, and B. Hall, 1997. Seasonal variation of carbon dioxide exchange rates above and below a boreal jack pine forest. *Ag. For. Met.* 83, pgs. 147-170.
- Barr, A.G., T.A. Black, E.H. Hogg, N. Kljun, K. Morgenstern, and Z. Nescic, 2004. Inter-annual variability in the leaf area index of a boreal aspen-hazelnut forest in relation to net ecosystem production. *Ag. For. Met.* 126, pgs. 237-255.
- Chasmer, L., C. Hopkinson, B. Smith, and P. Treitz, 2006. Examining the influence of changing laser pulse repetition frequencies on conifer forest canopy returns. *PE&RS*. 72(12), pgs. 1359-1367.
- Chen, J., M. Falk, E. Euskirchen, K. Tha Paw U., T. Suchanek, S. Ustin, B. Bond, K. Brosofske, N. Phillips, and R. Bi, 2002. Biophysical controls of carbon flows in three successional Douglas-fir stands based on eddy-covariance measurements. *Tree Physiology*. 22:169-177.
- Chen, J.M., A. Govind, O. Sonnentag, Y. Zhang, A. Barr, and B. Amiro, 2006. Leaf area index measurements at Fluxnet-Canada forest sites. *Ag. For. Met.* 140, pgs. 257-268.
- Choudhury, B., and J. Monteith, 1988. A four-layer model for the heat budget of homogeneous land surfaces. *Quart. J. Roy. Meteorol. Soc.* 114, pgs. 373-398.
- Griffis, T. J., T. A. Black, K. Morgenstern, A. G. Barr, Z. Nescic, G. B. Drewitt, D. Gaumont-Guay, J. H. McCaughey, 2003. Ecophysiological controls on the carbon balances of three southern boreal forests. *Ag. For. Met.* 117, pgs. 53-71.
- Kljun, N., P. Calanca, M. Rotach, H. Schmid, 2004. A simple parameterisation for flux footprint predictions. *Bound.-Lay. Met.* 112, pgs. 503-523.
- Leblanc, S., J. Chen, R. Fernandes, D. Deering, and A. Conley, 2005. Methodology comparison for canopy structure parameters extraction from digital hemispherical photography in boreal forests. *Ag. For. Met.* 129, pgs. 187-207.
- Lindroth, A., A. Grelle, and A.-S. Morén, 1998. Long-term measurements of boreal forest carbon balance reveal large temperature sensitivity. *Global Change Biology*. 4:443-450.
- Magnussen, S., and P. Boudewyn, 1998. Derivations of stand heights from airborne laser scanner data with canopy-based quantile estimators. *Canadian Journal of Forest Research*. 28:1016-1031.
- Morsdorf, F., B. Kötz, E. Meier, K. Itten, and B. Allgöwer, 2006. Estimation of LAI and fractional cover from small footprint airborne laser scanning data based on gap fraction. *Rem. Sens. of Environ.* 104, pgs. 50-61.
- Monteith, J., and M. Unsworth, 1990. Principles of Environmental Physics. 2nd ed. Edward Arnold, New York. 291 pgs.
- Schmid, H. P., 1994. Source areas for scalars and scalar fluxes. *Bound. Lay. Met.* 67, pgs.293-318.
- Shuttleworth, W., and J. Wallace, 1985. Evaporation from sparse crops – An energy combination theory. *Quart. J. Roy. Met. Soc.* 111, pgs. 839-855.
- Vogel, J., and S. Gower, 1998. Carbon and nitrogen dynamics of boreal jack pine stands with and without a green alder understory. *Ecosystems*. 1(4):386-400.
- Wilson, K.B., A. Goldstein, E. Falge, et al. 2002. Energy balance closure at FLUXNET sites. *Agricultural and Forest Meteorology*. 113:223-243.

PROCESSING FULL-WAVEFORM LIDAR DATA: MODELLING RAW SIGNALS

Adrien Chauve^{1,2,3}, Clément Mallet¹, Frédéric Bretar¹, Sylvie Durrieu², Marc Pierrot Desilligny¹ and William Puech³

¹ Laboratoire MATIS - Institut Géographique National

2-4 av. Pasteur, 94165 Saint-Mandé, France - firstname.lastname@ign.fr

² UMR TETIS Cemagref/Cirad/ENGREF-AgroParisTech, Maison de la Télédétection
500, rue J.F. Breton 34093 Montpellier Cedex 5, France - firstname.lastname@teledetection.fr

³ Laboratoire LIRMM, UMR CNRS 5506, Université Montpellier II
161, rue Ada, 34392 Montpellier Cedex 05, France - firstname.lastname@lirmm.fr

KEY WORDS: lidar, waveform analysis, signal processing, modelling, generalized Gaussian

ABSTRACT:

Unlike airborne multi-echo laser scanner systems, full-waveform systems are able to digitize and record the entire backscattered signal of each laser pulse. It has been demonstrated that decomposing the return waveforms into a mixture of Gaussian components was suitable. In this paper, we focus on the improvement of peak detection and of raw signal modelling. Refined peak detection greatly increased the number of detected targets as well as their positional accuracy. Models more complex than the Gaussian model, such as the Lognormal or generalized Gaussian functions, were introduced and their contribution to waveform processing was studied. In this way, fitting of asymmetric, peaked or flattened echoes located both in urban and forested areas could be improved. Moreover, introduction of new echo parameters allowed the extraction of additional information on the target shape. This should make easier the decorrelation of geometric and radiometric influences on the signal and, as a consequence, the improvement of point cloud classification algorithms.

1 INTRODUCTION

Airborne laser scanning is an active remote sensing technique providing range measurements between the laser scanner and the Earth topography. Well-known direct georeferencing processes turn such distance measurements into 3D point clouds with high accuracy and relevancy. Even for small footprints, there may be several objects of different range within the travel path of the laser pulse that generate individual backscattered echoes. Consequently, conventional lidar systems measure the first echo of the incoming signal ("first pulse") and the last echo ("last pulse"). Some are able to measure up to six pulses and more advanced systems also provide signal intensity.

During the last decade, a new generation of airborne laser scanners that are able to digitize and record the entire backscattered signal of each emitted pulse has appeared. They are called **full-waveform (FW)** lidar systems.

Historically, the first FW lidar systems were designed in the 1980s for bathymetric purposes (Guenther and Mesick, 1988). The first operational topographic system, developed by the NASA, appeared in 1999. The LVIS sensor (Laser Vegetation Imaging Sensor) was an improved version of a former satellite system, SLICER, developed in 1994 (Blair et al., 1999). SLICER was designed to describe the vertical structure of the canopy over extensive areas (Harding et al., 2001). LVIS data processing demonstrated the potential of recording return waveforms to characterize woodland areas and to measure the Earth topography, even ground beneath the canopy. First algorithms for classifying ground points by analysing the return waveform were developed and then resumed for the following system, GLAS, carried by the ICESAT satellite (2003-2006) (Zwally et al., 2002).

The first airborne commercial full-waveform lidar system has been operational since 2004 (LiteMapper-5600 lidar system based on the Riegl LMS-Q560 laser scanner) (Hug et al., 2004) and several features are now available for cartographic purposes.

Full waveform data hold large potentialities since it may overcome many drawbacks of classical multi-echo lidar data. More

control is given to an end user in the interpretation process of the physical measurement. FW lidar data yield more than a basic geometric representation of the Earth topography. Instead of 3D point clouds, more detailed and additional information are provided about the structure of the illuminated surfaces with off-line processes. Thus, in addition to single range measurements, further physical properties of the objects included in the diffraction cone may be found with a backscattered waveform analysis. For example, in vegetated areas, more 3D points may be extracted, low vegetation can be separated from ground and both canopy and ground heights can be measured with higher accuracy (Dubayah and Blair, 2000).

Many studies have already been carried out to perform full waveform lidar data processing and analysis. Return waveform (1D signal) processing to extract more information than a single range measurement is the first main step. Non-linear least-squares (NLS) methods (Hofton et al., 2000, Reitberger et al., 2006) or maximum likelihood estimation using the Expectation Maximization (EM) algorithm (Persson et al., 2005) are typically used to fit the signal to a mixture of Gaussian functions to detect and parametrize the peaks. It was found in general that small-footprint lidar waveforms can be well modelled with a sum of Gaussian pulses (Wagner et al., 2006).

Geometric and radiometric influence of the hit targets have not been yet decorrelated. Therefore, point cloud segmentation algorithms using peak intensity and width still lead to a certain rate of misclassification without a good theoretical understanding of the waveform response for different targets (Ducic et al., 2006).

The aim of this study is to investigate further lidar return waveform processing. First, a raw signal modelling is proposed with Gaussian, Lognormal and generalized Gaussian functions. Indeed, waveforms can be very similar to an ideal Gaussian function (Wagner et al., 2006) whereas other laser impulse responses are slightly asymmetric (Hofton et al., 2000, Jutzi and Stilla, 2006). Consequently, approximating the waveforms using a sum of Gaussians may not be an accurate representation depending on the application and the target.



Figure 1: Amplitude image of the first echoes detected by the embedded real-time system, displayed in the sensor geometry.

A NLS algorithm is then performed with robust initial parameter estimates to improve usual approaches.

Finally, the contribution of proposed functions is discussed as well as the potentialities of new echo parameters for both urban and vegetation area mapping.

2 FULL-WAVEFORM LIDAR DATA

The data acquisition was performed in September 2006 with the RIEGL LMS-Q560 system over the city of Biberach (Bade Wutermberg, Germany). The main technical characteristics of this sensor are presented in (Wagner et al., 2006). The lidar system operated at a pulse rate of 100 kHz. The flight altitude was about 500 m and the footprint size was 0.25 m. RIEGL full-waveform system allows to determine the vertical distribution of targets within the diffraction cone with a temporal resolution of around 1 ns. The target resolution of the system is close to 0.6 m and the spatial resolution (*i.e.* the distance between two samples) is 0.3 m. The surveyed area includes both residential, industrial and dense vegetated areas (figure 1). The point density is about 2.5 pts/m².

Each return waveform is composed of one or two sequences of 60 samples that is to say an altimetric profile of 18 m (or 36 m). For each emitted pulse, the emitted signal (60 samples) and the echoes found by the embedded real-time detection algorithm are given as well as their amplitude and width (figure 2).

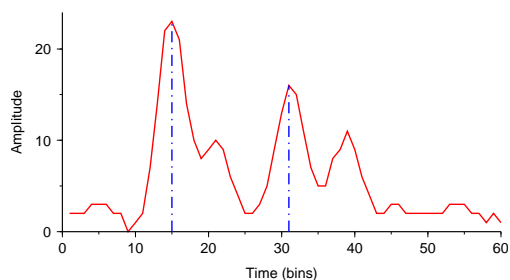


Figure 2: Example of a measured waveform for RIEGL LMS-Q560 system. Dashed lines indicate the position of the echoes detected by the system. The background noise is relatively low within the observed waveforms.

3 WAVEFORM PROCESSING

Waveform processing consists in decomposing the waveform into a sum of components or echoes, so as to characterise the different targets along the path of the laser beam. It is a parametric

approach to estimate a mathematical model. The aim of waveform processing is therefore to extract as many peaks from the signal as possible, but also information for each echo. It consists in two main steps : first, the number of components and initial values are estimated. Then the parameters are optimized. The optimization process is well-known and it has been demonstrated that either the Expectation-Maximization algorithm (Maximum Likelihood estimates) (Persson et al., 2005) or the Levenberg-Marquardt algorithm (non-linear least-squares method) (Hofton et al., 2000, Wagner et al., 2006) give good results. Nevertheless, optimization relies strongly on initial parameters. They therefore must be estimated very carefully to avoid erroneous results. In this study, an improvement of usual peak detection has been first performed. Then a new waveform modelling has been proposed with different functions to improve signal fitting.

3.1 Methodology

A full waveform extracted from the RIEGL LMS-Q560 system is composed of one or two sequences of 60 points uniformly-spaced $\{(x_i, y_i)\}_{i=1, \dots, N}$ sampled at 1 GHz. We aim at decomposing each sequence into a sum of components representing the targets located within the travel path of the laser beam as

$$y = f(x) = \sum_{j=1}^n f_j(x) \quad (1)$$

where n is the number of components, f_j a given function that may be a Gaussian, Lognormal or a generalized Gaussian (see section 3.3).

For each sequence, the background noise is first thresholded. Then, a basic detection method is used to estimate the number and the position of the components. Other function parameters are fixed with constant values. A first fit is computed, using a non-linear least-squares method. A fine detection using the fitting result is then performed to find missing peaks (cases of complex overlapping echoes, see figure 3). If new peaks are detected, a second fit is processed with the same method.

3.2 Peak detection and initial parameters estimation

The basic detection method is based on the zero crossings of the first derivative on the thresholded version of the waveform. The detection algorithm takes into account a minimal number of samples separating two detected peaks (spatial resolution of the system). A non-linear least-squares method with the Levenberg-Marquardt algorithm implemented in the GSL (GNU Scientific Library) is then used to compute the fit. The quality of the results

is evaluated by

$$\xi = \frac{1}{N-p} \sum_{k=1}^N (y_k - f(x_k))^2 \quad (2)$$

where the numerator is the sum of the residual differences between the observed waveform and the fitting function, N is the number of samples and p is the number of parameters of the fitting function.

In case of complex overlapping echoes, zero crossings of the first derivative are not sufficient to detect all real peaks. Indeed, a finer peak detection is needed when two overlapping echoes are so close that a single maximum is found, but three inflexion points (instead of two for a standard echo) exist. One solution is to perform a second pulse detection on the thresholded difference between the observed waveform and the previous fit. If a peak is detected, a new fit is run with the new component. The resulting ξ value is compared to the previous one and this step is repeated until the ξ factor stops decreasing.

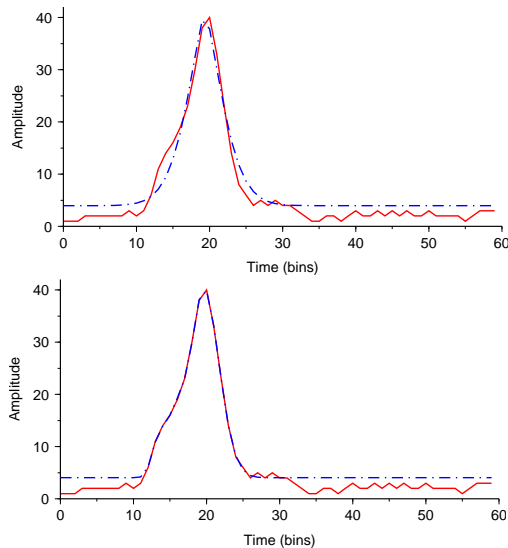


Figure 3: Example of complex waveform. The RIEGL system data is in red colour (continuous line) and the fitted result in blue (dashed line). Data is first thresholded to the value of 4 before pulse detection. **Top:** Fit with only a coarse pulse detection. **Bottom:** Fit with a fine detection. Two echoes are now found.

3.3 Modelling functions

Each laser output pulse shape is assumed to be Gaussian, with a specific and calibrated width. The collected pulse is therefore a convolution between this Gaussian distribution and a "surface" function, depending on the hit objects. It has been shown that if the vertical height distribution of the elements within the diffraction cone follows a Gaussian law, the reflected waveform can be approximated by a sum of Gaussians (Zwally et al., 2002). Wagner (Wagner et al., 2006) has shown that more than 98% of the observed waveforms with the RIEGL system could be fitted with a sum of Gaussian functions.

Nevertheless, this assumption is not always satisfactory. Depending on the lidar system, the transmitted signal is not always Gaussian but can be slightly distorted (asymmetric, flattened or peaked). For the LMS-Q560 waveforms, a steeper ascending part as well as a longer but weaker descending one than the Gaussian model can be noticed. Moreover, the Gaussian height distribution

of the targets has only been statistically shown for large-footprint lidar systems (Carabajal et al., 1999). For small-footprint systems, there is no assuming that the height distribution is Gaussian, even over vegetated areas. Therefore modelling full-waveform lidar data with a sum of Gaussian functions can be inaccurate. It is of interest to extend waveform processing capabilities by using more complex parametric models. It enables to both improve signal fitting and extract more information from the raw signal. Standard extensions of Gaussians are Lognormal and generalized Gaussian functions. The detected peaks can be asymmetric and modelled with a Lognormal function (see figure 4a). Besides, some symmetric waveforms are observed to be distorted over forested areas and over some building roofs. Using the generalized Gaussian model (see figure 4b) can improve signal fitting for complex waveform shapes.

Gaussian (G), Lognormal (L) and generalized Gaussian (GG) models have the following analytical expressions (see figure 4 for plots):

$$f_{G,j}(x) = a_j \exp\left(-\frac{(x - \mu_j)^2}{2\sigma_j^2}\right) \quad (3)$$

$$f_{L,j}(x) = a_j \exp\left(-\frac{(\ln(x - s_j) - \mu_j)^2}{2\sigma_j^2}\right) \quad (4)$$

$$f_{GG,j}(x) = a_j \exp\left(-\frac{|x - \mu_j|^{\alpha_j}}{2\sigma_j^2}\right) \quad (5)$$

The observation of data on the whole survey area shows that most of the asymmetric peaks are in fact so close overlapping echoes that the third inflexion point is hardly visible. As a consequence, with the coarse pulse detection, fitting the waveform with a mixture of Lognormal results in a better quality of fit (*i.e.* a lower value of ξ) than fitting with a sum of Gaussians. However, improving the peak detection as presented before leads to the detection of two echoes. Gaussian fitting is then better.

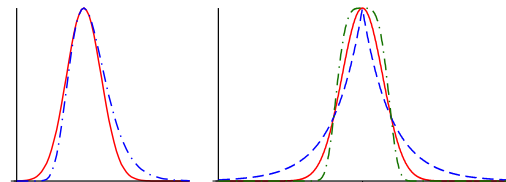


Figure 4: **Left:** Comparison between Gaussian (continuous line) and Lognormal (dotted line) functions. **Right:** The generalized Gaussian function: $\alpha=1$ = Laplace function (dashed line), $\alpha=\sqrt{2}$ = Gaussian function (continuous line) and $\alpha=2$ (dotted line).

The generalized Gaussian model enables to simulate both Gaussian shapes when $\alpha = \sqrt{2}$, peaked shapes when $1 \leq \alpha < \sqrt{2}$ ($\alpha = 1$ gives the Laplace function) and flattened shapes when $\alpha > \sqrt{2}$ (see figure 4b). Therefore it should improve the quality of the fit in most of the cases. But with a simple NLS algorithm, it will also increase the number of fits that do not converge, just like the Lognormal. It is due to the increasing number of degrees of freedom of the function and also to the more complex expression of the gradient (Aiazzi et al., 1999).

The generalized Gaussian is also used to model SAR amplitude (Moser et al., 2006), image texture or even outliers in image matching (Hasler et al., 2003). The α parameter is yet very interesting for waveform analysis because it provides another piece of information about the shapes of the echoes, in addition to their width, and it could be useful for classification purposes (see section 4.3).

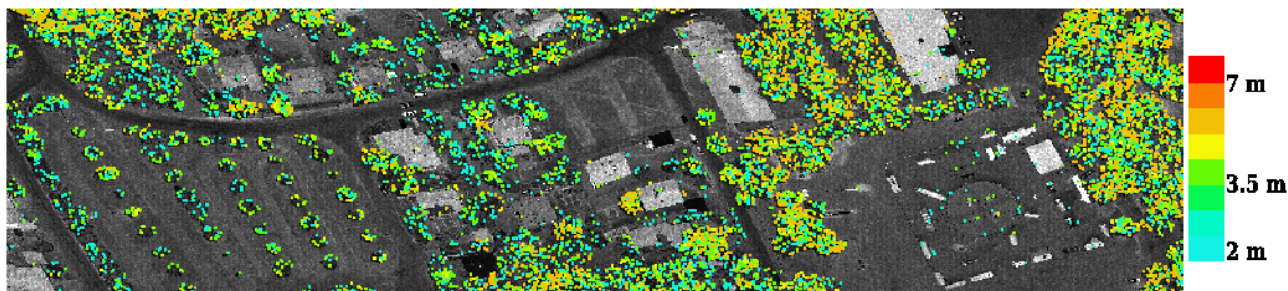


Figure 5: Difference of last pulse altitude between post-processing algorithm and real-time process. Only height differences greater than 2 m has been displayed.

4 RESULTS AND DISCUSSION

4.1 Point extraction

Lidar waveform post-processing allows to densify the final point cloud up to 50 % on forested areas (see table 1). The Gaussian fit was successful for about 99.3% of waveform profiles. A waveform was considered to be well fitted if the quality factor $\xi < 0.5$. It has been observed that $\xi < 0.1$ on urban areas with a single pulse of Gaussian shape and that $\xi \leq 0.5$ even for complex targets consistently fitted.

Analysing the differences between fitted waveforms and the delivered point cloud, one can notice that weak and overlapping echoes are now detected. As expected, the additional points are located near the tree canopy and in low ground vegetation areas. Only few points are additionally detected on the ground beneath the canopy, due to the survey low point density and the small laser footprint. Finally, more echoes are also detected on artificial objects in urban areas, because of multiple pulse reflections at building edges.

The fine peak detection performed after the first two steps (coarse detection and signal fitting) allows to detect up to 10 % more points than a unique coarse echo detection. Low intensity echoes close to strong ones are henceforth extracted (figure 3). The quality of the fit is therefore improved: figure 6 shows a significant decreasing of ξ median value. The fine peak detection enhances the stability of NLS method whatever the fitting function. Indeed, when providing relevant estimates of echo positions as input data, the fitting procedure finds a solution for almost all return profiles (99.99 % for the Gaussian, 99.8 % for the the generalized Gaussian and 99.05 % for the Lognormal function).

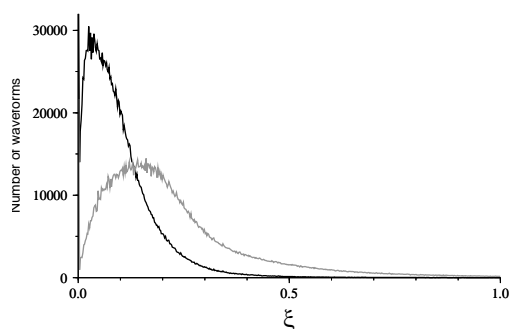


Figure 6: Histogram of ξ values for the Gaussian model : coarse detection (black) and fine detection (grey).

As expected, full-waveform lidar data enables to penetrate deeper in forested areas. Nevertheless, there is still no assuming

the last detected pulse is the ground. Figure 5 shows the difference of last pulse altitude between post-processing algorithm and real-time method. It illustrates that extracted points are significantly closer to the ground over vegetated areas (until 10 m). Moreover, the first pulse detection is also bettered over vegetated areas. Statistical results are summarized in table 1 where the mean difference Δ Height between post-processing detected pulse height and real-time one is always positive for the last pulse (e.g. +1.58 m for dense vegetation) and always negative for the first pulse (e.g. -0.42 m).

Area	Whole Area	Dense Vegetation	Vegetation	Residential	Downtown
Nb profiles	2027547	70074	23368	93690	66264
Non fitted (%)	0.01	0.004	0.008	0.01	0.02
Nb points extracted	2903976	147218	46246	120813	85520
Additional points (%)	24	55	51	9	10
Δ Height first (m)	-0.13	-0.42	-0.34	-0.04	-0.04
Δ Height last (m)	0.36	1.58	1.36	0.07	0.05

Table 1: Statistics on point extraction on different test areas. The figures of non-fitted profiles and difference of height measurement are given for the Gaussian model.

4.2 Comparison between modelling functions

As mentioned in other publications (Reitberger et al., 2006, Wagner et al., 2006), the Gaussian decomposition of lidar waveforms is a good approximation of the signal ($\xi < 0.5$ for 99.3% of the processed waveforms).

$\xi > 0.5$ means that the Gaussian model is not appropriate for modelling complex waveform. Such values are particularly observed on forested areas. Even for small ξ values, the Gaussian decomposition can be inaccurate. Indeed, for high and narrow echoes as well as for weak and large ones, Gaussian fitting could be improved. Such cases are difficult to quantify.

Modelling raw signals with the **Lognormal function** does not improve the waveform fitting for the whole survey area but locally. ξ values are globally higher than for the Gaussian model. Besides, inconsistencies are found for more than 5 % (i.e. $\xi > 5$) and the NLS algorithm diverges more often than for other functions (1 % compared to 0.01 % for the Gaussian model). Nevertheless, in very few cases, ξ values are lower for the Lognormal decomposition than for a sum of Gaussians. It shows that some backscattered echoes are asymmetric. Such cases are observed on streets and some building roofs. Further experiments have to be carried out to draw more conclusions.

It seems that a high value of ξ only means that the lidar waveform is not well modelled with Lognormal functions. But it does not mean that all the waveform echoes are inconsistently modelled. Thus modelling waveforms with a sum of different functions could be appropriate.

The **generalized Gaussian** function allows to model flattened, narrow and high pulses. ξ values are lower for such model than for the Gaussian function. Figure 7 shows the ξ histograms of Gaussian and generalized Gaussian models. The latter improves the global fitting quality. Still a higher number of inconsistent fitting results is noticed (about 0.4%). Theoretically the generalized Gaussian should always fit at least as well as the Gaussian function. But in practice, this is due to a minimization problem in the NLS method.

In the streets (asphalt or pavement), the fitting procedure works as well as for the Lognormal function. Indeed, the observed pulses have a high intensity and a low width ($\alpha \rightarrow 5$), what can be well modelled with the Lognormal function. But for asymmetric echoes, the generalized Gaussian model is not suitable.

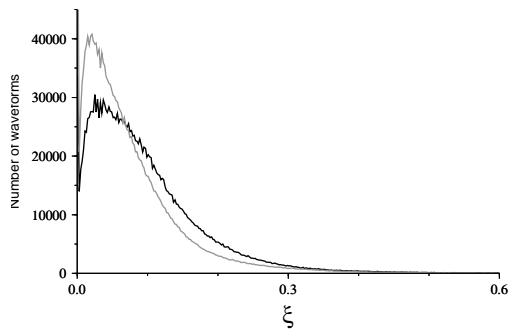


Figure 7: Histogram of ξ values for Gaussian fit (black) and generalized Gaussian fit (grey) using fine detection.

4.3 Contribution of the generalized Gaussian function

As expected, the generalized Gaussian model improves signal fitting. Furthermore, a new parameter α is estimated giving information about the sharpness of the detected echo. The parametric description of the targets given by the signal processing step contains significant information on the roughness, slope and reflectivity of the target surface. The main issue is that geometric and radiometric influences are correlated in one single shape. It seems difficult to decorrelate them with only return intensity and pulse width estimation.

A close observation of the data gives some hints on an empirical classification based on α :

- $\alpha > 1.9$ (rare) concerns pulses belonging to building edges and both to the top of the canopy and below the canopy. Simulations have to be performed to investigate whether echoes in forested areas concern low ground vegetation or bare ground;
- $1.6 < \alpha < 1.9$ is typical of vegetated areas (first echoes more than the other ones) but also of artificial planar areas (asphalt streets for example);
- $1.3 < \alpha < 1.6$ (associated to Gaussian shape) is found on natural ground (beaten-earth floor, grass) and building roofs;
- $\alpha < 1.3$ (very rare) concerns tree canopy and building boundaries.

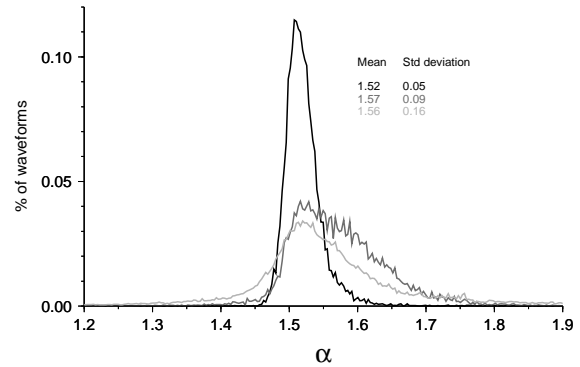


Figure 8: Histogram of α values over three homogeneous test areas (more than 15000 waveforms each) : building roofs (black), asphalt streets (dark grey) and dense vegetation (grey).

Figure 8 shows the distribution of α values over three test areas. The three mean values are all close to 1.55, meaning that the general shape of the backscattered echoes is close to a slightly flattened Gaussian. Extreme values (< 1.3 and > 1.9) are found on forested areas where, for small-footprint lidar systems, there is no assuming the value of the shape parameter. For urban areas, it can help to segment building and artificial ground areas. Further work have to be done to perform such classification algorithm, maybe with the help of both intensity and width pulse values.

The potentialities of the scale parameter α of the generalized Gaussian model can be shown on terrain areas. On flat areas, α seems less sensitive to radiometric changes than the two other ones. For example, intensity and width values are affected by the presence of zebra-crossings on the streets, of tracks on car parks, of moisture on natural surfaces, whereas α parameter is estimated almost constant. It could therefore be useful to classify geometrically similar areas as shown in figure 9. Although α values images are very noisy, α could be a discriminative parameter if associated to other variables in a supervised classification framework.

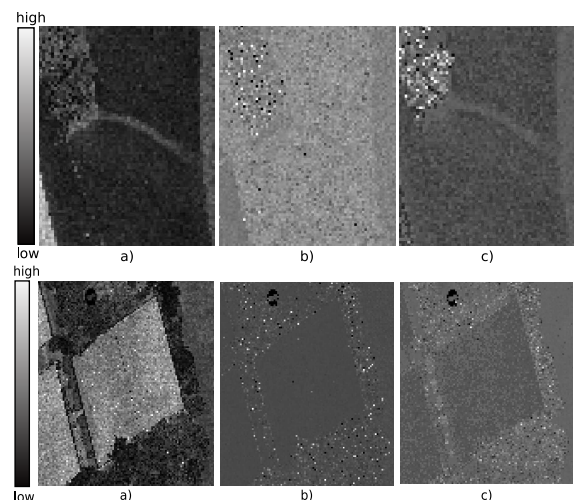


Figure 9: Comparison between the amplitude (a), α (b) and width parameters (c) on artificial (tracks on car park, **top**) and natural (moisture on tennis courts, **bottom**) ground areas.

5 CONCLUSIONS AND FUTURE WORK

The problem of modelling full-waveform lidar data has been investigated in this paper. It is known that the decomposition of an observed lidar waveform into its components not only improves the ranging accuracy of the measurement but also enables the determination of the heights of various reflecting surfaces within the laser diffraction cone. The traditional Gaussian fitting gives in general good results for all kind of areas. Providing the intensity and the width for each echo is however not sufficient for classification purposes.

We introduced the mixture of Lognormal functions to fit asymmetric echoes, especially on streets and roofs. Nevertheless, such model is not suitable for eclectic landscapes. The main limitation is that return bumps are not always of the same nature: it can be a mixture of Lognormal, Gaussian and other functions. We finally introduced the generalized Gaussian model to fit distorted peaks and still enables to fit Gaussian shapes. The modelling methodology is thus improved compared to the Gaussian adjustment. A practical limitation has however been observed since the fitting procedure gives inconsistent results for several waveforms due to optimization problems in the NLS method. But the contribution of this function is all the more significant since a new parameter is estimated for each peak, providing new information about its shape. A first visualization shows its potentialities for classifying extracted point cloud especially in urban areas. Waveform simulations have to be carried out to understand its global contribution.

Improving peak detection was shown in this paper to be very successful to extract additional targets in the return waveforms. However, for classification purposes, it could be more interesting to fit a wide flattened echo with only one generalized Gaussian instead of two basic Gaussians: parameter α would provide information to classify the group of two overlapping echoes that otherwise would not be available. Depending on the application, two approaches are conceivable. On the first hand a coarse pulse detection with a suitable model can be used for classification. On the other hand, an improved point detection with just a Gaussian model can be performed to describe accurately 3D vegetation structure.

Both Lognormal and generalized Gaussian functions contribute to improve lidar waveform modelling but not in the same way. Consequently, the three functions have to be gathered to take benefit from their specific advantages. Besides, other suitable functions have to be tested in order to best describe the return waveform. As the Gaussian fitting is already almost successful all the time, new modelling functions with different parameters have to be found. They could provide new information about the peaks and therefore contribute to lidar point cloud segmentation. A combination of several suitable functions have therefore to be performed to assess this solution. A Reversible Jump Monte Carlo Markov Chain (RJMCMC) method could, for example, be implemented thanks to its high flexibility. Jumps between models of different dimensions (the number of parameters) are possible and consequently each raw signal can be segmented by different functions.

ACKNOWLEDGEMENTS

The authors would like to thank Toposys for providing test data, as well as Boris Jutzi for fruitful discussions.

REFERENCES

Aiazzi, B., Alparone, L. and Baronti, S., 1999. Estimation based on entropy matching for generalized Gaussian PDF modeling. *IEEE Signal Processing Letters* 6(6), pp. 138–140.

Blair, J., Rabine, D. and Hofton, M., 1999. The Laser Vegetation Imaging Sensor: a medium-altitude digitisation-only, airborne laser altimeter for mapping vegetation and topography. *ISPRS Journal of Photogrammetry and Remote Sensing* 54, pp. 115–122.

Carabahal, C., Harding, D., Luthcke, S., Fong, W., Rowton, S. and Frawley, J., 1999. Processing of Shuttle Laser Altimeter range and return pulse data in support of SLA-02. In: *ISPRS Workshop 'Mapping Surface structure and topography by airborne and spaceborne lasers'*, Vol. XXXII-3/W14, La Jolla, United States.

Dubayah, R. and Blair, J., 2000. Lidar Remote Sensing for Forestry Applications. *Journal of Forestry* 98(6), pp. 44–46.

Ducic, V., Hollaus, M., Ullrich, A., Wagner, W. and Melzer, T., 2006. 3D Vegetation mapping and classification using full-waveform laser scanning. In: *Workshop on 3D Remote Sensing in Forestry*, Vienna, Austria.

Guenther, G. and Mesick, H., 1988. Analysis of airborne lidar bathymetric waveforms. In: *Proc. of SPIE Ocean Optics IX*, Orlando, United States, pp. 232–241.

Harding, D., Lefsky, M. and Parker, G., 2001. Laser altimeter canopy height profiles. Methods and validation for closed-canopy, broadleaf forests. *Remote Sensing of Environment* 76(9), pp. 283–297.

Hasler, D., Sbaiz, L., Susstrunk, S. and Vetterli, M., 2003. Outlier modelling in image matching. *IEEE Trans. on Pattern Analysis and Machine Intelligence* 25(3), pp. 301–315.

Hofton, M., Minster, J. and Blair, J., 2000. Decomposition of Laser Altimeter Waveforms. *IEEE Transactions on Geoscience and Remote Sensing* 38(4), pp. 1989–1996.

Hug, C., Ullrich, A. and Grimm, A., 2004. Litemapper-5600 - A Waveform-Digitizing LIDAR Terrain and Vegetation Mapping System. In: *ISPRS Laser-Scanners for Forest and Landscape Assessment*, Vol. 36, Frieberg, Germany.

Jutzi, B. and Stilla, U., 2006. Range determination with waveform recording laser systems using a Wiener Filter. *ISPRS Journal of Photogrammetry and Remote Sensing* 61, pp. 95–107.

Moser, G., Zerubia, J. and Serpico, S., 2006. Sar amplitude probability density function estimation based on a generalized gaussian model. *IEEE Trans. on Image Processing* 15(6), pp. 1429–1442.

Persson, A., Söderman, U., Töpel, J. and Alhberg, S., 2005. Visualization and Analysis of Full-Waveform Airborne Laser Scanner Data. In: *ISPRS workshop 'Laserscanning 2005'*, Enschede, The Netherlands, pp. 103–108.

Reitberger, J., Krzystek, P. and Stilla, U., 2006. Analysis of full-waveform lidar data for tree species classification. In: *ISPRS Photogrammetric Computer Vision (PCV)*, Bonn, Germany, pp. 228–233.

Wagner, W., Ullrich, A., Ducic, V., Melzer, T. and Studnicka, N., 2006. Gaussian decomposition and calibration of a novel small-footprint full-waveform digitising airborne laser scanner. *ISPRS Journal of Photogrammetry and Remote Sensing* 66, pp. 100–112.

Zwally, H., Schutz, B., Abdalati, W., Abshire, J., Bentley, C., Brenner, A., Bufton, J., Dezio, J., Hancock, D., Harding, D., Herring, T., Minster, B., Quinn, K., Palm, S., Spinhirne, J. and Thomas, R., 2002. ICESat's laser measurements of polar ice, atmosphere, ocean, and land. *Journal of Geodynamics* 34(3), pp. 405–445.

ICESAT FULL WAVEFORM ALTIMETRY COMPARED TO AIRBORNE LASER ALTIMETRY OVER THE NETHERLANDS

Hieu Duong^a, Roderik Lindenbergh^a, Norbert Pfeifer^b and George Vosselman^c

^aDelft University of Technology, Delft Institute of Earth Observation and Space systems, the Netherlands - v.h.duong@tudelft.nl, r.c.lindenbergh@lr.tudelft.nl

^bVienna University of Technology, Institute of Photogrammetry and Remote Sensing, Austria - np@ipf.tuwien.ac.at

^cInternational Institute for Geo-Information Science and Earth Observation - ITC, the Netherlands - vosselman@itc.nl

KEY WORDS: Full waveform; DTM; AHN; Laser altimetry; ICESat.

ABSTRACT:

Since 2003 the spaceborne laser altimetry system on board of NASA's Ice, Cloud and land Elevation Satellite (ICESat) has acquired a large world-wide database of full waveform data organized in 15 products. In this research three products are evaluated over The Netherlands. For this purpose the raw full waveform product, the derived Gaussian decomposition product and the global land evaluation product are compared to laser data from the Dutch national airborne laser altimetry archive AHN. Using the CORINE land cover 2000 database allows us to compare ICESat to AHN elevation profiles with respect to the land cover classes forest, urban, bare land/low vegetation and water. This comparison shows that a large average height difference of 5.7 m occurs over forest, while much smaller differences of 1.24 m over urban areas, of 0.43 m over bare land/low vegetation and of 0.07 m over water are found. The reason for this large difference over forests is that the standard processing of NASA does not take the position of the last Gaussian mode of the waveform into account. Incorporating results from a full waveform processing procedure allows us to determine improved ICESat profiles. Comparing the improved profiles shows that the average difference with the AHN profiles over forest is reduced to -0.38 m, while the average differences for the other land cover classes do not exceed -0.75 m. Encountered limitations are discussed in the conclusions.

1 INTRODUCTION

The Ice, Cloud and land Elevation Satellite (ICESat) was launched in January 2003 to observe the cryosphere, the atmosphere and also to measure land topography profiles and canopy heights (Zwally, 2002). These objectives are accomplished using the Geoscience Laser Altimeter System (GLAS) in combination with precise orbit determination (POD) and altitude determination (PAD). Since 2003 ICESat has acquired a huge database of raw and processed data, organized in the 15 data products GLA01, . . . , GLA15 (Brenner et al., 2003). The GLA01 level 1A product contains the raw full waveform data. The GLA05 level 2 altimetry product contains the centroid location of the full waveform as a result of NASA's waveform fitting method. The GLA14 product is also a level 2 product, consisting of global elevation data for non polar land regions.

The ICESat GLA14 elevation data are obtained by combining the GLA01 ICESat full waveform data with the precise position data as obtained by the POD/PAD system. The full waveform data are sampled as relative intensities in 200 bins for sea and 544 or 1000 bins for land, depending on which of the three lasers is used. A time stamp pair of each transmitted pulse and consecutively returned pulse (the full waveform) is recorded by the GLAS system and is used to calculate a travel time or range. This range is then used to compute the elevation of the area illuminated by the laser pulse. Moreover, the time stamp of the returned waveform can be measured at some typical bin positions of the waveform like the beginning, the centroid and the end. Consequently, the elevation will vary according to the variations in the range. The GLA14 elevation product is obtained on the basis of the range as derived from the centroid of the waveform. This elevation is therefore also called the mean elevation (Harding and Carabajal, 2005).

The accurate digital elevation model of the Netherlands (AHN) was acquired between 1996 and 2003 and is based on airborne laser altimetry, with a point density of at least 1 point per 4m×4m

area in leaf-off conditions. There are four levels of detail: raw point cloud, and interpolated grid data of 5m×5m, 25m×25m and 100m×100m (Heerd et al., 2000). The raw point cloud is separated into vegetation points and ground surface points. It has to be noted that the filtering of the entire point cloud concentrated especially on vegetation, building points may therefore remain in the set of ground surface points. All data is in ASCII format files with XYZ coordinates given in the RDNAP coordinate system (Rijksdriehoeksmeting and Normaal Amsterdams Peil) (RDNAP, 2007).

In this paper, we first compare elevation profiles derived from ICESat GLA14 data to profiles derived from AHN ground surface data. Second, we will propose and evaluate a method to determine the bare earth elevation on the basis of a combination of GLA14 data, waveform centroid data of GLA05 data and processed full waveform GLA01 data. As most improvement is expected for waveforms over complex terrain, comparison results are differentiated with respect to land cover type. Four classes are distinguished: forest, urban, bare land and water. Waveforms are divided into these land cover classes according to the CORINE Land Cover 2000 database (CLC2000, 2006). It will be shown how to use the obtained profiles to find individual waveforms showing particular behaviour. This is illustrated in detail in three examples of waveforms over forest.

2 STUDY AREA AND DATASET

2.1 Study area

The area of study is the Netherlands, bounded approximately by 3^oE to 7^oE longitude and 50^oN to 54^oN latitude which contains a large variety of land cover types. Figure 1 shows a map of the digital elevation model (AHN) of the Netherlands, colored by height.

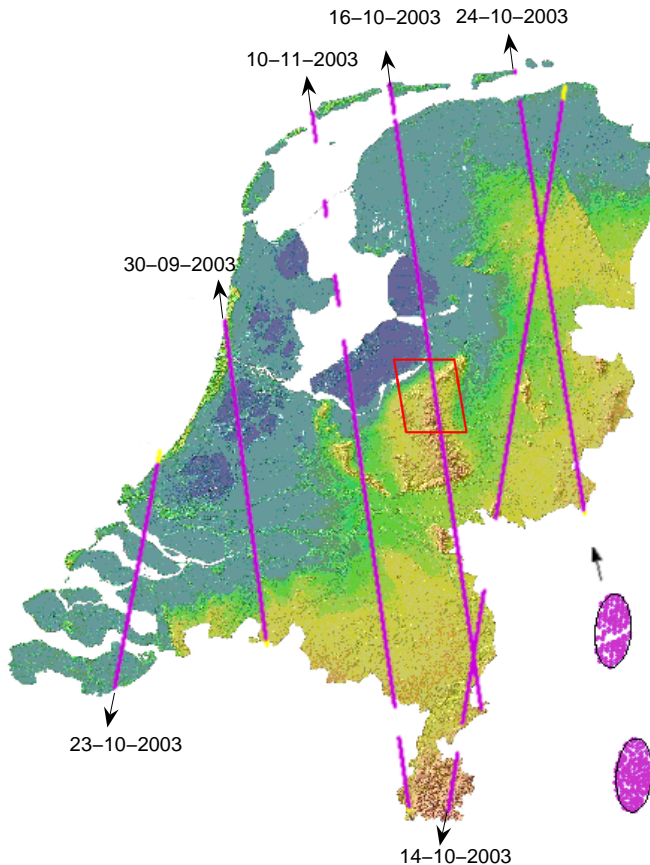


Figure 1. Study area: ICESat ground tracks (magenta) displayed with the actual height model of the Netherlands (AHN). The upward arrows indicate ascending tracks and the downward arrows descending tracks. In the bottom right corner two ICESat footprints filled with AHN points are shown.

2.2 CORINE Land Cover 2000 database (CLC2000)

The CORINE Land Cover 2000 database (CLC2000) was initiated by the European Environment Agency (EEA) and the Joint Research Centre (JRC). The CLC2000 database originated from the year 2000 but was actually obtained during a 3-year period from 1999 to 2001, with a horizontal geolocation accuracy of 25m based on satellite images of Landsat 7 ETM+ with 25m pixel resolution. The CLC2000 data product was obtained from the Landsat data via a computer-assisted visual interpretation of the satellite images, under the requirements of a scale of 1:100 000, a minimum mapping unit of 25 hectares and a pixel resolution of 100m (Perdigão and Annovi, 2006). The CLC2000 classification was hierarchical and distinguishes 44 classes at the third level, 15 classes at the second level and 5 classes at the first level. Detailed information of land cover levels can be found at the metadata section of the CLC2000 on the European Environment Agency website (CLC2000, 2006). The total thematic accuracy of the CLC2000 database was almost 95%. The database was geo-referenced in the European reference system (Hazeu, 2003).

2.3 ICESAT/GLAS

GLAS uses a laser altimeter to measure the distance between the satellite and the earth surface. The instrument time stamps each laser pulse emission, and measures the echo pulse waveform from the surface. GLAS acquires elevation profiles of the entire earth along tracks that are revisited in a 183-day repeat cycle, with 70m diameter footprints spaced every 175m. A waveform, recording

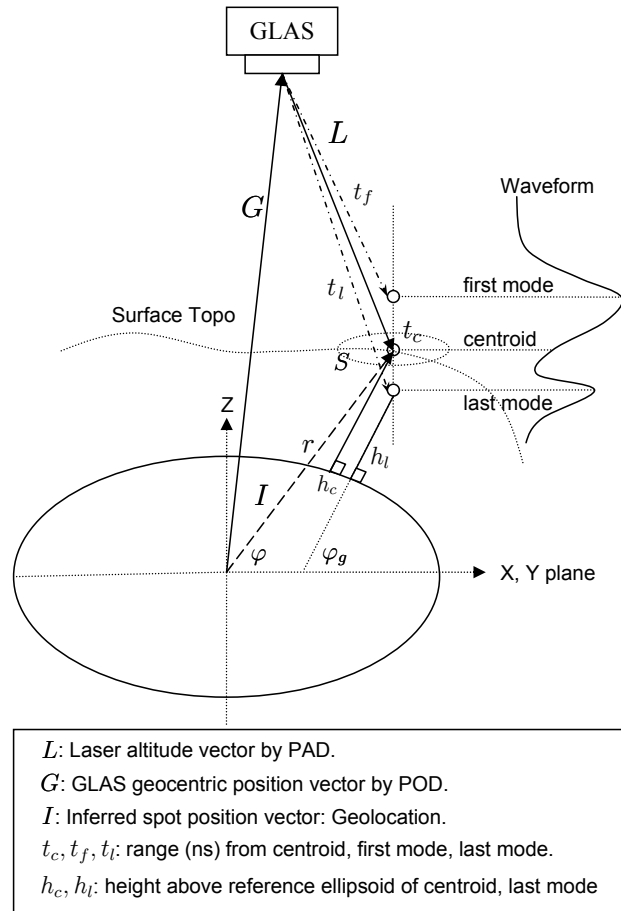


Figure 2. Principal of ICESat geolocation and surface elevation determination.

laser back-scatter energy as a function of time, is digitized in 544 consecutive bins at a temporal resolution of 1ns over land for each footprint (NSIDC, 2005). The land waveform of 15cm vertical resolution yields an 81.6m height range (544 waveform bins \times 15cm/bin) for laser L1 and 150m (1000 bins \times 15cm/bin) for laser L3 (Harding and Carabjal, 2005). GLAS carries three different laser altimeters, L1, L2 and L3. Laser 1 was turned off shortly after the Spring 2003 campaign, to be replaced by Laser 2. Laser 2 operates in both height ranges.

2.3.1 ICESat data overview: Among 15 GLAS data products, we investigate the products of GLA01, GLA05 and GLA14. The data sets we consider were acquired in the period from 2003-09-25 to 2003-11-18 and are all from release 26. There are six tracks with 6594 waveforms in total (Figure 1). The footprints of these waveforms are elliptical, its power distribution has a central maximum, while energy decreases towards the boundary. The size of the ellipse is 95m \times 52m on average (Harding and Carabjal, 2005).

The GLA01 is a raw level 1 product that contains the full waveform data. The GLA14 is a level 2 product of land surface elevation. Due to the potential complexities of land returns including possibly combined influences of slope, roughness, vegetation and cultural features, this level 2 land product was obtained by using a land-specific range¹. The land-specific range is defined as the travel time from the GLAS sensor to the centroid of the received waveform signal (see Figure 2) and stored in the GLA05. This

¹land-specific range means not in polar or ocean regions

land-specific range is then used for the computation of geolocated latitude, longitude and footprint elevation after all instrumental, atmospherical and tidal corrections have been applied (Brenner et al., 2003).

2.3.2 Principal of determination of geolocation and surface elevation: A geolocated surface elevation, S , is determined as a sum of a laser altimeter vector, L , and a ICESat/GLAS geocentric vector, G , with respect to the center of mass of the earth (see Figure 2). The laser altimeter vector includes the GLAS laser pointing angle and a range, t_i , between the GLAS instrument and the surface as identified by measuring a travel time of a transmitted pulse until its return as a waveform. The range is then calculated as a half-travel time multiplied with the speed of light. The geocentric vector represents the orbit position of the ICESat satellite with respect to the center of mass of the earth. Therefore the laser spot or geolocation is inferred by the sum of these two vectors. The surface elevation is obtained by converting the geocentric laser spot position (r, φ, λ) to ellipsoidal height and geodetic latitude and longitude (h, φ_g, λ) .

In Figure 2, the land-specific range from GLAS to the ground surface can be calculated based on different waveform parameters like the waveform centroid or the height of the first or last mode of the waveform. Using the first mode gives a shorter range and results in a higher elevation point. The first mode results from elevation points of trees, forest or artificial features like buildings. Using the centroid of the waveform gives an average elevation while the last mode potentially represents the ground surface.

3 METHODOLOGY

A flowchart of the methodology is shown in Figure 3. For comparison between ICESat and AHN, both data sets need to be available in the same georeferenced coordinate system, for which RD-NAP is chosen. The GLA14 data are first converted into RDNAP coordinates. Next those AHN ground data are extracted whose horizontal position is within the given GLA14 footprint ellipses. Because the ICESat footprint has an approximate diameter of 70 meter, the AHN points within the footprint need to be interpolated to a representative elevation point. For ICESat two profiles are determined, one based on the GLA14 ‘mean’ surface elevations only, the other derived from combining the GLA14 elevations with the results of the processing of the GLA01 waveforms and the centroid of GLA05. Both profiles are compared to the same profile of the corresponding interpolated AHN elevations, leading to the two results to be compared and discussed.

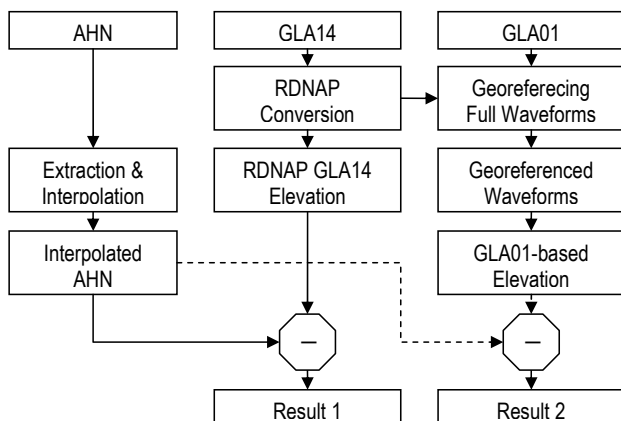


Figure 3. A methodology flowchart.

3.1 Interpolation of AHN data

A 70m-diameter ICESat footprint contains approximately 700 AHN data points. Therefore it is necessary to compute a mean AHN elevation for the purpose of comparing elevation profiles of AHN and ICESat data. To avoid effects of clusters in the spatial distribution of the AHN points, the AHN points are first interpolated to a regular grid, prior to the calculation of a mean AHN height. Based on the average point density of the AHN data of 0.20 point/m², a grid cell size of 4m×4m is chosen. Figure 4 shows a typical distribution of raw AHN points together with the regular grid points.

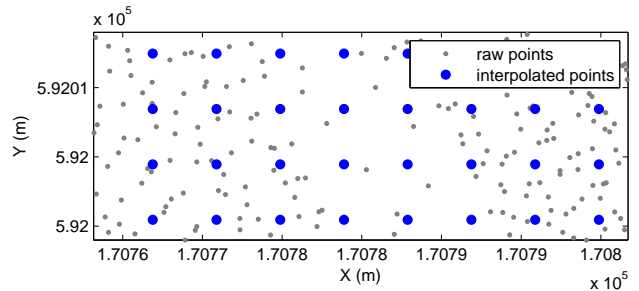


Figure 4. Raw AHN ground points (gray) and interpolated grid points (blue).

3.2 Height difference between GLA14 and interpolated AHN

A mean AHN elevation is obtained from interpolating the regular grid points within an ICESat footprint ellipse. This mean elevation is then subtracted from the ICESat GLA14 elevation of that footprint to obtain an AHN-GLA14 height difference. In this study, six ICESat tracks or six elevation profiles are used. Compare Table 1 and Figure 1 for an overview of the ICESat tracks. The differences over the total of the six tracks are averaged to obtain the final results as shown in Table 2.

3.3 Derivation of GLA01-based elevation data

The georeferenced waveform is decomposed into a maximum of six Gaussian components which allows to derive waveform parameters as amplitude, width and location of each Gaussian

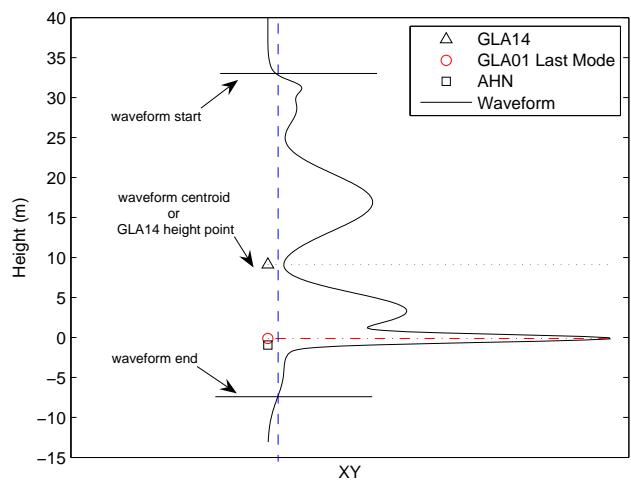


Figure 5. A waveform (black curve) is georeferenced by matching the waveform centroid (horizontal dotted line) to a GLA14 elevation point (black triangle). The GLA01-derived elevation is the centroid of the last peak (red circle).

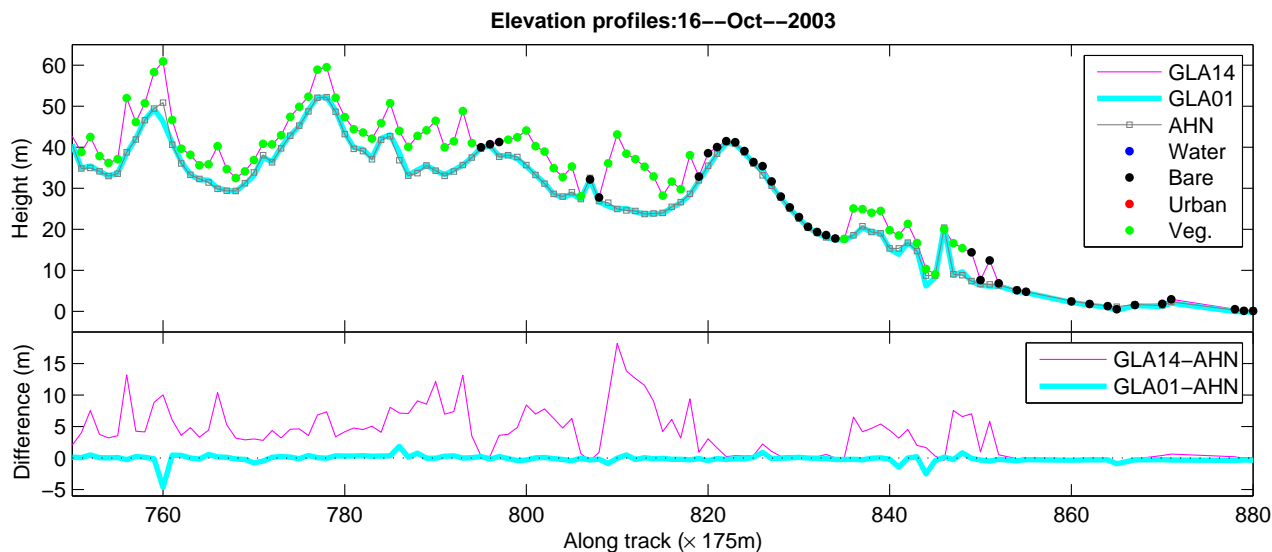


Figure 6. Top: Elevation profiles based on ICESat GLA14 data (red line), AHN data (black squared line) and ICESat GLA01 data (cyan line). Bottom: height differences between AHN and GLA14 (red) and AHN and GLA01 (blue). This profile corresponds to the red box in Figure 1.

mode (Duong et al., 2006). The first Gaussian refers to the highest point in the illuminated footprint which typically corresponds to a tree top or building roof. The centroid of the complete waveform corresponds to the average height of the objects in the footprint, while the last Gaussian mode is resulting from the lowest elevation in the footprint. Over flat terrain the lowest elevation mostly corresponds to the elevation of the ground surface. As Dutch topography is in general flat, the last Gaussian or last mode will be used in this research to obtain a ground surface elevation.

In Figure 5, the ICESat GLA14 elevation is represented by a black triangle; the black square represents the mean AHN elevation within the 70m-diameter footprint. For georeferencing the waveform (black curve), the waveform centroid (horizontal dotted line, black) is matched with the GLA14 elevation point. Therefore, the last mode is the most suitable representation of the ground elevation in the ICESat data (red circle). Finally the 'last mode elevation' of the ground surface is extracted by subtracting the distance between the centroid and the peak of the last mode from the GLA14 elevation.

4 RESULTS AND COMPARISON

4.1 Waveforms used

The waveforms from six ICESat tracks are assigned to different land cover classes based on the CLC2000 land cover database. On average, 97% of the ICESat measurements to the ground were successful, whereas in the remaining 3% percent, no data was acquired. One possible reason is the weather (e.g. cloud cover, data acquisition was in September-November). A number of 6594 waveforms is used, 595 waveforms are over vegetation, 790 over urban areas, 3472 over bare land and 149 over water (Table 1). About 20% of the waveforms was removed from analysis due to one of the following reasons:

- Some noisy waveforms could not be decomposed by the Gaussian fitting algorithm.
- No AHN points are available within the waveform footprint.

- Many ICESat pulses of the 24-10 track along 100km, see Figure 1, coincide with a cloud layer (our assumption) of at least 200m height and are therefore not considered reliable.

Track	Date	Number of ICESat waveforms					Total	Lost
		F	U	B	W			
1	30-09	72	158	456	28	795	81	
2	14-10	89	316	933	16	1534	180	
3	16-10	305	88	777	36	1515	309	
4	23-10	8	54	351	42	584	129	
5	24-10	2	17	361	0	979	599	
6	10-11	119	157	594	27	1187	290	
Total		595	790	3472	149	6594	1588	

Table 1. Number of ICESat waveforms used: F (Forest), U (Urban), B (Bare land) and W (Water). The column 'Lost' gives the number of waveforms that were discarded because of e.g. high noise level, large height differences (200m) between the GLA14 and the AHN elevation or missing AHN data.

4.2 Height differences AHN-GLA14 vs AHN-GLA01

Tr.	GLA14 - AHN terrain, (m)			
	F	U	B	W
1	4.68±4.5	2.01±3.2	0.26±1.4	-0.66±1.2
2	6.62±2.9	1.81±2.5	0.79±2.1	0.59±1.4
3	6.76±3.5	1.44±3.5	0.57±1.7	-0.13±0.9
4	7.47±5.7	0.85±1.5	0.48±1.1	0.21±0.7
5	4.52±1.0	1.12±1.3	0.35±1.2	N/A
6	3.89±3.1	0.19±2.0	0.14±1.8	-0.35±1.4
Total	5.66±3.5	1.24±2.3	0.43±1.5	-0.07±1.1

Table 2. Height differences and its standard deviation between GLA14 and AHN

In Tables 2 and 3 the average height differences between the AHN elevation profiles and the GLA14 'mean elevation' (Tables 2) and the GLA01 'ground elevation' (Tables 3) are given. As expected, it shows that the average height difference between the 'mean elevation' and the AHN profiles is maximal over forested areas (5.66m). The differences are smaller over urban (1.24m) and bare land (0.43m) and minimal over water (0.07m). This is further illustrated in Figure 6, where a profile of 22.5km is shown along

GLA01-derived – AHN terrain, (m)				
Tr.	F	U	B	W
1	-0.75±1.2	-0.84±3.0	-0.86±1.4	-1.81±1.8
2	-0.29±1.4	-1.11±2.3	-0.48±0.9	-0.49±0.7
3	-0.25±1.5	-1.73±2.0	-0.53±1.0	-1.54±1.4
4	-0.33±0.7	-0.58±0.8	-0.33±0.8	-0.22±1.0
5	-0.18±0.1	-0.45±0.8	-0.29±0.5	N/A
6	-0.49±1.8	-1.42±2.5	-0.58±1.1	-1.25±1.2
To.	-0.38±1.1	-1.02±1.9	-0.51±0.9	-1.06±1.2

Table 3. Height differences and its standard deviation between GLA01-derived elevation data and AHN

the ICESat track of October 16, 2003. Clearly, large differences of up to 20 m occur in forested areas. The difference between the waveform centroid, giving the GLA14 ‘mean elevation’ and the surface elevation as given by the AHN points is larger in case of a wide spread multi-modal waveform. These multi-modal waveforms occur in urban and certainly in forested areas. The width of the waveforms is further increased in case the terrain is not flat.

Table 3 shows the differences between the ICESat last mode or ‘ground elevation’ profile and the AHN profile. The average height difference over forest is significantly reduced from more than five meter to less than half a meter, while the spread in height difference is reduced by about 70% as well. For the other three land cover classes no significant improvement is found. The improvement over forest is visualized in Figure 6. The bottom image shows that the ICESat ‘ground elevation’ profile (in cyan) is always closer to the AHN profile than the ICESat ‘mean elevation’ profile. It is also visible that the ICESat ‘ground elevation’ profile is sometimes even lower than the AHN profile. This can be explained as follows. If the terrain is curved, interpolation of the AHN laser points within the ICESat footprint will result in a mean AHN elevation value higher than the lower terrain points. Meanwhile the height of the peak of the last mode can be positioned below the mean AHN elevation, resulting in a negative offset. Moreover, building points still remain in the set of the AHN ground points therefore it also results a height difference in a negative value.

4.3 Waveform examples

The profile in Figure 6 allows to look for specific examples that give insight in the differences between the three heights that are considered, the ICESat ‘mean elevation’, the ICESat ‘ground elevation’ and the AHN mean of the ground points. Below three typical examples are discussed. The first example is an ‘out of the book’ forest example, in the second case the canopy thickness is so large that the visible ICESat ground return is ignored by the decomposition algorithm while in the third example the ICESat ground return is totally absent due to the high canopy thickness.

4.3.1 Regular canopy thickness example: Figure 7(a) shows a case where taking the ICESat ‘ground elevation’ gives clearly a better value than the ICESat ‘mean elevation’, when compared to the mean AHN ground elevation. The AHN vegetation points (green) and ground points (black) precisely match to the ICESat raw full waveform (red) and to the fitted waveform (dashed black). The peak of the last Gaussian mode at 10m height corresponds to the average height of the AHN ground points within the ICESat 70m footprint. The peak of the second-last Gaussian mode corresponds to the average height of the low vegetation at 10m–15m that is also represented by the AHN points. The first Gaussian peak represents the average height of the canopy. The width of the first Gaussian gives a measure for the canopy depth. This example illustrates, that spaceborne full waveform altimetry can be a possible method for extraction of vegetation height

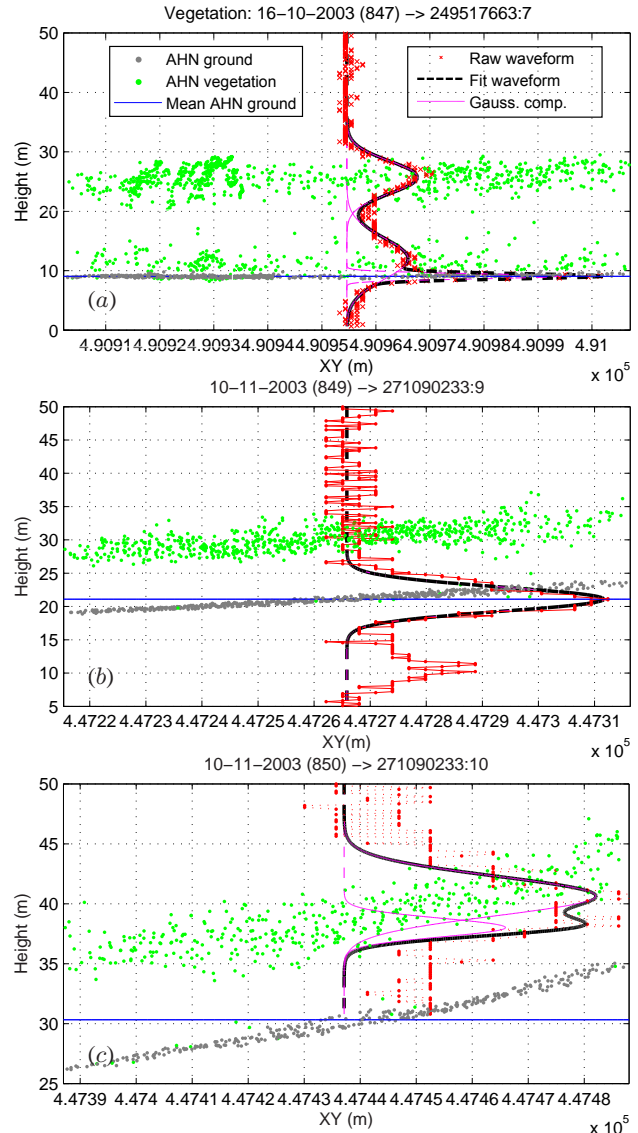


Figure 7. Three waveforms over forest. Good agreement between AHN and GLA14 is obtained for the top panel but insufficient results were found for the middle and bottom panel.

and vegetation characterization on single shot basis. The return energy, which is also recorded by GLAS, is about 20 fJ. This is well above the threshold of 5fJ (Fricker et al., 2005), under which the measurement noise increases. These high noise levels can be caused by atmospheric forward scattering and degradation of the laser transmitted power over time. Both effects lead to a decrease in received energy (and therefore SNR).

4.3.2 Higher canopy thickness: (i.) Figure 7(b) shows a raw waveform (red) with two dominant peaks. It agrees with the AHN data in the sense that it has one peak corresponding to the AHN ground points and one larger peak corresponding to the dense vegetation points. The last peak is ignored however by our waveform decomposition step due to the high noise level in the waveform. However, the distance between the lower and the higher peak of the raw waveform corresponds very well to the vegetation height whereas the absolute height may not be correct. Comparing Figure 7(b) and Figure 7(a) shows that the noise level is about three times higher in the lower example. In this case, the return waveform energy of 1.58 fJ which is very low compared to the threshold of 5 fJ (Fricker et al., 2005).

4.3.3 High canopy thickness: Figure 7(c) shows a case where the ICESat waveform shows only one mode, and where we need the AHN data to tell us that in fact this one mode corresponds to an unpenetrable forest canopy. In this case the ICESat 'mean elevation' and the ICESat 'ground elevation' are equal, but both higher than the AHN ground point elevation. This shot is a direct neighbor (175m) of the shot shown in Figure 7(b). The return energy is 3.40 fJ. This value is also below the 5fJ threshold.

4.3.4 'Glowing' effects: In Figure 8, a series of waveforms with systematic underestimation of the (surface) height is shown. Although the Gaussian components of the waveforms could be reconstructed, all but the first mode are weakly determined. Apparently these erroneous modes demonstrate some kind of 'glowing' effect. This assumption is supported by considering the orthophoto of the footprint locations: in most cases the footprints cover flat terrain which should result in one waveform mode only. Possible error sources for this behaviour are forward scattering by cloud cover or problems with the signal detection at the GLAS receiver unit for very low energy returns. In this case, the return energy ranges between 0.29 fJ to 2.72 fJ. Such waveforms could be automatically removed by increasing the requirements in the waveform decomposition step or by imposing a threshold on the minimal return energy.

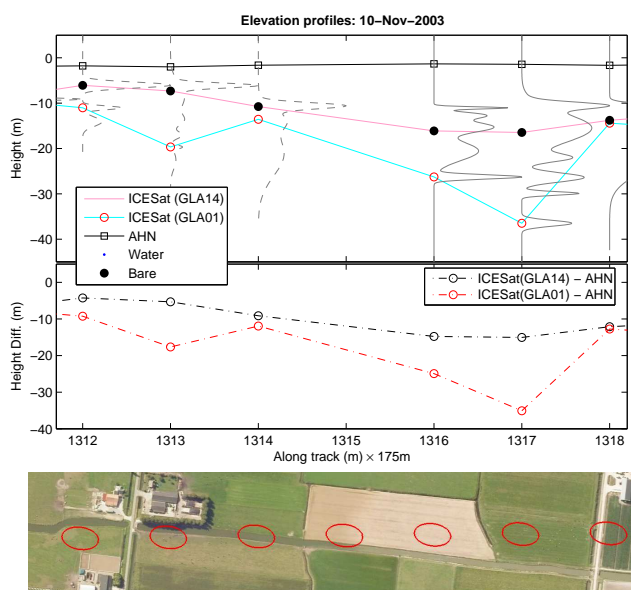


Figure 8. Elevation profiles (top) and height differences (middle) of ICESat, GLA14 and GLA01-derived elevations for some bad cases. At the bottom the ICESat footprints overlaid on a Google Earth image are shown.

5 CONCLUSIONS

In this paper we have compared three laser altimetry profiles. One based on ground return points from airborne laser data of the Dutch national height product AHN, and two based on ICESat data. NASA provides height data in the GLA14 product that are based on the centroid of the returned ICESat waveform. By considering the position of the last mode in ICESat's raw return waveforms a more realistic ground surface profile can be obtained from the ICESat data that is on average -0.38m below the mean AHN height, with an average standard deviation of ± 1.1 m.

Study of the three profiles gave us examples where the high forest canopy block almost all ICESat laser energy. This gives one

explanation for the remaining differences between ICESat ground elevation' profiles and the AHN ground surface profiles. Neglecting the terrain slope may be another error source that should be corrected for in future. Further research should focus on two directions: those footprints where the ICESat waveform shape match the shape of a waveform built up out of AHN points can be used to assess the accuracy of ICESat georeferencing. On the other hand, analysis of the height difference in the three profiles will lead us to further examples where current waveform processing still fails and should be improved.

ACKNOWLEDGEMENTS

The authors would like to thank the National Snow and Ice Data Center, Gerard Hazeu from Wageningen University - The Netherlands and the European Environment Agency for their guidelines and data distribution. This project is funded by the Delft Research Centre Earth.

REFERENCES

- Brenner, A. C., Zwally, H. J., Bentley, C. R., Csatho, B. M., Harding, D. J., Hofton, M. A., Minster, J. B., Roberts, L. A., Saba, J. L., Thomas, R. H. and Yi, D., 2003. Geoscience laser altimeter system algorithm theoretical basis document: Derivation of range and range distributions from laser pulse waveform analysis. 92pp. Available online at: <http://www.csr.utexas.edu/glas/atbd.html> (access 22 February 2006).
- CLC2000, 2006. Corine land cover 2000. european environment agency. Available online at: <http://dataservice.eea.eu.int/dataservice/metadetails.asp?id=822> (access 5 April 2006).
- Duong, H., Pfeifer, N. and Lindenbergh, R., 2006. Analysis of repeated ICESat full waveform data: methodology and leaf-on / leaf-off comparison. In Proceedings: Workshop on 3D Remote Sensing in Forestry. Available online at: <http://www.rali.boku.ac.at/3drsforestry.html>, pp. 239–248.
- Fricker, H. A., Borsa, A., Minster, B., Carabajal, C., Quinn, K. and Bills, B., 2005. Assessment of ICESat performance at the salar de uyuni, bolivia. Geophysical Research Letter. L21S06, doi:10.1029/2005GL023423.
- Harding, D. J. and Carabajal, C. C., 2005. ICESat waveform measurements of within-footprint topographic relief and vegetation vertical structure. Geophysical Research Letters. L21S10, doi:10.1029/2005GL023471.
- Hazeu, G. W., 2003. CLC2000 land cover database of the Netherlands. monitoring land cover changes between 1986 and 2000. Wageningen, Alterra, Green World Research. Alterra-rapport 775/CGI-rapport 03-006.
- Heerd, R., Kuijlaars, E., Teeuw, M. and 't Zand, R., 2000. Produktspecificatie AHN. Rijkswaterstaat, Adviesdienst Geo-informatie en ICT.
- Perdigão, V. and Annovi, A., 2006. Technical and methodological guide for updating CORINE land cover database. Joint Research Centre/European Environment Agency. Available online at: <http://www.ec-gis.org/document.cfm?id=197&db=document> (access on 29 December 2006).
- NSIDC, 2005. Frequently asked question. ICESat/GLAS Data at NSIDC, <http://nsidc.org/data/icesat/faq.html>. Last visit: 8-May-2007.
- RDNAP, 2007. Rijksdriehoeksmeting and Normaal Amsterdams peil. Dutch Geometric Infrastructure, <http://www.rdnap.nl/>. Last visit: 8-May-2007.
- Zwally, J., 2002. ICESat's laser measurements of polar ice, atmosphere, ocean, and land. Journal of Geodynamics 34, pp. 405–445.

SIMULATING SAMPLING EFFICIENCY IN AIRBORNE LASER SCANNING BASED FOREST INVENTORY

L. Ene^a, E. Næsset^b, T. Gobakken^b

^a Norwegian University of Life Sciences, Graduate student - liviue@student.umb.no

^b Norwegian University of Life Sciences, Dep. of Ecology and Natural Resource Management - (erik.naesset, terje.gobakken)@umb.no

KEY WORDS: Airborne laser scanner, Simulator, Forest inventory

ABSTRACT:

A simple simulator was developed to test whether airborne laser scanning can be used as a strip sampling tool for forest inventory purposes. The simulator is based on the existing two stages, grid based laser inventory procedure. A population of trees was created using an existing forest stand structure generator. Each tree was represented by means of its 3D-crown model derived from airborne laser scanning measurements and field measured parameters, i.e. total tree height, height of crown base and average crown diameter. Monte Carlo simulations were run to assess the efficiency of volume estimates obtained from airborne laser scanning and ground based inventory. The lowest RMSE for the laser based estimates was $5.1 \text{ m}^3\text{ha}^{-1}$ (2.0%) and the highest was $8.4 \text{ m}^3\text{ha}^{-1}$ (3.3%), while RMSE for the ground based estimates varied between $13.7 \text{ m}^3\text{ha}^{-1}$ (5.4%) and $18.4 \text{ m}^3\text{ha}^{-1}$ (7.2%). The LIDAR based estimation was on average 6.3 times more efficient in terms of MSE than ground based sampling. The RMSE of the volume estimates increased with increasing plot size, for a given sampling intensity. The results indicated that forest surveys over large areas carried out using airborne laser scanning as a strip sampling tool can provide accurate estimates, and can be more effective than traditional systematic ground plot based inventories.

1. INTRODUCTION

During the past two decades, remote sensing techniques have proven to meet some of the demand for environmental related data at fairly low cost. Among these techniques, small footprint LIDAR (LIght Detection and Ranging) has become one of the most common remotely sensed data sources for analyzing the canopy structure at the scale of operational forest management (Wynne, 2006).

Research has shown that profiling LIDAR can provide reliable biomass sampling based estimates at low costs (e.g. Nelson et al., 2006). The LIDAR based procedure consists of a two stage sampling scheme. LIDAR transects are taken by flying parallel flight lines separated by many kilometers over the area in question. Systematically distributed ground plots or ground transects are measured along the LIDAR transect. Ground based estimates are regressed against LIDAR measurements, and the resulting regression equation are used for prediction along the LIDAR transects across the entire sampled area (Nelson et al., 2004).

In contrast to profiling LIDAR systems which only collects a narrow line of data on the ground, commercial airborne laser scanners provide an accurately geolocated cloud of 3-dimensional observations, which can be related to ground measurements such as plots of various shapes and sizes. Scanning LIDAR is today used operationally for stand-based "wall-to-wall" inventories of forest stands in Norway (Næsset, 2004). For larger regions such as counties or nations, "wall-to-wall" inventories are not feasible. However, even scanning systems can be used in regional forest inventory, considering the flight lines as part of a strip sampling design by flying parallel, equally spaced strips over the study area and collecting sample plots only within strips, using for example systematic sampling schemes. Sampling applications are often relevant in areas with a size where it is not feasible to establish a ground

truth reference value. Consequently, designing an optimal inventory system has to rely on some kind of simulation, where different combinations of field and airborne data collection can be explored.

The aim of this study was to develop a prototype of a simple, small-scale simulator in order to assess the efficiency of laser scanning based volume estimates relative to the corresponding ground plot based estimates, when airborne laser scanning was used as a strip sampling tool. This simulator was based on the two stages, grid based sampling procedure developed and tested by Næsset & Bjercknes (2001) and Næsset (2002, 2004).

2. MATERIAL AND METHODS

Forest stand data and combinations of ground measurements of single tree parameters and airborne laser data were used to build 3D crown models for Norway spruce trees. Then, existing forest stand generator software and these models were employed to obtain a virtual forest as input for the simulations.

2.1 Stand data

The empirical stand data and single tree parameters were comprised in two datasets.

The first dataset (see Bollandsås & Næsset, 2007; Solberg et al., 2006) was collected in summer 2003. Twenty circular plots of 0.1 ha were collected from a boreal nature reserve located in south-eastern Norway. The forest was multilayered with a broad range of tree sizes and stand ages, and dominated by Norway spruce [*Picea abies* (L.) Karst.] and Scots pine (*Pinus silvestris* L.). The plots were established in subjectively selected spruce dominated sites. On each plot, all trees with height (d_{bh}) $\geq 3\text{cm}$ were callipered and tree heights were measured on trees selected with probability proportional to stem basal area. Mean

diameter was defined as diameter corresponding to mean stem basal area (d_{BA}) and mean height was defined as the average basal area weighted (Lorey's) height (h_L).

Both Global Positioning System (GPS) and Global Navigation Satellite System (GLONASS) were used to determine the planimetric coordinates (Euref89) of the plot centers. The average estimated accuracy of the plot coordinates was 10 cm.

For the first dataset, polar coordinates from the plot centre were registered for all trees with $d_{bh} \geq 3$ cm. Total tree height, height of crown base, crown radius in four cardinal directions, and average crown diameter were measured on trees selected from each plot. The final coordinates for all single trees were computed in Euref89, using plot centre coordinates and plot-wise polar tree coordinates.

The second dataset (see Næsset, 2004) comprised 60 large plots located in a productive forest area of approximately 5000 ha in the municipality of Krødsherad, south-eastern Norway. The forest composition was dominated by Norway spruce and Scots pine, while younger stands were dominated by deciduous species, mainly birch (*Betula pubescens* Ehrh.). The plot areas were from 3121 to 4219 m², with an average of 3739 m². Within each plot, all trees with diameter at breast height $d_{bh} \geq 4$ cm and $d_{bh} \geq 10$ cm were callipered in young and mature stands, respectively, using 2 cm diameter classes. Height measurements were taken from trees selected with probability proportional to stem basal area at breast height. For each plot, the mean height corresponding to Lorey's height was computed from the mean height of the individual diameter classes, weighted by total plot basal area for each diameter class.

2.2 Laser data

Laser scanner data were acquired during June 2005 (leaf-on canopy condition) from the same area as the first dataset, with an Optech ALTM 3100 sensor operating at 100 kHz laser pulse repetition rate and 70 Hz scanning frequency. The aircraft was flown approximately 750 m above ground with an average speed of 75 ms⁻¹. The maximum half scan angle was 10°, and the corresponding swath width was about 264 m. Pulses transmitted at scan angles that exceeded 8° were excluded from the final dataset. The average footprint size was about of 21 cm, with an average point density of 5.09 m⁻². First and last echo were recorded.

2.3 Laser-derived single tree models

Laser data and the ground measurements collected in summer 2003 from 0.1 ha stand plots comprised into the first dataset were used to obtain crown representation of Norway spruce trees. Laser pulse hits were related to tree crown projections by

the mean of planimetric coordinates, and then the resulted laser point clouds were considered as spatial crown models for Norway spruce trees. Laser pulses with heights below 2 m were considered as ground points.

The relationships between field and laser measurements were established for a total of 435 spruce trees. Hence, each of these trees were represented as unique combinations of diameter (d_{bh}), height (h), crown height (c_h), crown projection radius (c_r), stem volume (v) (Table 1), and the associated 3D crown models. For each of these trees, the volume was calculated by the means of functions for Norway spruce with bark (Vestjordet 1967). Further in this study, the trees were called "single tree models".

Metrics	Mean	S.D.	Min	Median	Max
d_{bh} (cm)	19.8	10.4	3.2	18.8	51
h (m)	15.8	6.1	3.6	16	29.5
c_h (m)	3.4	2.4	0.2	3.1	13.5
c_r (m)	1.3	0.4	0.6	1.3	2.9
v (m ³)	0.38	0.41	0.003	0.22	2.46

^a d_{bh} -diameter; h -height; c_h -crown height; c_r -crown radius; v -volume; S.D.-standard error

Table 1. Descriptive statistics for individual tree model parameters ^a.

2.4 Virtual forest

The program package SILVA 2.2 (Pretzsch et al., 2002) was used to generate a virtual forest. The stand generator provides a tree list with associated parameters. For each tree, the following information was recorded: tree species, diameter at breast height, total height and height of crown base, crown diameter and tree coordinates (x , y). To generate the tree lists, the input parameters were tree species, d_{BA} (cm), d_{max} (cm), h_L (m), and N , obtained from ground measurements. Only 13 plots from the first dataset and 25 plots from the second dataset provided acceptable combinations of input parameters which could be used to obtain tree lists by means of SILVA 2.2 (Tab. 2). The other plots were rejected due to inadvertencies between the test plot reference data and model calibration of the stand generator. Totally, a number of 38 tree lists were obtained and each of them was considered as a possible realization of a forest stand, given the ground-measured input parameters.

The virtual forest study area was defined in a 2D-local coordinate system with axes being multiples of 100 m, and the terrain was assumed to be flat. The frame of study area was considered to be a two-dimensional array, where each (i , j) position is a squared area representing a forest stand of 1.0 ha.

	Stand parameters															
	First dataset (0.1 ha plots)				Second dataset (large plots)											
	$d_{BA} s$	$d_{max} s$	$h_L s$	Ns	$d_{BA} s$	$d_{max} s$	$h_L s$	Ns	$d_{BA} p$	$d_{max} p$	$h_L p$	Np	$d_{BA} b$	$d_{max} b$	$h_L b$	Nb
Max	30.1	60.6	28.9	1040	27.6	51	22.2	904	36.3	49	23.6	622	23.9	47	20	286
Min	19.9	39.6	17.7	650	12	17	8.4	13	18.7	35	12.7	10	11.5	13	10.8	5
Mean	17.2	37.3	17	671	17.4	32.1	14.9	360	21.6	35.5	14.4	229	12.6	21.7	10.6	82

^a d_{BA} =basal area mean diameter (cm); d_{max} =maximum diameter (cm); h_L =basal area weighted mean height (m); N =stem number per ha; s =Norway spruce; p =Scots pine; b =deciduous trees (assimilated with birch).

Table 2. Summary of stand metrics for 13 selected plots from the first dataset and 25 plots from the second dataset ^a.

To create the population, one of the 38 virtual forest stands of 1.0 ha generated by means of SILVA 2.2 was randomly allocated to each (i, j) array position, and then the stand coordinates for each tree were translated according to the new location within the array. The neighborhood effects among forest stands were ignored. Thus, the spatial structure of each cell was supposed to be independent of the position in the array. The study area was defined as a square of 36 km².

Further, each tree from the tree list was substituted with a diameter-equivalent single tree model. Because of the relatively small number of single tree models (i.e. 435 trees) which could be derived from available dataset, only d_{bh} was used as key. The rest of the single tree model parameters, i.e. height, crown height, crown radius, laser pulse heights, and stem volumes, were then transferred to the corresponding diameter-equivalent trees from the tree list positioned at (x_i, y_i) coordinates in the study area. The matching results often consisted of more than one single tree model with equal diameters. In this situation, only one of these tree models was randomly selected to replace the tree at the position (x_i, y_i) from the generated forest stand. For the situations when diameter matching did not occur- which means that some trees from generated forest stands have diameters that were not among the diameters of single tree models, a single tree model with diameter closest to the missing value, either larger or smaller, was selected instead. Thus, the study area was re-populated with laser derived tree models, and the volume of the entire population was calculated as the sum of individual trees.

For other species than Norway spruce, i.e. Scots pine and birch, there were no available laser data for building 3D crown models. For this reason, diameter matching was done regardless of species, which means that trees of different species could be matched if they had the same diameter. After diameter matching, trees from the tree list generated by means of forest stand generator were replaced with diameter equivalent Norway spruce single tree models, regardless tree species.

Laser scanning data consist of clouds of laser hits related to tree crowns. In this study, each laser hit (first echo) has known x , y and z -coordinates, but in this analysis, the (x_i, y_i) coordinates of each laser hit were discarded. It was assumed that laser hits related to trees inside a grid cell fall inside the same cell where these trees are located, and that all the hits inside a tree crown projection belong only to that tree.

2.5 Simulator

The strip sampling simulation was based on the two-stage procedure described by Næsset & Bjerknes (2001) and Næsset (2002, 2004) and follows the approach proposed by Gobakken et al. (2006). In parallel, an estimation of mean volume by means of ground plot systematic sampling was done, as a kind of conventional inventory. The sampling units consist of equal strips containing the same number of grid cells. The total volume was estimated as the sum of predicted volume for all grid cells over all strips. Monte Carlo (MC) estimates of population mean volume and sampling error were derived running 50 iterations for each sampling scheme. Bias, standard deviation and RMSE for estimated mean values were used to assess the sampling estimates against the reference volume of the predefined population. The systematic samples of laser scanning strips and ground plots were treated as random samples. Relative efficiency of regression based estimates obtained from laser scanning strip sampling against ground

based systematic plot sampling estimates was assessed for each sampling scheme.

Computations

Multiple regression analysis was used to establish stratum-specific relationships between field measurements and laser derived metrics. Based on previous findings (e.g. Magnussen & Boudewyn, 1998; Næsset, 1997, 2002, 2004), two independent variables derived from first laser pulse returns were used for volume prediction within each grid cell: the percentile corresponding to the 9th quantile of laser canopy height (h_{90}) considering the lowest canopy height (≥ 2 m), and the canopy density corresponding to the proportion of the first pulse laser hits (d_0). Canopy density was defined as the proportions of first pulse laser hits above 2 m to total number of first pulse returns. To calculate the canopy density, it was necessary to find the total number of laser hits within each grid cell. Because the last echoes from initial laser scanning data were not available, it was assumed that each grid cell had a uniform coverage of laser hits. Thus, the total number of laser hits within a grid cell could be linearly extrapolated from the number of hits that fall inside the crown projection. Laser hits with heights below 2 m were considered as ground points as well.

The full second order regression model based on these variables was subject to stepwise variable selection to develop final models for prediction. Exploratory regression analysis was run to detect possible deviations from model assumptions. Various variance stabilizing transformations of the dependent variable (sample plot volume) were analytically assessed by the means of the Box-Cox method. Five regression models were finally proposed: (1) a multiplicative model, (2) a linear model without transformations, and three different models with transformed response variable: (3) $\log(y)$, (4) \sqrt{y} , and (5) $\text{asin}(\sqrt{y})$. For the multiplicative model, only two independent variables (h_{90} and d_0) were used, and consequently this model was not subject to stepwise selection.

For the other regression models, an empirical approach was used to obtain regression equations. Before each simulation, a number of 20 iterations were used to select the final regression models. First, a stripe sampling scheme was randomly generated over the study area, and the location of each stripe and correspondent sample plots were hold fixed. Initial sampling trials were run, and for each iteration a new population outcome was generated and sampled. Stepwise regression ($p_{in} = 0.05$, $p_{out} = 0.10$) was used for model selection, and each resulted subset model was registered. After running all iterations, the most frequently used model form for each regression model was selected as final model to be used for prediction during sampling simulations. Since serious multicollinearity problems occurred, best subsets regression models were also derived and compared to the stepwise regression subsets, in order to select unbiased regression models.

To estimate the population volume, Monte Carlo experiments were run to derive laser scanning and ground-based mean volume estimates. Initial tests showed that cumulated mean volume estimates over 50 iterations converged towards the value of MC estimates, while the sampling error decreased asymptotically. However, the number of iterations should vary with the study area, sample design, and population variability.

Squared sample plots of 200, 400, and 600 m² were used to provide ground estimates. Using squared plots significantly improves the computational performance during simulation.

Parallel laser strips with widths of 160, 180, and 200 m spaced at 1500 m were generated. The sampling intensity for different plot sizes was held almost constant around 0.6% of stripe sampling area, and the sample size varied with plots size. Compared to sampling intensities in ongoing research studies, which typically are less than 0.003% (Gobakken et al., 2006), the sampling intensity at stand plots level is much higher, but necessary to reach ground samples large enough to get reliable regression estimates.

Finally, the MC estimates for both laser strip and ground based systematic sampling were assessed by the means of a two-tailed t-test against the population value. Bias, standard deviation, and RMSE for the MC estimates of mean volume were then used to assess the sampling designs and regression models. Relative efficiency of regression based laser scanning estimates against corresponding ground based estimates was calculated as ratio of their respective MSE.

4. RESULTS

Except the multiplicative model, final regression equations were built using stepwise regression. A number of 45 mean volume estimates and their RMSE values were derived using five regression models (Table 4). In addition, for each sampling scheme, an estimate of mean volume and the corresponding RMSE were derived by ground based systematic plot sampling (Table 4). The reference value of mean volume per ha was 254 m³, i.e., total population volume of 914,400 m³ divided by the size of the study area of 3600 ha. The simulated study area included over 2.7 million trees. The number of iterations used for each simulation ensured convergence for both regression and ground plot based estimates. For mean timber volume estimates, the convergence occurred after ca 40-45 iteration for sampling schemes using ground plots of 200 m², ca 20-30 iterations for plots of 400 m², and after ca 15-25 iterations for plots of 600 m². As the number of iterations increased, the sampling error decreased asymptotically (Figure 1).

The regression models comprised two to five predictor variables. The most frequently used prediction variable was the interaction term, followed by squared height percentile and canopy density. Generally, the R² ranged between 0.79 and 0.96. The bias of mean volume estimates during iterations in each simulation ranged between -16.6 m³ha⁻¹ (6.5%) and 10.2 m³ha⁻¹ (4.0%) for regression estimates, while the bias of ground based estimates ranged from -34.1 m³ha⁻¹ (13.4%) to 31.8 m³ha⁻¹ (12.5%). MC estimates of mean volume derived by regression ranged between -5.7 m³ha⁻¹ (2.2%) and 0.3 m³ha⁻¹ (0.1%), and standard error between 5.0 m³ha⁻¹ (2.0%) and 7.4 m³ha⁻¹ (2.9%). For plot-based MC estimates, the range of bias was between -2.6 m³ha⁻¹ (1.0%) and 3.9 m³ha⁻¹ (1.5%), with a standard error between 13.7 m³ha⁻¹ (5.4%) and 18.4 m³ha⁻¹ (7.2%). The lowest RMSE for regression based MC estimates was 5.1 m³ha⁻¹ (2.0%) and the highest was 8.4 m³ha⁻¹ (3.3%). RMSE for ground plot MC estimates varied from 13.7 m³ha⁻¹ (5.4%) to 18.4 m³ha⁻¹ (7.2%). Among all regression models, only the multiplicative and linear models gave unbiased estimates ($p > 0.05$) under all sampling schemes. Ground based systematic plot sampling derived estimates provided unbiased estimates ($p > 0.05$) for all sampling designs. Relative efficiency of laser based estimates relative to ground plot estimates varied between 0.11 and 0.28, with an average of 0.16, which indicates efficiency in average 6.3 times higher for laser scanning strip sampling method (Table 5).

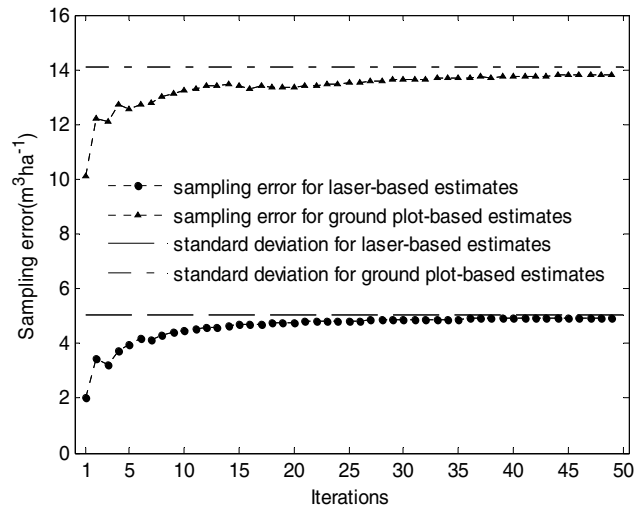


Figure 3. Example of sampling error estimation, for multiplicative regression model and ground plot base estimates using strip width of 180 m and plot size of 400 m².

5. DISCUSSION

The major findings of this study indicated that:

- 1) Laser scanning-based stripe sampling forest inventory can provide accurate and precise estimates of mean volume for relatively large forest areas. The LIDAR based estimation was on average 6.3 times more efficient in terms of MSE than ground-based sampling.
- 2) For both inventory methods, the inverse relationship between plot size and sample size seemed to be the dominant factors that led to a general increase of RMSE as the plot size increased.
- 3) For the ground-based systematic plot sampling method, the plot size was the dominant factor which led the overall trends for the MC estimates of mean volume. The RMSE of volume estimates increased by increasing plot size.

However, generalizations cannot be drawn from this study, since many assumptions were not realistic compared to real-world applications, i.e. small size of target area and small population variability. Another important issue is that all metrics derived from the population were considered to be "error free" and the effects of error propagation were neglected. As possible error sources could be mentioned errors concerning ground location of trees and ground plots, laser sampling and field measurements.

Nevertheless, we believe development and application of this first small-scale simulator has provided useful insight into some of the challenges we will have to face in the continued work to develop simulators that can operate on larger model forests where also spatial correlation and regional trends in the population value may be accounted for. Furthermore, a forest stand generator calibrated for Norwegian conditions should be developed, and there is also a need for building up an empirical database of laser derived individual tree models for all main tree species in Scandinavia.

Strip width (m)	Model	Plot area								
		200 m ²			400 m ²			600 m ²		
		bias	S.D	RMSE	bias	S.D	RMSE	bias	S.D	RMSE
Laser scanning based estimates (m ³ ha ⁻¹)										
160	1	-0.8 ^{ns}	5.5	5.6	-0.8 ^{ns}	5.7	5.8	-0.2 ^{ns}	6.4	6.4
	2	-2.2*	6.2	6.6	-1.3 ^{ns}	6.4	6.5	-0.8 ^{ns}	7.4	7.4
	3	-1.5*	5.2	5.4	-1.6 ^{ns}	5.7	5.9	-0.9 ^{ns}	6.5	6.5
	4	-5.5*	5.6	7.8	-3.6*	6.1	7.1	-4.3*	7.2	8.4
	5	-0.6 ^{ns}	5.5	5.5	-1.0 ^{ns}	5.7	5.8	-0.5 ^{ns}	6.3	6.4
180	1	-0.7 ^{ns}	5.5	5.6	-0.7 ^{ns}	5.0	5.1	-0.5 ^{ns}	5.6	5.7
	2	-3.0*	6.2	6.9	-0.4 ^{ns}	5.7	5.8	-0.8 ^{ns}	7.1	7.1
	3	-1.4 ^{ns}	5.3	5.4	-1.3 ^{ns}	5.1	5.3	-1.4 ^{ns}	6.0	6.2
	4	-5.7*	5.6	8.0	-3.6*	5.7	6.7	-4.1*	7.0	8.1
	5	-0.5 ^{ns}	5.4	5.4	-0.8 ^{ns}	5.0	5.1	-0.9 ^{ns}	5.5	5.6
200	1	-0.2 ^{ns}	5.4	5.4	-0.1 ^{ns}	5.1	5.1	-0.2 ^{ns}	6.0	6.0
	2	-2.5*	5.7	6.2	0.3 ^s	5.9	5.9	-0.7 ^{ns}	7.2	7.2
	3	-0.9 ^{ns}	5.3	5.4	-0.7 ^{ns}	5.0	5.1	-1.2 ^{ns}	6.3	6.4
	4	-5.2*	5.7	7.7	-3.2*	5.5	6.4	-3.1*	7.1	7.7
	5	0.0 ^{ns}	5.4	5.4	-0.2 ^{ns}	5.2	5.2	-1.0 ^{ns}	6.0	6.1
Ground plot based inventory (m ³ ha ⁻¹)										
160	-	-0.7 ^{ns}	13.7	13.7	3.9 ^{ns}	14.9	15.4	1.8 ^{ns}	18.4	18.4
180	-	-2.1 ^{ns}	14.8	15.0	2.2 ^{ns}	14.1	14.3	2.2 ^{ns}	17.5	17.6
200	-	-2.6 ^{ns}	14.5	14.8	2.2 ^{ns}	14.5	14.7	2.2 ^{ns}	18.2	18.4

^a significance level: * $p < 0.05$; not significant: ns > 0.05 ;
Models: 1–multiplicative; 2–log(y); 3–sqrt(y); 4–asin(sqrt(y)); 5–linear.

Table 4. Bias, standard error (S.D) and RMSE of mean volume estimates (m³ha⁻¹).

REFERENCES

Bollandsås, O. M. and Næsset, E. 2007. Estimating percentile-based diameter distributions in uneven-sized Norway spruce stands using airborne laser scanner data. *Scand. J. For. Res.*, 22:33-47.

Gobakken, T., Næsset, E. and Nelson, R. 2006. Developing regional inventory procedures based on scanning LiDAR. In: Hirata, Y., Awaya, Y., Takahashi, T., Sweda, T. & Tsuzuki, H. (Eds.). *Proceedings of the Silvilaser 2006 Conference*, Matsuyama, Japan. Pp 99-104.

Magnussen, S. and Boudewyn, P. 1998. Derivations of stand heights from airborne laser scanner data with canopy-based quantile estimators. *Can. J. For. Res.*, 28: 1016-1031.

Nelson, R., Short, A. and Valenti, M. 2004. Measuring biomass and carbon in Delaware using an airborne profiling LIDAR. *Scand. J. For. Res.*, 19: 500-511.

Nelson, R., Næsset, E., Gobakken, T., Ståhl, G. and Gregoire, T.G. 2006. Regional forest inventory using airborne profiling LiDAR. In: Hirata, Y., Awaya, Y., Takahashi, T., Sweda, T. & Tsuzuki, H. (Eds.). *Proceedings of the Silvilaser 2006 Conference*, Matsuyama, Japan. Pp 105-112.

Næsset, E. 1997. Determination of mean tree height of forest stands using airborne laser scanner data. *Photogramm. Eng. Remote Sensing*, 52: 49-56.

Næsset, E. and Bjerknes, K. 2001. Estimating tree heights and number of stems in young forest stands using airborne laser scanner data. *Remote Sens. Environ.*, 78: 328-340.

Næsset, E., 2002. Predicting forest stand characteristics with airborne scanning laser using a practical two-stage procedure and field data. *Remote Sens. Environ.*, 80: 88-99.

Næsset, E. 2004. Practical large-scale forest stand inventory using small-footprint airborne scanning laser. *Scand. J. For. Res.*, 19: 164-179.

Pretzsch, H., Biber, P. and Ďurský, J. 2002. The single tree-based stand simulator SILVA: construction, application and evaluation. *For. Ecol. Manage.*, 162: 3-21.

Solberg, S., Næsset, E. and Bollandsås, O.M. 2006. Single tree segmentation using airborne laser scanner data in a structurally heterogeneous spruce forest. *Photogramm. Eng. Remote Sensing*, 72: 1369-1378.

Vestjordet, E. 1967. Functions and tables for volume of standing trees. Norway spruce. *Rep. Norw. For. Res. Inst.* 22: 539-574. (In Norwegian with English summary).

Wynne, R. H. 2006. Lidar remote sensing of forest resources at the scale of management. *Photogramm. Eng. Remote Sensing*, 72:1311-1314.

Strip width (m)	Model	(MSE ^a / MSE ^b)		
		Plot size (m ²)		
		200	400	600
160	1	0.17	0.14	0.12
	2	0.23	0.18	0.16
	3	0.16	0.15	0.12
	4	0.32	0.21	0.21
	5	0.16	0.14	0.12
180	1	0.14	0.13	0.10
	2	0.21	0.16	0.16
	3	0.13	0.14	0.12
	4	0.28	0.22	0.21
	5	0.13	0.13	0.10
200	1	0.13	0.12	0.11
	2	0.18	0.16	0.15
	3	0.13	0.12	0.12
	4	0.27	0.19	0.18
	5	0.13	0.13	0.11

^a MSE of laser-based estimates

^b MSE of ground plot based estimates

Models: 1–multiplicative; 2–log(y); 3–sqrt(y); 4–asin(sqrt(y)); 5–linear.

Table 5. Relative efficiency of laser based against ground plot estimates.

DETECTION AND RECONSTRUCTION OF FREE FORM SURFACES FROM AIRBORNE LASER SCANNING DATA

Sagi Filin, Nizar Abo Akel, Yerach Doytsher

Dept. of Transportation and Geo-Information Eng., Technion – Israel Institute of Technology, Haifa 32000, Israel
{filin, anizar, doytsher}@tx.technion.ac.il

Commission III, WG 3

Keywords: LiDAR, City modeling, Building reconstruction, Free Form, Curved Surfaces.

ABSTRACT:

Building reconstruction from LiDAR data offers promising prospects for rapid generation of large-scale 3D models in an autonomous manner. Such reconstruction requires knowledge on a variety of parameters that refer to both the point cloud and the modeled building. The complexity of the reconstruction task has led many researchers to use external information, mostly in the form of detailed ground plans to localize the buildings and usually assume that buildings consist of only planar parts. These assumptions limit the reconstruction of complex buildings specifically when curved surfaces exist. We present in this paper a model that considers the point cloud as the only information source and analyzes the roof shapes. We extend the standard models to support free-form surfaces and reconstruct their shape. Since many of the buildings are still composed of planar faces, we maintain the planar based partitioning whenever possible but detect if non-planar surfaces exist and apply free-form surface models there. In such way, the standard models are extended to support general shape roofs without imposing an artificial model if not needed. In addition to the extension into non-planar roofs, our reconstruction involves the aggregation of the point set into individual faces, and learning the building shape from these aggregates. We show the effect of imposing geometric constraints on the reconstruction to generate realistic models of buildings.

1. INTRODUCTION

Three-dimensional reconstruction of buildings becomes a fundamental part in a growing number of applications. Among the data sources available for such reconstruction, airborne laser scanning has emerged in recent years as a leading source for that purpose (see e.g., Brenner and Haala, 1998; Wang and Schenk, 2000; Brenner, 2000; Voegtle et al. 2005; Rottensteiner 2005), particularly due to the direct measurements of the surface topography both accurately and densely.

Reconstruction of buildings from LiDAR data involves their detection in the point cloud, extraction of primitives that compose the building shape, and an agglomeration of the primitives into a geometric building structure. The detection will usually wear the form of object to background separation, e.g., via filtering, surface discontinuities analysis, segmentation, or with the support of external information, like ground plans (Vosselman and Dijkman, 2001; Haala et al. 2006). For the extraction of roof primitives, a segmentation of the data into planar faces will be applied in most cases. In Hoffman (2004) and Alharthy and Bethel (2004) a gradient based analysis is applied as a means to find roof planes. Voegtle et al. (2005) use classified data as an input, where the extraction of the roof planes is region growing based with a homogeneity predicate. Rottensteiner (2005) describes a roof delineation algorithm where the classified data is segmented in a similar fashion as in Voegtle et al. (2005). The boundaries of the detected planes are determined using the Voronoi diagram and the resulting edges are then grouped together into polyhedral models. The reconstruction of the roof model that follows, will usually involve modeling via geometrical representations such as, boundary representations, parametric models, or CSG trees.

Despite the large body of research into building reconstruction, many challenges are still remaining. One such challenge concerns the general planar roof-face assumption that is

common to almost all reconstruction models. While planar roof buildings are still the majority, buildings with general shape can be found in almost every scene. Using planar-based models for general curved or free-form surfaces, will lead to a wrong partitioning and a failure in the reconstruction process as the common outcome. Therefore, to increase the reliability of the building detection and modeling process, an extension of the reconstruction model to support a general shapes is a desired improvement. Nonetheless, as many of the buildings are still composed of planar faces, a planar based partitioning is an appealing concept to maintain whenever possible. An optimal reconstruction model will therefore not only involve finding a representation for curved surfaces but also deciding when planarity fails to hold and a more elaborate model is of need.

To support any form of reconstruction that deviates from the planarity assumption, the utility of turning into a curved surface description should be weighted. In this paper, we address the problem of identifying curved roof faces when such exist. The motivation is limiting such detection only to those cases where non-planarity is needed while avoiding over-parameterization elsewhere. We then demonstrate the reconstruction of non-planar roofs structures using data with moderate point density ($< 1 \text{ p/m}^2$). In the following Section we outline the roof face extraction model and then describe alternative methods for identifying deviations from planarity by looking into internal and external characteristics. We then study their applicability to the detection of curved segments and show the results of the surface reconstruction.

2. FEATURE EXTRACTION AND MODEL EVALUATION

As noted, a reconstruction framework that assumes no prior information from external sources requires, i) the detection of buildings in the point cloud, ii) segmentation of the roof into faces and analysis of the results, and iii) geometric adjustment

for the building primitives. Our focus here is on the segmentation and segment analysis part. An assumption is made here that buildings have been detected in the point cloud, and that following the roof face extraction and analysis, geometric/topological adjustment of the roof faces will take place.

2.1 Segmentation

Surface segmentation is the core of the primitive extraction process. It is aimed at identifying planar patches in the roof structure, which then allows learning about the roof shape and structure, and reconstructing its shape. The segmentation we apply here is based on cluster analysis that uses local surface parameters as attributes. With those attributes, solid surfaces as roofs tend to cluster as they share slope parameters. Clusters that share common surface properties constitute "surface classes" (all points that share similar surface parameters) that may consist of more than one physical segment. Therefore, following the "surface class" extraction, physical segments in object space are extracted by linking points according to proximity measures. The identified surface segments are validated via surface fitting, which involves testing whether the segment is homogeneous and composed of only one actual plane, and if that is the case, validating that all points in the cluster belong to the same class. The elemental segments are then extended, if possible, by adding unsegmented points and by merging segments that share similar surface properties. Merging of segments is decided by testing whether neighboring segments share similar mean (the estimated surface parameters) and standard deviation. The size of the segments is controlled by *std.* thresholds. An upper bound limit σ_{max} that reflects physical surface accuracy is set to avoid over-segmentation. Additionally a lower bound limit, σ_{min} , which is set in accordance with the expected accuracy of the laser points, is applied to avoid under-segmentation. When a segment is extended and its *std.* falls below the minimum threshold, σ_{min} is used instead.

2.2 Segment Analysis

When planar-surface based models are applied to non-flat surfaces, the reconstruction is likely to provide fractured segments (made of small/narrow) or a sporadic set of patches. From a geometric standpoint, all segments will conform to the segmentation guiding rules like minimum size and adequate *std.* as was defined with the segmentation. Therefore, the decision whether surface patches form a curved face, should not necessarily rely on segment accuracy but rather on internal, or external characteristics.

Internal characteristics – Segments can be considered potential parts of a curved surface if some shape properties indicate so and if the segment does not cover a large area within the building or included within a larger segment (as with dormers, chimneys, etc.). Shape properties can be linked with the arrangement of the offsets among the laser points composing the surface and the adjusted plane. According to adjustment theory, the observations taken should be statistically independent (namely, $E\{\varepsilon_i, \varepsilon_j\}=0 \quad \forall i \neq j$), with E the expectation, and ε , the random errors). Nonetheless, if a plane is fitted to a bended surface, offsets from the plane will tend to cluster and exhibit spatial correlation with offsets of nearby points sharing sign and magnitude. Figure 1.a shows a side view of a curved surface with its corresponding laser points, the

true surface passes among the points with random distribution of points above and below the surface. Figure 1.b shows the segmentation results which led to two planes that approximate the actual surface. As Figure 1.c, shows, the offsets have now some pattern. While the two detected plans have a *std.* that is limited by the segmentation, the residuals do not behave randomly.

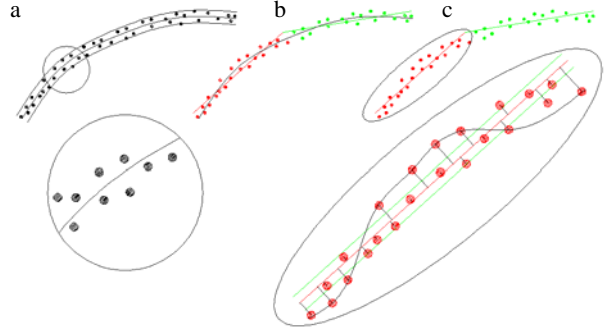


Figure 1: residual analysis, a) curved surface, b) segmentation results, with two planes detected, c) blowup of the left segment showing the spatial order in the residual distribution

Measures to quantify spatial correlation can be found in the literature, e.g., via autocorrelation analysis for time series, or variograms in the two dimensional case. The appealing variogram concept for segment analysis is costly, however, and therefore ineffective. Instead, we turn to non-parametric analysis of the error distribution via a quantitative analysis of the offsets variation. Generally, when a cluster of points will share the same residual sign, each point within this cluster will provide evidence to the non-planarity, and due to the minimum l_2 norm of the least-squares plane adjustment, positive and negative residual regions will be formed across the segment. Therefore, for the evaluation, our hypothesis is that the residual distribution can indicate potential curved segment. To translate this notion into a measure, we analyze the consistency of the residuals signs around a given point, so that

$$p_i = \begin{cases} 1 & \frac{\#\{\text{sgn}(p_j) = \text{sgn}(p_i) \mid p_j \in N(p_i)\}}{\#\{p_j \in N(p_i)\}} > t_p \\ 0 & \text{otherwise} \end{cases} \quad (1)$$

with N the neighborhood around a point p_i within the queried segment and t_p a threshold value that defines the ratio above which a point is considered correlated with its surrounding. Then, a segment is considered curved if $\sum p_i / \# p_i < t_r$, with t_r a

threshold ratio. The evaluation of the residual distribution has a very clear dependency on N , the neighborhood function toward which the p_i is evaluated. Filin and Pfeifer (2005) evaluate a set of neighborhood definitions for airborne laser scanning data and opt toward a slope adaptive neighborhood that adapt to a local fitted surface. However, as surfaces are given here by the segmentation, this model has little relevance to the current problem. For neighborhood definition we consider the following set of models:

1. **Euclidean neighborhood** – in which all neighboring points located within a given radius around a point are defined as neighbors, see Figure 2.a.

2. **Topological neighborhood** – in which the topological closest points within the maximal planar graph are considered neighbors. For the graph definition the pointset is triangulated using the Delaunay criterion; see Figure 2.b.

3. **Selective neighbors** – to maintain equal contribution in all direction around the point, a subdivision of the surrounding area is applied. Four quadrants are defined and the closest points in each sector are selected, see Figure 2.c. Around the edges of the segment, where a quadrant partitioning cannot be performed, this approach is maintained, but instead of quadrants the two halves covered by points are evaluated, see Figure 2.d (in narrow segment edge parts this evaluation is not performed, the information that can be drawn there is questionable from the outset).

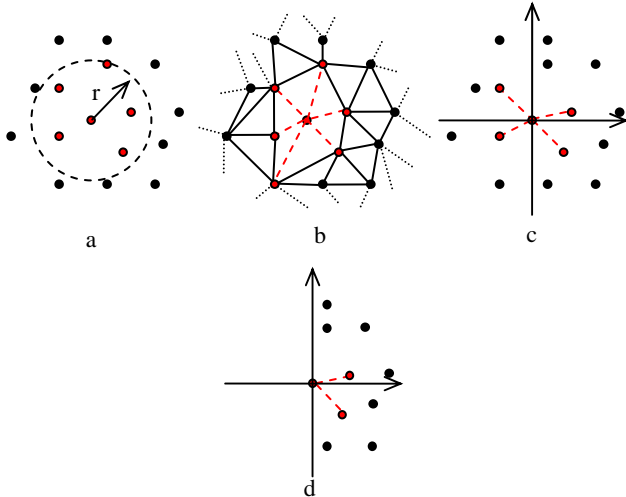


Figure 2. Neighborhoods a) Euclidean, b) topological, c) selective along quadrants, d) selective along edge points

External characteristics – Contrasting the internal characteristics evaluation that studies shape properties via laser points deviation from the surface, the evaluation of external characteristics concerns deciding which segments should be joined together into one curved surface and examining the utility in this. Neighboring planar segments can be grouped together by fitting a high degree parametric surface (e.g., cubic surface), and given the two models deciding which model is preferable. The measure we consider here is the Akaika Information Criterion (AIC) (Akaike, 1974; Boyer et al. 1994) that takes both model complexity and modeling accuracy into consideration, and is advantageous because of its simplicity. Under the reasonable assumption of normal distribution, the AIC values can be computed for each model using Equation (7)

$$AIC = 2k + n \ln \frac{\sigma}{n} \quad (2)$$

with k , the number of parameters in the model, n , the number of points, σ , the sum of the square errors. Errors here are the offsets of each point from the surface.

The evaluation is performed in a pair-wise manner, where for each pair of neighboring segments the AIC value is tested for the two individual segments against the merit of using one polynomial surface. Experimenting with polynomial surfaces of degrees 2-5 has shown that locally, bi-quadratic surfaces (six parameters) are sufficient to decide if the two surfaces are part of a curved surface. The ability to maintain a low-degree polynomial for the test is due to the local pair-wise evaluation. We note that such test can also be applied to evaluate internal characteristics, and refer to it in the following.

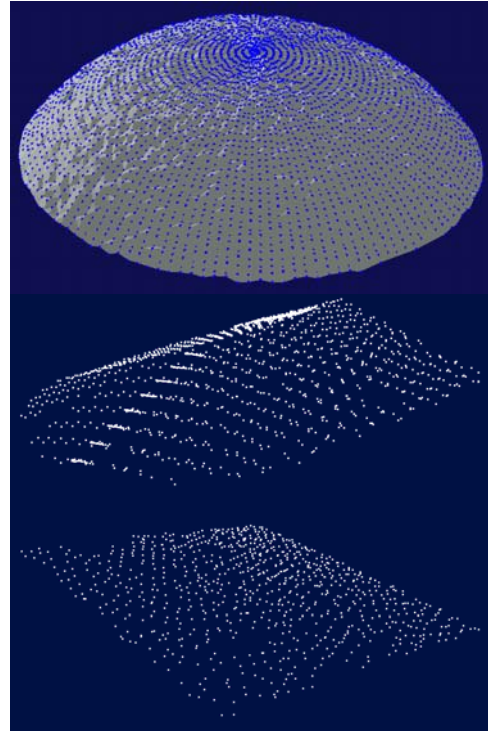


Figure 3: Curved roof datasets, top) a dome like shape, middle) a cross hip roof with curved end, bottom) a nearly flat roof

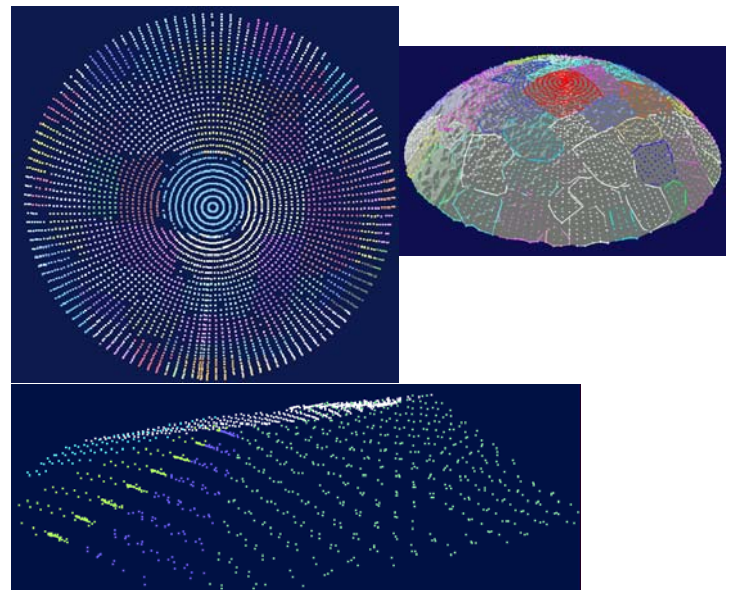


Figure 4: Segmentation results, top) the dome structure with top and isometric view, bottom) the hipped roof

3. RESULTS AND ANALYSIS

For the analysis of the metrics we use three datasets, a synthetic one with a dome like shape (see Figure 3 top), a hip roof with one facet having a cone like shape, (see Figure 3 middle), and a nearly flat roof with no distinct features (Figure 3 bottom), thus making it more challenging for the analysis. The choice of the synthetic dataset is driven the possibility to evaluate the robustness of the proposed methods, particularly to the increase of noise. Noise level ranging from 5 cm as an optimal case to 30 cm as a more extreme end, are applied to study the effect of noise on the surface evaluation model. We study the synthetic and winged roof examples and then analyze the nearly flat roof where further tests are applied. We point that other than the two

Method	Noise: 5 cm		Noise: 10 cm		Noise: 20 cm		Noise: 30 cm	
	Curved	Not Curved	Curved	Not Curved	Curved	Not Curved	Curved	Not Curved
Euclidean	90	2	86	3	74	4	1	57
	97.8%	2.2%	96.6%	3.4%	96.1%	3.9%	1.7%	98.3%
Topological	83	9	40	49	6	71	0	58
	90.2%	9.8%	44.9%	55.1%	7.8%	92.2%	0%	100%
Selective	92	0	88	1	77	0	53	5
	100%	0%	98.9%	1.1%	100%	0%	91.1%	8.6%

Table 1. Results of the segment analysis for different noise and neighbourhood methods

real world examples further tests were applied on other building datasets, both flat and free-forms.

The segmentation results for the first two datasets are given in Figure 4. In both cases $\sigma_{max}=\pm 15\text{cm}$ and a minimal segment size of 5 points were used as parameters. For the hipped roof, the two side wings were segmented as planes but the curved parts (the whole structure in the dome, and the front of the hipped roof) are broken into parts. Some holes in the point clouds can be noticed; these are small regions that fell outside the extent of the segments as they exceeded the accuracy threshold, but were too small to form an individual segment. In the overall roof reconstruction scheme, those holes will be "completed" when neighboring planes will be extended to intersect one another. In this regard, because of the actual non-planar shape of the roof, some topological inconsistencies may arise in the reconstruction. We point that for the dome structure some variations in the segmentation as a function of the noise increase can be seen but as they share more or less a similar structure, they are not presented here.

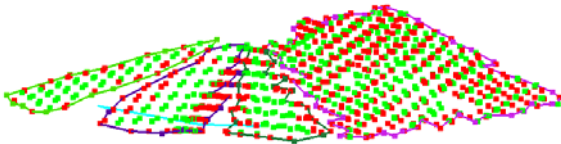


Figure 5: Residual distribution over the individual segments

As for the hip roof, Figure 5 shows the residual distribution over the segments, with green points as positive residuals and red points as negative ones. In all three curved segments a clear clustering of the errors can be noticed while the planar roof exhibits more or less random variations.

The application of the internal measures as a means to analyze the shape of the segment is now studied. The results are listed in Table 1 and illustrated graphically in Figure 6. For the experiment, noise level of 5, 10, 20, and 30 cm were applied to the data. For the case of 5 cm noise level all three models appear to perform well, with the Euclidean evaluation having only two misses out of 92 segments and the topological neighborhood giving rise to nine misses from the same amount of segments. The selective neighborhood scheme offers the best performance with no misses at all. As the noise level increases, the dissimilarity in results between the different measures starts growing. The Euclidean neighborhood system offers slight decrease in correct detection up to the 20 cm noise level, but then completely breaks apart at the 30 cm level. This behavior can be attributed to the noise level that exceeds by a factor of two the accuracy threshold of the segmentation. The

topological neighborhood shows a much weaker performance with more than 50% misses already at the 10 cm level and breaking apart from then on. Compared to the two others, the selective scheme appears to have the best performance, with a negligible miss up to the 20 cm level and five misses at the 30 cm level. This result can be attributed to the emphasis on the distribution of the evaluated points while maintaining a proximity criterion to the evaluated point. As Figure 6.b shows those misclassifications occur with the relatively small and narrow segments where the collection of a set of well distributed points is harder.

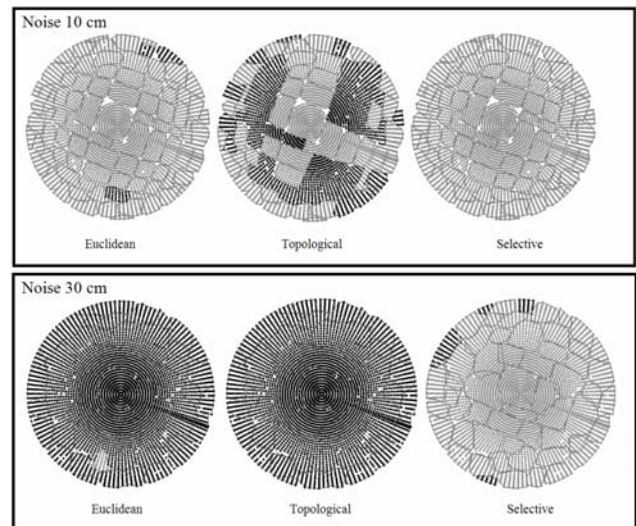


Figure 6: Classification of segment types (light tone – correct, dark tone – wrong)

An analysis of the results leads to the realization that one of the more affecting factors is the size and shape of the evaluated segments. Usually, with curved structures the resulting segments will tend to be small in size, and, depending on the surface geometry, narrow. Therefore, neighborhood models that try covering a relatively broad region, as the Euclidean model or the topological one, will exhibit greater sensitivity to the segment shape and size and as the level of noise increases lose the dominance of the residual distribution. Compared to them, the selective method shows, to some degree, less sensitivity as it weights in both point distribution and proximity in a more controlled manner.

For the segment characterization on the hipped roof the classification results based on the neighborhood systems are listed in Table 2 (for segment numbering see Figure 8).

Generally, both the Euclidean and the selective models classified correctly the three curved related segments, with the topological model misclassifying one of them. The more interesting result however is the classification of the two wing segments, where both the Euclidean and selective based models misclassified one segment. This result is due to the overlap between two different scans over the roof and a systematic scanning error that led to two sets of offsets. In term of the local analysis, it has led both surfaces, under different neighborhood schemes, to be classified as curved.

Method	Segment Number				
	0	1	2	3	4
Euclidean	Flat	Curved	Curved	Curved	Curved
Topological	Flat	Flat	Curved	Flat	Curved
Selective	Curved	Flat	Curved	Curved	Curved

Table 2: Results of the segment analysis for the hipped roof

External evaluation

The external evaluation of the segments' shape operates on a different level by assessing the utility in joining two neighboring segments into a one. The connectivity between the segments is established by identifying border points of each segment (those points that neighbor not only points with the same segment ID but such with others). When applying the AIC measure on the dome structure, the results yield correct classification for all segmentation under different noise levels. The successfulness of the AIC measure can be understood by the direct incorporation of noise level into the information criterion and to the fact that segments that are originally part of a curved object tend to show better results when joined.

When turning to the hipped roof that features both planar and curved part, the model should distinguish between curved parts that should be linked together and planar parts that should be kept as such. Table 3 lists the AIC values for the joining of the roof segments, with Figure 8 showing the resulting connectivity graph between the detected curved segments.

Segment		AIC Values			
I	II	I	II	I + II	curve
1	0	-3102	-3337	-6439	-1675
3		-1002	-3337	-4338	-2125
0	1	-3337	-3102	-6439	-1675
4		-419	-3102	-3521	-1646
3	2	-1002	-1482	-2484	-2688
4		-419	-1482	-1901	-2256
0	3	-3337	-1002	-4338	-2125
2		-1482	-1002	-2484	-2688
1	4	-3102	-419	-3521	-1646
2		-1482	-419	-1901	-2256

Table 3: AIC values - the best model to be selected is the one with the smallest AIC value

The results show that applying the AIC measure when evaluating the utility in joining the three curved segments has managed identifying them as part of a curved segment but when joining the flats with either one another or the curved ones, kept them as they are. We note that the systematic offsets due to the laser strips overlap have no effect on the results as with the

internal characteristics evaluation. This can be explained, again, by the global evaluation of the fitting accuracy and the model complexity that does not evaluate the individual points but rather the merit in joining surfaces.

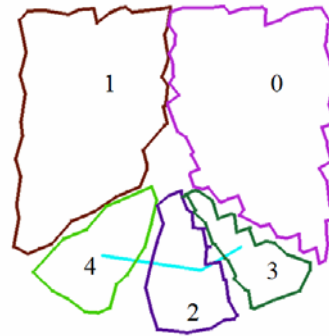


Figure 8: The connectivity graph between curved segments



Figure 9: Outline of the segments of the nearly flat roof

Turning to the nearly flat surface, the segmentation results are shown in Figure 9. Even though the accuracy level was raised to $\sigma_{max}=\pm 25cm$ the roof was segmented into two separate segments indicating its actual deviation from planarity. Here, internal measures are measured by the offset based analysis and by using the AIC as a means to assess flatness of the individual segments. Additionally, the external evaluation was performed. As the offsets distribution in Figure 9 show, the bigger segment was indeed classified as curved, but the smaller one as flat. Using the AIC measure to evaluate the two individual segments (flat vs. curved) identified, again, the big segment as curved but the other as flat. This can be explained by the segment size and dimensions that are small and elongated. Contrasting both internal evaluations, the global AIC measure that linked the two parts of the nearly flat roof showed higher gain by joining them into one curved segment. These results indicate that the merit of using the external evaluation lies not only in the information measure, but also in having a more global view of the surface joining utility.

3.2 Global Surface Approximation

Reconstruction of the curved roof shape can be in the form of a high order polynomial or a free-form surface. We demonstrate the application of a Non Uniform Rational B-Spline (NURBS) surface for the reconstruction (Cohen et al., 2001). The results can be seen in Figure 9. Using NURBS allows a mathematical representation that can accommodate and accurately describe surfaces of general shapes, ranging from simple 2D curves to complex 3D free-form surfaces or solids. In addition to the compact representation that NURBS geometry offers, NURBS can be graphically rendered in an efficient and accurate way.

Figure 10 (top) shows that NURBS surface that was fitted to the three curved surfaces, following their boundaries as extracted from the segmentation of the point cloud. Attempting to fit a high order polynomial to the joining of the three surfaces (that appear to be having a cone structure) did not yield satisfying results in terms of appearance and fitting accuracy. The result in Figure 10 (top) that follows the geometric shape of the roof face lacks the form of an actual building shape. In Figure 10(bottom) the application of geometric constraints and leveling the roof boundary is added to form the complete shape of the roof structure. This structure is composed now of two planar and one free-form surfaces. Finally, Figure 11 shows the effect of reconstruction when relying on flat surface based segmentation. It shows the clear role of free-form surfaces for building reconstruction, even for gentle deviations from planarity as the current building offers.

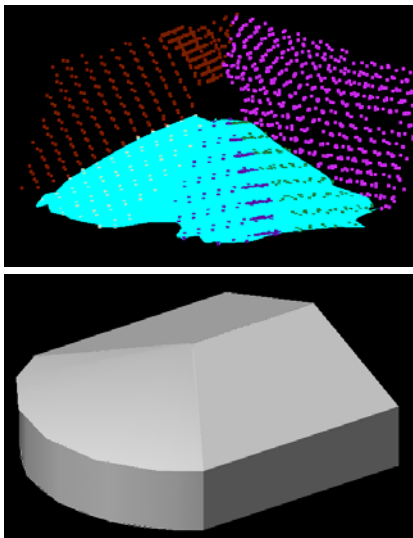


Figure 10: Reconstruction of the curved part and the roof shape via free-form surface

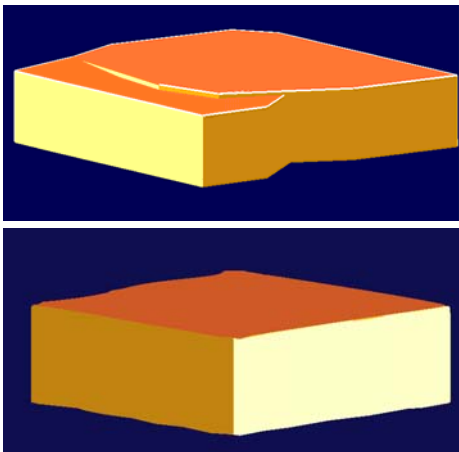


Figure 11: Reconstructing the nearly flat roof, with an example (top) of the effect of not using a free-form representation

4. CONCLUSIONS

Detection of curved roofs becomes an important component in building reconstruction over large areas, where some buildings are likely to wear such shapes. Such detection should be able identifying them while still maintaining the planarity of other roof faces, which still set the majority. In this paper, we evaluated methods to identify curved surfaces. The results have

shown that internal measures can be reach correct detection in most cases under a given neighborhood system. However, the dependency on the segments shape and laser scanning properties, like systematic offsets between strips, may lead to misclassification. In contrast, the external use of AIC criterion appears more robust to noise and to scanning artifacts, as the three examples show. The ability to distinguish correctly between planar surfaces and segments of a fractured curve are of great value in this regard. We note that other external measures may prove suitable as well.

Finally, the application of free-form surface coupled with geometric adjustment of the surface into a building shape has led to an optimal reconstruction of the building model, one that composed of three surfaces for the hipped roof, and of one global surface for the dome and the nearly flat one.

5. REFERENCES

- Akaike, H., 1974. A new look at the statistical model identification. *IEEE Trans. on Automatic Control*, **19**: 716-723.
- Alharty, A., Bethel, J., 2004. Detailed building reconstruction from airborne laser data using a moving surface method. *Int. Archives of Photogr. and Rem. Sens.* **35**(B3): 213-218.
- Boyer, K., Mirza, M., Ganguly, G., 1994. The robust sequential Estimator: A General Approach and its application to surface organization in range data. *IEEE Trans. on PAMI*, **16**(10): 987-1001.
- Brenner, C. and Haala, N., 1998. Rapid acquisition of virtual reality city models from multiple data sources. *Int. Arch. of Photogr. and Rem. Sens.* **32**(5): 323-330.
- Brenner, C., 2000. Towards fully automated generation of city Boundary points will be clustered at the maximum if they are within a limited spacing and above a certain threshold models. *Int. Arch. of Photogr. and Rem. Sens.* **33**(B3).
- Cohen, E., Riesenfeld, R., Elber, G., 2001. Geometric Modeling with Splines: An Introduction. A.K. Peters.
- Filin, S., Pfeifer, N. 2005. Neighborhood systems for airborne laser data. *Photogr. Eng. & Rem. Sens.* **71**(6): 743-755.
- Haala, N., Brenner, C., Anders, K.-H., 1998. 3D Urban GIS from Laser Altimeter and 2D Map Data. *International Archives of Photogrammetry and Remote Sensing*, **32**(3/1), 339-346.
- Haala, N., Becker, S., Kada, M., 2006. Cell Decomposition for the Generation of Building Models of Multiple Scales. *International Archives of the Photogrammetry, Remote Sensing and Spatial Information Sciences* **36**(3): 19-24.
- Hofmann A. D., 2004. Analysis of tin-structure parameter spaces in airborne laser scanner data for 3-d building model generation. *International archives of photogrammetry and remote sensing*, **34**(B3):302-307.
- Rottensteiner, F. 2006, Consistent Estimation of Building Parameters Considering Geometric Regularities by Soft Constraints. *Int. Arch. of Photogr. and Rem. Sens.* **36**(3):13-8.
- Rottensteiner, F., Trinder, J., Clode, S., Kubik, K., 2005. Automated Delineation of Roof Planes from LIDAR Data. *International Archives of the Photogrammetry, Remote Sensing and Spatial Information Sciences* **36**(3/W19): 221-226.
- Voegtle, T., Steinle, E., Tovari D. 2005, Airborne laserscanning data for determination of suitable areas for photovoltaics. *Int. Archives of Photogr. and Rem. Sens.* **36**(3/W19): 215-220.
- Vosselman, G., Dijkman S., 2001. 3D building model reconstruction from point clouds and ground plans. *Int. Arch. of Photogr. and Rem. Sens.* **34**(3/W4): 37-43.

TERRESTRIAL LIDAR MEASUREMENTS FOR ANALYSING CANOPY STRUCTURE IN AN OLD-GROWTH FOREST

S. Fleck^{a,*}, N. Obertreiber^b, I. Schmidt^a, M. Brauns^a, H.F. Jungkunst^a, C. Leuschner^a

^a Albrecht-von-Haller-Institute, Plant Ecology, University of Goettingen, 37073 Goettingen, Germany – (sfleck, ischmid1, mbrauns, hjungku, cleusch) @gwdg.de

^b Zoller+Froehlich GmbH, Simoniusstr. 22, 91577 Wangen im Allgaeu, Germany – n.obertreiber@zofre.de

KEY WORDS: tree height, old-growth forest, canopy structure, canopy projection, terrestrial lidar

ABSTRACT:

Terrestrial lidar measurements with the Leica HDS 4500 laserscanner (Imager 5003 from Z+F) were executed in a structurally highly diverse, at least 200-year-old natural 11-species forest with typical characteristics of an old growth forest in order to assess the species-specific differences of tree canopy structures growing in a forest stand. Accuracy of the method and completeness of the canopy measurement is evaluated based on independent height measurements and visual inspection of single tree canopies.

While canopy structure could be captured completely in the lower half of the canopies, the upper parts of the virtual canopies exhibited partly gaps along the axis of branches. Virtually executed vertical canopy projections could better represent indentations in the canopy borderline than field measurements – both measurements yielded comparable canopy projection areas (root mean square error, RMSE = 11.1m²). Lidar-derived heights of tree canopy base were in better agreement with field measurements than lidar-derived tree heights.

1. INTRODUCTION

The terms “old-growth forest” and “primeval forest” stand for undisturbed forests that were able to develop all features occurring in a forest within the natural life-span of its constitutive tree varieties, including those unique features that make the forest ecologically valuable as habitat for rare species depending on these features. Therefore, the typical aboveground characteristics of old growth forests comprise (Zenner 2004, Hunter and White 1997):

- large and old trees
- dead trees and wood, standing and on the ground
- standing, leaning, and fallen trees
- trees in all different ages due to natural regeneration
- high spatial complexity, e.g. several layers of vegetation
- naturally high tree species diversity

Out of these, spatial complexity of forests is a difficult and not satisfyingly defined feature that has not yet directly been measured. While it is recognized that species-specific differences in tree canopy structure exist (Hagemeier 2002), are ecophysiologicaly significant (Fleck et al. 2004), and contribute to structural complexity (Zenner 2004), they have not been quantified due to a lack of reliable and complete structure data of trees growing in competition with other trees in a forest.

Though terrestrial lidar principally provides an efficient tool to measure tree canopies in a forest, old-growth forests belong to the most difficult objects for laser-scanner measurements due to characteristics associated with structural complexity and size:

1. Inaccessibility of the canopy for the instrument leads to an unfavourable scanning geometry with all scanner positions on one side of the scanned object and in a considerable distance from it.

2. Irregularity of the geometrical shapes in old-growth forests (e.g. noncircular stems covered with moss or bulges from wound occlusion and hidden by twigs or epiphytes) limits the utility of semi-automated registration procedures (e.g. Henning and Radtke 2006) based on geometrical features of the scene, resulting in an unfavourable registration geometry with all control points lying on one side of the object.
3. Occlusions depend on the density of canopy elements per canopy volume, which is usually high. They make it difficult to completely capture the structure of the upper part of the forest canopy.
4. Instability of the objects due to wind and growth movements causes additional concerns about reliability and repeatability of the measurements.

This paper presents multiple laser-scanner measurements of single trees standing in a dense, species-rich old-growth forest and evaluates the reliability of these data for further steps in species-specific structure analysis.

2. MATERIAL AND METHODS

2.1. Study site

All measurements were executed on the 10th of March 2006 in a mixed broad-leaved forest in the Hainich national park, study site 3a (51.089° North, 10.523 ° East) of the collaborative research project Graduiertenkolleg 1086 “**The role of biodiversity for biogeochemical cycles and biotic interactions in temperate deciduous forests**” at the University of Göttingen (see <http://www.forest-diversity.uni-goettingen.de>). Average wind velocity on this sunny day was 11.5 km/h and the main wind direction was west.

The study site is a 65m x 55m fenced section of the natural forest with 11 different tree species inside the fence: small-leaved lime (*Tilia cordata*), large-leaved lime (*Tilia*

* Corresponding author.

platyphyllos), common ash (*Fraxinus excelsior*), Norway maple (*Acer platanoides*), European hornbeam (*Carpinus betulus*), pedunculate oak (*Quercus robur*), sycamore maple (*Acer pseudoplatanus*), field maple (*Acer campestre*), European beech (*Fagus sylvatica*) European field elm (*Ulmus minor*), and wild cherry (*Prunus avium*) in the order of stem numbers. The total number of 161 trees comprises 9 standing dead trees and equals 392 trees per ha (trees with diameter at breast height (DBH) >7cm). Due to natural regeneration there were trees in all different ages and sizes in the forest: patches of shrub-like young trees (mainly ash and lime trees), suppressed trees in the lowest canopy layer, up to approximately 200-year-old large trees, and large decomposing dead trees lying on the ground. Tree stems in the fenced area had a maximum DBH of 85cm. Leaning stems were inclined to up to 39° from vertical, the average stem inclination was 7°.

2.2 Measurement set-up

The measurements were set up in order to cope with the mentioned difficulties for terrestrial lidar measurements in an old-growth forest. 25 scans were performed with a Leica HDS 4500 laser-scanner produced by Zoller + Fröhlich, Germany. Scanning positions about 1.5m above ground level were chosen irregularly in order to take advantage of larger canopy gaps and to increase the measurement density in thickets (Fig. 1). The HDS 4500 scanner measures distances up to 53.5m (ambiguity interval) based on the phase-shift of a frequency modulated laser beam. The laser spot size is 3mm leaving the instrument and 8.5mm in a distance of 25m. Range measurements in a distance of 25m have a root mean square error of 9mm on dark grey surfaces.

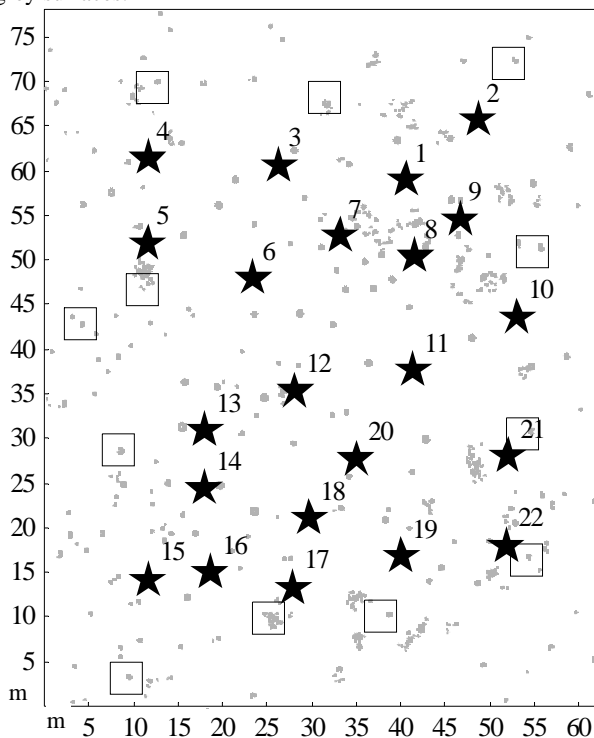


Fig. 1: Horizontal cut through the point-cloud in a height of 2m above ground-level, showing stem positions (grey spots), valid scan positions (filled stars), and the positions of elevated targets providing additional control points for the registration (open squares).

The scanning resolution was set to an angle of 0.036° in both, horizontal and vertical direction and to a total scan angle of 360°, resulting in a point spacing of 15.7mm in a distance of 25m.

The multiple scans were transformed into the same co-ordinate system based on 39 artificial chessboard pattern targets fixed to tree stems in a height up to 2m above the ground. Twelve elevated targets in a height between 8m and 10m on tree stems surrounding the forest stand were added in order to improve the registration geometry. They were directed towards the centre of the plot and fixed using a forest ladder of 10m length, which is equipped for leaning against stem surfaces and for stability on smooth ground. Geometric registration was performed using Z+F-LaserControl 6.8 (Zoller + Fröhlich, Germany). Single trees were extracted based on recognizable canopy elements using Cyclone 5.6.1 software (Leica Geosystems, Switzerland). Virtual canopy projections were performed on 20 trees viewing the single tree point-cloud in z-direction and keeping the actually surveyed part of the canopy in the zenith. Tree height was extracted of 45 single tree point-clouds as the vertical distance between the highest point and stem base (visually selected point at the bottom edge of the stem). A point representing canopy base was selected on 60 trees as the lowest point of the insertion area of the lowest main branch to the stem.

2.3 Forest Inventory data

8-point canopy projections were performed in January 2006 using a sighting tube equipped with a 45° mirror and cross-hairs to ensure vertical view of specified canopy elements from the ground (Johansson 1985). Eight points along the border of the canopy where chosen in order to approximate the canopy projection with a polygon and markers were set on the ground at each polygon corner point. Distance and direction of each point from the stem base were measured with a compass and a meter tape.

Height measurements in the stand were performed with the Vertex sonic clinometer and transponder (Haglöf, Sweden), aiming first to the stem at breast height (transponder height 1.30m a.g.l.) and then to the base and top of the canopy. Base of canopy was defined as the origin of the lowest main branch. Main branches were defined as branches with at least 10% of the cross-sectional area of the stem at this position.

3. RESULTS

3.1 Registration and Segmentation

Three scans were excluded from the evaluation due to target positions with offsets of more than 5cm in comparison to the grid of target positions represented by the other scans. The maximum positional deviation of control points in the remaining 22 scans was 2.1cm.

The extraction of single tree canopies based on visual recognition of canopy elements was safely possible for all branches with diameters of 4cm or more, but also smaller branches were usually well distinguishable due to the possibility to look at the point-cloud from many different viewpoints. Though the knowledge of species-specific tree habit accelerated the process of visual segmentation, this knowledge was not essential to distinguish tree canopies from each other.

Branches of adjacent tree canopies were visibly apart with gaps of more than 20cm between them. Gaps between canopies

could in less than 10% of all cases not safely be distinguished from the gaps between measured points on a branch. For these cases it was necessary to separate the tree point-clouds by an equidistant plane to those branches of the trees that could safely be identified. It cannot be excluded that this had a smoothing effect on the irregular form of the canopy surface due to

wrongly assigned points filling indentations of a neighbouring canopy. The result of this segmentation may be inspected in Fig. 2, 3, and 4. The point-clouds had up to 2 million points per tree. Point densities along branches were lower in the uppermost part of the canopy, but branches could still be identified.

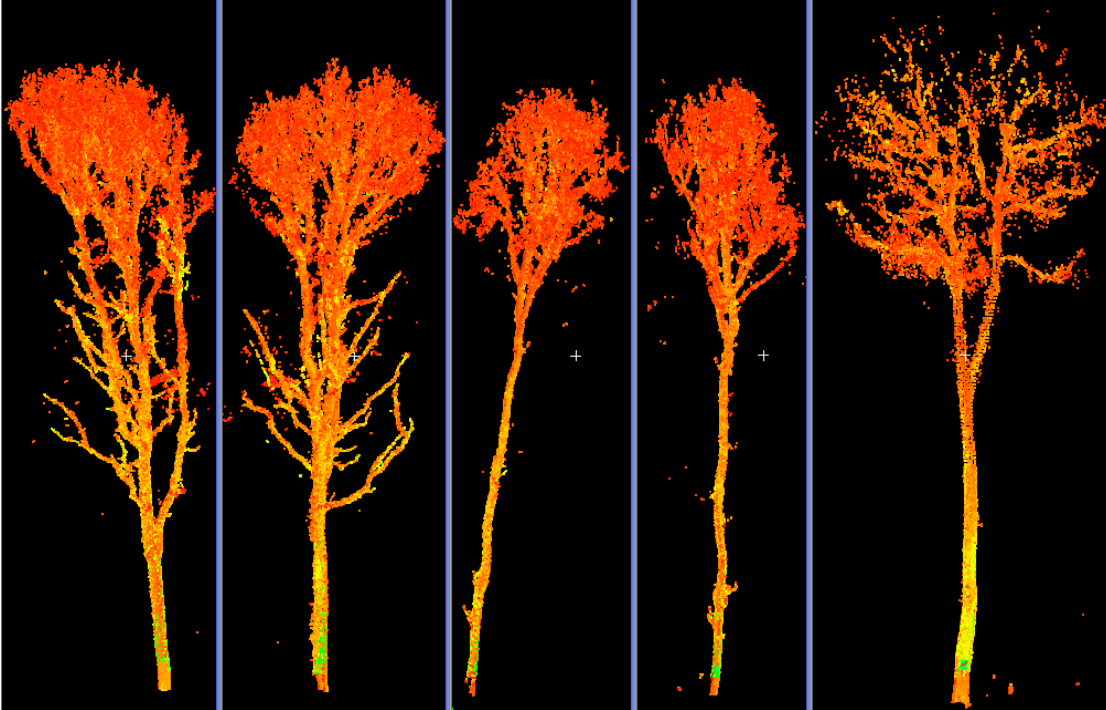


Fig. 2: Single tree point clouds of pedunculate oak #1 (south and east view), sycamore maple #2 (south and east), and common ash #3 (south view)

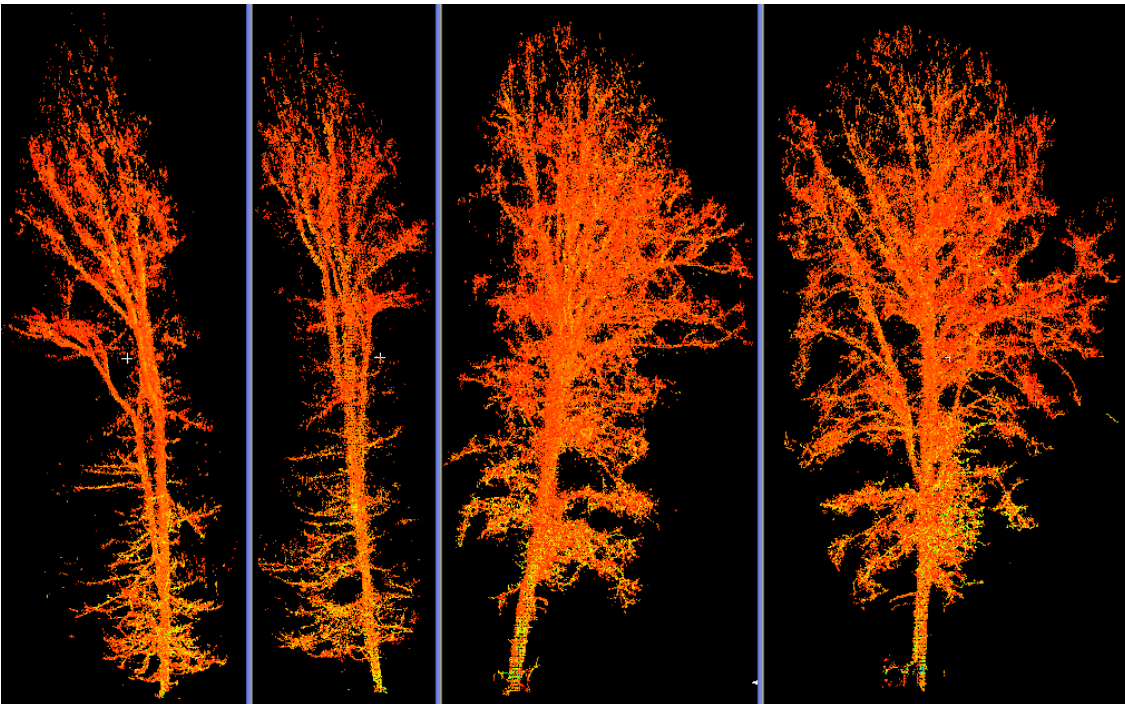


Fig.3: Single tree point clouds of European hornbeam #5 (south and east view) and small-leaved lime #12 (south and east view).

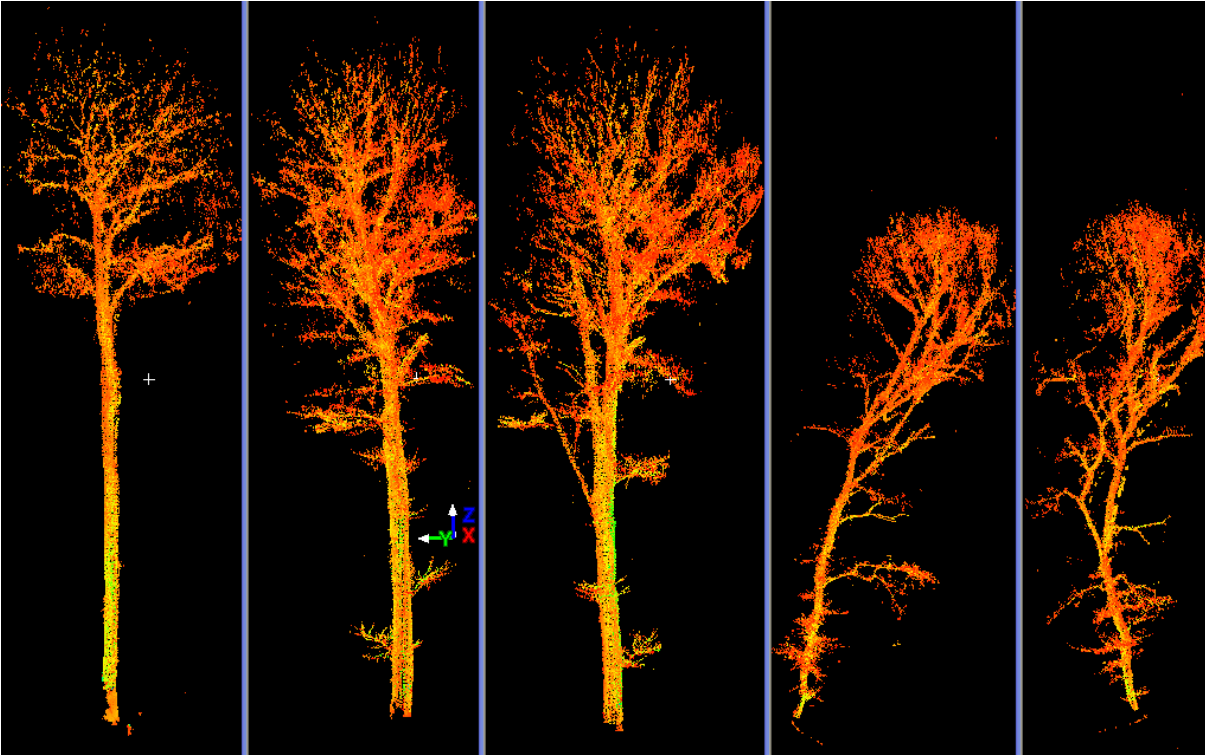


Fig. 4: Single tree point clouds of common ash #3 (east view), European beech #2 (south and east view), and field maple #15 (south and east view).

3.2 Virtual canopy projections

The 8-point canopy projections of 3 trees could not be evaluated due to obvious deviations from the virtual canopy projections. The area of 8-point canopy projections of 17 more trees ranged from 9m² to 112m² (mean = 47m²). The area of virtual canopy projections was well correlated with this measurement, yielding an r^2 of 0.90 and a root mean square error of 11.1m².

It was obvious from the measurement procedure that virtual canopy projections may capture indentations of the projected canopy surface line much better due to the higher number of polygon corner points, which were between 100 and 150.

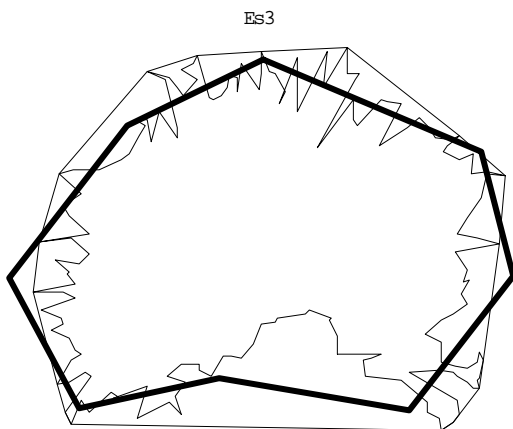


Fig. 5: Canopy projections of common ash #3: Contour lines of the 8-point canopy projection (thick line), the virtual canopy projection (inner thin line), and convex hull of the virtual canopy projection (outer thin line).

Both sorts of canopy projection were therefore compared to the area of their 2-dimensional convex hull (Fig.5): While 8-point-canopy projections were practically identical to their convex hull with an average area of 97% of their convex hull area (range: 87% - 100%), virtual canopy projections had on average 69% of the area that their convex hull would have (range: 56% to 79%). Virtual canopy projections were, thus, better suited for the representation of indentation-rich canopy shapes. While all virtual canopy projections represented a significant amount of canopy indentations, 53% of the 8-point projections did not.

The correlation of the 8-point-canopy projection area with the convex hull area of virtual canopy projections was even better than in the direct comparison of both projections ($r^2=0.95$, RMSE=11.1m²).

3.3 Height of canopy base and tree height

Vertex measurements and lidar-measurements of height of canopy base were well correlated ($r^2=0.99$), with a root mean square error of 0.52m, the mean height of canopy base being 9.18m.

The correlation of both measurement methods for absolute tree height was with an r^2 of 0.82 a bit weaker, RMSE being 2.41m and average tree height was 24.88m.

4. DISCUSSION

The segmentation of point clouds representing dense forest canopies into sub-clouds for each tree was visually not possible without a certain amount of insecurity at the canopy contact zones that lead to partly smoothed canopy surfaces.

The indentation-rich, irregular canopy surface of trees is on the other hand mostly well represented in its visual appearance (compare Figs. 2, 3, and 4).

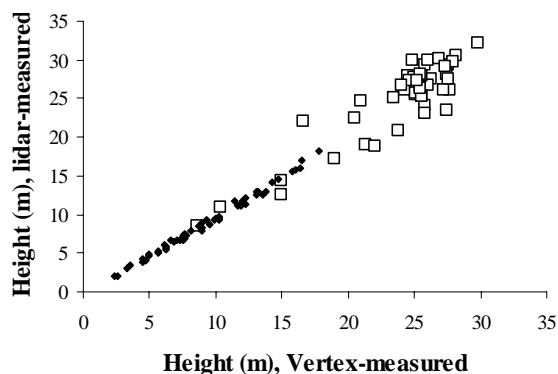


Fig. 7: Height measurements of top of the tree (open squares, $n=45$) and canopy base (black dots, $n=60$) as measured with the Vertex instrument (x-axis) and by terrestrial lidar (y-axis).

The low ratio of virtual canopy projection area to their convex hull area shows that this feature of tree canopies is well represented in lidar-measured point-clouds, while it cannot be captured by 8-point canopy projections.

Since 8-point canopy projections are a cheap and frequently used method to characterize forest composition, it needs to be specified that the arbitrary choice of corner points with the goal to approximate the projected canopy surface line with straight lines is essential for the accuracy of the method: The alternative use of the outermost points of the canopy projection would in many cases result in the convex hull area, which overestimates canopy cover up to 79% when compared with lidar data.

The slighter overestimation (23%) that was found comparing 8-point projections and virtual canopy projections may rather be explained by canopy indentations not represented than by branches that were not scanned due to occlusions or wrong segmentation, since the general shape of projected canopies was similar between both methods (compare Fig. 5) and completely missed branches would have been visible as gaps between canopies in the segmentation process. This interpretation is also supported by the better correlation of 8-point projection areas with the convex hull areas than with virtual canopy projections themselves.

A big practical advantage of virtual canopy projections is the possibility to view canopy contact zones from all necessary viewpoints before decisions on point-cloud segmentation are taken. This possibility does not exist when measuring projections with a vertical sighting tube which may have contributed to the deviation between both methods.

The agreement between Vertex measurement and lidar measured tree heights was much better for height of canopy base than for total tree height. This may have several causes: First, the canopy base is easily visible for both, the laser-scanner as well as the operator of the Vertex instrument. Second, canopy base and stem base are more probably in the same horizontal distance to the operator than the top of the tree would be. Though stems may be inclined a few degrees, same horizontal distance is a presupposition for correct measurement with the Vertex instrument. The highest point of the tree not necessarily has to be on the elongation of the stem axis. Third, branches in the uppermost part of the canopies had lower densities of lidar-measured points than below the canopy. It may, therefore, be that the tree top and its neighbouring points directly beneath have not been detected in some cases, though this is not likely in the visual

representations. Since both measurement methods may have contributed to these errors, it is difficult to judge the accuracy of tree height measurements without independent measurements. The data do show a reasonable agreement where the error sources are less severe, i.e., for measurements of height of canopy base.

5. CONCLUSIONS

(1) Not yet developed automated segmentation procedures for tree canopies in a forest will likely have the same problems as the visual segmentation of trees in a point-cloud with the consequence of partly smoothed canopy surfaces, unless the point density is even higher than in this example. (2) Terrestrial lidar measurements provide a tool to validate the performance of canopy projection methods. The arbitrary choice of border points of canopy projections leads to more accurate results than using the outermost points. (3) The validation of lidar-derived tree height measurements in a forest is not possible based on Vertex measurements, since these depend too much on visibility limitations.

6. REFERENCES

- Fleck, S., Schmidt, M., Köstner, B., Faltin, W., and Tenhunen, J. D., 2004. Impacts of canopy internal gradients on carbon and water exchange of beech trees. In: Matzner, E. (Eds.), *Temperate Forest Ecosystems response to Changing Environment: Watershed Studies in Germany*, Springer, Heidelberg, pp. 99-126.
- Hagemeyer, M. 2002. *Funktionale Kronenarchitektur mitteleuropäischer Baumarten am Beispiel von Hängebirke, Waldkiefer, Traubeneiche, Hainbuche, Winterlinde und Rotbuche*. Ph.D. Thesis University of Goettingen. 154 pages.
- Henning, J. G. and Radtke, P. J., 2006. Ground-based laser imaging for assessing three-dimensional forest canopy structure. *Photogrammetric Engineering and Remote Sensing* 72 (12), 1349-1358.
- Hunter, M. L. and White, A. S., 1997. Ecological thresholds and the definition of old-growth forest stands. *Natural Areas Journal* 17 (4), 292-296.
- Johansson, T., 1985. Estimating Canopy Density by the Vertical Tube Method. *Forest Ecology and Management* 11 (1-2), 139-144.
- Zenner, E. K., 2004. Does old-growth condition imply high live-tree structural complexity? *Forest Ecology and Management* 195 (1-2), 243-258.

ACKNOWLEDGEMENTS

We thank all doctoral students of Graduiertenkolleg 1086, especially Tobias Gebauer and Karl Maximilian Daenner, for basic contributions in the investigated forest stand and Heinz Coners for practical support of lidar measurements in the forest. This research was funded by the German Federal Ministry of Economics and Technology in the framework of the 3D-Canopy Analyzer project.

ADAPTIVE FILTERING OF AERIAL LASER SCANNING DATA

Gianfranco Forlani ^a, Carla Nardinocchi ^{b1}

^a Dept. of Civil Engineering, Parma University, Italy

^b Dept. ITS, University Roma La Sapienza, Rome, Italy

Commission III, WG 3

KEY WORDS: LIDAR, Classification, Algorithms, DEM/DTM, Automation

ABSTRACT

Filtering non-terrain points from raw laser scanning data is the most important goal to improve productivity in DTM generation. Filtering algorithms are built on assumptions about what discriminates terrain points from points on other objects (e.g. buildings and vegetation). In most cases, a single measure is used to accept or reject points. In this paper a three-stage raw data classification algorithm is presented. After a preliminary interpolation to a grid, a region growing based on height differences is applied. Segments from the region growing are classified as terrain, building or vegetation, based on their geometric and topological description. Terrain grid cells are conditionally low-pass filtered, to remove low vegetation. A piece-wise approximation of the terrain surface is computed, built from the grid cells classified as terrain. Finally, raw data are accepted as terrain within a given distance from the surface. Results obtained on a ISPRS filter test data set are shown to illustrate the effectiveness of the procedure.

1. INTRODUCTION

Airborne laser scanning is today the most effective data acquisition technology for the production of high resolution, high quality DTMs (Digital Terrain Models). The only competing technique might be aerial photogrammetry with direct camera orientation by GPS/INS (Inertial Navigation Systems) and DTM generation by digital image correlation; with aerial digital cameras the automation of the workflow should not be far from that of the laser scanner. Nevertheless, the preference for the laser scanner is clear and unlikely to be reversed. Because of its characteristics (first and last pulse, penetration rate in forested areas, narrow field angles, independence on shadows and object texture), laser scanning is indeed better suited and more versatile than photogrammetry for DTM production in urban areas as well as in forested areas. Penetration of pulses under the canopy provides a key advantage over photogrammetry, since it gives the filtering algorithms a chance to succeed in getting rid of spots on vegetation while retaining terrain hits.

Due to the scanning mechanism and aircraft movement, laser spots are scattered on terrain, vegetation, buildings and on whatever target that, hit by a pulse, reflects back enough energy to be detected. The result is a point cloud that must be filtered according to the survey purpose to get rid of unwanted echos: vegetation and buildings in DTM generation, vegetation in 3D city models, both the terrain and the buildings in tree counting and modeling.

To reduce production costs and processing time, filtering is performed automatically; in addition to visual inspection of the results for quality control, manual editing is still necessary, depending on the reliability of the filtering algorithms and on the complexity of the site.

2. PREVIOUS WORK

Many filtering algorithms have been proposed in the last decade; witnessing the difficulty of the task, none performs

equally well on any kind of landscape, because assumptions on terrain characteristics or the threshold values used do not always match reality.

A first group of algorithms looks for the lowest point in a neighborhood and label it as a terrain point. This is achieved mostly by applying morphological filters (Kilian et al., 1996; Vosselman, 2000; Sithole, 2001) where the structuring element is based e.g. on height difference or slope. Wack and Wimmer (2002) use grid data in a hierarchical scheme where non-object points are detected by using a Laplacian of Gaussian.

A second group fits an interpolating surface to the data and accept individual points measuring their distance to the surface. For instance, using linear prediction Kraus and Pfeifer (1998) iteratively get rid of points above the interpolating surface, so that it gets closer and closer to the lowest data points; Axelsson's (2000) algorithm works the other way around, i.e. a minimal set of (lowest) terrain points is progressively densified in a TIN structure by slope thresholding; Brovelli (2002) analyses the residuals from spline interpolation to detect objects contours.

A third group aim first to segment the data based on one or more criteria and then try to classify them: Filin (2002) clusters points in feature space, based on curvature and height difference, classifying low and high vegetation, smooth and planar surfaces; the neighbourhood used in feature evaluation is adaptively adjusted to the slope (Filin and Pfeifer, 2006); Roggero (2002) clusters points based on connectivity and a principal component analysis using geometric descriptors; Nardinocchi et al. (2003) segment data in regions bordered by discontinuities, retrieve their geometric and topological relationships and apply a rule-based scheme to classify the segments.

Recently proposed algorithms stress the need of segmentation and of context information to improve filter robustness: Sithole and Vosselman (2005) aim to separate objects (natural or man-made) from the terrain by extracting regions raised above their surroundings and classify them using geometric and topological relationships. Tóvári and Pfeifer (2005) group points in

¹ Currently visiting professor at Delft University of Technology, Dept. of Earth Observation and Space Systems

segments based on consistency of normal vectors, distance to the fitting plane and distance from seed point; robust filtering of the surface is then applied, where the same weights are applied to group of points, rather than to single points. In this paper a strategy for the classification and filtering of raw laser scanning data is presented. The main building blocks of the strategy (namely, data segmentation by region growing and region classification) have already been presented respectively in (Nardinocchi and Forlani, 2001) and (Nardinocchi et al, 2003). In (Forlani et al, 2006) the capability of the method in building detection was demonstrated, in the context of building reconstruction from laser data. In the following, Section 3 presents the main features of the strategy; Section 4 reviews the segmentation and the classification, pointing to the changes now introduced to earlier versions and showing the improvements. Section 5 presents the raw data filtering, that was just sketched in the previous papers. Finally, Section 6 reports on the results. Examples and results refer to site 5 of the ISPRS laser scanning test dataset (Sithole and Vosselman, 2003).

3. OUTLINE OF THE METHOD

The classification strategy comprises three-stages (see Figure 1). In the first one, raw data are interpolated to a grid, taking the lowest elevation in the cell as grid value. In the second stage, grid data are segmented by a region growing algorithm with adaptive threshold. The geometric characteristics and the topological relationships among the segments are reconstructed and, based on a set of rules, the segments are classified as outliers, vegetation, building or terrain. Although each cell was assigned to a class, the raw data it contains must still be classified individually. In the third and last stage of the procedure, the whole set of raw data is examined. For the former, consistency is measured with respect to the elevations of the neighbouring terrain cells. For the latter, a piecewise approximation of the terrain with a continuous surface is estimated using data from cells classified as terrain; consistency is measured thresholding the distance from the surface.

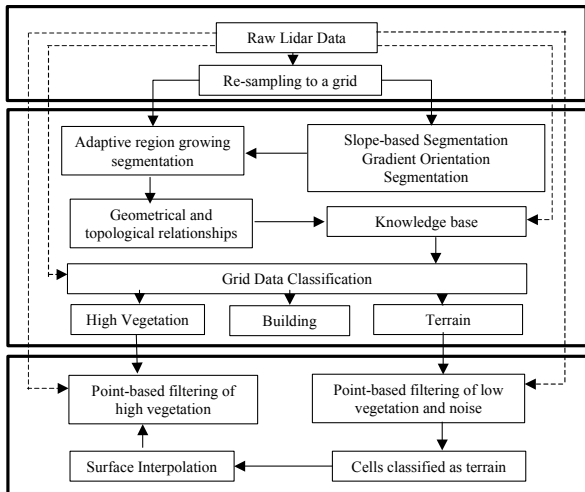


Figure 1. Components and main relationships of the framework for LIDAR data filtering. Solid lines refer to processing of grid data; dashed lines to processing of raw data

Aggregation of raw data in segments enables a richer description of geometric properties and the establishment of topologic relationships. This makes it possible reasoning about

their relationships and provides the contextual information essential to increase the probability of correct classification of single data point in the final stage. This is not to claim that the method is error free, but rather that a segment-based approach (as in feature-based matching) is more robust than just relying on point-to-point comparison in a local neighborhood (as in signal-based matching). Effective filtering cannot be separated by some sort of object recognition and identifying terrain patches or trees should not be seen as different from detecting buildings.

The final stage relies completely on the correctness of the classification of the cells labeled as terrain, since the overall approximation of the terrain is obtained only from cells classified as terrain. Some classification errors can be tolerated: small patches of low vegetation labeled as terrain are filtered out; buildings labeled as terrain, on the contrary, will not. On the other hand, the further a cell is from the nearest terrain region (or the less the terrain cells), the smaller the probability that the approximating surface will truly follow the terrain and so actually will help to correctly discriminate the point class. Data interpolation, segmentation and classification have to find the best compromise between correct labeling of the terrain regions and the attempt to extend them as much as possible, in order to penetrate into the high vegetation areas and to reduce the number of small patches of terrain that, if completely surrounded by vegetation, would be much more difficult to classify reliably.

4. DATA INTERPOLATION, SEGMENTATION AND CLASSIFICATION

In the following paragraphs the three stages of the strategy are reviewed, highlighting the changes introduced with respect to earlier versions and the improvements obtained. Attention is also paid to using First and Last pulse and how positive and negative outliers are dealt with. The behaviour of the procedure is exemplified on the Site 5 dataset of the ISPRS Laserscanning test which offers a great variety of environments, with step edges in the terrain, slopes with different orientation, high vegetation on a steep hillside and a built up area with vegetation with a relatively low density of raw data.

4.1 Grid Data Interpolation

Grid cells are assigned the elevation of the lowest raw point in the cell (see Figure 2). The larger the grid size, the more likely this prevents the noise (such as cars, low trees and so on) to affect the aggregation process. On the other hand, increasing it

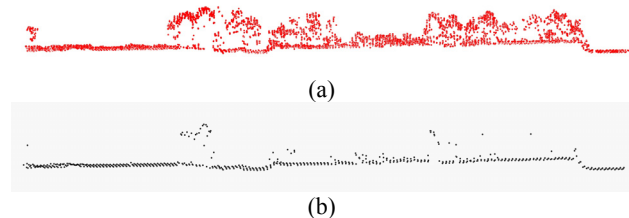


Figure 2. (a) Raw data Points; (b) Grid data Points

too much will affect the extraction of detailed information (slope, aspect, ...) from the grid, which may hamper the effectiveness of further steps. The best grid size should be between one or two times the raw data point spacing.

Empty grid cells are treated as no data, unless all 8-neighbours are non-empty: in this case, the cell value is set to the median of the 8-neighbours.

Figure 3 shows the TIN representation of the raw data (left) and of the grid data (right) in a smooth forest area. It is apparent that, due to the high penetration rate, in such cases the grid representation already constitutes a good, although noisy, approximation of the terrain.

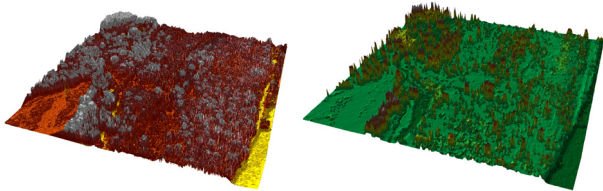


Figure 3. TIN of the raw data e TIN of the grid data on a wooded area.

4.2 Grid Data Segmentation

The region growing is the first step in data segmentation. From a seed pixel, every of the 8-connected neighbours with a height difference from the central pixel less than a threshold is enclosed in the region and becomes in turn a seed point for that region. The process goes on, until no points are added (i.e. the region border will feature a discontinuity larger than the threshold).

Although the result may depend on the cell size and the threshold, the region growing separates most of the high vegetation and of the buildings from the terrain: buildings raise above the terrain by well defined discontinuities (edges), larger than the threshold; laser spots on high vegetation get spread over many very small regions.

Unless some terrain patches are completely bordered by dense vegetation or, in case of bare earth, by a slope so steep that the threshold is exceeded, the whole terrain may end up all in a single region. This is because, from the seed point, the algorithm looks for a smooth path across all the 8-neighbours: therefore, even if in some area the terrain is steeper than the threshold would allow, the region growing may include it by “sneaking through” along a smoother path.

In the original implementation neither the choice of the seed points nor the threshold for the region growing were tied to the morphological features of the grid data. The threshold was set to 0.5 m (i.e. about two times the height error of the data), independently of cell size and terrain slope. The drawback was that, in steep roofs or in steep terrain, several narrow regions may be created, affecting the success rate of building and terrain identification. Figure 4 illustrates the problem that arose with a fixed threshold on a very steep roof.

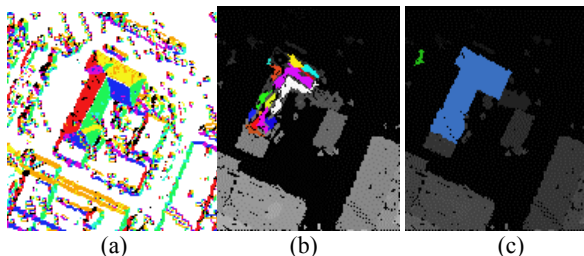


Figure 4. Steep roof segmentation. (a) Gradient orientation image; (b) region growing with fixed threshold: the roof is fragmented in several regions; (c) region growing with slope adaptive threshold: the house is included in one single region bordered by discontinuities.

For a given roof slope, the larger the cell size or the lower the point density, the likelier was a fragmented segmentation.

The same may happen with very steep terrain although, as already pointed out, in such cases the aggregation may come from a smoother adjacent terrain area.

Indeed, the region growing threshold should be coupled to the grid cell size and should also take into account evidence of surface continuity in the neighborhood. Several changes have been made to the original implementation of the method to address this problem. The region growing algorithm is now steered by both the gradient orientation of the grid heights and the slope. The seed pixels of the region growing algorithm are chosen from regions larger than 30 m² with homogeneous gradient orientation while the threshold value is adaptively adjusted to the slope of the region. Moreover, the process starts from the regions with the lowest threshold value.

In large regions with homogeneous gradient orientation the computation of the threshold will not be affected by vegetation.

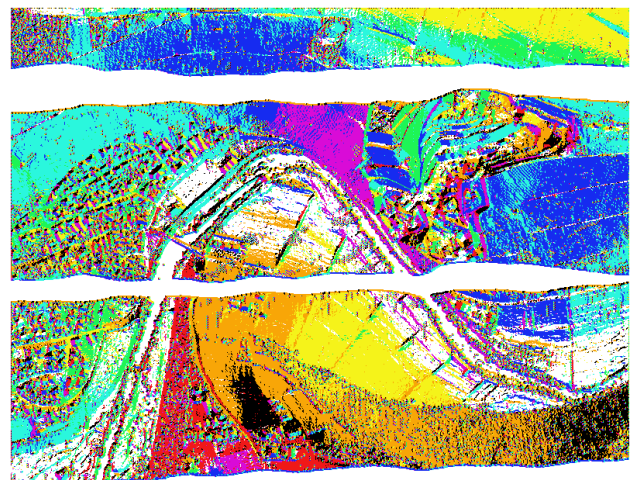


Figure 5. Gradient Orientation of the heights at Site 5. The orientation space is divided in 8 partitions.

The threshold value T for the segmentation based on height differences is computed, in each region obtained from the gradient orientation segmentation, as:

$$T = \min(T_{\max}, \max(T_{\min}, s \Delta + 2\sqrt{s^2 \sigma_{PL}^2 + \sigma_H^2}))$$

where: $T_{\max} = 2\Delta$; $T_{\min} = 0.5 \text{ m}$ $s =$ the 75th percentile of the slope distribution; $\Delta =$ cell size in m; σ_{PL} and σ_H are respectively the planimetric and height accuracy of laser data in m. With this modification the primary segmentation of the grid data becomes in fact a (bounded) slope based segmentation.

Figure 5 shows the gradient orientation (cell size = 2m). Large areas with the same colour correspond to regions having the same aspect (orientation intervals are 45° large). Data holes and flat areas are represented in white. Figure 6 shows the color coded threshold values T for the same dataset.

The seed points for the region growing based on height difference are taken from segments of the gradient orientation segmentation larger than 50 m², from the lower threshold values on. The 0.5 m fixed threshold value is applied to the remaining regions: in this way, areas with vegetation, that exhibit different gradient orientation, or very small patches with the same orientation, get separated in small regions.

Figure 7 shows the most significant segments with different colors. The red spots are very small regions (less than 3 pixels) that will be labeled as outliers or vegetation if several small regions are contiguous. Notice that segments from the region growing may encompass several regions with different gradient orientation or with different slopes.

4.3 Data Classification

Geometric characteristics of the regions and their topological relationships are computed and stored in a knowledge base. A rule-based scheme is applied to classify the regions: the outcome of the process labels each region as vegetation, building, terrain, outlier or unclassified (the last item typically being 1÷3% of the area size). Actually, each class may have sub-classes (e.g. courtyard as part of terrain); among unclassified regions, narrow regions are defined as those slender in shape. Points on high rise chimneys, towers, power line poles, etc may be classified as outliers or buildings, depending on shape, point density and cell size. Currently, no rules discriminate bridges, that are therefore included in the terrain.

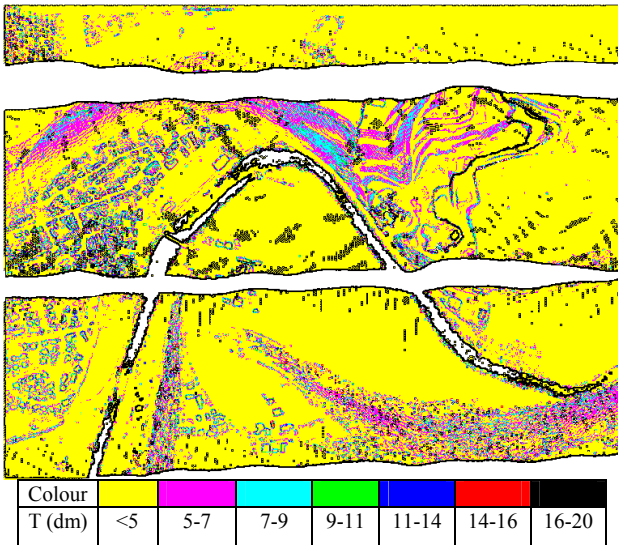


Figure 6. Color plot of the threshold values for the region growing



Figure 7. The most significant regions of the grid data segmentation by the adaptive threshold

The current set of rules has been drawn from simple models of characteristics and relationships between terrain, building and vegetation. The complexity of the task means that robustness of the rule set cannot be taken for granted and that more rules might have to be invoked in new scenarios. Most misclassification errors occur with trees labeled as buildings, buildings as terrain and terrain as buildings. The worst misclassification error is a building included in the terrain, because it will not be corrected in the next stage; on the

contrary, terrain pixels erroneously labeled as building might be recovered in the last stage. Figure 8 shows the result of grid data classification.

4.4 Using First and Last Pulse

Almost every laser scanner today provides first and last (F&L) pulse returns; the pattern of their difference is of great help in identifying vegetation. This is very important to improve both data classification as well raw data filtering: the percentage of grid points in a region where F&L pulse elevations differ is used to help the identification of terrain; raw data filtering (in terrain as well as non-terrain areas) can be robustified by this information (see Section 5).

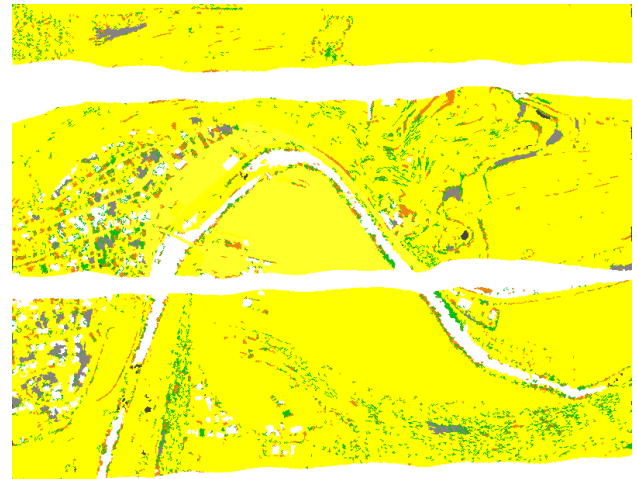


Figure 8. Grid Data Classification. Yellow: terrain; white: building; orange: narrow regions; grey: unclassified.

In the previous implementation of the strategy, cells with different height in the F&L pulses were classified as vegetation before applying the region growing and were not passed to the region growing. This led to more fragmentation of the terrain; now a terrain region penetrates much further into areas with high vegetation, because the (lowest) last pulse of the cell may have an acceptable height difference to nearby terrain cells (whether the pulse indeed hit the terrain or rather the vegetation, is to be clarified, of course).

Grid data under high vegetation are more noisy than those on bare Earth; together with F&L information, this can be used in the final filtering of raw data.

4.5 Outliers

Outliers in laser data are either “negative” (i.e. points below the surface, mostly due to multi-path) or “positive” (i.e. points above the surface, such as hits on birds, power cables, etc). The segmentation makes the classification insensitive to single cells with positive or negative outliers in two ways: if the outlier is the only point in the cell, it will be put in a 1-pixel region and classified as outlier. If there are several points in the cell, some outliers some not, the positive outliers will be recognized in the final filtering stage, because they are higher than the neighbourhood, whatever the class the cell was assigned. With negative outliers, the pixel has been labeled as outlier from the grid classification; other points of the cell may be assigned to terrain or vegetation, depending on the distance from the approximating surface.

Even in case several contiguous cells contain outliers, it is very unlikely that they end grouped in a region, because this would

happen only if they have similar gradient orientation or very small height differences.

5. EXTRACTING TERRAIN POINTS FROM RAW DATA

The output of the grid classification can be divided in two classes: terrain and non-terrain pixels (i.e. pixels classified as building, vegetation, outliers and pixels in unclassified regions). Each raw data in a grid cell is now examined to label it as terrain or as non-terrain point, comparing its distance from a reference surface with a threshold t depending on terrain slope and sensor error tolerance in horizontal and elevation.

The reference surface is computed from the local neighborhood for the former class, from a global approximation of the terrain for the latter. The reason for differentiating between the two classes is to allow more flexibility and fine-tuning for the terrain cells.

Some of or all the raw data points of a cell classified as terrain may in fact be low vegetation or noise. To check against this possibility, a reference value h_{ref} is computed from the neighborhood using a conditional averaging filter. Let m_n be the mean of the neighbouring terrain cells, h_c the elevation of the current cell and $t = 0.5$ m a threshold value for low vegetation:

$$\begin{aligned} \text{if } (h_c > m_n + t) & \quad h_{ref} = m_n \\ \text{else} & \quad h_{ref} = h_c \end{aligned}$$

Cells unclassified or classified as non-terrain may nevertheless contain raw data points that are in fact terrain points. Comparing the elevation of the raw data with the predicted elevation from a surface approximating the terrain, a decision will be made on the point class. To this aim, the most reliable information available (i.e. the raw data labeled as terrain points) is used to compute the approximating surface. The acceptance threshold is computed for each cell as a function of the slope of the surface.

Currently, the approximating surface is computed using bilinear splines with relatively short spacing (3÷4 times larger than the cell size); this may change in the future, to cope in a better way with discontinuities (see below).

Points in cells classified as building do not need filtering; a consistency check of the classification is performed, though: no point in such regions should fall in the acceptance band. If terrain points were erroneously identified as building, they might now be recognized as terrain, if close enough to the interpolating surface.

6. RESULTS ON ISPRS SITE 5

Figure 9 shows the behaviour of the raw data filtering in the forested hillside of Sample51 (ISPRS Site5). The cross-section (a) shows the reference data: terrain (pink) and vegetation (light blue). In (b) the red points are input to the spline, while the predicted value of the terrain in all cells classified as vegetation or in unclassified regions is shown in green. The approximation of the terrain is good and the ensuing raw data classification is correct. On the other hand, if the terrain shows step edges, as in the quarry in Sample53, the interpolation function typically undershoots at the bottom and overshoots at the top (see figure 10 (a)). This smoothing of sharp edges leads to rejection of true terrain points.

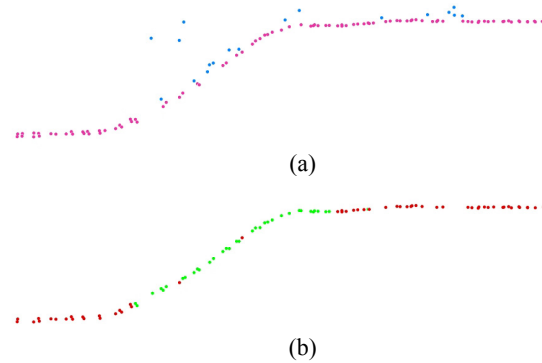


Figure 9. Cross-section of a forested area on a hill side; (a) Reference data: terrain: pink; vegetation or buildings: light blue. (b) Terrain surface approximation: spline input: red; spline prediction: green.

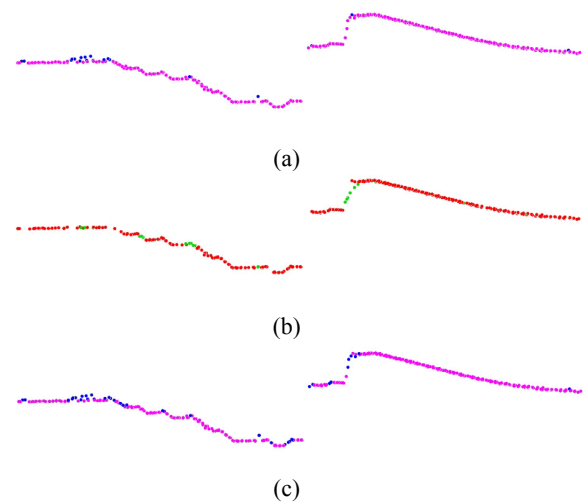


Figure 10. Cross-section of terrain with step edges; (a) Reference data: terrain: pink; vegetation: light blue. (b) Terrain surface approximation: input: red; spline prediction: green. (c) Filtering: accepted terrain points (pink), rejected points (light blue).

Figure 11 shows a cross-section in an area with buildings and vegetation (Sample54) with the same color coding as Figure 10.

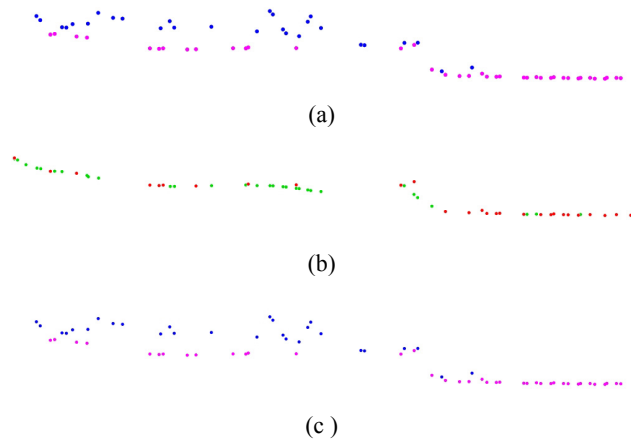


Figure 11. Cross section of an area with buildings and vegetation. (a) Reference data: terrain: pink; vegetation or buildings: light blue. (b) Terrain surface approximation: spline input: red; spline prediction: green; (c) Filtering: accepted terrain points (pink), rejected points (light blue).

Table 1 shows the overall results for the Samples available at Site 5; performance and correctness of the cell classification are measured respectively by the percentage of true terrain points with respect to the total number of terrain points in the Sample and by the percentage of misclassified points with respect to the number of cells labelled as terrain. Filtering errors are given according to the Laserscanning Test definitions.

	Terrain grid classification		Raw data filtering errors	
	#TrueTP in TG wrt #True TP in Sample (%)	#FalseTP in TG wrt #TG cells (%)	Type I	Type II
TP: Terrain Points; TG: Grid cells class. Terrain				
Sample 51	85.1	6.4	8.3	8.6
Sample 52	80.8	2.2	8.5	9.6
Sample 53	77.8	1.0	10.7	14.3
Sample 54	85.5	7.5	4.4	12.0

Table 1. Correctness of grid classification and terrain filtering for Site 5 Samples

Correctness of the terrain grid classification is normally high, taking into account that if a cell contains more than one TrueTP, the others were counted as errors. Classification errors on the grid are higher with high vegetation and buildings (Sample 51 and Sample 54) but filtering improved the results by more than 10% in both cases. With rough terrain, both types of filtering performed less effectively, especially the spline interpolation.

As far as raw data classification is concerned, Type I errors are good and better than most Test participants, Type II are among the largest.

7. CONCLUSIONS AND PERSPECTIVES

A strategy for classification and filtering of raw LIDAR data has been presented. The core of the procedure, i.e. the classification of data segments based on their geometric and topological relationships looks sound enough. On the ISPRS Laser Test Site 5, grid data classification led to the reliable identification of a percentage of true terrain points varying around 80%. Based on that information, a good approximation of the terrain surface can be computed. Terrain raw data close enough to the surface are also recognized as terrain, improving the percentage of success by up to 10%.

Problems arise with step edges in the terrain, because of over- and undershoot of the spline functions: alternative interpolation techniques will be tested soon (in this respect, our last stage needs a pre-filtered input as REIN (Kobler et al., 2007).

New approaches to rule definition in the grid classification are also being tried: an attempt is currently underway to automate the search for patterns in the data, using classification trees (Sutton, 2005) such as the AdaBoost algorithm.

Acknowledgements

George Vosselman and George Sithole are kindly thanked for allowing the use of the ISPRS data as well as of the manually classified control samples. Many thanks go to Simone Atzori for his invaluable support in using GIS software.

References

Axelsson P., 2000. DEM generation from Laser Scanner Data using adaptive TIN Models. IAPRS, Vol. 33 B4/1 pp. 110-117.

Brovelli M.A., Cannata M., Longoni U.M., 2002 Managing and processing LIDAR data within GRASS. Proc: Open source GIS - GRASS users conference. Trento, Italy, 11-13 Sept. 2002.

Filin, S. 2002, Surface Clustering from Airborne Laser Scanning Data. IAPRS, Vol. 34/3 A, Graz, Austria, 2002.

Filin S., Pfeifer N., 2006. Segmentation of airborne laser scanning data using a slope adaptive neighborhood. *ISPRS Journal of Photogrammetry and Remote Sensing*, 60(2):71-80, April 2006

Forlani G., Nardinocchi C., Scaioni M., Zingaretti P., 2006 Complete classification of raw LIDAR data and 3D reconstruction of buildings, *Pattern Analysis Applications*, 8: 357-374. DOI 10.1007/s1004-005-0018-2.

Kraus K., Pfeifer N., 1998. Determination of Terrain Models in Wooded Areas with Airborne Laser Scanner Data, *ISPRS Journal of Photogrammetry & R. S.*, vol. 53, pp. 193-203.

Kilian, J., Haala, N., English, M., 1996. Capture and evaluation of airborne laser scanner data. IAPRS, Vol. 31/B3, pp. 383-388.

Kobler A., N. Pfeifer, P. Ogrinc, L. Todorovski, K. Ostir, S. Dzeroski, 2007. Repetitive interpolation: A robust algorithm for DTM generation from Aerial Laser Scanner Data in forested terrain. *Remote Sensing of Environment*, 108 (2007), 1; pp. 9 - 23.

Nardinocchi C., Forlani G., 2001. Detection and segmentation of building roofs from Lidar data. *ISPRS Workshop 3D digital imaging and modelling applications of: Heritage, Industries, Medicine & Commercial Land*, Padova, 3-4 April 2001.

Nardinocchi, C., Forlani, G., Zingaretti, P. (2003). Classification and Filtering of laser data, IAPRS, Vol. 34 Part. 3/W13, 79-86.

Roggero, M., 2002. Object segmentation with region growing and principal component analysis. IAPRS, Vol. 34, Part 3A, Graz, Austria.

Sithole G., 2001. Filtering of laser altimetry data using a slope adaptive filter, IAPRS Vol. 34 3/W4, pp. 203-210.

Sithole G., Vosselman, G. 2003. Comparison of filtering algorithms. IAPRS, Vol. 34 3/W13, pp.71-78.

Sithole G., Vosselman, G. 2005 Filtering of airborne laser scanner data based on segmented point clouds. In: "Laser scanning 2005". IAPRS, Vol. 33,3/W19, pp. 66-71.

Sutton C.D., *Handbook of Statistics*, vol. 24, cap. 11: Classification and regression trees, bagging, and boosting, Elsevier, 2005

Tovari D., Pfeifer N., 2005 Segmentation based robust interpolation – a new approach to laser data filtering. In: "Laser scanning 2005". IAPRS, Vol. 33,3/W19, pp. 79-84.

Vosselman G., 2000. Slope based filtering of laser altimetry data. IAPRS, Vol. 33, Part B3, pp. 935-942.

Wack, R., Wimmer, A. 2002. Digital terrain models from airborne laser scanner data - a grid based approach. IAPRS, Vol. 34/3 B, Graz, Austria, 2002.

LIDAR-DERIVED SITE INDEX IN THE U.S. PACIFIC NORTHWEST – CHALLENGES AND OPPORTUNITIES

Demetrios Gatzliolis

USDA Forest Service, PNW Research Station, Forest Inventory and Analysis, Portland, Oregon USA – dgzatzliolis@fs.fed.us

KEY WORDS: LiDAR, Site Index, Forest Inventory, Pacific Northwest, Douglas-fir.

ABSTRACT:

Site Index (SI), a key inventory parameter, is traditionally estimated by using costly and laborious field assessments of tree height and age. The increasing availability of reliable information on stand initiation timing and extent of planted, even-aged stands maintained in digital databases suggests that information on the height of dominant trees suffices for assessing SI. Light Detection and Ranging (LiDAR) is a technology proven capable of providing reliable estimates of tree height even at the individual-tree level. A rigorous evaluation of LiDAR-enabled SI estimation performed on coniferous stands of the coastal U.S. Pacific Northwest indicates that where stand structure and topographic conditions support a high-fidelity assessment of ground elevation, accurate ($R^2 = 0.88$) estimates of SI should be anticipated. In more challenging conditions the accuracy of the estimates lessens substantially. A limited evaluation of spatial SI predictions indicates that the distribution of the index might not always conform to the expectations commonly held by forest managers and planners.

1. INTRODUCTION

Site index (SI) is the most commonly used indicator of site productivity (Hägglund, 1981), forms the basis for many forest management activities (Zeide and Zakrzewski, 1993), and it is an integral component of forest inventory systems (Hanson et al., 2002). It is calculated as a function of the height of dominant trees at some reference age, usually in even-aged stands (Monserud, 1984; MacFarlane et al., 2000). The formulation of the function can differ between species or ecoregions. Assessment of SI is typically performed at selected locations within the forest where estimates of tree height and age are obtained via standard forest field mensuration techniques. To avoid bias in SI estimates, it is essential that trees participating into its calculation, sometimes referred to as site trees, meet certain selection criteria (Nigh and Love, 1999), including dominant status, absence of injuries or growth suppression, and a preferred range of age.

Obtaining reliable estimates of individual tree height and age is a laborious and costly process often inhibited by visibility constraints, wood density that does not allow tree trunk boring to determine age, etc. Because of these limitations, SI estimates have traditionally been restricted to locations hosting inventory plots, and spatial predictions of SI have been rare. Recent efforts to assess the spatial distribution of SI have relied on relating multiple environmental variables in a geographic information system via regression tree analysis, geostatistics, and multiple regression (Iverson et al., 1997; Gustafson et al., 2003; McKenney and Pedlar, 2003). There has been speculation (Louw and Scholes, 2002), however, that the multiple-variable approach will be gradually replaced by superior, in terms of predictions accuracy, physiologically based simulation models such as 3-PG (Landsberg and Waring, 1997) or PROMOD (Battaglia et al., 1999). A recent implementation of the 3-PG spatial model in Oregon, USA, that used monthly averaged climatic data, estimates of soil attributes, and Forest Inventory and Analysis (FIA) data from thousands of plots in national forests to produce SI maps of Douglas-fir (*Pseudotsuga menziesii* (Mirb.) Franco) showed promising results ($R^2 = 0.55$), despite issues related to plot size, density and georeference precision (Swenson et al., 2005). The coarse resolution of the

3-PG model's prediction (1 km²) in Oregon, or of comparable multivariate models implemented elsewhere, limits their utility to forest planning and decision making at the strategic level only. The often substantial SI variability within a stand or tactical management units remains unknown.

The parsimonious parameterization of standard SI models indicates that where even-aged is the preferred or common forest stand structure and stand age is known, information on the height of dominant trees is sufficient for obtaining local estimates on forest productivity and SI. Because spatial predictions of tree height and other forest inventory parameters are restricted by financial and logistical constraints (St-Onge et al., 2004), forest managers and inventory specialists have long been regarding remote sensing as perhaps the only feasible alternative to field measurements for obtaining spatial predictions that meet established accuracy standards over entire management units (Turner et al., 2004). Remote-sensing-derived estimates of tree height are typically obtained via the classic parallax method. Applied either on stereopairs of analog aerial photographs (Worley and Landis, 1954) or more recently (and more efficiently) on digital high-resolution imagery (Korpela, 2004) the method was found to produce unbiased tree height estimates only where a precise the ground-level elevation could be assessed correctly at, or near, the base of trees, a prerequisite rarely met in closed-forest canopies (St-Onge et al., 2004).

Unlike aerial photography and other forms of optical remote sensing, Light Detection and Ranging (LiDAR), sometimes referred as airborne laser scanning (ALS), is capable of penetrating the forest canopy, and hence is well suited to describing the vertical structure of forests. Owing to the capacity of small footprint laser pulses emitted from the airborne scanning instrument to propagate through small canopy openings and echo at ground level, LiDAR is also capable of assessing ground elevation (Kraus and Pfeifer, 1998). Small-footprint scanning data comprise a set of points, sometimes known as 'returns', accurately and precisely georeferenced in three dimensions (Baltsavias, 1999). Assuming adequate return density (> 4 points / m²), processing of the point cloud data allows individual trees to be detected

(Brandtberg et al., 2003), and digital models of the vegetation canopy surface (CSM) and (bare-) ground surface (GSM) to be generated (Hodgson et al., 2003; Clark et al., 2004). Estimates of height for individual trees are obtained by subtracting from the CSM value, at selected locations believed to represent tree crown apices, the corresponding, in two-dimensions, GSM value. Variants of this approach have yielded height estimates for individual trees that rivaled the accuracy of those acquired in the field (Hyypä, 2000; Persson et al., 2002; Andersen et al., 2006).

Because the estimates of tree height depend on the fidelity of the LiDAR-derived forest canopy and bare-ground models, vegetation and topographical conditions that promote uncertainty, and perhaps bias, in model values became sources of error in tree height estimation. Choices of parameter values and assumptions embedded into the algorithms used in generating the models can also contribute uncertainty or bias (Kobler et al., 2007). Canopy models derived from LiDAR data tend to underestimate the true vegetation surface. The negative bias has been attributed to the laser pulse not always hitting the tree apex (Næsset and Økland, 2002) and having to penetrate the canopy surface before reflecting the first significant return (Hill et al., 2002). GSMs are generated under the assumption that enough pulses penetrate thoroughly through the stand profile to enable an accurate assessment of bare-ground elevation. Ackermann (1999) reported that 20 to 40 percent of pulses may reach the ground under dense forest canopies. Reutebuch et al. (2003) found that even in dense coniferous stands the density of ground returns enabled construction of a GSM with root-mean-square-error (RMSE) of only 0.31 m. Other studies have reported though that in increasingly complex vegetation, multiple-scattering reflection or absorption of the energy carried by a pulse reduces the number of ground returns or causes returns from understory vegetation or tree trunks to be erroneously labeled as representing the ground (Harding et al., 2001; Raber et al., 2002; Hodgson et al., 2003). In forest stands with complex profiles, GSM overestimation of at least 1.5 m is common (Hodgson et al., 2003; Clark et al., 2004) and bias should be expected to increase further with even moderate slopes (Kobler et al., 2007).

Although many studies have investigated the fidelity of LiDAR-derived estimates of tree height (Næsset, 1997; Popescu et al., 2002; Maltamo et al., 2004), very few were performed in dense forests or in terrain characterized by steep slopes (Clark et al., 2004). The paucity of studies where laser scanning is used for estimating tree heights in forests that are both dense and situated on steep slopes is likely due to the fact that, in such conditions, it is logistically and financially exceedingly difficult to obtain reliable field measurements of tree height necessary for evaluating the height estimates derived from LiDAR data. The challenge is further intensified where precise height estimates are needed over an area, a prerequisite for assessing inventory parameters with spatial support such as SI, instead of only at selected locations. The objectives of this study that address these challenges were a. to evaluate the fidelity of LiDAR-derived estimates of SI, and b. to investigate potential patterns in the spatial distribution of Site Index in the structurally complex temperate rainforest growing on the steep terrain of the coastal U.S. Pacific Northwest. The evaluation is based on rigorously calibrated field data obtained by using survey-grade equipment on plots established specifically for this study.

2. METHODS

2.1. Study area

The 9500-ha study area is on the coastal mountains of Lincoln County, in the State of Oregon, USA (Figure 1), and centered approximately at 44° 32'N, 123° 39'W. More than 90 percent of the area is temperate rainforest, with mean annual precipitation of 2005 mm. Forty seven percent of the forests are privately

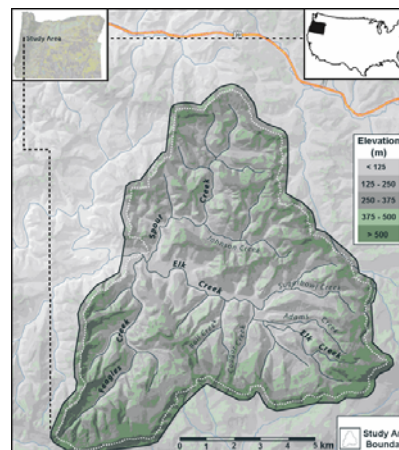


Figure 1. Study area

owned and under very intensive, timber-oriented management. 1550 ha are owned by the State of Oregon and 3850 ha are part of the Siuslaw National Forest where management has been limited to occasional non commercial thinnings, very few of which occurred after 1984. Prevalent species in the study area include Douglas-fir (*Pseudotsuga menziesii* (Mirb.) Franco), bigleaf maple (*Acer macrophyllum* Pursh), and red alder (*Alnus rubra* Bong.), with the hardwoods dominating buffer zones around the drainage network. Elevation ranges from 66 to 1123 m above sea level and terrain is characterized by steep slopes. Over the forest area the mean slope is 61 percent, and the 75th slope percentile is 84.

2.2. Field data

Forty five fixed-area plots of 15-m radius were established in the study area in summer 2005 stratified across classes of cover type (conifers, hardwoods, and mixed), tree size, and stand density. A three-member, veteran FIA crew visited each plot tallying all trees with diameter at breast height (DBH) exceeding 12.7 cm or of dominant or co-dominant status regardless of DBH. For each tree, the species and DBH was recorded, and the projection of its crown to the ground was delineated using distance and azimuth measurements from the tree base (Figure 2). Continuous feedback from the remaining crew members was used to guide a person operating a clinometer to on-ground locations that defined the shape of the crown being delineated. Estimates of tree height obtained via an electronic clinometer / distance finder were assigned a precision-class code reflecting the crew's confidence on the estimate. Two dominant trees in each plot were bored to determine age. Sketch maps depicting the presence, type, and height of understory vegetation were also produced.

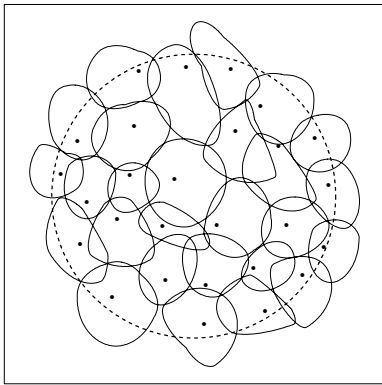


Figure 2. Field-delineated crowns of a plot and corresponding tree bases. The dashed line represents the plot boundary.

Management archives and stand maps from the Siuslaw National Forest and management plans or operation records kindly contributed by local tree farms were examined to determine the age of stands in nearly 75 percent of the forest land. After excluding all plots in uneven-aged or young (< 20 years) stands or where records suggested past stand improvement activities (fertilization, etc.), a set of 21 plots, all dominated by Douglas-fir, was selected and used in this study. The age of dominant trees ranged among the selected plots from 27 to 74 years. Plots comprising older and larger trees were in publicly owned stands.

The large percentage of height estimates assigned a low precision code in close-canopy stands confirmed skepticism that, in such conditions, traditional field mensuration techniques could not support the study's tree height precision requirements. To mitigate these limitations, an alternative, far more complex, approach was devised. It entailed a detailed survey of the bare ground and calibration of the tree crown apexes in each plot.

2.2.1. Plot registration and ground survey. For each plot a minimum of two locations was precisely referenced using a Real Time Kinematic (RTK) global positioning system instrument at leaf-off conditions. The instrument was set to record only when the expected, internally calculated, three-dimensional precision was better than 5 cm. Because the operation of the RTK instrument is limited to areas free from overstory vegetation, in 12 of the plots the closest two locations successfully recorded with the RTK were in canopy openings well outside the plot boundary. For those plots, transects connecting reference locations to corresponding plot centers were established and surveyed with a total station. For the remaining 9 plots, unobstructed, under canopy, lines of sight between the RTK reference locations and the plot centers supported direct plot georeferencing via the total station. Additional RTK reference locations and transects installed for 4 of the 12 plots revealed that the location error of the plot center ranged from 5.3 to 11.6 cm (mean 8.4 cm). Considering the difficult terrain and poor visibility conditions, the error level was deemed acceptable. With the total station positioned and oriented on the plot center, terrain inflection points were flagged over the plot area and a 5-m buffer around it. The flag density was higher in portions of the plots exhibiting variations in micro-topography. Across plots the density of flagged points had an average of 0.31 per square meter. Using Delaunay triangulation, the coordinates of flagged locations recorded with the total station were processed to generate a Triangulated

Irregular Network (TIN) for each plot, and the TINs were then converted to 1-m rasters via cubic convolution. Five 10-m wide corridors transcending the boundaries of stands with contrasting stem densities and structure were also surveyed in late summer 2006, but with smaller point density. Canopy and ground models for the corridors were generated following the methodology used for the regular plots.

2.2.2. Calibration of tree apexes. Tree-apex calibration was performed by using 14 additional plots of custom size and shape installed either in short (< 3 m) vegetation or along the edge of Douglas-fir stands exposed by recent clearcuts. The leader stems of the trees were surveyed during windless days with the total station from three reference positions in the clearcut area previously surveyed with the RTK instrument. The methodology used is similar to the one detailed by Andersen et al. (2006). Trees with apex measurement RMSE exceeding 7.5 cm were eliminated from further consideration. A comparison of the coordinates of the surveyed apexes to the coordinates of co-located (within 1 m in two dimensions) highest LiDAR returns for 120 trees of various sizes and ages revealed an elevation bias of -0.58 m (Figure 3). The calibration procedure was repeated at leaf-off conditions with nearly identical results.

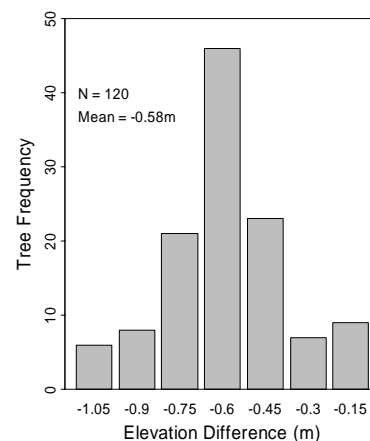


Figure 3. Histogram of discrepancies between surveyed and LiDAR-derived tree apex location at leaf-on conditions

2.2.3. Estimation of tree-height. To determine the heights of dominant and co-dominant trees in each plot, the field-delineated crowns were first overlaid with the return cloud. The elevation of the highest return within a crown was recorded and subsequently adjusted to account for the bias mentioned above. The calibrated tree height was then computed as the difference between the calibrated elevation of the highest return and the value of the GSM at the base of the tree. Calibrated heights for a total of 313 trees were computed.

2.3. LiDAR data

Laser scanning data were acquired at leaf-on conditions in July 2005 and leaf-off conditions in February 2006 using an aircraft-mounted Optech 3100 system from an average height of 1000 m above ground level. The LiDAR instrument operated on a 71 kHz laser repetition rate, captured a 20° scan width (10° from nadir) with adjacent flight line overlap of 50 percent, and yielded an average density of 9.81 returns per square meter for the leaf-on mission and 8.70 returns per square meter for the leaf-off mission. For both missions the spot spacing was 32 cm

with laser footprint diameter of 33 cm. Compared to horizontal, impermeable surfaces surveyed with the RTK, the laser returns sustained an RMSE of 2.6 cm during the leaf-on mission and 3.1 cm during the leaf-off mission. The scanning data delivered by the vendor had been processed with proprietary software to eliminate path reflectance points and to identify ground returns. The latter was enabled by an implementation of the adaptive TIN model (Axelsson, 2000). The raw (pre-filtered) data set for both missions was also obtained.

2.3.1. Canopy and ground models: For each plot, a 1-m canopy model was constructed by querying the returns cloud to determine the highest returns within the two-dimensional area occupied by each cell. Owing to the high return density and short pulse spacing, discontinuities in the canopy models were rare for both acquisitions and were observed only along the edge between adjacent crowns in plots with small canopy openings. GSMs were developed using the filtered returns classified as representing the ground via ordinary Kriging (Goovaerts, 1997) with a minimum of six nearest neighbors. Both canopy and ground surface models were co-registered to the GSMs generated from the survey data.

2.3.2. Tree identification and assessment. Individual trees were identified via the local maxima method (Wulder et al., 2000) using the LiDAR-derived canopy over the plot areas. After the elevation of GSM-identified tree apexes was bias-adjusted, the height of corresponding trees was computed as the difference between the tree apex elevation and the value of the co-located cell in the LiDAR-derived ground model. The local maxima method identified 294 trees. It was determined by visual examination of stem maps, delineated crowns, and the identified tree apexes that the tree list contained 26 errors of omission and 7 errors of commission.

2.4. Plot Site Index

The SI estimation for each plot followed the standard FIA protocol for Douglas-fir-dominated forest conditions. The protocol uses Equation 1, known as the King’s (1966) formula, to compute estimates of SI for the five largest (in terms of DBH) or five tallest SI-eligible trees present within a 0.2 ac (809 m²) area. The plot SI is then computed as the mean of the five estimates.

$$SI = \frac{25000 * (1.09757 + \frac{7.92236}{10^2} * A + \frac{1.97693}{10^3} * A^2) + 4.5 * (\frac{3.2808 * A^2}{H - 14.764} + \frac{9.5404}{10} - \frac{5.5818}{10^2} * A + \frac{7.3382}{10^3} * A^2)}{3.2808} \tag{1}$$

where SI = King’s SI in meters at reference age of 50 years
 A = breast-height age
 H = tree height in meters

Using classes of mean annual increment as reference, Equation 1 can be translated into a family of SI curves (Figure 4), commonly used to classify site productivity, instead of the actual SI values.

To investigate whether or to what extent tree selection affects the plot estimate, three SI versions were computed. The first (SI_D) was based on the trees with the largest, field-measured DBH. The second (SI_H) was based on the tallest trees identified

in the field survey. The last version (SI_L) employed the tallest trees whose height was derived from the laser data. All versions used the stand age retrieved from the management records, adjusted for 6 years, the average time required for a tree to reach breast height from seed.

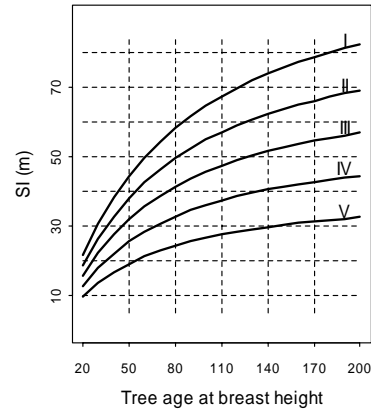


Figure 4. Douglas-fir Site Index classes for the coastal U.S. Pacific Northwest

2.4.1. Spatial predictions of SI. Investigations on the spatial continuity of SI focused on six areas, approximately 1 Km² each, where the stands present met the age and structure criteria for assessing SI. Given that reliable ground information, and therefore tree height, was available only for a single transect surveyed in each of these areas, the spatial investigations of SI were only exploratory in nature and employed omni- and directional variograms, along with an evaluation of potential trends (first-order spatial autocorrelation) in the predictions. The fidelity of SI maps produced was evaluated by visual, on-ground assessments performed while cruising the stands in the six focus areas.

3. Results

Tree age assessed by boring selected trunks was across plots, on average, 1.9 years (standard deviation 0.9) lower than the age expected from the stand history records. In the absence of cases showing the age determined by boring to exceed the age dictated by the records, and given that age underestimation for bigger trees where missed growth rings or failure to penetrate the trunk to its center is more common than in younger trees, there was no reason to doubt the accuracy of the stand age retrieved from management records.

Interesting insights into the interaction of dense coniferous vegetation and the laser pulses are obtained by subtracting the surveyed from the LiDAR-derived GSMs. For 10 of the 21 plots no macro-scale differences were observed between the surveyed ground surfaces and those computed from the leaf-on laser data. The paired discrepancies in cell values formed leptokurtic Gaussian distributions with means that ranged from -0.28 to -1.04 m. Nine of these 10 plots had little or no understory vegetation and the overstory had either been thinned in the past or contained regular canopy openings due to age progression. The 10th plot (Figure 5b) had a very dense overstory but was located on mild (51 percent) slope. For another five plots, the discrepancies between surveyed and derived surface elevation were larger, up to -2.19 m, and the distribution of paired cell value differences was wider than in the previous group. In three of the five plots the distribution

was bimodal. All five plots had dense multi-layer understory vegetation with overstory exhibiting occasional openings. For the remaining six plots large scale discrepancies were observed between the surveyed and LiDAR-derived surfaces. The distribution of cell value differences had Gaussian form with means ranging from -4.97 to -11.02 m (Figure 5a). The plots in this group were either located on very steep slopes or had dense, completely closed canopies. Substituting the leaf-on laser data with the leaf-off version caused a slight reduction in the discrepancies between the surveyed and derived ground surfaces for the first two groups of plots with the mean differences in the first group now ranging from -0.18 to -0.84 m and in the second from -0.46 to -1.58 m. No improvement in ground-surface discrepancies was observed for the third group. The third was also the only group of plots where returns located above the surveyed ground were eliminated during data preprocessing, an observation pertaining to both acquisitions.

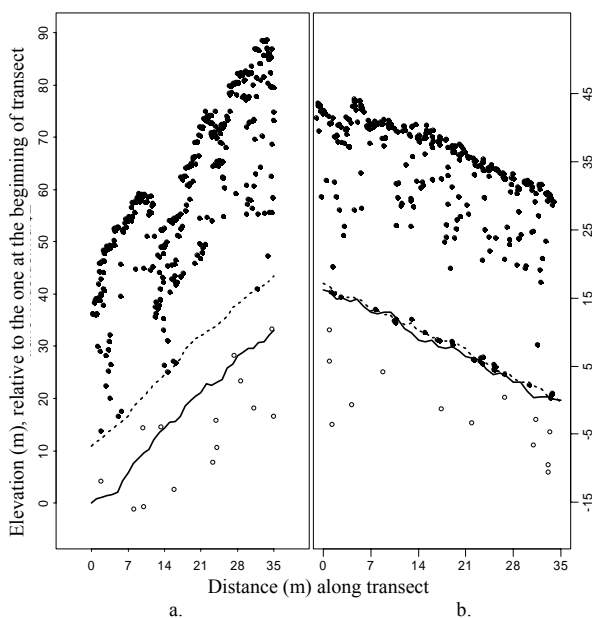


Figure 5. Plot profiles of 1 m depth depicting laser returns either maintained (dots) or filtered out (hollow circles) during data preprocessing, and surveyed (solid lines) and LiDAR-derived (dashed lines) ground surfaces.

In the process of overlaying the field-delineated tree crowns with the return cloud to evaluate the fidelity of individual tree identification procedure a pattern emerged that involved the relative location of tree apexes and bases. It was determined that for the majority of trees, the projection of the tree apex to the ground was downhill from the tree base, an indication that the trees were leaning systematically away from the slope. By considering that a tree was leaning if the horizontal distance between its apex and base exceeded 0.5 m, it was determined that 165 trees (53 percent) were leaning away from the slope, 50 trees (16 percent) were leaning in parallel to the contour lines, and 41 trees (13 percent) towards the slope. For the remaining 18 percent of the trees no appreciable leaning was observed. The intensity of the leaning was found to be positively correlated to slope and tree height, and negatively correlated to canopy closure, but the correlation was weak, with coefficients of 0.19, 0.16, and -0.17, respectively.

The option of selecting the trees with the largest DBH instead of the tallest ones was found to have little effect on the plot SI estimate. A t-test of the paired differences between SI values computed using the two alternative methods for tree selection failed to reject the hypothesis that the SI estimates were equal ($p > 0.5$). Substituting, however, either one of the alternative field-data-assessed SI estimates in the test with their LiDAR-derived equivalent, rendered the test significant ($p < 0.001$).

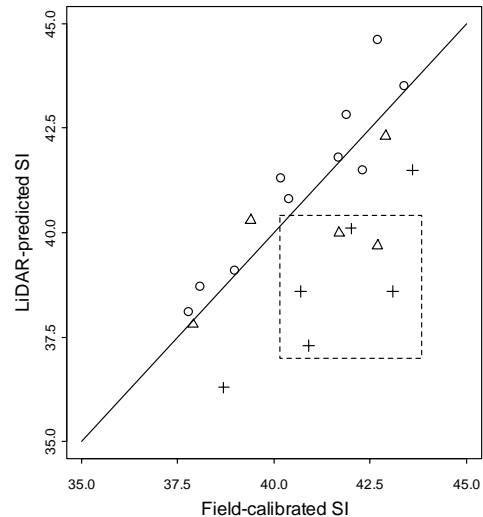


Figure 6. Plot Site Index values computed using the tallest trees surveyed in the field and their LiDAR-derived equivalent. Symbols indicate plot membership in classes of fidelity for the ground surface extracted from the laser data.

The causality behind the t-test findings becomes evident when examining the information in Figure 6, which compares the field calibrated and LiDAR-derived plot SI. Index values shown by circles in Figure 6 represent plots where the LiDAR-derived ground surfaces approximate the surveyed surfaces fairly well. In all but one of these plots, the predicted values exceeded the calibrated values, an indication that the tree height underestimation caused by the slight overestimation in ground elevation is somewhat overcompensated for by the trees leaning away from the slope. The values shown by crosses correspond to plots where the overestimation of ground elevation via LiDAR far exceeds the height overestimation due to leaning and results in index underestimation. With two exceptions, index values represented by triangles correspond to plots where elevation overestimation is somewhat balanced by tree height overestimation due to leaning. Note that 6 of the 11 plots in the last two groups (shown within a square in Figure 6) would be assigned an SI class of *II* when assessed via LiDAR and an SI class of *I* by using the calibrated field data. For the other 15 plots, the SI class assignment would not be affected by the method used to predict the index.

Regressions of the field-calibrated SI on the predicted values produced a low overall R^2 value of 0.42. The R^2 values pertaining to separate regressions computed using only the plot in each of the groups depicted in Figure 6 were substantially higher though, and for the group of plots established in medium density stands on moderate slopes, conditions that support assessment of ground elevation free from gross errors, it reached 0.88. Areas with conditions similar to those prevalent in the latter group of plot became the focus of investigations that evaluated the fidelity of spatial predictions of SI.

SI values predicted at 27-m intervals, the spacing equivalent to the size of field plots, were used to calculate omni- and directional variograms for each of the six, approximately 1km² areas where stand characteristics allowed computation of high-fidelity GSMS. A variogram quantifies how the values of a spatially distributed phenomenon change with distance. Typically, the value dissimilarity (semivariance) increases with distance until an asymptote (sill) is reached. The distance at which the sill is reached is known as the range of the variogram. Although there were notable differences in their form, all SI variograms computed for the six areas failed to reach a sill, thereby indicating the presence of low-order spatial autocorrelation(s), sometimes referred to as trend, affecting the predictions of SI. Of the many topographical covariates that were examined as a potential trend source (aspect, elevation, slope, wetness index, local ground curvature), only two were found to be significant at $\alpha = 0.05$: the distance to streams, which explained an average 9 percent of the SI variance across the six areas, and a composite variate computed as the natural logarithm of the slope cost distance away from streams, which explained 19 percent of the SI variance. Surprisingly enough, the percentage of SI variance explained increased to an average 31, almost a third of the total, when the variate was modified to be the natural logarithm of the absolute slope cost distance computed at 50 m from streams across contour lines. Variograms of the residuals of SI predictions (i.e. with the influence of the trend on the predicted SI values removed) regressed on the modified variate values did reach a sill, an indication that the remaining 69 percent of the SI variability is likely caused by genetic differences among the trees, soil characteristics, and variability in microclimate.

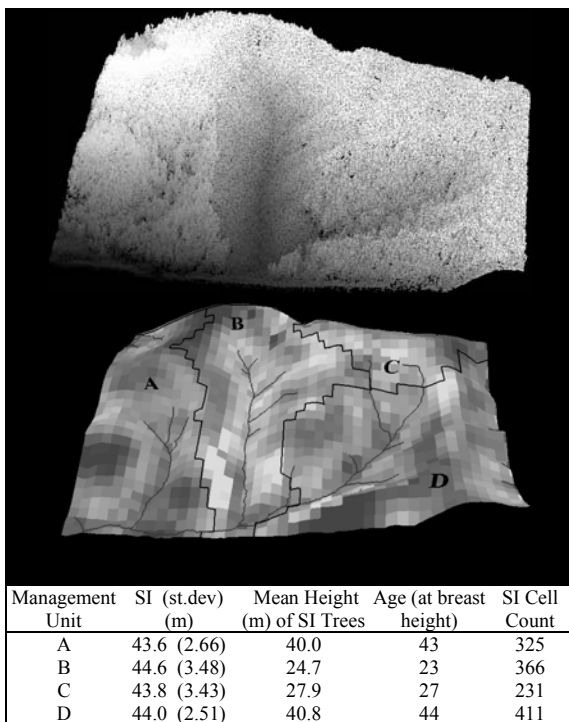


Figure 7. Top: Perspective view of the return cloud for a 1-km² area used in the evaluation of SI. Middle: Perspective view of SI predictions. Lighter tones indicate higher index values. The thick lines delineate management units; the thin lines represent

the drainage network. Bottom: Descriptive statistics of SI predictions for each management unit.

Although only a third of the variability in the SI has been accounted by spatial variates, the absence of discontinuities across management unit boundaries (Figure 7) suggests that at a coarser scale, LiDAR-enabled assessment of SI yields robust results. In the area depicted in Figure 7, the mean predicted value for SI is practically the same for all four management units despite the stand age differences. The higher variability in the predicted values for units B and C is likely due to the slope of the SI curves being much steeper at smaller reference tree ages (Figure 4) than at older ages. A set amount of height variability for a group of adjacent younger trees would produce a higher SI variance than for a group of older trees.

4. Discussion

Evidence from the surveys of ground surface in this study and the analyses of laser data profiles in dense, coniferous canopies appear to contradict the commonly held belief that, given a high pulse density per unit area, enough pulses would penetrate the vegetation profile to allow detection of the forest floor. There appears to be a limit in canopy density, albeit difficult to quantify and likely different among forest cover types, beyond which the percentage of pulses that manage to penetrate the upper canopy layers exhibit substantially higher levels of path reflectance compared to the pulses penetrating less dense canopies. The implication of this phenomenon is that the already small amount of returns that are indeed reflected by the ground surface, are perceived as originating from much below. In such conditions, the density of legitimate ground returns is too small over extended areas to support the detection of ground surface.

Steep terrain introduces additional difficulties in ground detection. The algorithms used for the assessment of bare-ground utilize, sometimes directly, sometimes implicitly via simulation, slope thresholds to eliminate above ground returns. In 100 percent slopes or higher, the search radii associated with the slope thresholds that are used by the algorithms to quantify the spatial relationships between adjacent returns become so large that, inevitably, cause legitimate, above ground returns to be eliminated. Employing a more advanced algorithm for scan data filtering and ground assessment might have improved slightly the fidelity of tree height estimates and ultimately of the SI estimates but only for the plots located on milder slopes and with non-continuous canopies.

To minimize acquisition costs while maintaining high return density coverage, LiDAR instruments capable of increasingly higher pulse rates have been developed. Personal communication with LiDAR data vendors in the western U.S. has revealed that the 15-fold increase in pulse rates over the last few years has not been accompanied by an even near increase in the power the instrument outputs. Simply put, modern instruments emit more but weaker pulses. Studies that have successfully retrieved the ground surface in tropical (Clark et al., 2004) or in dense, coniferous forests (Reutebuch et al., 2003) have used pulse rates much lower than the one used in this study. Unless the per-pulse energy could be increased, in laser data acquisitions where unbiased retrieval of the ground surface is of essence, lower pulse rates might warrant consideration.

The decent correspondence (R^2 of 0.88) between field-calibrated and LiDAR-assessed SI in nearly half of the plots used in this study suggests, that in ecosystems and biomes with

topography and vegetation complexity less challenging than those in the coastal U.S. Pacific Northwest, high-fidelity index estimates should be expected. If the assumptions about absence of gross ground surface errors in the areas where spatial evaluations were attempted were valid, then useful information can be gleaned from such data at the spatial domain as well. The finding, for example, that a lag of 50 m from streams added to a spatial variate improves the percentage of variance in spatial SI predictions explained by that variate, challenges common beliefs held by local forest managers. Regulations limiting harvesting or other management operations to only outside 15 to 45 m buffers around streams and creeks are thought anecdotally to exclude from timber production the portion of the land with the highest growth capacity. This study hints that this is not the case. Perhaps excessive soil moisture near the drainage network early in the growing season may actually shift the most productive land at some distance uphill. The limited influence topography is found to exert on the values of the index could relate to the limited range of index classes present within the study area and the relatively small extent of the six areas evaluated. Upcoming LiDAR acquisitions over Douglas-fir stands growing on shallow soils and higher elevation might enable a more precise quantification of topography's influence on SI.

The applicability of the methodology used in the study to predict SI is limited to stands with even-aged, usually planted overstory and where detailed stand initiation and management records are available. It is also limited to species that maintain substantial, and hence LiDAR-discernible, height growth until older age classes. The study also indicates that because of substantial local variability in the height of dominant trees even within short distances, it is important that SI estimates be based on an adequate sample of trees.

5. Conclusion

The ability of LiDAR to penetrate stand profiles renders it a useful technology for quantifying the vertical dimension of forests and for assessing key inventory parameters such as SI. As this study has demonstrated, however, in dense forests with continuous, closed canopies growing on steep terrain, laser pulses often fail to penetrate the stands and to adequately sample the ground. Substantial errors in the assessment of ground elevation propagate through the computation of tree height and introduce bias in the predicted SI values. Additional, albeit smaller, bias is introduced by the underestimation of tree apex elevation and tree leaning. A better understanding of the mechanisms governing the interaction of laser pulses and dense vegetation could help predict the conditions where tree height and SI estimates might exhibit bias or increased levels of uncertainty. Extending the study area to include forest lands with lower SI index classes may allow detection and quantification of topographical gradients influencing the values of the index.

References from Journals:

Ackermann, F. 1999. Airborne laser scanning – present status and future expectations. *Photogramm. Rem. Sens.* 54:64-67.

Andersen, H.E., S.E. Reutebuch, and R.J. McGaughey. 2006. Rigorous assessment of tree height measurements obtained using airborne lidar and conventional field methods. *Can. J. Rem Sens.* 32(5):355-366.

Axelsson, P. 2000. DEM generation from laser scanner data using adaptive TIN models. *International Archives of Photogramm. Remote Sens.* 35(B3), Turkey.

Baltsavias, E.P. 1999. A comparison of between photogrammetry and laser scanning. *Photogramm. Remote Sens.* 54: 83–94.

Battaglia, M., P.J. Sands, and S.G. Candy. 1999. Hybrid growth model to predict height and volume growth in your Eucalyptus globulus plantations. *For. Ecol. Manage.* 120:193-201.

Brandtberg, T., T.A. Warner, R.E. Landenberger, and J.B. McGraw. 2003. Detection and analysis of individual leaf-off tree crowns in small footprint, high sampling density lidar data from the eastern deciduous forest in North America. *Rem. Sens. Envir.* 85(3):290-303.

Clark, M.L., D.B. Clark, and D.A. Roberts. 2004. Small-footprint lidar estimation of sub-canopy elevation and tree height in a tropical rain forest landscape. *Rem. Sens. Envir.* 91:68-89.

Gustafson, E.J., S.M. Lietz, and J.L. Wright. 2003. Predicting the spatial distribution of aspen growth potential in the Upper Great Lakes region. *For. Sci.* 49:499-508.

Hägglund, B. 1981. Evaluation of forest site productivity. *Forestry Abstracts*, 42:515–527.

Harding, D.J., M.A. Lefsky, G.G. Parker, and J.B. Blair. 2001. Laser altimeter canopy height profiles: Methods and validation for closed-canopy, broadleaf forests. *Rem. Sens. Envir.* 76:283-297.

Hill, R.A., D.L.A. Gaveau, and M. Spendlove. 2002. Accuracy issues in the assessment of deciduous woodland canopy height by airborne laser scanning: a case study. In *Proc. ForestSAT 2002 Conference, Edinburgh, UK*, August 5-9, 2002. Forestry Commission England and Forestry Commission Scotland, Edinburgh, UK.

Hodgson, M.E., J.R. Jensen, L. Schmidt, S. Schill, and B. Davis. 2003. An evaluation of LIDAR- and IFSAR-derived digital elevation models in leaf-on conditions with USGS Level 1 and Level 2 DEMs. *Rem. Sens. Envir.* 84:295-308.

Hyyppä, J., U. Pyysalo, H. Hyyppä, and A. Samberg. 2000. Elevation accuracy of laser scanning-derived digital terrain and target models in forest environment. In *Proc. EARSEL-SIG-Workshop on LIDAR*, June 16-17, 2000, Dresden, Germany, pp. 139-147.

Iverson, L.R., M.E. Dale, C.T. Scott, and A. Prasad. 1997. A GIS-derived integrated moisture index to predict forest composition and productivity of Ohio forests (U.S.A.). *Landsc. Ecol.* 12:331-348.

Kobler, A., N. Pfeifer, P. Ogrinc, L. Todorovski, K. Oštir, and S. Džeroski. 2007. Repetitive interpolation: A robust algorithm for DTM generation from Aerial Laser Scanner Data in forested terrain. *Rem. Sens. Envir.* 109:9-23.

Kraus, K., and N. Pfeifer. 1998. Determination of terrain models in wooded areas with airborne laser scanner data. *Photogramm. Remote Sens.* 53:193-203.

- Landsberg, J.J. and R.H. Waring. 1997. A generalized model of forest productivity using simplified concepts of radiation-use efficiency, carbon balance and partitioning. *For. Ecol. Manage.* 95:209-228.
- Louw, J.H., and M. Scholes. 2002. Forest site classification and evaluation: a South African perspective. *For. Ecol. Manage.* 171:153-168.
- MacFarlane, D.W., E.J. Green, and H.E. Burkhart. 2000. Population density influences assessment and application of site index. *Can. J. For. Res.* 30:1472-1475.
- McKenney, D.W. and J.H. Pedlar. 2003. Spatial models of site index based on climate and soil properties for two boreal tree species in Ontario, Canada. *For. Ecol. Manage.* 175:497-507.
- Maltamo, M., K. Mustonen, J. Hyyppä, J. Pitkanen, and X. Yu. 2004. The accuracy of estimating individual tree variables with airborne laser scanning in a boreal nature reserve. *Can. J. For. Res.* 34:1491-1801.
- Monserud, R.A. 1984. Height growth and site index curves for inland Douglas-fir based on stem analysis data and forest habitat type. *For. Sci.* 30: 943-965.
- Næsset, E. 1997. Determination of mean tree height of forest stands using an airborne laser scanner data. *Photogramm. Remote Sens.* 52: 49-56.
- Næsset, E., and T. Økland. 2002. Estimating tree height and tree crown properties using airborne scanning laser in a boreal nature reserve. *Rem. Sens. Envir.* 79:105-115.
- Nigh, G.D., and B.A. Love. 1999. How well can we select undamaged site trees for estimating site index? *Can. J. For. Res.* 29:1989-1992.
- Persson, A., J. Holmgren, and U. Söderman. 2002. Detecting and measuring individual trees using an airborne laser scanner. *Photogramm. Eng. Rem. Sens.* 68(9): 925-932.
- Popescu, S.C., Wynne, R.H., and Nelson, R.F. 2002. Estimating plot-level tree heights with lidar: local filtering with a canopyheight based variable window size. *Comput. Electron. Agric.* 37:71-95.
- Raber, G.T., J.R. Jensen, S.R. Schill, and L. Schuckman. 2002. Creation of digital terrain models using an adaptive lidar vegetation point removal process. *Photogramm. Eng. Rem. Sens.* 68(12):1307-1315.
- Reutebuch, S.E., R.J. McGaughey, H.E. Andersen, and W.W. Carson. 2003. Accuracy of a high-resolution lidar terrain model under a conifer forest canopy. *Can. J. Rem. Sens.* 29(5):527-535.
- St-Onge, B., J. Jumelet, M. Cobello, and C. Véga. 2004. Measuring individual tree height using a combination of stereophotogrammetry and lidar. *Can. J. For. Res.* 34:2122-2130.
- Swenson, J.J., R.H. Waring, W. Fan, and N. Coops. 2005. Predicting site index with physiologically based growth model across Oregon, USA. *Can. J. For. Res.* 35(7):1697-1707.
- Turner, D.P., S.V. Ollinger, and J.S. Kimball. 2004. Integrating remote sensing and ecosystem process models for landscape- to regional-scale analysis of the carbon cycle. *Bioscience*, 54:573-584.
- Worley, D.P. and G.H. Landis. 1954. The accuracy of height measurements with parallax instruments on 1:12000 photographs. *Photogrammetric Engineering*, 20(1): 823-829.
- Wulder, M., K.O. Niemann, and D.G. Goodenough. 2000. Local maximum filtering for the extraction of tree locations and basal area from high spatial resolution imagery. *Rem. Sens. Envir.* 73:103-114.
- Zeide, B., and W.T. Zakrzewski. 1993. Selection of site trees: the combined method and its application. *Can. J. For. Res.* 23:1019-1025.

References from Books:

Goovaerts, P. 1997. Geostatistics for natural resources evaluation. New York, Oxford University Press.

Korpela, I. 2004. Individual tree measurements by means of digital aerial photogrammetry. *Silva Fennica Monographs*, 3:1-93.

References from Other Literature:

Hanson, E.J., D.L. Azuma, and B.A. Hiserote. 2002. Site index equations and mean annual increment equations for Pacific Northwest Research Station Forest Inventory and Analysis Inventories, 1985-2001, Portland, Oregon. USDA Forest Service, Pacific Northwest Research Station, PNW-RN-533.

King, J.E. 1966. Site index curves for Douglas-fir in the Pacific Northwest. *Weyerhaeuser For. Pap.* 8. Centralia, WA, USA: Weyerhaeuser Company, Weyerhaeuser Forestry Research Center, 49p.

ACCURACY OF FOREST PARAMETERS DERIVED FROM MEDIUM FOOTPRINT LIDAR UNDER OPERATIONAL CONSTRAINTS

C. Ginzler*, J. Boehl, R. Boesch, L.T. Waser

Swiss Federal Research Institute WSL, Research Unit Land Resources Assessment, Zuercherstr. 111, 8903 Birmensdorf, Switzerland - (ginzler, boehl, boesch, waser)@wsl.ch

ISPRS WG III/3, III/4, V/3, VIII/11

KEY WORDS: LiDAR, canopy height model (CHM), canopy closure, degree of composition, National Forest Inventory (NFI)

ABSTRACT:

The objective of this study is to test the feasibility of nation-wide medium footprint airborne laser scanning (ALS) data for derivation of forest parameters. The comparison of canopy closure as one important parameter for many forest functions derived from ALS data and aerial photo interpretation was conducted. The present study was carried out in the framework of the Swiss National Forest Inventory (NFI). Three study areas of different size, topographic and forest characteristics were selected. In a first step, canopy height models (CHM) were obtained by subtracting the interpolated terrain altitudes of LiDAR (Light Detection And Ranging) DTM from the interpolated canopy altitudes (LiDAR DSM). Then a binary forest layer with CHM larger or equal 3 m was calculated according to the Swiss NFI forest definition. The Distinction between deciduous and coniferous forest (degree of composition) was performed using the surface cover classes (broadleaved tree, coniferous tree, larch) of the aerial photo interpretation of the NFI for 7,696 sample plots. In a second step, canopy closure derived from the aerial photo interpretation was compared to canopy closure calculated from binary CHM. The study reveals that the canopy closure is underestimated in the binary CHM from LiDAR data and highlights significant differences between coniferous and deciduous predominated forest plots and significant differences between compared canopy closure from winter and summer data. The study shows limitations of canopy closure derived from national LiDAR data but also stresses its practical relevance for many protective functions of forests in alpine conditions.

1. INTRODUCTION

The present study focuses on a comparison of national medium footprint LiDAR data with aerial photo interpretation for deriving standard forest parameters as required by the Swiss National Forest Inventory.

Forests, as part of the landscape, represent an important natural resource for mankind and other living organisms. Exact information on forest extent, structure and composition is needed for environmental, monitoring or protection tasks (CIPRA, 2001; ALPMON work package 1, 1997). Especially alpine forests play a key role in the protection against natural hazards such as rock fall and avalanches. Furthermore, spatial extent of terrestrial ecosystems such as forests and their composition are a central issue in the discussion of carbon sinks and sources at national and continental level (Turner et al., 1995).

However, estimation of forest parameters for large territories (e.g. for national forest inventories) is either expensive if done in the field or imprecise when accomplished through automated stereophotogrammetry (Lefsky et al., 2001; St-Onge et al., 2004; Maltamo et al., 2004). Moreover, obtaining tree heights through measuring is often not feasible in dense and impenetrable forest stands (St-Onge and Achaichia, 2001). Especially the mapping of forests and the derivation of forest parameters is challenging when undertaken in alpine environments due to the specific terrain conditions (Hollaus et al., 2006). According to Wang et al. (2004), the costs of forest sampling can be reduced substantially by estimating forest and tree parameters directly from aerial photographs. The measurement of tree heights is one of the tasks that need to be

fulfilled for an appropriate estimation of these parameters. Due to the fact that parts of tree crowns are shadowed, it is obvious that not all important forest parameters can be derived from aerial photographs. Especially in dense forest stands and in mountainous regions the shapes of trees are varying with the geometrical position on the stereo images (St-Onge et al. 2004). Because seeing the ground is of critical importance, good results can only be obtained in open forest covers.

Recent progress in three dimensional remote sensing mainly includes digital stereophotogrammetry, radar interferometry and LiDAR (Hyypä et al. 2000; Lefsky et al. 2001; Naesset 2002). Meanwhile, several LiDAR systems are available on the market (e.g. Baltsavias, 1999; Heurich et al., 2003; Hyypä et al., 2000), enabling the derivation of DSMs and DTMs from such data as well. Some studies suggest the use of DSM data to detect changes in the forest stands (Schardt et al., 2002; Naesset & Gobakken, 2005). A number of studies reveal the successful use of LiDAR-based techniques to estimate tree and stand attributes such as tree height, crown diameter, basal area and stem volume (Naesset, 1997; Persson 2002; Morsdorf et al. 2004). Combining some of these attributes can be useful to evaluate forest stand parameters, e.g. the percentage of canopy cover (Ritchie et al., 1993).

However, some studies also show an underestimation of tree and canopy height, a result also found by scanning LiDAR studies (e.g. Magnussen et al. 1999; Means et al. 2000; Gaveau & Hill 2003). Estimations of the mean tree height are sensitive to forest structure and shape of the canopy (Nelson 1997; Schardt et al. 2002). Often a narrow tree apex is missed by LiDAR hits or the top of a small tree is covered by branches of a tall tree. However, for large monitoring programs or national

* Corresponding author

forest inventories there is a growing need to develop new remote sensing techniques that allow deriving quantitative forest parameters more directly. The objective of this study is to compare national medium footprint LiDAR data with aerial photo interpretation as applied in the Swiss National Forest Inventory (NFI) for the derivation of the degree of composition and canopy closure. Canopy closure is one of the most important parameters to determine the protective functions of forest in alpine conditions, in particular against avalanches (Meyer-Grass and Schneebeli, 1992). To ensure that the results are of practical relevance, only data and methods which are already applied and serve as operational applications are used (national LiDAR data and stereo image interpretation of NFI sample plots).

2. MATERIAL AND METHODS

2.1 Study area

Switzerland is divided into 26 cantons. For this study three cantons with different topographic and forest characteristics are used as test sites. An overview is given in figure 1. The first study area is located in the northern part of Switzerland (approx. 47°23' N and 8°2' E, 350-900 m a.s.l.) and covers the area of the canton Aargau (AG) with approx. 14,000 km². The highly fragmented landscape is characterized by a smooth terrain, forests, agricultural and urban areas. The forest covers 35 % of the area (4,930 km²) according to the second NFI (Brassel and Brändli, 1999). The forest consists of mixed deciduous trees (*Fagus sylvatica* as dominant tree species) and coniferous trees (*Picea abies* as dominant tree species). The second study area is located in the pre-alpine zone of central Switzerland (approx. 47°1' N and 9°4' E, 400-3600 m a.s.l.) and covers the area of the canton Glarus (GL) with approx. 7,000 km². The tree line in the area is around 1750-1800 m a.s.l. The landscape is characterized by steep slopes with the exception of the main valley and its plane, forests, pastures, few agricultural areas and settlements. The forest covers 29 % of the area (2,050 km²) (Brassel and Brändli, 1999). The forest is characterized by mixed deciduous trees (*Fagus sylvatica* as dominant tree species) in the lower parts and coniferous trees (*Picea abies* as dominant tree species) in the upper parts.

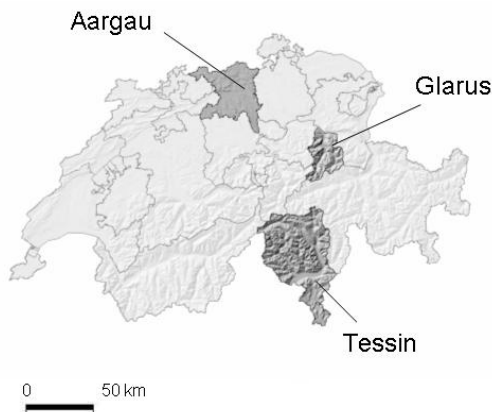


Figure 1. Overview of the three test sites: Cantons Aargau, Glarus and Tessin.

The third study area is located in the southern part of Switzerland (approx. 46°11' N and 9°1' E, 200-3400 m a.s.l.). It covers the area of the canton Tessin (TI) with approx. 28,100 km² whereas 49.4 % (13,900 km²) are forests (Brassel and Brändli, 1999). The landscape is mainly characterized by complex terrain with steep slopes, many valleys and forests (figure 2). The tree line in the area is around 2100-2150 m a.s.l. The forest consists of mixed deciduous trees (*Castanea sativa* as dominant tree species) and coniferous trees (*Picea abies* as dominant tree species).

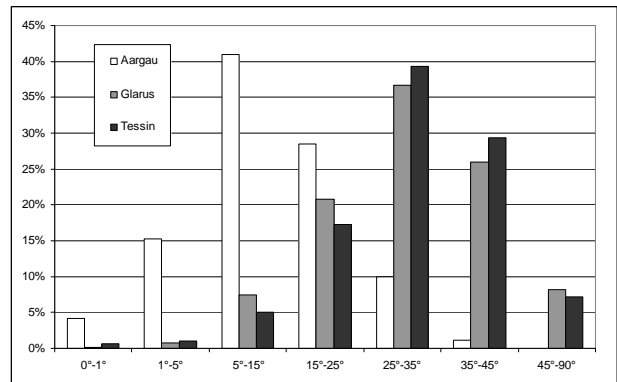


Figure 2. Distribution of the deciduous forest area in relation to the terrain slope for cantons Aargau (left), Glarus (middle) and Tessin (right). For test site Aargau most of the deciduous forest area is located in relatively flat topography, contrary to Tessin and Glarus where most of the forest area is located in steeper terrain.

2.2 National Forest Inventory Data (NFI)

In the Swiss NFI continuous parameters are assessed by aerial photo interpretation at each sample plot belonging to a regular 500 m grid. 25 raster points are distributed regularly (distance 10 m) on the sample plot. For each raster point height and surface cover information is gained and a forest boundary line is measured. The layout of a sample plot is illustrated in figure 3.

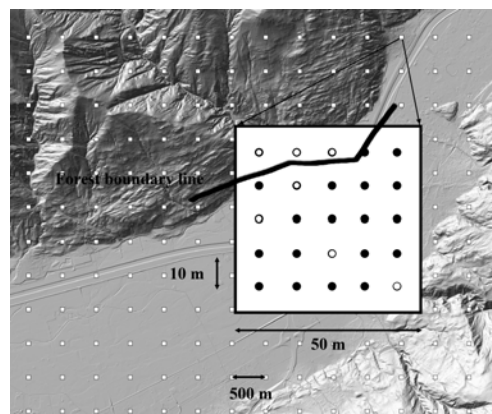


Figure 3. Design of the 50 x 50 m sample plot area with 25 raster points and a forest boundary line. Canopy closure is obtained by calculating the number of points falling on trees with a minimum height of 3 m (black points) within the forest boundary line in relation to the total number of raster points within the forest boundary line.

Each sample plot comprises an interpretation area of 50 x 50 m. The discrimination of forest and non-forest areas is one of the most important attributes resulting from aerial photo interpretation. This requires a non-ambiguous and reproducible forest definition. Summarised the following aspects are crucial: (1) the width of the stocked part of the interpretation area has to measure at least 25 m, (2) the crown coverage of the stocked part of the interpretation area has to be larger or equal 20 %, (3) the stocking has to have a dominant stand height of 3 m.

Stereo-measured variables were gathered on the aerial imagery at each of the 25 raster points within each sample plot. The analogue true colour photos were taken between 1998 and 2005 covering all of Switzerland at a scale of ~1:30,000 and where scanned at a resolution of 14 µm. The digitised photos have a ground resolution of ~0.45 m and a RMS error after aerial triangulation of < 1 m. A photo interpreter assigned each raster point to one of eleven thematic surface cover classes (broadleaved tree, coniferous tree, larch, shrub, grass vegetation, rock, bare soil, paved surface, construction object, water, glacier) using a 3D stereo softcopy station (Socet Set 5.0, BAE Systems).

In addition to surface cover, canopy height information was attributed to each raster point based on the difference between the surface elevation measured by the interpreter and the interpolated (Socet Set 5.0, BAE Systems) terrain elevation from an existing terrain model (25 m grid) provided by swisstopo (Swiss Federal Office of Topography). Finally, in cases with a forest border, a forest boundary line is digitised in addition to the raster points.

2.3 Airborne laser scanner data

National LiDAR data was acquired between 2001 and 2004 by swisstopo, the leaves partly off (figure 4). The project was realised with different companies so very little metadata are available. No detailed information on instruments or platforms is available. Average flight height above ground was between 1000 m and 1500 m. The footprint on ground varies between 0.8 m and 1.2 m. From the raw data, both a DTM and DSM are generated (as raw irregularly distributed points). The average density of the DSM data is 0.5 points / m² and the height accuracy (1 sigma) 0.5 m for open areas and 1.5 m for vegetation and buildings (Artuso et al. 2003). The DTM has an average point density of 0.5 points / m² and height accuracy (1 sigma) of 0.5 m (Artuso et al. 2003).

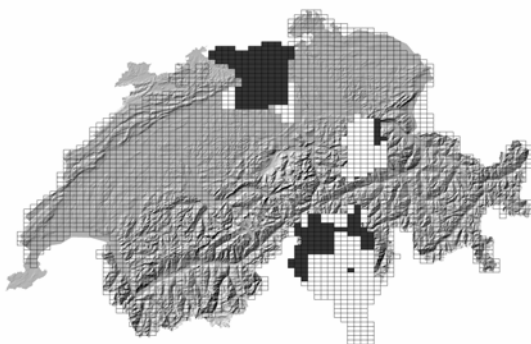


Figure 4. LiDAR data acquisition time of the three test sites. White areas were flown between November and March (leaves-off) and black areas during the vegetation season between April and October (mostly leaves-on).

2.4 Interpolation: DTM and DSM

The interpolation is based on the initial triangulation of all raw data points into a TIN. Depending on the expected point density of 0.5 points/m², a conservative grid size of 2.5 m has been chosen. The interpolation of raw data revealed that the measured point density varies more than expected. Initial results show, that 20 % of the test area in the canton Tessin has less than 0.4 points/m².

2.5 Canopy height model (CHM)

The Canopy height model (CHM) was obtained by subtracting the interpolated terrain altitudes from the interpolated canopy altitudes. Because only first and last pulse data is available, no further processing of pulse information was possible.

2.6 Derivation of forest parameters

According to the NFI forest definition the CHM was reclassified to a binary layer, where values ≥ 3 m are assigned to forest (1) and values < 3 m to non-forest (0). The sample plot area (50 x 50 m) was reduced to the actual forest area on the sample plot, if a forest boundary line was digitised in the aerial photo interpretation (see figure 5).

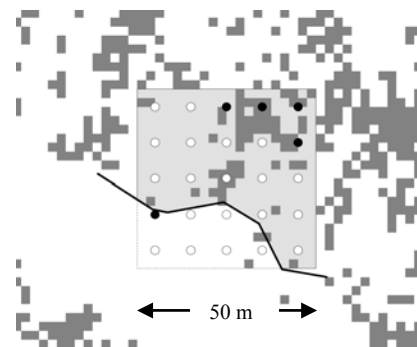


Figure 5. Binary CHM and the reduced sample plot area, with a forest boundary line and 25 raster points of the aerial photo interpretation.

As first forest parameter, the degree of composition was determined. The surface cover classes of the aerial photo interpretation were used to distinguish between plots dominated by deciduous trees and plots dominated by coniferous trees (degree of composition). Plots with more than 90 % of broadleaved tree raster points are assigned to the class 'deciduous forest' and plots with less than 10 % of broadleaved tree to the class 'coniferous forest'. Mixed plots were not used further in this study.

As second forest parameter, canopy closure was calculated as the sum of pixels of the binary CHM in the corresponding sample plot area. Canopy closure from aerial photo interpretation is obtained by calculating the number of points falling on trees with a minimum height of 3 m within the forest boundary line in relation to the total number of raster points (see figure 3).

3. RESULTS

3.1 Degree of composition

In total, in all three test sites 7,696 sample plots were classified into four classes of degree of composition using the raster points of the aerial photo interpretation (Table 1).

Fraction of deciduous trees on forest plots	Number of plots		
	AG (n=1,998)	GL (n=701)	TI (n=4,997)
Coniferous Plots (< 10%)	151	228	1565
Mixed Plots 10-50%	429	145	355
Mixed Plots 50-90%	673	165	486
Deciduous Plots (> 90%)	745	163	2591

Table 1. Degree of composition for the three test sites.

Table 1 shows that Aargau is characterised by mixed forests (55 %) and followed by deciduous forests (37 %) whereas Tessin is characterised by either predominant coniferous plots or predominant deciduous plots (83 %). In Aargau only 8 % are dominant coniferous forest plots. In Glarus most of the forest plots are mixed forest (44 %) followed by coniferous (33 %). In the following results only predominant coniferous and deciduous forest plots (n=5,443) are taken into account.

3.2 Canopy closure

The focus of this study lies on canopy closure obtained by means of aerial image interpretation and data derived from LiDAR.

3.2.1 Canopy closure obtained from aerial photo interpretation

Table 2 shows that canopy closure obtained from aerial photo interpretation is high in all test sites. Three quarters of the plots have a canopy closure between 75 % and 100 %. Deciduous plots are generally denser than coniferous plots. Only 0.7 % of deciduous plots and 6.8 % of coniferous plots are less dense than 30 %.

Canopy Closure %	Canopy closure from aerial photo interpretation			Canopy closure from LiDAR (%)		
	Number of deciduous forest plots			Number of coniferous forest plots		
	AG n=745	GL n=163	TI n=2,591	AG n=151	GL n=228	TI n=1,565
<30	7	1	19	9	15	109
30-50	10	4	78	3	31	239
50-75	44	17	284	12	65	429
75-100	684	141	2210	127	117	788

Table 2. Canopy closure as obtained by aerial photo interpretation. Deciduous forest plots are denser than coniferous forest plots. Three quarter of the plots is denser than 75 %.

Mean, median and standard deviation of canopy closure for both deciduous and coniferous forest plots are given in table 3. For deciduous trees the mean canopy closure varies between

89.7 % (TI) and 93 % (AG). Coniferous forest plots are less dense and vary between 70.8 % (TI) and 88.1 % (AG).

	Canopy closure from aerial photo interpretation (%)					
	deciduous forest plots			coniferous forest plots		
	AG n=745	GL n=163	TI n=2,591	AG n=151	GL n=228	TI n=1,565
Mean	93.0	90.2	89.7	88.1	71.2	70.8
Median	100.0	96.0	96.0	100.0	76.0	76.0
Std	13.9	15.0	15.7	23.1	23.7	23.6

Table 3. Mean canopy closure from aerial photo interpretation on deciduous forest plots and forest coniferous plot respectively.

3.2.2 Canopy closure obtained from LiDAR (binary CHM)

Table 4 shows the canopy closure obtained from LiDAR data and table 5 summarizes the canopy closure for deciduous and coniferous forest plots. For deciduous trees the mean canopy closure varies between 50.9 % (GL) and 62.7 % (AG). In contrary to aerial photo interpretation, coniferous forest plots obtained from LiDAR are denser than deciduous forest plots – with the exception of Tessin. They vary between 53.7 % (GL) and 67.1 % (AG).

Canopy Closure %	Canopy closure from LiDAR (CHM)					
	Number of deciduous forest plots			Number of coniferous forest plots		
	AG n=745	GL n=163	TI n=2,591	AG n=151	GL n=228	TI n=1,565
<30	59	40	132	21	43	312
30-50	139	37	344	16	56	355
50-75	301	53	1153	32	77	546
75-100	246	33	962	82	52	352

Table 4. Canopy closure from LiDAR (binary CHM). Deciduous forest plots are denser than coniferous forest plots. Only 30 % of the plots are denser than 75 %.

	Canopy closure from LiDAR (%)					
	deciduous forest plots			coniferous forest plots		
	AG n=745	GL n=163	TI n=2,591	AG n=151	GL n=228	TI n=1,565
Mean	62.7	50.9	66.2	67.1	53.7	53.8
Median	66.3	53.0	69.5	78.0	53.1	55.5
Std	21.0	26.9	18.6	28.7	24.6	24.1

Table 5. Mean canopy closure from CHM from LiDAR on deciduous plots and coniferous plot respectively

3.2.3 Aerial photo interpretation versus LiDAR

Overall, canopy closure is underestimated in all three test sites by the LiDAR CHM in comparison to the aerial photo interpretation. For the statistical analysis the plots were grouped into plots predominated by coniferous trees or deciduous trees respectively. Then a Kolomogorov-Smirnov-Test (alpha=0.05) as implemented in SAS's UNIVARIATE procedure was applied on the dataset. This test revealed that the plot wise calculated differences in canopy closure measurements from the aerial

photo interpretation and the LiDAR measurement are not normally distributed. Therefore a non-parametric test, the Wilcoxon two-sample test as implemented in SAS's NPAR1WAY Procedure (SAS, 2000), was chosen to account for significant differences. A significant difference ($\alpha=0.05$) between the calculated differences in canopy closure measurements for coniferous forest plots and deciduous forest plots ($p<0.0001$) was found. Finally, table 6 reveals that this underestimation is higher at deciduous than at coniferous plots.

	Difference of canopy closure (%)	
	deciduous forest plots	coniferous forest plots
Mean	25.7	17.4
Median	24.0	15.0
Std	16.9	19.2

Table 6. Mean differences of canopy closure from CHM and aerial photo interpretation on predominated deciduous plots and predominated coniferous plot respectively

3.2.4 LiDAR data acquisition: leaves-off versus leaves-on

For this analysis the plots were grouped into plots predominated by coniferous trees or deciduous trees and the flight date (in vegetation season yes or no). Again the calculated differences are not normally distributed. Therefore, the Wilcoxon two-sample Test was chosen, to account for significant differences of the canopy closure measure for the two datasets. A significant difference ($\alpha=0.05$) between the flight dates in both cases, coniferous forest plots ($p=0.0007$) and deciduous forest plots ($p=0.0316$) was found.

4. DISCUSSION AND CONCLUSION

ALS data covering large country wide areas is becoming more and more popular and is available for many countries. However, these data sets suffer from some limitations: First, in most cases these data are medium to large footprint ALS and do not meet the requirements for single tree detection and accurate derivations of relevant forest parameters as performed in many case studies. Second, although the acquisition time is not focused on single specific questions the data has to serve for different purposes.

The present study reveals that large area application of national LiDAR data for derivation of canopy closure as one important forest parameter is challenging since time of data acquisition varies. Therefore the accuracy of the obtained parameters is only partly satisfactory. Especially in predominated deciduous forest plots the differences of canopy closure obtained by aerial photo interpretation and LiDAR measurements are high. Therefore, the obtained information on canopy closure is reliable, since most protective functions of alpine forests are limited to coniferous forests (lower underestimation than for deciduous forests) in higher regions. Nevertheless, the influence of data acquisition time remains evident, in deciduous and in coniferous cases.

For a further quality assessment there is a strong need for more information on exact date of acquisition for each single LiDAR measurement. Summarized metadata for organizational units, like map sheets, are not appropriate. Furthermore, since both

forest parameters strongly depend on the quality of the CHMs a more extensive quality check of the CHMs has to be performed. Further reference data (e.g. tree heights) will be obtained using stereo photogrammetry and field measurements.

To summarize, the need to develop new remote sensing techniques for large NFIs is evident. The use of nation wide available LiDAR data is obvious, but further studies are needed to obtain more information on quality and characteristics of the data for forest specific questions.

5. REFERENCES

- ALPMON (Alpine Monitoring System), 1997. *Work package 1*, URL: <http://dib.joanneum.ac.at/alpmon/home.html>, Joanneum Research, Graz, Austria (last date accessed: 30 July 2007).
- Artuso, R., Bovet, St. and Streilein, A., 2003. Practical methods for the verification of countrywide terrain and surface models. *Proceedings of the ISPRS working group III/3 workshop XXXIV-3/W13*. 3-D reconstruction from airborne laserscanner and InSAR data, 8-10 March, 2003, Dresden, Germany.
- Baltsavias, E., 1999. Airborne laser scanning: existing systems and firms and other resources. *ISPRS Journal of Photogrammetry and Remote Sensing*, 54, 164-198.
- Brassel, P. and Brändli, U.B. (editors), 1999. Schweizerisches Landesforstinventar. Ergebnisse der Zweitaufnahme 1993-1995.
- CIPRA, 2001. 2. Alpenreport. Daten, Fakten, Probleme, Lösungsansätze. Verlag Paul Haupt, Bern, Stuttgart, Wien, 434 p.
- Gaveau, D. and Hill, R.A., 2003. Quantifying canopy height underestimation by laser pulse penetration in small footprint airborne laser scanning data. *Canadian Journal of Remote Sensing*, 29, 650-657.
- Heurich, M., Schneider, T. and Kennel, E., 2003. Laser scanning for identification of forest structure in the Bavarian forest national park. *Proceedings of the ScandLaser Scientific Workshop on Airborne Laser Scanning of Forests (pp. 98-107)*, 3-4 September 2003, Umea, Sweden, 2003, Hyypä J., Naeset H., Olssen H., Granqvist Pahlen T., Reese H. (eds) (Swedish University of Agricultural Sciences, Department of Forest Resource Management and Geomatics).
- Hollaus, M., Wagner, W., Eberhöfer, C., Karel, W., 2006. Accuracy of large-scale canopy heights derived from LIDAR data under operational constraints in a complex alpine environment. *ISPRS Journal of Photogrammetry and Remote Sensing*, 60, 323 - 338.
- Hyypä, J., Hyypä, H., Inkinen, M., Engdahl, M., Linko, S. and Yi-Hong, Z., 2000. Accuracy comparison of various remote sensing data sources in the retrieval of forest stand attributes. *Forest Ecology and Management*, 128, 109-120.
- Lefsky, M.A., Cohen, W.B. and Spies, T.A., 2001. An evaluation of alternate remote sensing products for forest inventory, monitoring, and mapping in Douglas-fir forests of western Oregon. *Canadian Journal of Forest Research*, 31, 78-87.

- Magnussen, S., Eggermont, P. and LaRiccia V.N., 1999. Recovering tree heights from airborne laser scanner data. *Forest Science*, 45, 407-422.
- Maltamo, M., Mustonen, K., Hyypä, J., Pitkänen, J. and Yu, X., 2004. The accuracy of estimating individual tree variables with airborne laser scanning in a boreal nature reserve. *Can. J. For. Res./Rev. Can. Rech. For.*, 34, 1791-1801.
- Means, J.E., Acker, S.A., Fitt, B.J., Renslow, M., Emerson, L. and Hendix, C.J., 2000. Predicting forest stand characteristics with airborne scanning lidar. *Photogrammetric Engineering and Remote Sensing*, 66, 1367-1371.
- Meyer-Grass, M., Schneebeli M., 1992. Die Abhängigkeit der Waldlawinen von Standorts-, Bestandes- und Schneebedingungen. International Symposium Interpraevent, Bern 2, 443-455.
- Morsdorf, F., Meier, E., Kötz, B., Itten, K.I., Dobbertin, M. and Allgöwer, B., 2004. LIDAR-based geometric reconstruction of boreal type forest stands at single tree level for forest and wildland fire management. *Remote Sensing of Environment*, 92, 353-362.
- Naesset, E., 1997. Determination of mean tree height of forest stands using airborne laser scanner data. *ISPRS Journal of Photogrammetry and Remote Sensing*, 52, 49-56.
- Naesset, E., 2002. Predicting forest stand characteristics with airborne scanning laser using a practical two-stage procedure and field data. *Remote Sensing of Environment*, 80, 88-99.
- Naesset, E. and Gobakken, T., 2005. Estimating forest growth using canopy metrics derived from airborne laser scanner data. *Remote Sensing of Environment*, 96, 453-465.
- Nelson, R. 1997. Modeling forest canopy height: the effects of canopy shape. *Remote Sensing of Environment*, 60, 327-334.
- Persson, Å., Holmgren, J. and Söderman, U. (2002). Detecting and measuring individual trees using an airborne laser scanner. *Photogrammetric Engineering and Remote Sensing* 68, 925-932
- SAS Institute Inc. 2000 // SAS Institute Inc. 2000: SAS/STAT® Users's Guide, Version 8. Cary, NC: SAS Institute Inc.
- Schardt, M., Ziegler, M., Wimmer, A., Wrack, R. and Hyypä, J., 2002. Assessment of forest parameters by means of laser scanning. *Proceedings from the International Society for Photogrammetry and Remote Sensing (ISPRS)*, Commission III Symposium, Vol. XXXIV, Part 3A, 9-13 September 2002, Graz, Austria, 302-309.
- St-Onge, A. and Achaichia, N., 2001. Measuring forest canopy height using a combination of LIDAR and aerial photography data. *International Archives of Photogrammetry and Remote Sensing*, XXXIV-3/W4, 131-137.
- St-Onge, B., Jumelet, J., Cobello, M. and Vega, C., 2004. Measuring individual tree height using a combination of stereophotogrammetry and lidar. *Canadian Journal of Forest Research*, 34, 2122-2130.
- Turner, M.G., Gardner, R.H. and O'Neill, R.V., 1995. Ecological dynamics at broad scales: ecosystems and landscapes. *BioScience Supplement*, 45, 29-35.
- Wang, L., Gong, P. & Biging, G.S., 2004. Individual Tree-Crown Delineation and Treetop Detection in High-Spatial-Resolution Aerial Imagery. *Photogrammetric Engineering & Remote Sensing* 70, 351-357.
- Watt, P.J. and Donoghue, D.N.M., 2005. Measuring forest structure with terrestrial laser scanning. *International Journal of Remote Sensing*, 26, 1437-1446.

ACKNOWLEDGEMENT

The study was carried out in the frame of the Swiss National Forest Inventory at the Swiss Federal Research Institute WSL and funded by the Swiss Agency for the Environment, Forest and Landscape and WSL. We are grateful to Adrian Lanz and Markus Keller for fruitful comments and statistical support.

ASSESSING EFFECTS OF LASER POINT DENSITY ON BIOPHYSICAL STAND PROPERTIES DERIVED FROM AIRBORNE LASER SCANNER DATA IN MATURE FOREST

T. Gobakken^{a,*}, E. Næsset^a

^a Norwegian University of Life Sciences, Dep. of Ecology and Natural Resource Management - (terje.gobakken, erik.naesset)@umb.no

KEY WORDS: Airborne laser scanner, Canopy density, Canopy height, Pulse density

ABSTRACT:

Canopy height distributions were created from small-footprint airborne laser scanner data for mature coniferous forest in two forest areas in Norway. In total, 82 and 70 georeferenced field sample plots and 39 and 38 forest stands were measured in the two areas, respectively. The average sampling densities were 1.2 m⁻² and 0.9 m⁻². Height percentiles, mean and maximum height values, coefficients of variation of the heights, and canopy density at different height intervals above the ground were computed from the laser-derived canopy height distributions from the first return data. The laser point clouds were thinned to approximately 1 point per 4 m² (0.25 m⁻²), 1 point per 8 m² (0.13 m⁻²), and 1 point per 16 m² (0.06 m⁻²). The mean difference and the standard deviation for the differences between laser-derived metrics derived from the original full density laser data and thinned data for the two areas were estimated and compared. For all comparisons, the maximum value of the canopy height distributions differed significantly between the full density laser datasets and the thinned data. The effects of different laser point densities on stand predictions of three biophysical properties of interest were also tested. The average standard deviation for mean tree height, stand basal area, and stand volume predicted at stand level showed only a minor increase by decreasing point density.

1. INTRODUCTION

For economical reasons, optimal specification of fieldwork, sensor, and flight parameters for laser data acquisition is important in practical forest inventory. A number of parameters for specifying airborne laser data acquisition have to be decided upon prior to survey, and they may influence on important properties such as the theoretical number of points per unit area, the ability to derive forest structural information, and survey costs.

In an area-based approach, i.e., individual forest stands are the basic units of the inventories, a large number of explanatory laser variables are extracted from the laser points and used to predict forest biophysical properties. A sampling density of about one laser point per square metre has shown promising results (Næsset, 2002b; Næsset, 2004b). The effects of point density have been assessed in a number of studies (e.g. Holmgren, 2004; Magnusson, 2006; Maltamo et al., 2006; Thomas et al., 2006). A study in Sweden indicated that the errors of predicted mean tree height, basal area, and stem volume did not differ much when the point density was changed from 0.1 to 4.3 m⁻² (Holmgren, 2004). Holmgren used a footprint diameter of 1.8 m and the large footprint size resulted in overlap between adjacent footprints on the ground. Oversampling may therefore have influenced on the results. In a Finnish study, where the point densities were 12.7, 6.3, 1.3, 0.6, and 0.13 m⁻² and the footprint diameter was 40 cm, no effects of point density on stem volume prediction were found (Maltamo et al., 2006). However, the basic dataset in the Finnish study was limited to 32 sample plots with size 0.09 ha. In contrast to the studies mentioned above, Magnusson (2006) found that the

RMSE for tree height and stem volume estimation increased when the point density was reduced from 2.5 to 0.004 m⁻². Many of the variables extracted from the laser point clouds are highly correlated. In addition, if some of these potential laser metrics are more sensitive to point density, then it would be best to select, as independent variables, those laser measures that are least affected by point density.

The objectives of this study were to assess the effects of different laser point densities on laser-derived metrics and to assess how laser point density may affect stand predictions of three biophysical properties of interest, i.e., mean tree height, basal area, and volume. Four different levels of laser point densities were assessed. The results were evaluated using an independent validation dataset.

2. MATERIAL AND METHODS

2.1 Study area

Two forest areas in southeast Norway were selected for this study: a forest area in the municipality of Våler (59°30'N, 10°55'E, 70-120 m a.s.l.) of about 1000 ha, and a forest area in the municipality of Krødsherad (60°10'N 9°35'E, 130-660 m a.s.l.) with size 6500 ha. The study sites in Våler and Krødsherad are hereafter denoted as sites A and B, respectively. The main tree species in the areas were Norway spruce (*Picea abies* (L.) Karst.) and Scots pine (*Pinus sylvestris* L.). Further details can be found in Næsset (2002b) and (Næsset, 2004b).

The present study was based on two different field datasets from each area: sample plots and forest stands. The sample

* Corresponding author

plots were used to assess the effects of different laser point densities on laser-derived metrics and to develop regression models for the three biophysical properties of interest. The forest stands were used to assess the influence of laser point density on the stand predictions for the three biophysical properties.

2.2 Sample plots

In total, 82 sample plots in site A and 70 in site B were distributed systematically in the mature forest across the entire study areas according to regular grids. The areas of the sample plots were 200 and 232.9 m² in sites A and B, respectively. The measurements were carried out during the summers 1999 (Næsset, 2002b) and 2001 (Næsset, 2004b). On each plot, all trees with $d_{bh} > 10$ cm were callipered. The d_{bh} was recorded in 2 cm classes. Basal area (G) was computed as the basal area per hectare of the callipered trees. The heights of sample trees were measured by a Vertex hypsometer. Mean height of each plot was computed as Lorey's mean height (h_L), i.e., mean height weighted by basal area. Volume of each tree was computed by means of volume equations of individual trees (Brantseg, 1967; Braastad, 1966; Vestjordet, 1967), with height and diameter as predictor variables. Total plot volume (V) was computed as the sum of the individual tree volumes.

Finally, to synchronize the h_L , G , and V values to the date the laser data were acquired the individual plot values were prorated by means of growth functions (Blingsmo, 1984; Braastad, 1975; Braastad, 1980; Delbeck, 1965). The prorated

values were used as ground-truth. A summary of the ground-truth sample plots data is displayed in Table 1.

Differential Global Positioning System (GPS) and Global Navigation Satellite System (GLONASS) were used to determine the position of the centre of each sample plot. The computed plot coordinates had an expected average accuracy of approximately 0.3 m.

2.3 Stand inventory

In site A, 39 stands were selected subjectively in order to represent different combinations of site quality classes and tree species mixtures. Field data were collected during summer 1998 (Næsset, 2002a). The average stand size was 1.7 ha. Each stand was inventoried by intensive sample of plots within each stand. The average number of plots per stand was 20. In site B, 38 large test plots located in subjectively selected stands were used. Ground reference data for the test plots were collected during summer 2001. Each plot was initially supposed to be a quadrat with an approximate size of 61 × 61 m, but the actual size varied somewhat. On each of these plots, all trees with size greater than the specified limits were callipered. The large test plots are hereafter denoted stands. The stand data values were synchronized to the date the laser data were acquired by prorating by up to 1.5 years. The prorated values were used as ground-truth. A summary of the ground-truth stand data is displayed in Table 1.

Characteristic	Sample plots		Stands	
	Range	Mean	Range	Mean
<i>Site A</i>	<i>(200 m², n=82)</i>		<i>(n=39)</i>	
h_L (m)	12.0 - 26.0	18.5	13.6 - 22.9	17.9
G (m ² ha ⁻¹)	7.5 - 50.6	24.2	12.6 - 38.8	24.9
V (m ³ ha ⁻¹)	53.2 - 632.7	219.2	90.8 - 410.9	216.9
Tree species distribution				
Spruce (%)	0 - 100	54	4 - 94	53
Pine (%)	0 - 100	41	0 - 92	38
Deciduous species (%)	0 - 27	5	1 - 22	9
<i>Site B</i>	<i>(232.9 m², n=70)</i>		<i>(n=38)</i>	
h_L (m)	9.9 - 26.0	18.1	12.2 - 24.4	17.9
G (m ² ha ⁻¹)	5.6 - 57.0	28.1	12.0 - 37.7	25.4
V (m ³ ha ⁻¹)	29.6 - 674.8	251.2	83.0 - 378.9	224.5
Tree species distribution				
Spruce (%)	0 - 100	38	1 - 100	50
Pine (%)	0 - 100	58	0 - 98	41
Deciduous species (%)	0 - 29	4	0 - 40	9

^a h_L =Lorey's mean height, G =basal area, V =volume.

Table 1. Summary of field inventory of sample plots and stands ^a.

2.4 Laser scanner data

A Piper PA31-310 aircraft carried the ALTM 1210 laser scanning system (Optech, Canada). The laser scanner data were acquired 8 and 9 June 1999 for site A (cf. Næsset, 2002b; Næsset and Bjerknes, 2001) and in the period between 23 July and 1 August 2001 for site B (cf. Næsset, 2004b). A summary of the laser scanner data is presented in Table 2.

All the first return laser points were spatially registered to the DTM derived from the last return echoes according to their coordinates. The relative height of each point was computed as the difference between the height of the return and the interpolated terrain surface height. Only these first returns were used for further analysis. Points that hit outside the plots and stands were excluded from further analysis.

2.5 Reduction of laser point density

In order to investigate the effects of laser point densities on the laser-derived metrics and on the predicted biophysical stand properties, the point clouds were thinned. The point clouds were thinned from about 1.2 m⁻² and 0.9 m⁻² for site A and B, respectively, to approximately 1 point per 4, 8, and 16

m² (0.25, 0.13, and 0.06 m⁻²) by randomly selecting one point within grid cells with the respective sizes (4, 8, and 16 m²). This thinning method was employed to insure a fairly regular distribution of the retained points. A similar approach has also been used in other studies (e.g. Magnusson, 2006).

	Number of obs.	No. of transmitted pulses (m ⁻²)			No. of canopy hits (m ⁻²) ^a			Mean rate of penetration (%)
		Range	Mean	Range	Mean			
<i>Site A</i>								
Sample plots	82	0.73 - 1.62	1.12	0.33 - 1.34	0.80	28		
Stands	39	1.04 - 1.41	1.19	0.60 - 1.33	0.88	26		
<i>Site B</i>								
Sample plots	70	0.40 - 2.00	1.03	0.24 - 1.62	0.80	23		
Stands	38	0.50 - 1.71	0.89	0.31 - 1.62	0.70	22		

^a Canopy hits: laser points with a height value of >2 m.

Table 2. Summary of characteristics of first return laser scanner data for sample plots and stands.

2.6 Computations

For each sample plot and stand inventoried in field, height distributions were created for those laser points that were considered to belong to the tree canopy, i.e., points with a height value of >2 m. Percentiles for the canopy height for 10% (h_{10}), 50% (h_{50}), and 90% (h_{90}) were computed. In addition, also the maximum (h_{max}) and mean values (h_{mean}) and the coefficient of variation (h_{cv}) of the canopy height distributions were computed. Furthermore, several measures of canopy density were derived. The range between the lowest laser canopy height (>2 m) and the 95% percentile for the canopy height distribution was divided into 10 fractions of equal length. Canopy densities were computed as the proportions of laser hits above fraction #0 (>2 m), 1, . . . , 9 to total number of points. The densities for fraction #1 (d_1), #5 (d_5), and #9 (d_9) were selected for further studies.

To assess how different laser point densities influenced on the laser-derived metrics, differences between corresponding metrics derived for the different alternatives were computed for each sample plot. The standard deviations of the differences were also computed to assess the stability of the respective metrics. Separate comparisons between laser scanner data with different point densities were made.

To assess the accuracy of laser-based predictions of mean tree height, basal area, and volume based on different laser point densities, we followed the two-step procedure proposed by Næsset & Bjerknes (2001) and Næsset (2002b) by (1) relating the three biophysical properties of interest to the laser data of the sample plots in the two sites using regression analysis, and by (2) applying the estimated regression models to predict corresponding values of the test stands. In addition, the differences between predicted values of the biophysical stand properties and ground-truth values were computed. The standard deviations of the differences were also calculated.

In the regression analysis, multiplicative models were estimated as linear regressions in the logarithmic variables. Stepwise selection was performed to select variables to be included in these models. No predictor variable was left in the models with a partial F statistic with a significance level greater than 0.05. The standard least-squares method was used (Anon., 1989).

Separate predictions were made for the two sites and the different laser point densities. In the prediction, each stand was divided into grid cells. Laser canopy height distributions were created for each cell and the biophysical properties were predicted at cell level using the estimated equations and the derived laser metrics. Finally, predicted values at stand level were computed as mean values of the individual cell predictions. The mean differences between predicted biophysical stand properties and ground-truth and corresponding estimates of the standard deviations of the differences were derived.

3. RESULTS

3.1 Laser-derived metrics

Height percentiles

None of the mean differences for the percentiles (h_{10} , h_{50} , h_{90}) between the full density data and the thinned data in site A and only one in site B were found to be statistically significant. In both sites and for all comparisons the standard deviations for the differences of the percentiles between the full density data and the thinned data increased by decreasing point densities, i.e., from 0.25 m⁻² to 0.06 m⁻². In general, the standard deviations were smallest in site A (Table 3).

Height maximum, mean, and variability

For all comparisons, the maximum values of the canopy height distributions (h_{max}) differed significantly between the full density laser data and the thinned data. The differences increased with decreasing point density for all comparisons. The h_{max} values were always highest for the full density data.

Only one of the comparisons of the differences for the mean height values (h_{mean}) between the full density laser data and the thinned data were found to be statistically significant.

The variability of the canopy height distributions expressed by the coefficient of variation (h_{cv}) did not differ significantly in any of the comparisons between the laser point intensities.

For both h_{max} , h_{mean} , and h_{cv} , the standard deviations of the differences increased with decreasing laser point density for

all the comparisons. The standard deviations of the differences were smaller in site B compared to site A.

Canopy density

For both sites, the differences of canopy densities (d_1 , d_5 , and d_9) between the full density laser data and the thinned data

were found to be statistically significant in four of the comparisons. In all of the comparisons the standard deviations for the differences of the canopy densities between the full density data and the thinned data increased by decreasing point densities, i.e., from 0.25 to 0.06 m⁻².

Metrics ^b	0.25 points m ⁻²		0.13 points m ⁻²		0.06 points m ⁻²				
	Mean <i>D</i>	S.D.	Mean <i>D</i>	S.D.	Mean <i>D</i>	S.D.			
<i>Site A</i>									
h_{10} (m)	0.15	ns	1.14	-0.06	ns	1.68	0.34	ns	2.80
h_{50} (m)	-0.13	ns	0.81	-0.31	ns	1.29	-0.24	ns	1.94
h_{90} (m)	-0.10	ns	0.77	-0.06	ns	1.21	0.10	ns	1.73
h_{\max} (m)	-0.96	***	1.12	-1.66	***	1.27	-2.53	***	1.88
h_{mean} (m)	-0.04	ns	0.50	-0.20	ns	0.87	0.00	ns	1.46
h_{cv} (m)	0.35	ns	3.42	1.88	ns	6.37	0.88	ns	11.41
d_1 (%)	-1.89	**	4.91	-1.97	ns	6.78	-1.46	ns	10.80
d_5 (%)	-2.53	***	5.11	-2.86	**	6.54	-0.76	ns	11.59
d_9 (%)	0.22	ns	4.03	0.66	ns	4.51	4.36	***	6.85
<i>Site B</i>									
h_{10} (m)	-0.06	ns	1.00	-0.08	ns	1.78	0.20	ns	2.35
h_{50} (m)	-0.34	**	0.78	-0.15	ns	1.19	-0.27	ns	1.78
h_{90} (m)	-0.18	ns	0.55	-0.28	ns	1.10	-0.24	ns	1.62
h_{\max} (m)	-0.93	***	0.90	-1.30	***	1.23	-2.06	***	1.61
h_{mean} (m)	-0.18	*	0.48	-0.22	ns	0.80	-0.22	ns	1.37
h_{cv} (m)	0.88	ns	3.41	1.26	ns	5.52	1.01	ns	10.72
d_1 (%)	-2.51	***	3.83	-2.74	**	6.59	0.06	ns	10.33
d_5 (%)	-2.99	***	4.46	-2.48	*	6.47	-1.60	ns	12.57
d_9 (%)	0.08	ns	4.54	0.09	ns	6.21	1.24	ns	8.89

^a Level of significance: ns = not significant (>0.05). * < 0.05; ** < 0.01; *** < 0.001.

^b h_{10} , h_{50} , and h_{90} = percentiles of the laser canopy heights for 10%, 50%, and 90%; h_{\max} = maximum laser canopy height; h_{mean} = arithmetic mean of laser canopy heights; h_{cv} = coefficient of variation of laser canopy heights; d_1 , d_5 , and d_9 = canopy densities corresponding to the proportions of laser hits above fraction # 1, 5, and 9, respectively, to total number of returns (see text).

Table 3. Differences (*D*) between laser-derived metrics of different point densities and standard deviation for the differences (S.D.) based on data from site A (200 m²) and from site B (232.9 m²) sample plots ^a.

3.2 Regression models

To assess effects of laser point density on the estimated regression models used in the two-stage inventory, stepwise regression analysis based on the 82 and 70 field training plots, for sites A and B respectively, was carried out to create relationships between the three biophysical properties of interest (h_L , G , and V) and the laser-derived metrics. The regression analysis was carried out using all points, 0.25, 0.13, and 0.06 m⁻², respectively. Separate models were estimated for the two sites. When all laser points were used, the selected log-log regression models explained 62-87% and 80-92% of the variability inherent in the log-transformed responses for the two sites.

However, when the lowest point density was used, the model fit was poor. In the model for basal area (G), only 45% and 73% of the variability were explained by the models for sites A and B, respectively. The selected models, R^2 , and RMSE when using all points in sites A and B are presented in Table 4. The selected models were slightly different for the other point densities. The models contained from one to three explanatory variables.

Response variable ^a	Expl. variables ^b	R^2	RMSE	κ
<i>Site A</i>				
$\ln h_L$	$\ln h_{10}$, $\ln h_{90}$	0.87	0.07	1.6
$\ln G$	$\ln h_{90}$, $\ln d_5$	0.62	0.25	1.5
$\ln V$	$\ln h_{\text{mean}}$, $\ln d_1$	0.71	0.27	1.9
<i>Site B</i>				
$\ln h_L$	$\ln h_{90}$	0.93	0.06	1.0
$\ln G$	$\ln h_{\text{mean}}$, $\ln d_1$	0.80	0.20	2.2
$\ln V$	$\ln h_{\text{mean}}$, $\ln d_1$, $\ln h_{90}$	0.90	0.20	6.9

^a h_L = Lorey's mean height (m), G = basal area (m²ha⁻¹), V = volume (m³ha⁻¹).

^b h_{10} and h_{90} = percentiles of the laser canopy heights for 10% and 90% (m); h_{mean} = arithmetic mean of first return laser heights (m); d_1 and d_5 = canopy density corresponding to the proportion of laser hits above fraction # 1 and 5, respectively, to total number of first returns (see text).

Table 4. Selected models for biophysical properties (response variables) from stepwise multiple regression analysis using

metrics derived using all points on the plots in site A and B as explanatory variables.

All the models selected to be the “best” ones for G and all the models except one for V were based on laser-derived variables related to canopy height and variables related to canopy density. The models for h_L were mainly based on canopy height variables. For all the 24 models developed, i.e., all possible combinations of point density (four densities) and sites (sites A and B) for each of the three variables (h_L , G , and V), at maximum three explanatory variables were selected. Multicollinearity issues were addressed by calculating and monitoring the size of the condition number (κ). None of the selected models had a condition number greater than 6.9, indicating that there was no serious collinearity inherent in the selected models (Weisberg, 1985). All the models developed using the plots in site B accounted for a larger proportion of the variability

inherent in the log-transformed responses compared to the models developed using the plots in site A.

3.3 Stand level predictions

The mean and the standard deviations for the differences between predicted mean height (h_L), basal area (G), and volume (V) and ground-truth values for the 39 and 38 stands in sites A and B respectively, are presented in table 5. The mean difference between the full density data and the thinned data varied between densities. However, no clear pattern was found.

The standard deviations for the differences increased in all except five cases when the point density decreased. Two of these five exceptions were for h_L and two were for V . The standard deviations of h_L did only increase to a minor extent when the point density decreased. The standard deviations for the differences were smallest in site B compared to site A in all except two cases.

Response variable ^a	1.2 points m ⁻²		0.25 points m ⁻²		0.13 points m ⁻²		0.06 points m ⁻²	
	Mean D	S.D.	Mean D	S.D.	Mean D	S.D.	Mean D	S.D.
<i>Site A</i>								
h_L (m)	-0.03	0.97	-0.01	0.96	-0.05	1.07	-0.06	1.15
G (m ² ha ⁻¹)	-0.30	2.67	-0.08	2.73	0.01	3.37	-0.93	3.59
V (m ³ ha ⁻¹)	2.78	30.11	3.02	29.70	3.09	37.30	-6.01	39.10
<i>Site B</i>								
h_L (m)	-0.35	0.55	-0.33	0.61	-0.06	0.85	-0.35	0.72
G (m ² ha ⁻¹)	1.74	3.19	1.78	2.99	1.68	3.05	0.93	3.58
V (m ³ ha ⁻¹)	8.94	27.80	7.24	26.52	12.41	28.19	2.34	38.23

Table 5. Mean differences (D) and standard deviation for the differences (S.D.) between laser-derived and observed Lorey's mean height (h_L), basal area (G), and volume (V) in sites A and B when using all points (1.2 m⁻²), 0.25 m⁻², 0.13 m⁻², and 0.06 m⁻².

4. DISCUSSION

The major findings of this study indicate that:

1) The maximum values of the canopy height distributions (h_{max}) differed significantly between the full density laser data and the thinned data. The differences increased with decreasing point density. In most cases the variability of h_{max} was larger than for the intermediate and upper height percentiles (h_{50} , h_{90}). A higher variability associated with h_{max} has also been found in other studies (Næsset, 2004a; Næsset and Gobakken, 2005). Since h_{max} is seriously affected by point density it should be avoided in practical applications.

2) The standard deviations for the differences for all the derived laser metrics increased by decreasing laser point density, i.e., from 0.25 m⁻² to 0.06 m⁻².

3) For other variables than h_{max} , no clear pattern of the mean differences between the laser metrics derived from full density data and the thinned data could be found.

4) Even if one of the prediction models only explained a quite low proportion of the variability (45%), the effects of reducing point density on the predicted mean height (h_L), basal area (G), and volume (V) at stand level were quite small.

When the laser point density was reduced by thinning to imitate data acquisitions with lower point densities, a random selection of points was carried out. A random selection of points within grid cells of size 4, 8, and 16 m² was carried out in order to maintain a fairly regular spatial distribution of the retained points. However, the modelled ground surface was all the time the same. Keeping the DTM constant might influence the results, although other studies indicate that this effect probably is small. Goodwin et al. (2006) indicated that the predicted surface closely matched the field measured even when a point density of 0.18 m⁻² was used. Magnusson (2006) found the RMSE of the terrain model to be quite low and unbiased up to a thinning level of 0.01 m⁻².

To conclude, the results of this study may indicate that the average point density used for the area-based operational forest stand inventory in Scandinavia utilizing airborne laser could be reduced from the current point density of around 1 m⁻² to 0.06 m⁻² without seriously reducing the quality of the inventory results. The effects of varying the point density reported here should, however, be verified on different forest types and in other regions than those considered here.

REFERENCES

Anon., 1989. *SAS/STAT User's guide, version 6*, 2. SAS Institute, Cary, NC, 846 pp.

- Blingsmo, K.R., 1984. *Diameter increment functions for stands of birch, Scots pine and Norway spruce*. Research Paper 7/84. Norw. for. Res. Inst., 22 pp.
- Brantseg, A., 1967. Volume functions and tables for *Scots pine*. South Norway. *Meddr. Norw. For. Res. Inst.*, 12: 689-739.
- Braastad, H., 1966. Volume tables for birch. *Meddr. norske SkogforsVes.*, 21: 265-365.
- Braastad, H., 1975. *Yield tables and growth models for Picea abies*, 31. Rep. Norw. For. Res. Inst., Ås, 364-537 pp.
- Braastad, H., 1980. Growth model computer program for *Pinus sylvestris*. *Rep. Norw. For. Res. Inst.*, 35: 272-359.
- Delbeck, K., 1965. *Methods for calculation of increment for open forests*. Melding 2, 5-45. Dept. of Forest Mensuration, Agric. Univ. of Norway, Ås.
- Goodwin, N.R., Coops, N.C. and Culvenor, D.S., 2006. Assessment of forest structure with airborne LiDAR and the effects of platform altitude. *Remote Sens. Environ.*, 1003: 140-152.
- Holmgren, J., 2004. Prediction of tree height, basal area and stem volume in forest stands using airborne laser scanning. *Scand. J. For. Res.*, 19: 543 - 553.
- Magnusson, M., 2006. *Evaluation of Remote Sensing Techniques for Estimation of Forest Variables at Stand Level*. Faculty of Forest Sciences, Department of Forest Resource Management and Geomatics, PhD. Swedish University of Agricultural Sciences, Umeå, 38 + appendix pp.
- Maltamo, M., Eerikainen, K., Packalén, P. and Hyypä, J., 2006. Estimation of stem volume using laser scanning-based canopy height metrics. *Forestry*, 79(2): 217-229.
- Næsset, E., 2002a. Determination of mean tree height of forest stands by means of digital photogrammetry. *Scand. J. For. Res.*, 17: 446-459.
- Næsset, E., 2002b. Predicting forest stand characteristics with airborne scanning laser using a practical two-stage procedure and field data. *Remote Sens. Environ.*, 80: 88-99.
- Næsset, E., 2004a. Effects of different flying altitudes on biophysical stand properties estimated from canopy height and density measured with a small-footprint airborne scanning laser. *Remote Sens. Environ.*, 91: 243-255.
- Næsset, E., 2004b. Practical large-scale forest stand inventory using a small-footprint airborne scanning laser. *Scand. J. For. Res.*, 19: 164-179.
- Næsset, E. and Bjerknes, K.-O., 2001. Estimating tree heights and number of stems in young forest stands using airborne laser scanner data. *Remote Sens. Environ.*, 78: 328-340.
- Næsset, E. and Gobakken, T., 2005. Estimating forest growth using canopy metrics derived from airborne laser scanner data. *Remote Sens. Environ.*, 96: 453-465.
- Thomas, V., Treitz, P., McCaughey, J.H. and Morrison, I., 2006. Mapping stand-level forest biophysical variables for a mixedwood boreal forest using lidar: an examination of scanning density. *Can. J. For. Res.*, 36: 34-47.
- Vestjordet, E., 1967. Functions and tables for volume of standing trees. Norway spruce. *Rep. Norw. For. Res. Inst.*, 22: 539-574.
- Weisberg, S., 1985. *Applied linear regression (2nd ed.)*. Wiley, New York, 324 pp.

ESTIMATION OF THE LIDAR HEIGHT OFFSET IN COASTAL VEGETATED AREAS

Jens Goepfert, Uwe Soergel

Institute of Photogrammetry and GeoInformation, Leibniz University of Hannover
(goepfert, soergel)@ipi.uni-hannover.de

KEY WORDS: lidar, laser scanning, vegetation, accuracy, feature extraction, intensity values

ABSTRACT:

Authorities operating in the field of coastal management require reliable area-wide height information for their responsibilities regarding to the safety of the coastal area. In this context the lidar technique replaces more and more traditional methods, such as terrestrial surveying, and is now the most important source for the generation of digital terrain models (DTM) in this zone. However, coastal vegetation interferes with the laser beam, resulting in a height offset for the lidar points depending on different vegetation types occurring in this region and their phenology. Various filter algorithms were developed for lidar data in vegetated areas, which are able to minimize this offset. But in very dense vegetation and hilly terrain these algorithms often fail resulting in certain residuals. In a previous approach the height offset was estimated based on grid data. In this algorithm the offset was linked to suitable features in the remote sensing data. A segment based supervised classification was performed using these features to partition the lidar data into different accuracy intervals. A major problem of this method arises from the fact that the accuracy intervals do not correspond to distinct and easily separable clusters in the feature space. Considering a single vegetation type the height offset exhibits a rather continuous characteristic. In a new approach this issue is tackled by modelling the offset with respect to the features using continuous functions. Additionally, feature extraction and classification are performed on raw data, in order to maintain the significance of the features by avoiding transformation artefacts and to increase the accuracy of the classification. On the basis of test data a comparison between the two methods is conducted to emphasize the problems and their solutions.

1. INTRODUCTION

Digital terrain models (DTM) of high accuracy are vital geographic information sources for various applications in coastal areas. For example, reliable height information is necessary for the calculation of flood risk scenarios, change detection of morphological objects and hydrographic numeric modelling. In former times traditional methods, such as terrestrial surveying, were used to acquire the data. However, in coastal areas with dense vegetation and frequently flooded terrain such measurement campaigns are very costly and time consuming as well as difficult to perform. Therefore, lidar technique is more and more used to collect the required amount of 3D points for the generation of the models. The advantage of this contactless remote sensing method leads on the other hand to an information loss about the measured objects (e.g., type and material). A serious problem for the generation of accurate DTM from lidar data is the influence of vegetation. The laser beam is not always able to fully penetrate the different layers of dense vegetation. Some echoes are produced by a mixed signal from vegetation as well as the ground and others are generated entirely in the canopy. This results in a positive height offset, because the laser beam is reflected before hitting the bare ground. In order to derive a DTM of high accuracy, these elevated points have to be eliminated from the dataset. Many filter algorithms were developed to remove such points. However, if there are only a few ground points, for example caused by dense vegetation, or points within low vegetation not significantly higher than the surrounding terrain present in the analysed area, the filter methods usually fail. Figure 1 visualizes a region in the dunes on the East Frisian Island "Langeoog" with standings of Japanese Rose, Beech Gras, Creeping Willow and Sea Buckthorn. The digital surface model (DSM) derived from unfiltered lidar data is illustrated on the left side (a) and the second picture (b) shows the DTM. Obviously, after the filtering process some height variations caused by vegetation still remain in the dataset. These considerations motivate efforts to determine the height offset of the lidar points depending on the vegetation type on the basis of different features.

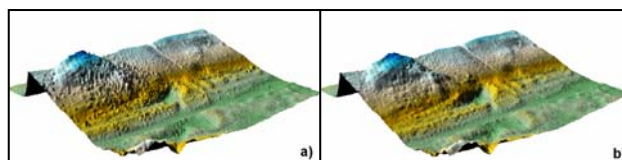


Figure 1. a) lidar DSM, b) lidar DTM

In preliminary studies the dependencies between the height offset of the lidar points and vegetation attributes (type, density and height) were investigated. In a next step the influencing factors had to be connected to features extractable from the available remote sensing data. These features were used for a supervised classification of the lidar data into different accuracy intervals.

In this paper, a new approach for the estimation of the height offset in the lidar data depending on the vegetation type is presented. While the previous classification algorithm was based on lidar data interpolated to a grid, now features are extracted directly from the 3D lidar raw data, in order to increase their significance with regard to the height offset. Another major problem of the former method arises from the aspect that the accuracy intervals, which represent the desired classes, do not correspond to distinguishable clusters in the feature space. The features describing the height offset show a rather continuous appearance. Thus, in this paper a relation between features and the height offset is established by continuous functions using reference data. Subsequently, the offset of each laser point can be determined on the basis of its related features and the connecting functions.

2. STATUS OF RESEARCH

In order to investigate the influence of different vegetation types on the accuracy of lidar measurements, understanding of the physical principles is essential that govern the interaction between the laser beam and different illuminated targets. Based on the radar equation Jelalian (1992) described the fundamental relations between the emitter, the reflecting object and the receiver applied to the lidar technique. Sensor and target

dependent parameters are separated and an object dependent cross section is defined. Additionally, Wagner et al. (2006) pointed out the dependencies between the spatial variations of the cross section and the amplitude as well as the width of the reflected echoes. Pfeifer et al. (2004) considered the influence of different parameters such as flying altitude, footprint size, echo detection and selection method as well as pulse width on the laser measurement in vegetated areas.

In addition, ground truth measurements can be used in comparison to the lidar data to estimate the height offset caused by the vegetation. In this manner Oude Elberink and Crombaghs (2004) found a systematic upwards shift of up to 15cm for low vegetated areas (creeping red fescue). Pfeifer et al. (2004) investigated the influence of long dense grass (+7.3cm), young forest (+9.4cm) and old willow forest (+11.6cm) on the accuracy of lidar data. In (Göpfert and Heipke, 2006) a positive offset for different coastal vegetation, such as Beach Grass (+19,3cm) and Sea Buckthorn (+18,4cm), was observed, too.

In the approaches described above the investigation of vegetation parameters influencing the lidar accuracy was limited to certain vegetation types. However, in the research of Hopkinson et al. (2004) the following relationship between the standard deviation of pre-processed laser heights (the ground elevation was subtracted from the first and last pulse measurement) and height of low vegetation in general (<1,3m) was given:

$$\text{vegetation height} = 2.7 * \text{standard deviation.}$$

The RMSE of the predicted vegetation heights was determined to be 15cm. Pfeifer et al. (2004) and Gorte et al. (2005) described the variation of the laser heights with texture parameters and showed their potential for correction of the height shift caused by low vegetation. Göpfert and Heipke (2006) linked vegetation attributes to features, such as echo intensity, in order to classify the lidar data into different accuracy intervals.

Many filter algorithms were developed to separate terrain and off-terrain points using geometric criteria exclusively, such as slope or height differences in a defined neighbourhood. Some methods are based on single lidar points, for example Axelsson (2000). Other approaches (e.g., Sithole and Vosselman, 2005), group the points to segments, which are classified afterwards. In contrast radiometric features of the lidar points are not very often included in standard filtering processes, if we distinguish between filtering and classification of objects. For example, in (Moffiet et al., 2005) the capabilities of the different returns (ground and vegetation, first, last, and single pulse) as well as the returned intensity were investigated to classify diverse tree types. Tóvári and Vögtle (2004) used the intensity values among other features, in order to discriminate buildings, vegetation, and terrain. In different studies a combination of height and multispectral data was proposed in order to detect and classify vegetation types. For instance, Mundt et al. (2006) explored the potential of this combination for mapping sagebrush distribution.

3. DATA

The research and tests are based on data of two flight missions. A detailed description of the reference and lidar data can be found in (Göpfert and Heipke, 2006). The first flight covering the East Frisian island Juist was conducted by the company TopScan with an ALTM 2050 scanner from Optech in March 2004. At a flying altitude of 1000m the system provided an average point density of 2 points/m². Unfiltered last pulse data

with intensity values, CIR-Orthophotos, ground and vegetation points were delivered. Simultaneously, 696 reference points with ground and vegetation heights, situated within a mixed habitat of rose and willow, were surveyed using tachymetry and GPS.

The data for the second measurement campaign were collected by the company Milan-Flug GmbH on the East Frisian island Langeoog in April 2005. The used LMS Q560 system of the company Riegl operating at an altitude of 600m realised an average point density of 2.9 points/m² and illuminated a footprint of 0,3m diameter. Raw data with up to three echoes per emitted pulse as well as the related intensity values, RGB-Orthophotos, ground and vegetation points were acquired. Supported by biologists several control areas of different vegetation types were surveyed. The results of this paper focus on coastal shrubberies including five test sites with Japanese rose and creeping willow.

Finally, a biotope mapping performed on aerial photos taken in 2002 and 2003 with a HRSC-AX and a DMC camera was used for the distinction of different predominant vegetation types.

4. METHODS

On the basis of previous research (Göpfert and Heipke, 2006) this paper introduces a new method to determine the height shift of lidar points in areas with typical coastal vegetation, where due to dense plant population no or only a few ground points exist and therefore standard filter algorithms usually fail.

Initially, section 4.1 explains briefly the characteristics of vegetation with respect to the lidar measurement and the connection between vegetation attributes and features generated from the remote sensing data. In section 4.2 the feature extraction method based on irregularly spaced lidar points is introduced. The next section gives a short overview about our previous classification algorithm emphasising its restrictions. Finally, in section 4.4 a new method for the estimation of the height offset in the lidar data caused by the vegetation is described.

4.1 Vegetation attributes and features

The interaction of the laser beam with complex objects, such as vegetation of different height and density, is difficult to model. In the corresponding literature this aspect is mathematically described as a convolution of the emitted signal with the cross section of the extended object. Every layer of the vegetation contributes to the signal received by the sensor. Low vegetation within the range resolution of the scanner system often generates a mixed echo with reflection from the ground. Therefore, the centre of gravity of this echo is situated above the terrain and an upwards shift is observed in the lidar data. In higher vegetation several distinctive echoes per laser pulse can occur. For the derivation of the DTM usually the last echo is used. However, also the last echo can be caused by a mixed reflection or within very dense plant population entirely created by vegetation layers. Thus, at locations of higher vegetation the last pulse data may also be biased upwards.

In order to assess the influence of vegetation attributes on the quality of the lidar height information, ground truth measurements were used in previous studies. For the purpose of comparison a DTM of the lidar data was generated and the heights were interpolated using the x- and y-coordinates of the terrestrial control points. In addition to the effect of the vegetation type on the lidar accuracy, the correlation between the height differences at the reference points and vegetation height and density were investigated. The vegetation density

was quantified by the analysis of the coverage rate of the plants in fish eye photos taken from the ground to the zenith.

In the next step the evaluated dependencies between the height shift and the vegetation attributes had to be related to the observables of the available remote sensing data. The significance of attributes as well as features depends strongly on the vegetation type. Therefore, without any context information a classification of vegetation types has to be performed in addition. In order to keep all features in the current remote sensing data exclusively for the distinction of accuracy levels with regard to the vegetation height and density, the separation of the vegetation types was realised using a biotope mapping.

The intensity value given with the data might be derived from the measurements in different manners by the providers. However, in any case it is a function of the signal amplitude, which is responsible for the main part of the spatial variation of the cross section (see Wagner et al., 2006). Reflectivity, directivity, and the effective area of the reflecting surface of an object are combined in the concept of the so-called cross section σ . Therefore, the amplitude of the echoes as well as the intensity values of the lidar points are related to the characteristics of the object, such as plant structure, and consequently to the vegetation density. In the basic case of normal incidence with uniform intensity, flat bare ground yields to a homogeneous cross section (coinciding with the circular beam footprint) as well as a narrow pulse width and high amplitude, while a mixed target consisting of terrain and low vegetation expands the pulse width and attenuates the amplitude. Considering coastal shrubberies in the leaf-off period, the higher the echo in the vegetation the thinner are the branches, which contribute to the cross section. Therefore, the amplitude as well as the intensity values decreases theoretically for elevated lidar points.

Due to in general higher reflectivity, bare ground in the investigation area appears brighter than shrubberies during the leaf-off time in the channels of multispectral data. Hence, the darker the pixel, the larger the proportion of vegetation and therefore the plant density is. Additionally, for evergreen plant population or measurement campaigns during the leaf-on period vegetation indices (e.g., the Normalized Difference Vegetation Index (NDVI)) are means to quantify the vegetation density, because a strong correlation between the leaf area index (LAI), describing the vegetation structure, and the NDVI exists (Pandya, 2004).

Higher vegetation areas cause larger variations in the height of the lidar points. Thus, the standard deviations as well as the contrast in the height data are correlated with vegetation height. Multiple echoes per laser beam can be separated by the system if the vegetation height is larger than the range resolution of the scanner. For pulsed scanner the range resolution corresponds to the half pulse length (e.g., LMS Q560 - $4ns \approx 0,6m$). Another premise for several echoes is a certain minimum vegetation density in the related height, which can generate a reflection strong enough to be detected by the photo diodes and the implemented signal processing software. In general, the occurrence of multiple echoes indicates larger vegetation height and density.

4.2 Feature extraction using raw data

The previous approach relied on transformation of the arbitrary distributed raw data to a regular spaced grid (3d to 2.5d mapping) in order to use conventional image segmentation and classification techniques. Disadvantages of the procedure are interpolation and smoothing artefacts reducing the significance

of the features related to the height offset in the lidar data. Additionally, the neighbourhood defined by the segments is not appropriate to the feature extraction especially for pixel near the borderline. Therefore, in this paper the features are determined using methods applied directly on 3D raw lidar data. A comparison is performed to evaluate the changes of the correlation between the different features, derived from grid and raw data, and the height shift caused by vegetation.

The raw data of the investigation area provided by the Milan Flug GmbH contains up to three echoes per laser pulse. The points were stored with x,y,z-coordinates together with intensity values in chronological order of their time stamps corresponding to the scan pattern. The different echoes are not assigned to a certain laser pulse, thus a separation into first, last and other pulses is performed based on geometric criteria. Afterwards, a file for the feature extraction is prepared, which only consists of last pulse data with the following attributes: coordinates, intensity values, number of associated returns and vertical differences between the last and related echoes. For the data of the first flight mission including only last echoes (Juist 2004) the separation step is omitted and the attributes related to multiple returns are not considered.

For feature extraction the n-nearest neighbours of each laser point are considered. The feature values for the intensity can be assigned directly from the examined point or the mean value in the neighbourhood is used alternatively, if a smoothing of noise effects is desired. Two additional features are calculated using the distribution of multiple echoes in the vicinity of the considered point: the ratio of laser pulses with several returns to all pulses and the average height difference between first and last echo in the defined neighbourhood. In order to analyse the variation of the height in the neighbourhood of the current laser point, the standard deviation and the contrast derived from a co-occurrence matrix are calculated. The influence of the terrain slope on the height variations is reduced by an adjusted plane fitted in the lidar points of the neighbourhood. The standard deviations of the point heights with respect to the plane are stored acting as features. The height values related to the plane are also used to determine the co-occurrence matrix. In Haralick (1979) the textural features were established based on grid data and Pfeifer et al. (2004) suggested their application to irregularly distributed points. The range of the height differences in the neighbourhood of the investigated point is divided into regularly spaced intervals. The number of these bins corresponds to the size of the square co-occurrence matrices. For each pair of points in the area of interest the horizontal distance is determined defining those pairs, which relate to a certain co-occurrence matrix. Afterwards, the height differences of the point pairs are calculated and assigned to the defined intervals. Like in (Pfeifer et al., 2004) all directions are considered, because in areas with natural vegetation, such as shrubberies, the direction dependency of the height variation should be marginal. The contrast is determined from the matrices using the following equation:

$$\text{Contrast} = \frac{\sum (i * (h_{diff})^2)}{N} \quad (1)$$

- i Number of counts in the matrix cell related to the height interval
- h_{diff} Related height interval
- N Number of all point pairs contributing to the values of a certain matrix depending on their horizontal distance

The features can be determined for lidar as well as for control points using the adjacent lidar points. For the purpose of comparison the features from the segments of the previous approach are assigned to the single points using their horizontal coordinates.

4.3 Previous classification approach

In the previous approach a supervised classification is performed based on different data sources (multispectral image, lidar data, biotope mapping), in order to divide the lidar data into different levels of accuracy depending on the predominant vegetation. For the classification a segment based algorithm was chosen in order to consider the local neighbourhood of the laser pulse and to calculate mean values and standard deviation as well as other texture parameters. Initially, the height and intensity values of the unfiltered lidar data are transformed to regular grids for a combined image classification with multispectral data. Unfiltered data are used, in order to preserve texture information stemming from the vegetation. The segmentation for the tests in this paper is performed using a watershed transformation applied to the low pass filtered lidar intensity image. Starting from the local grey value minima as seed points (corresponds to areas of low lidar accuracy), a flooding of the surface depending on the grey values is simulated. This procedure continues as long as water of different sources is only separated by the watershed lines. Afterwards, these lines are assigned to an adjacent segment using the minimum grey value difference between the segment and the line pixel. The significance of the features for the different accuracy intervals depends mainly on the vegetation type. Thus, the extension of the segments and, consequently, the area of the following classification are limited to one predominant vegetation type using the borderlines of the biotope mapping. Training areas are generated by slicing the height offset of the control points. For that purpose a difference model is calculated and transformed into an image, so that the grey values correspond to the height discrepancies. This image is segmented into different accuracy levels. These segments are used as training areas for supervised classification.

In the last step the feature vectors derived for the training areas and the segmentation are used to classify the lidar height data into different accuracy levels. In this paper a Minimum Distance Classifier (Euclidian distance) is applied to assign the current segment. For this method the features are normalised to the same overall value considering the distribution of the feature values, in order to weight the features equally.

4.4 New prediction algorithm

Studies indicated that the regular spaced accuracy intervals related to the classes do not correspond to separable clusters in the feature space. Considering one vegetation type the height offset and the related features show a rather continuous characteristic. Theoretically, lidar echoes can stem from reflection at any level of vegetation and hence every value in the range of the height offset for the current vegetation type is possible. Therefore, a standard classification is not the most suitable method to estimate the shift in the lidar data caused by vegetation. Hence, in the new approach the connection between the features and the height offset is realised by continuous functions. Initially, the parameters of the functions have to be determined using the reference data. For the unfiltered lidar data a DSM is calculated and the heights at the control points are interpolated. The height offset is determined based on comparison of the lidar and the reference height for every point.

Afterwards, the features for the control points are calculated depending on the adjacent lidar points (section 4.2). In order to eliminate outliers and attenuate the noise of the features a median filtering is performed. Subsequently, the parameters of the functions, which connect every chosen feature to the height offset, are estimated by least square adjustment. Polynomial functions of different order and exponential functions are implemented. For instance, if the lidar intensity values increase, the height offsets decrease implying the use of monotonic functions. Additionally, for high intensity values the height offset converges to zero. Therefore, in this case exponential functions are suitable to represent such dependency, while polynomials of higher order tend to oscillate between the interpolation points. For every single lidar point the height shift can be calculated based on its features and the estimated functions. Every feature and the related function generate an estimate of the shift. The final height shift of the current lidar point is computed by a weighted average of these single shifts. The weights are derived from the standard deviation of the points with respect to the fitted function for each feature (Equation 2) or from the correlation of the feature and the height shift (Equation 3).

$$\Delta H_f = \frac{\frac{\Delta H_1}{\sigma_1} + \frac{\Delta H_2}{\sigma_2} + \dots + \frac{\Delta H_n}{\sigma_n}}{\sigma_1^{-1} + \sigma_2^{-1} + \dots + \sigma_n^{-1}} \tag{2}$$

$$\Delta H_f = \frac{c_1 * \Delta H_1 + c_2 * \Delta H_2 + \dots + c_n * \Delta H_n}{c_1 + c_2 + \dots + c_n} \tag{3}$$

- ΔH_f Final height shift derived from all features
- $\Delta H_1 \dots \Delta H_n$ Height shift derived from single features
- $\sigma_1 \dots \sigma_n$ Standard deviation of the points regarding to the fitted function for single features
- $c_1 \dots c_n$ Correlation of the features and the height shift

The features correspond to the height offsets only for the vegetation type in the reference area, which is used to calculate the function's parameters. Therefore, the estimation of the height shift is conducted for the lidar points situated within the same kind of vegetation, which is realised using a biotope map.

5. RESULTS

5.1 Vegetation attributes and features

For all studied vegetation types in the coastal zone we observed a general upwards shift of the lidar DTM ranging from 10cm to 23cm for several control areas. The largest height shift was detected for beach grass (+19cm), sand couch grass (+20cm) and the mixed area sea buckthorn/willow (+23cm). Without considering the biotope type vegetation height and density did not show strong dependencies with respect to the height offset.

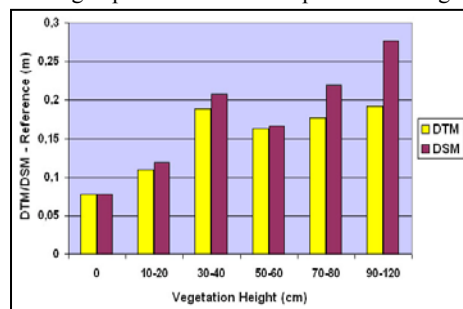


Figure 2. Average height shift plotted over vegetation heights for creeping willow (Langeoog, Riegl scanner)

However, a high correlation for height as well as density was determined observing exclusively one kind of vegetation. Hence, the knowledge of the vegetation type is crucial for the applicability of the other attributes. An example for the dependencies of the height shift and vegetation heights within an area of creeping willow is given in Figure 2.

The vegetation attributes are connected to features extracted from the remote sensing data (lidar and multispectral data), which are used to estimate the height shift of the lidar data in vegetated areas. For example, Figure 3 visualises the relations between the intensity of the lidar echoes and the height shift for an area covered with Japanese rose and creeping willow mapped by the ALTM 2050 scanner. A strong dependency and a continuous characteristic of the feature and the related offset are obvious. Maximal two clusters could be separated in the diagram. Intensity values lower than 60 indicate elevated targets, while for higher values mixed or ground echoes are expected.

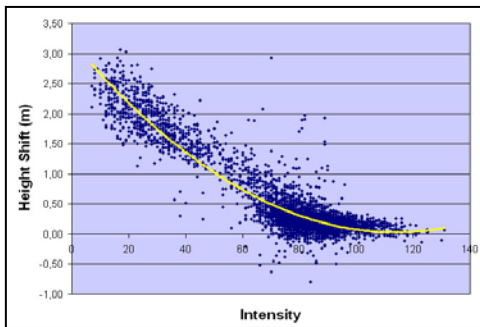


Figure 3. Dependencies between the height shift and the lidar intensity values (Juist 2004 TopScan)

5.2 Feature extraction using raw data

In order to increase the significance of the features the extraction is conducted using raw lidar data. Figure 4 depicts on the left side a part of a RGB-Image of the island Langeoog and on the right side the related density of multiple echoes extracted from the point cloud.

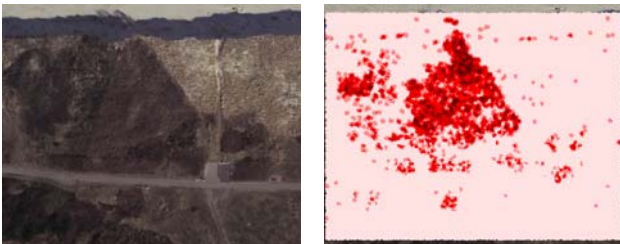


Figure 4. Left: RGB-photo of an area of the island Langeoog; Right: Density of multiple echoes (higher density is visualised with darker colour)

Reference area (flight mission)	Correlation between Height Contrast and Height Shift	
	Segments	Raw Data
Rose +Willow (2004)	0.45	0.51
Rose + Sea Buckthorn (2005)	0.36	0.55
Rose1 (2005)	0.38	0.48
Willow1 (2005)	0.46	0.72
Willow2 (2005)	0.65	0.69

Table 1. Correlation between the height shift and the height contrast extracted from the segments and raw data

In Table 1 the correlation of the offset to the height contrast extracted from raw and grid data (values for segments) is

compared. Obviously, the dependency of this feature to the height offset increases for all investigated reference areas using the raw data.

5.3 Previous classification approach

The previous and the new method are applied to a data set from the ALTM 2050 scanner covering the East Frisian island Juist in 2004. Figure 5 shows the terrestrial measured control points of the reference area, which is situated within a mixed habitat of rose and willow in the dunes. From the southern part of the points (green) the training areas are generated, which are used to learn the features for the classification. According to intensity values and height contrast the segments, created by the watershed transformation, are classified to five accuracy intervals using the minimum Euclidian distance.

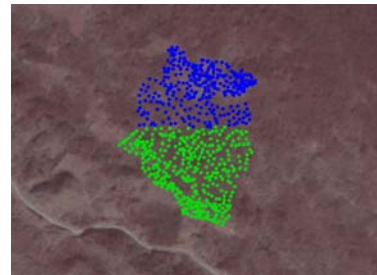


Figure 5. Control points of the test area on the island Juist (background: CIR-Orthophoto)

With the northern part of the reference points (blue) the classification result is checked. Table 2 visualises the related accuracy. The correctness for the different classes varies in the range of 54 – 75%. However, the proportion of the adjacent classes is quite high. These errors are caused by the arbitrarily chosen borders of the accuracy intervals. As shown before, the features and the related height offset have a rather continuous characteristic, which is not suitable to be modelled in clusters. Another reason for the errors is that the borderlines of the control areas and of the segments, which are classified in the aggregate, do not match.

Proportion of class with respect to the training area	Class 1 <20cm	Class 2 <50cm	Class 3 <100cm	Class 4 <150cm	Class 5 >150cm
Train Area 1	65,3	27,0	1,4	-	-
Train Area 2	32,7	56,9	18,7	2,01	0,3
Train Area 3	2,0	11,7	54,3	22,1	0,2
Train Area 4	-	4,0	22,0	54,0	24,5
Train Area 5	-	0,3	3,5	20,6	75,0

Table 2. Classification result

5.4 New prediction algorithm

In the new approach the control points are used to connect the height offset to the extracted features with continuous functions. In this test a second order polynomial is chosen both for the intensity and the height contrast. These features are weighted by their standard deviation with respect to the fitted functions. For the parameter estimation again the southern part of the control points is used as training area and the height offset of the northern points is calculated based on the features from the adjacent lidar data. The diagram in Figure 6 visualises a high correlation between the estimated height shift and the offset determined by the comparison of lidar and reference heights. This method shows potential for the estimation of the height offset in different coastal vegetation, because the continuous

characteristic of the accuracy in these vegetated areas is taken into account. But the algorithm depends strongly on the significance of the features.

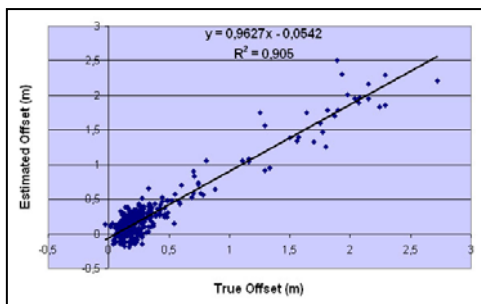


Figure 6. True height offset vs. estimated height offset

However, first tests using the lidar data acquired by the LMS Q560 system indicate that the correlation of the features and the height shift is not strong enough for some vegetation types, in order to fit robust functions. Therefore, the applicability of the features for the method has to be checked before.

6. CONCLUSION AND OUTLOOK

Starting from theoretical considerations about the interaction of the laser beam with different layers of vegetation, this paper compares two methods for the estimation of the height shift in the lidar data caused by coastal vegetation. Features, such as lidar intensity and height contrast, are connected to vegetation attributes, which influence the accuracy of lidar measurement. In a previous approach these features are used to classify the lidar data into different accuracy intervals. However, the characteristic of the accuracy of lidar data belonging to one vegetation type does not correspond to distinct and easily separable clusters in the feature space. Therefore, a new method is developed, which connects the feature to the height shift with continuous functions. The shift of a single lidar point can be easily calculated using its features and the parameters of the functions. However, this approach depends strongly on the significance of the extracted features, which is basically influenced by the scanner type and the echo detection algorithm. For future work upcoming scanning devices, which are able to record the full waveform, can provide new meaningful features. For instance, the pulse width can be a quality criterion by itself. It describes the uncertainty of the target surface and the range measurement for the related echo. Another idea combines the extracted feature with geometric criteria of filtering methods, in order to eliminate vegetation points and to generate a DTM for the vegetated coastal zone.

ACKNOWLEDGMENTS

This research has been financed by the Federal Ministry of Education and Research (BMBF) under project no. 03KIS050. We acknowledge the support of our project partners: Department of Rural Area Husum (ALR), Federal Waterways Directorate (WSD) and the Lower Saxony Water Management, Coastal Defence and Nature Conservation Agency Division Norden-Norderney (NLWKN).

REFERENCES

Axelsson, P. (2000). DEM Generation from Laser Scanner Data using adaptive TIN-Models. *The Int. Arch. of Photogrammetry and Remote Sensing*, Amsterdam, Netherlands, Vol. XXXIII, Part B4/1, pp. 110-117.

Göpfert, J., Heipke, C. (2006). Assessment of Lidar DTM Accuracy in Coastal Vegetated Areas: *The Int. Arch. of Photogrammetry, Remote Sensing and Spatial Information Sciences*, Vol. XXXVI, Part 3, pp. 79-85.

Gorte, B., Pfeifer, N., Oude Elberink, S. (2005). Height texture of low vegetation in airborne laser scanner data and its potential for DTM correction. *The Int. Arch. of Photogrammetry, Remote Sensing and Spatial Information Sciences*, Vol. XXXVI, Part 3/W19, pp. 150-155.

Haralick, R. M. (1979). Statistical and structural approaches to texture. *Proceedings of the IEEE*, 67(5), 786-804.

Hopkinson, C., Lim, K., Chasmer, L.E., Treitz, P., Creed, I.F., Gynan, C. (2004). Wetland grass to plantation forest – estimating vegetation height from the standard deviation of lidar frequency distributions. *The Int. Arch. of Photogrammetry, Remote Sensing and Spatial Information Sciences*, Vol. XXXVI, Part 8/W2, pp. 288-294.

Jelalian, A.V. (1992). *Laser Radar Systems*. Artech House, Boston and London.

Moffiet, T., Mengerson, K., Witte, C., King, R., Denham, R. (2005). Airborne laser scanning: Exploratory data analysis indicates variables for classification of individual trees or forest stands according to species. *ISPRS Journal of Photogrammetry & Remote Sensing* 59 (2005), pp. 289-309.

Mundt, J. T., Streutker D. R., Glenn N.F. (2006). Mapping Sagebrush Distribution Using Fusion of Hyperspectral and Lidar Classifications. In *Photogrammetric Engineering & Remote Sensing*, Vol. 72, No.1, January 2006, pp. 47-54.

Oude Elberink, S. and M. Crombaghs (2004). *Laseraltimetrie voor de hoogtemetingen van de kwelders Waddenzee*. Technical Report AGI-GAP-2003-50 (in Dutch), AGI, RWS.

Pandya, M.R. (2004). Leaf Area Index Retrieval Using Irs Liss-iii Sensor Data and validation of Modis Lai Product Over India. *The Int. Arch. of Photogrammetry and Remote Sensing*, Vol. XXXV, Part B7, pp. 144-149.

Pfeifer, N., Gorte, B., Oude Elberink, S. (2004). Influences of Vegetation on Laser Altimetry – Analysis and Correction Approaches. *The Int. Arch. of Photogrammetry, Remote Sensing and Spatial Information Sciences*, Vol. XXXVII, Part 8/W2, pp. 283-287.

Sithole, G., Vosselman, G. (2005). Filtering of Airborne Laser Scanner Data based on Segmented Point Clouds. *The Int. Arch. of Photogrammetry, Remote Sensing and Spatial Information Sciences*, Vol. XXXVI, Part 3/W19, pp. 66-71.

Tóvári, D., Vögtle, T. (2004). Object Classification in Laser-Scanning Data. *The Int. Arch. of Photogrammetry and Remote Sensing*, Vol. XXXVI, Part 8/W2, pp. 45-49.

Wagner, W., Ullrich, A., Ducic, V., Melzer, T., Studnicka, N. (2006). Gaussian decomposition and calibration of a novel small-footprint full-waveform digitising airborne laser scanner. *ISPRS Journal of Photogrammetry & Remote Sensing* 60 (2006), pp. 100-112.

AUTOMATIC CO-REGISTRATION OF TERRESTRIAL LASER SCANNER AND DIGITAL CAMERA FOR THE GENERATION OF HYBRIDS MODELS

Diego González Aguilera, Pablo Rodríguez González and Javier Gómez Lahoz

Land and Cartography Engineering Department, Univ. of Salamanca, Spain

daguilera@usal.es, pablorgsf@hotmail.com, fotod@usal.es

Commission V, WG V/3

KEY WORDS: Cultural Heritage, Laserscanning, Photogrammetry, Sensor Registration, Software Development.

ABSTRACT:

3D modeling and visualization of real world scenes is an important topic of research with applications in many areas such as virtual museums, game and entertainment, architecture description and restoration, virtual reality, archaeology, many industrial applications and last but not least important tourist applications. 3D modeling and visualization are the creation of a computer representation of real world environments that merges together data coming from one or more sensors. The representation of the geometric and texture information of a real scene is a very challenging task due to the acquisition of large-scale data, complexity of the geometry and difficulties to cope with reflectance properties of the objects and variations in the lighting in the scene. Two approaches, depending on the type of sensor (terrestrial laser scanner or digital cameras), are typically used to face the 3D reconstruction problem. Laser scanners provide 3D metric information in real time through an array of coordinates: range images. Digital cameras are used to acquire high-resolution images of the scenes. These images are 2D arrays of reflected light from objects but do not contain any explicit metric information. Further processing is necessary, to calibrate cameras and compute 3D models. This paper aims to demonstrate how active and passive sensors can be registered and combined through a hybrid approach to compute 3D models of complex scenes with photo-realistic quality. Particularly, the proposed approach tries to deal with two different images: a high-resolution image acquired with a digital camera and a range image obtained from a laser scanner model using collinearity condition. Our goal is to devise and implement a robust, automatic, and accurate hybrid-technique for registration of both sensors for efficient modeling (geometry) and rendering (radiometry) of complex environments. To this end, we have developed a novel application for laser scanning which allow us to test the approach developed over experimental results.

1. INTRODUCTION: A REVIEW

3D reconstruction of complex scenes is a very challenging task due to the variety of possible scenes to scan and difficulties to work with real data. Passive and active techniques used in 3D reconstruction have their limitations and, separately, none of these techniques can solve all the problems inherent to the modeling of real environments. To reinforce this need, next table (Table 1) illustrates a comparison based on the most important features with relation to laser scanner and digital camera.

Laser Scanner	Digital Camera
↓ Inaccurate lines and joints	↑ Accurate lines and joints
↓ Poor colour information	↑ Good colour information
↑ Prompt and accurate metric information	↓ Hard-working and slow metric information
↑ Excellent technique for the description of complex and irregular surfaces	↓ Time-consuming technique for the description of complex and irregular surfaces
↓ High-cost technique	↑ Low-cost technique
↓ The 3D model is an entity disorganized and without topology	↑ The 3D model is an entity organized and with topology
↑ Light is not required to work	↓ Light is required to work

Table 1: Comparison of features: laser vs. camera.

Up to now, several approaches have been developed trying to register both sensors. This problem of image-to-model registration is closely related to the problem of camera calibration, which finds a mapping between the 3D world (object space) and a 2D image. This mapping is characterized

by a rigid transformation and a camera model, also referred to as the camera's extrinsic and intrinsic parameters. This rigid body transformation takes 3D points from object space to 2D points in the camera's reference frame, and the camera model describes how these are projected onto the image plane. The camera calibration problem is solved by matching features in the 3D model with features in the image. These features are usually points, lines or special designed objects that are placed in the scene. The matching process can be automatic or user driven, and the number of feature pairs required depend on whether we are solving for the intrinsic, extrinsic or both parameters sets. In the context of image registration for 3D modeling using dense laser scanner data, several approaches have been developed: (Rocchini et. al., 1999) develop a new approach for mapping and blending textures on 3D geometries. The system starts from a 3D mesh which represents a real object and texture detail acquired via a common photographic process. Both datasets are integrated based on initial rough registration. However, this approach requires manual interaction and is applied to small objects; (Lensch et. al., 2001) develop an image registration approach based on silhouette matching, where the contour of a rendered version of the object is matched against the silhouette of the object in the image. No user intervention is required, but their method is limited to cases where a single image completely captures the object; in other range of methods applied to large distances, dealing with outdoor scenes and based on locating invariant image features, (McAllister et. al., 1999) suggest correlating edges common to the color image and the range map's intensity component. However, care must be taken to place the camera's nodal point at the same physical location as the laser's center of rotation, and to rotate both devices about this point. This homographic relationship simplifies the registration to the camera's three

rotations relative to the laser; (Elstrom, 1998) presents a novel stereo-based method for registering color and range images acquired from externally uncalibrated sensors. The multi-sensor alignment problem is solved by processing invariant features such as corner, edges or contours which are extracted from the raw data. The benefit of a feature-based approach is that it abstracts the data and thus simplifies the search for the registration parameters. Often, however, feature extraction leads to the loss of some information; (Stamos and Allen, 2001) present a semi-automatic method for image to model registration of urban scenes, where 3D lines are extracted from the point clouds of buildings and matched against edges extracted from the images. The method involves the utilization of parallelism and orthogonality constraints that naturally exist in urban environments. Therefore, their algorithm only operates in scenes which contain linear features with strong geometric constraints. Also a number of thresholds have to be manually set by the user in order to customize the segmentation; (Ikeuchi et. al., 2003) in their Great Buddha work, use reflectance edges obtained from the 3D points and match them against edges in the image to obtain the camera position. They align edges extracted from reflectance images with those in color images so that the 3D position error of those edges is minimized by iterative calculation. Nevertheless, this approach has been focused on small and simple objects; (Allen et. al., 2003) present a novel method for 2D to 3D texture mapping using shadows as cues. They pose registration of 2D images with the 3D model as an optimization problem that uses knowledge of the Sun's position to estimate shadows in a scene, and use the shadows produced as a cue to refine the registration parameters. However, they still have some limitations related to view planning and real-time model creation and visualization. More recently, (Aguilera and Lahoz, 2006) exploit the power of a single image-based modeling method to obtain an automatic co-registration of laser scanner and uncalibrated digital camera. Particularly, the problem of image registration is solved automatically through 2D and 3D points correspondences which are matched based on a search of spatial invariants: two distances and one angle. However, several input considerations such as especial targets, vanishing points and geometric constraints have to be taken into account; (Al-Manasir and Fraser, 2006) develop a strategy using a coded target placed on the object, which are registered by a calibrated digital camera, rigidly attached to the laser scanner. An automatic process is applied to solve the spatial position and orientation of the camera within the laser scanner coordinate system. The identified coded targets are used to apply a 3D similarity transformation. However, this approach needs a camera attached camera to laser scanner and placed some code target on the object; (Alshawabkeh et. al., 2006) propose a robust algorithm line detection within the high-resolution image, based on the mathematical properties of the mean which is invariant to arbitrary rotations and translation of surface. This segmentation is applied into 3D model, and can look for different types of edges. Finally, it uses the edge resulting to apply a matching between 2D and 3D datasheets.

The method that we have developed (Figure 1) exhibits significant improvements in flexibility, accuracy, and completeness over the approaches remarked above. Particularly, some relevant tasks have been automated; new strategies and algorithms integrating robust estimators have been adapted in each step guarantying more reliability and accuracy; considering that both sensors have been registered, a hybrid modeling process has been developed which allow us to complete and improve geometric and radiometric properties of

the laser model. Finally, a novel laser scanning tool has been developed in order to test experimental results.

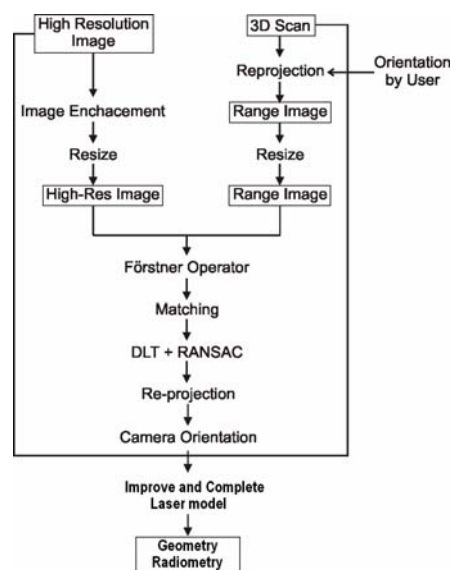


Figure 1. Full pipeline process.

The paper presents the following structure and organization: after this review, Section 2 develops the matching of both images: range and high-resolution. Section 3 explains in detail the co-registration approach developed for both sensors. Section 4 describes a hybrid modeling approach to improve and complete the laser model. Section 5 shows some experimental results using our own novel application of laser scanning. A final section is devoted to outline some conclusions and future works.

2. MATCHING RANGE AND HIGH-RESOLUTION IMAGES

Automated identification of image correspondences is a solved problem in aerial photogrammetry, since image geometry is more standard and relative camera rotations are small. However, in close range applications, each acquisition has its own image geometry, depending on the image scene, the baseline cannot be kept always constant and the rotations around the camera axis are significant. Moreover, more problems arise if we try to match two different types of images such as range and high resolution images. Therefore, the algorithm must be as robust as possible and extracted features should be invariant under different transformations to be re-detectable and useful in automatic procedures.

The matching strategy developed presents a robust and hierarchical approach with the aim of extracting and matching features (interest points) between high-resolution and range images. Firstly, an image pre-processing was applied based on some radiometric equalization and contrast enhancement. Particularly, a blue channel filter is applied in order to eliminate sky influence on high resolution image. With relation to range image, one problem is the 'air' or holes due to an insufficient density of points, so a bilinear interpolation is applied to reduce its influences. At last, both images are resized interactively based on some user information. The goal of the resizing is to apply a planar affine transformation to the range image to fit as well as possible to the high-resolution image. The resized images will be used in the matching process. Secondly, an

interest point detector method based on Förstner operator (Förstner and Gülch, 1987) has been applied. Many interest point detectors exist in the literature but only a few satisfy accuracy requirements. Through Förstner operator, the detection and localization stages are separated, into the selection of windows, in which features are known to reside and feature location within the selected windows. The windows of interest are computed with a gradient operator (1) and the normal matrix.

$$\begin{aligned} g'_x &= g'_{x+1,y} - g'_{x-1,y} \\ g'_y &= g'_{x,y+1} - g'_{x,y-1} \end{aligned} \quad (1)$$

The point of interest is determined as weighted centre of gravity of all points inside the window. Further statistics performed locally allow estimating automatically the thresholds for the classification, like trace of inverse matrix (Q) or form of the confidence ellipse. The algorithm requires a complicate implementation and is generally slower compared to other detectors.

Once interest points have been extracted, a hierarchical matching strategy based on ABM (Area Based Matching) and LSM (Least Square Matching) has been applied. At first, the cross-correlation coefficient is used to get a first approximation (2). Around the predicted position a search box is defined and scanned for searching the position which has the higher cross-correlation value. This position is considered a first approximation of the correct point to be matched.

$$\rho = \frac{\sigma_{HR}}{\sigma_H \sigma_R} \quad (2)$$

where ρ is the cross-correlation coefficient, σ_{HR} is the covariance between the windows of high-resolution and range image; σ_H is the high-resolution image deviation and σ_R is range image deviation.

Then, the approximation found with cross-correlation is refined using LSM algorithm (Grün, 1985), which provides precise and sub-pixel location of the matching elements. The cross-correlation process uses a small window around each point in the high-resolution image and tries to correlate it against all points that are inside a search area in the range image. The search area is given considering the resize of both images. The final number of possible matches depends on the threshold parameters of the LSM and on the disparity between the two images pairs; usually it is around 40% of the extracted points.

3. CO-REGISTRATION OF SENSORS

Due to the unguided matching process, the found matched pairs might contain outliers. Therefore, a filtering of false correspondences must be performed. Taking into account the authors' experience testing some robust approaches (Aguilera et. al., 2004), several assumptions can be confirmed:

- Least squares adjustments are not robust estimation techniques as wrong observations (like false interest points) can lead to completely wrong results and might even prevent convergence of the adjustment.
- The classical approach to detect blunders in the observations based on the reliability theory or data-snooping technique, developed by (Baarda, 1968) could

not solve some critical problems. Moreover, the blunder detection technique has a solid theoretical formulation but it is based on some hypothesis which can lead to unsuccessful results if not satisfied.

- When a large number of observations are available, robust estimators such as RANSAC or M-estimators can perform more efficiently to check for possible outliers. In robust estimations, gross errors are defined as observations which do not fit to the stochastic model used for the parameters estimation.

Taking into account the assumptions remarked upon above, a twofold approach for co-registration of both sensors has been developed:

I. An *estimation step* which allows us to obtain a first approximation of co-registration parameters based on Direct Linear Transformation (DLT) (Abdel-Aziz and Karara, 1971) combined with RANSAC (RANdom SAMpling Consensus) (Fischler and Bolles, 1981). As a result, the most important wrong matched interest points are rejected.

II. A *computation step*, which applies a re-weighted least square adjustment supported by modified Danish M-estimator (Domingo, 2000). A re-projection strategy based on collinearity condition and supported by Danish M-estimator allows us to refine the DLT solution and thus to compute accurate and reliable co-registration parameters.

In a first step, DLT is applied to solve camera orientation using pixel and terrain coordinates. Terrain coordinates are obtained from laser scanner file which relations every pixel of range image with its 3D point projection. This algorithm is used due to be a very well developed algorithm in computer vision, and it can obtain a first result without iterations. This process is upgraded with RANSAC in order to get a reliable camera position.

RANSAC computes several registrations based on a minimal subset of correspondences selected randomly. For each of these "random registrations", the technique searches for all supporting correspondences (correspondences with a DLT error below a given threshold). All correspondences are then used to compute a new camera registration. The process is repeated and the estimation that has the larger set of points and the minimum error is selected as the final registration. The algorithm needs three parameters: the maximum error (in pixels) to consider a correspondence pair as supporting a given registration (10 pixels); the subset of points used in each trial for the first evaluation (11 points); the number of trials (20-30). To estimate this last parameter, we need to know the number of outliers in the data. In our case, we do not know the percentage of outliers in the initial data; furthermore, it will depend on the type of image (the error will increase in poorly textured images where matching algorithms performance is worse). In order to provide more automatism and efficiency, adaptative thresholds have been introduced (Hartley&Zisserman, 2000).

In a second step, a final computation of the co-registration parameters has been obtained based on a re-projection strategy of range image into high-resolution image. An iterative process using collinearity-based approach has been applied to refine the DLT solution allowing us to improve the co-registration of both sensors. Particularly, a set of 2D range image points have been

re-projected over the image based on colinearity condition principles and the approximated camera parameters provided by DLT step. Small discrepancies remain between the projected range points and the original extracted high-resolution image points. The 2D coordinates of the extracted points and the re-projected corresponding range image points constitute the input to compute a new registration. This iterative process continues until the Euclidean distance between the re-projected points and the original interest points gets to a minimum (threshold distance). The general idea is that at each iteration the distance between the two datasets is reduced, allowing a better computation of registration parameters. To ensure the convergence of the algorithm and the improvement of the initial camera model estimation, the registration error of each correspondence is computed and recorded. In each new iteration, only matching pairs for which the registration error decreases are updated, and the other are kept unchanged.

Particularly, the method consists of minimizing the Euclidean distance between the re-projected points and the original interest points. Nevertheless, the presence of accidental and "light" gross errors in observations will make that each interest point does not have the same degree of participation in the adjustment. In this way, a re-weighted least square adjustment supported by modified Danish estimator (3) is applied. The numeric solution for this adjustment follows an iterative re-weighted approach, in which the iteration starts with some initial values for the weights of observations and a conventional least square adjustment. In the following iterations, new weights are calculated for each observation based on the residuals obtained in the previous iteration, and a least square adjustment with these new weights is repeated.

$$W(v) = e^{-(v/r)^2} \quad (3)$$

where w represents the weight function and v the residual vector.

The iterative process continues until the convergence is achieved (usually 3 to 10 iterations). After the computation of co-registration, a full model for the digital camera with relation to laser scanner is available and ready to be exploited. One of the most important advantages of modified Danish estimator regarding to RANSAC is its continuous approach without total loss of observations, providing more accuracy and reliability in the result.

4. A HYBRID MODELING APPROACH

The idea developed in this section, is based on the use of registered high-resolution image not only to texture mapping but also to complete and improve 3D laser model geometry.

4.1 Geometry.

For some modeling applications, like building reconstruction, where the object is mainly described with straight lines, laser scanner technology does not provide a final solution.

The goal of surface modeling can be stated as follows: given a set of sample points P_i assumed to lie on or near an unknown surface S , create a surface model S' approximating S . A surface modeling procedure based only in laser scanner dataset cannot exactly guarantee the recovery of S , since principal straight lines of the building are not provided by laser scanner. Sometimes additional information of the surface (e.g.

breaklines) can be available and thus the output result S' is more likely to be topologically correct and converges to the original surface S . A perfect scan system should be dense in detail area and sparse in featureless parts and performs automatically. But usually the measured points are unorganized and often noisy; moreover the surface can be arbitrary, with unknown topological type and with sharp features.

The approach presented in this section does not extract directly 3D information from a high-resolution image; it uses features detected in the high-resolution image to complete and improve segmentation in laser model. The process considers the laser model completely triangulated, and not the point's cloud, to make easier the detection and matching of 3D edges.

The co-registration of both sensors allows us to compute correspondences between 2D straight lines belonging to high-resolution image and 3D edges belonging to laser model. The final step of the correction process consists in the alignment of the laser model edges.

A first approximation to laser model has been obtained based on Delaunay triangulation, especially through an incremental strategy (Bourke, 1989). Furthermore, in order to make easier the process, laser model is filtered in order to isolate the main 3D edges. Topological information, as well as normal of triangles are used to isolate these features. As a result, two different types of 3D edges are isolated: *final edges*, those that constitute the surface perimeter and *breaklines edges*, those whose normal variation is greater than a predefined threshold (30-40°).

Afterwards, a robust straight line extraction is performed over the high-resolution image. Particularly, a combination of Canny (1986) and Burns (1986) operators is used to obtain accurate lines. Furthermore, a clustering of these segments based on the analysis of slope and orthogonal distance allow us to obtain the principal lines.

The hybrid modeling method that we propose should infer the correct geometry, topology and features based on the co-registration of both sensors. In this sense, the features extracted on the high-resolution image can provide geometric constraints as well as breaklines to model the object.

At this point, an iterative process starts in which the 3D edges isolated over the laser model start to be corrected based on the straight lines extracted over the high-resolution image. For each extracted segment in the high-resolution image, the algorithm selects the 3D edge points that are projected to the line defined by the segment (the orthogonal distance and the slope variation are used to validate the 3D edges candidates).

Finally, an algorithm corrects the 3D coordinates of points close to straight lines in the laser model. This is done in two steps. First, the parameterised equation of the 3D line is computed, and then 3D coordinates are modified so that the final points will lie in the computed line. The algorithm is applied iteratively with adaptative thresholds to correct as many edge points as possible. The algorithm stops when no correction is computed or when a user-defined number of iterations are reached.

4.2 Texture.

The visualization of a 3D model is often the only product of interest for the external world and remains the only possible

contact with the model. Therefore, a realistic and accurate visualization is often required.

Through a texture mapping technique, our registered high-resolution image is mapped onto the 3D laser model in order to achieve photo-realistic virtual models. Knowing the parameters of interior and exterior orientation of the image, for each triangular face of the 3D laser model the corresponding image coordinates are calculated. This approach is performed based on the Anchor Points method developed by (Krauss, 1993). This method has three main steps:

- (i) Firstly, laser model image-coordinates are computed through camera model and collinearity condition.
- (ii) Next, a correspondence between each face of the laser model with each face of the high-resolution image is established.
- (iii) Finally, a projection of the photographic texture between the face of the high-resolution image and its homologous in laser model is performed. In this sense, each triangular face receives a specific transformation model well known as affine transformation.

On the other hand, after the registration procedure, a full model for camera is available. Using this information, each 3D coordinate in the range image can be re-projected into the intensity high-resolution image according to the camera model. Since both images are directly registered, it is possible to establish an association between pixels in range and high-resolution images, and compute a new range image based on the high-resolution colour values. The final image is useful to evaluate the quality of the registration in an easy fast way. It can also be used directly to map texture on the 3D models, giving a much more realistic impression than for a model only textured with the range image. The 3D coordinates when projected in the high-resolution image, will not correspond normally to an integer pixel value. To avoid distortion in the colors, a bilinear interpolation is used to compute the resulting RGB value for the re-projected image. Furthermore, due to the different images resolution, the interpolation is used to compute the "extra" 3D positions.

Finally, regarding visualization, the VRML (Virtual Reality Modeling Language) format was the standard chosen to provide an interactive visualization of the results guaranteeing flexibility and scalability in the visualization at the same time, so different 3D laser models can be incorporated and managed easily. In this way, an automatic transformation of the reconstructed laser 3D model into a topological structure (points, lines and surfaces) sorted hierarchically in a nodes network was performed, allowing three different levels of visualization: wireframe, shaded and textured. Materials defined by their colours and radiometric properties (opaqueness, transparency, diffusion, reflection and emission) and high-resolution textures, are mapped through a uniform and continuous rendering supported internally by VRML. At last, in order to increase the level of realism and completeness of the scene, several basic primitives combined with spherical panoramas can be added.

5. EXPERIMENTAL RESULTS

In order to determine the accuracy, limitations and advantages of the hybrid approach proposed, a series of experiments are tested using our own tool developed.

5.1 The medieval wall of Avila

The medieval wall of Avila represents a fundamental reference point to the Spanish Cultural Heritage. Alfonso VI ordered the construction of this fortification after his conquest of Avila in 1090. Apparently, he used Moorish prisoners to build the wall.

5.1.1 Problem and goal. Two different sensors and images are used to put in practice the approach developed. Particularly, a time of flight laser scanner, Trimble GX200, is used to obtain range image, while a conventional digital camera, Nikon D70 is used to obtain high-resolution images.

The workspace is situated in the north of the medieval wall, in a popular place known as "Arco del Carmen". The principal problems with this experiment are related with its irregular patterns, battlements, which causes a lot of problems in matching phase, as well as its low density scan (about 300.000 points).

5.1.2 Methodology and results. The input data are constituted by a high-resolution image (3008 x2000 pixels) and a resized range image obtained from laser scanner point cloud and collinearity condition (Figure 2).

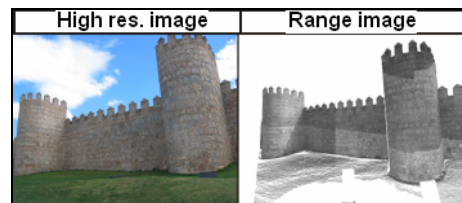


Figure 2. Input data: high-resolution and range image.

The Förstner detector (Figure 3) and a twofold matching strategy are applied to relate both images. A matching kernel of 35x35 pixels is used at first. The final deviation of the matching is 0.71 pixels.



Figure 3. Förstner detector applied to medieval wall.

Afterwards, a robust registration of both sensors is performed. In a first step, DLT and RANSAC are combined to obtain a first approximation of camera parameters (Table 2). Then, in a second step, a re-projection strategy supported by Danish robust estimator is applied iteratively (Table 3).

Sensor registration estimation: DLT + RANSAC

External Parameters (Unit: radians, metres)			
Axis: -1.16377	X: 1.195	σ_A : 0.163	σ_X : 0.70
Tilt: -1.0355	Y: -1.382	σ_T : 0.0178	σ_Y : 1.10
Swing: -0.3572	Z: -0.107	σ_S : 0.0037	σ_Z : 0.52

Table 2: Twofold registration process: estimation

Sensor registration computation: Collinearity + Danish estimator (7th iteration)

External Parameters (Unit: radians, metres)			
Axis: -1.1824	X: 1.607	σ_A : 0.0153	σ_X : 0.19
Tilt: -1.0521	Y: -2.035	σ_T : 0.0238	σ_Y : 0.14
Swing: -0.1687	Z: -0.204	σ_S : 0.0022	σ_Z : 0.13

Table 3: Twofold registration process: computation

Finally, once a complete camera model has been computed, an automatic high-resolution texture mapping is applied (Figure 4).



Figure 4. Mapping high-resolution textures.

5.2 The romanesque church of San Pedro

This romanesque church was founded on the XII century. The main facade is considered to have important examples of architectural sculpture, even though somewhat damaged.

5.2.1 Problem and goal. Two different sensors and images are used to put in practice the approach developed. Particularly, a time of flight laser scanner, Trimble GS200, is used to obtain range image, while a conventional digital camera, Canon IXUS400 is used to obtain high-resolution images.

The workspace is the main façade of the church. In this case, the scan density is high (over 1.5 millions of points), which allows obtain of range-image with enough texture to apply the matching process.

5.2.2 Methodology and results. The input data are constituted by a high-resolution image (2272 x 1704 pixels) and a resized range image obtained from laser scanner point cloud and collinearity condition (Figure 5).

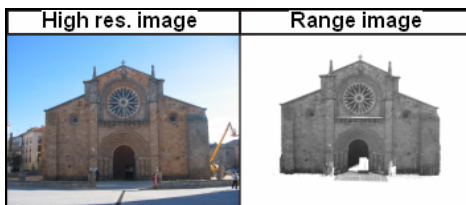


Figure 5. Input data: high-resolution and range image.

The Förstner detector and a twofold matching strategy are applied to relate both images (Figure 6). A matching kernel of 35x35 pixels is used at first. The final deviation of the matching is 0.51 pixels.



Figure 6. Twofold matching strategy

Afterwards, a robust registration of both sensors is performed. In a first step, DLT and RANSAC are combined to obtain a first approximation of camera parameters (Table 4). Then, in a second step, a re-projection strategy supported by Danish robust estimator is applied iteratively (Table 5).

Sensor registration computation: DLT + RANSAC

External Parameters (Unit: radians, metres)			
Axis: -1.429903	X: 8.048	σ_A : 0.0150	σ_X : 0.4433
Tilt: 0.09558	Y: -2.615	σ_T : 0.0226	σ_Y : 0.1928
Swing: 0.009088	Z: 0.277	σ_S : 0.0055	σ_Z : 0.6027

Table 4. Twofold registration process: estimation

Sensor registration computation: Collinearity + Danish estimator (4th iteration)

External Parameters (Unit: radians, metres)			
Axis: -1.451542	X: 8.456	σ_A : 0.0073	σ_X : 0.2143
Tilt: 0.098474	Y: -2.377	σ_T : 0.0111	σ_Y : 0.0981
Swing: 0.013599	Z: 0.585	σ_S : 0.0025	σ_Z : 0.2956

Table 5. Twofold registration process: computation

Finally, a hybrid modeling process has been developed in order to complete and improve laser model. Regarding geometry, several structural lines related to mesh model (breaklines and final edges) have been corrected based on the co-registration (Figure 7).

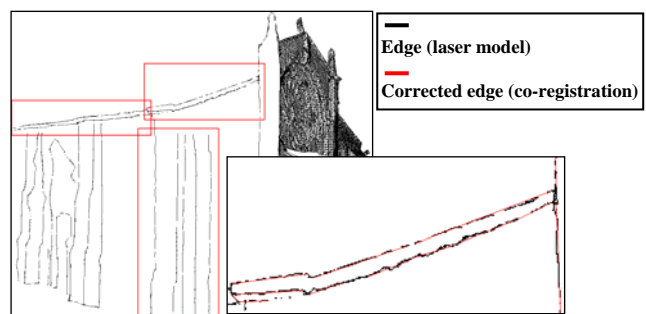


Figure 7. Hybrid modeling process in San Pedro Church.

The time effort required in both experimental results was irrelevant, only user interaction was required for providing an initial approximation of camera pose.

6. CONCLUSIONS AND FUTURE PERSPECTIVES

The presented paper has investigated and developed the automatic co-registration of two sensors: terrestrial laser scanner and high-resolution digital camera, as well as the hybrid modeling approach derived from this fusion. A consistent and reliable full process pipeline has been developed and presented. It was demonstrated with different practical examples tested through our own software.

With relation to the most relevant aspects of the proposed approach, we could remark on:

- Automation in the matching of both images has been achieved.
- No need for previous calibration.
- A robust registration of both sensors is obtained using RANSAC and Danish estimator.
- An alternative to improve and complete laser models is presented.

As for the most critical aspects, this approach has the following limitations:

- User interaction is required to provide a first approximation of the area of interest.
- High resolution scans is advisable to obtain fine texture and thus good quality in matching process.

We feel that we have attacked one of the most difficult problems in the laserscanning success. Nevertheless, several improvements could be considered in the next future. Focusing on geometry, the research could be extended to provide the improvement of complex geometries such as arcs and quadrics. Aiming on radiometry, also algorithms that allow handling the problem of occlusions, illumination properties and transition between junctions, could be developed.

Acknowledgements

We would like to thank to several local institutions, especially 'Ayuntamiento de Ávila' and 'Institución Gran Duque de Alba' for providing all technical and human assistance as well as for the partial economical support of the research work.

References from Journals:

Allen P. K., Troccoli A., Smith B., 2003. New methods for digital modeling of historic sites. *IEEE Journal*.

Burns, J.B., A.R. Hanson, E.M. Riseman, 1986. Extracting straight lines. *IEEE transactions on pattern analysis and machine intelligence*, Vol. 8 (4).

Canny J.F. 1986. A computational approach to edge detection. *IEEE Journal*.

Grün, A., 1985. Adaptive least squares correlation: a powerful image matching technique. *S. Afr. J. of Photogrammetry, Remote Sensing and Cartography*, 14, 3.

References from Books:

Domingo Preciado Ana, 2000. *Tesis Doctoral*. Universidad de Cantabria.

Elstrom M., 1998. A Stereo-Based Technique for the Registration of Color and LIDAR images, *Master's Thesis*, University of Tennessee, Knoxville.

Hartley R. and Zisserman A., 2000. *Multiple View Geometry in Computer Vision*, Cambridge Univ. Press.

Kraus, K. 1993. *Advanced Methods and Applications*. Vol.2. *Fundamentals and Standard Processes*. Institute for Photogrammetry Vienna University of Technology.

References from Other Literature:

Abdel-Aziz YI y Karara HM, 1971. Direct linear transformation from comparator coordinates into space coordinates in close range photogrammetry. Symposium on close range photogrammetry.

Aguilera D. G., Lahoz J. G., 2006. Terrestrial laser scanner and high-resolution camera registration through single image-based modeling. *Eurographics Book*.

Aguilera D., Claro-I. M. A., Gomez Lahoz J., Finat J., Gonzalo-T. M., 2004. Development of a simulator for reliable and accurate 3D reconstruction from a single view. ISPRS Congress. Istanbul.

Al-Manasir K., Fraser C. S., 2006. Automatic registration of terrestrial laser scanner data via imagery. *ISPRS Archives*. Dresden (Germany).

Alshawabkeh Yahya, Norbert Haala, Dieter Fritsch, 2006. 2D-3D feature extraction and registration of real world scenes. *ISPRS Archives*. Dresden (Germany).

Baarda, W., 1968. A Testing Procedure for use in Geodetic in Networks. *Publications on Geodesy, News Series*, 2(5), Netherlands Geodetic Commission.

Bourke P., 1989. Efficient Triangulation Algorithm Suitable for Terrain Modelling. Pan Pacific Computer Conference, Beijing, China.

Fischler, M. A., and R. C. Bolles, 1981. Random sample consensus. CM Communications.

Förstner, W. and Gülch, E., 1987. A Fast Operator for Detection and Precise Location of Distinct Points, Corners and Centres of Circular Features. ISPRS Workshop, Interlaken.

Ikeuchi, Nakazawa, 2003. Creating virtual buddha statues through observation. IEEE Workshop.

Lensch H.P., W. Heidrich, 2001. A silhouette-based algorithm for texture registration and stitching, *Graphical Models*, vol. 63, n4.

Levoy M., K. Pulli, B. Curless, 2000. The digital Michelangelo project: 3D scanning of large statues. Siggraph, CG Proceedings.

McAllister D. K., L. Nyland, V. Popescu, A. Lastra, and C. McCue, 1999. Real-time rendering of real world environments. In *Rendering Techniques*, EuroGraphics Rendering Workshop.

Rocchini C., P. Cignomi, C. Montani. Multiple textures stitching and blending on 3D objects, 1999. Eurographics, New York.

Stamos I. And P. K. Allen. Automatic registration of 2-D with 3-D imagery in urban environments, 2001. Proceedings ICCV.

ASSESSMENT OF SUB-CANOPY STRUCTURE IN A COMPLEX CONIFEROUS FOREST

N. R. Goodwin^a*, N. C. Coops^a, C. Bater^a, S. E. Gergel^b

^aDepartment of Forest Resource Management, ^bDepartment of Forest Sciences

University of British Columbia, Vancouver, Canada.

nicholas.goodwin@ubc.ca, nicholas.coops@ubc.ca, cbater@interchange.ubc.ca, sarah.gergel@ubc.ca

Key Words: LiDAR, understorey vegetation, vegetation cover.

ABSTRACT:

LiDAR technology emits narrow beams of laser light that are able to exploit gaps in the forest canopy and detect sub-canopy surfaces. In this study, we explore the potential of airborne LiDAR to quantify understorey vegetation cover in a dense and structurally diverse conifer forest on Vancouver Island, British Columbia, Canada. The cover of understorey vegetation, defined below an arbitrary height threshold of 4 m, was recorded in the field both horizontally and vertically at 12 plots for comparison with LiDAR data. Results showed significant relationships between field and LiDAR-based estimates of understorey vegetation cover at both the plot (30 x 30 m area, $r^2 = 0.87$) and sub-plot scale (15 x 15 m areas, $n = 4$ per plot, $r^2 = 0.68$) ($p < 0.05$). In addition, the variability (coefficient of variation) of understorey vegetation cover estimated in the field and with LiDAR data was found to be significantly correlated ($r^2=0.88$, $p < 0.001$). Overall, this work suggests that small-footprint LiDAR is sensitive to large changes in understorey vegetation cover which can benefit key forestry applications at the landscape scale such as examining stand regeneration success.

1. INTRODUCTION

Information about the forest understorey is critical for both ecological and forest management issues. Understorey vegetation provides food and habitat to a wide range of fauna (Fox & Fox 1984), whilst in multi-aged and mixed species stands, developing an understanding of regeneration success is important for ongoing stand management following a disturbance (Kozlowski 2002). Likewise the spatial distribution and structure of understorey vegetation (*e.g.* quantity, height, and cover) is critical to fire behaviour models which are difficult to parameterise over forested landscapes (Keane et al. 2001). For foresters, accurate and timely information on the understorey can also help in the assessment of nutrient retention and cycling (Yarie 1980), stand regeneration (Lormier et al. 1994), and species diversity (Gentry & Dobson 1987).

Conventionally, the approach to collecting information on the understorey has involved a range of field-based techniques. These generally require detailed, spatially dense field measurements (< 1 ha) (McLaughlin 1978; Scheller & Mladenoff 2002) so that the high spatial variability often present in the understorey can be captured and the ecological processes which occur at fine scales can be understood. For example, the distribution and composition of understorey vegetation has been shown to vary at fine spatial scales due to microtopography (*i.e.* pits and mounds), gaps in the overstorey vegetation, disturbances such as harvesting and nutrient availability (Beatty 1984; Bengtson et al. 2006; Miller et al. 2002). As a result, field-based assessments of the understorey are likely to be an expensive, difficult and time consuming task.

Light Detection And Ranging (LiDAR) however, has been recognised as a tool that might be suitable to quantify sub-canopy vegetation structure over large geographical areas. Earlier studies, for example, have shown that LiDAR can characterise fuel bed roughness (Seielstad & Queen 2003), discriminate understorey discrete LiDAR returns from overstorey returns within a mixed conifer and deciduous two-

tiered forest (Riaño et al. 2003), and estimate the Lorey's mean height of suppressed understorey trees in a boreal forest using regression models (Maltamo et al. 2005). Further, Mutlu et al. (2007) used the number of LiDAR hits within 0.5 m vertical bins from 0 to 2 m (2.5 x 2.5 m areas) normalised by the total number of LiDAR hits, to improve the accuracy of a surface wildfire fuel classification, which also involved multispectral passive optical data.

The focus of this work is to determine whether spatial estimates of understorey cover are possible within a conifer forest. To characterise the different types of understorey structure contained within a multi-use conifer forest, a number of sites (12 in total) were examined. The specific objectives were to: (1) assess whether understorey cover can be quantified within 30 x 30 m and 15 x 15 m areas using first return LiDAR data, and (2) determine whether the variability in understorey cover measured in the field was correlated to LiDAR estimates.

2. MATERIALS AND METHODS

2.1. Field site

The study area is Clayoquot Sound on Vancouver Island, British Columbia (49° 0' 35" N, 125° 37' 21" W). The area is classified as a Coastal Western Hemlock (CWH) zone, based on the biogeoclimatic ecosystem classification (BEC) system (Meidinger & Pojar 1996). Although the Vancouver Island Range is adjacent to the study area, the topography is subdued and dominated by Pleistocene glacial deposits with an annual precipitation of 3306 mm and mean daily minimum, average and maximum temperatures of 5.4, 9.1, and 12.8°C, respectively (Environment Canada 2006).

Clayoquot Sound is a multi-use forested area and includes both recently harvested Crown land, as well as mature first and second growth forest in Pacific Rim National Park. Western hemlock (*Tsuga heterophylla*) is the dominant or codominant tree species throughout. Western Redcedar (*Thuja plicata*), Amabilis fir (*Abies amabilis*), Yellow-Cedar

(*Chamaecyparis nootkatensis*), Sitka Spruce (*Picea sitchensis*), Douglas-fir (*Pseudotsuga menziesii* var. *mensiesii*), and Red Alder (*Alnus rubra*) also occur within this forest region. Common understorey species include: Salal (*Gaultheria shallon*), Salmonberry (*Rubus spectabilis*), Thimbleberry (*Rubus parviflorus*), Red Huckleberry (*Vaccinium parvifolium*), Evergreen Huckleberry (*Vaccinium ovatum*), Blueberries (*Vaccinium* spp.), and Devil's club (*Oplopanax horridus*). Several of these understorey species are important economically (for the floral industry), provide food for local communities, and include culturally important medicinal plants (Clayoquot Sound Scientific Panel 1995).

2.2 LiDAR characteristics

Airborne LiDAR data were acquired in July 2005 by Terra Remote Sensing (Sidney, British Columbia, Canada) using a TRSI Mark II discrete return sensor attached to a fixed wing platform. The sensor was configured to record first and last returns with a pulse repetition frequency of 50 kHz, platform altitude of 800 m, maximum off-nadir view angle of 23 degrees, wavelength of 1064 nm, and a fixed beam divergence angle of 0.5 mrad. The average pulse spacing equalled one laser pulse return per 1.5 m². Ground and non-ground returns were classified using TerraScan (Terrasolid, Finland).

2.2. Field estimates of understorey cover

Understorey cover was measured at 12 sites within a series of 2.5 x 2.5 m quadrats (n = 144) which collectively covered an area of 30 x 30 m. At each of the quadrat locations, understorey cover was visually estimated in 4 height intervals: 0.5 to 1, 1 to 2, 2 to 3, and 3 to 4 m above ground surface. A height pole was used as an aid and cover estimates were taken horizontally within 20% intervals.

A single integrated estimate of vertically projected understorey cover (UC) for each 2.5 x 2.5 m quadrat was then calculated using Equation 1. Given that:

$$UC = 1 - e^{-GF_{total}\bar{s}} \quad (1)$$

where: G refers to the G-function, the projection of leaf area into a given view direction (Ross 1981),

\bar{s} is the mean distance light will travel through understorey material (corresponding to the vertical height intervals used to estimate understorey cover), and

F_{total} is the foliage area index for each understorey sample location.

The calculation of vertically projected cover assumes homogenous volume of vegetation material and will depend on the leaf angles. Given the understorey is composed of mixed species and variable leaf angle distributions, a value between the two more extreme leaf angle distributions (planophile and erectophile) (Ross 1981; Ross & Marshak 1989) of 0.5 was used, which corresponds to a random foliage angle distribution. Since the field measured understorey cover is related to the understorey gap probability (P_{gap}) by the equation:

$$P_{gap,i} = 1 - UC_i \quad (2)$$

where: i = to the sub-quadrat cover measurement obtained at individual sample locations using the modified height pole (e.g. $i = 1$ for understorey cover estimated between 0.5 and 1 m above the ground).

We can also express Eq. 1 in terms of foliage area density for each understorey measurement as follows:

$$F_i = -\ln(P_{gap,i}) / G\bar{s} \quad (3)$$

and subsequently, derive the total foliage area index at each quadrat area by:

$$F_{total} = \bar{s} \sum_{i=1}^n F_i \quad (4)$$

Subsequently, understorey cover values were converted into mean estimates at the plot scale (30 x 30 m area) and sub plot scale (15 x 15 m areas) for comparison with LiDAR data.

2.3. Understorey vegetation cover comparison

Using coordinates recorded from a differential Geographic Position System ($dGPS$) (horizontal positional errors were approximately 1 to 5 m), LiDAR first return data were extracted for each plot. Returns > 0.5 and ≤ 4.0 m above ground surface were considered to be from understorey vegetation. Understorey cover was calculated at both the plot scale (30 x 30 m area) and sub plot scale (15 x 15 m areas), as the number of understorey returns divided by the total number of returns recorded ≤ 4.0 m. These values were then compared to field-based estimates. Additionally, the variability of understorey cover recorded at each site was computed in both datasets by computing the coefficient of variation (CoV) of the 4 sub-plot cover values derived at each site (15 x 15 m area, n = 4).

3. RESULTS

Strong positive relationships are shown between field and LiDAR-based estimates of understorey cover ($p < 0.001$) (Figure 1). The estimates of understorey cover however, were shown to be better correlated at the plot scale compared to the sub plot scale, which showed a weaker relationship ($p < 0.05$). Note one plot recorded no hits below 0.5 m and was excluded from analysis.

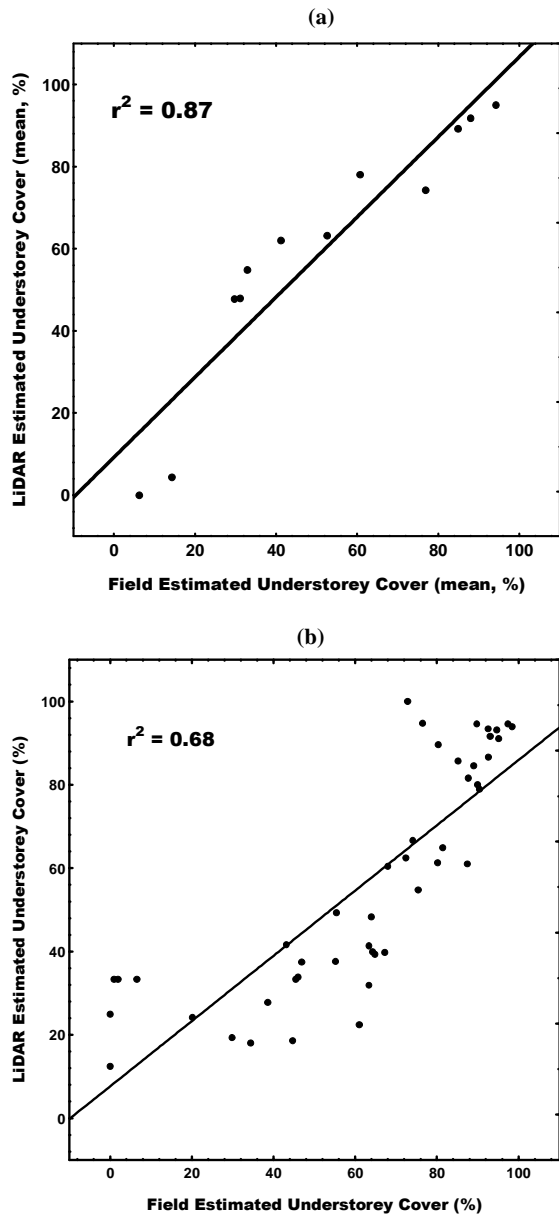


Figure 1. Relationship between field and LiDAR estimates of understorey cover: (a) plot scale (30 x 30 m areas) and (b) sub-plot scale (15 x 15 m areas). *Note:* outliers with an insufficient number of first returns were removed ($n < 3$).

Analysis of the variability in field and LiDAR estimates of understorey cover, within individual plots, was also shown to be positively correlated ($p < 0.001$) (Figure 2). This suggests that LiDAR is sensitive to changes in understorey cover within 15 x 15 m areas.

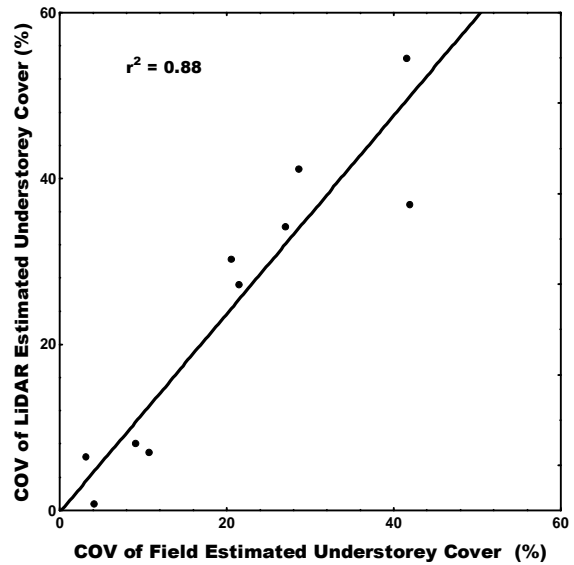


Figure 2. Field and LiDAR estimates of understorey cover variability within plots. *Note:* the CoV for each plot was calculated using four 15 x 15 m estimates of understorey cover per plot. Outliers with an insufficient number of first returns were removed ($n < 3$).

4. DISCUSSION

The results presented in this paper provide an insight into the capacity of airborne LiDAR to estimate both plot level understorey cover as well as cover at smaller spatial scales. Importantly, this work has shown a strong correlation between field and LiDAR estimates of understorey cover at the plot scale, with plots covering a wide range of cover values from 0 to 100% cover. When each plot was then subdivided into 4, the relationship weakened but remained significant. This suggests the relationships at the sub plot level might have been influenced by the number of LiDAR returns and the spatial registration of field and LiDAR data.

A limitation of this approach is that occlusion through the overstorey and understorey vegetation layers will reduce the number of first returns detected from ground and understorey surfaces. As a consequence, in areas with a dense canopy a larger mapping unit will be needed to capture a sufficient number of returns to derive understorey cover. At one of the 12 plots, for example, understorey cover could not be computed within a 30 x 30 m area as no LiDAR first returns were detected below 0.5 m (above ground surface).

Another important result is the relationship between LiDAR and field predicted understorey cover variation. This relationship is surprisingly strong, providing some confidence that regardless of the overall stand condition, the amount of variation in the LiDAR non-ground hits below 4 m is related to understorey cover variation. Additional work is needed however, to fully explore this relationship (*e.g.* sensitivity to scale).

Further, it should be mentioned that the spatial position of the ground plots becomes increasingly important when computing sub plot cover statistics at smaller spatial scales. Since the *d*GPS positional data for this study was recorded under dense forest canopies, which is known to affect the spatial accuracy

(Næsset & Jonmeister 2002), our analysis was restricted to scales that exceeded the horizontal positional errors. The measurement of understorey vegetation characteristics within 5 x 5 m however, may well be the smallest feasible unit to compare with LiDAR observations (assuming similar LiDAR pulse densities of around 1 pulse per m²).

5. CONCLUSION

We encourage more research into LiDAR's ability to map the understorey and believe that LiDAR can provide a suitable tool for mapping large differences in understorey cover (e.g. ~20% intervals), and its spatial pattern, at the landscape scale. Stronger relationships were found at the coarser spatial scale (30 x 30 m), possibly in response to a larger number of understorey hits being available to characterise the understorey.

6. REFERENCES

- Beatty, S.W., 1984. Influence of microtopography and canopy species on spatial patterns of forest understorey plants. *Ecology*, 65(5): 1406-1419.
- Bengtson, P., Ursula, F.G. and Bengtsson, G., 2006. Spatial distributions of plants and gross N transformation rates in a forest soil. *Journal of Ecology*, 94: 754-764.
- Clayoquot Sound Scientific Panel, 1995. Report 5: Sustainable Ecosystem Management in Clayoquot Sound, Halfmoon Bay, British Columbia, Canada.
- Environment Canada, 2006. Canadian Climate Normals 1971-2000. Tofino A., British Columbia. Downloaded from the World Wide Web on 9 September 2006 from http://www.climate.weatheroffice.ec.gc.ca/climate_normals/index_e.html.
- Fox, B.J. and Fox, M.D., 1984. Small-mammal recolonisation of open-forest following sand mining. *Australian Journal of Ecology*, 6: 29-41.
- Gentry, A.H. and Dobson, H.C., 1987. Contribution of non-trees to species richness of tropical rainforest. *Biotropica*, 19: 216-227.
- Keane, R.E., Burgan, R. and van Wagtenonk, J., 2001. Mapping wildland fuels for fire management across multiple scales: integrating remote sensing, GIS, and biophysical modelling. *International Journal of Wildland Fire*, 10: 301-319.
- Kozłowski, T.T., 2002. Physiological ecology of natural regeneration of harvested and disturbed forest stands: implications for forest management. *Forest Ecology and Management*, 158(1-3): 195-221.
- Lormier, C.G., Chapman, J.W. and Lambert, W.D., 1994. Tall understorey vegetation as a factor in the poor development of oak seedlings beneath mature stands. *Journal of Ecology*, 82: 227-237.
- Maltamo, M. Packalén P, Yu X, Eerikäinen K, Hyypä J, and Pitkänen J. 2005. Identifying and quantifying structural characteristics of heterogeneous boreal forests using laser scanner data. *Forest Ecology and Management*, 216(1-3): 41-50.
- McLaughlin, S.P., 1978. Determining the understorey production in southwestern ponderosa pine forests. *Bulletin of the Torrey Botanical Club*, 105(3): 224-229.
- Meidinger, D. and Pojar, J., 1996. *Ecosystems of British Columbia*. BC Special Report Series No. 6., British Columbia Ministry of Forests, Victoria, Canada.
- Miller, T.F., Mladenoff, D.J. and Clayton, M.K., 2002. Old-growth northern hardwood forests: spatial autocorrelation and patterns of understorey vegetation. *Ecological Monographs*, 72(4): 487-503.
- Mutlu, M., Popescu, S. C., Stripling, C., and Spencer, T., 2007. Mapping surface fuel models using lidar and multispectral data fusion for fire behavior. *Remote Sensing of Environment, In Press, Corrected Proof*.
- Næsset, E. and Jonmeister, T., 2002. Assessing point accuracy of dGPS under forest canopy before data acquisition, in the field and after postprocessing. *Scandinavian Journal of Forest Research*, 17: 351-358.
- Riño, D., Meier, E., Allgower, B., Chuvieco, E. and Ustin, S.L., 2003. Modelling airborne laser scanner data for the spatial generation of critical forest parameters in fire behaviour modelling. *Remote Sensing of the Environment*, 86: 117-186.
- Ross, J.K., 1981. *The radiation regime and architecture of plant stands*. Dr W. Junk Publishers, The Hague, Boston, London, 391 pp.
- Ross, J.K. and Marshak, A.L., 1989. The influence of leaf orientation and the specular component of leaf reflectance on the canopy bidirectional reflectance. *Remote Sensing of Environment*, 27: 251-260.
- Scheller, R.M. and Mladenoff, D.J., 2002. Understorey species patterns and diversity in old-growth and managed northern hardwood forests. *Ecological Applications*, 15(5): 1329-1343.
- Seielstad, C.A. and Queen, L.P., 2003. Using airborne laser altimetry to determine fuel models for estimating fire behaviour. *Journal of Forestry*, 101(4): 10-17.
- Yarie, J., 1980. The role of understorey vegetation in the nutrient cycle of forested ecosystems in the mountain hemlock biogeoclimatic zone. *Ecology*, 61(6): 1498-1514.

7. ACKNOWLEDGEMENTS

We thank Denis Collins, Andy McKinnon (BC Ministry of Forests and Range) and Warren Warttig (Interfor) for project support and encouragement. We thank Parks Canada and Interfor for providing access and Clayoquot Biosphere Trust for access to their field office. Yulia Stange, Kate Kirby, Andy Ackland, Yanny Barney, Selina Agbayani, Sam Coggins, Jessica Currie, and Jaime Pascoe provided significant help in the field program which accompanies this research. Components of the research were funded by BC Ministry of Forests and Range, British Columbia Forest Science Program (FSP), Interfor, UBC, and NSERC Discovery grants to Nicholas Coops and Sarah Gergel.

PLANAR FEATURE EXTRACTION IN TERRESTRIAL LASER SCANS USING GRADIENT BASED RANGE IMAGE SEGMENTATION

Ben Gorte

Department of Earth Observation and Space Systems (DEOS)
Delft University of Technology, Kluyverweg 1, 2629 HS Delft, The Netherlands
b.g.h.gorte@tudelft.nl

Commission WG V/3

KEY WORDS: Terrestrial Laser Scanning, Range Images, Segmentation.

ABSTRACT:

The paper presents a new segmentation algorithm, to be applied to terrestrial laser scans of urban environments. The algorithm works directly in a range image. This is the fundamental laser scan data structure as a laser recording can be regarded as a 2-dimensional grid of range measurements. The horizontal and vertical axes of the grid denote the horizontal and vertical angles at which the scanner emits the laser beam, receives the reflections, and measures the distance (the range) between the instrument and the reflecting surface at those angles.

The presented algorithm estimates for each measurement (pixel) in the range image three parameters of the 3D plane that contains the pixel: two angles (horizontal and vertical) and the distance between the plane and the origin. The estimates are based on the scan angles (the horizontal and vertical angles at which the laser beam was emitted from the scanner) and the image gradients, i.e. the rate of change in the distance that is observed between adjacent measurements. Since the three estimated parameters characterize a plane in 3D space, regions of adjacent pixels with similar parameter values are likely to be part of the same plane. Such pixels are grouped into segments by a region-growing image segmentation step, which takes the three parameters into account simultaneously.

The overall algorithm uses two complementary strategies to deal with the measurement noise affecting the gradients, during the gradient calculation and the region growing steps respectively.

1. INTRODUCTION

Range image segmentation has a long tradition in the computer vision research community. For example, Hoover *et al.* (1996) already set up a framework for experimental comparison of range image segmentation algorithm results, followed up by Xiang *et al.* (2000). At the time, range images were produced by photogrammetric interpretation of stereo imagery, by structured light techniques, or by early laser equipment, such as the Perceptron laser ranger. Commonly, those data were recorded in well-controlled conditions. Nevertheless, they tended to be noisy and have low point densities. They described relatively simple close-range scenes, to be used in industrial applications and in robot vision experiments.

Recent advancements in terrestrial laser scanning cause a renewed interest in segmentation of range data. Terrestrial laser scanners are being used in a multitude of applications, for example in 3D model reconstruction of complex outdoor scenes in urban environments. Nowadays scanners are able to record datasets with millions of points, and with recording speeds of several hundreds of thousands of points per second. The distance range has been increased to approx. 100 m for

phase scanners, and to several kilometres for time-of-flight scanners, with spatial accuracies in the cm-range (Staiger, 2007). These changes pose new requirements to segmentation algorithms.

The common perception of terrestrial laser scanning is that it results in a 3-dimensional point cloud, *i.e.* a collection of (x,y,z) coordinates, corresponding to locations in the scene where the laser beam was reflected by a surface. Additionally, most laser scanners record the intensity of the reflected beam as it is recorded by the instrument. Some types of laser equipment record a colour image of the scene, more or less at the same time and from approximately the same position as the laser scan. This image can be used to “colour” the point cloud, *i.e.* to assign (R,G,B) values to the (x,y,z) points of the laser scan. Many authors have reported on point cloud segmentation algorithms, amongst whom Rabbani (2006), who starts off with a Hough transform using (θ,ϕ,ρ) parameterization (see section 2). He also gives an overview of previous methods, stating that these either resample the data in a 2D or 3D grid, or build a topology on the point cloud using triangulation.

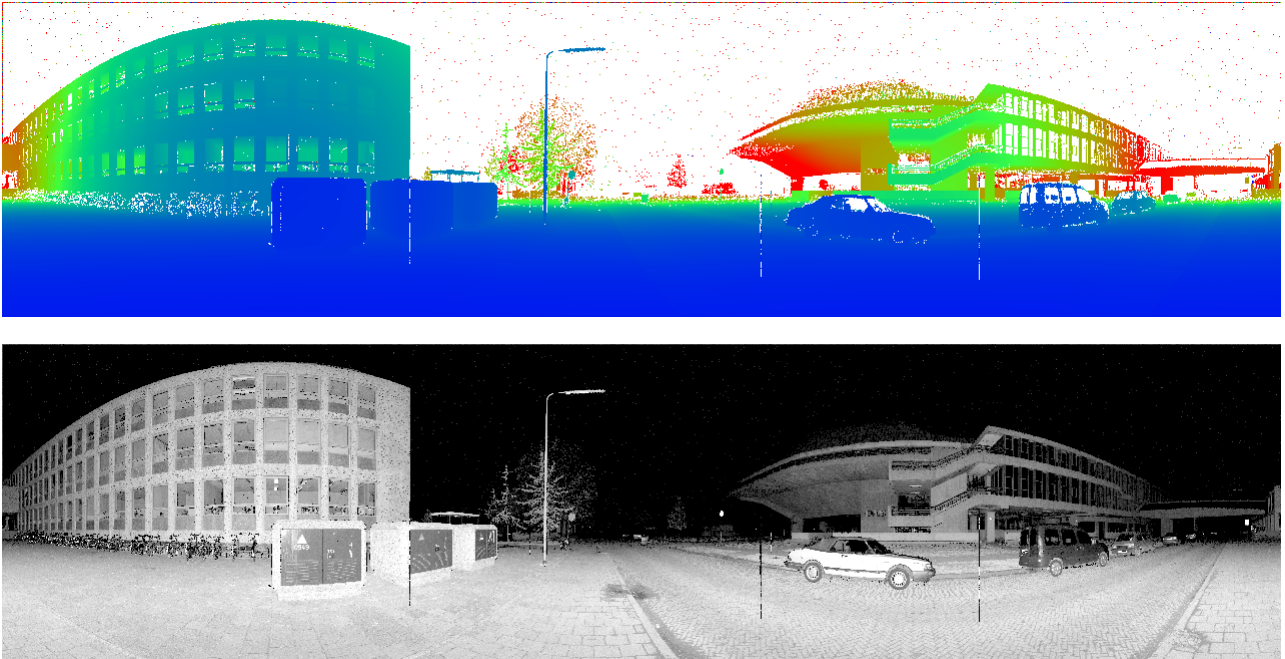


Figure 1. Upper: range image, lower: intensity image. The data were recorded by a FARO 880 phase scanner. Image size is approx. 8100 x 2200 pixels, covering 360° horizontally and 100° vertically. This corresponds to 1/5th of the scanner's maximum resolution.

As an alternative to the 3D point-cloud notion, and better in accordance with scanner operation, a laser recording can be regarded as a 2-dimensional grid of range measurements. The horizontal and vertical axes of the grid denote the horizontal and vertical angles (let these be called α and β respectively) at which the scanner emits the laser beam, receives the reflections, and measures the distance (the range) R between the instrument and the reflecting surface at those angles. The angles α and β are sampled at regular intervals $\Delta\alpha$ and $\Delta\beta$ (the angular resolutions). Therefore, laser scanning results in a 2D (often termed "2.5D") range image $R [i_\alpha i_\beta]$, with $\alpha=i_\alpha\Delta\alpha$ and $\beta=i_\beta\Delta\beta$. (Figure 1).

Figure 1 also shows the intensity image, which is recorded simultaneously with the range image. (The remainder of this paper only concerns range measurements and does not consider intensity or (R,G,B) -information.)

Pulli (1993) already described range image segmentation with some similarity to the method presented here, working with normal vectors and 3-feature image segmentation.

2. PLANES IN RANGE IMAGES

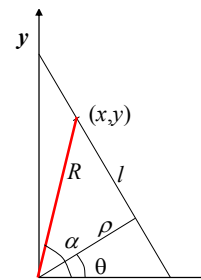


Figure 2. A line in 2D containing point (x,y) , and its normal vector

We will first establish a relation between the equation of a plane in 3D Cartesian coordinates, and the representation of that plane in a range image with 2d spherical image coordinates. The situation resembles the equation of a line l in 2D passing through a point (x, y) , as it is often used in Hough transforms:

$$\rho = x \cos \theta + y \sin \theta, \quad (1)$$

where θ is the direction of the normal vector of the line and ρ is the distance between the line and the origin. With varying θ (and therefore ρ) this yields all lines passing through a given point (x, y) (Figure 2). The point (x,y) may have been measured by a laser scanner at scanning angle α and range (distance from the scanner) R .

In analogy, Figure 3 shows that a parametric form of a plane in 3D, containing a point (x,y,z) is given by

$$\rho = x \cos \theta \cos \phi + y \sin \theta \cos \phi + z \sin \phi. \quad (2)$$

We will use this equation to establish the distance ρ between a plane and the origin of the Cartesian coordinate system, after having estimated the two angles θ and ϕ , denoting the orientation of the plane from the range image gradients. This will be done for every pixel in the range image. The resulting three “image features” will then be submitted to a three-band image segmentation algorithm.

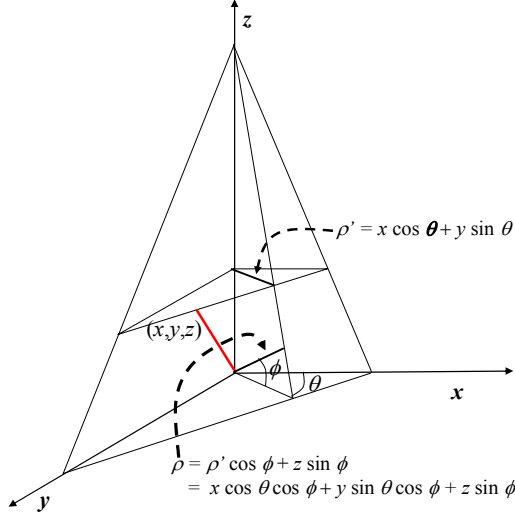


Figure 3. A plane in 3D containing point (x,y,z) and the normal vector to the plane.

Assuming that a certain pixel belongs to a plane P we want to compute the orientation angles θ and ϕ of the normal vector of P , θ being the angle between the x -axis and the projection of the normal vector in the xy -plane, and ϕ being the angle between the normal vector and the xy -plane. We will do this by computing the difference angles $\Delta\theta$ and $\Delta\phi$ between the normal vector and the scan angle, which is given by the coordinates α and β of the range image. This is illustrated in Figure 6, which shows the following relationship between scan angle and normal vector orientation:

$$\begin{aligned} \theta &= \alpha - \Delta\theta \\ \phi &= \beta - \Delta\phi. \end{aligned} \quad (3)$$

3. RANGE IMAGE GRADIENTS

The computation of the difference angles $\Delta\theta$ and $\Delta\phi$ between the normal vector of a plane and the scan angle is based on the gradients of the range image. The horizontal gradient is the change in the image (range) value that is observed when going one pixel to the right; the vertical gradient is the observed change when going one pixel up. Since the image coordinates are related to the scan angles α and β , the gradients can be considered estimates of the partial differences of the range with respect to the horizontal and vertical components of the scan angle, $\Delta R/\Delta\alpha$ and $\Delta R/\Delta\beta$, respectively, with $\Delta\alpha$ and $\Delta\beta$ denoting the angular resolution of the scanner in the horizontal and vertical directions.

To obtain the corresponding spatial resolution (the perpendicular distance between to neighbouring points), the

angular resolution has to be multiplied by the range R [i_{α}, i_{β}] itself. Finally, the arctangents of $\Delta R/(R \times \Delta\alpha)$ and $\Delta R/(R \times \Delta\beta)$ yield the required difference angles. The procedure is illustrated for the vertical angle ϕ in Figure 4.

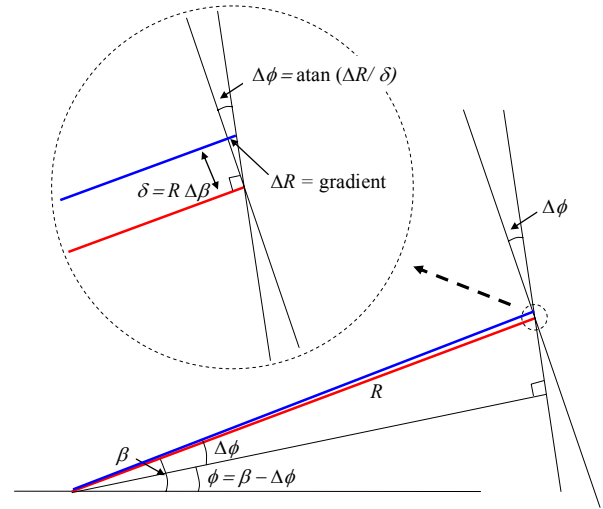


Figure 4. Computing difference angles from range image gradients

Unfortunately, laser scanner measurements are not entirely accurate. In a range image $R[\alpha, \beta]$, both the range measurement R , as well as the scan angles α and β , contain noise, which may severely affect the range image gradients and propagate into the derived estimates of difference angles and plane orientations.

Gradients are computed using convolution filtering with so-called gradient kernels. Examples are Sobel filters (Mather 1999). The noise problem is addressed firstly by using larger filtering kernels, having a smoothing effect, for the gradient computations. In the current example (see Figure 1) we used 5×5 kernels,

-1	-2	0	2	1
-2	-3	0	3	2
-3	-4	0	4	3
-2	-2	0	3	2
-1	-1	0	2	1

and

1	2	3	2	1
2	3	4	3	2
0	0	0	0	0
-2	-3	-4	-3	-2
-1	-2	-3	-2	-1

for horizontal and vertical gradients respectively.

A second countermeasure against laser measurement noise is applied during the segmentation step; see Section 4.

The last step in the feature extraction phase is the determination of the third parameter ρ , the distance between the plane containing the pixel at image coordinate [i_{α}, i_{β}] and the origin, using the plane equation

$$\rho = x \cos \theta \cos \phi + y \sin \theta \cos \phi + z \sin \phi \quad (4)$$

This equation contains for each range image pixel the 3D coordinate (x,y,z) of the point where the laser beam was reflected. It can be computed from the range image as:

$$\begin{aligned} x &= R[i_\alpha i_\beta] \cos(i_\alpha \Delta\alpha) \cos(i_\beta \Delta\beta) \\ y &= R[i_\alpha i_\beta] \sin(i_\alpha \Delta\alpha) \cos(i_\beta \Delta\beta) \\ z &= \sin(i_\beta \Delta\beta) . \end{aligned} \quad (5)$$

It is very important to note that a large plane, such as the façade of the building at the left in Figure 1, contains a large variety in range measurements, as the different colors indicate. However, after the above-described transformations, even such large plane should become rather homogeneous in the plane parameters θ , ϕ and ρ . This can be seen in Figure 6, which displays colour coded images of these three parameters.

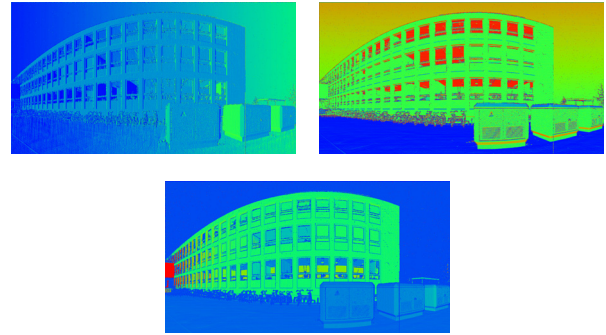


Figure 5. Images of plane parameters θ , ϕ and ρ .

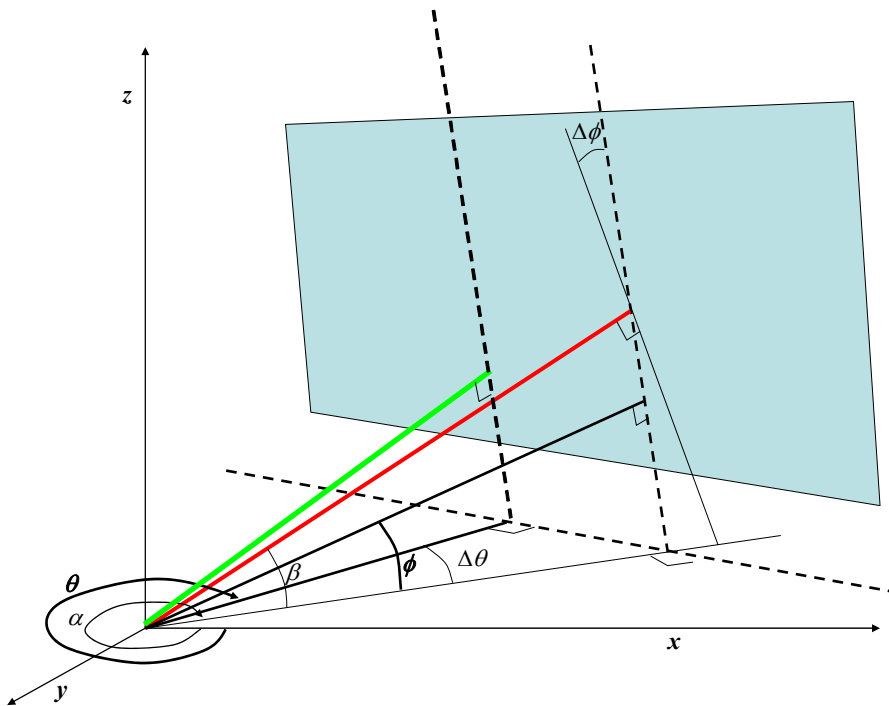


Figure 6. Relationship between scan angle and normal vector orientation

4. IMAGE SEGMENTATION

The purpose of image segmentation is to subdivide an image into adjacent groups of pixels, called segments, which (hopefully) coincide with meaningful objects in the scene. Image segmentation algorithms can be roughly subdivided into region based methods, where pixels within each segment obey some homogeneity criterion, and edge based methods, looking explicitly for boundaries between segments. Within the region based methods popular approaches are region growing (starting from seed pixels, pixels are added to regions as long as homogeneity is sufficiently maintained) and region merging (of adjacent regions that are similar enough).

The image segmentation algorithm used in this study is a region merging method (Gorte, 1999). It was designed for multi-spectral image segmentation, taking three image bands into

account simultaneously. It is a quadtree-based method that works bottom-up: merging pixels (quadtree leaves) into segments, and adjacent segments into larger segments while maintaining for each segment a mean feature vector, and as long as two criteria are satisfied:

- a) the Euclidian distance between feature vectors of adjacent segments should not exceed a threshold
- b) the elements of the variance-covariance matrix within a segment *after* merging should not exceed a threshold.

It has been previously shown that as the second threshold value the squared of the first one can be used, so only one value has to be specified. However, to prevent 'order dependency', the algorithm performs best when applied iteratively with a number of threshold values in a steadily increasing sequence (each iteration being recursive as previously stated). Therefore, the algorithm needs, in addition to the final threshold value, the number of iterations to be performed (usually 3 or 4).

Instead of using three bands of a multi-spectral image, we will now submit the three plane parameters images of Figure 5 to the segmentation algorithm. It will create segments of adjacent pixels that have similar values for θ , ϕ and ρ , and therefore are likely to belong to the same plane in the scene – the word ‘similar’ indicating that the values may still be contaminated by noise. The amount of noise expected within a single plane determines the threshold value.

Figure 7 shows the result of segmentation. Segments are displayed in arbitrary colours, just to distinguish them from each other. It should be noted, however, that each segment has its “mean feature vector”, containing average values for the plane parameters θ , ϕ and ρ . Also the size of each segments (the number of pixels) is known, and the pixels within very small segments can be considered not part of any plane, and can easily be removed from the result in a post-processing step, or assigned to a larger neighbour if required (Figure 8).

5. CONCLUSION AND OUTLOOK

The paper presents a new segmentation algorithm that subdivides a range image created by terrestrial laser scanning into segments that correspond to planar surfaces. Because it works in the 2.5D image domain, rather than in the 3D point cloud domain, the algorithm is quite straightforward and can be implemented very efficiently in a suitable image processing environment: it only requires standard processing steps: convolution, image calculation and multi-spectral segmentation.

Working in the original range image data, as delivered by the scanner, the algorithm cannot be applied to point clouds that are created by co-registering multiple scans. A future research topic may be, however, the usefulness of the segmentation method for extracting segments to be used in a feature (or object) based registration process.

A major obstacle in any segmentation effort is posed by measurement noise. It is clear that the effect of noise can be much better quantified, for example by regarding the specifications of the manufacturer (distinguishing between noise in angle and range measurements) and by taking the dependence of noise on the range into account.

REFERENCES

- A. Hoover et al., An experimental comparison of range image segmentation algorithms, *IEEE Transaction on Pattern Analysis and Machine Intelligence*, 18(7), 673-689, 1996
- X. Jiang, K. Bowyer, Y. Morioka, S. Hiura, K. Sato, S. Inokuchi, M. Bock, C. Guerra, R. E. Loke, J. M. H. du Buf. Some Further Results of Experimental Comparison of Range Image Segmentation Algorithms, *15th Int. Conference on Pattern Recognition*, Spain, Sept. 2000.
- Kari Pulli and Matti Pietikainen, Range Image Segmentation Based on Decomposition of Surface Normals, *Scandinavian Conference on Image Analysis (SCIA)*, Norway, 1993.
- R. Staiger, Selection criteria for terrestrial laser scanners, *FIG working week*, Hong Kong, May 2007.
- Paul M. Mather, *Computer processing of remotely sensed images: an introduction*, second edition, Chichester, NY, Wiley, 1999.
- Tahir Rabbani Shah, *Automatic reconstruction of industrial installations using point clouds and images*, PhD thesis, Delft, 2006.
- Ben Gorte, *Probabilistic segmentation of remotely sensed images*, PhD Thesis, ITC publication number 63, Enschede, 1999.

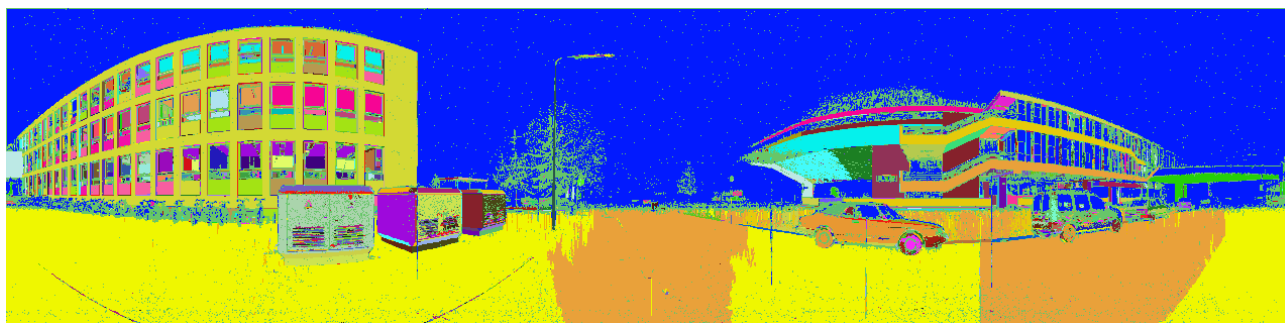


Figure 7. Segmentation result. Oversegmentation in the horizontal plane occurs because the angle θ is not well-defined

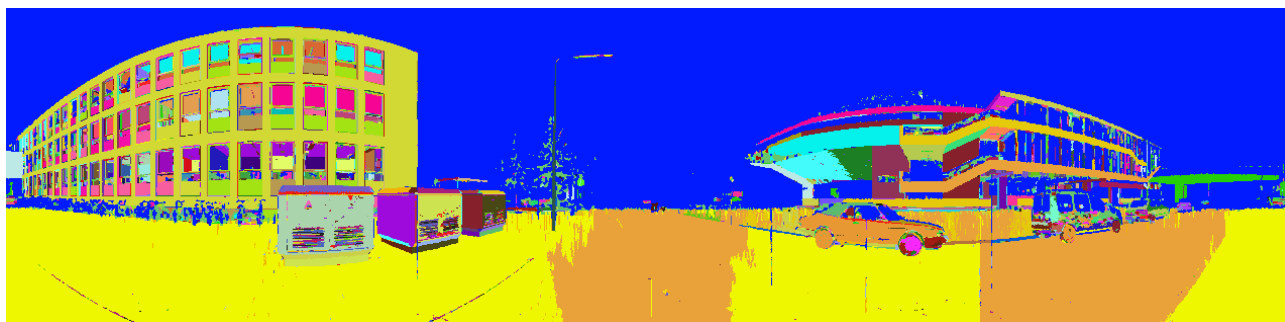


Figure 8. Segmentation result after post-processing to remove small segments

REGISTRATION OF AGIA SANMARINA LIDAR DATA USING SURFACE ELEMENTS

Wolfgang von Hansen

FGAN-FOM, Gutleuthausstr. 1, 76275 Ettlingen, Germany
wvhansen@fom.fgan.de

Commission V/3

KEY WORDS: Terrestrial, LIDAR, Building, Point Cloud, Registration, Algorithms, Automation, Performance

ABSTRACT:

Several approaches for automatic registration of terrestrial LIDAR data exist. However, they normally can not be compared to each other because of a lack of reference data. This is especially true for applications in urban areas. One dataset available for this purpose is a set of eight LIDAR scans from Agia Sanmarina, a Byzantine church in Greece, which has been made available by the ISPRS working group V/3 on terrestrial laser scanning.

We have tested our plane based approach for automatic registration on this particular dataset: The point clouds are first split into a regular raster, then for each raster cell, the dominant plane is robustly estimated and denoted as surface element. Coarse registration is carried out via grouping the surface elements to large planes and a generate-and-test strategy to find transformation parameters that maximize the inlier count. Pairwise fine registration is accomplished using a variant of the ICP (*iterative closest point*) algorithm that is based on matching surface elements instead of 3D points. In addition to this, the theoretical framework for a simultaneous fine registration of multiple datasets is presented in this paper.

1 INTRODUCTION

The registration of terrestrial LIDAR data is a topic that is currently under discussion within the laser scanning community. Several approaches based on different assumptions have been proposed recently, but there is not yet an overall conclusion which method could be regarded as the best one. Recently published work includes, but is not limited to, (Akca, 2003, Dold and Brenner, 2006, Ripperda and Brenner, 2005, Rabbani and van den Heuvel, 2005, Wendt, 2004) and other publications cited later.

In general, registration of point clouds from LIDAR systems can be divided in two steps. The first step is the coarse registration where no information about the particular setup of the scan positions is known. The task here is to determine a set of initial transformation parameters that bring (typically) two datasets into a common geometric reference frame.

Then the fine registration follows as the second step. Here, it can already be assumed that the datasets are aligned sufficiently, i.e. within the convergence radius of the method. Fine registration refines the initial transformation parameters into an optimal parameter set, usually by minimizing the squared sum of the residuals of some error term.

Although a number of approaches exist for registration, this is not true for datasets as each group works on their own data. This is probably caused by a lack of suitable standard datasets. For the specific case of LIDAR data from urban areas, there is currently only a single dataset available from ISPRS Commission V. Despite the publications from the originating group (Bae, 2006), there have not yet been other known attempts to process the data.

In this paper, we will apply the plane based registration strategy from (von Hansen, 2006) to the Agia Sanmarina LIDAR dataset in order to determine its suitability. This method only contains the coarse registration step. We have already extended the approach by a fine registration based on the surface elements (von Hansen, 2007b) for the case of two datasets. Since the Agia Sanmarina data consists of eight datasets in a ring shaped topology, pairwise fine registration inevitably leads to contradictions. Therefore, we have extended the pairwise fine registration to a bundle adjustment style registration for multiple datasets.

This paper is organized as follows: The generation of surface elements, the coarse registration method and the pairwise fine registration will be briefly summarized in section 2. In section 3, the bundle adjustment based on surface elements will be formulated. Section 4 will shortly introduce the Agia Sanmarina dataset and show the results obtained on it. The paper will conclude with some remarks regarding both the dataset and the tested methods.

2 PREVIOUS WORK

This section will briefly summarize the work this paper is based on. The original idea for the replacement of the point cloud by surface elements and the coarse registration based thereupon has been taken from (von Hansen, 2006). The pairwise fine registration is taken from (von Hansen, 2007b).

2.1 Surface elements

The raw data acquired by a LIDAR system is a huge set of (sometimes millions of) 3D points. The disadvantage of this representation is that the points are not related to each other. Sometimes, the neighborhood of points is known from the scan geometry so that region growing can be used to extract object surfaces from the data (Dold and Brenner, 2004). In the generic case, the neighborhood information is not available so that the data must be processed as true point data.

One possibility to bring structure into the data are surface elements, i.e. local plane patches that approximate the object surfaces. They are generated by a two step process. First, the point cloud is divided into a regular 3D raster of a given raster size. The raster size should be chosen such that an object surface is spread among several of the 3D cells, leading to an over-segmentation of the scene. In the second step, a single plane is robustly estimated from all points of a raster cell via a RANSAC scheme. This plane called the *surface element* and shall be a replacement for all the points in the cell. This way, the millions of raw 3D points are replaced by – depending on the raster size – a few hundred or thousand small planes.

2.2 Coarse registration

For the coarse registration, the surface elements are first grouped to larger planes based on neighborhood in the 3D raster and coplanarity. This way, each planar object surface is represented by one plane.

If plane based coarse registration would be tackled in a conventional way, the algorithms would be extremely slow due to a combinatorial explosion as three matching planes must be found in order to compute all six parameters of a rigid transform without scale (Dold and Brenner, 2004). The barycenter of a pair of matching planes can be used to compute the translation so that only two matches are required for the unknown rotation (He et al., 2005). (von Hansen, 2006) goes even further by assuming parallel zenith directions of two scan positions, thereby allowing to recover the transformation parameters from a single pair of matching planes only. A pre-rotation carried out separately for each dataset as shown in (von Hansen, 2007a) makes this approach suitable for generic sensor setups that include arbitrary rotations.

In this particular case, a complete search can be used to find the correct parameters: For each possible match, the transformation parameters are computed and a high number of inliers, planes matching for a given transformation, determines the correct transformation. This technique is fast for a small number of planes – up to a few hundred on modern hardware – but it should be noted that more elaborate search techniques have been proposed as well (He et al., 2005, Liu and Hirzinger, 2005).

2.3 Pairwise fine registration

The fine registration based on surface elements uses a variant of the well known ICP (*iterative closest point*) algorithm (Besl and McKay, 1992). This consists of two alternating steps that are repeated until convergence.

The first step transforms the data using initial transformation parameters – those returned by the coarse registration for the first run and the updated parameters for all consecutive runs. Then, matching pairs of surface elements are found on a nearest neighbor basis.

In the second step, the transformation parameters are updated by a least squares adjustment minimizing the residuals between the matching surface elements. For the mathematical model for the pairwise registration one dataset is kept fixed while the other is transformed. The bundle adjustment presented in section 3 extends this approach to a more general formulation.

Convergence can be determined by observing the pair matches. If they remain unchanged, then a stable solution has been found. However, sometimes the iteration procedure is cycling through a number of solutions because each set of matches leads to a slightly different parameter set that in turn leads to a set of slightly different matches. In this case, some attenuation must be introduced. This had to be done by changing the matching of surface elements in the first step. Instead of starting from scratch for each iteration, only those matches whose distance is above a certain threshold are reassigned to new partners.

3 BUNDLE ADJUSTMENT

Introduction This is an extension of the pairwise fine registration method shown in (von Hansen, 2007b). Opposed to the previous formulation where one dataset was kept fixed, the method



Figure 1. Agia Sanmarina and the Cyrax laser scanner. (By courtesy of ISPRS WG V/3)

as presented here can deal with multiple datasets in a free network. On the other hand, no ICP iterations are used, but a fixed set of input matches taken from the output of the pairwise registration.

This method will be called *bundle adjustment* here in reference to the idea of photogrammetric bundle adjustment even though LIDAR point clouds do not represent bundles in the strict sense.

Input data As input, the bundle adjustment relies on the output of a pairwise registration, requiring both the initial transformation parameters and the list of matching surface elements.

The first step is to determine initial transformation parameters for all datasets in a common reference frame. One dataset is used as starting point and, based on known relative registrations between datasets, all other datasets are subsequently added. Each of the n datasets is now given as a tuple

$$S_i = (\mathbf{R}_i, \mathbf{t}_i, \mathcal{P}_i), \quad i = 1 \dots n \quad (1)$$

where \mathbf{R}_i is the rotation matrix, \mathbf{t}_i the translation vector and \mathcal{P}_i the set of surface elements. A surface element

$$\mathbf{p} \in \mathcal{P} = (\mathbf{n}, \mathbf{x}) \quad (2)$$

is given by normal vector \mathbf{n} and barycenter \mathbf{x} that uniquely define a plane using the Hesse normal form

$$\mathbf{n}^\top \mathbf{x} - d = 0 \quad (3)$$

In addition there exists a set of matching surface elements

$$\mathcal{M} = \{(\mathbf{p}_i, \mathbf{p}_j), \mathbf{p}_i \in \mathcal{P}_i, \mathbf{p}_j \in \mathcal{P}_j\} \quad (4)$$

Vector notation for differential rotations For simplification, the datasets are transformed via the initial transformation parameters prior to the least squares adjustment. We will assume in the remainder, that these pre-transformations have been carried out implicitly. Therefore, one can assume the identity matrix as initial rotation ($\mathbf{R}_0 = \mathbf{I}$) and the null vector as initial translation ($\mathbf{t}_0 = \mathbf{0}$). The matrix for the differential rotation around angles α , β and γ is defined as

$$\mathbf{R} = \begin{pmatrix} 1 & -\gamma & \beta \\ \gamma & 1 & -\alpha \\ -\beta & \alpha & 1 \end{pmatrix}, \quad |\alpha|, |\beta|, |\gamma| \ll 1 \quad (5)$$

One can easily verify that

$$\mathbf{R}\mathbf{x} = \mathbf{r} \times \mathbf{x} + \mathbf{x}, \quad \mathbf{r} := (\alpha, \beta, \gamma)^\top \quad (6)$$

holds. This provides an easier way to write rotations for small angles using only vectors. Also, similar to \mathbf{t} , the initial rotation \mathbf{r} is a null vector ($\mathbf{r}_0 = \mathbf{0}$).

Matching constraints In the remainder, indices 1 and 2 will be used to denote two input datasets. Each match $\mathbf{m}_i \in \mathcal{M}$ of two surface elements will lead to three constraints. As all datasets are treated similarly, this easily extends to any number of input datasets. Each surface element (\mathbf{n}, \mathbf{x}) is transformed via the (unknown) parameters \mathbf{r}, \mathbf{t} to its ideal position $(\mathbf{n}', \mathbf{x}')$:

$$\mathbf{n}' := \mathbf{r} \times \mathbf{n} + \mathbf{n}, \quad \mathbf{x}' := \mathbf{r} \times \mathbf{x} + \mathbf{x} + \mathbf{t} \quad (7)$$

For an ideal solution a pair of transformed surface elements must be coplanar

$$\mathbf{n}_1'^\top \mathbf{n}_2' - 1 = 0 \quad (8)$$

$$\mathbf{n}_1'^\top \mathbf{x}_2' = d_1' = \mathbf{n}_1'^\top \mathbf{x}_1' \Leftrightarrow \mathbf{n}_1'^\top (\mathbf{x}_2' - \mathbf{x}_1') = 0 \quad (9)$$

$$\mathbf{n}_2'^\top \mathbf{x}_1' = d_2' = \mathbf{n}_2'^\top \mathbf{x}_2' \Leftrightarrow \mathbf{n}_2'^\top (\mathbf{x}_2' - \mathbf{x}_1') = 0 \quad (10)$$

i. e. the normal vectors are parallel (Eq. 8) and each barycenter lies on the corresponding plane (Eqs. 9/10). Using Eq. 7, Eqs. 8 to 10 transform to the conditions

$$C_1 = \mathbf{r}_1^\top \mathbf{r}_2 \cdot \mathbf{n}_1^\top \mathbf{n}_2 - \mathbf{r}_1^\top \mathbf{n}_2 \cdot \mathbf{n}_1^\top \mathbf{r}_2 + [\mathbf{r}_1, \mathbf{n}_1, \mathbf{n}_2] + [\mathbf{r}_2, \mathbf{n}_2, \mathbf{n}_1] + \mathbf{n}_1^\top \mathbf{n}_2 - 1 = 0 \quad (11)$$

$$C_2 = \mathbf{r}_1^\top \mathbf{r}_2 \cdot \mathbf{n}_1^\top \mathbf{x}_2 - \mathbf{r}_1^\top \mathbf{x}_2 \cdot \mathbf{n}_1^\top \mathbf{r}_2 + [\mathbf{r}_1, \mathbf{n}_1, \mathbf{x}_2] + [\mathbf{r}_1, \mathbf{n}_1, \mathbf{t}_2] - \mathbf{r}_1^\top \mathbf{r}_1 \cdot \mathbf{n}_1^\top \mathbf{x}_1 + \mathbf{r}_1^\top \mathbf{x}_1 \cdot \mathbf{n}_1^\top \mathbf{r}_1 + [\mathbf{r}_1, \mathbf{t}_1, \mathbf{n}_1] + [\mathbf{r}_2, \mathbf{x}_2, \mathbf{n}_1] + \mathbf{n}_1^\top \mathbf{x}_2 + \mathbf{n}_1^\top \mathbf{t}_2 - \mathbf{n}_1^\top \mathbf{x}_1 - \mathbf{n}_1^\top \mathbf{t}_1 = 0 \quad (12)$$

$$C_3 = \mathbf{r}_2^\top \mathbf{r}_2 \cdot \mathbf{n}_2^\top \mathbf{x}_2 - \mathbf{r}_2^\top \mathbf{x}_2 \cdot \mathbf{n}_2^\top \mathbf{r}_2 + [\mathbf{r}_2, \mathbf{n}_2, \mathbf{t}_2] - \mathbf{r}_2^\top \mathbf{r}_1 \cdot \mathbf{n}_2^\top \mathbf{x}_1 + \mathbf{r}_2^\top \mathbf{x}_1 \cdot \mathbf{n}_2^\top \mathbf{r}_1 + [\mathbf{r}_2, \mathbf{x}_1, \mathbf{n}_2] + [\mathbf{r}_2, \mathbf{t}_1, \mathbf{n}_2] + \mathbf{n}_2^\top \mathbf{x}_2 + \mathbf{n}_2^\top \mathbf{t}_2 + [\mathbf{r}_1, \mathbf{n}_2, \mathbf{x}_1] - \mathbf{n}_2^\top \mathbf{x}_1 - \mathbf{n}_2^\top \mathbf{t}_1 = 0 \quad (13)$$

where $[\mathbf{a}, \mathbf{b}, \mathbf{c}]$ denotes the triple product $(\mathbf{a} \times \mathbf{b})^\top \mathbf{c}$. Note that most terms cancel out because $\mathbf{r}_i = \mathbf{t}_i = \mathbf{0}$. This longer form of the constraints is only needed for proper linearization of the least squares adjustment.

Constraints and derivatives Eqs. 11 to 13 are an implicit representation of the conditions and can be used for least squares adjustment using the Gauss-Helmert model (McGlone et al., 2004). For this model, we require the equations of the constraints and the derivatives with respect to parameters and measurements. The constraints are directly available by removing all terms containing \mathbf{r}_i or \mathbf{t}_i because they have the null vector as initial values:

$$C_1 = \mathbf{n}_2^\top \mathbf{n}_1 - 1 = 0 \quad (14)$$

$$C_2 = \mathbf{n}_1^\top (\mathbf{x}_2 - \mathbf{x}_1) = 0 \quad (15)$$

$$C_3 = \mathbf{n}_2^\top (\mathbf{x}_2 - \mathbf{x}_1) = 0 \quad (16)$$

Note that the constraints are similar to Eqs. 8–10, which is obvious as the initial values assume that both datasets already are at their optimal position. The derivatives are

$$\begin{aligned} dC_1 &= (\mathbf{n}_1 \times \mathbf{n}_2)^\top d\mathbf{r}_1 + (\mathbf{n}_2 \times \mathbf{n}_1)^\top d\mathbf{r}_2 \\ &\quad + \mathbf{n}_2^\top d\mathbf{n}_1 + \mathbf{n}_1^\top d\mathbf{n}_2 \\ dC_2 &= (\mathbf{n}_1 \times \mathbf{x}_2)^\top d\mathbf{r}_1 - \mathbf{n}_1^\top d\mathbf{t}_1 \end{aligned} \quad (17)$$

Position	#elements	#planes
East	1250	50
Northeast	1917	79
North	1361	56
Northwest	4161	112
West	2339	75
Southwest	2547	82
South	1529	63
Southeast	2729	72

Table 1. Number of surface elements and large planes for each dataset.

$$\begin{aligned} &+ (\mathbf{x}_2 \times \mathbf{n}_1)^\top d\mathbf{r}_2 + \mathbf{n}_1^\top d\mathbf{t}_2 \\ &+ (\mathbf{x}_2 - \mathbf{x}_1)^\top d\mathbf{n}_1 - \mathbf{n}_1^\top d\mathbf{x}_1 + \mathbf{n}_1^\top d\mathbf{x}_2 \end{aligned} \quad (18)$$

$$\begin{aligned} dC_3 &= (\mathbf{n}_2 \times \mathbf{x}_1)^\top d\mathbf{r}_1 - \mathbf{n}_2^\top d\mathbf{t}_1 \\ &+ (\mathbf{x}_1 \times \mathbf{n}_2)^\top d\mathbf{r}_2 + \mathbf{n}_2^\top d\mathbf{t}_2 \\ &+ (\mathbf{x}_2 - \mathbf{x}_1)^\top d\mathbf{n}_2 - \mathbf{n}_2^\top d\mathbf{x}_1 + \mathbf{n}_2^\top d\mathbf{x}_2 \end{aligned} \quad (19)$$

Least squares adjustment Eqs. 14 to 19 can be used in a Gauss-Helmert model to solve for all unknown parameters \mathbf{r}_i and \mathbf{t}_i . The measurements are the plane parameters \mathbf{n}_{ij} and \mathbf{x}_{ij} of the surface elements.

It should be noted that the equation system defined the way shown here will be singular with a rank defect of 6. This is due to an overall rigid transformation (rotation, translation) that could be performed without changing the constraints. For this reason, the bundle adjustment as shown here is a free adjustment. In order to solve the equation system, one can compute the pseudo inverse using the singular value decomposition and the explicit knowledge of the rank defect.

4 EXPERIMENTS

4.1 Dataset

The purpose of this work is to test the surface element based registration approach on a standard dataset containing buildings. We have chosen the Agia Sanmarina data which is published by ISPRS working group V/3 on terrestrial laser scanning (ISPRS WG V/3, 2004). Agia Sanmarina is a Byzantine church near Kalamata in Greece and is approx. $10 \times 20 \times 15 \text{ m}^3$ in size. The scanner used was a Cyrax Cyra 2500. Both the church and the laser scanner are shown in Fig. 1.

There are eight datasets positioned around the church in 45° steps. Each dataset contains between 500 and 800 thousand 3D points. The opening angle of the scanner is rather small, so that the church fills most of the field of view. The object itself has many small and often highly structured surfaces which make it rather difficult for a plane based approach. Furthermore, it is difficult to find sufficient overlapping areas because the scanner has been positioned directly in front of one of the facades half of the time.

4.2 Generation of surface elements

The generation of the surface elements is straightforward and quite fast because the number of points is low compared to other laser scanners. Difficulties arose with the highly structured facades of the church because they are composed from many individual but small planes. The raster size of the 3D grid therefore had to be chosen rather small in order to get enough surface elements per object plane. On the other hand, the low point density

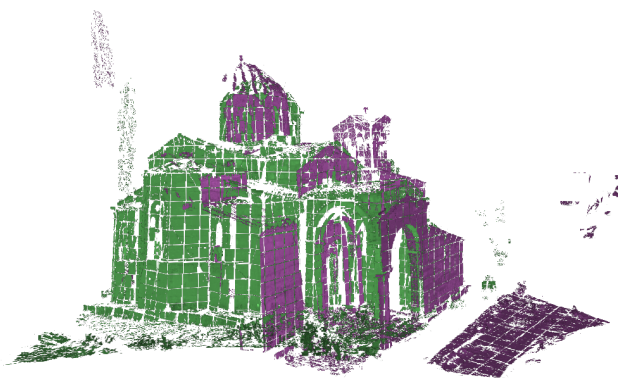


Figure 2. Coarse registration result for Northeast (green) and North (purple) positions.



Figure 3. Fine registration result for Northeast (green) and North (purple) positions.

on the church – the nominal sampling interval is given as 1 cm at 10 m distance – did not allow too small surface elements. The best compromise was a raster size of 0.5 m. The number of generated surface elements ranges roughly from 1200 to 4200 depending on scene complexity (see Tab. 1). Examples of the surface elements can be seen in Fig. 2 as the little square structures.

4.3 Coarse registration

The first step is the generation of large planes from the surface elements. Tab. 1 lists their number which ranges from 50 to 112. Too small planes below five surface elements have been dropped in order to eliminate noise. The coarse registration required careful choice of the algorithm's thresholds so that all eight neighboring positions could be processed successfully.

Basically it can be reported that the plane based automatic coarse registration works for the Agia Sanmarina dataset. The main reason for the success is that two neighboring positions contain a common facade completely so that there is a chance for the algorithm to generate correct transformation parameters. Difficulties arose because correct parameters are only accepted if they are supported by a number of other planes matches and besides the common facade, almost no other features overlap.

Another possible source for errors is the tilted sensor as the coarse registration algorithm assumes parallel zenith directions. Even though this influence is visible in the coarse registration result (see Fig. 2) it did not prevent the extraction of a valid solution.

	$\alpha/^\circ$	$\beta/^\circ$	$\gamma/^\circ$	x/m	y/m	z/m
Northeast	-6.4924	-1.1389	42.9209	-2.2892	15.6731	-0.3365
Southeast	3.7317	-1.1302	-28.8213	0.6569	-12.2696	0.1418
South	8.1701	-4.2542	-67.5171	-13.4374	-21.9461	-1.7592
Southwest	1.4909	-10.1123	-114.2456	-32.1951	-23.1324	-3.0601
West	-0.2914	-5.3232	-166.7708	-43.9244	-6.4330	-4.0994
Northwest	-1.7984	-9.5814	155.9213	-49.6421	9.6286	-5.2051
North	0.0711	-13.0660	91.4302	-20.8192	18.4335	-1.8945

Table 2. Resulting transformation parameters after bundle adjustment. They have been transformed such that the parameters for the East position are the identity transform ($\mathbf{r} = \mathbf{t} = 0$).

	$\Delta\alpha/^\circ$	$\Delta\beta/^\circ$	$\Delta\gamma/^\circ$	$\Delta x/m$	$\Delta y/m$	$\Delta z/m$
Northeast	0.24	-0.17	0.13	0.09	0.06	0.06
Southeast	-0.72	-0.55	-0.19	-0.10	-0.09	0.23
South	-0.30	-0.86	-0.46	-0.25	-0.14	0.12
Southwest	-0.31	-0.32	-0.37	-0.23	0.00	-0.06
West	-0.08	-0.36	-0.21	-0.14	0.04	-0.20
Northwest	0.14	-0.57	-0.04	-0.04	0.04	-0.31
North	0.07	-0.05	0.08	-0.14	0.00	0.03

Table 3. Differences to reference values taken from the results for the GP-ICPR method from (Bae, 2006).

Fig. 2 shows a coarse registration result for the Northeast and North positions. It can be observed that the North data (purple) is tilted a bit in one direction with respect to the other dataset. This is due to the tilted setup of the laser scanner that has not been accounted for by the registration algorithm. What can also be seen is the limited amount of overlapping areas between the positions which is typical for Agia Sanmarina data. There are hardly any purple planes pointing to other directions than North only. On the other hand, there are many green planes pointing North and East as this dataset had been taken from a corner of the church. However, matching object regions are close enough to each other so that a fine registration is possible.

4.4 Fine registration

The pairwise fine registration uses the initial transformation parameters output by the coarse registration and is carried out on the surface elements from which the large planes were composed. Even though a valid solution could be found rather easily, it turned out extremely difficult to find a set of thresholds that would work on all neighboring datasets.

Often, the plane based ICP gradually converged to a wrong solution. The reason is that the plane based adjustment step requires three independent planes to fix the translation. While this had not been a problem for other datasets tested previously, Agia Sanmarina data typically contains only one big facade. Often there is only little information on the orthogonal walls because the scanner had been positioned in front of the facade. The ground plane also is of bad quality since it is rough and does not display a suitable overlap.

An example for the fine registration is shown in Fig. 3. Matching parts now overlap quite well. Despite the difficulties with the convergence the fine registration also can be regarded as successful. As some manual intervention was needed for good choice of the thresholds, this step should be considered semi-automatic. However, it should be noted that only two out of the eight position pairs posed a problem and that the initial aim was to find a global set of thresholds.

Pairwise registration only leads to the propagation of errors. If the loop can be closed such as possible for Agia Sanmarina data, these errors become obvious. An example is shown in Fig. 4 (top). Especially at the top of the middle tower, the accumulated errors can be seen as a slight shift and rotation. Nevertheless, the overall quality of the fine registration seems to be quite well.



Figure 4. Top: Residual of the loop closing for consecutive fine registrations between Southeast (green) and East (purple) positions. Bottom: The same two positions after bundle adjustment.

4.5 Bundle adjustment

An improvement has been sought via a bundle adjustment of all datasets. The resulting transformation parameters are shown in Tab. 2. Similar to (Bae, 2006), an overall transformation had been carried out such that the East position has an identity transform as its parameters. As can be seen from Fig. 4 (bottom), the two positions are now registered with smaller residuals. There is a noticeable change in color because to a small remaining shift most of the surface elements from the East facade (purple) are slightly in front of those from the Southeast facade (green).

Tab. 3 shows the difference in the registration parameters obtained via the surface elements and those given in (Bae, 2006) that will be regarded as reference. Please note that the coordinate system used for our work is different from that of the reference data. Here, the z -axis is pointing upwards and the rotation angles are defined in a slightly different way. For comparison, the reference parameters had been transformed into our coordinate frame so that valid differences can be obtained.

(Bae, 2006) reports angular residuals that range from 0.0003° to 0.5° . Most of the time the residuals are less than 0.01° – we see

that the plane based method is roughly ten times worse. For the translation the situation is similar as the reference has residuals in the order of about 1 cm whereas we found about 10 cm.

5 CONCLUSIONS

In this paper, an automatic registration method for terrestrial LIDAR data has been applied to the Agia Sanmarina test data supplied by ISPRS WG V/3. Three different steps have been tested, coarse registration, fine registration and a refined solution that uses all datasets simultaneously.

All steps were able to generate a solution on the test data. Especially the coarse registration can be considered as successful as it quite easily returned usable initial solutions. The pairwise fine registration, however, required quite a lot attention to the selection of proper thresholds so that a correct solution could be obtained for all neighboring pairs.

The bundle adjustment was able to improve the results from the fine registration, but could not achieve a satisfying result as the accuracy is about a factor of ten worse than the ICP-based reference solution. A probable cause could be the rather coarse surface elements that might be less accurate than their planar appearance suggests.

On the other hand, the data is not optimal for plane based approaches because the scene consists of one convex object covered with a lot of small structures. The approach should work better if more objects with larger planar surfaces are available.

We can conclude that registration based on surface elements is especially successful for coarse registration. Pairwise fine registration as well as a bundle adjustment style registration of an arbitrary number of datasets are possible as well, but the resulting accuracy is limited.

REFERENCES

- Akca, D., 2003. Full automatic registration of laser scanner point clouds. In: *Optical 3-D Measurements VI*, pp. 330–337.
- Bae, K.-H., 2006. Automated Registration of Unorganised Point Clouds from Terrestrial Laser Scanners. PhD thesis, Curtin University of Technology. URL: adt.curtin.edu.au/theses/available/adt-WCU20060921.094236/.
- Besl, P. J. and McKay, N., 1992. A Method for Registration of 3-D Shapes. *PAMI* 14(2), pp. 239–256.
- Dold, C. and Brenner, C., 2004. Automatic Matching of Terrestrial Scan Data as a Basis for the Generation of Detailed 3D City Models. In: O. Altan (ed.), *Proc. of the XXth ISPRS Congress, IAPRS, Vol. XXXV-B3*. URL: www.isprs.org/istanbul2004/comm3/papers/429.pdf.
- Dold, C. and Brenner, C., 2006. Registration of terrestrial laser scanning data using planar patches and image data. In: H.-G. Maas and D. Schneider (eds), *Image Engineering and Vision Metrology, IAPRS, Vol. XXXVI Part 5*. URL: www.isprs.org/commission5/proceedings06/paper/DOLD_637.pdf.
- He, W., Ma, W. and Zha, H., 2005. Automatic registration of range images based on correspondence of complete plane patches. In: *Proceedings of the Fifth International Conference on 3-D Digital Imaging and Modeling*, pp. 470–475.

ISPRS WG V/3, 2004. Agia sanmarina test data.
URL: www.cage.curtin.edu.au/~gordonsj/isprs_wgv3/data.html.

Liu, R. and Hirzinger, G., 2005. Marker-free Automatic Matching of Range Data. In: R. Reulke and U. Knauer (eds), Panoramic Photogrammetry Workshop, IAPRS, Vol. XXXVI-5/W8. URL: www.informatik.hu-berlin.de/sv/pr/PanoramicPhotogrammetryWorkshop2005/Paper/PanoWS_Berlin2005_Rui.pdf.

McGlone, J. C., Mikhail, E. M. and Bethel, J. (eds), 2004. Manual of Photogrammetry. 5th edn, American Society of Photogrammetry and Remote Sensing.

Rabbani, T. and van den Heuvel, F., 2005. Automatic point cloud registration using constrained search for corresponding objects. In: 7th Conference on Optical 3-D Measurements.

Ripperda, N. and Brenner, C., 2005. Marker-free Registration of Terrestrial Laser Scans Using the Normal Distribution Transform. In: S. El-Hakim, F. Remondino and L. Gonzo (eds), 3D-ARCH 2005, IAPRS, Vol. XXXVI-5/W17. URL: www.commission5.isprs.org/3darch05/pdf/33.pdf.

von Hansen, W., 2006. Robust automatic marker-free registration of terrestrial scan data. In: W. Förstner and R. Steffen (eds), Photogrammetric Computer Vision, IAPRS, Vol. XXXVI Part 3. URL: www.isprs.org/commission3/proceedings06/singlepapers/O.08.pdf.

von Hansen, W., 2007a. Automatic detection of zenith direction in 3d point clouds from built-up areas. In: Photogrammetric Image Analysis, Munich, Germany.

von Hansen, W., 2007b. Pairwise registration of terrestrial lidar data using surface elements. Submitted to ISPRS journal, special issue on laser scanning.

Wendt, A., 2004. On the automation of the registration of point clouds using the metropolis algorithm. In: O. Altan (ed.), Proc. of the XXth ISPRS Congress, IAPRS, Vol. XXXV-B3. URL: www.isprs.org/istanbul2004/comm3/papers/250.pdf.

GOING UNDERCOVER: MAPPING WOODLAND UNDERSTOREY FROM LEAF-ON AND LEAF-OFF LIDAR DATA

R. A. Hill

School of Conservation Sciences, University of Bournemouth, Poole, Dorset, BH12 5BB, UK – rhill@bournemouth.ac.uk

ISPRS WG III/3, III/4, V/3, VIII/11

KEY WORDS: laser scanning, LiDAR, woodland, understorey, overstorey, broadleaf

ABSTRACT:

An understorey model is created for an area of broadleaf, deciduous woodland in eastern England using airborne LiDAR data from winter 2003 (leaf-off conditions) and summer 2005 (leaf-on). The woodland is ancient, semi-natural broadleaf and has a heterogeneous structure, with a mostly closed canopy overstorey and a patchy understorey layer beneath. In places, particularly in the centre of the study area, the top canopy is not mature, but is open and scrubby. The trees of the top canopy (i.e. dominants) together with trees and shrubs that occur in open areas (i.e. sub-dominants) can be sampled directly in leaf-on first return airborne LiDAR data, whereas trees and shrubs that occur hidden as understorey (i.e. suppressed) require a more sophisticated approach to map using airborne LiDAR data. This study makes use of the fact that in temperate deciduous woodland the understorey layer typically leafs out two weeks before the overstorey. Capturing winter (leaf-off) airborne LiDAR data during this time slot maximises the ability to map the understorey layer. Thus, leaf-on first return data were used to define the top canopy for overstorey trees and leaf-off last return data were used to model the understorey layer beneath. Field data from five stands were used to identify crown depth in relation to tree height for the six species of dominant trees in the study area. Thresholds were identified per tree species for crown depth as a percentage of canopy height, and the understorey layer was modelled where leaf-off last return data occurred below the relevant threshold. A minimum height of 1 m was applied to define woody understorey. Critical to this process were a Digital Terrain Model (extracted from the leaf-off last return LiDAR data) to normalise the first and last return LiDAR data to canopy height, and a digital tree species map (derived from the classification of time series airborne multi-spectral data) to guide the application of canopy depth thresholds per species.

1. INTRODUCTION

The vertical structure of woodlands or forest plays an important role in determining microclimatic conditions (including radiation levels at the forest floor), the availability of niche space, habitat quality, the distribution of fuels and subsequent fire behaviour (Brokaw and Lent, 1999, MacArthur and MacArthur, 1961, Pyne et al., 1996). Forests and woodlands can have simple, single-storey canopies or more complicated multi-storey canopies. In forests where there is a heterogeneous vertical structure, dominant trees form the overstorey canopy, whilst sub-dominant trees have free access to light but do not occupy the upper canopy, and suppressed trees have no direct access to light and grow underneath a relatively continuous cover of branches and foliage from adjacent dominant or sub-dominant trees. The understorey can be composed of seedlings and saplings of overstorey trees which persist as suppressed juveniles until a suitable canopy gap opens, and shade tolerant species of trees or shrubs which complete their life-cycles in an environment of lower light intensity and higher humidity than in the overstorey. Information on the understorey layer of woodland can be essential for the accurate modelling of carbon stocks and sequestration (Patenaude et al., 2003) and of bird habitat availability and quality (Broughton et al., 2006).

There are numerous case studies involving the application of airborne LiDAR data for detailed spatial modelling of forest structure (see Lim et al., 2003 for a review) and some techniques have become operational for forest inventory (see Næsset, 2004). At the stand level, measures such as mean tree height and diameter, timber volume, stem number, crown

height, biomass, canopy closure, and LAI have been derived using discrete-return small footprint LiDAR data (Magnussen and Boudewyn, 1998, Næsset, 2002, Næsset and Økland 2002). This typically involves regression-based methods in which percentiles of the distribution of canopy height measurements from LiDAR are used to predict forest characteristics within a spatial sampling frame based on empirical relationships. Where the density of laser returns is greater than 5-10 per m², then individual tree based approaches have been used (Persson et al., 2002), giving more direct measures of tree height, timber volume and stem number (Maltamo et al., 2004a). These studies tend to be focussed either on single layered forests or on the dominant tree layer if forests are multi-layered, thus deriving variables for dominant trees only (Maltamo et al., 2005). Such measures will not fully characterise the structure of forests with significant vertical heterogeneity. For example, Maltamo et al. (2004b) showed that for a mixed-species woodland of spruce, pine and birch in Finland it was possible to detect over 80% of dominant trees but only 40% of all trees in LiDAR data with approximately 10 hits per m². As a result, they found that predictions of timber volume and stem density were underestimated by 24% and 62% respectively, although this could be improved by predicting suppressed trees using theoretical distribution functions (Maltamo et al., 2004a).

The larger footprint, waveform recording LiDAR systems have an obvious advantage for characterising and quantifying forest vertical structure. For example, systems such as SLICER and LVIS have been demonstrated successfully for estimating stand height, mean stem diameter, basal area, and total biomass (Means et al., 1999, Drake et al., 2002, Lefsky et al., 2002), and

characterising the canopy height profile (Lefsky et al., 1999, Harding et al., 2001, Parker et al., 2001). However, there have been attempts to characterise forest vertical structure using small footprint discrete return LiDAR data, as it is recognised that the distribution of LiDAR returns over forests and woodland relates to the vertical structure of the tree canopy. Thus, Zimble et al. (2003) characterised woodland as either single or multi-storey by the analysis of LiDAR-derived tree height variance in 30 m grid cells, whilst Riaño et al. (2003) performed cluster analysis of LiDAR tree canopy returns to discriminate overstorey and understorey proportions in 10 m grid cells. Maltamo et al. (2005) developed a histogram thresholding method to designate the distribution of LiDAR canopy height returns as uni- or multi-modal and thus the canopy as single or multi-layered. They constructed regression models for the logarithmic number and Lorey's mean height of understorey trees, using independent variables derived from the LiDAR distributions. However, a common problem reported in these studies is that where the dominant trees form a dense and closed canopy it is not possible to identify understorey by analysing only one return of LiDAR data.

Where the overstorey is deciduous, what is required is LiDAR data from leaf-on and leaf-off conditions; using the leaf-on data to model the overstorey and leaf-off data to identify the understorey. To-date only two papers have touched on this. Hirata et al. (2003) showed, by a visual assessment, that the amount of information on both the ground and the understorey layers was significantly higher in leaf-off LiDAR data for temperate deciduous forests in Japan. Imai et al. (2006) examined LiDAR data from three dates across a growing season, also for temperate deciduous forests in Japan, and produced a canopy height model from leaf-on conditions and a canopy height difference model across all three dates. They then applied height thresholds of 0-1m, 1-5m, 5-10m and > 10m to both models to separate ten classes that distinguished what they called high tree canopy (evergreen and deciduous, with or without a shrub layer), sub-high tree canopy (again separating evergreen and deciduous, with or without a shrub layer), shrub layer (evergreen and deciduous) and ground layer.

The work reported in this paper makes use of dual return LiDAR data acquired in leaf-on and leaf-off conditions for a broadleaf deciduous woodland in the UK. Field data are used to identify the relationship between tree height and crown depth for overstorey tree species and this information is applied to the LiDAR data, using the leaf-on first return data to define the top canopy for overstorey trees, and leaf-off last return data to identify a discontinuous layer of suppressed trees or shrubs below the overstorey canopy. This is based on the identification of thresholds for crown depth as a percentage of canopy height per tree species. Critical to this understorey modelling process therefore, is a tree species map, which here is derived from the classification of time series airborne multi-spectral data.

2. MATERIALS AND METHODS

2.1 Field site

The study area is Monks Wood National Nature Reserve in Cambridgeshire, eastern England (52° 24' N, 0° 14' W). This is an ancient woodland of broadleaved deciduous species, which covers 157 hectares. Within this boundary are two cleared areas, totalling 6 ha, which are maintained by grazing. These two fields are not considered to be part of the spatial coverage

of Monks Wood in all following descriptions and statistical analyses. However, all other open areas within the boundary of Monks Wood, such as canopy gaps and paths, are included. The total area of Monks Wood is thus considered here to be 151 ha.

Monks Wood is extremely heterogeneous in terms of the woody species making up the tree canopy and understorey, their relative proportions in any area, canopy closure and density, tree height and stem density (Hill and Thomson, 2005). The overstorey tree species of Monks Wood are common ash (*Fraxinus excelsior*), English oak (*Quercus robur*), field maple (*Acer campestre*), silver birch (*Betula pendula*), aspen (*Populus tremula*) and small-leaved elm (*Ulmus carpinifolia*). Ash is the most common and widespread species, occurring mostly as coppice stems but regenerating naturally wherever the canopy is opened (Massey and Welch, 1993). Oak, maple and birch occur less frequently, the latter regenerating from seeds in canopy gaps. Aspen and elm form occasional clusters on the wetter soils, although the elm population declined significantly in the 1970s due to an outbreak of Dutch elm disease. The former elm stands have been left to regenerate naturally and today tend to be rather scrubby in nature. The dominant woody species making up the understorey and fringes of Monks Wood are hawthorn (*Crataegus monogyna*), common hazel (*Corylus avellana*), blackthorn (*Prunus spinosa*), dogwood (*Cornus sanguinea*) and common privet (*Ligustrum vulgare*). Hazel, along with ash, was coppiced until 1995. Hazel now occurs mixed with hawthorn and blackthorn throughout Monks Wood (Massey and Welch 1993). Also to be found in the understorey, especially in more open areas, are elder (*Sambucus nigra*), buckthorn (*Rhamnus catharticus*), grey willow (*Salix cinerea*), goat willow (*S. caprea*), downy birch (*B. pubescens*), crab apple (*Malus sylvestris*) and bramble (*Rubus fruticosus*).

2.2 Field data

The field data used in this study were collected in July 2000. Five contrasting stands were surveyed (see Table 1 in Patenaude et al., 2003). The stands ranged in size between 0.84 ha and 3.69 ha, and covered the range of species composition and structure present within Monks Wood (Tables 1 and 2). Each stand was divided into a grid of 10 equal areas (8 in stand 5), and in each of these grid cells a 20x20m sample plot was located randomly. For each of the 48 plots, the diameter at breast height (DBH) for all woody stems of at least 7cm DBH were recorded, totalling 2191 living stems. Each recorded stem was identified by species and designated as either overstorey or understorey. For the overstorey trees, crown height and crown depth (amongst other measures) were recorded for three randomly selected individuals of each species per plot. This totalled 101 individuals for ash, 62 for oak, 42 for maple, 15 for elm, 9 for aspen and 4 for birch.

	Overstorey		Understorey	
	# stems	Total BA	# stems	Total BA
Stand 1 (2.57 ha)	144	103891	224	18589
Stand 2 (3.35 ha)	248	104830	155	13293
Stand 3 (2.83 ha)	84	47682	325	24087
Stand 4 (3.69 ha)	394	108201	173	12672
Stand 5* (0.84 ha)	229	190687	215	19073

Table 1. Structural composition of the five stands enumerated in Monks Wood. Data per stand are for ten 20x20m plots; Total Basal Area values are in cm².

(* values for Stand 5 are weighted to the equivalent of 10 plots)

	Ash	Oak	Maple	Aspen	Elm	Birch
Stand 1	19	60	19	0	0	0
Stand 2	89	3	8	0	0	0
Stand 3	29	6	45	17	0	4
Stand 4	89	8	3	0	0	0
Stand 5	14	5	0	0	80	0

Table 2. Percentage composition of tree species in each stand enumerated from ten 20x20m plots.

The tree crown data were used to examine the relationship between canopy height and crown depth per overstorey tree species across Monks Wood, and to identify thresholds in crown depth as a percentage of canopy height. This information was used to model the understorey layer from the airborne LiDAR data. The field data on understorey stem count and basal area were used to validate the derived understorey model.

In addition to traditional forest mensuration data, a map of the six species of dominant trees which make up the overstorey of Monks Wood was available. This was produced from the supervised classification of a time-series of 2 m spatial resolution Airborne Thematic Mapper (ATM) data, acquired throughout the growing season of 2003. This map has a surveyed overall accuracy of 88% (kappa 0.84) for the identification of ash, aspen, birch, elm, maple and oak tree species in the overstorey canopy (Table 3). Note that for this product, the overstorey is defined as being greater than 8 m tall.

	Composition (%)	Users' Accuracy (%)
Ash	54.9	83.5
Aspen	7.2	71.4
Birch	2.3	90.7
Elm	0.5	84.6
Maple	14.3	84.1
Oak	20.8	97.3

Table 3. Percentage composition of overstorey tree species in Monks Wood based on digital image classification, and the surveyed User's Accuracy for each species.

2.3 Airborne LiDAR data

LiDAR data were acquired with an Optech Inc. Airborne Laser Terrain Mapper (ALTM-3033) on 14 April 2003 and 26 June 2005. These data sets are referred to in this manuscript as leaf-off and leaf-on respectively; however, the acquisition date for the leaf-off data was selected such that whilst the overstorey canopy was still dormant the understorey had already leafed out. For both data sets, the first and last significant return per laser pulse were recorded. The leaf-off data were acquired at an average flying altitude of 980m, with a scan half angle of 15° generating 1 laser hit per 1 m², whilst the leaf-on data were acquired at an average flying altitude of 1125m, with a scan half angle of 20° generating 1 laser hit per 2 m².

The first and last return data of both the leaf-on and leaf-off data sets were each processed into a Digital Surface Model (DSM) via Delaunay Triangulation (Figure 1). The selected spatial resolution was 0.5m, i.e. the approximate horizontal accuracy of data acquisition by the ALTM 3033 at the flying altitude. Comparison of the leaf-off and leaf-on DSMs revealed the need for more precise geo-registration between the two data sets. Thus, 32 ground control points were identified in the first return DSMs of the leaf-on and leaf-off data. These had a

predicted accuracy after first order polynomial transformation of 0.48m in x and 0.49m in y (total 0.69m). The same set of ground control points were used to register both the first and last return leaf-on DSMs to the leaf-off DSMs. The total shift after transformation was 0.33m in x and 1.68m in y. Nearest neighbour resampling was used to preserve individual pixel values in the transformed DSMs.

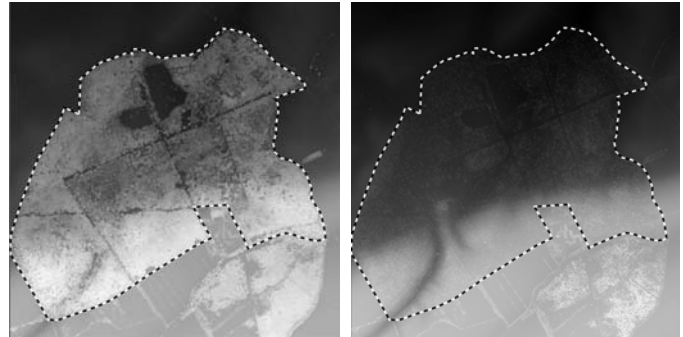


Figure 1. Leaf-on first return DSM (left) and leaf-off last return DSM (right) for Monks Wood, Cambridgeshire, UK. The boundary of the study area is shown by a dashed line.

A Digital Terrain Model (DTM) was generated from the leaf-off last return data, in which 48% of laser returns within the 151 ha Monks Wood were ground hits. This compared with a ground hit rate for the leaf-off first return of 3.1%, and the leaf-on last return (2.7%) and leaf-on first return (1.8%). Ground hits in the leaf-off last return data were identified by a process of adaptive filtering, whereby focal variance in the DSM was calculated over 10x10 and 40x40 pixel windows and thresholds in both were used to determine whether to extract a ground return as a 5x5, 10x10, or 20x20 pixel block minimum for any given area. A DTM was interpolated by applying a thin-plate spline to the extracted local elevation minima. This was carried out as an iterative process, comparing the DTM at each iteration with the leaf-off last return DSM and reducing the minimum filter size from which ground hits were extracted where the two surfaces were within tolerance limits. The accuracy of the resulting DTM was assessed using 244 terrain measurements recorded with an electronic total station (see Gaveau and Hill, 2003). The RMSE was ± 0.27 m (range -0.78 m to +0.59 m).

A Digital Canopy Height Model (DCHM) was then generated for the top canopy of Monks Wood by the per-pixel subtraction of the DTM from the leaf-on first return DSM. In line with the tree species map, the overstorey tree layer was considered as canopy taller than 8 m. The top canopy between 1 m and 8 m was considered to be sub-dominant trees and shrubs. This component of the understorey layer is directly exposed (i.e. not covered by an overstorey layer) and so is readily identifiable from airborne LiDAR data acquired during leaf-on conditions.

Extracting the proportion of the understorey layer that is hidden below the overstorey (i.e. suppressed trees and shrubs) made use of the difference between the leaf-on first return and leaf-off last return LiDAR data. The difference was calculated per-pixel between the leaf-on first return and leaf-off last return DSMs and expressed as a percentage of the leaf-on first return DCHM. The hidden understorey layer was identified as any point where the leaf-off last return occurred below the threshold identified from the field data of crown depth as a percentage of canopy height per tree species. The tree species information came from the co-registered tree species map. A minimum height of 1 m was applied to define woody understorey.

3. RESULTS

For the six species of dominant trees that constitute the overstorey layer in Monks Wood, only in the case of maple was there a strong significant relationship between canopy height and crown depth ($R^2 = 0.65$, $n = 42$, $p < 0.001$). Thus, rather than calculating the likely crown depth for a canopy of any given height for an individual species, an upper threshold was sought per species for percentage crown depth. Histograms of crown depth as a percentage of canopy height for the six overstorey tree species in Monks Wood are shown in Figure 2. The selected thresholds are also shown; these were 60% for ash, birch and elm, 70% for aspen and oak, and 80% for maple. These thresholds were subsequently applied to the leaf-on first return and leaf-off last return airborne LiDAR data to model the hidden understorey layer. The chosen thresholds of maximum crown depth as a percentage of canopy height were deliberately conservative; i.e. were more likely to miss larger trees or shrubs in the understorey where the overstorey canopy was tall but not deep (errors of omission) rather than to incorrectly map the base of deeper overstorey crowns as understorey (errors of commission).

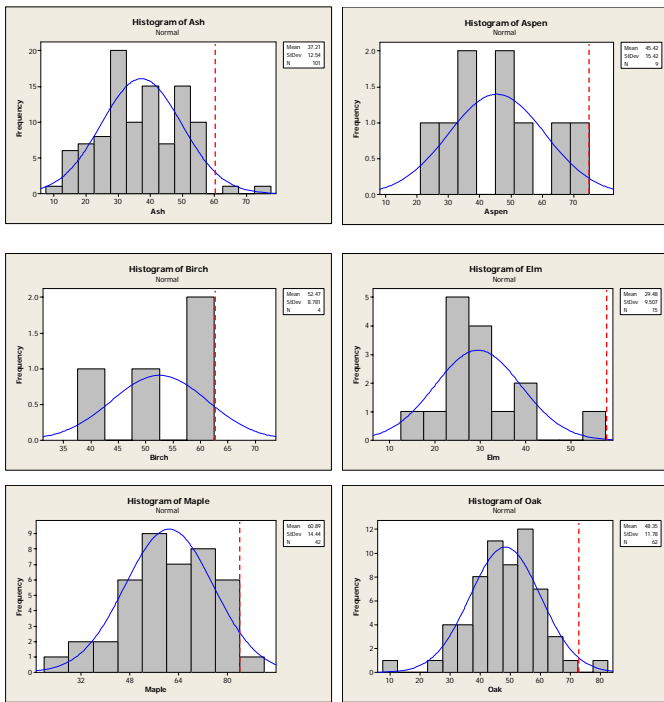


Figure 2. Histograms of crown depth as a percentage of canopy height for the six species of dominant trees that constitute the overstorey layer in Monks Wood. The chosen thresholds are shown by a dashed line.

The DSMs from leaf-on first return and leaf-off last return data clearly relate to two different surfaces, with the leaf-on first return reflecting the predominantly closed nature of the overstorey canopy and the leaf-off last return data supplying information from the understorey layer and ground (Figure 1). Statistics for the two DSMs normalised by the subtraction of terrain elevation are given in Table 4. The leaf-on first return data for Monks Wood had an average canopy height of 13.35 m (standard deviation of 5.10 m), with 83.2% having a canopy height > 8.0 m. This represents the overstorey tree layer, below which there could be a concealed understorey layer. Only 14% of the leaf-on first return data for Monks Wood had a canopy height of between 1 m and 8 m. This is the exposed proportion

of the understorey layer (composed of sub-dominant trees and shrubs), and occurs around the woodland margins and in distinct patches in those areas which have been left to regenerate naturally following the loss of elm trees. The exposed portion of the understorey had an average canopy height of 5.46 m (standard deviation 1.87 m). The leaf-off last return data had an average canopy height of 1.38 m (standard deviation 1.61 m), with only 0.3% being > 8 m, and 42.5% returning from canopy between 1 m and 8 m. This could represent either understorey or returns from lower levels within the crowns of overstorey trees.

	Leaf-on first return	Leaf-off last return
Minimum (m)	0.00	0.00
Maximum (m)	25.31	18.95
Mean (m)	13.35	1.38
Standard deviation (m)	5.10	1.61
0 m to 1 m (%)	2.8	57.2
1 m to 8 m (%)	14.0	42.5
> 8 m (%)	83.2	0.3

Table 4. Summary statistics for the normalised leaf-on first return and leaf-off last return LiDAR data for Monks Wood

Figure 3 gives histograms for the difference between the leaf-on first return and leaf-off last return DSMs; expressed in metres and as a percentage of overstorey canopy height. The summary statistics are given in Table 5. The obvious point to note is that there is a high level of penetration between the two LiDAR surfaces, with an average height difference of 11.98 m (standard deviation 5.28 m) and an average penetration rate of 90.2% (standard deviation 12.5%). In fact, just over half (50.5%) of Monks Wood overstorey has a penetration rate in the leaf-off last return data of > 95% of canopy height. This reflects a high level of ground penetration in the leaf-off last return LiDAR data. Note that negative values did occur where tree fall or felling took place between the two dates of LiDAR acquisition. However, these covered only 1% of the land area of Monks Wood and were not considered in the above statistics.

	Difference in metres	Difference as % canopy height
Minimum (m)	-12.97	0.06*
Maximum (m)	25.09	100.00
Mean (m)	11.98	90.23
Standard deviation (m)	5.28	12.45

Table 5. Summary statistics for the difference between leaf-on first return and leaf-off last return LiDAR data for Monks Wood

(* this value excludes negative height differences).

The concealed component of the understorey layer was modelled based on the difference between the leaf-on first return and leaf-off last return DSMs. This layer of suppressed trees and shrubs covers approximately 30% of the area within the Monks Wood boundary, i.e. some 46.4 hectares. The understorey model covers a range of height values from a chosen minimum of 1.0 m to a maximum of 10.18 m; although 99% has a height range between 1m and 6m. A histogram for the model of concealed understorey is shown in Figure 4. The mean height of the understorey is 2.64 m (standard deviation 1.16m).

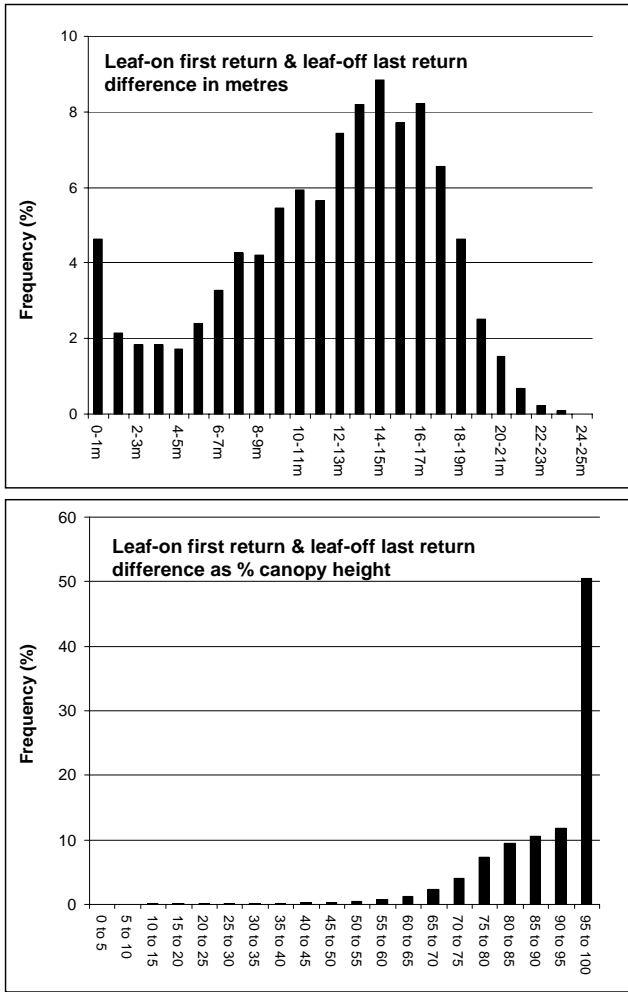


Figure 3. Histograms of the difference between leaf-on first return and leaf-off last return LiDAR data for Monks Wood.

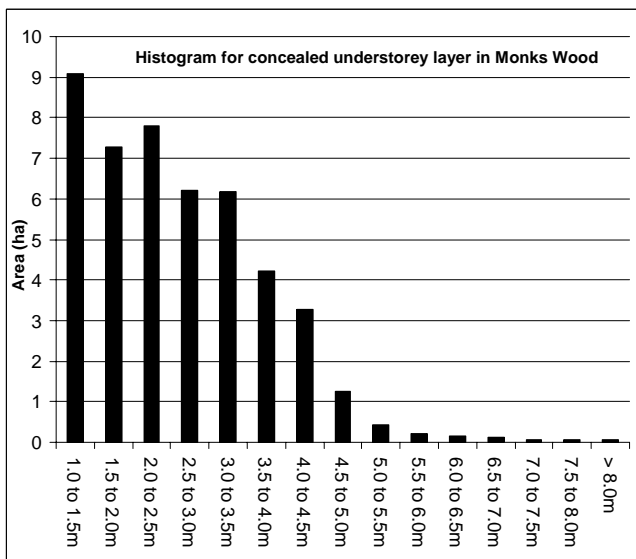


Figure 4. Histogram for the concealed portion of the understorey, as modelled from the leaf-on first return and leaf-off last return LiDAR data.

The total understorey layer of Monks Wood is thus made up of two components, a portion which is shaded below an overstorey and a portion which is exposed. These cover 46.4 ha and 21.2 ha respectively, which represents 30% and 14% of the land area within Monks Wood. The total understorey cover of Monks Wood is thus 67.6 ha, or 44% of the land area. Validation of this combined understorey model was carried out using the field plot measurements of understorey from five stands. For each stand the total Basal Area (in cm²) of all trees and shrubs designated as understorey was calculated and compared with the percentage cover of understorey modelled from LiDAR. A plot of this for the five stands (with stand 5 weighted by coverage) is shown in Figure 5, with the best fit line from least squares linear regression also plotted. The relationship between the two measures of understorey cover was strong and highly significant ($R^2 = 0.82$, $n = 5$, $p = 0.033$).

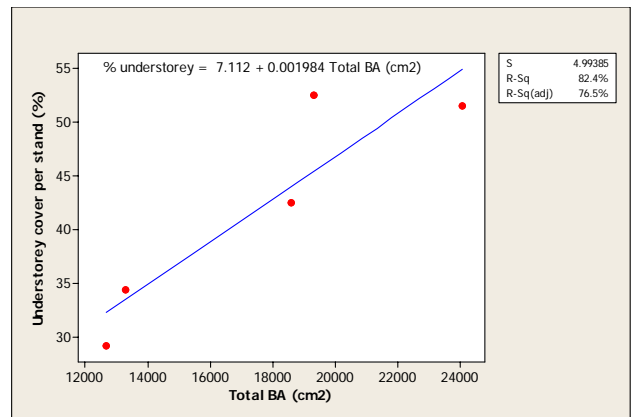


Figure 5. Plot showing the percentage cover of understorey as modelled from airborne LiDAR against field recorded total Basal Area of understorey trees and shrubs in five stands across Monks Wood.

4. DISCUSSION AND CONCLUSIONS

As has been well documented elsewhere, this work has shown that it is possible to map woodland canopy overstorey and scrubby areas along woodland margins and in overstorey canopy gaps from leaf-on first return airborne LiDAR data. Of greater significance is the demonstration of penetration rates of last return LiDAR data during leaf-off conditions. Thus, of the 83% of the study area classed as overstorey based on the leaf-on first return data, some 55.8% of leaf-off last returns came from the ground or ground vegetation layer and virtually all of the remainder came from the understorey. Less than 0.01% of leaf-off last return data came from the overstorey. Therefore, it would be possible to map all non-overstorey trees and shrubs within the study area simply by applying height thresholds of 1 m and 8 m to the leaf-off last return data (66.3 ha, ca 42% of the Monks Wood land area). However, this product would make no distinction between whether the understorey layer was shaded or exposed, which from an ecological perspective is a significant difference. A woodland understorey layer occurring beneath an overstorey is part of a mature and stable vegetation community. The woody species comprising that understorey layer will be shade tolerant. In Monks Wood the most common woody species comprising the shaded understorey are hawthorn, hazel, privet, and dogwood. By contrast, the exposed areas of understorey represent either edge communities or patches of secondary succession. In Monks Wood, blackthorn

and hawthorn are the most common edge species, whilst the scrubby successional areas often contain blackthorn, hazel, willow or juveniles of ash, aspen or elm. The shaded and exposed understorey components in Monks Wood, thus have different woody species compositions, associated species assemblages and future trajectories. Distinguishing this is important in terms of both ecological and carbon modelling.

5. ACKNOWLEDGEMENTS

This work was carried out whilst the author was based at the Centre for Ecology & Hydrology (CEH), at Monks Wood. The airborne LiDAR data were acquired by the NERC Airborne Research & Survey Facility, and pre-processed by the ULM at the University of Cambridge. The woodland mensuration data from Monks Wood were collected by Brian Briggs, now at the Edward Grey Institute of Field Ornithology, University of Oxford. The work presented here complements that of an M.Phil. thesis by Naga Raju Kotagari at the University of Cambridge, which was supervised by the author.

6. REFERENCES

- Brokaw, N.V.L., & Lent, R.A., 1999. Vertical structure. In M.L. Hunter (Ed), *Maintaining biodiversity in forest ecosystems*. Cambridge University Press, Cambridge, pp. 373-399
- Broughton R.K., Hinsley S.A., Bellamy P.E., Hill R.A., & Rothery P., 2006. Marsh Tit territory structure in a British broadleaved woodland. *Ibis*, 148, pp. 744-752.
- Drake, J.B., Dubayah, O., Clark, D.B., Knox, R.G., Blair, J.B., Hofton, M.A., Chazdon, R.L., Weishampel, J.F., & Prince, S.D., 2002. Estimation of tropical forest structure characteristics using large-footprint lidar. *Remote Sensing of Environment*, 79, pp. 305-319.
- Gaveau, D.L.A., & Hill, R.A., 2003. Quantifying canopy height underestimation by laser pulse penetration in small-footprint airborne laser scanning data. *Canadian Journal of Remote Sensing*, 29, pp. 650-657.
- Harding, D.J., Lefsky, M.A., Parker, G.G., & Blair, J.B., 2001. Laser altimetry canopy height profiles: methods and validation for closed-canopy, broadleaf forests. *Remote Sensing of Environment*, 76, pp. 283-297.
- Hill, R.A., & Thomson, A.G., 2005. Mapping woodland species composition and structure using airborne spectral and LiDAR data. *International Journal of Remote Sensing*, 17, pp. 3763-3779.
- Hirata, Y., Sato, K., Shibata, M., & Nishizono, T., 2003. The capability of helicopter-borne laser scanner data in a temperate deciduous forest. In Hyypä et al. (Eds.), *Proceedings of the Workshop Scandlaser Scientific Workshop on Airborne Laser Scanning of Forests*. September 3-4, 2003, Umeå, Sweden, pp 174-179.
- Imai, Y., Setojima, M., Funahashi, M., Katsuki, T., & Amano, M., 2006. Estimation of stand structure in the deciduous broad-leaved forest using multi-temporal LiDAR data. In Hirata, Y., et al. (Eds.) *Proceedings of the International Conference Silvilaser 2006*. November 7-10, 2006, Matsuyama, Japan, pp. 165-170.
- Lefsky, M.A., Cohen, W.B., Acker, S.A., Parker, G.G., Spies, T.A., & Harding, D., 1999. Lidar remote sensing of the canopy structure and biophysical properties of Douglas-fir and Western hemlock forests. *Remote Sensing of Environment*, 70, pp. 339-361.
- Lefsky, M.A., Cohen, W.B., Harding, D.J., Parker, G.G., Acker, S.A., & Gower, S.T., 2002. Lidar remote sensing of above-ground biomass in three biomes. *Global Ecology & Biogeography*, 11, pp. 393-399.
- Lim, K., Treitz, P., Wulder, M., St-Onge, B., & Flood, M., 2003. LiDAR remote sensing of forest structure. *Progress in Physical Geography*, 27, pp. 88-106.
- MacArthur, R.H., & MacArthur, J.W., 1961. On bird species diversity. *Ecology*, 42, pp. 594-598.
- Magnussen, S., & Boudewyn, P., 1998. Derivations of stand heights from airborne laser scanner data with canopy-based quantile estimators. *Canadian Journal of Forest Research*, 28, pp. 1016-1031.
- Maltamo, M., Eerikäinen, K., Pitkänen, J., Hyypä, J., & Vehmas, M. 2004a. Estimation of timber volume and stem density based on scanning laser altimetry and expected tree size distribution functions. *Remote Sensing of Environment*, 90, pp. 319-330.
- Maltamo, M., Mustonen, K., Hyypä, J., Pitkänen, J., & Yu, X. 2004b. The accuracy of estimating individual tree variables with airborne laser scanning in a boreal nature reserve. *Canadian Journal of Forest Research*, 34, pp. 1791-1801.
- Maltamo, M., Packalén, P., Yu, X., Eerikäinen, K., Hyypä, J., & Pitkänen, J., 2005. Identifying and quantifying structural characteristics of heterogeneous boreal forests using laser scanner data. *Forest Ecology & Management*, 216, pp. 41-50.
- Massey, M.E., & Welch, R.C., 1993. *Monks Wood National Nature Reserve: The experience of 40 years 1953-1993*. English Nature, Peterborough.
- Means, J.E., Acker, S.A., Harding, D.J., Blair, J.B., Lefsky, M.A., Cohen, W.B., Harmon, M.E., & McKee, W.A., 1999. Use of large-footprint scanning airborne Lidar to estimate forest stand characteristics in the Western Cascades of Oregon. *Remote Sensing of Environment*, 67, pp. 298-308.
- Næsset, E., 2002. Predicting forest stand characteristics with airborne scanning laser using a practical two-stage procedure and field data. *Remote Sensing of Environment*, 80, pp. 88-99.
- Næsset, E., 2004. Practical large scale forest stand inventory using a small airborne scanning laser. *Scandinavian Journal of Forest Research*, 19, pp. 164-179.
- Næsset, E., & Økland, 2002. Estimating tree height and tree crown properties using airborne scanning laser in a boreal nature reserve. *Remote Sensing of Environment*, 79, pp. 105-115.
- Parker, G.G., Lefsky, M.A., & Harding, D.J., 2001. Light transmittance in forest canopies determined using airborne laser altimetry and in-canopy quantum measurements. *Remote Sensing of Environment*, 76, pp. 298-309.
- Patenaude, G.L., Briggs, B.D.J., Milne, R., Rowland, C.S., Dawson, T.P., & Pryor, S.N., 2003. The carbon pool in a British semi-natural woodland. *Forestry*, 76, pp. 109-119.
- Persson, Å., Holmgren, J., & Söderman, U., 2002. Detecting and measuring individual trees using an airborne laser scanner. *Photogrammetric Engineering and Remote Sensing*, 68, pp. 925-932.
- Pyne, S.J., Andrews, P.L., & Laven, R.D., 1996. *Introduction to wildland fire*. Wiley & Sons, New York.
- Riáño, D., Meier, E., Allgöwer, B., Chuvieco, E., & Ustin, S.L., 2003. Modelling airborne laser scanning data for the spatial generation of critical forest parameters in fire behaviour modelling. *Remote Sensing of Environment*, 86, pp. 177-186.
- Zimble, D.A., Evans, D.L., Carlson, G.C., Parker, R.C., Grado, S.C., & Gerard, P.D., 2003. Characterizing vertical forest structure using small-footprint airborne LiDAR. *Remote Sensing of Environment*, 87, pp. 171-182.

MODELLING CANOPY GAP FRACTION FROM LIDAR INTENSITY

C. Hopkinson^a and L.E. Chasmer^{ab}

^a Applied Geomatics Research Group, NSCC Annapolis Valley Campus, Lawrencetown, NS, B0S 1P0, CANADA

^b Department of Geography, Queen's University, Kingston, ON, K7L 3M6, CANADA

Commission VI, WG VI/4

KEY WORDS: Lidar, gap fraction, leaf area index, intensity, Beer-Lambert.

ABSTRACT:

We reconstruct the vertical pulse power distribution returned from a commercial small footprint discrete pulse airborne laser terrain mapper within a mixed forest landscape. By modifying a Beer-Lambert approach, we relate the ratio of ground return power / total return power to the canopy gap fraction (P) as derived from digital hemispherical photography (DHP). The results are compared to the commonly cited and utilised ground-to-total returns ratio. Canopy gap fraction data were collected on five separate occasions from April to October of 2006, and analysed using standard DHP procedures. Five airborne lidar datasets were collected during dry conditions coincident with DHP, and all acquisitions were performed using the same sensor and survey configuration. It is found that for the mixed wood environment studied, a lidar intensity-based power distribution ratio provides a higher correlation with DHP gap fraction ($r^2 = 0.92$) than does the often used ground-to-total return ratio approach ($r^2 = 0.86$). Moreover, if the intensity power distribution ratio is modified to account for secondary return two-way pulse transmission losses within the canopy, the model requires no calibration and provides a 1:1 estimate of the overhead (solar zenith) gap fraction.

1. INTRODUCTION

1.1 Rationale

The premise of the study is that the interaction between forest canopy and laser pulses emitted from an airborne lidar (light detection and ranging) mapping system can be considered in some ways analogous to the interaction of direct beam solar radiation with canopy covered environments. We examine the reconstructed vertical pulse power distribution returned from a commercial small footprint discrete pulse airborne laser scanning system and relate properties of the distribution to canopy structural and radiative transfer characteristics. In particular, we compare published gap fraction (P) and plant area index (L_v) algorithms and compare these to new algorithms that utilize the return intensity information. From the algorithms tested we develop a non-parameterized physical model to map the spatiotemporal variation in canopy gap fraction for a mixed forest landscape.

1.2 Gap Fraction, Transmissivity and Leaf Area Index

Leaf area index (LAI) is defined as one half the total leaf area per unit ground surface area ($m^2 m^{-2}$) (Chen *et al.* 2006) and is an important parameter for understanding variability in energy, water and carbon fluxes within an ecosystem. LAI and canopy transmittance (T) are key input parameters in many ecological and hydrological models as they enable the prediction of energy transmission through the canopy to lower layers of biomass or to ground level (e.g. Pomeroy and Dion, 1996). This information is essential in growth (e.g. photosynthesis) and hydrological (e.g. melt and evaporation) process modeling in forested environments. Accurate and consistent LAI measurements are often labour intensive and may also be difficult to collect in remote or difficult to access areas.

FIPAR or the fraction of incoming photosynthetically active radiation absorbed by the canopy can be calculated based on the downwelling PAR at the top of the canopy, and downwelling PAR below the canopy (Gower *et al.* 1999). Chen (1996) states that downwelling PAR above the canopy does not tend to vary spatially during clear conditions, however, downwelling PAR below the canopy varies significantly both in space and time. The ratio of downwelling PAR below the canopy to downwelling PAR above the canopy is closely related to the canopy gap fraction (Gower *et al.* 1999). LAI can be estimated from the canopy transmittance Beer-Lambert's Law (from Gower *et al.* 1999; Leblanc *et al.* 2005):

$$P(\theta) = e^{-k(\theta)O(\theta)LAI / \cos(\theta)} \quad (1)$$

Where $P(\theta)$ is gap fraction along zenith angle (θ), $k(\theta)$ is the extinction coefficient (fraction of foliage area projected onto a perpendicular plane), and $O(\theta)$ is the clumping or non-randomness index (Gower *et al.* 1999; Leblanc *et al.* 2005). Gap fraction can also be difficult to estimate using hemispherical photography and radiation sensors (e.g. Licor LAI-2000) due to photograph over-exposure and variable light conditions.

1.3 Lidar estimates of P and LAI

Numerous studies have examined the use of lidar for obtaining gap fraction (P), leaf area index (LAI), the fraction of incoming photosynthetically active radiation absorbed by the canopy (FIPAR) and extinction coefficients (k) from lidar (e.g. Magnussen and Boudewyn, 1998; Parker *et al.* 2001; Todd *et al.* 2003; Morsdorf *et al.* 2006; Thomas *et al.* 2006).

For every emitted laser pulse, there can be several reflecting surfaces along the travel path. Those backscatter elements that are strong enough to register a sufficiently large energy spike at the sensor are known as 'returns'. For a discrete pulse return system such as the airborne laser terrain mapper (ALTM, Optech Inc., Toronto, Canada), the recorded ranges can be separated into single, first, intermediate and last returns. Single returns are those for which there is only one dominant backscattering surface encountered (e.g. a highway surface). For the ALTM, it is possible to also record two intermediate returns making a total of four possible returns from a single emitted pulse. While there is some slight loss of detection capability between adjacent returns (known as "dead time"), this multiple return capability means that there is a reasonable probability of sampling the dominant canopy and ground elements along the pulse travel path.

Laser pulses that are returned from within the canopy have intercepted enough foliage or branch material to be recorded by the receiving optics within the lidar system, while some of the remaining laser pulse energy continues until it intercepts lower canopy vegetation, the low-lying understory and the ground surface. Laser pulse returns from the ground surface have inevitably passed through canopy gaps both into and out of the canopy. Increasing numbers of gaps within the canopy will result in gap fractions approaching 100%, whereas fewer gaps within the canopy will result in a gap fraction closer to zero. Lidar estimates of canopy P and LAI are often based on the assumption that gap fraction is equivalent to canopy transmittance (T) and from Beer-Lambert's Law:

$$P = T = \frac{I_l}{I_o} = e^{-kLAI} \quad (2)$$

Where I_o is open sky light intensity above canopy, I_l is the light intensity after travelling a path length (l) through the canopy and k is the extinction coefficient, which can be approximated to a value of 0.5 in a canopy of spherical leaf distribution (Martens *et al.* 1993) but generally varies between about 0.25 and 0.75 for natural needle- and broad-leaf canopies (Jarvis and Leverenz, 1983). The main geometric difference between the canopy interaction of solar and airborne lidar laser pulse radiation is that solar radiation is incident at all zenith angles while laser pulses are typically incident only at overhead ($\theta = 0$ to 30 degrees) angles. Therefore, any direct lidar estimate of P will be for approximately overhead gap fraction only and for a path length close to the height of the canopy. However, by assuming randomly dispersed foliage elements, an isotropic canopy radiation environment (i.e. equal transmittance in all directions) and ignoring the division of woody and leafy foliage, it is possible to derive a first approximation of LAI as a function of the overhead gap fraction:

$$LAI = -\frac{\ln(P)}{k} \quad (3)$$

Several studies have used this or a similar approach to estimate P and LAI from lidar data. In particular, Solberg *et al.* (2006) used this approach and assumed that P could be approximated by the ratio of below canopy returns to total returns. A similar but simpler approach was taken by Barilotti *et al.* (2006) where the same ratio was found to linearly correlate with LAI. The assumptions of the two previous studies were corroborated by Riaño *et al.* (2004) and Morsdorf *et al.* (2006) where the ratio of lidar canopy returns to all returns was found to be a

reasonable indicator of the inverse of gap fraction; i.e. fractional canopy cover. Morsdorf *et al.* (2006) compared canopy lidar fractional cover estimates with field-based DHP fractional cover and found the best correlation was returned when using first return data only ($r^2 = 0.73$). A method for estimating LAI that utilised laser profiling techniques was presented by Kusakabe *et al.* (2000), where field plot data were compared to the cross-sectional area contained within the lidar surface profile across the plots. The rationale underlying this approach was that LAI would increase with tree height and stem density, and both of these physical attributes would act to increase the cross sectional area of a lidar profile across a plot.

Common to the studies mentioned is that they all used laser pulse return height attributes but not the intensity. Intensity has implicitly been used in estimates of canopy gap fraction in the full waveform lidar literature where the strength of the returned signal from within or below the canopy is considered to be directly related to the transmissivity of the canopy. For example, in Lefsky *et al.* (1999), it was suggested that canopy fractional cover can be estimated as a function of the ratio of the power reflected from the ground surface divided by the total returned power of the entire waveform. It was further suggested that this power ratio needed to be adjusted as a function of different reflectance properties at ground and canopy level.

For airborne laser pulses encountering and returning from a forested canopy at near-nadir scan angles, we cannot observe the incident pulse intensity as it enters the canopy; neither can we measure the transmitted intensity after it has passed through the canopy. However, by considering the total reflected energy from the canopy to ground profile as being some proportion of the total available laser pulse intensity, and the reflected energy from ground level as a similar proportion of the transmitted pulse energy, we have a means of estimating total canopy transmissivity at near-nadir angles. Further we can assume that atmospheric transmission losses for all outgoing and returning laser pulses are similar and small in magnitude relative to canopy losses. By building on the work of Lefsky *et al.* (1999), Parker *et al.* (2001) and adapting equation (2), a general pulse return power relationship can be described for gap fraction by:

$$P = f \frac{\sum I_b}{\sum I_t} \quad (4)$$

Where $\sum I_b$ is below canopy power (the sum of all ground return intensity) and $\sum I_t$ is the total power (sum of all intensity) for the entire canopy to ground profile. However, this model does not explicitly account for potentially different probabilities associated with receiving a return signal from the ground or canopy level; i.e. the ground and lower level canopy return signals might incur two-way transmission losses due to travelling both into and out of the canopy, while those return signals at the outer envelope of the canopy do not incur any canopy transmission losses. For discrete return data, it is fair to assume that first and single returns generally have not incurred appreciable transmission losses prior to being reflected back towards the sensor. However, intermediate or last returns are, by definition, a reflected component of the residual energy left over after a previous return was reflected from a surface encountered earlier in the travel path of the emitted pulse. From Beer-Lambert's Law and assuming uniform transmission losses per unit path length travelled, it can be assumed that a below canopy (ground level) return incurs a similar proportion of transmission loss during its exit from the canopy as it did on the

way into the canopy. This leads to a variation of equation (4) such that for secondary returns within or below the canopy:

$$P = f \sqrt{\frac{\sum I_b}{\sum I_t}} \quad (5)$$

The analysis presented in this paper builds on previous research in a number of ways: 1) to sample a range of canopy LAI and light conditions, data are collected from multiple sites across an entire growing season; 2) the previously published discrete return ratio method of computing gap fraction is compared to plot-level field DHP data; and 3) new discrete return gap fraction methods are developed and tested based on equations (4) and (5) utilizing the pulse intensity information as an indicator of transmission losses within the canopy.

2. STUDY AREA

The study was conducted over a flat to rolling valley site (< 50 m total elevation variation) near Nictaux in the Acadian forest ecozone of Nova Scotia. The study area was less than 1 km wide by approximately 2 km long and comprised a number of common land cover types for this region: predominantly Acadian mixed woodland (mostly yellow birch - *Betula alleghaniensis* Britton, with some mixed pine - *Pinus* and mixed spruce - *Picea* trees). The site is the subject of ongoing lidar and agro-forestry experiments, for which supplemental ground control, plot mensuration and DHP data exist (e.g. Hopkinson *et al.* 2006).

3. METHODS

3.1 DHP data collection and analysis

Canopy gap fraction data were collected and analysed using the DHP procedures outlined in Leblanc, *et al.* (2005). DHP data collection took place on five separate occasions: April 8th, May 12th, May 28th, August 18th and October 8th. The first collection was during early spring leaf off conditions, while the second was at the commencement of leaf flush. The May 28th dataset was at intermediate seasonal leaf area levels, while August 18th was close to maximum leaf area. The final dataset was collected during the autumn senescence and leaf drop period. These five datasets, therefore, represented the full seasonal growth cycle, capturing variable leaf area and transmittance conditions.

Six Acadian mixed wood plots were established and the centre of each located using Leica SR530 global positioning system (GPS) receivers differentially corrected to the same base coordinate that was used for the airborne lidar survey. (In total we set up nine plots but the data for plots 5, 6 and 7 were not collected). Each of the six plots contained five photograph stations: one at the plot centre and one at an 11.3 m radius out from the centre at each of the four cardinal compass directions. Each station (30 in total) was marked with a stake to allow each location to be revisited. The camera was always set up level at 1.3 m above ground level to ensure consistent data collection. In total, 150 individual photographs were collected during the growing season of 2006.

All photographs were collected late in the evening on each day, immediately prior to dusk, to minimize direct sunlight and ensure even background sky illumination conditions. Photographs were collected using a Nikon Coolpix E8800 camera with a 180° fisheye (FC-E9) lens set at 8 mega pixels with an exposure setting one f stop smaller than the automatic

exposure reading to slightly under-expose the image and increase contrast between vegetation and sky. Each photograph was processed using DHP and TracWin software (S. Leblanc, Canada Centre for Remote Sensing provided to L. Chasmer through the Fluxnet-Canada Research Network).

3.2 Lidar data collection and preparation

The lidar sensor used was an Optech Incorporated (Toronto, Ontario) airborne laser terrain mapper (ALTM) 3100 owned by the Applied Geomatics Research Group (AGRG) operating at a wavelength of 1064 nm. All data were collected and processed by the authors. Five datasets were collected in 2006 coincident (within two days) of the DHP field data collections. All airborne lidar acquisitions were collected during dry conditions and using the same sensor and platform configuration. The surveys were flown at 1000 m a.g.l., 70 kHz pulse repetition frequency, peak pulse power of 7.2 kW, 0.3 mrad beam divergence (1/e) producing a footprint diameter on the ground of approximately 0.3 m, ±15 degree from nadir scan angle (30 degree field of view), 50% swath overlap with roll compensation to keep survey swaths uniform. These settings provided a sampling density of approximately 3 points per m² and ensured that every point on the ground was observed from two directions at a mean viewing angle of 7.5 degrees.

The airborne GPS trajectories were differentially corrected to the AGRG GPS base station receiver less than 5 km from the centre of the survey site. Raw lidar ranges and scan angles were integrated with aircraft trajectory and orientation data using PosPAC (Applanix, Toronto) and REALM (Optech, Toronto) software tools. The outputs from these procedures were a series of flight line data files containing las binary xyz (easting, northing, elevation, intensity) information for each laser pulse return collected.

Following lidar point position computation, the xyz data files were imported into the *Terrascan* (Terrasolid, Finland) software package for plot subsetting and to separate canopy and below canopy returns. The data acquired for the leaf-off April 8th data collection were classified using the Terrascan morphological ground classification filter to provide a digital elevation model (DEM) to which all datasets could be normalised. After normalization, all elevations for all datasets were relative to the same ground level datum; i.e. possessed heights ranging from 0 m to approximately 25 m. This allowed all returns to be divided into canopy and below canopy returns using a height threshold of 1.3 m to coincide with the height of the DHP field data.

For each of the 30 DHP stations, all laser pulse return data were extracted within a circular radius of 11.3 m. This radius was chosen as it was: a) consistent with field mensuration practices; b) was the distance between adjacent photo stations and thus provided complete plot lidar coverage; and c) was close to the optimal radius of approximately 15 m observed in Mosdorf *et al.* (2006). In addition to the canopy and below canopy classes, the return data were further subdivided into four sub-classes related to the nature of the return itself; i.e. single, first, intermediate and last returns. For the canopy class, it is possible for a return to belong to any one of the four sub classes (provided the canopy is deep enough), however, ground returns can only belong to either the last or single return sub class. This subdivision was carried out as the return number and its position in the sequence indicates whether or not the pulse has been split and incurred any energy transmission losses on its way into and out of the canopy.

3.3 Lidar gap fraction analysis

For this analysis, gap fraction was estimated from the extracted photo station and plot-level lidar data using three methods. These lidar estimates of gap fraction were then compared with the photo and plot-level DHP estimates calculated from both the single overhead annulus ring (0 - 10 degrees) and nine ring hemispherical (0 - 80 degree) data. The first was using the ratio of ground level (below canopy) returns to total returns and was known as the pulse return ratio method (P_{pr}). This method is similar to that of Solberg *et al.* (2006) and has parallels to the fractional cover methods presented by Riaño *et al.* (2004) and Morsdorf *et al.* (2006). Further, laser pulse return power ratio methods were generated using return intensity data. Two variations were tested: 1) The simple pulse intensity power ratio is based on equation (4) with no modification; i.e. Gap fraction (P_{ipr}) is estimated as the ratio of the sum of all ground level return intensities divided by the sum of total return intensity; 2) The square root power ratio (P_{sqr}) is modified from equation (5) to account for the likelihood of two-way transmission losses for intermediate or last returns as follows:

$$P_{sqr} = \frac{\left(\frac{\sum I_{GroundSingle}}{\sum I_{Total}} \right) + \sqrt{\frac{\sum I_{GroundLast}}{\sum I_{Total}}}}{\left(\frac{\sum I_{First} + \sum I_{Single}}{\sum I_{Total}} \right) + \sqrt{\frac{\sum I_{Intermediate} + \sum I_{Last}}{\sum I_{Total}}}} \quad (6)$$

Where each subscript refers to the class and/or sub-class of pulse return. In this model, first and single returns incur no reverse transmission loss through canopy and so are not square rooted, while intermediate and last returns should lose similar proportions of energy due to interception on both incoming and outgoing transmission; i.e. a power function loss. It is possible that differences in ground and canopy reflectance could influence these results. However, an adjustment of equation (6) based on reflectance is not presented here, as ground level vegetation, canopy level woody material and spatio-temporal variations in both make most assumptions about systematic reflectance variations invalid.

4. RESULTS

The seasonal variation in DHP gap fraction (P_{DHP}) is clearly visible in Figure 1. The mean overhead (0 to 10 degrees zenith) and hemispherical (0 to 80 degrees zenith) P_{DHP} statistics, lidar ground-to-total return ratio (P_{pr}), the simple intensity power ratio (P_{ipr}) and the square root intensity power ratio (P_{sqr}), along with the coefficients of determination (r^2) are presented in Table 1. All results illustrate high correlations suggesting that any one of these methods can be used to estimate gap fraction (or fractional cover). While there are high correlations for all three lidar gap fraction methods, we see that the best correlation for both the 80 and 10 degree P_{DHP} results, however, is using the simple intensity power distribution ratio.

	Summary		r^2	
	Mean	SD	P_{DHP} 10 deg	P_{DHP} 80 deg
P_{DHP} (10 degree)	0.46	0.24		
P_{DHP} (80 degree)	0.36	0.17	0.92	
Ground return ratio (P_{pr})	0.62	0.18	0.81	0.86
Intensity power ratio (P_{ipr})	0.43	0.31	0.89	0.92
Square root Power ratio (P_{sqr})	0.46	0.25	0.86	0.92

Table 1. Gap fraction summary statistics (n = 150)

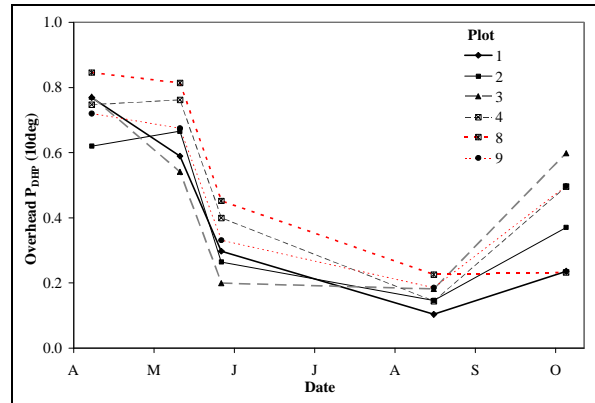


Figure 1. Plot-level seasonal DHP overhead gap fraction.

The r^2 values for the DHP 9 ring (0 to 80 degree) hemispheric gap fraction results are higher than those for the single overhead annulus ring (0 to 10 degree) due to the larger area sampled and subsequent increased stability in the data (Table 1). For the overhead DHP gap fraction, the small field of view (radius of ~ 3.5 m at a canopy height of 20 m), leads to an increased likelihood of localised variations in canopy gaps that are not representative of the overall canopy conditions. Regarding the absolute magnitude of P, we see that the intensity-based methods produce values (0.43 and 0.46 for P_{ipr} and P_{sqr} , respectively) that are within 6% of the overhead DHP value (0.46), while the pulse return ratio value (0.62) is over-estimated by 35%. In fact, the square root intensity-based method (P_{sqr}) provided the closest estimate both in magnitude and in variance (expressed as the standard deviation), despite a negligibly lower explanation of the variance ($r^2 = 0.86$) than for P_{ipr} ($r^2 = 0.89$).

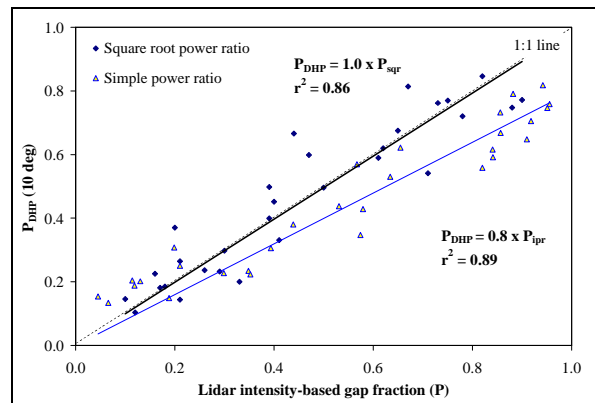


Figure 2. DHP overhead gap fraction (P_{DHP}) with lidar intensity power ratio (P_{ipr} and P_{sqr})

The high correlation and close match in absolute values is further illustrated in Figure 2, where we clearly see a 1:1 relationship between P_{DHP} and P_{sqr} . This result suggests that by applying a two-way Beer-Lambert Law transmission loss to the intermediate and last return intensity values, we are more accurately recreating the laser pulse power distribution. These results also demonstrate that by including the intensity data, we achieve both a better correlation with, and more accurate estimates of, canopy gap fraction. Of most significance here is that the lidar intensity based estimate of gap fraction appears to require no calibration.

5. CONCLUSION

While lidar ground-to-total return ratios have been demonstrated in the published literature to show strong correlation to canopy gap fraction and fractional coverage, it is shown here that for the mixed wood environment studied, the model can be improved slightly (r^2 increase from 0.86 to 0.92) by considering the lidar power distribution ratio as reconstructed from the laser pulse intensity data. Moreover, if the intensity power distribution is modified to account for secondary return two-way pulse transmission losses within the canopy, the resultant gap fraction model requires no calibration and provides a 1:1 direct estimate of overhead gap fraction. This is an improvement over the ground-to-total pulse return ratio where it was found that despite a good correlation with DHP gap fraction, the actual value predicted was over-estimated by approximately 35%. The implications of these observations are that: a) canopy transmissivity in overhead zenith directions can be directly quantified from lidar data without the need for ground calibration; and b) if the canopy extinction coefficient is *a priori* known or can be estimated from look up tables, the plant area index can also be mapped. If canopy clumping, woody-to-total and needle-to-shoot ratios are known, then such estimates of plant area index can be converted to leaf area index.

References

- Barilotti A., Turco S., Alberti G. 2006. *LAI determination in forestry ecosystems by LiDAR data analysis*. Workshop on 3D Remote Sensing in Forestry, 14-15/02/2006, BOKU Vienna.
- Chen, J.M. 1996. Optically-based methods for measuring seasonal variation in leaf area index of boreal conifer forests. *Agric. Forest Meteorol.* 80: 135-163.
- Chen, J.M., Govind, A., Sonnentag, O., Zhang, Y., Barr, A., and Amiro, B. 2006. Leaf area index measurements at Fluxnet-Canada forest sites. *Agric. Forest Meteorology*. 140:257-268.
- Gower, S.T., Kucharik, C. J. and Norman, J.M. 1999. Direct and indirect estimation of leaf area index, f_{APAR} , and net primary production of terrestrial ecosystems. *Remote Sensing of Environment*. 70:29-51.
- Hopkinson, C., Chasmer, L., Lim, K., Treitz, P., Creed, I. 2006. Towards a universal lidar canopy height indicator. *Canadian Journal of Remote Sensing*, 32(2):139-152.
- Jarvis P.G. and Leverenz J.W. 1983. Productivity of temperate, deciduous and evergreen forests. In: Lange OL, Nobel PS, Osmond CB, Zeigler H, eds. *Physiological plant ecology IV. Ecosystem processes: mineral cycling productivity and man's influence. Encyclopedia of plant physiology*, Vol. 12D. Berlin: Springer Verlag, 233-80.
- Kusakabe, T., Tsuzuki, H., Hughes, G. and Sweda, T. 2000. Extensive forest leaf area survey aiming at detection of vegetation change in subarctic-boreal zone. *Polar Biosci.*, 13, 133-146.
- Leblanc, S.G., Chen, J.M., Fernandes, R., Deering, D., and Conley, A. 2005. Methodology comparison for canopy structure parameters extraction from digital hemispherical photography in boreal forests. *Agric. and Forest Meteorology*. 129:187-207.
- Lefsky, M.A., Cohen, W.B., Acker, S.A., Parker, G.G., Spies, T.A., and Harding, D. 1999. Lidar Remote Sensing of the Canopy Structure and Biophysical Properties of Douglas-Fir Western Hemlock Forests. *Remote Sens. Environ.*, 70:339-361.
- Magnussen, S. and Boudewyn, P. 1998. Derivations of stand heights from airborne laser scanner data with canopy-based quantile estimators. *Can. Jnl of Forest Research* 28: 1016-1031.
- Martens, S.N. Ustin, S.L. Rousseau, R.A. 1993. Estimation of tree canopy leaf area index by gap fraction analysis. *For. Ecol. Manage.* 61:91-108.
- Morsdorf, F., Kotz, B., Meier, E., Itten, K.I., Allgower, B. 2006. Estimation of LAI and fractional cover from small footprint airborne laser scanning data based on gap fraction. *Remote Sensing of Environment*, 104(1):50-61.
- Parker, G.G., Lefsky, M.A., Harding, D.J. 2001. Light transmittance in forest canopies determined using airborne laser altimetry and in-canopy quantum measurements. *Remote Sens. Environ.*, 76:298-309.
- Pomeroy, J.W., Dion, K., 1996. Winter radiation extinction and reflection in a boreal pine canopy: measurements and modelling. *Hydrological processes*. 10: 1591-1608.
- Riaño, D., Valladares, F., Condes, S., and Chuvieco, E., 2004. Estimation of leaf area index and covered ground from airborne laser scanner (Lidar) in two contrasting forests. *Agricultural and Forest Meteorology*, 124(3-4):269-275.
- Solberg, S., Næsset E., Hanssen, K.H. & Christiansen, E. 2006. Mapping defoliation during a severe insect attack on Scots pine using airborne laser scanning. *Remote Sensing of Environment* 102: 364-376.
- Todd, K.W., Csillag, F., Atkinson, P.M. 2003 Three-dimensional mapping of light transmittance and foliage distribution using lidar. *Canadian Journal of Remote Sensing*, 29(5):544-555.
- Thomas, V; Treitz, P; McCaughey, J H.; Morrison, I. 2006. Mapping stand-level forest biophysical variables for a mixedwood boreal forest using lidar: an examination of scanning density. *Can. Jnl of Forest Research*, 36(1): 34-47.

Acknowledgements

The Canada Foundation for Innovation (CFI) and the Natural Sciences and Engineering Research Council (NSERC) is gratefully acknowledged for supporting this research. The AGRG post-graduate interns, Chris Beasy, Tristan Goulden, Peter Horne, and Kevin Garroay are thanked for their assistance with field data collection.

GLACIER SURFACE SEGMENTATION USING AIRBORNE LASER SCANNING POINT CLOUD AND INTENSITY DATA

B. Höfle^{a,b}, T. Geist^c, M. Rutzinger^{a,b}, N. Pfeifer^d

^a Institute of Geography, University of Innsbruck, Innrain 52, 6020 Innsbruck, Austria - (bernhard.hoefle,martin.rutzinger)@uibk.ac.at

^b alpS - Centre for Natural Hazard Management, Grabenweg 3, 6020 Innsbruck, Austria

^c FFG - Austrian Research Promotion Agency, Sensengasse 1, 1090 Vienna, Austria - thomas.geist@ffg.at

^d Institute of Photogrammetry and Remote Sensing, Vienna University of Technology, Gusshausstrasse 27-29, 1040 Vienna, Austria - np@ipf.tuwien.ac.at

KEY WORDS: Airborne Laser scanning, Point cloud, Segmentation, Classification, Intensity, Glaciology

ABSTRACT:

As glaciers are good indicators for the regional climate, most of them presently undergo dramatic changes due to climate change. Remote sensing techniques have been widely used to identify glacier surfaces and quantify their change in time. This paper introduces a new method for glacier surface segmentation using solely Airborne Laser Scanning data and outlines an object-based surface classification approach. The segmentation algorithm utilizes both, spatial (x,y,z) and brightness information (*signal intensity*) of the unstructured point cloud. The observation intensity is used to compute a value proportional to the surface property reflectance – the *corrected intensity* – by applying the laser range equation. The target classes *ice*, *firn*, *snow* and *surface irregularities* (mainly crevasses) show a good separability in terms of geometry and reflectance. Region growing is used to divide the point cloud into homogeneous areas. Seed points are selected by variation of corrected intensity in a local neighborhood, i.e. growing starts in regions with lowest variation. Most important features for growing are (i) the local predominant corrected intensity (i.e. the mode) and (ii) the local surface normal. Homogeneity is defined by a maximum deviation of $\pm 5\%$ to the reflectance feature of the segment starting seed point and by a maximum angle of 20° between surface normals of current seed and candidate point. Two-dimensional alpha shapes are used to derive the boundary of each segment. Building and cleaning of segment polygons is performed in the Geographic Information System GRASS. To force spatially near polygons to become neighbors in sense of GIS topology, i.e. share a common boundary, small gaps (< 2 m) between polygons are closed. An object-based classification approach is applied to the segments using a rule-based, supervised classification. With the application of the obtained intensity class limits, for ice $< 49\%$ (of maximum observed reflectance), firn 49-74% and snow $\geq 74\%$, the glacier surface classification reaches an overall accuracy of 91%.

1. INTRODUCTION

The cryosphere is a component of the Earth system that presently undergoes dramatic changes. Glaciers and ice sheets as important features of the cryosphere are sensitive to climate fluctuations and their mass balance can be used as an indicator of regional-scale climate change. Next to the quantification of glacier geometry and mass, the qualitative analysis of the glacier surface is important, as for example the identification of the snow line for subsequent parametrisation of glacier mass balance or the classification of different glacier surface facies (e.g. ice, firn, snow). Glaciological research is fundamentally based on field observations, which are rather costly and time-consuming. During the last two decades numerous studies have tested and discussed the possibilities offered by optical and radar remote sensing (summarized e.g. in Rees, 2005; Bamber and Kwok, 2004). Airborne Laser Scanning (ALS) allows for detailed mapping of glacier topography and the quantitative analysis of glacier geometry, such as changes in area and surface elevation, and subsequently mass. Not yet explored is the potential of ALS data for qualitative analysis (e.g. object detection, surface classification).

This paper presents a new method for glacier surface segmentation based on the unstructured point cloud using the full information of ALS data, namely geometry (x,y,z) and signal intensity. The proposed algorithm is fully implemented in a Geographic Information System (GIS). Hence, the GIS

vector data model and its topological processing tools can be used. The paper describes in detail the processing and segmentation steps and outlines an object-based classification. While this paper presents an application to glaciers, it shows that a common exploitation of geometry and radiometry provided by laser scanning can be jointly used to successfully segment and classify objects, where neither information source alone would suffice.

1.1 Related work

The last decade has seen increasing interest in the use of ALS for mapping and monitoring glaciers and ice sheets. One motivation was the ability of the technology to map areas of low surface texture (e.g. snow and firn) at high accuracy and resolution. To date, laser scanning for glaciological purposes has been widely and successfully applied in Antarctica and on the Greenland ice sheet (e.g. Abdalati et al., 2002), but only a few attempts have been made to utilize ALS or airborne laser profiling on mountain glaciers (e.g. Kennett and Eiken, 1997; Baltsavias et al., 2001). Geist et al. (2003) and Arnold et al. (2006) give an initial overview on potential applications of ALS in glaciology.

ALS intensity has been utilized in many fields of applications (e.g. road and building detection, strip adjustment, forestry) but only a few studies investigated its value for glaciological research (e.g. Lutz et al., 2003; Hopkinson and Demuth, 2006).

Point cloud segmentation is mostly used for anthropogenic objects/surfaces (e.g. Filin and Pfeifer, 2006; Rabbani et al., 2006). Natural surfaces, such as vegetation or glacier ice, are more likely to have a great variation in terms of geometry and reflectance characteristics. Thus, segmentation of such surfaces into homogeneous regions may be difficult. But separating homogeneous from heterogeneous surfaces already delivers valuable information, as for example the detection of glacier surface irregularities (e.g. crevasses, melt water channels, moulins, debris) surrounded by relatively homogeneous areas.

1.2 Glacier surface characteristics

The paper concentrates on the prevalent glacier surface classes *ice*, *firn*, *snow* and *surface irregularities*. The reflection characteristics of the glacier surface classes in the near-infrared wavelength of the laser scanner used in this study (1064 nm) exhibit a good spectral separability (Wolfe and Zissis, 1993). Due to the decrease of reflectance with age - metamorphosis from new to granular snow and increasing amount of absorbing particles (dirt) - different stages of snow/firn can be distinguished. Typical reflectance values are: glacier ice <0.2, firn 0.5-0.7 and fresh snow >0.7 (Rees, 2005; Hook, 2007). After correcting the laser signal intensity for spherical loss, topographic and atmospheric effects (Section 3.1), it can be used as a value proportional to surface reflectance (Ahokas et al., 2006; Höfle and Pfeifer, 2007). Lutz et al. (2003) and Hopkinson and Demuth (2006) state that the intensity is a good indicator for glacial surfaces (Fig. 1).

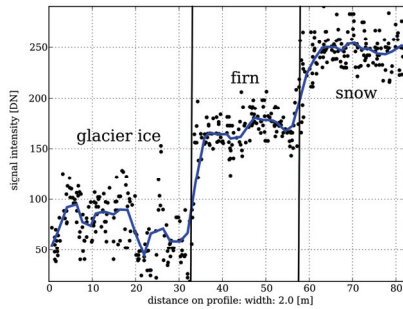


Figure 1. Corrected intensity cross-section along different surfaces: glacier ice, firn and snow. Moving average line clearly shows steps in intensity between the surface classes. Also high variability in intensity of glacier ice areas can be seen

Additionally to the corrected intensity, surface roughness can be used to describe the different classes. In general, terrain variation is increasing with proceeding melting from snow to uncovered glacier ice where irregularities due to glacier dynamics reach the upper surface, and hence are visible for the laser scanner.

2. STUDY AREA AND DATA SETS

2.1 Test site and data acquisition

Hintereisferner (Fig. 2) is a typical valley glacier with a length of approximately 6.5 km along the flow line (determined in 2005). The glacier shows a longitudinal profile with a relatively flat tongue and a steeper accumulation area. For the study described here data from 12 August 2003 is used, when most of the glacier, except the uppermost parts, was free of snow. The ALS flight campaign configurations are summarized in Table 1.

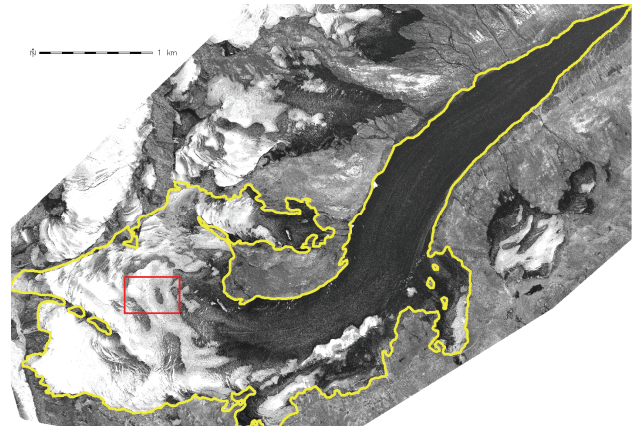


Figure 2. Corrected intensity image of Hintereisferner with glacier borders and rectangular test site

ALS campaign	
date, time	12.08.2003, 6:30–9:21
scanning system	Optech ALTM 2050
laser wavelength	1064 nm
avg. height above ground	1150 m
pulse repetition frequency	50 kHz
scan frequency	30 Hz
scan angle	+/- 20°
swath width	837 m (with 40% overlap)
avg. point density	1.7 points/m ²

Table 1. ALS flight campaign parameters

2.2 Reference data

Traditional aerial images were taken at the same day as the ALS campaign. These images were processed to orthophotos (0.5 m resolution). In order to obtain ground truth for validation, reference data for evaluating the results was created by a glaciologist aware of the local conditions. The classes ice, firn and snow were digitized using the orthophoto and the corrected intensity image. Surface irregularities were identified in the shaded relief of the ALS elevation model.

2.3 Datasets and data management

The ALS point cloud is managed within the LISA (Lidar Surface Analysis) framework (Höfle et al., 2006), which integrates full GIS functionality provided by the Open Source GIS GRASS. The results of the segmentation (segment polygons) are stored in the GRASS vector data model providing topologic geometry storage and attribute data management. For the glacier surface segmentation only single echo points are used. Plane positions, needed for intensity correction, are made available by LISA for each laser shot using linear interpolation of the GPS positions. A test site representing all target classes with 485 m x 318 m extent and 335.104 laser points was selected (Fig. 2).

3. METHODOLOGY

The developed methodology for glacier surface classification is shown in Fig. 3. The major processing steps will be described in detail below.

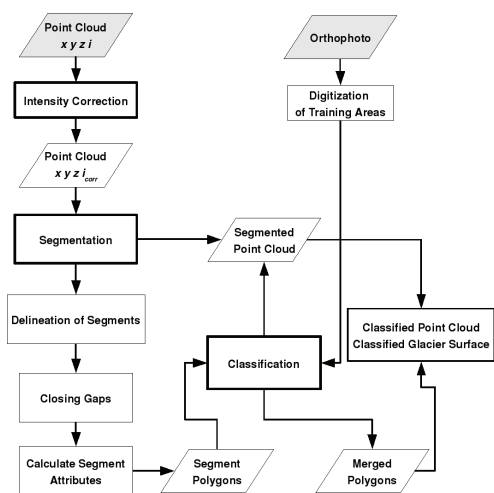


Figure 3. The workflow of glacier surface classification using the original, unstructured ALS point cloud

3.1 Intensity correction

To get a value proportional to surface reflectance, a correction procedure accounting for spherical loss, topographic and atmospheric effects has to be applied. The emitted power is assumed to be constant for the chosen flight campaign because scanner settings, such as pulse repetition frequency, are not changed. The existing data situation allows only for applying a model-driven correction approach (Eq. 1), due to the lack of multiple flying altitudes over homogeneously reflecting areas. Further details concerning intensity correction are described in Ahokas et al. (2006) and Höfle and Pfeifer (2007).

$$\rho \propto I \frac{R^2}{R_s^2} 10^{2Ra/10000} \frac{1}{\cos \alpha} \quad (1)$$

where ρ = reflectance
 I = signal intensity [digital number (DN)]
 R = range [m]
 R_s = standard/normalizing range [m]
 a = atmospheric attenuation coefficient [dB/km]
 α = angle of incidence [°]

The intensities are normalized to 1000 m range. Under the assumption of Lambertian scattering characteristics of the surface this value is proportional to surface reflectance and will be called *corrected intensity* in the following. The surface normal is estimated by fitting an orthogonal regression plane to the 30 nearest neighbors and a vertical atmospheric attenuation coefficient of 0.15 dB/km was derived by modeling the atmospheric conditions at time of flight. Fig. 4 shows the evident reduction of disturbance in intensity after correction and Fig. 2 the corrected intensity image of Hintereisferner.

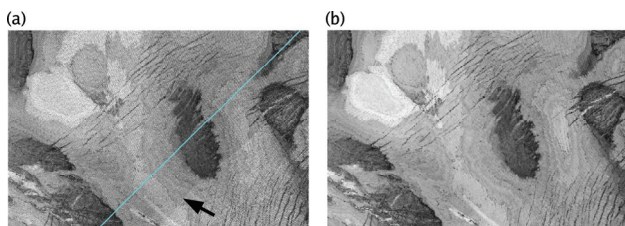


Figure 4. a) image of mean recorded intensity with flight path (cyan); strip offsets can be clearly seen (arrow), b) mean corrected intensity image

3.2 Segmentation

The point cloud is subdivided into homogeneous segments using a geometrical and intensity homogeneity criterion. Segments are defined as spatially connected regions, allowing only smooth terrain transitions (break at step edges, such as crevasses, water channels and glacier borders) and similar intensities. The segmentation steps are (i) point feature calculation, (ii) seed point selection and (iii) region growing.

3.2.1 Feature calculation: For each laser point the features are calculated from its 2D k nearest neighbors (kNN). The surface normal is estimated by fitting an orthogonal regression plane. Additionally, the standard deviation (SD) of the orthogonal fitting residuals is used as parameter for surface roughness. A representative corrected intensity value is found in the histogram by choosing the most frequent value (mode) for a given bin size. Hence, the predominant surface is selected and the influence of noise and outliers is reduced. Additionally, the coefficient of variation (c_v) of the corrected intensity is used as parameter for surface homogeneity in the local neighborhood.

3.2.2 Seed point selection: The laser points are sorted by homogeneity (c_v). The lower the variation, the more likely the point lies within a homogeneous area, representing a single surface class, well suited as start point for growing a segment. The seed points could be limited by a certain c_v threshold. Due to the inherent reflectance variation of natural surfaces and to reach an area-wide segmentation, all laser points are accepted as seed points ordered ascending by c_v .

3.2.3 Region growing: The local connectivity of segments is forced by using a small local neighborhood (e.g. $k=15$) and a maximum growing distance, as well as a maximum distance of a neighbor to the current adjusting plane of the segment (either the local surface plane of the starting seed, the current seed or the fitted plane to all current region points). To maintain similarity in terms of smoothness, the angle between the current segment plane and the surface normal of a candidate point is checked. The similarity in terms of reflectance is checked by comparing the current segment corrected intensity (either intensity feature of starting seed, current seed or mean of all current region points) with the corrected intensity feature of the candidate point. The difference must be lower than a defined percentage of the current segment intensity, i.e. for brighter objects higher absolute variation is allowed.

3.3 Delineation of point cloud segments

To be able to use an object-based classification procedure, the delineation (polygonization) of point cloud segments is necessary. The segment boundary line is derived individually for each segment by calculating a 2D basic alpha shape (i.e. based on the Delaunay triangulation of the point set) for a given alpha value (Edelsbrunner and Mücke, 1994; Da, 2006). Small alpha values not necessarily produce a convex shape. If alpha is chosen very large ($\alpha \rightarrow \infty$), the alpha shape represents the convex hull. Before calculating the alpha shapes a minimum segment size threshold (no. of points) is applied, which removes small, isolated points/regions, such as small snow spots or debris. The alpha value has to be chosen such that a connected exterior boundary can be produced. The alpha complex consists of non-ordered boundary line segments. Using GIS tools a clean polygon boundary is built (connect line segments; remove duplicate vertices and small islands; Fig. 5).

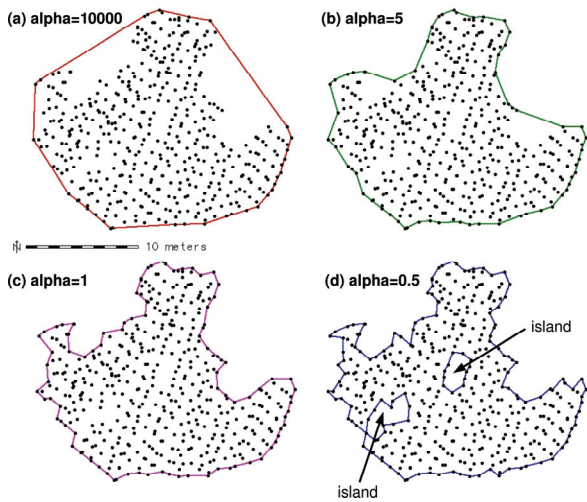


Figure 5. Segment boundary derived from point cloud alpha shape using different alpha values. a) With alpha=10000 the convex hull is reached, d) with small alpha values islands can occur

3.4 Removal of overlaps and closing of gaps between segment polygons

As the segment polygons are derived individually small overlaps and gaps may occur between the single segment polygons. With higher alpha values, more overlapping is necessarily produced. The lower the density of acquired points, the more areas are not covered by a polygon. Cleaning of segment polygons is proceeded as following (Fig. 6):

1. Buffer polygons (define max. gap size) and intersect with gap areas (areas not covered by any polygon).
2. Create Voronoi diagrams of segment boundary vertices. Voronoi polygons get ID of corresponding segment.
3. Intersect gap areas within buffer size with Voronoi diagrams. Assign segment ID to intersection polygons.
4. Merge intersection polygons with segment polygon sharing same ID.
5. Merge overlapping areas (intersections) and very small areas ($<2.0 \text{ m}^2$) with adjacent segment sharing longest boundary.

The buffer size should not be too large (e.g. half of estimated gap size) because the segments also grow into the areas not covered by any segment, which are later used to identify surface irregularities. After closing small gaps spatially near polygons share a common boundary line and therefore agree with the definition of neighbor in sense of GIS vector topology.

3.5 Calculate segment attributes

The segment attributes are directly derived from the point cloud (Sect. 3.2.1) but also from the segment polygon. Most important attributes are number of points, descriptive statistical values (e.g. min, mean, max) for elevation, corrected intensity, roughness (SD of plane fitting), as well as polygon area, point density and compactness ($\text{perimeter} / (2 * \sqrt{\text{PI} * \text{area}})$).

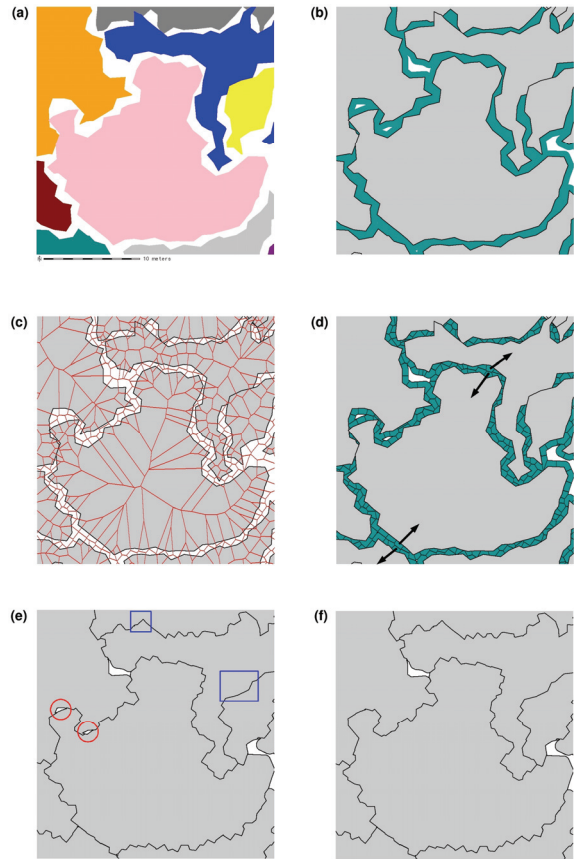


Figure 6. a) segment polygons derived from alpha shapes, b) 1.0 m buffer (green) c) Voronoi diagrams (red lines) of boundary points, d) intersection of Voronoi diagrams with buffer area, e) intersection areas attached to segment polygons; overlaps are already removed (blue squares), small leftover areas to be removed (red circles), f) resulting segment polygons after filling gaps and removing overlaps

3.6 Classification

To show the potential of the proposed segmentation for glacier surface mapping, a simple rule-based classification with manually defined training areas is applied. Training areas are digitized on basis of the orthophoto (Fig. 7b). In a first step the range of corrected intensity values for each target class is derived from the segments spatially selected by the training areas. The second classification feature roughness is preliminary grouped into three classes: low $<0.1 \text{ m}$, medium $0.1-0.25 \text{ m}$, and high $\geq 0.25 \text{ m}$ (Kodde et al., 2007). In a second step the segments are labeled according to the classification (e.g. snow with low roughness, ice with medium roughness). Polygons of areas not covered by any segment are derived and labeled as class *surface irregularities*. Using the compactness of the polygon shape the irregularities could be further divided into “longish” (e.g. if high roughness: crevasses, low roughness: superficial stream) and “compact” (e.g. moulins). Using the segment ID the classification can be assigned to the laser points resulting in a classified point cloud.

3.7 Merge of segments - dissolving of common boundaries

Due to the cleaning of the vector topology (e.g. close gaps, remove overlaps) neighboring segments falling into the same class can be easily dissolved along shared boundary lines to

larger polygons. The IDs of the segments are stored and therefore the connection to the segment attributes is kept.

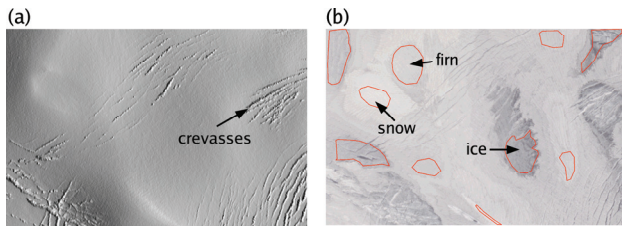


Figure 7. Test site: a) shaded relief b) orthophoto with training areas

4. RESULTS

A fundamental result of the proposed algorithm is the corrected intensity, which can be used to produce undistorted intensity images (Figs. 2 and 4b). Intensity offsets between flight strips and topographic effects have been successfully removed. Using the intensity mode of a given neighborhood for segmentation leads to a removal of outliers and small surface structures (e.g. debris), but also results in a certain classification of the intensity dependent on the chosen bin size of the histogram. A bin size of 5% of the total value range (max. 20 classes) for 50 kNN delivers appropriate values. If the bin size is too small, the mode is not representative anymore. If it is chosen too large, spectral classes are lost. To guarantee defined intensity homogeneity a maximum deviation of $\pm 5\%$ to the intensity of the segment starting seed point is set for growing. To allow smooth terrain transitions but stop growing at step edges, a maximum angle of 20° between the surface normals of current seed and candidate point is specified. The angle criterion is set low enough to get segment boundaries fitting well to the edges of crevasses (Figs. 7 and 8). The alpha shape value for segment delineation should be larger than the double average point spacing else too many islands are produced. An alpha value of 1.5 m was set due to the 0.7 m avg. point spacing of the test site. A larger alpha value would lead to more overlapping segments. Closing gaps between adjacent segment polygons is necessary because the boundaries are individually derived. The double of the buffer around the polygons determines the maximum gap size that is closed. A buffer size of 1.0 m was chosen, and hence gaps of max. 2.0 m are closed but also non-covered areas are shrinked or even fully closed, such as narrow crevasses. Filling gaps and cleaning of polygons is computationally very expensive (a lot of intersection with many polygons). If contextual information is not needed for classification, one could first classify the point cloud, merge the points of adjacent segments of the same class and then derive the boundaries and close gaps. But in comparison to our approach, the question of how to define a clear adjacency of point cloud segments can be more ambiguous.

The classification rules are determined using the manually delineated training areas. The distributions of the three classes partly overlap. The following corrected intensity values (in percentage of maximum observed value in test site) were extracted: ice 38% (11.3% SD), firm 64% (6.7% SD) and snow 85% (6.2% SD). In the ice areas of our test site also small snow and firm spots can be found, which results in a high SD for ice areas. The upper ice class limit is set to class mean+1 SD, whereas for firm and snow a class limit of mean \pm 1.5 SD is used. Hence, the classification rules are: ice <49%, firm 49-74% and snow \geq 74%. The roughness feature is not used to identify the surface classes but to independently subdivide the objects into the roughness classes low, medium and high (Sect. 3.6). The

areas remaining uncovered even after filling gaps emerge from areas with no laser points or areas with a high variability in intensity or elevation. These areas are summarized as “surface irregularities”. Once the segments are classified, the building of larger units by merging neighboring segments is straightforward.

Error assessment was performed using a point wise comparison method. For that purpose the classified point cloud was additionally labeled according to the reference map. The overall classification accuracy turned out to be 90.92%, whereas the spatial accuracy of the object boundaries strongly depends on point density and distribution. The given average point spacing of 0.7 m and closing of gaps <2.0 m fully agree with the state-of-the-art requirements for operational tasks in glacier monitoring, which state a min. horizontal accuracy of ± 2 m, in most cases even lower, to be sufficient (Jackson et al., 2001). Ice areas were found to have a good separability but there is a weak transition between firm and snow (Fig. 8), which can be explained by the advanced age of the snow (in August).

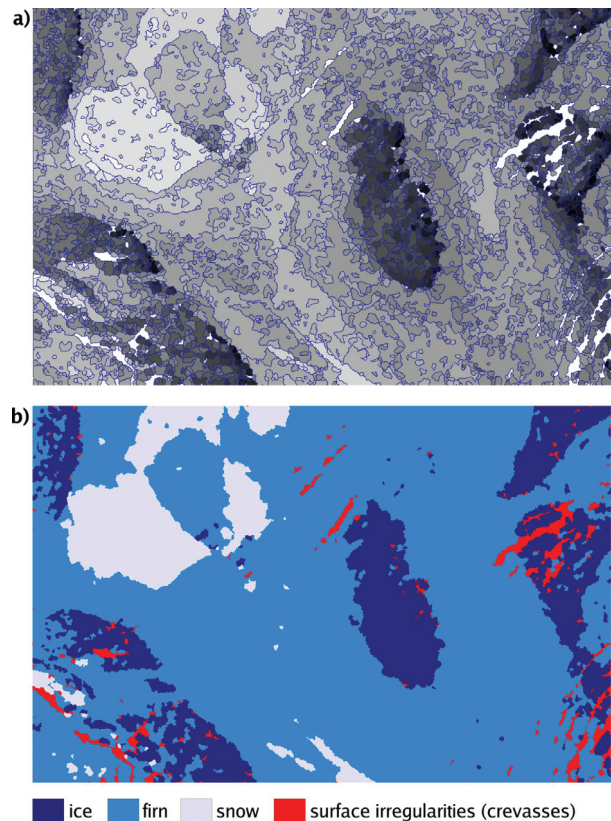


Figure 8. a) Segments colored by mean corrected intensity (black - low intensity, light gray - high intensity, white - unsegmented); b) glacier surface classification

5. CONCLUSIONS

The paper has presented a new workflow for glacier segmentation and classification using spatial and intensity information of the unstructured ALS point cloud. Most ALS sensors already record signal intensity, hence available without additional costs. Homogeneous objects concerning reflectance could be successfully derived. ALS intensity data surpasses the orthophoto in distinguishing between ice and firm (or snow), and in areas with shadows, which are very often in high mountainous areas. The accuracy of the classification is

certainly sufficient for glacier inventory mapping but should be assessed for applications in detailed scales, as for example collect GPS data of distinct objects (e.g. ice and snow spots, crevasses). The segmentation, i.e. the zoning of the glacier into areas with homogeneous surface characteristics, highly reduces data with defined loss of information (homogeneity criteria), and already represents a valuable input for energy balance and melt process models. For the conversion of corrected intensity (DN) to reflectance values defined reflectance targets are needed (Ahokas et al., 2006). The surface classification supports glacier monitoring and facilitates the creation of glacier inventories solely using ALS data. The class "surface irregularities" is important for multitemporal analyses, such as feature tracking of objects for flow velocity estimation or glacier dynamics monitoring (e.g. closing and opening of crevasses). Future work will concentrate on

- applying the methodology to larger areas with more surface classes (e.g. debris, water). Additional classification features have to be selected (e.g. use roughness for surface identification).
- utilization of geometrical and contextual relationships provided by the segment vector topology
- object-based error assessment (spatial and qualitative accuracy) of the classification. Ground truth data has to be collected.
- improving the intensity correction by applying individual reflectance functions for the detected surface classes (e.g. anisotropic reflectance for snow)

REFERENCES

- Abdalati, W., Krabill, W., Frederick, E., Manizade, S., Martin, C., Sonntag, J., Swift, R., Thomas, R., Wright, W., Yungel, J., 2002. Airborne laser altimetry mapping of the Greenland ice sheet: application to mass balance assessment. *Journal of Geodynamics*, 34(3), pp. 391-403.
- Ahokas, E., Kaasalainen, S., Hyypää, J., Suomalainen, J., 2006. Calibration of the Optech ALTM 3100 laser scanner intensity data using brightness targets. In: *The International Archives of the Photogrammetry, Remote Sensing and Spatial Information Sciences*, Marne-la-Vallée, France, Vol. XXXVI, Part A1, on CD-ROM.
- Arnold, N.S., Rees, W.G., Devereux, B.J., Amable, G.S., 2006. Evaluating the potential of high-resolution airborne LiDAR data in glaciology. *International Journal of Remote Sensing*, 27(5-6), pp. 1233-1251.
- Baltsavias, E.P., Favey, E., Bauder, A., Bösch, H., Pateraki, M., 2001. Digital Surface Modelling by Airborne Laser Scanning and Digital Photogrammetry for Glacier Monitoring. *Photogrammetric Record*, 17(98), pp. 243-273.
- Bamber, J.L., Kwok, R., 2004. Remote sensing techniques for observing land and sea ice. In: *Mass balance of the cryosphere: observations and modelling of contemporary and future changes*. Cambridge University Press, pp. 59-113.
- Da, T.K.F., 2006. 2D Alpha Shapes. In: *CGAL-3.2 User and Reference Manual (CGAL Editorial Board)*. http://www.cgal.org/Manual/3.2/doc_html/cgal_manual/content_s.html (accessed 1 May 2007).
- Edelsbrunner, H., Mücke, E.P., 1994. Three-dimensional alpha shapes. *ACM Transactions on Graphics*, 13(1), pp. 43-72.
- Filin, S., Pfeifer, N., 2006. Segmentation of airborne laser scanning data using a slope adaptive neighborhood. *ISPRS Journal of Photogrammetry and Remote Sensing*, 60(2), pp. 71-80.
- Geist, T., Lutz, E., Stötter, J., 2003. Airborne laser scanning technology and its potential for applications in glaciology. In: *The International Archives of the Photogrammetry, Remote Sensing and Spatial Information Sciences*, Dresden, Vol. XXXIV, Part 3/W13, pp. 101-106.
- Höfle, B., Rutzinger, M., Geist, T., Stötter, J., 2006. Using airborne laser scanning data in urban data management - set up of a flexible information system with open source components. In: *Proceedings of UDMS 2006: 25th Urban Data Management Symposium*, Aalborg, Denmark, pp. 7.11-7.23.
- Höfle, B., Pfeifer, N., 2007. Correction of laser scanning intensity data: data and model-driven approaches. *ISPRS Journal of Photogrammetry and Remote Sensing*, doi:10.1016/j.isprsjprs.2007.05.008 (in press).
- Hook, S.J., 2007. ASTER Spectral Library. Jet Propulsion Laboratory, Californian Institute of Technology, <http://speclib.jpl.nasa.gov/> (accessed 1 May 2007)
- Hopkinson, C., Demuth, M.N., 2006. Using airborne lidar to assess the influence of glacier downwasting on water resources in the Canadian Rocky Mountains. *Canadian Journal of Remote Sensing*, 32 (2), pp. 212-222.
- Jackson, M., Sharov, A.I., Geist, T., Elvehøy, H., Pellikka, P., 2001. OMEGA - User Requirement Document. Project Report, 16 p.
- Kennett, M., Eiken, T., 1997. Airborne measurement of glacier surface elevation by scanning laser altimeter. *Annals of Glaciology*, 24, pp. 293-296.
- Kodde, M.P., Pfeifer, N., Gorte, B.G.H., Geist, T., Höfle, B., 2007. Automatic glacier surface analysis from airborne laser scanning. In: *The International Archives of the Photogrammetry, Remote Sensing and Spatial Information Sciences*, this volume.
- Lutz, E., Geist, T., Stötter, J., 2003. Investigations of airborne laser scanning signal intensity on glacial surfaces - Utilizing comprehensive laser geometry modeling and orthophoto surface modeling (a case study: Svartisheibreen, Norway). In: *The International Archives of the Photogrammetry, Remote Sensing and Spatial Information Sciences*, Dresden, Vol. XXXIV, Part 3/W13, pp. 143-148.
- Rabbani, T., Heuvel, F.A. van den, Vosselman G., 2006. Segmentation of point clouds using smoothness constraint. In: *The International Archives of the Photogrammetry, Remote Sensing and Spatial Information Sciences*, Dresden, Vol. XXXVI, Part 5, pp. 248-253.
- Rees, W.G., 2005. *Remote Sensing of Snow and Ice*. Taylor & Francis.
- Wolfe, W.L., Zissis, G.J., 1993. *The Infrared Handbook*. Revised Edition. IRIA Series in Infrared and Electro Optics. The Infrared Information Analysis (IRIA) Center, Environmental Research Institute of Michigan.

RADIOMETRIC CALIBRATION OF ALS INTENSITY

S. Kaasalainen^{a,*}, J. Hyypää^a, P. Litkey^a, H. Hyypää^b, E. Ahokas^a, A. Kukko^a, and H. Kaartinen^a

^a Finnish Geodetic Institute, Department of Remote Sensing and Photogrammetry

^b Helsinki University of Technology, Laboratory of Photogrammetry and Remote Sensing

Commission WG III/3, III/4, V/3, VIII/11

KEY WORDS: Laser Scanning, Radiometric Calibration, Laboratory Measurements

ABSTRACT:

We have developed a new concept of empirical calibration scheme for airborne laser scanner (ALS) intensity by means of portable brightness calibration targets, which can be laid out in the flight target area. The accurate radiometric calibration of these targets is based on laboratory measurements with CCD-based laser backscatter instrument and terrestrial laser scanner reference measurements in laboratory and field conditions. We also discuss the extension of this method into the usage of commercially available industrial gravels or other (natural-type) targets available *ad hoc*. We demonstrate that airborne laser intensity calibration is feasible using this type of targets, but one must take carefully into account the physical parameters related to the experiment and the targets.

1. INTRODUCTION

1.1 The Radiometric Calibration of Laser Intensity

The previous use of uncalibrated laser intensity has mainly focused on estimation of planimetric shifts between ALS strips (Burman, 2000; Maas, 2001, 2002), segmentation of ALS data (Oude Elberink and Maas, 2000), and object classification (Song et al., 2002; Matikainen et al., 2003; Clode and Rottensteiner, 2005; Luzum et al., 2005; Moffiet et al., 2005). The first attempts to calibrate laser intensity have been presented by Luzum et al., (2004); Kaasalainen et al., (2005); Coren and Sterzai, (2006); Ahokas et al., (2006); Donoghue et al., (2006). Luzum et al., (2004) assumed a signal loss related to squared distance. In Donoghue et al., (2006) a linear correction approach for intensity was found adequate. Kaasalainen et al., (2005) proposed the intensity calibration by means of a known reference target. Coren and Sterzai, (2006) suggested a method that takes into account the loss of intensity with the diverging beam, the incidence angle, and the atmospheric attenuation. An asphalt road was used as homogeneous reflecting area. Ahokas et al., (2006) proposed a more general correction method, i.e., the intensity values need to be corrected with respect to range, incidence angle (both bidirectional reflectance distribution function (BRDF) and range correction), atmospheric transmittance, attenuation using dark object addition and transmitted power (because difference in the pulse repetition frequency (PRF) will lead to different transmitter power values).

Recently, it was proposed that the future ALS could be a hyperspectral sensor (Kaasalainen et al., 2007a). Under such circumstances the classification of laser hits could be highly automated if the used hyperspectral intensity responses could be radiometrically calibrated. The development of automatic data processing algorithms for, e.g., full-waveform digitizing lidars would also require calibrated intensity information. Therefore a systematic radiometric calibration method would have direct implications in more precise surface and target characterization.

1.2 Physics of ALS calibration

The recorded ALS intensity is related to the received power, which can be given in the form (Wagner et al., 2006; modified from Ulaby et al., 1982):

$$P_r = \frac{P_t D_r^2}{R^4 \beta_t^2 \Omega} \rho A_s. \quad (1)$$

where P_r and P_t are received and transmitted power, respectively. D_r is the receiver aperture size, R is the range, β_t is the beam divergence, Ω corresponds to the bidirectional properties of the scattering, ρ is the reflectivity of the target surface, and A_s is the receiving area of the scatterer. Thus, the recorded intensity is proportional to R^2 for homogenous targets spreading over the full footprint, to R^3 for linear objects (e.g. wire), and to R^4 for individual large scatterers.

The laser pulse illuminates a given surface area that consists of several scattering points. Thus, the returned echo comprises a coherent combination of individual echoes from a large number of points (as with radars, see Elachi, 1987). The result is a single vector representing the amplitude V and phase f ($I \sim V^2$) of the total echo, which is a vector sum of the individual echoes. This means that as the sensor moves, the successive beam intensities (I) will result in different values of I . This variation is called fading. Thus, an image of a homogeneous surface with constant reflectivity will result in intensity variation from one resolution element to the next. The speckle effect gives the images acquired with laser light a grainy texture. According to Ahokas et al., (2006), the original variability of the beam intensities was about 10% for the rough calibration target.

The effect of the incidence angle, i.e., the scanning angle, depends on the roughness of the surface. For rough surfaces, the variation with respect to incidence angle change is significantly smaller than for smooth surfaces and the main variation occurs for near-nadir measurements. Since surface smoothness is defined using Fraunhofer criterion (Schanda, 1986), most

* Corresponding author. E-mail: Sanna.Kaasalainen@fgi.fi

natural targets are considered to have low variation of intensity as a function of incidence angle compared to microwave radars, where the variations with the incidence angle are significantly larger. However, recent experiments with laboratory and terrestrial lasers show that the intensity variation with the angle of incidence needs to be taken into account (see also Kaasalainen et al., 2005; Kukko et al., 2007).

1.3 Calibration Scheme for ALS

The Finnish Geodetic Institute has managed a permanent photogrammetric test field in Sjököulla, Kirkkonummi since 1994. The test field contains permanent and transportable test targets for radiometric and geometric calibration of analogue and digital aerial cameras. Since 2000, airborne lidar testing has also been carried out using a set of eight portable 5x5 meter brightness targets (tarps) with calibrated reflectances of 70% (A), 50% (B), 40% (C), 26% (D), 20% (E), 16% (F), 8% (G), and 5% (H) (Kaasalainen et al., 2007b). These tarps have been used in airborne laser campaigns as well as laboratory and field reference measurements. This article presents the results from flight campaigns carried out in 2005-2006, and evaluates the feasibility of using these targets in brightness calibration and the accuracy of the results.

The radiometric calibration scheme of the Finnish Geodetic Institute, presented first in Ahokas et al. (2006), was based on using these brightness calibration tarps. The brightness targets were calibrated in the laboratory at two different wavelengths and repeated reference measurements have been carried out with both terrestrial laser scanner and a laboratory laser instrument (Kaasalainen et al., 2005, 2007b). The brightness targets act as a near-Lambertian reference, which are needed for the development of the radiometric calibration scheme for ALS.

Because of the inconveniences and limitations of the effective use of the large-size tarps, we also discuss the ongoing investigations of the usage of gravel and natural targets in radiometric measurement and calibration.

2. EXPERIMENTS

2.1 Airborne Laser Flights

The brightness calibration method based on the calibration tarps has been tested in several laser scanner flight campaigns. The first complete radiometric calibration of all the eight targets was carried out during the Optech ALTM 3100 airborne laser scanner surveys (July 12th and 14th, 2005) at the Sjököulla photogrammetric test field (Ahokas et al., 2006). The measurements were carried out at flight altitudes of about 200, 1000, and 3000 meters with a 1064 nm laser source. A more detailed description is in (Ahokas et al., 2006). At this campaign, the lowest flight altitudes (200 m and 1000 m) were found most suitable for intensity calibration.

The tarps were also used in the Espoonlahti full waveform flight campaign (Aug 31st, 2006), which used the TopEye MKII 1064 nm laser scanner. The flight altitude was 300 meters and the test area consisted of the Espoonlahti boat harbour and beach. The TopEye instrument recorded the entire waveform. Four of the targets (8%, 16%, 50%, and 70%, see also Fig. 1) were measured during these flights (Kaasalainen et al., 2007b). Another TopEye MK-II campaign occurred at the same site in December 2006, where the 5%, 20%, 26%, and 40% targets

were measured. Four targets (5%, 16%, 40%, and 70%) were also measured at the Nuuksio flight campaign (14-15 May 2006). The data were acquired at the altitude of 1097 m with the Optech ALTM laser scanner. The most important parameters of all the flight campaigns are summarized in Tables 1 and 2.



Figure 1. Four of the brightness calibration targets arranged for airborne laser measurement in Espoonlahti, Dec 2006. Each target is 5x5 m in size.

Location & Date	Instrument	Wavelength (nm)	Altitude (m)
Sjököulla Jul 05	Optech	1064	200
Nuuskio May 06	Optech	1064	1097
Espoonlahti Aug 06	Topeye	1064	300
Espoonlahti Dec 06	Topeye	1064	100 200 300 500 700

Table 1. Summary of some laser scanner flight parameters from different calibration flight campaigns. See also Table 2.

Altitude	Tarp 5 %	Tarp 20 %	Tarp 26 %	Tarp 40 %
100 m	702	645	413	1679
200 m	280	237	251	125
300 m	62	85	325	402
500 m	11	14	13	17
700 m	18	18	95	73

Table 2. Number of sample points at the Espoonlahti Dec 2006 campaign. The intensities were then sampled as an average of the entire set of points for each tarp. The hits near the edges of the targets were excluded (i.e., if there was a significant change in intensity in the vicinity of a data point, it was interpreted to be near the edge of the target and excluded).

2.2 Validation Measurements in the Laboratory

Laboratory measurements are the only means of correcting the directional effects from backscattered laser intensity, which have been found to be common and affect substantially to the lidar intensity. They also provide an accurate reference for the intensity measurement. The laboratory laser instrument has been constructed to operate in the similar illumination/observation geometry as in laser scanning (i.e., exact backscatter where the source and detector light paths coincide). The instrument (Fig. 2) comprises a 1064 nm Nd:YAG laser (wavelength similar to most airborne scanners), and 16-bit monochrome CCD-camera,

which is a commonly used detector in laboratory (laser) measurements in, e.g., optical physics (Yoon et al., 1993). More details on the laboratory experiment are found in (Kaasalainen et al., 2007). We averaged five 3-second images for each target. The backscattered laser intensities were measured from the CCD images by means of standard photometric techniques.

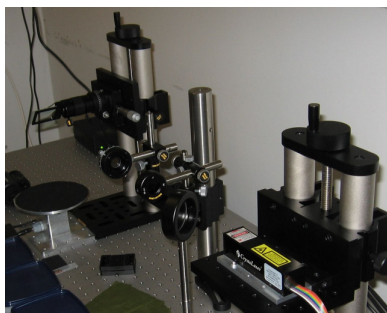


Figure 2. The laboratory laser measurement. The laser beam is reflected into the sample from a plate beam splitter (top left) and observed through the beam splitter with the CCD camera mounted above the instrument. Neutral density filters and a quarter-wave ($\lambda/4$) plate are used to avoid saturation of the detector and to scramble the linear polarization of the laser, respectively.



Figure 3. The FARO terrestrial laser scanner measuring a 4-step (12%, 25%, 50%, and 99%) Spectralon reflectance calibration plate (Labsphere Inc.).

The reflectance of a calibration target must be independent of the measurement technique and instrument, i.e. the relative intensities measured in different campaigns must be in agreement. To test this, we carried out laboratory reference measurements with the 785nm FARO LS HE80 terrestrial laser scanner. The scanner uses phase angle technique for the distance measurement with the accuracy of 3-5 mm and $360^\circ \times 320^\circ$ field of view. The detector of the FARO scanner is not optimized for intensity measurement: there are modifications in the detector that affect the intensity, e.g., a brightness reducer for near distances (<10 m) and a logarithmic amplifier for small reflectances. These all required an extensive and systematic distance and reflectance calibrations, which were carried out in the laboratory using the test targets and a calibrated 4-step Spectralon reflectance panel (see Fig. 3). We also made experiments for the calibration of distance and incidence angle effects (e.g., Kukko et al., 2007) and found the most suitable laboratory measurement distance to be about 1 m for brightness measurements.

3. RESULTS AND DISCUSSION

3.1 Comparison of laser intensities

The most important feature that makes a target suitable for intensity calibration is that its relative intensity is independent of the measurement system, i.e., the instrument, flight altitude, etc. To investigate this, we present a comparison of the relative intensities of the test tarps from different measurements in Table 3. The intensities of the 20% and 50% target are presented relative to the 70% target. It appears that the reflectances are generally well reproduced, but occasional deviations occur, because of random (laser) measurement errors (such as the saturation of the detector) and the contamination of the target itself due to, e.g., weather conditions. Furthermore, the angle of incidence turns out to be a crucial factor in laser intensity (Kukko et al., 2007) and causes variation in the measured intensities, which must be taken into account in surface models and intensity calibration. There is also a wavelength difference between FARO (785 nm) and the other measurements (1064 nm), which affects the relative intensities. There is a decrease in intensity towards longer wavelengths (see Fig. 4), which partially explains the differences for the targets measured with the FARO.

It is obvious that more data are needed for further testing and investigation of the materials most suitable for calibration, but these results indicate that the relative intensity calibration is possible by means of calibration targets.

Measurement (date & flight altitude)	Test tarp (%)	
	16/70	50/70
Sjökulla, Jul 05, 300 m	0.24	0.69
Espoonlahti, Aug 06, 200 m	0.37	0.72
Nuukio, May 06, 1097 m	0.21	0.58*
Laboratory, 785nm FARO	0.25	0.89
Laboratory, 1064nm Nd:YAG	0.23	0.73

Table 3. Comparison of the test target intensities from ALS flight campaigns and laboratory measurements. The intensities are scaled with the brightest (70%) target. *—The Nuukio value is for the 40% target, implying a response of 0.66 for 50% target (by interpolating the missing 50% value). (Also note that the corresponding 40%/70% value in Sjökulla measurements was 0.60.)

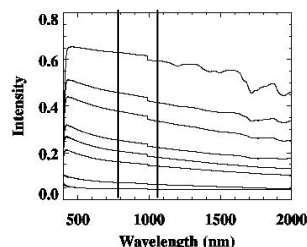


Figure 4. Reflectance spectra of the brightness tarps, measured using a flashlight illumination placed right on top of each sample (i.e. the zenith) and the detector placed at about 30° from the zenith (Kaasalainen et al., 2005). The intensities are relative to the 99% Spectralon reference plate. The 785 nm (FARO) and the 1064 nm (airborne and laboratory) wavelengths are marked with vertical lines.

We also made a further experiment on the effect from different flight altitudes on the calibration. The results are from a TopEye flight campaign in Espoonlahti, December 2006. The intensities, scaled at 100 m altitude, and relative to the brightest target (40% at this campaign) at four different flight altitudes, are presented in Table 4 and Fig. 5. (The scaling to the 100 m altitude was done by means of multiplying the original intensity by the ratio of the squared distance and the squared reference distance (100 m). The result was then divided by the squared atmospheric transmittance calculated with the MODTRAN software.) The intensity levels at different altitudes are in good agreement, i.e., the relative brightness calibration is independent on flight altitude. The relative results in Table 3 and Fig. 4, on the other hand, imply that the calibration would be independent on the instrument.

More data and a more accurate investigation on the effects of different parameters are needed to develop this concept into a well-established calibration procedure.

Altitude	Tarp 5 %	Tarp 20 %	Tarp 26 %
100 m	0.14	0.55	0.68
200 m	0.12	0.48	0.61
300 m	0.13	0.47	0.60
500 m	0.13	0.49	0.62
700 m	0.13	0.48	0.61

Table 4. Espoonlahti Dec 2006: Test target intensities relative to the brightest (40%) target. (Scaled in 100 m altitude.) The intensities are plotted in Fig. 5.

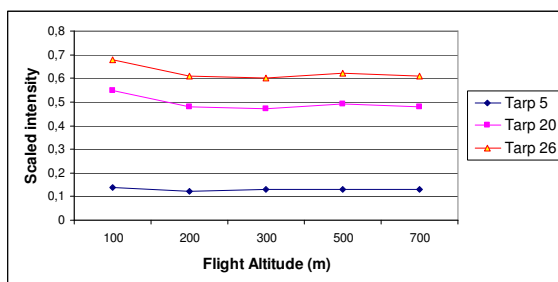


Fig. 5. Comparison of the intensities of the Espoonlahti (Dec 06) test targets (5%, 20%, 26%, and 40%) at different flight altitudes, scaled with the brightest (40%) target. (Cf. Table 4).

3.2 Discussion and Future Work

The calibration tarps provide a means to calibrate the laser scanner intensity in airborne flight measurements. They are, however, sensitive to errors caused by the weather effects, such as rain or wind changing the surface properties. The intensity signal from the wet or rugged and uneven surface may be substantially different from that of the flat and smooth or dry tarp. Because of these limitations, we are investigating the use of standard industrial gravels in brightness calibration. They would be less sensitive of, e.g., wind effects, and there could also be a possibility to calibrate, at some reduced accuracy at least, for the effects of moisture on their intensity. They have also proven more practical in field use because of easier logistics and mounting process, and their commercial availability.

The prospects of *in situ* calibration of the brightness targets (with the aid of, e.g., portable laser instruments) during a laser

scanner flight are also under study. This might enable the usage of natural targets (such as beach sands or roads) in the brightness calibration. Another alternative is to bring a sample of a natural calibration target into laboratory for more controlled reference measurement. More information is needed especially on the target reflectance properties in different weather conditions, especially because the actual targets to be calibrated also include complex vegetation surfaces. There is little information available on the laser-based reflectance calibration of vegetated surfaces, but strong directional effects have been found in the backscattered intensity of, e.g., forest understorey (Kaasalainen and Rautiainen, 2005).

In May 24, 2007, the European Spatial Data Research (EuroSDR) approved the proposal of the Finnish Geodetic Institute and the Technical University of Vienna to develop a practical ALS intensity calibration method for national mapping and cadastre agencies and companies during 2007-2008.

3.3 Applications

The intensity calibration procedure has applications in, e.g., the utilization and processing of the data from full-waveform lidars (which have recently become common) into calibrated backscatter cross-sections. This would offer a possibility of classifying the data based on the shape of the returned laser pulse and the cross-section amplitude, and thus facilitate the development of more accurate digital terrain models and more effective classification of targets. The calibration technique will also enhance the methods of monitoring and mapping of forests (e.g. tree growth), construction, and agriculture. There are also prospects for environmental change detection and monitoring, such as snowmelt or snow/glacier albedo variation, hydrological processes and climate change.

3.4 Acknowledgements

This work was financially supported by the Academy of Finland (projects "Improving the Applicability of Intensity Information in Laser Scanning", "The use of ICT measurement techniques for high-quality construction", and "Novel Aspects in Airborne Laser Scanning in Forests", and no. 121476, and the TEKES Waveform project.

REFERENCES

- Ahokas, E., Kaasalainen, S., Hyypä, J., and Suomalainen, J., 2006. Calibration of the Optech ALTM 3100 laser scanner intensity data using brightness targets. In: *The International Archives of the Photogrammetry, Remote Sensing and Spatial Information Sciences*, Marne-la-Vallee, France, Vol. 36, Part A1, CD-ROM.
- Burman, H., 2000. Adjustment of laserscanner data for correction of orientation errors. In: *The International Archives of the Photogrammetry, Remote Sensing and Spatial Information Sciences*, Vol. 33, Part B3/1, 125-132.
- Clode, S. P. and Rottensteiner, F., 2005. Classification of trees and powerlines from medium resolution airborne laserscanner data in urban environments. *Proceedings of the APRS workshop on digital image computing (WDIC)*, Brisbane, Australia, 2005, 191-196.

- Coren, F. and Sterzai, P., 2006. Radiometric correction in laser scanning. *International Journal of Remote Sensing*, 27 (15-16), 3097-3104.
- Donoghue, D., Watt, P., Cox, N., and Wilson, J., 2006. Remote sensing of species mixtures in conifer plantations using LiDAR height and intensity data. International Workshop 3D remote sensing in Forestry, February 2006, Vienna. (http://www.rali.boku.ac.at/fileadmin/_/H857-VFL/workshops/3drsforestry/presentations/6a.5-donoghue.pdf).
- Elachi, C., 1987. *Introduction to the physics and techniques of remote sensing*. John Wiley & Sons.
- Kaasalainen, S., Ahokas, E., Hyypää, J., and Suomalainen, J., 2005. Study of surface brightness from backscattered laser intensity: calibration of laser data. *IEEE Geoscience and Remote Sensing Letters*, 2 (3), 255-259.
- Kaasalainen, S. and Rautiainen, M. 2005. Hot spot reflectance signatures of common boreal lichens. *J. Geophys. Res.*, 110 (D20), D20102.
- Kaasalainen, S., Lindroos, T., Hyypää, J., 2007a. Toward hyperspectral lidar - Measurement of spectral backscatter intensity with a supercontinuum laser source. *IEEE Geoscience and Remote Sensing Letters*, 4 (2), 211- 215.
- Kaasalainen, S., Kukko, A., Lindroos, T., Litkey, P., Kaartinen, H., Hyypää, J., and Ahokas, E., 2007b. Brightness measurements and calibration with airborne and terrestrial laser scanners. *IEEE Trans. Geosci. Remote Sensing*, submitted for publication.
- Kukko, A., Kaasalainen, S., and Litkey, P., 2007. Effect of incidence angle on laser scanner intensity and surface data. Manuscript in preparation.
- Luzum, B., J., Starek, M., and Slatton, K. C., 2004. Normalizing ALSM intensities. Geosensing Engineering and Mapping (GEM) Center Report No. Rep_2004_07_001, Civil and Coastal Engineering Department, University of Florida, (http://www.aspl.ece.ufl.edu/reports/GEM_Report_2004_07_001.pdf), 8p.
- Luzum, B. J., Slatton, K. C., Shrestha, R. L., 2005. Analysis of spatial and temporal stability of airborne laser swath mapping data in feature space. *IEEE Trans. Geosci. Remote Sensing*, 43 (6), 1403-1420.
- Maas, H.-G., 2001. On the use of pulse reflectance data for laserscanner strip adjustment. In: *The International Archives of the Photogrammetry, Remote Sensing and Spatial Information Sciences*, Vol. 34, Part 3/W4, 53-56.
- Maas, H.-G., 2002. Methods for measuring height and planimetry discrepancies in airborne laserscanner data. *Photogrammetric Engineering and Remote Sensing*, 68, 933-940.
- Matikainen, L., Hyypää, J., and Hyypää, H., 2003. Automatic detection of buildings from laser scanner data for map updating. In: *The International Archives of the Photogrammetry, Remote Sensing and Spatial Information Sciences*, Vol. 34, Part 3/W13, 218-224.
- Moffiet, T., Mengersen, K., Witte, C., King, R., and Denham, R., 2005. Airborne laser scanning: Exploratory data analysis indicates potential variables for classification of individual trees of forest stands according to species. *ISPRS Journal of photogrammetry & remote sensing*, 59, 289-309.
- Oude Elbelink, S., and Maas, H.-G., 2000. The use of anisotropic height texture measures for the segmentation of laserscanner data. In: *The International Archives of the Photogrammetry, Remote Sensing and Spatial Information Sciences*, Vol. 33, Part B3/2, 678-684.
- Schanda, E., 1986. *Physical fundamentals of remote sensing*. Springer-Verlag, Berlin and New York.
- Song, J.-H., Han, S.-H., Yu, K., and Kim, Y.-I., 2002. Assessing the possibility of land-cover classification using lidar intensity data. In: *The International Archives of the Photogrammetry, Remote Sensing and Spatial Information Sciences*, Vol. 34, Part 3B, 259-262.
- Ulaby, F. T., Moore, R. K., and Fung, A. K., 1982. *Microwave remote sensing. Active and passive. Radar remote sensing and surface scattering and emission theory, vol. II*. Artech House Inc., Norwood.
- Wagner, W., Ullrich, A., Ducic, V., Melzer, T., and Studnicka, N., 2006. Gaussian decomposition and calibration of a novel small-footprint full-waveform digitising airborne laser scanner. *ISPRS Journal of photogrammetry & remote sensing*, 60, 100-112.
- Yoon, G.D., Roy, N.G., and Straight, R.C., 1993. Coherent backscattering in biological media: measurement and estimation of optical properties. *Applied Optics*, 32 (4), 580-585.

EXTENDING GENERALIZED HOUGH TRANSFORM TO DETECT 3D OBJECTS IN LASER RANGE DATA

Kourosh Khoshelham

Optical and Laser Remote Sensing Research Group, Delft University of Technology, Kluyverweg 1, 2629 HS Delft, The Netherlands
k.khoshelham@tudelft.nl

KEY WORDS: Laser scanning, Point cloud, Object Recognition, 3D Generalized Hough Transform, Automation

ABSTRACT:

Automated detection and 3D modelling of objects in laser range data is of great importance in many applications. Existing approaches to object detection in range data are limited to either 2.5D data (e.g. range images) or simple objects with a parametric form (e.g. spheres). This paper describes a new approach to the detection of 3D objects with arbitrary shapes in a point cloud. We present an extension of the generalized Hough transform to 3D data, which can be used to detect instances of an object model in laser range data, independent of the scale and orientation of the object. We also discuss the computational complexity of the method and provide cost-reduction strategies that can be employed to improve the efficiency of the method.

1. INTRODUCTION

Automated extraction of objects from laser range data is of great importance in a wide range of applications. Reverse engineering, 3D visualisation, industrial design monitoring and environmental planning are a few examples of the applications that require 3D models of objects extracted from images or laser range data. A 3D model provides an abstract description of the object, which can be processed and visualised more easily and efficiently. The process of object extraction consists of two main tasks. The first task is detection, in which the presence of an object in the data is verified, and its approximate location is found (usually by labeling the data points that belong to the object). The second task is modeling, where the detected object is represented with a 3D geometric model that is most adequate in terms of such criteria as accuracy, compactness, the domain of the object and the application requirements. The detection step plays a key role in the successful modeling of the object. If the object is properly detected in the data, the modeling can be carried out more reliably and accurately.

Existing approaches to the detection of objects in range data can be divided into two major categories: data-driven approaches and model-driven approaches. Data-driven approaches are mainly based on segmentation (Khoshelham, 2006; Rottensteiner and Briese, 2003; Sithole, 2005), clustering (Filin, 2002; Vosselman, 1999) and classification (Forlani et al., 2006; Oude Elberink and Maas, 2000). While these methods have been commonly applied to the laser range data of 2.5D surfaces, their application to more complex 3D scenes is not always possible. For instance, in laser range data of industrial installations many objects are partially occluded and data-driven methods fail to correctly detect these objects in the data. Model-driven approaches, on the contrary, are more robust in the presence of partial occlusion, since they incorporate some form of knowledge about the shape of the object. The object model can be represented, among other

representations, as a set of voxel templates (Greenspan and Boulanger, 1999) or spin images (Johnson and Hebert, 1999), which are matched against the data or as a set of parameters that mathematically define the object. In the latter case, Hough transform (Duda and Hart, 1972; Hough, 1962) has been used to determine the model parameters as well as the data points that belong to the object (Olson, 2001).

The application of Hough transform is restricted to simple objects that can be represented with few parameters, such as planes, spheres and cylinders. Vosselman et al., (2004) describe a Hough-based method for the detection of planes and spheres in a point cloud. Rabbani (2006) developed an extension of this method that can be used for the detection of cylinders. Figure 1 demonstrates the application of Hough transform to the detection of cylinders in a point cloud. As can be seen, the curved parts joining the cylinders have not been extracted because these parts cannot be expressed in parametric forms with few parameters.

This paper concentrates on the detection of 3D objects with arbitrary shapes in a point cloud. The objective of this paper is to develop a new extension of Hough transform, which can be used to detect instances of a complex object model in laser range data, independent of the scale and orientation of the object.

The paper has five sections. Section 2 provides an overview of the standard and generalized Hough transform as applied to 2D images. In section 3, the principles of the 3D generalized Hough transform is described. A discussion on the computational complexity of the method is presented in section 4. Conclusions appear in section 5.

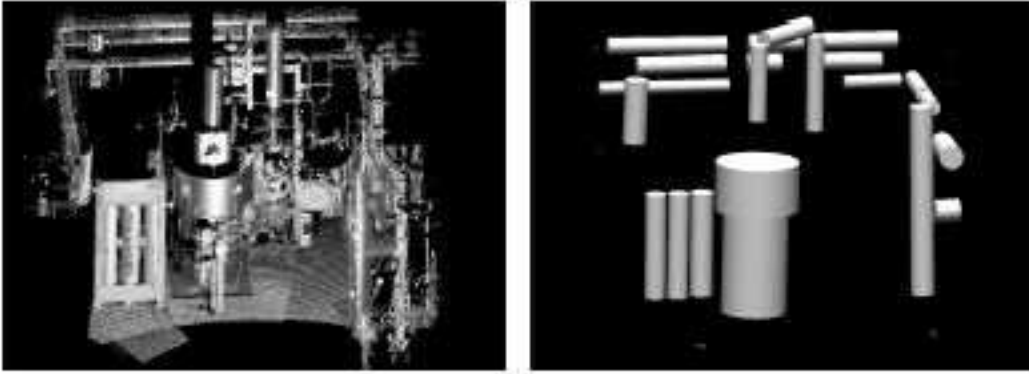


Figure 1. Detection of cylinders in a point cloud using Hough transform (from Rabbani (2006)). The curved parts joining the cylinders cannot be extracted using this method.

2. AN OVERVIEW OF THE STANDARD AND GENERALIZED HOUGH TRANSFORM

Hough transform is a well known method for the detection of objects in 2D intensity images. The standard Hough transform is applicable to objects with an analytical shape such as straight lines, circles and ellipses; whereas, with the generalized Hough transform any arbitrary curve can be detected in a 2D image. The following sections briefly describe the standard and generalized Hough transform.

2.1 The standard Hough transform

The idea of Hough transform for detecting straight lines in images was first introduced by Hough (1962). In the original Hough transform, a straight line is parameterized as $y = mx + b$ with two parameters m and b . According to the number of parameters, a 2D parameter space is formed in which every point in the image space corresponds to a line $b = -xm + y$. A set of image points that lie on a same line $y = mx + b$ in image space correspond to a number of lines in the parameter space, which intersect at point (m, b) . Finding this intersection point is, therefore, the basis for line detection in Hough transform. The parameter space is realized in the form of a discrete accumulator array consisting of a number of bins that receive votes from edge pixels in the image space. The intersection point is determined by finding the bin that receives a maximum number of votes.

In addition to straight lines, Hough transform has been used to detect also other analytical shapes, such as circles and ellipses, in 2D images. The underlying principle for the detection of other analytical shapes is the same as for the straight line detection, and is based on constructing a duality between edge pixels in the image and object parameters in the parameter space. The dimensions of the parameter space, however, vary with respect to the parameterization of the object.

2.2 The generalized Hough transform

Ballard (1981) proposed a generalization of Hough transform to detect non-parametric objects with arbitrary shapes in 2D intensity images. In the generalized Hough transform, the object model is stored in a so-called R-table format. An arbitrary reference point is selected for the object, and for every pixel on the object boundary the gradient direction as well as the length and direction of a vector connecting the boundary pixel to the reference point are computed (Figure 2). The gradient directions, φ , serve as indices in the R-table to look up the

length, r , and direction, β , of the connecting vectors. Table 1 illustrates a general form of an R-table.

Table 1: R-table

Point	φ	\mathbf{r}
0	0	$(r, \beta)_{01} - (r, \beta)_{02} - (r, \beta)_{03} - \dots$
1	$\Delta\varphi$	$(r, \beta)_{11} - (r, \beta)_{12} - (r, \beta)_{13} - \dots$
2	$2\Delta\varphi$	$(r, \beta)_{21} - (r, \beta)_{22} - (r, \beta)_{23} - \dots$
...	...	

The reconstruction of the object model from the R-table is straightforward:

$$\begin{cases} x_p = x_c - r \cdot \cos(\beta) \\ y_p = y_c - r \cdot \sin(\beta) \end{cases} \quad (1)$$

where (x_c, y_c) and (x_p, y_p) are respectively the coordinates of the reference point and a point on the boundary of the object. For the detection of the object model in the image, however, the coordinates of the reference point are not known. A 2D accumulator array is, therefore, constructed with the two parameters of the reference point as the axes. At every image edge pixel the gradient direction is obtained and then looked up in the R-table. The corresponding sets of r and β values are used to evaluate Equation 1, and the resulting x_c and y_c values indicate the accumulator array bins that should receive a vote. Once this process is complete for all edge pixels, the bin with the maximum vote indicates the reference point, and the edge pixels that cast vote for this bin belong to an instance of the object in the image.

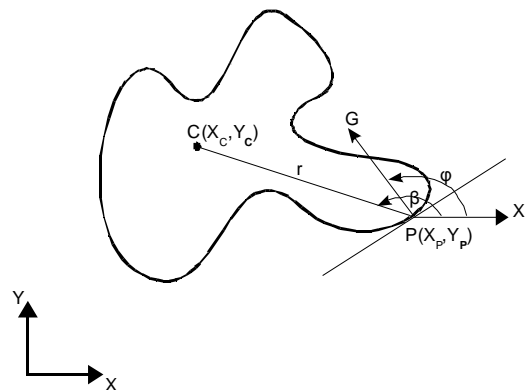


Figure 2: Parameters involved in the generalized Hough transform.

The generalized Hough transform can also be used to detect a rotated and scaled version of a model in an image. This is achieved by supplementing Equation 1 with a scale factor and a rotation angle, and the parameter space is expanded to a 4D accumulator array. The peak of the accumulator array determines the scale and rotation parameters in addition to the coordinates of the reference point, although at the price of a higher computational expense.

2.3 Modifications to Hough transform

Several modified variations of the Hough transform have been proposed to improve the performance of the method. Illingworth and Kittler (1988) provide a survey of these methods. Duda and Hart (1972) suggested a modification of the standard Hough transform by substituting the original slope-intercept parameterization of straight lines with a polar, angle-radius, parameterization. The polar parameterization leads to a bounded parameter space, unlike the original parameterization, and is, consequently, more computationally efficient. They also showed that standard Hough transform can be used to detect more general curves in an image. Gradient weighted Hough transform, as appears in Ballard's generalization, was first introduced by O'Gorman and Clowes (1976). The derivation of edge orientation information imposes very little computational cost, but greatly increases the efficiency of the method. Other methods that have been shown to improve the performance of Hough transform include Adaptive Hough transform (Illingworth and Kittler, 1987), Hierarchical Hough transform (Princen et al., 1990), and Randomized Hough transform (Xu et al., 1990).

3. EXTENSION OF GENERALIZED HOUGH TRANSFORM TO 3D DATA

In this section we present an extension of the generalized Hough transform to 3D data. The method will be referred to as 3D GHT in the subsequent parts of the paper. The 3D GHT follows the same principle as generalized Hough transform as outlined in Section 2.2. The main difference is that the gradient vector is replaced with a surface normal vector. The normal vectors can be obtained by triangulating the surface of the object or by fitting planar surfaces to small sets of points in a local neighbourhood. Vectors connecting each triangle to an arbitrary reference point are stored in the R-table as a function of the normal vector coordinates. A normal vector is constrained to be of unit length and is, therefore, defined by two orientation angles, φ and ψ , as depicted in Figure 3. A connecting vector is defined by two orientation angles, α and β , as well as its length r . These parameters can be derived from the coordinates of the reference point and the object boundary point:

$$\begin{aligned} r &= [(x_p - x_c)^2 + (y_p - y_c)^2 + (z_p - z_c)^2]^{1/2} \\ \alpha &= \arccos\left(\frac{z_c - z_p}{r}\right) \\ \beta &= \arccos\left(\frac{x_c - x_p}{r \sin(\alpha)}\right) \end{aligned} \quad (2)$$

This formulation results in a 2D R-table where all the connecting vectors, \mathbf{r} , are stored in cells whose coordinates are the orientation angles of the normal vectors. Figure 4 demonstrates how such a 2D R-table is constructed.

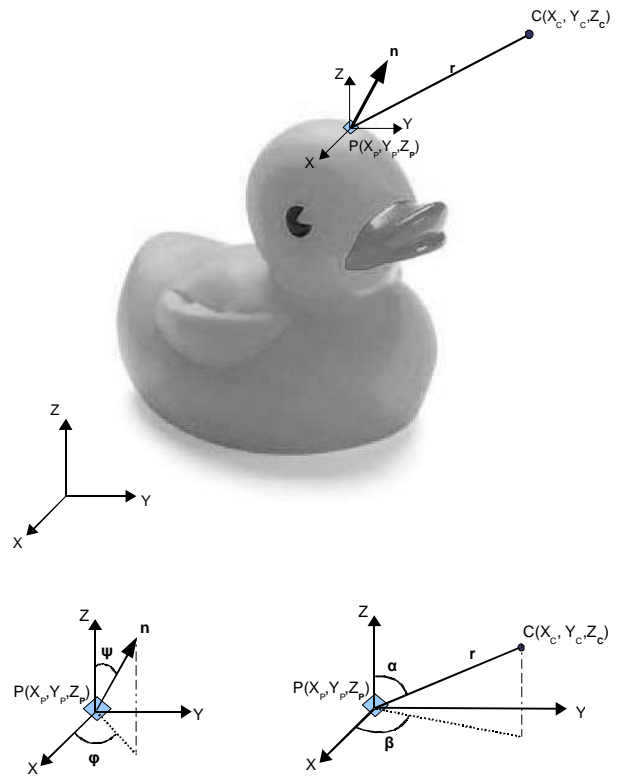


Figure 3: Parameters involved in the 3D GHT method.

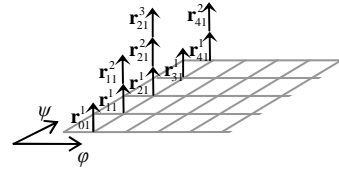


Figure 4: Storing \mathbf{r} vectors in a 2D R-table.

The reconstruction of the object model from the R-table is carried out by extending Equation 1 to 3D:

$$\begin{cases} x_p = x_c - r \cdot \sin(\alpha) \cos(\beta) \\ y_p = y_c - r \cdot \sin(\alpha) \sin(\beta) \\ z_p = z_c - r \cdot \cos(\alpha) \end{cases} \quad (3)$$

where α and β denote the orientation angles of the vector that connects a point p to the reference point c . For the detection of the 3D object model in a point cloud the three coordinates of the reference point are unknown parameters. Thus, the equations given in (3) are rearranged so as to express the unknown parameters as functions of the known variables:

$$\begin{cases} x_c = x_p + r \cdot \sin(\alpha) \cos(\beta) \\ y_c = y_p + r \cdot \sin(\alpha) \sin(\beta) \\ z_c = z_p + r \cdot \cos(\alpha) \end{cases} \quad (4)$$

Having obtained the object model in the form of the R-table, an algorithm for the detection of instances of this model in a point cloud can be outlined as follows:

1. Construct a 3D accumulator array with the three parameters of the reference point as the axes;

2. Compute the normal vector for every point in the point cloud and look up r vectors at coordinates (φ, ψ) of the 2D R-table;
3. Evaluate Equation (4) with the corresponding sets of r , α and β values to obtain x_c , y_c and z_c ;
4. Cast a vote (an increment) to the accumulator array bin corresponding to each set of x_c , y_c and z_c values;
5. Repeat the voting process for all the points in the point cloud;
6. The bin with the maximum vote indicates the reference point, and the 3D points that cast vote for this bin belong to an instance of the object in the point cloud.

In practice, the object appears in range data with an arbitrary rotation and scale. To account for the additional rotation and scale parameters, Equation (4) is modified as:

$$\mathbf{c} = \mathbf{p} + s\mathbf{M}_z \cdot \mathbf{M}_y \cdot \mathbf{M}_x \cdot \mathbf{r} \quad (5)$$

where $\mathbf{c} = (x_c, y_c, z_c)^T$, $\mathbf{p} = (x_p, y_p, z_p)^T$, $\mathbf{r} = (r \sin(\alpha) \cos(\beta), r \sin(\alpha) \sin(\beta), r \cos(\alpha))^T$ s is a scale factor and \mathbf{M}_x , \mathbf{M}_y and \mathbf{M}_z are rotation matrices around x , y and z axis respectively. The incorporation of a scale factor and three rotation parameters results in an expansion of the Hough space to seven dimensions. To evaluate Equation 5 and cast votes for the accumulator bins, a 4D space circumventing the entire range of scale factors and rotation angles must be exhausted. This implies that the crude application of the 3D GHT method to object detection can be very expensive. Therefore, cost-reduction strategies such as adaptive, hierarchical and randomized voting schemes are of great importance in the 3D GHT algorithm.

4. IMPLEMENTATION ASPECTS

The 3D GHT method as described in Section 3 is computationally expensive when the object appears in data with an arbitrary scale and rotation with respect to the model. The development of a cost-reduction strategy is thus the main challenge in the application of 3D GHT. In general, the execution time of Hough transform is more dominated by the voting process rather than by the search for a peak in the accumulator. In the absence of arbitrary scale and rotation, the number of required operations in the voting process is $O(M)$, where M is the number of points in the dataset. Thus, a desirable cost-reduction strategy must aim to reduce the number of points that are involved in the voting process. Randomized (Xu et al., 1990) and probabilistic (Kiryati et al., 1991) variations of the Hough transform work based on a random selection of a small number of data points, and are, therefore, suitable options for controlling the computational cost of the voting process..

In the presence of arbitrary scale and rotation, a 4D subset of the parameter space circumventing the entire range of scale factors and rotation angles is exhausted during the voting process. Consequently, the number of operations required in the voting process is $O(M \cdot N^4)$, where N is the number of intervals along each axis of the accumulator array. Clearly, a desirable cost-reduction strategy in this case must concentrate on the N^4 factor. The adaptive Hough transform (Illingworth and Kittler, 1987) reduces the number of intervals along axes since it begins with a coarse-resolution parameter space and increases the resolution only in the vicinity of the peak. The randomized Hough transform (Xu et al., 1990) also provides an efficient

strategy to reduce the number of bins that receive votes in the parameter space. In the randomized voting, instead of working with one point at a time, a number of points sufficient for the computation of all parameters are selected from the data. Once all the parameters are computed, only one bin in the accumulator array receives a vote. In the case of a 3D object with seven parameters, a set of three points must be selected from the data at each time. These points along with their respective \mathbf{r} vectors form nine equations of the form given in Equation 5, which can be solved for the seven parameters. Thus, for each randomly selected set only one vote is cast for a bin in the 7D accumulator array.

5. CONCLUSIONS

In this paper we presented an extension of the generalized Hough transform to detect arbitrary 3D objects in laser range data. The procedure of storing a 3D model in a 2D R-table was demonstrated, and a method for the detection of instances of the model in a point cloud, based on a voting process, was described. It was discussed that the voting process can be computationally expensive in the case that the object appears in data with an arbitrary scale and rotation with respect to the model. The employment of a voting process based on the randomized Hough transform was, therefore, suggested to reduce the computational cost of the method.

REFERENCES

- Ballard, D.H., 1981. Generalizing the Hough transform to detect arbitrary shapes. *Pattern Recognition*, 13(2): 111-122.
- Duda, R.O. and Hart, P.E., 1972. Use of the Hough transformation to detect lines and curves in pictures. *Communications of the ACM*, 15: 11-15.
- Filin, S., 2002. Surface clustering from airborne laser scanning data, *Proceedings of the Photogrammetric Computer Vision, ISPRS Commission III Symposium*, Graz, Austria, pp. 119-124.
- Forlani, G., Nardinocchi, C., Scaioni, M. and Zingaretti, P., 2006. Complete classification of raw LIDAR data and 3D reconstruction of buildings. *Pattern Analysis & Applications*, 8(4): 357-374.
- Greenspan, M. and Boulanger, P., 1999. Efficient and reliable template set matching for 3D object recognition, *2nd International Conference on 3-D Digital Imaging and Modeling*, Ottawa, Canada, pp. 230-239.
- Hough, P.V.C., 1962. Methods and means for recognizing complex patterns, US patent 3069654.
- Illingworth, J. and Kittler, J., 1987. The adaptive Hough transform. *IEEE Transactions on Pattern Analysis and Machine Intelligence*, 9(5): 690-698.
- Illingworth, J. and Kittler, J., 1988. A survey of the Hough transform. *Computer Vision, Graphics and Image Processing*, 44: 87-116.
- Johnson, A.E. and Hebert, M., 1999. Using spin images for efficient object recognition in cluttered 3D scenes. *IEEE Transactions on Pattern Analysis and Machine Intelligence*, 21(5): 433-449.
- Khoshelham, K., 2006. Automated 3D modelling of buildings in suburban areas based on integration of image and height data, *International Workshop on 3D Geoinformation (3DGeoInfo '06)*, Kuala Lumpur, Malaysia, pp. 381-393.
- Kiryati, N., Eldar, Y. and Bruckstein, A.M., 1991. A probabilistic Hough transform. *Pattern Recognition*, 24(4): 303-316.

- O'Gorman, F. and Clowes, M.B., 1976. Finding picture edges through collinearity of feature points. *IEEE Transactions on Computers*, 25(4): 449-456.
- Olson, C.F., 2001. A general method for geomtric feature matching and model extraction. *International Journal of Computer Vision*, 45(1): 39-54.
- Oude Elberink, S. and Maas, H.G., 2000. The use of anisotropic height texture measures for the segmentation of airborne laser scanner data, *International Archives of Photogrammetry and Remote Sensing*, 33 (Part B3/2), pp. 678-684.
- Princen, J., Illingworth, J. and Kittler, J., 1990. A hierarchical approach to line extraction based on the Hough transform. *Computer Vision, Graphics and Image Processing*, 52(1): 57-77.
- Rabbani Shah, T., 2006. Automatic reconstruction of industrial installations using point clouds and images PhD thesis Thesis, Delft University of Technology, Delft, 154 pp.
- Rottensteiner, F. and Briese, C., 2003. Automatic generation of building models from Lidar data and the integration of aerial images, *International Archives of Photogrammetry and Remote Sensing, Volume XXXIV/3-W13*, Dresden, pp. 170-184.
- Sithole, G., 2005. Segmentation and classification of airborne laser scanner data. PhD Thesis, Delft University of Technology, Delft, 185 pp.
- Vosselman, G., 1999. Building reconstruction using planar faces in very high density height data, *ISPRS Conference on Automatic Extraction of GIS Objects from Digital Imagery*, Munich, pp. 87-92.
- Vosselman, G., Gorte, B.G., Sithole, G. and Rabbani Shah, T., 2004. Recognising structure in laser scanner point cloud, *International Archives of Photogrammetry, Remote Sensing and Spatial Information Sciences*, Vol. 46, Part 8/W2, Freiburg, Germany, pp. 33-38.
- Xu, L., Oja, E. and Kultanen, P., 1990. A new curve detection method: randomized Hough transform (RHT). *Pattern Recognition Letters*, 11(5): 331-338.

TREE HEIGHT ESTIMATION METHODS FOR TERRESTRIAL LASER SCANNING IN A FOREST RESERVE

G. Király^{a*}, G. Broly^a

^a Univ. of West H, Dept. of Surveying and Remote Sensing, 9400 SOPRON, Bajcsy-Zs. 4, Hungary
(kiraly.geza, gbrolly)@emk.nyme.hu

Commission III, WG III/3, VIII/11

KEY WORDS: Terrestrial Laser scanning, Forestry, Photogrammetry, Modelling, Single tree

ABSTRACT:

A terrestrial laser scanning survey has been performed on a forest reserve site. This paper represents the processing of the dataset. Two new methods have been developed for tree positioning, which is necessary for height calculation. One of them is the clustering method, the other is the so-called crescent moon method. The stems were modelled, as high as possible, by both methods. Two methods were tested for height estimation. One was a direct method based upon the Digital Surface Model; however a new method was developed to predict the tree-top based upon the modelled trunk and then the nearest local maximum was selected to that predicted point in the DSM. The other was an indirect method, where the modelled stems were described as paraboloids, and the heights were extrapolated. The accuracies of the methods were investigated by means of photogrammetric measurements based on very high-resolution aerial images. Both the clustering and crescent moon methods were appropriate in tree positioning and stem modelling. The height estimation based upon the DSM yielded good results. The extrapolation method was tested for European Larch only. The height in one-third of the cases was estimated by this method within tolerance. This method can be taken into consideration in the case of leaves on scanning in very dense, multi-storey forests.

1. INTRODUCTION

Sixty-eight forest reserves have been established in Hungary to protect and study natural or semi-natural forest ecosystems. Some of these reserves are selected for long-term investigations, and a permanent sampling network has been established. These network points are the geometric base for the collection of different data, such as the forest stand parameters, soil, vegetation and so on (Horváth et al. 2001). Single-tree mapping is not the main objective of these networks, but some of them include stem maps created with conventional instruments, and demand is growing for remote sensing methods producing single tree maps. Terrestrial laser scanning is an available opportunity to automate data acquisition in forests. Several researchers have reported promising results in applicability in forest inventories, e.g. Thies & Spiecker (2004), Aschoff et al. (2004).

Forest Reserve 46, situated next to the Austrian border, was selected for this study. This reserve is a mountainous mixed, almost coeval forest stand with oak, hornbeam, beech, larch and spruce species. The spruces are dying of bark beetle disease.

2. MATERIAL

2.1 TLS data

The terrestrial laser scanning (TLS) was carried out on a permanent sample plot, No. 05-11, in leaf-off state, in April 2006 with a Riegl Z420i instrument. The configuration of the data acquisition can be seen in Figure 1. The scanning was done on the whole upper hemisphere at three different tilting angles, resulting in a vertical range from -40° to 90° with a 0.055° angle resolution. There were three further surveying points from

which the surveys were done toward the sample plot at approx. 180° horizontal, and from -40° to 90° vertical angles with a 0.12° angle resolution. The data acquisition, the registration and the colour coding were performed by the surveying company.

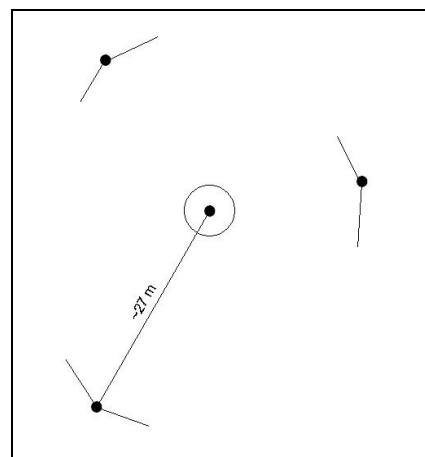


Figure 1. The configuration of the TLS data acquisition

2.2 Aerial images

Very large scale, colour metric aerial photographs were taken in April 2005. The parameters of the photography can be seen in Table 1.

Parameters	Value
Date	2 April 2005
Camera	Wild RC-20
Film type	KODAK AEROCROME III
Focal length	153.1 mm
FHAG	~600 m
GSD	4 cm

Table 1. Parameters of the aerial photography

3. METHODS

3.1 Creating Surface Models

The processing of the surface models was done based upon all four scanning positions (Figure 1). The first, and very important step, of the data-processing was the creation of the digital terrain model (DTM). The DTM was processed based upon an iterative, coarse to fine method. The points with the absolute minimum heights were selected within a cell, and then the first coarse triangulated irregular network (TIN) model was created. Then the heights relative to the previous DTM were calculated, and the points with the minimum relative heights were selected within a double resolution cell. In the raw data some points situated below the terrain surface were found to be faulty. A filtering method based upon the derivatives of the surface was applied, but some manual selections were also left. Finally the points situated on the terrain were selected and a TIN model was created.

The processing of the Digital Surface Model (DSM) was simpler, because there were no points above the tree-canopy surface. An iterative coarse to fine method was applied here as well, but always the absolute highest points were selected within the cell. A minimum curvature raster model was interpolated from the 'bumpy' selected points.

3.2 Stem modelling

Two new methods, a statistical and a geometric approach, were developed to automatically detect the position of single trees, and furthermore the stem position and size at each height layer. Both modelling methods initiate the process with the determination of a tree's position and diameter, based upon the selected points at breast heights (Figure 2).

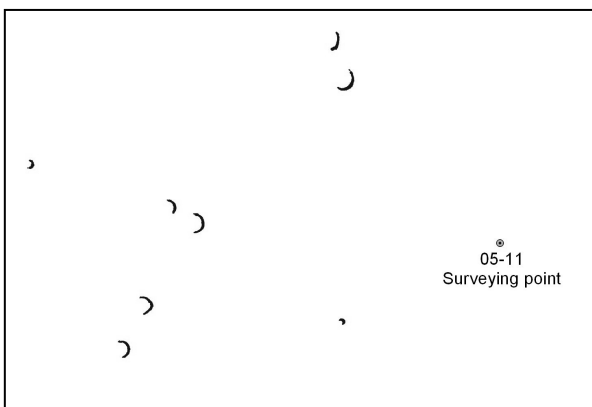


Figure 2. The shape of the points at breast heights

These processes were iterated for the selected points in slices of different height section above the terrain in both processes, but the processes differ from each other. The first approach was a statistical clustering method with a combination of a circle fitting by means of least square adjustments. The second approach was a geometric method utilising the crescent form of the points, which determines the position and diameter in one step. This method was called the crescent moon (CM) method.

3.2.1 Clustering

The point cloud was sliced for the clustering, with a surface parallel to the DTM from 1 to 18 metres above the ground by 1-metre steps. The thickness of the slices were 10 cm up to 5 meters, then it increased 10 cm for every 5 meters in elevation, because of the declining exposure of stems and the rising covering effect of neighbouring foliage.

The measurements reflected from stems form groups at each height layer, as seen in Figure 2. Grouping points of a dataset based on a similarity criterion was possible with clustering methods. Points that were measured from the same stem were much closer to each other than points measured from different stems, and thus points that were reflected from the same cross-section are represented by one cluster. The similarity was defined as the distance from the clusters' centroid. The number of clusters was usually not known at the beginning of the process. However, an interval for the approximate cluster size could be given, because the minimal and maximal diameter of trees on the sample plot could be roughly estimated. Let d_{max} denote the maximal diameter for all of the clusters. In our work d_{max} was 1.0 m. That also means the minimal distance between stems has to be larger than d_{max} , otherwise the clusters will be merged (Figure 3).

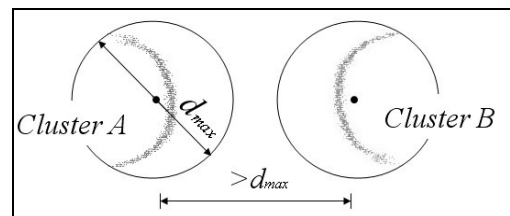


Figure 3. Rules of clustering

The algorithm worked iteratively. It read the points sequentially from a list. The actual point is labelled to the nearest cluster if it is closer than d_{max} , otherwise the point will be the centroid of a new cluster. At the end of the cycle the centroids were recalculated, and the clusters whose centroids were closer than d_{max} were merged. The iteration was continued until the changes in the coordinates of cluster centroids exceeded a given limit. After the last iteration the clusters containing fewer than 20 measurements were deleted, because these were usually bushes, branches, or other small objects.

3.2.2 Crescent Moon Method

This method utilises the more or less regular crescent moon (CM) shape of the selected points (Király et al. 2007). Starting from the surveying point, the first step was to find the nearest point. Next a test was applied to find whether the point was a CM point or a single or scattered point. The routine calculated a fitting circle in the first case, based upon three cardinal points of the shape (Figure 4). The points were sorted by the horizontal angle as seen from the surveying point. The means

were calculated for the points situated at the minimum, the mean and the maximum angle with a tolerance for the three points defining the circle.

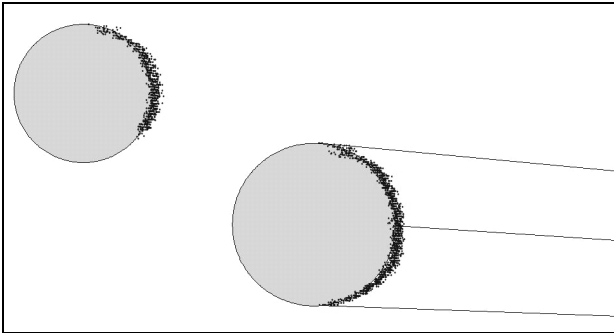


Figure 4. Fitting a circle to a crescent moon shape

When the fitting was successful and the calculated diameter at breast height (DBH) was within a tolerance, then the tree's position and DBH were recorded, the selected points – whether scattered or CM points – were deleted, and the routine was continued.

The next step of this method was the slicing. This was applied downwards from breast height to the ground, and upwards from the breast height to as high as possible by 10-cm steps. Some constraints can be defined based upon the diameter difference and the centre translation. At times the fitting was unsuccessful because of noisy points or branches, but the method allowed us to leave these slices out, and to continue normally when a successful fitting occurred.

3.2.3 Stem modelling from the fitted circles

A model of the stems could be produced based upon the circles from either of the above-mentioned methods. The model was suitable for volume calculations, demonstrations and so on (Figure 5).

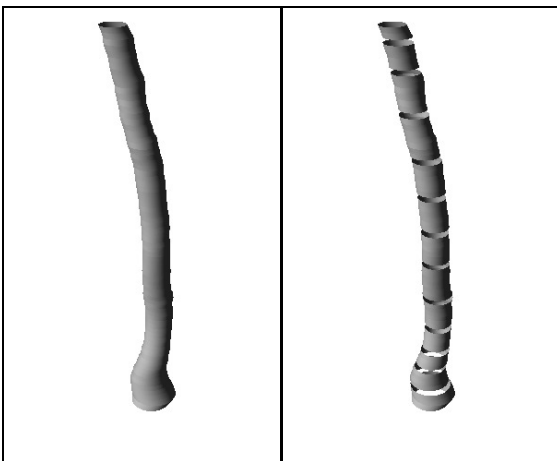


Figure 5. Two different representations of a stem model produced by the CM method

3.3 Calculating tree height by Terrestrial Laser Scanning

3.3.1 Stem form extrapolation

The lower halves of the trunks were well defined by the several fitted circles in leaves-off conditions. So one can assume that the upper half could be extrapolated to estimate the tree height.

The stems of trees can be approximated by a conoid-type geometric body of revolutions in general. For conoids the relative area of cross section is denotable with a power function of the relative length measured from the top. While the middle part of individual stems can usually be described as paraboloid, there is a linear relationship between the cross-section area and cross-section height that can be modelled with linear regression. The extrapolated value of the regression function at zero cross-section area predicts the individual tree height (Figure 6). The area of cross sections can be calculated by fitting circles onto them. In our study site the larch (*Larix decidua*) had the longest stem without branches, so only these trees were sampled. In a pre-processing step the deformed or noisy clusters were eliminated by visual inspection. Only those trees were evaluated upon which at least 10 circles could be fitted. In the next step the regression model was established for each individual tree. In spite of the manual elimination of irregular clusters, extreme diameters sometimes occurred that erroneously affected the regression models. Therefore a second filtering step was necessary, where the detection of outliers took place during an iterative regression. In every step the standard deviation of residuals (S_{xy}) was calculated, and if there was a diameter with a larger residual than $2 \cdot S_{xy}$ then it was deleted. Finally the intersection with the abscissa was calculated.

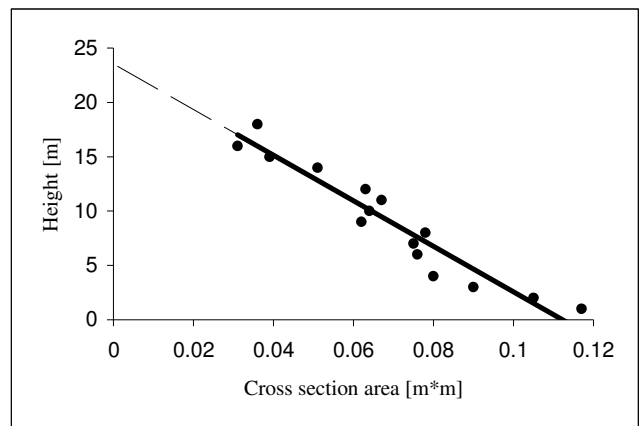


Figure 6. Estimated tree height versus cross section area

3.3.2 Calculating tree height using DSM

Tree height estimation can be done with the direct application of the digital surface model in the case of leaves-off scanning. The most problematic point in this method is finding the appropriate treetops on the DSM.

Accepting that the tree-tops are local maxima in the DSM, the task is to find the appropriate local maxima on the DSM. An inverse watershed modelling was applied to detect the local maxima (Gougeon 1995, and Király 1998).

The most obvious method is to find the nearest local maxima to the bottom of the tree in XY direction; however, this often causes mismatching. A new method was developed for predicting the treetop based upon the already modelled trunk. The modelled trunk was described as simple function of the heights. Then the predicted treetop was calculated based upon this function and the height estimated by the method above. The nearest local maximum was selected to that predicted point for the height calculation.

3.4 Reference Measurements

3.4.1 Field Measurements

A 30 m radius full circle sample with 208 trees was surveyed with total station around the sample point. Species and DBH were determined as attributes.

3.4.2 Photogrammetric Measurements on aerial images

The aerial images were evaluated using a digital photogrammetric workstation. The control points were measured by geodetic GPS surveys. The σ of the inner and relative orientations of the photos are less than 4 μ m. The RMS of the absolute orientation is better than 0.3 m. The primary mean error of Z measurements is -0.45 m. The 3D measurements on the oriented model were done manually. The measured larches were already grown green, so pointing the tip was usually effortless.

4. RESULTS AND DISCUSSION

The detection of the trees is a crucial point in automatic algorithms. There were 169 trees visible (or partly visible) from the sample point and 158 were sampled by more than 20 laser hits.

The efficiency of the modified sequential clustering in stem detection was examined visually and by means of spatial analysis in GIS software. This method clustered 158 stems altogether. The stem points were successfully clustered in 142 cases (89 %). The clustering merged two slight stems together in 4 cases. There were also 8 faulty clusters because of branches and noise. The main advantage of clustering is that it can handle point clouds from more than one scanning position in the same way. Although it is an easy and fast algorithm, it does not take account of shapes and is still unable to separate several stems if their outermost points are closer than the maximal cluster size. Noise reduction should be improved.

The CM method found 196 single trees from 169 ('116 %'), of which 166 were accurate (98 %). This method definitely over-detected the branches and noise, but was often successful with less than 20 hits. The over-detection can be reduced by the checking of the successfully detected stems. The stem modelling was not so successful; approximately half of the detected trees were modelled to at least 10 metres. The branches and junctions are difficult to model automatically with this method. The prediction of treetops worked well; the right crown was found in more than 95 % of the cases. The height calculation of this method depends on the quality of the DSM. This is the point where the height estimation from extrapolation can play a role: e.g., summer scanning with a high veil layer.

Twenty-seven larches were detected only with at least ten fitted circles along the stem, from thirty-nine total in the study area. The mean error of the prediction is 1.6 metres, which means significant underestimation. This presumably arises from the error of the model when the tops of trees are more conical than paraboloid formed. The main problem with the fitting cone is that accurate diameters above the two-third level of tree height are necessary. At such a height it is not possible to filter stem points with the methods presented here, due to the complexity of branches and crowns. We can say only in 9 cases (33%) that the accuracy of the prediction is comparable to the conventional field instruments, and gross errors often occurred (Table 2).

ID	H_photo	H_DSM	H_par	Diff_DSM	Diff_par
7	25.1	26.8	19.5	1.8	-5.6
11	25.7	26.8	25.0	1.0	-0.7
13	28.8	29.5	21.9	0.7	-6.9
20	26.1	28.9	25.6	2.7	-0.5
23	25.1	28.1	21.9	3.0	-3.2
24	27.2	27.4	30.5	0.2	3.3
25	26.6	28.2	18.8	1.6	-7.8
34	25.3	25.0	16.4	-0.3	-8.9
43	22.6	24.2	27.6	1.6	5.0
47	26.7	26.9	25.1	0.2	-1.6
53	26.5	27.3	22.3	0.8	-4.2
56	28.7	30.6	29.6	2.0	0.9
63	28.3	28.9	28.7	0.5	0.4
82	29.0	27.6	23.7	-1.4	-5.3
91	24.4	26.2	24.0	1.8	-0.4
93	28.1	28.3	23.8	0.1	-4.3
97	27.3	28.1	19.6	0.9	-7.7
99	31.1	28.1	25.6	-3.0	-5.5
100	24.8	25.7	23.0	1.0	-1.8
104	26.1	26.1	21.0	0.0	-5.1
108	28.8	28.7	24.8	-0.1	-4.0
111	27.3	26.3	25.0	-1.0	-2.3
134	25.5	26.2	25.3	0.7	-0.2
137	28.0	27.6	25.9	-0.5	-2.1
143	26.9	27.4	33.1	0.6	6.2
156	27.9	27.7	24.8	-0.2	-3.1
202	28.1	27.2	29.2	-0.9	1.1
Min				-3.0	-8.9
Max				3.0	6.2
Mean				0.5	-2.4
RMSE				1.4	4.4

Table 2. Results of the different height calculations

5. CONCLUSION

Two new methods were developed for positioning tree trunks automatically, and these methods are also suitable for positioning and measuring the slices of the stems. The right locations and directions are essential for height estimation. Both methods proved their suitability.

Height calculation based upon the DSM is not novel, but the algorithm predicting the tree top based upon the stem model is. It worked very well, although the method should be improved for curly trunks. Irrespective of the precision of the tree top, the accuracy of this method is based upon the accuracy of the DSM. The data acquisition in our study was adequate for DSM generation, but this is not always the case. Therefore, a new method was created calculating the height based upon the extrapolation of the stems. The accuracy of this method is not really adequate for practical tree height determination at this stage. With more precise filtering the upper third part of the stem should be sampled and an additional body of revolution (e.g., a cone) should be fitted.

6. REFERENCES

Aschoff, T.; Thies M.; Spiecker, H., 2004 Describing forest stands using terrestrial laser-scanning. International archives of Photogrammetry, Remote Sensing and Spatial Information Sciences Vol. XXXV, Part B, pp. 237-241.

Gougeon, F. A. 1995 A crown-following approach to the automatic delineation of individual tree crowns in highspatial resolution aerial images. Canadian Journal of Remote Sensing, 21(3): pp. 274-284

Horváth, F., Mázsa, K., Temesi, G. 2001 Forest Reserves Programme in Hungary. In: Results of the Forest Reserve Research, MTA ÖBKI, Vácrátót, Hungary pp. 6-20.

Király, G. 1998 Multiscale Images in Forestry. In ISPRS International Archives of Photogrammetry and Remote Sensing, Vol. XXXII Part 7, ISPRS Commission VII Symposium on Resource and Environmental Monitoring, September 1-4, 1998, Budapest, Hungary. pp 365-369.

Király, G., Brolly, G., Márkus, I., 2007 Application of Terrestrial Laser Scanning for Investigation on Single Trees. Bulletins of Geomatics, X. in press

Thies, M.; Spiecker, H., 2004 Evaluation and future prospects of terrestrial laser scanning for standardized forest inventories. In: Thies, M.; Koch, B.; Spiecker, H.; Weinacker, H. (ed.), Laser-Scanners for Forest and Landscape Assessment. International Archives of Photogrammetry, Remote Sensing and Spatial Information Sciences Vol XXXVI- 8/W2

REIN ALGORITHM AND THE INFLUENCE OF POINT CLOUD DENSITY ON NDSM AND DEM PRECISION IN A SUBMEDITERRANEAN FOREST

A. Kobler^{a,*}, P. Ogrinc^a

^a Slovenian Forestry Institute, Vecna pot 2, SI - 1000 Ljubljana, Slovenia - (andrej.kobler, peter.ogrinic) @gozdis.si

KEY WORDS: lidar, forest, DEM, nDSM, point cloud density, REIN algorithm

ABSTRACT:

The REIN algorithm makes use of the redundancy in lidar point cloud to generate bare ground DEM and vegetation canopy nDSM. The influence of the input lidar point density on the DEM precision and consequently also on the nDSM precision in the context of REIN have been analyzed in a rough-relief submediterranean karstic forested site. Different lidar point densities were simulated by thinning the density of the basic lidar dataset by factors of 2, 4, and 8. The DEMs and nDSMs were calculated separately from entire dataset and from the thinned lidar data. Strong smoothing effect of lidar data thinning was found in the study area both for DEM and nDSM. Based on the preset minimum precision criteria, the three highest point densities (i.e., 2.71, 5.43 and 10.85 last and only returns per m²) may be used for DEM generation in the study area, and the two highest point densities (i.e., 8.29 and 16.56 of all returns per m²) may be used to generate the nDSM. A coarser DEM raster resolution than 1 m is advised for all the lidar point densities except the highest one.

1. INTRODUCTION

Since nineteen-nineties the 3D representations of the bare ground relief under the forest canopy and of the forest canopy itself have been often captured and modeled using aerial laser scanning. Digital elevation models (DEMs) have been extracted from lidar data using a number of different approaches (e.g., Axelsson 2000, Kraus and Pfeifer 1998, Pfeifer et al. 2001, Sithole 2005, Vosselman 2000). Some of them were compared in Sithole and Vosselman (2004). Lidar DEMs are utilized among others in forest road construction and in archaeological studies. By subtracting the DEM from the corresponding forest DSM (digital surface model of the forest canopy) the nDSM (normalized DSM) can be computed, reflecting the relative forest vegetation heights. The nDSM are utilized, e.g., to detect tree tops and to analyze forest canopy closure and forest stand structure.

The REIN (REpetitive INterpolation) algorithm used in this study to extract the DEM and consequently the nDSM, was presented in detail in Kobler et al. (2007). Briefly, REIN is especially applicable in steep, forested areas where other filtering algorithms typically have problems distinguishing between ground returns and off-ground points reflected in the vegetation. REIN is applied after an initial filtering (Figure 1a) of the point cloud, which involves removal of all negative outliers and removal of many, but not necessarily all, off-ground points by some existing filtering algorithm (e.g., using the morphological filtering, Vosselman 2000). REIN makes use of the redundancy in the initially filtered point cloud (FPC) in order to mitigate the effect of the residual off-ground points. Multiple independent random samples are taken from the initial FPC. From each sample, ground elevation estimates are interpolated at individual DTM locations (Figure 1b). Because the lower bounds of the distributions of the elevation estimates at each DTM location are almost insensitive to positive outliers, the true ground elevations can be approximated by adding the

global mean offset to the lower bounds, which is estimated from the data (Figure 1c). While other filters behave deterministically, always generating a filter error in special situations, in REIN, because of its random aspects, these errors do not occur in each sample, and typically cancel out in the final computation of DTM elevations.

As the REIN algorithm makes use of the redundancy in the initially filtered point cloud, the input lidar point density has an influence on the DEM precision and consequently also on the nDSM precision. These influences have not yet been analyzed specifically in the context of REIN algorithm, so it is the aim of this study to estimate the influences of lidar point density on (1) the precision (i.e., spatial detail) of DEM extracted in a submediterranean karstic forested relief using the REIN algorithm, and on (2) the precision of the corresponding nDSM.

2. LIDAR DATA AND STUDY AREA DESCRIPTION

The study area (Figure 2) measures 400 m (E-W) by 250 m (N-S), spanning elevations between 71 m and 233 m. It is located in the submediterranean region of Kras in western Slovenia, 5 km from the Gulf of Trieste. The local Gauss – Krueger coordinates are: UL = 5394730, 5075590, LR = 5395130, 5075340. The relief of the study area is rough with slopes ranging up to 60°, the average slope being 22°. The micro-relief features include rock outcrops up to 1 m in size, due to karstic limestone geology, a narrow gorge, and some remains of frontline trenches (the Doberdob section of the World War I Isonzo front), which have been heavily vegetated since (Figure 2c). The study area is covered by submediterranean coppice forest. The main tree species are *Ostrya carpinifolia*, *Pinus nigra*, *Corylus avellana*, and *Ulmus minor*, the latter being found especially within the gorge. The average tree height in the study area is 9 m with the highest trees exceeding 20 m, estimated from the nDSM, using maximum available lidar point

* Corresponding author

density. The vegetation canopy coverage CC is between 5% and 91%, average value being 64%. CC was estimated as the ratio of the first and the only returns for each 10 by 10 sq. m area: $CC = N_{first} / (N_{first} + N_{only}) * 100$. The discrete lidar data of the study area were acquired on April 27, 2005, after beginning of vegetation, as part of a larger campaign, covering 2 by 20 sq. km. The aerial laser scanning was performed by an Optech ALTM-3100 lidar mounted onto a helicopter. The ground speed was 120 km/h and flying height was 1000 m above ground. The lidar pulse rate was 100 kHz, scan frequency 30 Hz, scan angle $\approx 20^\circ$, beam divergence 0.3 mrad, and up to 4 measurements including the last one were collected for each pulse. The following lidar point densities were obtained within the study area: 5.15 first returns / m², 0.56 intermediate returns / m², 7.64 last returns / m², and 3.21 only returns / m².

3. METHODS

Different lidar point densities were simulated by repeatedly thinning the density of the basic lidar dataset by a factor of 2, yielding the thinning factors of 2, 4, and 8, respectively. The points to be retained in the thinned dataset were selected by first ordering the points according to their respective GPS time-stamps and then selecting every second point. This procedure was performed separately for each point type. The resulting point densities are presented in Table 1. Total point densities used to calculate DEMs (last returns + only returns) and DSMs (all four return types) are given in the bottom two lines of Table 1.

Point density [m ⁻²]		Data thinning factor			
		1	2	4	8
Point type	First	5.15	2.58	1.29	0.64
	Intermediate	0.56	0.28	0.14	0.07
	Last	7.64	3.82	1.91	0.96
	Only	3.21	1.61	0.80	0.40
L + O		10.85	5.43	2.71	1.36
F + I + L + O		16.56	8.29	4.14	2.07

Table 1. Lidar point densities obtained by thinning the basic dataset. The starting point density is given in the first column (thinning factor = 1). Total point densities used to calculate DEMs (last returns + only returns) and DSMs (all returns) are given in the bottom 2 lines.

The DEMs, DSMs, and nDSMs were calculated separately from thinned lidar data corresponding to each thinning factor. The raster resolution of all the DEMs, DSMs, and nDSMs were 1 by 1 sq. m, the grids thus measuring 400 columns by 250 rows. The lidar DEMs were calculated from the last and the only returns, using the REIN algorithm, as presented in Section 1. The following REIN parameter values (see Kobler et al. 2007 for their detailed treatment) were used:

- threshold slope = 60° for the initial slope filtering,
- numsamples (i.e., number of repetitive TINs used to interpolate DEM elevations) = 20,
- samplesize (i.e., percentage of lidar points used to build a TIN at each repetition) = 10% of the last and the only returns, i.e., 1.09, 0.54, 0.27, and 0.14 points / m² respectively, corresponding to thinning factors of 1, 2, 4, and 8 respectively.

Each nDSM was calculated by subtracting the bare ground DEM from the corresponding forest canopy DSM. The elevation of each DSM pixel was estimated from the highest point of any type (first, intermediate, last, only) within each 1 by 1 sq. m. The DEM and nDSM calculated from the non-thinned dataset (DEM1, nDSM1) were used as the reference against which the “thinned” DEMs and nDSMs (DEMx, nDSMx; x = 2, 4, 8) were compared to estimate the decrease of precision due to lower point density.

The DEM precision was estimated by statistics of the image differencing DEM1 – DEMx, and by visual comparison and evaluation of the difference images, and of the wireframe DEM renderings. The nDSM precision was estimated using percentage of the empty pixels, i.e., pixels containing no lidar points, and using statistics of the image differencing nDSM1 –

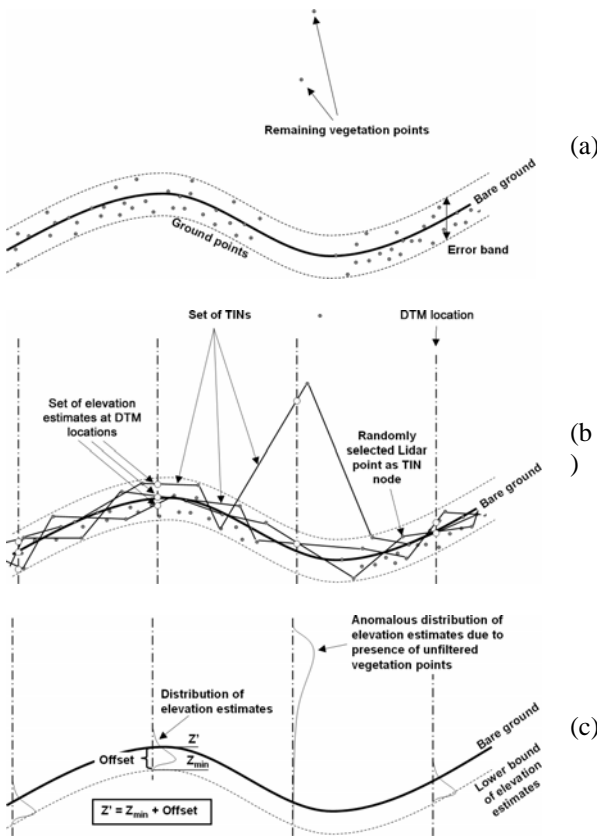


Figure 1. REIN algorithm is used after the initial filtering by any suitable deterministic filter. (a) The result of the initial filtering stage are ground points with few remaining unfiltered vegetation points and no negative outliers. Note the redundancy of ground points within the error band. The lidar point scattering within the error band is caused by measurement errors, grass and low herbal vegetation. (b) Repeated random selections of lidar points are used to build a set of TINs, out of which sets of elevation estimates are interpolated at the locations of DTM grid points. Note that also the remaining unfiltered vegetation points may become TIN nodes. (c) DTM elevations are approximated by adding global mean offset to the lower bounds of elevation distributions, which are unaffected by the unfiltered vegetation points.

nDSMx, and correlations between pixel values of nDSM1 and nDSMx within the nonempty pixels.

The minimum criteria for an acceptable DEM and nDSM precision were as follows:

- vertical DEM standard error ≤ 15 cm
- vertical DEM bias ≤ 5 cm
- percentage of nDSM empty pixels $\leq 2\%$
- vertical nDSM standard error ≤ 150 cm
- vertical nDSM bias ≤ 50 cm
- vertical nDSM correlation to the reference nDSM ≥ 0.9

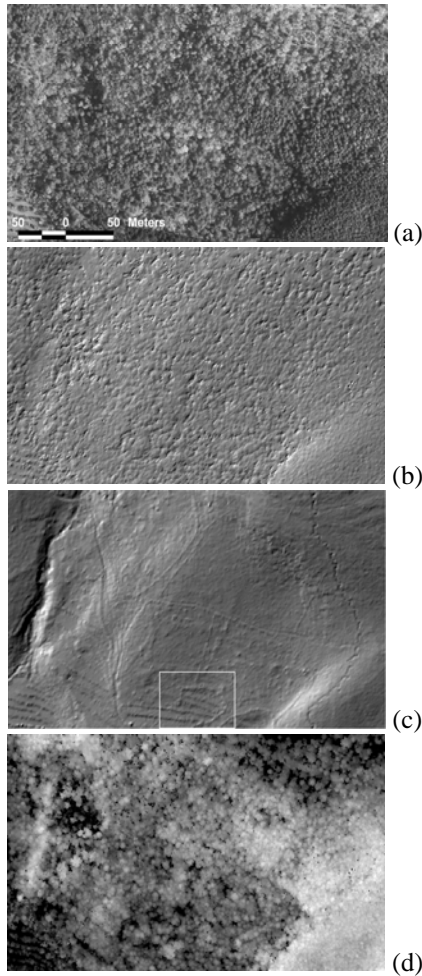


Figure 2. The study area measuring 400 m (E-W) by 250 m (N-S) is shown (a) on an aerial orthophoto, (b) on a shaded forest canopy DSM, (c) on a shaded DEM of the bare ground (the latter being computed using the REIN algorithm), and (d) nDSM. The maps shown in (b), (c), and (d) were computed using the highest available point densities. The white rectangle in (c) denotes the detail rendered as wireframe model in Figure 4. The DEM and the DSM have 1 m raster resolution. The average tree height in the study area is 9 m and the average forest canopy coverage is 64%. The average relief slope is 22° . There are several relief features to note in (c): the gorge on the left, the low manmade walls and footpaths appearing as crisscrossing lines, rock outcrops appearing as the rough surface, the abandoned agricultural terraces in the bottom part, and the jagged line on the right denoting the remains of the WW1 frontline trenches.

4. RESULTS

The DEM difference images $DEM1 - DEMx$ are given in Figure 3 and the corresponding statistics are given in Table 2. The DEM subsets are compared as wireframe models in Figure 4. The percentage of empty nDSM pixels due to data thinning is illustrated in Figure 6. The vegetation height images $nDSM1 - nDSMx$ are given in Figure 5. The statistics of the differences and the correlations between nonempty nDSM1 and nDSMx pixels are given in Table 3 and Figure 7, respectively.

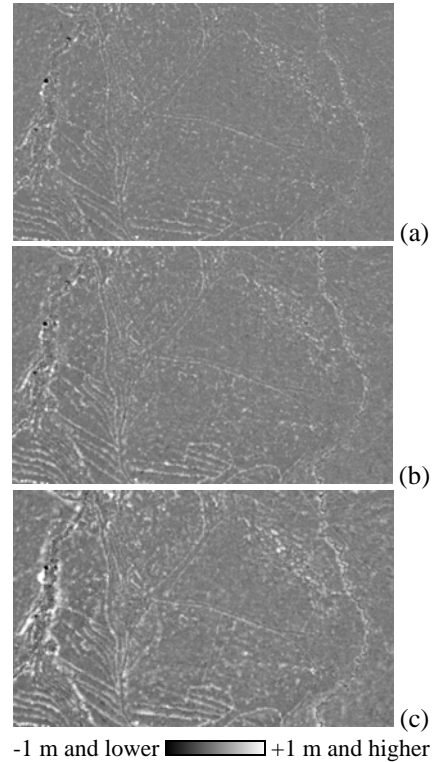


Figure 3. The elevation difference images due to data thinning: (a) $DEM1 - DEM2$, (b) $DEM1 - DEM4$, (c) $DEM1 - DEM8$. The differences are the greatest at sharp break-lines and at locations of pronounced micro-relief, e.g., low manmade walls, rock outcrops, or terraces (cp. Figure 2c).

[m]	x = 2	x = 4	x = 8
Minimum error	-2.34	-2.07	-1.98
Maximum error	1.92	1.85	2.87
Bias	0.02	0.03	0.05
Standard error	0.11	0.13	0.17

Table 2. The statistics for the difference images $DEM1 - DEMx$ (x in table header) shown in Figure 3.

[m]	x = 2	x = 4	x = 8
Minimum error	-18.04	-18.62	-20.54
Maximum error	1.63	1.55	2.13
Bias	-0.41	-1.39	-2.62
Standard error	1.18	2.72	3.95

Table 3. The statistics for the vegetation height difference images $nDSM1 - nDSMx$ (x in table header) shown in Figure 5. Only the non-empty nDSM pixels were taken into account.

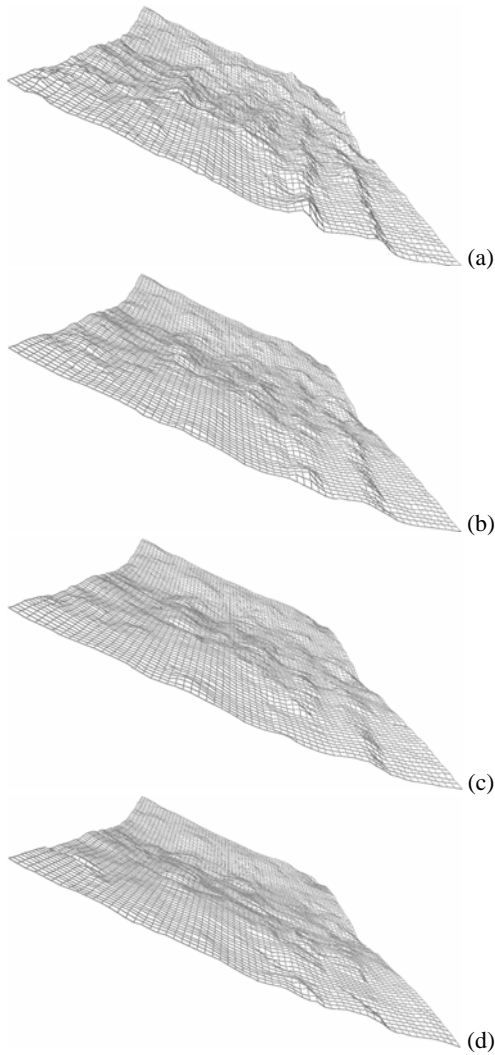


Figure 4. The wireframe DEM rendering of the DEM subset indicated in Figure 2c, as seen from the west. (a) DEM1 – based on lidar point density (i.e., last + only returns) 10.85 m⁻², (b) DEM2 – density 5.43 m⁻², (c) DEM4 – density 2.71 m⁻², (d) DEM8 – density 1.36 m⁻². The subset area is 80 m by 60 m. All wireframes are shown using 1 m raster. The main feature of the relief in the subset are the abandoned and overgrown agricultural terraces, which are increasingly smoothed out by REIN at greater data thinning factors.

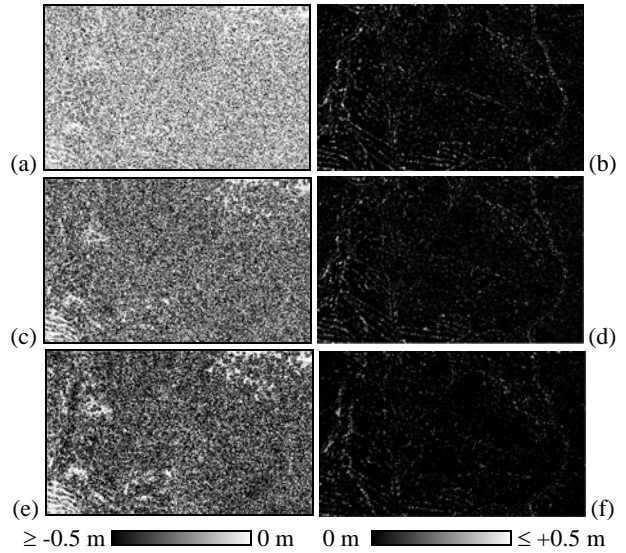


Figure 5. The vegetation height difference images: (a) and (b) nDSM1 – nDSM2, (c) and (d) nDSM1 – nDSM4, (e) and (f) nDSM1 – nDSM8. Due to different grayscale legends, the figures in (a), (c), and (e) in the left column highlight the negative difference values, and the figures in (b), (d), and (f) in the right column highlight the positive ones. Note the quasi-random pattern of differences in the left column, and spatial coincidence of differences with the microrelief features in the right column. The differences at the empty pixels were set to 0. Compare also with Figure 2d.

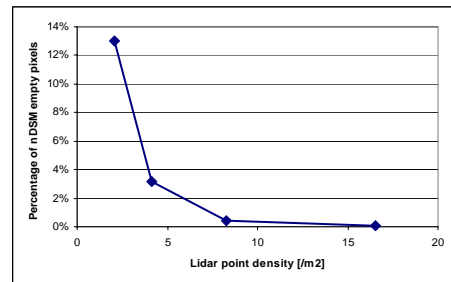


Figure 6. Percentage of the nDSM empty pixels (pixel size 1 m²) due to data thinning. Empty pixels are pixels containing no lidar points. Lidar point densities include all point types (first, intermediate, last, only).

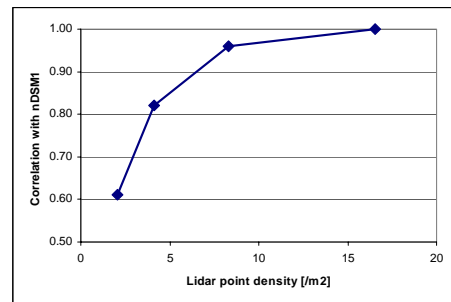


Figure 7. Correlations between the vegetation heights in the reference nDSM and the “thinned” nDSMs. Only the non-empty nDSM pixels have been taken into account.

5. DISCUSSION AND CONCLUSIONS

The REIN algorithm was designed to generate DEM in steep forested relief, where other filtering algorithms typically have problems distinguishing between ground returns and off-ground points reflected in the vegetation. REIN takes multiple independent random subsets of the initially filtered point cloud, making use of the redundancy in dense point clouds. Lowering the density of the input point cloud also reduces the size of the randomly selected point subsets that are used as nodes for TINs, generated in each repetition of REIN. This in turn affects the precision (i.e., spatial detail) of the generated DEMs, as illustrated in Figure 4. If one uses the DEM1 (i.e., the DEM based on the non-thinned point cloud) as the reference, this effect is mapped in Figure 3 and correspondingly quantified in Table 2. The largest elevation differences between DEM1 and the “thinned” DEMs (i.e., DEMs based on variously thinned point clouds) are found at sharp break-lines and at locations of pronounced micro-relief, e.g., low manmade walls, rock outcrops, terraces, and sharp depressions (Figure 3, Figure 2c). The standard deviation of the difference thus increases from 11 cm for DEM2 to 17 cm for DEM8 (Table 2). There is also a slight increase of the bias (i.e., average difference) from 2 cm to 5 cm for DEM2 and DEM8 respectively, which is due to a more biased estimate of REIN’s global mean offset calculation at lower point densities (Figure 1c). If a vertical DEM standard error of less than 15 cm, and a vertical DEM bias of less than 5 cm, respectively (Table 2), are used as criteria for acceptable DEM precision, then all but the most thinned lidar point cloud densities are suitable for REIN-based generation of DEM in the study area of rough relief covered with dense forest. However, the visual evaluation of the wireframe models (Figure 4) suggests coarser DEM raster resolutions than 1 m would be advised for all the lidar point densities except the highest one. This is partly due to the decision of the analyst to use aggressive REIN filtering in this study in order to exclude all DEM errors related to positive outliers (i.e., vegetation points). Less aggressive REIN operating parameters would yield more detailed micro-relief even given less dense lidar point clouds, however at the cost of some remaining vegetation errors in the DEM.

The smoothing effect of lidar point cloud thinning can also be observed in the resulting nDSMs. The comparison of nDSMs at different lidar point cloud densities reveals a strong influence of point density on the proportion of empty pixels, i.e., pixels containing no lidar points, where nDSM height has to be interpolated from the surrounding pixels. At a 1 m raster resolution, the number of empty nDSM pixels when low point density is used in the study area is proportionally much higher, compared to high point density (Figure 6). If 2 % are taken as the maximum allowable percentage of empty pixels, then only the two highest point densities should be used for the study area (considering all point types). Similarly as in DEM, the point cloud density influences the precision of forest canopy rendered in a nDSM. Because the vegetation height in a nDSM is calculated as the difference DSM – DEM, an additional factor in nDSM precision is also the underlying DEM precision. If one uses the nDSM1 (i.e., the nDSM based on the non-thinned point cloud) as the reference, these effects can be illustrated in Figure 5. Note the quasi-random pattern of differences due to varying fidelity of forest canopy in the left column of Figure 5, and the spatial coincidence of differences with the break-lines and with the micro-relief features, reflecting imprecision of the underlying DEMs, in the right column of Figure 5. These effects are quantified in Table 3, where the underlying DEM

imprecision is reflected in the maximum differences (1.63 m for nDSM2 and 2.13 m for nDSM8), and the forest canopy precision is reflected in the minimum differences (-18.04 m for nDSM2 and -20.54 m for nDSM8). The strong effect of lidar point cloud thinning on nDSM precision can also be observed in decreasing correlation of the reference nDSM1 with the “thinned” nDSMs (Figure 7). If a vegetation height bias of ± 50 cm, a standard error of 150 cm, and a vegetation height correlation of 0.9, respectively, are taken as the minimum criteria for the nDSM precision, then only the two least thinned point clouds (i.e., thinning factors 1 and 2) are suitable for nDSM generation.

In conclusion, the following can be summarized for the study area on the basis of the mentioned DEM and nDSM minimum precision criteria. The three highest point densities (i.e., 2.71, 5.43 and 10.85 last and only returns per m²) may be used for the REIN-based DEM generation in the study area. Coarser DEM raster resolutions than 1 m is advised for all the lidar point densities except the highest one. However, note that a less aggressive REIN operating parameters would yield more detailed micro-relief given even a less dense lidar point cloud, at the cost of some remaining vegetation errors in the DEM. To generate a precise enough REIN-based nDSM, the two highest point densities (i.e., 8.29 and 16.56 of all returns per m²) may be used.

6. ACKNOWLEDGEMENTS

The study was funded by the Slovenian Research Agency and by the Slovenian Ministry of Agriculture, Forestry, and Food within the research project “Processing of Lidar Data” (contract 3311-04-8226575), and by the Slovenian Ministry of Defense and by the Slovenian Research Agency within the research project “Forecasting GIS Model of Fire Danger in Natural Environment” (contract 3311-04-828032). The authors are thankful for fruitful comments by the anonymous reviewers.

7. REFERENCES

- Axelsson, P., 2000. DEM generation from laser scanner data using adaptive TIN models. In: *International Archives of Photogrammetry and Remote Sensing*, 33 (B4/1) 110-117.
- Kobler A., Pfeifer N., Ogrinc P., Todorovski L., Oštir K., Džeroski S., 2007. Repetitive interpolation: A robust algorithm for DTM generation from Aerial Laser Scanner Data in forested terrain. In: *Remote Sensing of Environment* 108 (2007) 9–23.
- Kraus, K., Pfeifer, N., 1998. Determination of terrain models in wooded areas with airborne laser scanner data. In: *ISPRS Journal of Photogrammetry and Remote Sensing*, 53, 193-203.
- Pfeifer, N., Stadler, P., Briese, C., 2001. Derivation of digital terrain models in the SCOP++ environment. In: *OEEPE workshop on airborne laserscanning and interferometric SAR for detailed digital elevation models*, Stockholm, Sweden.
- Sithole, G., 2005. *Segmentation and Classification of Airborne Laser Scanner Data*, Dissertation, TU Delft, ISBN 90 6132 292 8. In: *Publications on Geodesy of the Netherlands Commission of Geodesy*, Vol. 59.
- Vosselman, G., 2000. Slope based filtering of laser altimetry data. In: *International Archives of Photogrammetry and Remote Sensing*, Vol. 33, B3/2, 935–942.

AUTOMATIC GLACIER SURFACE ANALYSIS FROM AIRBORNE LASER SCANNING

M.P. Kodde^a, N. Pfeifer^b, B.G.H. Gorte^c, T. Geist^d, B. Höfle^e

- a. Fugro-Inpark, Dillenburgsingel 69, 2263 HW Leidschendam, The Netherlands - m.kodde@fugro-inpark.nl
 b. Institute of Photogrammetry and Remote Sensing, Vienna University of Technology - np@ipf.tuwien.ac.at
 c. Delft University of Technology, Kluyverweg 1, 2629 HS Delft, The Netherlands b.g.h.gorte@tudelft.nl
 d. FFG – Austrian Research Promotion Agency, Sensengasse 1, 1090 Vienna, Austria – thomas.geist@ffg.at
 e. Institute of Geography, University of Innsbruck, Innrain 52, 6020 Innsbruck, Austria – bernhard.hoefle@uibk.ac.at

KEY WORDS: Airborne Laser Scanning, DEM, Glacier, Crevasses, Mathematical Morphology

ABSTRACT:

Glaciers are interesting phenomena to scientists, mountaineers and tourists. Glaciers have a great impact on the local economy, power generation and water supply. Furthermore, the behaviour of glaciers is influenced by climate variations, such as changes in temperature. Monitoring glaciers can therefore give valuable insight to glaciologists. Two aspects of glaciers that can be monitored are the delineation of a glacier and the crevasses within a glacier. In this paper it is presented how these two aspects can be detected automatically from Airborne Laser Scanning (ALS) data.

The delineation of a glacier can be derived from ALS data by setting up a classification of the elevation model into the classes *glacier* and *non-glacier surface*. The smoothness, which is calculated from the ALS data, is used as classification criterion. Crevasses within the glacier can be detected by assuming that they are deviations from a regular glacier surface without any crevasses. Such a surface can be calculated with techniques from Mathematical Morphology. Given the assumption that crevasses have a V-like shape, the bottom of the crevasse and the two edges can be reconstructed from the point data. ALS data that was acquired at the Hintereisferner in Tyrol, Austria was used for testing the algorithms. Both the delineation of the glacier and the detection of crevasses give good results in the presented approach. However, the delineation of the glacier might fail if many crevasses cause exceptions to the smoothness criterion. Crevasses are sometimes not detected due to snow bridges. The quality of the reconstruction of crevasses is hard to assess due to the lack of reference data at the test location. Data acquisition with a higher point density and the acquisition of reference data for crevasses with Terrestrial Laser Scanning are recommended to independently check the result.

1. INTRODUCTION

Glaciers are sensitive indicators for climate change processes and have a significant impact on water supply in some regions. Several authors have shown that there is a relation between melting of glaciers and several climatologic parameters, including temperature (Oerlemans, 1994). Glaciers are also of great economic interest on a regional scale. In some regions hydro-power generation, drinking water supply and tourism rely heavily on the existence of glaciers. For these regions, a good understanding and monitoring of glaciers is of vital interest.

For many decades, measurements of glacier length variations and glacier mass-balance have been made in differing ways with the purpose of monitoring the dynamics of the glacier. This was done by means of terrestrial measurements, or by using aerial based data such as photogrammetry. In the European Union funded research project “Operational Monitoring System for European Glacial Areas (OMEGA)”, several methods for glacier monitoring were explored, including Airborne Laser Scanning (Geist et al., 2005). Results from this project show the potential of ALS data for different applications in glacier research, thereby following up earlier attempts to utilise ALS on mountain glaciers (Baltasvias et al., 2001; Kennett and Eiken, 1997; Rees, 2005).

With the increasing availability of ALS data, automated approaches can be used to find specific properties of glaciers. Some of the information that can be extracted from the datasets is the extent of the glacier and the location of glacier crevasses.

Crevasses are cracks in the upper surface of a glacier, formed by tension acting upon the brittle ice. They can be deep and thus dangerous for travellers on glaciers. Using ALS data to detect and reconstruct crevasses, will assist glaciologists to get more insight into ice dynamics.

Research in other fields of application has already shown that ALS data can be used with a high degree of automation. Objects such as buildings (Vosselman and Dijkman, 2001) and trees (Kraus and Pfeifer, 1998) can be detected automatically from the data. However, automated surface analysis has not yet been applied to glacier surfaces. Climate change sensitive objects, as glaciers are, will be monitored more intensively in future, necessitating automated approaches. In this paper methods for the automatic delineation of glacier areas will be presented and compared. Subsequently, a method for detecting and finally reconstructing crevasses will be presented.

2. DATA SETS

The methods presented were tested on ALS data that was acquired within the OMEGA project. One glacier in this project was the Hintereisferner in Tyrol, Austria. It is a typical valley glacier located in the Ötztal Alps. Up to now, 13 epochs of laser scanning data are available for the Hintereisferner. These datasets were acquired between October 2001 and September 2006 in different seasons of the glaciological year. The datasets acquired in the OMEGA project are documented in Geist and Stötter (2007). For the work in this paper, the data acquired on

August 12th 2003 (HEF9) and October 5th 2004 (HEF11) was used.

The acquisition of these two datasets was performed with the Optech ALTM 2050 and the Optech ALTM 1225 respectively. HEF9 had a mean flying height of 1150 m. For HEF11 the average flying height was 1000 m above the surface. The minimum slant range was 460 m, while the maximum was 1980 m. An average point distance of 0.8 m for HEF9 and 0.7 m for HEF11 was achieved. The vertical accuracy over a control area was $\sigma = 0.095$ m for HEF9 and $\sigma = 0.075$ m for HEF11. The full information of the points, i.e. values for first pulse, last pulse and intensity, is stored in a PostgreSQL database that can be connected to the GRASS GIS (Höfle et al., 2006). The other data sets were not yet added to the database at the time of writing. Additionally, the data was transformed to a 1 m resolution raster using a nearest neighbour interpolation method on the last pulse returns. The use of last pulse data increases the chance of getting points on the bottom of the crevasses. These resulting rasters form the input for the algorithms presented in the following sections.

3. GLACIER DELINEATION

For the detection and reconstruction of crevasses, it is required to limit the search area to the parts of a Digital Elevation Model (DEM) where a glacier can be found. This is done by automatically calculating the delineation of a glacier. Afterwards, the crevasse locations are detected and individual crevasses are reconstructed. The glacier delineation is not only of interest because it forms an important input to the crevasse detection algorithms, it is also an interesting result on itself. Delineations from repeated measurements can for instance be used to monitor the growth or decay of a glacier.

In the presented method it is assumed that the measurements are organised as a rasterised DEM. An example of such a DEM representing a glacier and the surrounding mountains is presented in Figure 1.

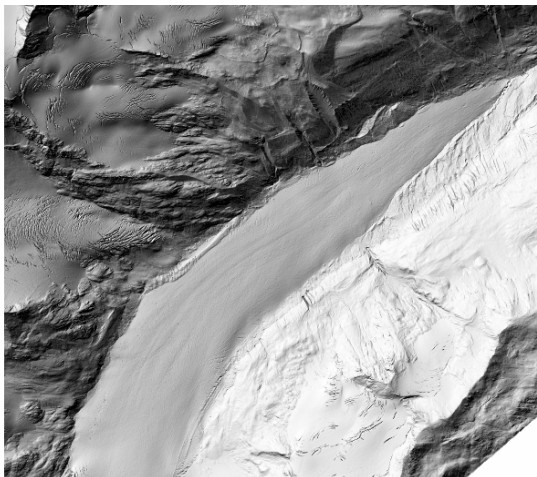


Figure 1. Shaded relief view of the tongue of Hintereisferner

Determining the delineation is essentially a classification of the pixels into the classes “glacier” and “non-glacier”. The process of classification is well-known from Remote Sensing where it normally involves the analysis of multispectral image data and the application of statistically based decision rules. This spectral

data is now absent, but other criteria can be developed for the decision rules:

- Criterion 1: Smoothness
- Criterion 2: Connectivity
- Criterion 3: Hydrological constraints

Criterion 1 is based on the surface characteristics as they can be derived from the elevation data. The ice surface that makes up the glacier is much smoother than the surface of the surrounding bedrock. There are several ways to find the smooth areas in the DEM. One method is to calculate the variance of the best fitting plane in a certain region of cells. The size of this region depends on some surface properties and the grid sampling interval. By setting upper and lower boundaries to the variance, the smooth areas can be classified as glacier. The result of this calculation is a new map Σ which contains the variance of n surrounding points in each pixel $\Sigma(r,c)$. The classification is now simply defined as applying a threshold t to this map:

$$\begin{cases} \mathbf{C}(r,c) = \text{TRUE} & \text{for } \Sigma(r,c) < t \\ \mathbf{C}(r,c) = \text{FALSE} & \text{for } \Sigma(r,c) \geq t \end{cases} \quad (1)$$

Alternatively, smoothness can be determined by segmenting the area first. For smooth areas we assume that the first derivative of the surface remains constant. Areas with constant first derivatives can be grouped in segments. If these segments are large enough, the surface that belongs to them can be considered smooth. In image processing, the first derivative of the data is usually called the gradient ∇_z .

$$\nabla_z = \left(\frac{\partial z}{\partial x} \quad \frac{\partial z}{\partial y} \right)^T \quad (2)$$

Numerically the gradient can be computed with the Sobel filter. Vosselman et. al. (2004) and Hoover et. al. (1996) treat different methods for segmentation in order to recognise structure in elevation models. One of the segmentation algorithms treated is the split-and-merge algorithm. For this work such a segmentation algorithm based on quad trees is used. The algorithm was designed by Gorte (1996) and has the advantage that it allows to segment on multiple bands simultaneously. In this case the x- and y-gradient images are the two bands on which the segmentation algorithm operates. After segmentation, we get a high number of different segments, which should now be classified in one of the classes ‘glacier’ and ‘non-glacier’. Only if a segment is relatively large, the surface can be called smooth. The problem of classifying glacier pixels can therefore be translated to the problem of selecting segments that are greater than a certain predefined area. By applying this classification method, the parts of the terrain that can be considered smooth are selected, resulting in the classification map \mathbf{C} .

Tests show that the results using the classification or the segmentation are practically equal. The size of differences observed fall within the grid resolution. In comparison to the variance based classification the segmentation method is computationally much more efficient because calculating the gradients requires less computational effort than fitting the planes through the data. However, when fitting the planes, slope

and aspect come as a side product, which may be interesting for other purposes.

Criterion 2 involves the connectivity of pixels classified as glaciers surface. In glaciology a glacier is considered as one large connected mass, mainly consisting of ice. Using connected component labelling, the result from the classification on criterion 1 can be improved by applying the connectivity constraint.

The last criterion that is used to improve the delineation is related to the hydrological properties of glaciers. Given some exceptional circumstances, glaciers generally flow downwards. Consequently, the notion of a catchment area also applies to glaciers. A catchment is the area in which all water, ice or snow flows to the same single outlet. Any pixel classified as glacier should therefore lie within the catchment area of the glacier. This criterion is therefore used to limit the extent of the glacier. Most GIS software contains methods to calculate such a catchment boundary from a DEM.

In the end, the results of the three criteria can be combined to get the final delineation of the glacier. A further improvement of the glacier surface could be obtained by using intensity based segmentation. (Höfle et al., 2007)

4. CREVASSE DETECTION

4.1 Detection using Mathematical Morphology

In order to extract crevasses from a DEM and visualise their locations, we try to create a flat surface with only non-zero values at crevasse locations. The part that has to be removed from the original DEM is the glacier surface as well as the elevation of underlying bedrock. The physical meaning of these elevations would be a glacier in which no crevasses were formed. In order to obtain this surface some techniques from mathematical morphology are used.

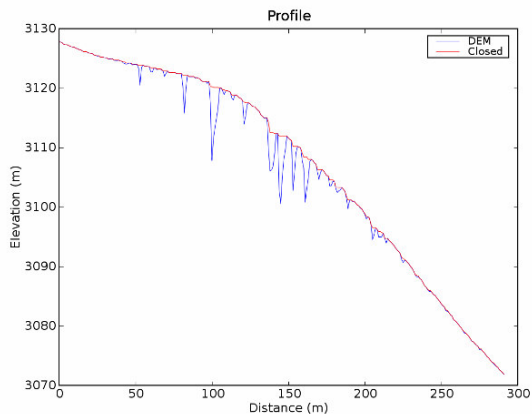


Figure 2. Cross section of a glacier with the result of the closing operation

Mathematical morphology is the theory of the analysis of spatial structures in data sets. It works like a convolution, but uses decision operators instead of multiplication. A morphological filter is used to detect or modify structural elements in the image, i.e. the morphology of the terrain. Provided that the structuring element is larger than the width of the crevasse, the closing filter will close all crevasses, effectively removing them

from the glacier surface. Figure 2 shows a profile of the glacier after performing the closing filter. Having generated this surface of a glacier without crevasses, the closed surface is subtracted from the original data, an operation that is known as Black Top Hat. Applied to the DEM, the resulting dataset will be zero over the whole terrain, except for the locations with a crevasse. Given the DEM \mathbf{H} , the Black Top Hat operation is now defined as:

$$\mathbf{H}_{\text{crev}} = BTH(\mathbf{H}) = \phi(\mathbf{H}) - \mathbf{H} \quad (3)$$

where $\phi(\mathbf{H})$ represents the closing operation over the DEM.

Because the filter closes the crevasses horizontally, the filtered surface is not exactly a surface without crevasses because this will be a sloped surface. This problem was solved by detrending the data first, so that the horizontal closing gives the correct result. This detrending of the DEM, i.e. removing the large scale relief features, can for instance be done by top-hat filtering with a very large window size.

4.2 Setting the structuring element size

After detrending, the crevasse-less glacier surface should be perfectly flat. This means that a flat structuring element can be used, i.e. a structuring element where the shape is defined by the value '1'. The size of the structuring element can be seen as a definition of how long (or how far) the morphology in the structuring element holds. Often, the correct filter size is hard to determine. In this work a novel method is explored to formalise the structuring element size using a variogram of the terrain. A variogram is a measure of the variance between data as a function of distance. The theoretical variogram is defined as:

$$\gamma(d) = \frac{1}{2} E \left\{ [\underline{h}(p+d) - \underline{h}(p)]^2 \right\} \quad (4)$$

Where p is a point in the DEM, $\underline{h}(p)$ the height of that point and d the distance from that point. Figure 3 gives the theoretical variogram based on the Gaussian model for a selected small part of the glacier surface. For comparison, the scatter- and experimental variograms are displayed as well. The values found after fitting the Gaussian model were a range of $R = 369$ m and a sill $\sigma^2 = 1.3$ m².

From the theoretical variogram, measures of variance in the terrain can be related to the size of the structuring element. For instance, field measurements with a Terrestrial Laser Scanner on the Hintereisferner in the summer of 2006 showed that a variance of 0.06 m² (0.25 m standard deviation) can be expected within a small area on the glacier. The variogram relates this to a structuring element size of 10 m in diameter.

The shape of the structuring element depends on the anisotropy of the glacier. The amount of anisotropy can be determined by calculating a directional variogram. On a perfect isotropic surface, the variogram will be equal in all directions, yielding a disk shaped structuring element. On anisotropic surfaces, the directional variogram is used to form an ellipse-shaped structuring element. In this study only isotropic structuring elements were applied.

Implementing the variogram method in the detection software, means that an operator can select the amount of variance he or she assumes on a glacier surface without crevasses. The program then takes care of setting the right parameters for the filter.

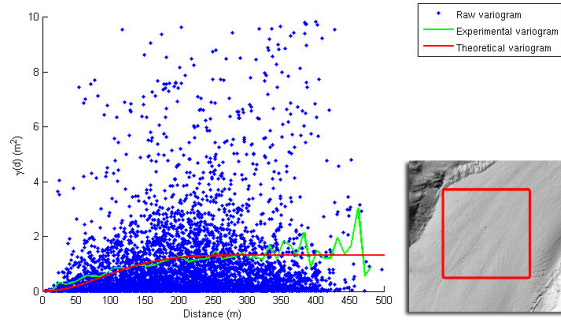


Figure 3. The fitted variogram of a part of the glacier surface

5. CREVASSE RECONSTRUCTION

Whilst the delineation of the glacier and the detection of crevasses were solely performed on height measurements that were interpolated to a grid, the reconstruction of crevasses will be done on the unprocessed point data. The point data for a crevasse is selected using the crevasse locations found in the previous step. A problem with reconstructing crevasses is the relative low point density of 1 point per square meter. This density is low compared to the average crevasse width of a few metres, which requires us to make some assumptions in the reconstruction.

If it is assumed that crevasses have a regular V-like shape, it is possible to parameterise this shape into a geometrical object. A simple parameterisation would consist of parameters for depth, width and length. Unfortunately, crevasses are not that simple: they are usually bended and do not have a constant depth. Describing this in parameters is infeasible; therefore the crevasses will be reconstructed using a boundary representation. Taking the V-shape as a basis, we can build a crevasse with three lines: a bottom line and two upper surface edges. These three lines are connected at the beginning and the end of the crevasse.

The bottom line is the first line to extract, using a process that consisting of two steps. The first step constitutes the determination of the horizontal position of the line. In the second step, z-coordinates are calculated for this line. It is unlikely that there are any laser points that lie exactly on the bottom line of the crevasse. The location of the bottom line must therefore be derived from the surrounding pixels. It can be assumed that the horizontal position of the bottom line lies in the middle of the crevasse. The program selects the lowest 25 percent of the points in the crevasses and calculates the centre by fitting a spline through these points. After fitting, the program removes points with a large residual and tries to fit the line again, giving an improved position.

The result of fitting the polynomial can further be improved by giving weights to the points used in the adjustment. Points with a large depth are given a higher weight in the adjustments, while points near the surface get a lower weight. We call the

estimated polynomial coefficients \hat{x} , the weight matrix W and the design matrix A . If the stochastic x and y coordinates are combined in the random vector y , the Least Squares

Adjustment is given by: $\hat{x} = (A^*WA)^{-1} A^*Wy$. Then the weights are derived as:

$$w_{ii} = \left(\frac{h_i - h_{\min}}{h_{\max} - h_{\min}} \right)^2 \quad i = 0, 1, \dots, n-1 \quad (5)$$

Taking these weights in an iterative approach, gives the horizontal position of the bottom line. The next step is to assign elevations to this line. This can be done by taking the convex hull over the lowest 25% of the points, like depicted in Figure 4. However, the reconstructed depth will be highly uncertain, as there might be snow in the crevasse, obstructing the bottom from the laser beam. The reliability will also depend on the sampling interval.

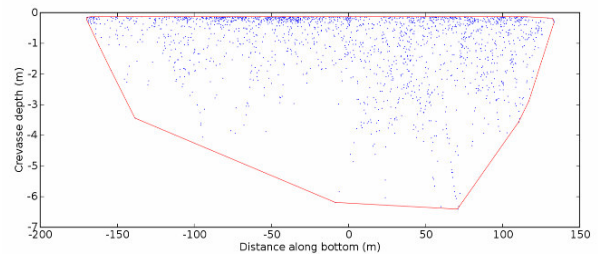


Figure 4. Laser points in a crevasse. The proposed bottom line is drawn in red

The remaining step comprises the modelling of the edge of the crevasse, the line where the glacier stops and the crevasse starts. For finding the edge, profiles of points were generated perpendicular to the bottom line that was found before. For the selected test crevasse, 152 profiles were made with an in-between spacing of 2 meters. In each of these profiles, the locations of the left and right edge were searched independently.

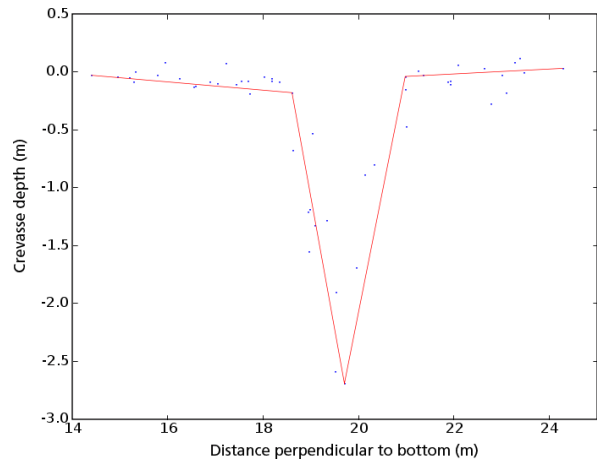


Figure 5. Cross section of a crevasse with generalisation result

To find the crevasse edges in the profiles, an algorithm was developed, based on the Douglas-Peucker line simplification algorithm. This algorithm reduces the number of points until

only the most important points for the profile shape remain. These points are the start and end points of the profile, the two edges and the bottom. Figure 5 shows one of these profiles with the laser points (in blue) and the profile (in red) after applying the simplification algorithm. When all edge points are found in the individual profiles, a spline fitting algorithm is used to connect and smooth the points for the final edge lines.

The points that are found on the bottom line and the two edge lines can be used for generating a Triangulated Irregular Network (TIN). From the TIN, it is possible to calculate values for the volume and shape of the crevasse.

6. RESULTS

The methods and algorithms described in the previous sections were implemented as a part of the LiSA toolbox, which is maintained by the University of Innsbruck. The program uses GRASS GIS (GRASS Development Team, 2006) for data storage and graphical output. The methods were tested on two epochs of the Hintereisferner ALS data.

6.1 Glacier delineation

The delineation of the Hintereisferner was determined by calculating the variance for all pixels in the DEM using the best fitting planes method that was presented in section 3. The window size used was 11 by 11 pixels with a resolution of 1 m per pixel. The surface variance that we find in the DEM is a combination of the measurement precision and the variation in the terrain: $\sigma_{DEM}^2 = \sigma_{ALS}^2 + \sigma_{SURFACE}^2$.

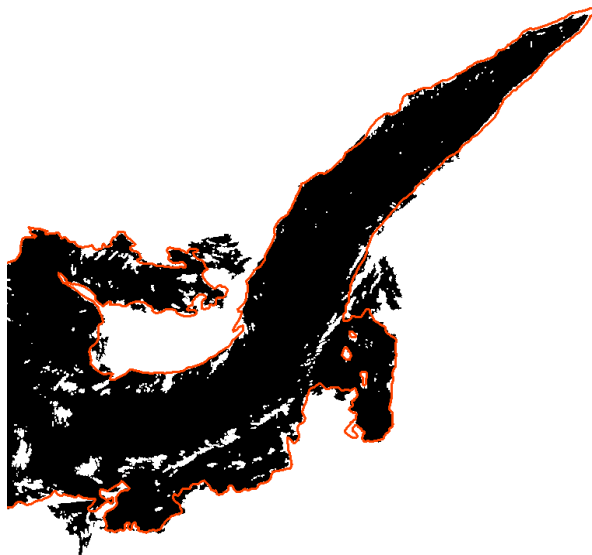


Figure 6. Area classified as glacier for the Hintereisferner DEM (black) and the manual delineation (red)

If we only look to pixels on the glacier surface of the Hintereisferner, variance values up to 0.06 m² were found, which implies a standard deviation of 0.25 m. This is approximately twice the specified laser scanning system variance σ_{ALS}^2 . This variance was used as the classification threshold *t* for assigning pixels to the classes “glacier” and “non-glacier”. The boundary of the “glacier” class will give the

delineation of the glacier. This delineation was further improved by smoothing it with a binary 3x3 morphological closing filter and intersecting it with the hydrological boundaries. Figure 6 shows the resulting area that has been classified as Hintereisferner.

The calculated delineation is a good representation of the real glacier extent. Only at some crevasse locations errors in the delineation occur. This is because the gaps at crevasse locations cause a higher surface variance, which is above the specified threshold value. Fortunately, these errors can easily be resolved, although they require manual intervention. One way to assess the quality of the delineation is to compare it with a delineation that was acquired manually by an experienced glaciologist. Comparing the computed delineation with the manual delineation gives an overall kappa value of 0.82. A comparison of the classified pixels in the manually made reference map and the classification result is given in Table 1 and Table 2.

Classes		Reference Map	
		No Glacier	Glacier
Classification	No Glacier	19665553	1122511
	Glacier	611266	5639118

Table 1. Number of pixels assigned to each class.

Classes	Commission	Omission	Estimated \hat{k}
No Glacier	5.88 %	3.29 %	0.780
Glacier	7.78 %	16.60 %	0.867

Table 2. Confusion matrix of glacier classification.

6.2 Crevasse detection

In the previous sections a method was presented for detecting crevasses in a glacier using mathematical morphology. Within the boundaries formed by the glacier delineation, the crevasse detection algorithm can now be applied. The crevasse detection was applied to two laser scanning epochs of the Hintereisferner dataset, taken in different seasons. Figure 7 shows the detected crevasse locations on a part of the glacier in the summer season. In this figure only crevasses deeper than 0.4 meters are shown.

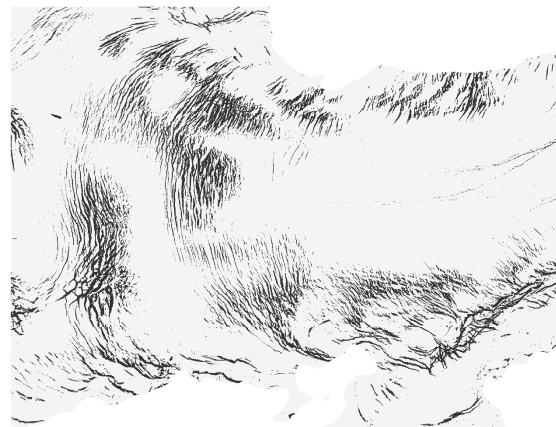


Figure 7. Detected crevasse locations.

From the variogram analysis it showed that a structuring element size of 10 m was most optimal for detecting the crevasses. In order to assess the quality of the crevasse detection one should consider the geometrical accuracy as well as the classification accuracy, i.e. how many crevasses are classified as glacier surface and how much glacier surface is classified as

crevasse? In the absence of any reference data, it was not possible to assess the quality of the results. However, by overlaying the detected crevasses over an orthophoto of the same time, a visual inspection was made. The visual inspection revealed that there were not crevasses found on the orthophoto that were missing in the automatic detection. The crevasse detection obviously gives wrong results when the crevasses are filled with snow or covered by snow bridges.

7. CONCLUSION

With the methods presented in this paper, it is shown that Airborne Laser Scanning is an accurate and reliable tool for monitoring glaciers and crevasses. Glaciers can be delineated from ALS data at an accuracy of the pixel size. The delineation used smoothness as well as some other classification criteria to find the outer boundaries of the glacier. This method takes the implicit assumption that glaciers can be recognised by a smooth surface. At crevasse locations this assumption doesn't hold and therefore the method still needs human supervision. It is also possible to detect the location of crevasses from ALS data, provided that the glacier surface is not covered by snow so the crevasses are visible for the laser beam. Additionally the crevasse should be wider than the pixel resolution. It also requires the glacier delineation as input.

Reconstructing crevasses is difficult because of the low sampling interval. The number of data points in the given dataset was too little to reliably reconstruct the crevasse without making assumptions. Additionally, specific situations, such as snow bridges, make the reconstruction even more unreliable. However, individually reconstructed crevasses do give a good indication of quantitative measures such as the volume and length of crevasses. Additionally, the area of the crevasses can be measured, even without reconstruction of its depth. For reconstructing crevasses, it is assumed that they are not covered by snow and have a V-like shape. In reality, some crevasses can have an A-shape, which can therefore not be reconstructed.

The results of the developed program can be used for the applications identified in the introduction of this paper. Interest has also been shown in some other fields, such as cartography of glaciers. To increase automation, studies on other (types of) glaciers and with data acquired in different seasons are necessary.

ACKNOWLEDGEMENTS

The authors would like to acknowledge alpS - Centre for Natural Hazard Management in Innsbruck, Austria for their support.

REFERENCES

Baltsavias, E.P., Favey, E., Bauder, A., Bosch, H., Pateraki, M., 2001. Digital Surface Modelling by Airborne Laser Scanning and Digital Photogrammetry for Glacier Monitoring. *The Photogrammetric Record*, Vol. 17, Part 98, pp 243-273.

Geist, T., Elvehøy, H., Jackson, M., Stötter, J., 2005. Investigations on intra-annual elevation changes using multitemporal airborne laser scanning data – case study

Engabreen, Norway. *Annals of Glaciology*, Vol. 42, pp 195-201.

Geist, T., Stötter, J., 2007. Documentation of glacier surface elevation change with multi-temporal airborne laser scanner data – case study: Hintereisferner and Kesselwandferner, Tyrol, Austria. *Zeitschrift für Gletscherkunde und Glazialgeologie*, Vol. 40.

Gorte, B.G.H., 1996. Multi-spectral quadtree based image segmentation. *International Archives of Photogrammetry and Remote Sensing*, Vol. 31, pp 251-256.

GRASS Development Team, 2006. Geographic Resources Analysis Support System (GRASS) Software. ITC-irst, Trento, Italy.

Höfle, B., Geist, T., Rutzinger, M., Pfeifer, N., 2007. Glacier Surface Segmentation using Airborne Laser Scanning Point Cloud and Intensity Data, ISPRS Workshop on Laser Scanning 2007, Espoo, Finland.

Höfle, B., Rutzinger, M., Geist, T., Stötter, J., 2006. Using airborne laser scanning data in urban data management - set up of a flexible information system with open source components, Proceedings of UDMS 2006: 25th Urban Data Management Symposium, Aalborg, Denmark, pp. 7.11-7.23.

Hoover, A., Jean-Baptiste, G., Jiang, X., Flynn, P.J., Bunke, H., Goldgof, D.B., Bowyer, K., Eggert, D.W., Fitzgibbon, A., Fisher, R.B., 1996. An Experimental Comparison of Range Image Segmentation Algorithms. *IEEE Trans. Pattern Anal. Mach. Intell.*, Vol. 18, Part 7, pp 673-689.

Kennett, M., Eiken, T., 1997. Airborne measurement of glacier surface elevation by scanning laser altimeter. *Annals of Glaciology*, Vol. 24, pp 293-296.

Kraus, K., Pfeifer, N., 1998. Determination of terrain models in wooded areas with airborne laser scanner data. *ISPRS Journal of Photogrammetry & Remote Sensing*, Vol. 53, pp 193-203.

Oerlemans, J., 1994. Quantifying Global Warming from the Retreat of Glaciers. *Science*, Vol. 264, pp 263-245.

Rees, W.G., 2005. Remote Sensing of Snow and Ice. Taylor & Francis.

Vosselman, G., Dijkman, S., 2001. 3D Building Model Reconstruction from Point Clouds and Ground Plans. *International Archives of Photogrammetry, Remote Sensing and Spatial Information Sciences*, Vol. XXXIV, Part 3/W4, pp 37-44.

Vosselman, G., Gorte, B.G.H., Sithole, G., Rabbani, T., 2004. Recognising Structure in Laser Scanner Point Clouds. *The International Archives of the Photogrammetry, Remote Sensing and Spatial Information Sciences*.

SINGLE-TREE FOREST INVENTORY USING LIDAR AND AERIAL IMAGES FOR 3D TREETOP POSITIONING, SPECIES RECOGNITION, HEIGHT AND CROWN WIDTH ESTIMATION

I. Korpela, B. Dahlin, H. Schäfer, E. Bruun, F. Haapaniemi, J. Honkasalo, S. Ilvesniemi, V. Kuutti, M. Linkosalmi, J. Mustonen, M. Salo, O. Suomi, H. Virtanen

Department of Forest Resource Management, POB 27, 00014 University of Helsinki, Finland –
ilkka.korpela@helsinki.fi

Commission III

KEY WORDS: Allometry, Modeling, Mapping, Sampling, Photo-plot, Calibration, Multi-Scale, Matching, Template

ABSTRACT:

An entire single-tree remote sensing (STRS) system was developed and tested in an inventory of timber resources of a 56.8-hectare forest. A semi-automatic approach with operator intervention is used in the system and it solves the essential tasks of STRS: 3D treetop positioning, height estimation, species recognition, crown width estimation and the model-based allometric estimation of the stem diameter. Large-scale aerial imagery, an accurate DTM and semi-dense LiDAR data are required. The relatively low sampling density of the LiDAR, 6 points per m² here, was considered appropriate for crown width estimation, when the 3D treetop position, tree height estimation and species classification are done first using the images. LiDAR-based crown width estimation was done using crown modeling, in which parametric crown instances are iteratively fitted with the LiDAR data. Image-based 3D treetop positioning and crown width estimation rely on multi-scale template matching (MSTM). Species recognition was done by visual photo-interpretation. In the experiment, a total of 59 circular 0.04-ha plots and 5294 trees were measured using STRS. The plots were investigated in the field and all STRS-trees and omission trees with a stem diameter of above 50 mm were mapped. The mapping was based on the use of the STRS-trees as geodetic control points. Redundant intertree azimuth and distance observations and a weighted least square adjustment of observations was used for the positioning of the omission trees. The commission error-rate was 2% in stem number and the omission trees constituted 10% of the total stem volume. Visual species recognition accuracy was 95% in classes of pine, spruce, broadleaved and dead trees. Height estimation accuracy of MSTM was 0.71 m or 4.7% in RMSE and it includes the DTM-errors. Stem diameter estimation RMSE was 29% and 20% when the crown widths were estimated using images and LiDAR, respectively. Underestimation of stem diameters was considerable, 3.4 and 1.0 cm. The inaccuracy of the stem diameter estimates degraded the accuracy of single-tree volume estimates and the results of estimating the proportion of assortments. Calibration of the STRS measurements and estimates are needed and this calls for field observations.

1. INTRODUCTION

1.1 Single-tree remote sensing from the viewpoint of forestry

The conventional way of measuring trees is giving way to new remote sensing applications, which have different scales of observation from individual trees to stands. Different sensors or methods that encompass certain levels of observation should not be taken as exclusionary alternatives. An optimal hybrid forest inventory most likely combines different data sources and furthermore, adjusts to the information needs that vary between stands and forest owners. Trees constitute a natural target of observation and single-tree remote sensing (STRS) aims at substituting the field measurements of position, species, height, stem diameter and volume. Preferably, a STRS-based forest inventory would be carried out without field visits, as it is largely based on direct measurements of the dimensions of the trees. However, STRS estimates seem to be prone to bias - e.g. the use of LiDAR often results in an underestimation of tree heights. This means that in situ data may be needed, at least for calibration.

The idea of photogrammetric STRS is old as early articles date back to the 1950s (e.g. Avery, 1958). Although the interest in the development has been extensive recently, especially in LiDAR-based methods (e.g. Persson et al. 2002), commercial STRS systems are essentially pending on the market. There are explicit difficulties to explain this. Scene complexity is an inherent aspect. Trees vary in crown size, shape and optical

properties. Crowns are often interlaced. Occlusion and shading are present and result in omission errors. In boreal canopies, the trees with a relative height of above 0.5-0.7 are detectable in images and 0-12% of the total stem volume and nearly all short trees remain unseen (Korpela, 2004). The fact that small trees remain undetected is a serious shortage for many applications. The detectable trees constitute 90-100% of the commercial timber, which motivates for applications in timber cruising. Reliable species recognition is needed by foresters and remains currently unsolved. A satisfactory level of accuracy is above 95% (Korpela and Tokola, 2006). This can be very difficult to achieve in for example temperate forests, where several species of one family or genus coexist in a stand. Foresters are interested in the current and future properties of the stems and the information on available timber assortments in a given area. Improved decisions are made in silvicultural and logging operations based on this information. This pays for the data. The estimates need to be accurate enough and the expenses of data acquirement and analysis need to remain tolerable. Objectives that are set for STRS systems should reflect these information requirements.

1.2 Reducing the ill-posedness of STRS

Because of the complexity and ill-posed nature of optical and LiDAR-based STRS, it seems necessary to adopt the semi-automatic approach and to use auxiliary information about the targets. Allometry, the knowledge on the relative sizes of plant

parts, is used in STRS, when the measurements of species (Sp), height (h) and crown width (d_{crm}) are used for estimating the stem diameter (dbh) with allometric equations (e.g. Kalliovirta and Tokola, 2005). They are imperfect and the inaccuracy, approximately 10% for dbh , defines an upper limit of attainable accuracy. Allometry varies between species and between trees in a stand as trees adapt to the intra- and interspecific competition and site conditions. The functioning and structure of trees are closely linked and it might be possible to improve the estimation accuracy of dbh , if, STRS could provide accurate measurements of the foliage density, foliage mass (Ilomäki et al., 2004) or crown length (Kantola and Mäkelä, 2004). Another aspect of allometry is to use the regularities for designing filters of rational STRS observations and for finding gross errors. In model-based STRS, allometry can provide initial approximations of the model instances (e.g. Larsen and Rudemo, 1998). In our STRS-system, the semi-automatic approach and allometric knowledge are used in solving the tasks of STRS.

1.3 Objectives

A set of semi-automatic STRS methods that use multiple images and airborne LiDAR data were developed to form an entire STRS system (Figure 1).

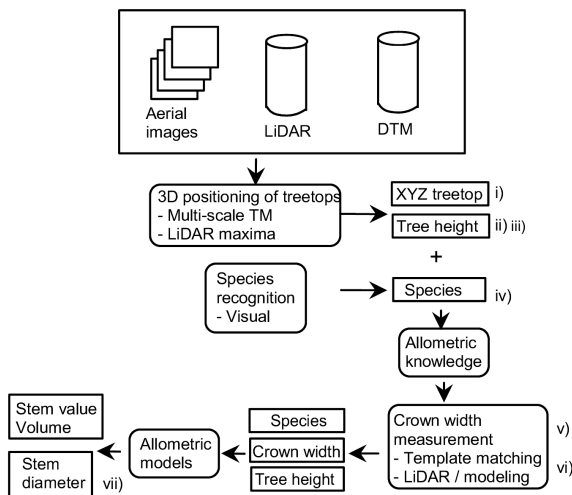


Figure 1. A schematic diagram of the STRS system with the data, tasks and output.

Allometric regularities are used for estimating the stem dimensions from STRS observations and for creating initial approximations of crown model instances. Following variables are measured by the system: i) Photogrammetric 3D treetop position using multi-scale template matching (MSTM), ii) photogrammetric tree height (h_{foto}) using the treetop position and a DTM, iii) LiDAR-based tree height (h_{LiDAR}), iv) species (Sp_{foto}) using visual image interpretation, v) image-based crown width ($d_{crm_{foto}}$) using MSTM, vi) LiDAR-based crown shape and width ($d_{crm_{LiDAR}}$) using least square adjustment of a crown model with the LiDAR point cloud and vii) stem diameter estimates (dbh_{foto} , dbh_{LiDAR}) using allometric equations. The system is described and a thorough performance test provided using a representative reference material from a systematic forest inventory. The rationales for our STRS system originate from the information needs in forestry and timber cruising in particular.

2. METHODS

2.1 Assumptions

It is assumed that multiple accurately oriented large-scale, >1:15000, aerial images and a semi-dense, 4-8 pulses per m^2 , leaf-on LiDAR data are available. An accurate DTM is needed for reliable tree height estimation. Here, an experienced photo-interpreter performed the visual species recognition.

2.2 Semiautomatic photogrammetric 3D treetop positioning, height and crown width estimation using multi-scale template matching

Single-scale template matching has been successfully applied in 2D and 3D treetop estimation of regular stands, where crowns show only moderate variation (Pollock, 1996; Larsen and Rudemo, 1998; Korpela, 2004; 2007a). The semi-automatic method that was presented in Korpela (2004; 2007a) and uses a single template per an aerial image was modified towards a more manual and reliable method. Instead of trying to position all treetops in an area, which fails when trees exhibit variation, a method that utilizes multi-scale template matching (MSTM) and operator assistance was developed. In it, the templates representing crown instances in the different views are copied from the real aerial images by first manually measuring the 3D treetop position of a model tree. Model trees are needed for as many species as there are in the area of interest. In the images, elliptic templates are defined by 3 metric parameters and the templates capture the upper part of the crown (Korpela 2004 p. #). For MSTM, these sub-images are copied, low-pass filtered and scaled into $N=11$ scales between 0.5 and 1.2 using bilinear re-sampling. For K images, this results in $N \times K$ templates. The semi-automatic 3D treetop positioning follows. A treetop is pointed manually in an image that is preferred by the operator. This image observation defines a reference image-ray, which is sampled over a range in Z (Figure 2).

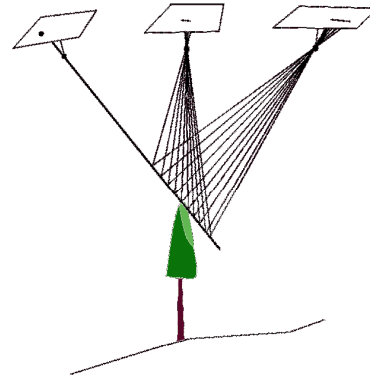


Figure 2. Illustration of the sampling of the reference image-ray over a search range in Z . The treetop position in the reference image is manually observed.

The search range in Z is one parameter that is set by the operator. It depends on the height variation of the trees and it is always centered on the Z of the previously measured treetop. At each 3D point along the reference image-ray, normalized cross-correlation (NCC) is computed in all images (along the epipolar lines) and templates (scales). The mean NCC of each scale is stored for each search point and the solution is the 3D point with the maximum NCC over all scales. Tree height (h_{foto}) is then given by the DTM by subtracting the terrain elevation from the elevation of the treetop.

Image-based crown width (*dcrm_foto*) estimation follows. The image with the smallest off-nadir angle is automatically selected for *dcrm_foto* estimation using MSTM. The 3D treetop position is mapped to this image and MSTM is tried in a small circular ($r=0.4$ m) image window near the projection point. The scale that gives the maximal NCC is used for the estimation of *dcrm_foto*: The crown width of the model tree, which is one of the 3 parameters that define the shape and position of the elliptic templates of the model tree, is multiplied by the scale factor to give *dcrm_foto* (Figure 3).

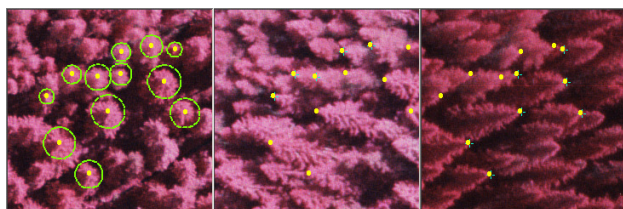


Figure 3. Results of MSTM in 3D treetop positioning and in *dcrm_foto* estimation: a CIR-image triplet of a pine-spruce stand. Solutions of twelve treetops are superimposed as yellow dots and the green circles depict estimates of *dcrm_foto*.

2.3 Species recognition

In tests with Vexcel Ultracam data (1:10000, GSD = 28 cm), it was found that the spectral values have considerable overlap between Scots pine, Norway spruce and birch. Within restricted areas in the front-lit parts of the images, the IR- and B-channels could potentially be used for species discrimination. The image-position seemed to cause variation in the spectral values. Also, young and old trees of the same species had varying spectral characteristics. The automatic approach was therefore discarded and visual interpretation of *Sp_foto* was applied. In an image set with 60% forward and side overlaps that was available here, there were always 1-2 views, where the crowns were seen back-lighted. These images are helpful for separating pine and spruce (Korpela et al., 2007). An experienced photo-interpreter carried out the visual interpretation.

2.4 Crown width estimation using LiDAR and least square adjustment of parametric crown models

A method was tried for LiDAR-based *dcrm* estimation, in which a parametric, non-linear crown model is iteratively fitted to the LiDAR point cloud (Figure 4; 5). The position and initial size and shape of the crown model are derived from the photogrammetric observations of *Sp_foto*, *h_foto* and the 3D treetop position. With these constraints, it was assumed that tree crown modeling is feasible even using rather a sparse LiDAR data. Crowns are approximated by a curve of revolution (1) that gives the crown radius $r(h_r)$ at a relative height $h_r \in [0, \pi/2]$ down from the treetop. The length of the crown is fixed to 40% of *h_foto*, which is a simplified approximation. The model is centered to the photogrammetric XYZ treetop position. If trees have only moderate slant, it can be assumed that the trunk is in the correct XY position. The crown model has three parameters and their initial values vary between species (Figure 4):

$$r(h_r) = a_1 \times h \times \sin(h_r)^{a_2} + a_3 \quad (1)$$

Parameter a_1 sets the relationship between tree height and the maximum crown radius; a_2 is a shape parameter and a_3 gives the width of the top. If $a_3 \neq 0$, the top is flat. Using allometric data from the National Forest inventory of Finland (Kalliovirta and

Tokola, 2005), conditional distributions of *dcrm* given h and Sp were derived. The relationship between *dcrm* and h was linear for all the three studied species: pine, spruce and birch. All broadleaved trees were treated as birches, as the proportion of other broadleaved trees is small in Finland. The conditional distributions were used in deriving initial values of parameter a_1 . Initial values for parameter a_2 were set such that pine and spruce had a conical crown and birch a more round crown (Figure 4). At the start of the iteration, the crown instance was made to overestimate the expected crown envelope through a_1 . Initial value of a_3 was 0.3 m for pine and spruce and 0.5 m for birch.

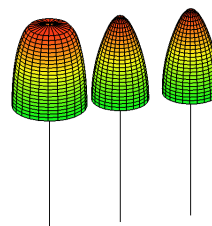


Figure 4. Illustration of three crown models for 22-m-high trees: a birch, a pine and a spruce. Birches have a 30-50% wider crown given the same tree height.

The LiDAR points that are inside the initial crown instance are collected and the relative height (h_r) down from the top and the XY distance (r) from the trunk is computed. These observations are used in solving a_1 , a_2 and a_3 by a least square adjustment procedure. The highest DTM-normalized height of a LiDAR point alternatively inside the initial crown instance or inside a 0.6-m wide cylinder is stored and used as height estimate h_{LiDAR} . *dcrm_LiDAR* is given by the adjusted model.

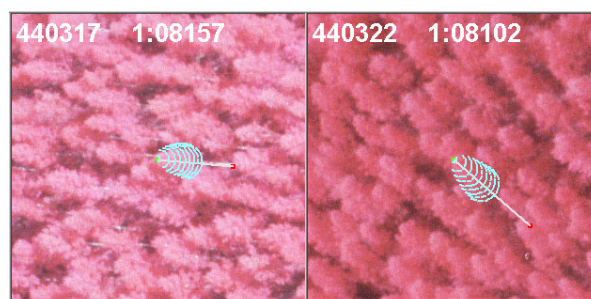


Figure 5. A view of an image pair after crown modeling of a birch. The "trunk" that is known from 3D treetop positioning is drawn in the images as well as the adjusted crown model. $dcrm_{LiDAR} = 4.5$ m, $h_{foto} = 22.1$ m and the RMSE of the model fit was 0.43 m. The texts give the image codes and the scale.

2.5 Allometric estimation of stem diameter and sortiment volumes

Equations by Kalliovirta and Tokola (2005) that predict *dbh* using h and *dcrm* for *Sp i* were applied:

$$\sqrt{dbh} = a_i \cdot \sqrt{h} + b_i \cdot \sqrt{dcrm} + \varepsilon_i \quad (2)$$

The models (2) assume maximal *dcrm*. Here, h_{foto} was always used as the h estimate and *dbh* was computed alternatively with *dcrm_foto* or *dcrm_LiDAR* giving two estimates for each STRS-tree: *dbh_foto* and *dbh_LiDAR*. The first case represents a

situation, where no LiDAR data is available. Assessment of different assortments was made by simulating stem bucking into logs of saw wood and pulp wood. The calculation of tree and log volumes was done using polynomial stem taper curves by Laasasenaho (1982). They use Sp , dbh and h for predicting the stem form. The bucking algorithm used rules for allowable log lengths and the minimum top diameters.

3. EXPERIMENT

3.1 Study area, image and LiDAR data

The study site is a 56.8 ha forest in southern Finland (61°50' N, 24°20' E). The area consists of 25-70 and 100-130-yr-old stands. A systematic 50×50-m grid of 0.04-ha circular plots was established. Every 4th plot was selected and two additional plots giving a total of 59 plots and 2.36 ha (Figure 6). The image data is given in Table 1. Images were orientated in a hybrid bundle block adjustment (c.f. Korpela, 2006). For visual interpretation, the 5-channel Vexcel images were fused into CIR-images having a 9-cm GSD.

Date	Image set	
	July, 18 2004	August, 5 2006
Time	11:25	09:27
Scale	1:8000	1:10000
Overlaps	60/60%	60/30%
Sun elev.	45°	30°
Camera	RC30	UltraCam D
Focal length	0.214 m	0.105 m
Film-type	CIR Kodak 1443	PAN, R, G, G, IR
Film-size	23 × 23 cm	10 × 6 cm
GSD	12 cm	9 cm PAN, 28 cm MS

Table 1. Parameters of the two image sets.

A LiDAR-DTM was estimated using TerraModeler software from leaf-on data from August, 2004 having 0.7-2 points per m^2 . Its accuracy was 0.27 m in a reference data of 8300 tacheometer points (Korpela and Välimäki, 2007). A semi-dense LiDAR from July 25, 2006 was available for tree crown modeling. An ALTM 3100 sensor with a pulse frequency of 100 kHz, a flying height of 800 m, a scan frequency of 70 Hz, a scan angle of $\pm 14^\circ$, a flying speed of 75 m/s and strip overlaps of 55% were applied in the mission. The density of the data varies from 6 to 9 pulses per m^2 and from 1 to 4 points per pulse. The data had a minimum range difference of 3 m between points in a pulse. The footprint was approximately 25 cm.

3.2 STRS and field measurements

In April 2007, 5294 STRS-trees in the vicinity of the photo-plots were measured using the methods of sections 2.2-2.4. The work took 32 hours giving an average rate of 165 trees per hour. Each tree was measured for 3D treetop position, h_{foto} , h_{LiDAR} , Sp_{foto} and estimated for $dcrm_{foto}$ and $dcrm_{LiDAR}$. From 3 to 6 images were used and the newest images from 2006 were included to reduce the underestimation of h caused by the 2-year mismatch of the 2004 images. There were always 6 images available on the computer screen for the visual species recognition into classes of pine, spruce, broadleaved and dead trees.

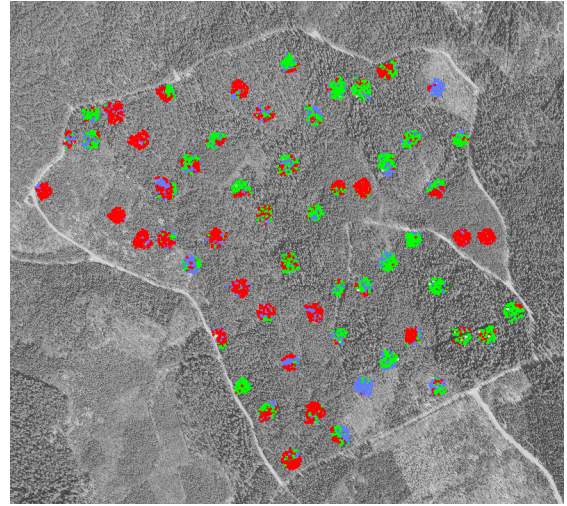


Figure 6. The 5294 STRS-treetops superimposed in a BW leaf-off topographic image from 1999. Forest roads define the borders of the 56.8-ha study area. The colors are: pine = red, spruce = green and broadleaved trees = blue.

The STRS-trees were processed into plot-wise maps (Figure 7). Labels to be fastened to the stems were printed. These had information of the STRS measurements and a map of the neighboring trees with azimuths as seen from the tree in question. A GPS-receiver with 1-m accuracy was used for finding the plot center. From then on, the field investigators used the map, intertree azimuths and a precision compass for identifying the STRS-trees. Cases, in which the STRS-tree did not have a unique counterpart in the field, the STRS-tree was made into a commission error. In addition to the STRS-trees, all omission trees with dbh of above 50 mm were mapped and included in the reference data and measured for Sp and dbh and assessed for the state of the crown. Every 3rd STRS-tree and every 6th omission tree were measured for h and crown length. The h -observations were done with a Suunto-hypsometer and the standard error (SE) was assumed to be 0.8 m. It undoubtedly varied between investigators, tree species and height classes.

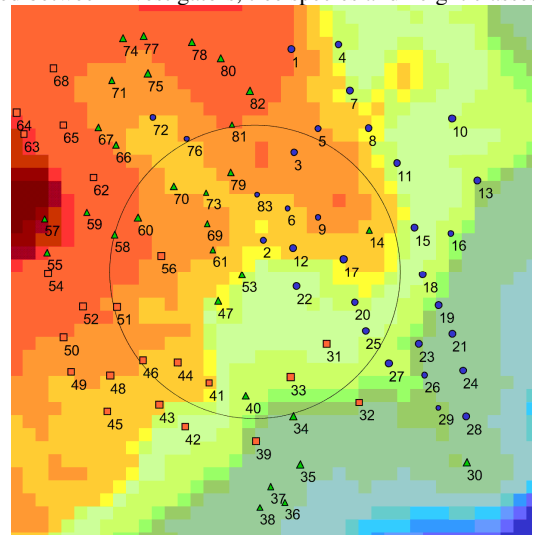


Figure 7. A tree map of STRS-trees that the investigators had in the field. The circle depicts the 0.04-ha plot and the STRS-trees are represented by species-specific symbols. A LiDAR-DTM in 1-m resolution is drawn in the background.

The mapping of the omission trees used a geodetic procedure, where the STRS-trees served the role of control points (Korpela et al., 2007). The investigators selected 3-4 STRS-trees with vertical stems and an unambiguous apex. These trunks were assumed to have an XY accuracy of 0.3 m. Intertree azimuths (spatial resection) were measured with a precision compass and intertree distances (trilateration) with a laser distance meter. Using weighted least square (WLS) adjustment of control point coordinates, intertree distances and azimuths, the omission trees were positioned with an average accuracy of 0.25 m in X and Y. The SE estimates of X and Y were above 0.75 m in 4 of 1410 omission trees. These trees had several gross observation errors and as the WLS adjustment could not be done in the field, it was arduous to track blunders. A leave-one-out technique was used to find cases with a single gross. Trees were also measured again.

3.3 Results - Performance of tree detection

2122 of 2205 STRS-trees were unambiguously found giving a commission error-rate of 3.7%. The commission error-rates were 1.8% for pine, 2.4% for spruce and 10.4% for the broadleaved trees.

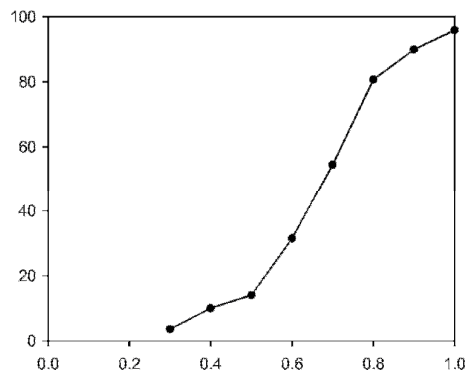


Figure 8. Results of tree detection. The curve gives the proportion (vertical axis, %) of correctly detected trees in 8 classes (0.3-1) of relative tree height.

Broadleaved trees can have round crowns, which affects the photogrammetric treetop positioning and makes the field identification of STRS-trees difficult. Broadleaved trees may have fused crowns, or the top of the crown consists of several upright thick branches, which are easily misinterpreted as individual trees. Commission errors were detected in 29/59 plots and the presence of broadleaved trees was associated with the number of commission errors. Since the detection of commission errors was a subjective process, it can be argued that a part of the commission errors were due to the prudence of the investigators. The true commission error-rate could only be examined by mapping the trees using tacheometry and by giving metric rules. From our field experience, we assumed that the true commission error-rate is approximately 2%. Omission trees constituted 38.8% of the stems ($dbh > 50$ mm) and 12% of the total stem volume. The omission error-rate in volume is thereby approximately 10%, if the “erroneous commission trees” are accounted for. (Figure 8).

3.4 Results - Species recognition

The species recognition accuracy was 93.7%, and if the 0-2% reference imprecision is accounted for, the accuracy is approximately 95% (Table 2).

<i>Sp_foto</i>	Field measured value				
	Pine	Spruce	Broadl.	Dead	All
Pine	896	37	8	6	947
Spruce	25	726	13	2	766
Broadl.	16	22	354	0	392
Dead	0	3	1	4	8
All	937	788	376	12	2113

Table 2. Error matrix of species recognition of the correctly found STRS-trees excluding 9 trees with tentative or missing reference measurements. Kappa = 0.90.

3.5 Results - Height estimation accuracy

The RMS-accuracy of h_{foto} was 0.71 m with an underestimation of 0.14 m (Table 3). Imprecision was largest in the broadleaved trees. Differences of up to 4 m were found. These may have resulted from errors in the 3D treetop positioning, the reference height observations or from errors in the DTM. h_{LiDAR} underestimated true h by 0.58 m (Table 4). The residuals of h_{foto} and h_{LiDAR} had an R^2 of 0.78. It is evident that a large part of the correlation is a result of the measurement errors in the field data. The underestimation of h_{LiDAR} was largest with spruce, which is explained by the peaked crown form.

<i>Sp</i>	N	Mean	SD	RMSE	RMSE-c
Pine	322	+0.17	0.93	0.94	0.50
Spruce	256	+0.19	1.07	1.08	0.73
Broadl.	128	-0.02	1.30	1.30	1.02
All	706	+0.14	1.06	1.07	0.71

Table 3. Accuracy of height estimates h_{foto} [m]. RMSE-c was calculated by subtracting the expected 0.8-m SE error of the field measurements from the observed RMSE. Mean reference h of all trees was 15.6 m.

<i>Sp</i>	N	Mean	SD	RMSE	RMSE-c
Pine	322	+0.58	0.88	1.05	0.69
Spruce	256	+0.69	1.01	1.22	0.92
Broadl.	128	+0.36	1.15	1.20	0.90
All	706	+0.58	0.99	1.14	0.82

Table 4. Accuracy of the height estimates h_{LiDAR} [m].

3.6 Results - Stem diameter estimation accuracy

The accuracy of dbh_{foto} estimates that were based on the use (2) of variables Sp_{foto} , h_{foto} and $dcrm_{foto}$ was 28.7% in RMSE. The plot-level RMSEs were 15.8%-47.3%, which means that in the best cases the $dcrm_{foto}$ measurement by MSTM had succeeded reasonably well. The 3.45-cm underestimation is most likely caused by the fact that the maximal crown width could not be seen in the images (Table 5). The estimates dbh_{LiDAR} that were predicted with models (2) using Sp , h_{foto} and $dcrm_{LiDAR}$, underestimated true dbh by 1 cm (Table 6). The overall RMSE was 19.6% with plot-level values ranging from 12.1% to 35.4%. The average $dcrm_{foto}$ was 2.1 m, while the mean of $dcrm_{LiDAR}$ was 2.9 m, which explains the differences in dbh_{foto} and dbh_{LiDAR} .

<i>Sp</i>	N	Mean	SD	RMSE
Pine	945	+3.96	3.33	5.17
Spruce	792	+3.24	3.08	4.47
Broadl.	376	+2.58	3.60	4.42
All	2113	+3.45	3.33	4.79

Table 5. Accuracy of stem diameter estimates dbh_{foto} [cm]. Mean diameter of all reference trees was 16.7 cm.

<i>Sp</i>	N	Mean	SD	RMSE
Pine	945	+0.73	3.12	3.21
Spruce	792	+1.39	2.99	3.30
Broadl.	376	+0.80	3.33	3.43
All	211	+0.99	3.13	3.28

Table 6. Accuracy of stem diameter estimates *dbh_LiDAR* [cm].

3.7 Results - Volume estimation accuracy

An RMSE of 60% was observed in the single tree volume estimates calculated with *dcrm_foto*. The plot-level RMSEs were 29.5%-108.1% (Table 6). The volume estimates that were based on the use of LiDAR in the estimation of crown width were more reliable. The RMSE for all trees was 46% and the plot-level RMSEs ranged from 24.6% to 101.4% (Table 7).

<i>Sp</i>	N	Mean	SD	RMSE
Pine	945	+82	102	131
Spruce	792	+74	107	130
Broadl.	376	+55	106	120
All	2113	+74	105	128

Table 6. Accuracy of single tree volume estimates [dm³] calculated using *Sp*, *h_foto* and *dbh_foto* and the taper curves by Laasasenaho (1982). Mean reference volume was 214 dm³.

<i>Sp</i>	N	Mean	SD	RMSE
Pine	945	+21	88	91
Spruce	792	+36	100	106
Broadl.	376	+24	94	98
All	2113	+28	94	98

Table 7. Accuracy of single tree volume estimates [dm³] calculated using *Sp*, *h_foto* and *dbh_LiDAR*.

3.8 Results - STRS forest inventory

Variable	Inventory method		
	STRS		Field
Standing stems, n	53137	64.8 %	82042
Total volume, m ³	9783	80.8 %	12110
Saw wood, m ³	3522	67.6 %	5212
Pulp wood, m ³	5926	94.6 %	6264
Volume, Pine, m ³	4511	86.8 %	5198
Volume, Spruce, m ³	3919	73.0 %	5372
Volume Broadl., m ³	1262	80.9 %	1560

Table 8. Timber resources of the 56.8-ha forest with the STRS and field inventory. The STRS-results were computed using measurements of *Sp_foto*, *h_foto*, *dcrm_LiDAR* and *dbh_LiDAR*.

The timber resources were computed for the 56.8-ha forest using both STRS and the field measurements (Table 8). The STRS inventory lead to an underestimation of volume by 19.2%, which is explained by the omission errors (10 % in volume) and the 1-cm underestimation and 3-cm imprecision of the *dbh_LiDAR* estimates. An average STRS-tree had a *dbh* of 16.7 cm and an *h* of 15.6 m. A 1-cm underestimation in *dbh* for such a tree results in a 10-% underestimation of volume. The inaccuracy of the *dbh* estimates affected especially the accuracy of saw wood and pulp wood volume estimates. When the *dbh* of a single tree reaches 17-19 cm, the stem can be cut to provide a single log of saw wood, which constitutes 50% of the stem volume. Because *dbh_LiDAR* was biased and, above all, averaged due to regression modeling (2), saw wood volume was underestimated as much as 32.4%. Averaged *dbh* estimates

induce systematic errors in the volume estimates, because the relationship between *dbh* and the volume is non-linear. Only 5% of the underestimation in saw wood volume was assessed to be due to omission errors, as the largest trees were measurable in the images (Figure 8). The rest of the underestimation, 27%, was due to the inaccuracy of *dbh_LiDAR*. Pulp wood volume was underestimated by only 5.4%. The seemingly good result is fallacious and a result of errors in stem bucking, which overestimated the proportion of pulp wood and underestimated the volume and number of saw wood logs because of the bias in *dbh_LiDAR*. Thereby, the results of Table 8 suggest strongly that a calibration of the STRS measurements and model estimates is required to avoid large systematic errors in the total estimates. The smaller underestimation in the volume of pine (13.2%) in comparison to spruce and the broadleaved trees is mainly explained by the differences in the relative height of the detected STRS-trees and the height variation of the species. Pine and Silver birch are light-demanding and spruce is a semi-shade-tolerant species. Also, the underestimation of *dbh_LiDAR* was largest for spruce.

4. DISCUSSION

The main result was that a STRS forest inventory was shown feasible, but that the results are subject to systematic errors that can only be eliminated with calibration. The STRS system provided the timber volume estimates per species and per sortiment, which is a must in a forest inventory. We demonstrated many difficulties that are inherent to STRS. Sampling, measurement and model errors all affected the results. Omission errors and biased measurements caused considerable systematic errors in the estimates of the timber resources. The use of the allometric regression models results in averaged *dbh* estimates even with error-free measurements. These, although free from systematic errors, resulted in biased volume estimates because of the non-linear dependencies. In all, the allometric estimation chain needs improvement.

The STRS measurements took 32 man-hours and the field work 500 with an extra 80 man-hours of data recording. The ratio was 1:18 between the two inventories. If larger photo-plots were used, less time per STRS-tree would have been needed, as the selection and measurement of the model tree in each plot was time-consuming. The costs should also include the image (~2€/ha) and LiDAR data (~3€/ha). Also, there was a high risk that no image data from 2006 was available because of bad weather. The weather risk is lesser with LiDAR and field work.

Multi-scale template matching (MSTM) was accurate in treetop positioning and *h* estimation. However, up to six large-scale images and an accurate LiDAR-DTM were available. The RMSE of *h* estimates was 0.5 m for pine, 0.7 m for spruce and 1.0 m for the broadleaved trees. The photogrammetric XY positioning accuracy was approximately 0.3 m, as the average σ_0 was close to 1, when a 0.3-m a priori SE was applied in the WLS-adjustment of photogrammetric coordinates, intertree azimuths (SE = 0.03 rad) and intertree distances (SE = 0.1 m) In all, the field mapping method of the omission trees, in which the STRS-trees were used as control points was satisfactory. In dense stands, where broadleaved trees formed the upper canopy, the mapping become tedious and subject to errors.

MSTM in near-nadir images for *dcrm* estimation resulted in badly biased *dbh* estimates with an RMSE of 29%. A plot-level RMSE of below 20% was observed in 7/59 plots. In first tests with the method (Korpela, 2007b), the accuracy of *dbh* estimates ranged from 16% to 21%, but the results were

obtained in well-structured stands and using images with a very low off-nadir angle. The technique needs further improvement. The use of synthetic templates should be tested (Larsen and Rudemo, 1998). The computation of NCC was done for gray-scaled versions of the images. Better results may be possible using a combination of channels. Also, the system could learn from good and compatible measurements, where the LiDAR-based estimates of h and d_{crm} are used to teach the system in the selection of better templates. The MSTM-based 3D treetop positioning algorithm was based on monoscopic observations by an operator and the process is slow. It might be possible to implement MSTM to find trees automatically. However, the very high computational costs of NCC need consideration. The 3D search space for photogrammetric treetop positioning is accurately known, if LiDAR data is available. This was not exploited here and the LiDAR data could be used more effectively by using the monoplotted principle (e.g. Baltsavias, 1996). In it, LiDAR data would be processed into a canopy surface model to be intersected by the reference (treetop) images rays. The search space could then be adjusted to the height variation measured by the LiDAR (c.f. Korpela, 2007a).

The accuracy of the visual species recognition was 95% for classes of pine, spruce, broadleaved and dead trees. The achieved 95% classification accuracy is at the requisite level for Finnish forestry. However, in some areas a separation of the broadleaved trees at the species level would be needed. The automatic species recognition remains to be solved. Here, we see possibilities in the combined use of LiDAR and image data.

The crown modeling procedure with LiDAR needs further improvement, although it resulted in a dbh estimation accuracy of 20% with 14/59 plot-level RMSEs of below 15%. Avoiding LiDAR points of neighboring trees to affect the modeling might be possible by constructing geometric filters that take into account the spatial pattern of trees, which is partially known from photogrammetric 3D treetop positioning. This would mean that the LiDAR-based crown modeling is done only after the tree map is attained. The dbh_{LiDAR} underestimated true dbh by 1 cm, because the d_{crm} was not measured correctly by the crown model. The LiDAR pulses do not seek their way to the tips of the branches and when LS adjustment is applied, the extent of the crown envelope is inherently underestimated. The nominal density of the LiDAR data was 6-9 pulses per m^2 here - a lesser density may possibly suffice for crown modeling.

Generalization of the results requires care. Most trees had peaked and uniform crowns. One experienced photo-interpreter was tested. The orientation of the images was exact and the image sets had a faultless match. Also, the LiDAR from 2006 did not have XYZ offsets, which was examined using multi-temporal large-scale images. Using network-RTK, a height offset of 0.18 m was detected in the LiDAR-DTM from 2004 and corrected for. Performing such revisions is not feasible in practice. The stands were older than 25 years. In timber cruising young stands are less important, but in an inventory for forest management planning, they cannot be overlooked.

5. REFERENCES

Avery, G. 1958. Helicopter stereo-photography of forest plots. *Photogrammetric Engineering*, 24(4), pp. 617-624.

Baltsavias E., 1996. Digital ortho-images - A powerful tool for the extraction of spatial- and geo-information. *ISPRS JPRS*, 51(2), pp. 63-77.

Iiomäki, S., Nikinmaa, E. and Mäkelä, A., 2003. Crown rise due to competition drives biomass allocation in silver birch. *Canadian Journal of Forest Research*, 33(12), pp. 2395-2404.

Kalliovirta, J. and Tokola, T. 2005. Functions for estimating stem diameter and tree age using tree height, crown width and existing stand database information. *Silva Fennica*, 39(2), pp. 227-248.

Kantola, A. and Mäkelä, A., 2004. Crown development in Norway spruce [*Picea abies* (L.) Karst.]. *Trees - Structure and Function*, 18(4), pp. 408-421.

Korpela, I., 2004. Individual tree measurements by means of digital aerial photogrammetry. *Silva Fennica Monographs*, 3, pp. 1-93.

Korpela I., 2006. Geometrically accurate time series of archived aerial images and airborne lidar data in a forest environment. *Silva Fennica*, 40(1), pp. 109-126.

Korpela, I., 2007a. 3D treetop positioning by multiple image matching of aerial images in a 3D search volume bounded by lidar surface models. *PFG 1/2007*, pp. 35-44.

Korpela, I., 2007b. Incorporation of allometry into single-tree remote sensing with lidar and multiple aerial images. ISPRS Hannover Workshop, May 29-June 1, 2007. 6 p.

Korpela, I. and Tokola, T., 2006. Potential of aerial image-based monoscopic and multiview single-tree forest inventory - a simulation approach. *Forest Science*, 52(3), pp. 136-147.

Korpela, I. and Välimäki, E., 2007. Talousmetsän maanpintamallinnus arkistoilmakuvilta ja laserkeilauksella. [Terrain modeling using archived aerial images and airborne laser scanning]. Accepted in *Maanmittaus*.

Korpela, I., Tuomola, T. and Välimäki, E., 2007. Mapping forest plots: An efficient method combining photogrammetry and field triangulation. Accepted in *Silva Fennica*.

Laasasenaho, J., 1982. Taper curve and volume functions for pine, spruce and birch. *Communicationes Instituti Forestalis Fenniae*, 74, pp. 1-74.

Larsen, M. and Rudemo, M., 1998. Optimizing templates for finding trees in aerial photographs. *Pattern Recognition Letters* 19(12), pp. 1153-1162.

Persson, Å., Holmgren, J. and Söderman, U. 2002. Detecting and measuring individual trees using an airborne laser scanner. *PERS*, 68(9), pp. 925-932.

Pollock, R.J., 1996. The automatic recognition of individual trees in aerial images of forests based on a synthetic tree crown model. PhD-thesis in Computer Science. The University of British Columbia. 158 p.

ACKNOWLEDGEMENTS

We thank Professor Markus Holopainen for letting the study to be a part of the forest inventory course at the University of Helsinki. Our thanks are due to Timo Melkas and Reija Haapanen for helping us in the field.

LASER SCANNER SIMULATOR FOR SYSTEM ANALYSIS AND ALGORITHM DEVELOPMENT: A CASE WITH FOREST MEASUREMENTS

Antero Kukko*, Juha Hyypä

Finnish Geodetic Institute, Department of Remote Sensing and Photogrammetry, P.O. Box 15, 02431 Masala, Finland –
Antero.Kukko@fgi.fi, Juha.Hyypa@fgi.fi

Commission VI WG VI/4

KEY WORDS: Airborne, Terrestrial, Laser scanning, LIDAR, Simulation, Waveform, Quality

ABSTRACT:

LIDAR systems have come to be extensively used in photogrammetry and mapping sciences. The accuracy of 3D information is mainly affected by navigational and system-dependent uncertainties, but also by the laser beam properties and the nature of the light interaction on the object surface. At the moment, the system-dependent sources of error are much better known than those arising from laser light interaction. In this paper, a simulation approach for scanning LIDAR systems is presented and discussed. Simulating light interaction on an object surface provides an opportunity to measure well-defined objects under controlled conditions. The simulated object remains unchanged over time, and when various sensor and system parameters are applied, it is possible to compare the 3D point clouds created. Furthermore, well-established simulation software makes it possible to study and verify future LIDAR systems and concepts.

1. INTRODUCTION

Airborne LIDAR systems have been extensively adopted for mapping purposes in recent years. Uses of laser scanning include digital elevation model (DEM) production (e.g. Kraus and Pfeifer, 1998; Pereira and Janssen, 1999; Axelsson, 2000; Reutebuch et al., 2003), building extraction (e.g. Brenner, 2005; Haala et al. 1998; Hofmann et al. 2002; Hofmann, 2004; Hofton et al., 2000; Maas, 2001; Rottensteiner, 2003; Rottensteiner and Jansa, 2002; Rottensteiner et al. 2005; Vosselman, 2002; Vosselman and Süveg, 2001), and forest management (e.g. Naesset, 2002; Hyypä et al. 2001; Persson et al. 2002; Yu et al. 2004; Matikainen et al., 2003). In these applications the algorithm development is usually based on data retrieved using commercial LIDARs. Consequently, mapping algorithms are often adapted to the laser data used.

Earlier attempts at three-dimensional simulation modeling include modeling of the scanning angle effect in the measurement of tree height and canopy closure in boreal forest with an airborne laser scanner (Holmgren et al. 2003) and the establishment of optimal LIDAR acquisition parameters for forest height retrieval (Lovell et al. 2005). In these cases two assumptions are made: the simulated laser pulse is assumed to be a single ray without any divergence and the coarse objects simulated are assumed to be solid. In general, such simulation methods were useful, but the implementation was relatively simple. Thus, in Holmgren et al. (2003), the simulation method systematically overestimated the laser height percentiles by 2.25 m since beam interaction, waveform, and threshold detection were not simulated.

There are possible applications in which simulation together with good models for the sensors, target and beam interaction would provide further insights. Simulation may also supply answers to some questions, which are not properly understood. Optimization of the laser acquisition parameters is one feasible application area. Opportunities for the use of waveform data has been long delayed due to the lack of experimental data.

However, waveform data can be simulated with some accuracy (Filin & Csathó, 2000; Thiel & Wehr, 2004; Jutzi et al. 2005). Also, the capabilities of future laser instruments can be estimated using simulation and appropriate models.

The quality of products derived from laser scanning is influenced by a number of factors, which can be grouped as follows: errors caused by the laser system (the laser instrument, GPS and INS) and data characteristics (e.g. first/last pulse, point density, flight height, scan angle, beam divergence), errors created during processing of the data (interpolation errors, filtering errors, errors caused by improper break-line detection, segmentation and smoothing of the data), and errors due to characteristics of the target (type and flatness of the terrain, density of the canopy above). By adding simulations to single data experiments, the effect of most of these errors can be estimated in a more reliable way than it is when an experimental approach is adopted.

This article presents ideas and development of a simulation method for existing LIDAR systems, but also general user defined sensors are supported. The purpose of this work is to provide a tool for analyzing systematic properties of scanning LIDAR systems, and factors affecting the quality of the LIDAR end products. Utilization of the simulation method developed also aims at intensifying the algorithm development for specific mapping applications and waveform processing. A case with forest measurements is depicted in more detail.

2. LASER SCANNING PRINCIPLE

A laser scanner transmits a short laser pulse, typically 3-10 ns. This laser pulse, or beam, is transmitted in a certain direction to reach the object surface. The beam diverges from its nominal direction and creates a narrow conic shape, and thus the transmitted energy spreads over a larger footprint area. The reflections of the pulse also come from this footprint area and their intensity decreases towards the edges of the beam.

* Corresponding author.

The illuminated footprint area may consist of a variable amount of surface materials at variable ranges and orientations. This affects the power and shape of the backscattered echo, or waveform, of the received signal. This situation is illustrated in Figure 1, which schematically depicts one laser beam and its reflection from a building. The different orientations and locations of the building surfaces cause sequential reflections from the building and ground. The amount of beam divergence from the nominal beam direction causes the decrease in accuracy in both the planar and height directions, since all echoes are considered to be reflected from the axis of the nominal beam direction. A good overview on the basic relations for the laser scanning can be found in (Baltasvias 1999).

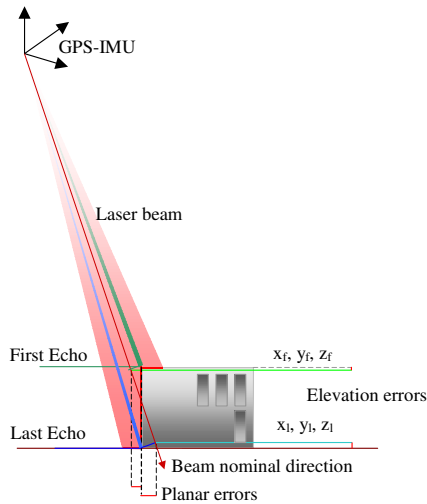


Figure 1. Principle of a LIDAR observation. Beam divergence causes the spread of a beam over the footprint area from which multiple echoes are collected. The nominal beam direction determines the final 3D position.

Three basic scanning geometries are engineered for commercial airborne scanning LIDARs. These operate mainly in line, oscillating (sinusoidal or z-shaped lines) and elliptical geometries, all of which form a different point pattern on the ground. These general patterns are illustrated in Figure 2. The point density on the ground surface is determined by the field of view, pulse repetition rate and scanning frequency as the sensor overflies the area with a known velocity and direction and at a specified altitude.

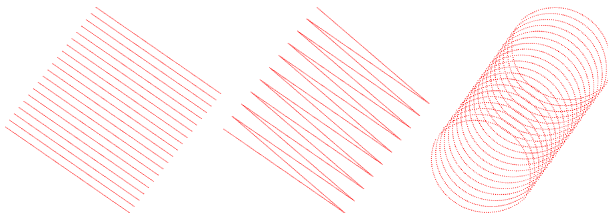


Figure 2. Scanning patterns for three basic measuring principles: A: Line, B: Oscillating, and C: Conic.

Table 1 sums up some principal parameters of commercial airborne laser scanning systems, which are adopted in the simulation software. The main operational differences are in the pulse and scanning frequency, the scanning angle, the beam divergence and the pulse length. It is also expected that the shape of the pulse is different for each of the sensors. The

parameter variability increases if the terrestrial scanners are taken into account, but here they are excluded.

3. SIMULATION METHODS

This section describes the basic implementations in the simulation software. The methodology includes emulation of the geometric properties of the scanner system, laser radiation and scattering on the target surface, as well as the signal waveform processing.

A complete LIDAR simulator deals with platform and beam orientation, pulse transmission, beam interaction with the target surface, computation of waveform prototype, and eventually digitization of the waveform:

- Platform and beam orientation – Controls platform movements and scanner operation according to the system and flight parameters.
- Pulse transmission – Deals with the laser beam properties according to the beam angular divergence and the spatial distribution of the transmitted energy.
- Beam interaction – Laser beam division into sub-beams and their interaction with the target surface are computed. Elevation, surface orientation, reflectivity, and distance from the beam center are considered.
- Waveform – The echo waveform prototype is created by summing up the energy returned from different parts of the laser beam according to their range and surface orientation dependent reflectivity. Returned energy is collected by a telescope aperture.
- Threshold detection and waveform digitizing – in this phase the echoes exceeding a given power threshold are detected. Recorded output echo waveform is created in digitization of the simulated echo prototype using system-dependent sampling interval and detection parameters.

3.1 Scanning geometries

Airborne LIDARs typically have three basic scanning geometries, as shown in Figure 2. These are implemented into the simulation software. The other relevant system-specific parameters affecting the achieved scanning pattern, and thus the data coverage on the ground surface, are pulse frequency, scanning rate, scanning angle, and the along track velocity of the platform.

One swath of a scanner consists of a certain amount of beams, defined by the ratio of pulse frequency and scanning rate, and is produced by rotation geometry around the origin of the laser scanner. The field of view of the scanner was divided according to the pre-set parameters to achieve the correct orientation for each beam in the ground coordinate system. Each single laser beam shot was modeled using multiple rays with uniform angular distribution around the center line of sight. The angular separation between adjacent rays, sub-beams, was chosen according to the flight altitude and surface model grid spacing in use.

3.2 Pulse transmission

The power distribution of the transmitted pulse can be approximated by a Gaussian as a function of time. The second element in the transmission sub-system controls the laser beam divergence, in other words, the laser footprint size at ground

Table 1. Characteristics of some commercial airborne laser scanning systems.

Sensor	Mode	Scan Freq.	Pulse Freq.	Scanning Angle	Beam Div. $1/e^2$	Pulse Energy	Range Resolution	Pulse Length	Digitizer
Optech 2033	Oscillating	0-70 Hz	33 kHz	$\pm 20^\circ$	0.2/1.0 mrad	N/A	1.0 cm	8,0 ns	N/A
Optech 3100	Oscillating	0-70 Hz	33-100 kHz	$\pm 25^\circ$	0.3/0.8 mrad	<200 μ J	1.0 cm	8,0 ns	1 ns
TopEye MkII	Conic	35 Hz	5-50 kHz	14°, 20°	1.0 mrad	N/A	<1.0 cm	4,0 ns	0.5 ns
TopoSys I	Line	653 Hz	83 kHz	$\pm 7.15^\circ$	1.0 mrad	N/A	6.0 cm	5,0 ns	N/A
TopoSys II Falcon	Line	630 Hz	83 kHz	$\pm 7.15^\circ$	1.0 mrad	N/A	2.0 cm	5,0 ns	1 ns
Leica ALS50	Oscillating	25-70 Hz	83 kHz	$\pm 37.5^\circ$	0.33 mrad	N/A	N/A	10 ns	N/A
Leica ALS50-II	Oscillating	35-90 Hz	150 kHz	$\pm 37.5^\circ$	0.22 mrad	N/A	N/A	10 ns	1 ns
LMS-Q560	Line	160 Hz	<100 kHz	$\pm 22.5^\circ$	0.5 mrad	8 μ J	2.0 cm	4,0 ns	1 ns

level. The size of the footprint on the ground is a simple function of the divergence angle and the flight altitude, or more precisely the range:

$$D = 2z \tan \Delta\theta/2, \quad (1)$$

where D is the beam footprint diameter, $\Delta\theta$ is the beam divergence angle and z the distance to the ground surface.

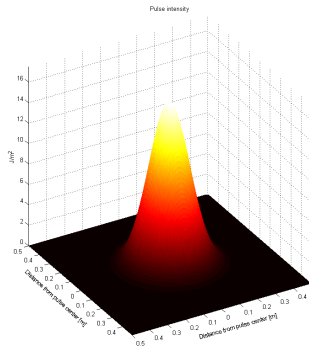


Figure 3. Intensity pattern of a 8 μ J Gaussian TEM₀₀ pulse with a beam divergence angle of 1.0 mrad ($1/e^2$) at range of 400 m. The resulting footprint diameter is approximately 40 cm.

The intensity of a laser pulse is modeled using transverse mode TEM₀₀, which gives one centralized Gaussian spot on the target surface. As it travels in the air, the laser-beam wavefront acquires curvature and begins to spread as follows:

$$w(z) = w_0 \left[1 + \left(\frac{\lambda z}{\pi w_0^2} \right)^2 \right]^{1/2}, \quad (2)$$

where z is the distance propagated from the plane where the wavefront was flat, λ is the wavelength of light, w_0 is the radius of the $1/e^2$ irradiance contour at the plane where the wavefront is flat, $w(z)$ is the radius of the $1/e^2$ contour after the wave has

propagated a distance z . Eventually attained energy per unit area is:

$$I(r) = \frac{2P}{\pi w^2} \exp\left(\frac{-2r^2}{w^2}\right), \quad (3)$$

where $I(r)$ is the intensity function, P the total energy, w the laser footprint radius measured between $\pm 2\sigma$ points, and r the distance from the centre of the laser beam. Thus, the energy decreases as a function of the distance from the beam centre leading to less energy returning from the outer parts of the beam than from the centre. Intensity pattern of a typical airborne laser scanner pulse is illustrated in Figure 3.

The transmitted laser pulse is modeled by a predefined number of discrete rays. The returned energy is calculated using the intensity of the transmitted pulse at the range in question, the surface reflectivity and the area of interaction, which here depends on the beam sub-division parameters:

$$E_{ret}(r) = \tau R(\theta) I_0(r) A, \quad (4)$$

where E_{ret} is the returned energy, τ is atmospheric transmission, R anisotropic surface reflectance at given angle of incidence θ , I_0 pulse intensity at range r from the scanner, and A the receiving area of the scatterer. Surface reflectance R depends on the angle of incidence θ , and the type of the surface. Scatterer cross section area A was calculated using angular distribution of sub-beam rays. Each scatterer (ray intersection) is then summed to an echo waveform prototype. Finally, the recorded intensity is affected by the aperture of the receiver telescope.

3.3 Scattering and attenuation

The wavelength of the laser used affects the scattering from the object surface. This scattering can be assumed to be isotropic, but the anisotropy should be taken into account for better precision. Scattering anisotropy depends greatly on the surface orientation relative to the light source, and on the surface

properties (Nicodemus et al., 1977; Hapke et al., 1996; Sandmeier and Itten, 1999).

Variation in the light scattering from different surfaces can be carried out by introducing different object types and incidence angle dependent scattering functions. Models introducing multiple scattering could also be considered. In this paper, the scattering was assumed to conform to the cosine of the angle of incidence. Laboratory measurements of backscattered intensity as a function of the angle of incidence using 1064 nm laser light have been performed for a set of natural and artificial surface types, and the data are being processed for description and use in a future paper. It is an interesting question, how much this kind of behaviour affects the accuracy of LIDAR range measurement.

Atmospheric transmission is of little interest within this context, since it can simply be considered constant, and thus only adds a scale term to the simulated energy, not altering the shape of the recorded waveform. This should be taken into account when data acquired using different flight altitudes and possible wavelengths are compared.

3.4 Waveform sampling

The transmitted pulse was modeled as energy vs. time function, with known time interval sampling. For simulation purposes 100 ps sampling was chosen to obtain the prototype echo waveform. This provides time sampling that is 5-10 times better than that provided by widely available scanners.

Every sub-beam of a modeled laser beam results in a distance, or range, from scanner to target surface. Thus one beam results in a number of distance measurements. Ranges are converted into time units and sub-echoes are summed into a sum echo as a function of time according to their scattering angle dependent reflectance. By summing up all the sub-echoes we obtain a sum waveform, including approximated noise, at a given 100 ps sampling interval. This provides a high-resolution view of the target, which could be regarded as an approximation of its physical properties.

The output echo waveform is then digitized from the higher resolution prototype waveform with a given system dependent sampling. By using the detector threshold, the information exceeding the selected noise level is found and digitized. This gives the first approximation for the point location, but more importantly captures the meaningful signal from the time slot. The recorded waveform is though more often analyzed in post processing, and could be used for more exact point extraction and range detection algorithm development.

One of the most crucial factors for exact range determination is the echo detection algorithm applied (Wagner et al., 2004, Wagner, 2005). Since the length of the laser pulse is longer than the accuracy needed (a few meters versus a few centimeters), a specific timing of the return pulse needs to be defined.

In a non-waveform ranging system, analogue detectors are used to derive discrete, time-stamped trigger pulses from the received signal in real time during the acquisition process (Wagner, 2005). The timing event should not change when the level of signal varies, which is an important requirement in the design of analog detections as discussed by (Palojärvi, 2003). For full-waveform digitizing ALS systems several algorithms can be used at the post-processing stage (e.g. leading edge

discriminator/threshold, center of gravity, maximum, zero crossing of the second derivative, and constant fraction) (Wagner, 2005).

The most basic technique for pulse detection is to trigger a pulse whenever the rising edge of the signal exceeds a given threshold (leading edge discriminator), which was also implemented in this first version of the simulation system. Although it is conceptually simple and easy to implement, this approach suffers from a serious drawback: the timing of the triggered pulse (and thus the distance measurement) is rather sensitive to the amplitude and width of the signal. If the amplitude of the pulse changes then the timing point also changes. The same applies for the center of gravity when computed over all points above a fixed threshold.

More sophisticated schemes are based on finite differences of numerical derivatives (e.g. the detection of local maxima or the zero crossings of the second derivative) or, more generally, the zero-crossings of a linear combination of time-shifted versions of the signal. An example of the latter approach is the constant fraction discriminator, which determines the zero crossings of the difference between an attenuated and a time-delayed version of the signal (Gedcke and McDonald, 1968). Maximum, zero crossing, and constant fraction are invariant with respect to amplitude variations and therefore also, to some degree, changes in pulse width (Wagner, 2005).

3.5 Surface and object models

In this paper, the surfaces used for simulation were modeled as high-resolution rasters. A grid spacing of a few centimeters was used. The height resolution of the models was 1.0 cm. Artificial building and forest models, and those based on multiple overlapping laser scanning strips, were used. Artificial models consist of areas much smaller than those in natural test areas, for example single buildings or a randomly generated forest stand as seen in Figure 4, which presents a forest canopy model expressing deciduous forest, 150x150 m² in area.

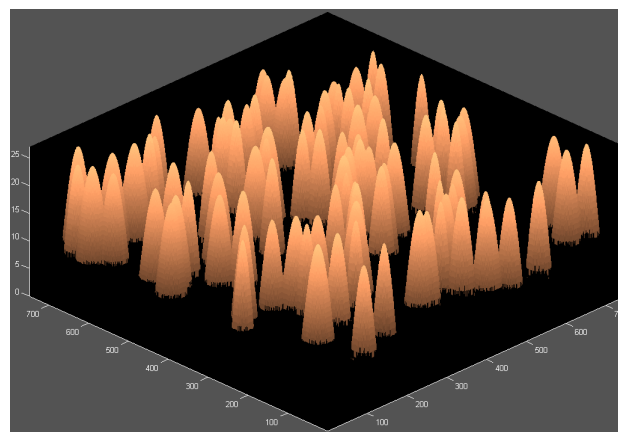


Figure 4. Randomly generated forest canopy model.

4. TESTS AND RESULTS

In this section we present one case, which demonstrate the versatility of the developed simulator in an airborne forest mapping, as the forest parameter extraction using LIDAR techniques is common practice nowadays. Here we present some preliminary results achieved by simulating TopEye MK-II laser scanner over a model forest 150x150 m² in size. The

total number of trees was 100, with a mean height of 25.97 m and a standard deviation of 0.58 m. The tree crowns were characterized by a 10.31 m mean crown diameter with 1.40 m deviation, and modeled by means of a sinusoidal surface with 5.0 cm grid spacing,

The simulated data presented in Figure 5 was acquired at an altitude of 200 m, and a flight speed of 25 m/s. The pulse repetition frequency was set at 30kHz, and the scanning angle at 20 degrees. The sub-sampling of the 1.0 mrad laser beam was set according to the model grid spacing and the flight altitude used, thus giving 53 sub-beams within the foot print area of 20 cm in diameter at ground level. Furthermore, a constant detector energy threshold was used to extract the first echo 3D-points from the 1.0 GHz sampled waveform data produced by the simulator.

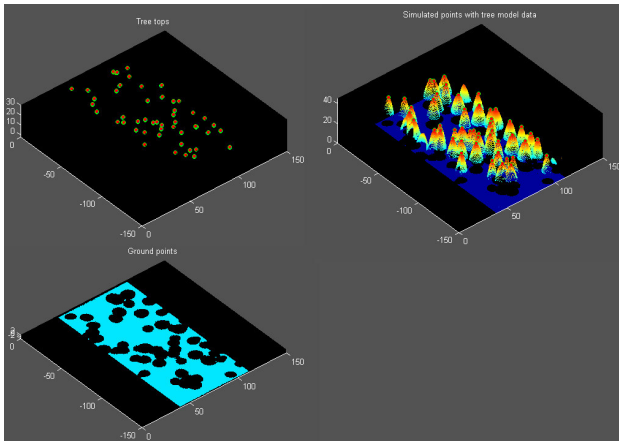


Figure 5. Composite presentation of the simulated measurements for a forest model. The tree tops of the forest model (top left), the tree tops expressed on top of the simulated points (top right), and ground points extracted from the simulated data (bottom left).

The tree tops were extracted from the simulated data using a priori model information on the tree locations. The maximum height point within a 0.5 m radius of the model tree top was chosen. On average this tree top estimator indicates a 0.33 m underestimation of the tree heights compared with the known ground level in the model. When simulated ground points within a one-meter wide circular belt around the tree canopy were considered, the tree height underestimation decreased to 0.02 m. This could be explained by the fact that the model trees had relatively flat tops with approximately the same surface orientation as the ground surface around the trees. Also, no distinction was made between the tree canopy and the ground reflectivities.

Tree location was extracted to 0.15 m accuracy by considering the selected maximum height point as a good representative. This was a rather good estimation thanks to the relatively dense point spacing and smooth shape of the tree canopy model. According to the international Tree Extraction comparison (Hyyppä and Kaartinen, 2007), the best models using a point density of 2-8 pt/m² resulted in a median error of 0.5 m in location. However, in this study the segmentation errors of individual trees were the main source of errors. Also, the tree trunks were not always vertical.

Based on this test case it is clear that this novel simulation method provides reasonable and accurate results for forest parameter extraction, compared with those presented by Holmgren et al. (2003) and Lovell et al. (2005). The advantages lie in the modeled beam divergence, and in the consideration of the incidence angle effect and waveform detection.

The full capability of the simulation system is expressed by a simulation over a ground model based on multi-strip point data acquired with TopoSys Falcon in August 2006. The simulated data were acquired using system characteristic parameter values for the Optech ALTM 3100 and TopoSys Falcon determining the spatial distribution of the laser beams, pulse transmission and waveform detection. The resulting simulated point cloud data and detailed profile for data comparison are presented in Figure 6, along with the original point data, in which the point colors are coded by elevation.

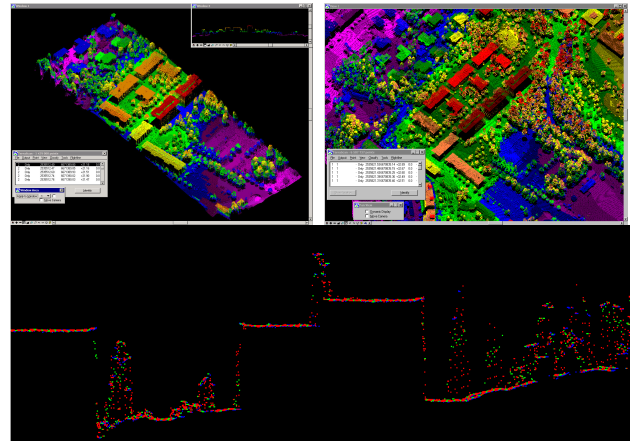


Figure 6. Point cloud presentation of the simulated data (top left) and the original laser scanning data (top right). Comparison of the original data (blue) with the simulated TopoSys Falcon (green) and Optech ALTM 3100 (red).

The level of details in the original first pulse data is reproduced by the simulation. The point spacing and elevation information are comparable to the original. The differences in the color mapping in Figure 6 are due to the larger elevation range of the original data as the data area is larger. More comparative statistical data analysis is beyond the scope of this issue.

The simulation method developed was intended to be a universal tool for studies on multiple parameters affecting the laser scanning accuracy and end products. This kind of approach is suggested for use in finding relevant system dependent differences affecting the data quality and suitability for desired mapping tasks. Simulation also makes it possible to better understand the particular measurement technique and its properties.

5. CONCLUSIONS

In this paper the simulation approach to laser scanning data is introduced and discussed. The simulation method implemented is the first to combine both spatial and radiometric components to produce realistic point cloud and waveform data for system analysis and algorithm development. Simulation provides a tool for demonstrating the effect of different factors on a LIDAR measurement. When integrated into an implementation of

sensor and platform geometry, simulation is a powerful tool for verification and comparison of different laser scanning systems, and analysis of the technique itself. Furthermore, simulator provides artificial data on known targets for algorithm development purposes in many fields of application. It is also clear that simulation of this kind is an important adjunct to the analytical error modeling and estimation performed creditably in recent years (Balsavias, 1999; Schenk, 2001; Wagner et al., 2006).

Preliminary results show that different system-dependent factors affecting the quality of LIDAR-based end products can be studied by simulation. It is also expected that the applicability of the simulation in this kind of research will be very varied. Since simulation makes it possible to acquire data from an unchanged object with different scanning geometries, it is possible to perform thorough analysis of the effect of scanning geometry on the quality of laser products. This is not usually possible with the real data.

Simulation provides a promising and efficient method for studying application-dependent parameters to optimally fulfill the demands of different LIDAR mapping tasks. Greater understanding of the particular measurement technique and its properties is possible. This kind of approach could be used to find relevant system-dependent differences affecting data quality and suitability for desired mapping tasks. Furthermore, the effects of positioning and scanner inaccuracies can be studied by varying the magnitude of these errors, or alternatively they can be completely omitted and attention given only to instrument-dependent sources of uncertainty in the data.

Further development of the LIDAR simulation method will deal with more precise scattering models as the results of the laboratory measurements become available.

ACKNOWLEDGEMENTS

Academy of Finland, Jenny and Antti Wihuri Foundation and Finnish Foundation of Technology are gratefully acknowledged for their financial support. Dr. Sanna Kaasalainen is acknowledged for her valuable comments.

REFERENCES

- Axelsson, P., 2000. DEM generation from laser scanner data using adaptive TIN models. *International Archives of Photogrammetry and Remote Sensing*, XXXIII, Part B4, Amsterdam, Netherlands.
- Baltsavias, E.P., 1999. Airborne Laser scanning: basic relations and formulas. *ISPRS Journal of Photogrammetry and Remote Sensing*, 54 (2/3), 199-214.
- Brenner, C., 2005. Building reconstruction from images and laser scanning. *International Journal of Applied Earth Observation and Geoinformation* 6(3-4), 187-198.
- Filin, S. & B. Csathó, 2000. An efficient algorithm for the synthesis of laser altimetry waveforms. Byrd Polar Research Center, Technical Report 2000-2.
- Gomes-Pereira, L. & L. Janssen, 1999. Suitability of laser data for dtm generation: A case study in the context of road planning and design. *ISPRS Journal of Photogrammetry and Remote Sensing*, 54, 244-253.
- Haala, N., Brenner, C. & K.-H. Anders, 1998. 3D urban GIS from laser altimeter and 2D map data. In: *International Archives for Photogrammetry and Remote Sensing (IAPRS)*, Columbus, Ohio, XXXII, Part 3/1, 339-346.
- Hapke, B., DiMucci, D., Nelson, R., Smythe, W., 1996. The cause of the hot spot in vegetation canopies and soils; shadow-hiding versus coherent backscatter. *Remote Sensing of Environment*, 58, pp. 63-68.
- Hofmann, A. D., Maas, H.-G. & A. Streilein, 2002. Knowledge-Based Building Detection Based On Laser Scanner Data And Topographic Map Information, *Symposium on Photogrammetric Computer Vision, ISPRS Commission III*, September 9 - 13, 2002, Graz, Austria.
- Hofmann, A.D. 2004. Analysis of TIN-structure parameter spaces in airborne laser scanner data for 3-D building model generation, *International Archives of Photogrammetry and Remote Sensing*, 35, B3 III, 302-307.
- Hofton, M. A., Blair, J. B., Minster, J.-B., Ridgway, J. R., Williams, N. P., Bufton, J. L. & D. L. Rabine, 2000. An Airborne Scanning Laser Altimetry Survey Of Long Valley, California. *International Journal of Remote Sensing*, 21(12), 2413-2437.
- Holmgren, J., Nilsson, M. & H. Olsson, 2003. Simulating the effects of lidar scanning angle for estimation of mean tree height and canopy closure. *Canadian Journal of Remote Sensing*, 29 (5), 623-632.
- Hyypä, J. & H. Kaartinen, 2007. Tree extraction comparison, To be published in EuroSDR report series, manuscript in preparation.
- Hyypä, J., Kelle, O., Lehtikainen, M., & M. Inkinen, 2001. A segmentation-based method to retrieve stem volume estimates from 3-D tree height models produced by laser scanners. *IEEE Transactions on Geoscience and Remote Sensing*, 39(5), 969-975.
- Jutzi, B., Neulist, J., & U. Stilla, 2005. High-resolution waveform acquisition and analysis of laser pulses. *ISPRS Hannover Workshop 2005 'High-Resolution Earth Imaging for Geospatial Information'*, Hannover, Germany, 17-20 May 2005.
- Kraus, K., & N. Pfeifer, 1998. Determination Of Terrain Models In Wooded Areas With Airborne Laser Scanning Data. *ISPRS Journal of Photogrammetry and Remote Sensing*, 53 (4), 193-203.
- Lovell, J.L., Jupp, D.L.B., Newnham, G.J., Coops, N.C. & D.S. Culvenor, 2005. Simulation study for finding optimal lidar acquisition parameters for forest height retrieval. *Forest Ecology and Management*, 214, 398-412.
- Maas, H. G., 2001. The suitability of airborne laser scanner data for automatic 3D object reconstruction. In: Balsavias, E. P., Gruen, A., Van Gool, L. (eds): *Automatic Extraction of Man-made Objects From Aerial and Space Images (III)*, Lisse, Balkema.
- Matikainen, L., Hyypä, J., & H., Hyypä, 2003. Automatic detection of buildings from laser scanner data for map updating. In: *International Archives of Photogrammetry, Remote Sensing and Spatial Information Sciences, Dresden, Germany, Vol. XXXIV, Part 3/W13*, 218-224.

- Montemerlo, M., Thrun, S., Dahlkamp, H., Stavens, D. & S. Strohband, 2006. Winning the DARPA Grand Challenge with an AI Robot. Proceedings of the 21st National Conference on Artificial Intelligence AAAI-06, July 16–20, Boston, Massachusetts.
- Nelson, R., 1997. Modeling forest canopy heights: The effects of canopy shape. *Remote Sensing of Environment*, 60, 237-334.
- Naesset, E., 2002. Predicting forest stand characteristics with airborne scanning laser using a practical two-stage procedure and field data. *Remote Sensing Environment*, 80, 88–99.
- Nicodemus, F. E., Richmond, J. C., Hsia, J. J., 1977. Geometrical considerations and nomenclature for reflectance. U.S. National Bureau of Standards Monograph 160.
- Persson, Å., Holmgren, J. & U. Söderman, 2002. Detecting and measuring individual trees using an airborne laser scanner. *Photogrammetric Engineering and Remote Sensing*, 68, 925-932.
- Reutebuch, S., R. McGaughey, H-E Andersen, and W. Carson, 2003. Accuracy of a high resolution LIDAR-based terrain model under a conifer forest canopy. *Canadian Journal of Remote Sensing*, 29, 527-535.
- Rottensteiner, F., 2003. Automatic Generation of High-Quality Building Models from Lidar Data. *IEEE Computer Graphics and Applications*, 23(6), 42 – 50.
- Rottensteiner, F. & J. Jansa, 2002. Automatic Extraction of Buildings from Lidar Data and Aerial Images. Commission IV Symposium "Geospatial Theory, Processing and Applications" - WG3, Ottawa, Canada, 34(3).
- Rottensteiner, F., Trinder, J. & S. Clode, 2005. Data Acquisition for 3D City Models from LIDAR - Extracting Buildings and Roads. Proceedings of the 25th IEEE International Geoscience And Remote Sensing Symposium (IGARSS), July 25-29, Seoul, South Korea, 521-524.
- Rönnholm, P., Hyypä, J., Hyypä, H., Haggrén, H., Yu, X. & H. Kaartinen, 2004. Calibration of laser-derived tree height estimates by means of photogrammetric techniques. *Scandinavian Journal of Forest Research* 19(6), 524-528.
- Sandmeier, S., Itten, K., 1999. A field goniometer system (FIGOS) for acquisition of hyperspectral BRDF data. *IEEE Transactions on Geosciences and Remote Sensing*, 37 (2), pp. 978-986.
- Schenk, T., 2001. Modeling and analyzing systematic errors in airborne laser scanners. Technical notes in photogrammetry No. 19, Department of Civil and Environmental Engineering and Geodetic Science, The Ohio State University, Columbus, OH.
- Talaya, J., Bosch, E., Alamús, R., Bosch, E., Serra, A. & A. Baron, 2004. GEOMOBIL: the Mobile Mapping System from the ICC. In: Proceedings of 4th International Symposium on Mobile Mapping Technology (MMT'2004). Kinming, China.
- Thiel, K.-H. & A. Wehr, 2004. Performance capabilities of laser scanners – an overview and measurement principle analysis. *International Archives of Photogrammetry Remote Sensing and Spatial Information Sciences*, XXXVI-8/W2, 14-18.
- Vosselman, G., 2002. Fusion of Laser Scanning Data, Maps and Aerial Photographs for Building Reconstruction. *IEEE International Geoscience and Remote Sensing Symposium and the 24th Canadian Symposium on Remote Sensing, IGARSS'02*, Toronto, Canada, June 24-28.
- Vosselman, G. & I. Suveg, 2001. Map Based Building Reconstruction from Laser Data and Images. *Automatic Extraction of Man-Made Objects from Aerial and Space Images (III)*, Ascona, Switzerland, June 11-15, Balkema Publishers, 231-239.
- Wagner, W., Ulrich, A., Ducic, V., Melzer, T., & N. Studnicka, 2006. Gaussian Decomposition and Calibration of a Novel Small-Footprint Full-Waveform Digitising Airborne Laser Scanner. *ISPRS Journal of Photogrammetry and Remote Sensing*, 60 (2), 100 - 112.
- Yu, X., Hyypä, J., Kaartinen, H., & M. Maltamo, 2004. Automatic detection of harvested trees and determination of forest growth using airborne laser scanner, *Remote Sensing of Environment*, 90, 451-462.

ROAD ENVIRONMENT MAPPING SYSTEM OF THE FINNISH GEODETIC INSTITUTE - FGI ROAMER -

Antero Kukko^{a,*}, Constantin-Octavian Andrei^b, Veli-Matti Salminen^c, Harri Kaartinen^a, Yuwei Chen^b, Petri Rönholm^d, Hannu Hyyppä^d, Juha Hyyppä^a, Ruizhi Chen^b, Henrik Haggrén^d, Iisakki Kosonen^c, Karel Čapek^e

^aFinnish Geodetic Institute, Department of Remote Sensing and Photogrammetry, P.O. Box 15, 02431 Masala, Finland – Antero.Kukko@fgi.fi

^bFinnish Geodetic Institute, Department of Navigation and Positioning, P.O. Box 15, 02431 Masala, Finland

^cHelsinki University of Technology, Department of Surveying, Laboratory of Geoinformation and Positioning Technology, P.O. Box 1200, 02015 TKK, Finland

^dHelsinki University of Technology, Department of Surveying, Institute of Photogrammetry and Remote Sensing, P.O. Box 1200, 02015 TKK, Finland

^eHelsinki University of Technology, Department of Civil and Environmental Engineering, Laboratory of Transportation Engineering, P.O. Box 2100, 02015 TKK, Finland

**Commission III, WG III/3
Commission V, WG V/3**

KEYWORDS: Mobile mapping, Laser scanning, Positioning, IMU, GPS, RTK, Traffic environment

ABSTRACT:

The Finnish Geodetic Institute has been developing a mobile road environment mapping system, named as ROAMER, since 2003. The vehicle-borne ROAMER system consists of a carrying platform, positioning and navigation systems, and a 3D data acquisition system. The system employed a 3D laser scanner operated in a profiling mode. The laser scanner can be mounted in several different positions to meet the special needs of some planned applications of the mobile mapping system. In order to be able to accomplish the high automation in 3D modeling, a laser scanner capable to provide dense point clouds was set as the requirement for the system. Additionally, the system is aimed to be a flexible moving laboratory for various road environment applications. The wide field of view and a high point measurement frequency of 120 kHz provided by the laser scanner in use, makes the ROAMER unique. This paper describes the hardware and the navigation solution of the FGI ROAMER. We also discuss the applicability of mobile mapping system in the field of traffic engineering as data source. There is a wide range of laser sensors applicable, as the MMS presented in this paper, but also static laser profilers could be used for real-time traffic flow measurements. This data could be used as input to the MMS based 3D virtual models of the different traffic places to help traffic planners to increase the traffic safety. The detailed 3D models of the transport systems can be used for traffic modeling and traffic simulation systems. In 3D models the interactions between vehicles, pedestrians and bicycles can be examined in high detail. Also the interaction with traffic environment can be studied.

1. INTRODUCTION

Modern transportation planning is becoming an increasingly interactive process between planners, authorities, road users, and private companies requiring more communication between various parties. On the other hand, the traffic systems are becoming more and more complex and difficult to understand as a whole. Thus, more complex modeling techniques are needed, which makes it more difficult to maintain the dialog between involved parties. In many other technology fields, virtual reality and 3D modeling techniques have made it possible to describe complicated systems. However, in the field of transportation engineering, the use of virtual reality and 3D modeling has so far developed slowly. The 3D modeling of a whole city or its transportation system is a time-consuming and expensive process, and road environments are not modelled with accuracy that would provide solutions to transportation engineering. These bottlenecks slow down the use of 3D in road

environments and, thus, new solutions are needed for fast and automatic data collection.

The detailed 3D models of the transport systems can be used for traffic modeling and traffic simulation systems. In 3D models the interactions between cars, pedestrians and bicycles can be examined in high detail. Also the interaction with traffic environment can be studied. As an example, the number of vehicle-train accidents in Finland is four times larger than that in other Scandinavian countries. Poor visibility due to vegetation and low density of gates (appr. 20%) are the main reason for these accidents. Virtual reality information in 3D of these interchanges could help in reducing future accidents.

There is also a growing need to improve of the efficiency of urban traffic. It is now recognized that this objective requires not only the improvement of traffic monitoring and management schemes in traffic control centres but also the provision of information services for ordinary road users. New ICT technologies can provide a new source of up-to-date, real-

* Corresponding author.

time traffic information (time as the fourth dimension). Especially, when the dynamic traffic data is combined with the static model of the city, it is possible to produce new services for drivers and improve the traffic management. Also if computational methods, such as simulation or neural networks are integrated, it is possible to produce short-time predictions of the traffic situation and derive indicators about traffic fluency, safety, economy and environmental aspects.

In transportation engineering, the transport telematics is the most rapidly developing area. Transport telematics is used for collecting traffic data, for processing it and creating new services for driver and authorities (Kulmala, 1995; Kosonen, 1999). Land vehicle navigation has advanced significantly over the past 20 years (El-Sheimy, 1996). First this was largely due to the advancement of navigation and computer related technologies (Krakiwsky, 1991). During that period, land vehicle navigation was known as, or associated with, Automatic Vehicle Location and Navigation (AVLN), Intelligent Vehicle Highway Systems (IVHS), Intelligent Transportation Systems (ITS), and Mobile Mapping Systems (MMS) (El-Sheimy, 1996). The integration of navigation sensors with sighting devices, e.g. digital cameras and laser imaging, extends the application of AVLN systems to inventory and mobile mapping (MMS), some of which are capable of collecting 3D information of the surroundings (El-Sheimy, 1996).

A modern MMS can be today considered as a multi-sensor system that integrates various navigation and data acquisition sensors on a rigid, moving platform (van, car) for determining the positions of the surrounding objects remotely. The navigation sensors typically include GPS (Global Positioning System) receiver and IMU (Inertial Measurement Unit), while in the data acquisition sensors some of the most sophisticated systems use both terrestrial laser scanners and digital cameras or videos. Other possible data acquisition sensors include film cameras, multi-spectral linear scanners, CCD cameras, imaging laser, laser profilers, laser scanners, impulse radar, and ultrasonic sensors depending on the needed information (see e.g. El-Sheimy, 2005 for more details).

Typical requirements for a MMS are that visible objects should be measured with accuracy of few decimetres with a maximum speed of 50-60 km/h and desired objects should be collected at distance of several tens of meters from the sensor. Because of the high costs of the MMS, mainly due to navigation-grade IMU used, the systems are one-off systems that are operated by the companies or institutions that build them. (El-Sheimy, 2005).

Mobile mapping systems have become an independent field of research and a short summary of state-of-the-art of systems can be found in El-Sheimy (2005). He concluded his overview in mobile mapping systems by stating "Considerable work is needed in the areas of real-time and post-mission quality control, automation of GPS/INS integration in case of frequent lock of loss, automatic feature extraction in post mission processing, and the efficient and user-oriented manipulation of extremely large databases."

Recent papers in the MMS field includes El-Sheimy (2005), Clarke (2004), Grejner-Brzezinska and Toth (2003), Habib et al. (2001), Joo et al. (2005), Karimi et al. (2000), Manandhar and Shikbasaki (2001,2002,2003), Reulke and Wehr (2004),

Talaya et al (2004), Tao (2001), Tao et al. (2001), Zhang and Xiao (2003), Zhao and Shibasaki (2003ab, 2005).

Finnish Geodetic Institute initiated a MMS development in 2003 with an aim to develop a system that would maximize the automation of feature extraction at the post processing phase. Additionally, the MMS system should be a moving MMS laboratory flexible for various road environment applications. To accomplish the high automation, a laser scanner capable of providing dense point clouds was set as the requirement for the system. This paper describes the hardware of the FGI ROAMER equipment for the first time.

2. MOBILE MAPPING UNIT/PLATFORM

The MMS platform is manufactured of hardened aluminium plates and profile tubes. The base plate is approximately 63 cm in length and width. The height of the scanner origin/mirror is approximately 97.5 cm above the base plate in the normal position, where the scanner is in upright position, and between 36-57 cm when some of the tilted (fixed) positions are used. The tilt angles are 60°, 45°, 30°, and 15° below the horizon of the platform. The design of the MMS/ROAMER integration platform is presented in Figure 1. The total weight of the intended instrumentation and the platform sums up to approximately 40 kg.

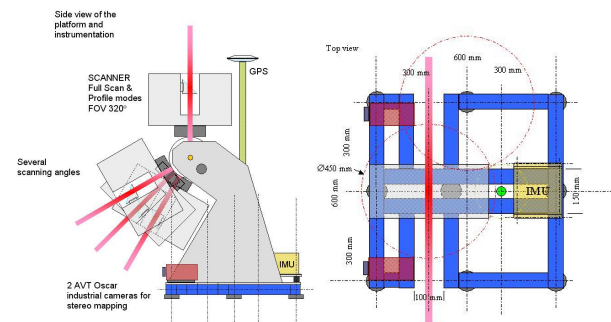


Figure 1. Side and top views of the platform design and instrumentation.

The integration platform is mounted on three standard off-the-self racks designed for the railings on top of the vehicle. Between the rack and the platform there is a suspension layer of nine shock absorption dampers to attenuate vibrations. The idea is to provide a compact and robust platform, isolated from the carrier vehicle, for the instrumentation to be mounted on, as seen in Figure 2.

The GPS antenna is attached on top of a mast in front of the scanner socket/holder. The height of the antenna can be adjusted using mast pieces with known length to avoid unnecessary wobble of the antenna. The root of the antenna mast is made of 30 mm square aluminum profile. The additional antenna mast pieces are at 10, 20 and 30 cm in length and made of 20 mm round aluminum bar.



Figure 2. The ROAMER instrumentation on its first field run. The scanner is tilted to the backward direction.

For the attitude determination of the MMS an inertial measurement unit (IMU) is applied. The IMU unit is mounted on its own rack at the front end of the platform base plate, with a suspension of four additional rubber absorbers. The unit is centered by tight fittings designed for the openings found in its feet. Two aluminium brackets are used to fasten the IMU-unit into its position.

The laser scanner is mounted on a steel socket/holder at the upper end of the instrument arm. The scanner socket can easily be tilted to acquire full scene and profile scans at different scanning angles. Both scanning modes can be utilized, which makes the versatility of the platform unique.

The normal scanner position can be used when structures lying above the lanes, i.e. bridges and traffic signs, have to be included in the model. The normal position is also good for measurements for the building facades and other similar structures, though many of them can be captured also at any of the tilted positions.

The tilted scanner positions are used in the extraction of the road surface. Tilted scanning plane also produces multiple hits even from narrow pole structures usually present on the both sides of the road. This is due to the high profile repetition frequency (scan rate), high point density along the profile, and especially due to the fact that the wide FOV makes it possible to acquire multiple hits from several sequential profiles from an object as the mapping unit passes by, as illustrated in Figure 3. The speed of the vehicle determines the number of profiles sweeping the object in the end.

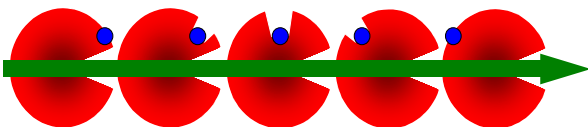


Figure 3. Wide FOV and tilted laser plane produces multiple hits from sequential profiles even from narrow vertical objects (blue circle presents a pole) lying on the side of the road. The height of the hits in each profile gets lower, though, giving a good estimation for the location of the pole.

3. LASER SCANNER SYSTEM

The mobile mapping system utilizes the FARO LS 880HE80 (FARO LS) terrestrial laser scanner for 3D measurements. FARO LS is based on phase difference technique providing high-speed data acquisition. The disadvantage for this is the relatively modest measurement distances ranging in practice up to 30-40 meters. Wide field of view (FOV) and good angular resolution however compensate this. Some of the technical properties of the scanner are summed up in the Table 1. In Figure 4 the modular construction of the FARO LS is presented.

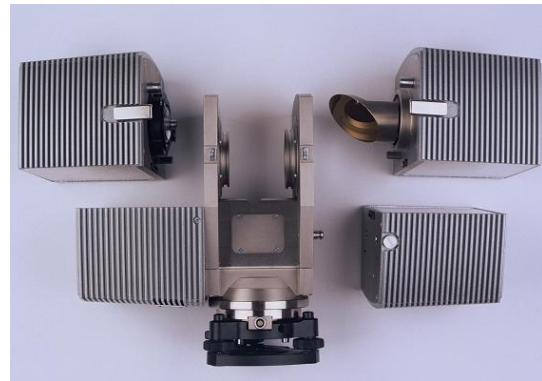


Figure 4. FARO LS 880HE80 terrestrial laser scanner. Top left: the laser ranging unit. Top right: Deflection unit. Bottom right: The data storage unit. Bottom left and center: The scanner electronics and base structure.

Table 1. Technical properties of the FARO LS 880HE80.

Maximum range	~76 m
Measurement rate	120 kHz
Field of view	320°x360°
Beam divergence	0.2 mrad, 3 mm at aperture
Maximum angular resolutions	
Vertical	0.009°
Horizontal	0.00076°
Ranging error	±3 mm, linearity e.
Mirror frequencies	3,6,12,15,24,30 Hz
Temp. limit	> 0°C, dry conditions

With slightly modified hardware, the FARO LS provides a so-called tunnel mode, or profile measurements, with synchronization to be used with external positioning and data logging systems. The deflection unit sends a synchronization pulse for every profile to the navigation hardware to be logged. This information is needed to derive the position and attitude information for each 3D-point produced by the laser scanner.

The mirror rotation frequency, or scan rate of the FARO LS can be set between 3 and 30 Hz, thus giving the vertical angular resolution of 0.0096-0.096 degrees (0.17-1,7 mrad), respectively. The corresponding point spacing at a typical scanning range of 15 meters in road mapping is thus 2.5-25 mm in the scanning plane. More general illustration of the point spacing at a given range and resolution level are summarized in Figure 5. It is seen that the point density is reasonable at any resolution level within the scan profile.

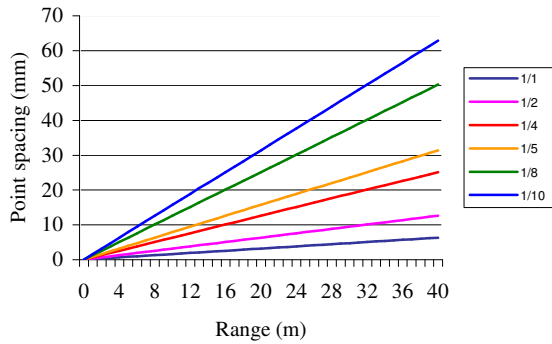


Figure 5. Point spacing at ranges from 0 to 40 meters for different scanning resolutions.

In Figure 6 the achievable along-track distances between two sequential profiles are shown as a function of platform velocity at different scan frequencies. Along-track profile spacing is less than one meter even for the speeds up to 70-80 km/h when high mirror speeds are used. For the platform speeds of 50-60 km/h the profile spacing around one meter is achieved also for the mid-frequencies for the mirror. The resulting point pattern cast on the scene depends on whether the scanner is in the normal or in the tilted position.

In the profile measurement mode the operator can determine the number of profiles to be measured. The number of profiles can be calculated by estimating the time needed for driving the planned route, and according to the selected mirror frequency. The operator can choose to automatically split the accumulating data into separate files of selected size, i.e. the number of profiles.

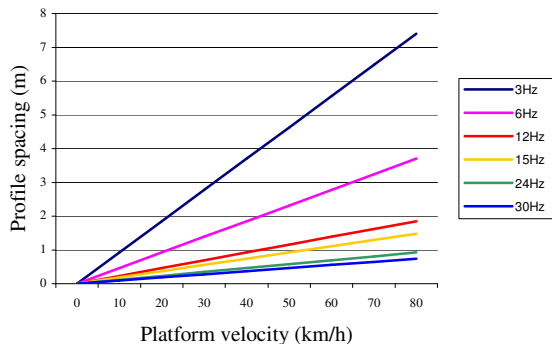


Figure 6. Movement of the scanner origin between two sequential profiles at different scan frequencies and platform velocities.

The operator controls the data recording with an external device. Using this device the operator can pause the data recording, and synchronization signal output, without stopping the scanner mirror rotation. This is useful in situations where the measurement vehicle has to stop due to other traffic, or for example in traffic lights.

Full scans can be used in the so called stop-and-go procedure, where the mapping unit stops to one position to acquire a full scene scan, and then proceeds. Full scene scans are also used for the calibration of the MMS sub-systems to a common coordinate frame. Full scans can be acquired in both normal and

tilted positions of the scanner. One full FOV scan at $\frac{1}{4}$ of the full resolution produces approximately 40 million 3D-points, and an external calibrated digital camera (Nikon D70s) with fisheye lens can be used to produce RGB values for the scan points.

4. NAVIGATION SYSTEM

For orientation of the data acquisition sensors in to the external coordinate system, the instantaneous rotations and the position of the MMS platform is determined by the navigation system. Navigation solution for the MMS is produced by a NovAtel's SPAN (Synchronized Position Attitude Navigation) Technology that integrates GPS and inertial data for applications requiring greater functionality and reliability than traditional stand-alone GPS can offer. The SPAN system also operates in RTK (Real-Time Kinematic) mode with an Internet-based application, named vDiff, developed by the Finnish Geodetic Institute.

Table 2. SPAN's IMU (HG1700 AG11) specifications.

Gyro Input Range	± 1000 deg/s
Gyro Rate Bias	1.0 deg/s
Gyro Rate Scale Factor	150 ppm
Angular Random Walk	0.125 deg/hr
Accelerometer Range	± 50 g
Accelerometer Linearity	500 ppm
Accelerometer Scale Factor	300 ppm
Accelerometer Bias	1.0 mg

The GPS receiver is a NovAtel DL-4plus, containing the OEM-G2 engine. Additionally, A GPS-702 antenna that offers access to the GPS L1 and L2 frequencies is included. The inertial measurement unit is a tactical-grade, ring laser gyro (RLG)-based IMU manufactured by Honeywell, and its specifications are given in the table 2.

To establish correct navigation solution the offset between the IMU and the GPS antenna phase center should be measured as accurately as possible, preferably within millimeters especially for RTK operations. This is a task to be carried out in the MMS system calibration.

4.1 Results from driving test

To measure the performance of SPAN system in a more realistic setting, data were collected while driving a route of 18 km and the vehicle passed 4 bridges and areas covered by forest that offered possibility to test the solution under full outages. Figure 7 shows the trajectory travelled during the test as calculated for the GPS/INS filter, and for the RTK filter alone, without inertial aid. Table 3 shows the quantified position error during the test for both GPS and GPS/INS solutions.

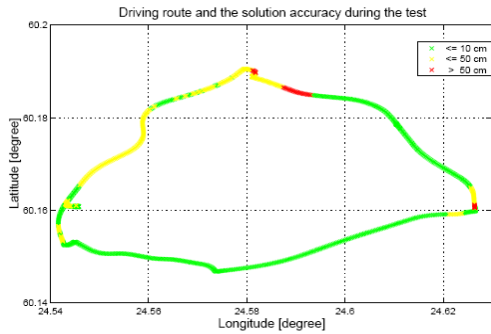


Figure 7. Driving route and solution accuracy during the test.

Table 3. Position Accuracy during the drive test.

Solution type	Positional Error (m)			
	Horizontal		Vertical	
	RMS	Max	RMS	Max
GPS-only	3.765	61.980	4.046	57.102
GPS/INS	0.232	1.043	0.124	0.650

Due to the shadowing of the forests and the passed bridges during the test drive and the instability of GPRS connection, the availability of a GPS-only solution was limited. Table 4 shows the solution availability for the GPS-only and GPS/INS filters, confirming that the addition of inertial data results in more reliable positioning solution.

Under the conditions of this test, the GPS-only solution could be computed for 82,6 percent of the time elapsed. The SPAN combined GPS/INS solution gave 100 percent availability, and from which 60,4 percent was RTK solution.

Table 4. Positioning solution availability during the drive test.

Solution type	Number of epochs	Percentage of solution
GPS-only	925	82,6%
RTK-fixed (GPS-only)	677	60,4%
GPS/INS	1120	100%

4.2 Results from a test with the entire MMS system in a static mode

The research team carried out a field test with all the major components/sensors in Otaniemi, Espoo. Also the SPAN system was involved together with the laser scanner. All the sensors were mounted on the common integration platform. The offset from the GPS antenna to IMU was measured within one-centimeter accuracy. All data were logged from the GPS receiver serial port to a laptop. A Thales ZX-Sensor GPS receiver was setup on the roof of FGI’s office building as the reference station. The RTK baseline length was approximately 20 kilometers during the test and GPRS communication was stable.

Data were collected through two test runs in a static mode. When the laser scanner starts, it sends a pulse for each profile via the synchronization device connected to USB port to GPS receiver and a log called MARKPOS is generated and recorded.

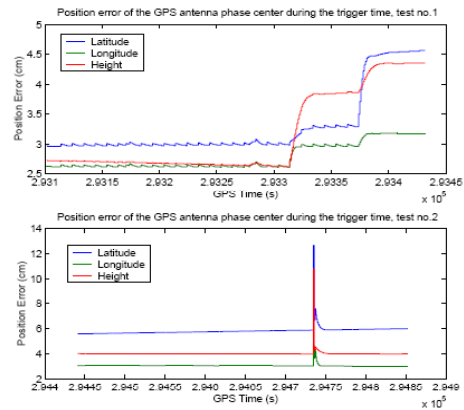


Figure 8. Position Error of the GPS/IMU solutions.

In Figure 8, the upper part shows the results of the first test, while the lower part shows that of the second test. In the second test, a larger error at the epoch between (294735.044 294736.026) occurred because the solution for this epoch was based on the wide-lane ambiguity. Table 5 summarizes the statistics of positioning solutions for the first test and the second test. It can be seen that a standard deviation is far below 2.0 cm.

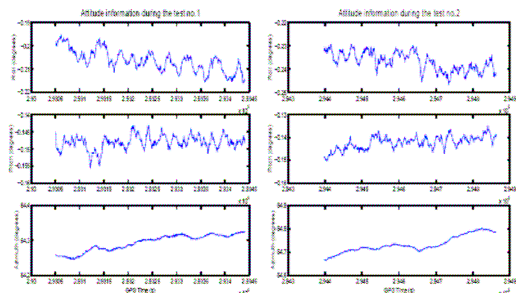


Figure 9. Attitude information of test no. 1 (left column) and test no. 2 (right column).

The INS solution was also initialized before the test start. The attitude information was logged with 1 Hz frequency. During the tests, as it is presented in Figure 9, the variations around the X-axis (roll) and Y-axis (pitch) were quite small within the interval of 0.03 degrees and 0.02 degrees, respectively. Moreover, the azimuth (heading) during the tests is almost constant, the small variation being determined by the Earth rotation around its own axis that are sensed by the IMU.

Table 5. Position of the antenna phase-center during the test.

Stats.	Cartesian coordinates in WGS 84		
	X	Y	Z
	Test no.1		
MIN	2885684.477	1333906.568	5510884.178
MAX	2885684.550	1333906.605	5510884.244
MEAN	2885684.528	1333906.586	5510884.205
STD	0.0150	0.0074	0.0157
Test no.2			
MIN	2885684.478	1333906.547	5510884.194
MAX	2885684.543	1333906.599	5510884.247
MEAN	2885684.513	1333906.574	5510884.221
STD	0.0117	0.0107	0.0090

5. APPLICABILITY OF MOBILE MAPPING SYSTEM FOR TRAFFIC ENGINEERING, FUTURE ADD-ON'S AND DISCUSSION

In the following, some of the potential applications are delineated.

Industry - The Mobile Mapping System under development can be applied to various applications such as map and GIS database updating, 3-D mapping, virtual reality modeling and highway feature inventory acquisition.

Safety - In Finland there is four times higher number of vehicle-train accidents than in other Scandinavian countries. Poor visibility due to vegetation and low density of gates (appr. 20%) are the main reasons for accidents. Virtual reality information of these interchanges could help in reducing future accidents by showing the danger of these environments to decision makers.

Modeling of the traffic system - The capability of using modern simulation and modeling techniques in transport planning is not so much limited by the models themselves, but due to the difficulties in obtaining the large amount of input data required. The benefits of high computing power and state of the art modeling systems are lost, because the collecting and organizing of the input data is mostly done manually. The need for automatically generated data models of transportation infrastructure is very urgent. The mobile mapping technology can provide a solid solution to the bottleneck of data input.

Traffic simulation - As detailed static models of the traffic system get available the extensive use of microscopic traffic simulation is much more simple and cost effective. This would be a very significant improvement in traffic and infrastructure planning since micro-simulation can provide large scale of traffic indicators regarding traffic fluency, safety, economy and environmental aspects.

Improvement of traffic efficiency - There is also a growing need for measuring of the efficiency of urban traffic. It is possible to measure the traffic efficiency by indicators provided by real-time traffic simulation. This way the present situation can be monitored and compared with past situations in order to figure out trends of effects of traffic improvement and control operations. It is possible to produce short-term prediction for improving the traffic management capabilities.

In real-time simulation, a static model of the traffic site is first needed. For dynamic modeling of the traffic situations, the simulation model is able to digest various sources of traffic information (data fusion). The basic input for real-time simulation are vehicle detectors. However, the problem of using detector data only is the cumulative error in the traffic situation model. Therefore additional sources and an on-line calibration facility are needed. The use of laser scanning in direct measurement of the traffic density and queue length could be a very important new data source. This would be of great advance in development of comprehensive system for real-time modeling of the traffic.

The future hardware development of the MMS will concentrate on the calibration of the sub-systems to a common reference frame. Also, a camera system is planned to be included to the MMS, and it may consist of two or three AVT Oscar 5 Mpix color cameras. The frame rate at full image size is five frames per second. The synchronization of the camera system to the

other instrumentation of the MMS uses TTL signals, and the image data transfer is done via FireWire (IEEE 1394) connection.

One of the cameras may point forward, and will be used to drape the labels captured from the traffic signs to the modeled road environment data. The two other cameras are planned to be used to capture backward looking stereo pairs along-track to provide complementary image measurement power, navigational aid and colour information to the road mapping system.

ACKNOWLEDGEMENTS

Academy of Finland (project Transportation Data Acquisition by Means of ICT-Derived 3D Modeling) and Henry Ford Foundation are gratefully acknowledged for their financial support. Jürgen Gittinger and Reinhard Becker from FARO Technologies and Rolf Berlin from ATS AB are acknowledged for their technical support.

REFERENCES

- Clarke, Keith C., 2004. Mobile mapping and geographic information systems. *Cartography and Geographic Information Science*, 31 (3), 131-136.
- El-Sheimy, N., 1996. The Development of VISAT-A Mobile Survey System for GIS Applications. Ph.D. Thesis, Department of Geomatics Engineering, University of Calgary, Calgary, Alberta, Canada, UCGE Report No. 20101.
- El-Sheimy, N., 2005. An Overview of Mobile Mapping Systems. FIG Working Week 2005 and GSDI-8, Cairo, Egypt April 16-21, on-line publication, 24 p.
- Grejner-Brzezinska, D. and C. Toth, 2003. Driving the line: multi-sensor monitoring for mobile mapping. *GPSWorld*, 14 (3), 16-22.
- Habib, A., Morgan, M. and Y.R. Lee, 2001. Integrating data from terrestrial mobile mapping systems and aerial imagery for change detection purposes. The 3rd International Symposium on Mobile Mapping Technology, Cairo, Egypt.
- Joo, I.-H., Hwang, T.-H. and K.-H. Choi, 2005. Updating geospatial database : An automatic approach combining photogrammetry and computer vision techniques. *Lecture Notes in Computer Science*, 3708, 324-331.
- Karimi, H.A., Khattak, A.J. and J.E. Hummer, 2000. Evaluation of mobile mapping systems for roadway data collection. *Journal of Computing in Civil Engineering* 14 (3), 168-173.
- Krakiwsky E., (1991). The method of least squares: a synthesis of advances, Dept. of Surveying Engineering, University of Calgary.
- Kosonen I. (1999). HUTSIM - Urban Traffic Simulation and Control Model: Principles and Applications. Helsinki University of Technology, Transportation Engineering, Publication 100. Espoo, Finland, 249 p.
- Kulmala, R., 1995. Safety at rural three- and four-arm junctions: development and application of accident prediction

models. VTT Publication 233, Technical Research Centre of Finland, Espoo.

Manandhar, D. and R. Shibasaki, 2001. Vehicle-borne Laser Mapping System (VLMS) for 3-D Urban GIS Database. Proceedings of the 7th International Conference on Computers in Urban Planning and Urban Management, University of Hawaii at Manoa, USA, July 18-20, CD-ROM.

Manandhar, D. and R. Shibasaki, 2002. Auto-extraction of urban features from vehicle-borne laser data. International Archives of Photogrammetry, Remote Sensing and Spatial Information Sciences, 34 (4), 6 p.

Manandhar, D. and R. Shibasaki, 2003. Accuracy assessment of mobile mapping system. Proceedings of the 24th Asian Conference on Remote Sensing, 3 p.

Reulke, R. and A. Wehr, 2004. Mobile panoramic mapping using CCD-line camera and laser scanner with integrated position and orientation system. Proceedings of the ISPRS working group V/1, IAPRS, 34.

Talaya, J., Bosch, E., Alamús, R., Serra, A., Baron, A.: GEOVAN: The mobile mapping system from the ICC. Proceedings of 4th International Symposium on Mobile Mapping Technology (MMT'2004). Kumming, 2004.

Tao, C.V., 2001. Mobile mapping technology for road network data acquisition. Journal of Geospatial Engineering, 2 (2), 1-13.

Tao, C.V., Chapman, M.A. and B.A. Chaplin, 2001. Automated processing of mobile mapping image sequences. ISPRS Journal of Photogrammetry and Remote Sensing 55 (5-6), 330-346.

Zhang, Kefei and Benlin Xiao, 2003. Current status of low-cost GPS and mobile mapping systems. Department of Geospatial Science, RMIT University, Melbourne, Australia, 10 p.
http://www.gs.rmit.edu.au/news/april03/Zhang+Xiao_Low%20cost%20GPS.pdf

Zhao, H. and R. Shibasaki, 2003a. A vehicle-borne urban 3-D acquisition system using single-row laser range scanners. IEEE Transactions on Systems, Man and Cybernetics, part B: Cybernetics, 33 (4), 658-666.

Zhao, H. and R. Shibasaki, 2003b. Reconstructing a textured CAD model of an urban environment using vehicle-borne laser range scanners and line cameras. Machine Visions and Applications, 14 (1), 35-41.

Zhao, H. and R. Shibasaki, 2005. Updating digital geographic database using vehicle-borne laser scanners and line cameras. Photogrammetric Engineering & Remote Sensing, 71 (4), 415-424.

ESTIMATION OF LAI USING LIDAR REMOTE SENSING IN FOREST

Doo-Ahn Kwak^a, Woo-Kyun Lee^a, Hyun-Kook Cho^b

^aDivision of Environmental Science and Ecological Engineering, Korea University, Seoul 136-701, South Korea – tulip96@korea.ac.kr

^bKorean Forest Research Institute, Cheongryangri-Dong, Dongdaemun-Ku, Seoul 136-012, Korea – hcho@foa.go.kr

KEY WORDS: LiDAR, Leaf Area Index (LAI), Point density, Vegetation Index, Photosynthetically Active Radiation

ABSTRACT:

Light Detection and Ranging (LiDAR) has been used to extract surface information as it can acquire highly accurate object shape characteristics using geo-registered 3D-points. Therefore, LiDAR can be used to effectively measure tree parameters in forested areas. In this research, we estimated the LAI (Leaf Area Index) for *Pinus koraiensis*, *Larix leptolepis* and *Quercus* spp. using LiDAR data. For calculating the LAI (Leaf Area Index), the LPI (Laser Penetration Index) and LII (Laser Interception Index) were generated by LiDAR data having High Vegetation Returns (HVR), Medium Vegetation Returns (MVR), Low Vegetation Returns (LVR) and Ground Returns (GR). The LPI was calculated with point density using first returns ($h \geq 1\text{m}$) and ground returns ($h < 1\text{m}$), and the LII was computed with the ratio of all returns to HVR and MVR. The LAI is calculated through the regression analysis by tree species with the LPI and LII. Afterward, we assessed the accuracy of LiDAR-derived and field-measured LAI with the coefficient of determination and root mean square error. As a result, the slope of *Pinus koraiensis* was the steepest, and the slope of *Quercus* spp. was the gentlest of three tree species. This can be explained by the fact that the amount of transmitted sunlight through the canopy in *Quercus* spp. can be different by seasons. Moreover, in the LAI generated by the LII, the coefficients of determination were estimated higher than those by the LPI. This can be attributed to the fact that the original information of the number of laser points was lost when the point data was transformed to raster data for generating the LPI. And the LII allows normalizing biased local variation of the number of laser points while the raster data has some noise due to unbalanced distribution of laser points.

1. INTRODUCTION

There are several definitions for the LAI in the field according to Jonckheere *et al.* (2004). The LAI can be defined as the total one-side area of leaf tissue per unit ground surface area (Watson, 1947). But this is only used for deciduous forests. Schulze *et al.* (2005) mentioned that the LAI could be determined as the sum of the projected leaf surface per soil area and Myneni *et al.* (1997) defined the LAI as the maximum projected leaf area per unit ground surface area. By these definition, the LAI can derive both the within and the below canopy microclimate, control canopy water interception, radiation extinction, water and carbon gas exchange (Bréda, 2003). Moreover, they provide as the information for biosphere modeling (Bonan, 1993) and fire behavior models (Finney, 1998), since they have information for a number of relevant ecological process (Morsdorf *et al.*, 2006). Therefore, the LAI can play a key role of biogeochemical cycles in ecosystem. Various methods for the LAI can be classified into two categories as direct and indirect estimation (Bréda, 2003). The direct methods can be measured as harvesting vegetation but these methods are destructive and exhaustive. Furthermore, such methods are suitable for the vegetation of small structure, not applied to large area or trees (Bréda, 2003). And previous methods have time-consuming and labor-intensive problems when the LAI is measured in the field. On the other hands, indirect methods can be estimated without destructive works and easily with the radiative characteristic of the sunlight, which is dispersed or penetrated around the vegetation area. In such methods, remote sensing techniques using satellite imagery and aerial photograph have applied to deriving this measurement. Such many approaches were based on passive optical sensor system and regression models (Cohen *et al.*, 2003) or radiative transfer modeling (Koetz *et al.*, 2004). However, a serious problem of remote sensing using passive

sensor system is that it can not describe the canopy shape and structure because it doesn't have the elevation information by itself. However, Light Detection and Ranging (LiDAR) with active sensor system, especially, has recently been used to extract surface information, as it can acquire highly accurate object shape characteristics using geo-registered 3D-points (Kwak *et al.*, 2006). Therefore, the LiDAR system can measure both vertical and horizontal forest structures in forested areas, such as tree heights, sub-canopy topographies and distributions, with high precision (Holmgren *et al.*, 2003). As such characteristic of the LiDAR is used for extracting the forest information, some research derived the LAI and the fCover (fractional cover) (Morsdorf *et al.*, 2006) and Rião *et al.* (2004) obtained the LAI using the gap fraction distribution. Moreover, Lovell *et al.* (2003) used the ground-based laser scanner to model the LAI using canopy profile and Koetz *et al.* (2006) applied the LiDAR waveform model to generating the fCover and the LAI from large footprint LiDAR data. However, it is difficult for the large footprint LiDAR used to extract forest information for small area. The use of the ground based Laser scanner is limited by topography conditions of study area and can estimate only limited small forest area, not broad forest area. Therefore in this research, we verified the usefulness of small footprint LiDAR data for estimating the LAI. Furthermore, we compared the LAI extracted from our study with previous research, which Barilotti *et al.* (2006) analyzed the LAI with the LPI (Laser Penetration Index). Thereby, we examined which method would be suitable for estimating the LAI in the forests of South Korea.

2. MATERIALS AND METHODS

2.1 Study area

The study area was located in Mt. Yumyeong (the upper left 127°28'45.76074"E, 37°35'59.75109"N and lower right 127°30'6.98627"E, 37°35'6.27425"N), central South Korea. Situated from 321m to 573m above sea level, the study area was dominated by steep hills, with the main tree species being *Pinus koraiensis* (Korean Pine), *Larix leptolepis* (Japanese Larch) and *Quercus* spp. (Oaks). Approximately 312ha were selected for this study and the 30 plots (10 plots by tree species) of the study area were investigated for measuring the LAI. These plots were selected in such a way that the composition of tree species was homogeneous.

2.2 LiDAR data

In this study, Optech ALTM 3070 (a small footprint LiDAR system) was used for acquisition of the LiDAR data, with the flight performed on 28th April 2004. The study area was measured from an altitude of 1,500m, with a sampling density of 1.8 points per square meter, and the radiometric resolution, scan frequency and scan width were 12bits, 70Hz and $\pm 25^\circ$, respectively. Field data were obtained on 28~30th April 2007, although the LiDAR data were acquired on 28th April 2004. However, the difference in the tree height growth relevant to the period between the acquisition of the ground data and LiDAR-derived values was not considered, as an increase in the quantity of needle leaf (*Pinus koraiensis* and *Larix leptolepis*) during 3 years is relatively small and broad leaf were come out little. In order to calculate the LAI from the LiDAR data, pre-classified points were used with the TerraScan software (Terrasolid Corporation); therefore, raw LiDAR points were classified into one of 4 groups; Ground Return (GR), Low Vegetation Return (LVR), Medium Vegetation Return (MVR) and High Vegetation Return (HVR) (Lim *et al.*, 2001). The HVR and GR were used to estimate the LPI, and the LII was calculated from the GR and all point data.

2.3 Field data

The number of sample plots was 10 sites by tree species. Each plot was composed of 20m \times 20m (400m²) size and the LAI of plots was measured using the AccuPAR-80 Linear PAR/LAI Ceptometer of Decagon Devices, INC. The LAI was calculated automatically, as shown equation 1 in the device (Decagon INC, 2001).

$$LAI = \frac{\left[\left(\left(1 - \frac{1}{2K} \right) f_b - 1 \right) \right] \ln \tau}{A(1 - 0.47 f_b)} \quad (1)$$

where f_b is the fraction of incident PAR (Photosynthetically Active Radiation) which is beam, K is the extinction coefficient for the canopy, and τ is scattered and transmitted PAR. A is defined as below equation 2 and the a of equation 2 is the leaf absorptivity in the PAR band.

The f_b was estimated at 0.85 in the barely field before beginning the measurement of the LAI below the canopy and used the same value for all tree species. The a was determined as 0.9 which was assumed by AccuPAR in LAI sampling routines. K could be calculated with zenith angle (37°) of the

sun in the study area (Equation 3) (Campbell, 1986). And τ could be computed as the ratio of PAR measured below the canopy to PAR above the canopy (Equation 4).

$$A = 0.283 + 0.785a - 0.159a^2 \quad (2)$$

$$K = \frac{(x^2 + \tan^2 \theta)^{\frac{1}{2}}}{x + 1.744(x + 1.182)^{-0.733}} \quad (3)$$

$$\tau = \frac{PAR_{\min}}{PAR_{\max}} \quad (4)$$

where θ is the zenith angle of the sun and x is a leaf angle distribution parameter. When the LAI was estimated in the study area, x was determined as 1 which means that the angle distribution was spherical. Therefore K can be simplified to equation 5.

$$K = \frac{1}{2 \cos \theta} \quad (5)$$

Through this process of the AccuPAR, we acquired the average LAI as estimating 9 positions for avoiding the LAI value fluctuating by changing the value according to the directions. The LAI estimation was begun at the centers of the plots and determined at 8 positions with 8 directions as we moved with 45° from the north and 10m distant from the center. The LAI value per 1 position was also estimated 4 times with 4 directions, where were East, West, South and North. Therefore we could obtain the one average LAI per a plot and compare field-derived LAI with LiDAR-derived LPI and LII through 30 LAI values totally. The measurement was carried out from 11 A.M to 14 P.M. since the solar altitude was the highest during a day. The positions of the plots were acquired at the breast height of the center of each plot, using GPS Pathfinder Pro XR[®] manufactured by Trimble[™].

2.4 Estimation of LAI

2.4.1 Potential of LiDAR for estimating LAI

It is possible to apply various remote sensing techniques for estimating the LAI. However, the LiDAR has the potential for obtaining geo-registered 3D-points whereas satellite imagery and aerial photograph are difficult to extract the 3 dimensional information of forested area. Moreover, the laser is similar to the sunlight at the aspect based on reflectance or transmission through the canopy; therefore, we could estimate the LAI as acquiring the 3D points reflected on the canopy and the ground in forested area. On the other hands, instead of the radiation reach from the sun to the ground and vegetation, with the number of ground returns and vegetation returns (including HVR, MVR and LVR) reach from an aircraft, we could analyze the LAI. Monsi and Saeki (1953) estimated the LAI as measuring both incident (I_0) and below-canopy radiation (I)

like equation 6 .

$$LAI = -1/k \ln(I/I_0) \quad (6)$$

where I_0 is the incident radiation, I is the radiation transmitted below-canopy, k is the extinction coefficient. In above equation, I/I_0 describes the ratio of sunlight interception. With such aspect of interception or penetration, we could estimate the LAI when using total amount of laser point emitted from an aircraft and reflected from the canopy although physical and chemical characteristics of laser and sunlight were different each other. In other words, the total emitted laser point from an aircraft could be considered as the total amount of sunlight, and the total intercepted or penetrated laser point through the canopy could be regarded as the total amount of blocked or incident sunlight. Therefore, for estimating the LAI, we applied the LPI and LII which could be generated using the density and number of laser point penetrated and intercepted through the canopy. However, we didn't apply the equation 6 directly because that equation was applied to only natural radiation. Thereby, in our study, new regression functions were used instead of equation 6 after regression analysis was performed with field-derived LAI and LiDAR-derive LPI and LII. Furthermore, we didn't consider the extinction coefficient as k of equation 6 because we conducted this study with only the number of laser point, not laser intensity value.

2.4.2 Laser Penetration Index (LPI)

For estimating the LAI, Barilotti *et al.* (2006) suggested the LPI using point density of ground returns and vegetation returns in the sample plots. The classification of LiDAR points into ground returns and vegetation returns was conducted by Terracan™ software. Afterward, vegetation returns were divided into two classes; one was first returns (height ≥ 1 m), the other was ground returns (height < 1 m). For generating the LPI, the ground and high vegetation returns were used only.

$$LPI = \frac{D_{gnd}}{D_{gnd} + D_{high}} \quad (7)$$

where D_{gnd} is the density of ground returns and D_{high} is the density of first returns. The LPI was calculated with raster data by a neighbor statistical analysis using a radius of 5m because of the heterogeneous distribution of LiDAR points. If the LPI value is close to 0, it means the vegetation is dense, however, if the value is close to 1, it describes the vegetation is sparse. We generated the LPI using the same methods and then compared the accuracy with the result of the LII as conducting the regression analysis with the LPI value and the field-derived LAI.

2.4.3 Laser Intercept Index (LII)

The LII can be generated from the number of ground and low vegetation returns and all returns including HVR, MVR, LVR and GR. Practically, however, the LII can be described as shown equation 8 because the LII means the ratio of laser points intercepted by the canopy.

$$LII = \frac{N_{(high+mid)}}{N_{all}} = 1 - \frac{N_{gnd} + N_{low}}{N_{all}} \quad (8)$$

where $N_{(high+mid)}$ is the sum of high and medium vegetation returns, N_{gnd} and N_{low} are the number of ground and low vegetation returns respectively and N_{all} is the sum of all returns in a plot. With above equation 6, we could predict that the LII is proportioned to the LAI since the LAI increases when the ratio of points intercepted by the canopy increase. We generated the LII by three tree species with the number of laser points, and then created the relationship function as comparing with field-derived LAI values.

3. RESULTS AND DISCUSSION

For the accuracy analysis of estimated regression function with field-derived LAI and LiDAR-derived LPI and LII, the coefficient of the determination (R^2) and root mean square error (RMSE) were calculated. As a result, on the whole tree species, coefficients of the determination of the LII were higher than those of the LPI. The coefficients of determination for the LPI were 0.81, 0.73 and 0.81 respectively for *Pinus koraiensis*,

Species	Statistics	LPI	LII
<i>Pinus koraiensis</i>	Function	$LAI = -54.561 \cdot LPI + 7.3411$	$LAI = 50.184 \cdot LII - 42.573$
	Range	0.04~0.07	0.92~0.96
	R ²	0.81	0.88
	RMSE	0.31	0.24
<i>Larix leptolepis</i>	Function	$LAI = -8.3405 \cdot LPI + 3.5776$	$LAI = 8.2604 \cdot LII - 4.6359$
	Range	0.07~0.19	0.78~0.91
	R ²	0.73	0.85
	RMSE	0.25	0.18
<i>Quercus spp.</i>	Function	$LAI = -1.7093 \cdot LPI + 1.2168$	$LAI = 1.8422 \cdot LII - 0.6043$
	Range	0.02~0.34	0.66~0.98
	R ²	0.81	0.86
	RMSE	0.09	0.08

Table 1. Accuracies of the LAI estimations with LPI and LII

Larix leptolepis and *Quercus* spp. (Table 1). The LII were estimated at 0.88, 0.85 and 0.86 respectively. Likewise with the result of the coefficient of determination, RMSEs of the LII were evaluated higher than those of the LPI. RMSEs of the LPI were determined as 0.31, 0.25 and 0.09 by three tree species, and LIIs were estimated at 0.24, 0.18 and 0.08 respectively.

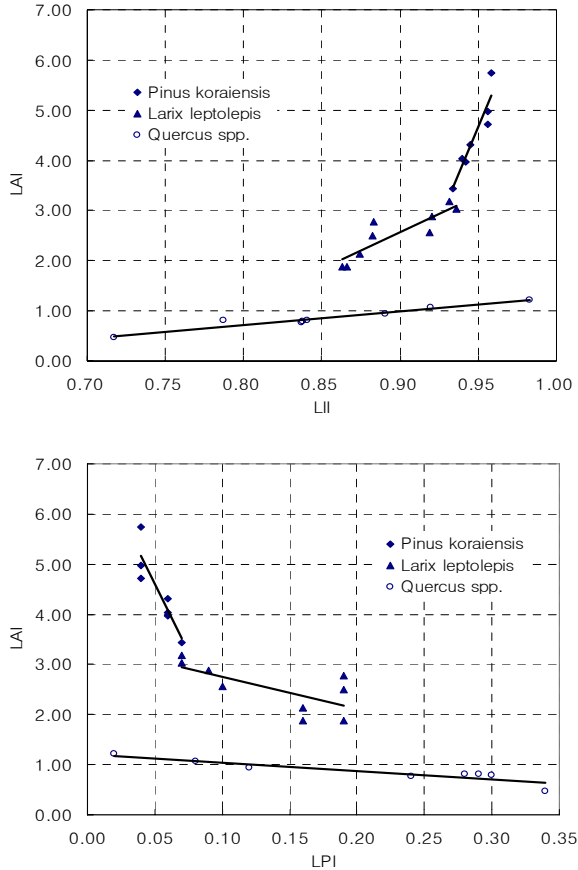


Figure 1. Distribution of LAI according to LPI and LII, and comparison of slope by tree species

When seeing the results, we could find out the accuracy of regression function was rarely different. However, the coefficient of determination for the LPI was totally lower than those of the LII. The reason for the difference could be judged as the original information of laser point was lost when the point data was transformed to raster data for generating the LPI. On the other hands, because the LII maintains the properties of laser points without losing peculiar individual value of laser points according to being changed into raster data, it can represent the LAI close to the sunlight through the canopy. Furthermore, the LII allows normalizing biased local variation of laser points since it uses only the number of laser points in a plot, whereas raster data has some noise which is caused by unbalanced distribution of laser points due to different distance of across track and along track (Kwak *et al.*, 2007).

And in the estimated regression functions, the slopes by functions show large difference by tree species (Table 1 and Figure 1). We can guess that the tendency of slope (the absolute value of slope) in estimated regression functions keeps up with the ratio of the amount of intercepted sunlight. In the equation 1, the LAI is affected by only τ value because the other variables are fixed as constant number in the study area. The τ

is defined as the ratio of PAR measured below the canopy to PAR above the canopy. Therefore, the τ has a nearly 1 value due to little difference between minimum and maximum PAR in the case with little leaf as *Quercus* spp. in the spring. It means, when the τ is close to 1, $\ln \tau$ is close to 0. Thus, the absolute value of the slope in regression function for *Quercus* spp. is smaller than those of the others because the τ of *Quercus* spp. is close to 1 due to little difference between maximum and minimum PAR. However, τ s of *Pinus koraiensis* and *Larix leptolepis* are very small due to large difference between minimum and maximum PAR. Thereby, the absolute values of slopes in *Pinus koraiensis* and *Larix leptolepis* are relatively higher than those of *Quercus* spp. because the increment of the LAI per unit of the LPI or LII is large. By the way, in coniferous trees, the slope of *Pinus koraiensis* is higher than that of *Larix leptolepis*. The reason for the difference is that the leaf density of *Larix leptolepis* is low since leaves of *Larix leptolepis* were rarely come out in April. We can expect that the slope of *Larix leptolepis* will become similar with *Pinus koraiensis* in summer season.

In this study, we used the LiDAR data which had 3 years gap with field measurement. However, we didn't consider the difference of leaves increment according to tree growth for 3 years because we tried to examine the tendency and relationship between field-derived LAI and LiDAR-derived information such as the LPI and LII. For the quantitative analysis of the LAI with the LPI and LII, the growth gap by the lapse of time must be considered. And based on above mentioned objective, we just examined the tendency and relationship of the LAI by LPI and LII without comparison with new sample area (test area). For proving the accuracy of our study, however, we have to estimate the LAI and compare the result with filed-derived LAI with new sample area not included in our training area.

4. CONCLUSION

In this study, we estimated the LAI using LiDAR data classified into 4 type points such as HVR, MVR, LVR and GR. For calculating the LAI, firstly the LPI and LII were generated. The LPI was created with first returns ($h \geq 1m$) and ground returns ($h < 1m$), and the LII was prepared with ground returns, low vegetation returns and all returns. As the result, the accuracy of the LPI was evaluated rather lower than the LII for *Pinus koraiensis*, *Larix leptolepis* and *Quercus* spp.. This is can be attributed to the fact that the characteristic of point data was removed when the LPI was calculated because the LPI was generated using a density map of raster data type which was assigned to point density of plot. Another reason was that the LII allows normalizing biased local variation of the number of laser points while the raster data has some noise due to unbalanced distribution of laser points. The slopes of estimated regression functions were also appeared differently each other. The slope of *Pinus koraiensis* was the steepest and that of *Quercus* spp. was the gentlest of three species. The reason was that the difference between minimum and maximum PAR is large in *Pinus koraiensis* because the sunlight and the LiDAR points were much intercepted above canopy by dense leaf density of *Pinus koraiensis*. However, in the case of *Quercus* spp., the difference of minimum and maximum PAR was small because of sparse leaf density. Therefore we can expect the

increase of the slope of *Quercus* spp. from summer because leaf density is gradually higher and higher. In the case of *Larix leptolepis*, the absolute value of slope was between *Pinus koraiensis* and *Quercus* spp. because leaves of *Larix leptolepis* were rarely come out in April.

5. ACKNOWLEDGMENT

We would like to thank Kang-Won Lee, Managing Director of Hanjin Information System & Telecommunication Corporation, South Korea, for offering the LiDAR data.

REFERENCES

- Barilotti, A., Turco, S., and Alberti, G., 2006. LAI determination in forestry ecosystem by lidar data analysis, Proceedings of Workshop on 3D Remote Sensing in Forestry, Vienna, Austria, February, 14~15, 2006., pp.248~252
- Bonan, G. B., 1993. Importance of leaf area index and forest type when estimating photosynthesis in boreal forests. *Remote Sensing of Environment*, 43(3), pp.303~314
- Bréda, N. J. J., 2003. Ground-based measurements of leaf area index: a review of methods, instruments and current controversies. *Journal of Experimental Botany*, 54(392), pp.2403~2417
- Campbell, G. S., 1986. Extinction coefficients for radiation in plant canopies calculated using an ellipsoidal inclination angle distribution. *Agricultural and Forest Meteorology*, 36, pp.317~321
- Cohen, W. B., Maersperger, T. K., Gower, S. T., and Turner, D. P., 2003. An improved strategy for regression of biophysical variables and landsat etm+ data. *Remote Sensing of Environment*, 84(4), pp.561~571
- Decagon devices, INC., 2001. Operator's manual of AccuPAR, U.S.A,
- Finney, M., 1998. Farsite: Fire area simulator-model. Development and evaluation. Research Paper RMRS-RP-4, USDA Forest Service
- Holmgren, J., Nilsson, M., Olsson, H., 2003. Estimation of tree height and stem volume on plots using airborne laser scanning, *Forest Science*, 49(3), pp.419~428.
- Jonckheere, I., Fleck, S., Nackaerts, K., Muys, B., Coppin, P., Weiss, M. and Baret, F., 2004. Review of methods for in situ leaf area index determination: Part i. theories, sensors and hemispherical photography. *Agricultural and Forest Meteorology*, 121(1~2), pp.19~35.
- Koetz, B., Morsdorf, F., Sun, G., Ranson, K. J., Itten, K., and Allgöwer, B., 2006. Inversion of a lidar waveform model for forest biophysical parameter estimation. *IEEE Geoscience and Remote Sensing Letters*, 3, pp.49~53
- Koetz, B., Schaepman, M., Morsdorf, F., Itten, K., and Allgöwer, B., 2004. Radiative transfer modeling within a heterogeneous canopy for estimation of forest fire fuel properties. *Remote Sensing of Environment*, 92(3), pp.332~344
- Kwak, D. A., Lee, W. K., Lee, J. H., 2006. Predicting Forest Stand Characteristics with Detection of Individual Tree, Proceedings of the MAPPs/ASPRS 2006 Fall Conference, San Antonio, Texas, U.S.A., November 6~10, 2006.
- Kwak, D. A., Lee, W. K., Lee, J. H., Biging, G. S., Gong, P., 2007. Detection of individual trees and estimation of tree height using LiDAR data, *Journal of Forest Research*, Revised submission
- Lim, K., Treitz, P., Groot, A., St-Onge, B., 2001. Estimation of individual tree heights using LIDAR remote sensing, Proceedings of the Twenty-Third Annual Canadian Symposium on Remote Sensing, Quebec, QC, August 20~24, 2001.
- Lovell, J., Jupp, D., Culvenor, D., and Coops, N., 2003. Using airborne and ground-based ranging lidar to measure canopy structure in Australian forests. *Canadian Journal of Remote Sensing*. 29(5), pp.607~622
- Monsi, M. and Saeki, T., 1953. Über den Lichtfaktor in den Pflanzengesellschaften und seine Bedeutung für die Stoffproduktion. *Japanese Journal of Botany* 14, pp.22~52
- Morsdorf, F., Kötz, B., Meier, E., Itten, K. I. and Allgöwer, B., 2006. Estimation LAI and fractional cover from small footprint airborne laser scanning data based on gap fraction. 104(1), pp.50~61
- Myneni, R., Nemani, R., and Running, S., 1997. Estimation of global leaf area index and absorbed par using radiative transfer models. *IEEE Transactions on Geoscience and Remote Sensing* 35, pp.1380~1393
- Riaño, D., Valladares, F., Condés, S., Chuvieco, E., 2004, Estimation of leaf area index and covered ground from airborne laser scanner (Lidar) in two contrasting forests. *Agricultural and Forest Meteorology*, 124, pp.269~257
- Schulze, E. D., Beck, E., Müller-Hohenstein, K., Lawlor, D., 2005. *Plant ecology*, Springer eds., Berlin
- Watson, D. J., 1947. Comparative physiological studies in the growth of field crops. I. Variation in net assimilation rate and leaf area between species and varieties, and within and between years. *Annals of botany* 11, pp.41~76

DECIDUOUS-CONIFEROUS TREE CLASSIFICATION USING DIFFERENCE BETWEEN FIRST AND LAST PULSE LASER SIGNATURES

X. Liang*, J. Hyypä, L. Matikainen

Finnish Geodetic Institute, Department of Remote Sensing and Photogrammetry, Masala, Finland
(Xinlian.Liang, Juha.Hyypä, Leena.Matikainen)@fgi.fi

Commission III

KEY WORDS: Leaf-off, First-last pulse, Species identification, Airborne laser scanners

ABSTRACT:

In this paper, a deciduous-coniferous tree classification mechanism is proposed, tested and analyzed using solely laser scanner data. The data were acquired under leaf-off conditions by Toposys II system. Under such circumstance, sources of last pulse hits of deciduous and coniferous are different, which allows concise discrimination between these two species. Tree positions were located from first pulse DSM, species were identified by the difference between two pulse data and field measurements were used for validation. The classification results demonstrate that first-last pulse laser data, under leaf-off condition, is ideal for deciduous and coniferous trees classification; and also indicate that the data collected for high accuracy DEM production is also suitable for forest investigation.

1. INTRODUCTION

Airborne laser scanners (ALS), providing small footprint diameters (10 – 30 cm), allow accurate forest information estimation (e.g. Næsset 1997; Magnussen and Boudewyn, 1998). Two main approaches in deriving forest attributes using laser scanner data have been those based on laser canopy height distribution and on individual tree detection. In former approach, percentiles of laser canopy heights distribution are used as predictors to estimate forest characteristics. Næsset (2002), Lim et al. (2003) and Holmgren and Jonsson (2004) have shown that this approach produces highly reliable estimates of stand variables. If the number of laser pulses is increased to several measurements per square meter, individual trees can be recognized (Hyypä and Inkinen, 1999; Hyypä et al. 2001, Persson et al., 2002; Popescu et al., 2002; Leckie et al. 2003). From individual tree, height, crown diameter and even species can be derived using laser scanner data. Then, more tree and stand attributes, e.g. timber volume, can be quite reliably estimated using existing forest models based on height, diameter and specie information (Hyypä and Inkinen, 1999).

Tree species is an essential index in forest studies, inventories, managements and other forest applications. In practice, species classification is performed using range and optical/near-infrared data, together or individually.

In Brandtberg (2002), features describing branch structure, crown shape and color were extracted from high spatial resolution color infrared aerial photographs and then input into a classification system. In Bohlin et al. (2006), spectral values, corresponding to sunlit part of detected crown, were extracted from high spatial resolution color infrared aerial photographs and applied in tree species identification. In the June and October images, 88% and 89% of the detected trees, respectively, could be separated into three classes, pine (*Pinus Sylvestris*), spruce (*Picea Abies*) and deciduous.

The airborne laser scanning data has also been tested for tree species classification. Holmgren and Persson (2004) stated that it is possible to separate pine and spruce using laser scanner data. That approach was tested at individual tree level between Scots pine and Norway spruce. The portion correctly classified trees on all plots was 95%. Moffiet et al. (2005) proposed that the proportion of laser singular returns is an important predictor for the tree species classification. Brandtberg et al. (2003) used laser data under leaf-off conditions for the detection of individual trees. Additionally, classification results of different indices suggest a moderate to high degree of accuracy using single or multiple variables between deciduous trees. Brandtberg (2007) presented a framework to express interactions of the laser beams with individual tree canopy, and proposed species classification strategies for selecting group of laser points, where variables used were quantifications of independent events and statistics/geometric measurements. Overall, 64% classification accuracy is achieved, for three leaf-off deciduous trees, oaks (*Quercus spp.*), red maple (*Acer rubrum*) and yellow poplar (*Liriodendron tuliperifera*).

Persson et al. (2006) identified individual tree species through combining features of high resolution laser data with high resolution multi-spectral images. Classification experiment was conducted in southern Sweden with forest dominated by Norway spruce (*Picea abies*), Scots pine (*Pinus sylvestris*), and deciduous trees, mainly birch (*Betula spp.*). The results implied that by combining structure and spectral features, the classification could be improved (95 % accuracy).

As a summary, laser data has been used for tree species classification successfully, but there are unsolved problems. Firstly, the accurate classification between deciduous and coniferous trees requires the aid of optical or near-infrared data. Secondly, in practical applications, there can only be few training trees for a large area. Therefore, in order to receive

* Corresponding author.

good classification accuracies, more research is needed in deriving good features for tree species classification.

The increasing use of laser scanning for nation-wide elevation data collection also supports use of the data for other purposes. Up to now, airborne laser scanning data can be available for whole countries (Switzerland, Netherland) and for large districts (South Tyrol / Italy, Vorarlberg / Austria, Saxon-Bohemian Switzerland / Germany, Baden-Württemberg / Germany). All this data has been collected with leaf-off conditions in order to get the highest accuracy in DEM. In Finland, the leaf-off data is also the first candidate for the national laser scanning. Forest inventory authorities are, however, planning to have a laser and aerial imaging survey during summer time in order to get more reliable information also for the tree species.

In the present work, we analyzed airborne laser data acquired in a suburban site in 2003 under leaf-off conditions. The objective was to demonstrate that leaf-off laser data is ideal for tree species classification between deciduous and coniferous trees. In previous studies, it has already been demonstrated that deciduous trees can be reconstructed using leaf-off data.

2. MATERIAL AND METHODS

The test site locates in Espoo, 15 km west of Helsinki. Toposys II (wavelength of 1.54 μm , maximum scan angle $\pm 7.1^\circ$) campaigns were carried out in 14th May 2003. At that time, the leaves were off and in some cases there were small buds depending on the tree species. The flying altitude was 400 m above ground and the beam divergence was 1 mrad giving a footprint of 0.40 m in diameter. In the Toposys II, there are 128 parallel beams (pushbroom type scanner) that are sampled in a fast rate. The point spacing between consecutive beams was 80 cm in the across track direction and between 10-15 cm in the along track direction (depending on the flight speed). Therefore, there was a high autocorrelation between the consecutive hits in the along track direction. We expect that the data corresponded to a nominal pulse density of 4 to 5 pulse per square meter organized in even spacing. Thus, the sampling density of the data was not significantly higher than that used in nation-wide data collection (for example, in Switzerland, the surveying company has collected laser data for their own use with a density of about 4 pulses per square meter).

Reference data included 295 identified trees, which were of direct access and were evenly scattered across the test site. Among them, 176 were coniferous (spruce and pine) and 119 were deciduous trees. Tree species information, coniferous or deciduous, was collected from those trees in summer 2006.

Coordinate transformations, geoid correction, strip adjustment and systematic shift correction were first performed on laser points cloud. Then, last pulse data were classified in TerraScan software (see www.terrasolid.fi) to separate the ground points from others (low and high vegetation). In TerraScan, the ground points were triangulated using TIN densification method developed by Axelsson (2000). The following parameters, cite dependent, were used for the classification: max. building size 100m, terrain angle 75° , iteration angle 6° , iteration distance 1.2m, and reduce iteration angle when edge length < 5 m. The raster image file corresponding to the Digital Elevation Model (DEM) was created from the classified ground points using the

following parameters: lowest hit within 0.5 m grid spacing and gaps filled up to 10 pixels.

The Digital Surface Model (DSM) was calculated for both pulses respectively, with a 0.5 m grid from the highest hits. Gaps were filled up to 3 pixels using interpolation. The final Canopy Height Model (CHM) was then calculated as the difference between the DSM and the DEM.

In the tree top detection, a simplified process to that presented in Hyypä et al. (2001) was applied. The prefiltering was done with a one step convolution of a 3 x 3 filter

$$\frac{1}{25} \begin{bmatrix} 1 & 3 & 1 \\ 3 & 9 & 3 \\ 1 & 3 & 1 \end{bmatrix} \quad (1)$$

and then the possible tree top position was found by a 5 x 5 maximum filter: if the current pixel was the highest in the 5 by 5 window, it was labelled as possible tree top. Lower local maxima, with height less than 3 m, were neglected from further analyses.

Tree crown radius was estimated using the tree top position and corresponding value of the CHM, which was taken as the tree height. The radius of the tree was assumed, according to Pitkänen et al. (2004), to be

$$R_{\text{Org}} = (1.2 + 0.16 \times H) \times 0.5 \quad (2)$$

In our analysis, the radius was reduced by 40%.

$$R_{\text{Est}} = R_{\text{Org}} \times 0.6 \quad (3)$$

It was assumed that the main difference in first-last pulse signature between coniferous and deciduous trees lies in the crown centre and that smaller radius leads to more reliable estimation for different tree species.

Then, a neighbourhood window $[2R_{\text{Est}} + 1, 2R_{\text{Est}} + 1]$ was defined as the estimated crown area.

It was expected that, under leaf-off conditions, first pulse signals correspond to reflections from treetops, even with the deciduous trees, as discovered by Brandtberg et al. (2003); and that the source of last pulse hits of deciduous trees is the ground and of coniferous tree, it is the tree top. Based on this assumption, tree species were classified by the absolute height difference between two DSMs, and defined as a function of two thresholds. If the proportion of pixels within the estimated crown area (defined in threshold 1) does not present significant height difference (defined in threshold 2), the tree was classified as coniferous tree. Otherwise, it was identified as deciduous tree.

3. RESULTS

Figure 1 and 2 show points cloud and DSM corresponding to coniferous and deciduous trees respectively. Points are in local coordinates. First and last pulses are marked in green and red,

whereas tree top and estimated crown area are marked by cross and circle, respectively.

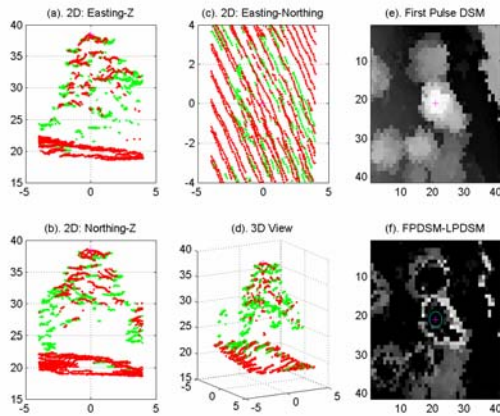


Figure 1. Points cloud and DSM corresponding to a coniferous tree. (a) Points cloud in vertical projection perpendicular to Northing, referred as Easting-Z. (b) Points cloud in vertical projection perpendicular to Easting, referred as Northing-Z. (c) Points cloud in horizontal projection, referred as Easting-Northing. (d) Points cloud in 3D space. (e) DSM based on first pulse laser data. (f) Difference between first and last pulse data.

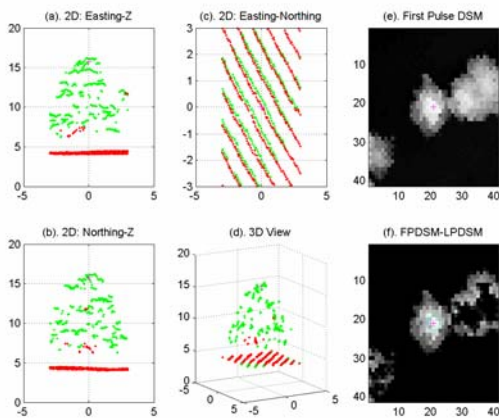


Figure 2. Points cloud and DSM corresponding to a deciduous tree, where a-f corresponds to cases in Fig. 1.

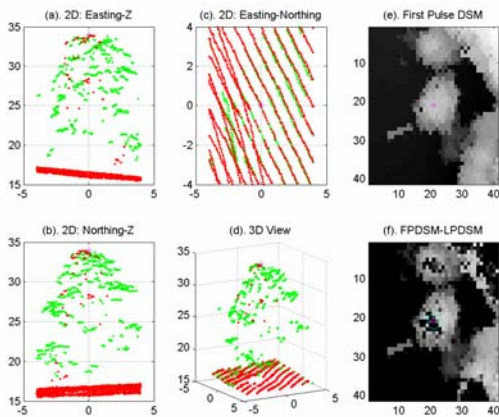


Figure 3. Points cloud corresponding to a deciduous tree, where a-f corresponds to cases in Fig. 1. Obviously, tree crown has been hit by the last pulse.

Figure 3 gives an example of how misclassification could be introduced. In that case, a deciduous tree's crown was hit by both pulses at the centre of the tree, leading to small height difference between first and last pulse data.

The classification results between coniferous and deciduous trees are reported in Table I and Figure.4.

Table I shows the confusion matrix of classification, where Th1 refers to the proportion of pixels within the estimated crown area and Th2 refers to the height difference in meter. The overall accuracy is 89.83%. Figure 4 shows the producer accuracy as a function of parameter Th2, where Th1 equals to 40%.

	Actual Coniferous	Actual Deciduous	Total
Classified as Coniferous	157	11	168
Classified as Deciduous	19	108	127
Total	176	119	295

Table 1. Confusion matrix (Th1 = 40% and Th2 = 0.3)

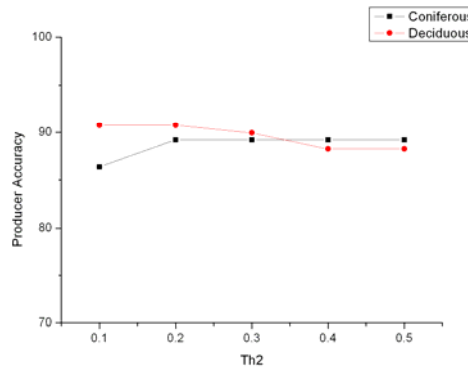


Figure 4. Producer accuracy as a function of threshold 2

4. DISCUSSION

The result indicates that a simple signature, i.e. the range difference between first and last pulse hits under leaf-off conditions, is suitable for deciduous-coniferous tree classification. In order to improve the quality of the classification and to understand where the proposed methodology failed, the misclassified cases were analysed. The reasons for the misclassification could be grouped into categories (1) branch structure, (2) only pulse hits (3) crown shape (4) tree top position, (5) parameter and (6) data processing. Yet, in practice, the misclassification is mostly introduced by several, rather than solely one, factors.

Branch structure: The basic assumption for this study was that, under leaf-off condition, last pulse would penetrate deciduous

tree crown and would be reflected from coniferous tree top. However, under certain circumstance, e.g. when coniferous trees are heavily defoliated, this is not always the case. For the deciduous, the denser the crown is, the more last pulse points are reflected from upper branches, which reduces difference between the two pulse modes, and possibly leads to misclassification. On the other hand, small buds also caused that some last pulses were reflected by upper branches.

Number of only pulse hits: In first and last pulse data set, there are some points with same planar coordinates and small, even zero, height differences. We assumed that they corresponded to only pulse hits. In Toposys II, about 1 m vertical difference was needed to separate between first and last pulse mode. Accompanied with incidence angle and crown shape, the only pulse hit may happen to be the ones adopted in DSM generation, thus leading to smaller differences between first and last pulse data. This explains that some deciduous trees were misclassified as coniferous.

Crown shape: particularly, for spruce with cone shaped crown and small open angle, it is possible that both lower and upper crown parts happen fall into the same raster cell, due to relative large cell size. In such case, the height difference, between two pulses, is exaggerated, and then leads to misidentification.

Tree top position: In general, tree top is expected to locate at crown centre and correspond to local height maximum. However, in practice, branches' configuration may be complicated and then makes it hard to define a necessary and sufficient condition of treetops. For instance, tree top may incline to one side and then not be local height maximum; outstretched branches may be higher than real tree top. Therefore, it is possible that some tree tops locate apart from crown centre and some mis-located tree tops exist. In former case, the height difference, around the estimated crown area, may be larger than what is supposed to be for coniferous, due to the edge area. And then the trees would likely be misclassified as deciduous ones. To overcome this problem, it would help to first determine crown area and then find possible, or assumed, tree top position. In the latter case, mis-located trees were neglected from analyses.

Parameter: Figure 4 shows how overall classification accuracy changes according to threshold 2. Clearly, the fluctuation of accuracy is moderate and the classification is not sensitive to parameter TH2. However, selected parameter also plays its own role in the classification. In general, larger Th1 and smaller Th2, which means larger proportion pixels presents smaller height difference between first and last pulse data, lead to higher producer accuracy for the coniferous, smaller producer accuracy for the deciduous, and vice versa. Between the two parameters, the classification is more sensitive to Th1. Considering the overall accuracy, 40% keeps a balance and leads to accuracy around 89% for both species.

Data processing: data processing, which enhances the different reflectance pattern between the deciduous and coniferous, also contributes to identification accuracy amelioration. One example could be the process in last pulse DSM production. When the highest hits are assigned to DSM cells, like in this study, the confusion caused by several last hits reflected by lower coniferous branches does not, generally, introduce large height differences between the DSMs, and the coniferous identification accuracy therefore improves. On the other hand, if the lowest hits were assigned to DSM cells, the confusion

caused by a few last hits reflected by upper deciduous branches would be effectively eliminated, which would contribute to high deciduous identification accuracy.

5. CONCLUSIONS

The results in this paper indicate that the difference between first and last pulse is a valuable feature for trees species classification. It reliably (89 % accuracy) gives the difference between coniferous and deciduous trees under leaf-off conditions. In order to conclude the optimal accuracy it could achieve, more experiments based on difference mechanisms are needed.

REFERENCES:

- Bohlin, J., Olsson, H., Olofsson, K. and Wallerman, J., 2006. Tree species discrimination by aid of template matching applied to digital air photos. Workshop on 3D Remote Sensing in Forestry, 14th-15th Feb. 2006, Vienna. pp. 199-203.
- Brandtberg, T., 2002. Individual tree-based species classification in high spatial resolution aerial images of forests using fuzzy sets. *Fuzzy Sets and Systems*, 132(3), pp. 371-387.
- Brandtberg, T., 2007. Classifying individual tree species under leaf-off and leave-on conditions using airborne lidar. *ISPRS Journal of Photogrammetry and Remote Sensing*, 61, pp. 325-340.
- Brandtberg, T., Warnera, T. A., Landenberger, R. E., McGraw, J. B., 2003. Detection and analysis of individual leaf-off tree crowns in small footprint, high sampling density lidar data from the eastern deciduous forest in North America. *Remote Sensing of Environment*, 85(3), pp. 290-303.
- Holmgren, J. and Jonsson, T., 2004. Large scale airborne laser-scanning of forest resources in Sweden. *International Archives of Photogrammetry, Remote Sensing and Spatial Information Sciences*. 36(8/W2), pp. 157-160.
- Holmgren, J. and Persson, Å., 2004. Identifying species of individual trees using airborne laser scanner. *Remote Sensing of Environment*, 90(4), pp. 415-423.
- Hyypä, J. and Inkinen, M. 1999. Detection and estimating attributes for single trees using laser scanner. *The Photogrammetric Journal of Finland*, 16(2), pp. 27-42.
- Hyypä, J., Kelle, O., Lehtikainen, M. and Inkinen, M. 2001. A segmentation-based method to retrieve stem volume estimates from 3-D tree height models produced by laser scanners. *IEEE Transactions on Geoscience and Remote Sensing*, 39, pp. 969-975.
- Leckie, D., Gougeon, F., Hill, D., Quinn, R., Armstrong, L., Shreenan, R., 2003. Combined high density LiDAR and multispectral imagery for individual tree crown analysis. *Canadian Journal of Remote Sensing*, 29(5), pp. 633-649.
- Lim, K., Treitz, P., Baldwin, K., Morrison, I., Green, J., 2003. Lidar remote sensing of biophysical properties of tolerant northern hardwood forests. *Canadian Journal of Remote Sensing*, 29(5), pp. 658-678.
- Magnussen, S., and Boudewyn, P. 1998. Derivations of stand heights from airborne laser scanner data with canopy-based

quantile estimators. *Canadian Journal of Forest Research*, 28(7), pp. 1016-1031.

Moffiet, T., Mengersen, K., Witte, C., King, R., Denham, R., 2005. Airborne laser scanning: exploratory data analysis indicates potential variables for classification of individual trees or forest stands according to species. *ISPRS Journal of Photogrammetry and Remote Sensing*, 59(5), pp. 289–309.

Næsset, E., 1997. Determination of mean tree height of forest stands using airborne laser scanner data. *ISPRS Journal of Photogrammetry and Remote Sensing*, 52(2), pp. 49-56.

Næsset, E. 2002. Predicting forest stand characteristics with airborne scanning laser using a practical two-stage procedure and field data. *Remote Sensing of Environment*, 80(1), pp. 88–99.

Persson, Å., Holmgren, J. and Söderman, U. 2002. Detecting and measuring individual trees using an airborne laser scanner. *Photogrammetric Engineering and Remote Sensing*, 68(9), pp. 925-932.

Persson, Å., Holmgren, J., Söderman, U., and Olsson, H. 2006. Tree Species Classification of Individual Trees in Sweden by Combining High Resolution Laser Data with High Resolution Near-Infrared Digital Images. *International Archives of the Photogrammetry, Remote Sensing and Spatial Information Sciences*, 37(8/W2), pp. 204-206.

Pitkänen, J., Maltamo, M., Hyypä, J. and Yu, X., 2004. Adaptive methods for individual tree detection on airborne laser based height model. *International Archives of Photogrammetry, Remote Sensing and Spatial Information Sciences*, 36 (8/W2), pp. 187-191.

Popescu, S.C., R.H. Wynne and R.E. Nelson, 2002. Estimating plot-level tree heights with lidar: local filtering with a canopy-height based variable window. *Computers and Electronics in Agriculture*, 37, pp. 71-95.

WAVEFORM FEATURES FOR TREE IDENTIFICATION

P. Litkey^{a,*}, P. Rönholm^b, J. Lumme^b, X. Liang^a

^a Finnish Geodetic Institute, Geodeetinrinne 2, 02431 Masala, Finland, (paula.litkey, xinlian.liang)@fgi.fi

^b Helsinki University of Technology, Institute of Photogrammetry and Remote Sensing, P.O.Box 1200, 02015 TKK, Finland, (petri.ronholm, juho.lumme)@tkk.fi

KEY WORDS: Laser scanning, Waveform, Tree identification, Close-range photogrammetry, Trunk detection

ABSTRACT:

Interest in full-waveform airborne laser scanning (ALS) data has significantly increased with the release of waveform digitizers by commercial vendors. Despite the recent widespread availability of full-waveform data, the full potential of this type of data has yet to be realised. Some of the most promising applications for waveform data can be found in various fields of forestry, in which ALS data can aid in understanding single-tree characteristics. Waveform data can provide both vertical and horizontal information on forests. In this article, we study the feasibility of using full waveform data for tree identification. This study also considers the applicability of methods designed for use with conventional data, the possibility of generating methods that could use considerably denser point clouds extracted from full-waveforms, as well as the applicability of single descriptive or distinct waveform characteristics for tree species classification and tree parameter extraction. In addition, waveform data is compared with terrestrial close-range images. Superimposing waveform data on registered close-range images offers an excellent opportunity for understanding the waveform in greater detail.

1. INTRODUCTION

Airborne laser scanning (ALS) has become a commercially accepted tool for modelling our environment. For the past decade, the majority of commercial applications have concentrated on using the last and first pulses. Recently, ALS vendors have expanded the provided number of returns, thereby enabling users to more easily gain information between the first and last pulses. Typically, between two to five returns have been employed, though some ALS systems can register the full-waveform.

The methods and problems of interpreting recorded waveforms have recently been studied by Hofton et al. (2000) and Wagner et al. (2006). Current methods for waveform processing focus on using a Gaussian decomposition of the signal to derive individual echoes, derived from the main scatterers in the path of the laser beam (Wagner et al., 2006; Reitberger et al., 2006a).

ALS data has become popular for estimating forest parameters. The two main feature extraction approaches for deriving forest information from ALS point clouds have been based on statistical canopy height distribution (e.g., Næsset 1997) and individual tree detection (e.g., Hyypä and Inkinen, 1999; Persson et al., 2002). Distribution-based techniques typically use regression, non-parametric or discriminant analysis for forest parameter estimation. Individual-tree-based approaches use the neighbourhood information of canopy height point clouds and the pixels of CHMs for extracting such features as crown size, as well as individual tree height and location. Finally, forest inventory data are estimated using existing models and statistical techniques.

Before current commercial small-footprint waveform digitizers became available, some forest parameters were statistically

extracted using large-footprint waveform laser altimeters such as "Scanning Lidar Imager of Canopies by based on Echo Recovery" (SLICER) and "Laser Vegetation Imaging Sensor" (LVIS) (Ni-Meister et al. 2001, Harding et al. 2001).

Tree species is an essential index in forest studies, inventories, managements and other forest applications. Pyysalo and Hyypä (2002) investigated a method for describing the tree shape by its 3D point cloud density distribution in both height and width dimension (Reitberger, 2006a). Holmgren and Persson (2004) showed that pine and spruce can be separated with 95% accuracy using laser scanner data. Knowledge of the echo type (first, last, only) together with elevation information was used to extract features from tree crowns. In Brantberg (2007), a digraph process was used for tree species classification, and the shape characteristics of a marginal height distribution were used to improve the tree height estimate. The potential use of waveform data for tree species classification has been presented, e.g., in Reitberger et al. (2006b).

If a size-independent representation of the point cloud structure can be formed, the corresponding features can be represented using primary components or other data compression methods. Waveform-induced point cloud densification could enable the generation of structural features that are detailed enough to allow for species classification.

In this article, we present various experiments on tree identification using waveform laser data. Two types of methods are used: methods based on single descriptive or distinct waveform characteristics and those that use considerably denser point clouds extracted from the full-waveforms. In addition, we also present the integration of ALS waveform echoes with terrestrial close-range images.

* Corresponding author.

2. DATA

2.1 Waveform Data from Espoonlahti

The study data are from the Espoonlahti area and were recorded August 31st 2006 with a TopEye MKII Palmer scanner. A flying altitude of 300m was used, with the scan angle varying between 9 and 25 degrees, as measured from the scanner position to the recorded point position. The waveform sample interval was 1 ns, corresponding to approximately a 15-cm resolution in the beam direction. The pulse length was 5 ns. The footprint of a single laser beam on the ground was approximately 30 cm caused by a beam divergence of 1 mrad. The mean point density was 16.6 points/m².

2.2 Reference Lidar Data

As a reference, we use the automatically extracted points from the TopEye MKII system, which produces first and last pulse data. For comparison of structural features, we also used the data from Optech ALTM3100 flight on July 12th 2005 with combined point cloud from 1000 and 400 m flying heights. Fig. 1 presents the point distributions of the systems used in the case of a birch.

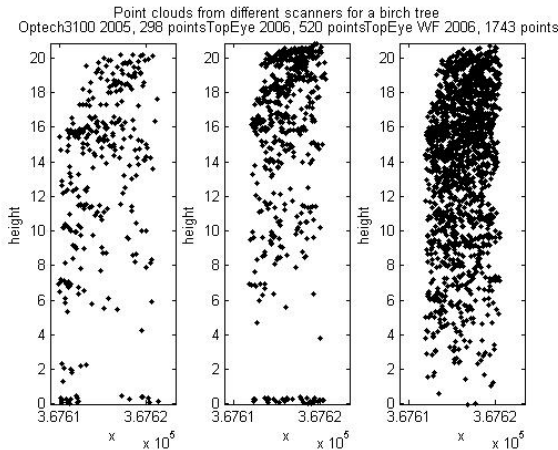


Figure 1. Birch tree example of point distribution for the data types used.

2.3 Photographs

Close-range images were captured using a Nikon D100 camera with a Nikkor 24-85 mm lens. The size of the CCD array was 3,008 x 2,000 pixels. A zoom setting of 24 mm was used during the image capture. The camera was calibrated in the test field at the Helsinki University of Technology (TKK). The original images were resampled in order to eliminate the effect of lens distortions.

3. EXPERIENCES WITH WAVEFORM METHODS FOR TREE SPECIES IDENTIFICATION AND FINDING TRUNK LOCATIONS

3.1 Methods Based on Points Extracted from Waveform

3.1.1 Tree Top Shape Identification

It is more convenient to detect and locate treetops rather than crowns, especially when occurring in clusters. Certain species have distinctive top shape; for example, the spruce usually

shows a cone-shape crown with a small open angle. Ideally, the shape of the crown can be modeled in 3D space by surface fitting (e.g., Holmgren and Persson, 2004). In our study, the crown top was explored in vertical projection and described with 2D curve parameters. At first, the crown points were projected onto four vertical planes through the assumed trunk position, in cardinal and half-cardinal directions. The final projection was constructed as a superposition of these four planes, which roughly expressed the convex hull of the crown. In the description phase, top shape was described by discharging all inner points and fitting a parabola based on the points lying in the topmost two meters.

Fig. 2(a) and Fig. 2(b) plot fitted curves in North-South projection for typical pine and spruce; Fig. 2(c) and Fig. 2(d) show the curves for 8 pine and 8 spruce trees, respectively. In general, the open angle for spruce is smaller than that for pine, thus providing a likely indicator for species identification.

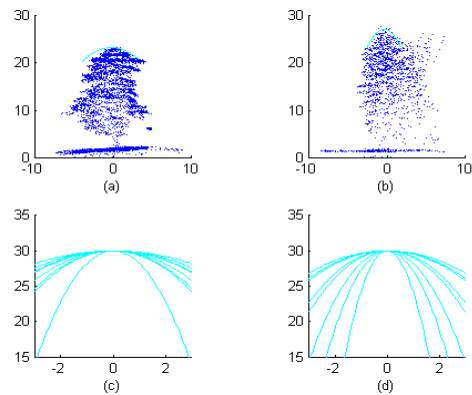


Figure 2. Tree top shape identification. (a) Pine with fitted curve, (b) spruce with fitted curve, (c) curves of eight pines and (d) curves of eight spruces. For comparison, curves were plotted at the same vertex in (c) and (d).

Mean increase WF/system %	Crown top points	Points used in tree top algorithm
Spruce	139%	115%
Pine	132%	106%

Table 1. The second column describes the mean points increase in the tree crown top, comparing the available points extracted from the waveform with points from first/last pulses. The third column presents the points increase in the treetop shape identification algorithm.

Table 1 shows that the points extracted from the waveform located inside the canopy are of little practical use, when employing shape predicting methods developed for first and last pulse data. The result is only indicative due to the small sample size. Verifying this result would require more data from different species and other environments.

3.1.2 Vertical and Horizontal Density Features

First and last pulse and waveform densified data are studied to determine those features that both represent the characteristic tree shape of different species and are independent of tree size. In our examples, the height of each tree is divided into ten

equal-sized bins. As a height feature, we use the percentage of points falling into each height bin.

Fig. 3 plots the height features of eight trees for each of the four tree species. It can be seen that the feature describing the height of a pine has the greatest point density near ground level. In contrast, the deciduous trees, birch and willow, have a maximum density in the upper canopy. The spruce tree has the most uniform point distribution along height bins. These height features only consider the point cloud distribution in the vertical direction. As structural features, we use both height and distance from the assumed trunk position. For simplicity, the location of the highest laser point is assumed to be trunk position. If the treetop is clearly asymmetrical, the centre of the point cloud is used. The point cloud is divided into ten height bins and five distance bins. The distance bins are cylindrical volumes around the trunk. Thus, distance bins located far from the trunk have larger sample percentages than would the inner distance bins. Different grey levels of the structural feature matrix elements in Fig. 4 describe the percentage of all the points falling into single height-width bin.

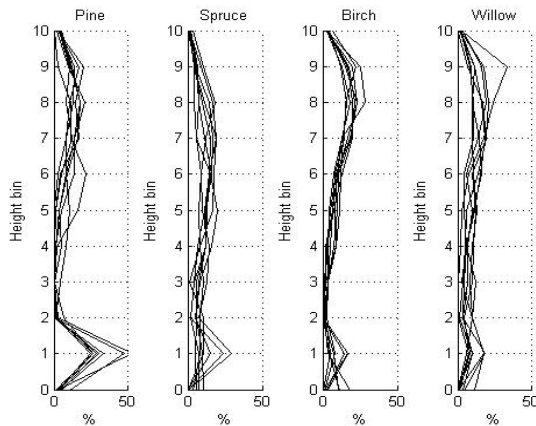


Figure 3. Eight representatives from each of four species are plotted to visualize the stability of the height feature in dense point clouds.

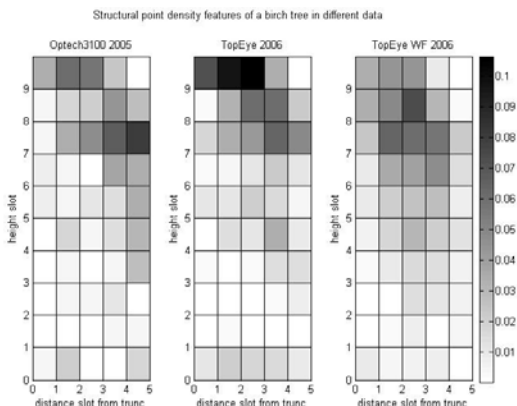


Figure 4. Structural density representations of the birch tree created from the point cloud in Fig. 1. The darker the structural element, the more points are located in the corresponding volume.

The advantage of using structural or height features to represent trees is that trees of different physical dimensions and point cloud size can be compared and dimension reduction methods can be used to enhance the computation.

The usability of height and structural features for species classification was tested using a sample of 32 trees, 8 samples from each of four species: pine, spruce, birch and willow (*Salix Siberica*). In the tests, the Euclidean distance between feature vectors was used as the distance metric. The leave-one-out method was employed for classifying each tree to one of the four species; for each tree in turn, the species information of other trees is used for determining the species of the current tree. In a nearest neighbour test, the distance to the feature vectors of 31 other tree samples was calculated, and each tree was classified to the same species as the closest neighbour. In the centre distance test, we computed the mean feature vectors for each species. Each tree was classified to the species whose feature centre was closest to the tree feature.

Height:	pine	spruce	birch	willow	Total
Dense 1-nn	75%	13%	75%	0%	41%
Thin 1-nn	88%	25%	75%	0%	47%
Dense cd	88%	75%	88%	25%	69%
Thin cd	100%	13%	63%	13%	47%
Structural:	pine	spruce	birch	willow	Total
Dense 1-nn	50%	63%	88%	63%	66%
Thin 1-nn	88%	75%	88%	75%	81%
Dense cd	50%	50%	88%	75%	66%
Thin cd	100%	13%	63%	75%	63%

Table 2. For each species, the percentage of correctly classified trees for waveform densified (Dense) and first and last pulse (Thin) TopEye data in nearest neighbour (1-nn) and centre distance (cd) methods.

In Table 2, two different distance metrics have been used to study whether the densified point cloud improves the separation between feature vectors of different tree species using height and structural features. The nearest neighbour method is likely to suffer from outlier samples. In larger samples, the nearest neighbour method should be k-nn, with a k variable of at least three. This result is only suggestive due to the small sample size. In a more realistic scheme, the sample centres would be calculated using a small training sample from each of the species.

Recently, Reitberger (2006a) compared the number of TopEye System points and waveform-extracted points. The increase in points for leaves on deciduous areas was 123%, but 230% for coniferous trees. For our sample, the respective values are 376% (Birch, Willow, leaf on) and 254% (Pine, Spruce). The difference in the percentages above is probably due to different area determination around the tree. We have not yet found an explanation for the fact that Reitberger et al. (2006) found a larger increase in the points for coniferous trees, whereas our study found a higher increase for deciduous ones.

3.2 Methods Using Single Waveform Features

In this section, we consider the possibility of examining the individual waveforms hitting a single tree. Such waveforms could be used to find information on tree trunk location or tree species. The use of the features extracted from the waveform is considered in Wagner et al. (2006), in which the authors studied the range, amplitude, pulse width and backscatter cross section information for target discrimination.

Fig. 5 describes the number of details in the waveform data. The left graph plots the points extracted from waveforms,

hitting the manually delineated tree canopy. Because of the relatively large scan angle, the extracted points occupy a much larger area than the original point cloud. This is of particular concern when analysing a dense forest. In the middle plot, only those waveforms are selected that travel across the point cloud centre. The right plot shows a densely sampled plane that slices the canopy when consecutively sent pulse waveforms are used together. In order to use features to measure characteristics such as trunk hits, it is essential that these features can be found computationally efficiently from large waveform data sets.

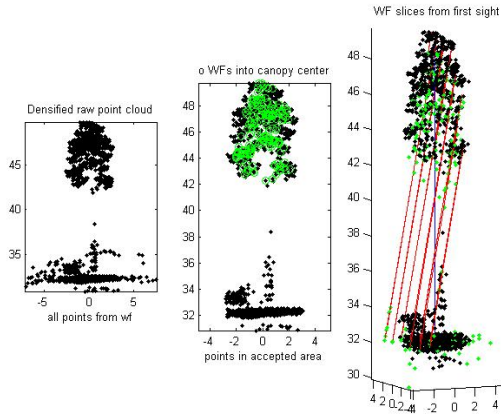


Figure 5. The left image shows all of the extracted points. In the middle image, the points with waveform directed into the tree canopy are plotted in green. The right image visualises a single slice from the consecutive waveforms.

3.2.1 Distinctive waveform profiles

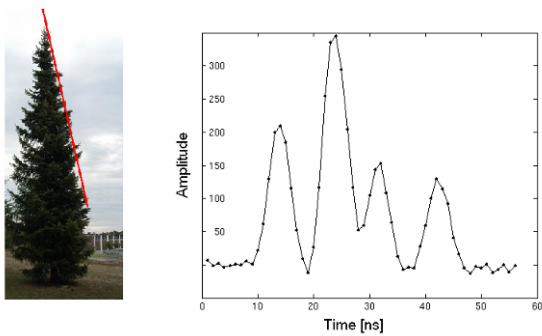


Figure 6. A multi-peaked waveform profile (right) is characteristic for signals that hit the spruce at a certain angle (left).

A laser beam that passes through spruce at a certain angle produces a multi-peaked waveform profile, as shown in Fig. 6. The return signal, composed of reflections from branch peaks and waveform amplitude, varies strongly as the signal passes through the foliage. To automatically determine multi-peaked waveforms, we developed an algorithm based on the divergence of signal amplitudes. The divergence was calculated from the part of the signal that originated from the tree crown, taking into account the fact that divergence was found throughout that part of the signal. Using this algorithm, we found several multi-peaked waveforms among each studied spruce. These waveforms were also found among pine data, though not as often as was the case with the spruce samples. Spruce can be identified based on the assumption that they cause more multi-

peaked waveforms than do pines. In this study, 0-50 % more multi-peaked waveforms were found from the spruce data compared to the pine data, though the results depend on algorithm parameters and several other factors. At the moment, only a few trees have been analyzed and more waveform data is needed to gain statistically reliable results.

3.2.2 Trunk echoes

Typically, two strong echoes were found in the case when the signal first hit the tree foliage and then the trunk, as seen in Fig. 7. Based on this information, an algorithm was developed to find tree trunk waveforms. The algorithm uses waveform data originating from the upper part of trees and restricts the distances between strong echoes. This was important to avoid confusion with signals of similar appearance originating from foliage and the ground. Several trunk waveforms were found from each spruce and pine, most of which seem to suggest roughly the same trunk location, thus allowing divergent points to be filtered out and the trunk position to be determined. In the future, field survey data are required to detect absolute errors arising from the determined trunk points.

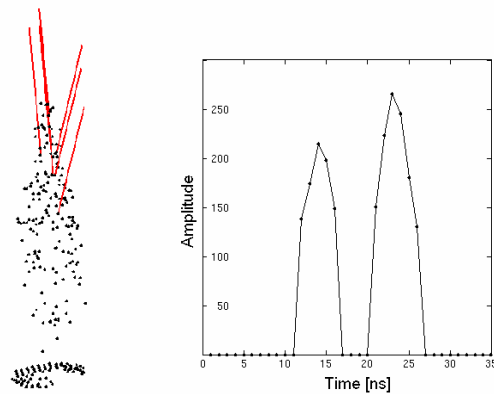


Figure 7. The spruce point cloud and waveform signals that hit the tree trunk (left). The waveform profile on the right is typical for signals that hit both the foliage and the trunk.

3.3 Integration of the ALS Waveforms with Terrestrial Close-Range Images

Registered close-range images are the most illustrative references when trying to understand the behaviour of the ALS. Unlike images derived with ALS, the internal geometry of the images is well known. In addition, the further perspective gained from terrestrial close-range images adds supplementary information to the laser scanning data. Such a comparison can reveal, for example, the effect of weather conditions.

During the test flight in Espoonlahti, the wind was relatively strong. The effect of the wind is clearly visible when the ALS data was superimposed onto the example images (Fig. 8). The registration of the images and ALS was completed using the interactive orientation method (Rönholm et al., 2003). For registration, the most stable features were observed, such as house roof, antennas, chimneys, pipes, and lamps. Unfortunately, movement of the treetop prevented sensible stereo viewing of the canopy, as the location and the shape of the treetop differed slightly in all images as well as in the ALS data. Fig. 8 shows how the tree canopy of the pine in the laser data does not fit perfectly with either of the two registered

images. Nevertheless, the laser point cloud fits very well with the roof of the building.

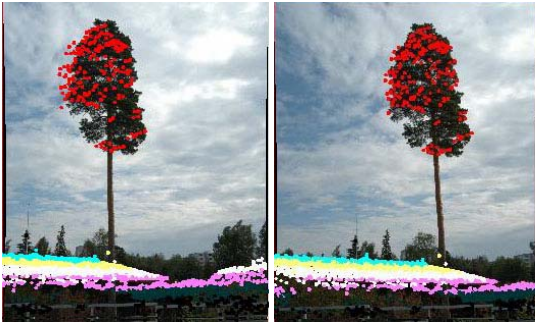


Figure 8. The first pulses are superimposed onto two registered terrestrial images. The colour coding is chosen to visualise the heights of the point cloud. The effect of the wind is clearly visible – the canopy of the tree has moved between the capture of the first and second images.

The full-waveform ALS data can be visualised by superimposing the echo rays onto the images. In Fig. 9, the ALS data is superimposed in two convergent images that are captured at an almost 90-degree angle to each other. The chosen camera locations and viewing directions make it easier to perceive the 3D shape and the behaviour of ALS data. If the canopy had been more stable, the stereo views from these two viewing directions would have been even more informative. For visualisation of the waveform data in Fig 9, we calculated the 3D location of each intensity value along the waveform echoes. The smallest intensity values were considered noise and thus rejected. The brightness of the colour describes the measured intensity values.

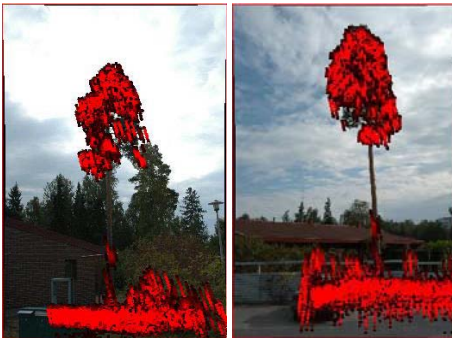


Figure 9. The full-waveform superimposed onto images. The difference in the viewing angles of the images is close to 90 degrees.

The superimposed ALS data is very informative. For example, the echoes that have hit the trunk can be selected using images (Fig. 10). Perpendicular image capturing can aid in this purpose. First, the area around the trunk is selected from the first image. The result is a cross-section of the echoes that can then be superimposed onto the next image. The different perspective of the second image visualises the cross-section from the side. Second, the area around the trunk is now selected from this second image. The intersection between these two cross-sections includes potential echoes that have hit the trunk.

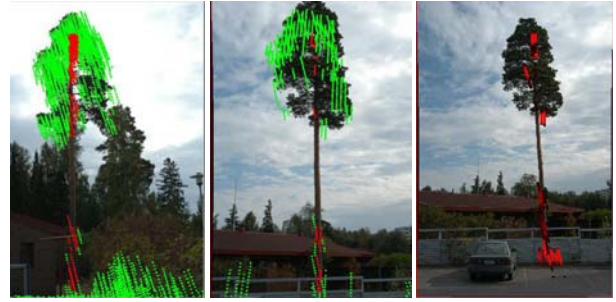


Figure 10. Using images for finding the trunk of the tree from the waveform data. The intersection of two perpendicular cross-sections finds potential echoes that have hit the trunk.

Although the total number of echoes that have hit the trunk is small, the waveform data includes significantly more information about the trunk than that provided by the first pulses alone. The first pulses have succeeded in detecting the trunk only in the lowest part of the tree and the number of hits is less than half of the number of trunk hits in the waveform data. Figs. 11 and 12 present some examples in which the information concerning the trunk is not located in the first pulse.

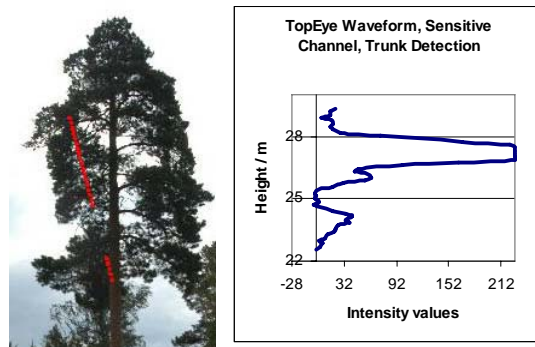


Figure 11. Waveform echo passes through the thick upper foliage before reaching the trunk. The echo is denoted in the image by uniform colour in order to enhance visibility of small intensity values.

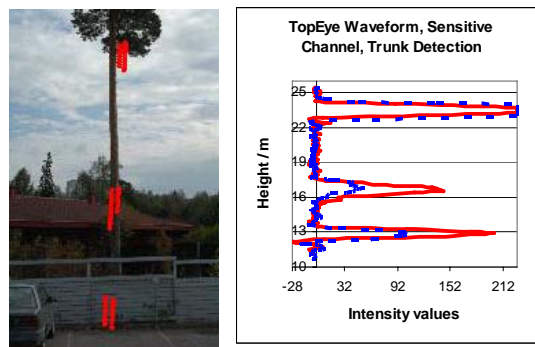


Figure 12. Two similar waveform echoes pass through thin branches of the upper foliage, detecting the trunk and continuing to the ground. The echoes are denoted in the image by uniform colour in order to enhance visibility of small intensity values.

4. CONCLUSIONS

Full-waveform data have great potential for improving the classification of tree species. The waveform can be used for densifying tree point clouds for more detailed information on tree structure. The benefit of densification is likely to be moderate for algorithms that use the special characteristics of the first and last pulse data, as described in section 3.1.1. However, those features based on density are likely to benefit more, since the large amount of data suppresses the effect of outlier points, different scan patterns and differences in the sampling resolutions. Table 2 presents preliminary classification results for height and structural features. The results show reasonable separation between the tree features of different species, despite the small size of the test sample. With larger data sets, we expect to gain more reliable estimates of the feature distribution for each species.

Single descriptive waveforms, studied in section 3.2, present a different approach for tree classification: instead of solving compute-intensive statistical densities, our method searches for simple descriptors of each species. Such waveforms could be used, for example, in decision-tree-based classification systems. In addition, this method enables detection of tree properties such as precise trunk position to be determined. To find the most informative single waveform types, a detailed knowledge is needed of the different types of waveforms and the typical locations in which they may occur.

Full-waveform data can be superimposed onto registered close-range images in order to obtain detailed information on the behaviour of the data. Visually, it is easy to find interesting waveforms if their nature can be verified from images. These waveforms can be chosen and examined separately. Stereo images would provide an easy interface for visualising waveform data. Unfortunately, windy conditions may cause instability of the tree canopies, thereby preventing sensible stereo examination, especially when images are not captured simultaneously. Alternatively, images can be taken convergently from different sides of a target. However, such convergent image acquisition would not allow stereo viewing, though it also provides a good impression of how light rays are located in the 3D space.

The usefulness of the superimposed ALS data is based on the human ability to find correspondences and similarities between images. It is very difficult to understand the true behaviour of ALS data if it cannot be compared with real images. Terrestrial close-range images give detailed reference data, and the viewing perspective which differs from that offered by ALS data gives additional information concerning the targets. A fuller understanding of these waveforms should make it possible in the future to develop improved tools for interpreting and classifying full waveform data.

5. REFERENCES

- Brantberg, T., 2007. Classifying individual tree species under leaf-off and leaf-on conditions using airborne lidar. *ISPRS Journal of Photogrammetry & Remote Sensing*, 61, pp 325-340.
- Harding, D.J., Lefsky, M.A., Parker, G.G, Blair J.B., 2001. Laser altimeter canopy height profiles: Methods and validation for closed-canopy, broadleaf forest. *Remote Sensing of Environment* 76(3), pp. 283-297.
- Hofton, M., Minster, J.B., Blair, B., 2000. Decomposition of Laser Altimeter Waveforms. *IEEE Trans. On Geoscience and Remote Sensing* 38(4), pp. 1989-1996.
- Holmgren, J., Persson, Å., 2004. Identifying species of individual trees using airborne laser scanner. *Remote Sensing of Environment* 90(4), pp. 415-423.
- Hyypä, J., Inkinen, M., 1999. Detecting and estimating attributes for single trees using laser scanner. *The Photogrammetric Journal of Finland* 16, pp. 27-42.
- Ni-Meister, W., Jupp, D.L.B, Dubayah, R. 2001, Modeling Lidar Waveforms in Heterogenous and Discrete Canopies, *IEEE Trans. On Geoscience and Remote Sensing* 39(9), pp. 1943-1958.
- Næsset, E, 1997. Determination of mean tree height of forest stands using airborne laser scanner data. *ISPRS Journal of Photogrammetry & Remote Sensing* 52, pp. 49-56.
- Persson, Å., Holmgren, J., Söderman, U., 2002. Detecting and measuring individual trees using an airborne laser scanner. *Photogrammetric Engineering and Remote Sensing* 68 (9), pp. 925-932.
- Persson, Å., Holmgren J., Söderman U., 2006. Identification of tree species of individual trees by combining very high-resolution laser data with multispectral images. In: *Workshop on 3D Remote Sensing in Forestry*, 14-15 Feb 2006, Vienna, Austria.
- Pyysalo, U., Hyypä, H., 2002. Reconstructing tree crowns from laser scanner data for feature extraction. *IAPRS, vol XXXIV, Part 3B*, pp. 218-221.
- Reitberger, J., Krzystek, P., Heurich, M., 2006a. Full-waveform analysis of small footprint airborne laser scanning data in the Bavarian forest national park for tree species classification. In: *Workshop on 3D Remote Sensing in Forestry*, 14- 15 Feb 2006, Vienna, Austria.
- Reitberger J., Krzystek P., Stilla, U., 2006b. Analysis of Full Waveform Lidar Data for Tree Species Classification. In: *PCV06, Photogrammetric Computer Vision*, 20 – 22 September 2006, Bonn, Germany.
- Rönholm, P., Hyypä, H., Pöntinen, P., Haggrén H. and Hyypä, J., 2003. A Method for Interactive Orientation of Digital Images Using Backprojection of 3D Data, *the Photogrammetric Journal of Finland*, Vol 18, No. 2., pp. 58-69.
- Wagner, W., Ullrich, A., Ducic, V., Melzer, T., Studnicka, N., 2006. Gaussian decomposition and calibration of a novel small-footprint full-waveform digitising airborne laser scanner *ISPRS Journal of Photogrammetry & Remote Sensing*, 60(2), pp. 100-112.

6. ACKNOWLEDGEMENTS

The authors would like to thank the TEKES Full-Waveform Project (210435) for funding and Arttu Soinen from TerraSolid Oy for providing us with the software tools for handling waveform data.

GENERATING LIDAR DATA IN LABORATORY: LIDAR SIMULATOR

Bharat Lohani* and R K Mishra

Department of Civil Engineering, Indian Institute of Technology Kanpur, Kanpur 208016, INDIA – blohani@iitk.ac.in

Commission VI, WG VI/4

KEY WORDS: Altimetric LiDAR, Simulator, Modelling of sensor, Software, Research and Education tool

ABSTRACT:

This paper describes the methodology adopted for developing a simulator for airborne altimetric LiDAR. The goal is to model LiDAR sensor functioning so LiDAR data can be generated for a user specified terrain with given parameters of the sensor and aerial platform. The simulator is conceived having three components: 1) Terrain component, 2) Sensor component and 3) Platform component. Terrain component is formed using multiple mathematical surfaces for bare terrain and for objects on top of the surface. Further, the terrain can be represented using a raster. The sensor component permits a user to opt for the commercially available sensors or a generic sensor and accordingly generates data. The third component attempts to model the platform parameters, viz., velocity, roll, pitch, yaw and accelerations. LiDAR data are generated by first finding the equation of laser vector that changes with each pulse and then determining the point of intersection of this vector with the mathematical surface or the raster representing terrain. This GUI based simulator, developed in JAVA, is an ideal tool for research and education.

1. INTRODUCTION

The last decade has seen manifold growth in the use of airborne altimetric LiDAR (Light Detection and Ranging) technology. Due to the main advantage of measuring topography through highly dense and accurate data points which are captured at high speed, the LiDAR technology has found several interesting applications (Lohani, 2001; Quejja, et al., 2005).

1.1 What is a simulator?

A LiDAR simulator is aimed at faithfully emulating the LiDAR data capture process with the use of mathematical models under a computational environment. Basically, data generated by simulator should exhibit all characteristics of data acquired by an actual LiDAR sensor.

Literature reveals that only a few attempts have been made by researchers to develop simulator for LiDAR instrument. These efforts are limited in their scope as either these consider effect of only single parameter on one kind of object (Holmgren et al., 2003) or inaccurate scanning pattern (Beinat and Crosilla, 2002). More focused and comprehensive efforts have been made to simulate the return waveform from a footprint (Sun and Ranson, 2000; Tuldahl and Steinvall, 1999).

1.2 Why a simulator?

LiDAR data with varying specifications are fundamental for success of a research. To judge the optimality of algorithms or suitability of data for an application one needs to work with data with varying characteristics. Collecting these data in field is not feasible in view of extensive time and resource involvement. Further, for success of a research (e.g., building extraction from LiDAR data), availability of accurate and complete ground truth is crucial, which is difficult and

expensive to collect in field. LiDAR simulator can generate data with all user specified specifications at no cost. Data can be generated even with those specifications that are not available in commercially available sensors. Also, in the case of simulator complete and 100 per cent accurate ground truth is available. Simulated data can help in evaluation of the effect of noise and/or systematic error in final outcome.

A simulator is also a useful tool for education, as data generation process and the effect of error and various flight parameters can be understood in laboratory. In view of the cost and sometime the security/proprietary concerns associated with LiDAR data, the same are not cheaply and readily available for classroom activities. Simulator can help by producing data for various laboratory exercises aimed at understanding LiDAR data, their errors and information extraction algorithms.

2. DESIGN BENCHMARKS FOR THE SIMULATOR

The following benchmarks are set for an ideal simulator:

1. Simulator should employ a user-friendly GUI (Graphical User Interface.)
2. Simulator should be designed for wider distribution over various computational platforms.
3. The simulator should come along with a help/tutorial system which can explain concepts of LiDAR using user-friendly multimedia techniques.
4. It should simulate a generic LiDAR sensor and some other sensors available in market.
5. The simulator should facilitate selection of trajectory and sensor parameters as in actual case along with the facility of introducing errors in various component systems of LiDAR.
6. Simulator should facilitate data generation for actual earth-like surfaces.

7. The output data should be available in commonly used LiDAR formats.

3. METHODOLOGY

3.1 Coordinate systems used

As shown in Figure 1 two coordinate systems are considered. The first coordinate system is (X, Y, Z), which is absolute. All trajectory and terrain coordinates are determined in this system. A system which translates with platform and remains parallel to absolute coordinate system is considered at the laser head and is henceforth referred to as gyro coordinate system. The second coordinate system is the body coordinate system(x,y,z), which has its origin at laser head and is affected by roll, pitch and yaw rotations. Scanning takes place in this coordinate system, i.e., in y-z plane. The laser vector at any instance is defined using direction cosines and coordinates of laser head in gyro coordinate system.

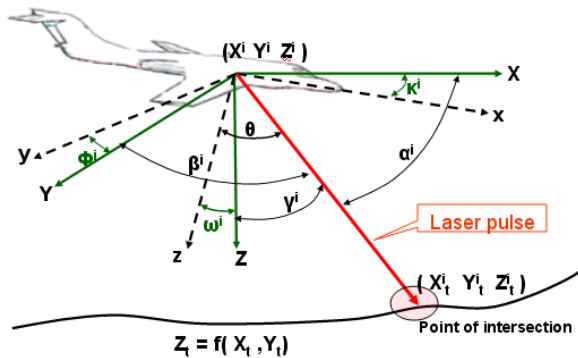


Figure 1. Schematic of laser vector intersection with a surface and coordinate systems

3.2 Simulator components and programming environment

Simulator components are shown in Figure 2. These components take form as per user input, while their integration generates LiDAR data. Following paragraphs describe development of these components as implemented in the latest version of simulator. The simulator has been improved substantially from its previous version (Lohani et al., 2006). This paper will focus more on description of these improvements. However, to make it complete a few parts are reproduced from Lohani et al. (2006) with modifications.

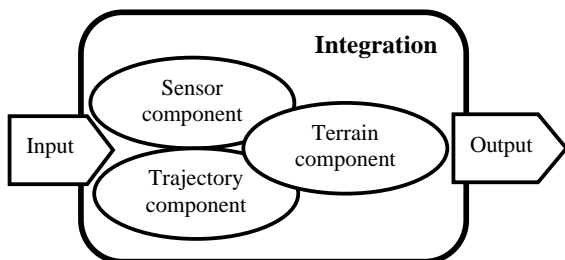


Figure 2. Basic components and their integration

Programming language JAVA has been chosen, as it offers good numerical and graphical programming besides, and most

importantly, being platform independent. The parameters required to define three individual components and output data format are input through user-friendly GUIs.

3.3 Terrain component

Vector and raster approaches are chosen for simulating bare earth surface and above ground objects as described below. Through a GUI, as shown in Figure 3, a user is prompted to select an area of interest, by marking it using the mouse on screen. The area selected from the underlined mathematical surface or raster becomes available for LiDAR data generation.

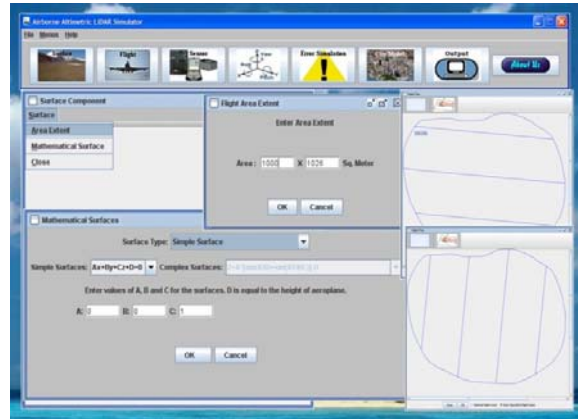


Figure 3. GUI showing selection of underlying mathematical surface, its extent and area of interest on it for LiDAR flight along with flight lines

3.3.1 Vector approach

In this, a terrain is represented using mathematical equations, which yield earth like surfaces. The GUI permits selection of these surfaces and their parameters. A few of these are:

$$\begin{aligned}
 Z &= AX + BY + C \\
 Z &= A[\sin(X/B) - \sin(XY/C)] + D \\
 Z &= A[\sin(X/Y) - \sin(XY/B)] + C
 \end{aligned}
 \tag{1}$$

3.3.2 Raster approach

In this the surfaces resulting from the above equations are rasterized. Most importantly, this approach permits populating the raster with above ground objects. Those cells, where an over ground object is desired to be placed, take new values as per the height and shape of object. In addition, it is possible to import an existing raster file (say DEM) for which LiDAR data can be simulated.

3.4 Sensor component

The GUI prompts user to select any one of the two commercially available sensors (ALTM3100 or ALS50) or a generic sensor. While the range of parameters is constrained in commercial sensors, as per their specifications, the generic sensor permits selection of any range of parameters. Having selected the sensor, the user is prompted to enter the sensor parameters which are desired for LiDAR data generation, viz., scan angle, scan frequency, firing frequency, type of scanning etc. (Figure 4.)

Depending the type of scanning (which may be zig-zag or sinusoidal) the instantaneous scanning angle is determined by

the following model. Let time taken to complete $1/4^{\text{th}}$ of a scan is T and there are P numbers of points in this. The maximum scan angle is θ_{max} . For the i^{th} point, which is fired at time t_i from the beginning of scan, the scan angle will be:

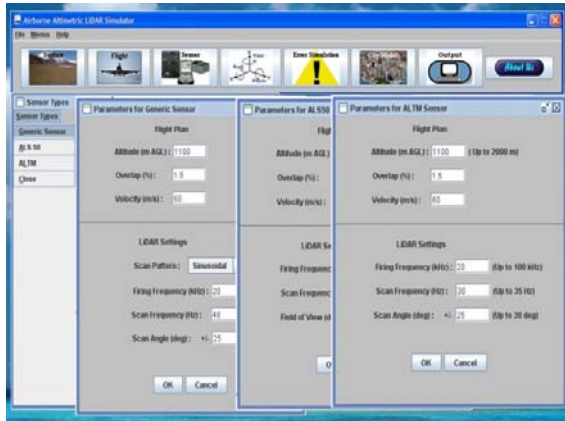


Figure 4. Parameter input for different sensors

$$\theta_i = \frac{\theta_{\text{max}}}{P} i \quad \text{For zig-zag} \tag{2}$$

$$\theta_i = \theta_{\text{max}} \sin\left(\frac{\pi}{2T} t_i\right) \quad \text{For sinusoidal}$$

where, $t_i = \frac{T}{P} i$

The resulting trajectories are shown in Figure 5. By changing the parameters listed above the spread of points within scan can be altered.

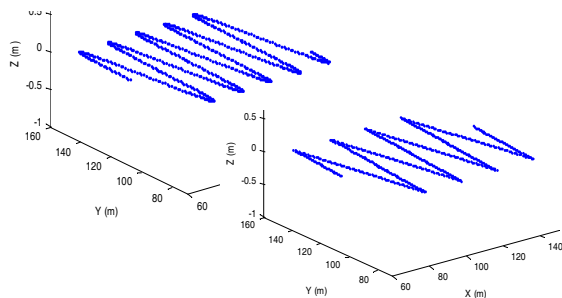


Figure 5. Sinusoidal and zig-zag scan generation

3.5 Trajectory component

Complete trajectory of aircraft is made of several flight lines as shown in Figure 6. Depending the area chosen for LiDAR data generation (gray area in Figure 6) and sensor parameters (i.e., swath width and per cent overlap) the direction of flight lines is either chosen by the user or an optimum direction is determined by the software. In latter case, the flight direction is determined by making use of the principal direction of area. For this, first using Douglas-Peucker algorithm (Douglas and Peucker, 1973) the number of vertices defining the area of interest marked by the user are reduced, which ensures that the area marked has no small kinks which are the artefacts of drawing on screen by hand. Covariance matrix is generated for the coordinates of all points forming the area of interest polygon. The first eigen vector of this is used to determine the principal direction of the polygon. The flight direction is oriented in the principal

direction, which makes the total flight line length required to cover the area a minimum (in most of the cases.)

The software also determines the location of flight lines (thick lines in Figure 6) so as to cover entire area considering the overlap specified. The algorithm places the first flight line (top flight line in Figure 6) in such a way that the swath covers up to the edge of area. The last flight line is placed considering the spacing between flight lines for given overlap. It is shown in Figure 6 that in order to cover full area of interest some extra area (*union of all swath rectangles – area of interest*) is also scanned. Using the points of intersection of periphery of area and the flight line the starting and ending points of flights are determined. The following section describes computations for an individual flight line. The same procedure is followed for other flight lines also.

3.5.1 Location

A trajectory (referred as flight line henceforth to indicate a single flight) is defined by the location of laser mirror centre (point of origin of laser vector) in the absolute coordinate system at each instance of firing of laser pulse. To simulate the flight line and to incorporate a possibility of introducing errors in parameters the following procedure is employed.

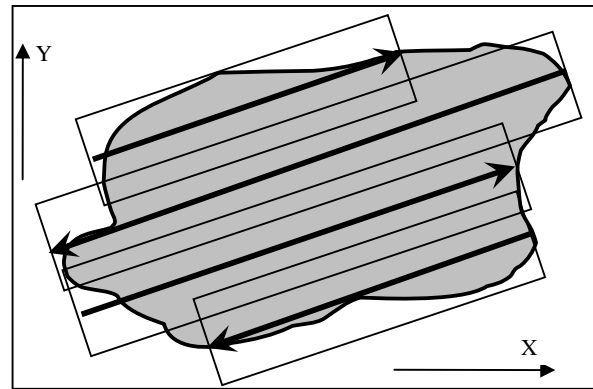


Figure 6. Area of interest (gray), flight lines in optimum direction (thick arrows) and swaths with overlap (thin rectangles)

Let, time interval between firing of successive pulses is d_t , which is equal to $1/F$, where F is firing frequency. Total number of points on flight line wherefrom pulses are fired is n , which will depend upon the length of flight line. Velocity of platform in flight direction at i^{th} point on flight line is u^i . Let the laser head coordinates at i^{th} point on trajectory are (X^i, Y^i, Z^i) .

At each successive d_t interval one needs to compute the location of laser head. The aerial platform is subject to internal and external force fields with the net effect that the platform is subject to random accelerations in three axes directions. The following system is employed to simulate accelerations. This system ensures a pseudo-random generation of acceleration values.

$$a_x^i = \sum_{j=1}^J A_j \sin(B_j (\frac{2\pi}{T}(id_t))) + \sum_{k=1}^K C_k \cos(D_k (\frac{2\pi}{T}(id_t))) \tag{3}$$

Where a_x^i is the acceleration at i^{th} point in X direction. T is the total duration of a flight line. The parameters of this equation J, K, A, B, C and D control the direction and quantum of acceleration. Developed software permits selection of these parameter values within ranges that generate accelerations as may be observed in a normal flight. Similarly, a_y^i and a_z^i are also generated with different values of parameters in above equation. Using the acceleration values at i^{th} point the new location of laser head (i.e., $X^{i+1}, Y^{i+1}, Z^{i+1}$) after d_i interval is computed using equations similar to:

$$X^{i+1} = X^i + u_x^i d_t + \frac{1}{2} a_x^i d_t^2 \quad (4)$$

Where, u_x^i is the velocity in X direction.

3.5.2 Attitude

As in case of acceleration, due to internal and external force fields, the attitude will change within certain limits and may exhibit a random behaviour. To realise this, the attitude values (i.e., $\omega^i, \phi^i, \kappa^i$) at any i^{th} point are determined using the equation (3). Similar to the case of acceleration, the developed simulator permits selection of these parameters in the ranges which generate attitude values as in case of a normal flight.

The outcome of aforesaid is that at each point wherefrom a laser pulse is fired the attitude values and coordinates of point are known in the absolute coordinate system.

3.6 Integration of components

The components discussed above are integrated by generation of the laser vector and its intersection with simulated terrain. The point of intersection yields the coordinate of terrain point. As shown in Figure 1, for any i^{th} point on trajectory there exists a laser vector. Equation of laser vector is given as:

$$\frac{X - X^i}{a^i} = \frac{Y - Y^i}{b^i} = \frac{Z - Z^i}{c^i} \quad (5)$$

Where $a^i, b^i,$ and c^i are direction cosines ($\cos\alpha^i, \cos\beta^i,$ and $\cos\gamma^i$, respectively) of laser vector with respect to gyro coordinate system at i^{th} point. The values of $\alpha^i, \beta^i,$ and γ^i are determined from known values of attitude ($\omega^i, \phi^i, \kappa^i$) and instantaneous scan angle (θ).

The point where laser hits the terrain, following the above laser vector, is computed by solving for intersection of equation (5) and equation (1) or the rasterized terrain. Solution is realised using specially formulated numerical methods. These methods differ for vector and raster terrain and also depend upon the basic equations employed to create terrain. The raster data size becomes very large (raster cell is taken 10 cm). Therefore, to solve the intersection it is not feasible to store entire data in memory. Special data structuring is adopted by tiling the raster and reading the data only from those tiles which fall under the swath of flight line. This is ensured by using the ‘‘point in polygon’’ algorithm which determines whether a tile intersection is within the area covered by flight line (i.e. $Swath \times Flight\ length$). Full description of these methods is beyond the scope of this paper. At this stage coordinates of all points of intersection (X_i^i, Y_i^i, Z_i^i) are known.

3.7 Error introduction in data

LiDAR data suffer from systematic and random errors of different kinds (Huising and Pereira, 1998). Errors in position and orientation of platform and in angle and range measurement by sensor propagate in final coordinates. It is proposed to provide facility for introduction of these errors in the future version of simulator. In present version a normal error is introduced in the terrain coordinates computed in the above step in X, Y and Z directions separately. The system for introducing error in X direction is shown below:

$$X_T^i = X_i^i + N(\mu_X, \sigma_X^2) \quad (6)$$

Where X_T^i is the X coordinate value with error. Similar systems with different values of parameters are used for Y and Z coordinates. It is assumed that errors in X, Y and Z directions follow normal distribution. Further, when introducing these errors it is ensured in algorithm that there is no spatial auto-correlation of error. The parameters of this distribution are known from field experience and are reported by the vendors of sensors. The simulator facilitates variation of these parameters.

3.8 Output generation

The software facilitates output of LiDAR coordinates in simple ASCII format or standard LAS format. Further, a variety of other reports are generated, e.g., sensor parameters, flight parameters and parameters used to generate terrain (Figure 7). These reports are output in textual format which can be employed by user for further study.

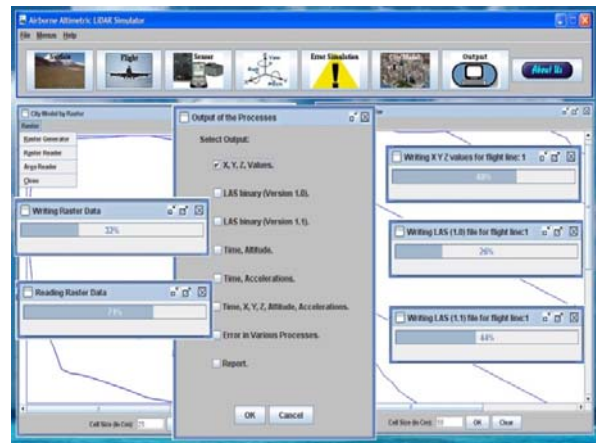


Figure 7. LiDAR data output menu and options

4. RESULT AND DISCUSSION

Simulated trajectory and attitude parameters are shown for a duration of 5 seconds (Figure 8). Though, it is statistically difficult to compare simulated data with any set of actual flight data, as these two represent two different populations, the former amply exhibit the random nature of parameters as in any normal flight.

A hypothetical terrain (2km by 2km) is created over a flat surface and is populated with building like shapes (length and breadth ranging from 150 m to 300 m) along with 6 cylindrical objects (50 m diameter and 90m height). Large objects are chosen here to fill the 2km by 2km area. The flat surface and

objects on top of it are rasterized. The raster takes values as per the underlying surface or the object. A view of this is shown in Figure 9, which is generated using surface feature of Surfer. This view also shows the location and direction of the four flight lines. This view will help understanding the results presented later. LiDAR data were generated for this terrain with the parameters: Flight velocity: 60 m/s; Altitude: 600m; Firing frequency: 20000 Hz; Scan frequency: 48 Hz.; Scan angle: 50°; No. of flight lines: 4; Overlap 1.5 %

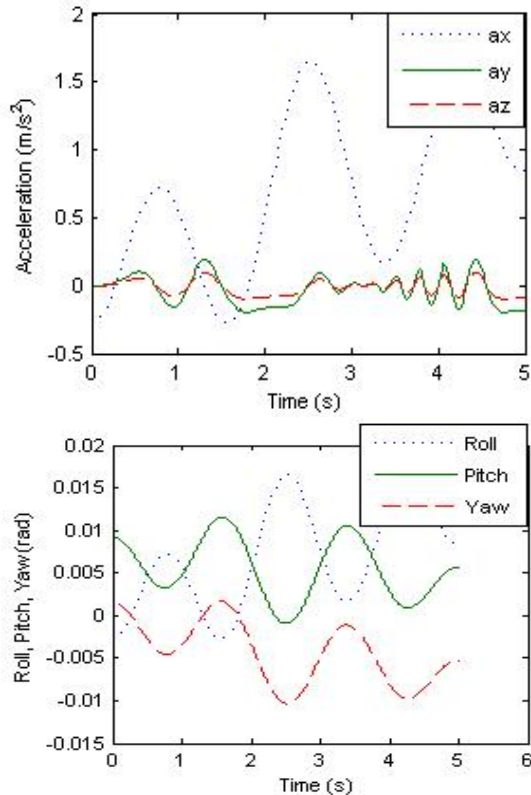


Figure 8. Acceleration (top) and attitude (bottom) values

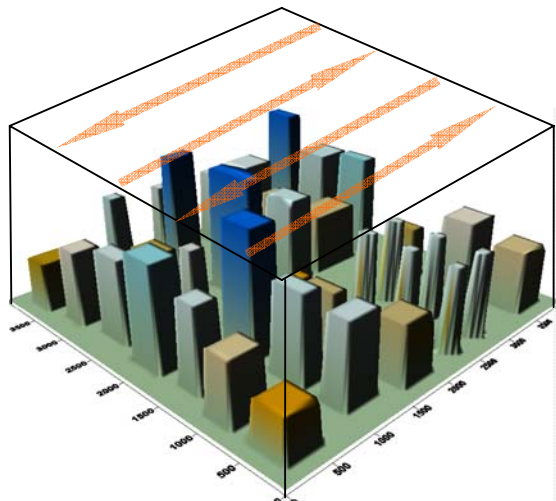


Figure 9. Surfer surface view of the chosen terrain (heights are exaggerated)

Resulting LiDAR data are imported in Terrascan software and displayed. Only few views are being presented for the sake of space as shown in Figure 10 and Figure 11. Data generation for objects of different shapes and sizes and as well as for objects situated at different locations w.r.t. the flight line can be understood from these figures. In Figure 10(a) a perspective view is shown, which shows various buildings where data are captured, while the interplay of object and shadow is also evident. Not all black areas (i.e. where data are not captured) are shadows. This can be understood from the profile drawn about A-A and shown in Figure 10 (b). For example, the roof of building marked by white oval is not fully captured. The reason for this can be understood in profile (also marked by white oval.) The black area is not being covered by either flight lines. This also serves as an example of poor choice of scan angle and flying height, which can be understood by simulator.

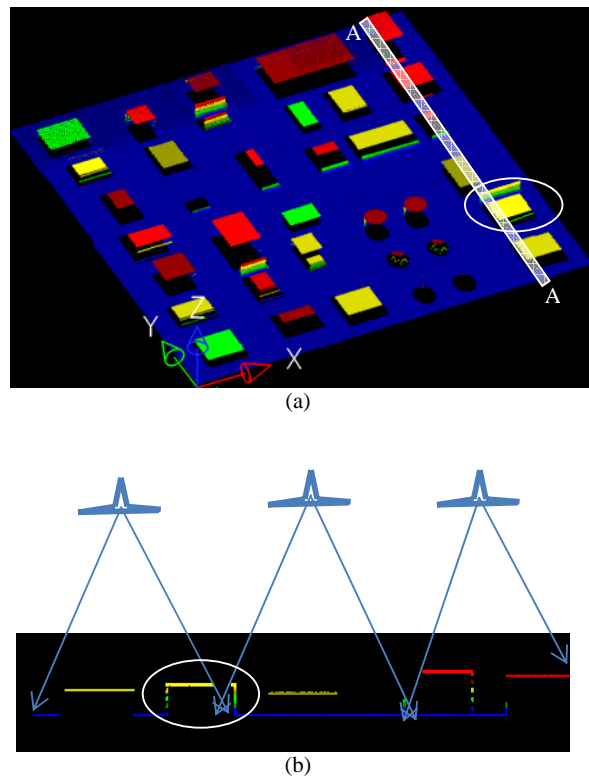
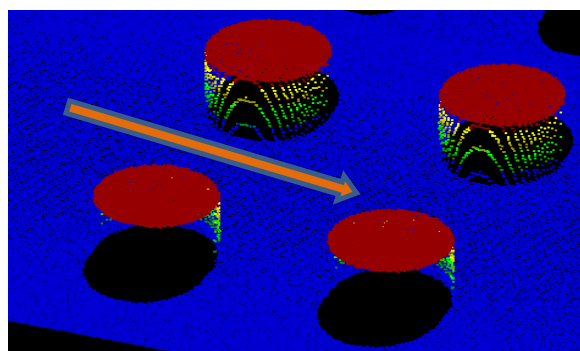
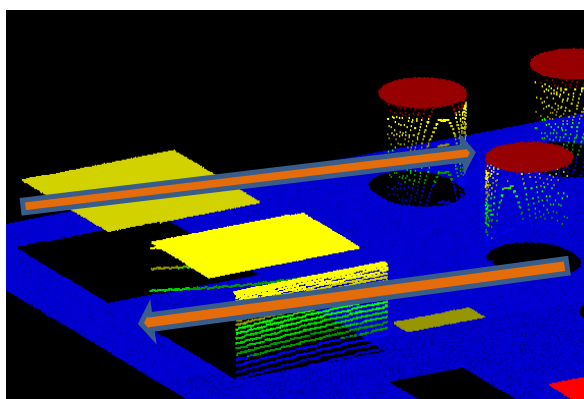


Figure 10. (a) LiDAR data display in Terrascan-perspective view; (b) Profile along A-A band shown by white colour in top image. The profile is shown along with the flight lines and swaths. The building within oval is not fully measured.

The zoomed out views (shown in Figure 11 (a) and (b)) of the same data show the point cloud as obtained for different objects. Location of flight lines is also shown. The spread of point cloud depends on the location of the object with respect to flight line and the parameters chosen for sensor. LiDAR data points are available on the vertical walls facing flight line, while no data points are captured on the other wall. Data in these examples are produced with error. This is evident as the points do not fall in smooth scan lines.



(a)



(b)

Figure 11. Zoomed out display of point cloud

5. CONCLUSION

The presented simulator emulates existing commercial sensors and models a generic LiDAR sensor to generate data over a user specified terrain. A user can alter the sensor and trajectory parameters with ease and generate the resulting LiDAR data. Error can also be incorporated in output. The simulator has a user friendly GUI designed in architecture independent JAVA language.

The simulator can be useful to generate LiDAR data for research to test algorithms. It is also useful in a classroom for demonstrating LiDAR data capture process and understanding the effect of flight and sensor parameters and their errors.

Terrain representation using raster has solved to a large extent the problem of representation of bare earth and objects. However, this results in large data size which is managed through data structuring so the data are brought into the simulator in chunks as needed.

A MATLAB based system has been developed in parallel for simulating full waveform digitization for a Gaussian pulse. Efforts will be made in future to integrate this with the present simulator, thus to generate multiple return data and waveform digitization.

References

Beinat, A., and Crosilla, F., 2002. A generalized factored stochastic model for optimal registration of LIDAR range images, *International Archives of photogrammetry and remote sensing and spatial information sciences*, 34(3/B), pp. 36-39.

Douglas, D., and Peucker, T., 1973, Algorithms for the reduction of the number of points required for represent a digitized line or its caricature, *Canadian Cartographer*, 10(2), pp. 112-122.

Holmgren, J., Nilsson, M., and Olsson, H., 2003. Simulating the effect of lidar scanning angle for estimation of mean tree height and canopy closure. *Canadian Journal of Remote Sensing*, 29(5), pp. 623-632.

Husing, E. J. and Pereira, L. M., 1998, Errors and accuracy estimates of laser data acquired by various laser scanning systems for topographic applications, *ISPRS Journal of Photogrammetry & Remote Sensing*, 53(5), pp. 245-261.

Lohani, B., Reddy, P., and Mishra, R., 2006, Airborne Altimetric LiDAR Simulator: An education tool, *International Archives of the Photogrammetry, Remote Sensing and Spatial Information Science*, XXXVI(6), Tokyo, Japan.

Lohani, B., 2001, Airborne altimetric LiDAR for topographic data collection: Issues and application., *Proc. of International conference MAPINDIA-2001*, 7-9 February 2001, New Delhi.

Queija, V. R., Stoker, J. M., and Kosovich, J. J., 2005, Recent U.S. geological survey applications of LiDAR, *PE&RS*, 71(1), pp. 5-9.

Sun, G. and Ranson, K. J., 2000. Modeling Lidar returns from forest canopies, *IEEE trans. On geosciences and remote sensing*, 38(6), pp. 2617-2626.

Tulldahl, H. M. and Steinvall, K. O., 1999, Analytical waveform generation from small objects in lidar bathymetry, *Applied optics*, 38(6), pp. 1021-1039.

5.1 Acknowledgements

This work is supported under RESPOND programme of ISRO. Authors are grateful to two anonymous reviewers and editor.

EXPERIENCES AND POSSIBILITIES OF ALS BASED FOREST INVENTORY IN FINLAND

Maltamo, M.^a, Packalén, P.^a, Peuhkurinen, J.^a, Suvanto, A.^a, Pesonen, A.^a & Hyyppä, J.^b

a) University of Joensuu, Faculty of Forest Sciences, P.O. Box 111, FI-80101 Joensuu, Finland. Tel.+358 13 2513615. E-mail: matti.maltamo@joensuu.fi, petteri.packalen@joensuu.fi, jussi.peuhkurinen@joensuu.fi, aki.suvanto@joensuu.fi, annukka.pesonen@joensuu.fi

b) Finnish Geodetic Institute, Geodeetinrinne 2, P.O. Box 15, FI-02431 Masala, Finland, E-mail: juha.hyyppa@fgi.fi

KEY WORDS: remote sensing, forestry, inventory, modelling, prediction, recognition, lidar, accuracy

ABSTRACT

During last ten years the research concerning airborne laser scanning based forest inventory applications has been very active in different parts of the world. In Finland, both basic approaches, single tree detection and area based modeling have been widely examined. In the following the results of the ALS based forest inventory experiments and further possibilities in Finland are reviewed and discussed. A short review of Finnish forestry in relation to possibilities of ALS based forest inventories is included as well. Finally, some examples concerning the comparison of single tree detection and area based modeling and the usability of spatial information provided by ALS data are presented.

1. INTRODUCTION

During last ten years the research concerning airborne laser scanning (ALS) based forest inventory applications has been very active in different parts of the world (e.g. Næsset, 1997; Magnussen & Boudewyn, 1998; Hyyppä et al., 2001; Persson et al., 2002; McCombs et al., 2003; Takahashi et al., 2005; Tickle et al., 2006; Koch et al., 2006). Most of the studies have been conducted by using discrete return small footprint systems but there are also large footprint lidar applications as well (Drake et al., 2002).

In Finland, both basic approaches to utilize ALS data, single tree detection (Hyyppä & Inkinen, 1999; Hyyppä et al., 2001; Maltamo et al., 2004a; Yu et al., 2006; Korpela, 2007; Peuhkurinen et al., 2007) and area based modeling (Suvanto et al., 2005; Maltamo et al., 2006a; c; Packalén & Maltamo, 2007) have been examined. In the following, the results of the ALS based forest inventory experiments and further possibilities in Finland are reviewed and discussed. Forest inventories are usually multipurpose but here we concentrate mainly on prediction methods of living tree stock. Some examples concerning the comparison of single tree detection and area based modeling as well as spatial information provided by ALS data are also presented. However, to understand the growing conditions and forest inventory traditions in Finland a short review of Finnish forestry in relation to possibilities of ALS based forest inventories is also included.

2. FOREST INVENTORIES IN FINLAND

The forests of Finland are located in boreal vegetation zone. The number of existing tree species is rather low, including coniferous pine (Scots pine [*Pinus sylvestris* L.]) and spruce species (Norway spruce [*Picea abies* L. karst]), and as deciduous birches (Silver birch [*Betula pendula* Roth], downy birch [*Betula pubescens* Ehrh.]), alders (grey alder [*Alnus incana*], red alder [*Alnus glutinosa*]) and aspen (European aspen [*Populus tremula*]) species. At stand level,

most of the forests are dominated either by pine or spruce. There is no pure plantation forestry in Finland. Although considerable proportion of regenerated stands have been planted by one tree species the rotation age is so long that other species usually naturally regenerate to stand. As a result, a considerable proportion of stands are mixed at least in some level. Only the least fertile stands, usually located in northern Finland consist of pine only. Of course, silvicultural treatments may also favour certain tree species. One specific phenomenon in boreal forests is also high stand density by means of number of stems whereas trees are rather small. For example, in managed forests of Matalansalo test area, used in several ALS studies, the average stand density is about 1500 stems per hectare and in mature stand strata still over 1250 stems per hectare (Suvanto et al., 2005). As a comparison, in the study data by Heurich and Weinacker (2004) the stand density in southeastern Germany on temperate forests was on average 540 stems per hectare.

In Finland forest inventory is carried out on two levels: National forest inventory (NFI) and forest management planning. NFI is based on systematic cluster sampling of field plots and covers whole country (Tomppo, 2006a). This data is used for calculation of national and regional forest resources and for national level planning. In addition, satellite images are used in the multi-source National Inventory as an auxiliary material (Tomppo, 2006b).

ALS data based sample plots is not a realistic alternative for replacing field measured NFI sample plots. This is due to the fact that one of the main requirements of NFI is that forest resource results should be unbiased and this cannot be guaranteed by using ALS data. Furthermore, information concerning tree stock is only a minor part of the measurements in these plots. Some other data needs consist e.g. of forest health, biodiversity and forest soil variables and most of these cannot be remote sensed (the head of the NFI of Finland, Dr. Kari T. Korhonen, personal comm.). On the other hand, large scale ALS data such as National Laser Scanning (e.g. Artuso et al., 2003) could provide auxiliary information for multi-source inventory in the form of digital

terrain model (DTM), canopy height model (CHM) or stand characteristics interpretation on systematic grid.

Forest management planning in private forests is usually based on information collected by forest compartments (stands) (Poso, 1983). A conventional inventory by compartment includes expensive field work, but the number of assessments per stand is typically small, resulting in low precision of estimated stand variables. All assessments are made on tree species level already in the field and as a final product tree species specific timber sortiments are calculated. The accuracy of prediction of stand total volume achieved in compartment inventory usually varies between 15 and 30% (Haara & Korhonen, 2004). For tree species the results are even considerably worse. In fact, during recent years, the costs and accuracy of conventional field work based small area forest inventories have been at unsatisfactory levels (e.g., Kangas & Maltamo, 2002). There is, therefore, an increasing pressure to improve methods of carrying out field inventories in small areas. The main approaches to developing a compartment inventory have been the modification of field measurements and the application of remote sensing methods to support, or even replace, field measurements. For the purpose of replacing current inventory, ALS based methods have a very high potential.

Other forest inventory applications in Finland include specific inventories for detailed purposes, such as wood procurement planning or forest protection survey. These inventories should produce very fine grained information of variables of interest. In addition, the area they cover can vary from one marked stand to large scale level. The usability of ALS data in these inventories varies. For wood procurement planning ALS based methods could provide detailed information but due to the small area of target stands the cost efficiency of data may not be sufficient. Concerning characteristics of forest protection, some of them may be mapped by ALS data and the others may be almost impossible to recognise. In general, ecological information can be obtained from ALS data (Hill et al., 2003; Hashimoto et al., 2004)

All in all the characteristics of Finnish forests (low number of tree species but usually more than one in stand, high stand density, no fast growing plantations) and inventory output needed (stand variables by tree species) define the possibilities for ALS data to be applied. These possibilities are further discussed later in this paper.

3. ALS EXPERIENCES OF FOREST INVENTORY IN FINLAND

3.1 General

The first ALS based forest inventory studies in Finland were based on single tree detection and high pulse density data (Hyypä & Inkinen, 1999; Hyypä et al., 2001). In fact, Hyypä and Inkinen (1999) were among the first ones to apply single tree detection with ALS data. The accuracy was found to be superior already in these first studies the standard error (without bias) being about 10% for stand volume. In the studies by Hyypä and Inkinen (1999) and Maltamo et al. (2004b) the proportion of detected trees was only about 40%. This was due to the multilayered and unmanaged stand structure of the study area. Detailed information concerning ALS studies in Finland before 2004 can be found from

review by Hyypä et al. 2003. More recent developments in Nordic countries and in boreal forests in general have been reported e.g., by Næsset et al. (2006) and Hyypä et al (2007). In Finland, there has also been active research going on concerning the quality of DTM construction in forested areas (e.g. Hyypä et al., 2005; Korpela & Välimäki, 2007). In addition, the TerraScan software (by Arttu Soininen) from Terrasolid Oy is assumed to be the global market leading software concerning laser scanning processing.

3.2 Single tree detection

More recently the research of single tree approach has concentrated on detection algorithms, recovery of undetected trees, height growth and change detection. In addition, crown height estimation and, especially, tree species recognition are under growing research interest in Finland.

Concerning detection algorithms one problem on raster canopy height models is handling of tree crowns of different sizes. On laser scanner data one size attribute, height, is directly available. This gives possibilities to develop processing methods that adapt to the object size. In the study by Pitkänen et al. (2004) three adaptive methods were developed and tested for individual tree detection on CHM. In the first method, the CHM was smoothed with canopy height based selection of degree of smoothing and local maxima on the smoothed CHM were considered as tree locations. In the second and third methods, crown diameter predicted from tree height was utilised. The second method used elimination of candidate tree locations based on the predicted crown diameter and distance and valley depth between two locations studied. The third method was modified from scale-space method used for blob detection. Instead of automatic scale selection of the scale-space method, the scale for Laplacian filtering, used in blob detection, was determined according to the predicted crown diameter.

Possibility to characterize suppressed trees that cannot be detected has also been of interest. Maltamo et al. (2004a) combined theoretical distribution functions and laser scanning data to describe small and suppressed trees, which tree crown segmentation methods was not able to detect. The use of original point clouds instead of digital surface models (DSM) or CHMs also gives possibilities for detection of small trees. Since, some of the laser pulses will penetrate under the dominant tree layer, it is also possible to analyze multilayered stands. In Maltamo et al. (2005), the existence and number of suppressed trees was examined. The results showed that multilayered stand structures can be recognised and quantified using quantiles of laser scanner height distribution data. However, the accuracy of the results is dependent on the density of the dominant tree layer.

Correspondingly, Mehtätalo (2006) used theoretical approach to describe small trees. The probability of a tree being observed was related to its height and was equal to the proportion of the forest area not covered by taller trees. Mehtätalo (2006) presented mathematical formula which was based on the following assumptions: (i) trees are randomly located within the stand and crown diameters within a stand are uncorrelated, (ii) tree height increases as a function of crown diameter, (iii) the tree crown forms a circle around the tree tip, and (iv) a tree is invisible if the tree tip locates within the crown of a taller tree. Furthermore, different approaches were proposed for the correction of the censoring effect upon

the observed distribution of crown areas. The used approach provided theoretically accurate estimates for the distribution of crown areas and the number of stems.

Yu et al. (2004) demonstrated the applicability of airborne laser scanners in estimating height growth and monitoring fallen or cut trees. Out of 83 field-checked fallen or cut trees, 61 were detected automatically and correctly. All the mature cut trees were detected; it was mainly the smaller trees that were not. Height growth was demonstrated at plot and stand levels using an object-oriented tree-to-tree matching algorithm and statistical analysis. In Yu et al. (2006) the potential of measuring individual tree height growth of Scots pine in boreal forest was analysed. Three different types of variables were extracted from the point clouds representing each tree: (i) the difference of highest z value, (ii) difference between DSMs of tree tops and, (iii) difference of 85, 90 and 95% quartiles of the height histograms corresponding to a crown. The results indicate that it is possible to measure the height growth of an individual tree with multi-temporal laser surveys.

Maltamo et al. (2006b) compared the results of the prediction of crown height characteristics using ALS data and intensive field measurements. Crown height models were constructed both at the tree and plot level for Scots pine, Norway spruce and birches. The ALS based models included independent variables of tree levels, such as tree height, crown area and independent plot-level variables, i.e. canopy height and density quantiles and proportion of vegetation hits. The results indicated that the ALS-based crown height models were more accurate than the field-measurement-based models when plot-level information was used as independent variables. However, the field-measurement-based tree-level models for Scots pine and Norway spruce were more accurate than the ALS-based models. Even so, the accuracy of the different models was very similar.

Related to wood procurement planning Peuhkurinen et al. (2007) applied ALS data and field measurements to characterize timber assortments of two pure Norway spruce marked stands. Pre-harvest measurement was realized by using different methods as follows: (i) lidar-based individual tree detection (see Pitkänen et al., 2004) and local constructed dbh model (tree height as predictor), (ii) lidar-based individual tree detection and existing regional dbh model for spruce presented by Kalliovirta and Tokola (2005), (iii) lidar-based individual tree detection and existing regional dbh model (both tree height and maximum crown diameter as predictors), (iv) systematic field plot sampling data, (v) field inventory by compartments and, (vi) area based canopy height distribution approach. The mean stand variables were predicted with the models presented by Suvanto et al. (2005). As a ground truth data harvester measurements were used and the comparison of the methods was based on bucking simulations.

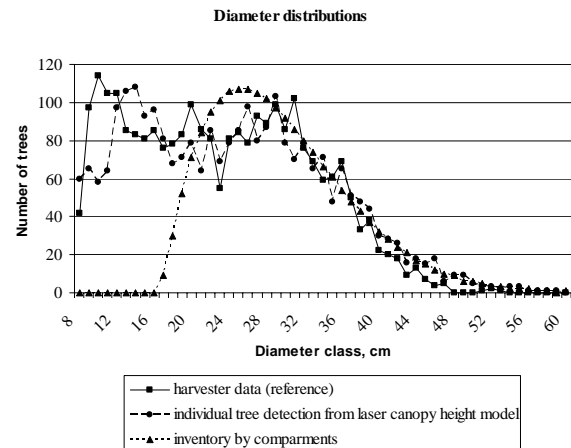


Fig. 1. Comparison of diameter distributions of single tree detection, compartment inventory and harvester reference data in a marked stand (Peuhkurinen et al. 2007).

The results of Peuhkurinen et al. (2007) illustrated considerable advantage of lidar-based single tree detection procedure compared to other studied methods in producing pre-harvest measurement information. Single tree detection with local dbh model (method (i)) was the most accurate method by means of error index of diameter distribution (Reynolds et al., 1988), saw wood and pulp wood volumes and apportionment indexes used in relation with distribution of logs. In fact, single tree detection found 2561 trees whereas harvester data included 2638 trees, corresponding figures for saw wood volumes were 1262 m³ and 1267 m³, respectively. Predicted tree diameters were even able to produce bi-modal shape of diameter distribution (Fig. 1). Though, it must be noticed that the study by Peuhkurinen et al. (2007) was done using two marked stands only and, thus, has the nature of a case study.

Pyysalo (2006) developed 3D vector models of single trees from ALS data in order to derive geometry features. The vector model construction included four stages: (i) laser point classification, (ii) DTM construction, (iii) extraction of points from each individual tree and, (iv) vector model creation. The extracted features were tree height, crown height, trunk location, and crown profile. According to the derived results tree shape is underestimated in vector models in both vertical and horizontal direction. Tree location were extracted with an accuracy of 2 m and tree heights with an accuracy of 1.5 m (Pyysalo, 2006).

Säynäjoki (2007) examined tree species classification between aspen and other deciduous trees by using single tree recognition of ALS data. Watershed segmentation was used to create crown segments on the smoothed CHM (Pitkänen et al., 2004). Crown segments of deciduous trees were used to classify trees to aspen or other deciduous trees using linear discriminant analysis. Classification accuracy between aspen and other deciduous trees was as its best 79.1%. Predictors in this classification function were proportion of vegetation hits, standard deviation of pulse heights, accumulated intensity on 90th percentile and relation of proportions of laser points reflected on 95th and 40th height percentiles. In addition to the study by Säynäjoki (2007) there is a lot of research interest going on in Finland to recognise tree species from single tree detected ALS data. In Liang et al. (2007), it was shown that the difference between first and last pulse is a valuable feature for trees species classification. It gives reliable (89%

accuracy) classification between coniferous and deciduous trees under leaf-off conditions.

Finally, international EuroSDR/ISPRS Tree Extraction project is coordinated by Finland (Hyypä & Kaartinen 2006). The project includes twelve partners and the study area is located in southern Finland. The aims of the project are: (i) to compare different algorithms in tree extraction, (ii) to study the effect of pulse density and (iii) to improve results by combining ALS data and aerial images. The characteristics to be compared are tree and tree species detection and tree height estimation. The results clearly showed that the variability of tree location accuracy is small as a function of pulse density and it mainly changes as a function of the provider. With the best models for all the trees, the mean location error was less than 1 m and the difference with 2, 4 and 8 pulses per m² was negligible. With trees over 20 m, the accuracy of tree location of 0.5 m was obtained. Tree height quality analysis using selected 70 reference trees, the reference height was known with accuracy of 10 cm, showed again that the variability of the pulse density was negligible compared to method variability. With best models RMSE of 50 to 80 cm was obtained for tree height. Even the 2 pulses per m² seemed to be feasible for individual tree detection. Percentage of the found trees by partners showed that the best algorithms found 90% of those trees that were found at least by one of the partners. There was again higher variation with the method used rather than pulse density. The results of the test showed that the methods of individual tree detection vary significantly and that the method itself is more significant for individual tree based inventories rather than the applied pulse density (Harri Kaartinen and Juha Hyypä, personal comm.).

3.3 Area based modelling

Research concerning area based modelling by using canopy height distribution approach and low pulse density ALS data started year 2004 in Finland (Suvanto et al., 2005; Maltamo et al., 2006a). First studies confirmed the corresponding accuracy observed in other Nordic countries (e.g. Næsset, 2002; 2004; Holmgren, 2004; Næsset et al., 2004). Juntunen (2006) also made cost plus loss comparisons between ALS based stand variables and characteristics of conventional inventory by compartments (see e.g., Eid et al., 2004). When compared to optical sensors canopy height distribution approach was found to be more suitable alternative for the next generation method for compartment inventory in Finland (Utterra et al., 2006). Instead of using regression models in construction of stand variable models k-MSN model was used by Maltamo et al. (2006c). The k-MSN method is a non-parametric method, which uses canonical correlation analysis to produce a weighting matrix used in the selection of k Most Similar Neighbors from reference data. Most Similar Neighbors are observations that according to predictor variables are similar to the target of prediction. When using k-MSN model the accuracy of stand volume was improved when compared to regression models (Maltamo et al., 2006). Additional information of aerial photographs or stand register data further slightly improved the accuracy.

When constructing area based forest inventory application a ground truth sample of accurately measured field plots is needed. One possibility for reducing the costs lies in the use of existing field plots for ground truth purposes. The most obvious alternative in Finland is to use truncated angle count sample plots of the National Forest Inventory. Due to the

lack of suitable angle count ground truth data and corresponding laser data, Maltamo et al. (2007a) tested this possibility using data on fixed area sample plots, in which tree locations were simulated. The trees for a truncated angle count sample plot were then chosen and the resulting data together with the characteristics of an ALS -based canopy height distribution were used to construct regression models to predict stem volume, basal area, stem number, basal area median diameter and the height. The accuracy of the stand attributes was found to be almost as good as in the case of models of fixed area plots. However, one drawback of this study was that there were no field plots which were located on stand edge. Such plots are typical for systematic sampling based forest inventory applications, such as NFI of Finland.

Närhi (2007) tested the usability of area based canopy height distribution approach to define the need and timing of silvicultural treatment on Norway spruce sapling stands. Two approaches were used: (i) ALS characteristics were directly used to classify sapling stands according to treatment need by using discriminant analysis and, (ii) regression models were constructed for mean height and stand density correspondingly as Næsset and Bjerknes (2001). After that, the need and timing of silvicultural treatment was classified according to these predicted characteristics. The results indicated that overall accuracy of about 70% was achieved in classification. The stands where there is a need for treatment were found more accurately than those who did not have need for that.

Basically, area based canopy height distribution approach produces stand variables, usually stand volume, stem number, basal area, basal area median diameter and tree height. However, ALS data can also be used to predict parameters of a theoretical diameter distribution model of a stand (Gobakken & Næsset, 2004; 2005). In Finland, Maltamo et al. (2006a) compared prediction of diameter percentiles and the use of predicted stand characteristics to further predict Weibull parameters. More flexible and local percentile based distribution was able to better describe diameter distribution of heterogeneous stands.

In Maltamo et al. (2007b) the accuracy of ALS-based stem frequency and basal area diameter distribution models by using Weibull distribution were compared. Furthermore, the usability of calibration estimation (see, e.g., Kangas & Maltamo, 2002) to adjust the predicted distributions to be compatible with the ALS based estimated stand volume was presented. As a main result, the authors state that when diameter distributions are predicted using ALS data, basal area diameter distributions may not be needed. This represents a considerable improvement in the inventory system, since basal area is not in itself an interesting end-product variable. When stem frequency distributions are directly usable, this would provide a more realistic description of the stand structure and generate simulations for the further development of the tree stock.

Pesonen et al. (2007) analysed the potential of ALS data for estimating coarse wood debris (CWD) volumes in conservation area of the Koli National Park. The accuracy of the ALS data proved adequate for predicting the downed dead wood volume (RMSE 51.6%), whereas the standing dead wood volume estimates were somewhat poorer (RMSE 78.8%). The downed dead wood volume estimates were found to be substantially more accurate than traditional predictions based on field measurements. Correspondingly,

Kotamaa (2007) analysed the potential of ALS data for estimating downed dead wood volumes in managed forests in Juuka, eastern Finland. The accuracy was found to be considerably worse. However, ALS data was able to satisfactorily classify plots whether they included downed dead wood or not.

In all abovementioned studies (excluding Säynäjoki, 2007 and Liang et al., 2007) tree species have been ignored and total tree stock has been considered. However, species-specific stand characteristics are essential in Finland. To solve this problem Packalén and Maltamo (2006) combined information from ALS data with digital aerial photographs to predict stand volume by tree species. Furthermore, Packalén and Maltamo (2006; 2007) applied the non-parametric k-MSN method to predict species-specific forest variables volume, stem number, basal area, basal area median diameter and tree height simultaneously for Scots pine, Norway spruce and deciduous trees as well as total characteristics as sums of the species-specific estimates. The combination of ALS data and aerial photographs was used in these studies. The predictor variables derived from the ALS data were based on the height distribution of vegetation hits, whereas spectral values and texture features were employed in the case of the aerial photographs. The results showed that this approach can be used to predict species-specific forest variables at least as accurately as from the current stand-level field inventory for Finland.

4. CALCULATION EXPERIMENTS

4.1 Comparison of single tree detection and canopy height distribution approaches

Area based canopy height distribution and single tree based approaches to utilise ALS data have been compared and discussed in some reviews (Næsset et al., 2004; Hyypä et al., 2007). However, reliability figures presented earlier have been based on different reliability characteristics and study areas as well. Peuhkurinen et al. (2007) observed the better accuracy of single tree detection in pre harvest measurement case study. The example stand had rather low stand density (465 stems per hectare). However, for forest inventory purposes, comprehensive forest resource estimate should be provided in relation to area to be considered, not just for mature stands.

In this paper we theoretically compare these two approaches in Matalansalo test area. This area has been earlier used in several ALS studies (Suvanto et al., 2005; Maltamo et al., 2006c; 2007a; b; Packalén & Maltamo, 2006; 2007). The total size of the area is about 1200 hectares. There are a total of 472 field sample plots (radius 9 meters) located in the area and ALS campaign was conducted in summer 2004 using an Optech ALTM 1233 laser scanning system operating at an altitude of 1500 m above ground level. Sampling density of the data was about 0.7 measurements per one square metre. The pulse density does not allow individual tree detection and, therefore, we simulated single tree approach as follows: (i) it was expected that all trees were found, i.e. true tree heights of all field measured trees were used, (ii) tree species recognition produced 100% accuracy, i.e., tree species recorded for each field measured tree was used and, (iii) tree diameter was predicted with the help of tree height (h) either by using existing, i.e. no calibration, regional regression models by Kalliovirta and Tokola (2005) or from sample tree

material, i.e. calibrated by using about 1200 measurements, constructed local tree diameter models. The model forms were for Scots pine $\sqrt{dbh} = f(\sqrt{h})$ and for Norway spruce and deciduous tree species $\sqrt{dbh} = f(h)$. After that we calculated stand volumes by using volume functions of Laasasenaho (1982). As a result RMSE's of 25.3% and 22.9% for plot level volumes were obtained for regional and local models, respectively. When compared these figures to canopy height distribution approach based estimates of regression models 19.9% (Suvanto et al., 2005), k-MSN estimate 15.6% (Maltamo et al., 2006c), species-specific k-MSN estimates summed to plot level 20.5% (Packalén & Maltamo, 2007) and diameter distribution based plot volume estimate 20.6% (Maltamo et al., 2007b) it can be seen that the accuracy is slight worse although it was expected that tree and tree species detection totally succeeded. This is due to the fact that the relationship between tree height and diameter is far from deterministic. Allometric relationship between tree diameter and height defines only certain limits for the variation of these to variables, but characteristics such as stand density, stand silvicultural history, genetic factors of tree seed, tree position in a stand, site fertility, height above sea level, distance from sea, mineral soil/peatland and stand development class effect considerably to this relationship

In real world applications all trees and tree species would not be detected, tree groups would cause some problems and tree heights would be underestimates (e.g. Maltamo et al., 2004b), but, the errors obtained here might not be increased considerably due to the correlations between different errors (Kangas, 1999). On the other hand, our simulation was not able to take into consideration other variables produced by single tree detection, usually tree crown area or diameter (Hyypä et al., 2001; Persson et al., 2002; Maltamo et al., 2004a). In the study by Kalliovirta and Tokola (2005) the increase in accuracy when maximum width of tree crown was added to dbh/h model was 2.5 %-units in tree diameter prediction. Furthermore, in Finnish conditions the effect of tree crown area or diameter to increase accuracy of volume prediction has been found to be 5-7 %-units (Maltamo et al., 2004a; Villikka et al., 2007). Furthermore, the use of height and density distributions of 3D point cloud of each detected tree would additionally slightly improve the accuracy as suggested by Villikka et al. (2007). Also some of the characteristics mentioned in previous paragraph could be used in dbh/h models or in the stratification of the data.

In fact, it is obvious in statistical manner that if the target variable is stand volume, direct prediction model, as in the case of canopy height distribution, is the most accurate alternative to predict it. To further compare these two approaches by using diameter distribution estimates we also calculated error index presented by Reynolds et al. (1988):

$$e = \sum_{i=1}^K \left| \hat{f}_i - f_i \right| \quad (1)$$

where \hat{f}_i and f_i are the predicted and true frequency of diameter class i , respectively, and K is the number of diameter classes. The error index was calculated in 1-cm-diameter classes for stem numbers at the plot level. Thus, the error index of a given plot was the sum of the absolute differences between the actual and predicted stem frequencies of the diameter classes. Diameter distribution

estimate was in the case of canopy height distribution approach based on Weibull distribution (Maltamo et al., 2007b). Correspondingly, diameter estimates of local diameter models were used in the case of single tree detection. Tree species recognition was not used in these comparisons, i.e. distributions described tree total stock. As a result, the average values of error indexes were 30.1 for Weibull distribution based estimates and 30.8 for single tree detection. In 239 plots Weibull distribution was more accurate and in 211 plots single tree detection, in the rest (n=22) these methods were as accurate by means of Reynold's error index.

Finally, RMSE figures for volumes of saw wood sized trees (dbh>17 cm) were calculated. This characteristic approximates saw wood proportion, an important variable when deriving value or final cut decision of the stand. In the case of Weibull distribution the RMSE was 32.2% and for detected single trees, which diameters were predicted with local tree diameter models, the RMSE was 40.3%.

At least when only tree height is used to predict tree diameter single tree detection is not able to produce more accurate common forest resource estimates than area based methods. This is true for the stand volume as well as derived diameter distribution or certain detailed part of tree stock. Single tree detection does directly measure physical dimension of a tree but tree height in itself is not an interesting variable in most of the forest inventory applications. When considering biodiversity aspects or certain habitat requirements stand vertical structure is of primary interest but usually diameter distribution and end products derived from it together with tree height and tree species information are most important output variables of forest inventory.

The accuracy of single tree detection could be improved by calibrating tree diameter estimates at stand level. This would, however, need field visit and measurement of GPS mapped tree(s) and their height/diameter -relationship almost in each target stand, i.e. extensive and very expensive reference data for calibration is needed. Alternatively, single tree detection based estimates, such as number of trees and stand volume, could also be calibrated by using corresponding area based ALS estimates. For general forest resource information field calibration would not be cost-efficient, since such field visits could take as much time as current compartment inventory in Finland (on average 10 minutes per stand). Without calibration there is, however, a high possibility of large errors in operational inventories. For certain purposes, such as pre harvest measurement of a marked stand in Finland single tree detection could still be very interesting alternative expecting that tree and tree species detection algorithms are highly successful.

4.2 Usability of spatial information provided by ALS data

Both basic approaches to process ALS data for forest information purposes also include some spatial information which has not yet been utilised as much as possible. In the case of single tree detection location and height of each detected trees are obtained as well as same characteristics of neighbouring trees. This allows us to calculate height based competition indexes. In the following we calculate additive competition index based on elevation angle sums (see Miina & Pukkala, 2000):

$$CI = \sum_{i=1}^n a \tan\left(\frac{h_{neighbour} - 0.8 * h}{dist}\right) \quad (2)$$

where $h_{neighbour}$ is height of neighbour tree, n is number of neighbouring trees and $dist$ is distance between target and neighbour trees, maximum distance of 8 meters was taken into consideration in the calculations.

This index was calculated for trees of two pine dominated mapped field sample plots and corresponding individual tree recognised ALS data including point density of 3.88 pulses per square meter. ALS data was acquired in summer 2005 using an Optech ALTM 3100 scanner operating at a mean altitude of 900 m above ground level. Example sample plots were located on Koli National park and algorithms of Pitkänen et al. (2004) were used for tree detection. Tree coordinates and heights were needed in the calculations.

In the case of sparse density sample plot almost all trees were detected and distributions CI-indexes were quite close to each other (Fig. 2). All in all, ALS data was capable of producing realistic estimates of competition indexes. On the other hand, in dense sample plot less than 50% of trees were detected and ALS data based CI estimates are not realistic (Fig. 3). In the case of small trees there are only a few ALS detected trees and also for larger trees underestimates are obtained since there are too few neighbouring trees taken into consideration in these estimates.

Further use of spatial indexes lies, e.g., in situation where tree level distance dependent growth models are constructed (e.g. Miina & Pukkala, 2000). Additional information that ALS data could provide for such models would be spatial indexes as described here, past height growth estimates from multitemporal ALS data either at single tree level or plot level as suggested by Yu et al. (2004, 2006) and information included in laser based DTM, e.g. slope. Field measurements including at least time series of two measurements are, of course, needed for model construction, but when applying such models a considerable amount of independent variable information could come from ALS data.

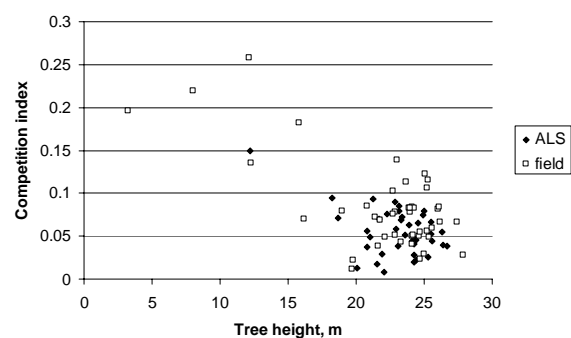


Fig. 2. An example plot of spatial competition indexes calculated from field measurements (n=44) and ALS detected trees (n=39). Stand variables: basal area=24.5 m²ha⁻¹, mean height=24.7 m and number of stems = 489 per hectare.

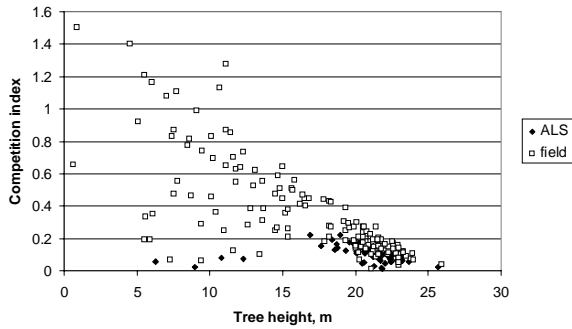


Fig. 3. An example plot of spatial competition indexes calculated from field measurements (n=151) and ALS detected trees (n=67). Stand variables: basal area=31.7 m²ha⁻¹, mean height= 24 m and number of stems= 1677 per hectare

In the case of canopy height distribution approach spatial information can be considered by using within stand information provided by ALS based grid cells. In our example two stands in Juuka test area are used. ALS data were collected during summer 2005 using an Optech ALTM 3100 scanner operating at an altitude of 2000 m above ground level resulting point density of about 0.6 pulses per square meter. Field ground truth consists of systematic sample (30 m distance) of angle count sample plots measured originally for stand delineation purposes (Mr. Jukka Mustonen, personal comm.). ALS based stand variable estimation was based on the principle presented by Packalén and Maltamo (2007). The size of the systematic grid cell was 16 m * 16 m which was close to original field sample plot (radius 9 m).

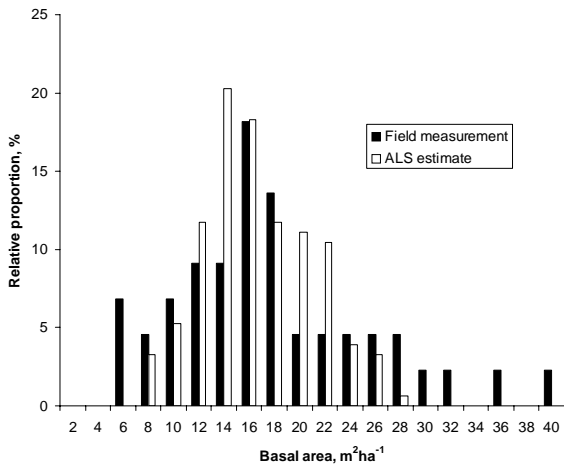


Fig. 4. Within stand distributions of field measured and ALS based basal area estimates. Field measurements: mean basal area 18 m²ha⁻¹ and number of field measured angle count plots 44. ALS: mean basal area 15.6 m²ha⁻¹ and number of grid cells 153. Area of the stand is 3.9 hectares.

As shown in the example figures (4 and 5) ALS data can reproduce realistic estimates of within stand variation of basal area. The averaging effect of models can be seen on both ends of the distribution since extreme values are not predicted. Compared to current field estimate of compartment inventory which is only average value of basal area in the stand this kind spatial information is of primary interest. As within stand variation can be described, the need for silvicultural operations such as thinnings can be more

accurately timed and spatial pattern at stand level can also be defined. Of course, information presented in Figures 4 and 5 can also be produced by using single tree detection if as a result of it high proportion of trees are detected and accurate calibrated tree diameter model is used.

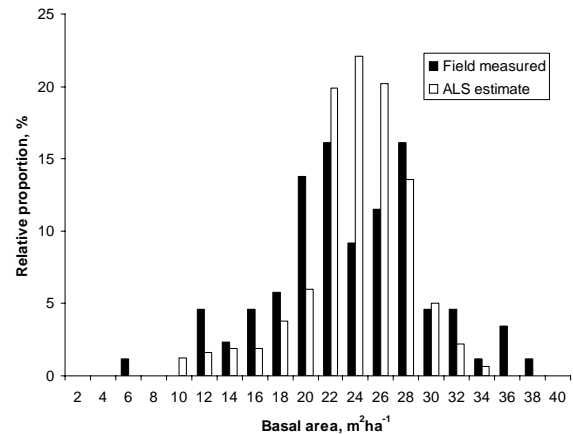


Fig. 5. Within stand distributions of field measured and ALS based basal area estimates. Field measurements: mean 24 m²ha⁻¹ and number of field measured angle count plots 87. ALS: mean basal area 22.9 m²ha⁻¹ and number of grid cells 327. Area of the stand is 8.4 hectares.

5. CONCLUSIONS

In Finland there are numerous research activities going on concerning the utilisation of ALS data in forest applications. First commercial ALS applications for forest inventory purposes were also introduced in Finland year 2006. This paper reviewed and discussed most of research works concentrating especially on forest inventory purposes. Some further utilisation possibilities, such as spatiality and biodiversity aspects in terms of CWD and large aspens, were also considered and proposed. There are also numerous other research topics, such as canopy cover, tree quality, forest condition, stand delineation, forest planning, site classification and forest structure which are currently examined in Finland by using ALS data. From the point of forest research both area based and single tree approaches have a very high potential to be further developed and used in novel applications. One possible application would also be a combination of area based and single tree detection methods. Also the rapid technological development of laser technology gives new possibilities all the time.

A lot of interest is currently being shown especially in remote sensing-based forest inventories in Finland, the driving force being the possibility for reducing costs, although the potential for improved accuracy is also important. Species-specific stand characteristics are essential in Finland, because they are used as an input to forest management planning. The accuracies achieved in the study by Packalén and Maltamo (2007) in the estimation of species-specific characteristics were at least as good as those achieved with the current inventory practise, but more testing must be carried out in different types of forests with varying species compositions, different geographical locations and different age distributions before it is fully justified to conclude that the combined use of ALS and aerial photographs prove superior to a conventional inventory by compartments (Packalén,

2006). The inclusion of young forests to inventory chain is also one research topic to be further examined.

ALS-based tree-level forest inventories may become a realistic alternative in the near future. Tree-level inventories require denser ALS data but technological development will mean that costs will decrease rapidly. An approach in which aerial photographs are not needed for species recognition would also be interesting at the individual tree level, but more development work must still be done in the fields of individual tree recognition, tree species classification, modelling tree variables, especially tree diameter and the inventory chain as a whole before tree-level inventories can be valid operationally.

6. REFERENCES

- Artuso, R., Bovet, S. & Streilein, A., 2003. Practical Methods for the Verification of Countrywide Terrain and Surface Models. ISPRS WG III/3 Workshop '3-D reconstruction from airborne laser scanner and InSAR data', Dresden, Germany 8-10 October 2003. *The International Archives of Photogrammetry, Remote Sensing and Spatial Information Sciences*, Vol. XXXIV, part 3/WG13.
- Drake, J. B., Dubayah, R. O., Knox, R. G., Clark, D. B. & Blair, J. B. 2002. Sensitivity of large-footprint lidar to canopy structure and biomass in a neotropical rainforest. *Remote Sensing of Environment*, 81, pp. 378–392.
- Eid, T., Gobakken, T. & Næsset, E., 2004. Comparing stand inventories based on photo interpretation and laser scanning by means of cost-plus-loss analyses. *Scandinavian Journal of Forest Research*, 19, pp. 512-523.
- Gobakken, T. & Næsset, E., 2004. Estimation of diameter and basal area distributions in coniferous forest by means of airborne laser scanner data. *Scandinavian Journal of Forest Research*, 19, pp. 529-542.
- Gobakken, T. & Næsset, E., 2005. Weibull and percentile models for lidar-based estimation of basal area distribution. *Scandinavian Journal of Forest Research*, 20, pp. 490-502.
- Haara, A. & Korhonen, K.T., 2004. Kuvioittaisen arvioinnin luotettavuus. *Metsätieteen aikakauskirja*, 4/2004, pp. 489-508. (In Finnish).
- Hashimoto, H., Imanishi, J., Hagiwara, A., Morimoto, Y. & Kitada, K., 2004. Estimating forest structure indices for evaluation of forest bird habitats by an airborne laser-scanner. *International Archives of Photogrammetry, Remote Sensing and Spatial Information Sciences*, Vol. XXXVI, Part 8/W2, pp. 254–258.
- Heurich, M. & Weinacker, H., 2004. Automated tree detection and measurement in temperate forests of Central Europe using laser-scanning data. *International Archives of Photogrammetry, Remote Sensing and Spatial Information Sciences*, VOL. XXXVI(8/W2), pp. 198-203.
- Hill, R.A., Hinsley, S.A., Gaveau, D.L.A. & Bellamy, P.E., 2004. Predicting habitat quality for Great Tits (*Parus major*) with airborne laser scanning data. *International Journal of Remote Sensing*, 25, pp. 4851-4855.
- Holmgren, J. 2004. Prediction of Tree Height, Basal Area and Stem Volume in Forest Stands Using Airborne Laser Scanning. *Scandinavian Journal of Forest Research*, 19, pp. 543-553.
- Hyypä, H., Yu, X., Hyypä, J., Kaartinen, H., Honkavaara, E. & Rönnholm, P., 2005. Factors affecting the quality of DTM generation in forested areas. In *Proceedings of ISPRS Workshop Laser scanning 2005*, September 12-14, 2005, Enschede, Netherlands, (Netherlands: GITC bv), XXXVI (Part 3/W19), pp. 85-90.
- Hyypä, J. & Inkinen, M., 1999. Detecting and estimating attributes for single trees using laser scanner. *The Photogrammetric Journal of Finland*, 16, pp. 27-42.
- Hyypä, J., Kelle, O., Lehikoinen, M., & Inkinen, M., 2001. A segmentation-based method to retrieve stem volume estimates from 3-dimensional tree height models produced by laser scanner. *IEEE Transactions on geoscience and remote sensing*, 39, pp. 969-975.
- Hyypä, J., Hyypä, H., Maltamo, M., Yu, X., Ahokas, E. & Pyysalo, U., 2003. Laser Scanning of Forest Resources - Some of the Finnish Experience. In *Proceedings of the ScandLaser Scientific Workshop on Airborne Laser Scanning of Forests*, September 3-4, 2003, Umeå, Sweden, pp. 53-59.
- Hyypä, J. & Kaartinen, H., 2006. EuroSDR/ISPRS test on tree extraction. *Proceedings of the international conference Silvilaser 2006*. November 7-10, 2006. Ehime Prefectural Convention Hall Matsuyama, Japan, pp. 75-79.
- Hyypä, J., Hyypä, H., Leckie, D., Gougeon, F., Yu, X & Maltamo, M., 2007. Methods of small-footprint airborne laser scanning for extracting forest inventory data. *International Journal of Remote Sensing*, In press.
- Juntunen, R., 2006. Puustotiedon laadun vaikutus metsänkäsittelyn optimoinnin tuloksiin – UPM Metsän laserkeilausaineiston ja kuviotiedon vertailu. University of Helsinki, Department of Forest Economics, Helsinki, Finland. M.Sc. thesis, 94 p. (In Finnish).
- Kalliovirta, J. & Tokola, T., 2005. Functions for estimating stem diameter and tree age using tree height, crown width and existing stand database information, *Silva Fennica*, 39, pp. 227-248.
- Kangas, A., 1999. Methods for assessing the uncertainty of growth and yield predictions, *Canadian Journal of Forest Research*, 29, pp. 1357-1364.
- Kangas, A. & Maltamo, M., 2002. Anticipating the variance of predicted stand volume and timber assortments with respect to stand characteristics and field measurements. *Silva Fennica*, 36, pp. 799-811.
- Koch, B., Heyder, U. & Weinacker, H., 2006. Detection of individual tree crowns in airborne lidar data. *Photogrammetric Engineering & Remote Sensing*, 72, pp. 1339-1348.
- Korpela I., 2007. 3D treetop positioning by multiple image matching of aerial images in a 3D search volume bounded by lidar surface models. *Photogrammetrie, Fernkundung, Geoinformation*, 1/2007, pp. 35-44.

- Korpela, I. & Välimäki, E., 2007. Talousmetsän maanpintamallinnus arkistoilmakuvilta ja laserkeilauksella. *Maanmittaus*, 82. (In Finnish).
- Kotamaa, E., 2007. Lahopuun määrän ennustaminen laserkeilauksella talousmetsissä. University of Joensuu, Faculty of Forest Sciences, candidate's thesis in in Forest Planning and Economics. (In Finnish).
- Laasasenaho, J., 1982. Taper curve and volume function for pine, spruce and birch. *Communications Instituti Forestalis Fenniae*, 108, pp. 1-74.
- Liang, X., Hyyppä, J. & Matikainen, L., 2007. Deciduous-coniferous tree classification using difference between first and last pulse laser signatures. *ISPRS Workshop on Laser Scanning 2007 – Silvilaser 2007*.
- Magnussen, S., & Boudewyn, P. 1998. Derivations of stand heights from airborne laser scanner data with canopy-based quantile estimators. *Canadian Journal of Forest Research*, 28, pp. 1016-1031.
- Maltamo, M., Eerikäinen, K., Pitkänen J., Hyyppä, J. & Vehmas, M., 2004a. Estimation of timber volume and stem density based on scanning laser altimetry and expected tree size distribution functions. *Remote Sensing of Environment*, 90, pp. 319-330.
- Maltamo, M., Mustonen, K., Hyyppä, J., Pitkänen, J. & Yu, X., 2004b. The accuracy of estimating individual tree variables with airborne laser scanning in a boreal nature reserve. *Canadian Journal of Forest Research*, 34, pp. 1791-1801.
- Maltamo, M., Packalén, P., Yu, X., Eerikäinen, K., Hyyppä, J. & Pitkänen, J., 2005. Identifying and quantifying structural characteristics of heterogeneous boreal forests using laser scanner data. *Forest Ecology and Management*, 216, pp. 41-50.
- Maltamo, M., Eerikäinen, K., Packalén, P. & Hyyppä, J., 2006a. Estimation of stem volume using laser scanning based canopy height metrics. *Forestry*, 79, pp. 217-229.
- Maltamo, M., Hyyppä, J. & Malinen, J., 2006b. A comparative study of the use of laser scanner data and field measurements in the prediction of crown height in boreal forests. *Scandinavian Journal of Forest Research*, 21, pp. 231 - 238
- Maltamo, M., Malinen, J., Packalén, P., Suvanto, A. & Kangas, J., 2006c. Non-parametric estimation of stem volume using laser scanning, aerial photography and stand register data. *Canadian Journal of Forest Research*, 36, pp. 426-436.
- Maltamo, M., Korhonen, K.T., Packalén, P., Mehtätalo, L. & Suvanto A., 2007a. A test on the usability of truncated angle count sample plots as ground truth in airborne laser scanning based forest inventory. *Forestry*, 80, pp. 73-81.
- Maltamo, M., Suvanto, A. & Packalén, P., 2007b. Comparison of basal area and stem frequency diameter distribution modelling using airborne laser scanner data and calibration estimation. *Forest Ecology and Management*, In press.
- McCombs, J.W., Roberts, S.D. & Evans, D.L., 2003. Influence of fusing lidar and multispectral imagery on remotely sensed estimates of stand density and mean tree height in a managed loblolly pine plantation. *Forest Science*, 49, pp. 457-466.
- Mehtätalo, L., 2006. Eliminating the effect of overlapping crowns from aerial inventory estimates. *Canadian Journal of Forest Research*, 36, pp. 1649-1660.
- Miina, J. & Pukkala, T., 2000. Using numerical optimization for specifying individual tree competition models. *Forest Science*, 46, pp. 277-283.
- Närhi, M., 2007. Kuusen taimikoiden inventointi ja taimikonhoidon kiireellisyyden määrittäminen laserkeilauksen avulla. University of Joensuu, Faculty of Forest Sciences, master's thesis in Management of Forest Ecosystems. (In Finnish).
- Næsset, E., 1997. Estimating timber volume of forest stands using airborne laser scanner data. *Remote Sensing of Environment*, 51, pp. 246-253.
- Næsset, E., 2002. Predicting forest stand characteristics with airborne scanning laser using a practical two-stage procedure and field data. *Remote Sensing of Environment*, 80, pp. 88-99.
- Næsset, E., 2004. Practical large-scale forest stand inventory using a small airborne scanning laser. *Scandinavian Journal of Forest Research*, 19, pp. 164-179.
- Næsset, E & Bjercknes, K-O., 2001. Estimating tree heights and number of stems in young forest stands using airborne laser scanner data. *Remote Sensing of Environment*, 78, pp. 328-340
- Næsset, E., Gobakken, T., Holmgren, J., Hyyppä, J., Hyyppä, H., Maltamo, M., Nilsson, M., Olsson, H., Persson, Å. & Söderman, U., 2004. Laser scanning of forest resources: the Scandinavian experience. *Scandinavian Journal of Forest Research*, 19, pp. 482-499.
- Næsset, E., Gobakken, T., Kangas, A., Maltamo, M. Bollandssås, O.M., Aasland, T. & Solberg, S., 2006. Extending and improving methods for operational stand-wise forest inventories utilizing multi-resolution airborne laser scanner data. In *Proceedings of the international conference Silvilaser 2006*. November 7-10,2006. Ehime Prefectural Convention Hall Matsuyama, Japan, pp. 75-79.
- Packalén, P., 2006. Using airborne laser scanning data and digital aerial photographs to estimate forest growing stock. Licentiate thesis. University of Joensuu.
- Packalén, P. & Maltamo, M., 2006. Predicting the volume by tree species using airborne laser scanning and aerial photographs. *Forest Science*, 52, pp. 611-622.
- Packalén, P. & Maltamo, M., 2007. The k-MSN method in the prediction of species specific stand attributes using airborne laser scanning and aerial photographs. *Remote Sensing of Environment*, 109, pp. 328-341.

- Persson, Å., Holmgren, J. & Söderman, U., 2002. Detecting and measuring individual trees using an airborne laser scanner. *Photogrammetric Engineering & Remote Sensing*, 68, pp. 925-932.
- Pesonen, A, Maltamo, M., Eerikäinen, K. & Packalén, P., 2007. Airborne laser scanning-based prediction of coarse woody debris volumes in a conservation area. Submitted manuscript.
- Peuhkurinen, J., Maltamo, M., Malinen, J., Pitkänen, J. & Packalén, P., 2007. Pre-harvest measurement of marked stand using airborne laser scanning. *Forest Science*, In press.
- Pitkänen, J., Maltamo, M., Hyypä, J. & Yu, X., 2004. Adaptive methods for individual tree detection on airborne laser based height model. *International Archives of Photogrammetry, Remote Sensing and Spatial Information Sciences*, XXXVI(8/W2), pp. 187-191.
- Poso, S., 1983. Kuvioittaisen arvioimismenetelmän perusteita. English summary: Basic features of forest inventory by compartments. *Silva Fennica*, 17, pp. 313-349.
- Pyysalo, U., 2006. Single tree feature extraction from airborne laser scanner data applying vector models. Thesis for degree of Licentiate of Science In Technology. Department of Surveying at Helsinki University of Technology.
- Reynolds, M.R. JR., T.E. Burk, & Huang, W.-C., 1988. Goodness-of-fit tests and model selection procedures for diameter distribution models. *Forest Science*, 34, pp. 373-399.
- Säynäjoki, R., 2007. Classification of aspen and other deciduous trees using high resolution remote sensing data. University of Joensuu, Faculty of Forest Sciences, master's thesis in Forest Planning and Economics.
- Suvanto, A., Maltamo, M., Packalén, P. & Kangas, J., 2005. Kuviokohtaisten puustotunnusten ennustaminen laserkeilauksella. *Metsätieteen aikakauskirja*, 4/2005, pp. 413-428. (In Finnish).
- Takahashi, T., Yamamoto, K., Senda, Y. & Tsuzuku, M., 2005. Predicting individual stem volumes of sugi (*Cryptomeria japonica* D. Don) plantations in mountainous areas using small-footprint airborne LiDAR. *Journal of Forest Research*, 10, pp. 305-312.
- Tickle, P.K., Lee, A., Lucas, R.M., Austin, J. & Witte C., 2006. Quantifying Australian forest floristics and structure using small footprint LiDAR and large scale aerial photography. *Forest Ecology and Management*, 223, pp. 379-394.
- Tomppo, E., 2006a. The Finnish National Forest Inventory. In: Kangas, A. & Maltamo, M. (eds.). *Forest inventory. Methodology and applications*. Managing Forest Ecosystems, Vol 10, Springer, Dordrecht, pp. 179-194.
- Tomppo, E., 2006b. The Finnish multi-source National Forest Inventory - small area estimation and map production. In: Kangas, A. & Maltamo, M. (eds.). *Forest inventory. Methodology and applications*. Managing Forest Ecosystems, Vol 10, Springer, Dordrecht, pp. 195-224.
- Utterä, J., Anttila, P., Suvanto, A. & Maltamo, M., 2006. Yksityismetsien metsävaratiedon keruuseen soveltuville kaukokartoitusmenetelmillä estimoitujen puustotunnusten luotettavuus. *Metsätieteen aikakauskirja*, 4/2006, pp. 507-519. (In Finnish).
- Villikka, M., Maltamo, M., Packalén, P., Vehmas, M. & Hyypä, J., 2007. Alternatives for predicting tree-level stem volume of Norway spruce using airborne laser scanner data. Submitted manuscript.
- Yu, X., Hyypä, J., Kaartinen, H. & Maltamo, M., 2004. Automatic Detection of Harvested Trees and Determination of Forest Growth using Airborne Laser Scanning. *Remote Sensing of Environment*, 90, pp. 451-462.
- Yu, X., Hyypä, J., Kukko, A., Maltamo, M. & Kaartinen, H., 2006. Change detection techniques for canopy height growth measurements using airborne laser scanner data. *Photogrammetric Engineering & Remote Sensing*, 72, pp. 1339-1348

CLASSIFICATION TREE BASED BUILDING DETECTION FROM LASER SCANNER AND AERIAL IMAGE DATA

Leena Matikainen*, Harri Kaartinen, Juha Hyyppä

Finnish Geodetic Institute, Department of Remote Sensing and Photogrammetry
P.O. Box 15, FI-02431 Masala, Finland – firstname.lastname@fgi.fi

KEY WORDS: Building, Detection, Classification, Segmentation, Automation, Laser scanning, Aerial image

ABSTRACT:

A classification tree based approach for building detection was tested. A digital surface model (DSM) derived from last pulse laser scanner data was first segmented and the segments were classified into classes 'ground' and 'building or tree' on the basis of preclassified laser points. 'Building and tree' segments were further classified into buildings and trees by using the classification tree method. Four classification tests were carried out using different combinations of 44 input attributes. The attributes were derived from the last pulse DSM, first pulse DSM and an aerial colour ortho image. In addition, shape attributes calculated for the segments were used. The attributes of training segments were presented as input data for the classification tree method, which constructed automatically a classification tree for each test. The trees were then applied to classification of a separate test area. Compared with a building map, a mean accuracy of almost 90% was achieved for buildings in each test. The classification tree method appeared to be a feasible and highly automatic approach for distinguishing buildings from trees. If new data sources become available in the future, they can be easily included in the classification process. The results also suggest that satisfactory building detection results can be obtained with different combinations of input data sources. By using a statistical method, it is possible to find useful attributes and classification rules in different cases. The use of an aerial image or both first pulse and last pulse laser scanner data does not necessarily improve the results significantly, compared with a classification that uses only last pulse laser scanner data.

1. INTRODUCTION

Most methods presented for automatic building detection from laser scanner data use step-wise classification approaches to distinguish buildings from other objects (see, for example, Hug, 1997; Morgan and Tempfli, 2000; Vögtle and Steinle, 2000; Rottensteiner et al., 2005a; Forlani et al., 2006; Zhang et al., 2006). The methods normally begin by extracting the ground surface using a filtering algorithm. After this, the most important task is to distinguish buildings from trees. Features or attributes commonly used for building detection include height texture (e.g. Hug, 1997; Maas, 1999) or surface roughness (e.g. Brunn and Weidner, 1998), reflectance information from images (e.g. Haala and Brenner, 1999; Vögtle and Steinle, 2000) or laser scanning (e.g. Hug, 1997), the difference between first pulse and last pulse laser scanner data (e.g. Oude Elberink and Maas, 2000; Alharthy and Bethel, 2002), and shape and size of objects (e.g. Tóvári and Vögtle, 2004). The attributes calculated for predefined segments or single pixels are presented as input data for a classification method which can be a general-purpose supervised or unsupervised method but more commonly is a rule-based method or other similar method specifically designed for the task.

Each building detection method typically uses a certain set of attributes and rules selected by its developers on the basis of their knowledge and experience on the subject and/or training data available for the study. This approach is a feasible one and can lead to satisfactory results, as shown by many previous studies. The disadvantage of the approach, however, is that the development of the methods is time consuming. When new datasets become available, considerable time is needed to study their potential in building detection and include them in the methods. Comparative studies between different datasets and

input attributes are also rare (for examples of comparative studies, see Rottensteiner et al., 2005b; Pfeifer et al., 2007), which makes it difficult to evaluate the usefulness of and need for different datasets for practical applications. For example, many of the methods use aerial image data in addition to laser scanner data, but whether this improves the results significantly is largely an open question. The same applies to the combined use of first pulse and last pulse laser scanner data.

A method that has been increasingly used in the classification of remotely sensed data in recent years is classification trees (also called decision trees) (Breiman et al., 1984; Safavian and Landgrebe, 1991). Classification trees can be created automatically with data mining or statistical software tools, and they have many useful properties which make them attractive for the analysis of remotely sensed data (see Breiman et al., 1984; Safavian and Landgrebe, 1991; Hansen et al., 1996; Friedl and Brodley, 1997; Huang and Jensen, 1997; Lawrence and Wright, 2001; Thomas et al., 2003; Lawrence et al., 2004). The classification tree method is non-parametric and does not require assumptions on the distribution of the data. It is thus particularly interesting when multisource datasets with different types of possible input attributes are used. A large number of different attributes can be presented for the method, and it automatically selects the most useful ones. This makes the classification process highly automatic and different from most other approaches, in which the user must select suitable attributes before classification. Different attributes can be used for distinguishing different classes. The structure of the classification tree is easy to understand and it gives information on the roles and usefulness of different attributes in the classification task, although caution is needed in the interpretation of this information (see Breiman et al., 1984).

* Corresponding author.

There are still few applications of the classification tree method to the analysis of laser scanner data. Hodgson et al. (2003) studied the mapping of urban parcel imperviousness using colour aerial photography and laser scanner derived height information. Ducic et al. (2006) used the classification tree method to classify laser points as vegetation points and non-vegetation points on the basis of full-waveform information. Matikainen (2006) tested the classification tree method for building detection to distinguish buildings from trees. This approach proved to be highly automatic and provided an accuracy that was very near the accuracy obtained earlier using the same dataset and manually created classification rules.

This article presents further tests of the classification tree method in building detection. A large set of input attributes derived from last pulse and first pulse laser scanner data and an aerial ortho image were used. In addition to testing the feasibility of the method, the objective of the study was to acquire basic information on the importance of different datasets and attributes in building detection.

2. STUDY AREA AND DATA

Data from a study area in Espoonlahti, near Helsinki, were used. The area is a suburban area with small hills and plenty of coniferous and deciduous trees, as well as lower vegetation. When the laser scanner data were acquired on 14 May 2003, some deciduous trees were without leaves and others had small leaves. Colour aerial images were taken on 26 June 2003, when all trees were in full leaf. Separate areas covering about 0.4 km² and 1.4 km² were used for training and testing the classification tree method. The test area was divided into two parts, one of which is mainly a high-rise residential area and the other is mainly a low-rise residential area.

The laser scanner data were acquired simultaneously in first pulse and last pulse modes with the TopoSys FALCON system. The flying altitude was 400 m above ground level (a.g.l.), which resulted in a point density of about 10 points per m². The average point density in the datasets, including overlap between adjacent strips, is about 17 points per m². First pulse and last pulse digital surface models (DSM) in raster format and with a pixel size of 30 cm × 30 cm were created using the TerraScan software (Soininen, 2005; Terrasolid, 2007). The highest (first pulse DSM) or lowest (last pulse DSM) value within the pixel was assigned to each pixel, and interpolation was used to determine values for pixels without laser points. The original laser points were also classified in TerraScan to detect points located above 2.5 m a.g.l.. This classification for the last pulse points was used for distinguishing buildings and trees from the ground surface before application of the classification tree method. An aerial colour ortho image with a pixel size of 30 cm × 30 cm was created from the aerial images, which were taken with a Leica RC30 camera and had red, green and blue channels. The images were acquired and scanned by FM-Kartta Oy.

Two additional raster images were derived from the DSMs: slope calculated from the last pulse DSM and difference between first pulse and last pulse DSMs. Both of these were filtered using morphological opening and closing operations to remove building edges and to smooth areas covered with trees.

A building map from 2003 obtained from the city of Espoo and a forest map obtained from FM-Kartta Oy were used as training

data. The building map was also used for estimating the accuracy of the building detection results. The map data were converted from vector to raster format (pixel size 30 cm × 30 cm). Before this, neighbouring building polygons were merged to obtain one polygon for each building and polygons smaller than 20 m² were eliminated to exclude very small buildings and other constructions from the analysis. Compared with some ground measurements in the study area, the positional accuracy of buildings in the original building map is 0.5 m or higher. There are, however, many differences in the appearance of the buildings on the map and in the laser scanner and aerial image data. For example, building outlines on the map represent the ground plans of the buildings instead of roof edges. Some more details of the laser scanner, aerial image and map data can be found in Matikainen et al. (2004; 2007).

3. METHODS

3.1 Classification tree tools

The classification (and regression) tree tools available in the Statistics Toolbox of the Matlab software (The MathWorks, 2007) were used in the study. These tools can be used to construct a classification tree with a binary tree structure and to apply the tree to classification (for a detailed description of the classification tree method, see Breiman et al., 1984). A classification tree has a root node, non-terminal nodes and terminal nodes. The root node and each non-terminal node contain a question that asks whether a given attribute satisfies a given condition. Beginning from the root node, an object to be classified goes to the left or right descendant node, depending on whether or not it satisfies the condition of the node. Finally, it ends up at one of the terminal nodes and is assigned to the corresponding class. When a classification tree is constructed, the most useful attributes and splits are selected using a splitting criterion. The Gini's diversity index was used as the splitting criterion in our study. This criterion is a measure of node impurity and is defined as

$$impurity(t) = \sum_{i \neq j} p(i|t)p(j|t), \quad (1)$$

where t is the node, and $p(i|t)$ is the proportion of cases $x_n \in t$ which belong to class i (x is the measurement vector). At each node of the tree, a search is made for the split that most reduces node impurity. (Breiman et al., 1984; The MathWorks, 2003.)

The resulting tree is normally large and can overfit the training data. Therefore, it must be pruned, which means that a set of smaller subtrees is obtained. The best level of pruning can be estimated by computing the cost of each subtree in the optimal pruning sequence (for details, see Breiman et al., 1984; The MathWorks, 2003). This was carried out using the training data and 10-fold cross-validation. The costs were based on the misclassification costs of classes (default; 1) and probabilities of the terminal nodes. The best level of pruning was the level that produced the smallest tree within one standard error of the minimum-cost subtree. When the tree was initially created, a threshold value of 10 (default) was used for splitting nodes, which means that a node had to contain at least 10 training objects to be split.

3.2 Workflow for building detection

The building detection method used in the study included the following stages:

1. Segmentation of the last pulse DSM into homogeneous regions. The segments were the objects to be classified. The multiresolution segmentation method (Baatz and Schäpe, 2000) of the Definiens Professional software (Definiens, 2006; 2007) and a homogeneity criterion based completely on the height values in the DSM were used. The software also provides a large number of different attributes for each segment.
2. Exportation of the segments and various attributes for the segments from Definiens Professional.
3. Classification of the segments into classes 'ground' and 'building or tree' on the basis of the preclassified laser points. A segment was classified as 'building or tree' if most of the last pulse laser points within it had been classified as having a height value of 2.5 m or over (a.g.l.). Within each pixel, only the lowest point, which was also used in forming the last pulse DSM, was considered.
4. Definition of training segments on the basis of training data. A segment from the training area was defined as a training segment for building or tree if over 80% of its area was labelled as building or forest in the map data (some forest areas were excluded because they included a considerable area covered by roads). Segments classified as ground were excluded from the training data. The total number of training segments was 2464, which included 396 building segments and 2068 tree segments. The building segments covered an area of about 3.2 ha and the tree segments covered an area of about 0.8 ha.
5. Construction of a classification tree on the basis of the attributes of the training segments.
6. Classification of all 'building or tree' segments on the basis of their attributes and the classification tree.

The classification tree method has also been applied to segments and attributes obtained from the Definiens (previously eCognition) software in some previous studies. For example, Thomas et al. (2003) used this approach for land-cover/land-use mapping.

3.3 Attributes and classification experiments

Four sets of attributes were selected to be used as input data for the classification of buildings and trees (Table 1, left column). Attributes calculated from the last pulse DSM included standard deviation, texture and the mean slope of the segments. In addition to these more common attributes, two attributes that were available in the Definiens Professional software and were expected to be potentially useful were included. Contrast to neighbour pixels is an attribute that describes the difference (in this case, height difference) between a segment and its surrounding area. Standard deviation of neighbour pixels is the standard deviation of the surrounding area. The surrounding area of a segment consisted of pixels that were located inside the bounding box of the segment (extended by one pixel at the edges) but did not belong to the segment. Attributes calculated using the first pulse DSM comprised standard deviation, texture, and the mean difference between the first pulse and last pulse DSMs. Aerial image attributes included the mean value, standard deviation and texture in different channels. Shape

attributes comprised 27 different shape descriptors available in Definiens Professional.

The texture attribute used in the study, Grey Level Co-occurrence Matrix (GLCM) homogeneity, is one of the texture measures originally presented by Haralick et al. (1973). It can take into account grey level variations between neighbouring pixels in different directions. We used the option 'all directions'. For a more detailed description and formulas of this and other attributes, the reader should refer to Definiens (2006).

Four classification tests were carried out, each with a different combination of attributes (Table 1, middle column). These tests could correspond to four practical situations with different data sources available. The last pulse DSM, which was also used for segmentation, was considered as the primary data source and was available in each test. The shape attributes calculated for the segments could also be used in each case.

3.4 Accuracy estimates

Completeness (corresponds to interpretation accuracy or producer's accuracy), correctness (corresponds to object accuracy or user's accuracy) (Helldén, 1980; Congalton and Green, 1999) and mean accuracy (Helldén, 1980) were calculated for buildings by comparing the classification results with the reference map pixel by pixel in the test area. As described in Section 2, the test area was separate from the training area.

4. RESULTS

Attributes selected automatically for the classification tree in each of the classification tests are listed in the right-hand column of Table 1. The corresponding pruning level is also mentioned (for example, 'pruning level 3/8' means that there were 8 pruning levels in the tree and level 3 was selected; level 0 is the full tree without pruning). In each classification test, the script created for the construction of the tree was run five times to find the best level of pruning. The estimated level may vary slightly between the runs because the subsamples for cross-validation are selected randomly. If different levels were selected as the best in different runs, the classification was carried out using each of these. The level that gave the best mean accuracy for buildings in the whole test area is shown in Table 1 and following figures and tables. In practice, the differences in mean accuracy between the different levels were very small (less than 1 percentage unit).

To give an idea of the relative importance of different attributes in the classification, the total number of training segments passing through nodes with a given attribute is shown in brackets in Table 1. Some training segments had undefined values for one of the shape attributes (main direction) and were not taken into account in the construction of the trees. The total number of training segments used by the algorithm was 2224 (391 building segments and 1833 tree segments). If one segment passed more than one node with the same attribute, it was counted more than once for this attribute. The number of training segments per attribute can thus exceed the total number of training segments.

The classification tree obtained for Test 3 is shown in Figure 1 (pruning level 3/8). Classification results for Test 1 and Test 3 in the high-rise area and Test 2 and Test 4 in the low-rise area

Table 1. Attributes and classification tests. The complete set of attributes used in the study is shown on the left, attributes available for the classification tests are shown in the middle and attributes selected automatically by the classification tree method in the different tests are shown on the right. The number of training segments passing through nodes with the given attribute is given in brackets. The accuracy obtained in the classification (completeness/correctness/mean accuracy) is also shown for each test.

Attributes	Attributes available for the classification tests	Attributes selected for classification and accuracy obtained (completeness/correctness/ mean accuracy)
<p>Attributes from the last pulse (LP) DSM LP DSM, standard deviation LP DSM, GLCM homogeneity LP DSM, contrast to neighbour pixels LP DSM, standard deviation of neighbour pixels Slope from LP DSM, mean</p> <p>Attributes from the first pulse (FP) DSM FP DSM, standard deviation FP DSM, GLCM homogeneity FP DSM - LP DSM, mean</p> <p>Attributes from the aerial image Aerial image, red, mean Aerial image, red, standard deviation Aerial image, red, GLCM homogeneity Aerial image, green, mean Aerial image, green, standard deviation Aerial image, green, GLCM homogeneity Aerial image, blue, mean Aerial image, blue, standard deviation Aerial image, blue, GLCM homogeneity</p> <p>Shape attributes Area Area (polygon-based, excluding inner polygons) Area (polygon-based, including inner polygons) Asymmetry Average length of edges Border index Border length Compactness Compactness (polygon-based) Density Edges longer than 10 pixels Elliptic fit Length Length of longest edge Length/Width Main direction Number of edges Number of inner objects Number of right angles with edges longer than 10 pixels Perimeter Radius of largest enclosed ellipse Radius of smallest enclosing ellipse Rectangular fit Roundness Shape index Standard deviation of length of edges Width</p>	<p>Test 1 Attributes from the LP DSM Attributes from the FP DSM Attributes from the aerial image Shape attributes</p> <p>Test 2 Attributes from the LP DSM Attributes from the aerial image Shape attributes</p> <p>Test 3 Attributes from the LP DSM Attributes from the FP DSM Shape attributes</p> <p>Test 4 Attributes from the LP DSM Shape attributes</p>	<p>Test 1 (Pruning level 3/8) Aerial image, blue, mean (2224 segments) FP DSM - LP DSM, mean (2186) Length of longest edge (1872) Average length of edges (38) Area (12) -> Accuracy 92.0/85.8/88.8%</p> <p>Test 2 (Pruning level 1/6) Aerial image, blue, mean (2224 segments) LP DSM, standard deviation (2183) Length of longest edge (1872) Aerial image, blue, standard deviation (1834) Slope from LP DSM, mean (344) Edges longer than 10 pixels (48) Average length of edges (38) -> Accuracy 92.1/86.4/89.2%</p> <p>Test 3 (Pruning level 3/8) FP DSM - LP DSM, mean (4022 segments) FP DSM, GLCM homogeneity (1881) Average length of edges (1805) LP DSM, GLCM homogeneity (1803) Slope from LP DSM, mean (560) LP DSM, standard deviation (343) Radius of largest enclosed ellipse (36) -> Accuracy 92.5/87.4/89.9%</p> <p>Test 4 (Pruning level 3/10) Length of longest edge (2224 segments) Slope from LP DSM, mean (2189) LP DSM, GLCM homogeneity (1921) LP DSM, contrast to neighbour pixels (420) Area (330) LP DSM, standard deviation of neighbour pixels (55) -> Accuracy 92.8/86.7/89.7%</p>

Table 2. Numerical accuracy estimates for the building detection results (%) (Test 1/Test 2/Test 3/Test 4).

	Test area		
	High-rise residential	Low-rise residential	All
Completeness	92.6/92.3/92.6/92.3	91.5/91.9/92.5/93.2	92.0/92.1/92.5/92.8
Correctness	91.0/91.1/91.9/91.0	82.2/83.2/84.4/83.8	85.8/86.4/87.4/86.7
Mean accuracy	91.8/91.7/92.2/91.6	86.6/87.4/88.3/88.2	88.8/89.2/89.9/89.7
Buildings classified as trees	0.6/0.9/0.6/0.9	2.6/2.2/1.6/0.9	1.8/1.6/1.2/0.9
Buildings classified as ground	6.8/6.8/6.8/6.8	5.9/5.9/5.9/5.9	6.3/6.3/6.3/6.3

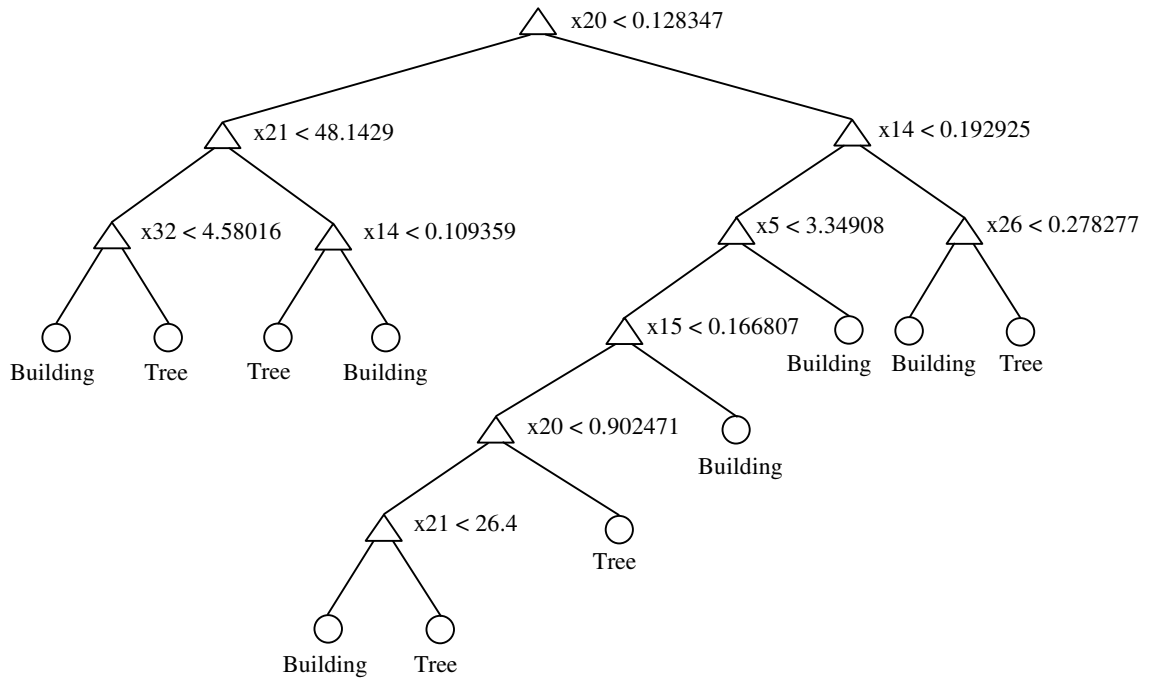


Figure 1. Classification tree obtained for Test 3. Attributes are: x20: FP DSM - LP DSM, mean; x21: slope from LP DSM, mean; x14: FP DSM, GLCM homogeneity; x32: LP DSM, standard deviation; x5: average length of edges; x26: radius of largest enclosed ellipse; x15: LP DSM, GLCM homogeneity.

are presented in Figure 2. Figure 3 shows classification results for Tests 1–4 in a smaller area of the low-rise residential area. Four input data sources derived from the laser scanner data are also shown for this subarea. The accuracy estimates for the building detection results are shown in Table 2. The percentage of building pixels classified as trees or ground is also presented (here, it should be noted that the ground classification was the same in each test). The accuracy estimates obtained for the whole test area are also shown in Table 1.

5. DISCUSSION

The classification tree approach allowed rapid and automatic testing of different attribute combinations for the classification of buildings and trees. Different attributes were selected for the trees, but the quality of the results, evaluated either visually or numerically, was very similar in each test and relatively good, taking into account the differences between the remotely sensed data and reference map. This suggests that satisfactory building detection results can be obtained with different combinations of input data sources. By using a large training dataset and a statistical approach, it is possible to find useful rules for separating buildings and trees in different cases. The highest mean accuracy, 89.9%, was obtained in Test 3, which used attributes calculated from the last pulse and first pulse DSMs, in addition to the shape attributes, which were used in each test. The mean accuracy obtained in Test 4, using the last pulse DSM alone, was only slightly lower, i.e. 89.7%. The lowest accuracy, 88.8%, was obtained in Test 1, which used both last pulse and first pulse DSMs and the aerial image. The difference in accuracy between this and other tests, however, was very small. The percentage of building pixels misclassified as trees was remarkably small in each test. Direct comparison of classification results from different studies is not possible, but the accuracy estimates are also in accordance with those

obtained in other studies (e.g. Rottensteiner et al., 2005a; 2005b).

Many of the attributes were selected in several trees. These included the mean value of the segment in the blue channel of the aerial image, the mean difference between first pulse and last pulse DSMs, the mean slope calculated from the last pulse DSM, standard deviation and texture calculated from the last pulse DSM, and shape attributes 'length of longest edge', 'average length of edges' and 'area'. These are obviously useful attributes for distinguishing buildings from trees. Some other attributes appeared occasionally in the trees, but most attributes were never selected. It should be noted, however, that there can also be useful attributes among those that were not selected (see Breiman et al., 1984). At each node, the algorithm selects the best split according to the splitting criterion, but there can be several attributes and splits that would be almost equally good. The lower splits in the tree also depend on the splits selected earlier. This can explain the difference in the attributes selected in different tests. The tree obtained in Test 2 was also different from the tree obtained in our earlier study (Matikainen, 2006), which used basically the same input data sources but somewhat different attributes and training data.

The classification tree based method seems to be a feasible approach for building detection. Satisfactory results can be obtained rapidly and with a high level of automation. When new data sources become available, they can be easily included in the classification. Once the input data are in the correct format, the construction of the tree can be carried out in seconds. This means a remarkable saving of time compared with the typical manual (or semi-automatic) process of attribute selection and rule development. The classification process itself is also fast. The method could thus be well suited to automatic processing of large areas. A training area with up-to-date map data, or manually delineated buildings and trees, is required for

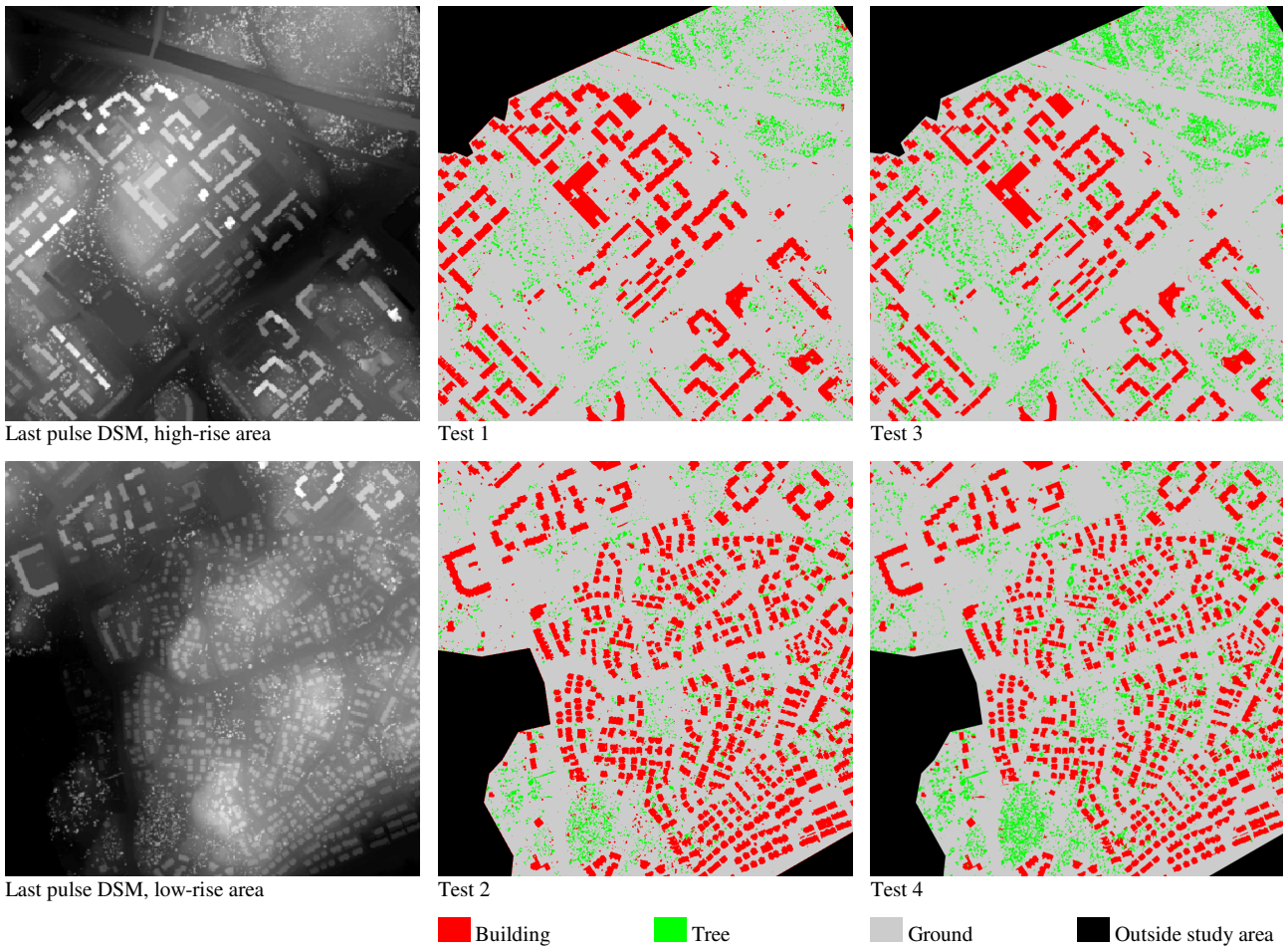


Figure 2. Last pulse DSM and building detection results for Test 1 and Test 3 in the high-rise residential area and Test 2 and Test 4 in the low-rise residential area.

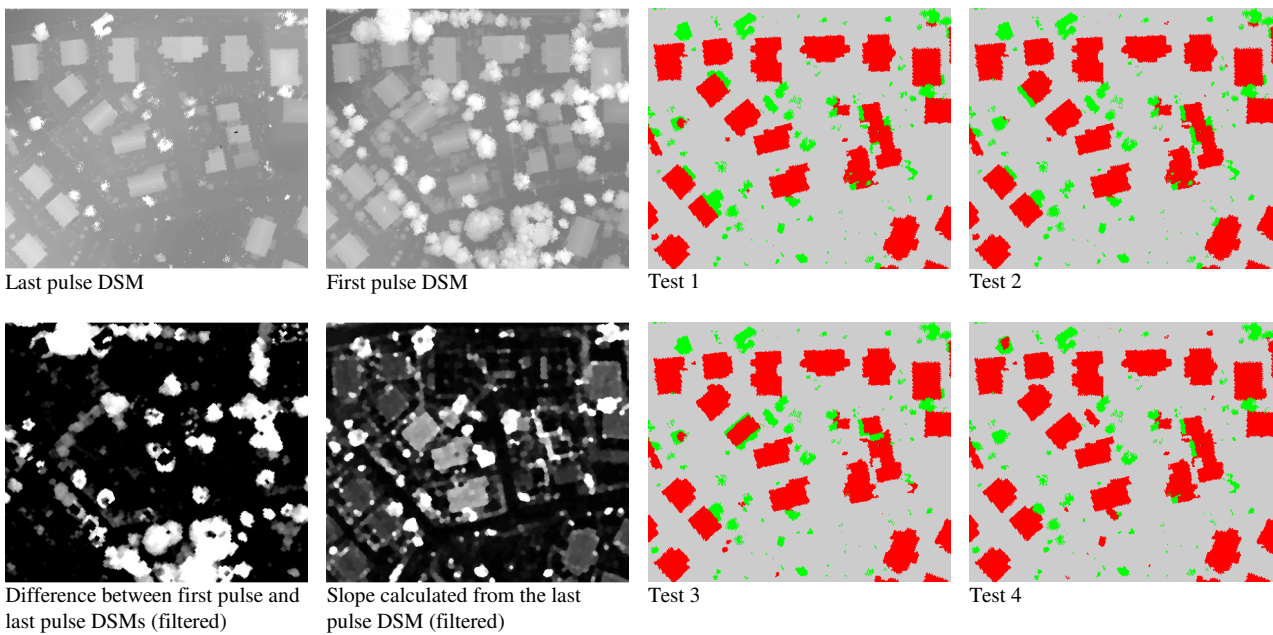


Figure 3. Four input data sources and classification results for Tests 1-4 in a subarea of the low-rise residential area.

training, but it is likely that the classification rules created in one training area could be applied to classification of other similar areas if the characteristics of the laser scanner and aerial image data are stable. For example, the rules from our training area could be largely applicable to other suburban areas in Finland. Further improvements of the classification method might be achieved by testing multivariate trees, alternative splitting rules and pruning methods, and advanced methods of using training data (see, for example, Breiman et al., 1984; Safavian and Landgrebe, 1991; Lawrence et al., 2004).

The classification tree based results can be improved by eliminating obvious misclassifications. This was tested by filling holes (classified as trees) in buildings and removing buildings smaller than 20 m². This increased the mean accuracy of the building detection results in Tests 1–4 to 90.0%, 90.1%, 90.6% and 90.4%, respectively. The use of aerial imagery with an infrared channel should also be tested in the future. The application of the classification tree method to the first classification step of building detection, i.e. distinguishing buildings and trees from the ground surface, could also be tested. Some preliminary experiments related to this were carried out and promising results were obtained, although further study is needed. The use of the classification tree method for ground classification too, could further speed up and simplify the process of building detection.

6. CONCLUSIONS

A classification tree based approach for building detection was tested. Segments derived from the last pulse DSM were first classified into classes 'ground' and 'building or tree' on the basis of preclassified laser points. 'Building and tree' segments were further classified into buildings and trees by using the classification tree method. Four classification tests were carried out by using different combinations of 44 input attributes. These included attributes calculated from the last pulse DSM, first pulse DSM and aerial colour ortho image, as well as shape attributes. The classification tree method appeared to be a feasible and highly automatic approach for distinguishing buildings from trees. The attributes of 2224 training segments were used as input data in the method, which automatically constructed a classification tree for each test. The trees were then applied to classification of a separate test area (1.4 km²). Compared with a building map, a mean accuracy of almost 90% was achieved for buildings in each test. The best results were obtained using attributes derived from the last pulse and first pulse DSMs, and the shape attributes. The differences in accuracy between the different tests, however, were very small. The results thus suggest that satisfactory building detection results can be obtained with different combinations of input data sources. By using a statistical method, it is possible to find useful attributes and classification rules in different cases. Most importantly for practical applications, the use of only last pulse DSM may be sufficient. The use of aerial images or first pulse DSM does not necessarily improve the results significantly. However, if new and potentially useful data sources become available in the future, they can be easily included in the classification process.

REFERENCES

Alharthy, A., Bethel, J., 2002. Heuristic filtering and 3D feature extraction from lidar data. In: *The International Archives of the*

Photogrammetry, Remote Sensing and Spatial Information Sciences, Graz, Austria, Vol. XXXIV, Part 3A, pp. 29-34.

Baatz, M., Schäpe, A., 2000. Multiresolution segmentation – an optimization approach for high quality multi-scale image segmentation. In: Strobl, J., Blaschke, T., Griesebner, G. (Eds.), *Angewandte Geographische Informationsverarbeitung XII: Beiträge zum AGIT-Symposium Salzburg 2000*, Wichmann, Heidelberg, pp. 12-23.

Breiman, L., Friedman, J. H., Olshen, R. A., Stone, C. J., 1984. *Classification and regression trees*. Wadsworth, Inc., Belmont, California, 358 p. (The Wadsworth Statistics/Probability Series.)

Brunn, A., Weidner, U., 1998. Hierarchical Bayesian nets for building extraction using dense digital surface models. *ISPRS Journal of Photogrammetry & Remote Sensing*, 53, pp. 296-307.

Congalton, R. G., Green, K., 1999. *Assessing the Accuracy of Remotely Sensed Data: Principles and Practices*. Lewis Publishers, Boca Raton, 137 p.

Definiens, 2006. Definiens Professional 5 Reference Book. Definiens AG, München, Germany, 122 p.

Definiens, 2007. <http://www.definiens.com/>

Ducic, V., Hollaus, M., Ullrich, A., Wagner, W., Melzer, T., 2006. 3D vegetation mapping and classification using full-waveform laser scanning. In: *Proceedings, International Workshop, 3D Remote Sensing in Forestry*, Vienna, 14–15 February, pp. 222-228. http://www.rali.boku.ac.at/fileadmin/_/H85/H857/workshops/3drsforestry/Proceedings_3D_Remote_Sensing_2006_rev_20070129.pdf (accessed 5 July 2007)

Forlani, G., Nardinocchi, C., Scaioni, M., Zingaretti, P., 2006. Complete classification of raw LIDAR data and 3D reconstruction of buildings. *Pattern Analysis and Applications*, 8(4), pp. 357-374.

Friedl, M. A., Brodley, C. E., 1997. Decision tree classification of land cover from remotely sensed data. *Remote Sensing of Environment*, 61, pp. 399-409.

Haala, N., Brenner, C., 1999. Extraction of buildings and trees in urban environments. *ISPRS Journal of Photogrammetry & Remote Sensing*, 54, pp. 130-137.

Hansen, M., Dubayah, R., Defries, R., 1996. Classification trees: an alternative to traditional land cover classifiers. *International Journal of Remote Sensing*, 17(5), pp. 1075-1081.

Haralick, R. M., Shanmugam, K., Dinstein, I., 1973. Textural features for image classification. *IEEE Transactions on Systems, Man, and Cybernetics*, SMC-3(6), pp. 610-621.

Helldén, U., 1980. A test of Landsat-2 imagery and digital data for thematic mapping, illustrated by an environmental study in northern Kenya. Lunds Universitets Naturgeografiska Institution, Rapport och Notiser 47, Lund, Sweden, 63 p.

Hodgson, M. E., Jensen, J. R., Tullis, J. A., Riordan, K. D., Archer, C. M., 2003. Synergistic use of lidar and color aerial photography for mapping urban parcel imperviousness.

- Photogrammetric Engineering & Remote Sensing*, 69(9), pp. 973-980.
- Huang, X., Jensen, J. R., 1997. A machine-learning approach to automated knowledge-base building for remote sensing image analysis with GIS data. *Photogrammetric Engineering & Remote Sensing*, 63(10), pp. 1185-1194.
- Hug, C., 1997. Extracting artificial surface objects from airborne laser scanner data. In: Gruen, A., Baltsavias, E. P., Henricsson, O. (Eds.), *Automatic Extraction of Man-Made Objects from Aerial and Space Images (II)*, Birkhäuser Verlag, Basel, pp. 203-212.
- Lawrence, R. L., Wright, A., 2001. Rule-based classification systems using classification and regression tree (CART) analysis. *Photogrammetric Engineering & Remote Sensing*, 67(10), pp. 1137-1142.
- Lawrence, R., Bunn, A., Powell, S., Zambon, M., 2004. Classification of remotely sensed imagery using stochastic gradient boosting as a refinement of classification tree analysis. *Remote Sensing of Environment*, 90, pp. 331-336.
- Maas, H.-G., 1999. The potential of height texture measures for the segmentation of airborne laserscanner data. In: *The Fourth International Airborne Remote Sensing Conference and Exhibition / 21st Canadian Symposium on Remote Sensing*, Ottawa, Ontario, Canada, 21-24 June.
<http://www.lr.tudelft.nl/live/binaries/3666d89e-a329-4c97-8d59-13d30c96b34e/doc/Maasthepotential.pdf> (accessed 5 July 2007)
- The MathWorks, 2003. Online documentation for Statistics Toolbox, Version 4.0. The MathWorks, Inc.
- The MathWorks, 2007. <http://www.mathworks.com/>
- Matikainen, L., 2006. Improving automation in rule-based interpretation of remotely sensed data by using classification trees. *The Photogrammetric Journal of Finland*, 20(1), pp. 5-20.
- Matikainen, L., Hyypä, J., Kaartinen, H., 2004. Automatic detection of changes from laser scanner and aerial image data for updating building maps. In: *The International Archives of the Photogrammetry, Remote Sensing and Spatial Information Sciences*, Istanbul, Turkey, Vol. XXXV, Part B2, pp. 434-439.
- Matikainen, L., Hyypä, J., Kaartinen, H., 2007. Comparison between first pulse and last pulse laser scanner data in the automatic detection of buildings. Manuscript accepted to *Photogrammetric Engineering & Remote Sensing*.
- Morgan, M., Tempfli, K., 2000. Automatic building extraction from airborne laser scanning data. In: *International Archives of Photogrammetry and Remote Sensing*, Amsterdam, The Netherlands, Vol. XXXIII, Part B3, pp. 616-623.
- Oude Elberink, S., Maas, H.-G., 2000. The use of anisotropic height texture measures for the segmentation of airborne laser scanner data. In: *International Archives of Photogrammetry and Remote Sensing*, Amsterdam, The Netherlands, Vol. XXXIII, Part B3, pp. 678-684.
- Pfeifer, N., Rutzinger, M., Rottensteiner, F., Muecke, W., Hollaus, M., 2007. Extraction of building footprints from airborne laser scanning: comparison and validation techniques. In: *2007 Urban Remote Sensing Joint Event, URBAN 2007 – URS 2007*, Paris, 11-13 April, 9 p. (on CDROM).
- Rottensteiner, F., Trinder, J., Clode, S., Kubik, K., 2005a. Using the Dempster-Shafer method for the fusion of LIDAR data and multi-spectral images for building detection. *Information Fusion*, 6, pp. 283-300.
- Rottensteiner, F., Summer, G., Trinder, J., Clode, S., Kubik, K., 2005b. Evaluation of a method for fusing lidar data and multispectral images for building detection. In: *International Archives of Photogrammetry, Remote Sensing and Spatial Information Sciences*, Vienna, Austria, Vol. XXXVI, Part 3/W24.
http://www.commission3.isprs.org/cmrt05/papers/CMRT05_Rottensteiner_et_al.pdf (accessed 5 July 2007)
- Safavian, S. R., Landgrebe, D., 1991. A survey of decision tree classifier methodology. *IEEE Transactions on Systems, Man, and Cybernetics*, 21(3), pp. 660-674.
- Soininen, A., 2005. TerraScan User's Guide (03.10.2005). Terrasolid, 169 p.
- Terrasolid, 2007. <http://www.terrasolid.fi/>
- Thomas, N., Hendrix, C., Congalton, R. G., 2003. A comparison of urban mapping methods using high-resolution digital imagery. *Photogrammetric Engineering & Remote Sensing*, 69(9), pp. 963-972.
- Tóvári, D., Vögtle, T., 2004. Classification methods for 3D objects in laserscanning data. In: *The International Archives of the Photogrammetry, Remote Sensing and Spatial Information Sciences*, Istanbul, Turkey, Vol. XXXV, Part B3, pp. 408-413.
- Vögtle, T., Steinle, E., 2000. 3D modelling of buildings using laser scanning and spectral information. In: *International Archives of Photogrammetry and Remote Sensing*, Amsterdam, The Netherlands, Vol. XXXIII, Part B3, pp. 927-934.
- Zhang, K., Yan, J., Chen, S.-C., 2006. Automatic construction of building footprints from airborne LIDAR data. *IEEE Transactions on Geoscience and Remote Sensing*, 44(9), pp. 2523-2533.

ACKNOWLEDGMENTS

The authors wish to thank TopoSys GmbH for laser scanner data, FM-Kartta Oy for aerial image and map data, and the city of Espoo for map data. The financial support from Tekes (project 'NewSAR') is gratefully acknowledged.

RECOVERING PLOT-SPECIFIC DIAMETER DISTRIBUTION AND HEIGHT-DIAMETER CURVE USING ALS BASED STAND CHARACTERISTICS

Mehtätalo, L*., Maltamo, M., & Packalén, P.

University of Joensuu, Faculty of Forest Sciences, P.O. Box 111, FI-80101 Joensuu, Finland. ([lauri.mehtatalo](mailto:lauri.mehtatalo@joensuu.fi), [matti.maltamo](mailto:matti.maltamo@joensuu.fi), [petteri.packalen](mailto:petteri.packalen@joensuu.fi))@joensuu.fi

KEY WORDS: Airborne laser scanning, forest inventory, Weibull, Korf, Scots pine

ABSTRACT:

Density, diameter distribution and height-diameter (H-D) pattern of a forest stand are of primary importance in deriving various stand characteristics, but measuring diameters and heights of a tree stock is rather time-consuming. That is why theoretical diameter distribution and H-D models are usually employed. We examine the prediction of them for Scots pine sample plots using information obtained with airborne laser scanning (ALS). We propose a parameter recovery approach, where such values for the parameters of assumed diameter distribution and H-D models are determined, that satisfy the mathematical relationships between the predicted plot-specific characteristics. If the solution for the formulated system of equations exists, it is always compatible with the predictions of stand characteristics. The method is developed and tested with a dataset of 213 Scots pine stands. A solution was found for all but 2 plots. The proposed method appears to be a reasonable alternative for predicting stand structure from ALS data.

1. INTRODUCTION

Information on tree diameters and heights from a forest stand can be used for deriving various stand characteristics, such as basal area, volume and timber assortments, which are of primary interest in forest management. Since measuring standing tree diameters and heights is rather time-consuming, a theoretical model for the structure of the growing stock is usually employed in growth and yield simulators. We call such a model *stand description*. A stand description characterizes stand structure with only a few parameters. The level of detail in a stand description varies according to information needs of the application. In this study, we use a triplet including stand density (i.e. number of trees per hectare), diameter distribution, and height-diameter (H-D) curve. Assuming that tree volume and taper curve are known functions of tree diameter and height, such a stand description is sufficient for computing timber assortments. In a mixed species stand, such a description would be needed for all tree species, but this study will consider only single species stands.

Numerous approaches for describing the diameter distribution of a stand have been presented, including beta, Weibull and Johnson SB functions, as well as percentile-based and non-parametric approaches (Bailey and Dell, 1973; Loetsch et al., 1973; Hafley and Schreuder, 1977; Borders et al., 1987; Maltamo and Kangas, 1998). Correspondingly, two main methods have been used to predict parameters of an assumed theoretical distribution, namely the parameter prediction method (PPM) and the parameter recovery method (PRM) (Hyink and Moser, 1983). In PPM, field measured stand variables, such as basal area and mean diameter, are used as predictors in regression models that are applied in predicting the diameter distribution for a target stand. In PRM, stand variables, moments or percentiles of diameter distribution are predicted or measured for the target stand, and parameters of an assumed diameter distribution are then

recovered using mathematical relationship between them and the utilized characteristics (see Knoebel and Burkhardt, 1991).

This study generalizes the idea of PRM to recovery of a stand description of an assumed form. Instead of recovering the parameters of a diameter distribution, we will simultaneously recover the parameters of diameter distribution and H-D curve. In addition to stand density, as many predicted stand variables are needed as the assumed stand description has stand-specific parameters to make recovery possible.

The development of small footprint and discrete return airborne laser scanning (ALS) technology has offered possibilities for accurate prediction of forest variables, such as standing tree volume. Numerous studies have shown that both the recognition of individual trees and plot level utilization of the characteristics of canopy height distributions can produce highly accurate predictions of forest variables (e.g. Næsset, 1997; Hyyppä et al., 2001; Persson et al., 2002; Lim et al., 2003; Holmgren, 2004; Næsset et al., 2004; Hopkinson et al. 2006; Maltamo et al., 2006). ALS-based variables have usually been stand mean and sum characteristics, but in Norway and Finland, ALS data have also been used to predict the parameters of assumed diameter distribution models (Gobakken and Næsset, 2004; 2005; Maltamo et al., 2006; Bollandås and Næsset, 2007). These studies have employed either Weibull function or percentile-based distributions, and have applied parameter prediction method. Recently, Maltamo et al. (2007) applied Weibull distribution, PPM, and calibration estimation (see Deville and Särndal, 1990; Kangas and Maltamo, 2000) to predict distributions that are compatible with ALS based stem number, basal area and stand volume.

The aim of this study was to apply the parameter recovery method to estimate diameter distribution and H-D curve of Scots pine (*Pinus sylvestris*) by using ALS based stand variables. First, stem number, stand volume, basal area median diameter, and the corresponding tree height were

* Corresponding author

regressed on independent variables based on ALS data, and the obtained models were applied for prediction in the modelling data. A parameter recovery system, developed for this study, was then utilized to recover such values for the parameters of two parameter Weibull distribution and Korf's height curve that are compatible with these predictions. The system was validated by calculating the proportion of plots where recovery was possible, and RMSE and bias of volume predictions for trees above given diameter limits.

2. STUDY MATERIAL

2.1 Field data

The Juuka test area (about 10 000 hectares) in eastern Finland is a typical Finnish managed boreal forest area. The field data were acquired during summers 2005 and 2006. A total of 506 circular sample plots with a radius of 9 metres were established on the area. Sample plots were located rather systematically to the young, middle-aged and mature forests; sapling stands were left out. Subsequently, the Global Positioning System (GPS) was used to determine the position of the centre of each of the 506 plots to the accuracy of about 1 meter. The diameter at breast height (*DBH*), tree and storey class, and tree species were recorded for all trees with *DBH* over 5 cm, and the height of one sample tree of each species in each storey class was measured on each plot. For prediction of heights for other trees, a Näslunds height model with a random constant for each plot was fitted to the data of measured heights (Aki Suvanto, personal communication). The model with predicted plot effects was utilized to predict heights for trees without height measurement. The volume models of Laasasenaho (1982) were used to compute tree volumes. Finally, the stand characteristics of interest were scaled up to per hectare level. Of those 506 plots, pure Scots pine plots (the proportion of Scots pine over 90 % of volume) were selected to the study data of 213 plots (Table 1).

	mean	min	max	sd
Volume, m ³ ha ⁻¹	122.8	14.7	317.8	61.8
Number of stems, ha ⁻¹	903.8	196	2122	377.3
Basal area median diameter, cm	18.1	9.4	40.0	4.8
Height of a basal area median tree, m	14.0	6.0	23.4	3.3

Table 1. Mean characteristics of the study data. Sd is standard deviation.

2.2 Laser scanning

Georeferenced point cloud data were collected from Juuka on 13th July 2005 using an Optech ALTM 3100C laser scanning system. The test site was measured from an altitude of 2000 m above ground level using a field of view (FOV) of 30 degrees. This resulted in a swath width of approximately 1050 m and a nominal sampling density of about 0.6 measurements per square meter. The divergence of the laser beam (1064 nm) was set at 0.26 mrad. Optech ALTM 3100C laser scanner captures 4 range measurements for each pulse, but here the measurements were reclassified to represent first and last pulse echoes.

In order to generate a digital terrain model (DTM) from the laser scanner data, the points reflected from objects, e.g. from trees, were classified as vegetation hits. The laser point

clouds were first classified to ground points and other points (the method is explained by Axelsson, 2000). Then a DTM raster with a cell size of 2.5 meters was created by computing the mean of the ground points within each raster cell. Values for raster cells with no data were derived using Delaunay triangulation and bilinear interpolation.

Laser canopy height at a given location was calculated as the difference between the *z* value of laser hit and the estimated DTM raster. Points having canopy height over 0.5 meters were classified as vegetation hits. Different height metrics were calculated using the vegetation hits of each sample plot. Percentiles for the canopy height were computed for 5, 10, 20, ... , 90, 95 and 100 % (h_5, \dots, h_{100}) (see Næsset, 2004), and proportional canopy densities were calculated for each of these quantiles (p_{05}, \dots, p_{100}). For example, h_{10} means the height where 10% of all vegetation hits are accumulated, and p_{10} the proportion of laser hits that is accumulated at the height of 10%. Moreover, the standard deviation (h_{std}), mean (h_{mean}), and proportion of vegetation hits (*veg*) were computed. In addition to height and density metrics the intensity of reflection of backscattered laser pulse was utilized. Intensity variables were calculated as percentiles (i_{10}, \dots, i_{90}) within a plot using vegetation hits only. All these characteristics were calculated for both first (*f*) and last (*l*) pulse data.

3. METHODS

3.1 Modeling stand characteristics using ALS data

Regression models were constructed for standing tree volume (*V*), stem number (*N*), basal area median diameter (*D*) and height of a basal area median tree (*H*) using ALS based characteristics as independent variables. The models were fitted using ordinary least squares. A stepwise procedure was applied in the choice of independent variables. The obtained models were applied for prediction in the modelling data.

3.2 Recovering the stand description

In parameter recovery, a stand description of an assumed form was determined that is compatible with all four predicted stand variables. The stand description includes stand density, diameter distribution and H-D curve. The stand density is directly obtained as the predicted number of stems, whereas the other components are recovered using the other three predicted stand variables. We assume that the growing stock is fully described with the stand variables we have, and PRM is used to find a compatible stand description.

Denote the predicted values of stand variables by \hat{V} , \hat{G} and \hat{H} and the values based on an assumed stand description by $V(\theta, \hat{N})$, $D(\theta)$ and $H(\theta)$, which depend on the parameters of the stand description, θ , and the predicted stand density, \hat{N} . A stand description that is compatible with all the predicted stand variables is obtained as a solution to the following system of equations:

$$\begin{cases} V(\theta, \hat{N}) - \hat{V} = 0 \\ D(\theta) - \hat{D} = 0, \\ H(\theta) - \hat{H} = 0 \end{cases} \quad (1)$$

The system is infeasible if no stand description of the assumed form exists that complies with \hat{V} , \hat{D} , \hat{H} and \hat{N} .

Denote tree diameter by x , height by h and volume by v . We assume a diameter distribution with density $f(x|\alpha, \beta)$, height $h(x|\gamma)$ for a tree with diameter x , and volume $v(x, h)$ for a tree with diameter x and height h , where the parameters of the stand description are $\theta = (\alpha, \beta, \gamma)$. Thus, the diameter distribution is characterized by two plot-specific parameters, α and β , and the H-D curve with one plot-specific parameter, γ . A general volume function with no stand-specific parameters is assumed for all trees. The stand variables based on such a stand description are

$$V(\theta, \hat{N}) = \hat{N} \int_0^{\infty} f(x|\alpha, \beta) v(x, h(x|\gamma)) dx$$

$$D(\theta) = F_G^{-1}(0.5|\alpha, \beta)$$

and

$$H(\theta) = h(\hat{D}|\gamma),$$

where $F_G^{-1}(p|\alpha, \beta)$ is the inverse (quantile) function of the basal-area weighted diameter distribution

$$F_G(x|\alpha, \beta) = \int_0^x f_G(u|\alpha, \beta) du,$$

where

$$f_G(x|\alpha, \beta) = \frac{x^2 f(x|\alpha, \beta)}{\int_0^{\infty} x^2 f(x|\alpha, \beta) dx}$$

is the density of basal-area weighted diameter distribution (see e.g. Gove and Patil, 1998).

We described the diameter distribution with the two-parameter Weibull distribution. It has density

$$f(x|\alpha, \beta) = \left(\frac{\alpha}{\beta}\right) \left(\frac{x}{\beta}\right)^{\alpha-1} \exp\left(-\left(\frac{x}{\beta}\right)^{\alpha}\right),$$

where α is a shape and β is a scale parameter. As the H-D curve, we used the model of Mehtätalo (2005)

$$h(x|\gamma) = \max\left[1.4, \exp(\gamma - \delta y(x))\right].$$

The independent variable is a transformation of tree diameter

$$y(x) = \frac{(x+7)^c - (\hat{D}+17)^c}{(17)^c - (37)^c},$$

where $c = 0.98 + 0.058\hat{D}$. This transformation gives interpretations to the two parameters: γ is the logarithmic height of trees with diameter $\hat{D}+10$ and δ is the expected difference in logarithmic height between diameters \hat{D} and $\hat{D}+10$. We allowed only γ vary between plots in recovery and δ depended on basal area median diameter according to $\delta = 0.62 - 0.027\hat{D} + 0.00094\hat{D}^2$ (Mehtätalo, 2005). As the volume function, we used that of Laasasenaho (1982),

$$v(x, h) = 0.036x^{2.01} 0.997^x h^{2.07} (h-1.3)^{-1.07}.$$

Using the functions presented above, we solved the system of equations given in (1) for $\theta = (\alpha, \beta, \gamma)$. The estimation was carried out in two stages: we first searched initial estimates for the parameters by minimizing function $(V(\alpha, \beta, \gamma, \hat{N}) - \hat{V})^2 + (D(\alpha, \beta) - \hat{D})^2 + (H(\gamma) - \hat{H})^2$ for $\theta = (\alpha, \beta, \gamma)$, using the algorithm of Nelder and Mead with $\theta = (5, \hat{D}, 3)$ as initial guesses. The obtained estimates were used as initial guesses for the Newton-Raphson algorithm, which was used for finding the final estimates. The required integrals and differentials were evaluated numerically. The basal-area weighted quantile function was solved using a simple up and down algorithm. R-software (R Development core team 2006) was used for computations.

3.3 Evaluation of results

The results were first evaluated using the proportion of plots where the system of equations was feasible. For plots with feasible solution, the obtained stand description was used to compute the total volumes for trees with diameter above a predefined lower diameter limit L . The volume was computed as

$$\hat{V}_L = \hat{N} \int_L^{\infty} f(x|\hat{\alpha}, \hat{\beta}) v(x, h(x|\hat{\gamma})) dx.$$

We used values 10, 15 and 20 cm as the values for L . As criteria of comparison, we used the bias and RMSE of these volumes, together with the bias and RMSE of the predicted stand characteristics. In addition, we evaluated the predictions visually and report graphs of selected sample plots of our data.

4. RESULTS

4.1 Prediction models for stand characteristics.

The models for plot volume, number of stems, basal area median diameter and corresponding height are:

$$\ln V = 0.134 + 1.202 \ln(f - h_{50}) + 0.198 \sqrt{f - veg} + 0.114 \ln(l - veg)$$

($R^2 = 0.924$, s.e. = 0.155, relative s.e. 16.3%)

$$\ln N = 7.803 - 1.027 \ln(f_{-h_{95}}) + 0.251 \sqrt{f_{-veg}}$$

$$+ 7.988 \left(\frac{1}{f_{-i_{50}}} \right) - 0.319 \ln(l_{-p_{20}})$$

($R^2 = 0.497$, s.e. = 0.311, relative s.e. 30.8%)

$$\ln H = -26.075 + 5.747 \ln f_{-h_{95}} + 3.581 \ln f_{-h_{40}}$$

$$+ 38.371 \frac{1}{f_{-h_{60}}} + 0.605 \ln l_{-veg} + 4.907 \ln l_{-h_{50}}$$

($R^2 = 0.783$, s.e. = 0.119, relative s.e. 12.9%)

$$\ln D = 2.697 - 2.605 \frac{1}{f_{-i_{50}}} - 37.812 \frac{1}{f_{-p_{20}}}$$

$$+ 2.004 \ln f_{-h_{50}} - 1.231 \ln f_{-h_{40}}$$

($R^2 = 0.860$, s.e. = 1.230, relative s.e. 8.7%)

where f or l denotes the laser pulse type (first or last pulse), h_p denotes the height at which $p\%$ of the height distribution has accumulated, veg is the proportion of vegetation hits, i_{50} is the 50th percentile of intensity reflection, and p_{20} is the proportion of laser hits which is accumulated at the height of 20%.

The RMSEs of predicted volume, number of stems, basal area median diameter and the corresponding height (Table 2) were at the same level as they have been in previous studies with laser scanning data (Holmgren, 2004; Næsset, 2002; 2004; Maltamo et al. 2007). The predictions of the number of stems and total volume are slightly downward biased.

	RMSE		Bias	
	Absolute	%	Absolute	%
H , m	1.22	8.70	0.00	-0.01
D , cm	2.35	12.96	-0.15	-0.80
N , ha ⁻¹	279.8	31.00	-35.30	-3.91
V , m ³ ha ⁻¹	20.02	16.29	-1.64	-1.33

Table 2. RMSE and bias of predicted stand characteristics in the data of feasible solutions (211 plots).

4.2 Recovery of stand description

A stand description of the assumed form could be found for almost all stands. In only two out of the 213 plots, the system of equations was infeasible. In addition, the resulting distribution was highly peaked (recovered shape parameter $\alpha > 20$) for 2 stands.

The accuracy of predicted volume above diameters 10, 15 and 20 cm is given in table 3. The RMSE of volume above 10 cm is slightly lower than that of total volume in absolute terms, but slightly higher in relative terms. For higher diameter limits, the RMSE gets higher both in absolute and relative terms, being 24.33 m³ha⁻¹ (42%) for the volume of trees above 20 cm in diameter. The volumes are slight underestimates in all cases; an expected result because the predictions of stand characteristics were underestimates, too.

	RMSE		Bias	
	Absolute	%	Absolute	%
V_{10} , m ³ ha ⁻¹	19.70	16.67	-0.79	-0.67
V_{15} , m ³ ha ⁻¹	22.20	22.70	-2.20	-2.25
V_{20} , m ³ ha ⁻¹	24.33	42.76	-1.72	-3.02

Table 3. RMSE and bias of volumes above 10, 15 and 20 cm diameter limit in the data of feasible solutions (211 plots).

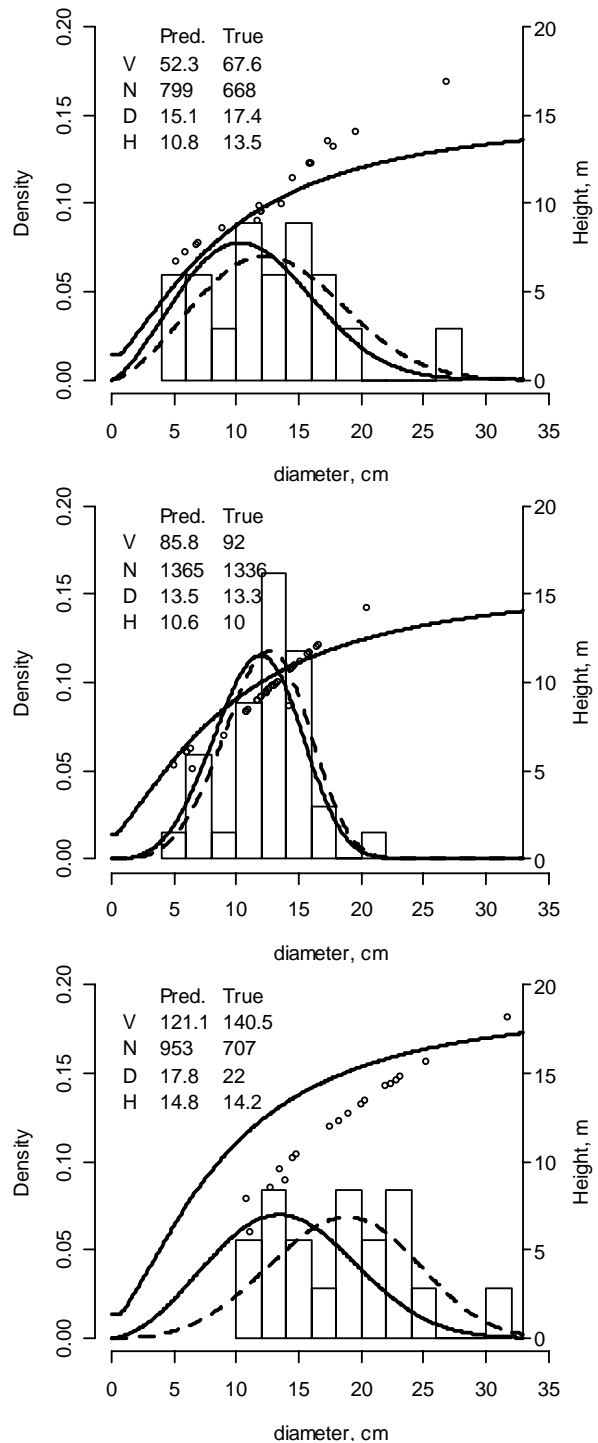


Figure 1. Examples of true and recovered stand descriptions. The histogram shows the observed diameter distribution and the open circles the tree heights. The dashed line shows a Weibull-distribution fitted to the observed data using ML. The solid lines show the recovered diameter distribution and H-D curve.

Visual evaluation of predictions showed that they are, in most cases, fair (the two uppermost stands in Figure 1). However, especially errors in predicted basal area median diameter made the location of the distribution inaccurate, causing large errors in the predicted structure of the growing stock (The lowest plot in Figure 1). The recovered H-D curve did not agree very well with the “true” heights, which are based on plot-specific Näslund’s curve. These differences result from different model forms.

5. DISCUSSION

This study generalized the parameter recovery of diameter distribution to the recovery of stand description, including stand density and models for diameter distribution and H-D curve. Such a method is useful in laser scanning approaches, where accurate predictions are obtained for characteristics that depend on both tree diameter and height. In the proposed parameter recovery approach, diameter distribution and H-D curve of assumed forms are recovered so that the obtained stand description is compatible with predicted stand characteristics. The approach appears to be a reasonable alternative for obtaining estimates of stand structure using laser data.

With the stand description of this study, the parameter recovery would be possible with any four stand characteristics, given that they are mathematically related to the stand description and at least one of them depends on tree height. In addition, the parameters of the assumed stand description can further be increased if the number of predicted parameters is increased. Total volume, stand density, basal area median diameter and corresponding height were selected as the variables being predicted because they can be rather accurately predicted using laser data. However, attention was also paid to the correlation of the prediction errors. Using two accurately predicted variables with highly correlated prediction errors (e.g. volume and basal area) might have lead to worse results than using variables with lower accuracy but less correlated prediction errors (e.g. volume and the number of stems). However, analysis of this requires further efforts.

A problem with the proposed approach is that a solution to the system of equations cannot necessarily be found. In our data, this happened with two plots. For those plots, a stand description that simultaneously satisfies the three equations does not exist. This may result from too restricted form of the assumed stand description: three parameters are not enough to realistically describe all possible forms of diameter distribution and H-D curve. A solution would be to assume a more flexible stand description, including more parameters and, for example, allowing bimodal diameter distributions. However, the number of parameters in the stand description would be increased, and that would also require more ALS-predicted stand variables. Another possible cause for infeasibility is an illogical set of predictions. Especially, if the models are based on small plots, sampling errors may cause the modeling data to include such combinations of stand variables that cannot be described with the simple description we used. This may affect also to the prediction models, making them it more likely for them to give illogical predictions. To prohibit this effect, the plot size of the modeling data should be large enough. However, the above solutions do not guarantee feasibility, and for operational utilization, predictions are required for all plots. One

alternative would be using the solution that minimizes the sum of squared distance between the predicted values and the values based on the stand description. Appropriate weights should be used for different terms to make them comparable. The solution would no more be compatible but, however, as compatible as possible.

The approach presented in this study would allow conversion of old inventory results, where stand mean characteristics are predicted by using ALS data (e.g. Næsset, 2002, 2004; Holmgren, 2004; Suvanto et al.; 2005), to stand descriptions as used in this study. Compared to earlier ALS data based diameter distribution studies (Gobakken and Næsset, 2004;2005; Maltamo et al. 2006;2007) the benefit of the proposed method is that no additional modelling is needed since the approach recovers possible parameter values without the use of tree level data. Finally, this study also confirms the result by Maltamo et al. (2007) that in the case of ALS data, basal area diameter distributions are not needed to obtain accurate volume estimates.

This study considered stand description in Sots pine stands. It was assumed that it is known prior to prediction that these forests are pure pine stands (pine proportion of volume over 90%). In practical applications, information concerning species proportions could be obtained by using non-parametric species-specific forest inventory approach which utilises both ALS data and digital aerial photographs (Packalén and Maltamo, 2007). This kind of method would also recognise stands where pine exists but it is not the main tree species. The usability of stand description approach of this study could be worse in some of those stands, i.e., the system of equations might be infeasible due to inconsistency with mean characteristics of pine. Crude information about species proportions could also be obtained from old stand register data or site fertility class. Photo interpretation could also be used for estimation of species proportions, as it was done in Norway (e.g. Næsset, 2004)

This study expected that the diameter distribution of a pure pine stand can be characterized with a unimodal function. In managed stands, this is, in fact, true in most cases. In unmanaged stands, conservation areas, or forest reserves, the situation would be more complex since fire ecology and gap dynamics may result in diameter distributions of a multimodal shape (Esseen et al. 1997).

6. REFERENCES

- Axelsson, P., 2000. DEM generation from laser scanner data using adaptive TIN models. In: *Proc. of XIXth ISPRS Conference, Amsterdam, The Netherlands. IAPRS, Vol. XXXIII*, pp. 110–117.
- Bailey, R.L. & Dell, T.R., 1973. Quantifying diameter distributions with the Weibull function. *Forest Science*, 19(2), pp. 97-104.
- Bollandsås, O.M. & Næsset, E., 2007. Estimating percentile-based diameter distributions in uneven-sized Norway spruce stands using airborne laser scanner data. *Scandinavian Journal of Forest Research*, 22, pp. 33-47.
- Borders, B.E., Souter, R.A., Bailey, R.L. & Ware, K.D., 1987. Percentile-based methods characterize forest stand tables. *Forest Science*, 33(2), pp. 570-576.

- Deville, J.-C. & Särndal, C.-E., 1992. Calibration estimators in survey sampling. *J. Am. Stat. Ass.* 87, pp. 376-382.
- Esseen, P.-A., Ehnström, B., Ericson, L. & Sjöberg, K., 1997. Boreal forests. *Ecological Bulletin*, 46, pp.16-47.
- Gobakken, T. & Næsset, E., 2004. Estimation of diameter and basal area distributions in coniferous forest by means of airborne laser scanner data. *Scandinavian Journal of Forest Research*, 19, pp. 529-542.
- Gobakken, T. & Næsset, E., 2005. Weibull and percentile models for lidar-based estimation of basal area distribution. *Scandinavian Journal of Forest Research*, 20, pp. 490-502.
- Gove, J. H. & Patil, G. P., 1998. Modeling basal area-size distribution of forest stands: a compatible approach. *Forest Science*, 44(2), pp. 285-297.
- Hafley, W.L. & Schreuder, H.T., 1977. Statistical distributions for fitting diameter and height data in even-aged stands. *Canadian Journal of Forest Research*, 7, pp. 481-487.
- Holmgren, J., 2004. Prediction of Tree Height, Basal Area and Stem Volume in Forest Stands Using Airborne Laser Scanning. *Scandinavian Journal of Forest Research*, 19, pp. 543-553.
- Hopkinson, C., Chasmer, L., Lim, K., Treitz, P. & Creed, I., 2006. Towards a universal lidar canopy height indicator. *Canadian Journal of Remote Sensing*, 32, pp. 139-152.
- Hyink, D.M. and Moser, J.W. Jr., 1983. A generalized framework for projecting forest yield and stand structure using diameter distributions. *Forest Science*, 29(1): 85-95.
- Hyypä, J., Kelle, O., Lehikoinen, M., & Inkinen, M., 2001. A segmentation-based method to retrieve stem volume estimates from 3-dimensional tree height models produced by laser scanner. *IEEE Transactions on geoscience and remote sensing*, 39, pp. 969-975.
- Kangas, A & Maltamo, M., 2000. Calibrating predicted diameter distribution with additional information. *Forest Science*, 46(3): 390-396.
- Knoebel, B.R. & Burkhart, H.E., 1991. A bivariate distribution approach to modeling forest diameter distribution at two points in time. *Biometrics*, 47(1), pp. 241-253.
- Laasasenaho, J. 1982. Taper curve and volume functions for pine, spruce and birch. *Communications Instituti Forestalis Fenniae*, 108, pp. 1-74.
- Lim, K., Treitz, P., Baldwin, K., Morrison, I. & Green J., 2003. Lidar remote sensing of biophysical properties of tolerant northern hardwood forests. *Canadian Journal of Remote Sensing*, 29, pp. 648-678.
- Loetsch, F., Zöhler, F. & Haller, K.E., 1973. *Forest inventory 2*. BLV Verlagsgesellschaft, Munic, Germany. 469 p.
- Magnussen, S., & Boudewyn, P., 1998. Derivations of stand heights from airborne laser scanner data with canopy-based quantile estimators. *Canadian Journal of Forest Research*, 28, pp. 1016-1031.
- Maltamo, M. & Kangas, A., 1998. Methods based on k-nearest neighbor regression in the prediction of basal area diameter distribution. *Canadian Journal of Forest Research*, 28, pp. 1107-1115.
- Maltamo, M., Eerikäinen, K., Pitkänen J., Hyypä, J. & Vehmas, M., 2004. Estimation of timber volume and stem density based on scanning laser altimetry and expected tree size distribution functions. *Remote Sensing of Environment*, 90, pp. 319-330.
- Maltamo, M., Eerikäinen, K., Packalén, P. & Hyypä, J., 2006. Estimation of stem volume using laser scanning based canopy height metrics. *Forestry*, 79, pp. 217-229.
- Maltamo, M., Suvanto, A. & Packalén, P., 2007. Comparison of basal area and stem frequency diameter distribution modelling using airborne laser scanner data and calibration estimation. *Forest Ecology and Management*, In press.
- Mehtätalo, L., 2005. Height-diameter models for Scots pine and birch in Finland. *Silva Fennica*. 39(1), pp. 55-66.
- Næsset, E., 1997. Estimating timber volume of forest stands using airborne laser scanner data. *Remote Sensing of Environment*, 51, pp. 246-253.
- Næsset, E., 2002. Predicting forest stand characteristics with airborne scanning laser using a practical two-stage procedure and field data. *Remote Sensing of Environment*, 80, pp. 88-99.
- Næsset, E., 2004. Practical large-scale forest stand inventory using a small airborne scanning laser. *Scandinavian Journal of Forest Research*, 19, pp. 164-179.
- Næsset, E., Gobakken, T., Holmgren, J., Hyypä, J., Hyypä, H., Maltamo, M., Nilsson, M., Olsson, H., Persson, Å. & Söderman, U., 2004. Laser scanning of forest resources: the Scandinavian experience. *Scandinavian Journal of Forest Research*, 19, pp. 482-499.
- Packalén, P. & Maltamo, M., 2007. The k-MSN method in the prediction of species specific stand attributes using airborne laser scanning and aerial photographs. *Remote Sensing of Environment*, 109, pp. 328-341.
- Persson, Å., Holmgren, J. & Söderman, U., 2002. Detecting and measuring individual trees using an airborne laser scanner. *Photogrammetric Engineering & Remote Sensing*, 68, pp. 925-932.
- R Development Core Team, 2006. R: A language and environment for statistical computing. R Foundation for Statistical Computing, Vienna, Austria. ISBN 3-900051-07-0, URL <http://www.R-project.org>.
- Suvanto, A., Maltamo, M., Packalén, P. & Kangas, J., 2005. Kuviokohtaisten puustotunnusten ennustaminen laserkeilauksella. *Metsätieteen aikakauskirja*, 4/2005, pp. 413-428. (In Finnish).

RAY TRACING FOR MODELING OF SMALL FOOTPRINT AIRBORNE LASER SCANNING RETURNS

Felix Morsdorf^a, Othmar Frey^a, Benjamin Koetz^b, Erich Meier^a

a) Remote Sensing Laboratories, Department of Geography, University of Zurich
email: felix.morsdorf, othmar.frey, erich.meier@geo.uzh.ch

b) ESA-ESRIN, Exploitation & Services Division, Project Section
email: Benjamin.Koetz@esa.int

Commission III, WG 3

ABSTRACT:

Airborne Laser Scanning (ALS) has been established as a valuable tool for the estimation of biophysical canopy variables, such as tree height and vegetation density. However, up to now most approaches are built upon empirical stand based methods for linking ALS data with the relevant canopy properties estimated by field work. These empirical methods mostly comprise regression models, where effects of site conditions and sensor configurations are contained in the models. Thus, these models are only valid for a specific study, which renders inter-comparison of different approaches difficult. Physically based approaches exist e.g. for the estimation of tree height and tree location, however systematic underestimation depending upon sampling and vegetation type remains an issue. Using a radiative transfer model that builds on the foundation of the Open-Source ray tracer povray we are simulating return signals for two ALS system settings (footprint size and laser wavelength). The tree crowns are represented by fractal models (L-systems), which explicitly resolve the position and orientation of single leaves. The model is validated using ALS data from an experiment with geometric reference targets. We were able to reproduce the effects of target size and target reflectance that were found in the real data with our modeling approach. A sensitivity study was carried out in order to determine the effect of properties such as beam divergence (0.5, 1, and 2 mrad), canopy reflectance (laser wavelength, 1064 and 1560 nm) on the ALS return statistics. Using the two laser wavelengths above, we were able to show that the laser wavelength will not significantly influence discrete return statistics in our model. It was found that first echo return statistics only differ significantly if the footprint size was altered by a factor of 4. Last return distributions were significantly different for all three modelled footprint sizes, and we were able to reproduce the effect of an increased number of ground returns for large footprint sizes. These forward simulations are a first step in the direction of physically based derivation of biophysical ALS data products and could improve the accuracy of the derived parameters by establishing correction terms.

1 INTRODUCTION

In recent years, Airborne Laser Scanning (ALS) was established as a valuable tool for the horizontal and vertical characterization of the vegetation canopy. A number of studies prove ALS to be capable of deriving canopy height, be it for stands [Lefsky et al., 1999; Means et al., 2000; Næsset and Bjerknes, 2001] or single trees [Hyypä et al., 2001; Persson et al., 2002; Morsdorf et al., 2004]. Furthermore, ALS was used to derive measures of vegetation density such as fractional cover (fCover) and/or leaf area index (LAI) [Harding et al., 2001; Lovell et al., 2003; Morsdorf et al., 2006b]. These approaches can be divided into two classes, empirical and physical methods. Tree height and crown width are mostly directly computed from either a gridded canopy height model (CHM) or the point cloud itself, making it a physical approach as e.g. the tree segmentation algorithm proposed by Morsdorf et al. [2004] (Figure 1). On the other hand approaches deriving fCover and LAI most often use regression models to link ground measurements with laser predictor variables, making it an empirical method.

These products comprise site and instrument specific properties, such as different sensor types, vegetation types and viewing geometry. This makes the comparison of results from different sites and sensor configurations hard, if not impossible. For instance, it is expected that laser wavelength and footprint size have an influence on the magnitude of these parameters. Some research has already been pointing in this direction. A study of Yu et al. [2004] showed that tree height underestimation was larger for higher flying heights (and consequently larger footprint size), as well as that fewer trees were detected the higher the flying altitude was. These results are backed (among others, e.g. Gaveau

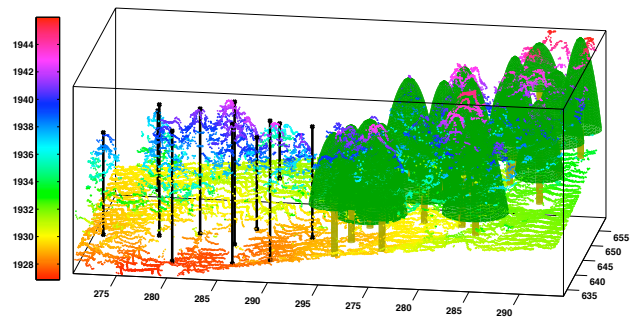


Figure 1: Illustration of physically based tree segmentation algorithm based on cluster analysis of raw data. For details see Morsdorf et al. [2004].

and Hill [2003]) by Morsdorf et al. [2006a], who showed that tree height underestimation in a mountain pine forest would increase by about 30 cm when changing the flight altitude from 500 m AGL to 900 m AGL. However, it remains unclear how much the lower sampling density or the larger footprint size contribute to this increase in tree height underestimation. As it is very hard to separate these effects in empirical studies such as the one of Morsdorf et al. [2006a], one has to find alternative solutions in retrieving information on the magnitude of these effects on biophysical parameter estimation. Modelling of laser returns using geometrical-optical models might help here. Such approaches have been carried out for large footprint data, where the tree crowns were represented by cones filled with a turbid medium [Sun and Ranson, 2000; Ni-Meister et al., 2001; Koetz

et al., 2006], but so far not for small-footprint ALS data. For small footprint data, the tree models need to be more complex and should explicitly resolve the tree structure at the leaf level, whereas for modeling large footprint data it was sufficient to spatially resolve the canopy at the crown level [Sun and Ranson, 2000]. In recent years, fractal models of tree geometry have been developed which resolve the tree geometry at the leaf level. These models are used for ecological studies as well as for producing realistically looking computer rendered images of vegetation. Thus, our objective is to use such fractal models of tree geometry and a commonly used ray-tracer to study the effect of footprint size and laser wavelength on ALS return distributions, which are the basis for most ALS based biophysical vegetation products. This approach should enable one to simulate individually the effects of acquisition properties such as incidence angle, point density, terrain slope, laser footprint size, laser wavelength and canopy reflectance on the accuracy of biophysical vegetation data products opposed to real-world scenarios, where all these effects contribute indifferently to differences between ground truth and ALS based estimations of biophysical parameters. A special challenge will be to model the sensor characteristics of the Toposys FALCON II system used for validation. This needs to be done, since we use discrete return data for validation, which is highly susceptible for the methods of echo detection applied by the system provider.

2 METHODS

2.1 Modeling of ALS data

2.1.1 Ray-tracing using povray Povray¹ is an open-source ray tracing software that is widely used in computer graphics for the visualization of scenes with arbitrary complex geometry. It has as well been used for scientific visualizations [Solenthaler et al., 2007], but so far not for simulating optical devices, except for optical benches. However, we believe that it might be used for the simulation of ALS return signals, since it allows for representing complex geometries as well as differences in object reflectance and transmission. Povray uses backward ray-tracing to infer whether a beam from a light-source is reflected from an object in a scene into the camera. The description of the scene including object, light and camera location and properties, is done using its own scene description language. A series of commands is written into include files (.inc) and is then parsed by the program. Povray allows for several lights and camera modes, we use a spotlight with a defined beam divergence resembling that of the Toposys instrument. Inside the beam, the energy distribution is not uniform, but of Gaussian shape. According to the system manufacturer, the beam divergence defines the point where the intensity of the beam has fallen off to $1/e$ of its peak (center) energy. The spotlight used in our simulations has been configured accordingly. An orthographic camera is used which is placed directly above the object. The spotlight distance was set to 500 meters, the incidence angle to zero degrees, and for each of the experiments the tree was sampled at a regular grid of 25 cm spacing in both x and y direction, summing up to about 1000 waveforms.

2.1.2 Constructing an ALS return signal We use a special version of povray, MegaPov², which additionally is able to write a depth image from the rendered scene based on the camera position. The resolution of the images was 400 by 400 pixels, resulting in a spatial resolution in the model domain of about 1.5 mm. A combination of the intensity image (povray's primary rendering product) with the depth image will then yield a *return*

waveform. This is achieved by summing up the pixels P for each range bin $R_i - R_{i+1}$ based on the depth image and multiplying it with the respective mean intensity \bar{I} from the intensity image according to Equation 1. This method is based on the assumption that the leaves are behaving in a lambertian manner.

$$\sigma(R_i, R_{i+1},) = 4 * \sum_{R_i}^{R_{i+1}} P * \bar{I}_{R_i}^{R_{i+1}} \quad (1)$$

This *waveform*, however, represents the range dependent description of the cross-section of the scattering elements in the path of the laser beam rather than the real return waveform of a laser pulse. For obtaining a real waveform, this cross-section still needs to be convoluted with a specific laser pulse [Wagner et al., 2006]. For the Toposys system (see Table 1), this pulse is Gaussian shaped and has a duration of 5 nanoseconds, which equivalents to 1.5 meter in range. Such a pulse is used for the simulations in this study. An illustration of the waveform generation process from the rendered images can be found in Figure 2.

Falcon II Specifications	
Maximum Range	1600 m
Range Resolution	2 cm
Scanning Angle	$\pm 7.15^\circ$
Line-scan Frequency	653 Hz
Pulse Frequency	83 kHz
Laser Wavelength	1560 nm
Number of Fibers	127
Beam Divergence	1 mrad
Pulse length	5 ns

Table 1: Specifications of Falcon II Sensor Platform

2.1.3 Converting the waveform to discrete return data Since most of the currently available ALS systems are discrete return systems, which do not record the full waveform, but trigger distinct echos in real time from the return signal, we had to simulate this feature as well. For detecting discrete returns from the modelled waveform, we use a Gaussian decomposition as proposed by e.g. Wagner et al. [2006] or Hofton et al. [2000]. This Gaussian decomposition will as well have the advantage of describing the physically meaningful cross-section of the scatterer opposed to plain echo locations in the range dimension. The algorithm we implemented first detects local maxima's from a smoothed version of the return waveform. The location of these maxima's is then used to fit Gaussian functions to the waveform using non-linear least squares regression. An illustration of the decomposition process can be found in Figure 3. From the reconstructed waveform, adaptive thresholding is used to detect first and last returns as is done for most time-of-flight based LIDAR systems. The height of the threshold is adapted to the maximum intensity of each peak to avoid trigger walk. Using a constant threshold would produce range errors for peaks of different intensity, even if they are at the same location in the range dimension.

2.1.4 Validation For simulating discrete ALS return data, we faced two challenges. One was the modeling of the return signal (the full waveform) itself and the other was to model the sensor and detector characteristics correctly. For the latter, we were able to use ALS data from an experiment with geometric reference targets on an airstrip close to Zürich. This study was published as Wotruba et al. [2005] and dealt with determining the effects of target size and reflectivity on echo detection and echo separation. We used this data to qualitatively validate our approach by comparing modeled and measured point clouds and studying the effect of target size and reflectance on the echo distribution.

¹www.povray.org

²http://megapov.inetart.net/

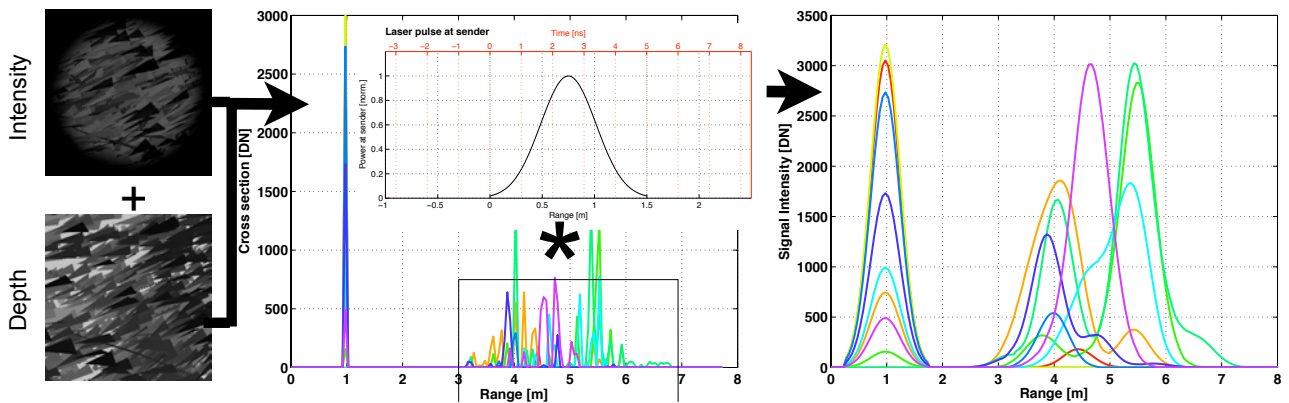


Figure 2: Illustration of waveform generation process based on intensity and depth image and using convolution (denoted by asterisk in middle panel) with a laser pulse of 5 nanoseconds length.

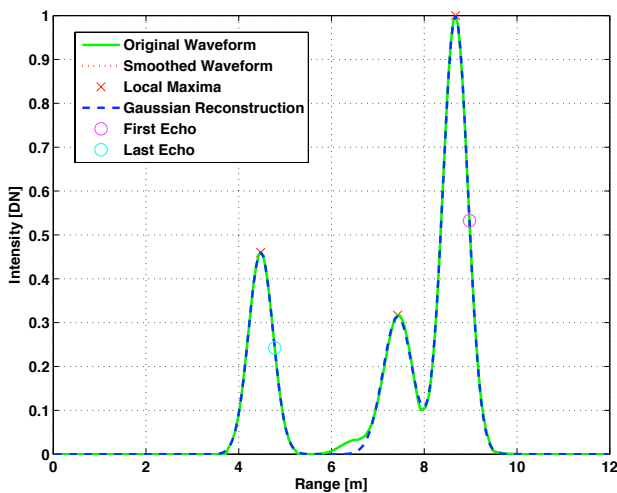


Figure 3: Illustration of Gaussian decomposition for triggering of first and last returns.

In Figure 4 point clouds both from modeled and real data are displayed, the targets consisted of slats of different width and reflectance's. Reflectance values were measured using an ASD field-spec and assigned to the scene description in povray, which as well contained the explicit geometry of the targets. The modeled scene was sampled at exactly the same location as the real data, based on the location of the real echo locations. In order to obtain this modeled echo distribution, we needed to emulate noise in the echo detection process, which will lead to small peaks in the return signal not being detected. We used a simple intensity threshold to eliminate peaks that are too small to be detected. Doing so, we were able to reproduce the *measured* thicknesses of the slats, which is a function of slat width and slat reflectance in conjunction with the characteristics of the detection methodology. We were able to reproduce the effect of target reflectivity of the dark slats in the modeled data. A slat being 5cm wide, and white (third from right in Fig. 4, ρ at 1560 nm : 0.52) will trigger more returns than a black one with a reflectance of only 0.02 (right most in Fig. 4). For more details regarding the experiments on the airstrip, please refer to Wotruba et al. [2005].

2.2 Simulating effects of ALS system specification

Two parameters which are supposed to severely influence ALS return statistics are the footprint size, that is the size of the illu-

minated area on the earth's surface and the different laser wavelengths used in ALS systems. The footprint size depends on beam divergence γ and flight altitude h (and in some cases the aperture D of the transmitter/receiver optics):

$$A = D + 2h \tan\left(\frac{\gamma}{2}\right) \quad (2)$$

Since D can be neglected in most cases, and γ is generally very small, Equation 2 can be rewritten to:

$$A = h * \gamma \quad (3)$$

It is known that the size of the footprint alters the ability of the laser pulse to penetrate vegetation [Nilsson, 1996; Chasmer et al., 2006]. The smaller the footprint is, the larger is the chance of not receiving a last echo from the ground in denser vegetation. Thus, for systems recording first and last echo, the penetration of vegetation will in fact be better for systems using larger footprints [Schnadt and Katzenbeisser, 2004]. We will alter the footprint size with the factors of 0.5 and 2, which yields three footprint sizes in total together with the nominal footprint size of the Toposys FALCON II system. The other effect we wanted to study is the effect of using different laser wavelengths. Two commonly used wavelengths are 1064 (e.g. Optech ALTM series) and 1560 nm (e.g. Toposys and Riegl systems), and when one studies spectra of canopy elements, one will find large differences in reflectance for these two wavelengths (see Table 2).

	Reflectance		Transmission	
	1064 nm	1560 nm	1064 nm	1560 nm
Bark	0.172	0.365	0	0
Leaf	0.559	0.217	0.188	0.033
Understory	0.332	0.152	0	0

Table 2: Spectral properties of canopy elements for two laser wavelengths.

How sensitive the return statistics are in respect to laser wavelength is yet not known. Thus, we construct two different pine trees for both 1064 nm and 1560 nm wavelength and sample those in the same way as we did for the footprint diameter analysis. The trees are constructed being *gray scale* as we use for all three of R,G,B the same values of reflectance at the particular wavelength, as they are displayed in Table 2.

2.2.1 Fractal models of tree geometry Fractal models (also known as L-systems) have a long tradition in computer graphics

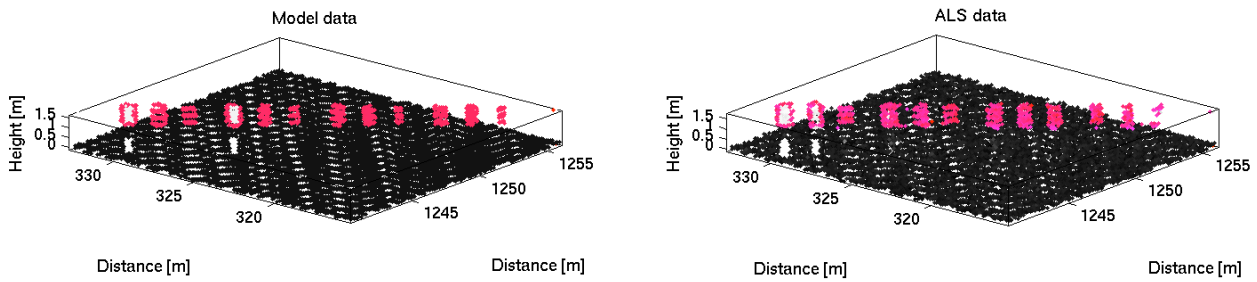


Figure 4: Real ALS data for slats target (right) and modeled data (left). The slats are grouped in 4 colors, with three different widths (15,10 and 5 cm from left to right). The white slats are left, the black ones right. Note the difference in sampled width due to both difference in reflectance and difference in actual width.



Figure 5: Rendered image of modelled pine tree.

for the generation of realistically looking plants. Several Open-Source tools exist which can produce such models for the use in rendering software such as povray. One of these tools, namely Tomtree³ will be used in this study. A pine tree constructed of the canopy elements leaf and bark is virtually planted on a horizontal patch of soil. These three scene elements (bark, leaf and understory) are assigned with reflectance's and transmissions according to model output of a model for leaf optical properties (PROSPECT, Jacquemoud and Baret [1990]) and ASD field-spec⁴ measurements. These values are displayed in Table 2. A side-view rendering of the pine tree used in this study is displayed in Figure 5. The leafs are represented by simple triangles, which are rotated randomly around their elongated axis.

3 RESULTS

3.1 Full waveform

The results for full waveform data are depicted in Fig. 7. The waveforms are averaged from the single simulations and not treated for first and last echo detection as in the previous section, and

³www.aust-manufaktur.de/austtx.html

⁴www.asdi.com

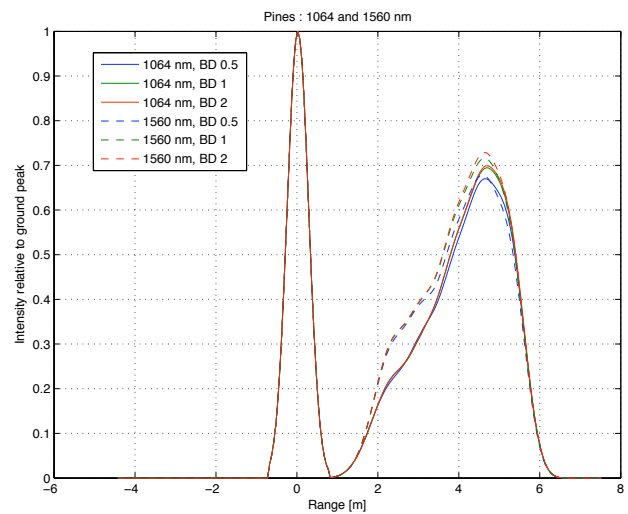


Figure 7: Averaged waveforms for two wavelengths and three footprint sizes.

thus resemble a height distribution that are being used for e.g. biomass estimation. The different waveforms have been normalized to their ground return, in order to visualize relative differences in the canopy part of the waveforms. We can do this here, since we know that exactly the same area containing the same object has been sampled in our modeling study. In a real world application, normalizing waveforms with the ground peak would not be suitable. For different footprint size, only little (and not significant) differences of about 3 to 5 % in the magnitude of the canopy maximum can be observed. However, for different wavelengths, a significant increase of return energy (about 25 %) below the canopy maximum at about 4.5 m can be observed. The mean energy of the vegetation peak does not significantly change between laser wavelengths of 1064 and 1560 nm. Thus, except for a difference in total energy not shown here (due to normalizing of waveforms), the only significant difference in waveforms is between the 1064 and 1560 nm laser wavelength.

3.2 Discrete returns

In Table 3 the mean height differences of the discrete return statistics for different footprint size are depicted. Bold values indicate that first or last echo distributions are significantly differing from each other based on a two sided Kolmogorov-Smirnow test. First echo statistics are lower on average for large footprint sizes, with this effect being in the order of almost 20 cm, when comparing the returns for 0.5 and 2 mrad beam divergence. For these two

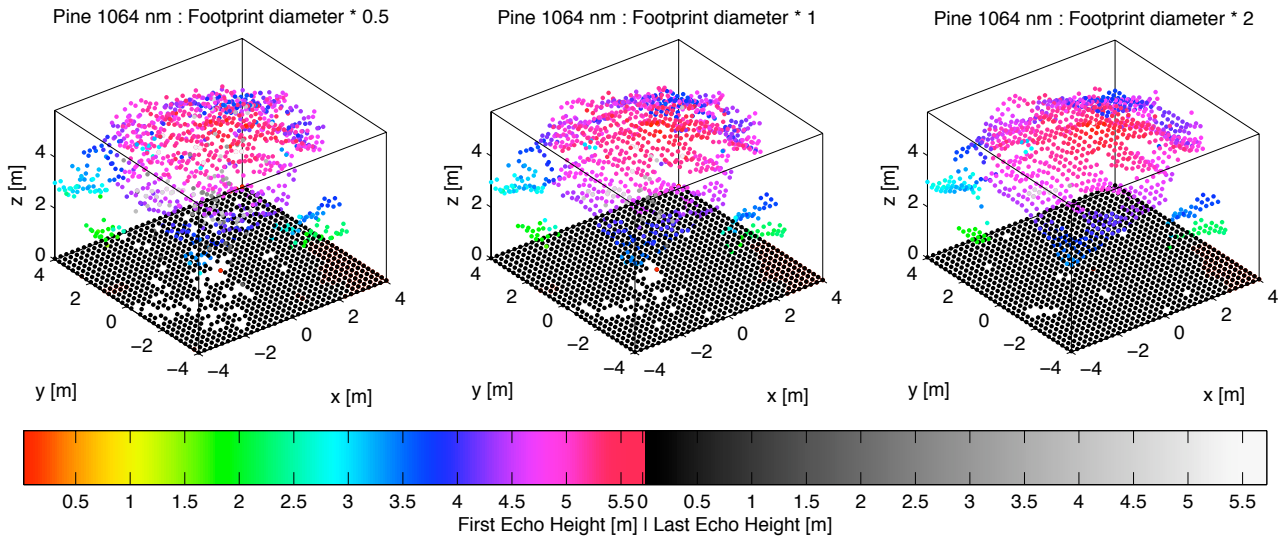


Figure 6: First and last echo distribution inside modelled tree for three different footprint sizes. Note the increased number of ground returns and the smoothing effect due to increase in footprint size.

beam divergences, the difference in first echo distributions is significant. For smaller differences (factor 2) of beam divergence the mean height difference of the first return statistics is not significant. However, last echo distributions are more affected by differences in footprint, as for all three combinations of footprint sizes the distributions are significantly different. Furthermore, a systematic height difference exist when comparing the different footprint sizes. Opposed to first echo statistics, for last echo a positive difference is found when comparing distributions gathered from smaller footprint with those of larger footprints. Thus, one can state that for larger footprint diameters, last echo distribution will be biased upwards. Changing the laser wavelength from 1064 to 1560 nm did not produce significantly different return statistics, neither for first nor for last echo. Thus, these results are not included in Table 3.

Height difference of return statistics [cm]			
Returns Beam diverg. [mrad].	0.5/1	1/2	0.5/2
First echo @ 1064 nm	-10	-6.7	-17
First echo @ 1560 nm	-9.6	-5.3	-15.2
Last echo @ 1064 nm	19.3	10.1	29.5
Last echo @ 1560 nm	18.7	9.3	28.4

Table 3: Mean height differences in return statistics comparing different footprint diameters. Bold values denote significantly different echo distributions

4 DISCUSSION AND CONCLUSIONS

Using povray and fractal models of tree geometry, we were able to study the effect of two ALS sensor settings on both discrete return statistics and the full return waveform. The model was validated using discrete return data from an experiment on an airstrip, where geometric targets where used to infer information on the effect of target size and reflectance on target visibility. We were able to reproduce the distribution of real data with our model, and could demonstrate that it is sensitive not only for the geometric structure of the modelled objects, but as well for differences in object reflectance. In a sensitivity analysis using a modelled pine tree, we tested the impact of footprint size and laser wavelength on two types of return statistics, discrete return and full waveform. For discrete return data, the return distribution of both first

and last echo do not significantly change in respect to the two laser wavelengths used in this study. For first echo data, the effect of altering footprint size is only significant when changing the footprint diameter by a factor of 4, otherwise the difference of return statistics is not significant. For the last echo statistic, however, even smaller changes in footprint size lead to significantly different return statistics. Furthermore, our results were in conjunction with the statement from Schnadt and Katzenbeisser [2004], showing an increasing number of ground returns when footprint size was increased. First echo distributions will be biased towards the ground, when increasing the footprint size, in the order of some decimeters for our modelled tree. This effect could partly explain the observed increase in tree height underestimation, as was found by Morsdorf et al. [2006a] or Gaveau and Hill [2003], which was in the order of about 30 cm for doubling the flying altitude (and thus the footprint size). Another finding from Morsdorf et al. [2006a] was that there are more last echos triggered inside the canopy for higher flying altitudes. This was said to be related to illumination issues due to the larger footprint, and our modeling results back this behavior to some extent by the observed positive bias in last echo return statistics for larger footprint sizes. In our simulations, first echo data seems to represent an outer hull of the tree crown and does not penetrate deeper into the canopy. This effect was as well observed by Chasmer et al. [2006] in real data, and it might explain why it can be hard to derive canopy density metrics from first echo data alone. For the full waveform, the lower part of the canopy seems to contribute more energy to the return signal at 1560 nm than for 1064 nm laser wavelength. This could be explained by the significantly higher reflectance of leaves at 1064 nm. The canopy elements higher in canopy would already scatter back a large part of the energy of the laser pulse, which in turn would not be available for illuminating the lower part of the canopy.

These forward simulations are a first step in the direction of physically based derivation of biophysical ALS data products and could improve the accuracy of the derived parameters by establishing correction terms for different sensor settings. The model presented in this work can be further used to study the effect of point density, sampling distribution and scanning angle on various canopy types. However, the model might need ecologically calibrated fractal tree models (e.g. AMAP, Castel et al. [2001]) and needs to be validated not only for geometric reference tar-

gets, but as well using real world trees. This will be a difficult task and will most likely be accomplished by incorporating terrestrial laser scanning data. Such modelling will become increasingly important with the availability of small-footprint full waveform data, which needs to be interpreted in a meaningful way. If one knows how much ALS system settings contribute to differences in these waveforms, it should be easier to derive accurate descriptions of biophysical parameters from this highly anticipated data, which might provide an even more detailed insight into the vertical structure of vegetation than discrete return data ever could.

5 ACKNOWLEDGMENTS

This research was funded by the research credit of the University of Zürich.

References

- Castel, T., Beaudoin, A., Floury, N., Toan, T. L., Caraglio, Y. and Barczy, J., 2001. Deriving forest canopy parameters for backscatter models using the amap architectural plant model. *IEEE Transactions on Geoscience and Remote Sensing* 39(3), pp. 571–583.
- Chasmer, L., Hopkinson, C. and Treitz, P., 2006. Investigating laser pulse penetration through a conifer canopy by integrating airborne and terrestrial lidar. *Canadian Journal of Remote Sensing* 32(2), pp. 116–125.
- Gaveau, D. and Hill, R., 2003. Quantifying canopy height underestimation by laser pulse penetration in small-footprint airborne laser scanning data. *Canadian Journal of Remote Sensing* 29, pp. 650–657.
- Harding, D., Lefsky, M., Parker, G. and Blair, J., 2001. Laser altimeter canopy height profiles: Methods and validation for closed-canopy, broadleaf forests. *Remote Sensing of Environment* 76, pp. 283–297.
- Hofton, M. A., Minster, J. B. and Blair, J. B., 2000. Decomposition of laser altimeter waveforms. *IEEE Transactions on Geoscience and Remote Sensing* 38, pp. 1989–1996.
- Hyypä, J., Kelle, O., Lehtikainen, M. and Inkinen, M., 2001. A segmentation-based method to retrieve stem volume estimates from 3-d tree height models produced by laser scanners. *IEEE Transactions on Geoscience and Remote Sensing* 39, pp. 969–975.
- Jacquemoud, S. and Baret, F., 1990. Prospect: A model of leaf optical properties spectra. *Remote Sensing of Environment* 34(2), pp. 75–91.
- Koetz, B., Morsdorf, F., Sun, G., Ranson, K. J., Itten, K. and Allgower, B., 2006. Inversion of a lidar waveform model for forest biophysical parameter estimation. *IEEE Geoscience and Remote Sensing Letters* 3, pp. 49–53.
- Lefsky, M. A., Cohen, W. B., Acker, S. A., Parker, G. G., Spies, T. A. and Harding, D., 1999. Lidar remote sensing of the canopy structure and biophysical properties of douglas-fir western hemlock forests. *Remote Sens. Environ.* 70, pp. 339–361.
- Lovell, J., Jupp, D., Culvenor, D. and Coops, N., 2003. Using airborne and ground-based ranging lidar to measure canopy structure in Australian forests. *Canadian Journal of Remote Sensing* 29(5), pp. 607–622.
- Means, J. E., Acker, S. A., Fitt, B. J., Renslow, M., Emerson, L. and Hendrix, C., 2000. Predicting forest stand characteristics with airborne scanning lidar. *Photogrammetric Engineering & Remote Sensing* 66(11), pp. 1367–1371.
- Morsdorf, F., Frey, O., Meier, E., Itten, K. and Allgöwer, B., 2006a. Assessment on the influence of flying height and scan angle on biophysical vegetation products derived from airborne laser scanning. In: *3d Remote Sensing in Forestry*, 14–15. Feb. 2006, Vienna, Austria.
- Morsdorf, F., Kotz, B., Meier, E., Itten, K. and Allgower, B., 2006b. Estimation of LAI and fractional cover from small footprint airborne laser scanning data based on gap fraction. *Remote Sensing of Environment* 104(1), pp. 50–61.
- Morsdorf, F., Meier, E., Kötz, B., Itten, K. I., Dobbertin, M. and Allgöwer, B., 2004. Lidar-based geometric reconstruction of boreal type forest stands at single tree level for forest and wildland fire management. *Remote Sensing of Environment* 3(92), pp. 353–362.
- Næsset, E. and Bjercknes, K.-O., 2001. Estimating tree heights and number of stems in young forest stands using airborne laser scanner data. *Remote Sensing of Environment* 78(3), pp. 328–340.
- Ni-Meister, W., Jupp, D. L. B. and Dubayah, R., 2001. Modeling lidar waveforms in heterogeneous and discrete canopies. *IEEE Transactions on Geoscience and Remote Sensing* 39(9), pp. 1943–1958.
- Nilsson, M., 1996. Estimation of tree heights and stand volume using an airborne lidar system. *Remote Sensing of Environment* 56, pp. 1–7.
- Persson, A., Holmgren, J. and Söderman, U., 2002. Detecting and measuring individual trees using an airborne laser scanner. *Photogrammetric Engineering & Remote Sensing* 68(9), pp. 925–932.
- Schnadt, K. and Katzenbeisser, R., 2004. Unique airborne fiber scanner technique for application-oriented lidar products. *International Archives of Photogrammetry and Remote Sensing* XXXVI - 8/W2, pp. 19–23.
- Solenthaler, B., Schäfli, J. and Pajarola, R., 2007. A unified particle model for fluid-solid interactions. *Computer Animation and Virtual Worlds* 18(1), pp. 69–82.
- Sun, G. and Ranson, K., 2000. Modeling lidar returns from forest canopies. *IEEE Transactions on Geoscience and Remote Sensing* 38(6), pp. 2617–2626.
- Wagner, W., Ullrich, A., Ducic, V., Melzer, T. and Studnicka, N., 2006. Gaussian decomposition and calibration of a novel small-footprint full-waveform digitising airborne laser scanner. *ISPRS Journal of Photogrammetry and Remote Sensing* 60(2), pp. 100–112.
- Wotruba, L., Morsdorf, F., Meier, E. and Nüesch, D., 2005. Assessment of sensor characteristics of an airborne laser scanner using geometric reference targets. *International Archives of Photogrammetry and Remote Sensing* XXXVI(3/W19), pp. 1–6.
- Yu, X., Hyypä, J., Kaartinen, H. and Maltamo, M., 2004. Automatic detection of harvested trees and determination of forest growth using airborne laser scanning. *Remote Sensing of Environment* 90, pp. 451–462.

UTILIZING AIRBORNE LASER INTENSITY FOR TREE SPECIES CLASSIFICATION

H. O. Ørka, E. Næsset, O. M. Bollandsås

Dept. of Ecology and Natural Resource Management, Norwegian University of Life Sciences, P.O. Box 5003, N-1432 Ås, Norway – (hans-ole.orka, erik.naesset, ole.martin.bollandsas@umb.no)

KEY WORDS: Laser scanning, High resolution, Forest, Inventory, Analysis, Classification

ABSTRACT:

High-resolution datasets from Airborne Laser Scanning (ALS) provide information to extract the outline of single tree crowns. Laser echoes with spatial coordinates inside these single-tree crowns give the ability of measuring biophysical properties and to classify species of these single-trees. Species classification by ALS-data is based on differences in crown shape, crown density, reflectivity and distribution of foliage and branches between tree species. All of these parameters may be expressed by spatial coordinates of the point cloud or by the intensity of the backscattered signal measured by ALS. In this study we investigate mean intensity and standard deviation of intensity computed for single trees by explorative data analysis and linear discriminant analysis. We explore differences in spruce, birch, and aspen trees for different echo categories from a multiple return ALS system. We found that intensity could assist species discrimination. The overall classification accuracies obtained were from 68 to 74 %, depending on number of variables considered. In spite of the heterogeneous structure of the forest studied, the classification accuracy was fairly high. Intensity metrics computed from different echo categories influence overall accuracies by 3 to 4 %, depending on the intensity metric used in the classification. Both species reflectivity and structural characteristics within the tree crown will influence intensity recorded by ALS.

1. INTRODUCTION

In the past two decades, the capabilities of Airborne Laser Scanning (ALS) in forest structural assessment have been documented in a many research studies as well as in operational inventories. Today, ALS-sensors provide high-resolution datasets with 5-10 points per square meter. From these high-density datasets single trees can be extracted and measured (e.g. Persson et al. 2002; Morsdorf et al. 2004; Solberg et al. 2006). The distribution of laser echoes in a tree is a result of crown shape, crown density, distribution of foliage mass and branches, surface reflectivity, etc. Since many of these parameters may represent distinct characteristic of different tree species, ALS have been proposed and tested to support single-tree species classification. In addition to the distribution of the spatial coordinates x , y , and z for the returned echoes, most proprietary airborne lasers are also capable of measuring the reflectivity of the surface hit by the laser pulses. The reflectivity measured by pulse lasers represents the intensity of the maximum energy of the returned echo (Wehr and Lohr 1999). This intensity recorded by ALS could also assist tree species classification if species are separable in the spectral domain at the wavelength emitted by the laser (e.g. 1064 nm). Already in 1985, Schreier et al. (1985) found that the mean reflection and reflection variability measured by a airborne laser system could be used to differentiate between coniferous and deciduous trees. Later, intensity metrics derived from ALS have been used in tree species classification studies in boreal conifer forest in Scandinavia (Holmgren and Persson 2004), North American deciduous forest (Brandtberg et al. 2003; Brandtberg 2007), and sub-tropical Australian forest (Moffiet et al. 2005). In some of these classification studies the echo categories, i.e., first and last echoes, are treated separately, in other studies echo categories are joined together. However, combining all echo categories are not recommended because separate echo categories may play an important role in achieving better total classification accuracies (Brandtberg 2007). As use of ALS

systems capable of record multiple echoes become more common, knowledge of intensity behavior of different echo categories will be important in further species classification studies. The objectives of the present study were to characterize and analyze ALS-derived intensity metrics for (1) different tree species and 2) for different echo categories, and 3) to test and report classification performance of ALS-derived intensity metrics in a heterogeneous boreal forest.

2. MATERIAL

2.1 Study area

The study area is located in the Østmarka natural reserve, in southeastern Norway (59°50'N, 11°02'E, 190-370 m a.s.l.). The area has not been logged or managed over the last 60 years. Today the forest appears with large within-stand variation of tree ages and tree sizes. The dominating species are Norway spruce (*Picea abies* L.) and Scots Pine (*Pinus silvestris* L.). In addition, deciduous species, mainly Birch (*Betula ssp.*) and Aspen (*Populus tremula* L.), are found scattered in the landscape.

2.2 Field data

The field inventory was carried out during summer 2003 on 20 sample plots of size 0.1 ha. The sample plots were located in the spruce-dominated areas. Polar coordinates relative to plot center of all trees with diameter at breast height greater than 3 cm were registered. Plot center coordinates were determined by differential Global Navigation Satellite Systems (GNSS). On each plot, sample trees were selected according to two different sampling schemes. First, eight trees were selected by choosing the first dominant tree in each cardinal direction and the nearest tree to each of the four dominant ones. Second, all deciduous trees on the plot and some deciduous trees just outside the plot were selected. This was done to increase the

number of deciduous trees in the sample. On sample trees height, diameter in breast height, and crown radius were measured. Crown radius was determined as the mean of the radii measured in the four cardinal directions. Further details about the field work and the georeferencing procedures can be found in Solberg et al. (2006) and Bollandsås and Næsset (2007).

2.3 Airborne laser scanner data

ALS-data used in this study were acquired 18 June 2005 with the Optech ALTM 3100 sensor. Table 1 provides information about laser scanner settings planned for the acquisition. The initial processing of laser data was accomplished by the contractor (Blom Geomatics, Norway). First, all echoes outside a half scan angle of 8 degrees were deleted. Ground points were classified using the Terrascan software (Anon. 2004) and the ground-classified points were used to build a Triangular Irregular Network (TIN) terrain model. The TIN heights were then subtracted for each laser echo to produce height above the ground surface. Furthermore, all echoes with height less than 1.3 m were deleted from the dataset. In previous studies, this Ground Threshold Value (GTV) has typically been set to 2 m (Nilsson 1996; Næsset 2002, 2004). The choice of 1.3 m as GTV is based on the requirement of consistency with other measurements on the trees. For example, stem diameter and age are usually measured at breast height (1.3 m). In this multi-layered forest, we also wanted to keep as much information about small trees as possible and for that reason we did not want to exclude tall under-vegetation.

Parameters	
Flying altitude AGL (m)	750
Pulse repetition frequency (Hz)	100000
Scanner frequency (Hz)	70
Half scan angle (deg.)	10
Flying speed (m/s)	75
Swath (m)	264
pt/m ²	5.09
Beam divergence (mrad)	0.26

Table 1. Planned laser scanner settings for data acquisition

The elapsed time between field measurements and ALS data acquisition represented two years of growth. The forest in the nature reserve is in general old and little growth is seen. Hence, the field measurements were not adjusted for growth.

The Optech ALTM 3100 sensor is a multiple return system capable of recording up to four echoes per pulse. Older systems (e.g. Optech ALTM 1233) record two echoes for each pulse, i.e., first and last echoes. The number of echoes recorded by the ALTM 3100 depends on the returned energy of the laser pulses and the vertical resolution, i.e., the minimum distance between separate echoes. For the ALTM 3100, the vertical resolution is 2.1 m between the two first returns and 3.8 m for the other returns. If four returns are detected the sensor label them as “first echo of many”, “second echo”, “third echo” and “last echo”. If only two echoes are identified, these are labeled “first echo of many” and “last echo”. If three echoes are recorded, these are labeled “first echo of many”, “second echo” and “last echo”. If only one significant return is identified, this is labeled as an “only echo”. In this study, the ALS data were delivered by the contractor to be as close as possible to the structure of data provided by the old ALTM 1233 sensor. This

was done by combining “first echoes of many” and “only echoes” in one dataset and “last echoes” and “only echoes” in another dataset. The reason for this was to be able to compare the two different sensors, i.e., the ALTM 1233 and 3100 instruments. However, in this particular study we split the dataset into the original echo categories, i.e., “first echoes of many”, “last echoes”, and “only echoes”. We did this by extracting and labeling echoes with the same spatial coordinates in the two datasets as “only echoes” and deleting them from the two original datasets. These three echo categories were used in our analysis and for short they are denoted “first”, “only” and “last” echoes.

3. METHODS

In this study, no single-tree detection based on the ALS-data was carried out. Instead we buffered the field-derived tree stem positions with the mean crown radius. Laser echoes inside these circular crown segments were then tied to the buffered tree. The forest in the nature reserve is partly multi-layered and in case of overlapping tree crowns echoes were tied to the tallest tree.

For each tree we computed the mean intensity (MI) and the standard deviation of intensity (SDI) based on the laser point cloud. These two metrics are selected for this study because they are the most frequently used in other single-tree species classification studies (Schreier et al. 1985; Brandtberg et al. 2003; Holmgren and Persson 2004; Moffiet et al. 2005; Brandtberg 2007). These two intensity metrics were computed for each echo category. In total, six variables were therefore derived. In this paper, the last character of the variable name represents the echo category, i.e., F=first, O=only and L=last. For example, mean intensity of first echoes of many are denoted MIF, mean intensity of only echoes MIO, etc. To be able to calculate the SDI at least two echoes are needed. Thus, in order to have a consistent dataset without missing values, all trees hit by less than two echoes in an echo category were discarded from further analysis. In addition, only Norway spruce (S), birch (B), and aspen (A) trees were considered.

Explorative data analysis was performed using graphical methods by means of box-and-whisker plots (Tukey 1977; Anon. 2006). The box-and-whisker plot will give an overview of the data showing first and third quartile as the box (“hinges”), the median as the horizontal line dividing the box and extreme values as points outside the “whisker” defined as:

$$\pm 1.58 \frac{IQR}{\sqrt{n}} \quad (1)$$

where n = number of observations

IQR = Inter Quartile Range (i.e. difference between first and third quartiles)

In addition to this graphical representation of summary statistics, we explored relationships between intensity metrics by computing Pearson correlation coefficients. We also carried out a Principal Component Analysis (PCA) to explore and visualize variance in all computed metrics. The PCA calculation was done by a singular value decomposition of the centered data matrix.

The investigation of classification performance was conducted with Linear Discriminant Analysis (LDA). LDA was carried out using equal prior probabilities and leave-one-out cross validation by *lda* function of the R-package MASS (Venables and Ripley 2002). Classification was tested for all variables on independent basis. Overall accuracy was calculated as the percent trees correctly classified over total number of trees in the analysis. Then two to six (all) variables were combined and the combination(s) with the highest overall accuracy were selected. These overall accuracies are reported in Table 4. An error matrix for the combination of variables that produced the highest overall accuracy is also reported (Table 5).

4. RESULTS

Of the 260 field measured trees a total of 224 trees were of the tree species considered and hit by at least three echoes of each category and included in the analysis. Summary statistics of trees used in analysis appear in Table 2.

	Spruce	Birch	Aspen
Number of trees	133	70	21
Tree height (m)	23.1 (4.7)	18.6 (4.2)	23.8 (3.9)
Stem diameter (cm)	31.7 (8.3)	22.8 (7.5)	33.4 (8.3)
Crown radius (m)	1.78 (0.46)	2.02 (0.56)	2.51 (0.81)

Table 2. Mean values and standard deviations (in parenthesis) of field measured trees used the in analysis.

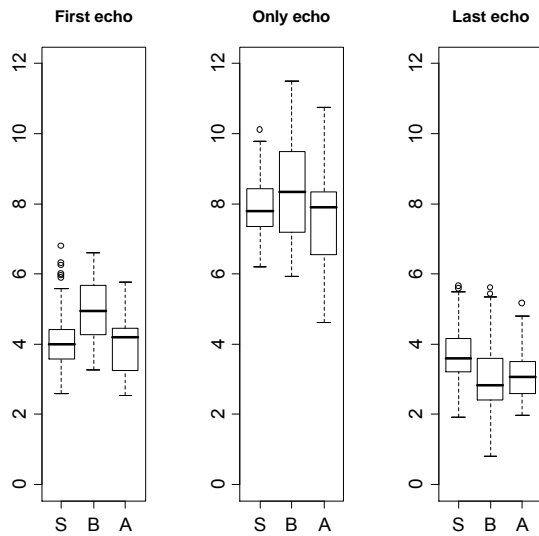


Figure 1. Mean intensity for different echo categories and tree species

Explorative data analysis by means of box-and-whisker plot of MI and SDI provides an overview of the variables (Figures 1 and 2).

The correlation matrix of intensity-derived metrics (Table 3) unveiled two relationships, i.e., (1) a positive correlation between MI and SDI in each echo category and (2) a positive correlation between metrics computed from first echoes and only echoes. Correlations between first and only echoes are found between MI and SDI computed from these echoes and between

MIO and SDIF. All correlations in the matrix are stronger for birch and aspen compared to spruce when correlation analyses were performed on subsets containing separate tree species.

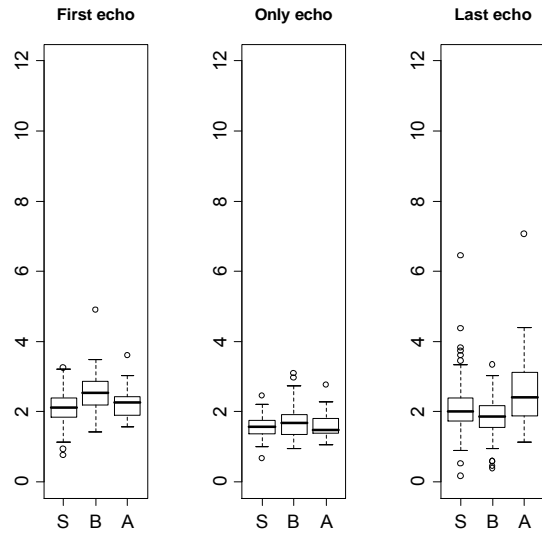


Figure 2. Standard deviation of intensity for different echo categories and tree species

	MIF	MIO	MIS	SDIF	SDIO	SDIS
MIF	1.00					
MIO	0.57	1.00				
MIS	-0.17	0.13	1.00			
SDIF	0.44	0.59	0.02	1.00		
SDIO	0.29	0.47	0.06	0.45	1.00	
SDIS	-0.08	0.01	0.42	0.11	0.14	1.00

Table 3. Correlations between intensity metrics

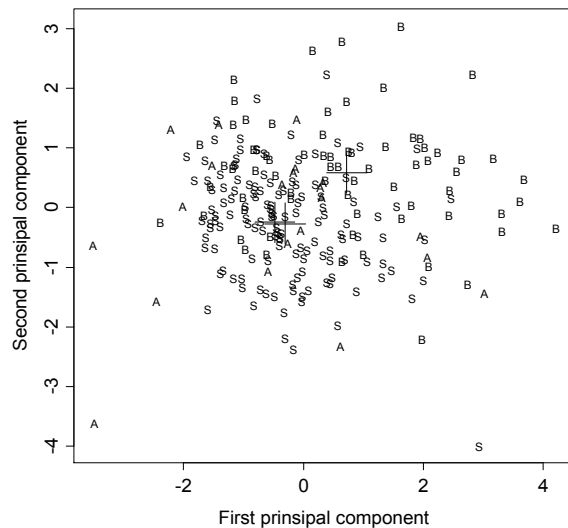


Figure 3. PCA score plot of first and second principal component. Class centers indicated by crosses.

The two first components of the PCA explained 73 % of the variation in intensity-derived metrics whereas the first component explained 46 % only. The score plot of the two first components is displayed in Figure 3 labeled with tree species.

LDA classification was performed both by using only one variable at a time and for combinations of variables (Table 4). The best classification obtained included mean intensity for first and last echoes and standard deviation of intensity for all echo categories. The error matrix (Table 5) for this classification provided an overall accuracy of 74.1 % and a *Kappa* coefficient of 0.49. The classification accuracies for the single species were 87.2 % for spruce, 64.3 % for birch and 23.8 % for aspen.

Combination of intensity metrics	Overall accuracy (%)
MIF	68.3
MIO	65.2
MIS	66.5
SDIF	64.3
SDIO	62.5
SDIS	60.3
MIF, MIS	71.4
MIF, MIS, SDIF	72.8
MIF, MIS, SDIO	72.8
MIF, MIS, SDIF, SDIS	73.7
MIF, MIS, SDIF, SDIO	73.7
MIF, MIS, SDIF, SDIO, SDIS	74.1
All intensity metrics	73.2

Table 4. Overall accuracy of species classification for different combinations of laser intensity metrics

Classification	Field reference		
	Spruce	Birch	Aspen
Spruce	116	25	12
Birch	13	45	4
Aspen	4	0	5

Table 5. Error matrix for tree species classification

5. DISCUSSION

The distribution of trees on different species and size classes in the natural reserve is different from what we will find in a managed forest. The structure of the forest limits the number of deciduous trees. The birch trees in this study are also somewhat smaller than the spruce trees and the aspen trees are in general large and old with tick branches that dominates the crown. However, our goal was to get some basic experience with intensity metrics for three species discrimination and for this purpose we found the data relevant.

In the box-and-whisker plots, the most pronounced pattern is the higher values of mean intensity of only echoes (Figure 1). The mean intensities of only echoes are about the size of the sum of first and last echoes. This is reasonable size only echoes are recorded when there is not enough energy to produce a second return (or vertical distance is too short). However, both first and only echoes should be returned from the same canopy surface. The difference in intensity from these echoes indicates that they have different origins not only depending on species reflectivity. Thus, it seems that laser intensity is a result of other tree characteristics than the species-specific reflectivity (Moffiet et al. 2005). It is therefore likely that only echoes are returned from denser parts of the tree like the stem or thick branches. However, the observed differences between echo categories are important and indicate that treating different

echoes separately in species classification may provide more information than combining them.

The box-and-whisker plots (Figures 1 and 2) indicate that the differences between tree species are relatively small. The median values of each species are in general between the first and third quartile of the other species they are compared to. The exception is first echoes which are different in both MI and SDI for spruce compared to birch. We expected that deciduous species would have nearly the same reflection in the wavelength emitted by the laser. Surprisingly, intensity metrics from first and only echoes of aspen trees were more similar to spruce than birch. This similarity may be explained by reflectivity of bark (branches and stems) and by crown characteristics such as density and structure in addition to foliage reflectivity. Last echoes of spruce have higher mean intensity than the two deciduous species. A likely reason is the relation to first echoes where spruce trees have more energy left to produce a second return. However, the correlations between metrics derived from first and last echoes are weak (Table 3).

Correlations between mean intensities and standard deviations within echo categories at plot level are also reported by Moffiet et al. (2005). They explain the correlation between mean intensity and standard deviation of intensity by the interaction of the features of forest and trees on the footprint. A permeable surface will return a small portion of the pulse energy and it will need more time before a significant return will be recorded. This will lower the mean intensity and increase the standard deviation of intensity compare to a denser surface. However, we found that these relationships are stronger in deciduous species. Hence, the effect is different between tree species. The correlations between metrics from first echoes and only echoes are also interesting, especially as first echoes seem to be more important in separating species than only echoes. The correlations between metrics of first echoes and only echoes indicate effects which influence both echo categories in the same way. However, first echoes are better in discriminate species. Hence, first echoes are probably less affected by these overall effects.

The explorative data analysis and the principal component analysis indicated large variation in the intensity metrics. Only parts of the variation were explained by the first two components of the PCA, indicating that much of the variation in these metrics will be difficult to explain. A factor of variance that may be used in further studies is the incident angle of the laser pulse. However, as shown in Figure 5, some of the variation is explained by tree species. The birch and spruce trees are nearly separated into two groups in the PCA score plot. This separation of tree species in the score plot supports the use of laser intensity in discriminating between these two species. The score values for aspen trees are found more scattered and mixed with score values of spruce trees in the plot. The scattered score values of aspen trees may be an effect of the special crown structure or by the limited number of observations in the dataset. However, the observation of different score values in aspen and birch trees indicate that these tree species should be treated separately and not as a common group. In addition, both the box-and-whisker plots and the score plot point out that the variance in intensity metrics, e.g. MIO, is smaller for spruce than for deciduous species. This may be due to the fact that spruce trees have a more uniform crown than deciduous trees.

The study site is located in a heterogeneous forest with a number of suppressed trees. They are indeed difficult to detect and segment by automated single-tree segmentation as well (Solberg et al. 2006), and these trees may also be the most difficult ones to classify. In spite of the complex stand structure, the classification accuracy was fairly high. The cross validated classification indicated that intensity of first echoes are the most appropriate ones to separate spruce, birch, and aspen trees. In addition, intensity metrics from last echoes and the standard deviation of intensity from only echoes will contribute with information separating the three species. The classification is explorative and more appropriate training- and testing datasets are required to verify these initial findings.

6. CONCLUSION

The results of this study indicate that intensity from high-resolution airborne laser could assist species discrimination. Of the tested echo categories the "first echoes of many" provided most information for discriminating between species. Last echoes provided additional information and "only echoes" provided least information for separating species. Intensity measured by ALS is also highly variable. The high intensity of "only echoes" compared to first echoes and relationships between echo categories indicated that other tree structural characteristics than species reflectivity are of importance for the intensity value. The classification accuracies obtained were from 68 to 74 %, depending on number of variables considered. Using additional ALS-derived metrics, like canopy density- or height metrics, will probably improve classification performance. Hence, additional metrics and information will be used in and operational application. In the near future, use of integrated systems like sensors combining laser and image sensors are likely to become more common. Data from such systems will have a great advantage in tree species classification (Persson et al. 2004).

7. REFERENCES

- Anon. (2004). TerraScan user's guide. Terrasolid, Helsinki. <http://terrasolid.fi>
- Anon. (2006). R: A Language and Environment for Statistical Computing (R Development Core Team). R Foundation for Statistical Computing, Vienna, Austria. <http://www.R-project.org>
- Bollandsås, O.M., & Næsset, E. (2007). Estimating percentile-based diameter distributions in uneven-sized Norway spruce stands using airborne laser scanner data *Scandinavian Journal of Forest Research*, 22(1), pp. 33-48.
- Brandtberg, T. (2007). Classifying individual tree species under leaf-off and leaf-on conditions using airborne lidar. *ISPRS Journal of Photogrammetry and Remote Sensing*, 61(5), pp. 325-340.
- Brandtberg, T., Warner, T.A., Landenberger, R.E., & McGraw, J.B. (2003). Detection and analysis of individual leaf-off tree crowns in small footprint, high sampling density lidar data from the eastern deciduous forest in North America. *Remote Sensing of Environment*, 85(3), pp. 290-303.
- Holmgren, J., & Persson, Å. (2004). Identifying species of individual trees using airborne laser scanner. *Remote Sensing of Environment*, 90(4), pp. 415-423.
- Moffiet, T., Mengersen, K., Witte, C., King, R., & Denham, R. (2005). Airborne laser scanning: Exploratory data analysis indicates potential variables for classification of individual trees or forest stands according to species. *ISPRS Journal of Photogrammetry and Remote Sensing*, 59(5), pp. 289-309.
- Morsdorf, F., Meier, E., Kotz, B., Itten, K.I., Dobbertin, M., & Allgower, B. (2004). LIDAR-based geometric reconstruction of boreal type forest stands at single tree level for forest and wildland fire management. *Remote Sensing of Environment*, 92(3), pp. 353-362.
- Nilsson, M. (1996). Estimation of tree weights and stand volume using an airborne lidar system. *Remote Sensing of Environment*, 56(1), pp. 1-7.
- Næsset, E. (2002). Predicting forest stand characteristics with airborne scanning laser using a practical two-stage procedure and field data. *Remote Sensing of Environment*, 80(1), pp. 88-99.
- Næsset, E. (2004). Practical large-scale forest stand inventory using a small-footprint airborne scanning laser. *Scandinavian Journal of Forest Research*, 19(2), pp. 164-179.
- Persson, Å., Holmgren, J., Söderman, U., & Olsson, H. (2004). Tree species classification of individual trees in Sweden by combining high resolution laser data with high resolution near-infrared digital images. In: M. Thies, B. Koch, H. Spiecker & H. Weinacker (Eds.), *Laser-Scanners for Forest and Landscape Assessment*. Freiburg, Germany.
- Persson, Å., Holmgren, J., & Söderman, U. (2002). Detecting and measuring individual trees using an airborne laser scanner. *Photogrammetric Engineering and Remote Sensing*, 68(9), pp. 925-932.
- Schreier, H., Loughheed, J., Tucker, C., & Leckie, D. (1985). Automated measurements of terrain reflection and height variations using an airborne infrared laser system. *International Journal of Remote Sensing*, 6(1), pp. 101-113.
- Solberg, S., Næsset, E., & Bollandsås, O.M. (2006). Single tree segmentation using airborne laser scanner data in a structurally heterogeneous spruce forest. *Photogrammetric Engineering and Remote Sensing*, 72(12), pp. 1369-1378.
- Tukey, J.W. (1977). *Exploratory data analysis*. Addison-Wesley Reading, pp. 688
- Venables, W.N., & Ripley, B.D. (2002). *Modern Applied Statistics with S*. Springer, New York, pp. 495
- Wehr, A., & Lohr, U. (1999). Airborne laser scanning - an introduction and overview. *ISPRS Journal of Photogrammetry and Remote Sensing*, 54(2-3), pp. 68-82.

QUALITY ANALYSIS OF 3D ROAD RECONSTRUCTION

Sander Oude Elberink and George Vosselman
 International Institute for Geo-information Science and Earth Observation (ITC),
 Hengelosestraat 99, P.O. Box 6, 7500 AA Enschede The Netherlands
 oudeelberink@itc.nl, vosselman@itc.nl

KEY WORDS: Quality analysis, 3D road reconstruction, topographic features, data fusion, laser scanner data

ABSTRACT:

Quality of 3D reconstructed roads strongly depends on input data and following processing steps. Quality analysis is essential for building up a reliable reconstruction process and for a proper use of 3D data. It is therefore of interest to analyse which error sources influence the final result, and what is the sensitivity of each of these error sources. In this paper we explicitly describe quality of 3D reconstructed roads as a function of input data. These 3D roads have been reconstructed automatically by a fusion process of two input data sets: topographic map data and airborne laser data. Heights of map points are calculated by least squares plane fitting through a selection of neighbouring laser points. We determine the precision of map point heights by using error propagation techniques and properties of least squares adjustment. Map points heights have been calculated with a precision varying from a few centimetres to a few decimetres, depending on the point density and distribution of laser data. Even more important is that independent reference data showed the correctness of predicted quality by testing the actual quality against the predicted quality.

1. INTRODUCTION

Reconstructing 3D topographic objects has been an active research topic in the last decade, driven by the growing need for 3D geo-information and the growing technical possibilities. Researchers proposed several acquisition techniques varying in terms of level of automation, focus on specific objects, and kinds of data sources like stereo imagery or laser altimetry data. Quality parameters of these 3D reconstructed models strongly depend on input data and how well these objects can be extracted from the data. (Kaartinen et al, 2005) reviewed the quality of building models submitted by 11 participants, and relate this to the acquisition methods, divided into image based and laser altimetry based approaches. In other individual papers sections on quality assessment are often limited to a value of success rate and completeness or a table of differences between reference data and reconstructed models.

While users of 3D geo-information also gained experiences in their applications, requirements on data quality became more specific. For one purpose users need a higher accuracy than for others. Quality descriptions are therefore essential for a proper use of data. For users as well as for researchers it is of interest to analyse which error sources influence the final result, and what is the sensitivity of each of these error sources.

In this paper we explicitly describe quality as a function of input data, using error propagation techniques and properties of least squares adjustment. Our focus is on the quality of 3D road reconstructions. We will examine the precision of only the height component in these models. Three-dimensional roads are important features for infrastructural analysis, like traffic noise simulations, but are also essential features in 3D city models, besides 3D buildings. Roads can automatically be reconstructed in 3D using airborne laser scanner data in combination with existing 2D map data (Oude Elberink and Vosselman, 2006). Their method recognises and models height discontinuities to allow roads to cross in 3D. Results have been shown for a complex interchange, but quality assessment was limited to a section about completeness of the reconstructed model. First we will generally describe the reconstruction approach, which is an extension to the method of (Oude Elberink and Vosselman, 2006). By using formulas from least squares adjustments and

error propagation techniques, we are able to analyse the precision and reliability of our reconstructed model. Finally, we check our reconstructed model by comparing it with independent reference data. Differences between these two datasets should be explainable by the predicted quality measures. Detailed insight in the quality of 3D reconstructed roads is important to analyse critical steps in the reconstruction process. This is especially true in situations in which laser points are scarce like on lower parts at interchanges. This paper gives insight in the quality of the 3D road reconstruction process and results.

2. 3D ROAD RECONSTRUCTION

Essential in our quality analysis is the integration of functional and stochastic information, using error propagation and least squares adjustment techniques. In this section we describe the functional information, covering the subsequent steps to reconstruct 3D roads. Our aim is to reconstruct 3D road models by adding height values from laser data to 2D planar coordinates of map polygons.

2.1 Pre-processing

In a pre-processing stage laser data has been segmented into piecewise smooth laser segments. We have filtered small segments to remove points on objects like cars and traffic signs.

2.2 Assigning laser data to map data

Roughly, our approach assigns laser points to a map polygon and then reconstructs its 3D boundaries by fitting a plane through a selection of the assigned laser points. When reconstructing complex interchanges, assigning laser points to the map needs extra attention. Simple points-in-polygon operations will fail because the existence of roads on multiple height levels. Laser points should be assigned to a road part on the correct height level. In Figure 1 a part of an interchange is shown, visualizing map polygons bounded by black lines, and laser points coloured by height. Colours indicate height above mean sea level varying from yellow (~0 meter), green (~6 meter), blue (~14 meter) and purple (~21 meter).

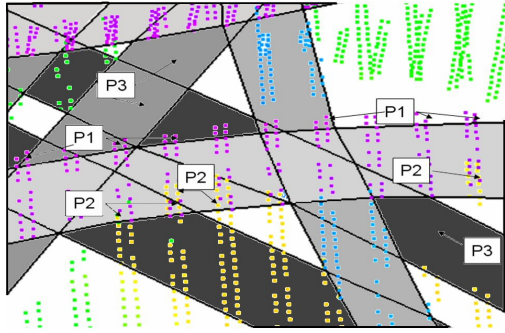


Figure 1. Laser points and map polygons at four height levels of a complex interchange, see text for explanations of P1, P2 and P3.

Looking at a complex infrastructural object like in Figure 1, the following characteristic problems may occur:

P1. Due to a horizontal displacement between map and laser data, laser points will be assigned to the wrong (neighbouring) polygon.

P2. Height data might be acquired at different levels at the same horizontal location because of the across track scanning angle. When reconstructing this map polygon at different height levels, we have to select the right laser points for the right height level, and remove the false laser points.

P3. Problems arise when handling polygons with only a few points, due to the size of the polygon or due to the surface material of the object feature resulting in a low point density.

Problems mentioned above are solved in a special map growing algorithm. Map polygons are merged together if they belong to the same road. Geometric and topological information from two neighbouring polygons decides if they belong to the same road. Laser points are added during map merging if they fit to the height and slope of the growing map polygon. This assignment procedure is a recently added step to the approach of (Oude Elberink and Vosselman, 2006), making it possible to reconstruct complex interchanges completely and automatically, at all height levels. Now that laser points have been assigned to map polygons, the actual reconstruction consists of adding height values to each map point. To correctly capture the 3D shape of polygons, additional map points have been generated and inserted at every 10 meters. This height value is calculated by fitting a plane through a selection of laser points within a certain radius, see Figure 2. This plane is calculated by least squares adjustment. To reduce influences of single laser points, only points from the largest segment have been used. The height of the plane at the location of the map point is taken as map point height. At road crossings multiple heights will be calculated and stored to make a full 3D description possible.

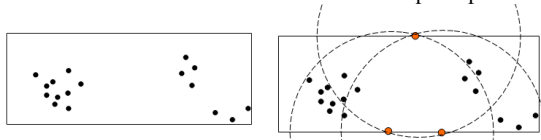


Figure 2. Laser points assigned to map polygon (left); map points (orange bullets) and search radius for selecting laser points (right).

Our plane parameters (p) can be written in the form:

$$z = f(x, y) = -xp_1 - yp_2 + p_3 \quad (1)$$

Where p_1 and p_2 are two slope parameters and p_3 a distance parameter. We can write the plane calculation in a system of linear equations:

$$E\{y\} = Ax. \quad (2)$$

In equation (2), y contains observations (z -values of laser points), x is a vector of the three unknown plane parameters and matrix A contains information about the configuration of laser points. Each row consists of the horizontal location of a single laser point ($-x, -y, 1$).

$$E \begin{Bmatrix} z_1 \\ z_2 \\ z_3 \\ \dots \\ z_n \end{Bmatrix} = \begin{Bmatrix} -x_1 & -y_1 & 1 \\ -x_2 & -y_2 & 1 \\ -x_3 & -y_3 & 1 \\ \dots & \dots & \dots \\ -x_n & -y_n & 1 \end{Bmatrix} \begin{Bmatrix} p_1 \\ p_2 \\ p_3 \end{Bmatrix}. \quad (3)$$

To solve these equations in a least squares adjustment, observations are given a weight, and plane parameters are estimated by:

$$\hat{x} = (A^* Q_y^{-1} A)^{-1} A^* Q_y^{-1} y; Q_{\hat{x}} = (A^* Q_y^{-1} A)^{-1}. \quad (4)$$

After map height calculation, 3D boundaries are triangulated to get a solid surface description of the road. In the next section a quality description is given concerning the height values of 3D roads.

3. QUALITY DESCRIPTION

By using formulas from network design analysis, we can predict the quality of our reconstructed model before the actual reconstruction. For researchers quality prediction is useful for optimizing parameters used in their algorithms ("designing the network"). For users, predicting quality is important because it answers the question whether the input data and the processing steps can fulfil the user requirements.

We distinguish three components in the precision of the map point:

$$\sigma_{map_pnt}^2 = \sigma_{plane}^2 + \sigma_{laser_block}^2 + \sigma_{plane_mdl}^2 \quad (5)$$

σ_{plane}^2 is the uncertainty caused by variations in the plane parameters, which are influenced by laser point noise.

$\sigma_{laser_block}^2$ represents a stochastic value for systematic errors in laser data, and $\sigma_{plane_mdl}^2$ stands for discrepancies between the fitted plane and the actual shape of the road.

3.1 Quality of plane at map point location

To predict uncertainty in the plane parameters we need information about the quality and configuration of the input data. (Crombaghs et al., 2002) present a practical method to describe quality of laser data sets as a function of four error sources (error 1 to 4, denoted as E1 to E4). These error sources are point noise (E1), GPS (E2) and INS noise (E3) and strip adjustment noise (E4). Influence of each of these error sources depend on the size of the area of interest. Within the radius for selecting laser data, it can be expected that all laser points are influenced by the same E2, E3 and E4. When using least squares adjustment, these three error sources act as systematic errors, not stochastically influencing the quality of the plane

equation. These error sources will be added later to the precision of the map point (see eq. 9). When only assuming influence of point noise in equation (4), Q_y turns into a diagonal matrix and (4) can then be written in the form:

$$\hat{x} = (A^* A)^{-1} A^* y. \tag{6}$$

Equation (6) shows that a diagonal matrix Q_y does not have an effect on the estimation of plane parameters. However, it does affect the quality of the plane parameters.

$$Q_{\hat{x}} = (A^* Q_y^{-1} A)^{-1} = \frac{1}{\sigma_z^2} \begin{pmatrix} \sum_{i=1}^n x_i^2 & \sum_{i=1}^n x_i y_i & \sum_{i=1}^n -x_i \\ \sum_{i=1}^n x_i y_i & \sum_{i=1}^n y_i^2 & \sum_{i=1}^n -y_i \\ \sum_{i=1}^n -x_i & \sum_{i=1}^n -y_i & n \end{pmatrix}^{-1} \tag{7}$$

In order to avoid singularity when inverting the 3x3 normal matrix, columns of A^*A have to be linearly independent. This can be achieved by selecting at least three laser points that do not lie in a straight line. For a stable calculation we proceeded with local coordinates by subtracting the mean location of the laser points. Once the quality of plane parameters is known, we can calculate the height precision of the plane at the location of the map point.

$$\sigma_{plane}^2 = x^2 \sigma_{p_1}^2 + y^2 \sigma_{p_2}^2 + \sigma_{p_3}^2. \tag{8}$$

3.2 Quality of laser block

Remember that equation (5) consisted of multiple components: plane uncertainty, systematic errors in laser data and model uncertainty. Laser point noise was taken into account in the plane uncertainty; other errors in laser data (E2, E3, and E4 as mentioned in section 3.1) did not reflect the plane equations. However, they influence the precision of the map point height. We can group these errors by

$$\sigma_{laser_block}^2 = \sigma_{E_2}^2 + \sigma_{E_3}^2 + \sigma_{E_4}^2 \tag{9}$$

3.3 Quality of plane model

Plane model quality covers the discrepancy at the map point between the actual shape of the road and the modelled plane. If the horizontal distance between map point and laser points is small it can be expected that a plane through these laser points accurately represents the road height at the map point. Model uncertainty becomes of interest when we need to extrapolate over a certain distance, in case we are short of laser points. We can quantify the differences between a local plane and the actual shape, by analysing the curvature of roads. This quantification is a function of horizontal distance between plane origin and map point. To estimate the idealisation precision, we have to use height differences between plane and reality instead of curvatures. For distances smaller than a few hundred meters, we can approximate the difference between the road and a plane by a quadratic term.

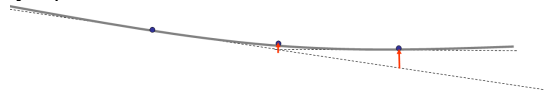


Figure 3. Extrapolation error caused by model uncertainty.

Figure 3 can be translated into a stochastic measure for model uncertainty by calculating the standard deviation of extrapolation errors as a function of the distance. We have approximated this value by dividing maximum extrapolation error, calculated by integrating curvatures, by three.

Now that we have described three components that contribute to the uncertainty in map point heights, we analyse the influence of one of the reconstruction parameters –radius– to this uncertainty. Increase of the radius results in the increase of laser points. Generally this will improve the quality of the fitted plane, because the number of observations in the plane calculation increases. However, increasing radius results in larger extrapolation uncertainties. Remember that this extrapolation error increases quadratically with larger radius. The optimum value can be found by minimizing the sum of these two components as a function of the radius value. For practical reasons, our program starts with an initial radius value, which will be increased if there are too few laser points to precisely fit a plane.

4. TESTING WITH REFERENCE DATA

In the previous sections we have described our 3D road reconstruction method and its stochastic model. To be able to test our –functional and stochastic– model, heights on reconstructed roads have been compared with independent reference data.

4.1 Reference data

Accurate geometric information of highways in the Netherlands is stored in a photogrammetrically derived topographic database, called DTB. Terrestrial measurements have been added to complete road information underneath interchanges and in tunnels. The DTB contains 3D geometric and semantic information of points, boundaries, centrelines and surface features of national roads, at a map scale of 1:1000. This also includes information on road details like locations of paint strips, traffic lights, road signs and other detailed infrastructural objects. DTM information (2.5D) has been integrated into the DTB by photogrammetric measurements on breaklines in the terrain. An example of DTB data is given, showing a complex interchange Prins Clausplein near The Hague.

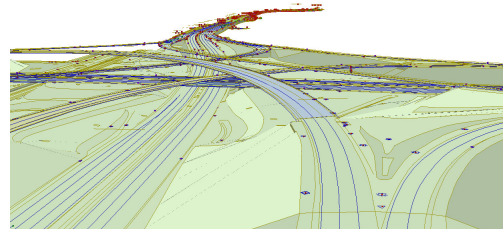


Figure 4. DTB data is used for reference information. Paint strips, shown as blue lines, have been selected to test reconstructed roads.

Paint strips have been measured by manual photogrammetric or tachymetric measurements. Paint strips belong to the so-called ‘hard topography’ category, what means that this object can be identified and measured with high precision. The standard deviation of heights of these points is required to be 9 cm or better.

4.2 Quality of 3D roads by comparing to reference data

In this section we will describe our testing configuration by comparing reference data with our reconstructed model. As we have seen in section 2 roads are represented as a TIN surface, using 3D map points on the boundary as TIN nodes. Figure 5 explains the set-up of our height testing procedure. Orange bullets represent three map points that form one TIN triangle. Green plus marks represent 3D positions on paint strips, which are measured with high accuracy in the reference dataset. At these green plus marks height differences have been calculated.

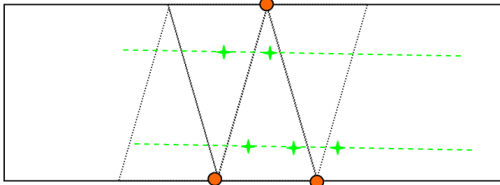


Figure 5. Configuration of height testing: TIN patches and points on paint strips.

Our expectation is that the height difference between reference data and our 3D model should vary around zero. Deviations should be explainable by uncertainty in the 3D model and in the reference data.

$$\Delta h_i = h_{\text{mod}_i} - h_{\text{ref}_i} \sim N(0, \sigma_{\Delta h_i})$$

$$\sigma_{\Delta h_i}^2 = \sigma_{h_{\text{mod}_i}}^2 + \sigma_{h_{\text{ref}_i}}^2 \quad (10)$$

The term $\sigma_{h_{\text{mod}_i}}^2$ contains the height variance of the model, at the location of the reference point. We therefore have to propagate precisions of the map points, calculated as described in section 3.2, to the location of the reference point. Looking again at Figure 5, we see that the precision of three map points influence the precision at reference point location.

First, the location of the reference point within the TIN mesh is important to describe the influence each of the map points. If the reference point is close to one of the three map points, the precision of the TIN height is highly influenced by the precision of the height of this single map point.

Then we investigate the influence of covariance between the three map points. Extreme cases here are no covariance and full covariance. If the three map point heights have been calculated by three different groups of laser points, we can assume that the correlation equals zero. This occurs when using a small radius to select laser points. If the three map point heights have been calculated by the same group of laser points, the correlation equals one.

$$\sigma_{\text{mod}} = \frac{TIN(\sigma_{\text{map_point } s})}{\alpha} \quad (11)$$

Equation shows the calculation of the precision of the reconstructed model, at locations of reference points, by TIN interpolation of 3 precision values of three map points, divided by a correlation term α ($1 < \alpha < \sqrt{3}$).

4.3 Testing our predicted quality

In section 3 we have calculated the precision of map point heights by using error propagation techniques and properties of least squares plane fitting, in this section followed by an actual quality check using reference data. To test the stochastic model

we check if the actual differences can be explained by the predicted accuracy. With the outcomes of equation (10), we test if the difference is significant by using a modified version of the w-test statistics or local error detection as described by (Baarda, 1968 and Teunissen, 1991). In their approaches, the w-test calculates normalized residuals of geodetic observations. If the test exceeds a critical value, this observation will be recognized as a possible outlier. In an iterative procedure the observation with the highest w-test value has been removed from the adjustment.

$$w_i = \frac{\Delta h_i}{\sigma_{\Delta h_i}} \sim N(0,1) \quad (12)$$

A closer look at the w_i learns that it indicates how well one can predict the actual quality. This is an informative measure to show if the predicted quality represent the actual quality. If the stochastic model is correct, the total of all w-test values should have a standard normal distribution. To rely on predicted quality is important for future users who want to predict the quality of 3D reconstructed roads, without checking on highly detailed reference data. Besides this, reference data might not be available at some locations. Large w-test values indicate that the actual quality is worse than predicted. In our approach it is of interest to find reasons for large w-test values, because the functional or stochastic model might not be correct at those locations.

5. RESULTS

5.1 Data specifications

For a complex interchange we assigned coarse laser data (~1 point/ 9m²) to a medium scale topographic map (1:10.000). Laser point noise has been determined in a quality control procedure at the Survey Department of Rijkswaterstaat. For this project the laser point noise (E1) has been stated to be 8 cm, GPS noise (E2) 3 cm, INS noise (E3) 4 cm and block uncertainty (E4) 3 cm. To estimate extrapolation errors due to model uncertainty, we analysed curvature of road heights. Maximum slope differences on highways can be found near interchanges, hillsides and exits. Terrestrial measurements show that slope differences at such locations are about 2% per 100 meter.

$$\Delta y'(d) = 2 \cdot 10^{-4} d \quad (13)$$

We can derive the formula for maximum height difference as a function of distance by integrating formula (13).

$$\Delta y(d) = 1 \cdot 10^{-4} d^2 \quad (14)$$

And its standard deviation:

$$\sigma_{\text{plane_mdl}}^2 = \left(\frac{1}{3} \cdot 10^{-4} d^2\right)^2 \quad (15)$$

Theoretically, we have to optimize the radius for each map point, because of varying laser point configuration and (thus) plane uncertainty. Instead, we decided to use a default radius of 15 meter, which will be doubled in case less than three laser points are found in this radius.

5.2 Predicted standard deviation of map point heights

Figure 6 shows predicted standard deviations of map point heights. The figure shows the position of map points, coloured by predicted standard deviation of the map point height. For

visibility reasons the standard deviation has been classified into three categories: standard deviations larger than 50 cm (shown in red), larger than 20 cm (yellow), and below 20 cm (green). To better understand the cause of large variations at some locations, the blue box in Figure 6 shows the laser points used for 3D road reconstruction. The relation between lack of laser data and large height variations can easily be seen for locations in black ellipses. Point densities in these black ellipses drop to 1 point per 100 m², with extremes to 1 point per 600 m². At map point locations in those areas, map point heights show standard deviations of more than 50 cm. Two factors play an important role here. First, the plane has been determined by just a few laser points; standard deviations of laser points will have a great influence because they are not averaged out. Secondly, the search radius for finding enough laser points increases up to 50 or even 100 m. This results in extrapolation errors rising up to 50 cm or more.

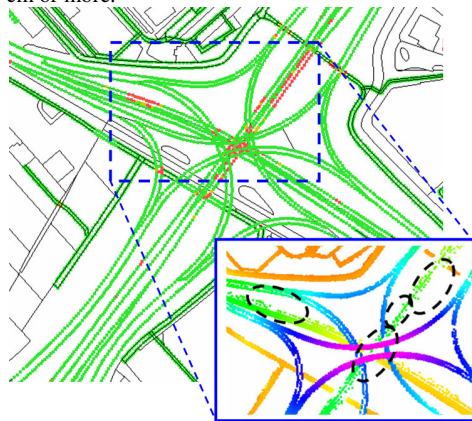


Figure 6. Standard deviations of map point heights. Compare with available laser points (lower right corner).

Bad configuration of the laser points leads to large standard deviations. Figure 7 shows a situation where the majority of laser points lie on a straight line, in this case clearly measured in just one or two scan lines. Fitted planes are badly determined in the direction perpendicular to this scan line. Blue circles have a radius of 15 meter.

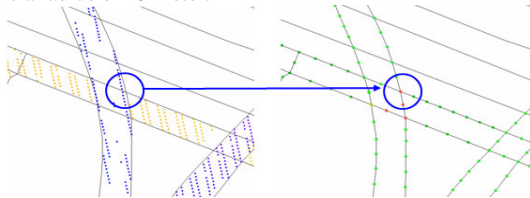


Figure 7. Bad configuration of laser points (left) leads to large predicted standard deviations (right).

5.3 Comparison with reference data

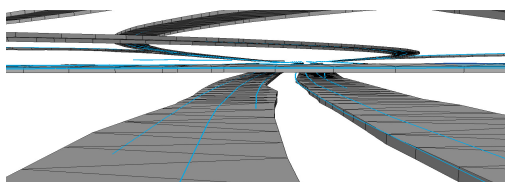


Figure 8. Visual inspection of 3D roads by superimposing reference data.

Results of calculated differences at paint strip locations can be seen in Figure 9, where differences are coloured as red (larger

than 50 cm), yellow (larger than 20 cm) and green (below 20 cm). Note that reference data is not completely covering the interchange. Some parts of flyovers have not been measured in the reference data, test results are therefore locally missing. Still we calculated over 10.000 height differences for this area of 1.2 x 1.2 km.

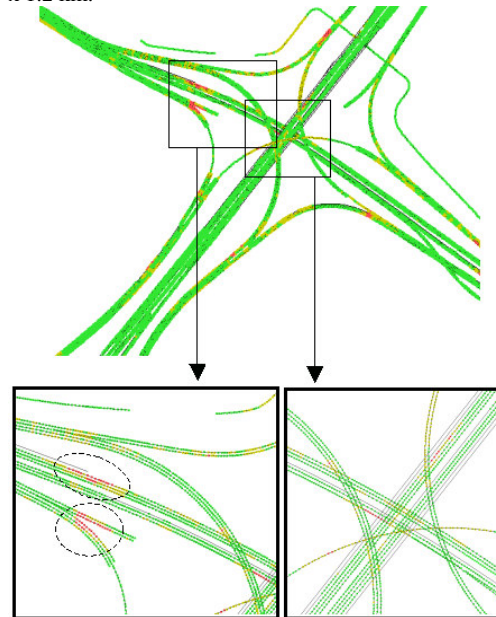


Figure 9. Height difference between reconstructed model and reference data.

A further look at Figure 9 learns that in the centre of the interchange (highlighted in the lower right corner box), where laser points were scarce at all height levels, the calculated differences are remarkably small. A few differences are more than 50 cm, some below 50 cm and many below 20 cm (green). In the lower left corner box, two situations are highlighted which show large height differences with a systematic character. In the higher circle height differences could be expected, due to the lack of laser points, see Figure 6. The reason for differences in the lower circle is that the search radius selects laser points from both road parts, which happen to curve strongly at those locations. Therefore, fitting a plane through the selected points will differ from reality.

Number of reference points inside test area	10922
Mean difference	0.5 cm
Standard deviation of vector of differences	15.4 cm
Maximum absolute difference	121 cm

Table 1. Statistical results of comparing heights of 3D roads.

Table 1 summarizes most important statistic information of height differences between reference data and 3D reconstructed model. The mean difference includes systematic errors between reference data and our reconstructed model. Normally, it is expected to be in the order of 0-5 cm, due to systematic errors in laser data (Crombaghs et al., 2002). In this case, the mean difference happens to be very small (0.5 cm). Looking at the standard deviation of the differences of 15.4 cm, and knowing that it includes uncertainty in the reference data ($\sigma_{ref} = 9$ cm), we can calculate the uncertainty of our reconstructed model ($\sigma_{mod} = \sqrt{15.4^2 - 9^2} = 12.5$ cm). It should be noted that this value is biased by some systematic errors in the reconstructed model.

5.4 Testing predicted standard deviations

Now that the actual difference is known, we divide each difference with the expected standard deviation of the difference. In Figure 10 large w -test values have been coloured yellow (larger than 3) and red (larger than 4). At these points the actual height difference was three or four times larger than expected, meaning that either the standard deviation was too small or the calculated height was significantly wrong. Note that the former case deals with the stochastic model, and the latter case with the functional model. Due to the systematic character of large w -test values, we assume a functional error causes the problems at those locations, mostly where one road splits into two roads. However, the distribution of all w -tests is close to the standard normal distribution, as 68% of the w -test values are less than 1 and 92% are less than 2. If we remove outliers, standard deviation is 1.06 (with outliers 1.22). This means that the predicted stochastic model is a bit too optimistic, but still realistic.

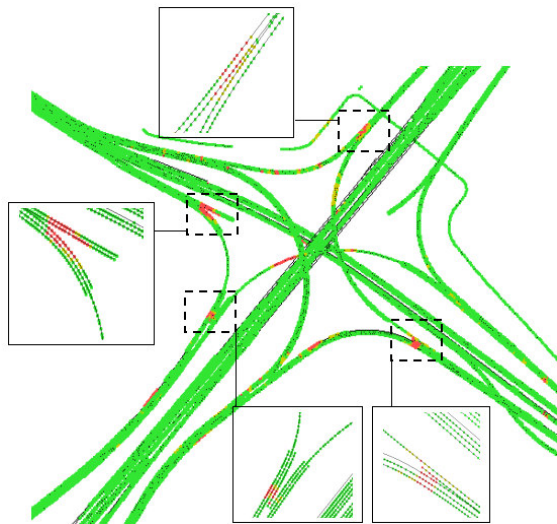


Figure 10. W -test values at reference point locations.

6. DISCUSSION

In this paper we have described a method to calculate quality of 3D reconstructed roads by error propagation. These 3D reconstructed models have automatically been acquired by a fusion process of map data and airborne laser data. After assigning laser data to map polygons, heights of map points have been calculated by least squares plane fitting through a selection of laser points inside the polygon. These 3D map points are nodes in the 3D boundary description. Precision of the map point have been calculated by error propagation of laser point noise and the configuration of the laser points used for plane fitting. Also, influences of model uncertainty have been taken into account. Average predicted standard deviation of map point heights is about 10 cm.

Our method combines a 2D topographic data set with an airborne laser scanner dataset (2.5-3D). Even at locations where no height information is available, our method can reconstruct 3D roads with a height precision in the order of 10-15 cm. Input data sets used in this project are parts of national databases. Now that we can predict quality of 3D roads, we can predict the height quality for all roads in the national database without actually having to reconstruct them, and without testing them with reference data.

Independent reference data has been used to test our reconstructed model and its derived quality parameters. Predicted standard deviations realistically represent the actual quality for most of the situations. Exceptions are found at road splitting situations, where actual differences are more than four times higher than expected. The reason is the wrong assumption that a least squares fitted plane through the selected laser points, realistically represent the shape of the road. Future work will focus on improvement of reconstruction of these splitting roads. This can be achieved by selecting only those laser points that lie on the front side of the map point. The search algorithm for laser points should therefore not cross the polygon border. Quality analysis as presented in this paper is not limited to 3D road reconstruction, but can be extended to other reconstruction applications. For example, building reconstruction can benefit from quality measures by error propagation. Decisions on conflicts between building knowledge and data driven information can be made more reliable if data driven approaches come with quality measures.

ACKNOWLEDGEMENT

We would like to thank the Dutch research programme Space for Geo-Information for funding this research, and Survey Department of Rijkswaterstaat, Topographic Service as well as the Steering Committee AHN for providing the data.

REFERENCES

- Baarda, W. (1968). A testing procedure for use in geodetic networks, Netherlands Geodetic Commission, New Series 2, No 4.
- Crombaghs, M., Oude Elberink, S., Brügelmann, R. and de Min, E., 2002. Assessing height precision of laser altimetry DEMs. Photogrammetric Computer Vision 2002, IAPRS, Graz, Austria, pp. 85-90.
- Kaartinen, H., Hyyppä, J., Gülch, E., Vosselman, G., Hyyppä, H., Matikainen, L., Hofmann, A., Mäder, U., Persson, Å., Söderman, U., Elmqvist, M., Ruiz, A., Dragoja, M., Flamanc, D., Maillet, G., Kersten, T., Carl, J., Hau, R., Wild, E., Frederiksen, L., Holmgaard, J. and Vester, K. (2005). Accuracy of 3D City Models: EuroSDR comparison. International Archives of Photogrammetry, Remote Sensing and Spatial Information Sciences 36 (3/W19), 227-232, Enschede, the Netherlands.
- Oude Elberink, S. and Vosselman, G., 2006. Adding the Third Dimension to a Topographic Database Using Airborne Laser Scanner Data, Photogrammetric Computer Vision 2006. IAPRS, Bonn, Germany.
- Teunissen, P.J.G. (1991). An integrity and quality control procedure for use in multi sensor integration. In: Proceedings of ION GPS-90, 19-21 September 1990, pp. 513-522, Colorado Springs, USA.
- Vosselman, G., 2003. 3D Reconstruction of Roads and Trees for City Modelling, ISPRS working group III/3 workshop '3-D reconstruction from airborne laserscanner and InSAR data'. IAPRS, Dresden, Germany, pp. 231-236.

GEOMETRICAL ASPECTS OF AIRBORNE LASER SCANNING AND TERRESTRIAL LASER SCANNING

Norbert Pfeifer^a and Christian Briese^{ab}

^a Institute of Photogrammetry and Remote Sensing, Vienna University of Technology,
Gußhausstrasse 27-29/E122, 1040, Vienna, Austria, np@ipf.tuwien.ac.at, cb@ipf.tuwien.ac.at

^b Christian Doppler Laboratory "Spatial Data from Laser Scanning and Remote Sensing"

KEY WORDS: Airborne Laser Scanning, Terrestrial Laser Scanning, LiDAR, Geometry, Orientation, Registration, Segmentation, Calibration, Digital Terrain Model, DTM

ABSTRACT:

This paper reviews the current state of laser scanning from airborne and terrestrial platforms for geometric reconstruction of object shape and size. The current performance figures of sensor systems are presented in an overview. Next, their calibration and the orientation of the acquired point clouds is discussed. For airborne deployment this is usually one step, whereas in the terrestrial case laboratory calibration and registration of point clouds are (still) two distinct, independent steps. As laser scanning is an active measurement technology, the interaction of the emitted energy with the object surface has influences on the range measurement. This has to be considered in order to explain geometric phenomena in the data. While the problems, e.g. multiple scattering, are understood well, there is currently a lack of remedies. Then, in analogy to the processing chain, segmentation approaches for laser scanning data are reviewed. Segmentation is a task relevant for almost all applications. Likewise, DTM (digital terrain model) reconstruction is relevant for many applications of airborne laser scanning, and is therefore discussed, too. This paper reviews the main processing steps necessary for many applications of laser scanning.

1 INTRODUCTION

Laser scanning, often also referred to as LiDAR (light detection and ranging), has been operational for surface and object reconstruction since the mid 1990s. It is continuously developing in sensor as well as in data processing aspects. Higher measurement rates, increased precision, wider range spectrum, and extraction of target or object properties beyond the range are some of the developments on the sensor side. The development of calibration procedures for both airborne and terrestrial devices is one important development for the early stages of data processing. Additionally, a diversification in applications can be seen. The first applications were in capturing terrain elevation (Kilian, Haala, and English 1996), but forestry (see e.g. the overview in (Hyypä et al. 2004)) and industrial reconstruction became standard areas of application (e.g. Rabbani, Dijkman, van den Heuvel, and Vosselman (2007)) in the meantime, too.

This paper reviews the state of art in airborne and terrestrial laser scanning. The first publications on laser scanning (and laser profiling) in photogrammetric journals and conference proceedings were often linked to one or more applications: laser profiling for terrain elevation (Lindenberger 1989; Lindenberger 1993), laser scanning (Lohr and Eibert 1995), terrain elevation and buildings (Kilian, Haala, and English 1996), power lines (Reed and Lynch 1996), forest stand parameters (Naesset 1997), terrain elevation (Flood and Gutelius 1997), surface characteristics (Lin 1997; Ritchie and Pachepsky 1998), digital terrain modeling (Kraus and Pfeifer 1998), and a wide range of applications in Vol. 54(2-3) of the ISPRS Journal, special issue on airborne laser scanning. Only later dedicated data pre-processing algorithms were published, especially on strip adjustment and segmentation (Burman 2000; Crombaghs, Brügelmann, and de Min 2000; Behan, Maas, and Vosselman 2000; Filin 2002). Terrestrial laser scanning went through a similar history but matured and entered the photogrammetric community a bit later. A special issue of the ISPRS Journal on terrestrial laser scanning is in preparation. With over ten years of development it stands to reason to review the current

state of these pre-processing algorithms, give an overview of the relevant literature, and judge the development.

The so-called intensity measurements are rarely used (Höfle and Pfeifer 2007), and also full waveform laser scanning (Wagner et al. 2006), and even more so, multispectral laser scanning (Wehr et al. 2006; Wehr et al. 2007), still have to prove their value for exploitation in different applications. Thus this review will be confined to the geometrical aspects of airborne laser scanning (ALS) and terrestrial laser scanning (TLS) and will not go into details of retrieving material properties of objects scattering back an incident laser beam. For the physical principles of *laser radar* the reader is referred to Jelalian (1992) and Wehr and Lohr (1999). With the diversification of applications, it would also be impossible to review the state in each application, and this review will concentrate more on laser scanning itself and procedures useful or necessary in all applications.

We are therefore mainly treating the point cloud, starting from the sensors acquiring the data, and proceeding, in steps, to model generation. While reporting the state of the art according to our best knowledge, we allow ourselves to point out fields, where we expect research to concentrate in the coming year(s). This is solely the opinion of the authors and necessarily speculative. The paper is structured by first reviewing the state of the art in data acquisition and pre-processing, where the latter term means that the original measurements are processed and a specific application is not the driving force behind the processing. Next, the geometrical consequences, i.e., effects on the point cloud, of the interaction of the laser signal with the object are investigated. Naturally, this has physical causes, formulated in terms of multiple scattering properties, object transparency, and the like. However, at least currently, this cannot be handled on a physical basis and has to be analyzed, and if possible corrected, in a data driven manner. Then generic processing steps as segmentation are reviewed, including also DTM reconstruction. The latter, while being an application itself, is used in many further applications, which justifies including it in this review.

2 DATA ACQUISITION

This section presents the state of the art in laser scanning systems, their calibration and transformation of the point clouds acquired into a superior, possibly global, coordinate system.

Due to the fact that the sensor technology is developing fast we will not describe specific scanners of different vendors, as at the moment of printing the article, the information may be outdated already. Therefore, rather the main performance parameters are given. Surveys of currently available devices are regularly published (GIM 2007; POB 2007). Airborne and terrestrial (also called close-range) deployment will be treated separately, as the different deployment of the scanners, at fixed positions over periods of time vs. on a moving platform, has a large impact on the first steps of data processing. However, with the advent of scanning from moving platforms on the ground (also termed mobile laser scanning), and the longer history of using profile scanners on trains, it would be more appropriate to distinguish between *dynamic and static scanning*. In the first case scanning is performed by a univariate beam deflection unit and area wise data acquisition is established by the dynamics, i.e. the movement, of the scanning platform (aircraft, land vehicle or a boat). In the second case the exterior orientation of the platform is constant for one scan position, and two dimensional coverage in the angular domain is performed by rotating components of the device (e.g., a mirror or the upper instrument part). Profiling (Lindenberger 1989), on the other hand, is what is obtained by univariate beam distribution, e.g. obtained from satellite platforms (Zwally et al. 2002) or used for continuous monitoring or elongated structures (Hesse, Neuner, and Kutterer 2005).

2.1 Airborne Laser Scanning

2.1.1 Current Systems ALS systems use almost solely the pulse time of flight measurement principle for ranging (Riegl 2007; Optech 2007; Leica 2007; TopEye 2007; TopoSys 2007; Fli-Map 2007). One exception is the research system ScaLARS, which applies the phase difference measurement principle (Hug and Wehr 1997). Currently, there are two different types of commercial ALS sensor systems available: discrete echo and full-waveform scanners. While discrete echo scanners detect a representative trigger signal for multiple echoes in real time using analogue detectors, full-waveform ALS systems digitize the entire analogue echo waveform, i.e. the time-dependent variation of received signal power, for each emitted laser pulse. Digitization is performed typically with an interval of 1 ns (corresponding to 15cm one-way distance) and the determination of the individual echoes has to be performed in post-processing (Wagner, Ullrich, Melzer, Briese, and Kraus 2004). In ALS mainly two laser wavelengths are in use: 1.06 μ m and 1.5 μ m. The pulse repetition rate (PRR) of current "top end" devices is 100kHz to 200kHz¹. The operating altitude of the systems is different, with some systems restricted to a flying height of less than 1000m above ground, whereas others can be used 5km above ground level. Many ALS systems are currently only able to record the reflections of one laser pulse before the next is emitted. This restricts high PRR to lower flying heights (not more than 100kHz for 1500m maximum one-way slant range). Recent sensor developments lead to the ability of multipulse systems which allow to have multiple laser signals in the air simultaneously (Optech 2007; Leica 2007).

The maximum field of view in ALS data acquisition, measured perpendicular to the forward movement of the aircraft is depending on the scanner used and reaches from $\pm 7^\circ$ to $\pm 30^\circ$. ALS

¹Next to increasing the pulse generation rate of the laser, an option to increase the measurement rate is mounting two laser scanners on one platform, as offered currently e.g. by (Diamond Airborne Sensing 2007).

systems are used on fixed-wing aircraft as well as on helicopters. While fixed-winged aircraft are typically used for the acquisition of large project areas, helicopters are preferred for following a linear feature (e.g. for corridor mapping) or for difficult topography.

The scanning mechanisms applied are mainly those deflecting the laser beam in a plane perpendicular to the flying direction, using an oscillating or a multi-faceted rotating mirror (Latypov 2005). For rotating mirror scanners the PRR is typically only a burst measurement rate, and the number of pulses used for measuring ranges, i.e. the effective measurement rate, is lower (Riegl 2007). The rays with larger nadir angles are not provided to the users or are reflected within the scanner housing. Oscillating mirrors have the advantage that the turning points can be set to angles appropriate for a specific project. However, as the mirrors have to be accelerated the point distribution on the ground can be less homogeneous than for rotating mirror scanners, especially when using a harmonic angle acceleration. By using mirrors with different angles at the facets, forward, nadir, and backward looking can be performed with one scanner (Fli-Map 2007). The fiber scanner used in one of the TopoSys scanners is special in the sense that no angle position of the mirror has to be measured as the emission direction is fixed and governed by the single fibers directly. Palmer scanners (Wehr and Lohr 1999) are used by TopEye, ScaLARS and NASA's ALTM (Finnegan et al. 2005). While generating a less regular ground point pattern they offer an advantage in calibration, as each "point" is measured twice.

2.1.2 Calibration and Strip Adjustment For the transformation of the ALS data (range and angle observations) into one common coordinate system the position and angular attitude, i.e. the exterior orientation, of the platform have to be known in order to allow direct geo-referencing. Typically, this is realized by a combination of a global navigation satellite system (GNSS) receiver and an inertial measurement unit (IMU). Together with the laser scanner they form a multi sensor system. During data acquisition data streams are recorded by each instrument at different frequency and are synchronized via the GNSS time measurements. Calibration of this multi sensor system is the process of determining the relative orientation, i.e. shifts and rotations, between the components (GNSS antenna, IMU, and laser scanner) and time lags in the synchronization. To some extent these parameters can be determined by total station measurements on the ground, but a number of parameters, e.g. the IMU-laser scanner relative orientation or time lags, are better determined during flight. Scanner vendors provide special software that allow derivation of these parameters if dedicated flight patterns are performed. Typically only flat surfaces are used for this alignment, but as Filin (2003) has shown, inclined surfaces with different aspect are a prerequisite for determining all relative orientation parameters of the multi sensor system.

Approaches for the calibration have been presented in (Burman 2002; Filin 2003; Kager 2004). In Skaloud and Lichti (2006) a method for dedicated determination of the three bore-sight angles and the range finder offset is described. These models are all based on the observations range, angle (of beam deflection), and observations of exterior orientation (i.e. position and angular attitude). The points measured by the ALS system are either related to ground truth and/or to points of another strip (control and tie information in the form of surface patches, respectively). The discrepancies encountered in those are minimized by determining the calibration parameters.

In calibration the task is, as described above, to reconstruct the geometric layout of the multi sensor system. For applications of

ALS data, the effects of an insufficient calibration and of errors in the exterior orientation determination are more of interest. The task of strip adjustment is to correct these errors. This can be done either by calibration, or by applying corrections to the points directly: $\mathbf{p}'_{i,j} = \mathbf{p}_{i,j} + \mathbf{c}_j(\mathbf{p}_{i,j})$. The point $\mathbf{p}_{i,j}$ with index i in strip j is corrected by applying a correction function \mathbf{c}_j for strip j . The first publications on strip adjustment chose that approach.

In the simplest case the functions \mathbf{c}_j are only shift vectors, $\mathbf{c}_j = (x_j, y_j, z_j)$ and do not depend on the location within the strip. In (Crombaghs, Brügelmann, and de Min 2000) and (Kraus and Pfeifer 2001) the correction function applies to the height component only, using a linear function (vertical offset and tilts in and across flight direction), and polynomials, respectively. The approach of Kraus and Pfeifer (2001) allows correcting shorter wavelength deformations, too. A method that is not restricted to vertical correction, but also removes discrepancies in planimetry was developed by Kilian, Haala, and English (1996), where the function \mathbf{c}_j has parameters for constant offset and time dependent drifts for shift in and rotation around the three coordinate axes, requiring that the time of the measurement is known. Vosselman and Maas (2001) describe a similar method, mentioning, that this model does not allow to correct short time effects caused by the limited GNSS accuracy. Knowledge on the measurement time is not required but replaced by parameterization along the strip axes.

Contrary to these approaches which model effects, not causes, calibration procedures can be extended to perform strip adjustment, too. This has been demonstrated by Burman (2002) and Kager (2004).

In ALS there is still a process of model identification going on. Calibration methods and strip adjustment should be generic enough to allow handling all airborne laser scanners on the one hand, and correct the causes of the errors, and not only effects, on the other hand. Specialized developments are often beneficial for data acquisition (e.g. the roll angle compensation of Optech), but less practical for implementation of on-the-job sensor calibration techniques. Especially the lack in the availability of the original observations (i.e., trajectory, angles, and ranges) complicates these efforts from a scientific point of view.

Although methods have been published, and the increase in precision is notable, on-the-job calibration is not standard yet. There is a lack of software available to data providers. Next to calibration, also efforts to improve the flight path are necessary. The global navigation satellite system can be seen as correction for the low frequency errors in the high frequency observations of the flight path and sensor attitude by IMU measurements. However, the GNSS component itself is subject to errors that occur over the entire strip or parts of it (e.g., wrong ambiguity fixes)². Under such circumstances an offset and drift component as unknowns in strip adjustment are not enough (Ries, Kager, and Stadler 2002). Also polynomial models do not work satisfyingly, and spline models for modeling the dynamic exterior orientation require careful balancing of the number of knots and their placing. Summarizing, solutions modeling the flight path have not been very successful yet, which may be attributed partly also to unexpected behavior encountered in flight path information, e.g. "jumps" in the flight path (Ries, Kager, and Stadler 2002).

The authors hold the view, that a tighter integration of the determination of the sensor trajectory with Kalman filtering of the

²It shall be noted that satellite positioning is performed in a geometrical coordinate system (geocentric cartesian or ellipsoidal coordinates) whereas IMU measurements depend also on the local geoid.

GNSS/IMU data with the determination of sensor calibration and exploitation of homologous patches on the ground will provide the most precise solution. It allows to introduce redundancy in the determination of the flight path, which is absent in direct georeferencing (Skaloud 2006). Introducing redundancy increases, at least in theory, reliability and allows estimating the precision. There is also a potential to account for changing satellite constellations, GNSS outages, or periods with less than four satellites visible. In aero-triangulation the combined adjustment of images and GNSS observations is investigated in (Schmitz, Wuebbena, Bagge, and Kruck 2001) and (Ellum and El Sheimy 2006).

For well defined surfaces the precision of ALS, applying a rigorous model of laser strip calibration as described above, can reach a few centimeter. The determination of the flight path with GNSS gives a precision of $\pm 5\text{cm}$ to $\pm 10\text{cm}$ in each coordinate direction and becomes a limiting component of ALS precision (Csanyi and Toth 2007). Solutions may come from improvements in the GNSS, also by using multiple reference stations, or from more ground control. The latter can be in the form of surface patches, which is economically and practically less viable. Alternative navigation systems may emerge, although the current alternatives to GNSS for navigation in cities or inside buildings, e.g. based on mobile communication and other wireless networks (Karimi and Hammad 2004) are far from the accuracy provided by GNSS yet.

For full exploitation of the measurements of ALS not only the geometric aspects should be considered, but also the radiometry. The backscattered energy, in the form of photons, is typically converted to a voltage or current and then converted further into a digital number, not necessarily by a linear function. This is discussed in (Wagner et al. 2006; Ahokas et al. 2006; Höfle and Pfeifer 2007). Many airborne systems have two receivers (so-called low channel and high channel for detection of echoes with small and large amplitude, respectively), which has not been considered in calibration efforts so far.

2.2 Terrestrial Laser Scanning

2.2.1 Current Systems In contrast to ALS systems more variation in the sensor design of TLS systems can be observed. The wavelengths used are between $0.5\mu\text{m}$ and $1.5\mu\text{m}$. Longer wavelengths are affected less by the atmosphere, but shorter wavelengths can provide smaller footprints. Terrestrial laser scanners use the pulse time of flight measurement principle (Riegl 2007; Leica 2007; Trimble 2007; Optech 2007; Callidus 2007; I-SiTE 2007) as well as phase based ranging (Zoller+Fröhlich 2007; Faro 2007; 3rdTech 2007). The second systems use the phase difference between the emitted and received backscattered signal of an amplitude modulated continuous wave (AM CW) to infer the range. Pulse time of flight ranging scanners are suited better for outdoor operation where longer ranges have to be measured and are typically panoramic scanners, with a field of view of 360° by e.g. 80° . The PRR of these sensors is around 10kHz and less, and precision lies between $\pm 5\text{mm}$ and $\pm 2\text{cm}$.³ Some systems offer the possibility to either measure the first or last echo, but simultaneous recording is usually not available.

Scanners applying the phase based ranging are typically hemispherical scanners that allow to scan into almost all directions (e.g. 360° by 135°). However, due to their ranging principle (limited range uniqueness, mostly below 100m) they are well suited for indoor usage and outdoor environments with a larger number of objects (e.g. piping installations, inner city areas), restricting

³Leica recently introduced a terrestrial laser scanner with 50kHz PRR, but at the time of writing (August 2007) no independent reports of performance were available.

the view. The measurement rate is typically above 100,000 points per second, and the precision is $\pm 2\text{mm}$ or better. With this ranging principle only one distance can be determined, because the backscattered signals from different reflectors are always overlapping each other. This results in a phase angle corresponding to a distance between the two or more reflectors.

Triangulating scanners, similar to structured light systems, are not discussed here. In (Blais 2004) a review is given. Additionally it shall be noted that currently efforts are on the way to generate standards for terrestrial scanners (Beraldin et al. 2007; Breuckmann et al. 2007).

2.2.2 Calibration Terrestrial laser scanners are, from the construction principle, similar to theodolites and total stations. This holds especially for strictly monostatic systems, where the axis of laser beam emission and the optical axis of the receiver are the same. Additionally, if the rotation around the vertical axis is performed by instrument rotation and the beam deflection in the vertical plane is performed by a rotating mirror inclined 45° against the beam, then an analogy between the instrument axes of a terrestrial laser scanner and a theodolite can be established.

Lichti (2007) models deviations in the observations by correction functions, some of which are based on the sensor model (e.g., trunnion axis error), whereas other parameters are found empirically (e.g., sinusoidal error in horizontal angle as a function of elevation angle). The physical corrections for the range measurement errors are a constant offset and harmonic functions at the wavelengths used in the amplitude modulation for the phase based ranging (Rueger 1990). This approach is driven by the model of the sensor and for a Faro laser scanner it resulted in an improvement of about 30% in each coordinate direction (Lichti 2007).

Abmayr et al. (2005) use the similarity of a terrestrial laser scanner to a theodolite and determine for a Z+F Imager 5003 consecutively trunnion axis error, collimation axis error and vertical circle index error. In (Parian and Gruen 2005) a different approach for the same scanner is presented. The TLS observations in the spherical coordinate system are transformed to observations of a cylindrical coordinate system, which is possible if not the entire hemispherical field of view is used. Then a calibration approach for panoramic cameras is applied, reducing systematic errors in the angle observations. By this method residuals at target points identified in intensity images for a Z+F Imager 5003 are reduced by 90%.

The approaches presented so far rely on targeted points. While such a well-controlled experiment allows to make observations in the entire (angular and range) domain, it is not typical for project execution. As the stability of the parameters cannot be guaranteed (Lichti 2007), the development of on-the-job calibration methods appears to be necessary (Reshetyuk 2006).

It should also be noted that special device constructions, e.g. the dual window design of the Leica Scan stations, have not been investigated, yet.

2.2.3 Registration/Orientation In TLS relative orientation, also termed registration, is currently performed standard-wise by either of two methods: ICP type algorithms on the one hand and explicit tie features on the other hand. With a sufficient number of homologous tie features (points, lines, or surfaces) the transformation parameters can be computed. For points this is possible without approximate values (Horn 1987). ICP algorithms do not require homologous points, and the exact correspondence is replaced by iteratively determined approximate correspondence of points or small surface elements.

The terms relative orientation and registration are used almost synonymously. Brenner, Dold, and Ripperda (2007) note that 'registration' is putting more emphasis on the active role of the point cloud in the process itself (Brenner, Dold, and Ripperda 2007). The term 'relative orientation', on the other hand, also refers to the relation between device coordinate systems. Next to registration and orientation also the terms (co)-alignment, consolidation, and stitching are regrettably in use.

If only the object itself is of interest, it is sufficient to determine the relative orientation between scans. If the object also has to be placed in a superior coordinate system, absolute orientation becomes necessary, too. If the superior coordinate system is earth fixed it becomes the task of geo-referencing.

Using homologous features for relative orientation, they have to be extracted first. This becomes simple, if artificial targets are placed in the scene, e.g. with retroreflective material. In that case, due to the high intensity value, they can be found automatically. Natural tie elements can be identified with lower accuracy in the intensity images by visual inspection or automatic procedures. Alternatively, object surfaces can be used as tie elements (e.g., cylinders and planes). A method for automatic extraction of these patches and computation of transformation parameters has been presented by Rabbani, Dijkman, van den Heuvel, and Vosselman (2007), Dold and Brenner (2006), and Brenner, Dold, and Ripperda (2007). Finding the correct correspondences between features of two scans automatically can be seen as a graph search problem and methods for pruning the graph become necessary to reduce the search time, e.g. by computing and comparing parameters as patch boundary length. Another way to increase automation is relying on high resolution images, where the task has been studied for a longer time and (e.g.) the technique of coded targets has been developed. Al-Manasir and Fraser (2006) presented an approach where artificial targets are automatically found in a digital image, taken with a camera with known relative orientation to the laser scanner. Böhm and Becker (2007) suggests using the SIFT operator (Lowe 2004) to find homologous points in the intensity image. For two scans from notably different viewpoints of a house, including even repetitive texture, the relative orientation could be computed correctly, although with limited precision.

The ICP (iterative closest point) method does not require homologous points and performs the orientation of two scans, given approximate values of sufficient quality, entirely automatically. This is advantageous, because placing targets can be impossible, especially if the object is not accessible, additionally it can become time consuming. ICP has been suggested by Besl and McKay (1992) and variants are studied in (Rusinkiewicz and Levoy 2001). Much research effort is currently spent in order to automate finding approximate parameters for ICP. This leads to finding corresponding features as described above, possibly with lower quality requirements.

The authors believe that the registration task will run fully automatically for certain applications in some years. However, in the general case (including terrestrial scanning in a forest, etc.), or not relying on domain knowledge, the task will remain difficult. An alternative may come from cheap exterior orientation devices, allowing to obtain approximate exterior orientation, which can be used for reducing search spaces.

In order to transform one or multiple scans, generally one point cloud, into a superior coordinate system control points and/or patches are required. This control information can either be distributed in the scene or the coordinates of a laser scanner stand point can be observed, e.g. by centering over a known point or by mounting a GNSS antenna on top of the scanner. Deviation of

the stand axis from the vertical, defined by the local gravity field, may be observed and corrected with an electronic spirit level (inclinometer). Such a device is built into many terrestrial laser scanners. Concerning the targets used for absolute orientation the same as mentioned for relative orientation applies.

3 GEOMETRICAL ASPECTS OF SIGNAL–OBJECT INTERACTION

In laser scanning backscattered energy is used for range measurement. If the backscattering surface is flat, reflecting diffusely, oriented orthogonal to the laser beam, reflection appearing only at the material top surface (i.e., there is no penetration of the incident energy into the material), and the surface is not too close to the scanner (especially in the case of bistatic systems)⁴, the systems in use measure the quantity of interest. Furthermore, no other targets may be in the instantaneous field of view. In many cases in ALS and TLS these requirements do not hold.

- Depending on the echo detection method (Fox, Accetta, and Shumaker 1993; Katzenbeisser 2003; Jutzi and Stilla 2003b) used, the angle of incidence or surface roughness may have an impact on the range. For flat, slanted targets, discrete return systems that analyze the leading edge of the signal may report ranges shorter than the range to the beam center (Jutzi and Stilla 2003a). This effect is diminished for smaller footprints and shorter pulses.
- In TLS the dynamic range of the backscattered energy is quite high. This originates in the larger range spectrum of 1:100 to 1:1000 (e.g., minimum distance 2m, maximum distance 1km), and in the variety of backscattering surfaces, too. The surfaces reach from dark materials to retro reflective targets. Quantized in terms of Lambertian scatterers, the detectable reflected energy may vary from 5% to 1000%⁵. This results, using the laser range equation (Jelalian 1992), in return energies with a ratio of 1 : 10⁹. Effects depending on the intensity have been reported by many authors for terrestrial scanning (Hanke, Grussenmeyer, Grimm-Pitzinger, and Weinold 2006; Valanis and Tsakiri 2004). It is also reported that runway markers found on air-strips have caused similar effects in ALS.

It shall be noted that most airborne and terrestrial systems require a measure of the return energy for applying a range correction. Some preliminary results on the relation between observed intensity and range (and between intensity and object reflectivity) for a pulse time of flight terrestrial laser scanner have been presented by Pfeifer, Dorninger, Haring, and Fan (2007).

- In TLS penetration of the energy into different materials is generally not very well studied. For marble surfaces and red light Godin et al. (2001) have demonstrated the effect. This effect can reach significant magnitude, in the order of millimeter, for close ranges, typically encountered for triangulating laser scanners and for phase-based range measuring laser scanners.
- In ALS the terrain and (vegetation) objects upon it are the object of interest, but often it is impossible to measure only one, either the ground or the vegetation. Low (herbaceous)

⁴For bistatic (two-eyed) systems the emitter and receiver field of view overlap only after a certain distance.

⁵Lambertian scatterers have a maximum backscatter of 100% (no absorption), but retro-reflective material scatters back more energy into the direction of the source.

vegetation offsets the ground measurements. While the cause is basically well understood, i.e. scattering at all objects within the footprint and multiple scattering, the amount and the influencing factors are not very well known. They can be reported for a specific experiment, but prediction is not possible yet. In any case, the effects are in the order of cm to dm.

Ahokas, Kaartinen, and Hyypä (2003) have reported systematic influences of grass on the measured range. Bollweg and de Lange (2003) reported systematic upward shifts for long dense grass. In (Oude Elberink and Crombaghs 2004) it is shown that upward shifts occurred up to 15cm on low vegetation areas (creeping red fescue, thrift). A relation could be seen between the density of the vegetation coverage and the systematic error: 0% coverage meant no upward shift, 100% coverage showed a 15cm shift. The study of (Hodgson and Bresnahan 2004) fits less well into that picture, as the systematic shifts reported are all very small, i.e. below 6cm. Pfeifer, Gorte, and Oude Elberink (2004) reported shifts of 7cm for long dense grass and 10cm for a young forest.

Hopkinson et al. (2004) have correlated height of low vegetation with standard deviation of heights and other textural characteristics. Concentrating on the experiments over low vegetation (below 0.5m) the errors are comparatively large with respect to the vegetation height and a functional relationship is not obvious.

Contrary to the research efforts and solutions presented in the sections 2.1.2 and 2.2.2 (ALS and TLS calibration) these problems cannot be confined to the measurement system itself, but target properties have to be considered, too. Even when recording the full waveform of the backscattered echoes, not much information beyond spatial and absorption/scattering characteristics can be extracted. The echo width holds information on the range distribution within the footprint, but this is not necessarily connected to the discrepancy between ground elevation and systematically shortened range measurement. Thus, material properties can only be derived if additional knowledge is provided by external sources as imagery, maps, or possibly range information at another wavelength.

Phantom points, also called virtual points, also hinder automatic exploitation, especially in TLS data sets. These points are encountered, when the footprint is distributed over different, hard targets in close proximity⁶. The measured range is then between those two or more surfaces. First steps for automatic removal of these points were made (e.g. Sotoodeh (2006)) by analyzing the spatial distribution of points (without consideration of the scanner position). There is no reliable method available yet. Considering the geometry of the measurement setup can contribute in identifying these points, as they are aligned along bundles or rays with the origin in the laser scanner.

Furthermore, multi-path reflections can occur (not only in TLS, but also in ALS data), resulting in too long ranges. A typical situation is that a surface along the propagation path of the laser beam features (some) specular reflection onto another, diffusely reflecting surface. A portion of its diffuse backscatter travels via the specularly reflecting surface back to the detector. In (Lichti, Gordon, and Tipdecho 2005) an overview of errors in TLS, including the influence of geo-referencing and beam width, is given.

⁶For pulse time of flight systems this depends on the pulse duration, whereas phase-based systems are always affected.

We believe that the above items will continue to play a role. For natural surfaces, thus rather in the airborne case, the “range errors” induced change spatially, as the vegetation is not entirely homogeneous. Surfaces encountered in terrestrial scanning are often more homogenous, especially compared to the measurement density, and the “error” is more of systematic nature. Applications requiring higher precision will become possible when tackling and solving these problems.

4 DATA PROCESSING

The early steps of data processing, which are not directly linked to an application, are typically segmentation or clustering of the laser scanning point cloud, removal of erroneous points, and thinning.

Segmentation and clustering are means to organize points, measured by laser scanning, into homogeneous groups. Points of a group shall be neighbors, and in this way larger entities are generated and the data is organized on a higher level. A *classification* of such groups or sets is then in the domain of a certain application, which provides a “meaning”, a class attribute (e.g. “house roof”, “vegetation”, or “tree”) for each segment. In many publications segmentation is presented as one step for a certain application, e.g. building reconstruction. In this section we want to specifically concentrate on general purpose approaches.

Segmentation and clustering have been studied for a long time in image processing where the neighborhood of elements, i.e. pixel, is given implicitly by the matrix layout. For point clouds of laser scanning, on the other hand, neighborhood is often defined via Euclidean distance, TIN topology, or a number k defining the k nearest points as neighbors (kNN). An overview for neighborhood in ALS data is given in (Filin and Pfeifer 2005).

A general overview on segmentation algorithms is provided by (Hoover et al. 1996), and overviews dedicated to laser scanning data are given in (Vosselman, Gorte, Sithole, and Rabbani 2004) and (Geibel and Stilla 2000). Most often region growing from a seed point is applied (Vosselman, Gorte, Sithole, and Rabbani 2004) where the features used as similarity measure are

- height difference for airborne laser scanning data,
- normal vector similarity, or
- distance to a plane.

Differences and similarity may either be measured from the seed point to a currently investigated point, or from the previously accepted segment point to its new neighbors. The latter strategy allows to grow over bent surfaces, the first one not. These region growing approaches generally deliver smooth (gently curved) or planar (flat) regions.

The watershed transform is used to segment digital surface models, not point clouds, by a notably different approach. In forestry it is one standard method to extract the single trees from a canopy model. While most general purpose approaches are performed on the point cloud, Vögtle and Steinle (2004) and Rottensteiner, Trinder, Clode, and Kubik (2005), for example, apply 2.5D techniques on gridded versions of the original data. This is only applicable for ALS data and reduces the range of extractable structures. Operating on the point cloud enables also the extraction of vertical planes or planes stacked on top of each other, thus the full 3D content of the data.

Clustering performs the grouping of point sets not in object space, but in a feature space. The features used may be an estimated normal vector for each point, a local roughness measure, the intensity measure, etc. The connectivity in object space is realized by adding the coordinates of the points as elements of the feature vector. Such approaches have been presented for laser point clouds by, e.g., Filin and Pfeifer (2006) and Melzer (2007).

The normal vector, a frequently used feature, is often estimated by computing an orthogonal regression plane. In this eigenvector/eigenvalue approach all three eigenvalues can be used to classify points as belonging to a surface, a volumetric distribution of points, a single point or a linear feature (Medioni, Lee, and Tang 2000). In (Belton and Lichti 2006) also the recognition of surface boundaries is discussed.

Voting schemes such as the Hough transform are hardly applied on large data sets. Their disadvantage is that connectivity is not considered. Such approaches are more typically used, if some organization of the entire point cloud into smaller entities has already been performed. Rabbani and van den Heuvel (2005), e.g., first apply segmentation based region growing, and then use a Hough transform to detect and reconstruct cylinders in the individual segments. von Hansen, Michaelsen, and Thonnessen (2006) apply the RANSAC algorithm (Fischler and Boller 1982) for detecting planes. In order to overcome the problem of connectivity, they first divide the space into larger 3D cells and apply RANSAC plane detection to the point cloud within the cell. Then a grouping step connects similar planes of neighboring cells.

There is a number of strategies to *reduce the volume* of the data. Modeling itself, especially model reconstruction with the help of analytical surfaces, can be seen as a means to reduce the data volume, and by fitting surfaces also a means of reducing noise. The same holds for the interpolation of a digital surface model (DSM) or a DTM by qualified interpolation methods that consider the stochastic properties of the data. Methods to decimate dense point clouds and reduce noise are given in (Pauly, Gross, and Kobbelt 2002). An overview on decimation of polygonal meshes is given in (Heckbert and Garland 1997).

Close range scanning systems based on the phase shift measurement principle are capable of producing very dense point clouds, e.g. 5 points per cm^2 . The footprints of the laser beam on the object surface are then overlapping. It is therefore justified to reduce the volume of the data and also reduce the noise in the data in one step. According to the authors view there is currently a lack of studies that investigate these possibilities considering the properties of laser scanning data (next to noise e.g. measurement position, or missing points) and not treating the measurements as a set of discrete points.

5 DTM DETERMINATION FROM ALS DATA

During the ALS data acquisition process no interpretation or classification of the determined echoes, which were reflected from different objects, is performed. However, for the generation of a DTM the classification of the ALS data into terrain and off-terrain points is essential. This separation, which is important for other applications (e.g. vegetation and power line mapping), is often also entitled as “filtering”.

In the past, many different solutions for the filtering of the ALS data were published (cf. Sithole and Vosselman (2004)). On one hand these methods can be classified by the input data they use (one type of methods uses rasterized ALS data while others use the original ALS point cloud) whereas on the other hand they can

be grouped by the different concepts they use in order to classify the data. One group of algorithms are the morphological filters (e.g. Vosselman (2000)), which use a structure element, describing admissible height differences as a function of the horizontal distance. Another group are the progressive densification methods (Axelsson 2000; von Hansen and Vögtle 1999). They start with a rough approximation of the DTM with initial terrain points (typically the lowest point within a certain grid cell) and iteratively densify the DTM by the evaluation of a set of rules (e.g. maximal distance to the DTM approximation, angle criteria, etc.). The third group of filter methods work surface based (Kraus and Pfeifer 1998; Elmqvist, Jungert, Lantz, Persson, and Söderman 2001). They use a surface model that iteratively approaches the DTM calculated based on the entire point set by adapting the influence of the individual input points. Finally, recently a set of segmentation based methods were published (e.g. Sithole and Vosselman (2005) and Tóvari and Pfeifer (2005)). In the first step, these methods segment the ALS data with a local neighborhood analysis and subsequently classify the segments by different strategies. Most of the existing methods do not consider further input data (e.g. ortho photos) and only analyze the geometric relation between neighbored ALS points. A comparison of the performance of different methods can be found in (Sithole and Vosselman 2004).

Doneus and Briese (2006) studied the advanced possibilities for DTM generation using full-waveform ALS data. They used the echo width, which was determined with the help of a Gaussian decomposition of the full-waveform (FWF) signal for each echo (Wagner, Ullrich, Ducic, Melzer, and Studnicka 2006). The potential of this further information for the elimination of low vegetation could be demonstrated. With the help of a pre-filter step that eliminates echoes with a higher echo width a significant improvement of the DTM could be achieved. However, up to now it is not studied in detail how (and if) the additional FWF information can be used for advanced modeling tasks.

6 SUMMARY

In this paper an overview on data acquisition and the first processing steps was given for airborne and terrestrial laser scanning. There is a small number of standard products, e.g. the DTM, that are produced routinely and efficiently. In order to increase automation for other applications, further development of the first processing steps, especially registration, segmentation, and error/outlier removal, is necessary. For calibration, geometric and physical aspects will have to be considered simultaneously. Also the application-specific approaches are still matter of research, e.g. building reconstruction. The hardware development in the recent years has been fast, considering for example the increase in pulse repetition rate. However, the success rate in object reconstruction did not grow linearly with it. Therefore, most research effort will have to be spend in these application specific fields.

REFERENCES

IAPRS= International Archives of Photogrammetry and Remote Sensing Conf. on O3D= Conference on Optical 3-D Measurement Techniques 3rdTech, 2007. www.3rdtech.com. Homepage of the company 3rdTech, accessed: June 2007.

Abmayr, T., Dalton, G., Hines, D., Liu, R., Härtl, F., Hirzinger, G., and Fröhlich, C., 2005. Standardization and visualization of 2.5d scanning data and color information by inverse mapping. In: Gruen and Kahmen (Eds.), *7th Conf. on O3D*, Vienna, Austria, pp. 164–173.

Ahokas, E., Kaartinen, H., and Hyypä, J., 2003. A quality assessment of airborne laser scanner data. In: *IAPRS, XXXIV, 3/W13*, Dresden, Germany.

Ahokas, E., Kaasalainen, S., Hyypä, J., and Suomalainen, J., 2006. Calibration of the Optech ALTM 3100 laser scanner intensity data using brightness targets. In: *IAPRS, XXXVI, 1*, Paris, France.

Al-Manasir, K. and Fraser, C., 2006. Registration of terrestrial laser scanner data using imagery. *The Photogrammetric Record* 21(115), 255–268.

Axelsson, P., 2000. DEM generation from laser scanner data using adaptive TIN models. In: *IAPRS, XXXIII, B4*, Amsterdam, Netherlands, pp. 111–118.

Behan, Maas, and Vosselman, 2000. Steps towards quality improvement of airborne laser scanner data. In: *Proceedings of the 26th annual conference of the Remote Sensing Society*, Leicester, UK.

Belton, D. and Lichti, D., 2006. Classification and segmentation of terrestrial laserscanner point clouds using local variance information. In: *IAPRS, XXXVI, 5*, Dresden, Germany.

Beraldin, J.-A., El-Hakim, S., and Blais, F., 2007. Traceable 3d imaging metrology: evaluation of 3d digitizing techniques and commercial 3d systems/scanners in a dedicated metrology laboratory. In: *8th Conf. on O3D*, Zurich, Switzerland.

Besl, P. and McKay, N., 1992. A method for registration of 3D shapes. *IEEE Transactions on Pattern Analysis and Machine Intelligence* 14(2), 239 – 256.

Blais, F., 2004. Review of 20 years of range sensor development. *Journal of Electronic Imaging* 13(1), 231–240.

Böhm, J. and Becker, S., 2007. Automatic marker-free registration of terrestrial laser scans using reflectance features. In: *8th Conf. on O3D*, Zurich, Switzerland.

Bollweg, A. and de Lange, R., 2003. Wat ruist er door het struikgewas. Technical Report AGI-GAR-2003-22 (in Dutch), Adviesdienst Geo-Informatie en ICT, Rijkswaterstaat, The Netherlands.

Brenner, C., Dold, C., and Ripperda, N., 2007. Coarse orientation of terrestrial laser scans in urban environments. *ISPRS Journal of Photogrammetry and Remote Sensing*. Accepted for publication.

Breuckmann, B., Rein, H., Pfeifer, J., and Mutsch, J., 2007. Acceptance test of topometric 3d-scanners: experiences with the guideline vdi/vde 2634. In: *8th Conf. on O3D*, Zurich, Switzerland.

Burman, H., 2000. Adjustment of laserscanner data for correction of orientation errors. In: *IAPRS, XXXIII, B3/1*, Amsterdam, The Netherlands, pp. 125–132.

Burman, H., 2002. Laser strip adjustment for data calibration and verification. In: *IAPRS, XXXIV, 3*, Graz, Austria, pp. 67–72.

Callidus, 2007. www.trimble.com. Homepage of the company CAL-LIDUS precision systems GmbH, accessed: June 2007.

Crombaghs, M., Brügelmann, R., and de Min, E., 2000. On the adjustment of overlapping strips of laseraltimeter height data. In: *IAPRS, XXXIII, 3A*, Amsterdam, Netherlands, pp. 230–237.

Csanyi, N. and Toth, C., 2007. Improvement of lidar data accuracy using lidar-specific ground targets. *Photogrammetric Engineering & Remote Sensing* 73(4), 385–396.

Diamond Airborne Sensing, 2007. www.diamond-air.at. Homepage of the company Diamond Aircraft, accessed: August 2007, in German.

Dold, C. and Brenner, C., 2006. Registration of terrestrial laser scanning data using planar patches and image data. In: *IAPRS, XXXVI, 5*, Dresden, Germany, pp. 78–83.

Doneus, M. and Briese, C., 2006. Digital terrain modelling for archaeological interpretation within forested areas using full-waveform laser-scanning. In: *The 7th International Symposium on Virtual Reality, Archaeology and Cultural Heritage VAST*, Zypern.

Ellum, C. and El Sheimy, N., 2006. New strategies for integrating photogrammetric and GNSS data. In: *IAPRS, XXXVI/5*, Dresden, Germany, pp. 103–108.

Elmqvist, M., Jungert, E., Lantz, F., Persson, A., and Söderman, U., 2001. Terrain modelling and analysis using laser scanner data. In: *IAPRS, XXXIV, 3/W4*, Annapolis, MD, USA.

Faro, 2007. www.faro.com. Homepage of the company FARO Technologies, Inc., accessed: June 2007.

Filin, S., 2002. Surface clustering from airborne laser scanning data. In: *IAPRS, XXXII, 3A*, Graz, Austria, pp. 119–124.

- Filin, S., 2003. Recovery of systematic biases in laser altimetry data using natural surfaces. *Photogrammetric Engineering & Remote Sensing* 69(11), 1235–1242.
- Filin, S. and Pfeifer, N., 2005. Neighborhood systems for airborne laser data. *Photogrammetric Engineering & Remote Sensing* 71(6), 743–755.
- Filin, S. and Pfeifer, N., 2006. Segmentation of airborne laser scanning data using a slope adaptive neighborhood. *ISPRS Journal of Photogrammetry and Remote Sensing* 60(2), 71–80.
- Finnegan, D. C., Krabill, W., Lichvar, R. W., Ericsson, M. P., Frederick, E., Manizade, S., Yungel, J., Sonntag, J., and Swift, R., 2005. Using NASA's Airborne Topographic Mapper IV to Quantify Geomorphic Change in Arid Southwestern Stream Systems. In: *AGU Fall Meeting Abstracts*.
- Fischler, M. A. and Bolter, R. C., 1982. Random sample consensus: A paradigm for model fitting with applications to image analysis and automated cartography. *Communications of the ACM* 24(6), 381–395.
- Fli-Map, 2007. www.fli-map.nl. Homepage of FLI-MAP, accessed: August 2007.
- Flood, M. and Gutelius, B., 1997. Commercial implications of topographic terrain mapping using scanning airborne laser radar. *Photogrammetric Engineering & Remote Sensing* 63, 327–365.
- Fox, C. S., Accetta, J. S., and Shumaker, D. L., 1993. *Active Electro-Optical Systems*, Volume 6 of *The infrared and electro-optical systems handbook*. SPIE Optical Engineering Press.
- Geibel, R. and Stilla, U., 2000. Segmentation of laser altimetry data for building reconstruction: different procedures and comparison. In: *IAPRS, XXXIII, B3*, Amsterdam, the Netherlands, pp. 326–334.
- GIM, 2007. www.gim-international.com/productsurvey. Product surveys of GIM international, accessed: August 2007.
- Godin, Rioux, Beraldin, Levoy, Cournoyer, and Blais, 2001. An assessment of laser range measurement on marble surfaces. In: *5th Conf. on O3D*, Vienna, Austria.
- Hanke, K., Grussenmeyer, P., Grimm-Pitzinger, A., and Weinold, T., 2006. First experiences with the trimble gx scanner. In: *IAPRS, XXXVI, 5*, Dresden, Germany.
- Heckbert, P. S. and Garland, M., 1997. Survey of polygonal surface simplification algorithms. Technical report, School of Computer Science, Carnegie Mellon University, Pittsburgh, PA. Technical Report.
- Hesse, C., Neuner, H., and Kutterer, H., 2005. Statistical analysis of kinematic lasers scans. In: *7th Conf. on O3D*, Vienna, Austria, pp. 103–112.
- Hodgson, M. E. and Bresnahan, P., 2004. Accuracy of airborne lidar-derived elevation: Empirical assessment and error budget. *Photogrammetric Engineering & Remote Sensing* 70(3), 331–339.
- Höfle, B. and Pfeifer, N., 2007. Correction of laser scanning intensity data: Data and model-driven approaches. *ISPRS Journal of Photogrammetry and Remote Sensing*. Accepted for publication.
- Hoover, Jean-Baptiste, Jiang, Flynn, Bunke, Goldgof, Bowyer, Eggert, Fitzgibbon, and Fisher, 1996. An experimental comparison of range image segmentation algorithms. *IEEE Transactions on Pattern Analysis and Machine Intelligence* 18(7), 673–689.
- Hopkinson, D., Chasmer, L., Zsigovics, G., Creed, I., Sitar, M., Treitz, P., and Maher, R., 2004. Errors in lidar ground elevation and wetland vegetation height estimates. In: *IAPRS, XXXVI, 8/W2*, Freiburg, Germany.
- Horn, B., 1987. Closed-form solution of absolute orientation using unit quaternions. *Journal of the Optical Society of America A* 4, 629–642.
- Hug, C. and Wehr, A., 1997. Detecting and identifying topographic objects in imaging laser altimetry data. In: *IAPRS, XXXII, 4/W2*, pp. 16–29.
- Hyypä, J., Hyypä, H., Litkey, P., Yu, X., Haggren, H., Roennholm, P., Pyysalo, U., Pitkaenen, J., and Maltamo, M., 2004. Algorithms and methods of airborne laser-scanning for forest measurements. In: *IAPRS, XXXVI, 8/W2*, Freiburg, Germany.
- I-SiTE, 2007. www.isite3d.com. Homepage of the company I-SiTE Pty Ltd, accessed: June 2007.
- Jelalian, A. V., 1992. *Laser Radar Systems*. Artech House, Boston.
- Jutzi, B. and Stilla, U., 2003a. Analysis of laser pulses for gaining surface features of urban objects. In: *2nd GRSS/ISPRS Joint Workshop on Remote Sensing and data fusion on urban areas. URBAN 2003, IEEE*, pp. 13–17.
- Jutzi, B. and Stilla, U., 2003b. Laser pulses analysis for reconstruction and classification of urban objects. In: *IAPRS, XXXIV, 3/W8*, Munich, Germany, pp. 151–156.
- Kager, H., 2004. Discrepancies between overlapping laser scanning strips - simultaneous fitting of aerial laser scanner strips. In: *IAPRS, XXXV, B/1*, Istanbul, Turkey, pp. 555–560.
- Karimi, H. A. and Hammad, A., 2004. *Telegeoinformatics: location-based services and computing*. CRC Press, Boca Raton.
- Katzenbeisser, R., 2003. Technical note on: Echo detection. TopoSys GmbH, Germany.
- Kilian, J., Haala, N., and Englich, M., 1996. Capture and evaluation of airborne laser scanner data. In: *IAPRS, XXXI, B3*, Vienna, Austria, pp. 383–388.
- Kraus, K. and Pfeifer, N., 1998. Determination of terrain models in wooded areas with airborne laser scanner data. *ISPRS Journal of Photogrammetry and Remote Sensing* 53, 193–203.
- Kraus, K. and Pfeifer, N., 2001. Advanced DTM generation from LIDAR data. In: *IAPRS, XXXIV, 3/W4*, Annapolis, MD, USA, pp. 23–30.
- Latypov, D., 2005. Effects of laser beam alignment tolerance on lidar accuracy. *ISPRS Journal of Photogrammetry and Remote Sensing* 59(6), 361–368.
- Leica, 2007. www.leica-geosystems.com. Homepage of the company Leica Geosystems, accessed: August 2007.
- Lichti, D., 2007. Error modelling, calibration and analysis of an amcw terrestrial laser scanner system. *ISPRS Journal of Photogrammetry and Remote Sensing* 61(5), 307–324.
- Lichti, D., Gordon, S., and Tipdecho, T., 2005. Error models and propagation in directly georeferenced terrestrial laser scanner networks. *Journal of Surveying Engineering* 131(4), 135–142.
- Lin, 1997. Waveform sampling lidar applications in complex terrain. *International Journal of Remote Sensing* 18(10).
- Lindenberger, 1989. Test results of laser profiling for topographic terrain survey. Technical Report 13, Institute of Photogrammetry, University of Stuttgart.
- Lindenberger, J., 1993. *Laser-Profilmessungen zur topographischen Geländeaufnahme*. Ph. D. thesis, University Stuttgart, Institute of Photogrammetry.
- Lohr, U. and Eibert, 1995. The toposys laser scanner-system. In: Fritsch and Hobbie (Eds.), *Photogrammetric Week*.
- Lowe, D. G., 2004. Distinctive image features from scale-invariant keypoints. *International Journal of Computer Vision* 60(2), 91–110.
- Medioni, G., Lee, M.-S., and Tang, C.-K., 2000. *A computational framework for segmentation and grouping*. Elsevier, Amsterdam.
- Melzer, T., 2007. The mean shift algorithm for clustering point clouds. *Journal of Applied Geodesy*. Accepted for publication.
- Naesset, E., 1997. Determination of mean tree height of forest stands using airborne laser scanner data. *ISPRS Journal of Photogrammetry and Remote Sensing* 52(2), 49–56.
- Optech, 2007. www.optech.ca. Homepage of the company Optech, accessed: June 2007.
- Oude Elberink, S. and Crombaghs, M., 2004. Laseraltimetrie voor de hoogtemetingen van de kwelders Waddenzee. Technical Report AGI-GAP-2003-50 (in Dutch), Adviesdienst Geo-Informatie en ICT, Rijkswaterstaat, The Netherlands.
- Parian, J. A. and Gruen, A., 2005. Integrated laser scanner and intensity image calibration and accuracy assessment. In: *IAPRS, XXXVI, 3/W19*, Enschede, the Netherlands, pp. 18–23.
- Pauly, M., Gross, M., and Kobbelt, L., 2002. Efficient simplification of point-sampled surfaces. In: *Proceedings of the conference on Visualization '02*, Boston, Massachusetts, pp. 163–170. IEEE Computer Society.
- Pfeifer, N., Dorninger, P., Haring, A., and Fan, H., 2007. Investigating terrestrial laser scanning intensity data: Quality and functional relations. In: *8th Conf. on O3D*, Zurich, Switzerland.
- Pfeifer, N., Gorte, B., and Oude Elberink, S., 2004. Influences of vegetation on laser altimetry – analysis and correction approaches. In: *IAPRS, XXXVI, 8/W2*, Freiburg, Germany, pp. 283–287.

- POB, 2007. www.pobonline.com. Product surveys of Point of Beginning, accessed: August 2007.
- Rabbani, T., Dijkman, S., van den Heuvel, F., and Vosselman, G., 2007. An integrated approach for modelling and global registration of point clouds. *ISPRS Journal of Photogrammetry and Remote Sensing* 61, 355–370.
- Rabbani, T. and van den Heuvel, F., 2005. Efficient hough transform for automatic detection of cylinders in point clouds. In: *IAPRS, XXXVI, 3/W19*, Enschede, the Netherlands, pp. 60–65.
- Reed and Lynch, 1996. Near field airborne remote sensing using a laser mapping system on electric transmission line corridor surveys and capacity analyses. In: *International Airborne Remote Sensing Conference and Exhibition – Technology, Measurement & Analysis*, San Francisco, USA.
- Reshetyuk, Y., 2006. Calibration of terrestrial laser scanners for the purposes of geodetic engineering. In: *3rd IAG Symposium on Geodesy for Geotechnical and Structural Engineering and 12th FIG Symposium on Deformation Measurements*, Baden, Austria.
- Riegl, 2007. www.riegl.com. Homepage of the company RIEGL Laser Measurement Systems GmbH, accessed: August 2007.
- Ries, C., Kager, H., and Stadler, P., 2002. High-quality geo-referencing of GPS/IMU-supported multi-spectral airborne scanner data - experiences and results. In: *IAPRS, XXXIV/3*, Graz, Austria, pp. 222–226.
- Ritchie and Pachepsky, 1998. Seasonal changes in fractal landscape surface roughness estimated from airborne laser altimetry data. *International Journal of Remote Sensing* 19(13).
- Rottensteiner, F., Trinder, J., Clode, S., and Kubik, K., 2005. Automated delineation of roof planes from lidar data. In: *IAPRS, XXXVI, 3/W19*, Enschede, the Netherlands.
- Rueger, J., 1990. *Electronic Distance Measurement: an introduction* (3 ed.). Springer-Verlag, Heidelberg, Germany.
- Rusinkiewicz, S. and Levoy, M., 2001. Efficient variants of the icp algorithm. In: *Third International Conference on 3-D Digital Imaging and Modeling (3DIM '01)*, Los Alamitos, CA, USA, pp. 145.
- Schmitz, Wuebbena, Bagge, and Kruck, 2001. Benefit of rigorous modelling of gps in combined at/gps/imu-bundle block adjustment. In: *OEEPE Workshop*, Hannover, Germany.
- Sithole, G. and Vosselman, G., 2004. Experimental comparison of filtering algorithms for bare-earth extraction from airborne laser scanning point clouds. *ISPRS Journal of Photogrammetry and Remote Sensing* 59(1-2), 85–101.
- Sithole, G. and Vosselman, G., 2005. Filtering of airborne laser scanner data based on segmented point clouds. In: *IAPRS, XXXVI, 3/W19*, Enschede, The Netherlands, pp. 66–71.
- Skaloud, J., 2006. Reliability of direct georeferencing phase 0 – an overview of current approaches and possibilities. In: *EuroSDR Official Publication 51*, pp. 143–168.
- Skaloud, J. and Lichti, D., 2006. Rigorous approach to boresight self-calibration in airborne laser scanning. *ISPRS Journal of Photogrammetry and Remote Sensing* 61(1), 47–59.
- Sotoodeh, S., 2006. Outlier detection in laserscanner point clouds. In: *IAPRS, XXXVI, 5*, Dresden, Germany.
- TopEye, 2007. www.blomasa.com. Homepage of the BLOM GROUP, accessed: August 2007.
- TopoSys, 2007. www.toposys.com. Homepage of the company TopoSys GmbH, accessed: June 2007.
- Tóvari, D. and Pfeifer, N., 2005. Segmentation based robust interpolation - a new approach to laser data filtering. In: *IAPRS, XXXVI, 3/W19*, Enschede, The Netherlands, pp. 79–84.
- Trimble, 2007. www.trimble.com/. Homepage of the company Trimble, accessed: June 2007.
- Valanis, A. and Tsakiri, M., 2004. Automatic target identification for laser scanners. In: *Proceedings of XXth ISPRS Congress*, Istanbul, Turkey.
- Vögtle, T. and Steinle, 2004. Detection and recognition of changes in building geometry derived from multitemporal laserscanning data. In: *IAPRS, XXXV*, Istanbul, Turkey.
- von Hansen, W., Michaelsen, E., and Thonnessen, U., 2006. Cluster analysis and priority sorting in huge point clouds for building reconstruction. In: *18th International Conference on Pattern Recognition (ICPR'06)*, pp. 23–26.
- von Hansen, W. and Vögtle, T., 1999. Extraktion der Geländeoberfläche aus flugzeuggetragenen Laserscanner-Aufnahmen. *Photogrammetrie Fernerkundung Geoinformation* 4, 229–236.
- Vosselman, G., 2000. Slope based filtering of laser altimetry data. In: *IAPRS, XXXIII, B3*, Amsterdam, Netherlands, pp. 935–942.
- Vosselman, G., Gorte, B. G. H., Sithole, G., and Rabbani, T., 2004. Recognising structure in laser scanner point clouds. In: *IAPRS, XXXVI, 8/W2*, Freiburg, Germany.
- Vosselman, G. and Maas, H.-G., 2001. Adjustment and filtering of raw laser altimetry data. In: *Proceedings of OEEPE Workshop on Airborne Laserscanning and Interferometric SAR for Detailed Digital Terrain Models*, Stockholm, Sweden.
- Wagner, W., Ullrich, A., Ducic, V., Melzer, T., and Studnicka, N., 2006. Gaussian decomposition and calibration of a novel small-footprint full-waveform digitising airborne laser scanner. *ISPRS Journal of Photogrammetry and Remote Sensing* 60(2), 100–112.
- Wagner, W., Ullrich, A., Melzer, T., Briese, C., and Kraus, K., 2004. From single-pulse to full-waveform airborne laser scanners: potential and practical challenges. In: *IAPRS, XXXV*, Istanbul, Turkey.
- Wehr, A., Hemmler, M., Thomas, M., and Maierhofer, C., 2007. Moisture detection on building surfaces by multi-spectral laser scanning. In: *8th Conf. on O3D*, Zurich, Switzerland.
- Wehr, A., Kleusberg, A., and Schiele, O., 2006. CW-laser-scanning state-of-the-art at INS and future multispectral sensors. In: L. Gruendig and O. Altan (Eds.), *Turkish-German Joint Geodetic Days "Geodesy and Geoinformation in the Service of our Daily Life"*, Berlin, Germany.
- Wehr, A. and Lohr, U., 1999. Airborne laser scanning an introduction and overview. *ISPRS Journal of Photogrammetry and Remote Sensing* 54(2-3), 68–82.
- Zoller+Fröhlich, 2007. www.zofre.de. Homepage of the company Zoller+Fröhlich GmbH, accessed: June 2007.
- Zwally, H., Schutz, B., Abdalati, Abshire, Bentley, Brenner, Bufton, Dezio, Hancock, Harding, Herring, Minster, Quinn, Palm, Spinhirne, and Thomas, 2002. Icesat's laser measurements of polar ice, atmosphere, ocean, and land. *Journal of Geodynamics* 34(3), 405–445.

EXTRACTING WINDOWS FROM TERRESTRIAL LASER SCANNING

Shi Pu and George Vosselman

International Institute for Geo-information Science and Earth Observation (ITC),
Hengelosestraat 99, P.O. Box 6, 7500 AA Enschede, The Netherlands
spu@itc.nl, vosselman@itc.nl

Commission V, WG 3

KEY WORDS: 3D modeling, terrestrial laser scanning, TIN; evaluation

ABSTRACT:

With the high density point clouds obtained with terrestrial laser scanning, detailed building facade structures, such as windows, can be recovered. There are usually only a few laser points available for windows, because window frames are small parts on walls, and window glass reflects no laser beam. Insufficient raw laser information makes it very difficult to recover reliable geometry of a window without human interaction. In this paper, we describe an approach to automatically extract windows from terrestrial point clouds. First, a segmentation process will group laser points in planar segments. Walls, doors and extrusions will be detected by applying feature constraints. Then, two detection strategies for windows are presented, depending on whether a window is covered with curtains or not. Windows which are not covered with curtains reflect no laser beam during the scanning process, and therefore cause holes on the wall segments. Laser points are available for windows which are covered with curtains, but they usually are not on the same plane as its wall and will therefore be grouped into other segments than wall segments. This again results in holes on wall segments. Holes on the wall are recognized by searching long edges from the TIN, generated for wall segments. After filtering out the holes caused by doors and extrusions, the remaining holes are believed to be caused by windows, and hence fitted to rectangles. The result from our approach is evaluated and discussed with examples of reconstructed building facades.

1. INTRODUCTION

Recently, the topic of building reconstruction has become a popular research of interest. This is because various applications, such as virtual tourism, urban planning, and cultural documentations, require realistic building models. Many algorithms and systems have been proposed towards the topic of building reconstruction after several years' research. According to the position of data acquisition, the reconstruction algorithms can be categorized to airborne based (Brenner 2005, Maas 2001, Suveg and Vosselman 2004) and terrestrial based (Haala et.al. 2006, Remondino and El-Hakim 2006).

Taking the airborne images or airborne laser points as primary data source, airborne reconstruction approaches are able to reconstruct building roofs well. However, it is very difficult to recover facade structures from airborne approaches, because the oblique acquisition aspect makes it very difficult to retrieve sufficient raw data for facades. Only a few pixels or laser points are available for facade is the usual case. In contrast, terrestrial approaches are able to provide abundant facade information. In particular, terrestrial laser scanning gives explicit 3D information, which enables the rapid and accurate capture of the geometry of a complex building facade; terrestrial laser scanning also provides high density point clouds, which gives enough raw data from which accurate and detailed 3D models can be obtained.

Many researchers are active in the field of extracting geometry features from laser point cloud. Edge based approaches (Gross and Thoennessen 2006, Sotooth 2006, Wani and Arabnia 2003) aim at detecting boundary points from point cloud, and then fit to lines. The surfaces based approaches use local surface

properties as a similarity measure, and merge together the points which are spatially close and have similar surface properties. These surfaces can be either planar surface (Dold and Brenner 2004, Schuster 2004), or curved surfaces such as cylinder, sphere and cone (Rabbani et.al. 2006).

With the extracted geometry features, we can extract higher level of features with semantic meanings. In (Pu and Vosselman 2006) the authors described an automatic method to extract building features from terrestrial laser scanning. The method first defines several important building features (walls, roofs, doors, extrusion) with building constraints. Then the terrestrial laser point cloud for a building facade is segmented, so that points belonging to the same planes are grouped together. Finally each segment is compared with different building feature constraints to determine which feature this segment represents. It is possible to extend this approach, so that more detailed structures, such as windows, can be extracted. The recognized wall segments usually contain many holes, which mostly result from windows. A feature based method is employed to recognize door and extrusion segments. This can be used to discard holes caused by doors and extrusions. Combination of feature extraction and holes detection leads to a robust algorithm for extracting windows.

In section 2 we first give a brief introduction on building feature extraction. Section 3 describes how windows are extracted from holes on wall segments, and evaluates this approach. Some concluding remarks are given in section 4.

2. FEATURE EXTRACTION

2.1 Building feature extraction

An automatic method to extract building features has been demonstrated in a previous paper. Here we give a brief introduction because of its strong relevance to the window

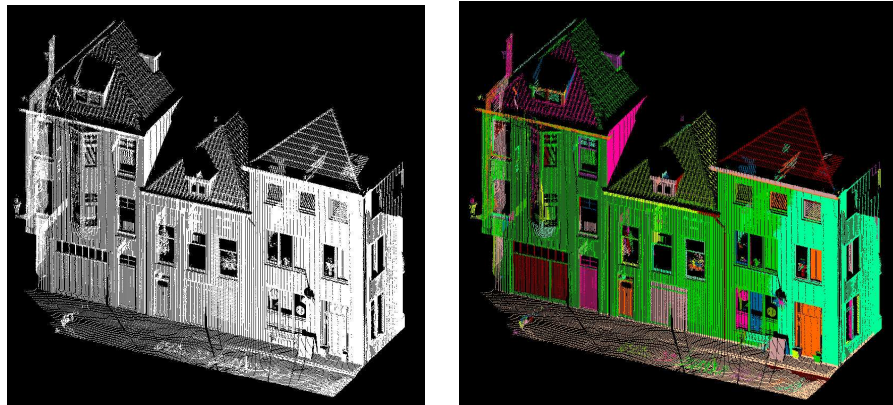


Figure 1. Left: terrestrial laser scanned building facade; right: segmentation result

	Size	Position	Direction	Topology
Wall	Segment(s) with larger area		Vertical	May intersect ground
Roof	Segment(s) with large area	Above wall	Not vertical	Intersects a wall
Door	Area within certain range	On the wall	Vertical	Intersects the ground
Extrusion		A little outside the wall/roof		

Table 1. Constraints for building features

seed surfaces which consist of a group of nearby points that fit well to a plane. Then seed surfaces are grown to their nearby points. Only the points within certain distance to the seed surface and with a perpendicular distance to the seed plane below some threshold can be added to the seed surface. Figure 1 shows a terrestrial laser scanned building facade, and its segmentation result.

- Feature constraints.** Some important building features (wall, roof, door, extrusion) are defined with feature constraints, related to size, position, direction and topology. All feature constraints are derived from human knowledge about building structures. For example, we know that a wall is a large vertical patch, and that a wall intersects the ground. The feature constraints for wall feature can be defined as: a large area (size) on a vertical plane (direction) with an intersection with the ground plane (topology). Table 1 gives the constraints for different features. Most of the tolerance values are independent of different data set because of the semantics. For example, the tolerance for how vertical can a wall be, is at least 80 degree with XOY plane. An extrusion must be at least 25 centimeters outside the wall plane. These tolerance values are set appropriate for most buildings.
- Feature extraction.** Convex hulls for all segments are computed first to approximate segments, because it is much easier to derive geometry properties (area, directions, etc.) from polygons than point sets. Next, the convex hull for each segment is checked with the feature

extraction approach. There are three main steps:

- Segmentation.** The planar surface growing algorithm by (Vosselman et.al. 2004) is adopted because it is suitable for segmenting planar surfaces. The planar surface growing algorithm first selects

constraints defined in Table 1, to determine which of the four features (wall, roof, door, and extrusion) the segment is. Figure 2 gives the recognition results. Sometimes a feature might be over-segmented, when the global threshold value is too strict. Therefore all attached feature segments are found and merged to combine a bigger feature segment. For example, the two wall segments in Figure 2 attach to each other, so they will be combined to a bigger wall segment.

2.2 Feature based window extraction

Theoretically, windows can also be extracted as a feature, with the similar method of extracting wall, door, roof, and extrusion. From knowledge about windows, a window feature can be defined as: area not too large (size), on the wall (position), on a vertical plane (direction). Figure 2 also gives the recognized window feature segments.

The result in Figure 2 is not satisfactory. Not all windows are recognized, and even recognized feature segments give incomplete and inaccurate geometry. The main reason for the failure is that the feature extraction algorithm mainly counts on a relatively good segmentation. Window frames are usually small parts of wall, so terrestrial laser scanning retrieves only a few laser points for windows. When a window is not covered with a curtain, the terrestrial laser beam will just penetrate the glass, and no laser points will be reflected in the window center. Insufficient information leads to bad segmentation for windows, and in turn leads to bad window recognition.

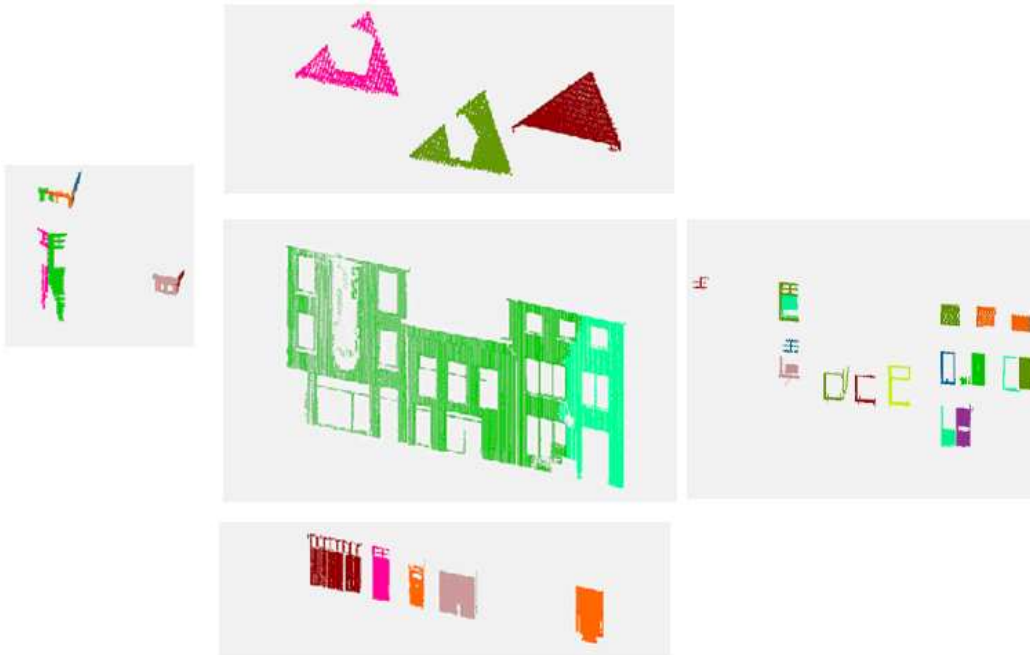


Figure 2. Feature recognition results (extrusion, roof, wall, door, window)

3. WINDOW EXTRACTION

3.1 Hole-based extraction method

The feature based approach is able to recognize large building features such as walls and roofs, but doesn't work well for windows, because of the lack of laser points on windows or window frames. Figure 2 illustrates the recognized wall feature segment, with some holes on it. It is obvious that these holes are caused by windows, doors and extrusions on the wall. An alternative method, which extracts windows from wall holes, is developed. The main steps are:

- **Triangulation.** A TIN for each wall segment is generated first, as shown in Figure 3.
- **Extracting boundary points.** Long TIN edges appear only at the outer boundary (wall outline) or inner boundary (holes) of a wall. Boundary points are just the end points for the TIN edges with long length. Figure 4a gives the extracted boundary points.
- **Clustering.** Points belonging to the same hole are grouped together. The clustering algorithm is given as follows:
 - 1) Choose a boundary point A which has no label value yet. Label A with an integer value: i.
 - 2) Finds all the long TIN edges which connect to this A. For all of these long edges, determine the other end points: B.
 - 3) Give B the same label value: i, if B is not labeled yet.
 - 4) Make B the new A, iterate step 2) to step 4), until no more unlabelled points can be found.
 - 5) Choose another unlabelled boundary point A, give it a label value: i+1, repeat step 2) to step 5), until all boundary points are labeled.

The different colors in Figure 4a, 4b, 4c, 4d are because different point clusters are colored with their labels.

- **Extracting holes.** Among a TIN mesh, the interior triangles always have three neighbor triangles, while the

triangles on the outer boundary have only one or two neighbor triangles. Therefore we first get all the triangles that have a boundary point as a vertex, and check these triangles about the number of their neighbor triangles. If three, then the checked triangle is an interior triangle, and the boundary point is an interior boundary (hole) point. Otherwise the boundary point is an outer boundary (wall outline) point. Figure 4b and 4c illustrates the two kinds of boundary points.

- **Removing holes caused by extrusion and door.** The holes in Figure 4d are compared with the extrusion and door segments in Figure 2. If a hole doesn't have overlap with any extrusion or door segment, it is considered a window hole. Figure 4d gives the result after this step.
- **Filtering.** Remove some noise holes which have irregular shapes, such as extremely long and narrow, or very small (longest edge shorter than 40 centimeter).
- **Fitting rectangles.** Assuming windows to be rectangular, the window holes are finally fitted to rectangles as shown in Figure 4e. This is done by choosing the most left point (L), most right point (R), top point (T) and bottom point (B) from each point cluster. The x, y coordinates of the left-bottom corner of the rectangle equal the x, y coordinates of point L, and the z coordinate equals the z coordinate of B. In this way the coordinates for the other three corners can also be determined. We are aware this method is only accurate for the following assumption:
 - The wall is vertical.
 - The left and right border of the window is vertical.
 - The window is rectangle.

The first two assumptions are true for most windows. If a window is not rectangle, then a minimum bounding rectangle will be fitted.

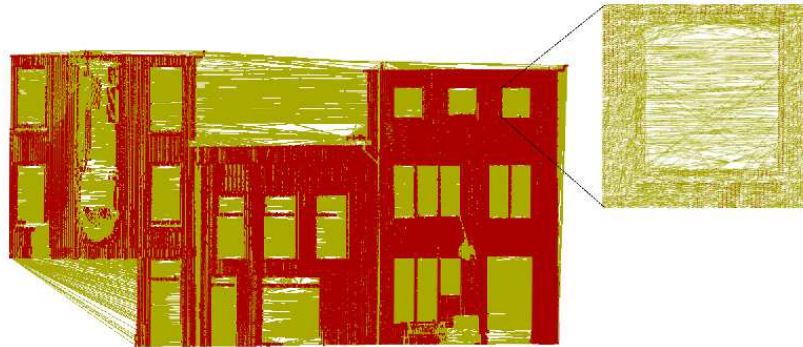


Figure 3. TIN of a building facade, with zooming in a hole corner

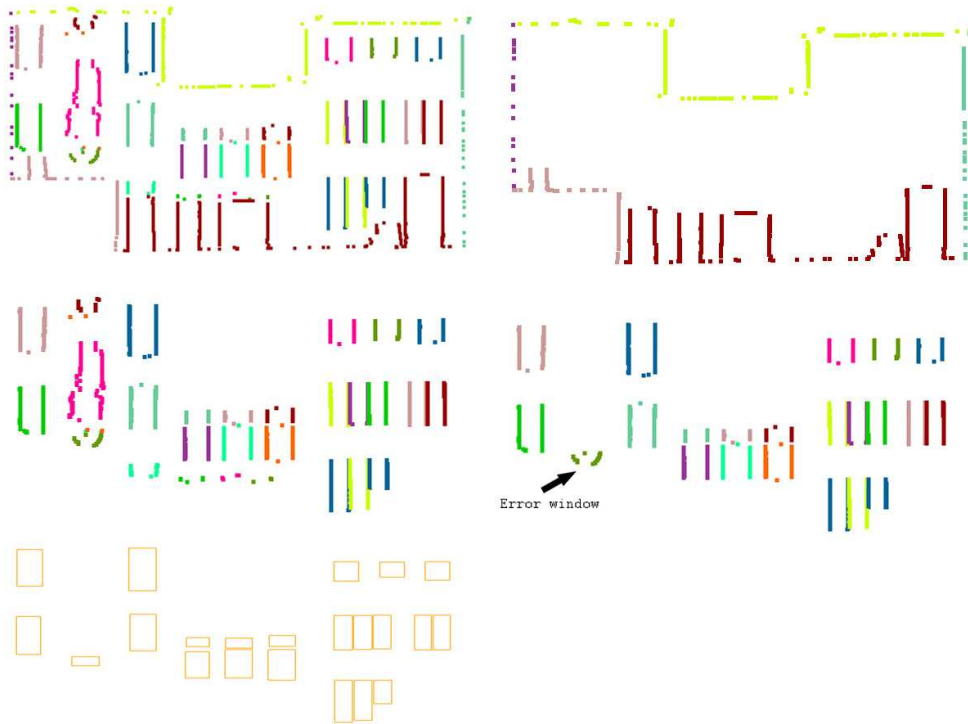


Figure 4. Extracting windows from wall holes (from left to right, top to down): (a) boundary points (b) outer boundary points (c) hole points (d) hole points after filtering (e) reconstructed windows by fitting points to rectangles

3.2 Method evaluation

The hole-based extraction method provides a robust approach to extract windows from terrestrial laser scanning. Our experiments on 12 building facades show that more than 90% of the windows can be accurately recognized. Figure 5 illustrates some experiment result. As the rule “windows are holes on walls” is valid for almost every building, we can expect the method achieving high accuracy also for other data sets. The algorithm only takes a few seconds, because no heavy computation is involved.

Sometimes a few windows are extracted which don't exist in reality, such as the indicated error window in Figure 4d. These error windows usually appear at places of a building extrusion. This is because the feature recognition algorithm still doesn't

work perfectly for extrusion. When an extrusion has a complex shape, e.g. the extrusion in Figure 2 has a curved patch on the bottom, not all segments of this extrusion can be recognized. The extrusion segments, which are not correctly recognized, still result in holes on wall segments. These extrusion holes are not removed when all the holes are compared with extrusion segments, so they remain and are treated as window holes. This kind of error windows seldom appears for doors, because doors have simple shapes and recognition of doors is very reliable.

Another unsolved issue is that the real holes on the wall are recognized as windows. For example, the building in Figure 5 left has 3 holes on the wall bottom. These holes satisfy all the definitions for windows in our approach: they are holes on the wall segments; they don't overlap with any door or extrusion

segments. Further research is required to distinguish the real holes and holes caused by windows, door and extrusions. The extracted windows can be smaller than reality, when there are obstacles on these windows. In Figure 6, the most right window on the ground floor is partly covered with some decorations. This is why the fitted rectangle is actually only the top half of this window. In Figure 7 the bigger window on the 1st floor is firstly extracted as three holes as a result of the frame decorations. The left and right holes are filtered out because



Figure 5. An example showing holes in the wall recognized as windows.



Figure 6. An example showing an extracted window is smaller than reality, as a result of obstacles on this window



Figure 7. Another example showing extracted window is smaller than reality

they have very narrow shape. Only the middle hole is fitted to rectangle. In the same façade, the second most right window on the ground floor is also smaller than reality, because some plants obstacle a big part of this window.

Furthermore, only windows on walls can be extracted so far. Extracting windows from dormers and extrusions are still need to be investigated.

4. CONCLUDING REMARKS

In this paper we have presented an automatic method to extract windows from terrestrial laser scanning. First, terrestrial laser points for a building facade are segmented and then wall segments are recognized by comparing each segment with feature constraints. A TIN of the wall segments is generated and both exterior boundary points and the hole boundary points are extracted from the end points of long edges in the TIN. After filtering out exterior boundary points, the hole points are further classified into window points, extrusion points and door points. This is done by comparing each hole with the recognized extrusion and door segments.

The hole-based window extraction method proved to be a very promising approach. In the future we will focus on how to add semantic knowledge to improve the extraction accuracy. Especially, knowledge about windows will be helpful to remove wrong windows which is caused by miss recognized extrusions, holes on walls, and other unpredictable cases. Next, considering terrestrial imagery provides confident edge information, we will explore the possibility to reconstruct more detailed building structure by fusing terrestrial laser points and terrestrial imagery.

REFERENCES

- Brenner, C., 2005. Building Reconstruction from Images and Laser Scanning. *International Journal of Applied Earth Observation and Geoinformation* 6 (3-4), 187-198.
- Dold, C., Brenner, C., 2004. Automatic Matching of Terrestrial Scan Data as a Basis for the Generation of Detailed 3D City Models. In *International Archives of Photogrammetry and Remote Sensing*, Vol. XXXV, Part B3, Proceeding of the ISPRS working group III/6, Istanbul, pp. 1091-1096
- Haala, N., Becker, S., Kada, M., 2006. Cell Decomposition for the Generation of Building Models at Multiple Scales. *International Archives of Photogrammetry, Remote Sensing and Spatial Information Sciences*, vol. 36, part 3, Bonn, Germany, September 20-22, pp. 19-24.
- Gross, H., Thoennessen, U., 2006. Extraction of Lines from Laser Point Clouds. *International Archives of Photogrammetry, Remote Sensing and Spatial Information Sciences*, vol. 36, part 3, Bonn, Germany, September 20-22, pp. 86-91.
- Maas, H.-G., 2001. The Suitability of Airborne Laser Scanner Data for Automatic 3D Object Reconstruction. *Automatic Extraction of Man-Made Objects from Aerial and Space Images (III)*, A.A. Balkama Publishers, pp. 291-296.
- Pu, S., Vosselman, G., 2006. Automatic extraction of building features from terrestrial laser scanning. *International Archives of Photogrammetry, Remote Sensing and Spatial Information*

Sciences, vol. 36, part 5, Dresden, Germany, September 25-27, 5 p. (on CD-ROM).

Rabbani, T., Heuvel, F.A. van den, Vosselman, G. , 2006, Segmentation of point clouds using smoothness constraints, International Archives of Photogrammetry, Remote Sensing and Spatial Information Sciences, vol. 36, part 5, Dresden, Germany, September 25-27, pp. 248-253.

Remondino, F., El-Hakim, S., 2006. Image-based 3D Modeling: A Review, The Photogrammetric Record 21 (115), 269-291.

Schuster, H.F., 2004, Segmentation of Lidar Data Using The Tensor Voting Framework, XXth ISPRS Congress, 12-23 July 2004 Istanbul, Turkey, pp1073

Sotoodeh, S., 2006. Outlier Detection In Laser Scanner Point Clouds, International Archives of Photogrammetry, Remote Sensing and Spatial Information Sciences, vol. 36, part 5, Dresden, Germany, September 25-27, pp. 297-302

Suveg, I., Vosselman, G., 2004. Reconstruction of 3D Building Models from Aerial Images and Maps. ISPRS Journal of Photogrammetry and Remote Sensing 58 (3-4), 202-224.

Vosselman, G., B. Gorte, G. Sithole and Rabbani, T., 2004. Recognizing Structure in Laser Scanner Point Clouds. International Archives of Photogrammetry, Remote Sensing and Spatial Information Sciences, vol. 46, part 8/W2, Freiburg, Germany, October 4-6, pp. 33-38.

Wani, M. A. and Arabnia, H. R., 2003, Parallel edge region based segmentation algorithm targeted at reconfigurable multiring network. Journal of Supercomputing 25(1), 43-62.

CLASSIFICATION OF BUILDING DAMAGES BASED ON LASER SCANNING DATA

M. Rehor

Institute of Photogrammetry and Remote Sensing (IPF), Universität Karlsruhe (TH), Englerstr. 7, 76128 Karlsruhe, Germany – miriam.rehor@ipf.uni-karlsruhe.de

KEY WORDS: Change detection, LIDAR, DEM/DTM, Disaster, Comparison, Segmentation, Fuzzy Logic, Classification

ABSTRACT:

Due to the possibility of acquiring precise height data of large areas rapidly, airborne laser scanning systems are particularly suitable for obtaining information about the damage situation immediately after a disaster in large scale. This paper presents a technique for the detection and classification of damages occurring on buildings in affected areas. It is based on the comparison of pre-event building models composed of planar surfaces with planar surfaces extracted from laser scanning data acquired directly after the disaster. In a first step, segments are created by superposing the pre- and post-event surfaces. Subsequently, for every segment the geometrical characteristics of the corresponding pre- and post-event surface are compared. Finally, the segments are assigned to damage types using a fuzzy logic classification approach. The results achieved for each processing step by applying the method on data containing real building damages are presented and analysed.

1. INTRODUCTION

Disasters like earthquakes cause many casualties every year. In many cases people are trapped in collapsed buildings and have to be rescued. Mostly, time plays a very critical role in this process. Furthermore, resources are short and have to be employed efficiently to save as many lives as possible. This shows the necessity of a fast and extensive damage analysis. Therefore, one project of the German Collaborative Research Centre (CRC) 461 “Strong Earthquakes: A Challenge for Geosciences and Civil Engineering” deals with the development of methods for the automatic detection and classification of building damages. Since the resources required for rescue activities depend among others on the damage types of the affected buildings (Schweier and Markus, 2004), it is not only important to find out whether a building is damaged or not but also to receive information about how it is collapsed.

The damage analysis described in this paper is based on the comparison of planar surfaces composing pre-event building models and planar surfaces derived from post-event airborne laser scanning data. Airborne LIDAR data are used because laser scanning allows a rapid and extensive acquisition of height data without the necessity of entering destroyed areas. The use of laser scanning data for the detection of building damages after disasters has already been proposed in several publications, e.g. (Murakami et al., 1998), (Vögtle and Steinle, 2004), (Vu et al., 2004). Most of these approaches have originally been developed for the detection of changes in urban areas. Until now, they have never been tested on data containing real building damages.

The results of this damage interpretation represent one main input of the Disaster Management Tool (DMT) also developed within the CRC 461 (Markus et al., 2006). The aim of the DMT is the support of decision makers, surveillance and intervention teams during disaster response.

In this paper a building damage detection and classification technique is presented. It is based on a segmental fuzzy logic approach. However, only the situation of the buildings

contained in the pre-event data set can be regarded. The results achieved by applying this method on data containing buildings with different damage types are demonstrated and interpreted.

2. DAMAGE TYPES

During a classification process unknown patterns are assigned to a priori given classes. Therefore, the classes which shall be discriminated have to be defined before the classification. Due to this, a damage catalogue was developed containing the different damage types of entire buildings after earthquakes (Figure 1) (Schweier and Markus, 2004; Schweier and Markus, 2006). Moreover, the damage catalogue includes for every damage type a description and some geometrical features like *volume* and *height reduction*, the *change of the inclination of building surfaces* as well as the *surface structure* and the *size of the recognisable planes*. For these features qualitative or quantitative values were determined by analysing pictures of more than 100 damaged buildings. Quantitative information is defined by numeric values, e.g. a *heap of debris* has a *volume reduction* of 60-80%. To express qualitative information linguistic terms are used, e.g. the *volume reduction* of a *multi layer collapse* is *small*. For the development of the damage catalogue the special characteristics of aerial data acquisition

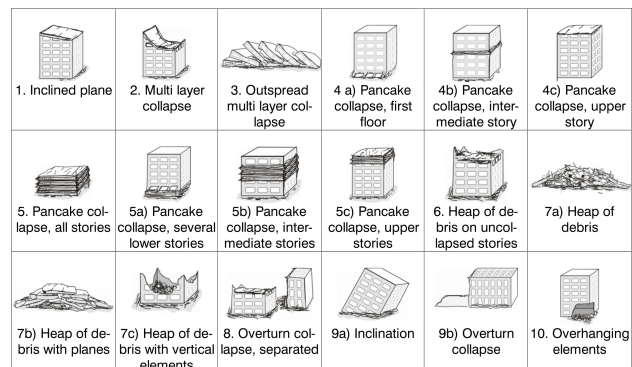


Figure 1: Compilation of damage types (Schweier and Markus, 2004)

were taken into account. This means that attention was paid to the fact that the geometrical features characterising the single damage types can be derived from aerial data (e.g. laser scanning).

As in the presented approach only changes inside the pre-event building outlines are examined (see section 1), features like *debris structure outside the footprint* cannot be used for the discrimination of the various damage types. This implicates that damages characterised very well by these features (e.g. *overturn collapse*) may not yet be identified within the current classification procedure which should be extended in future.

Concerning damage types 4a), 4b), 4c) and 5, 5a), 5b), 5c), respectively, it seems to be impossible to find out which storey has collapsed by using aerial data only. Hence, these damage types were summarised as follows:

- Pancake collapse of one storey
- Pancake collapse of more than one storey

The difference of a *pancake collapse of one storey* and a *pancake collapse of more than one storey* is characterised by the quantity of the *volume* and *height reduction*. Obviously, damage type 5 has a higher *volume* and *height reduction* than damage type 4. But since the number of collapsed storeys can only be determined reliably if the height of a floor is known, this discrimination is very fuzzy if it is unknown.

Furthermore, the different types of debris heaps (7a), 7b), 7c)) are also very difficult to distinguish. As a consequence, they are merged as well. Damage type number 10 (*overhanging elements*) cannot be recognised if only aerial data (e.g. LIDAR) are used. As a result, the following damage types are distinguished in the classification process:

0. Unchanged
1. Inclined plane
2. Multi layer collapse
3. Outspread multi layer collapse
4. Pancake collapse of one storey
5. Pancake collapse of more than one storey
6. Heap of debris on uncollapsed storeys
7. Heap of debris
8. Overturn collapse, separated
- 9a. Inclination

3. DATA

The test site of this study is an area of the *Swiss Military Disaster Relief* used for practising search and rescue activities (Figure 2). It is located close to Geneva and has a size of about 500 m × 800 m. The specialty of this area is that undamaged buildings as well as damaged buildings with different damage types are located on it. Table 1 summarises the damage types occurring on the buildings marked in Figure 2.

Building no.	1	2	3	4	5	6a	6b	7	
Damage type	5	5 + 9a	1	0	5	0	5	7	
Building no.	8	9	10	11	12	13	14	15	16
Damage type	7	3	7	7	0	0	0	0	0

Table 1: Damage types of the buildings marked in Figure 2

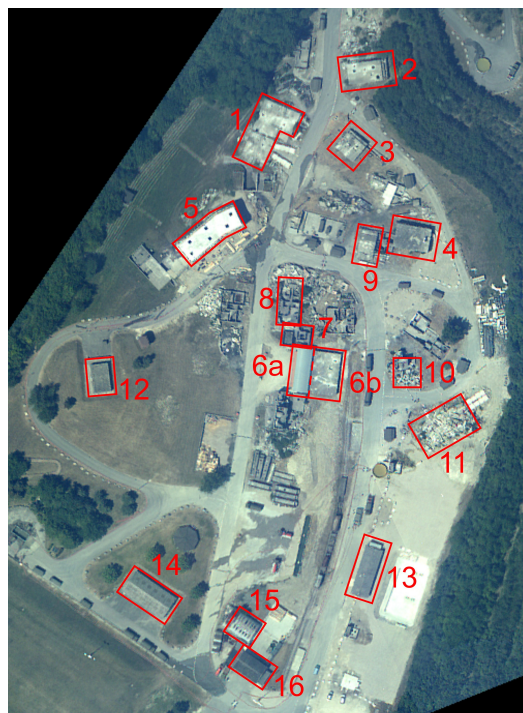


Figure 2: Aerial image of the test site

In 2004 a laser scanning flight was carried out in order to acquire height data of this test area. Therefore, a TopoSys Falcon II sensor was used. The original point clouds were transformed into DSMs (1 m raster width) having an accuracy of ± 0.5 m in position and ± 0.15 m in height. The described approach is based on raster data because of the better performance concerning memory access and the well defined neighbourhood. But it has to be mentioned that in principle the method can also be adapted to point clouds.

Normally it is a problem to get LIDAR data of areas containing damaged buildings. In this study it is exactly the other way round. This means that no real laser scanning data of the pre-event state are available. On this account CAD models of the undamaged buildings were reconstructed by means of construction plans and photographs.

4. CLASSIFICATION OF BUILDING DAMAGES

In this section the whole workflow of the approach for classifying building damages is described. First of all a normalised DSM (nDSM) is needed for the post-event date. An nDSM contains only the 3D objects on the Earth's surface like buildings and vegetation. It can be derived from the DSM by subtracting a digital terrain model (DTM) (Oude Elberink and Maas, 2000; Steinle and Vögtle, 2001). For the generation of DTMs from laser data many methods have been proposed (e.g. Weidner and Förstner, 1995; Axelsson, 2000; Vosselman, 2000; Tóvári and Pfeifer, 2005). In this study the approach of (von Hansen and Vögtle, 1999) is applied which uses a convex-concave hull (TIN densification).

Figure 3 displays the pre-event data of the test site. In Figure 4 the post-event nDSM derived from last echo data is visualised. It has to be indicated that terrain and vegetation have not been modelled in the pre-event data based on CAD models.

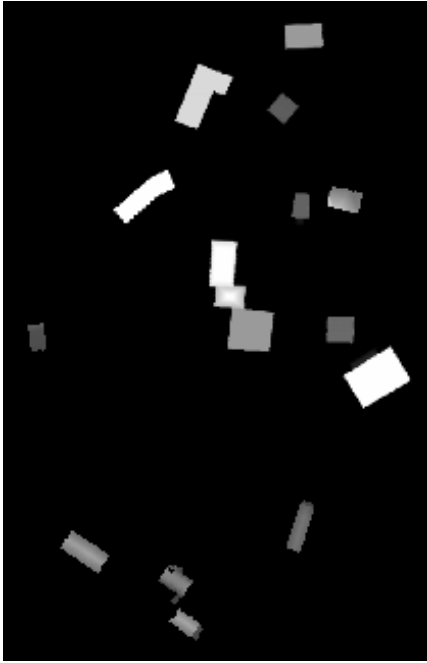


Figure 3: Pre-event data generated from CAD models

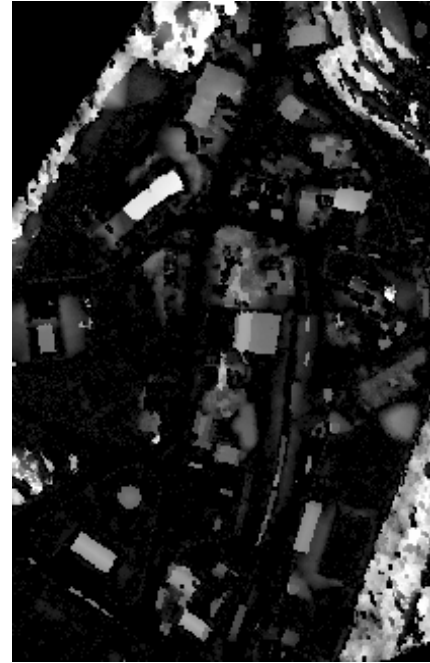


Figure 4: Last echo post-event nDSM

4.1 Generation of pre-event building models

As already mentioned in section 1, pre-event building models are needed as basis for the classification. These models can be created by using different methods such as photogrammetry, terrestrial measurements or construction plans (Figure 5(a)). Airborne laser scanning itself is a suitable technique for the extraction of building models (Brenner and Haala, 2000; Vosselman and Dijkman, 2001; Rottensteiner et al., 2005; Schwalbe et al., 2005). For this purpose, (Steinle, 2005) proposed a method which starts with the extraction of planar surfaces from a laser scanning derived nDSM (see section 4.2). Afterwards, the neighbourhood relations (topology) of these surfaces are analysed and adjacent planes are intersected. This results in building edges which can be intersected again in order to determine the corners of the building (CAD model).

Since only changes within buildings included in the pre-event data are inspected during the classification step, the building outlines have to be extracted from these building models before the further analysis can start.

4.2 Creation of segments for the classification

Two main features that characterise the different damage types are the *size of the recognisable planes* and the *change of inclination of the building surfaces* (see section 2). For this reason, planar surfaces are extracted from the post-event nDSM (see Figure 5(b)) by applying a region growing algorithm starting from a seed region which fulfils the condition that the assigned points are approximately lying in a plane (Steinle, 2005; Rehor and Bähr, 2006). For testing the affiliation of a neighbouring pixel to the currently considered plane, a global test and a test for blunders in a Gauss-Markov model are used as homogeneity criterion. For every detected segment the plane of best fit is estimated by least squares adjustment. Due to taking into account only planar surfaces lying inside building contours (section 4.1) during the further processing steps, the segmentation algorithm is only applied on points lying inside a building outline plus a buffer of 3 m.

After planar surfaces have been extracted from the post-event laser data, new segments are created by superposition of the pre- and post-event planar surfaces (Figure 5(c)). This means that each of these new segments corresponds to one of the pre- and one of the post-event surfaces. As a consequence, for these segments features like the *change of inclination* or the *volume* and *height reduction* can be calculated (see section 4.3).

During the segmentation of planar surfaces not all pixels are assigned to segments. Some pixels remain unsegmented. For these pixels no plane of best fit can be estimated. In consequence, the *change of inclination* cannot be determined. So these pixels are excluded from the building damage classification and treated in a special way. For each pixel staying unsegmented the difference of its pre- and its post-event elevation is calculated. This height difference h_{diff} is analysed and classified as follows:

$$\begin{aligned} |h_{diff}| < t_1 &: \text{unchanged} \\ h_{diff} > t_1 &: \text{reduction} \\ h_{diff} < -t_1 &: \text{increase} \end{aligned}$$

Due to the fact that damage types like *heaps of debris*, *outspread multi layer collapses* or *overturn collapses* have a very irregular *structure of surface*, the assumption can be made that many unsegmented pixels occur in areas affected by these damage types.

4.3 Feature extraction

In order to assign the segments to a priori determined classes (see section 2), features have to be defined and extracted for each segment (see section 4.2). These features should be chosen in such a way that they cause a high discrimination between the different classes. With respect to the damage catalogue the following parameters were determined for every segment:

- Volume reduction
- Height reduction
- Change of inclination
- Size

The volume reduction expresses the ratio of the difference between pre- and post-event volume of the segment and the pre-event volume. The height reduction is defined as the ratio of the difference between the maximum pre-event and the maximum post-event height of the segment to the maximum pre-event height. The change of inclination is defined as the angle between the normal vectors of the corresponding pre- and post-event planes. Due to the usage of raster data, the segment size can be calculated easily by multiplying the number of pixels associated with the segment by the pixel size.

4.4 Fuzzy logic classification of building damages

For the classification of building damages a *fuzzy logic* based technique has been developed. The theory of fuzzy sets was introduced by (Zadeh, 1965) in order to model uncertainties. While in ordinary Boolean logic an element either belongs to a class or not, fuzzy logic enables to define a grade of membership (Tilli, 1993).

A fuzzy logic classification always starts with the definition of membership functions for every class and every feature (*fuzzification*). To simplify matters in this study, they are composed of line segments although in general they do not have to be linear. Furthermore, the a priori knowledge about the damage types defined in the damage catalogue is taken into account during this step (see section 2). This means that the qualitative and quantitative descriptions of the features are converted into membership functions for every damage type. By means of membership functions a degree of membership μ_{ij} can be calculated for every segment with every parameter j (here $j=4$ (section 4.3)) according to every class i (here $i=10$ (section 2)).

The combination of the single membership values μ_{ij} for the j different features results in the degree of match μ_i for every class i (*inference process*). It can be realised by different operators (e.g. minimum and maximum operator (Zadeh, 1965), algebraic product (Tilli, 1993), etc.). (Weidner and Lemp, 2005) propose the employment of the mean or the median of the single values. Among a lot of other possibilities these five operators have been tested in this study.

Finally, a decision for one class is made by applying the maximum operator, i.e. the currently considered segment is assigned to the class i with the highest value μ_i .

5. RESULTS

In the following the results obtained by applying the whole approach on the data of the test site are presented. Figure 5(a) shows the planar surfaces of the pre-event buildings (section 4.1). The post-event planar surfaces are visualised in Figure 5(b). The segments resulting from the superposition of the pre- and post-event surfaces are displayed in Figure 5(c). The classification is based on these segments.

The comparison of the five different operators for the inference process shows that the best results are achieved by the algebraic product, while the other operators prove to be less suitable. Therefore, the results obtained by the product operator are visualised in Figure 5(d). This verifies the achievements of (Tóvári and Vögtle, 2004). During their investigations concerning the classification of 3D objects in laser scanning data the product operator also provided the results with the highest classification rate.

A closer look at Figure 5(d) in combination with Table 1 shows that main parts of the buildings 1, 3, 4, 6a, 6b, 7, 8, 10, 11, 12, 13, 14 and 16 are classified correctly. For building 5 a *pancake collapse of one storey* was determined instead of a *pancake collapse of more than one storey*. As mentioned in section 2 the discrimination between these two damage types is very difficult if the height of a floor is not known. But if the two types of *pancake collapse* would be fused, a correct decision would be gained.

A similar case occurs at building 2 (Figure 5(e)). Its real damage type is a combination of a *pancake collapse of more than one storey* and an *inclination*. The classification proposes damage type number 4. Due to the fact that each segment can be assigned to only one damage type the general solution *pancake collapse* would be acceptable. Furthermore, it has to be mentioned that the class with the second highest degree of match for the main segment of building 2 is *inclination*. As a consequence, further research should examine if an improvement can be achieved by taking not only the class with the highest degree of match into account but also the one with the second highest value. This means that for example specific combinations of damage types could be allowed.

Figure 5(d) in connection with Table 1 and Figure 2 confirms the assumption that many unsegmented pixels showing a height reduction occur in case of debris heaps (section 4.2). If this is taken into account the determined damages of the buildings 7, 8, 10 and 11 can be considered as correct.

Building 9 is one of the misclassified buildings (Figure 5(f)). In reality it is affected by an *outspread multi layer collapse* but it is classified as an *inclination*. This can be explained by the fact that an *outspread multi layer collapse* is characterised by the extension of debris outside the former building contour line which is not yet regarded in this status of the approach. Therefore, it is not surprising that the classification is not correct.

Building 15 is an exception because it has a barrel-shaped roof (Figure 5(g)). Hence, this roof type is not composed by planar surfaces in the CAD model (section 2). Since the whole approach is based on the comparison of planar surfaces, the region growing algorithm described above (section 4.2) is applied on the pre-event data of this building. But although building 15 is unchanged (Table 1), the surfaces extracted from the pre- and post-event data are not the same. Thus, the inclination change of the corresponding pre- and post-event planes is significantly larger than zero and the segments are classified as *inclined planes* instead as *unchanged*. As the only difference between the damage types 0 and 1 is the change of the orientation that is a bit larger for damage type 1, it is obvious that building 15 is the only misclassified building without any damage. In addition, more pixels remain unsegmented during the segmentation of planar surfaces than in case of buildings with gable or flat roofs.

6. CONCLUSION

A new approach for the classification of building damages after disasters like earthquakes was presented. It is based on the comparison of building models derived from pre- and post-event data. It starts with a segmentation of planar surfaces, followed by the generation of segments on which the fuzzy logic classification can be applied. Finally, these segments are

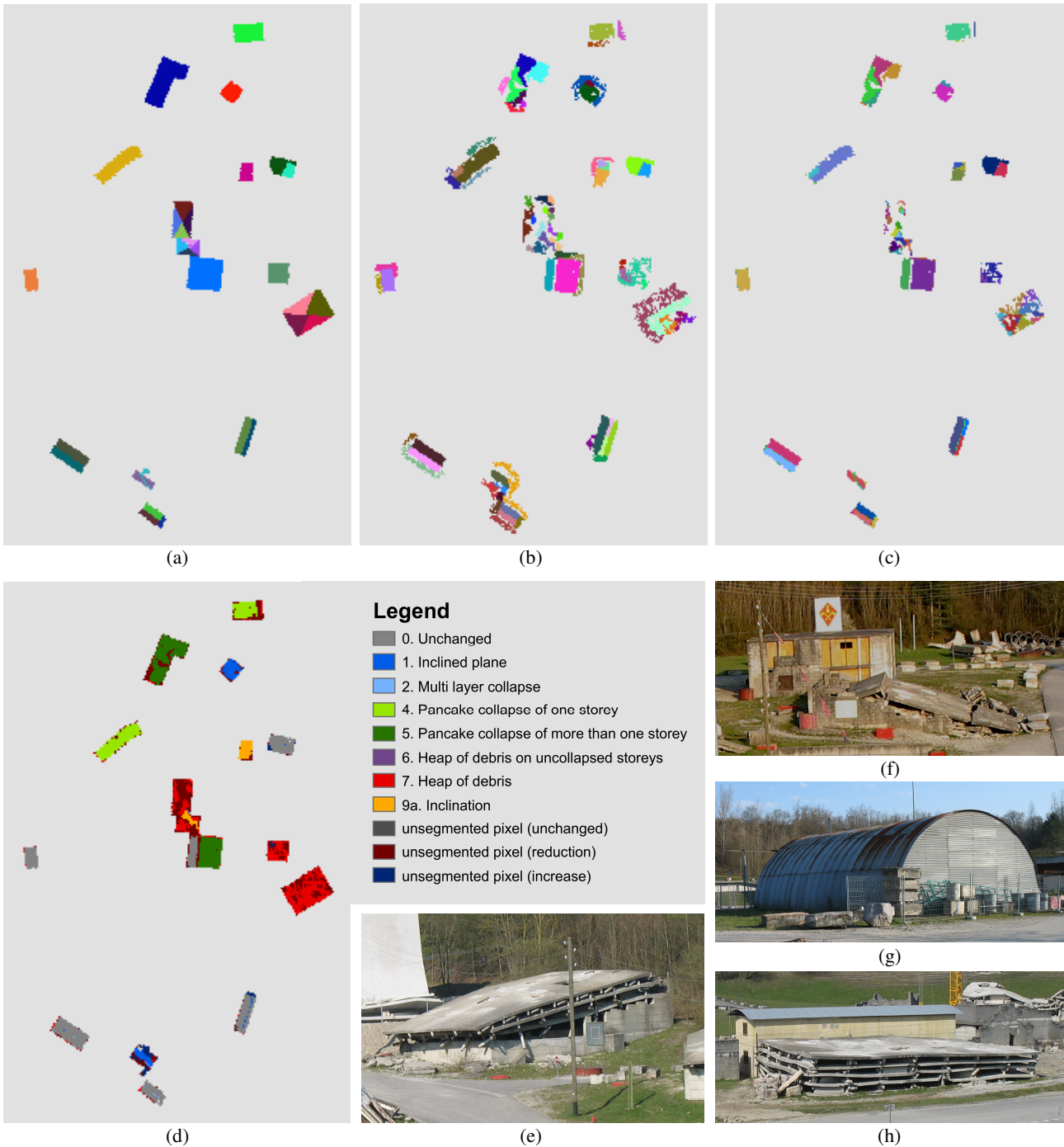


Figure 5: a) Planar surfaces of the pre-event buildings. b) Planar surfaces extracted from the post-event data. c) Segments used for the classification; they are created by a superposition of the pre- and post-event planar surfaces. a) - c) Each segment is displayed in another random colour. d) Classification results achieved by using the product operator for the inference process. e) Photograph of building 2. f) Photograph of buildings 4 and 9. g) Photograph of building 15. h) Photograph of building 6.

assigned to damage types according to their height and volume reduction, their size, and their change of inclination.

The results achieved for data of a test area containing real building damages are very promising although only changes inside the pre-event building contour are analysed so far. Thus, in future further investigations should be carried out to extend the approach in order to include the situation outside the former building areas into the analysis.

During the classification process each of the segments is classified on its own. As a result, different segments belonging to one building may be assigned to different damage classes. On the one hand, this is advantageous because one building can be affected by more than one damage type (e.g. building 6 (Figure 5(h))). On the other hand, the possibility exists that most of the segments belonging to one building are classified correctly as the same damage type but some small segments are misclassified (e.g. building 13). As a consequence, it should be

investigated in further research if an improvement can be achieved by considering the damage types of adjacent segments. Besides, the results might be optimised if the class with the second highest degree of match is also taken into account.

Another aspect requiring further research is the treatment of pixels not assigned to a planar surface in one of the two states. It was pointed out that they concentrate in areas affected by specific damage types. Hence, they should also be classified based on triangulated surface description instead of planes.

ACKNOWLEDGEMENTS

The presented work has been funded by the Deutsche Forschungsgemeinschaft (DFG) as part of the Collaborative Research Centre (CRC) 461: "Strong Earthquakes". Furthermore, the author would like to thank the Swiss Disaster Relief Coordination and Control Centre DDPS for providing their facilities.

7. REFERENCES

- Axelsson, P., 2000. DEM generation from laser scanner data using adaptive TIN models. In: *International Archives of Photogrammetry and Remote Sensing (IAPRS)*, Amsterdam, The Netherlands, Vol. XXXIII, Part B4, pp. 111-118.
- Brenner, C. and Haala, N., 2000. Erfassung von 3D Stadtmodellen. *Photogrammetrie – Fernerkundung – Geoinformation (PFG)*, Nr. 2/2000, pp. 109-118.
- von Hansen, W. and Vögtle, T., 1999. Extraktion der Geländeoberfläche aus flugzeuggetragenen Laserscanner-Aufnahmen. *PFG*, Nr. 4/1999, pp. 229-236.
- Markus, M., Engelmann, H., Gehbauer, F., Leebmann, J., and Schweier, C., 2006. The Disaster Management Tool - Concept and application experiences. In: *Proceedings "100th Anniversary Earthquake Conference - Managing Risk in Earthquake Country"*, Paper No. 1253, San Francisco, USA.
- Murakami, H., Nakagawa, K., Shibata, T., and Iwanami, E., 1998. Potential of an airborne laser scanner system for change detection of urban features and orthoimage development. In: *IAPRS*, Stuttgart, Germany, Vol. XXXII, Part 4, pp. 422-427.
- Oude Elberink, S. and Maas, H.-G., 2000. The use of anisotropic height texture measures for the segmentation of laserscanner data. In: *IAPRS*, Amsterdam, The Netherlands, Vol. XXXIII, Part B3/2, pp. 678-684.
- Rehor, M. and Bähr, H.-P., 2006. Segmentation of damaged buildings from laser scanning data. In: *The International Archives of Photogrammetry, Remote Sensing and Spatial Information Sciences (IAPRSIS)*, Bonn, Germany, Vol. XXXVI, Part 3, ISSN 1682-1750, pp. 67-72.
- Rottensteiner, F., Trinder, J., Clode, S., and Kubik, K., 2005. Automated delineation of roof planes in LIDAR data. In: *IAPRSIS*, Enschede, The Netherlands, Vol. XXXVI, Part 3/W19, ISSN 1682-1777.
- Schwalbe, E., Maas, H.-G., and Seidel, F., 2005. 3D building model generation from airborne laserscanner data using 2D GIS data and orthogonal point cloud projections. In: *IAPRSIS*, Enschede, The Netherlands, Vol. XXXVI, Part 3/W19, ISSN 1682-1777, pp. 209-214.
- Schweier, C. and Markus, M., 2004. Assessment of the search and rescue demand for individual buildings. In: *Proceedings of the 13th World Conference on Earthquake Engineering*, Vancouver, Canada.
- Schweier, C. and Markus, M., 2006. Classification of collapsed buildings for fast damage and loss assessment. *Bulletin of Earthquake Engineering*, Vol. 4, No. 2, pp. 177-192.
- Steinle, E. and Vögtle, T., 2001. Automated extraction and recognition of buildings in laserscanning data for disaster management. In: *Automatic Extraction of Man-Made Objects from Aerial and Space Images (III)*, E. Baltsavias et al. (eds.), Swets & Zeitlinger, Lisse, The Netherlands, pp. 309-318.
- Steinle, E., 2005. Gebäudemodellierung und -änderungs-erkennung aus multitemporalen Laserscanningdaten. PhD dissertation, Deutsche Geodätische Kommission, Reihe C, Heft Nr. 594, Verlag der Bayerischen Akademie der Wissenschaften, München, http://129.187.165.2/typo3_dgk/docs/c-594.pdf (accessed 14 May 2007).
- Tilli, T., 1993. *Mustererkennung mit Fuzzy-Logik*. Franzis-Verlag GmbH, München.
- Tóvári, D. and Pfeifer, N., 2005. Segmentation based robust interpolation - a new approach to laser data filtering. In: *IAPRSIS*, Enschede, The Netherlands, Vol. XXXVI, Part 3/W19, ISSN 1682-1777, pp. 79-84.
- Tóvári, D. and Vögtle, T., 2004. Classification methods for 3D objects in laserscanning data. In: *IAPRSIS*, Istanbul, Turkey, Vol. XXXV, Part B3, ISSN 1682-1750.
- Vögtle, T. and Steinle, E., 2004. Detection and recognition of changes in building geometry derived from multitemporal laserscanning data. In: *IAPRSIS*, Istanbul, Turkey, Vol. XXXV, Part B2, ISSN 1682-1750, pp. 428-433.
- Vosselman, G., 2000. Slope based filtering of laser altimetry data. In: *IAPRS*, Amsterdam, The Netherlands, Vol. XXXIII, Part B3, pp. 935-942.
- Vosselman, G. and Dijkman, S., 2001. 3D Building Model Reconstruction from Point Clouds and Ground Plans. In: *IAPRSIS*, Annapolis, USA, Vol. XXXIV, Part 3/W4, pp. 37-44.
- Vu, T. T., Matsuoka, M. and Yamazaki, F., 2004. Employment of LIDAR for Disaster Assessment. In: *Proceedings of the 2nd International Workshop on Remote Sensing for Post-Disaster Response*, Newport Beach, California, USA.
- Weidner, U. and Förstner, W., 1995. Towards automatic building extraction from high resolution digital elevation models. *ISPRS Journal of Photogrammetry and Remote Sensing*, 50(4), pp. 38-49.
- Weidner, U. and Lemp, D., 2005. Objektorientierte Klassifizierung. In: *Digitale Bildverarbeitung – Anwendungen in Photogrammetrie, Fernerkundung und GIS*, Bähr, H.-P. and Vögtle, T. (eds.), Wichmann Verlag, Heidelberg, 4. edn., pp. 106-122.
- Zadeh, L. A., 1965. Fuzzy Sets. *Information and Control*, Vol. 8, pp. 338-353.

COMBINED TREE SEGMENTATION AND STEM DETECTION USING FULL WAVEFORM LIDAR DATA

J. Reitberger^{a,*}, P. Krzystek^a, U. Stilla^b

^a Dept. of Geoinformatics, Munich University of Applied Sciences, 80333 Munich, Germany
(reitberger, krzystek)@fhm.edu

^b Photogrammetry and Remote Sensing, Technische Universitaet Muenchen, 80290 Munich, Germany
stilla@tum.de

Commission III, WG III /3

KEY WORDS: LIDAR, Analysis, Segmentation, Forestry, Vegetation

ABSTRACT:

The study highlights a new method for the delineation of tree crowns and the detection of stem positions of single trees from dense airborne LIDAR data. At first, we combine a method for surface reconstruction, which robustly interpolates the canopy height model (CHM) from the LIDAR data, with a watershed algorithm. Stem positions of the tallest trees in the tree segments are subsequently derived from the local maxima of the CHM. Additional stem positions in the segments are detected in a 3-step algorithm. First, all the points between the ground and the crown base height are separated. Second, possible stem points are found by hierarchically clustering these points. Third, the stem is reconstructed with a robust RANSAC-based adjustment of the stem points. The method was applied to small-footprint full waveform data, which have a point density of 25 points per m². The detection rate for coniferous trees is 61 % and for deciduous trees 44 %, respectively. 7 % of the detected trees are false positives. The mean positioning error is 0.92 cm, whereas the additional stem detection improves the tree position on average by 22 cm. The analysis of waveform data in the tree structure shows that the intensity and pulse width discriminate stem points, crown points and ground points significantly. Moreover, the mean intensity of stem points turned out to be the most salient feature for the discrimination of coniferous and deciduous trees.

1. INTRODUCTION

Laser scanning has been widely used in mapping the Earth's surface and especially in forest application. Conventional LIDAR, which records the first and last pulse, was successfully applied to retrieve forest parameters like tree height, crown diameter, number of stems, stem diameter and basal area on the tree level (Hyypä et al., 2004). Also, tree species classification became feasible with first/last pulse scanning systems providing high point density (Holmgren et al., 2004; Heurich, 2006; Brandtberg, 2007). Recently, studies reported about the successful application of novel small footprint full waveform systems to DTM generation (Doneus et al., 2006) or to tree species classification (Reitberger et al., 2006) using advantageously the intensity and the pulse width.

Approaches to tree species classification are usually based on a single tree segmentation that delineates the tree crown from the outer geometry of the forest surface. The methods have in common to reconstruct – at least locally – the CHM to find the local maximum as the best guess for the stem position and to delineate a segment polygon as the tree crown. For example, the CHM is locally interpolated from the highest laser reflections (Hyypä et al., 2001), derived with the active contour algorithm (Persson et al., 2002), or is interpolated with special gridding methods (Solberg et al., 2006). Stem positions are determined from the interpolated CHM at the highest positions (Solberg et al., 2006) or from a special local tree shape reconstruction (Brandtberg, 2007). Tree crowns are typically derived with the watershed algorithm (Pyysalo et al., 2002), by a slope-based segmentation (Persson et al., 2002; Hyypä et al., 2001) or by a region growing method that starts from local surface maximums and finds crown polygons optimised in shape (Solberg et al., 2006).

The drawback of the segmentation methods is that they solely base on the CHM, which is reconstructed from the raw data in an interpolation process that smoothes the data to some extent. The degree of smoothing directly affects the success rate in terms of false positives and negatives. Moreover, in some cases neighbouring trees do not appear as two clear local maximums. Thus, approaches that solely use the CHM will be restricted in the success rate anyway, especially in heterogeneous forest types where groups of trees grow close together. So far, little focus has been given to reconstruct trees using information like laser hits on the stems or the reflectance, mainly because of the low spatial point density and the lack of information about the reflecting characteristics of the tree structure. Detected tree stems could be used to improve the CHM-based segmentation in terms of the detection rate and the position of the trees. Moreover, the analysis of the internal tree reflecting characteristics will gain more insight about salient tree features which are significant for instance for tree species classification or DTM generation. New full waveform systems have the potential to overcome these drawbacks since they detect significantly more reflections in the tree crown and provide the intensity and the pulse width as reflecting parameters.

The objective of this paper is (i) to present a method that segments single trees with a robust surface reconstruction method in combination with the watershed algorithm, (ii) to introduce a novel approach to stem detection that clusters hierarchically potential stem reflections and reconstructs the stem with a RANSAC-based adjustment, (iii) to show how the detection rate and position of single trees is improved, and (iv) to analyse the distribution of the parameters intensity and pulse width of the reflections in the tree structure.

* Corresponding author.

The paper is divided into five sections. Section 2 focuses on the segmentation of the single trees and the reconstruction of the tree stems. Section 3 shows the results which have been obtained from full waveform data acquired in May 2006 by the Riegl LMS-Q560 scanner in the Bavarian Forest National Park. Finally, the results are discussed with conclusions in sections 4 and 5.

2. METHODOLOGY

2.1 Decomposition of full waveform data

Let us assume that full waveform LIDAR data have been captured in a region of interest (ROI). A single waveform is decomposed by fitting a series of Gaussian pulses to the waveform which contains N_R reflections (Figure 1).

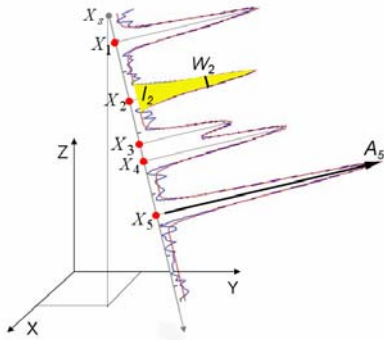


Figure 1. 3D points and attributes derived from a waveform

The vector $X_i^T = (x_i, y_i, z_i, W_i, I_i) (i=1, \dots, N_R)$ is provided for each reflection i with (x_i, y_i, z_i) as the 3D coordinates of the reflection. Additionally, the points X_i are given the width $W_i = 2 \cdot \sigma_i$ and the intensity $I_i = \sqrt{2 \cdot \pi} \cdot \sigma_i \cdot A_i$ of the return pulse with σ_i as the standard deviation ($=$ half pulse width at A_i / \sqrt{e}) and A_i as the amplitude of the reflection i (Reitberger et al., 2006; Jutzi and Stilla, 2005). Note that basically each reflection can be detected by the waveform decomposition. This is remarkable since conventional LIDAR systems – recording at most five reflections – have a dead zone of about 3 m which makes these systems effectively blind after a reflection.

Class	Single	First	Middle	Last
Definition	$N_R=1$ $i=1$	$N_R \geq 2$ $i=1$	$N_R \geq 3$ $i=2, \dots, N_R-1$	$N_R \geq 2$ $i=N_R$

Table 1. Subdivision of points into classes in dependence on the number of reflections N_R and the position i of the reflection in the waveform

The sensor data are calibrated by referencing W_i and I_i to the pulse width W^e and the intensity I^e of the emitted Gaussian pulse and correcting the intensity with respect to the run length s_i of the laser beam and a nominal distance s_0 .

$$W_i^c = W_i / W^e \quad (1)$$

$$I_i^c = (I_i \cdot s_i^2) / (I^e \cdot s_0^2) \quad (2)$$

Note that the correction assumes a target size larger or equal to the footprint (Wagner et al., 2006). The points from a waveform

are subdivided into 4 point classes depending on the number of reflections within a waveform (Table 1).

2.2 Segmentation

The segmentation of the tree crowns is achieved by deriving the CHM from 3D points which are best representing the outer tree crown geometry. The ROI is subdivided into a grid having a cell spacing of cp and N_C cells. Within each cell of size cp^2 , the highest 3D point is extracted and corrected with respect to the ground level z_j^{ground} , i.e. $z_j^{CHM} = z_j - z_j^{ground} (j=1, \dots, N_C)$. The

ground level z_j^{ground} is estimated from a given DTM by bilinear interpolation. In the next step, all the highest 3D points $X_j^T = (x_j, y_j, z_j^{CHM}) (j=1, \dots, N_C)$ of all N_C cells are robustly interpolated in a grid that has N_X and N_Y grid lines and a grid width gw . The special adjustment approach (Krzysztek et al., 1992) interpolates the $N_{CHM} = N_X * N_Y$ grid points

$$X_{Int_j}^{CHM T} = (x_{Int_j}^{CHM}, y_{Int_j}^{CHM}, z_{Int_j}^{CHM}) (j=1, \dots, N_{CHM})$$

and filters the 3D points X_j in a 2-phase iterative Gauß-Markoff process. Thanks to constraints on the curvature and torsion of the surface, the interpolation smoothes and regularises the surface in case of an ill-posed local situation. The iterative adjustment scheme is similar to an edge preserving filter that discards outliers, closes gaps in the surface if no 3D points could be found in the cells, and preserves surface discontinuities. The result is a smoothed CHM having N_{CHM} equally spaced posts. Finally, the tree segments are found by applying the watershed algorithm (Vincent and Soille, 1991) to the CHM. The local maximums of the segments define the N_{seg} tree positions $(X_{stem_i}^{CHM}, Y_{stem_i}^{CHM}) (i=1, \dots, N_{seg})$.

2.3 Stem detection

Tree stems in the individual tree segments are detected in a 3-step procedure:

Step 1: The N_S points $X_j^{Seg} (j=1, \dots, N_S)$ within a tree segment are cleared from ground points by discarding all points within a given height bound $Z_{threshold} = 1$ m to the DTM.

Step 2: The goal of the second step is to derive the crown base height h_{base} of the tree in order to subdivide the tree into the stem area and the remaining crown area. This coarse tree subdivision is achieved by (i) splitting the tree into l layers with height of 0.5 m, (ii) calculating the number of points n_i per layer, (iii) forming the vector $N_P = \{n_i / N_S\} (i=1, \dots, l)$, (iv) smoothing N_P with a 3x1 Gaussian filter and, finally, (v) defining h_{base} as the height that corresponds to 0.15 % of the total number of points per segment. All the N_{stem} points below h_{base} are potential stem points. Note that the remaining points can result from one or even several stems or from the understorey. The following hierarchical clustering scheme is applied to these points after calculating the Euclidian distance matrix $D_{stem} = \{d_{ij} = \sqrt{(x_i - x_j)^2 + (y_i - y_j)^2}; i=1, \dots, N_{stem}; j=1, \dots, N_{stem}; i \neq j\}$ (Heijden et al., 2004).

1. Assign each point to its own cluster, resulting in N_{stem} clusters.
2. Find the closest pair of clusters and merge them into one cluster. The number of clusters reduces by one.

3. Compute the distance d between the new clusters and each of the old clusters.
4. Repeat steps 2 and 3 until all items are clustered into a single cluster of size N_{stem} or a predefined number of clusters is reached.

In this clustering process the distance between two clusters C_i and C_j is defined as the shortest distance from any point in one cluster to any point in the other cluster. The clustering yields a dendrogram which shows at which distance the clusters are grouped together. By defining a minimum distance d_{min} between the cluster centres the number of clusters $N_{cluster}$ is selected. The value of d_{min} must be larger than the maximum distance of stem points and smaller than the distance of points belonging to different stems. A value of 1.2 m was found to be most useful.

Step 3: The final finding of the stems is achieved by applying a RANSAC-based 3D line adjustment to all the $N_{cluster}$ clusters and labelling all 3D lines with an incident angle smaller than $\alpha = 7^\circ$ and a minimum number of 3 points as stems g_{stem} . This robust procedure eliminates clusters that result from the understorey and do not show a vertical main direction. Also, it cleans the cluster points from non-stem points. The detected stem positions $(x_{stem}^{det}, y_{stem}^{det}) = \{DTM \cap g_{stem}\}$ are calculated as the intersection of the stem g_{stem} with the DTM. Note that several stems can be found within a tree segment.

3. EXPERIMENTS

3.1 Material

Experiments were conducted in the Bavarian Forest National Park which is located in south-eastern Germany along the border to the Czech Republic (49° 3' 19" N, 13° 12' 9" E). 11 sample plots with an area size between 1000 m² and 3600 m² and a mean tree density of 390 trees per ha were selected in the mixed mountain forests. The plots comprise forest in the regeneration phase, the late pole phase and the optimal phase. Reference data for all trees with diameter at breast height (DBH) larger than 10 cm have been collected in May 2006 for 438 Norway spruces (*Picea abies*), 477 European beeches (*Fagus sylvatica*), 74 fir trees (*Abies alba*), 20 Sycamore maples (*Acer pseudoplatanus*) and 3 Norway maples (*Acer platanoides*). Several tree parameters like the DBH, total tree height, stem position and tree species were measured and determined with the help of GPS, tacheometry and the 'Vertex' III system. A DTM with a grid size of 1 m and an absolute accuracy of 25 cm was available (Heurich, 2006). Full waveform data have been collected by Milan Flug GmbH with the Riegl LMS-Q560 scanner in May 2006 after snowmelt but prior to foliation with an average point density of 25 points/m². The vertical sampling distance was 15 cm, the pulse width at half maximum reached 4 ns and the laser wavelength was 1550 nm. The flying altitude of 400 m resulted in a footprint size of 20 cm.

3.2 Single tree detection

The procedures for segmentation and subsequent stem detection were applied to all the plots in a batch procedure without any manual interaction. Figure 2 shows a typical sample area containing several coniferous trees. The tree tops derived from the local maximums of the CHM correspond in some cases with the reference trees reasonably. However, some tree tops are deviating considerably from the true position. Moreover, some

segments contain more than one reference tree. The main reasons are that (i) a group of trees form locally a well-defined maximum and (ii) the surface reconstruction smoothes too much so that neighbouring trees cannot be isolated. In both cases the single trees are not detected and hence the segment represents a group of trees rather than a single tree.

The stem detection takes advantage of additional high-density point information the waveform decomposition provides underneath the CHM. In case that only sparse understorey is below the base height stem points are successfully detected by the hierarchical clustering and the RANSAC-based stem reconstruction. Figures 3a and 3b show the stem points for the segment in the centre of Figure 2 found by the clustering scheme given in section 2.3. The two stems are clearly isolated by applying the angle constraint of 7° to the stems approximated with RANSAC. Moreover, the single stem position derived from the CHM maximum is significantly improved by the new stem position. Thus, the stem detection provides additional single trees that constitute no local maximum in the CHM and improves the position of trees derived from the CHM maximum in the majority of cases.

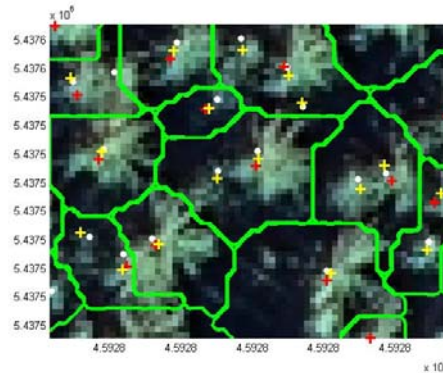


Figure 2. Orthophoto of sample area with segments (green lines), reference coniferous trees (white dots), detected stems (yellow crosses) and the local CHM maximums (red crosses)

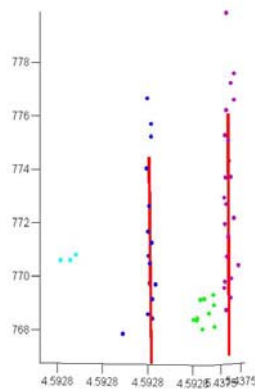


Figure 3a. Stem point clusters and stems reconstructed with RANSAC

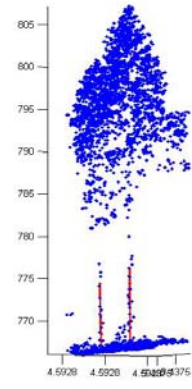


Figure 3b. The neighbouring trees and the reconstructed stems

Let us now evaluate the accuracy and reliability of the presented method. Table 2 contains the percentage of detected trees for all the plots. The trees are subdivided into 3 layers with respect to the mean height h_{top} of the 100 highest trees per ha. The lower layer contains all trees below 50 % of h_{top} , the intermediate layer refers to all trees between 50 % and 80 % of h_{top} , and, finally, the upper layer contains the rest of the trees.

Number of reference trees in lower layer		229
Number of reference trees in intermediate layer		161
Number of reference trees in upper layer		622
Percentage of deciduous [%]		49
Without "stem detection"	Detected trees lower layer [%]	3
	Detected trees intermediate layer [%]	13
	Detected trees upper layer [%]	74
	Total number of detected trees [%]	49
	False detected trees [%]	5
With "stem detection"	Detected trees lower layer [%]	3
	Detected trees intermediate layer [%]	21
	Detected trees upper layer [%]	78
	Total number of detected trees [%]	53
	False detected trees [%]	7

Table 2. Detection of trees in the reference plots

Mean positioning error	Without "stem detection"	With "stem detection"
Coniferous	0.80 m	0.70 m
Deciduous	1.65 m	1.22 m
Total	1.16 m	0.92 m

Table 3. Accuracy of the tree position

At first, we focus on the detection rate of trees that are derived from the CHM without stem detection and hence refer to a local maximum in the CHM. The overall detection rate of 74 % evidences that most of the trees are detected in the upper layer. In comparison, in the intermediate and lower layer the detection rate is considerably smaller. Especially, in the lower layer only a few trees can be found since most of these trees are covered by taller trees. The mean number of false detected trees amounts to 5 % and indicates a remarkable reliability. When applying the stem detection we get an overall improvement of the detection rate in the intermediate layer of 8 % and in the upper layer of 4 %. However, no improvement is achieved in the lower layer since (i) laser hits at the stem of small trees happen rarely, (ii) the base height h_{base} is inaccurate for trees beneath taller trees, and (iii) some trees have no clear h_{base} since their green branches start close to the ground. Additionally, we found that the detection rate is on average for coniferous trees 61 % and for deciduous trees 44 %, respectively. Finally, Table 3 shows the absolute positional improvement of the trees derived from the stem positions $(x_{stem}^{det}, y_{stem}^{det})$ and the position of the reference trees. As expected, the mean positioning error of deciduous trees gets better by 26 %, which corresponds to 43 cm. The overall improvement of the tree position amounts to 24 cm, which is equivalent to 21%.

3.3 Analysis of full waveform data

Based on the segmentation, the stem detection, and the known DTM all the points within a tree segment were subdivided into the three categories "stem points" below the base height, "ground points" and "crown points" representing the tree crown. Possible stems points in the tree crown were excluded by discarding all the points within the stem cylinder V_{stem} , where V_{stem} is defined by the 3D stem line g_{stem} as the centre line of the cylinder and the radius $R = 1$ m. Ground points were found within a height bound of 1 m to the DTM. Furthermore, I_i^c and W_i^c of the points were analysed with respect to the

incident angle of the laser beam. Because of the scanning angle of 45° the maximum incident angle amounted to 22.5° . Thus, mean values and standard deviations were calculated in an angle interval of 5° for the point classes given in Table 1 and are used in the following for visual analysis in Figures 4 to 10.

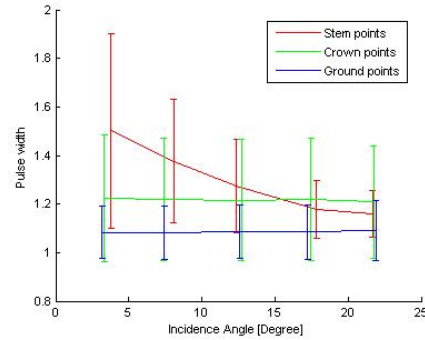


Figure 4. Mean pulse width and standard deviation (single and last points) for the three point categories

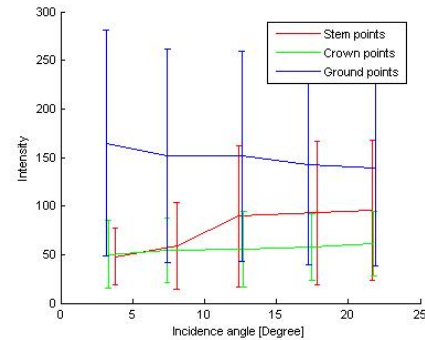


Figure 5. Mean intensity and standard deviation (single and last points) for the three point categories

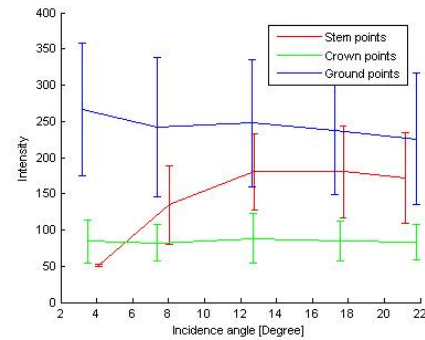


Figure 6. Mean intensity and standard deviation (single points) for the three point categories

In general, we found that roughly 75 % of the stem points are single and last points. Since ground points are also only composed by single and last points we focussed primarily on these point classes. The Figures 4 and 5 show for these point classes the mean values for pulse width and intensity and their standard deviations in dependence on the incident angle. Apparently, the ground points differ from stem points and crown points considerably. Both crown and ground points show no angle dependence. The undulating ground, the undergrowth, and the varying reflecting targets in the crown average the individual values for pulse width and intensity. As expected, the pulse width for the stem points decreases with increasing incident angle since with increasing incident angle the angle between laser beam and the normal to the stem surface gets smaller. This leads to a smaller broadening of the pulse.

Accordingly, the slight increase of the intensity with increasing incident angle can be interpreted the same way. Figure 6 focuses especially on the intensity of single points. Apparently, the three point categories differ fairly well for an angle range of 10° and 22.5° . This was the only point class that indicated the best discrimination between the stem points and crown points. Most notably, ground points and crown points can be clearly separated. These results correspond with experiences of the study (Doneus et al., 2006), which recommends the use of intensity and pulse width along with point coordinates to generate a DTM from full waveform data.

We focus now on the important question in how far intensity and pulse width discriminate tree species. We restrict ourselves to coniferous and deciduous trees, which are the dominating trees in the study area. Crown points and stem points are assigned to the two tree species using the reference data. Again, the mean values and the standard deviation for I_i^c and W_i^c are analysed with respect to the incident angle. From Figure 7 we can conclude that the mean pulse width W_i^c of single crown points is different for coniferous and deciduous trees and is independent on the incident angle. Interestingly, we found that the difference in the pulse width was significant especially for single points. However, the difference of the mean intensity I_i^c was distinctive for all the four point classes, again without any dependence on the incident angle (Figure 8).

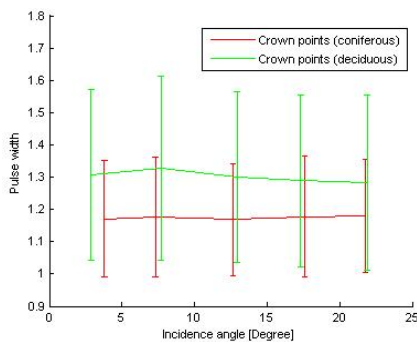


Figure 7. Mean pulse width and standard deviation (single points) for coniferous and deciduous crown points

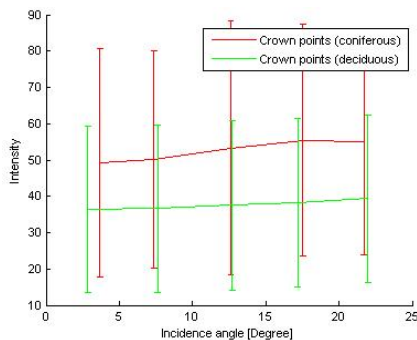


Figure 8. Mean intensity and standard deviation (all point classes) for coniferous and deciduous crown points

Finally, we concentrate on the stem points. The mean pulse width W_m^c is practically the same for the two tree species using all four point classes and decreases slightly with increasing incident angle (Figure 9). Apparently, the shape of coniferous and deciduous tree stems influences the pulse width the same way. Of course, the incident angle still plays a role likewise in Figure 4. Surprisingly, the mean intensity for single points is

clearly different for coniferous and deciduous tree stems (Figure 10). Probably, the absorption and reflecting characteristics of stems have a clear impact on the mean intensity.

We have corrected the intensity of all point classes according to equation (2) assuming that the target size is equal or larger the laser footprint. This assumption is true for ground points and – probably – for most of the stem points. Since the target size of the crown points is not known we corrected them like stem or ground points.

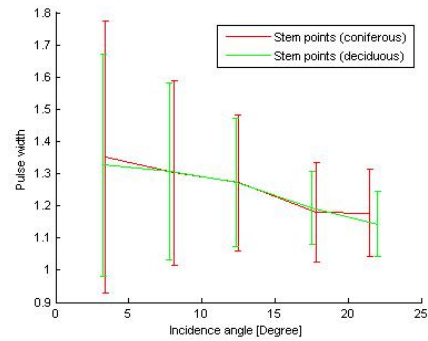


Figure 9. Mean pulse width and standard deviation (all point classes) for coniferous and deciduous stem points

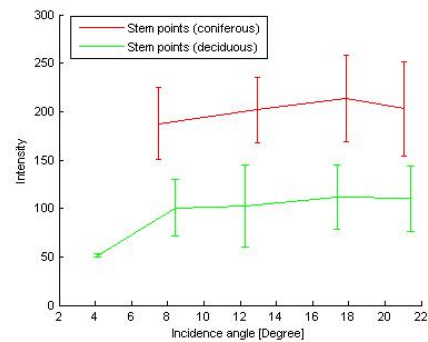


Figure 10. Mean intensity and standard deviation (single points) for coniferous and deciduous stem points

4. DISCUSSION

Conceptually, the presented approach to single tree detection from airborne LIDAR data goes one step further by using the CHM and additional information inside the tree. It leads to an improvement of the detection rate of single trees in the intermediate and upper forest layer by detecting tree stems. This refinement of the detection rate could be expected since (i) in many cases neighbouring trees do not appear as two clear maximums in the raw data and (ii) the smoothing of the CHM blurs the maximums. Apparently, as already pointed out by some other authors (e.g. Solberg et al., 2006), the smoothing of the reconstructed CHM influences the quality of the single tree detection considerably. The second advantage of the presented method is that the position of detected trees is improved. This is also not very surprising since the intersection of the detected tree stem with the DTM must be more precise than the tree position derived from the CHM maximum. Thirdly, the stem detection checks the hypothesis of a stem position which has been derived from the CHM. The restrictions of the approach are that only trees in the upper and intermediate forest layer can be additionally detected. It fails in the under layer where stem hits are rare and stems points can not be clearly clustered. Moreover, so far we have not implemented to go back to the

raw data and to find a new segmentation of the tree crowns using the stem information.

The analysis of the waveform data shows that the intensity and pulse width can be advantageously used for the discrimination of crown, stem and ground points, if the reflections are distinguished with respect to their position in the waveform. This information can be helpful for a true 3D segmentation. Moreover, we found that the mean pulse width and the mean intensity are characteristic for coniferous and deciduous trees. Thus, these experiences are very useful for (i) a DTM generation in forest areas, (ii) an improvement of the stem detection, (iii) and a tree species classification. For instance, ground or stem points can be more reliably detected using the intensity and pulse width as explained in the Figures 4, 5 and 6. Furthermore, the classification of coniferous and deciduous trees in leaf-off situation can advantageously use features that are composed from the mean intensity and pulse width of the tree crowns. If stem points can be detected the mean intensity of single points is the most meaningful feature. The pulse width of stem points is useless for classification purposes.

5. CONCLUSIONS

The study presents a novel single tree detection based on a combined surface reconstruction and stem detection. The results attained in heterogeneous forest types show that the detection rate and position of single trees can be improved in the upper and intermediate layer. Based on the stem detection the analysis of the waveform data shows a clear dependency of the intensity and the pulse width with respect to crown points, stem points, ground points, and tree species, resp. Future research should be focussed on the improvement of the segmentation of the tree crowns using the stem information.

ACKNOWLEDGEMENTS

We thank Dr. Marco Heurich and the Administration of the Bavarian Forest National Park for their productive contributions and for giving us the opportunity to use their remote sensing test sites.

REFERENCES

- Brandtberg, T., 2007, Classifying individual tree species under leaf-off and leaf-on conditions using airborne lidar. *ISPRS Journal of Photogrammetry and Remote Sensing*, 61, pp. 325 – 340.
- Doneus, M., Briese, C., 2006, Full-waveform airborne laser scanning as a tool for archaeological reconnaissance. In: Campana S., Forte M. (eds.), *From Space to Place. Proceedings of the 2nd International Conference on Remote Sensing in Archaeology*. BAR International Series 1568, 2006, 99-106.
- Heijden, F. van der, Duin, R.P.W., Ridder, D. de, Tax, D.M.J., 2004. *Classification, parameter estimation and state estimation – An engineering approach using MATLAB*. John Wiley & Sons Ltd, The Attriium, southern Gate, Chichester, West Sussex PO19 8SQ, England.
- Heurich, M., 2006, Evaluierung und Entwicklung von Methoden zur automatisierten Erfassung von Waldstrukturen aus Daten flugzeuggetragener Fernerkundungssensoren. *Schriftenreihe des Wissenschaftszentrums Weihenstephan für Ernährung, Landnutzung und Umwelt der Technischen Universität München und der Bayerischen Landesanstalt für Wald und Forstwirtschaft*, Forstlicher Forschungsbericht München, Nr. 202, ISBN 3-933506-33-6. <http://meadiatum2/ub.tum.de/>. (Accessed February 18, 2007)
- Holmgren, J., Persson, Å., 2004, Identifying species of individual trees using airborne laser scanner. *Remote Sensing of Environment* 90 (2004) 415-423.
- Hyypä, J., Kelle, O., Lehikoinen, M., Inkinen, M., 2001. A segmentation-based method to retrieve stem volume estimates from 3-D tree height models produced by laser scanners. *IEEE Transactions on Geoscience and Remote Sensing*, 39:969-975.
- Hyypä, J., Hyypä, H., Litkey, P., Yu, X., Haggren, H., Rönnholm, P., Pyysalo, U., Pikänen, J., Maltamo, M., 2004, Algorithms and methods of airborne laser scanning for forest measurements. *Proceedings of the ISPRS working group VIII/2 Laser-Scanners for Forest and Landscape Assessment*, Volume XXXVI, PART 8/W2, 3 – 6th October, Freiburg, pp. 82 – 89.
- Jutzi B., Stilla U. 2005. Waveform processing of laser pulses for reconstruction of surfaces in urban areas. In: *Moeller M, Wentz E (eds) 3th International Symposium: Remote sensing and data fusion on urban areas, URBAN 2005. International Archives of Photogrammetry and Remote Sensing*. Vol 36, Part 8 W27.
- Krzystek, P., Wild, D., 1992, Experimental accuracy analysis of automatically measured digital terrain models. *Robust Computer Vision: Quality of vision algorithms*. Förstner, Ruhwedel (ed.). Wichman Verlag, Karlsruhe, pp. 372 -390.
- Persson, A., Holmgren, J. and Söderman, U., 2002. Detecting and measuring individual trees using an airborne laserscanner. *Photogrammetric Engineering & Remote Sensing* 68(9), pp. 925–932.
- Pyysalo, U., Hyypä, H., 2002. Reconstructing Tree Crowns from Laser Scanner Data for Feature Extraction. In *ISPRS Commission III, Symposium 2002 September 9 - 13, 2002, Graz, Austria*, pages B-218 ff (4 pages).
- Reitberger, J., Krzystek, P., Stilla, U. 2006. Analysis of Full Waveform Lidar Data for Tree Species Classification. *Symposium ISPRS Commission III "Photogrammetric Computer Vision" PCV06*, 20 – 22th September, Bonn, Germany.
- Solberg, S., Naesset, E., Bollandsas, O. M., 2006. Single Tree Segmentation Using Airborne Laser Scanner Data in a Structurally Heterogeneous Spruce Forest. *Photogrammetric Engineering & Remote Sensing*, Vol. 72, No. 12, December 2006, pp. 1369-1378.
- Vincent, L., Soille, P., 1991, Watersheds in Digital Spaces: An Efficient Algorithm Based on Immersion Simulations. *IEEE Transactions of Pattern Analysis and Machine Intelligence*, Vol. 13, No. 6, June 1991, pp. 583-598.
- Wagner, W., Ullrich, A., Ducic, V., Melzer, T. and Studnicka, N., 2006, Gaussian decomposition and calibration of a novel small-footprint full-waveform digitising airborne laser scanner. *ISPRS Journal of Photogrammetry and Remote Sensing*, 60, pp. 100-112

FROM POINT CLOUD TO SURFACE: MODELING STRUCTURES IN LASER SCANNER POINT CLOUDS

Pablo Rodríguez González, Diego González Aguilera and Javier Gómez Lahoz

Land and Cartography Engineering Department, Univ. of Salamanca, Spain

pablorgsf@hotmail.com, daguilera@usal.es, fotod@usal.es

Commission V, WG V/3

KEY WORDS: Laserscanning, Photogrammetry, Feature Extraction, Segmentation, Modeling, Software Development.

ABSTRACT:

The automatic modeling of precise structures from randomly distributed laser points derived from laser scanner data is a very hard problem, not completely solved and problematic in case of incomplete, noisy and sparse data. The generation of polygonal models that can satisfy high modeling and visualization demands is required in different applications, like architecture, archaeology, city planning, virtual reality applications and other graphics applications. The goal is always to find a way to create a computer model of an object which best fits the reality. Polygons are usually the ideal way to accurately represent the results of measurements, providing an optimal surface description. While the generation of digital terrain models has a long tradition and has found efficient solutions, the correct 3D modeling of closed surfaces or free-form objects is of recent nature, a not completely solved problem and still an important issue investigated in many research activities.

In this paper we develop an approach for converting a laser scanner point cloud into a realistic 3D polygonal model that can satisfy high modeling and visualization demands. Close range photogrammetry deals since many years with manual or automatic image measurements. Now laser scanners are also becoming a standard source for input data in many application areas, providing millions of points. As a consequence, the problem of generating high quality polygonal models of objects from randomly distributed laser points is getting more and more attention. After reviewing some results in this context, we will describe a full approach for turning a usual unstructured point cloud into a consistent polygonal model. Finally, the polygonal model is turned into a hierarchical nodes network similar to VRML. A novel laserscanning processing tool, LSM3D (Laser Scanner Modeling 3D), has been developed and tested over different examples related with architectonic buildings.

1. INTRODUCTION

The automatic 3D modeling of precise structures from randomly distributed laser points is a problem which has been approached in several ways in computer graphics and computer vision literature and which has currently produced a growing interest in close range photogrammetry due to the emergence of terrestrial laser scanner. The generation of polygonal models which can satisfy high modeling and visualization demands is required in different applications, like architecture, archaeology, virtual reality applications and other graphics applications. The goal is always to find a way to create a computer model of an object which best fits the reality, remember that the models, if they are even very accurate, are idealizations of the reality. Polygons are usually the ideal way to accurately represent the results of measurements, providing an optimal surface description. While the generation of DTMs has a long tradition and has found efficient solutions, the correct 3D modeling of closed surfaces or free-form objects is of recent nature, a not completely solved problem and still an important issue investigated in many research activities.

Several methods and approaches have been developed for the recognition of object surfaces in laser scanner point clouds. Following the proposal of (Vosselman et. al., 2004), methods for the extraction of surfaces can roughly be divided into two categories: those that segment a point cloud based on criteria like proximity of points and/or similarity of locally estimated surface normals and those that directly estimate surface

parameters by clustering and locating maxima in a parameter space.

The first approach shares large similarities to the image segmentation problem, so equivalent techniques and algorithms of image processing could be extrapolated and adapted. For example, an important type of 2D image processing operators and filters like neighborhood, labeling, skeletonisation or even morphologic operators could be adapted for the detection of three dimensional linear structures and boundaries: (Palagyi and Kuba 1999), (Jiang and Bunke, 1994) and (Sithole and Vosselman, 2003) are several examples where scan line segmentation and growing surfaces methods could be comparable in strategy to the split-and-merge methods and region growing algorithms in image segmentation respectively.

In this line, polygonal meshes, volume grids and parametric piecewise functions NURBS (Non Uniforms Rational B-Splines) are others alternatives to obtain a final description of the surface: (Polis and McKeown, 1992) and (Oda et. al., 2004) develop several methods for creating simple polygonal meshes linked to surveying applications; (Chew, 1997), (Shewchuk, 2001) and (Watson, 1981) present several approaches based on 3D polygonal meshes; finally, (Han and Medioni, 1996) develop several parametric piecewise functions based on NURBS. Nevertheless, one of the main drawbacks of complex polygonal meshing is that requires high rates of computing time

and do not always represent the wealth of information contained in the original points cloud.

On the other hand, regarding the second category of methods, these are more robust but can only be used for modeling basic primitives supported by a few parameters. There are several authors (e.g. (Krishnamurthy and Levoy, 1996), (Curless and Levoy, 1996), (Pottmann et. al., 2002) and (Vosselman et. al., 2004)) who have developed automatic methods and algorithms for polynomial 3D modeling, but only applied to structured or small points clouds corresponding to independent objects. In these approaches, the use of a parameter space based on the generalized Hough transform (Ballard, 1981) and Gaussian Sphere (Barnard, 1983) have been the most successful techniques for modeling basic primitives such as planes, cylinders, spheres, etc. Nevertheless, the main disadvantage of these methods is its high computational cost, as well as the presence of outliers. Outlier detection in point clouds is not a trivial task since there are: geometrical discontinuities caused by occlusions, no prior knowledge of the statistical distribution of points, existence of noise, and different local point densities.

The approach that we propose follows a combination of both categories, since segmentation and clustering techniques are applied over unorganized laser scanner dataset. In order to avoid outliers, RANSAC robust estimator (Fischler and Bolles, 1981) has been adapted before the fitting step.

The complete full pipeline process in 3D modeling structures from laser scanner dataset is illustrated in Figure 1.

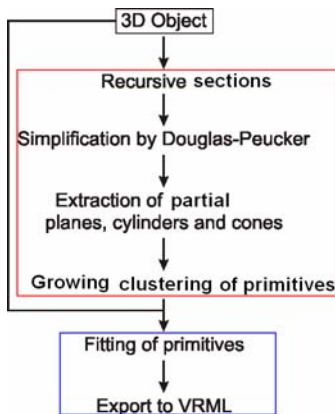


Figure 1. Full pipeline process.

The paper presents the following structure and organization: after this introduction, Section 2 explains in detail the segmentation approach of point clouds. Section 3 develops the basic primitives fitting process. Section 4 describes the novel laserscanning processing software developed. Section 5 shows the experimental results tested with our own software. A final section is devoted to give some conclusions and future works.

2. SCAN SEGMENTATION

In the process of 3D modeling structures from randomly distributed laser points, a number of steps are involved. One of the critical steps is segmentation, which contributes to segment the structures from the background of the original laserscanning point cloud. The reliability and accuracy of the segmentation method affect the result of the final structures extraction to a

large extent. Therefore, image segmentation plays an important role in laserscanning modeling. Recently, several segmentation techniques for laser scanner have been reported (Min et. al., 2004) and (Bellon and Silva, 2002). In the first approach, the authors develop an automated framework for evaluating the performance of range image segmentation algorithms. This framework should make it possible to objectively and reliably compare the performance of range image segmentation algorithms; allow informed experimental feedback for the design of improved segmentation algorithms. The framework is demonstrated using range images, but in principle it could be used to evaluate region segmentation algorithms for any type of image. In the second approach, the authors present new improvements for range image segmentation based on edge detection techniques. The developed approach better preserves the object's topology and shape even in noisy images. The algorithm also does not depend on rigid threshold values, thus being useful in unsupervised systems. Experiments are performed in a popular range image database and the results are compared to four other traditional range image segmentation algorithms, demonstrating the efficiency of the proposed algorithm.

In our case, laser points have been processed with various well-known segmentation algorithms following a triple process.

In a first step, orthogonal sections to the vertical are obtained (Figure 5). This segmentation requires a previous definition of the Z axis which coincides with the vertical, due to the vertical is the mainly character of the shapes of the buildings. Afterwards, sections and profiles are simplified automatically based on Douglas-Peucker algorithm (Douglas&Peucker, 1973) which keeps the basic geometric features of every section (Figure 2). This step also includes a process to localize circumferences, and in this way, the final results of all these sections are polygonal lines and circles.

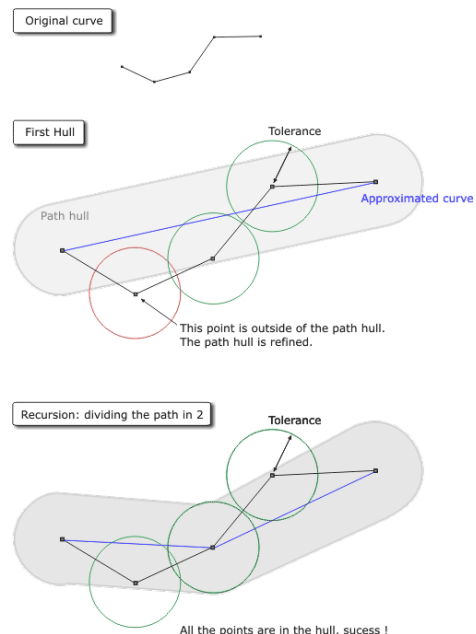


Figure 2. Simplification of laser sections based on Douglas-Peucker.

In a second step, a clustering of different sections allows us to extract partial primitives such as planes, cylinders and cones,

working recursively with groups of three sections to verify the results.

The algorithm is completely automatic. Two adaptive thresholds are selected:

- The threshold α is used to decide whether two sections have a similar orientation.
- The threshold d is used to decide whether two sections have a logical position in space, in order to discriminate between sections which are in different parts of the scene, like regular patterns.

For each straight segment belonging to the first section, similar features such as position, orientation and size are searched in segments belonging to the second and third sections. This processing is based on the regularity of the facade, and for every three segments which verify the previous condition, a new partial extraction of planes is obtained. The process with cylinders and cones is similar, but this time, values such as the position and radius are the main goal. Discrimination between cylinders and cones is established based on the radius variation.

To improve the efficiency and reliability of the process, RANSAC robust estimator is implemented with a twofold purpose in order to check for possible outliers. Firstly, through Douglas-Peucker simplification, allowing that possible outliers do not take part during the process. Secondly, in the clustering of sections, determining the best three combinations of sections and profiles for extracting basic primitives.

The final step is a growing clustering of each partial primitive in order to obtain a global primitive. To do this, geometric characteristics of each primitive such as the diedric angle between planes, the angle between the axes of the cylinders, or the relationship between the radius of cylinders, as well as its neighbouring relations are checked. Moreover, each threshold of geometric characteristics can be modified by the user interactively.

3. PRIMITIVES FITTING

At a final level, the segmented range dataset is fitted to basic surfaces. Particularly, the results from segmentation give potential architectural elements, but it is required to fit these features to the real object accurately.

Particularly:

3D planes are extracted by an automatic fitting of planar primitives with points of the object.

3D lines are extracted as a result of planar surface intersections. The extraction of 3D lines involves two steps:

- i) Intersection of neighbouring 3D planes to produce 3D lines of infinite extent.
- ii) Verification of the infinite 3D lines. This step involves the computation of the distance between the bounded primitives and the produced 3D line.

Cylinders and cones are processed in the same way that planes, using the segmentation results to limit the workspace that is used in the fitting.

At last, an analytical and simplified parameterization of the basic extracted geometries is performed.

On the other hand, the visualization of a 3D model is often the only product of interest for the external world and remains the only possible contact with the model. Moreover, an interactive visualization of the object enables us to obtain impossible views and perspectives to support further analysis tasks. Therefore, a realistic and accurate visualization is often required. However, working with laser scanner dataset complexity increases considerably, especially if we consider the volume of information, so the modeling pipeline described before remains crucial to transform our laser polygonal models to VRML automatically.

The VRML (Virtual Reality Modeling Language) format was the standard chosen to provide an interactive visualization of the results guaranteeing flexibility and scalability in the visualization at the same time, so different 3D models can be incorporated and managed easily. In this way, an automatic transformation of the reconstructed 3D model into a topological structure (points, lines and surfaces) sorted hierarchically in a nodes network was performed, allowing three different levels of visualization: wireframe, shaded and textured. Materials defined by their colours and radiometric properties (opaqueness, transparency, diffusion, reflection and emission) and photographic textures, are mapped through a uniform and continuous renderization supported internally by VRML.

4. THE LSM3D SOFTWARE

Nowadays, laser scanner technology continues relying on a strong hardware and software dependence. In fact, some companies have invested heavily on digital implementations of laserscanning principles, and lead the market in order to obtain massive range data production. Consequently, prices remain high and the access to laser scanner equipment continues being limited only to those who can afford it.

Our aim tries to improve this 'bottleneck' through the development of free laser scanner software and tools. The basic idea is to develop laserscanning tools that can be used as didactical elements for Computer-assisted teaching and training on Internet, regular Classes, Summer Courses and Seminars, in order to ease the students' assimilation of main laserscanning concepts.

In principle, the laserscanning tool LSM3D consists of two parts: Knowledge and Tasks. In the 'Knowledge' part, LSM3D describes the synergies between disciplines such as close-range photogrammetry, computer vision and computer graphics, as well as the methodology developed for laser scanner modeling. These contents are interlaced with hyperlinks to a glossary of technical terms and definitions, as well as supported with graphic illustrations. In the 'Tasks' part, LSM3D allows to carry out exercises and simulations (Figure 3). This interface allows to work in different levels, from students who use the program only with learning purposes to PhD students who develop new tools and even professionals who are interested in applying the software to an specific context.

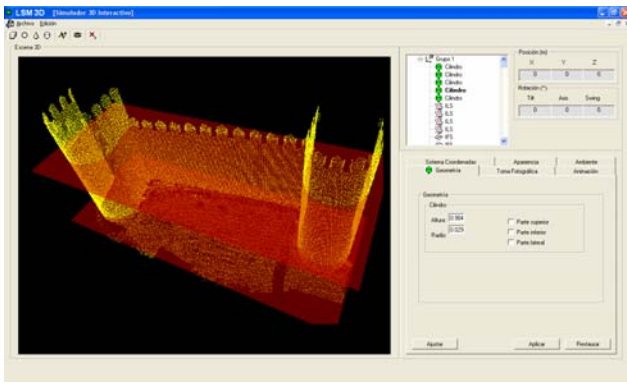


Figure 3. LSM3D: 'Tasks' interface.

Particularly, LSM3D allows:

- Importing and exporting point clouds and high resolution digital images;
- Projecting the texture of high resolution image onto the point cloud.
- Obtaining sections over the point cloud (Figure 4).
- Modeling simple structures through the extraction of basic primitives.
- Modeling complex structures through mesh triangulation algorithms and using the previous structures as geometric constraints.
- Gaining feedback between image re-projection and primitive extraction to improve the results.
- Exporting results to VRML language.

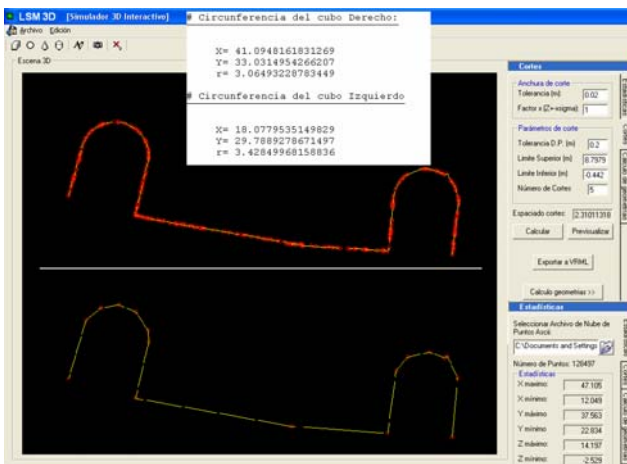


Figure 4. LSM3D: laserscanning segmentation.

As a result, LSM3D represents a clear contribution in the laserscanning context, destined to the synergic integration of different methodologies and tools. Therefore, teaching and research work can be presented as an interactive learning program. The 'knowledge' is presented by dynamic figures and hypertexts, while 'tasks or experiments' can be carried out with different free tools such as LSM3D.

5. EXPERIMENTAL RESULTS

In order to determine the accuracy, limitations and advantages of the 3D modeling approach proposed, a series of experiments are tested using our own developed tool.

5.1 The medieval wall of Avila

Problem and goal

The aim of this study is the automatic 3D modeling of the basic structures of the medieval wall of Avila. A time of flight laser scanner, Trimble GX200, is used to obtain laser scanner dataset. The main problems are focused on the own complexity and irregularity of an emblematic object like that.

Methodology and results

A first segmentation approach based on orthogonal sections with an equidistance of 1 meter and a tolerance of 200 millimeters for Douglas-Peucker is applied (Figure 5).

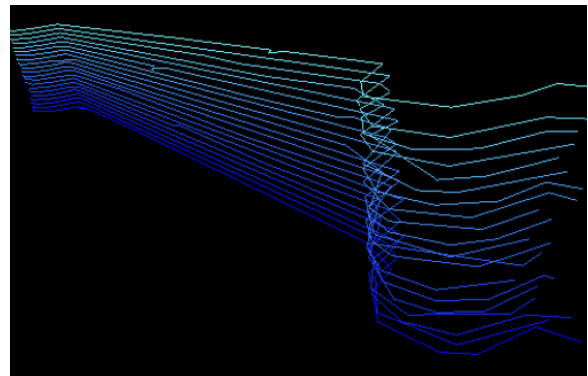


Figure 5. Laserscanning segmentation with orthogonal sections and Douglas-Peucker simplification before circle extraction

A second segmentation approach based on the clustering of sections allows us to extract partial primitives (Figure 6), which are transformed into global primitives following a growing surface strategy.

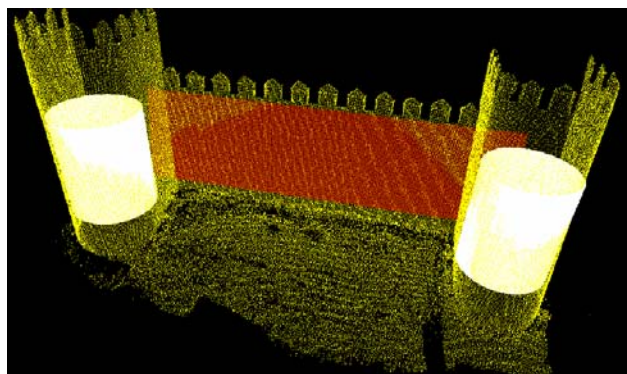


Figure 6. Partial extraction of primitives.

A maximum threshold of 3° corresponding to the diedric angle between planes has been used to clustering adjacent planes, preserving the basic geometric characteristic of each primitive. Regarding cylinders, a maximum threshold of 2° and 1 meter between cylinders axis have been considered to validate them.

Finally, a fitting of basic primitives is performed using object coordinates as reference. Particularly, 3D planes corresponding to the main wall and cylinders corresponding to towers are extracted by an automatic fitting of basic primitives with points of the object (Figure 7).

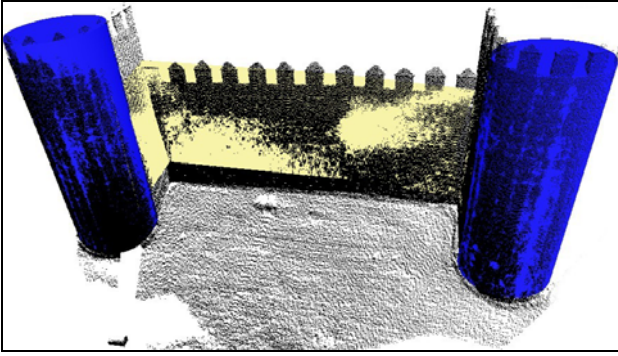


Figure 7. Automatic medieval wall 3D modeling.

The final fitting error for 3D planes and cylinders is around 50 millimetres. However, some problems remain in the battlements, due to their irregular shape and discontinuity in the transition with towers.

5.2 The romanesque church of San Pedro

Problem and goal. The workspace is focused on the two main façades of the church. The aim of this study is the automatic modeling of the basic structures of the romanesque church of San Pedro. A time of flight laser scanner, Trimble GX200, is used to obtain laser scanner dataset.

Methodology and results

A first segmentation approach based on orthogonal sections with an equidistance of 1 meter and a tolerance of 100 millimetres for Douglas-Peucker is applied (Figure 8).

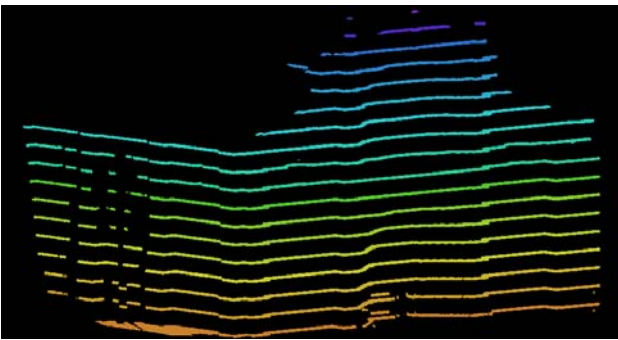


Figure 8. Laserscanning segmentation with orthogonal sections and Douglas-Peucker simplification.

A maximum threshold of 2° corresponding to the diedric angle between planes has been used to clustering adjacent planes, preserving the basic geometric characteristic of each primitive.

Finally, a fitting of basic primitives is performed using object coordinates as reference. Particularly, 3D planes corresponding to the main façades are extracted by an automatic fitting of basic primitives with points of the object (Figure 9).

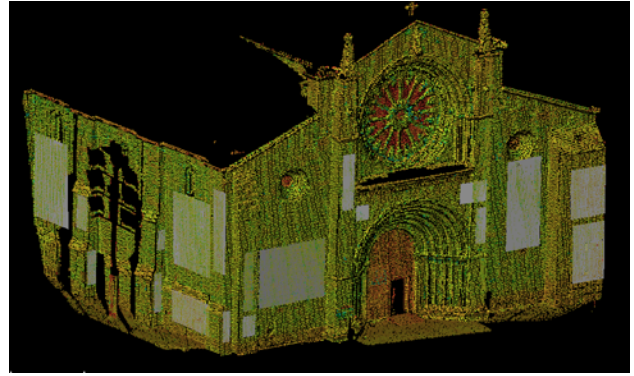


Figure 9. Automatic romanesque church 3D modeling.

The final fitting error for 3D planes is around 30 millimetres.

6. CONCLUSIONS AND FUTURE PERSPECTIVES

The presented paper has investigated and developed a range segmentation and 3D feature modeling from laser scanner dataset. We proved the applicability of these algorithms in architectural scenes. A consistent and reliable full process pipeline has been developed and presented. It was demonstrated with different practical examples tested through our own software, LSM3D.

We feel that we have attacked one of the most difficult problems in laserscanning. Regarding the most relevant aspects of the proposed approach, we could remark on:

- Automation in the modeling of basic primitives.
- Creation of geometrically correct solid models.
- Simplification of laser scanner models through VRML transformation.
- More reliability in segmentation step through the incorporation of RANSAC robust estimator.
- Original approach which provide a new point of view to solve the problem of laserscanning 3D modeling.

Due to the scope of the system, there are still a number of open technical issues that need to be addressed:

- A number of thresholds have to be tested by the user before obtaining good results.
- The object must be linear in order to apply orthogonal sections.

As for the future perspectives, we believe that this novel laser scanner tool could be improved towards the automatic, accurate and reliable construction of CAD models of urban structures from laser scanner dataset.

Acknowledgements

First of all, we would like to thank to the students Luis García, Fernando Castro and Esteban Ruiz for their support during this project. Furthermore, we are especially grateful with several local institutions, especially 'Ayuntamiento de Ávila' and 'Institución Gran Duque de Alba' for providing all technical and human assistance as well as for the partial economical support of the research work.

References from Journals:

Ballard D. Generalizing the Hough transform to detect arbitrary shapes. *Pattern Recognition*, 13(2):111-122, 1981.

Barnard S., 1983. Interpreting perspective images. *Artificial Intelligence*, vol. 21.

Douglas D. & Peucker T. Algorithms for the reduction of the number of points required to represent a digitized line or its caricature. *The Canadian Cartographer* 10(2), 112-122 (1973)

Jiang, X., Bunke, H. and Meier, U., 2000. High-level feature based range image segmentation. *Image and Vision Computing*, 18(10), pp. 811/822.

Min J., Powell M. and Bowyer K. Automated performance evaluation of range image segmentation algorithms. *Systems, Man and Cybernetics, Part B, IEEE Transactions on*, vol. 34, n° 1, 2004.

Sithole, G., Vosselman, G., 2004. Experimental Comparison of Filter Algorithms for Bare Earth Extraction from Airborne Laser Scanning Point Clouds. *ISPRS Journal of Photogrammetry and Remote Sensing* 59 (1-2): 85-101.

Watson D. Computing the n-dimensional Delaunay Tessellation with Application to Voronoi Polytopes. *Computer Journal* 24(2):167-172, 1981.

References from Other Literature:

Bellon O. R. and Silva L. New improvements to range image segmentation by edge detection. *Signal Processing Letters, IEEE*, vol.9, n° 2, 2002.

Chew L. Guaranteed-Quality Triangular Meshes. Technical Report TR-89-983, Department of Computer Science, Cornell University, 1989.

Curless, B. Levoy, M. 1996: A volumetric method for building complex models from range images. *ACM Proc. Of Siggraph*, pp. 303-312.

Fischler, M. A., and R. C. Bolles, 1981. Random sample consensus. *CM Communications*.

Han S. and Medioni G.: Triangular NURBS surface modeling of scattered data. *Proceedings of the 7th conference on Visualization '96 table of contents*. San Francisco, California, United States, 1996.

Krishnamurthy V. and Levoy M. Fitting smooth surfaces to dense polygon meshes. *Proceedings of SIGGRAPH 96*, pages 313-324, August 1996. Held in New Orleans, Louisiana.

Oda K., Wei Lu Osamu Uchida Takeshi Doihara: Triangle-based visibility analysis and true orthoimage generation. *International Congress of ISPRS. Istanbul 2004*.

Palagyi K. and A. Kuba, A Parallel 3D 12-Subiteration Thinning Algorithm, pp. 199-221.

Polis M. and D. McKeown: Iterative TIN Generation from Digital Elevation Models, in: *Proceedings of IEEE Conference on Computer Vision and Pattern Recognition, Illinois, 1992*.

Pottmann H., Stefan Leopoldseeder, Johannes Wallner and Martin Peternell: Recognition and reconstruction of special surfaces from point clouds. *ISPRS archives 2002*.

Shewchuk J.: Delaunay Refinement Algorithms for Triangular Mesh Generation. Department of Electrical Engineering and Computer Science. University of California at Berkeley, 2001.

Vosselman G., B.G.H Gorte, G. Sithole, T. Rabbani : Recognising structures in laser scanner point clouds. *International ISPRS Congress. Istanbul (Turkey) 2004*.

A METHOD OF DIRECTLY ESTIMATING STEMWOOD VOLUME FROM GLAS WAVEFORM PARAMETERS

J. A. Rosette^{a,*}, P. R. J. North^a, J. C. Suárez^b

^a University of Wales Swansea, Climate and Land-Surface Systems Interaction Centre (CLASSIC), Department of Geography, Swansea, SA2 8PP, United Kingdom - (ggrosette, p.r.j.north)@swansea.ac.uk

^b The Agency of the Forestry Commission Great Britain, Northern Research Station, Roslin, Midlothian, EH25 9SY, United Kingdom – juan.suarez@forestry.gsi.gov.uk

KEY WORDS: Lidar, Satellite, Vegetation, Forestry, Inventory

ABSTRACT:

Methods of estimating stemwood volume from ICESat/ GLAS lidar waveforms are explored for a mixed temperate forest, the Forest of Dean, Gloucestershire, UK. Previous methods have used maximum canopy height estimations incorporating a digital terrain model (DTM) and requiring calibration using a sample of within-footprint tree heights. This study focuses on deriving methods which do not require such supplementary data. Maximum canopy height is estimated as the distance between Signal Begin and the ground peak within the waveform. The ground peak is determined using the centroid of either Gaussian Peak 1 or 2, identified by whichever has the greatest amplitude. This canopy height estimation was used to isolate the region of the waveform returned from the vegetation, from which heights of cumulative energy percentiles were calculated. For the tallest species within footprints, stemwood volume estimates for conifers produced R^2 of 0.59, RMSE 98.3 m³/ha and for broadleaf species, R^2 of 0.75, RMSE 59.1 m³/ha were found. Stemwood volume estimates taking account of the mixed species composition within stands were also calculated. For mixed stand estimates, R^2 of 0.66, RMSE 82.5 m³/ha was found for stands dominated by conifers whilst stands with greatest percentage cover provided by broadleaf species produced R^2 of 0.47, RMSE 75.6 m³/ha. Potential is shown for satellite lidar stemwood volume estimates to be derived directly from waveforms and therefore suggests that similar techniques could be applied where a suitable DTM or field measurements are not available.

1. INTRODUCTION

Quantifying changes in biomass distribution is acknowledged by the Global Climate Observing System as an essential variable for the monitoring of global climate. Satellite-derived estimates can contribute to biomass estimation on a global scale; the aim being to achieve an accuracy of 10-20% which is comparable with *in situ* methods (GCOS 2006).

Airborne lidar has been shown to offer a means of estimating biophysical parameters such as above ground biomass at a local scale. This has been demonstrated using discrete return lidar (e.g. Hyypä *et al.* 2001, Patenaude *et al.* 2004) and waveform recording devices (e.g. Lefsky *et al.* 1999, Drake *et al.* 2003). Opportunities for USA state-wide biomass estimation using first return lidar profiling are also shown by Nelson *et al.* (2004) and Nelson *et al.* (2006), whilst Bufton (1989), Gardner (1992), Harding *et al.* (1994), Brenner *et al.* (2003) and Hese *et al.* (2005) discuss the concepts of full waveform satellite lidar.

Therefore, given the near-global coverage of the Ice, Cloud and land Elevation Satellite (ICESat), there is potential for satellite lidar to contribute to regional or national scale forest monitoring and quantification (e.g. GCOS 2004, Hese *et al.* 2005, Helmer and Lefsky 2006). However, previous methods of estimating above ground biomass/ volume have relied upon supplementary data to estimate maximum canopy heights. This has involved a two-stage process, deriving maximum canopy height from a multiple regression using the Waveform Extent (distance between Signal Begin and Signal End) plus a terrain index (using a DTM centred on the footprint co-ordinates) and calibrating against field measurements of within-footprint tree height. These maximum canopy height estimates were then used

to develop methods of estimating stemwood volume (Lefsky *et al.* 2005, Rosette *et al.* submitted).

This paper explores an alternative means of estimating stemwood volume which does not necessitate additional information and therefore aims to simplify the process, potentially allowing broader application.

2. METHODS

2.1 Study Site

The Forest of Dean, Gloucestershire, UK covers an area of approximately 11,000 hectares and was crossed by ICESat between 51.74° N and 51.88° N latitude and 2.54° W and 2.51° W longitude. The data used for this study were captured on 22nd October 2005 while vegetation was predominantly still in leaf. Most frequently occurring species within stands sampled by ICESat were Norway Spruce (*Picea abies*), mixed broadleaf species, Oak (*Quercus* spp), Corsican Pine (*Pinus nigra* var *maritima*), Douglas Fir (*Pseudotsuga menziesii*), Scots Pine (*Pinus sylvestris*) and European Larch (*Larix decidua*). It is a highly mixed, temperate forest managed by the Forestry Commission of Great Britain. Forest Enterprise is responsible for maintaining a sub-compartment database for management purposes which lists details of species, habitat conditions and management criteria for each discrete component contained within sub-compartments (Forestry Commission 2006).

* Corresponding author.

2.2 Yield Models

The sub-compartment database allows reference to be made to yield models which predict stand parameters including top height, individual tree volume, volume per hectare and mean diameter at breast height by age (Edwards and Christie, 1981). These models are empirically-derived and initial spacing of individuals, species, yield class (annual increment $\text{m}^3/\text{ha}/\text{year}$) and management (e.g. thinning regime) determine the anticipated growth curve.

Stemwood volume is defined as living over-bark volume in m^3/ha (for conifers this comprises the main stem diameter greater or equal to 7cm). Forestry Commission yield models were used to calculate stemwood volume for stands covered by ICESat footprints and, for this study, two calculations of stemwood volume were used:

2.2.1 Single species stemwood volume: Few footprints covered stands containing a single species and therefore, to indicate the potential for pure stands, a proxy was used. Stemwood volume was calculated for the tallest species within each footprint (identified from the sub-compartment database). This was based on the principle that this species could also be identified within waveforms (maximum canopy height estimates). Differentiation was then made between footprints in which the tallest species was broadleaf or coniferous to consider whether this would improve the relationship with waveform parameters described in 2.3.2.

2.2.2 Mixed stand stemwood volume: Sub-compartments may contain several distinct components and additionally, a number of ICESat footprints crossed sub-compartment boundaries. The second measure of stemwood volume therefore represents the mixed composition of stands and is calculated using the percentage cover of species within all components of each sub-compartment sampled by footprints. Footprints were then discriminated according to whether broadleaf species or conifers formed the greatest percentage cover and correlations with waveform parameters (section 2.3.2) were calculated.

2.3 GLAS Data

2.3.1 Data description: The Geoscience Laser Altimeter System (GLAS) is carried on the Ice, Cloud and land Elevation Satellite (ICESat) and is operated at intervals to capture measurements for three seasons each year: usually for approximately month-long periods during February-March, May-June and October-November. GLAS simultaneously emits 1064nm and 532 nm pulses which produce NIR elliptical footprints of 64m average equivalent circular area diameter at 172m intervals along the ground track. Footprint horizontal geolocation is unknown for the laser operation used in this study (L3D), however is expected to vary between 0.0 ± 2.7 metres (L3A) and 17.4 ± 22.8 metres (L3B).

Footprints are broader than the ideal diameter for vegetation analysis (approximately tree crown width) and this increases the likelihood of vegetation and ground signals being combined within the returned waveform thereby complicating interpretation. For footprints containing complex topography and vegetation distribution, apparent vegetation heights derived from waveforms may therefore differ from actual vegetation heights. A further consideration when studying the vegetation profile within waveforms is that laser energy diminishes towards the margins of the footprint and therefore waveforms are most representative of the footprint centre.

Zwally *et al.* (2002), Brenner *et al.* (2003), Kichak (2003), Abshire *et al.* (2005), Harding and Carabajal (2005), Schutz *et al.* (2005) and NSIDC (2006) provide further details regarding the ICESat mission and data.

For this study, the following products were used from data release V026 (Zwally *et al.* 2006): level 1A GLA01 (Global Altimetry data - raw waveform) and level 2 products GLA06 (Global Elevation data - footprint geolocation) and GLA14 (Global Land Surface Altimetry data - alternate model fit).

Waveform structure is formed by the returned energy for intercepted surfaces at and above the ground surface within footprints. Signal Begin and Signal End positions within the waveform indicate the highest canopy surface and lowest ground elevation within footprints and are identified by the signal exceeding a background noise threshold. Waveform amplitude is determined by both area of intercepted surfaces and the intensity of the returned laser pulse. Vegetated footprints on relatively flat terrain are expected to produce a bimodal waveform with a narrow peak from the ground surface and a broader, more complex return from the overlying canopy. The canopy return represents, in part, the surface area of intercepted canopy elements and is therefore explored with regard to the potential to estimate vegetation volume. To facilitate interpretation, the GLA14 product provides a model fit to the waveform using the sum of six Gaussian peaks (Figure 1). These are used in the identification of waveform parameters for this study.

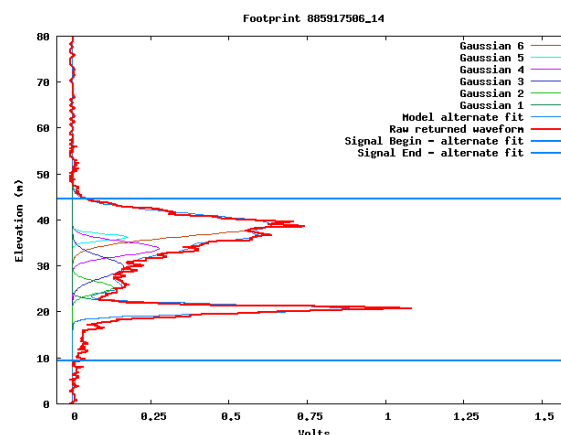


Figure 1. Raw waveform showing alternate fit Signal Begin and Signal End waveform positions plus model decomposition (the sum of six Gaussian peaks)

2.3.2 Waveform parameters: Several waveform parameters were used to explore their potential to estimate stemwood volume for the Forest of Dean. Firstly a method of estimating maximum canopy height presented in Rosette *et al.* (in press) was used. Of the lowest two Gaussian peaks (Figure 1), the centroid of that with the greatest amplitude was used to identify the ground surface. Maximum canopy height was then estimated as the elevation difference between this location within the waveform and the Signal Begin position. This estimated maximum canopy height was used to isolate the region of the waveform assumed to be returned from the vegetation. Percentiles of cumulative energy within the vegetation return were calculated (adapted from Harding *et al.* 2001).

Waveform-derived maximum canopy height, plus heights of cumulative energy percentiles were then explored as potential estimators of stemwood volume (2.2.1 and 2.2.2).

Previous work has shown that, for this site, area under the canopy return of the waveform did not provide a robust estimator of stemwood volume. However, multiple regression was carried out using the maximum canopy height and heights of percentiles together with area under the canopy return, to assess whether an improvement on the relationships could be achieved. Canopy return area was assumed to be the sum of areas under Gaussian peaks 2-6 if peak 1 had been identified as the ground peak or the total of areas under Gaussian peaks 3-6 if the ground position was assumed to be the centroid of peak 2.

3. RESULTS

3.1 Tallest species stemwood volume estimation

Using the waveform parameters described in 2.3.2, regression analysis was carried out against yield model stemwood volume estimates for the tallest species within each footprint (section 2.2.1). The results for key parameters are shown in Table 1.

Parameters	All species	Conifers	Broadleaf
Max. canopy	0.59 (100.8)	0.59 (99.0)	0.75 (61.0)
99 th percentile	0.58 (100.5)	0.59 (98.3)	0.75 (59.9)
98 th percentile	0.58 (101.2)	0.58 (99.4)	0.75 (59.1)
95 th percentile	0.56 (103.5)	0.56 (102.2)	0.74 (59.1)
90 th percentile	0.47 (113.1)	0.46 (114.9)	0.74 (59.0)

Table 1. Waveform-derived estimation of stemwood volume for the tallest species within footprints. Results shown are: R² (RMSE m³/ha)

For stemwood volume estimation of the tallest species within all footprints, the estimated maximum canopy height produced the best relationship with R² of 0.59 and RMSE of 100.8 m³/ha.

3.1.1 Coniferous species: Differentiating between coniferous and broadleaf species did not significantly improve the estimation of stemwood volume for conifers. Using the height of the 99th percentile of cumulative energy produced R² of 0.59 and RMSE of 98.3 m³/ha. This relationship is shown in Figure 2.

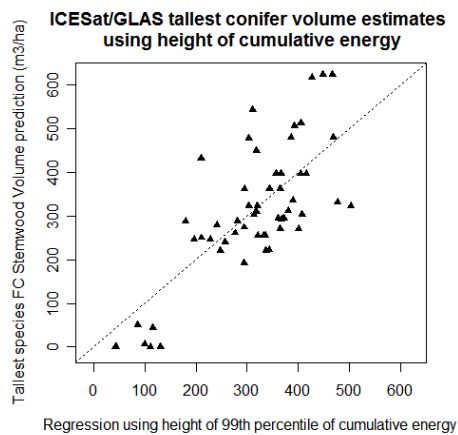


Figure 2. Relationship between stemwood volume estimates and height of 99th percentile of cumulative energy for footprints in which conifers form the tallest species.

3.1.2 Broadleaf species: Considering broadleaf species in isolation however, resulted in a substantial improvement in correlation (R² of 0.75 and RMSE of 59.1 m³/ha using height of the 98th percentile of cumulative energy). This is shown in Figure 3.

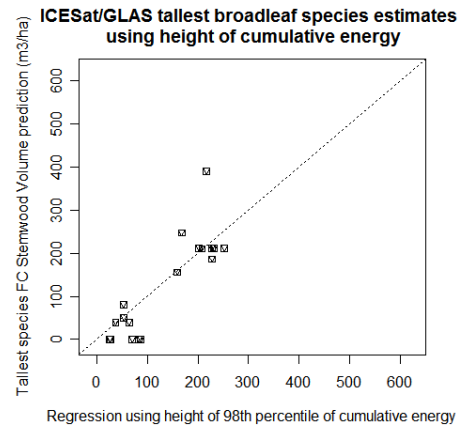


Figure 3. Relationship between stemwood volume estimates and height of 98th percentile of cumulative energy for footprints in which the tallest trees are broadleaf.

3.2 Mixed stand stemwood volume estimation

Weighted stemwood volume estimates accounting for the mixed species composition of stands (section 2.2.2) were used to regress waveform-derived maximum canopy height estimates and heights of cumulative energy percentiles. Key results of these calculations are found in Table 2.

Parameters	All species	Conifers	Broadleaf
Max. canopy	0.46 (102.1)	0.63 (86.6)	0.46 (76.6)
99 th percentile	0.47 (100.7)	0.64 (85.5)	0.47 (75.8)
98 th percentile	0.48 (99.6)	0.65 (84.3)	0.47 (75.6)
95 th percentile	0.50 (97.8)	0.66 (82.5)	0.46 (75.8)
90 th percentile	0.49 (97.6)	0.65 (83.7)	0.36 (82.3)

Table 2. Waveform-derived estimation of mixed stand weighted stemwood volume. Results shown are: R² (RMSE m³/ha)

Greatest correlation was seen for all mixed stand weighted stemwood volume estimates using the height of the 95th percentile of cumulative energy. This produced R² of 0.50 and RMSE of 97.8 m³/ha.

3.2.1 Coniferous species: Height of the 95th percentile of cumulative energy also produced the best estimate when only considering coniferous species. R² of 0.66 and RMSE of 82.5 m³/ha was seen and the relationship is shown in Figure 4.

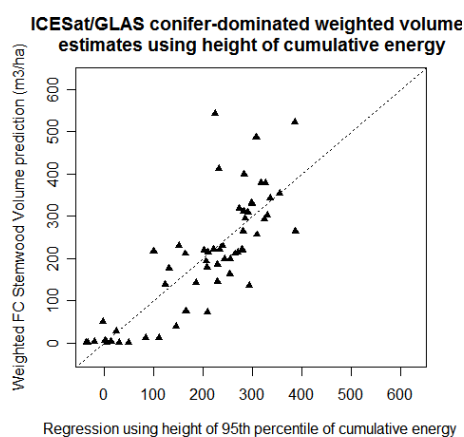


Figure 4. Relationship between mixed stand stemwood volume estimates and height of 95th percentile of cumulative energy for footprints dominated by conifers.

3.2.2 Broadleaf species: However, considering broadleaf species separately produced a poorer correlation with R^2 of 0.47 and RMSE of 75.6 m³/ha for height of the 98th percentile of cumulative energy (Figure 5).

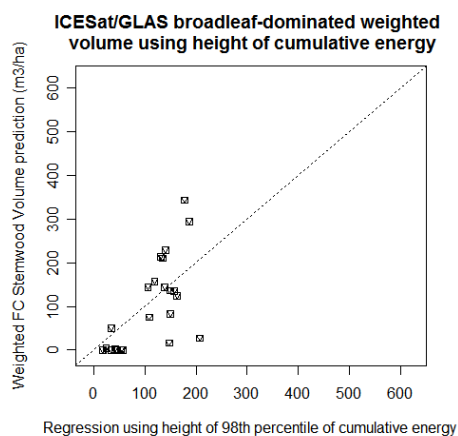


Figure 5. Relationship between mixed stand stemwood volume estimates and height of 98th percentile of cumulative energy for footprints dominated by broadleaf trees.

3.3 Area under the waveform

Area under the waveform canopy return (2.3.2) did not produce a statistically significant improvement on the results using either stemwood volume estimate for either broadleaf species or conifers.

4. DISCUSSION

A previously developed method of estimating maximum canopy height (Rosette *et al.* in press) has enabled a new approach to estimating stemwood volume using waveform-derived parameters to be explored. Percentiles of cumulative energy were calculated using the region of the waveform returned from vegetation. Using the heights of these percentiles has allowed different elevations within the canopy return to be considered with respect to their ability to estimate stemwood volume derived from yield models. It is anticipated that, whilst higher elevations are largely the result of returns from the tallest

species within footprints, returns from lower canopy elevations might better represent the mixed species composition within stands.

Overall, results for the Forest of Dean are less consistent than previous methodologies which produced similar correlations for both broadleaf and coniferous species (Rosette *et al.* submitted). Stemwood volume estimates for the tallest species within footprints are considerably better for broadleaf species than for conifers (a possible effect of upper canopy shape), whilst for mixed stand estimates, greater correlation is seen for stands with greatest cover formed by conifers than by broadleaf species.

However, improvements are noted on previous methods for stemwood volume estimates for the tallest broadleaf trees (from R^2 of 0.65, RMSE 68.2 m³/ha to R^2 of 0.75, RMSE 59.1 m³/ha) and for mixed stands dominated by conifers (from R^2 of 0.57, RMSE 92.3 m³/ha to R^2 of 0.66, RMSE 82.5 m³/ha). Mixed stand estimates show marginally higher correlations at higher percentiles of cumulative energy for broadleaf species than for conifers, possibly due to canopy structure and leaf area affecting laser penetration.

Area under the waveform canopy return failed to significantly improve estimates of stemwood volume. An explanation for this could be the considerable variation in reflectivity that may be expected between species. Therefore, for such a species diverse forest, the principal reason for differing waveform amplitude may be reflectivity as opposed to intercepted surface area (anticipated to be related to volume).

Where multiple scattering within the canopy produces a 'tail' below the visible ground peak (Figure 1), this method may offer a more constant means of identifying the ground surface within the waveform as it is not dependent on the assumption that the Signal End position represents the lowest ground surface or on the accuracy of a DTM. However, sufficient laser penetration to produce a ground peak may be problematic under dense canopies whilst combined vegetation and ground returns may prevent reliable identification of the ground surface for steep vegetated slopes. For the Forest of Dean, only the greatest slopes (15.5m – 18m within-footprint elevation difference) with continuous vegetation cover did not produce a clear ground return. A further source of error may be dense ground cover vegetation which could cause misidentification of the ground peak.

Limitations of stemwood volume estimations using yield models to assess the potential of using waveform-derived parameters are recognised. Stands are unlikely to respond precisely as anticipated within yield models due to habitat anomalies or changes to management practices for example. In terms of long-term production forecast, Edwards and Christie (1981) suggest this may result in errors of 20% (however, updates are made to the sub-compartment database annually).

Forestry Commission yield models are not dynamic and therefore do not take account of changes in growth or stand composition due to competition, damage affliction or mortality. Estimates for coniferous stands for example, have been found to overestimate actual volume.

Stemwood volume estimates used in this study include some common stands which were contained within the sub-compartment database but not listed as planted. These zero volume values may have improved the relationships and may go some way to explaining the spread among lower waveform estimates: initial observations at footprint locations have revealed the presence of unmanaged trees, shrubs or buildings in some cases which are contributing to waveforms.

An assumption is also made in the calculation of stemwood volume for mixed stands, that components are regularly distributed within sub-compartments rather than individuals

forming clusters or being dispersed along a linear feature such as a footpath.

Nevertheless, at a stand level, calibration of yield model estimates using field measurements has produced vegetation height accuracy of 98%. Furthermore, in the course of this study, tree height measurements within 21 footprints at the Forest of Dean produced R^2 of 0.94 when compared with corresponding yield model estimates.

The Forestry Commission sub-compartment database and yield models are widely used in forest management and have provided the best available indication of vegetation distribution throughout the forest. They have therefore formed useful points of reference against which to explore methods of estimating stemwood volume from waveforms.

The study presented in this paper refers to relationships using waveforms acquired whilst vegetation was predominantly still in leaf. Correlation may be anticipated to vary with seasonal differences in LAI.

5. CONCLUSION

This paper has described a method of estimating stemwood volume directly from ICESat/GLAS waveforms. Waveform-derived maximum canopy height and heights of cumulative energy percentiles for the estimated waveform canopy return were compared with yield model stemwood volume coincident with footprints.

Stemwood volume estimates for the tallest species within footprints produced R^2 of 0.59, RMSE 98.3 m³/ha for conifers and for broadleaf species, R^2 of 0.75, RMSE 59.1 m³/ha.

Further stemwood volume estimates taking account of the mixed species composition within stands were calculated. Footprints were distinguished depending on whether the greatest percentage cover was formed by coniferous or broadleaf species. For mixed stand estimates, R^2 of 0.66, RMSE 82.5 m³/ha was found for stands dominated by conifers whilst stands in which broadleaf species are prevalent produced R^2 of 0.47, RMSE 75.6 m³/ha.

The results demonstrate the opportunity for waveform-derived stemwood volume estimates from satellite lidar to be applied where an appropriate digital terrain model and field data are not available.

REFERENCES

- Abshire, J., Sun, X., Riris, H., Sirota, J., McGarry, J., Palm, S., Yi, D. and Liiva, P., 2005. Geoscience Laser Altimeter System (GLAS) on the ICESat Mission: On-orbit measurement performance. *Geophysical Research Letters* **32**: L21S02
- Brenner, A., Zwally, H., Bentley, C., Csathò, B., Harding, B., Hofton, M., Minster, J.-B., Roberts, L., Saba, J., Thomas, R. and Yi, D., 2003. Derivation of Range and Range Distributions From Laser Pulse Waveform Analysis for Surface Elevations, Roughness, Slope, and Vegetation Heights. *Algorithm Theoretical Basis Document* V4.1. Available online at: http://www.csr.utexas.edu/glas/pdf/Atbd_20031224.pdf (accessed March 2005)
- Buften, J., 1989. Laser Altimetry Measurements from Aircraft and Spacecraft. *Proceedings of the IEEE*, **77**, pp.463-477
- Drake, J. B., Knox, R. G., Dubayah, R. O., Clark, D. B., Condit, R., Blair, J. B. and Hofton, M. A., 2003. Above-ground biomass estimation in closed canopy Neotropical forests using lidar remote sensing: factors affecting the generality of relationships. *Global Ecology and Biogeography*, **12**, pp. 147-159
- Edwards P.N. and Christie J. M., 1981. *Yield Models for Forest Management, Booklet 48*. Edinburgh, The Forestry Commission.
- Forestry Commission, 2006. *Operational Guidance Booklet Number 6, Survey Handbook*. Edinburgh, The Forestry Commission.
- Gardner, C. 1992. Ranging Performance of Satellite Laser Altimeters. *IEEE Transactions on Geoscience and Remote Sensing*, **30**, pp. 1061-1072
- GCOS 2004. Implementation Plan for the Global Observing System for Climate in support of the UNFCCC. *Global Climate Observing System WMO/TD No. 1219*, Available online at: http://www.wmo.int/pages/prog/gcos/Publications/gcos-92_GIP.pdf (accessed July 2007)
- GCOS 2006. Systematic Observation Requirements for Satellite-Based Products for Climate. Supplemental details of the GCOS Implemental Plan. *WMO/TD 1338*, Available online at: <http://www.wmo.int/pages/prog/gcos/Publications/gcos-107.pdf> (accessed July 2007)
- Harding, D., Buften, J. and Frawley, J., 1994. Satellite Laser Altimetry of Terrestrial Topography: Vertical Accuracy as a Function of Surface Slope, Roughness and Cloud Cover. *IEEE Transactions on Geoscience and Remote Sensing*, **32**, pp. 329-339
- Harding, D. J., Lefsky, M. A., Parker, G. G. and Blair, J. B., 2001. Laser altimeter canopy height profiles; Methods and validation for closed-canopy, broadleaf forests. *Remote Sensing of Environment*, **76**, pp. 283-297
- Harding, D. and Carabajal, C., 2005. ICESat waveform measurements of within-footprint topographic relief and vegetation vertical structure. *Geophysical Research Letters* **32**: L21S10
- Helmer, E.H. and Lefsky, M.A., 2006. Forest Canopy Heights in Amazon River Basin Forests as Estimated with the Geoscience Laser Altimeter System (GLAS). *USDA Forest Service Proceedings RMRS-P-42CD*
- Hese, S., Lucht, W., Schmulilius, C., Barnsley, M., Dubayah, R., Knorr, D., Neumann, K., Riedel, T., and Schroter, K., 2005. Global biomass mapping for an improved understanding of the CO₂ balance – the Earth observation mission Carbon-3D. *Remote Sensing of Environment*, **94**, pp. 94-104
- Hyypää, J., Kelle, O., Lehtikoinen, M. and Inkinen, M., 2001. A Segmentation-based Method to Retrieve Stem Volume Estimates from 3-D Tree Height Models Produced by Laser Scanners. *IEEE Transactions on Geoscience and Remote Sensing*, **39** (5), pp. 969-975
- Kichak, R. 2003. Chairman's Executive Summary, Technical Report. Independent GLAS Anomaly Review Board, Available online at: <http://icesat.gsfc.nasa.gov/docs/IGARB.pdf> (accessed June 2005)
- Lefsky, M. A., Harding, D. Cohen, W. B., Parker, G. and Shugart, H. H. 1999. Surface Lidar Remote Sensing of Basal

Area and Biomass in Deciduous Forests of Eastern Maryland, USA. *Remote Sensing of Environment*, 67, pp. 83-98

Mike Barnsley of the University of Wales, Swansea plus Heiko Balzter, University of Leicester.

Lefsky, M., Harding, D., Keller, M., Cohen, W., Carabajal, C., Del Bom Espirito-Santo, F., Hunter, M., de Oliveira Jr., R. and de Camargo, P., 2005. Estimates of forest canopy height and aboveground biomass using ICESat. *Geophysical Research Letters* 32: L22S02

Nelson, R., Short, A. and Valenti, M., 2004. Measuring Biomass and Carbon in Delaware Using an Airborne Profiling Lidar. *Scandinavian Journal of Forest Research*, 19, pp. 500-511

Nelson, R., Næsset, E., Gobakken, T., Ståhl, G., Gregoire, T., 2006. Regional forest inventory using an airborne profiling lidar. *Proceedings of the International Conference Silvilaser 2006*, 7th-10th November 2006, Matsuyama, Japan

NSIDC, 2006. The Attributes for ICESat Laser Operations Periods. Available online at: <http://nsidc.org/data/icesat/data.html> (accessed June 2006)

Patenaude, G., Hill, R., Milne, R., Gaveau, D., Briggs, B., Dawson, T., 2004. Quantifying forest above ground carbon content using lidar remote sensing. *Remote Sensing of Environment* 93, pp. 368-380

Rosette, J., North, P. and Suárez, J., in press. Vegetation Height Estimates for a Mixed Temperate Forest using Satellite Laser Altimetry. *International Journal of Remote Sensing, 3D Forestry Special Issue*

Rosette, J., North, P. and Suárez, J., submitted. Stemwood Volume Estimates for a Mixed Temperate Forest using Satellite Lidar. *Journal of Forest Planning, Lidar application in Forestry Special Issue*

Schutz B., Zwally, H., Shuman, C., Hancock, D. and DiMarzio, J., 2005. Overview of the ICESat Mission. *Geophysical Research Letters* 32: L21S01

Zwally, H., Schutz, B., Abdalati, W., Abshire, J., Bentley, C., Brenner, A., Bufton, J., Dezio, J., Hancock, D., Harding, D., Herring, T., Minster, B., Quinn, K., Palm, S., Spinhrne J. and Thomas, R., 2002. ICESat's Laser Measurements of Polar Ice, Atmosphere, Ocean and Land. *Journal of Geodynamics*, 34, pp. 405-445

Zwally, H.J., Schutz, R., Bentley, C., Bufton, J., Herring, T., Minster, J., Spinhrne, J. and Thomas, R., 2006. GLAS/ICESat L1A Global Altimetry Data and L2 Global Elevation Data and Global Land Surface Altimetry data V026. Boulder, CO: National Snow and Ice Data Center. Digital media.

ACKNOWLEDGEMENTS

This research is funded by the UK Natural Environment Research Council (NERC), forming part of the objectives of the Climate and Land-Surface Systems Interaction Centre (CLASSIC). Recognition is given to the Forestry Commission GB for their assistance with this work; in particular to Peter Burnett, staff at the Forest of Dean District Office and Genevieve Patenaude. Thanks are also due to Sietse Los and

USING AIRBORNE LASER SCANNER DATA IN FORESTRY MANAGEMENT: A NOVEL APPROACH TO SINGLE TREE DELINEATION

Jürgen Rossmann, Michael Schluse, Arno Bücken, Petra Krahwinkler

Institute of Man-Machine-Interaction, RWTH Aachen, Ahornstr. 55, 52074 Aachen, Germany –
{rossmann,schluse,buecken,krahwinkler}@mmi.rwth-aachen.de

KEY WORDS: Laser Scanning, Single Tree Delineation, Forestry, 3D, GIS

ABSTRACT:

Lately, laser scanning even of huge areas has become economically sensible due to new airborne laser-scanners delivering higher resolutions and measurement frequency. In this paper we will describe a novel approach for single tree delineation based on airborne laser-scanner-data for use in forestry applications. This currently leads into the development a forestry management tool as a part of a new three-dimensional geoinformation system (3D-GIS).

By enhancing the well-known watershed-algorithm by adding a third dimension, we developed a novel volumetric approach, which is able to accurately — and robustly — detect positions and dimensions of the individual trees in a forest. Each tree's "business card" is then stored in a database, the "Virtual Forest" which serves as the integration platform for a new single-tree-based forestry management system currently being developed in Northrhine-Westfalia, Germany. Combining the single-tree-data with known statistical methods, the system will provide the user with a detailed view on forestry units, on single trees or on the complete forest within an administrative district. The presented algorithms and methods were integrated into our 3D-GIS and successfully tested in a 82km² test-area close to Arnsberg, Germany.

1. INTRODUCTION

In recent years, laser-scanner technology has responded to the demands of the market by increasing resolution and measurement-frequency. Today's devices are capable of performing up to 150.000 measurements per second at helicopter flight level (Leica) or up to 100.000 measurements per second at airplane flight-level (Riegl). Multiple echoes or even a full-waveform recording provide information not limited to the surface of a forest (fig. 1). Lower levels are also monitored. Using the first echo it is possible to calculate a digital surface model (DSM), an (interpolated) grid-based representation of the vegetation surface. On the other hand the last received echo can be processed into a digital terrain model (DTM). The DTM calculated this way might contain remains of vegetation as well as buildings and other objects that are not penetrable by laser. By removing this perturbation and by interpolating the resulting gaps a so-called filled digital terrain model (FDTM) is calculated. The difference between the DSM and the FDTM is called differential model (DM). It is the DM that is actually used to locate and parameterise individual trees.

Adding high-resolution aerial photos it is possible to calculate "true-ortho-photos", which are free of parallax distortions. In true-ortho-photos the roof of a building covers exactly the buildings footprint. The image looks like every pixel was taken with a perpendicular optical axis.

This paper introduces our new single tree delineation algorithm which takes the differential model or true-ortho-photos as input data. The results of the algorithm using DM-data and true-ortho-photos will be compared later in this paper.

2. PROCESSING OF THE DATA

2.1 Data Acquisition

All examples in this paper are based on data recorded in spring 2004 and summer 2005 using a Toposys Falcon II scanner (Schnadt, 2004, Toposys). The data shows the area around "Glindfeld", a small town located close to Winterberg, Germany. The size of the recorded area was about 82km². The dominating tree species in the forestry units used for examination of the presented algorithm is spruce, but there were also other coniferous species like Douglas Fir and European Larch.

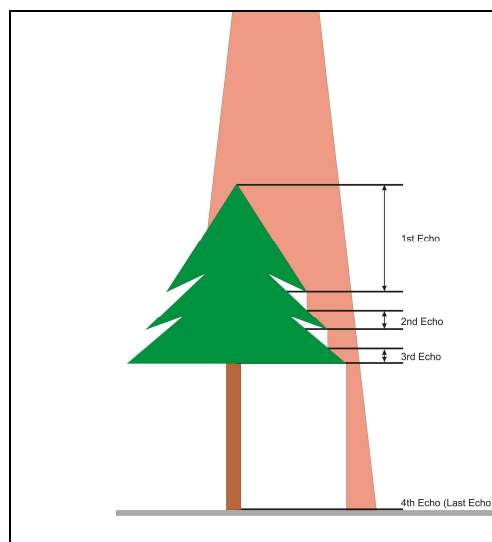


Figure 1. Multiple Echoes in LIDAR Data Recording

The resolution of the LIDAR data was specified to be one point per square-meter, the true-ortho-photos were specified to have a resolution of four pixels per square-meter.

Furthermore, a smaller area was recorded with a nominal resolution of 4 points per square meter.

The pointcloud of the first echo has been rastered into a digital surface model grid (DSM), while the last echo has been converted into a digital terrain model raster (DTM). Due to the limited penetrability of the canopy, there may be (small) regions where no ground echo occurred. For these points the last echo is identical with the first echo. During the process of the DTM generation a semi-automatic filter was applied by the data provider in order to eliminate trees and bushes as well as artificial objects like buildings and bridges. This leads to a DTM representation with gaps. The DTM with interpolated gaps is referred as filled digital terrain model (FDTM). The difference between the DSM and the FDTM is a differential model (DM, also known as canopy height model CHM or normalized digital surface model nDSM).

The overlapping high-resolution photos captured by a rgb-ir line-scanner were projected on the DSM. The result is a set of "true-ortho-photos", which are free of paralactic distortions.

2.2 LIDAR Processing

A popular way for single-tree-delineation in LIDAR maps is the use of the watershed-algorithm. (Diedershagen, 2003) With a standard watershed-algorithm the z-axis of the three dimensional data is only used to generate gradients and calculate affiliations, resulting in a set of areas, each annotated with its size. So the size of the region would be the only criterion to decide whether a region represents a tree or a branch of a tree. We decided to look at the volume of a peak pointing out of the canopy, rather than restricting the investigation to 2-D simplifications.

By increasing the amount of raindrops simulated in the watershed-algorithm up to a level that floods the whole canopy, this algorithm can easily be modified to work on three-dimensional data. To illustrate the volumetric algorithm we will use a sectional drawing — a cut through a three-dimensional DM. Fig. 2a shows several trees and the canopy above them. To make it easier to associate this drawing with rainfall and water-flow, we turned the canopy upside down in the subsequent images with the most significant points – the maximum heights in the original data that may represent tree-tops – as local minima of the graph. Fig. 2b illustrates the idea of a standard watershed algorithm. Water is poured across the area uniformly. The water-flow is simulated and the amount of arriving water is measured at all local minima. The amount of water is equivalent to the area covered by the peak.

To get the volumetric information, we fill the DM with water. Then, in each cycle, we puncture the point with the highest water-pressure acting on it and measure the amount of water flowing out of this opening. (Fig. 2c) The result is a value, which is always greater than or equal to the real volume of the peak. The interesting feature is that the result is far away from the real volume for the most extreme points (for the most likely treetops) but very close to the real volume for the critical peaks that are hard to decide. For each opening which receives a volume greater than a user-specified threshold a tree is generated in the map. The tree is annotated with its height that can be read out of the DM. Fig. 2d shows a

situation where only one peak is left. The remaining volume is below the threshold, so no tree will be generated at this position.

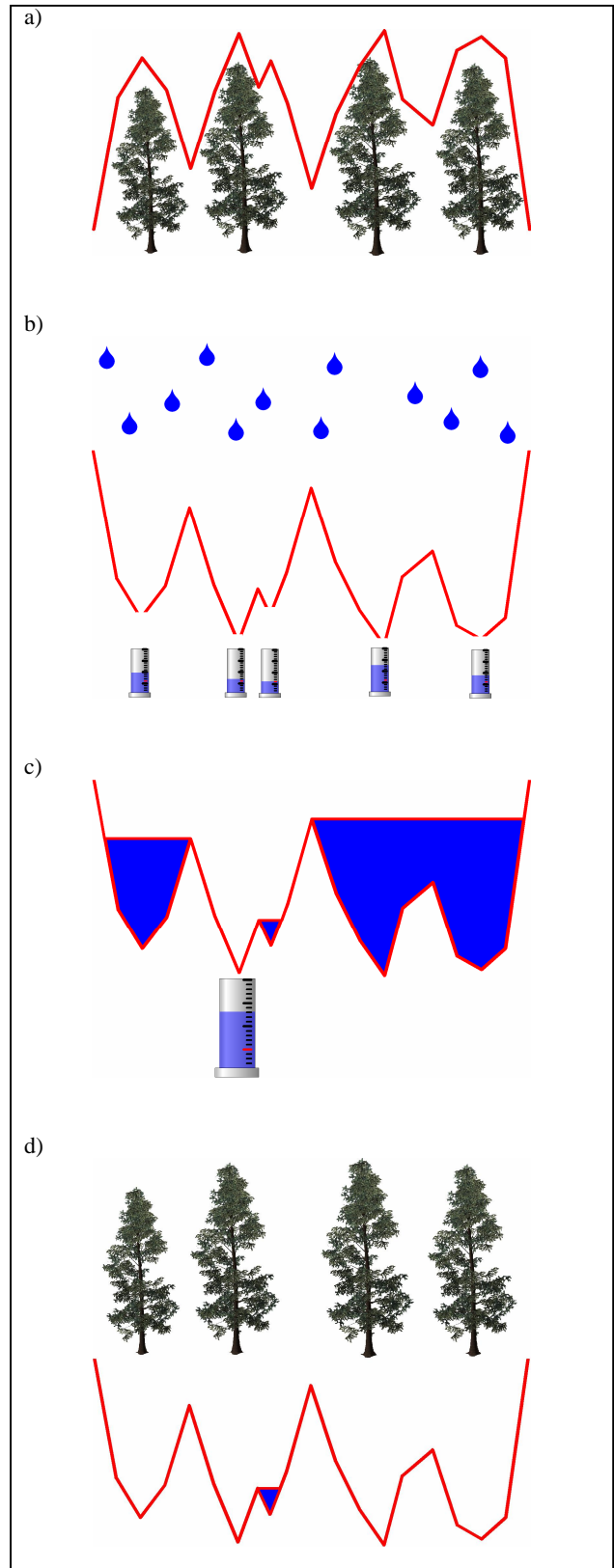


Figure 2. Single Tree Delineation a) Laser-Surface and Trees, b) Watershed-Algorithm, c) Volumetric Algorithm, d) Last Decision for the Volumetric Algorithm

The volumetric approach introduces an additional dimension to the data used for the calculation and makes it easier to decide whether a peak is a tree or just a branch of a tree. This is especially valuable for our test-data because the z-axis of the rasterized LIDAR data features a resolution of 1cm compared to the 1m-resolution of the x- and y-axis.

Especially for coniferous forests, the detection results using the volumetric approach were significantly better compared to the ones of the standard watershed algorithm applied to the same data. Not surprisingly it turned out that the results for the four points per square meter data were better than the ones for the 1m data.



Figure 3. RGB True-Ortho-Photo and Image after Colour-Tone-Based Brightness Reduction

2.3 Aerial Photo Processing

While analysing the source of the LIDAR DM, the point-cloud recorded by the laser-scanner, we encountered some gaps in the coverage, which led us to the question whether homogeneity of the source data is also important for the detection results. The true-ortho-photos are stored at a resolution of four pixels per square meter. So they are comparable to the high-resolution LIDAR data as far as resolution is concerned. But the true-ortho-photos have a

better homogeneity compared to the LIDAR data so they are a good candidate for the comparison. In order to transfer the volumetric watershed idea to the ortho-photos, we simply associated brightness-levels of the photos with an artificial height and *directly applied the same volumetric algorithm to the images*. The results were amazingly promising.

A minor problem was, that in addition to the trees, a few artificial landmarks like white road markings were “detected”. We implemented a colour-tone-depending brightness-reduction-filter (fig. 3). The filter takes four channels (R, G, B and IR) as its input. Each pixel in the destination image is mixed of the rgb-values of the source and a defined brown colour. The ratio between the source and the constant brown colour is determined by the values of the four input channels. Basically it can be said that bright objects with a colour different to all typical green-tones are reduced in brightness by adding the brown colour. In the resulting image, we chose the green-channel of the RGB image – obviously a sensible choice for trees – for detection. At the first glance, this data looks very similar to a greyscale representation of the LIDAR-data. We associated height-levels with brightness-levels in the green-channel and applied the volumetric algorithm described above to this data in order to find the tree-positions. The true-ortho-photos are geo-referenced so we read the height of each detected tree out of the DM again.

The detection rate was significantly improved compared to the volumetric approach on LIDAR-data. In older forestry units, close to their harvesting age, we achieved detection rates of about 95%.

2.4 Extraction of Forestry Attributes

In addition to the position and the height of an individual tree, attributes like diameter at breast height (DBH) and timber volume are interesting when judging the value of the log. In addition to the height of a tree, the diameter (of the visible part) of its crown can also be calculated using the DM by performing a gradient descent for all detected trees. Note that this must be done simultaneously for all trees in order to divide areas that are reachable by gradient descent from several trees centres correctly between the adjacent crowns. The DBH was the most important characteristic of a tree in former times and is still very important for the forester. According to (Hyypä, 1999), the DBH can be calculated using the height and crown-diameter of a tree by:

$$DBH = \alpha L + \beta h + \gamma$$

In this equation α , β , and γ are parameters depending on the local situation of the tree. L is the crown-diameter and h represents the height. The parameters α , β and γ can be calculated using regression formulas and measured data triplets DBH, L and h .

Other important attributes like the timber volume of a stem can be derived by using the DBH and the height of the tree or other known attributes. In (Kramer, 1995) and (Landesanstalt, 1989) the authors specify – ordered by tree-species – the relation between several attributes of an average tree. Knowing the DBH, the height of the tree and the quality of the habitat, it is possible to estimate the other attributes of the tree that are relevant in forestry management.

2.5 Implementation

The described algorithms were integrated into the VEROSIM 3D GIS, a software solution for virtual reality systems and GIS. The threshold needed for the decision in the volumetric algorithm is set interactively by using a slider (fig. 4). The varying results, depending on the threshold, are displayed in real-time in order to help the user to find the correct value for each forest unit. Older units will require higher thresholds because smaller peaks will most likely represent only branches whereas a peak with the same volume in a younger unit will most likely be a treetop.

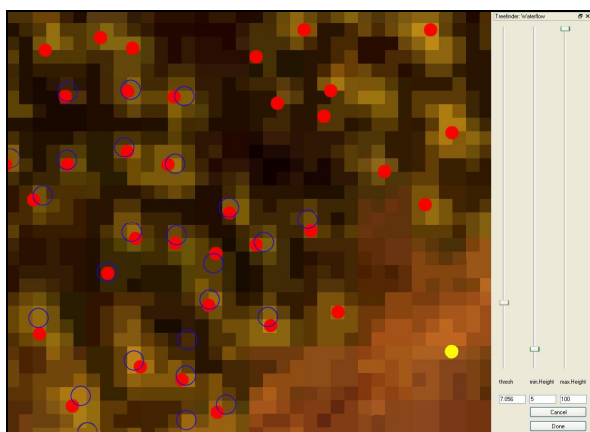


Figure 4. Detection Results and User Interface

2.6 Results

It turned out, that not only resolution but also homogeneity of the data improves the quality of the single tree delineation. Although the detection rate gets better using the additional visual information as explained above, LIDAR-data will mostly deliver better tree-positions. On the other hand RGB and CIR fotos depend on the actual lighting situation. At noon, the treetops will be the brightest point of a tree giving correct results. If the image was taken during the later afternoon, the lower sun will light one side of a tree moving the “optically detected centre” of the brightest part of a tree away from its treetop. Within the 82km² test-area, we found several places where lightning conditions made it hard to recognize trees – even for a human.

3. ONGOING WORK

The results shown in this paper are a first step towards the “Virtual Forest”, a database containing each individual tree in Northrhine-Westfalia. We already delineated a number of forestry units with a total of about 120.000 trees (Fig. 5). During this work we discovered several points which will need ongoing work and attention.

- It turned out that the detection quality is best on homogeneous high-resolution data. Promising sensors that seem to be capable of delivering the required resolution at a homogenous point-distribution are DLR’s HRSC stereo-camera (Scholten, 1999), using an appropriate algorithm for stereo matching, as well as the latest rotating and oscillating mirror laser-scanners. We will implement import-filters for this data and evaluate its quality for single-tree delineation using the volumetric algorithm presented in this paper.

- The boundaries of the units used for detection of the 120,000 trees were based on current administrative units that consider ownership and historical borders as well as forestry office districts. In many units we found several species of trees or a huge spectrum of sizes. It became apparent that different classes of trees also need different parameters for the detection. In order to support the single-tree-delineation, we will integrate an algorithm that separates current units or even the whole forest into biologically reasonable areas that contain a homogeneous tree structure.
- Some of the formulas used for the calculation of the individual tree’s attributes base on statistical data. The Hyypä-formula uses constants α , β and γ as a description of the habitat. It turned out that the variance of these parameters is rather high. A promising approach to adapt the parameters to an area is to combine airborne measured data with terrestrial measurements. We will develop new methods to extract the DBH and position of individual trees from terrestrial laser-scanner data and match the positions of these trees with the ones detected in the airborne LIDAR data in order to get sample sets of completely characterized trees. These trees will serve as an input to a mathematical regression tool that can be used to determine the local parameters.
- Other modules will be added to the Virtual Forest GIS. Some of these modules will be: Classifying the tree species out of aerial and satellite images, segmenting a forest into units with similar structure and species, calculating terrain attributes for each unit, simulating forest growth and calculating the profit of a harvesting action.



Figure 5. View into the Virtual Forest

4. CONCLUSIONS

By using the novel volumetric approach the detection rate was significantly improved compared to the well-known watershed-algorithm. The algorithm works well on LIDAR data as well as on a combination of aerial photos (which deliver tree positions) and laser-scanner-data (for the determination of the tree-height). It works best on homogeneous high-resolution data.

Additional attributes of the individual tree were estimated using the DBH formula invented by Hyypä and Inkinen and statistical relations between DBH and other attributes of a tree.

We stored the complete single-tree data set, the tree’s “business card”, in a geo-database. The user is now able to

select trees in the database using SQL-statements or a database GUI. Using this tool a forester is able to react on requests of the timber market faster and more efficiently, because it becomes possible to determine exact locations in the forest where the customer-ordered number of trees of a given species with a certain height and diameter can be harvested. The database is used as a warehouse management system for the natural warehouse forest.

The tree attributes generated by the presented combination of algorithms make up the most significant part of the data a forester needs to collect to evaluate and to further develop forestry units. Thus, there is a strong demand to make our forest-optimized 3D-GIS available as a standard tool for foresters in NRW.

By passing the gathered information to other modules of the 3D-GIS, it will be possible to project the development of the forest into the future in a kind of "time-machine" (Klemmt, 2004) and to be able to exactly calculate the cost and gain of a thinning.

The generated virtual forests can also be used on harvester simulators during the training of new drivers to give them an impression of the areas they will work in (Fig. 6).

Recapitulating, one can state that the volumetric approach for single-tree delineation in the VEROSIM 3D-GIS is a foundation for many different new applications in forestry management.



Figure 6. Forest Machine Simulation in the Virtual Forest

REFERENCES

- Diedersshagen, O., Koch, B., Weinacker, H., Schütt, C., 2003. Combining LIDAR- and GIS-Data for the Extraction of Forest Inventory Parameters. *Proceedings of the Scandlaser Scientific Workshop on Airborne Laser Scanning of Forests*, Umea, Schweden, pp. 157-165
- Holmgren, J., 2003. Estimation of Forest Variables using Airborne Laser Scanning, *Acta Universitatis Agriculturae Sueciae - Silvestria*, 2003 (No. 278) 43 pp. + Appendices I-V
- Holmgren, J., Persson, A., Södermann, U., 2006. Identification of tree species of individual trees by combining very high resolution laser data with multi-spectral images. *Workshop on 3D Remote Sensing in Forestry*, Vienna

Hyypä, J., Inkinen, M., 1999. Detecting and estimating attributes for single trees using laser scanner. *The Photogrammetric Journal of Finland*, Vol. 16, No. 2, s. 27-42

Klemmt, H.-J., Biber, P., Pretsch, H., 2004. Mit SILVA in die Zukunft des Waldes blicken, *LWF aktuell*, Bayrische Landesanstalt für Wald und Forstwirtschaft, No. 46

Kramer, H., Akça, A., 1995. Leitfaden zur Waldmesslehre. 3. erw. Aufl. Frankfurt a.M., Sauerländer. 266 S.

Landesanstalt für Ökologie, Landschaftsentwicklung und Forstplanung, 1989. Nordrhein-Westfalen. Hilfstafeln für die Forsteinrichtung. 3. Auflage

Leica ALS50-II Technical Specification, Leica Geosystems, Heerbrugg Switzerland, www.leica-geosystems.com

Naesset, E., 1997. Determination of mean tree height of forest stands using air-borne laser scanner data, *ISPRS Journal of Photogrammetry and Remote Sensing* 52: 49-56

Riegl LMS-Q560 Technical Specification, Riegl Laser Measurement Systems, Horn, Austria, www.riegl.com

Schnadt, K., Katzenbeisser, R. 2004. Unique Airborne Fiber Scanner Technique for Application-Oriented Lidar Products, *International Archives of Photogrammetry, Remote Sensing and Spatial Information Sciences*, Vol. XXXVI - 8/W2

Scholten, F., Sujew, S., Wewel, F., Flohrer, J., Jaumann, R. et al, 1999. The High Resolution Stereo Camera (HRSC) - Digital 3D-Image Acquisition, Photogrammetric Processing and Data Evaluation. "Sensors and Mapping from Space 1999" ISPRS Joint Workshop, Hannover

Toposys Falcon II Technical Specification, Toposys GmbH, Biberach, Germany, www.toposys.de

INTEGRATION OF LASER SCANNING AND PHOTOGRAMMETRY

P. Rönnholm ^{a,*}, E. Honkavaara ^b, P. Litkey ^b, H. Hyypä ^b, J. Hyypä ^b

^a Helsinki University of Technology – petri.ronnholm@tkk.fi

^b Finnish Geodetic Institute - (eija.honkavaara, paula.litkey, hannu.hyypa, juha.hyypa)@fgi.fi

Commission III/3, III/4, V/3, VIII/11

KEY WORDS: Laser Scanning, Photogrammetry, Registration, Integration

ABSTRACT:

The term “integration” can be defined as the fusion of two separate entities, resulting in a new entity. Integrating laser scanning with photogrammetry allows us to compensate for the individual weaknesses of each method alone, thus providing more accurate modelling, interpretation and classification of the surroundings. Laser scanners produce data that can vary in terms of point density, field of view, amount of noise, incident angle, and distribution method. Similarly, the accuracy requirements or level of automation may also vary. Therefore, no single registration method overcomes others. The most suitable method is usually case-specific. This paper presents a short overview of current registration approaches and proposes four levels of integration: object-level integration, photogrammetry aided by laser scanning, laser scanning aided by photogrammetry, and tightly integrated laser scanning and optical images. In addition, some examples are presented of integrated laser scanning and photogrammetric data.

1. INTRODUCTION

Both terrestrial (TLS) and airborne (ALS) laser scanning (LS) offer improvements over photogrammetric methods (Hyypä et al., 2000; Jansa et al., 2004). LS methods are based on using active sensors that transmit and receive light rays for range measurements. In addition to range information, LS data can also include information on the backscattered intensity of the returning light. If the full-waveform is available, the accuracy of the range information can be improved in the post-processing phase, and other information can also be derived, such as the length of the returned echo. Some advantages of LS include the immediate generation of a 3D point model, ability to partially penetrate through vegetation and water, accuracy of the range measurements, ability to measure areas without texture, the ability to measure even in the dark, and competitive expenses.

Soon after LS devices had been developed to a commercial level, many people speculated that photogrammetry would be totally replaced by LS. After the initial enthusiasm, however, it has become more obvious that integrating optical information with LS has many advances. The major advantages of images are similarity to human vision, well-known internal geometry, good interpretability, ability to capture texture and multichannel reflectance information, ability to model moving objects, re-measurability, and use of a frame-based acquisition method. Because of the geometric stability of images, they are the most suitable references for inspecting laser point clouds.

The term “integration” can be defined as the fusion of two separate entities, resulting in the creation of a new entity. Properly integrating laser scanning with photogrammetry allow us to compensate individual weaknesses of each method alone, thus providing more accurate applications for modelling, interpretation and classification of surrounding objects.

LS devices can be categorized into two major classes based on the physical measuring method: triangulation and time-of-flight (TOF) (Blais, 2004). TOF methods have two major variants: pulse-based systems and those based on the phase differences of modulated light rays. In the triangulation method, the camera comprises a constant part of the device. In the case of TOF systems, an external camera is usually attached to a scanner or images are taken separately. In addition to normal lenses, cameras can have panoramic or fish-eye lenses or the panoramic camera can be based on line sensor.

Registration plays a key role when combining different types of data. If the registration fails or is incomplete, the integration may give misleading information. Since different laser scanners produce data that can vary in terms of point density, field of view, amount of noise, incident angle, distribution method, and the accuracy requirements or the level of automation may significantly vary, there is no single general registration method that would outperform the others. The most suitable method is typically case-specific.

This paper presents an overview of various registration approaches, proposes four levels of integration and provides examples of integrated LS and photogrammetric data.

2. REGISTRATION

Registration can be considered the foundation on which the integration is based. In principal, registration is completed either by determining the sensor orientations of the images and LS separately for the common coordinate system or by directly determining the relative orientation of the data sets (Fig. 1). By default, the latter method ensures better mutual accuracy, because it includes only one transformation and always uses the common tie features. In those cases in which a camera is permanently mounted to the laser scanner, the system only

* Corresponding author.

occasionally needs to be calibrated in order to ensure the registration of LS point clouds and images.

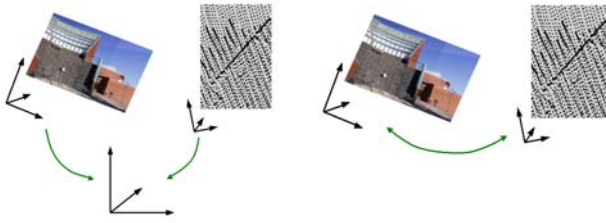


Figure 1. LS point clouds and images can be registered either separately into the common coordinate system (left) or by directly determining one relative orientation (right).

2.1 Registration through the common ground coordinate system

ALS obtains the position and attitude information from the Global Positioning System (GPS) and Inertial Navigation System (INS) sensors. The accuracy of these direct orientation sensors even challenges the conventional photogrammetric aerial triangulation (Heipke et al., 2002). If transformation to a local coordinate system is needed, the datum is typically found using planar areas. GPS and INS observations are nowadays used as additional observations in the block adjustment for determining the camera locations in aerial triangulation.

Both TLS and terrestrial images are typically registered to a known coordinate system using targets, since targets can be interpreted easier and measured more accurately than natural features.

2.2 Direct registration between laser scanning data and images

Registration of LS data and images basically follows the same workflow as registration of two or more images. According to Zitova (2003), the majority of registrations have four steps: feature detection, feature matching, transform model estimation, and transformation. Transformation may also include resampling.

The main problem with feature detection lies in finding features that can be robustly interpreted from both LS data and images. Moreover, possible perspective differences can further hinder interpretation. Appropriate feature selection depends greatly on the density of the LS point cloud. The resolution of currently available terrestrial laser scanners is high, especially when measuring short distances. In such dense point clouds, even small details are visible, thus enabling the detection and measurement of photogrammetric targets, for example. Typically, the intensity information from LS is used for identifying centres of 2D circular targets (Parian and Gruen, 2005) or natural features (Elstrom et al., 1998; Forkuo and King, 2004) that are also easy to identify from images. Most LS devices operate at an infrared band, which must be taken into account when natural tie features are selected from intensity images (Smith and Elstrom, 1999).

The point density of ALS is usually sparser than TLS data and can vary significantly depending on the LS device and flying altitude. In addition, customers may have specific desires for point density. Noise, outliers and the large footprint of the

single laser beam, as well, may prevent the identification of finding robust and accurate tie features.

Several alternatives to the use of corresponding features have been proposed for the registration of LS data and images, including the edges of buildings (Schenk and Csatho, 2002; Zhang et al., 2005), conjugate straight-line segments (Habib et al., 2005), planar objects (Roux, 2004), and surfaces (Habib and Schenk, 1999; Postolov et al., 1999; Wendt and Heipke, 2006).

In addition to numerical methods, manual methods can also be useful for registration. Rönholm et al. (2003) describe how ALS data and terrestrial images can be registered using an interactive orientation method. Similar to numerical methods, the interactive orientation method requires enough tie features within the image footprint. LS data usually include many small details, such as hits from street lamps, pipes, antennas, and trunks. In numerical registrations, all these details are filtered out because they are considered to be outliers. Nevertheless, small details can be valuable during the registration using interactive methods.

Physical models describe the geometrical aspects of the data acquisition process. In the case of images, the physical model is typically the collinearity model extended by suitable additional parameters. Physical models can also be determined for LS (Schenk, 2001).

Finally, the data sets are transformed using the selected transformation model. If regularly spaced data (e.g., image or laser data organized in a grid) is transformed, the new coordinates are non-integer and will require some interpolation. In the case of irregularly spaced laser data, interpolation is not needed.

2.3 Errors that affect registrations

Both images and LS data can have internal errors which can affect registration. Frame-based photogrammetry uses interior orientation for solving these errors. The internal errors of cameras can be minimized by accurately determining the principle point, the principle distance and lens distortions.

According to Schenk (2001), ALS data typically include LS range errors, scan angle errors, LS mounting errors, GPS mounting errors, INS errors, systematic GPS errors, error in the geoid normal, synchronization error, and interpolating error. These errors can be reduced using, e.g., overlapping laser strips, ground control features and photogrammetric references. Pushbroom images have GPS and INS errors similar to those for LS. It would be interesting to acquire simultaneously pushbroom images, frame-based images and LS data, and to investigate whether comparison of pushbroom and frame-based images could be used for eliminating GPS and INS errors from LS data.

Terrestrial laser scanners can suffer from physical errors similar to those of total stations. Physical parameters, however, are not sufficient to describe all errors in TLS data. Therefore, also empirical parameters should also be used. Lichti and Licht (2006) give good information on calibrating terrestrial laser scanners.

Different surface materials may cause systematic shifts in the LS data (Boehler et al., 2004). Pfeifer et al. (2004) pointed out that surface types other than those used for calibration cannot

be expected to have correct heights. One factor causing variation in the range with different surface materials is the selected triggering method of the returning echo. Katzenbeisser (2003) gives illustrative presentation of how LS echoes interact with various surfaces. Wagner et al. (2004) proposed that different triggering methods or a combination of methods should be used to achieve optimal performance for each surface type. If full-waveform LS data is not available, it is not possible to re-process the triggering phase. Nevertheless, the effect of false triggering can be reduced by class- or object-based registration. Fig. 2 illustrates how some ALS echoes from white road paintings are shifted downwards from the level of the asphalt.



Figure 2. The cross-section of ALS data reveals how some echoes are shifted downwards from the asphalt level when hitting the white road markings.

In addition to internal error sources, the interpretation of tie features can reduce the accuracy of registration. Interpretation can be difficult, if the data is coarse, noisy or difficult to perceive.

3. LEVELS OF INTEGRATION

The integration of laser point clouds and images can have different levels depending on the desired end-product, the nature of the original data or differences in emphasis. The four main levels of integration are:

1. Object-level integration
2. Photogrammetry aided by laser scanning
3. Laser scanning aided by photogrammetry
4. Tightly integrated laser scanning and optical images

In this chapter, the levels of integration are described in greater depth and some examples from the literature are presented as examples to illustrate the applications of each integration type.

3.1 Object-level integration

In object-level integration, LS and photogrammetric data are processed and interpreted separately (Fig. 1). A typical example of object-level integration is the creation of hybrid 3D virtual models, in which digital terrain model is created from laser point clouds, but breaklines and buildings are measured from images. Integration is not limited to involve only either airborne or terrestrial data. Actually, the most complete 3D virtual models may integrate information from ALS, TLS, aerial images, terrestrial images, and geodetic observations.

Orientation to the common coordinate system is usually done separately for LS and images. However, if common features can

be found, registration of interpreted 3D objects can also be used.

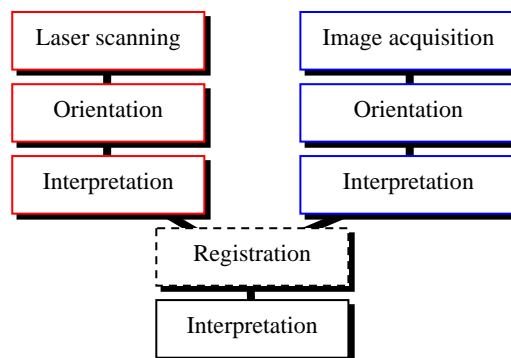


Figure 3. Object-level integration of LS and photogrammetry.

3.2 Photogrammetry aided by laser scanning

The second level of integration is photogrammetry aided by LS. Although the main focus is on images, LS data is also necessary. In this approach, LS data and images are either separately oriented or directly registered into a common coordinate system. A typical example of this level is the creation of orthophotos using LS-based surface modes (e.g., Wehr and Wiedemann, 1999). The relief displacement errors are eliminated from the original images using the information from the LS-based object models or, in the case of aerial images, digital terrain models.

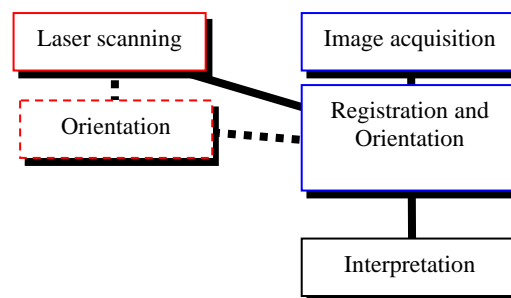


Figure 4. Photogrammetry is aided by LS.

By augmenting photogrammetry with laser data, the popularity of mono-plotting can be significantly improved. The principle is that the features can be selected from the image plane, and the depth information is derived from laser data. Mono-plotting applications have been proposed, for example, by Abdelhafiz et al. (2005) and Ressel et al. (2006).

Kern (2001) made an interesting proposal to reduce the effects of shadows from the original images using LS-derived 3D models. The idea was that circumstances similar to those occurring during image exposure are reconstructed using 3D model and ray-tracing software. Although this approach has yet to be implemented, it could be beneficial both with aerial and terrestrial photogrammetry.

Haala and Brenner (1999) used an ALS-derived normalized digital surface model with colour-infrared aerial images to improve image-based classification of streets, grass, trees, buildings, and shadows.

Wendt (2007) used TLS point clouds for choosing planar tie features from image-derived set of interest points. This method enabled automatic registration of images and laser scans.

Visualization of 2D images or videos in 3D is possible, e.g., using 3D depth maps (Harman, 2000; Fehn et al., 2002). Similar methods are used with some autostereoscopic displays, such as lenticular or barrier displays, in which several sub-images are created from one 2D image and the depth map. With this technique, only one image and a depth map need to be stored, instead of five sub-images, for example. The conversion of regular 2D video stream with associated depth maps to autostereoscopic displays will be included in the new MPEG-C standard, ISO/IEC 23002-3 (Bourge et al., 2006).

3.3 Laser scanning aided by photogrammetry

The third level of integration is LS aided by photogrammetry. The main focus is on LS point clouds, though image data provide additional information. The most typical approach involves the colour coding of the laser point cloud. In this approach, the colour values are taken from registered images and are attached to 3D laser points. In addition, the textures can be extracted from images and attached to LS-derived 3D meshes. This approach is useful for creating detailed and photorealistic impressions even with quite an approximate mesh.

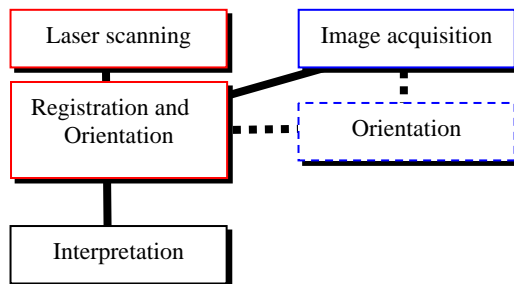


Figure 5. LS is aided by photogrammetry.

One interesting approach is the registration of separate terrestrial laser scans using the relative orientations of images from a camera integrated into a laser scanner (Al-Manasir and Fraser, 2006; Kang et al., 2007). Image-based registration provided better registration than the commonly used Iterative Closest Point (ICP) method (Al-Manasir and Fraser, 2006).

St-Onge and Achaichia (2001) proposed integrating laser-derived digital terrain models and photogrammetric tree height models to bring out the temporal aspect that is essential for many practical applications.

St-Onge (1999) overlaid the rectified multispectral videography onto the canopy height model to help in locating trees. He also suggested using imagery for providing information on tree species. Later (St-Onge and Achaichia, 2001), the canopy height models were extracted from historical aerial images bringing out the temporal variations of forests.

Matikainen et al. (2003) used colour information from aerial images to classify segmented ALS point clouds with fuzzy logic. Lichti (2005) classified TLS point clouds using the colours of terrestrial images together with near infrared information from TLS as input for the thematic classifier.

Persson et al. (2004) presented a method for tree species classification using integrated data. Individual trees were first extracted from the ALS data. Then, the corresponding spectral information was taken from near-infrared images and was used to separate different tree species.

Rönnholm et al. (2004) suggests that terrestrial images can be used for understanding how ALS data interact with various structures. Their examples illustrated cases in which ALS data underestimated tree heights.

3.4 Tightly integrated laser scanning and optical images

The last level of integration contains tightly integrated LS and optical images. The main difference between this level and the previous ones is that registration after data acquisition is unnecessary. Typically, the laser scanner and camera are integrated at the device level by mounting both sensors rigidly on the same platform. After system calibration, the relationship between LS data and images is known. However, the data can be used identically to three other levels of integration. The trend in the development of laser scanners is towards tightly integrated systems.

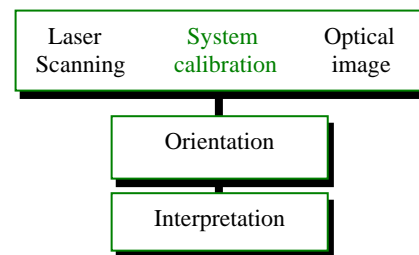


Figure 6. Tightly integrated laser scanning and photogrammetry with simultaneously data acquisition.

The first impression is that in each case when the laser scanner and camera are attached to a common platform, the system is tightly integrated. In principle, this is the case. However, there is some doubt as to whether all TLS devices with externally mounted cameras and mobile systems can truly be categorized as tightly integrated, or whether they are only approximately integrated. In the case of TLS, the point density can be very high. Thus, the registration of images and LS data should be accurate. In many cases, the position of the camera slightly changes when the camera is remounted onto the system, creating the need for on-site system calibration. Laser scanners that are based on triangulation can be categorised with more certainly as tightly integrated systems.

Despite a few exceptions (e.g. Zhao and Shibasaki, 2003), current air- and vehicle-borne mobile systems typically employ frame-based image acquisition and non-frame-based laser scanners. Even if the location of the laser scanner can be accurately known at the time of image exposure, the scanner can take only a few observations before the location is changed. Therefore, a laser point cloud that covers the footprint of the image can have non-homogeneous internal geometry, and the data acquisition perspective is changing continuously.

The most desired application would be a simultaneously taken frame-based optical and range images. In applications that require high accuracy, the data acquisition of both methods should share the same line of collimation. The imaging system based on focal plane arrays fulfils these demands (Steinval,

2003). Frame-based 3D range cameras using the time-of-flight principle already exist, such as SwissRanger, in which the optical image and range information can be collected simultaneously. Thus, the resolution of the range image is still low compared to optical images.

4. EXAMPLES OF INTEGRATING ALS DATA AND IMAGES, EXPERIENCES AT TKK

In this section, we present our experiences in integrating LS with images at the Helsinki University of Technology (TKK). All registrations of ALS point clouds and terrestrial or oblique images are solved using the interactive orientation method (Rönnholm et al., 2003).

4.1 Coloured point clouds

Coloured point clouds can be very photorealistic if the viewing distance is set to meet the resolution of the LS data (Fig. 7). With some limitations, increasing the point size can fill the gaps between individual points in visualizations. Image data can also include information from various bandwidths. In Fig. 8 false-colours from UltraCam-D are associated with the ALS point cloud. The point cloud is visualized with both ortho and perspective projections.

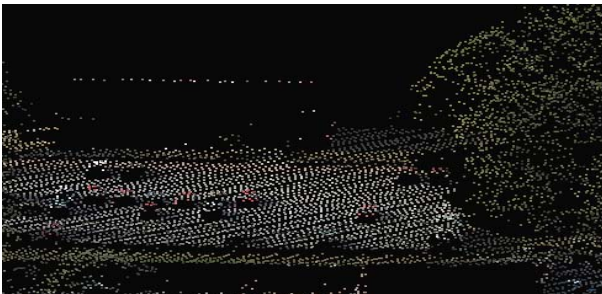


Figure 7. Top: coloured 3D ALS point cloud looks photorealistic when viewed from a distance that meets the resolution of ALS data. Bottom: the structure of the ALS point cloud becomes visible when the viewing location is close enough. The images are created with TerraScan.

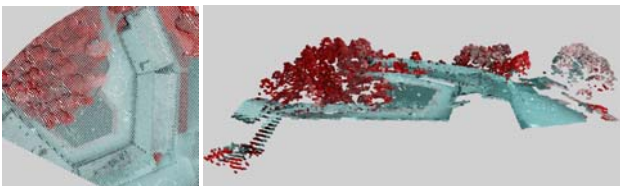


Figure 8. False-colours from UltraCam-D’s digital aerial images have been associated with the laser point cloud. Left: the point cloud in ortho projection. Right: perspective side view.

4.2 The significance of the perspective

Typically, LS data and images are acquired as closely as possible from the same perspective. Such data acquisition is ideal for colouring LS point clouds, because each LS point is separately visible when superimposed onto an image. In addition, both sensors can see all objects identically with no shadows caused by perspective differences. Fig 9. illustrates the typical integration of ALS and an image. In this case, all low points are discarded leaving only upper tree canopies, street lamps, and signs visible. Because the perspective of both data sets is very close to each others, it is easy to detect planimetric correspondences. Using single images, the height correspondences can be inspected only at the sides of the images. For practical purposes, however, stereo images are needed.

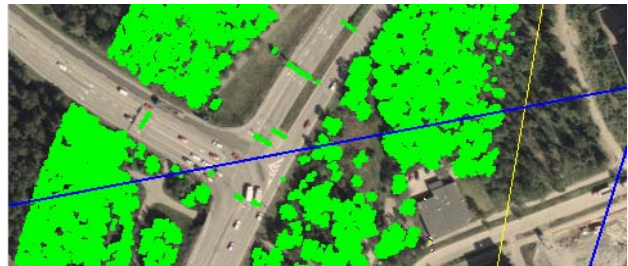


Figure 9. Typical integration of orthoimage and an ALS point cloud (TopoSys-1).

If the LS point cloud is integrated with an image that has a different acquisition perspective, the vertical structure of LS data is seen (Fig. 10). Because of perspective differences some LS points have no corresponding feature in the image, because they are located at the backside of a solid object.

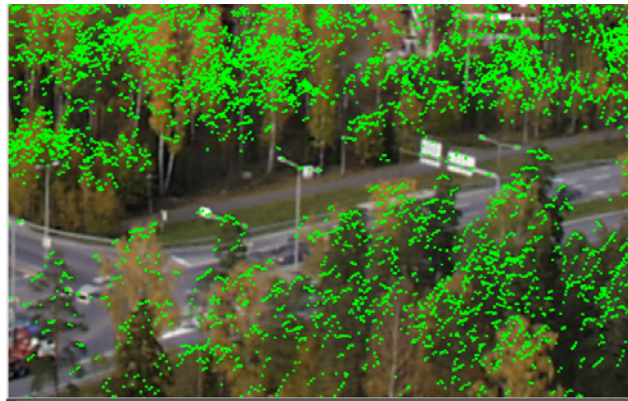


Figure 10. The vertical structure of the ALS point cloud (TopoSys-1) is visible, when data is superimposed onto an oblique image.

Fig. 11 illustrates the usefulness of stereo images when examining LS point clouds. Using stereovision enables comparison of the 3D correspondences between optical images and LS data. In addition, possible gaps in the LS data can be filled with photogrammetric stereo measurements. On the other hand, the LS can also assist in the interpretation of images. For example, the altitude-based colour coding of LS data attaches the height scale to the images, thus allowing the relative heights of objects, at very different distances from the camera, to be understood more easily.



Figure 11. Cross-eye stereo images with superimposed LS point cloud (TopEye MK-II).

4.3 Comparing more than one LS data sets on the image plane

Sometimes, it is advantageous to compare LS point clouds from different devices. Laser scanners produce point clouds that can differ in density, accuracy and distribution. Comparison with the image as a background (Fig. 12) can help significantly, when the usability of point clouds is evaluated for some specific purposes.

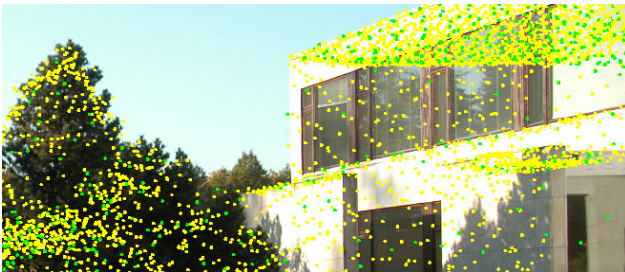


Figure 12. Comparison of two TopEye's laser scanners: yellow (TopEye MK-II), green (TopEye).

In Fig. 13 Toposys-1 data from 800 m and TopEye data from 200 m flying height are superimposed onto the image. Because the data sets are collected at different years, some temporal changes can be detected: two deciduous trees in the middle do not have any hits in TopEye data (black spots).



Figure 13. White spots (TopoSys-1) are scanned from 800 m with a pulse repetition rate of 83 kHz and black points (TopEye) are scanned from 200 m at a scanning rate of 7 kHz. (Rönholm et al., 2003)

4.4 Understanding LS data using images

In Fig. 14a, a perspective side view of the ALS point cloud gives the impression of a building. When the point cloud is superimposed onto the image (Fig. 14b), we gain additional information on the building, such as the textures of facades, the amount of floors and the temporary structure on the roof build to cover repairs, for example. After half a year, the temporary structure is removed from the roof, though its shape remains in the ALS data (Fig. 14c). This example reveals one disadvantage

of LS, if it is used without any other information source: range information alone is not enough for advanced understanding of target.

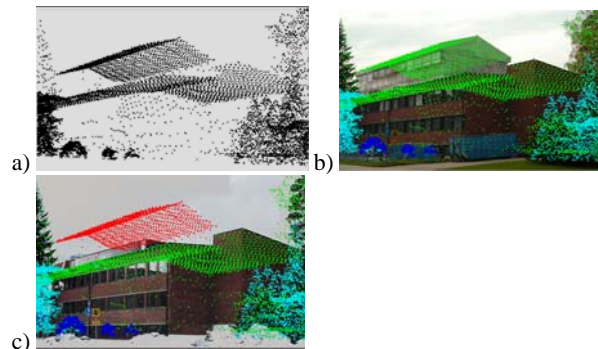


Figure 14. a) Perspective view of the ALS point cloud b) ALS data is integrated with the terrestrial image c) after half a year, the temporary structure was removed from the roof.

In Fig. 15, the full-waveform LS data is superimposed onto the image. Close-range images are the most suitable reference for increasing our understanding of waveform data and extracting the most interesting echoes from the entity (Litkey et al., 2007).



Figure 15. Full-waveform ALS data is superimposed onto the terrestrial image (Litkey et al., 2007).

5. DISCUSSION AND CONCLUSIONS

Integration of LS and photogrammetry is an essential step towards being able to provide accurate and photorealistic 3D modelling methods. LS alone does not include enough information for an advanced understanding of the target. Combined use of all variations of optical imagery and all properties of LS data will provide us with material for robust classification and interpretation of our surroundings. The intensity information for LS should be calibrated (Kaalainen et al., 2007) if it is to be used for automatic classification.

Registration provides the fundamental basis for any integration. Incompletely registered data sets may disturb automatic decision-based algorithms. In addition, misalignments are easily seen during visualizations giving an unreliable impression of the accuracy of the entire data. Accurate registration, especially automatic ones, is not an easy task. Although functional examples of registration methods exist, there is still need for developing more robust and computationally more feasible methods.

Integration, in this context, can be divided into four levels: object-level integration, photogrammetry aided by laser scanning, laser scanning aided by photogrammetry, and tightly integrated laser scanning and optical images. We have discussed these levels of integration and given some illustrative examples. More examples can be found, e.g., from Kaartinen et al. (2006). The full potential of integration is, however, not yet utilised and more research is needed on this subject.

In the future, 3D modelling systems that have tightly integrated LS and images will become increasingly popular. The final revolution in 3D modelling will occur when frame-based LS devices are developed to meet the resolution of optical images. Although the resolution of frame-based range sensors is currently too coarse for accurate modelling, the direction of development is obvious. It will, probably, take considerable time before such 3D ranging cameras can be used for commercial aerial data acquisition.

In some conditions, LS and images must be acquired separately. For example, when the laser scanner is an active sensor, the lighting conditions do not prevent measuring campaigns. Commercially, it is not tempting to wait proper weather conditions for optical images, if LS could operate. To conclude, the need for robust registration methods will not disappear even if the devices become highly integrated.

In addition to integrating of images and LS data, other sources, such as geodetic observations, maps, and CAD design models should also be used. Complete integration of all available data sources would be beneficial in the fields of mapping, planning, constructions, simulation, and in the entertainment industry, to just mention a few.

6. REFERENCES

- Abdelhafiz A., Riedel B., Niemeier W., 2005. "3D Image" As a Result From the Combination Between the Laser Scanner Point Cloud and the Digital Photogrammetry. In: *Optical 3-D Measurement Techniques VII*, Volume 1, pp. 204-213
- Al-Manasir, K. and Fraser, C., 2006. Registration of Terrestrial Laser Scanner Data Using Imagery. *The Photogrammetric Record* 21(115), pp. 255-268.
- Blais, F., 2004. Review of 20 Years of Range Sensor Development. *Journal of Electronic Imaging*, 13(1), pp. 231-240.
- Boehler, W., Bordas Vicent, M. and Marbs, A., 2003. Investigating laser scanner accuracy. In: *Proc. of XIXth CIPA Symposium*, Antalya, Turkey, 30 Sept. – 4 Oct. 2003.
- Bourge, A., Gobert, J. and Bruls, F., 2006. MPEG-C Part 3: Enabling the Introduction of Video Plus Depth Contents. In: *Workshop on "Content generation and coding for 3D-television"* June 2nd 2006, Eindhoven, The Netherlands.
- Elstrom, M., Smith, P. and Abidi, M., 1998. Stereo-Based Registration of Ladar and Color Imagery. In: *Proceedings of the SPIE Conference on Intelligent Robots and Computer Vision XVII: Algorithms, Techniques, and Active Vision*, 3522, pp. 343-354.
- Fehn, C., Kauff, P., Op de Beeck, M., Ernst, F., IJsselsteijn, W., Pollefeys, M., Van Gool, L., Ofek, E., and Sexton, I., 2002. "An Evolutionary and Optimised Approach on 3D-TV". In: *Proceedings of International Broadcast Conference*, Amsterdam, The Netherlands, September 2002, pp. 357-365.
- Forkuo, E. and King, B., 2004. Automatic Fusion of Photogrammetric Imagery and Laser Scanner Point Clouds. In: *Int. Archives of Photogrammetry, Remote Sensing*, Vol. XXXV, pp. 921-926.
- Haala, N. and Brenner, C., 1999. Extraction of Buildings and Trees in Urban Environments, *ISPRS Journal of Photogrammetry and Remote Sensing*, 54(2-3), pp. 130-137.
- Habib, A., Ghanma, M., Morgan, M., and Al-Ruzouq, R., 2005. Photogrammetric and Lidar Data Registration Using Linear Features, *Photogrammetric Engineering & Remote Sensing*, Vol. 71, No. 6, pp. 699-707.
- Habib, A. and Schenk, T., 1999. A New Approach for Matching Surfaces from Laser Scanners and Optical Scanners. In: *Int. Archives of Photogrammetry and Remote Sensing*, Vol. XXXII, pp. 55-61.
- Harman, P., 2000. Home Based 3D Entertainment – An Overview. In: *Proceedings of International Conference on Image Processing, ICIP00, Vol I*, pp. 1-4.
- Heipke, C., Jacobsen, K., Wegmann, H., Andersen, H., and Nielsen Jr., B., 2002. Test Goals and Test Set Up for the OEEPE Test "Integrated Sensor Orientation". In: *Test Report and Workshop Proceedings*, OEEPE, Official Publication No. 43, pp. 11-18.
- Hyypä, J., Pyysalo, U., Hyypä, H., Samberg, A., 2000. Elevation accuracy of laser scanning-derived digital terrain and target models in forest environment. In: *20th EARSeL Symposium and Workshops, Dresden, Germany, 14-17 June, 2000*, pp. 139-147.
- Jansa, J., Studnicka, N., Forkert, G., Haring, A., Kager, H., 2004. Terrestrial Laserscanning and Photogrammetry – Acquisition Techniques Complementing One Another. In: *International Archives of Photogrammetry and Remote Sensing*, Vol XXXV, Part B/7, pp. 948-953.
- Kaartinen, H. and Hyypä, J., 2006. Evaluation of Building Extraction. In: *EuroSDR, Official Publication No. 50*, pp. 9-110.
- Kaasalainen, S., Hyypä, J., Litkey, P., Hyypä, H., Ahokas, E., Kukko, A., and Kaartinen, H., 2007. Radiometric Calibration of ALS Intensity. In: *Int. Archives of Photogrammetry and Remote Sensing* (this workshop proceeding).
- Kang, Z., Zlatanova, S. and Gorte, B., 2007. Automatic Registration of Terrestrial Scanning Data Based on Registered Imagery. In: *Proc. 2007 FIG Working Week*, 13-17 May 2007, Hong Kong SAR.
- Katzenbeisser, R., 2003. Technical Note on: Echo Detection. <http://www.toposys.de/pdf-ext/Engl/echo-detec3.pdf> (10 May 2007).
- Kern, F., 2001. Supplementing Laserscanner Geometric Data with Photogrammetric Images for Modelling. In: *Int. Symposium CIPA*, pp. 454-461.

- Lichti, D., 2005. Spectral Filtering and Classification of Terrestrial Laser Scanner Point Clouds, *The Photogrammetric Record* 20(111), pp. 218-240.
- Lichti, D. and Licht, G., 2006. Experiences with Terrestrial Laser Scanner Modelling and Accuracy Assessment. In: *International Archives of Photogrammetry, Remote Sensing*, Vol XXXVI, Part 5, pp. 155-160.
- Litkey, P., Rönholm, P., Lumme, J., Liang, X., 2007. Waveform features for tree identification. In: *Int. Archives of Photogrammetry and Remote Sensing* (this workshop proceeding).
- Matikainen, L., Hyypä, J. and Hyypä, H., 2003. Automatic Detection of Buildings from Laser Scanner Data for Map Updating. In: *International Archives of Photogrammetry, Remote Sensing*, Vol XXXIV, Part 3W13, pp. 218-224.
- Parian, J. and Gruen, A., 2005. Integrated Laser Scanner and Intensity Image Calibration and Accuracy Assessment. In: *Int. Archives of Photogrammetry and Remote Sensing*, Vol. XXXVI, part 3/W19, pp. 18-23.
- Pfeifer, N., Gorte, B. and Elberink, S., 2004. Influences of Vegetation on Laser Altimetry – Analysis and Correction Approaches. In: *Int. Archives of Photogrammetry, Remote Sensing*, Vol. XXXVI, part 8/W2, pp. 283-287.
- Postolov, Y., Krupnik, A. and McIntosh, K., 1999. Registration of Airborne Laser Data to Surfaces Generated by Photogrammetric Means. In: *Int. Archives of Photogrammetry and Remote Sensing*, Vol. XXXII, part 3W14, pp. 95-99.
- Persson, Å, Holmgren, J., Söderman, U., and Olsson, H., 2004. Tree Species Classification of Individual Trees in Sweden by Combining High Resolution Laser Data with High Resolution Near-Infrared Digital Images. In: *Int. Archives for Photogrammetry and Remote Sensing*, Vol. XXXVI, Part 8/W2, pp. 204-207.
- Ressl, C., Haring, A., Briese, C., and Rottensteiner, F., 2006. A Concept For Adaptive Mono-Plotting Using Images and Laserscanner. In: *Int. Archives for Photogrammetry and Remote Sensing*, Vol. XXXVI/3, pp. 98 - 104.
- Roux, M., 2004. Registration of Airborne Laser Data with One Aerial Image. In: *Int. Archives of Photogrammetry and Remote Sensing*, Vol. XXXV, pp. 1043-1048.
- Rönholm, P., Hyypä, H., Pöntinen, P., Haggrén H. and Hyypä, J., 2003. A Method for Interactive Orientation of Digital Images Using Backprojection of 3D Data. *The Photogrammetric Journal of Finland*, Vol 18, No. 2, pp. 58-69.
- Rönholm, P., Hyypä, J., Hyypä, H., Haggrén, H., Yu, X., and Kaartinen, H., 2004. Calibration of Laser-derived Tree Height Estimates by means of Photogrammetric Techniques, *Scandinavian Journal of Forest Research*, Vol. 19, No. 6, pp. 524-528.
- Schenk, T., 2001. Modeling and Analyzing Systematic Errors of Airborne Laser Scanners. *Technical Notes in Photogrammetry* No. 19, Department of Civil and Environmental Engineering and Geodetic Science, The Ohio State University, Columbus, OH., 40 pages.
- Schenk, T. and B. Csatho, 2002. Fusion of Lidar Data and Aerial Imagery for a More Complete Surface Description. In: *Int. Archives of Photogrammetry and Remote Sensing*, XXXIV/3A, pp. 310–317.
- Smith, P. and M. Elstrom, 1999. Automatic Feature Correspondence for Scene Reconstruction from Multiple Views. In: *2nd international conference on 3-D digital imaging and modeling, IEEE proceeding, Ottawa, Canada*, pp. 463-472.
- St-Onge, B., 1999. Estimating Individual Tree Heights of the Boreal Forest Using Airborne Laser Altimetry and Digital Videography. In: *International Archives of Photogrammetry and Remote Sensing*, Vol 32, part 3-W14, pp. 179-184.
- St-Onge, B, and Achaichia, N., 2001. Measuring Forest Canopy Height Using a Combination of Lidar and Aerial Photography Data. In: *International Archives of Photogrammetry and Remote Sensing*, XXXIV-3/W4. pp. 131-137.
- Steinval, O., 2003. Laser Systems for Vegetation and Terrain Mapping – a Look at Present and Future Technologies and Capabilities. In: *Proceedings of the ScandLaser Scientific Workshop on Airborne Laser Scanning of Forests*, September 3.-4. 2003 Umeå, Sweden, pp. 8–19.
- Wagner, W., Ullrich, A., Melzer, T., Briese, C., and Kraus, K., 2004. From Single-Pulse to Full-Waveform Airborne Laser Scanners: Potential and Practical Challenges. In: *Int. Archives of Photogrammetry and Remote Sensing*, Vol. XXXV, pp. 201-206.
- Wehr, A. and Wiedemann, A., 1999. Fusion of Photogrammetric and Laser Scanner Data. In: *Int. Archives for Photogrammetry and Remote Sensing*, Vol. XXXIV, Part 5C1B.
- Wendt, A. and Heipke, C., 2006. Simultaneous Orientation of Brightness, Range and Intensity Images. In: *Image Engineering and Vision Metrology, ISPRS Commission V Symposium, Dresden, 25.-27. September 2006*, pp. 315-322.
- Zhang, A., Hu, S., Jin, X., Sun, W., 2005. A Method of Merging Aerial Images and Ground Laser Scans. In: *Geoscience and Remote Sensing Symposium. IGARSS '05*, pp. 222-225.
- Zhao, H. and Shibasaki, R., 2003. Reconstructing a Textured CAD Model of an Urban Environment Using Vehicle-Borne Laser Range Scanners and Line Cameras. In: *Machine Vision and Applications*, vol. 14, no. 1, pp. 35-41.
- Zitova, B, Flusser, J., 2003. Image Registration Methods: a Survey. In: *Image and Vision Computing*, No. 21, pp. 977-1000.

7. ACKNOWLEDGEMENTS

The authors are grateful for the financial support of the Academy of Finland (36801) and TEKES (210435).

AN IMPLEMENTATION OF THE ASPRS LAS STANDARD

Andre Samberg

AVAPROedu, Training & Consulting, P.O. Box 1408, 00101 Helsinki, Finland – info@avaproedu.com

ISPRS WG III/3, III/4, V/3, VIII/11

KEY WORDS: Lidar, Airborne, Terrestrial, Laser Scanning, Data Format, LAS, ASPRS, Standards

ABSTRACT:

The laser scanning technology has become de-facto as a successful measuring mean in numerous applications of remote sensing and mapping. A development of hardware has been followed by a development of a new data file format standard known as the American society for Photogrammetry and Remote Sensing (ASPRS) Lidar Exchange Format (LAS). This data format standard has been designed in order to make the exchange of lidar data, (pre-/post-) processing, analysis, and storing less time consuming and more convenient. There are three versions of the ASPRS LAS standard: 1.0, 1.1, and 2.0 (draft). A number of the manufacturers of hardware and software, laser scanning service providers and end users have already accepted a concept of ASPRS LAS as an industry standard. However, a less experienced end user might be confused by the different definitions of the term LAS that appear in literature and are used by various software vendors. The following main LAS definitions in remote sensing and geomatics exist: Land Analysis System by USGS, Log ASCII Standard by the Canadian Well Logging Society, LAS image format by ER Mapper, and ASPRS LAS by the ASPRS Lidar Committee. This paper explains the different common meanings of those terms. Several popular software products used for lidar data processing are also reviewed and the terminology associated with the file format defined. At this time there is no common tool available for converting from one ASPRS LAS format to another, and this can be a challenge when working with multiple formats. Only in one study case a version number of ASPRS LAS was clearly identified in the Import/Export tool. This paper also provides a comparison feature matrix of the different versions of ASPRS LAS.

1. INTRODUCTION

1.1 Abbreviations

ANSI – American National Standards Institute
 ALS – Airborne Laser Scanning
 ASPRS – The American Society for Photogrammetry and Remote Sensing
 ASTM – The American Society for Testing and Materials
 EDC – U.S. Geological Survey's EROS Data Center
 GIS – Geographic Information System
 GPS – Global Positioning System
 IEEE - The Institute of Electrical and Electronics Engineers
 INCITS L1 – InterNational Committee for Information Technology Standards
 ISPRS – The International Society for Photogrammetry and Remote Sensing
 ISWG - The IEEE Committee on Earth Observations Standards Working Group
 ISO – The International Organization for Standardization
 .LAS – the file extension of the ASPRS lidar data exchange format
 LAS – Land Analysis System
 LAS image USGS/AVHRR – raster image format in ERMapper
 LAS – Log ASCII Standard
 Laser – Light Amplification by the Stimulated Emission of Radiation
 Lidar – Light Detection And Ranging
 NIST – The National Institute of Standards and Technology
 OGC – The Open Geospatial Consortium, Inc. (= OpenGIS®)
 PRR – Pulse Repetition Rate
 SPIE – The International Society for Optical Engineering
 TC211 – Technical Committee 211 “Geographic information/ Geomatics” in the ISO

TC211 WG6 – ISO/TC211 Working Group #6 “Imagery”

TLS – Terrestrial Laser Scanning

U.S. ATEC – U.S. Army Topographic Engineering Center

USGS – U.S. Geological Survey

1.2 Background

Laser scanning has become a new trend in the areas of applications where precise 3D data collection of a remote scene and capturing of high resolution elevation point data are required. During the last decade a large number of the projects, where this technique has been studied, evaluated and assessed, have been conducted. Numerous reports reported that it is an efficient and trustable method for 2.5D and 3D digitizing remotely located objects and large scenes, and mapping. The big advantage of this technique is that it can provide a much more reliable representation of the actual surface shape for 3D modeling and 3D mapping as compared to traditional remote sensing means like photogrammetry.

The laser scanning technology continues to become more mature and advanced. Since the middle of 90th, when the first commercial airborne laser scanning systems penetrated a market (Samberg, 1996), progress in the development of hardware has occurred dramatically. Also laser data post-processing, analysis, and utilization has been significantly improved and increased. There is already a variety of the areas of applications where both airborne laser scanning (ALS) and terrestrial laser scanning (TLS) are widely used. They are, for example, 3-D city modeling, man-made feature extraction, the forestry, flood mapping, plant industry, documentation of cultural heritage, and homeland security. Nowadays, a number of projects in mapping and civil engineering extensively utilize the laser/lidar data.

1.3 Lidar Data Acquisition Techniques

Briefly, a laser source of laser scanning system can be operated in a pulsed or continuous wave mode. A narrow laser beam is deflected across a scene. A distance between a laser sensor and a target is typically determined based on the time-of-flight (TOF) principles. When this information is combined with information about scan angle and positional (i.e. INS/POS) and navigation (i.e. GPS, GLONASS, and GALILEO) data, then a 3D position of a footprint of the laser beam can be precisely calculated in a local co-ordinate system. Nowadays, both ALS and TLS provide a laser point cloud which is stored as a file which consists of XYZ coordinates, intensity, and time tags, at least. A 3D model is generated from that lidar dataset. Further, the post-processed lidar dataset is usually converted in a suitable format by using appropriate software. Thus, the lidar data can be taken to any commercial GIS or CAD software.

In the middle of 1990, topographic laser scanning systems were much less powerful than modern systems. Their typical main operating performances were the following: a pulse repetition rate (PRR) in the order of 2-7 kHz, scan rate of 2-25 Hz, and the flight operating altitude above ground level up to 300 m (á 1000 feet). The obtained average laser point density was 0.25 points/m² at the flight speed of a carrying platform of 70 m/s (136 knots). Although ALS was able to distinguish between multiple reflections, it was not capable of recording and storing the single returns (echoes) of the first and the last pulse simultaneously (Samberg, 1996). Commercial terrestrial laser scanners were not yet well studied and exploited in everyday practice at that time.

Product specific technical information about currently available commercial hardware can be found from (Lemmens, 2007b; Lemmens, 2007c), and directly on the web sites of vendors of topographic and terrestrial laser scanning systems, i.e. Optech, Leica Geosystems, Riegl, Toposys, Blom, and Zoller+Fröhlich. Briefly, the summarized main operating performances of ALS are the following: PRR up to 200 kHz, scan rate up to 653 Hz, and the flight operating altitude above ground level up to 4000 m (á 13120 feet). The achievable average laser point density is typically 40 points/m² at the flight speed of a carrying platform of 70 m/s (136 knots). Furthermore, modern ALS can benefit from a full wavelength digitizing technology. TLS can today operate at PRR up to 190 kHz in pulsed mode, and up to 500 kHz using phase shift measurements. Operating distance is up to 4000 m (á 13120 feet). Achievable scan angle step size can be as low as 0.00067° x 0.009° (Lemmens, 2007c). (Fowler et al, 2007) provides a comprehensive overview of the entire technologies.

1.4 Existing Laser Data File Formats

There are three major parts of a laser scanning process: data capture, data processing, and data archiving for future applications. In the beginning, various hardware manufacturers developed a number of their own propriety laser data file formats depending on the customer requirements of the commercial firms, and on the kind of product required. A continuing development of hardware and the new areas of applications demand more suitable file formats for the new purposes.

There are many different laser data file formats existing. Table 1 shows a summary of those file formats only which more often appear in the technical documentations, reports and literature.

Additional data file formats, which are used in a production process of a digital elevation model (DEM) or a digital terrain model (DTM), are listed in (Maune et al., 2007), page 466. Among them is ASPRS LAS, which is a binary file format used for delivering and managing of laser scanner data.

As it is well known, a typical output of a laser scanning campaign is raw point clouds which are stored in files. These file can be stored in generic ASCII format, i.e. .TXT, .CVS, and .DBF. In general, they are the text files containing lists of XYZ points arranged in columns. Any regular columned ASCII format can be used, if it consists, in general, of the following main information: number of lines to skip at the beginning of the file, X (Easting) column, Y (Northing) column, Z (Altitude) column, and, optionally, intensity column, and RGB columns.

Format	Type	Notes
.3DD	binary	Riegl
.ASC	ASCII	text file
.BIN	binary	TerraScan
.CMP	propriety	Optech's REALM, comprehensive format
.CSD	propriety	Optech's REALM
.DAT	ASCII	text file
.DVZ	propriety	project file in FUSION/LDV
.IXF		Optech's ILRIS parser
.LAS	binary	ASPRS LAS
.LDA	binary	FUSION/LDV
.LDI	propriety	index file in FUSION/LDV
.LDX	propriety	index file in FUSION/LDV
.PTC		TerraScan classification file
.PTS	ASCII	Leica Geosystems
.PTX	ASCII	Leica Geosystems
.QTC	propriety	QT Modeler, ungridded point clouds, no interpolation or approximation
.QTT	propriety	QT Modeler, surface model, gridded data set
.RAW	ASCII	raw lidar points
.TEW	binary	TopEye Mark II
.TS	binary	TerraScan
.TXT	ASCII	text file
.WRL	ASCII	used in 3D range imaging
.XLS	worksheet	Microsoft Excel
.XML		DTM file
.XYZ	ASCII	text file
.ZFC	binary	Zoller+Fröhlich
.ZFS	binary	Zoller+Fröhlich

Table 1. A summary of existing common laser data file formats

Furthermore, lidar data can be also delivered for importing in the following file formats: 3dp, 3di, 3dv, dxf, dxb, dwg, obj, 00t, dgd, pt, vml, iv, Cyclone native IMP object database format, Cyclone Object Exchange (COE) format, ASCII SVY, Leica's X-Function DBX format, and Land XML.

Other possible data export formats are 3dp, 3di, 3dv, txt, obj, dxf, dxb, dwg, ma, vrml, jpg, arch_d, 00t, zfs, zfc, pt, ptx, pts, ptc, rle, img, dxf, asc, vml, Cyclone Object Exchange (COE), ASCII (XYZ, SVY, PTS, PTX, TXT, customized format), BMP, TIFF, JPEG, SDNF 3.0 (Intergraph Steel Detailing Neutral File) PCF (Alias Piping Component File) Leica System 1200, LandXML, ASCII point data (XYZ, SVY, PTS, PTX, TXT), DFX, Leica's X-Function DBX format, and Land XML.

1.5 Motivation

It is obvious that inputs and outputs can vary significantly. Thus, it is necessary to develop a friendly interface and have a unique flexible lidar data file standard which will support different inputs and outputs as well as the integration with different software packages for the distribution and management of complex information.

There are several major reasons why ASPRS LAS has been proposed several years ago.

- Manufacturers’ data file specifications vary from system to system.
- As it was shown in Table 1, there are a large number of various lidar data file formats existing. This makes data exchange very challenging.
- Uniform software support for different inputs and outputs is required for both ALS and TLS.
- Originally lidar data file, which is a text file, can consist of ten of millions of points. Therefore, the text file can consists of ten of millions of lines what requires a significant amount of hard disk space.
- Depending on lidar project specifications, lidar data files can be much larger than post-processed files, even, up to many Gigabytes, because, for example, there are too many decimals units as compared to actual lidar data accuracy.

In addition, this particular study was motivated by the below following needs:

- A less skilled and proficient end user can be confused by the different meanings of the term LAS which appears in literature.
- Various vendors of lidar data processing tools refer to the ASPRS LAS file format in different ways in their products.

1.6 Activities on Lidar Data Format Standardization

The first steps towards lidar data format standardization were taken by the ASPRS Lidar Committee in the beginning of 2000. In 2003, the version 1.0 of ASPRS LAS, a binary file format, was approved by ASPRS and delivered to the remote sensing and mapping communities. Initially, it was designed and developed for the needs of ALS. In 2005, ASPRS LAS 1.0 was substituted by ASPRS LAS 1.1 with the minor changes. At the same time, TLS has become increasingly popular, in particular, for laser scanning of cultural heritage.

As laser scanning techniques, ALS and TLS, are becoming more mature and everyday practice, they have been attracting more attention of various groups of professionals. For example, (Barber et al., 2003) reported about a lidar initiative started by a Heritage3d consortium (<http://www.heritage3d.org>). (Barber, 2006) provided an interesting overview of a foreseeing application of ASPRS LAS for purposes of TLS, in particular.

Also other professional organizations started to look over ASPRS LAS (Table 2). The participants of the different ISO projects in the working group 6 of geographic information and geomatics, i.e. 19101-2 (Preference model – Imagery), 19115 (Metadata – Extensions for imagery and gridded data), and 19130 (Sensor and data models for imagery and gridded data),

have initiated work to update those projects with a lidar standard. In 2003, NIST in co-operation with ASTM has begun a research for lidar calibration, and evaluation of performances of 3D imaging systems. The aim of this research is to “facilitate the development of consensus-based standards for 3D imaging systems. These standards are expected to include terminology, test protocols for performance evaluation and reporting of test results, and data exchange formats. The availability of standards would i) help clarify manufacturers’ specifications to enable meaningful comparisons between various commercially available instruments, ii) encourage uniform guidelines for manufacturers’ specifications, testing, and reporting, and iii) facilitate interoperability”. ISWG has recently issued a call for developing lidar standards. SPIE and its lidar group of interest are more participating in co-operation with NIST, and have no initiative of its own in developing lidar standard. In 2007, the ANSI INCITS L1 committee initiated a project to make ASPRS LAS 2.0 a U.S. National Standard.

	ALS	TLS
ANSI	x	x
ASPRS	x	x
ASTM	na	x
ISO	x	o
ISPRS	x	x
ISWG	o	o
NIST	na	x
SPIE	na	na

Table 2. A participation of the different organizations in the development work of lidar standards (x – active, o – passive, na – no special activities)

1.7 Materials

From a list of commercial terrain visualization software tools, which consists of more than 500 products, we focused our attention on the most popular lidar data post-processing and management utilities (U.S.ATEC, 2006):

- PCI Geomatica Focus 10.0 from PCI Geomatics, Inc.
- PCI Geomatica Lidar Engine 1.0 from PCI Geomatics, Inc.
- Leica Photogrammetry Suite 9.1 from Leica Geosystems
- ERDAS Imaging 9.1 from Leica Geosystems
- ERmapper 7.1 from Leica Geosystems (former ER Mapper)
- MapInfo 8.5 Pro from MapInfo, Corp.
- ENVI 4.3 from ITT Visual Information Solutions
- IDL 6.3 from ITT Visual Information Solutions
- TerraScan build 007.004 from Terrasolid Ltd.
- LIDAR 1 CuePac 4.0 from GeoCue, Corp.
- LAS Reader for ArcGIS 9 from GeoCue, Corp.
- ArcGIS 9.2 Workstation from ESRI, Inc.
- FME Pro 2007 from Safe Software Inc.
- Quick Terrain Modeler 6.0.2 from Applied Imagery
- Global Mapper 8.0 from Global Mapper Software, LLC
- LIDAR Analyst 4.1 from Visual Learning Systems, Inc.
- MARS Explorer Pro 4.0 from Merrick & Company
- FUSION/LDV 2.51 by Robert J. McGaughey from USDA Forser Service
- MATLAB R2007a from MathWorks, Inc.

Those software utilities can be divided in three groups: stand-alone, plug-ins, and development tools. PCI Geomatica Focus 10.0, Leica Photogrammetry Suite 9.1, ERDAS Imaging 9.1, ER Mapper 7.1, MapInfo 8.5 Pro, ENVI 4.3, IDL 6.3, LIDAR 1 CuePac 4.0, ArcGIS 9.2 Workstation, FME Pro 2007, QT Modeler 6.0.2, Global Mapper 8.0, MARS Explorer 4.0 Pro, FUSION/LDV 2.51, and MATLAB R2007a are stand-alone. TerraScan build 007.004 and LIDAR Analyst 4.1 are optional modules for MicroStation, and ERDAS Imaging and ArcGIS, respectively. LAS Reader for ArcGIS 9 is a plug-in for ArcGIS 9.x. PCI Geomatica Lidar Engine 1.0 is a plug-in for PCI Geomatica software. MATLAB is only mentioned, because it is widely used by the academic community and R&D people, who deal with laser scanning, although there is no ASPRS LAS support directly. From the other side, there is available a toolbox called SeisLab, which supports the Log ASCII Standard developed by the Canadian Well Logging Society: LAS 2.0 and LAS 3.0 (SeisLab, 2007). Those files also have .las extension.

2. EXISTING LAS DEFINITIONS

Remote sensing community including different vendors of hardware and software (U.S.ATEC, 2006; Lemmens, 2007) has already widely accepted a lidar data exchange file format standard called ASPRS LAS. However, the term LAS is widely used somewhere else too. This can be sometime confusing, especially, when end user is familiar with another application of the term LAS than in the ALS and TLS applications. In order to clarify a situation in this case, we gathered in this section the several most common definitions of LAS which were pulled out from the different open information sources too.

2.1 ASPRS LAS

The ASPRS LAS file format is a public binary file format for exchanging of lidar data between vendors and customers, and maintains information specific to the nature of the data. It is an alternative to proprietary systems or generic ASCII files, which can be very large and slowing down the interpretation of data as a consequence. Also in ASCII files lidar specific information can be lost.

There are currently two active ASPRS LAS versions: 1.0 and 1.1. The version 2.0 is undergoing a final revision and approval. The INCITS L1 project will consider ASPRS LAS as a basic lidar file format for approval as a lidar standard by ANSI.

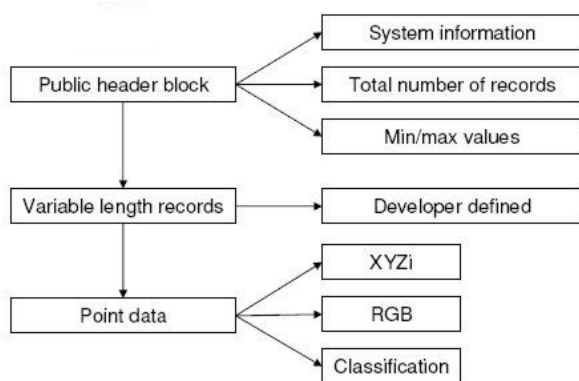


Figure 1. Simplified structure of ASPRS LAS ver. 1.1 (adopted from (Barber, 2006))

In general, the latest release of ASPRS LAS version 1.1 has the following file structure (Fig. 1). There are three block: public header block, variable length records, and point data block. A name of generating software, version number, and statistics like minimum and maximum values of XYZ are stored in the public header block. Variable length records can consist of project specific information. Laser point data, i.e. XYZ values, intensity value, and the results of classification are recorded in the point data block. More detailed specifications can be found at

http://www.asprs.org/society/divisions/ppd/standards/lidar_exchange_format.htm.

2.2 Log ASCII Standard

In 1990, the Canadian Well Logging Society designed a floppy disk format standard, and named it LAS (Log ASCII Standard). Its purpose was to complement the LIS (Log Information Standard) and DLIS (Digital Log Interchange Standard) formats which, in own turn, were designed for own specific purposes. Each LAS file had an extension ".LAS". The first official ver. 1.2 was released in September 1990. The LAS file ver. 1.2 consisted of the header information which described optical curves only (LAS format specifications for ver. 1.2, 1990). A media used at that time was a 3.5 inch 720K DOS compatible floppy disk. The floppy disks in the LAS format must be MS/DOS or PC/DOS compatible. Its version 2.0 was released in 1992. In 2000, the LAS file format standard received a version 3.0 with expanded features in order to meet the increasing demands of the end users (LAS format specifications for ver. 3.0, 2000).

This type of the data file format standard was promoted and widely used by the members of the Canadian Well Logging Society, i.e. the petroleum industry and organizations involved in exploring mineral resources. However, this file format standard is not a common practice among the remote sensing and mapping communities.

2.3 Land Analysis System

In comparison with the data file format standards, an entirely specific use of the LAS term is the Land Analysis System (LAS). This is a software system which has been widely used by the U.S. Geological Survey's EROS Data Center (EDC) as an image processing, image and statistical analysis, and raster GIS system originally developed in co-operation with the NASA's Goddard Space Flight Center. The EDC has provided the LAS software to outside users since 1983. It is public-domain software which is available to any government or private institution.

The LAS installation package consists of three main modules: Transportable Applications Executive (TAE), Land Analysis System (LAS), and AVHRR Data Acquisition and Processing System (ADAPS). TAE acts as a user interface between the end-users and the system. It manages the execution of the LAS applications. The LAS consists of image analysis routines designed to ingest, manipulate, and analyze digital image data and provide the user with a wide spectrum of functions and statistical tools for image analysis. The ADAPS module has been originally used for receiving, archiving, and processing the data of Advanced Very High Resolution Radiometer (AVHRR) from Tiros-N polar orbiting satellites (System Manager's Guide of the Land Analysis System, 2004). The last LAS version was

release 7.4 in November 2001. LAS 7.4 has been used on the computer systems that support the following configurations: SGI IRIX 6.5 using the SGI MIPSpro C and Fortran compilers (version 7.3.1.2m), SUN Solaris 2.7 on a SPARC processor using gcc and g77 (version 2.95.2), various RedHat, Mandrake, and SuSe Linux distributions with gcc 2.95 and 2.96 RH compilers. Previous versions of LAS have also been installed on DEC/VAX computers running VMS 4.7 or higher operating systems, SUN2 and SUN3 computers running SUN/OS operating system, Gould PowerNode computers running UTX 2.0 or higher operating systems, IBM RS6000 computers running AIX operating system, IBM RT computers running AIX operating system, and Data General running DG/UX 5.4.1.

This LAS development work stopped in 2004. Now, LAS 7.4 distribution is available from the ftp site at the Pennsylvania State University: <ftp://dbftp.essc.psu.edu/pub/code/las>.

2.4 LAS image format

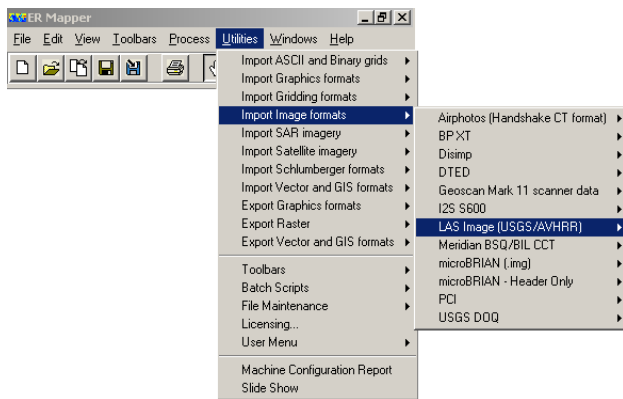


Figure 2. Import tool in ER Mapper 7.1

Import LAS Image reads LAS USGS/AVHRR Image file format data and creates an ER Mapper raster dataset. The source file must be a LAS Image format file (.img). This is the image file (raster) LAS format.

The LAS 5.0 Image file format is supported for read access by the GDB library. The LAS image (USGS/AVHRR) format is used to store various types of geocoded image data. Typically, a LAS image will consist of several related files. The two used by the GDB library are the .ddr and .img files. The .ddr file contains header information and geocoding, while the .img file contains the actual imagery. Either file may be used to refer to the LAS image, but both must exist in the same directory with the same base name (ER Mapper online help).

3. IMPLEMENTATION OF ASPRS LAS

For a visualization purpose and demonstration, there are the following examples of different geospatial utilities which have integrated a lidar processing routing and support ASPRS LAS.

3.1 FME Pro 2007

FME Pro 2007 (Feature Manipulation Engine) typically allows reading from and writing to a supported data format. However, it supports ASPRS LAS reading only (Fig. 3). The lidar reader extracts features from a LAS file, and passes them on to further processing.

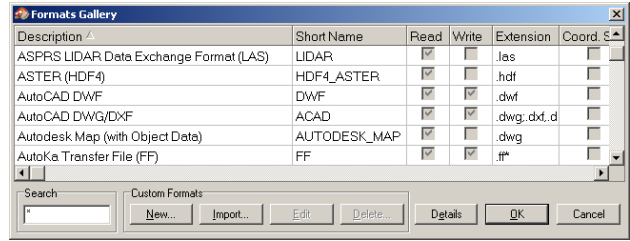


Figure 3. ASPRS LAS support in FME Pro 2007

3.2 Quick Terrain Modeler 6.0.2

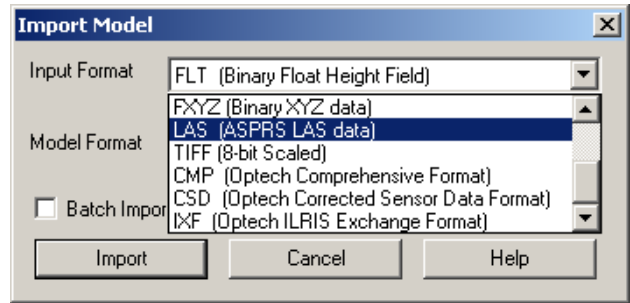


Figure 4. Import file formats in QT Modeler 6.0.2

3.3 LiDAR Tools for ENVI 4.3 and IDL 6.3

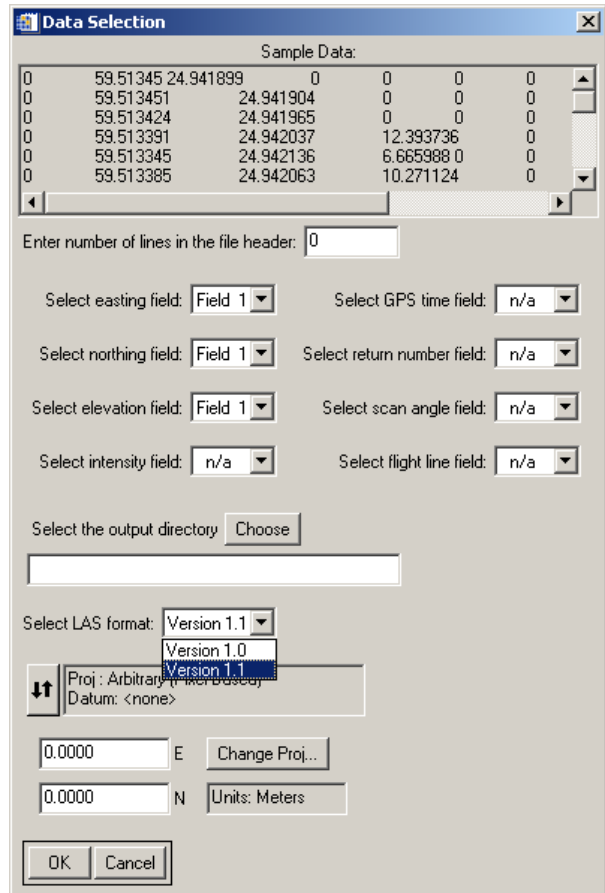


Figure 5. Import ASCII-to-LAS wizard in LiDAR Tools for ENVI 4.3 version dated 20 July 2007

3.4 LIDAR 1 CuePac 4.0

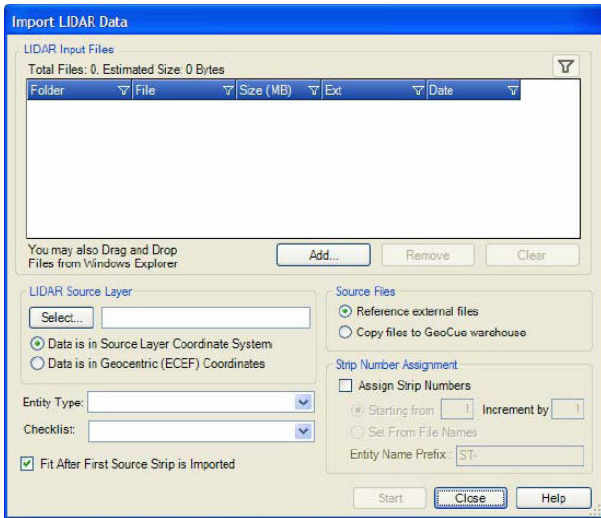


Figure 6. Lidar data import wizard in LIDAR 1 CuePac 4.0

3.5 Global Mapper 8.3

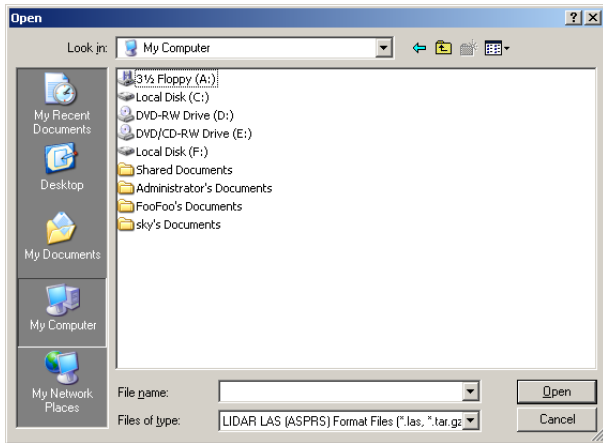


Figure 7. Input file formats in Global Mapper 8.0.3

3.6 PCI Geomatica Focus 10.0

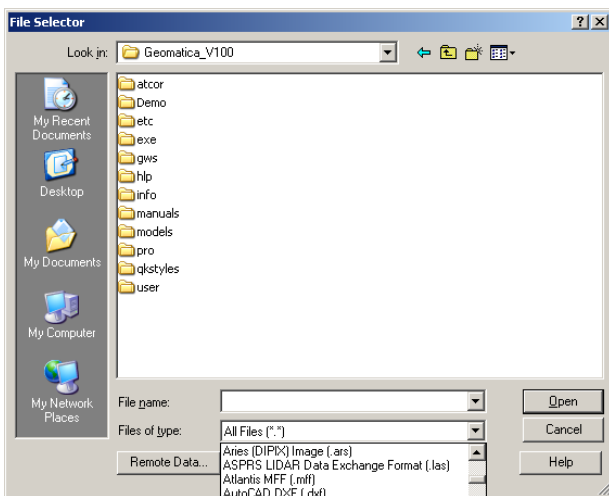


Figure 8. Laser data import window in Geomatica Focus 10.0

3.7 FUSION/LDV 2.51

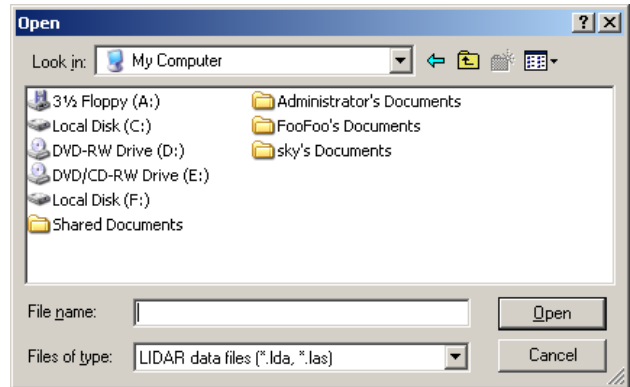


Figure 9. Import/Export tool in FUSION/LDV 2.51

3.8 LIDAR Analyst 4.1

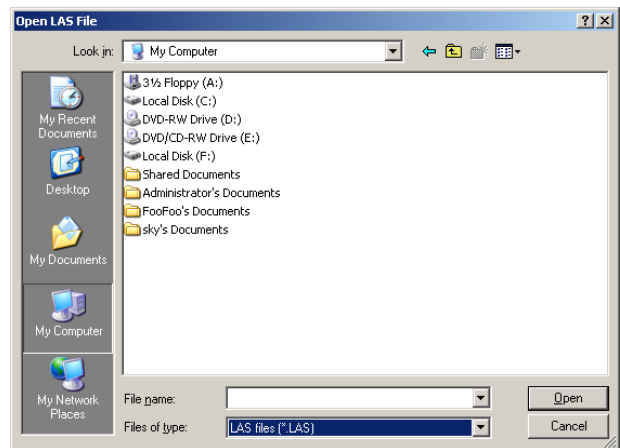


Figure 10. Input LAS file in LIDAR Analyst 4.1

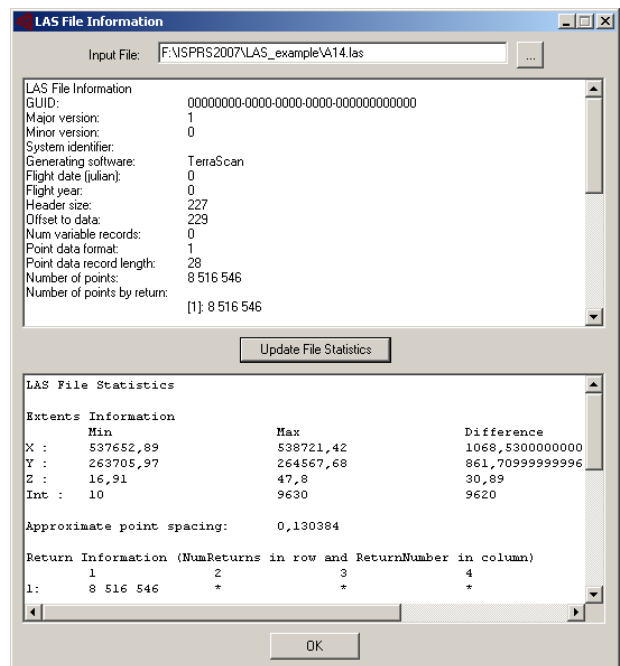


Figure 11. Attributes of ASPRS LAS file in LIDAR Analyst 4.1

3.9 TerraScan 007.004

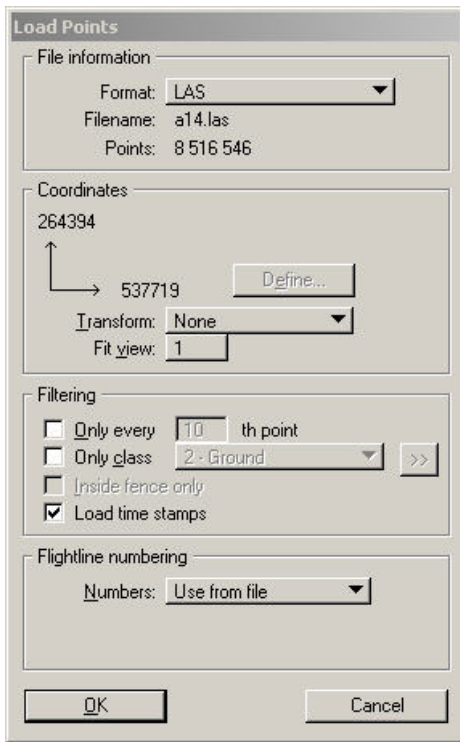


Figure 12. Import laser points from LAS file in TerraScan

3.10 MARS Explorer Pro 4.0

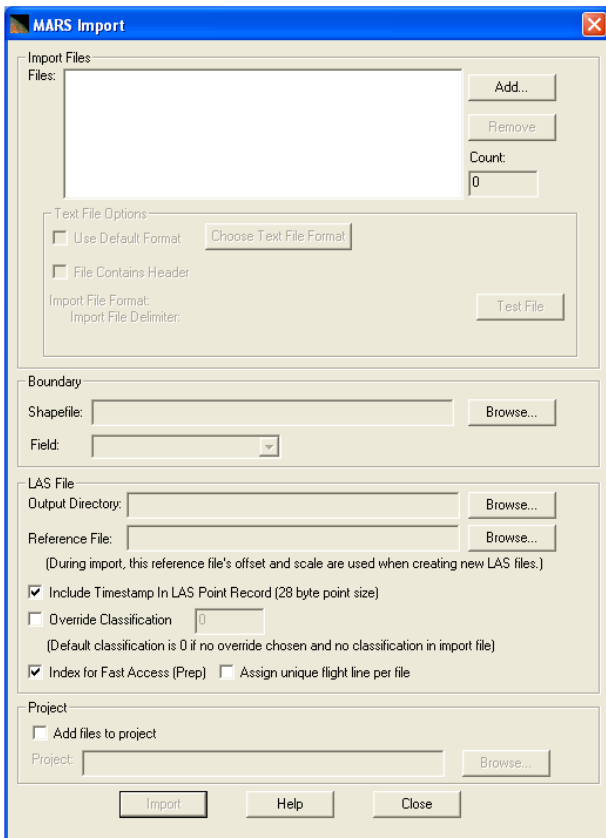


Figure 13. Import wizard in MARS Explorer Pro 4.0

3.11 Leica Photogrammetry Suite 9.1 / ERDAS Imaging 9.1

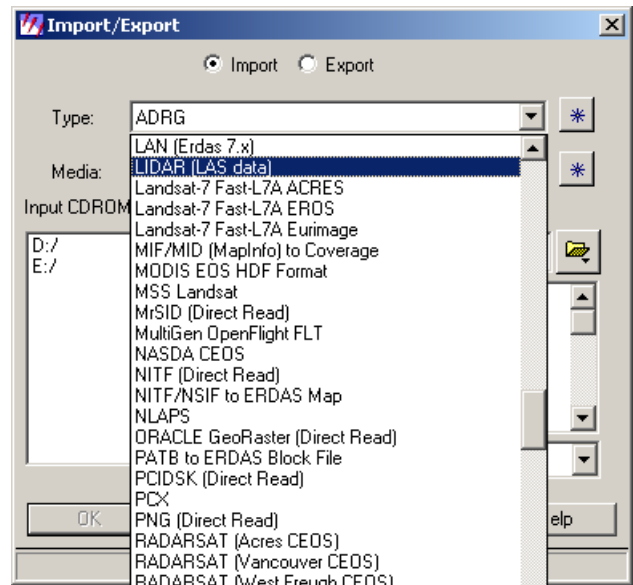


Figure 14. Import/Export tool in LPS 9.1/ERDAS Imaging 9.1

4. CONCLUSIONS AND RECOMMENDATIONS

4.1 Conclusions

19 software packages have been studied. It is obvious that the ASPRS LAS file format has reached its worldwide popularity. A number of stand-alone lidar data processing utilities have already added the ASPRS LAS support to their import tools (Fig. 3, 4, 6, 7, 8, 9, 13, and 14). However, only few of them are capable of delivering of (post-)processed lidar data in the ASPRS LAS file format (Table 3). Also there are available optional modules for lidar data processing like LIDAR Analyst 4.1 for ERDAS Imaging (Fig. 14), LIDAR Analyst 4.1 for ArcGIS, LiDAR Tools for ENVI (Fig. 5), and TerraScan (Fig. 12), which runs on top of MicroStation.

Only LiDAR Tools for ENVI clearly identifies the different versions of ASPRS LAS supported, for example, in its ASCII-to-LAS importing tool what was a bit surprise (Fig. 5).

There are the different lidar file format names. They appear in import/export tools of various SW packages as follows:

- LAS
- LAS files (*.LAS)
- ASPRS LIDAR Data Exchange Format (LAS)
- ASPRS LIDAR Data Exchange Format (*.las)
- LIDAR LAS (ASPRS) Format Files (*.las, *.tar.gz)
- LIDAR (LAS data)
- LIDAR data files (*.lda, *.las)
- LAS (ASPRS LAS data)
- LAS format

Advantages:

- ASPRS LAS has been already recognized and accepted as in industry lidar standard worldwide
- Binary file format allows to speed up entire lidar data processing and project management processes

- Applied binary file format allows to significantly reduce a space required for lidar data storage
- Allows to share entire lidar data set between different end user's over a net or the Internet, and manipulate in small pieces independently
- The ANSI INCITS L1 committee initiated a project to make ASPRS LAS 2.0 a U.S. National Standard

Disadvantages:

- No ASPRS LAS conversion tool exist
- Various vendors use different names of ASPRS LAS in their software packages
- Absence of a version number in the import tools
- Help documentation does not always well explain what ASPRS LAS version is supported by a particular software

Software	Read	Write
PCI Geomatica Focus 10.0	+	-
PCI Geomatica LidarEngine 1.0	+	-
Leica Photogrammetry Suite 9.1	+	+
ERDAS Imaging 9.1	+	+
ER Mapper 7.1	-	-
MapInfo 8.5 Pro	-	-
ENVI 4.3	+	-
IDL 6.3	+	+
LIDAR 1 CuePac 4.0	+	+
ArcGIS 9.2 Workstation	+	-
FME Pro 2007	+	-
QT Modeler 6.0.2	+	+
Global Mapper 8.0	+	+
MARS Explorer 4.0 Pro	+	-
TerraScan build 007.004	+	-
LIDAR Analyst 4.1	+	+
LAS Reader for ArcGIS 9	+	-
MATLAB R2007a	-	-

Table 3. A summary of reading and writing capabilities of ASPRS LAS by various geospatial software utilities

4.2 Recommendations

Initially, ASPRS LAS has been intended for the use with ALS only. However, its practical application and increasing popularity have proved that the ASPRS LAS concept can be used somewhere else. It seems to be already accepted as a defacto of industry standard worldwide. For example, the Heritage3D group has proposed to adopt ASPRS LAS as an attractive generic solution for the delivery, archiving, and exchange of both ALS and TLS data. However, in its present form (version 1.1) it is not suitable for storing and handling of TLS data. Some useful TLS practical examples and standard considerations are well presented in (Staiger, 2003; Aschoff, 2004; Mamatas, 2004).

There is one cosmetic issue. It appeared that a name of ASPRS LAS varies between various hardware and software manufacturers. Therefore, it is necessary to make this name unique like ASPRS LAS. We suggest updating their import and export tools, and simply changing the existing names to ASPRS LAS in the following releases or service packs. Also the version number of the ASPRS LAS file must be clearly identified in the import and export tools for a more convenience usage.

It is expected that the designers and developers of the next version of ASPRS LAS will take in consideration other existing laser scanning systems like bathymetric and active hyperspectral lidar systems in addition to ALS and TLS. At least, it must be possible to store their attributes in the existing or forthcoming variables, which must be easily recognized and interpreted.

It is expected that the proposed next version of the ASPRS LAS file format (version 2.0) will help establish a consistent understanding and should clear up a lot of the confusions (http://www.asprs.org/society/divisions/ppd/standards/lidar_exchange_format.htm).

4.3 References

Applied Imagery LLC, 2007. *Quick Terrain Modeler Version 6 – User's Manual*. 148 p.

Aschoff, T., Spiecker, H., 2004. Algorithms for the automatic detection of trees in laser scanner data. In: *International Archives of Photogrammetry, Remote Sensing and Spatial Information Scienc.*, Vol. XXXVI - 8/W2. pp. 71-75

ASPRS LAS format. <http://www.lasformat.org> (accessed 20 May 2007)

ASPRS LIDAR Data Exchange Format Standard version 1.0. <http://www.lasformat.org/documents/ASPRS%20LAS%20Format%20Documentation%20-%20V1.0%20-%202005.09.03.pdf> (accessed 20 May 2007)

Barber D., Mills J., Bryan P., 2003. Towards A Standard Specification for Terrestrial Laser Scanning of Cultural Heritage. In *Proceedings XIX International CIPA Symposium*, Antalya, Turkey, pp. 619-624

Barber, D., 2006. *The LAS format*. The Heritage3d Workshop, 15 p., 29-30 June, Newcastle upon Tyne, The United Kingdom, www.ceg.ncl.ac.uk/heritage3d/downloads/workshop2006 (accessed 20 May 2007)

Blak, T.A., 2007. Ch. 12 "DEM quality assessment". *Digital Elevation Model Technologies and Applications: The DEM Users Manual*, 2nd Edition, Editor Maune D.F., January, ASPRS, pp. 425 – 448

Bloomquist, D., Shrestha, R., Slatton, C., 2005. *Early Sinkhole Detection and Verification Using Airborne Laser and Infrared Technologies*. Final report BC-354-54, Department of Civil and Coastal Engineering, University of Florida, November, 114 p., http://www.dot.state.fl.us/Research-Center/Completed_Proj/Summary_GT/FDOT_BC354_54_rpt.pdf (accessed 20 May 2007)

Bryan, P. G., Barber, D. M., Mills, J. P., 2004. Towards a Standard Specification For Terrestrial Laser Scanning In Cultural Heritage – One Year On. On *CD-ROM Proceedings XX ISPRS Congress "Geo-Imagery Bridging Continents"*, Commission 5, 12-23 July, Istanbul, Turkey, 6 p., www.isprs.org/istanbul2004/comm5/papers/187.pdf (accessed 20 May 2007)

Cheok, G. S. Lytle, A. M. Stone, W. C., 2005. *Standard Requirements for LADARs?* In: *Proceedings of the SPIE Laser Radar Technology and Applications X conference*. Vol. 5791, Gary W. Kamerman (editor), pp. 250-261

- Crosby, C.J., 2006. *A Geoinformatics Approach To Lidar Data Distribution And Processing With Applications To Geomorphology*. Master of Science thesis, August, Tempe, Arizona, Arizona State University, 119 p. http://www.public.asu.edu/~cjcrosby/downloads/Crosby_MSthesis.pdf (accessed 20 May 2007)
- Di, Lining, 2002. The ISO TC211 Standard Project 19130: Sensor and Data Models for Imagery and Gridded Data. PowerPoint presentation in CEOS Grid Workshop & CEOS WGISS subgroup meeting, ESRIN, ESA, 6-10 May, 20 p.
- ER Mapper 7.1 online help.
- ERDAS Imaging 9.1 online help.
- Flood, M., 2004. ASPRS guidelines – vertical accuracy reporting for lidar data version 1.0. 24 May 2004, 20 p. (http://www.asprs.org/society/committees/lidar/Downloads/Vertical_Accuracy_Reporting_for_Lidar_Data.pdf)
- Fowler, R.A., Samberg, A., Flood, M.J., Greaves, T.J., 2007. Ch. 7 “Topographic and terrestrial lidar”. *Digital Elevation Model Technologies and Applications: The DEM Users Manual*, 2nd Edition, Editor Maune D.F., January, ASPRS, pp. 199 – 252
- GeoCue, 2007. *GeoCue LIDAR 1 CuePac Version 4.0 – Workflow document*. 15 June, 241 p. <http://www.geocue.com/Products/LIDAR%201%20CuePac%20Workflow%20Document%20V4%20-%20R0.pdf> (accessed 1 July 2007)
- Geomatica 10.0 online help
- Graham, L., 2007. LAS specification version 2.0 (final draft). March 7, 2007, ASPRS Lidar Committee
- Heslop, K., Karst, J., Prensky, S., Schmitt, D., 2000. Log ASCII Standard – LAS 3.0 File Structure Specifications. The Canadian Well Logging Society, 6 June, 44 p.
- http://www.asprs.org/society/divisions/ppd/standards/lidar_exchange_format.htm
- <http://forsys.cfr.washington.edu/fusion/fusionlatest.html>
- <http://geology.isu.edu/BCAL/tools/EnviTools/>
- [http://www.blomasa.com/sweden/en/products--services/laser-scanning/rotary-wing-\(lidar\)](http://www.blomasa.com/sweden/en/products--services/laser-scanning/rotary-wing-(lidar))
- <http://www.globalmapper.com/>
- <http://www.heritage3d.org/>
- <http://www.optech.ca>
- <http://www.riegl.com>
- <http://www.safe.com/>
- <http://www.toposys.com>
- http://www.vls-inc.com/lidar_analyst.htm
- http://www.zofre.de/e_index.html
- ISO/TC 211 Geographic information, Geomatics. <http://www.isotc211.org> (accessed 20 May 2007)
- Kresse, W., 2003. Status of Standardization Project ISO 19130. PowerPoint presentation, CEOS/ISPRS Workshop on Rad/Geo Cal, 3 December, Gulfport, MS, USA, 21 p.
- Kresse, W., 2006. Standardization of Sensor and Data Models. In: *Proceedings of Workshop 2 - International Standards Seminar 1. XXIII FIG Congress*, Munich, Germany, 8-13 October, 5 p.
- Kresse, W., Di, Liping, 2002. Status report of ISPRS WG II/4 "Image data standards" 2000 – 2002. In: *Proceedings ISPRS Commission II Symposium*, 20–23 August, Xi'an, China, pp. 229 – 230
- LAS file reader plug-in for ArcGIS 9.x. <http://www.geocue.com/Products/LAS%20Reader%20for%20ArcGIS%209.htm> (accessed 20 May 2007)
- LAS format specifications for ver. 1.2., 1 September 1990. http://cwls.org/docs/LAS12_Standards.txt (accessed 20 May 2007)
- LAS format specifications for ver. 2.0., 25 September 1992. http://cwls.org/docs/LAS20_Standards.txt (accessed 20 May 2007)
- LAS format specifications for ver. 3.0., 6 June 2000. http://cwls.org/docs/LAS_3_File_Structure.PDF (accessed 20 May 2007)
- LAS image file format 7.4 of the USGS LAS system. <http://dbwww.essc.psu.edu/lasdoc/lastoc.html> (accessed 20 May 2007)
- LAS image format 5.0. <http://www.pcigeomatics.com/cgi-bin/pcihlp/GDB%7CSupported+File+Formats%7CLAS+Image+Format> (accessed 20 May 2007)
- Leica Cyclone 5.7 SCAN: product specifications. 2007, 2 p. http://www.leica-geosystems.com/images/new/product_solution/753558enUS_Cyclone_Scan_low.pdf (accessed 20 July 2007)
- Leica HDS3000 3D laser scanner: product specs. 2006. 2 p. www.avat.com/documents/products/hardware/leica/Leica_HDS3000_datasheet.pdf (accessed 20 June 2007)
- Lemmens, M. 2006. *Product Survey: 3D Laser Scanner Software*. GIM International. September, Volume 20, Issue 9, pp. 49-53
- Lemmens, M. 2007a. *Product Survey: Airborne Lidar Processing Software*. GIM International. February, Volume 21, Issue 2, pp. 52-55
- Lemmens, M. 2007b. *Product Survey: Airborne Lidar Sensors*. GIM International, February, Volume 21, Issue 2, pp. 24-27
- Lemmens, M. 2007c. *Terrestrial Laser Scanners*. GIM International. August, Volume 21, Issue 8, pp. 52-55
- Lidar tools for ENVI (updated 15 March 2007). <http://geology.isu.edu/BCAL/tools/EnviTools> (accessed 20 May 2007)

Mamatas, A., Starek, M., Slatton, K.C., 2004. *ILRIS-3D Ground Based Laser and PolyWorks*. GEM Center Report No. Rep_2004-06-002, Civil and Coastal Engineering Department, University of Florida, USA, 3rd June, 6 p. http://www.aspl.ece.ufl.edu/reports/GEM_Rep_2004_06_002.pdf (accessed 20 May 2007)

Manifold System Release 7.x Formats: Import/Export. <http://www.manifold.net/products/mfd/formats.html> (accessed 20 May 2007)

Maune, D.F., Maitra, J.B., McKay, E.J., 2007. Ch. 3 “Accuracy standards”. *Digital Elevation Model Technologies and Applications: The DEM Users Manual*, 2nd Edition, Editor Maune D.F., January, ASPRS, pp. 65 – 98

Rodarmel C, Samberg A., Theiss H., Johanesen T., 2006. A Review of the ASPRS Guidelines for the Reporting of Horizontal and Vertical Accuracy in Lidar Data. *CD-ROM Proceedings “From sensors To Imagery” ISPRS Commission I Symposium Paris, France, 3-6 July, 6 p.*

Samberg, A., 1996. Airborne Laser Mapping Systems. *Maankäyttö #3* (special international edition), pp. 6-9

Samberg, A., 2006. The ASPRS lidar guidelines for horizontal accuracy reporting version 0.91. 14 February, 48 p.

Samberg, A., 2007. The ASPRS lidar guidelines for horizontal accuracy reporting version 1.0. May, 48 p.

Samberg, A., 2006. The definitions of the LAS terms. A report for the ISO 19101-2 and ISO 19130 projects, 28 August, 1 p.

SeisLab, 2007. *MATLAB Software for Seismic Data Analysis – A Tutorial*. Version 3.0 Release 7.0722, 13 July, 72 p.

Staiger, R. 2003. Terrestrial Laser Scanning – Technology, Systems and Applications. In: *Proceedings of 2nd FIG Regional Conference*. Marrakech, Morocco, 2-5 December, 10 p. http://www.fig.net/pub/morocco/proceedings/TS12/TS12_3_staiger.pdf (accessed 20 May 2007)

Staiger, R., 2005. The Geometrical Quality of Terrestrial Laser Scanner. In *Proceedings “From Pharaohs to Geomatics” FIG Working Week 2005 and GSDI-8*, 16-21 April, Cairo, Egypt, 11 p.

System Manager’s Guide of the Land Analysis System (LAS), 2004. ftp://dbftp.essc.psu.edu/pub/code/las/lasinstall_74.txt (accessed 20 May 2007)

The Canadian Well Logging Society. Log ASCII Standard (LAS). http://cwls.org/las_info.php (accessed 20 May 2007)

The USGS Center for LIDAR Information Coordination and Knowledge. <http://lidar.cr.usgs.gov> (accessed 20 May 2007)

U.S.ATEC, 2006. Survey of terrain visualization software. U.S. Army Topographic Engineering Center Topography, Imagery and Geospatial Research Division, Data Representation Branch, 7 December, 1051 p.

4.4 Acknowledgements

Special thanks go to Dr. Richard A. Pearsall from the National Geospatial-Intelligence Agency for his valuable comments and proof reading.

INTEGRATED BUNDLE ADJUSTMENT WITH VARIANCE COMPONENT ESTIMATION – FUSION OF TERRESTRIAL LASER SCANNER DATA, PANORAMIC AND CENTRAL PERSPECTIVE IMAGE DATA

D. Schneider *, H.-G. Maas

Institute of Photogrammetry and Remote Sensing, Dresden University of Technology,
Helmholtzstraße 10, 01069 Dresden, Germany – (danilo.schneider, hans-gerd.maas)@tu-dresden.de

Commission V, WG V/3

KEY WORDS: Bundle adjustment, variance component estimation, laser scanner, camera, panorama, calibration

ABSTRACT:

Terrestrial laser scanners and digital cameras can be considered largely complementary in their properties. Several instruments combine a laser scanner and a camera, with the laserscanner providing geometry information and the camera supplying point of surface colour. These approaches of data fusion make sub-optimal use of the complementary properties of the two devices, as they assign a master-and-slave casting to laser scanner and camera. A thorough exploitation of the complementary characteristics of both types of sensors should start in 3D object coordinate determination with both devices mutually strengthening each other. For this purpose a bundle adjustment for the combined processing of terrestrial laser scanner data and central perspective or panoramic image data, based on an appropriate geometric model for each sensor, was developed. Since different types of observations have to be adjusted simultaneously, adequate weights have to be assigned to the measurements in a suitable stochastic model. For this purpose, a variance component estimation procedure was implemented, which allows to use the appropriate characteristics of the measurement data (e.g. lateral precision of image data, reliability of laser scanner range measurement), in order to determine 3D coordinates of object points. Finding optimal weights for the different groups of measurements leads to an improvement of the accuracy of 3D-coordinate determination. In addition, the integrated scanner and camera data processing scheme allows for the optimal calibration of the involved measurement devices (scanner+camera self-calibration). Moreover, it is possible to assess on the accuracy potential of the involved measurements. The presented paper describes the basic geometric models as well as the combined bundle adjustment with variance component estimation. First results, based on data in a 360° test field, are presented and analysed.

1. INTRODUCTION

Several software packages nowadays provide the possibility of combined processing of terrestrial laser scanner data and photogrammetric image data, since the combination of three-dimensional point clouds and images presents promising prospects due to their complementary characteristics. For this reason manufactures of terrestrial laser scanners also integrate digital cameras in their scanning hardware (Ullrich et. al., 2003; Mulsow et. al., 2004). In these integrated systems, the laser scanner usually represents the dominant device, while the image information is only used secondarily for the colouring of point clouds, texturizing of surfaces or to support the interpretation in interactive laser scanner data handling. Beyond this, the use of images for the automatic registration of laser scanner datasets was suggested in previous approaches (Al-Manasir & Fraser, 2006; Dold & Brenner, 2006), as well as the automatic generation of orthophotos on the basis of image and range data (Reulke, 2006).

The integrated analysis of terrestrial laser scanner data and photogrammetric image data provides a much larger potential (Jansa et. al., 2004; Wendt & Heipke, 2006). Using the complementary characteristics of both sensor types consistently in a combined adjustment, laser scanner and camera may mutually benefit from each other in the determination of object geometry and in calibration (Ullrich et. al., 2003).

In particular, high resolution cameras may be rather beneficial in a combined system, since the high angular accuracy of sub-pixel accuracy image measurements may help to improve the

lateral accuracy of laser scanners. Adapting to the operating mode of most laser scanners, which cover a 360° field of view, the use of panoramic cameras may be an interesting alternative to conventional central perspective cameras. Panoramic cameras often have a very high resolution and a large accuracy potential for the determination of 3D object coordinates (Luhmann & Tecklenburg, 2004; Schneider & Maas, 2005).

Based on the geometric models of laser scanner and camera, as well as a geometric model of panoramic cameras, which was developed at the Institute of Photogrammetry and Remote Sensing of the TU Dresden (Schneider & Maas, 2006), a combined bundle adjustment tool for the integrated processing of terrestrial laser scanner data, central perspective and panoramic image data was developed.

Since the procedure requires the simultaneous adjustment of different types of observations, it is necessary to assign adequate weights to the groups of measurements at the combined adjustment. These weights may be specified by the user, based on manufacturer specifications or practical experience. More rigorously, the weights can be determined automatically in the adjustment procedure by variance component estimation. Thus, the respective characteristics of the involved measurement devices will be optimally utilised, and an improvement of the adjustment results can be achieved (Klein, 2001; Sieg & Hirsch, 2000). Results of variance component estimation in a combined adjustment of laser scanner and image data are also presented in (Haring et. al., 2003).

* Corresponding author.

In this paper the implementation of a combined bundle adjustment with variance component estimation is described and analysed on the basis of multiple laser scans, central perspective and panoramic images in a 360° test field at TU Dresden.

2. GEOMETRIC MODELS

One precondition for the combined analysis of measurements from different devices (laser scanner, camera, panoramic camera) is the knowledge about the basic geometric models as well as their mathematical description. This allows for the calculation of object information (e.g. coordinates of object points) using different observations (range, angles, image coordinates) on the one hand and for the calibration of the involved measurement devices on the other hand, if the geometric models are extended by an appropriate set of additional parameters.

2.1 Central perspective and panoramic images

Cameras with area sensors comply with the known central perspective model (Figure 1). Mathematically this is described by the collinearity equations. Usually these equations are extended by correction terms, which contain additional parameters (Brown, 1971; El-Hakim, 1986) to compensate errors caused by lens distortion and other effects.

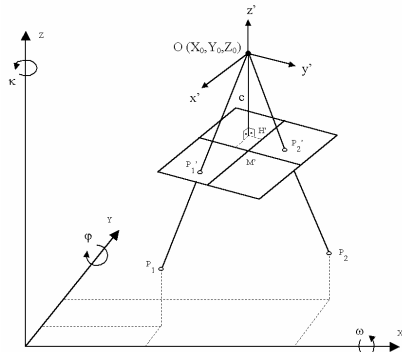


Figure 1. Central perspective camera model

Panoramic cameras are able to record a 360° horizontal field of view in one image, which is in particular beneficial for the recording of big interiors. Technically this is mostly realised by the rotation of a linear sensor. Panoramic cameras provide a very high resolution and accordingly a high accuracy potential. The panoramic camera model can be described by central perspective geometry only in one coordinate direction. The mapping process (Figure 2) can be represented by the projection onto a cylinder (Schneider & Maas, 2006; Amiri Parian, 2007).

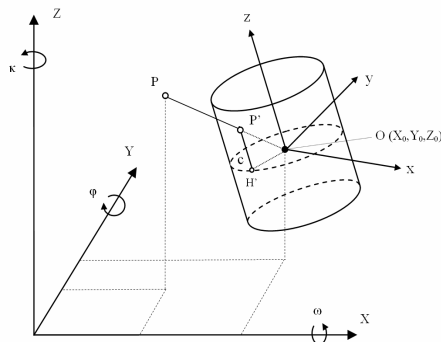


Figure 2. Panoramic camera model

The mathematical descriptions of the geometric models of central perspective and panoramic cameras (see Schneider & Maas, 2006 for the derivation) are:

$$x' = x_0' - \frac{c \cdot x}{z} + dx' \quad (1)$$

$$y' = y_0' - \frac{c \cdot y}{z} + dy'$$

$$x'_{pano} = x_0' - c \cdot \arctan\left(\frac{-y}{x}\right) + dx'_{pano} \quad (2)$$

$$y'_{pano} = y_0' - \frac{c \cdot z}{\sqrt{x^2 + y^2}} + dy'_{pano}$$

The transformation into a uniform coordinate system occurs by:

$$\begin{aligned} x &= r_{11}(X - X_0) + r_{21}(Y - Y_0) + r_{31}(Z - Z_0) \\ y &= r_{12}(X - X_0) + r_{22}(Y - Y_0) + r_{32}(Z - Z_0) \\ z &= r_{13}(X - X_0) + r_{23}(Y - Y_0) + r_{33}(Z - Z_0) \end{aligned} \quad (3)$$

- where
- c = principal distance
 - x', y' = image coordinates
 - x_0', y_0' = principal point coordinates
 - x'_{pano}, y'_{pano} = panoramic image coordinates
 - X_0, Y_0, Z_0 = coordinates of projection center
 - X, Y, Z = coordinates of object points
 - r_{ij} = elements of rotation matrix
 - x, y, z = coordinates of object points in the local camera coordinate system

The correction terms dx', dy' as well as dx'_{pano} and dy'_{pano} contain additional parameters for the compensation of systematic errors, which are caused by the physical characteristics of the cameras.

2.2 Laser scanner

Original measurement data of terrestrial laser scanners are spherical coordinates, i.e. range (D), horizontal (α) and vertical (β) angle. Therefore the geometric model can be described easily by the conversion of Cartesian into spherical coordinates (eq. 4). Applying equation (3), the local laser scanner coordinate system can be integrated into the uniform object coordinate system.

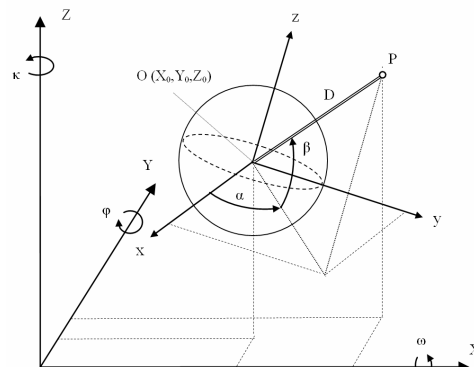


Figure 3. Laser scanner basic model

$$D = \sqrt{x^2 + y^2 + z^2} + dD \tag{4}$$

$$\alpha = \arctan\left(\frac{y}{x}\right) + d\alpha$$

$$\beta = \arctan\left(\frac{z}{\sqrt{x^2 + y^2}}\right) + d\beta$$

Analogous to the camera model, additional parameters can be considered within the correction terms dD , $d\alpha$ and $d\beta$ as an extension of the geometric model of terrestrial laser scanners. This allows for the compensation of systematic deviations from the basic model and thus for the calibration of laser scanners.

However, the calibration of terrestrial laser scanners is complicated by the fact that the manufacturers already implement geometric corrections inside the scanner, whose underlying model equations are mostly not known. Subsequently, significant systematic effects can often not be detected in the residuals of the observations. Therefore only a distance offset (k_0) and scale (k_s) parameter were used in the geometric model (eq. 5) so far, but no corrections of the horizontal and vertical angle were considered.

$$dD = k_s \cdot D + k_0 \tag{5}$$

3. INTEGRATED BUNDLE ADJUSTMENT

Bundle adjustment allows for the orientation of an arbitrary number of images, using the image coordinates of object points as observations. The results of the calculation are the orientation parameters of the images, the 3D coordinates of object points and possibly camera self-calibration parameters. Extending this approach to the combined bundle adjustment means the integration of all laser scans, central perspective and panoramic images of each involved measurement device (scanner, camera, panoramic camera). The calculation follows the geometric constraint that all corresponding rays between object point and the instrument should intersect in their corresponding object point.

The spherical coordinates of object points measured with a laser scanner as well as the image coordinates of a camera respectively a panoramic camera are introduced as observations in one combined coefficient matrix. Figure 4 shows a synthetic example of the structure of a design matrix.

The calculation is performed as a least squares adjustment. The results are the coordinates of object points, the position and orientation of each involved scan and image, the calibration parameters of the measurement devices as well as statistical values for the assessment of accuracies and correlations.

For the calculation of the bundle adjustment a software was developed at the Institute of Photogrammetry and Remote Sensing of TU Dresden, which also allows exporting a protocol and a visualisation file. All settings are displayed in a graphical user interface (Figure 5) and can be changed if necessary. In order to detect and to eliminate outliers a data-snooping procedure following (Baarda, 1968) is applied.

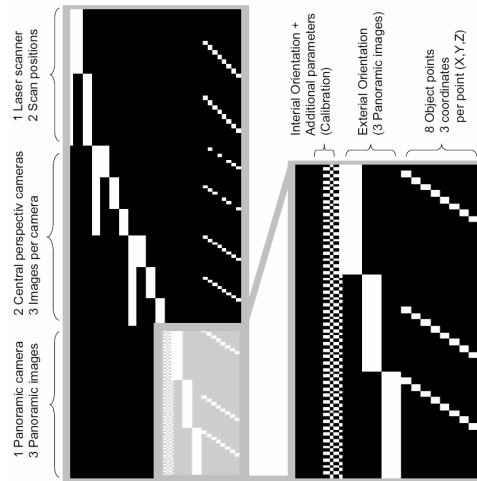


Figure 4. Structure of design matrix (example)

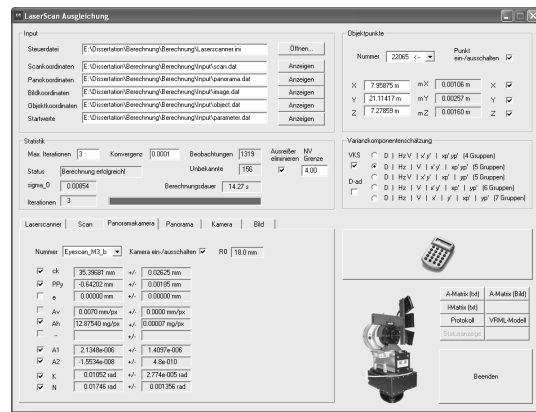


Figure 5. User interface of combined adjustment

Within a courtyard at TU Dresden a 360° test field with ca. 100 retroreflective targets (circles with 5 cm diameter) was installed to practically verify the combined bundle adjustment. The dimensions of this courtyard are 45 m × 45 m, the surrounding façades are 20 m high. The scanner used in the practical tests was a Riegl LMS-Z420i, whose operating software allows for the automatic determination of the centre of retroreflective targets applying a centroid operator to the intensity image. Furthermore multiple panoramas were captured with the KST Eyescan M3metric panoramic camera (Schneider & Maas, 2006), as well as a large number of images from digital SLR cameras Kodak DCS 14n and Nikon D100. The target image coordinates were determined using centroid and ellipse operators. In the following, the results of processing the data of several different sensor combinations in the test field will be shown.

3.1 Example 1

This example shows the calculation of the 3D coordinates of 10 object points of a façade of the test field. Two laser scanner positions and two panoramic camera positions were stepwise introduced into the combined bundle adjustment in different constellations, and the standard deviation of the estimated object coordinates were analysed. Figure 6 shows the used configuration schematically.

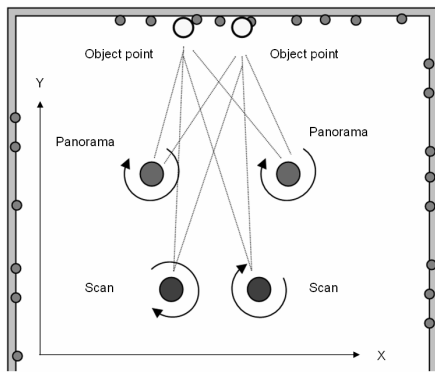


Figure 6. Imaging configuration 1 (schema)

Using only 2 panoramic images for the bundle adjustment, the precision of the resulting object coordinates (mainly in imaging direction Y) is worse than the precision obtained from one laser scan (see Table 1). This can be explained by poor intersection geometry of the used panorama positions. Furthermore the potential of the high-resolution panoramic camera could not be exploited, since the retroreflective targets could not be illuminated properly and the subpixel potential of the image analysis operators could not be used to full extent. Nevertheless, the combination of both devices (at least one scan and one panoramic image) leads to a significant precision improvement.

Number of scans	Number of panoramas	$\hat{\sigma}_D$ (mm)	$\hat{\sigma}_{\alpha,\beta}$ (mgon)	$\hat{\sigma}_{xp,yp}$ (pixel)	RMS_X (mm)	RMS_Y (mm)	RMS_Z (mm)
1	–	7.45	4.92	–	2.82	6.83	3.36
1*	–	5.56	4.91	–	2.55	5.22	2.93
–	2	–	–	0.55	4.18	14.15	4.99
1	1	5.56	4.85	0.59	2.25	5.07	2.61
1	2	5.84	4.88	0.62	1.96	4.81	2.51
2	–	6.87	6.30	–	2.53	4.83	2.95
2	1	6.48	5.65	0.68	2.12	4.47	2.51
2	2	6.21	5.42	0.65	1.91	4.33	1.88

Table 1. Example 1: Calculation results of different configurations (calculated with variance component estimation – see chapter 4)

While the laser scanner measurements improve the accuracy in depth direction, the image observations of the panoramic camera ensure a better precision in lateral coordinate direction. If further scans or images are added, the RMS of the standard deviations of object point coordinates can be minimized accordingly, as long as good intersection angles are maintained.

3.2 Example 2

The next example analyses the precision improvement achieved by the use of additional central perspective images. For this purpose 4 laser scans, 5 panoramic images and a total of 62 images with the Kodak DSC 14n were recorded (Figure 7 shows a reduced number of camera positions). The recording configuration was chosen with regard to good intersection geometry. Furthermore additional images with a camera Nikon D100, which was mounted on top of the Riegl laser scanner,

were captured and included into the calculation. Figure 8 shows the devices involved into this calculation example.

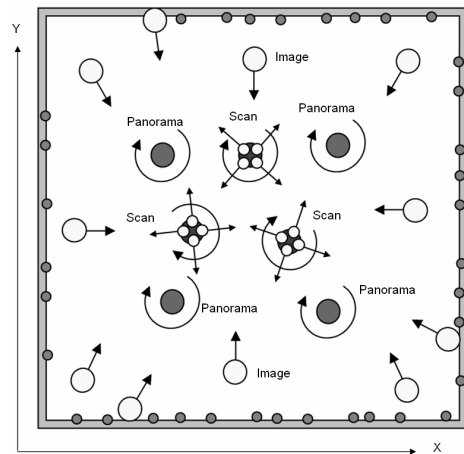


Figure 7. Imaging configuration 2 (schema)



Figure 8. Combined devices (Riegl laser scanner LMS-Z420i, panoramic camera Eyescan M3, Kodak 14n, Nikon D100)

The results of this example show, that the integration of additional panoramic or central perspective images has the potential to improve the accuracy of the calculated results in general. This can be realized in practice, if the user takes additional images while the laser scan runs automatically, subsequently feeding the images into the calculation process. Similarly the images of a camera mounted on top of a laser scanner respectively a camera integrated within the laser scanner hardware can contribute to increase the accuracy. The large number of additional images of the last calculation example in Table 2 may be unrealistic for practical use, but shows the accuracy potential of the combined bundle adjustment.

4. VARIANCE COMPONENT ESTIMATION

The combined bundle adjustment uses different types of observations simultaneously in order to estimate the unknown parameters. For this reason it is necessary to assign suitable weights to the different groups of observations (image coordinates in central perspective and panoramic images, range measurement and angle measurements of the laser scanner). The definition of weights can be performed in terms of fix values, in case of known a-priori standard deviations of the measurements (e.g. specifications of the manufacturer) or if experience values are available. However, the information content of the observations is not fully exploited in this case.

* with consideration of scale and offset, according to eq. (4)

Number of scans	Number of panoramas	Number of central perspective images		Unknown object points	$\hat{\sigma}_D$ (mm)	$\hat{\sigma}_{\alpha,\beta}$ mgon	$\hat{\sigma}_{x_p',y_p'}$ (pixel)	$\hat{\sigma}_{x',y'}$ (pixel)	RMS _X (mm)	RMS _Y (mm)	RMS _Z (mm)
		Kodak	Nikon								
3	—	—	—	35	5.22	5.62	—	—	2.28	2.19	1.75
3	4	—	—	35	5.19	5.45	0.59	—	1.89	1.67	1.26
3	—	18	—	35	5.27	5.76	—	0.30	1.86	2.08	1.55
3	—	—	18	35	5.19	5.70	—	0.18	1.81	2.04	1.52
3	4	18	—	35	5.23	5.55	0.59	0.29	1.51	1.62	1.12
3	4	—	18	35	5.20	5.63	0.60	0.19	1.50	1.61	1.12
3	—	18	18	35	5.24	5.79	—	0.24	1.80	2.03	1.49
4	5	62	42	8	5.59	5.91	0.63	0.25	0.49	1.12	0.60

Table 2. Example 2: Calculation results of different configurations (calculated with variance component estimation – see chapter 4)

Using the variance component estimation procedure (VCE) it is possible to estimate optimal weights for each group of observations as well as standard deviations of the observations in the course of the bundle adjustment. This allows for the qualification of each group of measurement on the one hand and for an improvement of the adjustment results on the other hand, since the individual characteristics of the involved measurement devices can be optimally utilised (Klein, 2001; Sieg & Hirsch, 2000). By separating the horizontal and vertical angle measurement of the laser scanner as well as the horizontal and vertical image coordinates of the panoramic camera into different groups of observation, it becomes possible to draw conclusions on the characteristics of each instrument.

Furthermore, also cameras or laser scanners with different accuracies can be considered simultaneously.

The weights p_i of the observations are determined by the ratio of the variance of the unit weight σ_0^2 and the variance of the observations σ_i^2 , which can be derived from manufacturer's data or from empirical values. A constant value will be set for σ_0 (e.g. 0.01 in the presented examples). Subsequently, the standard deviation of unit weight $\hat{\sigma}_0$ shows if the a-priori standard deviations of the observations were defined too pessimistic ($\hat{\sigma}_0 < \sigma_0$) or too optimistic ($\hat{\sigma}_0 > \sigma_0$).

Calculation example	Weighting	$\hat{\sigma}_0$	RMS _X (mm)	RMS _Y (mm)	RMS _Z (mm)	RMS _{XYZ} (mm)
1	Balanced (but too pessimistic overall)	0.00573	1.58	1.71	1.16	2.60
2	Balanced (but too optimistic overall)	0.02296	1.63	1.83	1.15	2.71
3	Balanced and realistic constant weights	0.01046	1.59	1.74	1.19	2.64
4	Unbalanced (range too optimistic)	0.01309	1.78	1.78	2.03	3.23
5	Unbalanced (angles too optimistic)	0.01479	2.03	2.62	1.33	3.57
6	Unbalanced (panoramic coordinates too optimistic)	0.01320	2.12	2.31	1.32	3.40
7	Unbalanced (central perspective coordinates too optimistic)	0.01061	2.68	3.05	1.94	4.50
8	VCE, 4 groups: D α, β x_p', y_p' x', y'	0.01000	1.51	1.64	1.13	2.50
9	VCE, 5 groups: D α β x_p', y_p' x', y'	0.01000	1.56	1.68	1.04	2.52
10	VCE, 5 groups: D α, β x_p' y_p' x', y'	0.01000	1.47	1.60	1.16	2.46
11	VCE, 6 groups: D α β x_p' y_p' x', y'	0.01000	1.52	1.63	1.05	2.46
12	VCE, 7 groups: D α β x_p' y_p' x' y'	0.01000	1.52	1.63	1.05	2.46

Table 3. Combined bundle adjustment with different stochastic models

Standard deviation of observations	too optimistic/ too pessimistic			Unbalanced weights				Variance component estimation				
	1	2	3	4	5	6	7	8	9	10	11	12
Range (mm)	(10.0) 5.73	(3.0) 6.89	(5.3) 5.54	(2.0) 2.0	(10.0) 14.8	(10.0) 13.2	(10.0) 10.6	(7.5) 5.23	(7.5) 5.21	(7.5) 5.24	(7.5) 5.22	(7.5) 5.23
Horizontal angle (mgon)	(10.0)	(2.0)	(5.6)	(10.0)	(2.0)	(10.0)	(10.0)	(10.0)	4.23	(10.0)	(10.0)	4.21
Vertical angle (mgon)	(10.0) 5.73	(2.0) 4.59	(5.6) 5.86	(10.0) 13.1	(2.0) 3.0	(10.0) 13.2	(10.0) 10.6	(10.0) 5.57	(10.0) 6.61	(10.0) 5.58	(10.0) 6.64	(10.0) 6.64
Panoramic x_p' (pixel)	(1.00)	(0.25)	(0.6)	(1.00)	(1.00)	(0.25)	(1.00)	(0.5)	(0.5)	(0.5)	(0.5)	(0.5)
Panoramic y_p' (pixel)	0.57	0.66	0.63	1.31	1.48	0.38	1.06	0.60	0.60	(0.5) 0.66	(0.5) 0.66	(0.5) 0.66
Central perspective x'	(0.5)	(0.12)	(0.24)	(0.5)	(0.5)	(0.5)	(0.12)	(0.2)	(0.2)	(0.2)	(0.2)	(0.2)
Central perspective y'	0.29	0.29	0.25	0.65	0.74	0.66	0.13	0.24	0.24	0.24	0.24	(0.2) 0.23

Table 4. Combined bundle adjustment with different stochastic models (in brackets: standard deviation for the a-priori definition of observation weights; hereunder: estimated a-priori standard deviations of observations)

If observations of the same type have to be processed, the variance-covariance matrix Σ is calculated as product of σ_0^2 and the cofactor matrix Q . In case of a combined adjustment of different observation groups the matrix Σ will be split into components $\Sigma_i = \sigma_i^2 Q_i$. The factors σ_i^2 are the variance components to be estimated which represent the a-priori measurement inaccuracies of each observation group. The calculation is carried out as described in (Koch, 1997; Sieg & Hirsch, 2000).

Table 3 and 4 show the results of 12 different practical examples. The weighting of examples 1 and 2 was balanced but too pessimistic respectively too optimistic. For example 3 well balanced and realistic weights were used as constant values. Examples 4-7 started with unfavourable unbalanced observation weights, examples 8-12 were calculated with integrated variance component estimation, each with different constellations (compare table 4) of observation groups.

Generally it is noticeable that the variance component estimation has the potential to contribute to the improvement of the accuracy, in particular, if the precision of the involved instruments is not sufficiently well known a-priori (see table 3). Table 4 demonstrates the capability of the calculation with variance component estimation to estimate the precision of the involved groups of measurements – widely independent from the definition of a-priori approximate weights.

The values in brackets served for the definition of weights for each observation. The values below are the estimated a-priori standard deviations as results of the bundle adjustment. This value is better than the value in brackets if the weighting was too pessimistic and worse if the weighting was too optimistic. This is in particular noticeable with example 1 and 2. In Examples 4-7 only one group of observations started with too optimistic standard deviations which lead to overemphasized weights for this group of observations (in table 4 highlighted with boldface). Anyway, the adjustment results change for the worse in these cases (see RMS of object coordinates in table 3). The variance component estimation (examples 8-12) results in balanced weights and therefore in optimal adjustment outcomes. The values in brackets in table 4 serve in these cases only for the definition of a-priori approximate weights. The values below are the variance components estimated within the adjustment with VCE. These variance components give realistic information about the precision of each observation group.

Furthermore, it is even possible to draw conclusions on differences of the horizontal and vertical angle precision of the laser scanner, as well as on differences in the horizontal and vertical image coordinate accuracy, in particular for panoramic cameras. In future the separation into more observation groups will be analysed (e.g. by use of different cameras or scans with different resolution, separation in constant and distance-dependent variance components). In addition, the implementation and assessment of a free net adjustment (without datum points) with variance component estimation is planned. In order to assess the accuracy more realistically, independent test measurements respectively a comparison of the estimated object point coordinates with known object coordinates, measured with a higher accuracy, will be performed.

5. REFERENCES

- Al-Manasir, K. & Fraser, C., 2006: Automatic registration of terrestrial laserscanner data via imagery. *ISPRS Archives*. Vol. XXXVI, Part 5.
- Amiri Parian, J., 2007: Sensor modelling, terrestrial panoramic camera calibration and close-range photogrammetric network analysis. *Dissertation ETH Zürich*.
- Baarda, W., 1968: A testing procedure for use in geodetic networks. *Netherlands Geodetic Commission*, Vol. 2 (5), Delft.
- Brown, D., 1971: Close-Range Camera Calibration. *Photogrammetric Engineering*, Vol. 37, No. 8.
- Dold, C. & Brenner, K., 2006: Registration of terrestrial laser scanning data using planar patches and image data. *ISPRS Archives*. Vol. XXXVI, Part 5.
- El-Hakim, S.F., 1986: Real-Time Image Meteorology with CCD cameras. *Photogrammetric Engineering and Remote Sensing*, Vol. 52, No. 11, pp. 1757-1766
- Haring, A.; Briese, M.; Pfeifer, N., 2003: Modellierung terrestrischer Laserscanner-Daten am Beispiel der Marc-Anton-Plastik. *Österreichische Zeitschrift für Vermessung und Geoinformation (VGI)*, 91. Jahrgang (2003), 4: 288-296.
- Jansa, J.; Studnicka, N.; Forkert, G.; Haring, A.; Kager, H., 2004: Terrestrial laserscanning and photogrammetry – acquisition techniques complementing one another. *ISPRS Archives*. Vol. XXXV, Part B5.
- Klein, B., 2001: Untersuchungen zur Feldprüfung geodätischer Instrumente mittels Varianzkomponentenschätzung. *Diplomarbeit, Technische Universität Darmstadt*, unpublished.
- Koch, K.-R., 1997: *Parameterschätzung und Hypothesentests in linearen Modellen*. Dümmler Verlag, Bonn, 3. Auflage.
- Luhmann, T. & Tecklenburg, W., 2004: 3-D object reconstruction from multiple-station panorama imagery. *ISPRS Archives*. Vol. XXXIV, 5/W16.
- Mulsow, C.; Schneider, D.; Ullrich, A.; Studnicka, N., 2004: Untersuchungen zur Genauigkeit eines integrierten terrestrischen Laserscanner-Kamerasystems. *Beiträge der Oldenburger 3D-Tage 2004*: 108-113, Herbert Wichmann Verlag, Heidelberg.
- Reulke, R., 2006: Combination of distance data with high resolution images. *Image Engineering and Vision Metrology, ISPRS Archives*. Vol. XXXVI, Part 5.
- Schneider, D. & Maas, H.-G., 2005: Combined bundle adjustment of panoramic and central perspective images. *ISPRS Archives*. Vol. XXXVI, Part 5/W8.
- Schneider, D. & Maas, H.-G., 2006: A geometric model for linear-array-based terrestrial panoramic cameras. *The Photogrammetric Record*, 21(115): 198-210, Blackwell Publishing Ltd., Oxford, UK.
- Sieg, D. & Hirsch, M., 2000: Varianzkomponentenschätzung in ingenieurgeodätischen Netzen; Teil 1: Theorie. *Allgemeine Vermessungsnachrichten*, 3/2000: 82-90.
- Ullrich, A.; Schwarz, R.; Kager, H., 2003: Using hybrid multi-station adjustment for an integrated camera laser-scanner system. *Optical 3-D Measurement Techniques VI*, Vol. 1 (2003), 298-305.
- Wendt, A. & Heipke, C., 2006: Simultaneous orientation of brightness, range and intensity images. *ISPRS Archives*. Vol. XXXVI, Part 5.

MAPPING DEFOLIATION WITH LIDAR

S. Solberg ^{a *}, E. Næsset ^b

^a Norwegian forest and landscape institute, P.O. Box 115, N-1431 Ås, Norway – svein.solberg@skogoglandskap.no

^b Dept. of Ecology and Natural Resource Management, Norwegian University of Life Sciences, P.O. Box 5003, N-1431 Ås, Norway - erik.naesset@umb.no

KEY WORDS: Leaf area index, LAI, LIDAR, defoliation, woody area

ABSTRACT:

The aim of this article is to present a concept of using airborne laser scanning (LIDAR), with one scan only, to map defoliation as a forest health variable. The idea is to apply two independent algorithms on the LIDAR data set, to produce both actual and expected leaf area index (LAI) values for every cell in a grid over the area. LAI is estimated based on laser pulse penetration through the canopy layer, and expected LAI values are derived from stand density based on position and height of single trees as obtained from a single-tree segmentation algorithm. The results are preliminary findings from four ongoing and related studies. In the first study repeated laser scans had close to equal extinction coefficients for LAI estimation although the instruments and flight specifications were different. In the second study, based on the findings in the first we derived normal LAI values from existing and large scale data sets with LIDAR and field data. The main independent variable was stand density, defined as the ratio between mean tree height and mean distance between the trees. The ratio between LAI and stand density was around 0.5, and this is a preliminary standard for a healthy pine forest. In a third study the woody area fraction of LAI was estimated from 14 total harvested trees, and turned out to be slightly below 50% for a healthy pine tree, which means that a totally defoliated pine forest would have an LAI/stand density ratio around 0.2. In the fourth study, these LAI standard values were confirmed with LIDAR data from a severe insect defoliation event in Norway 2005. In conclusion, the present preliminary results demonstrate a potential for application of airborne laser scanning for monitoring or mapping of defoliation as a forest health variable.

1. INTRODUCTION

In two test cases with Norway spruce and Scots pine in Norway, it has been demonstrated that airborne laser scanning (LIDAR) can be used for mapping of leaf area index (LAI) (Solberg et al., 2005), and repeated scans can be used for mapping of defoliation events (Solberg et al., 2006a). However, normally defoliation events are not known in advance, and it would be useful to be able to map defoliation based on one laser scanning after a forest damage event. This would be useful for obtaining an overview of the damage area for actions such as sanitary cutting, prevention of further spread of the damage, for forest insurance companies, and for general interests of having damage overviews.

There are some problems that need to be resolved in order to realize such a one-scan defoliation mapping. First, there is a need for data on normal LAI values for the given site and stand properties of the forest in question. Second, the LAI obtained is so-called effective LAI which includes woody areas of branches and stems. Hence, there is a need for knowing the woody area fraction of the actual forest, which would be the LAI value for a totally defoliated forest. This woody area is the area of branches and stems. Both the normal LAI values and the woody area will depend on the number of trees and their size. Hence, we see here a potential for modelling both the normal LAI values and the woody area as a function of single-tree data obtained from automated single-tree segmentation routines (Solberg et al. 2006b).

The major objective of this article is to present preliminary results of such a one-scan forest health mapping concept, applying two independent algorithms on the same LIDAR data set. First, LAI is estimated from LIDAR pulse penetration through the canopy layer, and second, expected LAI values are obtained for the forest if it was healthy and if it was totally defoliated based on modelling on single tree segmentation data. One specific aim was to test whether already existing LIDAR data sets could be used to generate normal LAI values, i.e., do technical differences between airborne laser scans influence the extinction coefficient of the laser pulses through a forest canopy layer (Næsset & Solberg, 2007)? A second aim was to generate normal LAI with key stand and site property variables, mainly based on single tree data (Solberg & Næsset, 2007). Third, how can the woody area fraction be estimated (Solberg, 2007a)? The fourth and final aim was to apply the results of the above mentioned steps in a test case with severe insect defoliation on a Scots pine forest (Solberg, 2007b).

2. MATERIALS AND METHODS

Solberg et al. (2006) used calibration from point-based measurements on the ground with LAI-2000 and hemispherical photography to estimate LAI. The calibration was done with the formula:

$$[1] \quad LAI = (1/k) \ln(N_a/N_b)$$

* Corresponding author

where k is an extinction coefficient, and the term $\ln(N_a/N_b)$ is the inverse of the gap fraction. N_a is the total number of echoes and N_b is the number of below-canopy echoes for a 30m-diameter circle around each ground measurement point.

A number of studies have already addressed the effects of differences between laser data acquisitions using different sensors, flying altitudes, footprint sizes, and sensor specifications on basic laser-derived forest data metrics (e.g. Næsset 2004, 2005; Chasmer et al, 2006). Significant effects of flying altitude, sensor and repetition frequency have been reported, but the influence on biophysical properties may be limited by selecting operational parameters that are similar across acquisitions. For example, the effects of repetition frequency for a given instrument can be more significant than effects of different instruments operated with similar settings (Næsset, in prep). It also seems to be a general tendency for first return data to be more stable across flight specifications than last return data. The current application is based on first return data only. It is therefore not unlikely that the technical properties of the laser scanning turns out to have a limited effect on the extinction coefficient.

2.1 Stability of laser canopy penetration across LIDAR campaigns

In this part of the study, we utilized existing data sets from previous laser data acquisitions of forests in Norway, where the scanning is repeated over the same area with different technical properties. Important here is that we don't need to calibrate the LAI data with ground measurements. It is sufficient to compare the $\ln(N_a/N_b)$ term in equation [1], which is proportional to LAI. This is valid if the laser scanning is repeated for an area and LAI was the same on both occasions.

2.2 Modelling normal LAI values

The idea is that LAI will normally vary with tree species, site index and stand density, where the latter reflects both the number of trees per unit area and the spacing between them. For each species and site index the normal LAI should be proportional to stand density (SD) which we initially defined as:

$$[3] \quad SD = h/dist,$$

where h is the mean tree height, and $dist$ is the mean distance between the trees.

We used existing and comprehensive data sets with airborne LIDAR to produce normal values of LAI for Scots pine, and for various values of stand density and site index. We had at hand a considerable amount of extensive airborne LIDAR data sets for forests in Norway. In each of these study areas, a number of field plots with complete measurements of trees and site productivity were available for analysis.

2.3 Correction for woody area fraction

From the forest area with insect attacks in 2005, 14 pine trees were sampled. They were located one in each of 14 sample plots in age classes from young, intermediate age and old stands. The sample trees, having heights of 10-30 m, were felled and all branches harvested. The branches, having a total mass of 591 kg d.w., were dried and separated into

needles, twigs, and coarser branches for detailed measurements of hemisurface areas and clumping factors, mainly by photographing techniques (Fig. 1). From the total area, the area fraction of branches and stems, i.e., woody area, was calculated. Also, the woody area was modelled as a function of single-tree measurements, such as tree height and crown width. Such variables might be derived from single-tree segmentation algorithms using LIDAR data.



Figure 1. Example of branch photography.

2.4 Example of the method applied on insect defoliation event

For testing the method, a laser scanning data set covering a 21 km² area with severe insect defoliation of Scots pine from 2005 was applied. First, we used the single-tree segmentation algorithm (Solberg et al., 2006b) in order to detect all local maxima in the digital canopy height model (DSM), most likely being tree tops. The entire area was then divided into 10m x 10m grid cells. For each cell, the stand density (SD) was calculated based on the height and position of the local maxima. Second, for each cell LAI was calculated according to model [1], where $1/k$ was set to 1.48 (Solberg et al., 2006a). Finally, each grid cell was then provided with a forest health indicator value, c , defined as:

$$[4] \quad c = LAI / SD$$

This health proportionally factor was then assigned to forest health classes based on training sites within the damage area where the degree of defoliation was known based on

- a) field observations;
- b) changes in LAI during the insect defoliation period June – July obtained by repeated laser scanning;
- c) the normal LAI values obtained above from other sites; and
- d) minimum LAI values set to woody area as a function of single tree variables.

3. RESULTS

3.1 Stability of laser canopy penetration across LIDAR campaigns

Fortunately, different laser scans had equal extinction coefficients for LAI estimation, although the instruments and flight specifications were different (Fig. 2).

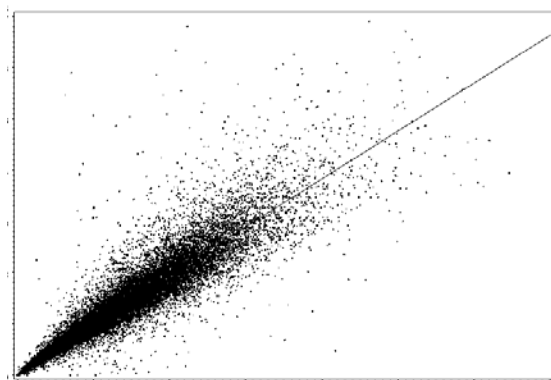


Figure 2. Relationship between $\ln(N_d/N_b)$ for two laser scans done with two different scanners at two points of time over a forest reserve with no forest management. The 1:1 line is shown. The $\ln(N_d/N_b)$ range is 0-7, which corresponds to an LAI range of about 0-14. The spatial resolution is 10m x 10m, $n=19399$, and the no-intercept model was $Y = 0.98X$.

3.2 Modelling normal LAI values

The result of the modelling of normal LAI values for forests produced quite stable ratios between $\ln(N_d/N_b)$ and stand density values. However, no effect of site index was found. Random errors might be present due to a limited number of plots for the lowest and highest site index classes. The ratios ranged from 0.29-0.38, which would correspond to health indicator ratios (c) in the range 0.43-0.56 after scaling with the $1/k$ factor being 1.48 (Solberg et al. 2006a).

Site index, H40	factor r
6	0.34
8	0.37
11	0.32
14	0.29
17	0.38
20	0.32

Table 1. Proportionality factor between $\ln(N_d/N_b)$ and stand density for various combinations of site index for Scots pine.

3.3 Correction for woody area fraction

The woody area fraction was around 50% for those trees not affected by the insect defoliation, and increased to 85% of the area for trees with severe defoliation. The woody area fraction of LAI can be estimated based on regression models with input variables such as crown size and tree height (Table 2). It is notable that crown projected area was a stronger predictor for woody area than tree height, which indicates that the spacing between the trees are important for the amount of branching and woody area.

Variable	Parameter r estimate	R^2
Height, m	1.25	0.46
Crown volume, m^3	0.96	0.61
Projected crown area, m^2	2.99	0.83
Crown length, m	2.76	0.47

Table 2. Results of no-intercept regression models for woody area against various tree size measures that were

derived from an automated routine for single tree segmentation on the LIDAR data for the 14 sample trees.

3.4 Example of the method applied on insect defoliation event

In total, 1.5 million local maxima were found over the 21 km^2 area, and the process was quite time-consuming with 35 hours computing time with a Pentium 4 processor with a 3.2 GHz clock frequency. From the training sites we obtained different values for the forest health indicator (c). First, the training sites subject to severe defoliation had c values around and lower than 0.25. A second set of training sites consisted of grid cells having no change in LAI from May to August. This is likely to be sites with a moderate degree of defoliation, i.e., where the amount of insect defoliation equalled the amount of new needles produced during the summer. These sites had a mean forest health indicator value $c = 0.32$. Finally, sites where we did not observe any signs of defoliation had c values in the range 0.3–0.6. All these results were from pine-dominated grid cells, having 90% or more of the standing volume being pine.

It turned out that the pine forest in this case was in general quite defoliated, and in order to visualize some spatial variability we produced a map with more arbitrary threshold values for the forest health indicator c (Figure 3):

- Class 1, most defoliated: $c < 0.225$
- Class 2, moderately defoliated: $0.225 < c < 0.275$
- Class 3, least defoliated: $c > 0.275$.

These values are lower than what was obtained from the normal LAI values, and visualizes degrees of defoliation severity.

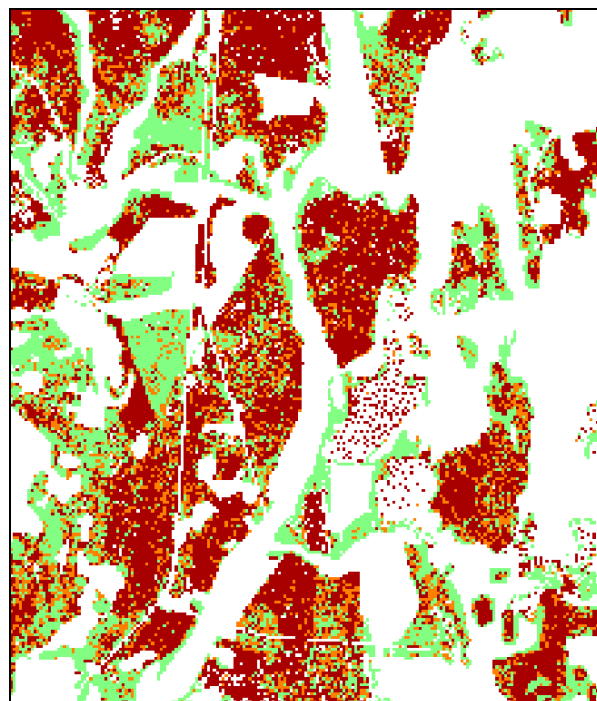


Figure 3. Map of defoliation in 2005 with an extent of 2 km x 2.3 km. Red (dark grey) = severe defoliation; orange (grey) = moderate defoliation; green (light grey) = less severe defoliation; white = areas other than pure pine forest.

4. DISCUSSION

The presented results are all preliminary. However, as a whole, they indicate a potential for using one laser scanning only for mapping defoliation. Two independent algorithms are used to process the laser datasets. First, LAI is estimated based on the degree of laser pulse penetration through the canopy layer. Second, tree heights and locations are derived by a single-tree segmentation algorithm, and these data are recalculated into a stand density variable. Then, a grid with a given spatial resolution is overlaid and the two variables are combined into a LAI/SD ratio which can be used as a forest health indicator. It appears that a healthy pine forest should have a LAI/SD ratio around 0.5, while a completely defoliated forest would have an LAI/SD values around 0.2, which would be woody areas of branches and stems only.

We will fine-tune the results further on. In our model of normal LAI values there is a linear relationship between LAI and tree height, and this needs to be refined. As trees grow in height, and the stand is closed, the canopy will be moved upwards, and LAI should not continue to increase linearly. Hence, we will try other non-linear models for tree height in future work. The denominator in the ratio is the mean distance between the trees, which can be recalculated to the inverse of the square root of the number of stems per unit area, and this is a non-linear function of LAI against the number of trees, which is reasonable.

5. CONCLUSION

In conclusion, the present preliminary results demonstrate a potential for application of airborne laser scanning for monitoring or mapping of defoliation as a forest health variable based on one scan only. Standard threshold values for LAI in healthy forests remains to be developed for various tree species and for various combinations of site index and stand density.

6. REFERENCES

- Chasmer, L., Hopkinson, C., Smith, B., and Treitz, P., 2006. Examining the influence of changing laser pulse repetition frequencies on conifer forest canopy return. *Photogrammetric Engineering & Remote Sensing*, 72, pp. 1359-1367.
- Næsset, E., 2004. Effects of different flying altitudes on biophysical stand properties estimated from canopy height and density measured with a small-footprint airborne scanning laser. *Remote Sensing of Environment*, 91, 243-255.
- Næsset, E., 2005. Assessing sensor effects and effects of leaf-off and leaf-on canopy conditions on biophysical stand properties derived from small-footprint airborne laser data. *Remote Sensing of Environment*, 98, 356-370.
- Næsset, E., and Solberg, S., 2007. LAI standards for healthy forests derived by airborne LIDAR. *In prep.*
- Solberg, S., 2007a. Detailed LAI measurements in defoliated Scots pine from destructive sampling and airborne laser scanning. *In prep.*

Solberg, S., 2007b. Mapping areas with defoliated pine from a single laser scan. *In prep.*

Solberg, S., Næsset, E., Aurdal, L., Lange, H., Bollandsås, O.M., and Solberg, R., 2005. Remote sensing of foliar mass and chlorophyll as indicators of forest health: preliminary results from a project in Norway. In: Olsson, H. (Ed.) *Proceedings of ForestSat 2005, Borås, May 31-June 3*. Rapport 8a.

Solberg, S., Næsset, E., Hanssen, K.H., and Christiansen, E., 2006a. Mapping defoliation during a severe insect attack on Scots pine using airborne laser scanning. *Remote Sensing of Environment*, 102, 364-376.

Solberg, S., Næsset, E., and Bollandsås, O.M., 2006b. Single-tree segmentation using airborne laser scanner data in a structurally heterogeneous spruce forest. *Photogrammetric Engineering & Remote Sensing*, 72, 1369-1378.

Solberg, S., and Næsset, E., 2007. Estimating LAI in multitemporal airborne LIDAR. *In prep.*

ACKNOWLEDGEMENTS

This paper is a result of studies from several projects, however, mainly from the ongoing REMFOR project funded mainly by the Norwegian Research Council.

HIERARCHICAL CLUSTERED OUTLIER DETECTION IN LASER SCANNER POINT CLOUDS

S. Sotoodeh

Institute of Geodesy and Photogrammetry, ETH Zurich, Switzerland
Soheil.Sotoodeh@geod.baug.ethz.ch

Commission V/3

KEY WORDS: Point cloud, Laser Scanner, Outlier detection, EMST, Gabriel graph, Clustering

ABSTRACT:

Cleaning laser scanner point clouds from erroneous measurements (outliers) is one of the most time consuming tasks that has to be done before modeling. There are algorithms for outlier detection in different applications that provide automation to some extent but most of the algorithms either are not suited to be used in arbitrary 3 dimensional data sets or they deal only with single outliers or small scale clusters. Nevertheless dense point clouds measured by laser scanners may contain surface discontinuities, noise and different local densities due to the object geometry and the distance of the object to the scanner; Consequently the scale of outliers may vary and they may appear as single or clusters. In this paper we have proposed a clustering algorithm that approaches in two steps with the minimum user interaction and input parameters while it can cope with different scale outliers. In the first step the algorithm deals with large outliers (those which are very far away from main clusters) and the second step copes with small scale outliers. Since the algorithm is based on clustering and uses both geometry and topology of the points it can detect outlier clusters in addition to single ones. We have evaluated the algorithm on a simulated data and have shown the result on some real terrestrial point clouds. The results explain the potential of the approach to cope with arbitrary point clouds and different scale erroneous measurements.

1 INTRODUCTION

Simple, efficient and direct capturing of 3D information are the main reasons for the fast growing popularity of laser scanners. Although the generated point clouds are direct and dense measurement of objects, the appearance of single or cluster outliers cause serious problems for the next modelling steps. Therefore, a pre-process is required to detect and remove outliers. However, the number of points in the generated point cloud is in the order of million points, so (semi) automatic approaches are necessary.

Outlier detection in point clouds is not a trivial task since there are: geometrical discontinuities caused by occlusions in silhouette boundaries, no prior knowledge of the statistical distribution of points, the existence of noise, and different local point densities. The typical outlier detection approaches are classified as distribution-based, depth-based, distance-based, density-based and clustering approaches (Papadimitriou et al., 2002).

In the previous work (Sotoodeh, 2006), we have introduced an outlier detection algorithm for laser scanner point clouds, which is categorized in density-based approaches, and have investigated the advantages and the deficiencies of the algorithm in different data sets. The algorithm needs a predefined minimum density for inlier clusters and a threshold to distinguish outliers from inlier. There it is shown that even though the algorithm is capable to detect single and small clustered outliers but it simply does not detect clustered outliers that are denser than the predefined cluster density (large β -error). Also we have tried the algorithm in an iterative manner however it removes a large amount of the inlier and consequently results in a bigger value of α -error.

In this paper we have presented a new algorithm that applies more sophisticated information of the point cloud to detect single and clustered outliers with a minimum user interaction. It uses two proximity graphs and performs in two steps. In addition to the algorithm description, the results of applying the algorithm to a

real close-range data is reported in this article. Also some implementation issues are discussed.

This article contains a brief review of several outlier detection approaches in section 2. Section 3 presents the algorithm and some implementation issues. Results of applying the algorithm on different data sets is presented and discussed in Section 4 and the last Section concludes the article by discussing the achievements.

2 RELATED WORK

While an extensive amount of research has been presented in literature for outlier detection it is still a critical problem in laser scanner point clouds. The proposed approaches have weak potential to perform well with surface discontinuities, they need some prior knowledge of the statistical distribution of the samples (Hawkins, 1980, Vanicek and Krakiwsky, 1982) or they are sensitive to noise and different local densities (Breunig et al., 2000). Nevertheless, the mentioned criteria are typical cases in laser scanner point clouds.

According to (Papadimitriou et al., 2002) outlier detection approaches are classified into the distribution-based (Hawkins, 1980), depth-based (Johnson et al., 1998), clustering approaches (Jain et al., 1999), distance-based (Knorr et al., 2000) and density-based (Breunig et al., 2000). Distribution-based approaches deploy some standard stochastic distribution model (Normal, Poisson, etc.) and flag as outliers those objects that deviate from the model according to a significant level (Vanicek and Krakiwsky, 1982, Rousseeuw and Leroy, 1987, Barnett and Lewis, 1994). However, for arbitrary data sets without any prior knowledge of the distribution of points, determination of the suitable distribution model which fits to the data set (if any) needs to perform expensive tests (in laser point clouds the distribution of points varies according to the distance of objects to laser scanner and the object geometry). Local surface fitting approaches, for instance moving least squares, is also used for outlier detection. The algorithms perform well if the point cloud is dense and obtained

from a smooth surface. However, discontinuities or high curvature areas would get severe smoothing effect. The description of these algorithms and their application is beyond the scope of this article.

The depth-based approach is based on computational geometry and computes different layers of k -dimensional convex hulls (Johnson et al., 1998). Objects in the outer layer are detected as outliers. However, it is a well-known fact that the algorithms employed cannot cope with large, arbitrary data sets in 3 dimensions. The above two approaches for outlier detection are not appropriate for large, arbitrary data sets (Papadimitriou et al., 2002). Nevertheless, this is often the case with laser point clouds.

The distance-based approach was originally proposed by (Knorr et al., 2000). An object in a data set P is a distance-based outlier if at least a fraction b of the objects in the object set is further than r from it. This outlier definition is based on a single, global criterion determined by the parameters r and b . This can lead to problems when the data set has both dense and sparse regions (Breunig et al., 2000).

The density-based approach was proposed by (Breunig et al., 2000) for KDD (Knowledge Discovery in Database) applications and (Sotoodeh, 2006) adopted the algorithm for application in laser scanner point clouds. It relies on a local outlier factor (LOF) of each object, which depends on the local density of its neighborhood. The neighborhood is defined by the distance to the M nearest neighbor. The $MinPts$ is a predefined value, which corresponds to the minimum number of points in the calculation of density. The algorithm is not only independent of the prior knowledge of the scanned objects, the distribution or density of sampled points but also does not suffer from the different local point densities. It is capable to detect single and small clustered outliers. Nevertheless it does not detect clustered outliers that are denser than the predefined cluster density (large β -error).

Many clustering algorithms detect outliers as by-products (Jain et al., 1999). From the viewpoint of a clustering algorithm, outliers are objects not located in the clusters of dataset. These algorithms, in general, consider outliers from a more global perspective, which also has some major drawbacks (Breunig et al., 2000). Clustering algorithms, also called as classification methods, are performing by two main approaches: supervised and unsupervised. In the supervised approach the algorithm needs some representatives of different classes the supervisor expects. Providing such samples differs in various laser data set and so makes the approach very dependent on the scanned objects.

In the unsupervised case, the goal is to cluster the input data in such a way as to provide clusters $C_k, k = 1, \dots, K$ which correspond to some underlying (interesting or useful) unobserved class labels. A fundamental difficulty in clustering is determining K , the number of clusters. Once K is determined, one proceeds to group the observations. One may approach clustering from a density estimation viewpoint. For instance, a common approach is to model the density as a mixture of K components (again, choosing K can be difficult) and then use these components to determine clusters. A related method is k -means clustering. The idea is to cluster the data into clusters centered on k centers. The centers are initialized arbitrarily, and points are assigned to the cluster associated with their closest center. The centers are then recomputed using the assigned points, and this continues until convergence. Besides the problem of selecting the value of K , the k -means algorithm suffers from sensitivity to the initial cluster centers. For this reason, some practitioners advise trying several initializations, with various methods for selecting or combining the result clusters. Others suggest various methods for selection of initial centers (Marchette, 2004).

The minimum spanning tree can be used for clustering, using a local criterion for defining clusters. This idea is described in some detail in (Zahn, 1971). The idea is to break (remove edges from) the minimum spanning tree at edges that are "inconsistent". This results in a collection of connected graphs, one for each cluster. Many definitions of inconsistent are possible. One could compute the standard deviation of the edge lengths incident on a vertex and eliminate edges which are large relative to this scale. However since this cutting is based on a global criterion, the clustering result would be rough and outliers close to the object surface cannot be detected. This is described in more detail in Section 3.

(Sithole, 2005), has also applied minimum spanning tree to segment airborne laser scanner (ALS) data. The algorithm is scan line based and performs in different directions. The author has reported well performance of the algorithm in different ALS data set to separate terrain, trees, house roofs and bridges (segmentation). The outliers are detected as points that are not in the predefined classes. It has a fast run time performance and runs in case there are overlapping point clouds. However the extension of the algorithm to close-range data, in case either there is no information about scan lines or if the point cloud is a combination of different scan positions (topologically 3D data from object surfaces), does not seem trivial and limits the application to ALS datasets.

3 HIERARCHICAL OUTLIER DETECTION (HOD) ALGORITHM

According to the general definition of outliers form (Hawkins, 1980), "Observations that deviate so much from other observations as to arouse suspicion that it was generated by a different mechanism", an outlier in a dense point cloud can be identified using its sampling interval deviation from the others. In laser scanner point clouds the sampling interval is not a fixed value since the sampling is performed based on two fixed angular resolution and objects might have different distance to the measurement instrument and so outliers might appear in various scales in a scan; Therefore applying a global and then a local outlier detection should provide useful results. Based on this observation we have developed an algorithm that runs in two phases. The first phase tries to capture some statistical information of a global sampling interval, while the second phase provides a local criteria to cluster the point cloud. Flowchart of the algorithm is depicted in Figure 1.

First, a rough global approximation of the sampling intervals is estimated over the Euclidean Minimum Spanning Tree (EMST) edges. Then the tree edges that are not in a predefined confidential interval are pruned. The result is a rough clustering of the point cloud. In the next step, each cluster is treated separately. For points in each cluster a graph, so called Gabriel Graph (GG), is generated. Edges of GG are used for estimating the sampling interval statistics in each cluster. Then graph edges that are not in a predefined confidential interval are pruned. This gives the final clustering in which single outliers are removed as a by product. The clustered outliers are also removed if they have less point density than a predefined value.

Initially the algorithm computes the Delaunay triangulation of the point cloud. The underlying topology of the Delaunay graph is the base for the generation of the next graphs. In the first phase of the clustering, EMST of the point cloud is generated and the edges of the tree are pruned based on the statistical analysis of the edge lengths. This gives a rough clustering of the point cloud and might disconnect some big clustered outliers that their distance to

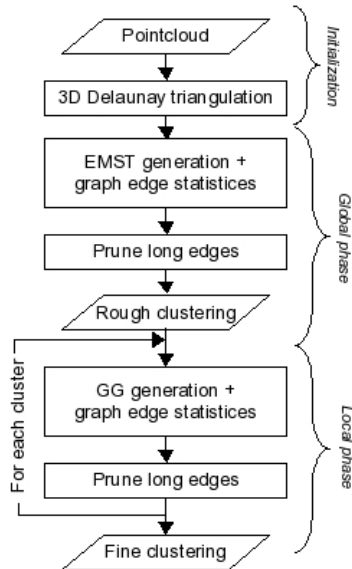


Figure 1: Flowchart of the hierarchical outlier detection algorithm

the other clusters are large. Clusters that are denser than a predefined threshold are kept and the rest are removed. Second phase starts with the generation of GG for the point clouds of each cluster from the last phase. Having pruned the long edges of each GG according to the statistics computed over edges of that GG, a finer clustering of the point cloud is obtained. Removing clusters less denser than a predefined value removes the final outliers and cleans the data. In another viewpoint, the algorithm in the first stage removes relatively large scale erroneous measurements and in the second phase it detects and removes the outliers that might not be as large as the first ones but according to the scanned object surfaces they are considered as wrong measurements. In the following sections, the above process is described in more details.

3.1 Global phase (rough clustering)

In the first step we use edges of EMST to obtain a global sampling interval measure. The Euclidean minimum spanning tree or EMST is a minimum spanning tree of a set of points in R^n , where the weight of the edge between each pair of points is the Euclidean distance between those two points. In simpler terms, an EMST connects a set of points using edges such that the total length of all the edges is minimized and any point can be reached from any other by following the edges.

This definition gives a clue that edges of EMST contain some global information about the sampling interval, since they span the points by a global minimum edge weight (distance). Additionally in case of some clusters apart from each other, EMST connects them by single edges that are logically longer than the other edges of the tree (Figure 2b).

Having assumed that sampling intervals obey a normal distribution, an edge of the tree is statistically long if its distance to the median of the all edge lengths is longer than the distance corresponding to a predefined confidential interval. Median is used since it is statistically less sensitive to outliers. Removing the long edges of the tree according to such a threshold results in some sub trees that each corresponds to a cluster of points (Figure 2c).

Since today laser scanners provide dense point clouds of objects, splitted clusters that are less dense than a threshold are most probably outliers. In our implementation the minimum inlier cluster

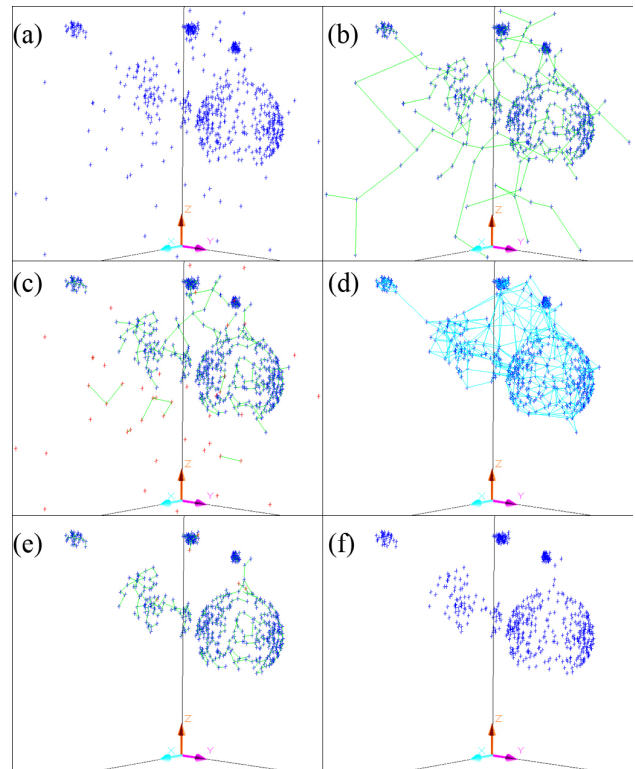


Figure 2: Proposed algorithm steps in a simulated data. Steps (a) to (c) and (d) to (f) illustrate the first and the second phases of the algorithm respectively. (a) input data set (b)EMST of the point set (c) pruned EMST by 99% confidential interval (d) GG of the clusters of the first phase (e) pruned GG by 95% confidential interval (f) ultimate result which is cleaned out of the outliers.

density (the threshold) is a user defined single value that might be different for various scanning resolutions and object size.

In this stage the algorithm has cleaned outliers according to a global criteria that is performing well in the scale of the whole scan but might not be suitable to remove local outliers. So we need a local and more rich measure of sampling intervals. The next stage describes an approach to reach this goal.

3.2 Local phase (fine clustering)

Since EMST provides a rough skeleton of the scanned object, the estimated sampling interval is also not so precise. Applying a denser structure (graph) that has more edges on the underlying scanned surface provides a denser sample of the edges and consequently the estimation of the parameters of the related population is more reliable. Gabriel Graph is such a structure.

Gabriel graphs, also known as Least Squares Adjacency Graphs, were introduced by (Gabriel and Sokal, 1969) and named after their originator. GG has originally been defined for 2D and has been used for geographic variation of data, but the definition is generalized to higher dimensions in a straightforward way (Veltkamp, 1994). It also has widely been applied in the analysis of labeled data (Aupetit, 2003) and widely in boundary/surface reconstruction algorithms; (Veltkamp, 1994, Attene and Spagnuolo, 2000, Adamy et al., 2000) to name a few. A Gabriel Graph on a point set P in R^n is defined to be the graph on P in which two points are connected if the largest open ball passing through the two points is empty. In a three dimensional Euclidean space two points make an edge if the largest sphere passing through these two points contains no other point. On the other hand since

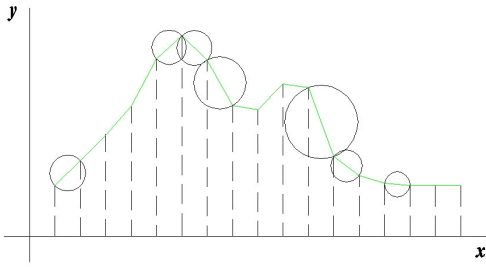


Figure 3: Gabriel graph edges and sampling intervals of a sampled curve in a plane. Two points are connected by GG edges if the largest circle passing through the points is empty (Only some circles are shown in the figure).

GG is a sub graph of each Delaunay triangulation of the point set, the edges of the GG are also edges of each Delaunay triangulation and inherit their properties (Marchette, 2004).

According to the definition, the graph contains edges that resemble the sampling intervals in three dimensions and the structure is quit like a wireframe of the scanned object surface (Figure 2d). Figure 3 illustrates the Gabriel Graph for a sampled curve in a plane. It shows how the edges of GG are similar to the sampling intervals.

Based on the above property the proposed algorithm performs the second phase. For each cluster obtained in the previous stage, GG is computed and its edges considered as the samples of the sampling distance in that particular cluster. Like the first step, the median value of the edge lengths is assumed as the estimation of the sampling distance with a standard deviation equal to the standard deviation of the edge lengths. Considering the predefined confidential interval, long edges of the graph are cut. It results in sub graphs each indicating a cluster. Clusters that have a density less than the predefined cluster size are considered as outliers (Figure 2e).

3.3 Implementation

Although the algorithm seems straight forward, computation of EMST and GG needs some considerations. The simplest algorithm to find an EMST, given n points, by constructing the complete graph on n vertices requires $O(n^2)$ time. The same approach constructs GG in $O(n^3)$ in 3 dimensions. Having noticed that EMST and GG are the subgraphs of every Delaunay triangulation of a point set even in 3 dimensions, applying Delaunay triangulation structure reduces the complexity to $O(n \log n)$ for each. Thus, we first compute the 3D Delaunay triangulation of the point set and use that structure for computing the EMST and then GG for each cluster resulting from the first phase. CGAL¹ is used as a geometric core library and for the Delaunay triangulation computations. Boost Graph library² is also employed for the EMST computations.

4 RESULTS AND DISCUSSION

To assess the explained algorithm, it was examined on a simulated data and some terrestrial laser scanner point clouds, with dense clusters and most of typical outliers. Below the result of all tests are reported.

¹<http://www.cgal.org>

²<http://www.boost.org>

4.1 Simulated data

Figures 2a-f show the algorithm sequence on a simulated data containing 656 points. Reference outlier and inlier are separated manually and the result of the algorithm is compared with the reference data. Table 1 shows some statistics, the number of outlier/inlier points and the first and second error types, of the result in the two phases. At the first phase points and clusters that are too far from the main clusters are detected while the second phase deals with local outliers. High β -error value at the first phase explains planes that there are still some outliers among the intermediate cleaned data that are not detected. Having run the second phase remained outliers are detected and removed (the lower value of β -error). Of course the second phase increases the α -error too (some correct points are detected as outlier) however this is a trade off one has to consider between decreasing β -error and increasing α -error.

The HOD algorithm (phase-1)

Reference	Inlier	Outlier		α -error
	569	3	572	correct outlier
	9	75	84	correct inlier
	578	78	656	β -error

α -error	0.45%	β -error	1.37%
-----------------	-------	----------------	-------

The HOD algorithm (phase-2)

Reference	Inlier	Outlier	
	565	6	571
	3	4	7
	568	10	578

α -error	1.04%	β -error	0.52%
-----------------	-------	----------------	-------

Table 1: Result of the proposed algorithm on the simulated data, phase one (upper table) and phase two (lower table).

4.2 Terrestrial case

Point clouds from Sternwarte³ building, which was measured by Faro⁴ LS880 laser scanner, used as the terrestrial test data set. Figure 4 left column, illustrates the original laser scanner data in different scan positions with different object facets. The right column of the figure shows each data set after has been cleaned by the algorithm. 99% and 95% confidential intervals are used for the global and local clustering phases respectively. The minimum inlier cluster density is considered as 100 points, according to the object size, distance of the scanner to the object and sampling resolution. Comparing the data set before and after outlier detection clearly shows the importance of the process and how the proposed algorithm performed. Close look at the results shows that not only the algorithm detected single outliers, but also clustered outliers with different densities have been detected.

The figure shows direct result of the algorithm on the data set. However in some cases it might happen that some cluster of outliers denser than the minimum inlier size exist in the data set

³ETH Sternwarte in Zurich, an astronomical observatory planned and constructed by the two ETH-Professors Gottfried Semper (Architecture) and Rudolf Wolf (Astronomy and Mathematics) from 1859 to 1864

⁴<http://www.faro.com>

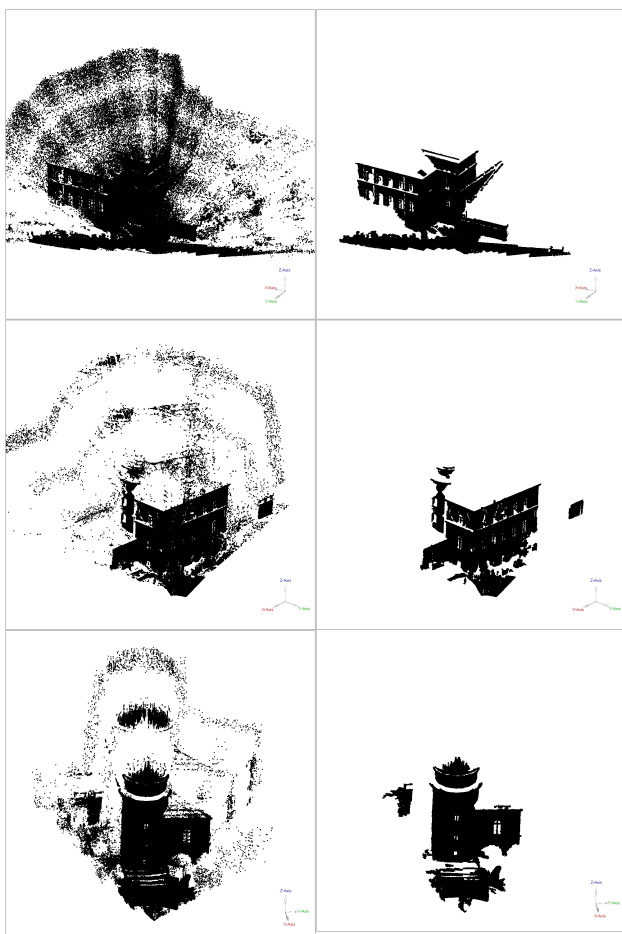


Figure 4: Results of applying the proposed outlier detection algorithm on some scans of the Sternwarte building which are captured by Faro laser scanner. Left column shows 3 different raw point clouds and the right column shows the cleaned point clouds after applying the algorithm.

which the algorithm consider them as inlier. This happens specially in case there are some real objects on the scene further than the main object that has to be measured. In that case detecting those objects as outliers is beyond the potential of the algorithm and needs some further information other than the point cloud itself. User interaction to determine if the cluster is an outlier or an object is required. The result of the algorithm seems quite handy again; User just needs to select a cluster to remove the whole outlier cluster and comparing to the case that the user has to remove the points of the outlier cluster separately, the user saves time for editing.

5 CONCLUSIONS AND FUTURE WORK

Detecting outliers in laser scanner point cloud using a hierarchical algorithm is proposed and investigated in this paper. The algorithm approaches in two stages. In the first stage it removes relatively large scale erroneous measurements and in the second phase it detects and removes the outliers that might not be as large as the first ones but according to the scanned object surfaces they are considered as wrong measurements. The algorithm has unconstrained behavior to the preliminary knowledge of the scanned scene and it does not suffer from the varying density of the points. The algorithm efficiency is assessed by a test on a simulated point cloud, which contained single and clustered outliers. The assessment is done with respect to a manual separation

of outlier/inlier points. The α -error and β -error (type I and II errors) are estimated and the results show that most of the detected outliers are really outliers according to the definition of the outliers (Hawkins, 1980). In addition some examples in terrestrial laser scanner point clouds are presented and the behavior of the algorithm on the data sets are shown and discussed. Results show that the algorithm detects single and even clustered outliers almost without user interaction. Also, in case that the user editing is required, the result of the algorithm provides easier editing procedure due to the selection of point clusters rather than individual points. Test of the algorithm on airborne laser scanner data set is another challenge that the author is currently working on.

ACKNOWLEDGMENTS

This research was partially supported by the Ministry of Science, Research and Technology (MSRT) of IRAN. The author appreciates the cooperation of Faro company, who provided the author a laser scanner for measurements.

REFERENCES

- Adamy, U., Giesen, J. and John, M., 2000. New techniques for topologically correct surface reconstruction. *IEEE Visualization 2000* pp. 373–380.
- Attene, M. and Spagnuolo, M., 2000. Automatic surface reconstruction from point sets in space. *Computer Graphics Forum (Proc. of EUROGRAPHICS '00)* 19(3), pp. 457–465.
- Aupetit, M., 2003. High-dimensional labeled data analysis with gabriel graphs. *ESANN'2003 proceedings - European Symposium on Artificial Neural Networks (ISBN 2-930307-03-X)*, pp. 21–26.
- Barnett, V. and Lewis, T., 1994. *Outliers in Statistical Data*. John Wiley and Sons, Inc., Hoboken, New Jersey.
- Breunig, M., Kriegel, H., Ng, R. and Sander, J., 2000. Lof: Identifying density-based local outliers. In *Proc. ACM SIGMOD Conf* p. 93104.
- Gabriel, K. R. and Sokal, R. R., 1969. A new statistical approach to geographic variation analysis. *Systematic Zoology* 18, pp. 259–278.
- Hawkins, D., 1980. *Identification of Outliers*. Chapman and Hall, London.
- Jain, A., Murty, M. and Flynn, P., 1999. Data clustering: A review. *acm computing surveys*. *ACM Computing Surveys* 31(3), pp. 264323.
- Johnson, T., Kwok, I. and Ng, R., 1998. Fast computation of 2-dimensional depth contours. *Proc. KDD 1998* p. 224228.
- Knorr, E., Ng, R. and Tucakov, V., 2000. Distance-based outliers: Algorithms and applications. *VLDB Journal* 8, pp. 237253.
- Marchette, D. J., 2004. *Random Graphs for Statistical Pattern Recognition*. John Wiley and Sons, Inc., Hoboken, New Jersey, ISBN 0471221767.
- Papadimitriou, S., Hiroyuki, K., Gibbons, P. B. and Faloutsos, C., 2002. Loci: Fast outlier detection using the local correlation integral. Intel Corporation, IRP-TR-02-09.
- Rousseeuw, P. and Leroy, A., 1987. *Robust Regression and Outlier Detection*. John Wiley and Sons, Inc., Hoboken, New Jersey.

Sithole, G., 2005. Segmentation and Classification of Airborne Laser Scanner Data. Ph.D. Thesis. Publications on Geodesy, 59. Publication of Netherlands Geodetic Commission, ISBN 90 6132 292 8.

Sotoodeh, S., 2006. Outlier detection in laser scanner point clouds. International Society of Photogrammetry and Remote Sensing.

Vanicek, P. and Krakiwsky, E., 1982. Geodesy: The Concepts. University of New Brunswick, Canada, ISBN 0-444-86149-1.

Veltkamp, R., 1994. Closed Object Boundaries from Scattered Points. Lecture Notes in Computer Science 885, Springer, ISBN 3-540-58808-6.

Zahn, C. T., 1971. Graph theoretical methods for detecting and describing gestalt clusters. IEEE transactions on Computers 20(1), pp. 68–86.

ESTIMATION OF CARBON STOCKS IN NEW ZEALAND PLANTED FORESTS USING AIRBORNE SCANNING LIDAR

P.R. Stephens¹, P. J. Watt², D. Loubser¹, A. Haywood³, M.O. Kimberley⁴

¹ Ministry for the Environment, PO Box 10362, Wellington, New Zealand – (Peter.Stephens, David.Loubser)@mfe.govt.nz

² Pöyry Forest Industry, PO Box 105891, Auckland, New Zealand – pete.watt@poyry.com

³ Pöyry Forest Industry, Box 22, 437 St. Kilda Road, Melbourne, Australia – andrew.haywood@poyry.com

⁴ Forest Research Institute, Private Bag 3020, Rotorua, New Zealand – mark.kimberley@ensisjv.com

KEY WORDS: Kyoto Protocol, forest inventory, sampling, carbon models

ABSTRACT:

To meet obligations under Article 3.3 of the Kyoto Protocol, New Zealand is required to estimate, in an unbiased manner, forest carbon stock change, over the Protocol's first commitment period (2008-2012). New Zealand has three categories of forest, namely: natural forest; forests planted prior to 1990; and forests planted in non-forest land after 1990. Carbon credits can be earned from net carbon accumulated in the last forest category: these forests are referred to as 'Kyoto forests'. However, field access to these Kyoto forests for sampling is not guaranteed, and a plot-based forest carbon inventory system, which relies on the use of airborne scanning LiDAR, was therefore developed. Circular plots, 0.06 ha in area, will be located within these forests on a systematic 4 km grid. This paper describes investigations to confirm the relationship at the plot scale between LiDAR variables and (a) forest carbon, and (b) the key inputs (namely height, basal area, age, and silvicultural regime) to a New Zealand-specific forest growth model. The study has demonstrated that airborne scanning LiDAR provides an alternative approach to estimate carbon stock change for the first commitment period of the Kyoto Protocol, and can provide inputs to forest growth and carbon models enabling forecasts of carbon sequestration beyond 2012. The paper also describes some considerations for an operational forest carbon inventory system which will be implemented in early 2008.

1. INTRODUCTION

New Zealand is a signatory to the Kyoto Protocol and the United Nations Framework Convention on Climate Change. A requirement under Article 3.3 of the Protocol is annual reporting of carbon stock changes arising from land use, land-use change and forestry (LULUCF) activities. Reporting is required for the Protocol's first commitment period, from 2008 to 2012. Good Practice Guidance for LULUCF activities requires carbon stock changes to be estimated in an unbiased, transparent, and consistent manner. Further, uncertainties must be determined and these are required to be reduced over time.

To meet LULUCF reporting requirements, New Zealand will be classifying forests into three categories: natural forest; forests planted prior to 1990; and forests planted after 1990 into non-forest land. The latter category is referred to as 'Kyoto forests'. Forests to be measured by New Zealand under the Protocol have been selected by the following parameters: minimum area of 1 ha; at least 30 % canopy cover; at least 5 m in height; and a width of 30 m. Carbon credits (net carbon stock change) derived from Kyoto forests over the first commitment period can then be used to either offset greenhouse gas emissions and/or for carbon trading. New Zealand planted forests are comprised predominantly (89 %) of radiata pine (*Pinus radiata*), with the remainder made up of other species, mostly (6 %) Douglas-fir (*Pseudotsuga menziesii*) (MAF, 2006).

A plot-based forest inventory system has been developed for Kyoto forests. Circular plots, 0.06 ha in area, will be located within these forests on a systematic 4 km grid across New Zealand. Field access to the mostly privately-owned Kyoto forests is not guaranteed. Accordingly, airborne scanning Light Detection and Ranging (LiDAR) will be used to inventory those

plots without field access. Plot measurements are then used as inputs to a New Zealand specific radiata pine growth model, the 300 Index (Kimberley et al., 2005) and a carbon allocation model, called C_Change (Beets et al., 1999). These two models can be linked, with the growth model used to parameterise the carbon allocation model. Under the Kyoto Protocol the four biomass carbon pools that must be reported are aboveground biomass, belowground biomass, dead wood, and litter. The amount of carbon in each of the four biomass carbon pools, at any stage of tree growth and stand development, is determined by running these two linked models.

In recent years researchers have published a wide range of methods using remotely-sensed data to help identify forest type and forest structure. Much of this work has been focused on mapping at a small scale using satellite imagery. New digital metric cameras and airborne LiDAR scanning instruments allow forest information to be measured in three dimensions with precision over moderately large areas at low unit cost. In some countries the data derived from digital airborne surveys and/or scanning LiDAR are being used (Næsset, 2002; Holmgren and Wallerman, 2006).

Airborne LiDAR has been studied for its application in forestry since 1978. However, it is only in recent years that the combination of global positioning systems (GPS), inertial navigation systems and improvements in post-processing capabilities have allowed the scanning LiDAR and digital camera technology to progress to operational use (Næsset, 2002; Nilsson, 1996; Watt, 2005).

This study was undertaken to determine the potential of airborne scanning LiDAR to determine forest characteristics at

the plot scale (Watt and Haywood, 2007a). The criteria used to test the potential of airborne scanning LiDAR included accuracy with which the key inputs to the 300 Index growth model could be determined, and the accuracy of predicting total carbon at the inventory plot scale. The key inputs to this growth model include: mean top height; basal area; tree age; and silvicultural regime (stocking (trees per ha), pruning, and thinning). Mean top height is the mean height of the 100 largest diameter stems per ha, and its method of calculation is described by Dunlop (1995). Mean top height is derived from plot tree total heights and stem diameters measured in the field.

2. MATERIALS

2.1 Study Area

The study was located in the central area of the North Island, New Zealand (39° S, 176° E) and consisted of both planted forest inventory plots and experimental trial plots for which we had unrestricted field access. Field and LiDAR data were collected between August and October 2006. The forests in these plots were representative of the radiata pine dominated forests in New Zealand.

2.2 Field Plot Data and Carbon Stocks

To determine how well LiDAR could predict inputs to the growth model, 121 plots were used ranging in size from 0.04 to 0.245 ha, and arrangement: circular, square and/or rectangular. The circular plots had been measured in 4 plot clusters (a central plot with three satellite plots within 35 m of the central plot), while the square and rectangular plots were generally measured as part of existing experiments. Measurements recorded for each plot included: age; stocking; tree diameter at breast height; tree heights; and pruned height. Radiata pine plantations occurred in 117 of these plots. A summary of the field measurements and statistics is provided in Table 1.

Field plot centres were located using a 12-channel differential GPS. The positional accuracy of the survey is expected to be within ± 3 m. In a majority of plots individual tree locations were also recorded in relation to the plot centre.

	Mean	SD	Median	Min	Max
Top Height (m)	22.9	8.6	22.7	2.8	39.1
Basal Area (m ² /ha)	33.3	13.6	35.9	0.4	62.0
Stocking (trees/ha)	468	446	468	81	4435
Age (years)	16.1	5.5	19	4	26

Table 1. Summary of plot statistics ($n=121$).

To determine the accuracy of LiDAR variables to predict total carbon per plot, 140 plots were used. Thirty six Kyoto forest radiata pine plantation plots with a pasture land-use history were added to the original (121) plot set, and 17 of the original plots, comprised of very young trees, were excluded. The total carbon for each of the 140 plots was determined by using field measured and derived inputs to the 300 Index growth model. The mean total carbon for the 140 plots was 117 t/ha, with a range from 36 - 261 t/ha.

2.3 LiDAR and Photographic Data

The LiDAR data were acquired using a small footprint (0.2 m) Optech ALTM 3100EA system at 8-10 returns/m². The 3100EA system is capable of recording the return time of up to four pulses, the first is usually reflected from the top of the canopy and intermediate pulses from the lower canopy or ground. Aerial photographic data were captured, for reference only, using a natural colour Rollei AIC medium format digital camera. These data had a pixel size corresponding to 20 cm on the ground.

3. METHODS

3.1 LiDAR Data Analysis

The analysis of the LiDAR data involved a five-stage process, as listed below.

1. Calculation of LiDAR plot-level variables, such as height percentiles and coefficient of variation of above ground pulse responses. LiDAR data were also used to determine ground height within the plots.
2. Exploratory analysis of the two datasets - field measurements and LiDAR data - to investigate their underlying data structure.
3. Generation, using bivariate and multiple regression methods, of relationships at plot level between field measurements (mean top height, stocking, and basal area) and total carbon per plot to LiDAR-derived variables.
4. Determination of stocking using an individual tree detection method.
5. Progressive decimation of the number of LiDAR returns on the ability of LiDAR to predict top height and basal area at the plot level.

3.2 Variables Derived from LiDAR Data

The following variables were calculated from the LiDAR data and extracted over co-located field plots for quantitative analysis: LiDAR height percentiles; mean intensity percentiles; standard deviation of laser dispersals; percentage of ground returns; coefficient of variation; skewness and kurtosis.

LiDAR height percentiles provide information on the structure of the forest canopy at different height levels. Using the LiDAR data the pulses above 0.5 m were divided into quantiles corresponding to every 10th percentile from the 10th to the 100th, as well as the 5th, 95th and 99th percentiles. The 0.5 m was used as a threshold to account for undulations in terrain. This provided 13 variables of an average LiDAR canopy height by percentile.

Laser intensity, the intensity of each return pulse (sometimes referred to as laser amplitude), represents this reflected energy and provides a concentrated measurement of the object's reflectance unaffected by shadows or occlusions. This reflectance may vary based on the reflectance properties and porosity of the targeted material, path length and incidence angle of the pulse. Accordingly, for this study the data are regarded as uncalibrated, and is only used as a relative measure of intensity. For each plot the mean intensity for each of the 13 height percentiles was calculated.

The standard deviation of laser dispersals provides a simple measurement of the variation or dispersal within the laser height distribution of each field measurement plot.

The percentage of ground returns (*pczero*) provides a measure of canopy density, and is calculated by dividing the sum of all above ground returns by ground observations with height values below 0.5 m by the total number of returns. All returns above this threshold are considered to be canopy hits. Areas with large numbers of ground returns will be those with sparser, more open canopies.

The coefficient of variation (C_V) summarises the relative variation, or dispersion, of the LiDAR height distribution within each sample plot. It is the ratio of standard deviation and mean, and is expressed as a percentage. As a measure of crown density, higher C_V values indicate sparse, open canopies and low C_V values dense, closed canopies (e.g. <20%). The inclusion of C_V has proven useful to other researchers for estimating basal area, volume and biomass (Næsset, 1997; Nelson et al., 1997; Næsset & Økland, 2002).

Skewness (*skew*) and kurtosis (*kurt*) of LiDAR height distribution also provide measures of canopy structure and density. If returns from the forest canopy only are considered, then as trees increase in height and the canopy develops, skewness and kurtosis of the laser height distribution change.

3.3 Exploratory Data Analysis

This analysis was used to explore, organise and summarise patterns in the LiDAR data, to explain variation and strength of relationships between the LiDAR-derived variables. Firstly, computation of summary statistics (Table 1) and the exploration of the distributional properties of all variables using histograms was undertaken. This was important to both detect and remove errors in the dataset and to identify factors such as outliers (due to uncertainty in location of field plots) that may potentially influence any modelling. Secondly, the correlation between each variable within the datasets was calculated as an initial step to the identification of potential relationships.

3.4 Regression Modelling

Regression equations were fitted to predict five forest structural variables, namely: top height; basal area; stocking; age; and total carbon. LiDAR data from the 117 radiata pine plots were used to calculate the predictor variables in these regression equations. Eight types of predictor variables were used in this analysis. These are: mean LiDAR height by height percentile; mean intensity by height percentile; standard deviation of LiDAR dispersion; percentage of ground returns (*pczero*); reciprocal of *pczero* (*pcveg*); coefficient of variation (C_V); skewness (*skew*); and kurtosis (*kurt*).

Two regression modelling approaches were used given the relationships between the datasets. These approaches were bivariate (for top height) and multiple regression (for basal area, stocking, age, and total carbon).

Bivariate regression uses the different LiDAR derived data individually as predictor variables for the estimation of the structural parameters. For each variable, the laser height percentile with the highest R^2 and lowest residual mean square (RMS) error values was used. Selection was guided first by the R^2 and then RMS values. This approach was only applied to top height, as previous studies showed that although bivariate regression worked well with top height, it would not be sufficient for the estimation of the other forest structural parameters (Donoghue and Watt, 2006; Watt and Haywood, 2006).

Multiple regression analysis was conducted to determine if further variation in the models could be explained by the inclusion of LiDAR-derived measures of intensity and canopy structure/density.

3.5 Progressive decimation of LiDAR returns

To test the sensitivity of the relationships to changes in LiDAR point density, returns classed as vegetation and ground data surrounding the plots were progressively decimated (reduced in number) using a randomised sampling routine (Watt and Haywood, 2007b). A ground surface model was generated for the area around each plot cluster for each iteration. It is necessary to process an area larger than the plot extent to ensure that there are an adequate number of LiDAR ground returns to generate the ground surface model. Using the surface model as a reference, relative height of each LiDAR return above the ground was calculated for the area in and surrounding the plot.

The impact of progressively reducing the number of laser returns on regression model error was tested using tenfold cross-validation. In tenfold cross validation each dataset is divided into 10 subsets of approximately equal size; the model is re-run 10 times, each time leaving out one of the subsets and utilising it for testing the model. The sample error is then calculated each time and averaged to obtain an estimate of the true error. For each run the 'optimal model' was selected measured in terms of the model with the lowest RMS error.

3.6 Automatic Tree Detection

An individual tree detection algorithm was also used as a method for determining tree stocking. The algorithm uses canopy returns to detect individual tree crowns, and is based on the work conducted by Holmgren and Wallerman (2006). The algorithm was evaluated over 10 stands with the accuracy of the detection compared plot-level stocking.

4. RESULTS

4.1 Top Height Prediction Using LiDAR Percentiles

The percentile height with highest R^2 and lowest RMS error was selected as the predictor for estimation of top height. In this case, laser height values corresponding to the 70th percentile (*p70*) were used. Figure 1 illustrates there is a strong linear relationship ($R^2 = 0.96$) between the 70th height percentile (*p70*) and field-measured top height.

With an R^2 of 0.96 using a single variable it is clear that a simple model that uses a single height percentile is the most effective approach to a prediction of top height. Canopy density variables did not add any additional value to the predictive model in terms of explaining the remaining variation.

4.2 Basal Area Prediction Using LiDAR Data

Multiple regression showed that none of the intensity measurements were significant (with $p > 0.05$). Accordingly, the 30th height percentile (*p30*) measurement and skewness (*skew*) were the only variables included in the model. This model had an R^2 of 0.66 with an RMS error of 8.02 m² (25%). Figure 2 shows the relationship between basal area and the two significant variables (*p30* and *skew*). The 30th height percentile

is positively correlated with basal area, while skewness is negatively correlated.

Figure 2 shows that there are no strong outliers in the dataset causing undue influence on the regression. There are no major patterns or structure in the residuals, which indicates that the model predicts basal area reasonably well at both high and low basal area.

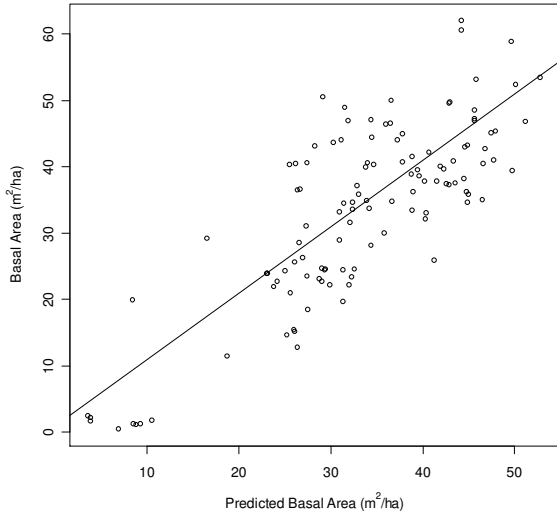


Figure 1. Top height against LiDAR 70th height percentile (*p70*) ($n=117$).

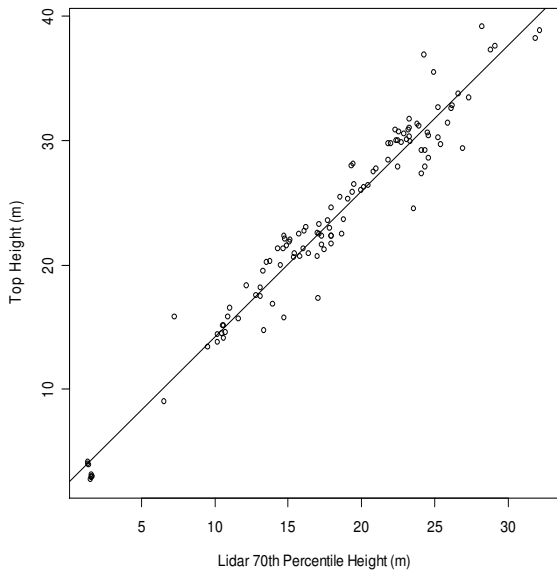


Figure 2. LiDAR-derived basal area against field measured basal area ($n=117$).

4.3 Stocking (Stems per ha)

Multiple regression analysis showed that the only models found to be significant were models with a single height percentile measurement. The model with the highest R^2 and lowest RMS error was the model that included maximum height (*p100*). The stocking model based on the highest R^2 ($R^2 = 0.26$ and RMS error = 167 stems/ha (35%)) does not provide a good relationship. There are no strong outliers in the dataset causing

undue influence on the regression. The RMS error is high, limiting its practical use for providing stocking estimates.

4.4 Tree Age Prediction Using LiDAR Percentiles

The best model for predicting age included both height and a canopy structural measure. A model that includes height (*p60*) and kurtosis (*kurt*), explained 74% of the variation with an RMS error of 2.85 years (18%).

4.5 Total Carbon Per Plot Using LiDAR Data

Bivariate regression showed that there was a strong relationship between modelled total carbon per plot and tree height. A single LiDAR canopy height percentile (*p30*) explained 71 % of the variation in modelled total carbon. When combined with canopy structure (*pczero*) there was a significant improvement with fit, with 80 % variance explained (Figure 3). It was established that if a robust measure of stocking were available for LiDAR, then 87% of the variation in modelled total carbon could be explained.

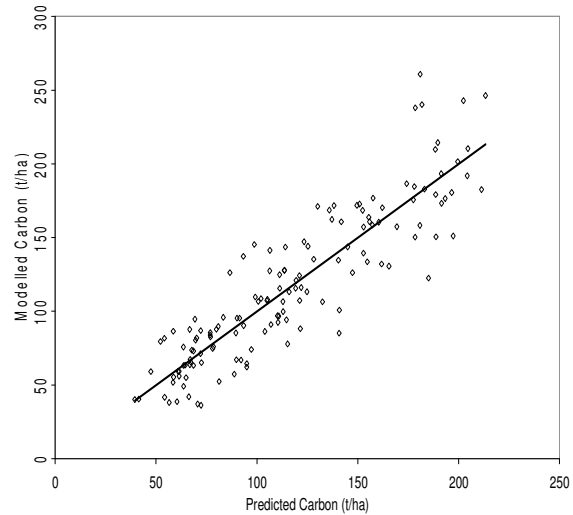


Figure 3. Modelled versus predicted carbon using LiDAR-derived inputs to the 300 Index growth model and the C_Change carbon allocation model ($n=140$).

4.6 Decimation of LiDAR Returns

Top height and basal area relationships behaved in a similar manner with the decimation model structure, remaining relatively stable throughout all runs. As expected the RMS error tends to increase as laser point density decreases with the greatest observed once densities fall below 1%, a nominal point density of 0.1 returns/m². At densities below this the models start to perform poorly.

4.7 Stocking Estimates From Automatic Tree Detection

The ability of the algorithm to detect trees depends on the laser return density, crown size, tree height and growth stage. The RMS error of the non-linear least square regression is 140 stems/ha. Overall the algorithm underestimated the number of trees, with larger errors observed in plots that contain higher numbers of trees. The proportion of detected trees saturates once stocking levels exceed 1200 stems/ha.

5. DISCUSSION

This study sought to determine the potential benefit of airborne scanning LiDAR as an input to carbon models and to estimate carbon per plot for New Zealand Kyoto forests. It is anticipated that some of the methods described in this paper will become operational and that LiDAR data will be used routinely to provide plot-based estimates of carbon as well as some key carbon model parameters. Based on work reported here, we have demonstrated that LiDAR is able to provide estimates of total carbon per plot ($R^2=0.80$), mean top height ($R^2=0.96$), basal area ($R^2=0.66$), and age ($R^2=0.74$). The following discussion compares this research against an earlier South Island study in New Zealand (Watt and Haywood, 2006) and also attempts to place the results in a wider international context.

Total carbon per plot could be predicted with a reasonable level of precision ($R^2=0.80$; RMS error = 23 t (carbon) per ha (19%)), where LiDAR derived height at the 30th percentile ($p30$) has an $R^2 = 0.71$. Predictive performance was improved by including stocking in the regression model ($R^2=0.87$; RMS error = 19 t (carbon) per ha (16%)). These results were superior to results from the earlier South Island study (Watt and Haywood, 2006), where the regression model with three LiDAR variables had an $R^2=0.59$ and an RMS error = 24 t (carbon) per ha (37%). This inferior result is likely to be due to difficulties in precisely matching ground and LiDAR plot locations, and a result of the time of LiDAR data acquisition being up to 1.5 years after the plot measurements were made for the 74 plots.

In this study a strong relationship ($R^2 = 0.96$; RMS error = 1.82 m (8%)) between mean top height and LiDAR derived heights above the 70th percentile ($p70$) was established. This result is similar to that obtained in the earlier New Zealand study (Watt and Haywood, 2006) which yielded R^2 values of ≥ 0.87 with an RMS error of ≤ 1.36 m. Again, the results from the Watt and Haywood (2006) study suggest that the linear model is relatively insensitive to LiDAR height distribution percentiles above 60%. Combined, these results agree with international findings where the accuracy of LiDAR-derived height is comparable to that of manual field survey methods (Donoghue and Watt, 2006; Næsset, 1997; Watt, 2005; Lim and Treitz, 2004). To achieve a good level of accuracy the density of laser returns must be sufficient to (a) define the underlying terrain and (b) capture variations in terms of tree crop height and spatial arrangement. Generally a survey that records at least 1 to 2 first returns/m² at a scan angle of $\leq 10^\circ$ either side of nadir should be sufficient to capture the detail required (Watt, 2005; Watt and Haywood, 2007b).

Basal area estimates based on LiDAR measurements were found to be less accurate than top height; the best model found had an R^2 of 0.66 with an RMS error of 8.02 m² (25%). The error found in this study is of a similar magnitude to that found in the earlier New Zealand study (Watt and Haywood, 2006). The field-measured basal area was found to be strongly correlated with top height ($R^2 = 0.73$). The final model included height ($p30$) and skewness. The height measure can be interpreted as being a measure of the development phase of the plot which is related directly to basal area. In European conifer-dominated forest Næsset (2002) reported R^2 values of 0.86 for basal area in southern Norway, and Lim et al. (2003) reported basal area estimates of $R^2=0.86$ in a Canadian hardwood forest.

Stocking was not reliably predicted using LiDAR measurements in this study. The RMS error is high (167 stems/ha (35%)) limiting its practical use for providing accurate estimates of tree

density. This result is in contrast to other studies where the inclusion of measures of canopy characteristics derived from the LiDAR height distribution, in combination with selected LiDAR height percentiles, have proven useful for estimating stocking (Næsset, 2002). One explanation is that after stocking has changed (a standard silvicultural treatment) in New Zealand conifer forests the tree crowns expand to fill the canopy gaps and so while the stocking may change the distribution of LiDAR points may be similar to areas that have received no treatment once the canopy has closed.

The evaluation of the single tree detection algorithm shows that the RMS error is marginally lower than the plot-based method. Overall the algorithm provides better results in stands less than 1200 stems/ha. Above this stocking level the method saturated, especially in areas with coalescing crowns. To measure higher density stands it would be necessary to sharpen the tree top extraction algorithm. The detection rate would probably also improve if a higher density laser dataset was used. However, according to the simulations, the detection rate would still decrease as a function of stem density even if a high density laser dataset (20 returns/m²) were available. Therefore, it would be necessary to have a method for the estimation of the number of sub-dominant or suppressed trees.

Estimates of age were improved by including more than just LiDAR-derived height. A model that includes height ($p60$) and kurtosis (*kurt*) explains 74% of the variation with RMS error of 2.85 years (18%). Here, kurtosis provides a measure of canopy permeability which is related to tree crop development stage. Both variables included in the model are uncorrelated, so assist in explaining variation associated with the prediction.

Any reduction in the point density (number of pulses/m²) of a LiDAR survey has the potential to reduce acquisition costs of data. This study evaluated for basal area and top height the effect of systematically reducing the laser point density and showed that basal area and top height estimates are stable even after 95% of the original data has been removed. This is equivalent to reducing the initial point density of 9 returns/m² to 0.5 returns/m². A plausible explanation is the simple structure of top height and basal area models, as for both, height percentiles are the most significant variables. Consequently, the models are relatively insensitive to the decimation process. These findings are similar to other research that has evaluated different laser point densities and their impact on plot-level forest predictions (Næsset, 2002; Goodwin et al., 2006). Also of relevance to this work is that little change is observed in predictions if pulse density is kept constant and footprint size (0.2 to 0.6 m) and platform altitude are increased (Næsset, 2002; Goodwin et al., 2006).

While silvicultural status was not assessed in this study, an earlier study in New Zealand (Watt and Haywood, 2006) noted that for Kyoto forest plots, prune heights can be determined by visual assessment of LiDAR data. If automatic methods do not show promise in determining this aspect of management, then visual methods could be employed.

6. CONCLUSIONS

Where field access to forest plots is not possible, the study has demonstrated that airborne scanning LiDAR provides an alternative operational approach to estimate, at the plot-level, total carbon change for the first commitment period of the Kyoto Protocol. Forest top height, basal area, and age can be

determined with acceptable accuracy. It is expected that either visual assessment of either digital photography and/or LiDAR data can address the stocking (stems per ha) issue.

This study suggests that laser point density can be taken as low as 0.5 to 1 returns/m² without unduly affecting predictions of basal area and top height. Assessment of stocking using laser returns will require a much higher density. Given there will be variation in the number of returns across a survey area (in the study the range was 3-19 returns/m² due to overlapping LiDAR swaths), it is prudent to acquire data at more than 4 returns/m². This should provide a margin of safety and reduce the possibility of plots being excluded from the analysis due to insufficient laser returns, and to support use of LiDAR data to assess stocking should visual assessment of photographic imagery not be possible.

The ability of LiDAR to provide inputs to the linked forest growth and carbon models with some degree of accuracy will assist in forecasting carbon sequestration beyond 2012.

Operationally, adequate measurements to estimate carbon stock change for the first commitment period of the Kyoto Protocol could be achieved by surveying the Kyoto forest plot network located on a 4 km grid in 2008 and in 2012. The Kyoto forest plots will be circular, and 0.06 ha in area. During this five year period, as more data are acquired, the regression relationship between LiDAR variables and carbon per plot will be reviewed and improved. This will enable more accurate relationships to be applied to past plot data, which subsequently will lead to updated carbon assessments and a reduction in uncertainties, as is required under the Kyoto Protocol.

7. REFERENCES

- Beets, P.N., Robertson, K.A., Ford-Robertson, J.B., Gordon, J., and Maclaren, J.P., 1999. Description and validation of C_Change: A model for simulating carbon content in managed *Pinus Radiata* stands. *New Zealand Journal of Forestry Science*, 29(3), pp. 409-427.
- Donoghue, D.N.M., and Watt, P.J., 2006. Using LiDAR to compare forest height estimates from IKONOS and Landsat ETM+ data in Sitka spruce plantation forests. *International Journal of Remote Sensing*, 27(11), pp. 2161-2175.
- Dunlop, J., 1995. Permanent sample plot system User Manual. New Zealand Forest Research Institute Bulletin No. 187, Rotorua, New Zealand.
- Kimberly, M.O., West, G.G., Dean, M.G., Knowles, L.R., 2005. The 300 Index – a volume productivity index for radiata pine. *New Zealand Journal of Forestry*, 50, pp. 13-18.
- Lim, K., Treitz, P., Wulder, M., St-Onge, B., Flood, M., 2003. LiDAR remote sensing of forest structure. *Progress In Physical Geography*, 27(1), pp. 88-106.
- Lim, K.S., and Treitz, P.M., 2004. Estimation of above ground forest biomass from airborne discrete return laser scanner data using canopy-based quantile estimators. *Scandinavian Journal of Forest Research*, 19(6), pp. 558-570.
- Goodwin, N. R., Coops, N.C., Culvenor, D.S., 2006. Assessment of forest structure with airborne LiDAR and the effects of platform altitude. *Remote Sensing of Environment*, 103(2), pp. 140-152.
- Holmgren, J., and Wallerman, J., 2006. Estimation of tree size distribution by combining vertical and horizontal distribution of LiDAR measurements with extraction of individual trees. In: *Proceedings, EARSeL ISPRS Workshop, 3D Remote Sensing in Forestry*, Vienna, pp. 157-163.
- Næsset, E., 1997. Estimating timber volume of forest stands using airborne laser scanner data. *Remote Sensing of Environment*, 61(2), pp.246-253.
- Næsset, E., and Økland, T., 2002. Estimating tree height and tree crown properties using airborne scanning laser in a boreal nature reserve. *Remote Sensing of Environment*, 79(1), pp. 105-115.
- MAF, 2006: A National Exotic Forest Description as at 1 April 2005. Edition 22, Ministry of Agriculture and Forestry, Wellington, New Zealand.
- Næsset, E., 2002. Predicting forest stand characteristics with airborne laser using a practical two-stage procedure and field data. *Remote Sensing of Environment*, 80, pp. 88–99.
- Nelson, R., Oderwald, R., Gregoire, T.G., 1997. Separating the ground and airborne laser sampling phases to estimate tropical forest basal area, volume, and biomass. *Remote Sensing of Environment*, 60(3), pp. 311-326.
- Nilsson, M., 1996. Estimation of tree heights and stand volume using an airborne lidar system. *Remote Sensing of Environment*, 56, pp. 1–7.
- Watt, P.J., 2005. An evaluation of LiDAR and optical satellite data for the measurement of structural attributes in British upland conifer plantation forestry. Doctoral thesis. Department of Geography, University of Durham, England.
- Watt, P.J., and Haywood, A., 2006. Evaluation of airborne scanning LiDAR generated data as input into biomass/carbon models. Pöry Forest Industry, contract report 38A08068 to Ministry for the Environment, Wellington, New Zealand.
- Watt, P.J., and Haywood, A., 2007a. Evaluation of airborne scanning LiDAR generated data as input into biomass/carbon models. Pöry Forest Industry, contract report 38A07375 to Ministry for the Environment, Wellington, New Zealand.
- Watt, P.J., and Haywood, A., 2007b. Evaluation of the impact of varying LiDAR point density on the accuracy of LiDAR-derived forest estimation models. Pöry Forest Industry, contract report 38A08467 to Ministry for the Environment, Wellington, New Zealand.

EXTRACTING STRUCTURAL CHARACTERISTICS OF DORMANT HERBACEOUS FLOODPLAIN VEGETATION FROM AIRBORNE LASER SCANNER DATA

Menno Straatsma*, Hans Middelkoop

Department of Physical Geography, Utrecht University, PO Box 80115, 3508 TC Utrecht, The Netherlands (m.straatsma, h.middelkoop)@geo.uu.nl

KEYWORDS: Floodplains, Herbaceous vegetation; Leaf-off; vegetation height; vegetation density

ABSTRACT:

To map spatial patterns of floodplain vegetation structure for hydrodynamic modelling, airborne laser scanning is a promising tool. In a test for the lower Rhine floodplain, vegetation height and density of herbaceous vegetation were measured in the field at 42 georeferenced plots of 200 m² each. Simultaneously, three airborne laser scanning (ALS) surveys were carried out in the same areas resulting in three high resolution, first pulse, small-footprint datasets. The laser data surveys differed in flying height, gain setting and laser diode age. Laser points were labelled as either vegetation or ground using three different methods: (1) a fixed threshold value, (2) a flexible threshold value based on the inflection point in the normalised height distribution, and (3) using a Gaussian distribution to separate noise in the ground surface points from vegetation. Twenty-one statistics were computed for each of the resulting point distributions, which were subsequently compared to field observations of vegetation height. Additionally, the Percentage Index (PI) was computed to relate density of vegetation points to hydrodynamic vegetation density. The vegetation height was best predicted by using the inflection method for labelling and the 95 percentile as a regressor ($R^2 = 0.74 - 0.88$). Vegetation density was best predicted using the threshold method for labelling and the PI as a predictor ($R^2 = 0.51$). The results of vegetation height prediction were found to depend on the combined effect of flying height, gain setting or laser diode age. We conclude that high resolution ALS data can be used to estimate vegetation height and density of herbaceous vegetation in winter condition, but field reference data remains necessary for calibration until a standard measure of sensitivity is supplied together with the laser data.

1. INTRODUCTION

In response to the increased awareness of the socio-economic importance of river flooding in the past decades, considerable effort has been undertaken in recent years in the development of hydrodynamic models of overbank flow to predict extreme flood water levels for the design of flood defence structures. Hydrodynamic roughness of the floodplain surface is one of the key parameters of these models, and depends to a large extent on vegetation height and density (Baptist, 2005). Vegetation density is the projected plant area in the direction of the flow per unit volume (m²/m³ or m⁻¹). For cylindrical vegetation, this equals the product of number of stems or stalks per unit area multiplied by the average stem diameter. Traditional methods to map vegetation patterns within the floodplain are based on classification of vegetation units or a uniform roughness is applied to the whole floodplain area. This leads to a considerable loss of within-class variation. There is thus a need for a fast and adequate approach to assess vegetation structure of floodplain surfaces.

Airborne laser scanning (ALS) provides information on the distribution of vegetation directly, and therefore has been used extensively in forestry surveys to estimate forest characteristics (Straatsma and Middelkoop, 2006; Lim et al., 2003). It has been used to map vegetation *height* in floodplains as well, but only in summer when vegetation was in leaf-on condition (Davenport et al., 2000; Cobby et al., 2001; Hopkinson et al., 2004; Mason et al., 2003). However, the portability of the established relations in these studies was low. Moreover, in the Netherlands most floods occur in winter and relations derived for summer vegetation may therefore be unrepresentative. No studies were found on the extraction of vegetation *density* of herbaceous vegetation. The main goal of this study was to estimate vegetation height and density of dormant herbaceous floodplain vegetation on a field plot level using ALS data and assess the

influence of flying height and amplification of the return signal at the receiver of the laser scanner.

2. MATERIALS AND METHODS

2.1 Study area and field measurements

This study is based on laser data collected in three floodplain sections of the distributaries of the River Rhine in The Netherlands: 'Duursche Waarden' floodplain (DW) along the right bank of the River IJssel, and the 'Afferdensche en Deestsche Waarden' (ADW) and the 'Gamerensche Waarden' (GW) floodplains along the left bank of the River Waal. Vegetation consisted of hardwood and softwood forest and shrubs, but is dominated by herbaceous vegetation. Vegetation is characterized by a heterogeneous pattern of vegetation types and structure. Herbaceous vegetation consists mostly of sedge [*Carex hirta* L.], sorrel [*Rumex obtusifolius* L.], nettle [*Urtica dioica* L.], thistle [*Cirsium arvense* L.] and clover [*Trifolium repens* L.].

We measured vegetation height and density in 42 field plots of homogeneous vegetation: 12 plots in the DW and ADW floodplain in March 2001, and 30 plots in the GW floodplain in March 2003. Field measurements were carried out simultaneously with the ALS survey. The plots were geolocated using a Garmin GPS12 resulting in a horizontal accuracy of 5 meter.

2.2 Laser scanning data

The laser data were acquired by Fugro-Inpark using the FLI-MAP system. FLI-MAP, Fast Laser Imaging and Mapping Airborne Platform, is a first-pulse scanning laser range finder combined with a dGPS and an Inertial Navigation System for

Table 1. Metadata for the three laser scanning campaigns

Acquisition Time	Floodplain location	scan angle	no. of sensors	sensor age	Flying height	Gain	point density	Flight strips
March 2001	DWADW	$\pm 30^\circ$	1	old	80 m	100%	12 pts/m ²	Single
March 2003a	GWhigh	$\pm 30^\circ$	2	new	80 m	80%	75 pts/m ²	Double
March 2003b	GWlow	$\pm 30^\circ$	2	new	55 m	100%	60 pts/m ²	Single

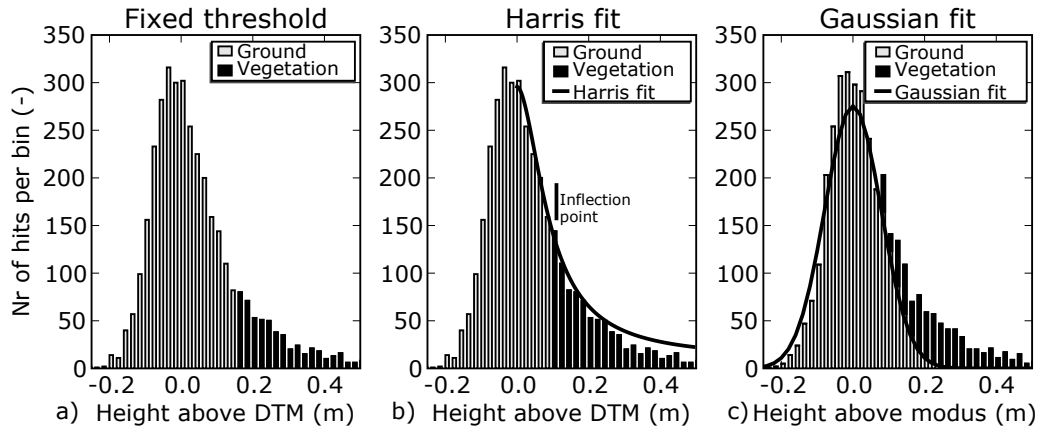


Figure 1. Labelling of vegetation point (black bars) and ground points (grey bars); a) threshold value of 0.15 m, b) inflection point, c) difference between Gaussian fit and point distribution.

positioning. FLI-MAP has an additional option to change the gain setting. The gain is the amount of amplification of the return signal before it is converted to a digital signal. Surveyors may increase the gain to compensate for the declining emission of energy due to ageing of the laser diode. Table 1 summarizes the characteristics of the three laser scanning campaigns carried out in three floodplain sections in the Rhine distributaries. The laser data collected in 2001 in the 'Duursche Waarden' and the 'Afferdensche en Deestse Waarden' floodplains is referred to as 'DWADW' dataset. Between 2001 and 2003, Fugro-Inpark added a second laser range finder to FLI-MAP, resulting in a doubling of the data collection rate and a re-orientation of the scanners. Instead of one nadir looking scanner, the two scanners were facing 7° forward and backwards to decrease the number of occlusions in built-up areas. With the new FLI-MAP configuration two datasets were collected in the 'Gamerensche Waard' floodplain in 2003. One was acquired from a height of about 80 m and with normal gain setting of the receiver, resulting in the 'GWhigh' dataset, the second from a minimum height of 55 m and with the maximum gain, called the 'GWlow' dataset. The GWhigh dataset covers the entire GW floodplain, while each flight line was flown twice to increase the point density resulting in a point density of 75 points/m². The GWlow dataset only covers 10 field plots. The three datasets enable the evaluation of the resulting regression equations to estimate vegetation height, which are influenced by the different flight parameters (table 1).

2.3 DTM extraction and labelling

For the determination of the vegetation height, the effect of the undulations of the terrain was eliminated. We constructed a Digital Terrain Model (DTM) for each plot using iterative residual analysis based on a simplified version of the method of

Kraus and Pfeifer (1998). In each step, a surface was computed as a local second order trend surface in a moving window. The window radius was 1.5 m to ensure enough points are available for a robust fit. The residual distance to this surface was computed for each point. Points with positive residuals are likely to be vegetation points. Since the range of values for an unvegetated, flat surface was computed and proved to be approximately 30 cm, a simple weight function was applied to compute the surface in the next iteration: points with a residual value of more than 15 cm were excluded from further analysis in the DTM processing. With the remaining points a new DTM surface was computed. Iterations were continued until all points had residuals less than 15 cm. The final DTM was a smooth surface running through the middle of these ground points. Heights relative to the DTM were used in subsequent computations.

In a second step, a detailed study was carried out to decide which points should be labelled as vegetation. Three different methods were evaluated: (1) a threshold method, (2) an inflection method, and (3) a Gaussian method. The first method is based on a fixed threshold value above the DTM, the other two are based on histogram analysis of normalised heights. For the threshold method, we used 15 cm above the DTM as a threshold (figure 1a), similar to the DTM filtering setting. For the second and third method laser points were binned in 2 cm vertical bins. Narrower bin intervals led to very spiky histograms, wider intervals to a loss of detail. The vertical point distribution was considered as a combination of a noise distribution of ground points and a uniform distribution of vegetation points. The inflection method finds the point of maximum concave-up curvature in the upper limb of the histogram, the so-called inflection point. The rationale behind the selection of this point as a threshold value is that the sum of

a noise distribution of the ground points and the uniform distribution of the vegetation points gives a strong concave up curvature. Any point that lies above the inflection point value is labelled as a vegetation point, all points below are ground points. To find the inflection point, a Harris function was fitted through the upper part of the histogram for each field plot (figure 1b). The Harris function is defined as:

$$y(h) = (a+b*h^c)^{-1} \quad (1)$$

where $y(h)$ is the frequency of occurrence in a bin at height h . Parameters a , b and c are estimated from a least squares fit using a minimum of 15 bins to ensure stability of the fit. The inflection point was obtained by determining the height at which the second derivative of the Harris function reaches the maximum value. The height of the inflection point in the example is 0.09 m (figure 1b). The Gaussian method fits a Gaussian curve to the histogram. The Gauss curve is defined as:

$$p(h) = (2\pi\sigma)^{-0.5} \exp\left(-\frac{1}{2}\left(\frac{h-\mu}{\sigma}\right)^2\right) \quad (2)$$

where $p(h)$ is the frequency of noise occurrence at height h , μ is the mean, σ is the standard deviation. Fitting the Gauss curve boils down to finding the mean and standard deviation of the ground points. The mean of all points in the plot however also considers the vegetation points. Therefore, we used the mode of the distribution instead of the mean to estimate μ . The disadvantage of the mode is that the data have to be binned which introduces a dependence on the choice of the bin boundaries. Moreover, the mode can be undetermined. To counteract this effect we used the weighted mode, the average of the seven most frequent values in the point distribution, weighed by frequency. The standard deviation was based on the points lower than the weighted mode. The Gauss curve was then scaled by the product of twice the number observations below the weighted mode and the bin width (figure 1c). The difference between the histogram values and the fitted Gauss curve in the range above one standard deviation above the mode provided the number of points per bin that were assumed to represent vegetation. In each bin, points were labelled randomly as vegetation up to the predicted number of vegetation points. This ensured a spatially random distribution of the vegetation points.

2.4 Normalized point height distribution and comparison with field data

The three methods, described in the previous section, result in three height distributions of vegetation points for each plot. With respect to predicting the vegetation height, each point distribution was described by 21 different statistics:

- Central tendency: mean, median, mode
- Variability: standard deviation and variance
- Shape: skewness and kurtosis
- Percentiles: D_{10} , D_{20} , ..., D_{100} + D_{95} , D_{96} , D_{97} , D_{98} , D_{99}

The observed vegetation heights in the field were subsequently compared to these statistics using correlation as an indicator of the strength of the relation. Forward stepwise linear regression was subsequently carried out to determine the strongest predictors (Wonnacott and Wonnacott, 1990). The effects of gain setting and flying height were tested using two statistical tests; a t-test on differences in means and a paired sample t-test of the D_{95} percentiles of the GWhigh and GWlow data set. Samples could be paired for the GW datasets since the same reference plots were used. To gain insight in the effect of laser

diode age and the flight parameters, the slopes of the regression models for vegetation height were compared using three Student's t-tests.

Vegetation density was predicted using the Percentage Index (PI), which computes the percentage of laser hits that fall within the height range of the vegetation ($h1$ to $h2$):

$$PI_{h1-h2} = \frac{1}{h2-h1} * \frac{N_{h1-h2}}{N_{tot}} \quad (3)$$

in which N_{h1-h2} is the number of vegetation points between height 1 and 2 above the ground surface, N_{tot} is the total number of points in the field plot including vegetation points and ground surface points. The height interval for PI is equal to the height of the vegetation. The first term in the equation is added, because higher vegetation would increase N_{h1-h2} , but does not necessarily increase the vegetation density. Ideally, $h1$ should be set to zero, and $h2$ to the maximum height of the vegetation. However, $h1$ should not include noise of the ground surface. Therefore we chose the lower limit of the vegetation point height distribution as a minimum value.

3. RESULTS

3.1 Vegetation height and density

Vegetation height in the 42 sample plots ranged from 0.26 to 1.66 m. Vegetation density varied between 0.0003 and 0.72 m^{-1} . For each plot, three different labelling methods were applied and 21 laser-derived statistics were computed. The correlations between the field vegetation heights and the laser statistics were shown in figure 2. The following parameters showed the highest correlations: (1) D_{30} for the threshold method ($r = 0.72$), (2) D_{90} to D_{98} plus the standard deviation and variance for the inflection method ($r > 0.85$), and (3) D_{70} for the Gaussian fit ($r = 0.70$).

The parameter with the highest correlation was chosen for vegetation height prediction for each labelling method. For the inflection method, a few parameters showed a high correlation. The 95 percentile was selected to maintain congruency in the selection of any additional parameters for any of the regression models, due to multicollinearity constrictions. Table 2 summarizes the regressions. Results of the prediction of vegetation density using the Percentage Index (PI) are shown as scatter plots (figure 4). The threshold and Gaussian method show a positive relation with vegetation density ($R^2 = 0.51$ and 0.49 respectively). Conversely, prediction based on the inflection labelling shows a weak negative relation ($R^2 = 0.09$). Table 3 summarizes the equations.

3.2 Effect of flying altitude and gain setting

The GWhigh and GWlow laser datasets share 10 field plots, which allowed to compare the combined effect of lower flying altitude and increased the gain setting (cf. table 1). The following tests were performed using the inflection labelling method and the D_{95} percentile:

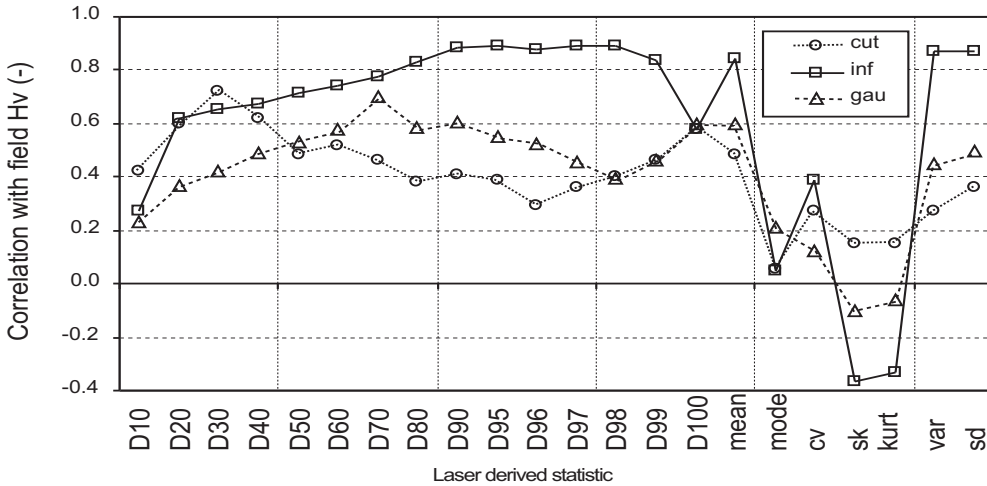


Figure 2. Effect of point labelling methods on the strength of correlation between laser-derived statistics and field vegetation heights. Dx = X percentile of the vegetation points, cv = coefficient of variation, sk = skewness, kurt = kurtosis, var = variance, sd = standard deviation

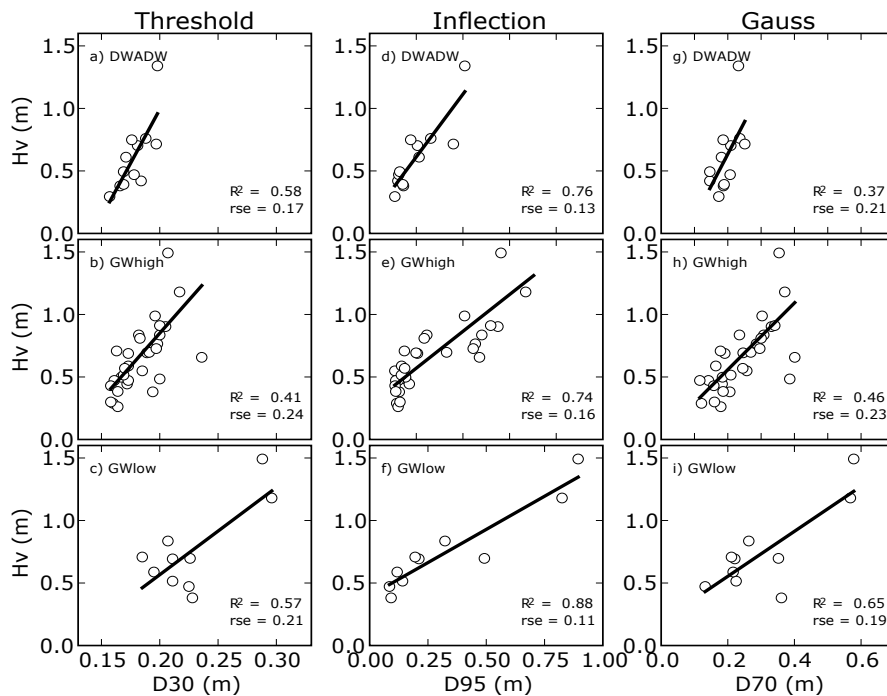


Figure 3. Scatter plots of predictions of vegetation height per dataset using three different point labelling methods: a), b), and c) threshold method, d), e) and f) inflection method, g), h) and i) Gaussian method

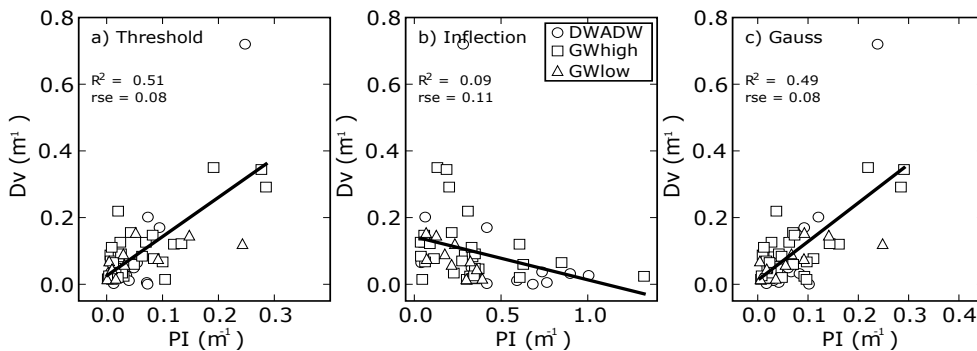


Figure 4. Scatter plots of predictions of vegetation density per dataset using three different point labelling methods: a) threshold method, b) inflection method and c) Gaussian method

Table 2. Regression equations for vegetation height

Labelling method / dataset	Regression equation	R ²	RSE (m) ^a
Threshold			
DWADW	Hv = 17.20D ₃₀ - 2.45	0.58	0.17
GWhigh	Hv = 10.57D ₃₀ - 1.26	0.41	0.24
GWlow	Hv = 6.98D ₃₀ - 0.83	0.57	0.21
Inflection			
DWADW	Hv = 2.51D ₉₅ + 0.11	0.76	0.13
GWhigh	Hv = 1.47D ₉₅ + 0.28	0.74	0.16
GWlow	Hv = 1.06D ₉₅ + 0.40	0.88	0.11
Gaussian			
DWADW	Hv = 5.13D ₇₀ - 0.39	0.37	0.21
GWhigh	Hv = 2.67D ₇₀ + 0.02	0.46	0.23
GWlow	Hv = 1.80D ₇₀ + 0.19	0.65	0.19

^a Residual Standard Error

Table 3. Regression equations for vegetation density using three different methods

	Regression equation	R ²	RSE (m ⁻¹) ^a
Threshold	Dv = 1.18PI + 0.03	0.51	0.08
Inflection	Dv = -0.13PI + 0.14	0.09	0.11
Gaussian	Dv = 1.16PI + 0.01	0.49	0.08

^a Residual Standard Error

A paired sample t-test revealed significant differences between the height of the D₉₅ percentile of the GWhigh and GWlow datasets ($\alpha = 90\%$, $p = 0.08$). These results indicate that a low flying height, combined with a high gain improves detection of the top of the vegetation.

The slope of the regression lines between laser data and observed vegetation height also indicates the ability of the laser signal to detect the top of the vegetation. A steeper slope indicates a poorer detection of the vegetation top. Figure 3 shows the regression lines for the DWADW, GWhigh and the GWlow data sets. The slope of the DWADW is steepest, and the slope of the GWlow dataset is mildest. Based on three Student's t-tests, all differences in slope were significant at the 95 % level of confidence.

4. DISCUSSION

4.1 Vegetation height and density estimation

Vegetation height of herbaceous floodplain vegetation can be predicted reliably at the plot level using high-density first-pulse airborne laser scanning data ($R^2 = 0.74$ to 0.88 using the inflection labelling method), while estimation of vegetation density is less accurate ($R^2 = 0.51$ using the threshold method). The inflection method shows the best predictions of vegetation height for all three datasets (figure 3). The threshold and the Gaussian method in general selected fewer points, and are therefore more sensitive to outliers in the height distribution. Conversely, vegetation density was predicted better by the threshold and Gaussian method (figure 4). The PI relates point density of vegetation points to hydrodynamic vegetation density. The inflection method labels more points as vegetation than the two other methods, but the PI values did not correlate well with field reference values, and are even negatively correlated. This could be caused by the height at which the vegetation density

was measured in the field, which was at least at 13 cm above the ground surface (half the minimum vegetation height). This is well above a typical inflection height of 5 cm. The threshold method performed marginally better than the Gaussian method. The inverse dependence of PI on h_2 minus h_1 (eq. 3) could lead to unrealistic values in case h_2 nears or equals h_1 . This should not be a problem for vegetation higher than 25 cm as in this study.

The quality of prediction of vegetation height in this study is similar to the results obtained in regression models for forests: Means et al. (1999), Naesset and Bjercknes (2001), and Naesset (2002) reported regression models explaining 74 to 95 percent of the variance in the field reference data of vegetation height. Similar to our study, forestry studies obtained better results for vegetation height than for parameters related to vegetation density. Given the small range in height of herbaceous floodplain vegetation, it is remarkable that the results obtained in our study are of similar quality as those obtained in forestry surveys.

Davenport et al. (2000), Cobby et al. (2001) and Hopkinson et al. (2004) studied vegetation height of low vegetation in leaf-on condition. Conversely, in our study, we predicted vegetation height of dormant herbs. This means that the vegetation signal is much weaker, due to the smaller plant surface. Still, the predictive quality of vegetation height found in this study is comparable to the studies on low vegetation in leaf-on condition. The differences found in the regression equations from this study and previous studies (Davenport et al., 2000; Cobby et al., 2001; Hopkinson et al., 2004) demonstrate that portability of the derived relations is low. It points to the need for future field reference data. A standardized empirical measure of sensitivity could be provided together with the laser data by laser scanning of artificial objects with varying reflectivity as suggested by (Wotruba et al., 2005). Further improvements are expected from a decrease in laser point accuracy. Our data showed a 4 cm standard deviation, but present day scanners show standard deviations down to 1.5 to 2 cm, which might allow mapping vegetation heights of meadows.

4.2 Effects of flight parameters; flying height, laser diode age and gain setting

The DWADW and GWhigh data sets yielded different slopes of the regression models to estimate vegetation height, which was significant at the 99.9 confidence level. The reason for this difference might be the age of the laser diode age, the calibration settings or the larger average incidence angle in the GWhigh dataset, due to the reorientation of the laser scanners between 2001 and 2003. The slope of the GWlow dataset was significantly steeper than for the GWhigh dataset. The paired sample t-test also showed significant differences between the GWhigh and GWlow datasets. Remarkably, the increase in the regression slope of the GWhigh and GWlow dataset was significant even though the field and laser data were collected on the same day. The reason for the difference in slope and 95 percentile must therefore be the combination of the reduced flying height and increased gain setting for the GWlow dataset. Together these effects result in a larger amount of energy reaching the analogue to digital converter in the laser scanner from an equally reflective object. Consequently, small objects are detected better, and the regression slopes are lower. Naesset (2004) concluded for spruce and pine forest that the effect of flying altitude is marginal and that the flying altitude can be increased by 60 % without any serious effect on the estimated stand properties. These conclusions for forests are contrary to our conclusions for herbaceous floodplain vegetation. The reason for this difference might lie in the shape and structural properties of the vegetation involved. Trees are larger and Naesset's data were collected in leaf-on conditions, which make

detectability of trees better than thin floodplain herbs, which seem at the edge of detectability. With these datasets, it is impossible to assess the influence of the individual parameters. However, as long as the parameters influencing the regression equations are unclear, field reference data will remain necessary to establish the regressions.

5. CONCLUSIONS

Laser scanning provides detailed and accurate estimates of vegetation height and to a lesser extent of vegetation density. Three different vegetation labelling methods were evaluated (threshold, inflection and Gaussian). Vegetation height estimation was most successful using the inflection method for point labelling. The 95 percentile proved the best predictor, ($R^2 = 0.74$ to 0.88). However, regression models differed significantly for datasets that were acquired with different flying height, gain, and laser diode age. The validity range for vegetation height is the height range order of 0.2 to 2 m. Vegetation density was predicted using the Percentage Index (PI), which relates vegetation point density to hydrodynamic vegetation density. The PI based on the threshold ($R^2 = 0.51$) and Gaussian ($R^2 = 0.49$) labelling method proved better estimators of vegetation density than the PI based on the inflection method ($R^2 = 0.09$). This might be caused by difference in reference heights between field and laser data. The validity range for vegetation density is in the order of 0.001 to 0.7 m^{-1} .

Because these herbs in winter are low and thin, height estimation is sensitive to the combined effect of flying height, gain setting and age of the laser diode. The common factor in these parameters is that they influence the amount of energy at the receiving end of the laser scanner. With increasing energy, the vegetation detection increases too. We conclude that airborne laser scanning data can be used to map vegetation height and density of dormant floodplain vegetation for floodplain roughness parameterization. Field observations of vegetation structure remain, however, necessary to calibrate the regression models until a standard measure of laser sensitivity is supplied together with the laser data.

ACKNOWLEDGEMENTS

This work was funded by NWO, the Netherlands Organization for Scientific Research, within the framework of the LOICZ program under contract number 01427004.

REFERENCES

Baptist, M.J., 2005. Modelling floodplain biogeomorphology, Delft Technical University, Delft, 195 pp.

Cobby, D.M., Mason, D.C. and Davenport, I.J., 2001. Image processing of airborne scanning laser altimetry data for improved river flood modeling. *ISPRS Journal of Photogrammetry and Remote Sensing*, 56: 121-138.

Davenport, I.J., Bradbury, R.B., Anderson, G.R.F., Hayman, J.R., Krebs, J.R., Mason, D.C., Wilson, J.D. and Veck, N.J., 2000. Improving bird population models using airborne remote sensing. *International Journal of Remote Sensing*, 21: 2705-2717.

Hopkinson, C., Lim, K., Chasmer, L.E., Treitz, P., Creed, I.F. and Gynan, C., 2004. Wetland grass to plantation forest - estimating vegetation height from the standard deviation of lidar frequency distributions. In: M. Thies, B. Koch, H. Spiecker and H. Weinacker (Editors), *Laser-scanners for forest and landscape assessment*. Institute for forest growth, Freiburg, Germany.

Kraus, K. and Pfeifer, N., 1998. Determination of terrain models in wooded areas with airborne laser scanner data. *ISPRS Journal of Photogrammetry and Remote Sensing*, 53: 193-203.

Lim, K., Treitz, P., Wulder, M., St-Onge, B. and Flood, M., 2003. Lidar remote sensing of forest structure. *Progress in Physical Geography*, 27: 88-106.

Mason, D.C., Cobby, D.M., Horrit, M.S. and Bates, P., 2003. Floodplain friction parameterization in two-dimensional river food models using vegetation heights derived from airborne scanning laser altimetry. *Hydrological Processes*, 17: 1711-1732.

Means, J.E., Acker, S.A., Harding, D.J., Blair, J.B., Lefsky, M.A., Cohen, W.B., Harmon, M.E. and McKee, W.A., 1999. Use of large-footprint scanning airborne lidar to estimate forest stand characteristics in the Western Cascades of Oregon. *Remote Sensing of Environment*, 67(3): 298-308.

Naesset, E., 2002. Predicting forest stand characteristics with airborne scanning laser using a practical two-stage procedure and field data. *Remote Sensing of Environment*, 80: 88-99.

Naesset, E., 2004. Effects of different flying altitudes on biophysical stand properties estimated from canopy height and density measured with a small-footprint airborne scanning laser. *Remote Sensing of Environment*, 91: 243-255.

Naesset, E. and Bjercknes, K.-O., 2001. Estimating tree heights and number of stems in young forest stands using airborne laser scanner data. *Remote Sensing of Environment*, 78: 328-340.

Straatsma, M.W. and Middelkoop, H., 2006. Airborne laser scanning as a tool for lowland floodplain vegetation monitoring. *Hydrobiologia*, 565: 87-103.

Wonnacott, T.H. and Wonnacott, R.J., 1990. *Introductory Statistics*. John Wiley & Sons, New York, 711 pp.

Wotruba, L., Morsdorf, F., Meier, E. and Nüesch, D., 2005. Assessment of sensor characteristics of an airborne laser scanner using geometric reference targets. In: G. Vosselman and C. Brenner (Editors), *ISPRS workshop laser scanning 2005*, Enschede.

ASSESSMENT OF LIDAR-DERIVED TREE HEIGHTS ESTIMATED FROM DIFFERENT FLIGHT ALTITUDE DATA IN MOUNTAINOUS FORESTS WITH POOR LASER PENETRATION RATES

T. Takahashi^{a,*}, Y. Awaya^a, Y. Hirata^b, N. Furuya^a, T. Sakai^a, A. Sakai^c,

^a Forestry and Forest Products Research Institute, 1, Matsunosato, Tsukuba, Ibaraki, 305-8687, Japan - (tomokun, awaya, n Furuya, torus)@ffpri.affrc.go.jp

^b Shikoku Research Center, Forestry and Forest Products Research Institute, Asakura-Nishi, Kochi, 780-8077, Japan - hirat09@affrc.go.jp

^c Japan International Research Center for Agricultural Sciences, 1-1, Ohwashi, Tsukuba, Ibaraki 305-8686, Japan - golgo@affrc.go.jp

KEY WORDS: Forestry, Remote Sensing, LIDAR, Laser scanning, DEM/DTM

ABSTRACT:

In this study, the effects of different flight altitudes on tree height estimates with a small-footprint scanning lidar were investigated and assessed in mountainous forests with poor laser penetration rates. The study area was closed-canopy evergreen coniferous plantations dominated by Japanese cedar (*Cryptomeria japonica*) and hinoki cypress (*Chamaecyparis obtusa*) in Japan. The stand age ranged from 33 to 100 years and the area was undulating terrain with a variation in elevation ranging from 135 to 391 m above sea level. A total of 33 circular sample plots (0.04 ha) were established and predominant mean tree heights for each plot were calculated using individual tree heights within each sample plot. Data from three different flight altitudes (500 m, 1000 m, and 1500 m) were acquired with Optech ALTM3100 sensor in late summer 2006. The settings of lidar system were paid attention as the laser footprints should cover the targeted area without omission, i.e. the laser spot spacing should be close to footprint diameter in the resultant data. Owing to this idea, we were able to theoretically avoid missing treetops and passing through the canopy gaps just by chance for a given transmitted laser pulse. The results of this study demonstrate that the higher platform altitude would reduce both the penetration rates and the intensities of laser pulses, and affect not only the quality of digital surface model, but also the quality of digital terrain model more significantly in forests with undulating topographies, thus indicating the less accurate estimates of lidar-derived tree heights.

1. INTRODUCTION

Small-footprint scanning lidar systems have been often used for forest measurements because such systems have become widely available on a commercial basis (St-Onge et al. 2003). In the previous studies, especially the accuracy of lidar-derived tree height estimates was really high and comparable with the accuracy of field measured tree heights in some vegetation types of forests (e.g. Hyypä et al., 2001; Holmgren et al., 2003; Magnussen and Boudewyn 1998; Maltamo et al., 2004; Næsset 1997, 2004; Persson et al., 2002; Popescu et al., 2002; Takahashi et al., 2005; Yu et al., 2004). Because it takes much time and energy to measure tree heights in the field, it seems that small-footprint scanning lidar has a good potential to become an operational technique for forest inventories if the costs of data acquisition can be reduced (Yu et al., 2004).

For the purpose of reducing costs of data acquisition and measuring wider areas, one way is to increase the flight altitude. When the flight altitude increases, laser-sampling density decreases if both the pulse-repetition frequency and scan angle are kept fixed. On this point, some researchers have focused on the effects of laser-sampling density on the estimation of forest parameters using small-footprint lidar (Næsset, 2004; Hirata, 2004; Yu et al., 2004). In general, when the sampling density decreases, not only does the number of detected trees decrease (Zimble et al., 2003), but also the accuracy of tree height estimates deteriorates because of missing treetops (Gaveau and

Hill, 2003). Moreover, we also have to note that when the flight altitude increases, footprint size increases if the beam divergence is kept fixed. On this point, for example, Perrson et al. (2002) concluded that estimates of lidar-derived individual tree heights and crown diameters were not affected much by different footprint diameters of 0.26 m, 0.52 m, 1.04 m, and 2.08 m in a boreal coniferous forest dominated by Norway spruce (*Picea abies* L. Karst), Scots pine (*Pinus sylvestris* L.), and birch (*Betula spp.*) on flat terrain. Moreover, Nilsson (1996), Yu et al. (2004), and Goodwin et al. (2006) also showed similar results for the estimation of tree height or canopy height profile with varying footprint sizes in some vegetation types of forests on comparatively flat terrain. Now, there is an interesting consistent report in both Yu et al. (2004) and Goodwin et al. (2006). Yu et al. (2004) found that as a result of increasing flight altitude, no reflections received by laser from most of tree canopies were observed for data from 1500 m flight altitude when using a Toposys Falcon lidar system. They assumed this relates to the problem of insufficient laser-transmitted power (laser class I) or insufficient sensitivity of the receiver, as the received power strongly depends on the distance between the target and laser. Goodwin et al. (2006) found that the proportion of first/last return combinations were reduced by higher platform altitudes with more than 70 % of pulses recording a single return at 3000 m in some types of eucalyptus forests when using an Optech ALTM3025 sensor. They hypothesized that greater platform altitude and footprint size reduce the intensity of laser beam incident on a given surface

* Corresponding author. Tomoaki Takahashi; E-mail: tomokun@ffpri.affrc.go.jp

area, thus decreasing the probability of recording a last return above the noise threshold.

Considering these reports, it is considered that the penetration rates of laser pulses would decrease as increasing flight altitude in any type of forest. Thus, the accuracy of a digital terrain model (DTM) derived from higher altitude data would be less. In our previous study, we showed that the difference of the laser penetration rates in between closed canopy, middle-aged Japanese cedar (*Cryptomeria japonica*) and hinoki cypress (*Chamaecyparis obtusa*) plantations that had similar levels of canopy openness was significant ($P < 0.001$). (Takahashi et al., 2006). Although we acquired high laser-sampling density data (over 10 points/m²) with footprint diameter of 0.15 m from approximately 300 m flight altitude, the penetration rate within each stand was 8.1 % and only 1.1 % in the Japanese cedar and hinoki cypress plantations, respectively. Therefore, we concluded that the generation of accurate DTMs in dense hinoki cypress stands with complex topographies is likely to be difficult when using such poor laser penetration data, although DTMs were not created and validated in the study. In Japan, many dense Japanese cedar and hinoki cypress plantations exist in mountainous areas. Many of the forests have not been adequately thinned and the canopy in such instances would be closed. Therefore, in order to evaluate the potential of airborne small-footprint lidar as an operational technique for forest inventories in Japan, we should investigate the effects of lidar data from different flight altitudes on the estimation of forest parameters in such forests.

Therefore in this study, we simply assessed lidar-derived tree heights estimated with data from different flight altitudes in closed-canopy Japanese cedar and hinoki cypress plantations with varying stand characteristics in mountainous areas. For the tree heights, we targeted predominant mean tree heights in this analysis because some previous researches have shown that lidar can usually give more information of predominant trees than that of lower trees in dense or closed-canopy coniferous forests (Persson et al., 2002; Takahashi et al., 2005).

2. MATERIALS AND METHODS

2.1 Study area and ground reference data

The study area was a national forest located in Ibaraki Prefecture in central Japan (lat. 36° 10' N, long. 140° 10' E). The size of the area was approximately 75.2 ha and over 80 % of this area was dominated by planted hinoki cypress and Japanese cedar which are evergreen coniferous tree species, and the rest of the area was dominated by some deciduous broadleaved tree species. The stand age ranged from 33 to 100 years in the coniferous area, and the area was essentially undulating terrain with a variation in elevation ranging from 135 to 391 m above sea level (Figure 1). During fall and winter of 2006, we established 33 circular sample plots (0.04 ha) within the coniferous plantations and differential global positioning system was used to determine the position of the center of each sample plot. Twelve plots consisted of purely planted Japanese cedar and the understory vegetations consisting of *Aucuba japonica* and *Eurya japonica* which are evergreen shrubs with a height of less than approximately 3 m. Meanwhile, 19 plots consisted of purely young to middle-aged planted hinoki cypress and the understory vegetations hardly existing except short shrubs or herbs with a height of less than approximately 1 m. Especially in Japan, closed-canopy

unthinned hinoki cypress plantations have so low light intensity on the floor that there is scarcely understory vegetations (Hattori et al., 1992). On the other hand, the forest floors of two plots in old and matured hinoki cypress stands consisted of *Aucuba japonica* and *Eurya japonica*, and some types of deciduous shrubs with a height of less than approximately 3 m. Moreover, there is an important information about the topographic locations of Japanese cedar stands and hinoki cypress stands in this study site. In Japan, applying the idea of right tree on right site, Japanese cedar is usually planted around mountain valleys, while hinoki cypress is usually planted around mountain ridges. In this site, the same thing can be found as seen in Figure 1.

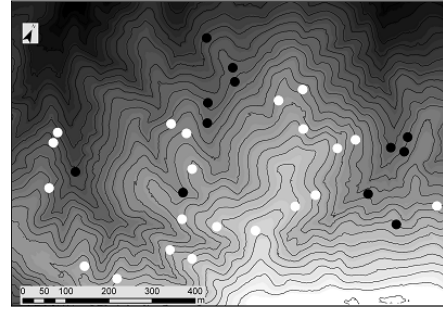


Figure 1. The topographic map created by a digital terrain model (500 m-altitude data) within the study area. The gray-scale color represents the elevation ranging from 135 to 391 m a.s.l. (black to white). Black lines, black circles, and white circles denote the contour (10 m interval) and the field sample plots in Japanese cedar and hinoki cypress stands, respectively.

	Japanese cedar			Hinoki cypress		
	Min	Max	Mean	Min	Max	Mean
Stand age	38	100	59	33	99	44
Density (per 1 ha)	475	2800	1575	475	2575	1899
No. of trees	19	112	63	19	103	76
No. of predominant trees ^a	9	58	33	11	63	43
Mean DBH (cm)	14	37	24	15	37	20
Basal area (m ² /ha)	37.6	76.8	59.1	42.1	66.5	53.4
Mean tree height (m)	10.8	24.8	18.8	9.6	22.2	14.7
Predominant mean tree height ^a (m)	11.5	26.8	20.2	11.1	22.8	15.5

^aFor trees whose heights were greater than the mean tree height within each plot

Table 1. Summary statistics of field data for 33 sample plots

Within each sample plot, all trees with diameter at breast height (DBH) > 4 cm were callipered. Tree heights were measured on sample trees within plots for young and middle-aged forests and all trees within plots for old and matured forests with Vertex hypsometer. For the young and middle-aged forests, sample trees were selected with equal probability and over 50 % of the number of trees within each plot. Next, height-diameter curve

was produced for each plot and unmeasured tree heights were estimated from each model. Then the arithmetic mean tree height (H) was calculated with all individual tree heights within each plot. Finally, the trees whose heights were greater than H within each plot were targeted and the arithmetic mean value was regarded as field measured predominant mean tree height (H_{dom}) in this study. A summary statistics for 33 field sample plots is shown in Table 1.

2.2 Lidar data collection

Lidar data acquisition was performed on 31st August 2006 using a helicopter-airborne laser scanner (Optech ALTM 3100) operated by Aero Asahi Co., Ltd., Japan. The study site was flown at three flight altitudes, namely, 500 m, 1000 m, and 1500 m (a.g.l.), providing data with different point densities and footprint sizes. In this study, these data were referred to as 500 m-, 1000 m-, and 1500 m-altitude data, respectively. Assuming that laser footprints should cover the targeted area without omission, i.e. the laser spot spacing should be close to footprint diameter in the resultant data, we changed flight speed, scan frequency, and pulse-repetition frequency at each flight altitude. At each flight altitude, several parallel flight lines were recorded to cover the entire area with average overlapping of 64 % between adjacent flight lines. Maximum scan angle was 11° and pulses transmitted at scan angles that exceeded 8° were excluded from the final data in order to avoid the low quality data at the edge of strips (Lovell et al., 2005) and be average overlapping of 50 % between adjacent flight lines. The beam divergence of 0.31 mrad produced footprint diameters of 0.16 m, 0.31 m, and 0.47 m for 500 m-, 1000 m-, and 1500 m-altitude data, respectively. The resultant laser-sampling densities within the study area were approximately 57, 25, and 9 points/m², respectively. Both first and last returns and also intermediate returns were recorded as well as the intensity of all returns for each flight altitude data.

2.3 Processing lidar data and estimating predominant mean tree heights

Firstly, the unevenly distributed laser reflection point data were converted into one raster layer with a pixel size of 0.5 m. The raster layer, referred to as DSM_{raw} , was assigned the height value of the highest laser reflection point within each pixel using only first pulse data. To create a continuous surface model, the values of the no-data pixels in DSM_{raw} were interpolated by an inverse distance weighting (IDW) method that does not change the original value (Popescu et al., 2002). The interpolated DSM_{raw} was defined as DSM.

Next, in the noise (i.e. lidar vegetation point) filtering processes for DTM creation, we firstly applied an automatic method used in Holmgren et al. (2003) and Takahashi et al. (2005). Parameter settings were not changed during the processing for all data within the study area in order to evaluate objectively the quality of the resultant DTM for all data. Firstly, the unevenly distributed laser reflection point data were converted into one raster layer with a pixel size of 0.5 m. The raster layer, referred to as DTM_{raw} , was assigned the lowest laser reflection point within each pixel using only last pulse data which had a distance between the first and the last pulse in the same laser beam was more than 2.0 m in this study. Each center pixel of DTM_{raw} was compared with the other pixels within a 6 m horizontal distance, and if the vertical angle of the neighbouring pixels from the center pixel exceeded 45° , the center pixel was classified as ground laser data and the neighbouring pixels were

removed. Then, the remaining pixels were referred to as ground laser data. Finally, DTM was created with the remaining pixels by spline interpolation (Magnussen and Boudewyn, 1998).

Then we also applied a semi-automatic method which requires human edits by the contractor (Aero Asahi Co., Japan) in the noise filtering processes for DTM creation. In this study, this semi-automatic method is denoted as a processing which requires a human operator to not only determine the input parameters for the noise removal algorithms (e.g. the parameters of 6 m and 45° as used in the automatic method), but also edit data manually with intensive visual checks. Normally, such methods seem to be often applied for DTM products by any contractor. Although such semi-automatic methods are nonobjective and largely depend on the operator's experience and technical intuition, it is considered that the method can produce much better quality of DTM than that of automatic method when the ground laser data exist enough to discriminate high or low vegetation laser data and ground laser data visually (Raber et al., 2002). On the other hand, it seems to be difficult to distinguish objectively high or low vegetation laser data from ground laser data when the ground laser data is poor. In this study, we found that both 1000 m- and 1500 m-altitude data had really poor ground laser data especially in some young and middle-aged hinoki cypress stands, conversely 500 m-altitude data had little more than many ground laser data in the stands. Therefore in this study, firstly the semi-automatic method in the noise filtering processes was applied for 500 m-altitude data by the contractor intensively, and a DTM was created with the remaining pixels by spline interpolation as mentioned above. Hereafter, the DTM was regarded as a reference terrain data and referred to as DTM_{ref} . Because the DTM_{ref} was created by similar noise filtering processes as mentioned above but a little bit different process by the contractor (Yokota et al., 2006), so we created DTM uniformly for three flight altitude data using the DTM_{ref} as follows. If a given pixel value of DTM_{raw} of each flight altitude data is greater than that of corresponding pixel of DTM_{ref} , the pixel is ideally regarded as noise and removed. But in order to avoid the effect of the interpolation error (e.g. overestimation of elevation) within the DTM_{ref} on excessive removing pixels, if the difference between DTM_{raw} and the DTM_{ref} is greater than 1 m, such pixel of DTM_{raw} is regarded as noise and removed for all data. Finally, DTM for each data was created with the remaining pixels by spline interpolation as mentioned above.

To estimate lidar-derived predominant mean tree heights ($H_{dom,L}$), firstly a canopy height model (CHM) was calculated by subtracting DTM from DSM for each flight altitude data. Previous researches have shown that the raster-based CHM can usually give more information of predominant trees than that of lower trees in dense or closed-canopy forests (Persson et al., 2002; Takahashi et al., 2005). We then smoothed the DSM with a low-pass filter (3 by 3 pixels) used in the previous researchers (Hyypä et al., 2001; Maltamo et al., 2004) and applied a 3 by 3 local maximum filtering (Wulder et al., 2000) to detect predominant treetops for each data. Then individual tree heights were derived from the CHM at the horizontal location of the local maxima of the smoothed DSM. Finally, the arithmetic mean value of the lidar-derived individual tree heights within each sample plot was calculated and regarded as $H_{dom,L}$.

2.4 Assessment of lidar-derived tree heights

Data assessments were made separately in Japanese cedar and hinoki cypress stands basically. Firstly, the relationships

between lidar-derived and field measured predominant mean tree heights were investigated by regression analysis. Next, systematic error (i.e. bias) and root mean square error (RMSE) for the tree height estimates were computed as follows:

$$RMSE = \sqrt{\frac{\sum (H_{dom_L} - H_{dom})^2}{n}} \quad (1)$$

where H_{dom_L} and H_{dom} are lidar-derived and field measured predominant mean tree heights, respectively and n is the number of sample plots. Then, in order to understand the errors of the tree height estimates, DTMs for different flight altitude data derived from both the automatic and the semi-automatic methods were compared with a reference DTM, i.e. DTM_{ref} , and the systematic errors were evaluated for each DTM. Also the laser penetration rates of last pulses within each sample plot were calculated for each data. Additionally, the arithmetic mean laser-intensity of first pulses within each sample plot was also calculated. Then we assessed the statistical significant differences for each factor (i.e. penetration rate and intensity) among three flight altitude data. In this study, Friedman test and the Scheffe procedure as a multiple comparison post hoc test were applied in the statistical tests. Moreover, these two factors were tested in between Japanese cedar and hinoki cypress stands for each flight altitude data by Mann-Whitney U test.

3. RESULTS

	Japanese cedar			Hinoki cypress		
	500 m	1000 m	1500 m	500 m	1000 m	1500 m
All trees	756	756	756	1595	1595	1595
Predominant trees ^a	393	393	393	902	902	902
Local maxima ^b	399	409	344	760	724	606

^aThe trees whose heights were greater than the mean tree height within each plot

^bLocal maxima derived from lidar data with 3 by 3 local maximum filtering were denoted as the number of predominant trees in this study

Table 2. The number of trees in the field and lidar-detected trees within all (33) sample plots for each flight altitude data

	Altitude	Automatic		Semi-automatic	
		Bias (m)	RMSE (m)	Bias (m)	RMSE (m)
Japanese cedar	500 m	-0.16	1.12	-0.46	1.11
	1000 m	-0.81	1.46	-0.74	1.28
	1500 m	-2.54	6.12	-1.15	1.63
Hinoki cypress	500 m	0.18	0.98	0.00	0.84
	1000 m	1.50	3.78	0.39	1.23
	1500 m	2.18	5.91	0.88	2.29

Table 3. Bias and root mean square error (RMSE) for predominant mean tree height estimates when using DTMs created by an automatic and a semi-automatic method

The number of detected predominant treetops, i.e. local maxima, for each altitude data is shown in Table 2. Although the number of local maxima within the DSM of 1000 m-altitude data was higher than that of 500 m-altitude data in Japanese cedar stands, there seems that greater platform altitude and footprint size reduced the number of local maxima. The magnitudes of the differences between the number of predominant trees in the field and lidar-detected trees were greater in hinoki cypress stands than in Japanese cedar stands.

The relationships between field measured and lidar-derived predominant mean tree heights are shown in Figure 2. The results show that the number of the outliers increased as the flight altitude increased in both two methods. Bias and RMSE for predominant mean tree height estimates are shown in Table 3. Japanese cedar stands had underestimates of height, conversely hinoki cypress stands had overestimates of height in both methods. Figure 3 shows that the cause of under and overestimations of predominant mean tree heights in Japanese cedar and hinoki cypress stands, respectively. That is, the underestimations of DTM would produce the overestimations of tree heights in hinoki cypress stands, in contrast, the overestimations of DTM would produce the underestimations of tree heights in Japanese cedar stands. In the semi-automatic method, the magnitude of the difference between maximum and minimum RMSEs in hinoki cypress stands was greater than that of Japanese cedar stands.

According to the statistical tests, the penetration rates of last pulses in 500 m-altitude data were significantly greater than that of other altitudes in both stands (Table 4). Moreover, there were statistically significant differences among the intensities of first pulses of all three flight altitude data in both stands.

	Altitude	Penetration rate (%)	Intensity
Japanese cedar	500 m	14.1	74.3
	1000 m	3.2	16.9
	1500 m	2.1	11.2
Hinoki cypress	500 m	2.3	99.0
	1000 m	0.6	23.6
	1500 m	0.4	16.3

Table 4. Mean values of laser penetration rates of last pulses and laser-intensity of first pulses

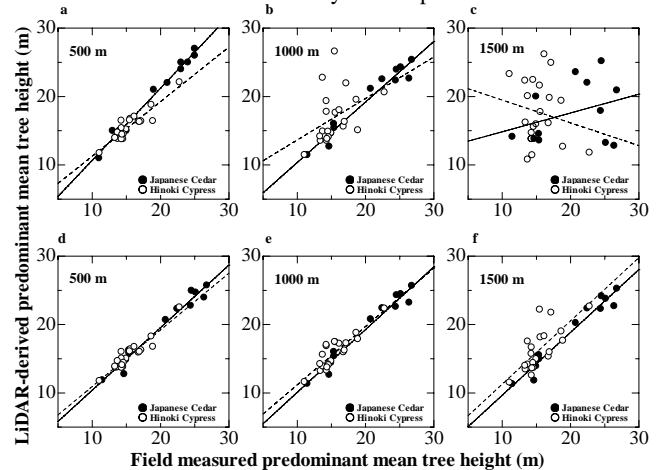


Figure 2. The relationships between field measured and lidar-derived predominant mean tree heights (H_{dom_L}) of three flight

altitude data. Solid and dashed lines denote regression lines of Japanese cedar and hinoki cypress data, respectively. H_{dom_L} in above three graphs (a, b, and c) and below three graphs (d, e, and f) are the estimates when using DTMs created by an automatic and a semi-automatic method, respectively.

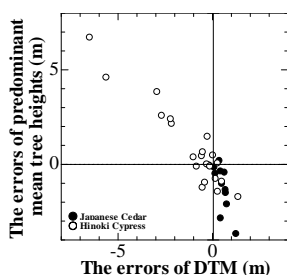


Figure 3. The relationship between the errors of DTM of 1500m-altitude data derived from a semi-automatic method and the errors of predominant mean tree height estimates for all sample plots. The errors of the DTM denote as the difference between the mean elevation within each plot of the DTM and that of a reference DTM (DTM_{ref}) created by a contractor.

4. DISCUSSIONS AND CONCLUSIONS

In order to investigate the effects of different flight altitudes on the estimation of tree heights in forests with poor laser penetration rates, we used lidar-derived predominant mean tree heights derived from the information of local maxima in DSM and heights in CHM in this study. The validity of this approach seems to be ensured by the results of regression analysis and the errors of the tree height estimates as shown in Figure 2 (d) and Table 3. In this study, the settings of lidar system were paid attention as the laser footprints should cover the targeted area without omission, i.e. the laser spot spacing should be close to footprint diameter in the resultant data. Owing to this idea, we were able to avoid theoretically missing treetops and passing through the canopy gaps just by chance for a given transmitted laser pulse. But in fact, the no-data pixels of DSM_{raw} (50 cm resolution) were found for all flight altitude data even though the mean laser-sampling density is high (at least over 9 points/m²). This problem is considered to be inevitable for any scanning lidar system as long as using airborne platform and targeting uneven surface, especially in mountainous forest areas.

On the assumption that the targeted area was fully covered with laser shots for all flight altitude data, the results of this study indicate that the higher platform altitude would deteriorate the quality or accuracy of lidar-derived variables such as the number of detectable local maxima in DSM, penetration rates and intensities of laser pulses, the elevation of DTM, and tree height estimates. These findings are partly similar to those previously reported in Yu et al. (2004) and Goodwin et al. (2006), even though the vegetation species and topographies were different from that of this study area. But there were some dissimilar points in this study. The most crucial failing at higher flight altitude seems to be less penetration rates of laser pulses, thus indicating the less accuracy of the resultant DTM in mountainous forests with undulating topographies. Judging from the low penetration rates in Table 4 and the outliers in Figure 2 (e and f) in hinoki cypress stands, lidar ground laser data did not seem to exist enough to recover the shape of the field topographies. Therefore, the results in Figure 2 (b and c) indicate that it is difficult to remove lidar vegetation points properly and correctly in such forests by using fixed input parameters for the noise removal algorithms, i.e. automatic

methods when the laser penetration rates are poor. Although we could use a good reference DTM (DTM_{ref}) in this study, whether another semi-automatic method which depends on human edits manually and visually without using such reference DTM can produce an equivalent to the quality of the DTMs created in this study for 1000 m- and 1500 m-altitude data remains unknown. However, judging from the results in Figure 2, it would be necessary semi-automatic noise filtering methods to acquire better DTM of such forests even if the resultant DTM is not objective product.

Figure 3 shows the positive and negative errors of tree height estimates would be mainly caused by the negative and positive errors of the DTM, respectively. Moreover, the tendencies that many hinoki cypress stands had larger negative errors of the DTM while many Japanese cedar stands had larger positive errors of the DTM can be understood by the topographic locations of each stand as seen in Figure 1. That is to say, because most hinoki cypress stands located around the mountain ridges, poorly penetrated laser pulses would be missing the top of the ridges, thus resulting in the lower elevation of the DTM and the greater estimates of tree heights. Meanwhile, although Japanese cedar stands in this study area might have the opposite effect from hinoki cypress stands, it is also considered that the existence of understorey bushes might be involved in the overestimations of the DTM. As indicated in Goodwin et al. (2006) and Hyypä et al. (2005), the all results of this study are highly site dependent as lidar-derived relationships will be influenced by its structural complexities. But the relationships between the topographic locations and the penetration rate of laser pulses would effect significantly on the resultant DTM in any type of forest.

Although lidar data was acquired in late summer (growing season) in evergreen Japanese cedar and hinoki cypress stands in this study, the assessment of different flight altitude data acquired in winter (leaf-off season) for the estimation of tree heights should be performed because the leaf biomass of evergreen forests differs between summer and winter (Tsutsumi 1989). Therefore, if such low laser penetration rates were improved in hinoki cypress stands in winter, the acquisition of lidar data should be performed in winter. Anyhow, the results of this study demonstrate that the higher platform altitude would reduce both the penetration rates and the intensities of laser pulses, and affect not only the quality of DSM, but also the quality of DTM more significantly in forests with undulating topographies, thus indicating the less accuracy of lidar-derived tree height estimates. In fact, the errors of tree height estimates increase with increasing flight altitude as shown in Table 2, and there are some hinoki cypress stands whose tree height errors are over 4 or 5 m in 1500 m-altitude data (Figure 2 (f)). Although the accuracy of tree height estimates in Japanese cedar stands was high in all flight altitude data, the penetration rates of laser pulses are not enough magnitude of 1500 m-altitude data (Table 4). Considering these results, if we ensure the accurate lidar-derived tree height estimates (the error is 1 m or so) in summer in both Japanese cedar and hinoki cypress plantations with varying stand characteristics, the flight altitude should be set lower than at least 1000 m.

Further work should be performed to investigate the effect of laser-sampling density on the accuracy and quality of DTM and tree height estimates in this study site, especially in closed-canopy hinoki cypress plantations, to establish optimal settings of lidar system for an operational technique for forest inventories in mountainous forests in Japan.

REFERENCES

- Gaveau, D.L.A., and Hill, R.A., 2003. Quantifying canopy height underestimation by laser pulse penetration in small-footprint airborne laser scanning data. *Canadian Journal of Remote Sensing*, 29, pp. 650-657.
- Goodwin, N. R., Coops, N. C., and Culvenor, D. S., 2006. Assessment of forest structure with airborne lidar and the effects of plot form altitude. *Remote Sensing of Environment*, 103, pp. 319-330.
- Hattori, S., Abe, T., Kobayashi, C., and Tamai, K., 1992. Effect of forest floor coverage on reduction of soil erosion in hinoki cypress plantations (in Japanese with English summary). *Bulletin Forestry and Forest Products Research Institute*, 362, pp. 1-34.
- Hirata, Y., 2004. The effects of footprint size and sampling density in airborne laser scanning to extract individual-trees in mountainous terrain. *The International Archives of the photogrammetry, Remote Sensing and Spatial information Sciences*, 36, part8/w2
- Holmgren, J., Nilsson, M., and Olsson, H., 2003. Estimation of tree height and stem volume on plots using airborne laser scanning. *Forest Science*, 49, pp. 419-428.
- Hyypä, J., Kelle, O., Lehtikoinen, M., and Inkinen, M., 2001. A segmentation-based method to retrieve stem volume estimates from 3-D tree height models produced by laser scanners. *IEEE Transactions on Geosciences and Remote Sensing*, 39, pp. 969-975.
- Hyypä, H., Yu, X., Hyypä, H., Kaartinen, H., Kaasalainen, S., Honkavaara, E., and Rönnholm, P., 2005. Factors affecting the quality of DTM generation in forested areas. *International Archives of Photogrammetry, Remote Sensing and Spatial Information Sciences*, 36, part3/W19
- Lovell, J.L., Jupp, D.L.B., Newnham, G.J., Coops, N.C., and Culvenor, D.S., 2005. Simulation study for finding optimal lidar acquisition parameters for forest height retrieval. *Forest Ecology and Management*, 214, pp. 398-412.
- Magnussen, S., and Boudewyn, P., 1998. Derivations of stand heights from airborne laser scanner data with canopy-based quantile estimators. *Canadian Journal of Forest Research*, 28, pp. 1016-1031.
- Maltamo, M., Eerikäinen, K., Pitkänen, J., Hyypä, J., and Vehmas, M., 2004. Estimation of timber volume and stem density based on scanning laser altimetry and expected tree size distribution functions. *Remote Sensing of Environment*, 90, pp. 319-330.
- Næsset, E., 1997. Determination of tree height of forest stands using airborne laser scanner data. *ISPRS Journal of Photogrammetry & Remote Sensing*, 52, pp. 49-56.
- Næsset, E., 2004. Effects of different flying altitudes on biophysical stand properties estimated from canopy height and density measured with a small-footprint airborne scanning laser. *Remote Sensing of Environment*, 91, pp. 243-255.
- Nilsson, M., 1996. Estimation of tree height and stand volume using an airborne lidar system. *Remote Sensing of Environment*, 56, pp. 1-7.
- Persson, A., Holmgren, J., and Soderman, U., 2002. Detecting and measuring individual-trees using an airborne laser scanner. *Photogrammetric Engineering and Remote Sensing*, 68, pp. 925-932.
- Popescu, S.C., Wynne, R.H., Nelson, R.F., 2002. Estimating plot-level tree heights with lidar: local filtering with a canopy-height based variable window size. *Computers and Electronics in Agriculture*, 37, pp. 71-95.
- Raber, T.G., Jensen, J.R., Schill, S.R., and Schuckman, K., 2002. Creation of digital terrain models using an adaptive lidar vegetation point removal process. *Photogrammetric Engineering and Remote Sensing*, 68, pp. 1307-1315.
- St-Onge, B., Treitz, P., and Wulder, M.A., 2003. Tree and canopy height estimation with scanning lidar. Concepts and case studies. In Wulder, M.A., and Franklin, S.E., (eds) *Remote sensing of forest environments*, Kluwer Academic Publishers, Boston, pp. 489-509.
- Takahashi, T., Yamamoto, K., Senda, Y., and Tsuzuku, M., 2005. Estimating individual-tree heights of sugi (*Cryptomeria japonica* D. Don) plantations in mountainous areas using small-footprint airborne lidar. *Journal of Forest Research*, 10, pp. 135-142.
- Takahashi, T., Yamamoto, K., Miyachi, Y., Senda, Y., and Tsuzuku, M., 2006. The penetration rate of laser pulses transmitted from a small-footprint airborne lidar: a case study in closed-canopy, middle-aged pure sugi (*Cryptomeria japonica* D. Don) and hinoki cypress (*Chamaecyparis obtusa* Sieb. et Zucc.) stands in Japan. *Journal of Forest Research*, 11, pp. 117-123.
- Tsutsumi T (Ed) (1989) *Forest ecology* (in Japanese). Asakura syoten, Tokyo, Japan, pp. 62-63.
- Wulder, M., Niemann, K.O., and Goodenough, D.G., 2000. Local maximum filtering for the extraction of tree locations and basal area from high spatial resolution imagery. *Remote Sensing of Environment*, 73, pp. 103-114.
- Yokota, H., Nakajima, T., and Tamino, T., 2006. Introduction of a filtering method named roller-method (in Japanese). *Journal of the Japan Society of Photogrammetry & Remote Sensing*, 45(4), pp. 18-21.
- Yu, X., Hyypä, J., Hyypä, H., and Maltamo, M., 2004. Effects of flight altitude on tree height estimation using airborne laser scanning. *The International Archives of the photogrammetry, Remote Sensing and Spatial information Sciences*, 36, part8/w2
- Zimble, D.A., Evans, D.L., Carlson, G.C., Parker, R.C., Grado, S.C., and Gerard, P.D., 2003. Characterizing vertical forest structure using small-footprint airborne lidar. *Remote Sensing of Environment*, 87, pp. 171-182

ACKNOWLEDGEMENTS

We thank Kenichi Shibuya and Kouji Oomori from Aero Asahi Co., Japan for planning the flight and acquiring the lidar data.

HOUGH-TRANSFORM AND EXTENDED RANSAC ALGORITHMS FOR AUTOMATIC DETECTION OF 3D BUILDING ROOF PLANES FROM LIDAR DATA

F. Tarsha-Kurdi*, T. Landes, P. Grussenmeyer

Photogrammetry and Geomatics Group MAP-PAGE UMR 694, Graduate School of Science and Technology (INSA), 24 Boulevard de la Victoire, 67084 STRASBOURG, France.
(fayez.tarshakurdi|tania.landes|pierre.grussenmeyer@insa-strasbourg.fr)

Commission III, WG III/4

KEY WORDS: LIDAR, Processing, Detection, Extraction, Building, Segmentation, Modelling

ABSTRACT:

Airborne laser scanner technique is broadly the most appropriate way to acquire rapidly and with high density 3D data over a city. Once the 3D Lidar data are available, the next task is the automatic data processing, with major aim to construct 3D building models. Among the numerous automatic reconstruction methods, the techniques allowing the detection of 3D building roof planes are of crucial importance. Three main methods arise from the literature: region growing, Hough-transform and Random Sample Consensus (RANSAC) paradigm. Since region growing algorithms are sometimes not very transparent and not homogeneously applied, this paper focuses only on the Hough-transform and the RANSAC algorithm. Their principles, their pseudocode - rarely detailed in the related literature - as well as their complete analyses are presented in this paper. An analytic comparison of both algorithms, in terms of processing time and sensitivity to cloud characteristics, shows that despite the limitation encountered in both methods, RANSAC algorithm is still more efficient than the first one. Under other advantages, its processing time is negligible even when the input data size is very large. On the other hand, Hough-transform is very sensitive to the segmentation parameters values. Therefore, RANSAC algorithm has been chosen and extended to exceed its limitations. Its major limitation is that it searches to detect the best mathematical plane among 3D building point cloud even if this plane does not always represent a roof plane. So the proposed extension allows harmonizing the mathematical aspect of the algorithm with the geometry of a roof. At last, it is shown that the extended approach provides very satisfying results, even in the case of very weak point density and for different levels of building complexity. Therefore, once the roof planes are successfully detected, the automatic building modelling can be carried out.

1. INTRODUCTION

The quick acquisition of 3D data as well as the automatic data processing are two key-tasks for the majority of surveying fields. Airborne laser scanning systems generate 3D data with high speed, good accuracy and density. Thus, the use of this technique in urban region is more and more frequent.

In order to construct automatically 3D city models, two successive steps have to be considered. The first one is the automatic segmentation of the point cloud into three classes which are terrain, vegetation and buildings. Once the city cloud is segmented, the modelling of buildings can start. Two types of approach called *model-driven* and *data-driven* approaches in the literature are proposed for constructing building models. The model-driven approaches search the most appropriate model among primitive building models contained in a model library (Maas and Vosselman, 1999). They consider that a primitive building can be described by a set of parameters. That implies to calculate the values of the parameters before constructing the 3D model. On the other hand, data-driven approaches try to simulate each part of the building point cloud for obtaining the nearest or the more faithful polyhedral model (Rottensteiner, 2003).

In the context of data-driven approaches which provide more universal models, the automatic detection of planes is a crucial operation. Many methods are proposed in order to carry out this procedure such as region growing, 3D Hough-transform and RANSAC. Only the two last techniques are studied in this paper since region growing algorithm are sometimes not very transparent and not homogeneously applied. Furthermore, the principles and the pseudocodes of 3D Hough-transform and

RANSAC algorithms are detailed and compared. In order to clarify their operating mode and assess them, they are applied on samples of buildings with different forms and complexity levels. At last, the RANSAC algorithm is extended to be able to solve the majority of building cases.

2. 3D HOUGH-TRANSFORM

2.1 Related works and principle

The 2D Hough-transform technique (Hough, 1962) is normally used in the field of digital image processing in order to detect geometric primitives. Many applications in this field as well as its algorithm are presented by (Davies, 1988; Gonzalez *et al.*, 2004; Nguyen *et al.*, 2005). This technique is used to detect the straight lines like building contour polygons, and curves such as circles and ellipses. With the 3D point cloud, the demand is increased for detecting 3D planes. In this context, the 2D Hough-transform has been extended to 3D (Vosselman and Dijkman, 2001; Oda *et al.*, 2004; Overby *et al.*, 2004). Later, its principle has been extended to the extraction of other 3D geometric forms like cylinders (Rabbani and Van den Heuvel, 2005).

The principle of the 2D Hough-transform is the representation of a points set, defined initially in the Euclidian space, in another space. This transform allows detecting the points composing specific geometric primitives. For example, in (OXY) space, the equation of a line has the form (1).

$$Y = a \cdot X + b \quad (1)$$

where (a, b) are the line parameters.

This line can be represented by a point with coordinates (a, b) in the parameter space (O' a b). In an opposite way, one point (X_i, Y_i) belonging to the space (OXY) is represented by a line in the parameter space (O' a b) as expressed in Equation 2.

$$b = -X_i \cdot a + Y_i \quad (2)$$

where (X_i, Y_i) are the parameters of this line.

Supposing that M₁, M₂, ... M_n are a set of points in the space (OXY) and that they belong to the line P following Equation 1. Each one of these points represents a line in the parameter space. The intersection of these lines in the parameter space is the point (a₁, b₁) which represents the parameters of the line P in a 2D-space.

If the line equation has the form $X = constant$, then it can not be presented in the parameter space (O' a b), because the Y-axis coefficient is equal to zero. In order to solve this problem, it is suggested to use the normal form of the line (Equation 3).

$$\cos \theta \cdot X + \sin \theta \cdot Y = \rho \quad (3)$$

where θ and ρ are the parameters of the normal passing through the origin (see Fig.1).

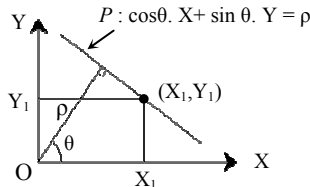


Figure 1. Presentation of one line and its normal in a 2D-space

So, θ and ρ are constant for one line. The parameter space in this case is (O' θ ρ). Hence, one point (X₁, Y₁) in the 2D-space represents a sinusoid in the parameter space (see Fig.2).

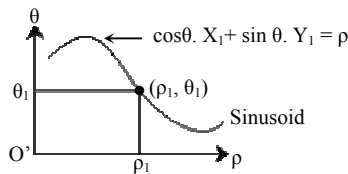


Figure 2. Presentation of a point in the parameter space using the normal form

The same principle can be applied in a 3D case in considering that one plane belonging to the (OXYZ) space (Equation 4) can be represented by a point (a, b, c) in the parameter space (O' abc).

$$Z = a \cdot X + b \cdot Y + c \quad (4)$$

In the same manner, if the plane equation has the form (5), then it can not be presented in the parameter space because the Z-axis coefficient is equal to zero. In order to solve this problem, (Overby *et al.*, 2004) suggest to use also the normal form of the plane (Equation 6).

$$a X + b Y + c = 0 \quad (5)$$

$$\cos \theta \cdot \cos \varphi \cdot X + \sin \theta \cdot \cos \varphi \cdot Y + \sin \varphi \cdot Z = \rho \quad (6)$$

where θ , φ and ρ are the parameters of the plane normal passing through the origin (see Fig.3).

So, θ , φ and ρ are constant and the parameter space is (O' θ φ ρ). In this case, one point (X₁, Y₁, Z₁) in the 3D-space represents a sinusoidal surface in the parameter space. Since the principles of the 3D Hough-transform are explained, the aim of the next section is to deliver its algorithm.

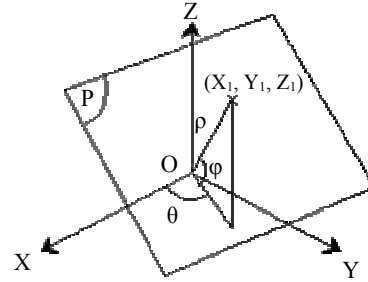


Figure 3. Representation of plane equation elements in the normal form

2.2 3D Hough-transform algorithm

The input data are the steps on θ , φ and ρ axis (discrete intervals), called θ_step , φ_step and ρ_step respectively. The 3D point cloud is represented by three coordinate lists X, Y and Z. Algorithm 1 presents the pseudocode of the 3D Hough-transform.

Algorithm 1: 3D Hough-transform for plane detection

1. $X_min = \min(X)$; $Y_min = \min(Y)$; $Z_min = \min(Z)$
2. $X_max = \max(X)$; $Y_max = \max(Y)$; $Z_max = \max(Z)$
3. Calculation of: Dis_min ; Dis_max
4. $\theta = \text{from } 0 \text{ to } 360$, $\text{step} = \theta_step$; $n_theta = \text{length}(\theta)$
5. $\varphi = \text{from } -90 \text{ to } +90$, $\text{step} = \varphi_step$; $n_phi = \text{length}(\varphi)$
6. $n_rho = 2 * (Dis_max - Dis_min) / \rho_step$
7. $\rho = \text{from } Dis_min \text{ to } Dis_max$; $\text{step} = \rho_step$
8. $\theta_mat(n_phi, n_theta) = [\theta \ \theta \ \dots \ \theta]^T * \pi / 180$
9. $\varphi_mat(n_phi, n_theta) = [\varphi \ \varphi \ \dots \ \varphi]^T * \pi / 180$
10. $H(n_theta, n_phi, n_rho) = 0$
11. $ratio = (n_rho - 1) / (\rho(n_rho) - \rho(1))$
12. for $k = 1$ to $\text{length}(X)$
13. $\rho_mat = \cos(\varphi_mat) * \cos(\theta_mat) * X(k) + \dots$
 $\cos(\varphi_mat) * \sin(\theta_mat) * Y(k) + \sin(\varphi_mat) * Z(k)$
14. $\rho_index = \text{round}(ratio * (\rho_mat - \rho(1) + 1))$
15. for $i = 1$ to n_phi
16. for $j = 1$ to n_theta
17. $H(j, i, \rho_index(i, j)) = H(j, i, \rho_index(i, j)) + 1$
18. next j ; next i ; next k

In this algorithm, Dis_min and Dis_max are the distances between the origin and the two extremities of the cloud points calculated at lines 1 and 2; H is a 3D matrix; θ_mat , φ_mat and ρ_mat are 2D matrices; θ , φ and ρ are three lists.

The result of the algorithm is the 3D matrix H which contains the representation of the original cloud in the parameter space. Each point of (OXYZ) space gives a sinusoidal surface in the parameter space.

Fig.-4a shows the visualization of one horizontal plane in the 3D matrix H . Fig.-4b shows the result of the roof planes detection. For improving this result, it is necessary to use parameter values as small as possible. But, in this case the processing time and the needed memory will be much higher. The sample used for this figure is a building whose characteristics are detailed in section 3.3.

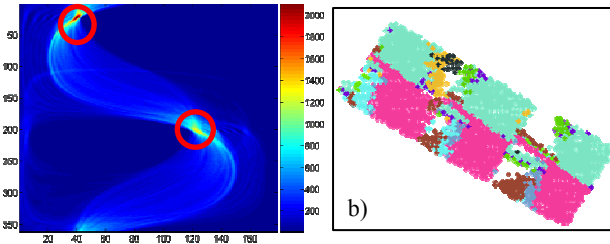


Figure 4. a) Horizontal plane in the 3D matrix H , (with plane number $\rho = 75$); b) Roof plane detection result using the 3D Hough-transform.

The next step consists in detecting the peaks from the 3D matrix H as marked by red circles in Fig.-4a. Each peak represents one plane in (OXYZ) space. This operation can be performed by searching voxels having the maximum values in the matrix H and then applying a 3D region growing algorithm.

2.3 Analysis

The 3D Hough-transform uses a pure mathematical principle in order to detect the best planes from a 3D point cloud. That means that it looks for point sets which represent statistically the best planes without taking into account their signification in the building point cloud. In this context, the *best plane* does not mean the most probable plane calculated according to the least squares theory. But it means the plane containing the maximum number of points. Therefore, it detects perhaps a set of points which represents several roof planes or which belongs to several planes.

Moreover, the 3D Hough-transform spends a long time for calculating the matrix H and for detecting the peaks in it. Furthermore, the application of 3D Hough-transform requires the use of four parameters. The first three one are the steps (discrete intervals) on θ , φ and ρ axis. When the used step values are small, the quality of the detected plane is improved, but the processing time and the needed memory are much higher and vice versa. The fourth parameter is a threshold entering in the 3D region growing algorithm. It represents the difference between the voxel value and its neighbours. The determination of the four threshold values are related to the characteristics of the point cloud and of the building roof planes. Thus, it is very difficult to determine them automatically.

3. RANSAC ALGORITHM FOR PLANE DETECTION

3.1 Related works and principle

In the digital image processing domain, RANdom SAMple Consensus (RANSAC) algorithm is used to detect mathematical features like straight lines and circles. Its principle is well explained by (Fischler and Bolles, 1981; McGlone McGlone *et al.*, 2004; Nguyen *et al.*, 2005). In the field of automatic buildings modelling based on Lidar data, many authors suggest its use for achieving different tasks. For example, (Ameri and Fritsch, 2000; Brenner, 2000) use RANSAC algorithm for detecting the building roof planes. (Forlani *et al.*, 2004; Forlani *et al.*, 2006) apply RANSAC algorithm in order to correct the building roof segmentation result which are obtained using a partition in 8 classes of the gradient orientation. Moreover, to carry out the 2D segmentation of the building contour polygon pixels in straight lines, the same technique is also applied. (Bretar and Roux, 2005) use the Normal Driven RANSAC

(ND-RANSAC) for extracting 3D planar primitives. For this purpose, they calculate the normal vectors for each point. Then, they select randomly three points but having the same orientation of normal vectors. In our case, RANSAC algorithm is used with the aim of roof planes detection.

The principle of RANSAC algorithm consists to search the best plane among a 3D point cloud. In the same time, it reduces the number of iterations, even if the number of points is very large. For this purpose, it selects randomly three points and it calculates the parameters of the corresponding plane. Then it detects all points of the original cloud belonging to the calculated plane, according to a given threshold. Afterwards, it repeats these procedures N times; in each one, it compares the obtained result with the last saved one. If the new result is better, then it replaces the saved result by the new one.

3.2 RANSAC algorithm

This algorithm needs four input data which are:

- The 3D point cloud (*point_list*) which is a matrix of three coordinate columns X, Y and Z;
- The tolerance threshold of distance t between the chosen plane and the other points. Its value is related to the altimetric accuracy of the point cloud;
- The *foreseeable_support* is the maximum probable number of points belonging to the same plane. It is deduced from the point density and the maximum foreseeable roof plane surface.
- The probability α is a minimum probability of finding at least one good set of observations in N trials. It lies usually between 0.90 and 0.99.

Algorithm 2 details the pseudocode of RANSAC algorithm.

Algorithm 2: RANSAC for plane detection

1. $bestSupport = 0$; $bestPlane(3,1) = [0, 0, 0]$
 2. $bestStd = \infty$; $i = 0$
 3. $\varepsilon = 1 - foreseeable_support / length(point_list)$
 4. $N = round(\log(1 - \alpha) / \log(1 - (1 - \varepsilon)^3))$
 5. **while** ($i \leq N$)
 6. $j =$ pick 3 points randomly among (*point_list*)
 7. $pl = pts2plane(j)$
 8. $dis = dist2plan(pl, point_list)$
 9. $s = find(abs(dis) \leq t)$
 10. $st = Standard_deviation(s)$
 11. **if** ($length(s) > bestSupport$ **or** ($length(s) = \dots$
 $bestSupport$ **and** $st < bestStd$)) **then**
 12. $bestSupport = length(s)$
 13. $bestPlan = pl$; $bestStd = st$; **endif**
 14. $i = i + 1$; **endwhile**
-

In this pseudocode, ε is a percentage of observations allowed to be erroneous; the function *pts2plane* calculates the plane parameters from three chosen points. It is advised to use the normal form of the plane instead of the classical form (see Equation 6) in order to consider the general expression of a plane; the function *dist2plan* calculates the signed distances between point set and given plane (the distance takes negative or positive value) as given in Equation 7.

$$dist2plan = \cos \theta \cos \varphi X + \sin \theta \cos \varphi Y + \sin \varphi Z - \rho \quad (7)$$

where X, Y and Z are the three columns of the matrix *point_list*; θ , φ and ρ are the plane parameters (see Equation 6).

It is important to note that the number of trials N can be considered directly as an input of the algorithm, instead of calculating it by a pure probability law. For this purpose, a table of different urban typologies and point densities can suggest the N value. Therefore, it replaces the introduction of values for *foreseeable_support* and α . This operation is one of the modifications proposed for improving the basic RANSAC algorithm.

In order to detect the whole roof planes, the algorithm is applied several successive times. In each iteration, the set of considered points is excluded from the original cloud. This operation is repeated until the number of non-modelled points becomes smaller than a given threshold.

3.3 Comparison and quantitative analysis

In order to assess the capacities of the algorithm, two samples of buildings are used. They contain buildings of different forms and complexity levels. Only some results are illustrated in this paper, but they are based on characteristic samples (covering simple as well as complex building types) and consider low and high point densities. The first sample contains 12 buildings and its point density is equal to 7 points/m². The second sample contains 46 buildings, with a point density of 1.3 points/m².

Fig.5 presents the results of roof planes detection using RANSAC algorithm.

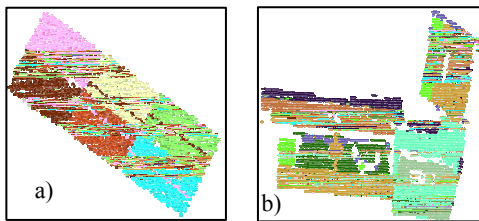


Figure 5. Visualisation of the 2D point clouds resulting from roof planes detection using RANSAC.

a) Point density: 7 pts/m². b) Point density: 1.3 pts/m².
The colours represent the different building roof planes.

The application of classic RANSAC algorithm on these samples gives successful results in 70% of cases for different building forms and different point cloud densities. It means that it detects correctly the roof planes for 41 buildings. For example, Fig.-5a illustrates very good plane detections, whereas Fig.-5b shows unsatisfying results. In extreme situations, the algorithm can provide unacceptable errors (see Fig.-7b). That can be explained by the use of a pure mathematical principle, without taking into account the particularity of the building Lidar data. The same remark has already been made for the 3D Hough-transform in section 2.3. That is why, it may detect a set of points which represents several roof planes or which belongs to several planes. Therefore, the classic algorithm needs to be adapted in order to detect the best roof planes instead of the best mathematical planes in a 3D point cloud.

(McGlone *et al.*, 2004) note that the RANSAC algorithm aims at significantly reducing the number of necessary trials for large N values. However, it reduces N at the expense of having no guarantee for a solution free of gross errors. That means that there is not any guarantee for obtaining the same result after each iteration.

Afterwards, several experiments have been made on the point cloud including the 41 buildings, i.e. the cloud for which RANSAC generated successful results. They demonstrate that the iterative application of RANSAC algorithm gives the same

set of roof planes, but in a different order. Since the plane order is not important here, the RANSAC algorithm can be considered as an algorithm which guarantees a successful result. Furthermore, the processing time, even in the case of a large point cloud, is negligible in comparison with the processing time required by 3D Hough-transform.

It is important to note that the segmentation quality could be actually evaluated only after the stage of 3D modelling. Moreover, the quantitative comparison between the results of 3D Hough-transform and RANSAC algorithms will not be correct. Indeed, the Hough-transform results are related to three aspects: the segmentation quality, the processing time and the needed memory, while the last two aspects are negligible for RANSAC algorithm.

3.4 3D Hough-transform or RANSAC algorithm?

As evoked in previous sections, RANSAC algorithm provides not only results in a shorter time but also results of higher quality with a large percentage of successful results in comparison with 3D Hough-transform. This assertion is made after several experiments carried out on the same data for both algorithms. For example, the result of 3D Hough-transform mentioned in Fig.-4b is based on the same building as those used with RANSAC and presented in Fig.-5a. Therefore it is chosen in our approach leading to detect automatically building roof planes using Lidar data. Therefore, in the next paragraph, the RANSAC algorithm is extended in order to increase the percentage of successful plane detection from 70% to more than 95%.

4. EXTENSION OF RANSAC ALGORITHM

Two directions are proposed for extending the capacities of RANSAC algorithm to a better roof plane detection. The first one is the improvement of the data quality; the second one is the adaptation of RANSAC algorithm to roof detection.

4.1 Improvement of data quality

It is well known that the point cloud coordinates contain errors related to position accuracy, artefacts, and multi ways. Moreover, noise and the small details composing building roofs are considered as obstacles. At last, variable point densities may occur for the same building roof. So, irregular distribution of points on a building roof is also a cause of errors in the calculated plane. All these reasons allow thinking about the necessity of improving the quality of the point cloud.

This remark leads to generate a new point cloud. On the one hand, the new cloud should present a homogeneous point density, and on the other hand, the errors of point coordinates and the noise should be eliminated or decreased.

For this purpose, a resampling of the building point cloud is performed firstly. The sampling value defining the generated DSM is deduced from the average point density (Tarsha-kurdi *et al.*, 2007); and then values are assigned to the DSM cells. In the latter operation, the original cloud is superimposed on the DSM grid. Hence, some cells are empty and other cells contain one or more points. In the case of a non empty cell, the corresponding DSM pixel takes the maximum of the Z values occurring among the points. In the case of an empty cell in the building body, the corresponding DSM pixel value takes the mean of the non null neighbouring pixels. On the one hand, this operation allows eliminating a high quantity of points describing the facades. On the other hand, it allows filling the

empty pixels, while respecting the mathematical characteristic of the plane.

Secondly, in order to decrease the errors of point coordinates and the noise, a simple low-pass filter is applied. The last step consists in converting the generated DSM into a 3D cloud. The analysis of the new point cloud shows that the position accuracy of the inner roof plane boundaries has decreased. This has to be related to the low-pass filtering. Hence, the new cloud is used exclusively for detecting the roof planes, but not for the future building modelling operations where the return to the original point cloud is inevitable.

4.2 Adaptation of RANSAC algorithm

The second enhancement consists in adapting RANSAC algorithm, in order to adapt the mathematical aspect of the algorithm with the geometry of a roof. Indeed, RANSAC algorithm searches to detect the best mathematical plane in a building cloud, regardless if the detected plane represents a roof plane or another plane.

The adaptation of RANSAC algorithm consists of improving its pseudocode, and of using additional procedures for improving the quality of the detected planes.

4.2.1 Improvement of RANSAC algorithm: In section 3.2, the 11th line is the essential line in the algorithm, because it represents a gate which allows to accept or to refuse the calculated plane. Indeed, the used condition is the number of points belonging to the calculated plane. Then the algorithm accepts the new plane if it contains more points than the last calculated one, else the new plane will be refused.

After the experiments, it was found that the best condition for validating plane detection is to take into account not only the number of points, but also simultaneously the standard deviation. Indeed, the use of standard deviation decreases the negative influence of the distance tolerance threshold t . As already mentioned, this threshold allows accepting whole points having distances to the plane smaller than t .

For example, let us take a "bad" plane which does not represent a roof plane, with a large standard deviation and containing a large number of points. In this case, in reason of the condition imposed by the number of points, the RANSAC algorithm will not accept another plane for replacing it. For solving this problem, a new threshold is introduced. This threshold is the number of points of the smallest foreseeable plane surface (PN_S). It is equal to the product of the smallest foreseeable plane surface by the point density. Then the 11th line in the algorithm becomes:

$$\text{if } st < \text{bestStd} \text{ and } \text{length}(s) > PN_S \text{ then} \quad (8)$$

After this modification, the percentage of successful results reached by the application of the adapted RANSAC algorithm reaches 85%.

4.2.2 Improvement of the detected planes quality: As already mentioned, the application of RANSAC algorithm allows the detection of planes which do not necessarily present roof planes. It represents perhaps one roof plane in addition to other noisy points which belong to other roof planes, as the points inside the red circles in Fig.-6a. These noisy points have to be eliminated from the detected plane, and have to be reassigned to the initial cloud.

Furthermore, inside the detected plane, there are some lost points (inside the blue circle in Fig.6a). These points have to be added to the fitted plane and extracted from the cloud in the same time.

The last two problems can be solved by applying mathematical morphology procedures on the binary Digital Surface Model (DSMb) calculated for the detected plane.

Results obtained by processing the data of Fig.-6a are shown in Fig.-6b. If the detected plane represents a set of points belonging to different roof planes and distributed stochastically, then the plane is rejected. Moreover, an additional condition checking if the new parameters never occurred previously is added automatically to the 11th line of the algorithm. So this plane is avoided in the next trials.

After detecting all planes covering perfectly the roof, the remaining points are normally either noisy points or small roof details (Fig.-6c). For classifying these points, a region growing algorithm is used, deciding if the set of points represents noise or roof details. Hence, the two criteria used are: the smallest foreseeable surface of a roof detail and the segment form. Thus, if the doubtful set of points represents noise, it is added to the nearest plane, else it is considered as a new plane. Fig.-6d presents the final result of roof planes detection obtained with the extended RANSAC algorithm.

4.3 Results and accuracy analysis

The building used for testing the approach in Fig.7 has numerous details on its roof (chimneys, dormers, windows). Moreover, the majority of roof plane surfaces are small regarding the point density. Furthermore, its point density is relatively weak (1.3 points/m²).

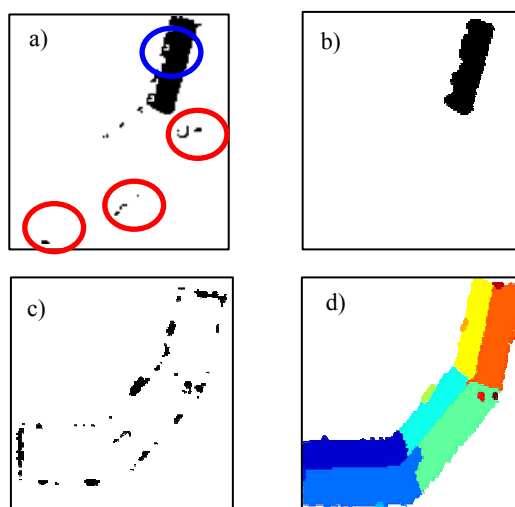


Figure 6. a) DSMb of the detected plane. It corresponds to the yellow plane in Fig.6d; b) DSMb of the improved detected plane; c) DSMb of the remaining points after detecting the roof planes; d) Final result of roof planes detection.

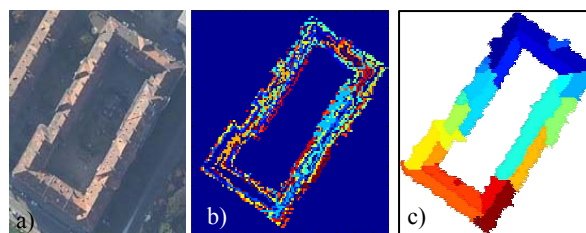


Figure 7. Roof planes detection results. a) Aerial image. b) Using classic RANSAC algorithm. c) After extension of RANSAC algorithm. The colours in b) and c) represent the different building roof planes

All these reasons lead to plane misdetection when the original RANSAC algorithm is applied (see Fig.-7b). On the other hand, after applying the extended RANSAC algorithm, the automatic roof plane detection over the same building is satisfactory. Fig.-7c illustrates clearly the improvements gained by the extension of RANSAC algorithm.

Finally, the same test has been achieved on almost 58 buildings with different forms and different Lidar point densities. The good results confirm the potentiality of the extended RANSAC algorithm. Although the improvements showed promising results, it must be noted that the level of generalisation and consequently the result quality depend obviously on the point cloud characteristics (point density, position accuracy, noise), on the architectural complexity of the building roof and on the dimensions of the building roof planes and their details.

5. CONCLUSION

This paper presented and compared two methods for automatic roof planes detection from Lidar data. These methods are 3D Hough-transform and RANSAC algorithm. The principle and the pseudocode of each one were detailed. In order to test the original and the improved algorithms, two sets of point clouds characterized by different densities and containing different building forms were used.

It is stated that both methods are based on pure mathematical principles in order to detect the best planes from 3D point clouds. This characteristic leads sometimes to the production of intolerable errors. The main advantage of RANSAC algorithm is its rapidity and the percentage of successful detected roof planes. These reasons were our main motivations.

Thus, two enhancements were suggested in order to increase its capacities. The first one was the improvement of the original data by generating a new point cloud. The second improvement was the adaptation of the algorithm, so that the extended algorithm allows detecting the best roof plane instead of the best mathematical one. At last, the satisfying results obtained for different clouds even with weak point density validate the proposed processing chain. Once the building roof planes are detected automatically, it becomes easier to complete the processing chain and achieve the last steps leading to the complete 3D building model.

REFERENCES

- Ameri, B. and Fritsch, D., 2000. Automatic 3D building reconstruction using plane-roof structures, Published by the ASPRS, Washington DC.
- Brenner, C., 2000. Towards fully automatic generation of city models. In: *Int. Arch. Photogrammetry and Remote Sensing*, vol. 32, Part 3. Amsterdam, pp. 85–92.
- Bretar, F. and Roux, M., 2005. Hybrid image segmentation using LiDAR 3D planar primitives. *ISPRS Proceedings*. Workshop Laser scanning. Enschede, the Netherlands, September 12-14, 2005.
- Davies, E. R., 1988. Application of the generalized Hough transformation to corner detection. *IEEE proceedings*, Vol 135, Pt. E, No. 1.
- Fischler, M. A. and Bolles, R. C., 1981. Random Sample Consensus: A paradigm for model fitting with application to image analysis and automated cartography. *Communications of the ACM*, 24(6): 381-395.
- Forlani, G., Nardinocchi, C., Scaioni, M. and Zingaretti, P., 2004. Building reconstruction and visualization from Lidar data. *Int. Arch. of the Photogrammetry, Remote Sensing and Spatial Information Sciences*, Vol. XXXIV, Part 5/W12.
- Forlani, G., Nardinocchi, C., Scaioni, M. and Zingaretti, P., 2006. Complete classification of raw Lidar data and 3D reconstruction of buildings. *Pattern Anal. Applic.* (2006) 8: 357–374. DOI 10.1007/s10044-005-0018-2.
- Gonzalez, RC., Woods, RE. and Eddins, SL., 2004. *Digital Image processing using MATLAB*. Printed in USA, Pearson Prentice Hall. ISBN 0-13-008519-7. 609p.
- Hough, P.V.C., 1962. Method and Means for Recognizing Complex Patterns. *U.S. Patent* 3.069.654.
- Maas, H.-G. and Vosselman, G., 1999. Two algorithms for extracting building models from raw laser altimetry data. *ISPRS Journal of Photogrammetry & Remote Sensing* Vol. 54, No. 2/3, pp. 153-163
- McGlone, J. C., M. Mikhail, E. and Bethel, J., 2004. *Manual of photogrammetry (5th edition)*. Published by the ASPRS, ISBN 1-57083-071-1, 1151p.
- Nguyen, V., Martinelli, A., Tomatis, N. and Siegart, R., 2005. A comparison of line extraction algorithms using 2D laser rangefinder for indoor mobile robotics. *IEEE/RSJ Proceedings. Int. conference on intelligent robots and systems, IROS*, Edmonton, Canada.
- Oda, K., Takano, T., Doihara, T. and Shibasaki, R., 2004. Automatic building extraction and 3-D city modeling from lidar data based on Hough transformation. *Int. Arch. of Photogrammetry and Remote Sensing*, Vol. XXXV, part B3.
- Overby, J., Bodum, L., Kjems, E. and Ilsoe, P. M., 2004. Automatic 3D building reconstruction from airborne laser scanning and cadastral data using Hough transform. *Int. Arch. of Photogrammetry and Remote Sensing*, Vol. XXXV, part B3.
- Rabbani, T. and Van den Heuvel, F., 2005. Efficient Hough transform for automatic detection of cylinders in point clouds. *ISPRS Proceedings*. Workshop Laser scanning. Enschede, the Netherlands, September 12-14, 2005.
- Rottensteiner, F., 2003. Automatic generation of high-quality building models from Lidar data. *IEEE Computer Graphics and Applications* 23(6), pp. 42-51.
- Tarsha-Kurdi, F., Landes, T. and Grussenmeyer, P., 2007. Joint combination of point cloud and DSM for 3D building reconstruction using airborne laser scanner data. *Urban Remote Sensing Joint Event URBAN/URS 2007*. 11-13 April Télécom Paris.
- Vosselman, G. and Dijkman, S., 2001. 3D building model reconstruction from point clouds and ground plans. *Int. Arch. of Photogrammetry and Remote Sensing*, XXXIV-3/W4: 37-43.

WAVEFORM ANALYSIS TECHNIQUES IN AIRBORNE LASER SCANNING

W. Wagner^a, A. Roncat^a, T. Melzer^a, A. Ullrich^b

^a Christian Doppler Laboratory for Spatial Data from Laser Scanning and Remote Sensing, Institute of Photogrammetry and Remote Sensing, Vienna University of Technology, Gusshausstrasse 27-29, 1040 Wien, Austria
(ww, ar, tm)@ipf.tuwien.ac.at

^b Riegl Research GmbH, 3580 Horn, Austria - aullrich@riegl.co.at

KEY WORDS: LIDAR, Waveform, Analysis, Pulse detection, Decomposition, Deconvolution, Point cloud

ABSTRACT:

Small-footprint airborne laser scanners with waveform-digitising capabilities are becoming increasingly available. Waveform-digitising is particularly advantageous when the backscattered echo waveform is complex because it allows selecting processing algorithms adjusted to the task. In addition, waveform-digitising laser scanners depict the physical measurement process in its entire complexity. This opens the possibility to derive the backscatter cross section which is a measure of the electromagnetic energy intercepted and reradiated by objects. In this paper approaches for deriving the cross section along the laser ray path are discussed. For data storage and processing reasons a practical approach is to model the waveform as the sum of a number of echoes backscattered from individual scatterers. This approach involves estimating the number of echoes, finding a match between the modelled echoes and the measured waveform, and estimating the cross section using calibration targets. For estimating the number and position of echoes the Average Square Difference Function (ASDF) method, which is a discrete time delay estimation technique, is tested. The results show that ASDF is a promising approach which appears to be less affected by noise compared to more traditional echo detection methods.

1. INTRODUCTION

Airborne laser scanning (ALS) is an optical measurement technique for obtaining information about the Earth's surface such as the topography of the land surface, the vegetation cover and the seafloor elevation in shallow waters. This technique is also often referred to as LIDAR, which stands for *Light Detection And Ranging*. Most ALS instruments use pulse lasers, i.e. they send out short laser pulses in the visible and/or infrared part of the electromagnetic spectrum and measure some properties of the backscattered light to find range and/or other information of a distant target. While many of the first ALS systems provided only range information, ALS systems that digitise and record the complete echo waveform are becoming increasingly available.

Bathymetric lidar instruments designed for measuring depth of relatively shallow, coastal waters were the first full-waveform systems. These sensors transmit pulses at green wavelengths that penetrate several meters into the water depending on water clarity and turbidity. According to Wozencraft and Millar (2005) the maximum detectable depth of the seafloor is about 60 m. Scattering and spreading of the laser pulse at the air-water boundary, within the water column and the seafloor results in relatively complex echo waveforms (Tulldahl and Steinvall, 1999). Therefore, as Guenther et al. (2000) point out, it has not been possible to calculate all depths with high accuracy and reliability in real time during data acquisition. Precise depths are determined via post-flight processing of stored waveforms. More recently, NASA developed a small-footprint waveform-digitising bathymetric lidar that is also capable of mapping topography and vegetation (Wright and Brock, 2002). Nayegandhi et al. (2006) demonstrate the capability of this sensor for depicting the vertical structure of vegetation canopies.

Also the echo waveform from vegetated areas is in general rather complex, in particular when the laser footprint is large (Sun and Ranson, 2000). Therefore also large-footprint airborne and spaceborne lidar systems designed for mapping of vegetation capture the complete echo waveform in order to allow the retrieval of geophysical parameters in post-processing. One of the airborne systems is the Laser Vegetation Imaging Sensor (LVIS) that transmits 10 ns long infrared pulses at repetition rates up to 500 Hz (Blair et al., 1999). Depending on flight altitude the footprint diameter is 1-80 m. So far, no satellite lidar system designed for the primary purpose of global vegetation mapping is available. However, the Geoscience Laser Altimeter System (GLAS) on-board of the ICESat satellite has acquired waveform data not only over the ice sheets but also over land surfaces. This will allow testing the usefulness of large-footprint (66 m) satellite-based waveform measurements for characterising forest structure and biomass (Harding and Carabajal, 2005).

For topographic mapping a small laser footprint and a high point density are required to collect a high number of geometrically well defined terrain echoes. Various filters that classify the echoes into terrain and off-terrain echoes based on purely geometric criteria can be used to reconstruct the terrain surface (Sithole and Vosselman, 2004). Given that this approach has worked well for lidar systems with ranging capabilities only, the need for waveform digitising lidar systems has not been evident for this application. Also, the benefit of waveform data for emerging ALS applications like 3D city modelling (Vosselman et al., 2005) and forest mapping (Hollaus et al., 2006) was not clear even though some early studies demonstrated the rich information content of small-footprint waveform data over land surfaces (Lin, 1997). Nevertheless, the first commercial waveform-digitising laser scanner system started appearing in the market in 2004. Even though research

on small-footprint waveform data can still be considered to be only in its beginning, a number of benefits start to emerge:

- Jutzi and Stilla (2003) point out that recording the waveform is advantageous because algorithms can be adjusted to tasks, intermediate results are respected, and neighbourhood relations of pulses can be considered. For example, Wagner et al. (2004) show that depending on the observed target the range determined by different echo detection methods may differ by several decimetres for a laser footprint diameter of 1 m. Recording the waveform allows applying different detectors for different targets.
- Over forested areas the number of detected echoes can be significantly higher for waveform-recording ALS systems compared to first/last pulse systems (Persson et al., 2005; Reitberger et al., 2006)
- In addition to geometric information, waveform digitising ALS systems also provide a number of physical observables such as the echo width, the echo amplitude and the backscatter cross section (Wagner et al., 2006). This opens the possibility to classify the echo point cloud based on geometric and physical properties.
- The echo from vegetation is in general broader than the echo from the ground surface (Persson et al., 2005). Doneus and Briese (2006) demonstrated that it is possible to improve the quality of terrain models by removing wide echoes before the filtering process.
- The intensity of laser echoes, respectively the backscatter cross section, can be calibrated using portable brightness targets (Kaasalainen et al., 2005). This is important to enable the comparison of measurements taken by different sensors over different areas.
- In electrodynamics, scattering processes are described quantitatively by the cross section. The cross section is hence a fundamental quantity in radar and lidar remote sensing. Since it can be derived from calibrated waveform data, the gap between experimental results and electromagnetic theory could be bridged (Wagner et al., 2007).

In this paper waveform analysis techniques as applied to small-footprint ALS data acquired over land surfaces are discussed. An advanced method for estimating the number and position of echoes in small-footprint waveforms is investigated in more detail.

2. THEORY

2.1 Waveform Generation

The shape of the waveform is determined by a number of sensor parameters and the backscattering properties of the targets. Important sensor parameters are the shape of the laser pulse, the receiver impulse function and parameters describing the pulse spreading (Jutzi and Stilla, 2006). The target is described by the differential backscatter cross section $\sigma(t)$, whereas t represents the round-trip time from the sensor to the target and back. Essentially, the received power $P_r(t)$, i.e. the waveform, is the result of a convolution of the ALS system waveform $S(t)$ and the cross section $\sigma(t)$ (Wagner et al., 2006):

$$P_r(t) \propto S(t) * \sigma(t) \quad (1)$$

where the symbol $*$ represents the convolution operator. The system waveform $S(t)$ takes into account the form of the laser pulse and the effects of the receiver and other hardware components. For extended targets the convolution function given in Eq. (1) has to be expanded to account for beam spreading effects.

2.2 Backscatter Cross Section

As one is interested in measuring target characteristics, the principal quantity of interest in Eq. (1) is the differential backscatter cross section $\sigma(t)$, here also referred to cross section profile. It can be estimated from the measured waveform using deconvolution or decomposition techniques, each of which rests on a set of different assumptions about the real form of the cross section $\sigma(t)$.

Depending on the intended purpose, the cross section is treated as a continuous variable or as the sum of discrete values at different ranges. If treated as a continuous parameter the differential cross section can be represented in a three-dimension grid (voxel space). According to the orientation of the scanner relative to the 3D world frame, each ray (laser pulse) traces out a line in the world frame (Figure 1). Each voxel is assigned the corresponding value of the differential cross section. Such 3D representations could be the starting point for advanced modelling efforts, such as ray-tracing simulations within vegetation canopies (Sun and Ranson, 2000). A major disadvantage of such a representation is the required data volume.

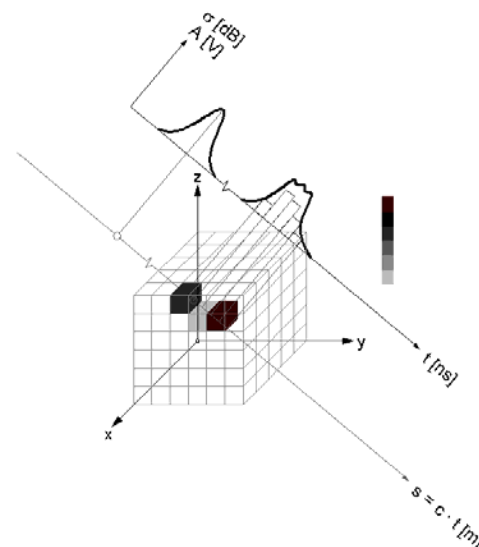


Figure 1. Voxel space representation of the cross section. The top half of the figure shows the emitted pulse (left) and the received echo (right), the lower half the embedding of the underlying cross section in a 3D voxel space.

For data storage and processing reasons a more practical approach is to model the waveform as the superposition of basis functions corresponding to the cross section of singular scatterers at different ranges (Wagner et al., 2006):

$$P_r(t) = \sum_{i=1}^N \frac{D_r^2}{4\pi R_i^4 \beta_i^2} \eta_{sys} \eta_{atm} S(t) * \sigma_i(t) \quad (2)$$

where N = number of targets
 D_r = receiver aperture diameter
 R_i = range from sensor to target i
 η_{sys} = system transmission factor
 η_{atm} = atmospheric transmission factor
 β_i = transmitter beamwidth
 σ_i = differential backscatter cross section of target i

Here, the waveform respectively cross section is represented by intermittent points irregularly distributed in 3D space (Figure 2). Neighbourhood relationships are not considered. An echo point is attributed a certain spatial dimension by adding the attribute "echo width". This approach is currently the standard in ALS processing.

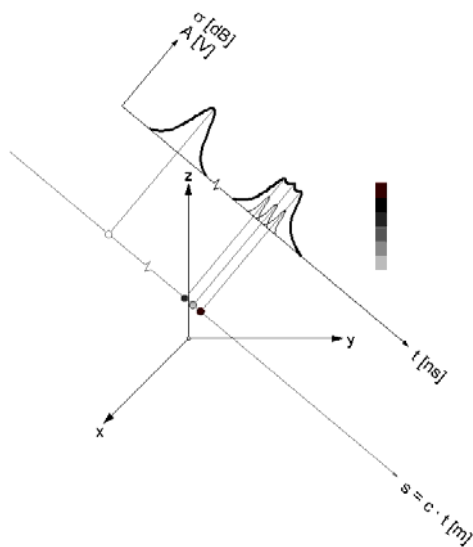


Figure 2. Discretisation of the ALS waveforms to obtain an irregularly distributed 3D point cloud. Here, the observed waveform is modelled explicitly as superposition of 3 Gaussian basis functions (targets).

2.3 Gaussian Decomposition

The decomposition of the waveform according to Eq. (2) becomes particularly simple, if both the individual cross sections and the emitted laser pulse can be described sufficiently well by Gaussian functions. In this case, the cross section can be computed in closed form using calibration targets (Wagner et al., 2006):

$$P_r(t) = \sum_{i=1}^N \hat{P}_i e^{-\frac{(t-t_i)^2}{2s_{p,i}^2}} \quad (3)$$

$$\sigma_i = C_{cal} R_i^4 \hat{P}_i s_{p,i} \quad (4)$$

where \hat{P}_i = amplitude of echo i
 $s_{p,i}$ = width of echo i
 t_i = round-trip time sensor to target i
 C_{cal} = calibration constant

Gaussian decomposition works by computing a nonlinear fit of the model Eq. (3) to the observed waveform. From the computed estimate (reconstruction), various target specific parameters such as echo width, intensity and position can be obtained. However, the number of targets as well as initial estimates for the distance of the targets have to be determined prior to the fit. This task is referred to as echo (pulse) detection.

Determining the number of echoes in ALS waveforms is not as simple as it may sound. Standard pulse detection methods such as *threshold*, *centre of gravity*, *maximum*, *zero crossing* of the second derivative, and *constant fraction* are discussed in Wagner et al. (2004). All these methods have their advantages and disadvantages. Problems occur when the waveforms have a complex shape and when the backscattered pulse is low compared to the noise level. In this case, advanced detection methods that minimise the influence of noise and account for non-ideal pulse forms should be sought. Thiel et al. (2005) tested a pulse correlation method and found almost no dependency on the signal to noise ratio. In our study we tested a time delay estimation technique as discussed in the next section.

3. ECHO DETECTION

For echo detection and time delay estimation, the *Average Square Difference Function* (ASDF) technique became relatively widespread during the last 15 years. Given two equidistantly sampled discrete time series, $x_1(t)$ and $x_2(t)$, the response value R of the ASDF is defined as (Jacovitti and Scarano, 1993):

$$R_{ASDF}(\tau) = \sum_{k=1}^n [x_1(kT) - x_2(kT + \tau)]^2 \quad (5)$$

where T is the sampling interval and $(n-1)T$ the estimation window length. Figure 3 (bottom) shows a typical example of $R_{ASDF}(\tau)$. As one can see, this function is closely related to the well-known direct cross-correlation function but has some computational advantages (Jacovitti and Scarano, 1993). In the case of full-waveform analysis, the reference pulse $x_1(t)$ can be of any shape required by the respective task, e.g.

- the emitted laser pulse itself (see Figure 3, top)
- a Gaussian Pulse (see Figure 4) or
- a mean reference system waveform (see Figure 4) derived from a set of original laser pulses.

The time delay estimator Δt of a tentative echo is the value of τ corresponding to the minimum of $R_{ASDF}(\tau)$. In full-waveform laser scanning, one has to expect multiple echoes of a single laser pulse. Therefore, not only the global minimum, but also the local minima have to be taken into account. Tentative echoes are located between local maxima (depicted with black circles in Figure 5). Due to the fact that only positive values of R_{ASDF} appear and due to zero-padding outside the time window of x_2 , the values of R_{ASDF} at the margins of its time window are always considered as local maxima (Figure 5). To distinguish real echoes from background noise, the detected minima must be separated from the neighbouring minima by a minimum distance ΔR_{min} . For our calculations we choose:

$$\Delta R_{min} = 0.3(\max(R_{ASDF}(\tau)) - \min(R_{ASDF}(\tau))) \quad (6)$$

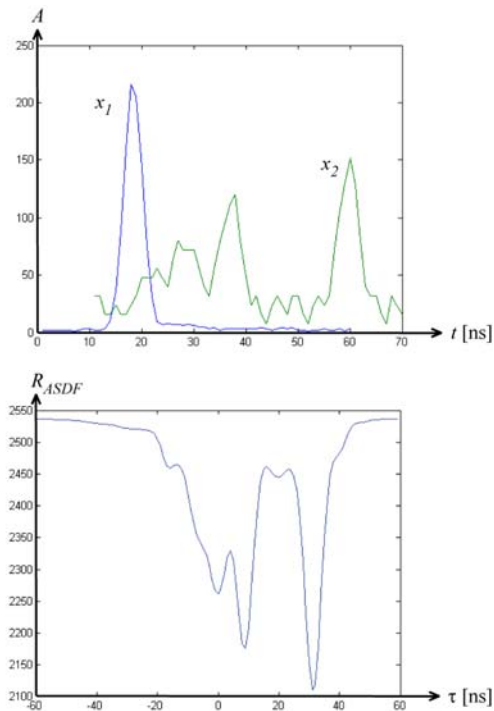


Figure 3. Top: Two discrete time series $x_1(t)$ (blue line) and $x_2(t)$ (green line) representing the system waveform and the backscattered waveform. Bottom: ASDF of these two time series.

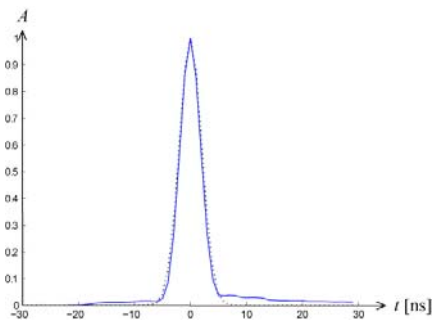


Figure 4. Mean reference pulse of the Riegl LMS-Q560 (blue solid line) and Gaussian pulse (black dotted line).

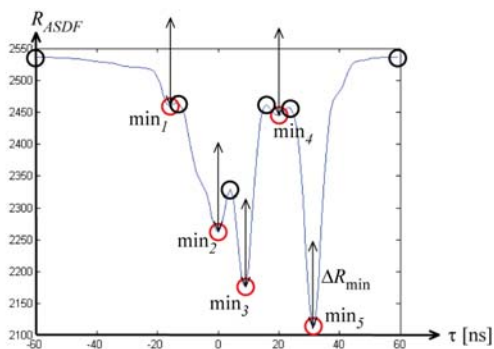


Figure 5. Principle of echo detection using ASDF.

Until now, the time delay of the detected echoes is only coarsely determined in the dimension of the sampling interval. According to Jacovitti and Scarano (1993), parabola fitting can be used for fine delay estimation. The peak of this parabola is located at

$$\Delta t_{fine} = -\frac{T}{2} \frac{R_{ASDF}(\Delta t + T) - R_{ASDF}(\Delta t - T)}{R_{ASDF}(\Delta t + T) - 2R_{ASDF}(\Delta t) + R_{ASDF}(\Delta t - T)} + \Delta t. \quad (7)$$

4. EXPERIMENTS

In this section, we present the results of two simple pulse detection and estimation experiments.

4.1 Data Sets

The data used in this study consist of two samples from the 2005 flight campaign over the Schönbrunn area of Vienna using the Riegl LMS-Q560 full-waveform laser scanner which uses a digitising interval of 1 ns. This campaign consisted of 14 flight strips (side overlap 60%) with an altitude of 500 m above ground and an average point density of 4 points per square metre within the strip. The data were acquired on April 5th, 2005 before the greening-up of the vegetation. Each sample contains the waveforms of 10,000 consecutive laser pulses and was taken from an area with rather dense vegetation (see Figure 6).

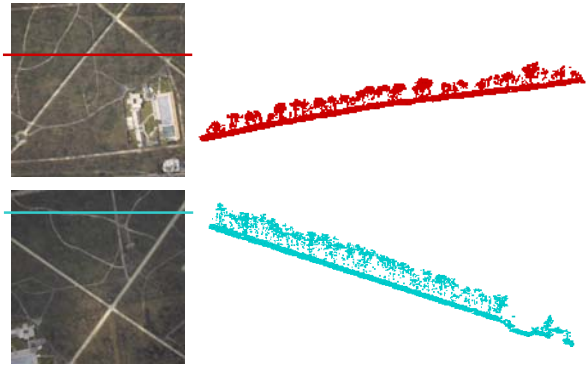


Figure 6. Aerial and perspective views of the sample areas. Top: Sample 1 (strip 2), bottom: Sample 2 (strip 5).

4.2 Results

In the first experiment, the number of echoes obtained with the max-detection method and two ASDF-based methods were compared. Max-detection considers those points as maxima whose intensity exceeds the respective intensities of its immediate neighbours. It is one of our standard pulse detection methods used in Gaussian Decomposition. The first ASDF-based technique uses a Gaussian Pulse with $s_p = 2$ ns as reference pulse (x_1 in Eq. (3)) whereas the second ASDF-based technique used the average of all emitted pulses of the respective sample as reference pulse. The results of this comparison are given in Table 1.

Method	# detected echoes (%)				
	1	2	3	4	>= 5
Max-Detection	58,08	32,20	7,73	1,08	0,09
ASDF (Gaussian Pulse)	66,23	21,09	9,22	1,81	0,18
ASDF (Mean Reference Pulse)	65,89	20,65	9,74	2,01	0,24

Method	# detected echoes (%)				
	1	2	3	4	>= 5
Max-Detection	51,54	35,23	10,86	1,67	0,27
ASDF (Gaussian Pulse)	60,96	24,24	11,48	2,47	0,24
ASDF (Mean Reference Pulse)	60,64	23,63	12,15	2,70	0,27

Table 1. Number of Echoes computed with Max-Detection vs. ASDF-based Pulse Detection. Top: Sample 1 (Strip 2), bottom: Sample 2 (Strip 5).

From Table 1 one can learn that the used reference pulse of the ASDF-based techniques does not influence the results of pulse detection significantly. However, it is not clear if this is mainly a consequence of the scanner's recording system. Comparing max-detection with the ASDF-based methods, one can see that the latter are more likely to detect single echoes than max-detection. It appears that ASDF is less sensitive to laser ringing effects, which may be pronounced particularly after strong echoes (Nordin, 2006). On the other hand, Table 1 shows that it is also more likely to detect three and more echoes with an ASDF-based technique than with max-detection.

In the second experiment, the echo estimation of the three different methods (Gaussian Decomposition and the two ASDF-based approaches mentioned above) was compared. Two echoes computed with different estimation methods were treated as identical (one and the same) if their respective delays Δt did not differ more than the sampling interval of 1 ns (see Table 2).

Comparison	Identical echoes (%)		Median of difference [ns]		RMS of difference [ns]	
	Sample 1	Sample 2	Sample 1	Sample 2	Sample 1	Sample 2
Gaussian Decomposition / ASDF (Gauss.Pulse)	86,7	86,4	-0,0004	-0,0004	0,12	0,13
Gaussian Decomposition / ASDF (Mean Ref. Pulse)	86,9	86,8	0,0002	-7E-05	0,12	0,13
ASDF (Mean Ref. Pulse) / ASDF (Gauss.Pulse)	98,7	98,7	-0,0008	-0,001	0,05	0,05

Table 2. Comparison of Echo Estimation

The results of Table 2 show that in most cases (more than 85 %), classical pulse detection methods and ASDF-based approaches yield identical pulses. Also here, the two ASDF-variants show nearly identical results. Furthermore, it is given empirical evidence that in most cases echo estimation with Gaussian decomposition and with parabola fitting of the ASDF lead to comparable results since the medians of difference are very close to 0 and the standard deviations of difference are not greater than 0.15 ns. In metric dimensions, this would conform to 2.25 cm in the direction of the laser pulse which is a very low value in comparison to the ranges appearing in ALS.

5. CONCLUSIONS

The experiments presented in this paper give empirical evidence that both pulse detection and pulse estimation using the Average Square Difference Function (ASDF) method is a

promising approach. To a high percentage, the results of ASDF-based techniques coincide with those achieved using standard methods. In these cases, it would not be necessary to determine the exact position of the echoes with non-linear fitting methods but could be done prior to Gaussian decomposition using the ASDF technique. This could accelerate the calculations, what is important given the increasingly large data volumes that novel laser scanner systems deliver. The remaining cases, where classical pulse detection methods and ASDF-based techniques do not coincide, need to be treated in more detail and are subject of further research.

6. REFERENCES

Blair, J. B., Rabine, D. L., and Hofton, M. A., 1999. The Laser Vegetation Imaging Sensor: a medium-altitude, digitisation-only, airborne laser altimeter for mapping vegetation and topography. *ISPRS Journal of Photogrammetry and Remote Sensing*, 54, pp. 115-122.

Doneus, M. and Briese, C., 2006. Digital terrain modelling for archaeological interpretation within forested areas using full-waveform laserscanning. In: M. Ioannides, D. Arnold, F. Niccolucci and K. Mania (Editors), *The 7th International Symposium on Virtual Reality, Archaeology and Cultural Heritage VAST (2006)*, in press.

Guenther, G.C., Cunningham, G.C., LaRocque, P.E., and Reid, D.J., 2000. Meeting the accuracy challenge in airborne lidar bathymetry. In: *Proceedings of the EARSeL-SIG-Workshop LIDAR*, Dresden, Germany, June 16-17, European Association of Remote Sensing Laboratories, 23 p.

Harding, D.J., and Carabajal, C.C., 2005. ICESat waveform measurements of within-footprint topographic relief and vegetation vertical structure. *Geophysical Research Letters*, 32, L21S10, pp. 1-4.

Hollaus, M., Wagner, W., Eberhöfer, C., and Karel, W., 2006. Accuracy of large-scale canopy heights derived from LiDAR data under operational constraints in a complex alpine environment. *ISPRS Journal of Photogrammetry and Remote Sensing*, 60(5), pp. 323-338.

Jacovitti, G., Scarano, G., 1993. Discrete Time Techniques for Time Delay Estimation. *IEEE Transactions on Signal Processing*, 41(2), pp. 525-533.

Jutzi, B., and Stilla, U., 2003. Laser pulse analysis for reconstruction and classification of urban objects. In: *International Archives of Photogrammetry and Remote Sensing*, Munich, Germany, 17-19. Sept., Vol. 34, Part 3/W8, pp. 151-156.

Jutzi, B., and Stilla, U., 2006. Range determination with waveform recording laser systems using a Wiener filter. *ISPRS Journal of Photogrammetry and Remote Sensing*, 61, pp. 95-107.

Kaasalainen, S., Ahokas, E., Hyypä, J., and Suomalainen, J., 2005. Study of surface brightness from backscattered laser intensity: Calibration of laser data. *IEEE Geoscience and Remote Sensing Letters*, 2(3), pp. 255-259.

- Lin, C.S., 1997. Waveform sampling lidar applications in complex terrain. *International Journal of Remote Sensing*, 18(10), pp. 2087-2104.
- Nayegandhi, A., Brock, J.C., Wright, C.W., and O'Connell, M.J., 2006. Evaluating a small footprint, waveform-resolving lidar over coastal vegetation communities. *Photogrammetric Engineering & Remote Sensing*, 72(12), pp. 1407-1417.
- Nordin, L., 2006. Analysis of waveform data from airborne laser scanner systems. Master Thesis, Luleå University of Technology.
- Persson, Å., Söderman, U., Töpel, J., and Ahlberg, S., 2005. Visualization and analysis of full-waveform airborne laser scanner data. In: *International Archives of Photogrammetry and Remote Sensing*, Vol. 36, Part 3/W19, pp. 103-108.
- Reitberger, J., Krzystek, P., and Heurich, M., 2006. Full-waveform analysis of small footprint airborne laser scanning data in the Bavarian forest national park for tree species classification. In: *Proceedings of the International Workshop on 3D Remote Sensing in Forestry*, Vienna, Austria, 14-15. Feb., pp. 218-227.
- Sithole, G., and Vosselman, G., 2004. Experimental comparison of filter algorithms for bare-Earth extraction from airborne laser scanning point clouds. *ISPRS Journal of Photogrammetry & Remote Sensing*, 59, pp. 85-101.
- Sun, G., and Ranson, K.J., 2000. Modeling lidar returns from forest canopies. *IEEE Transactions on Geoscience and Remote Sensing*, 38(6), pp. 2617-2626.
- Tiehl, K.-H., Wehr, A., and Hug, C., 2005. A new algorithm for processing fullwave laser scanner data. In: Proceedings of EARSEL Workshop "Use the third dimension for remote sensing purposed", Porto, Portugal.
- Tulldahl, H.M., and Steinvall, K.O., 1999. Analytical waveform generation from small objects in lidar bathymetry. *Applied Optics*, 38(6), pp. 1021-1039.
- Vosselman, G., Kessels, P., and Gorte, B., 2005. The utilization of airborne laser scanning for mapping. *International Journal of Applied Earth Observation and Geoinformation*, 6, pp. 177-186.
- Wagner, W., Ullrich, A., Melzer, T., Briese, C., and Kraus, K., 2004. From single-pulse to full-waveform airborne laser scanners: Potential and practical challenges. In: *International Archives of Photogrammetry and Remote Sensing*, XXth ISPRS Congress, Istanbul, Turkey, 12-23 July 2004, Vol. XXXV, Part B3, pp. 201-206.
- Wagner, W., Ullrich, A., Ducic, V., Melzer, T., and Studnicka, N., 2006. Gaussian decomposition and calibration of a novel small-footprint full-waveform digitising airborne laser scanner. *ISPRS Journal of Photogrammetry and Remote Sensing*, 60(2), pp. 100-112.
- Wagner, W., Hollaus, M., Briese, C., and Ducic, V., 2007. 3D vegetation mapping using small-footprint full-waveform airborne laser scanners. *International Journal of Remote Sensing*, in press.
- Wright, C.W., and Brock, J.C., 2002. EAARL: A Lidar for mapping shallow coral reefs and other coastal environments. In: *Proceedings of the Seventh International Conference on Remote Sensing for Marine and Coastal Environments*, Miami, Florida, unpaginated CDROM.
- Wozencraft, J., and Millar, D., 2005. Airborne lidar and integrated technologies for coastal mapping and nautical charting. *Marine Technology Society Journal*, 39(3), pp. 27-35.

7. ACKNOWLEDGEMENTS

We would like to thank the Schloß Schönbrunn Kultur- und Betriebsges.m.b.H for their support of the data acquisition campaign.

DEVELOPMENT OF A PROCEDURE FOR VERTICAL STRUCTURE ANALYSIS AND 3D-SINGLE TREE EXTRACTION WITHIN FORESTS BASED ON LIDAR POINT CLOUD

Yunsheng Wang ^{a,*}, Holger Weinacker ^a, Barbara Koch ^a
 a Dept. of Remote Sensing and Landscape Information Systems, University of Freiburg,
 – Tennenbacher Str. 4, 79106 Freiburg, Germany
 – (yunsheng.wang, holger.weinacker, barbara.koch)^a@felis.uni-freiburg.de

KEY WORDS: Canopy, Vertical structure, Tree crown, 3D model, Lidar, Point cloud

ABSTRACT:

A procedure for both vertical canopy structure analysis and 3D single tree extraction based on Lidar raw point cloud is presented in this paper. The whole study area is segmented into small study cells by a raster net. For each cell, a normalized point cloud whose point heights represent the absolute heights of the ground objects is generated from the original Lidar raw point cloud. The main tree canopy layers and the height ranges of the layers are detected according to a statistical analysis of the height distribution probability of the normalized raw points. For the 3D extraction of individual trees, the normalized raw points are resampled into a local voxel space. A series of horizontal 2D projection images at different height levels are then generated respect to the voxel space. Tree crown regions are detected from the projection images. Individual trees are then extracted by means of a pre-order forest traversal process through all the tree crown regions at different height levels. Finally, 3D tree crown models of the extracted individual trees are reconstructed.

1. INTRODUCTION

The vertical structures of stands are of high interest in forest management. The knowledge on the vertical structure improves regression models for estimation of wood volume and biomass. It is also of high interest for assessment of the regeneration success and biodiversity aspects. Lidar is especially suitable to reproduce the vertical structure of forest stand due to its capability of three-dimensional measurements with high accuracy. The utilization of Lidar in forest investigation can be generally divided into canopy height distribution based and single tree detection based. Several approaches for Canopy height distribution detection have been achieved in the past few years (Naesset, 2002; Lim et al, 2003; Hogmgren and Jonsson, 2004), these researches are mostly concentrated with the forest characteristics of the top canopy layer. Concern the vertical distribution of canopy layers, researches based on large-footprint Lidar data with continuous waveform have been accomplished by Lefsky et al.(1999) and Harding et al.(2001). Andersen et al.(2003) has presented a method for estimating vertical structure of forest through a group of regression functions based on field investigations. As for single tree delineation, the majority of the existed algorithms are DSM (Digital Surface Model) based (Hyypä and Inkinen 1999; Persson et al. 2002; Koch et al. 2006). Trees are delineated according to the features of crowns on the DSM, thus the individual trees in the lower canopy layer whose crowns are covered by the top canopy layer cannot be detected. Beside the detection of individual trees, Pyysalo and Hyypä (2002) has provided a process for reconstructing tree crowns, with a pre knowledge of the location and the crown size of single tree, raw points belong to the tree are extracted, the height of the tree, the height of the crown and the average radius of the crown at different heights are derived.

In this paper, we will present a procedure for both vertical structure analysis and single tree extraction within forest area based on Lidar raw point cloud. The major task of vertical structure analysis is to detect the number of main canopy layers and the height range of each canopy layer. A more detailed study of the spatial features of canopies is performed by the single tree extraction process. Individual trees are detected not

only from the upper canopy layer but also from the lower canopy layer in between the ground and upper canopy layer. Shapes of individual tree crowns are then delineated and 3D models of tree crowns are reconstructed.

The raw point cloud is the basis of our analysis. Due to the huge amount of data, it is not possible to analyse all the raw points within a study area in one step. Therefore the study area is segmented into a raster net firstly. Each grid cell is then a study cell, which with a size of $20\text{m} \times 20\text{m} = 400\text{m}^2$ in this case. Further analyses are carried out for each study cell separately. The results of each study cell can then be assembled for the whole study area at the end.

The study area is in “Kuernacher Wald”, the size of this study area is $2.7\text{km} \times 2.8\text{km}$, the dataset being used is a first-last returned Lidar data, the density of raw point cloud is 4~7 points per m^2 .

2. VERTICAL STRUCTURE ANALYSIS

2.1 Normalized Point cloud

To get the absolute object height of the raw points, the influence of terrain must be eliminated (Figure 1. Left). A raster DTM (Digital Terrain Model) is used for the normalization of raw point heights. The DTM is generated from the raw point clouds by TreesVis, a software for LIDAR data processing developed by Department of Remote Sensing and Landscape Information Systems (FeLis) (Weinacker et al., 2004).

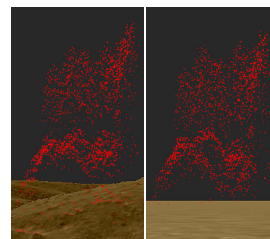


Figure 1. Comparison between original Lidar raw point cloud and normalized point cloud; Left: original Lidar raw point cloud and the DTM; Right: normalized point cloud over a zero height level surface

As been showed in Figure 1.(Left), raw points are projected above the DTM, the height difference between a raw point and its correspondent terrain is marked as the normalized height of the point. A normalized point cloud is then generated (Figure 1. Right), point heights of the normalized point cloud represent the absolute heights of the objects.

2.2 Detection of Canopy Layers

2.2.1 Height Distribution Probability of Normalized Points:

With a statistical process of the normalized points, a height distribution probability function $\phi(h)$ can be derived. According to the physical feature of Lidar data, most of the reflected points are located at canopy layers in the forest area. Therefore there should be an obvious increase of reflected points at each canopy layer. Thus, the problem of canopy layer detection is then transferred to a salient curve detection based on the height distribution probability function $\phi(h)$.

To reduce the influence of slight amplitude movements on the function, $\phi(h)$ is firstly smoothed with a gaussian function, a smoothed function $S(h)$ is generated, the second derivative $S''(h)$ is then calculated for the smoothed function $S(h)$.

As presented in figure 2., the magnitude of the second derivative is a useful criterion for salient curve detection. With each $S''(h) = 0$, there is an inflexion point of function $S(h)$. At the intervals of h where $S''(h) < 0$, there must be salient curves of function $S(h)$, so the intervals of h are considered as height ranges of tree canopy layers.

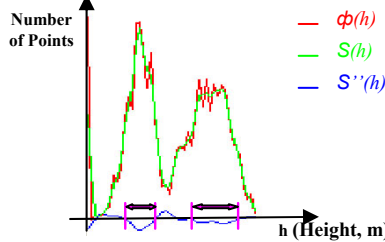


Figure 2. Relationship between $\phi(h)$, $S(h)$ and $S''(h)$, the ranges of canopy layers are extracted at the height intervals where $S''(h) < 0$

2.2.2 Attributes of Canopy Layers: The number of canopy layers in each study cell and the height range of each canopy layer are the main attributes derived from the vertical structure analysis. The range of a canopy layer starts from the height where the most rapid increase of point amounts occurred, the end of the range is marked at the height where the sharpest decrease of point amounts takes place (Figure 3.(a)).

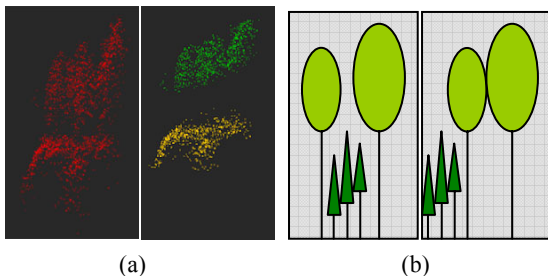


Figure 3. (a) Points within the ranges of the detected canopies with comparison of original point cloud; Left, Normalized point cloud; Right, Points within detected canopy ranges; (b) Two different forest stands with same height distribution probability density function; Left: Duple layer forest stand; Right: Single layer forest stand with trees of mixed height

As been illustrated in Figure 3 (b)., although there is no difference on height distribution of normalized points between the two cases, the spatial relationship of canopy layers is distinct. In the left case, the canopy layers overlap, such kind of situation can be considered as a real duple layer forest stand, on the contrary, the canopy layers in the right case are separated, this is actually a stand of trees with mixed heights. To detect the real duple layer stand, further studies on the spatial distribution of canopy layers are needed. This task is accomplished during the single tree extraction process.

3. SINGLE TREE EXTRACTION

3.1 2D Horizontal Projection Images

As being shown in Figure 4., a local voxel space is defined for each study cell, all the normalized points within the study cell will be resampled into the local voxel space.

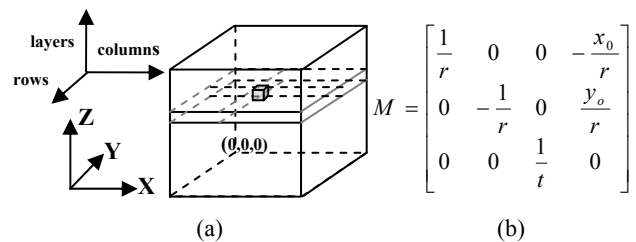


Figure 4. (a) Local voxel space with real world coordinate system (x,y,z) and voxel coordinate system (rows,columns,layers); (b) Definition of transformation matrix M

For the transformation of normalized points from real world coordinate system (x,y,z) to the voxel coordinate system (rows,columns,layers). A transformation matrix M is defined as figure 4.(b), of which: r represents the raster resolution of the horizontal surface in the voxel space; t represents the thickness of each layer in the voxel space; x_0, y_0 are the coordinates of the local origin, namely the x, y coordinate in real world coordinate system of the upper-left corner in the study cell; For each normalized point in real world $P(x,y,z)$, there is a correspondent point in voxel space $P'(row, column, layer)$, the relationship between P and P' can be defined with function:

$$[row \ column \ layer]^T = Round(M \times [x \ y \ z \ 1]^T)$$

According to the density of raw point cloud and the scale of r and t in transformation matrix M , it is possible that several normalized points are located within a same voxel. Take all the voxels of a single layer out of the voxel space, the voxels of the layer can be considered as pixels of an image. The number of normalized points within each voxel can be marked as the gray value of the correspondent pixel in the image.

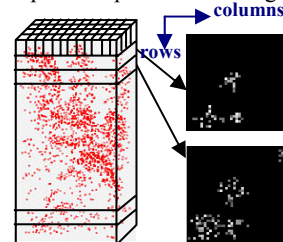


Figure 5. Normalized points in local voxel space and two examples of projection images of two vertical neighbouring layers of the voxel space

A 2D horizontal projection image of the selected layer is then generated (Figure 5.). The raw points of each individual tree crown will present a cluster feature on the horizontal projection image and the present of the cluster features is highly related with the horizontal resolution r and the thickness t of the voxel space. The values of parameter r and t in transformation matrix M rely on the density of the raw point cloud. According to our experiments, a horizontal resolution of 0.5 meter and a thickness of 2 meter are the ideal values for our dataset.

3.2 Extraction of Individual trees

The clusters on the horizontal projection image at each layer represent the distribution of tree crowns in the correspondent height level. Therefore an individual tree crown should be visible at the same location of several vertical neighbouring layers. The basic concept of single tree extraction is to trace the cluster features on the projection images from top to bottom through projection images at layers of different height levels.

3.2.1 Tree crown regions on 2D horizontal projection image: Potential tree crown regions in each layer are extracted based on the cluster features on the correspondent projection image. A hierarchical morphological opening and closing process with a group of predefined structuring elements (Figure 6.) is performed.

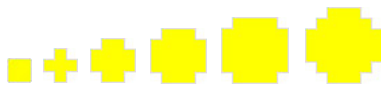


Figure 6. Structuring elements used in hierarchical morphological process

It can be presumed that the amount of raw points should be higher near the centre of each tree crown. Consider to the projection image, a higher gray value of a pixel represents a higher point amount in its correspondent voxel. Thus a higher significance should be assigned to the pixel with higher gray value and a larger neighbourhood of the pixel should be kept. The morphological process begins with the brightest pixels on the projection image, these pixels are taken as seeds and closed by the largest structuring element, then opened by the smallest structuring element, potential tree crown regions are then extracted based on the brightest pixels. Similar process is fulfilled with pixels of other gray value levels, the lower gray value the pixels have, the smaller structuring element is used for closing and the bigger structuring element is used for opening. Finally, potential regions from different gray value levels at same neighbourhoods are merged (Figure 7.). Levels of gray value are defined according to the histogram of the projection image at non-zero gray value area, of which highest level: $\alpha \geq 80\%$; middle level: $20\% < \alpha < 80\%$; lowest level: $\alpha \leq 20\%$.

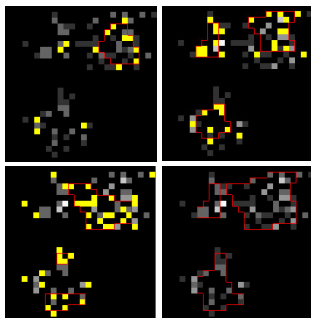


Figure 7. Hierarchical morphological process for tree crown region extraction from projection image; A

projection image is used as background, seed pixels are marked as yellow, contours of extracted tree crowns are marked as red. Upper left, Upper right, Lower Left: morphological process based on the pixels with highest, middle, lowest gray value level; Lower right: final result of tree crown extraction

3.2.2 Pre-order forest traversal: In computer science, forest traversal or more generally tree traversal refers to the process of visiting each node in a forest or tree data structure systematically. In our case, tree crown regions on the layers at different height levels can be considered as nodes at different levels of a forest data structure, crown regions on the top layer are the prime root nodes of the forest. A pre-order forest traversal process is fulfilled to visit all the crown regions of the forest.

Individual trees are extracted during the forest traversal process by grouping the vertical neighbouring crown regions from layers at different height levels. The main procedures of single tree extraction is illustrated in figure 8., a real case of single tree extraction is demonstrated in figure 9.. For each root node, namely the top region of each crown, the conditions of the existence of a child node, namely a vertical neighbouring crown region in next layer, are listed as follows:

$$\begin{aligned} A_i/A_r > C_a & \quad (1) \\ A_i/A_c > C_a & \quad (2) \\ D < \text{Min}(R_r, R_c) & \quad (3) \end{aligned}$$

where

- A_i = intersection area of root node and child node
- A_r = area of root node; A_c is the area of child node
- C_a = constant criteria in interval [0.5, 1.0], for which 0.8 is an ideal value in our study case
- D = distance between centre points of root node and child node
- R_r = average radius of root node
- R_c = the average radius of the child node

All the three conditions are sufficient condition, two regions can be considered as neighbouring regions no matter which condition is fulfilled.

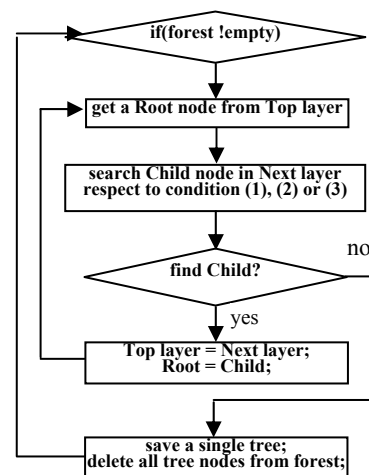


Figure 8. Main process of single tree extraction;

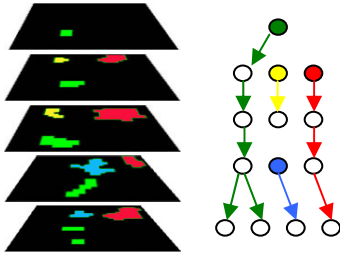


Figure 9. Demonstration of single tree extraction during a pre-order forest traversal process; Left: tree crown regions in different layers; Right: Result of single tree extraction, each tree is marked with a different colour, the root node of each tree is filled up with the same colour as the corresponding tree.

3.2.3 3D models of tree crowns: Each detected tree crown is described by an array of 2D tree crown regions in different layers at different height level. Since the layers in voxel space have certain thickness, 3D prisms can be constructed for the 2D crown regions in different layers with the thickness of layers as the height of the prisms. A group of 3D prisms at different height levels are then derived for each individual crown, and a prismatic 3D tree crown model can be reconstructed by a combination of all the tree crown prisms (Figure 10.).

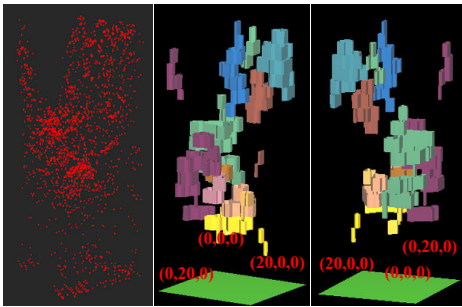


Figure 10. VRML(Virtual Reality Modeling Language) prismatic model of individual tree crowns within a single study cell with comparison of normalized point cloud; Left: Normalized raw points in a single study cell; Middle & Right: VRML models of individual tree crowns in the study cell visualized from different view directions, individual tree crowns are marked with different colours. The 3D models have the same vertical resolution with the local voxel space.

3.2.4 Features of study cell and individual trees:

1. For an individual tree the following parameters are available:
 - Height of the tree;
 - Height range of the crown;
 - Diameters of the crown at different height levels;
 - The largest diameter of the tree crown and its correspondent height;
 - Volume of the crown.
2. For a study cell, beside the number of individual trees, the number of crown layers is examined according to the spatial distribution of the extracted crowns. If there is an overlapping between individual crowns at different height levels, the study cell is considered as duple layered. This is a supplemental process for the study cells in which more than one canopy layers have been detected according to the vertical structure

analysis. After the analysis for all the study cells, the distribution of duple canopy layers in the whole study area can be mapped (Figure 11.)

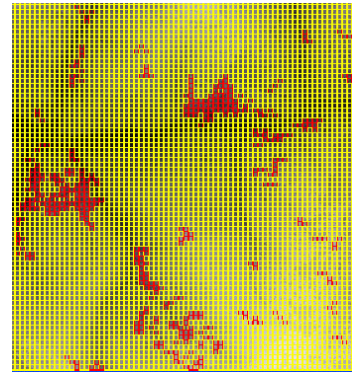


Figure 11. Map of duple canopy layer stands in one of the study area (Kuernacher Wald); Study cells with two canopy layers are marked as red; Study cells with single canopy layer are marked as yellow;

For 3D single tree extraction, a comprehensive reference data set based on field measurements is still missing. Coarse evaluations are based on ocular inspections of the raw data cloud points, aerial photographs and field information.

4. CONCLUSION

The statistical method seems to be efficient and reliable in detecting the existence and height range of canopy layers due to the first visual checks. The drawback is that it is incapable in distinguishing a real duple canopy layer structure and a single layer structure with trees of mixed heights. The existence of duple canopy layer structure is examined during the single tree extraction process according to the spatial distribution of canopy layers.

For the single tree extraction, the advantage of our algorithm is that not only the individual trees whose crowns are at the top canopy layer, but also the lower trees whose crowns are covered by the top canopy layer are extracted. The crown contours extracted from different height level of an individual tree crown will provide a higher approximation between the 3D crown model and the reality. The main problems still faced are due to the trees with big crowns and the conjunct neighbouring trees. For big tree crown with more than one crown peak, the crown might be split into more than one individual crowns. Trees whose crowns are tightly conjunct might be considered as a single tree. Another disadvantage of current algorithm is that the segmentation of study cells might split the trees along the border of the cells.

The main influence factors on the quality of the 3D single tree extraction algorithm are the density of the raw point cloud and the stand situation of the forest. Higher point density will improve the accuracy of tree extraction. Better result can be expected for a lower canopy closure forest stand.

Despite the mentioned challenges, the outcomes of recent single tree extraction algorithm are encouraging. Further studies will concentrate on the improvement of the single tree detection and modelling process, utilization of full waveform data could be helpful for the achievement of better tree crown models, and an enlargement of study cell size or a substitution of the raster grid by a moving window for study cell segmentation would reduce the over split of the trees along the border of each cell.

REFERENCES

- Andersen, H.E., Foster, J.R., Reutebuch, S.E. (2003). Estimating forest structure parameters on Fort Lewis Military Reservation using airborne laser scanner (LIDAR) data. Proceedings of the 2nd International Precision Forestry Symposium. Seattle, Washington. University of Washington, College of ForestResources, 45-53.
- Harding, D., Lefsky, M., Parker, G., Blair, J. (2001). Laser altimeter canopy height profiles: Methods and validation for closed-canopy, broadleaf forests. *Remote Sensing of The Environment* 76, 283-297.
- Holmgren, J. and Jonsson, T. (2004). Large scale airborne laser-scanning of forest resources in Sweden. In:Thies, M., Koch, B, Spiecker, H.and Weinacker, H.(eds.). *Laser scanners for forest and landscape assessment*. Proceedings of the ISPRS working group VIII/2. Freiburg, Germany, October, 3-6 2004. *International Archives of Photogrammetry, Remote Sensing and Spatial Information Sciences*. Volume XXXVI,Part 8/W2, 157–160.
- Hyypä, J. and Inkinen, M. (1999). Detecting and estimating attributes for single trees using laser scanner. *The Photogrammetric Journal of Finland* 16, 2742.
- Koch, B., Heyder, U., Weinacker, H.(2006) Detection of individual tree crowns in airborne lidar data. *Photogrammetric engineering and remote sensing* 72:4, 357-363.
- Lefsky,M., Cohen,W., Acker,S., Parker, G., Spies, T., & Harding, D. (1999). Lidar remote sensing of biophysical properties and canopy structure of forests of Douglas-fir and western hemlock. *Remote Sensing of Environment*, 70, 339-361.
- Lim, K, Treitz, P., Baldwin, K., Morrison, I. and Green J. (2003). Lidar remote sensing of biophysical properties of tolerant northern hardwood forests. *Canadian Journal of Remote Sensing* 29, 648–678.
- Næsset, E. (2002). Predicting forest stand characteristics with airborne scanning laser using a practical two-stage procedure and field data. *Remote Sensing of Environment* 80, 88–99.
- Persson, Å., Holmgren, J. and Söderman, U. (2002). Detecting and measuring individual trees using an airborne laser scanner. *Photogrammetric engineering & Remote Sensing* 68, 925–932.
- Pyysalo, U., Hyypä, H. (2002). Reconstructing tree crowns from laser scanner data for feature extraction. *Commission III Symposium Graz*, 293-296.
- Weinacker, H., Koch, B., Weinacker, R.(2004). TREESVIS- A software system for simultaneous 3D-Real-Time visualization of DTM, DSM, Laser row data, Multi-spectral data, simple tree and building models. Proceedings of the ISPRS working group on Laser-Scanners for Forest and Landscape Assessment, 03-06 October, Freiburg, Germany, *The International Archives of Photogrammetry, Remote Sensing and Spatial Information Sciences*, vol XXXVI part 8/W2, ISSN 1682-1750, 90-95

TERRESTRIAL LASER SCANNING VERSUS TRADITIONAL FOREST INVENTORY FIRST RESULTS FROM THE POLISH FORESTS

Wezyk P.*, Koziol K., Glista M., Pierzchalski M.

Laboratory of GIS & Remote Sensing, Faculty of Forestry, Agricultural University of Krakow, Poland
rlwezyk@cyf-kr.edu.pl

Commission WGIII/3, III/4, V3, VIII/1

KEY WORDS: terrestrial laser scanning, DBH, tree and stand basal area, manual and automatic methods

ABSTRACT:

The goal of this paper was to present the pilot study ongoing in the Polish State Forests on the application of gathering basic forest parameters using the terrestrial laser scanner (TLS) technology. The 3D point cloud was created using scanner based on the "phase-shift" technology. The first part of the paper shows the comparison of two manual methods of TLS data processing, i.e. the directly measurement on the planar image so called - „pixel method” and semi-automatic „pipe method”, in the context of the results obtained with traditional forest inventory. The second part of the article refers to author’s algorithms, the purpose of which was to make the process of obtained the stand basal area (G) from a scanned tree trunks (also partially scanned) automatic. The first stage of work over algorithms resulted in precise definition of the: location of tree trunks on the inventory plot and such elements: tree basal area (g), stand basal area (G) and BHD.

1. INTRODUCTION

The inventory of forest resources in Europe is based on well-elaborated standards and usually carried out in a very traditional way. To put it in a simple way - the measurement involves getting information on the diameters at breast height (DBH) of the trees, their mean height (H) and density (the number of trees) on circular plots, making statistical sample of respective stratification groups of tree stands. The works on forest inventory are very time-consuming and costly, thus methods and technologies accelerating the work and reducing costs have been looked for. The application of airborne and terrestrial photogrammetry in the forest inventory have been known for decades and the application of VHRS offering a pixel size below 1.0 metre becomes more and more common (de Kok, et al., 2005; de Kok and Wezyk, 2006; Weinacker, et al., 2004). One of dynamically developing technologies in the area of active remote sensing systems is LiDAR, both in the form of airborne laser scanning (ALS) and terrestrial laser scanning (TLS). This technology allows very quick information on the structure of forest in the form of the 3D point cloud, which is processed to gain such taxation features as: the number of trees in the stand, geoposition of individual trunks, diameter at breast height (DBH), crown base height and the height of trees (Aschoff and Spiecker, 2004; Bienert, et al., 2006; Næsset, et al., 2004; Simonse, et al., 2003; Hopkinson, et al., 2004). The purpose of presented paper was the comparison of the TLS technology to traditional forest inventory applied in Poland in the aspect of supporting these methods with modern technologies correcting the quality of elaborations. The paper presents subsequent stages of work over obtaining such parameters as: position of the tree in the 3D space, DBH, tree height and tree/stand basal area (g/G).

2. RESEARCH AREA

The tree stands located in the Forest District of Milicz, central-west Poland (51°27' N; 17°12' N) were selected for the study. In

these stands in November 2006, TLS was carried out on 30 circular plots (6 plots located in deciduous forest stands: beech, oak; 24 plots in coniferous stands: Scots pine). In the paper the results from 4 inventory plots are presented (Table 1).

Forest type	Deciduous		Coniferous		
	Plot number	3	5	15	19
Forest sub-compartment	140b	140g	232b	220d	
Radius [m] / Area [m ²]	12.62 / 500				
Tree species (number)	<i>Quercus</i> sp. (12); <i>Fagus silvatica</i> (1), <i>Pinus silvestris</i> (1)	<i>Fagus silvatica</i> (6)	<i>Pinus silvestris</i> (21)	<i>Pinus silvestris</i> (30)	
Mean DBH [cm]	42.7	56.7	22.0	28.5	
Mean height [m]	31.2	33.7	20.4	22.5	
Age [years]	142	152	107	67	

Table 1. Characteristic of selected forest inventory plots (Milicz Forest District PG LP)



Figure 1. Scanner FARO and the 5 spheres on the inventory plot

3. MATERIAL AND METHODS

3.1 Type of scanning

In the paper the method of TLS from 4 scanner locations is presented i.e., first position (S_1) was in the centre of the plot and the following three (S_2, S_3 and S_4) were distributed regularly along the plot. In practice the position of the scanner (so that they could be visible from each other) and reference spheres (k1+k5), was often problematic, because of the tree trunks and undergrowth. The condition of fitting 4 scans into one point cloud together is clear identification (max. in the distance of 15÷17 m) of at least 3 reference spheres from each scanner position. Scanning of one forest inventory plot from 4 stations, together with preparation work, took about 1 hour and 20 minutes.

3.2 Reference data

The forest inventory campaign was carried out in August 2006 by the company Taxus SI Ltd., based on the methods accepted in the Polish State Forests inventory guidelines (PGLP, 2003). The DBH measurement was carried out in a standard way with the calliper (accuracy 0.001 m) aiming its long arm towards the centre of the plot (this measurement further called reference inventory = Ref. Inv.), i.e., unfortunately exactly the opposite (90°) to the one imaging by scanner. Distances (L) in the polar measurement towards the tree were measured with an ultrasound range finder. The azimuth (Az) was read towards the centres of trunks with a compass (accuracy up to 1°). Due to the irregularity of trunks of the analysed trees, in April 2007 additional reference measurements were carried out by the authors (further called = Ref. 1_AUC), defining for each tree the DBH upright towards each of 4 scanner positions using calliper. At the same time the perimeter of the tree trunk on the height of 1.3 metre from the ground (further called = Ref. 2_AUC) was collected using measuring tape (accuracy 0.001 m). These works, although time-consuming, were necessary to test the usefulness of the FARO scanner fully objectively.

3.3 Hardware and software

In the forest the model LS 880 HE80 of a laser scanner of FARO company was used. It is based of the phase shift technology. Due to this technology up to 250 000 pps can be registered. The beams, in case of full resolution and distance 10.0 m from the scanner are located every 1.5 mm. The time of the scanner's full rotation is about 7 minutes for the resolution of about 1/4. The HE80 model, due to its modular structure, i.e. 4 components installed on a rotating base is very practical. The PC computer and HDD are integrated in the base module and they allow the set-up of the equipment in the office, without the need for a notebook in difficult field conditions. To manage the scans and combine them based on reference spheres, the Faro Scene ver. 4.0 software was applied. This also enables to apply proper filters and make measurements as well as give the geoposition to the point clouds. To achieve this, a static dGPS measurement (300 epoch; reference station: ASG-PL Wroclaw; distance ~50km; Polish Coordinate System PUWG 1992) was carried out for the position of the scanner (Wezyk, 2005). The mean fit scan error of joining 4 point clouds from respective positions of scanners, oscillated for the analysed inventory plots within the range: 2.8÷4.9 mm - long. mismatch and 2.1÷6.3 mm - orthogonal mismatch.

Manual measurements of DBH in FARO Scene, made by the operator between the pixels making the tree trunk in a planar

view, were (in a simplified way) called *pixel method* (Figure 2). The other alternative method (further called „pipe method” - Figure 3) involved semi-automatic fitting a cylinder into the tree trunk (on breast height). The distance and angle to tree trunks represented by the clouds of points were defined due to the author's algorithm operating in ArcView (ESRI) environment.

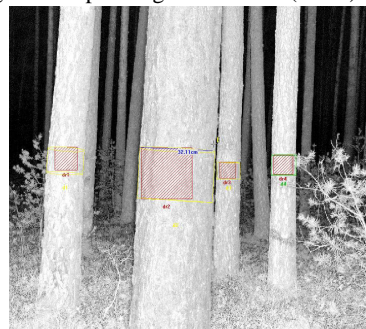


Figure 2. Manual „pixel method” (plot no. 19)

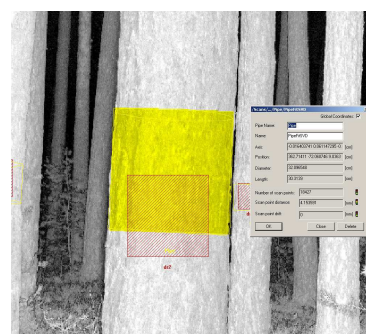


Figure 3. Semi-automatic „pipe method” (plot no. 19)

3.4 Data pre-processing

Advanced data processing (filtration, classification) was carried out by TerraScan and TerraModeler (Terrasolid Ltd.) software importing the cloud of points with added georeference in FARO Scene as XYZ (ASCII) sets. The classification of the point clouds involved generating a correct DTM in the first step, based on so-called *low points routine*. Not always was it a simple task due to so-called *ghost points* occurring below the ground, which should be reclassified. In the next step, points above DTM were put into a *High Vegetation* class (Figure 4). From this class slices were obtained and their thickness was 0.04 m (3D belt 1.28÷1.32 m from the DTM). If this place was covered with another object (e.g. undergrowth) the closest slice above was taken. In the subsequent step the slice was exported as XYZ set to ArcView 3.2 (ESRI) software.



Figure 4. The point cloud after classification (plot no. 5)

3.5 Algorithms

The process of manual fitting ellipses into slices of trunks obtained from the point clouds on BHD height is very time-consuming and it is hard to imagine obtaining this parameter for hundreds or even thousands of inventory plots.

Automatic methods allowing the detection of tree trunks are usually based on the application of Hough transformation (Aschoff and Spiecker, 2004). Fitting geometric figures (ellipse, circle) into trunk slices is also described in detail by Aschoff et al., (2004). The cluster analysis is often used in automatic recognition of tree trunks and extraction of parameters both in case of single scans (covering not more than 180°) of the tree trunk cylinder form, as well as images originating from the integration of several scans on one area (Bienert, et al., 2006).

The main purpose of making the algorithm in the discussed project was the need for automatic detection of tree trunks and obtaining the tree/stand basal area (g/G).

The tasks for the algorithm focussed on:

- the definition of the neighbourhood in the point cloud, in the surrounding of 2D or 3D space (filtering, significance definition);
- assignment of points to a concrete tree trunk,
- definition of the angle range for the trunks visible from subsequent scanner positions,
- recognition of tree trunks and definition of their sizes;
- definition of the visibility of trunks (overshadowing by other trees), and
- drawing a probable outline of the trunk in the places without measurement points.

The first step for the algorithm (Algorithm 1) was to define the number of points in the surroundings of the point for plane XY and XYZ. Points with only three neighbours were treated as auxiliary points. The algorithm of automatic definition of the assignment of points (XYZ) to a given trunk is realized by triangulation (TIN) between points and then by the elimination of triangles not fulfilling the initial prerequisites.

As testing parameters the values of triangle's angles and lengths of its sides were accepted. The border value for angles was defined on the level of 10°, while the border value for the length ranged from 0.04 m to 0.08 m. The threshold value for the distance depends on the size of the inventory plot (maximal distance from the scanner), scanning resolution, the number of trees on the plot and their thickness (the influence of the overshadowing).

After classifying the points belonging to one tree trunk, the convex hulls were generated through the points regarded as trunks, then their area, perimeter and the number of internal and border points (making convex hulls) were calculated (Figure 5a).

Respective objects of convex hulls were eliminated based on the attributes according to the following criteria:

- the number of internal points > 3,
- the number of border points > 3,
- polygon perimeter > 0.21991 m (DBH > 7cm),
- area > 0.00385 m² (DBH > 7cm).

As a result of the carried out elimination, we obtained the polygons representing tree trunks (Figure 5a, 5b) and objects of a great density of points such as: bushes, branches or undergrowth (Figure 5d). Through the analysis of azimuth and length (Figure 5c, 5e) between the centroid of the object and the point belonging to it - objects other than trees were eliminated. In the case of trees covered by the undergrowth - the closest possible slice of the trunk was taken.

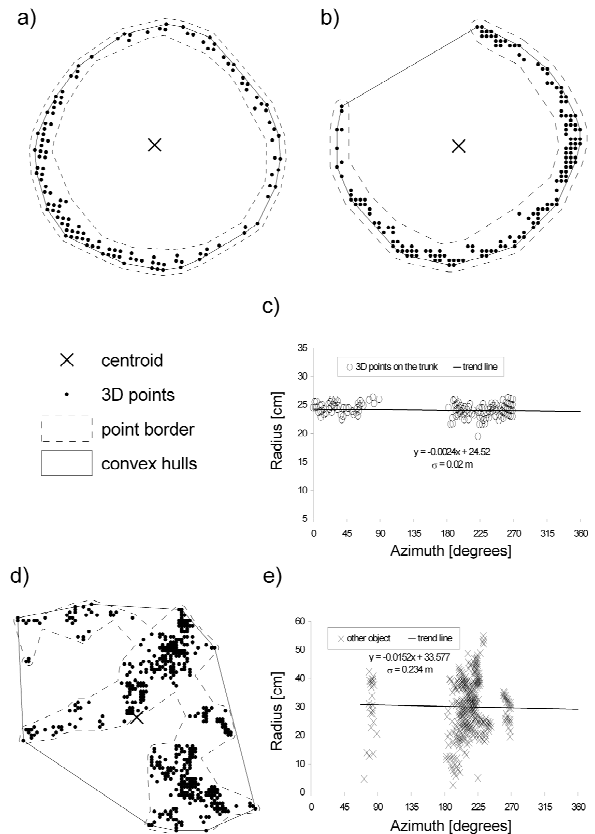


Figure 5. Points belonging to the tree trunk (a), partly to the trunk (b) and regression plots between radius and azimuth (c); not a tree objects (d) and their regression plot between radius and azimuth (e)

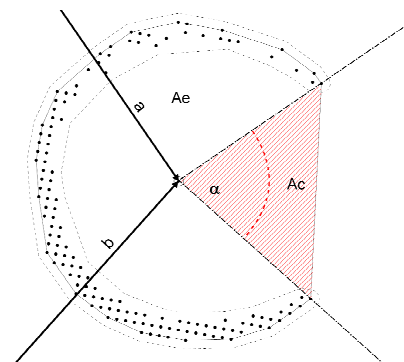


Figure 6. The cross section of tree trunk without a full point cover of TLS: a, b – lines between positions 2 and 4 of the scanner and centroid of the object, A_0 ; α - central angle describing the missing part of the slice

For trees not having points on fragment of the trunk (Figure 5b) – the correcting algorithm (Algorithm 2) was applied, based on the sector relayed on to central angle α . This algorithm acts in two ways based on the analysis of the interface based on the analysis of the length and the number of points on the perimeter of the convex hulls and the analysis of mutual situation of the objects and the positions of the scanner (Figure 6).

The area of the detected tree trunk by Algorithm 1 can be defined as:

$$A_o = A_e + A_c \quad (1)$$

where: A_e – part of trunk cross section with correct area,
 A_c – part of trunk cross section of an underestimated area.

The algorithm removed the determined part A_c to replace it by the corrected area (A_{cor}), calculated from the ratio between a full angle (360°) and angle α as well as the respective areas (Figure 6).

The correction values (A_{cor}) are expressed by the formula:

$$A_{cor} = A_e * \frac{2\pi}{\alpha} \quad (2)$$

The total tree basal area (g_t) is defined as:

$$g_t = A_e + A_{cor} \quad (3)$$

The majority of functioning algorithms for automatic calculation of the basal area of the trunk propose fitting of a circle (Aschoff, et al., 2004,), cylinder (Bienert, et al., 2006, Hopkinson, et al., 2004) or Hough’s transformation (Aschoff and Spiecker, 2004) assuming that a circle can approximately represent a trunk. In case of the listed algorithms the mean difference in the relation to the reference measurement DBH ranges from 1÷2 cm. Additionally the algorithm based on Hough transformation requires the conversion of vector data TLS (points XY) into raster. In algorithms based on the fitting of a cylinder, its height is connected with the size of the trees DBH. The larger DBH – the bigger height of the cylinder, thus it is necessary to make the mean base of cylinder. The proposed in this article algorithm is first of all based on a correct definition of the basal area of individual trees (g), from which DBH value could be calculated back as one of basic tree and stand parameters. The studies over the algorithm (Algorithm 1 and Algorithm 2) have been continued and the algorithm is gradually being improved.

4. RESULTS

4.1 The number of trees

Depending on the scanner position (S_1 ÷ S_4), the number of tree trunks on the reference plot, possible to be interpreted as full slices or their fragments, can be different. In case of plot 19 from the central position (S_1) one tree trunk could not be seen and two other were partially covered, which was stated only on the stage of detail work on the comparison with Ref. Inv. Making manual measurements with the pixel and pipe method is strictly dependent on full identification of tree trunk. The percentage of trees visible for manual measurement in plot number 19, ranges from 63.3% to maximal 90.0% from individual scanner positions. This has its consequences in calculating the stand basal area (Table 2).

4.2 Polar measurement

The process of getting slices of tree trunks leads to automatic gaining information on the centroid of the trunk and, this way,

making a precise map of trees on the forest inventory plot (Figure 7).

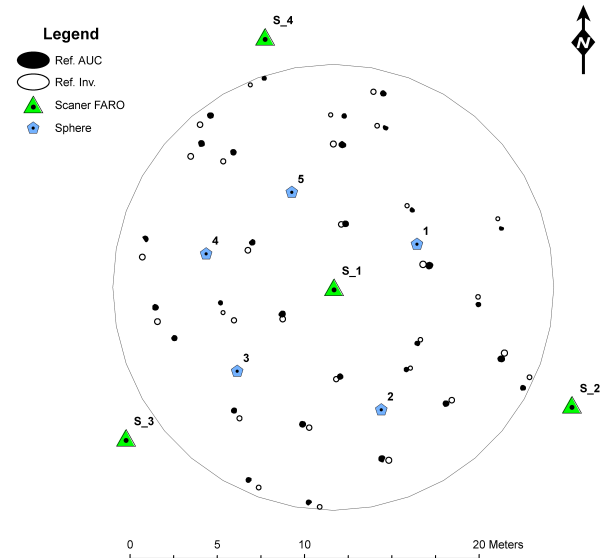


Figure 7. Map of tree trunks on the plot no. 19

Compared to traditional forest inventory, a constant angular shifting was observed (about 4°) resulting from the application of different instruments to measure azimuth from the centre of the plot to the tree trunk, as well as the situation of a survey pole northwards at the moment of scanning. So-called „gross errors” were relatively rare. They occurred e.g. during completing the paper forms in the “distance to the trunk” field (e.g. in case of plot 19, tree no. 21; the error was ca. 3.5m). The error in marking the north and inaccurate reading can cause the change of the position of the tree trunk to about 0.80÷1.0 m, on the border of the reference plot (radius = 12.62 m). Taking that the errors in the localization of respective laser points on the tree trunks can reach 1÷2 cm – this is still 50 to 100 times less than the accuracy of dGPS measurement (RMS 1.0÷1.5 m) under the forest canopy (Wezyk, 2005).

4.3 Tree DBH

The carried out statistic analysis of the measurements for all the scanner positions - i.e. for 141 visible pines, 36 oaks and 22 beech trees – showed that manual “pixel” and “pipe methods” provide precise results. A very clear relationship ($R^2 > 0.946$) between DBH defined with the “pixel method” and Ref. AUC is presented below (Figure 8).

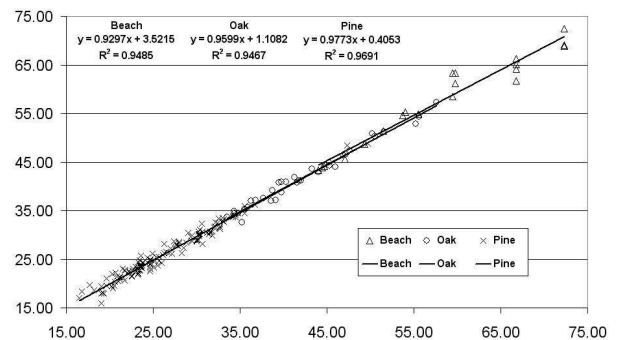


Figure 8. Regression plot of manual (Ref. 1_AUC) versus TLS DBH [cm] estimates (all trees from inventory plots)

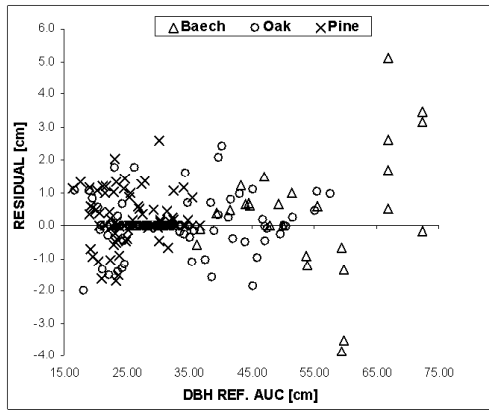


Figure 9. Residual plot for DBH from TLS of all the analysed trees

4.4 Tree height

After the application of several levels of data filtering to get rid of so-called *air points* and *ghost points*, the classification of point clouds was made. The height of tree was defined in a *High Vegetation* class in the TerraScan (Terrasolid) software. Compared to Ref. Inv., the TLS measurement of deciduous tree stands and the interpretation of point clouds turned out to be slightly underestimated. The arithmetic error if the reading of the highest points belonging to the canopy of deciduous trees was +0.44 m (beach -0.01 m; oak +0.61 m), an absolute mean error was about 1.10 m (beach 0.59 m; oak 1.30 m). Due to the late season in the tree crown remained about 15÷20% leaves, which on one hand enabled deep penetration with a laser beam, on the other hand the lack of leaves above 30 meters made small twigs not clearly seen target by the scanner. The beech stand, because of small density could be better measured by both methods, probably because of this the results were better. In case of coniferous tree stands the arithmetic mean of the height measurement was +0.35 m, which indicated a slight overestimation of the reading of the obtained points compared to Ref. Inv. The absolute mean value for these pine stands was 0.79 m.

4.5 Methods of the automatic definition of the tree (g) and stand basal area (G)

As a result of the application of two algorithms (Algorithm 1 and Algorithm 2; Table 2) in a fully automatic way, the information on stand basal area ($G \text{ m}^2 \text{ ha}^{-1}$) was obtained and compared to the results got from forest inventory (Ref. Inv.) and manual measurement in planar view of point cloud as well (methods: *pixel* and *pipe*).

The results clearly indicate that the accuracy of the automatic measurement with the application of Algorithm 2, in the coniferous stands (plots no. 15 and 19) gives mean error on the level of 0.26% (Table 2) in the situation when a traditional inventory measurement differs by about 2.88%. For the deciduous stands the mean values of the error in defining stand basal area (G) with Algorithm 2 are respectively 1.63% and, compared to Ref. Inv. (5.19%), are also several times smaller. Both manual measurements methods: *pixel* and *pipe* give much worse results, because every time they only refer to one direction of calliper.

The application of the Algorithm 2 correcting the area of the slice with incomplete cover of TLS points, very significantly reduced the error of the tree basal area (g) in deciduous tree

stands, from about 3.5 times to several dozens of times in the case of Scots pine stands (Table 3).

Plot no.	Method	G [$\text{m}^2 \text{ ha}^{-1}$]	Percentage of difference to Ref. 2_AUC
3	Ref. 2_AUC	42.1638	
	Ref. Inv.	42.0877	0.18%
	Pixel	40.5036	3.94%
	Pipe	40.9054	2.98%
	Algorithm 1	39.3390	6.70%
	Algorithm 2	41.3680	1.89%
5	Ref. 2_AUC	26.2230	
	Ref. Inv.	24.5319	6.45%
	Pixel	18.8020	28.30%
	Pipe	15.8495	39.56%
	Algorithm 1	25.4210	3.06%
	Algorithm 2	25.8640	1.37%
15	Ref. 2_AUC	17.1722	
	Ref. Inv.	16.6284	3.17%
	Pixel	15.6010	9.15%
	Pipe	15.5777	9.29%
	Algorithm 1	16.7250	2.60%
	Algorithm 2	17.1780	-0.03%
19	Ref. 2_AUC	40.8747	
	Ref. Inv.	39.8160	2.59%
	Pixel	34.8210	14.81%
	Pipe	35.0043	14.36%
	Algorithm 1	39.6220	3.06%
	Algorithm 2	41.0760	-0.49%

Table 2. The accuracy of the determination of stand basal area (G) of the forest inventory plots using different methods (Milicz Forest District).

Tree species	Method	Sum of tree basal area (g)	Percentage of difference to Ref. 2_AUC
European Beach	Ref. 2_AUC	1.4647	
	Ref. Inv.	1.3885	5.20%
	Pixel	1.0928	25.39%
	Pipe	0.9383	35.94%
	Algorithm 1	1.4006	4.38%
	Algorithm 2	1.4463	1.26%
Oak	Ref. 2_AUC	1.7649	
	Ref. Inv.	1.7398	1.42%
	Pixel	1.6858	4.49%
	Pipe	1.7235	2.35%
	Algorithm 1	1.6492	6.56%
	Algorithm 2	1.7270	2.15%
Scots pine	Ref. 2_AUC	3.0920	
	Ref. Inv.	3.0249	2.17%
	Pixel	2.7078	12.43%
	Pipe	2.7050	12.52%
	Algorithm 1	3.0056	2.79%
	Algorithm 2	3.1009	-0.29%

Table 3. The accuracy of the tree basal area (g) determination with different methods for respective tree species (Milicz Forest District)

5. CONCLUSIONS

The obtained results allow the statement that the application of TLS technology in the forest inventory work is already possible. Manual measurements of the point clouds using dedicated software give very good results, however only when the tree trunk is fully visible for the scanner.

Comparison or benchmarks of the TLS with the traditional forest inventory methods make sense only when the same parameter is gathered in right way. The perimeter of the irregular tree trunk on the DBH height is the best reference in case of using TLS.

The fact that such work is time-consuming made these methods applicable in e.g. observation of areas or monitoring and modelling the growth of trees and tree stands, but not very successful when it is necessary to make automatic data-gaining in the area of hundreds or thousands of hectares.

Further planned work of the research team is aimed at defining the possibilities of limiting the number of scanner positions and (at the same time) the improvement of the algorithm reconstructing missing fragments of tree trunk slices. However, the improvements require the following stages: data pre-processing (filtering) and their classification. The errors of the automatic determination of stand basal area (G) reach level of only a few percent. The application of algorithms in the automatic calculation of tree basal area (g) and stand basal area (G) significantly shortens the time of full data processing and provides high correctness of the results. This can contribute to the verification of present legal regulations and guidelines describing the standards of calculation the wood biomass of the stands.

At present high accuracy TLS data are hardly used in standard forest inventory. As long as the concept of „precise forestry” is not applied in practice, scanners will be regarded too expensive and unnecessary tools.

Finally, TLS seems to be a tool for objective obtaining of information on the forest structure, although fully automatic use of data will only be possible in the near future.

REFERENCES

- Aschoff, T., Spiecker, H., 2004. Algorithms for the automatic detection of trees in laser scanner data. *The International Archives of Photogrammetry, Remote Sensing and Spatial Information Sciences*, Freiburg, Deutschland, Vol. XXXVI, Part 8/ W2, pp. 66- 70.
- Bienert, A., Scheller, S., Keane, E., Mullooly, G., Mohan, F., 2006. Application of terrestrial laserscanners for the determination of forest inventory parameters. Image Engineering and Vision Metrology. ISPRS Commission V Symposium, WG 3, Dresden, 25.-27. September 2006, Vol. XXXVI, Part 5. <http://rcswww.urz.tu-dresden.de/~isprs/proceedings/pages/start.html> (accessed 10 May. 2007).
- Hopkinson, C., Chasmer, L., Young-Pow, C., Treitz, P., 2004. Assessing forest metrics with a ground-based scanning lidar. *Can. J. Forest Research*, 34, pp.573- 583.
- de Kok, R., Koziol K., Wezyk, P., 2005. Application of Object Oriented classification of QuickBird VHR satellite images and GIS spatial analysis in forest stand mapping. *Annals of Geomatics*, Vol. III, Number 4., pp. 99-108, (in polish).
- de Kok, R., Wezyk, P., 2006. Process development and sequential image classification for automatic mapping using case studies in forestry. ISPRS WG VIII/11 & EARSeL joint

Conference '3D Remote Sensing in Forestry', Vienna, 14-15 February. pp. 380-384.

Næsset, E., Gobakken, T., Holmgren, J., Hyypä, H., Hyypä, J., Maltamo, M., 2004. Laser scanning of forest resources: the Nordic experience. *Scandinavian Journal of Forest Research*, 19, pp. 482–499.

PGL LP 2003. Instrukcja Urzadzania Lasu. Czesc 1. Instrukcja sporzadzania planu urzadzania lasu dla nadlesnictwa. Zalacznik do Zarzadzenia nr 43 DGLP z dn. 18.04.2003

Simonse, M., Aschoff, T., Spiecker, H., Thies, M., 2003. Automatic Determination of Forest Inventory Parameters Using Terrestrial Laserscanning. Proceedings of the ScandLaser Scientific Workshop on Airborne Laser Scanning of Forests. Umeå. pp. 251- 257.

Weinacker, H., Koch, B., Heyder U., Weinacker R., 2004. Development of Filtering, Segmentation and Modelling Modules for LIDAR and Multispectral data as a Fundament of an Automatic Forest Inventory System. Proceedings of the ISPRS working group VIII/2 Laser-Scanners for Forest and Landscape Assessment, Freiburg, 03.- 06. Oct. 2004.

Wezyk P., 2004. GPS in Forestry: Myths and Facts. *Annals of Geomatics*. Vol. II. Number 4, pp. 19-32, (in polish).

ACKNOWLEDGEMENTS

We would like to thank the General Directorate of the Polish State Forest National Holding for financing the RTD project: “*Elaborating the method of forest inventory, based on the integration of selected geomatic techniques*” managed by Warsaw Agricultural University (SGGW). In this project the usefulness of selected geomatic technologies in forest inventory is tested, including: airborne laser scanning and digital photogrammetry (airborne and terrestrial).

CHANGE DETECTION VIA TERRESTRIAL LASER SCANNING

Reem Zeibak, Sagi Filin

Dept. of Transportation and Geo-Information Eng., Technion – Israel Institute of Technology, Haifa 32000, Israel
{reemz, filin}@tx.technion.ac.il

Commission V, WG 3

KEY WORDS: Terrestrial laser scanning, change detection, point clouds, morphology

ABSTRACT:

We present in this paper an algorithm for the detection of changes based on terrestrial laser scanning data. Detection of changes has been a subject for research for many years, seeing applications such as motion tracking, inventory-like comparison and deformation analysis as only a few examples. One of the more difficult tasks in the detection of changes is performing informed comparison when the datasets feature cluttered scenes and are acquired from different locations, where problems as occlusion and spatial sampling resolution become a major concern to overcome. While repeating the same pose parameters is an advisable strategy, such demand cannot always be met, thus calling for a more general solution that can be efficient and perform without imposing any additional constraints. In this paper, we propose a general detection strategy based on terrestrial laser scanning data. We analyze the different sources of complexity involved in the detection of changes and study their implication for terrestrial laser scans. Based on this analysis we propose a detection model, which is both aware of these hurdles and is efficient. We show that by finding an adequate representation of the data, efficient solutions can be derived. We then demonstrate the application of the model on several natural scenes and analyze the results.

1. INTRODUCTION

Differing from conventional mapping techniques like photogrammetry, laser scanners provide rapid and direct description of 3D geometry independent of lighting conditions, and without the need for a manual collection of the data. Furthermore, the point-cloud provided by high-resolution laser scanners is both dense and accurate, thereby allowing a detailed description of objects irrespective of their shape complexity. It is therefore, not surprising that laser-scanning technology is rapidly becoming the popular alternative for modeling 3D scenes, for site characterization, cultural heritage documentation and reverse engineering, as only a few examples.

A key application where terrestrial laser scanning technology offers great use is monitoring of changes that occur over time. One example is the need to update geographic information by comparing the existing information with current state; another, which is more extreme, follows disastrous events where comparison of pre- and post- events is required, preferably in an efficient manner. Change detection should not necessarily be related to large-scale events. Behavior of small size natural phenomena or changes of specific objects are of great importance for analyzing deformations or objects evolution, and require a more subtle analysis of the measured scene. We point that the detection of changes can find its use in the elimination of moving objects within a static scene; such application can find use when reconstructing static landmarks, while avoiding irrelevant objects in the scene.

To date, detecting changes is mainly performed via images, usually by using object to background separation or a simple subtraction between images. Such models are limited and usually impose rigid constraints like static mounting of the camera, recognizable (usually artificial) landmarks, and are sensitive to shadows and local illumination problems. With 3D data arriving from airborne laser platforms, change detection is mainly applied in the form of a Digital Surface Models (DSMs) subtraction, where the DSMs are created from the raw laser point cloud (e.g., Vu et al., 2004). Murakami et al. (1999) also add to this intensity images as an additional information layer to help revising GIS databases. Vogtle and Steinle (2004) propose

a methodology for detecting changes in urban areas following disastrous events. Instead of solely computing the difference between the laser-based DSMs, a region growing segmentation procedure is used to separate the objects and detect the buildings; only then, an object-based comparison is applied. Hofton and Blair (2001) propose waveforms correlation of coincident footprints between different epochs to study vertical or elevation changes in LIDAR data.

As for change detection via terrestrial laser scans, most works focus on deformation analysis for designated objects. Comparison can be performed by the subtraction of a resampled set of the data (Schäfer et al. 2004), or adjustment to surface models like cylinders (Gosliga et al., 2006) or planes (Lindenbergh and Pfeifer, 2005). For the comparison of a complete scene, Hsiao et al. (2004), propose an approach that combines terrestrial laser scanning and conventional surveying devices such as total station and GPS, in order to acquire and register topographic data. The dataset is then transformed into a 2D grid and is compared with information obtained by digitization of existing topographic maps. Such approach has very appealing use in practical applications, but is very limited in scope and cannot be generalized into a change detection scheme for 3D data. Girardeau-Montaut et al. (2005) discuss the detection of changes in 3D Cartesian world, and point to the possibility of scans comparison in point-to-point, point-to-model, or model-to-model manners. The authors then use point-to-point comparison with some adaptations and make use of an octree as a data structure for accessing the 3D point cloud. Comparison is carried out by using the Hausdorff distance as a measure for changes.

The review demonstrates the great potential of change detection via laser scanning data that allow assessing variations within the physical scene without resorting to interpretation of radiometric content, as is the case with images. It also shows that in most cases where terrestrial laser scanning is being applied, some constraints on the studied objects or on the scanner pose are being imposed. Since, the assessment of the actual change, and the ability to quantify and measure it (e.g., size, volume), offer great assets, we study in this paper the detection of changes without the imposition of external constraints (other than having

some overlap) and propose a model for the assessment of changes. Our goal is not only to develop a methodology for the detection of changes, but also to propose an efficient solution, aware of the unique characteristics of terrestrial laser data.

Before turning to the analysis and methodology presentation, we note that the detection of changes between scans from different location requires the establishment of registration between the point-clouds. Since scans are acquired in local reference frames whose origin is at the scanner position, the relative transformation parameters between the datasets should be known a priori (in practice, estimated). Our work considers the transformation parameters as known. This assumption is based on the fact that the registration between the scans is a common practice that can be treated either by using artificial targets within the scene (spheres, or corner reflectors) or in an autonomous manner.

The change detection model is presented as follows, in Section 2, we discuss various geometric and scanner related features that influence the detection of changes in laser scanning data. Section 3 presents the proposed change detection model; we outline first the proposed model, analyze it, and then present a processing sequence that addresses scanning related problems. Section 4 presents results of the application and the model, and Section 5 offers concluding remarks and outlook.

2. CHANGES BETWEEN LASER SCANS

When studying the detection of changes between terrestrial laser scans, concerns like data characteristics, level of comparison, and scene complexity, are key factors that affect the detection methodology. Data characteristics relate here to the three-dimensionality, the irregular point distribution, the varying scale and resolution within the scene (depending on depth), and the huge data volume in each scan. Regarding the level of comparison, it may be applied at the point level by comparing a point to its surrounding, at the feature level via primitive based comparison (e.g., planes or conics), and the object level by comparing objects and their shape variation between epochs.

Since laser scans provide point-clouds embedded within 3D space, we study the realization of changes in that space. For an efficient model, we focus on the prospects of point-level based change detection. We opt towards efficient models that do not impose elaborated processes with added computational overhead. Since changes in the point level are based on a comparison of points to their surroundings, we analyze first the potential artifacts that may affect the detection, particularly with reference to cases that raise the level of false alarms. Because of the unorganized nature of the 3D data, it is clear that some form of data arrangement (or structure) must be used for efficient access and association between the sets of points. Gorte and Pfeifer, (2004) use a voxel based organization as a means to impose regularity in the data (though not for change detection), and Girardeau-Montaut et al. (2005) use octree representation, which is more efficient and more aware of the fact that most of 3D space has no information. In the analysis, we study their applicability to point based comparison.

2.1 Resolution and object pose

We begin our analysis with assessment of the varying resolution both within and between scans. As angular spacing dictates the resolution of the acquired data, distant objects will have a lower resolution than those closer to the scanner. The most direct effect of the varying resolution is the level of detail by which objects are described. However, the fixed angular spacing also means that distances between consecutive ranges will keep

increasing the further the ranges from the scanner become. Figure 1 illustrates this effect, it also shows that the increasing point spacing is object-dependent – while the spacing of the ground points in the 'green' scan keeps growing, those related to vertical objects (poles, trunks, or standing people) are more or less fixed. Finding a point-to-surrounding comparison scheme that suits close and distant points is, therefore, hard. The use of volumetric arrangement models (that define surrounding by their nature) will fail covering both ends. Small size surroundings will lead to cells with no points from one scan but some from the other, and will therefore raise a "change" flag. Bigger size surroundings will lead to missed changes (e.g., accommodating for the decreasing ground resolution may cover complete vertical objects). Such effects will occur with both the voxel scheme and the adaptive, octrees based, partitioning.

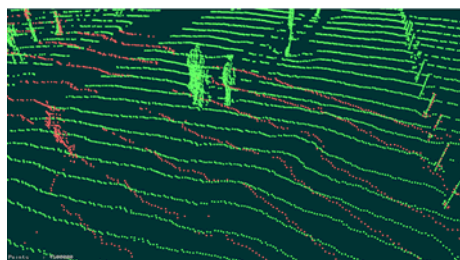


Figure 1. Overlaid scans from different positions, and the effect of the varying resolution.

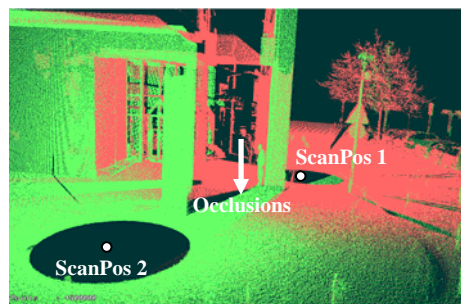


Figure 2. Occluded areas in one scan that are 'seen' from the other scan. Such regions will wear the form of a change by a plain point based comparison.

2.2 Occlusion

Occlusion of objects, or object parts, offers another type of "interference," with a likely consequence of false detection. Figure 2 shows a scene part in 3D space, which is seen in the 'green' scan but is occluded in the 'red' one due to the supporting pillar. Those points appearing in one scan but not in the other are natural change candidates. An additional related effect arises when the same object is partially visible in both scans, either with a region mutually seen by both scans, or when the visible parts are exclusive one to the other. To handle occlusion effects, the application of z-buffering must be applied. However, z-buffering considers by its nature a sense of surfaces, and therefore requires a level of interpretation that either involves data segmentation or the definition of connectivity among the points. With the varying resolution, such definition becomes hard, and in order to be applied properly, a sense of objects must be inserted.

2.3 Scanner related artifacts

The scanning system itself offers several features to consider when dealing with the detection of changes. Among them are the "no-reflectance" regions, range limits, and noisy ranges. Artifacts related to regions of **no-reflectance** refer to areas

towards which pulses have been transmitted, but due to absorption or specularity, not enough energy (if any) is returned to trigger a range measurement (objects like, windows, and low reflectance surfaces are some example to that). When data from the other scan exists in those "hole" regions they will be considered a change while not being so.

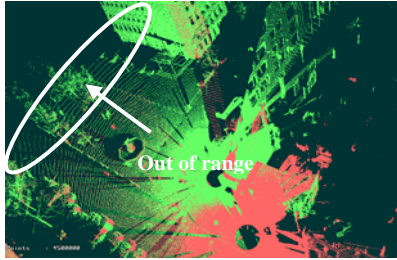


Figure 3. Regions covered by only one scan. By the simple comparison, it is impossible to distinguish between a "no data" area and an actual change.

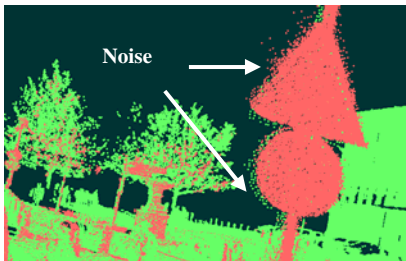


Figure 4. Noisy laser returns around object borders that can be interpreted as changes.

With **ranging limits**, the different scanning positions will leave areas seen in one scan uncovered by the other (see Figure 3). This relatively trivial fact suggest that the lack of information cannot be attributed only to actual changes (or geometric constraints that the scene imposes) but also to the lack of range measurements in a region. Therefore, the consideration of the range limits should be handled appropriately. Finally, we point to **noise** in the data (see Figure 4) which usually accompanies laser data, especially around object edges and corners. Unless treated properly, noise will be interpreted as changes in the scene.

All those features suggest that detection of changes between laser scans cannot be decimated into a mere point-to-surrounding comparison problem if such artifacts are to be resolved. In the following Section, we present a model for change detection that accommodates those features of the scan.

3. CHANGE DETECTION MODEL

The essence of point-level change detection in 3D space is comparing a point from one scan to its surrounding in the other. Change detection between scans can be approached however, from a different direction by asking whether a point that was measured in one scan can be seen in the other. For this question, three answers can be given, i) yes, but there is no object in the reference scan, namely a change, ii) yes, and it is lying on an object, namely no change, and iii) no, as there is an item hiding it, and due to lack of any other information we mark it as no change. In the rest of this Section we show that under an adequate data representation a decision among the three alternatives can be easily and efficiently made.

3.1 Data representation

3D laser scans can be seen as range panoramas whose axes are the latitudinal and longitudinal scanning angles, and the ranges are the intensity values. As the angular spacing is fixed (defined by system specifications), regularity becomes an established property of this representation. Relation between the Cartesian and the polar data representation is given in Eq. (1).

$$(x, y, z)^T = (\rho \cos \varphi \cos \theta, \rho \cos \varphi \sin \theta, \rho \sin \varphi)^T \quad (1)$$

with x, y and z the Euclidian coordinates of a point, φ and θ are the latitudinal and longitudinal coordinates of the firing direction respectively, and ρ is the measured range. $\Delta\theta$, and $\Delta\varphi$, the angular spacing, define the pixel size. Figure 5.a shows range data in this representation where the x axis represents the θ value, $\theta \in (0, 2\pi]$, and, the y axis represents the φ value, with $\varphi \in (-\pi/4, \pi/4]$ for this scan.

The arrangement of the irregular 3D point cloud into a panoramic form offers not only a compact representation (which is less of a concern here) but more importantly an organization of the ranges according to their viewing direction. To some degree, this representation can be viewed as tiling of the data, where the pixel size in angular terms defines a region where the measured range is the best information source. This contributes to the connectivity notion as featured in Figure 5.a. Since size is defined here in angular terms, the varying distance between consecutive points and scan-lines cease being a factor.

To assess if a point that was measured from the other scan can be seen by the reference one, the evaluated scan should be transformed into the same frame as the reference scan. Even though the range dataset are assumed registered, each range panorama is given in a local scanner frame. This transformation has the notion of asking how the scan will look from the reference scanner position. This transformation involves rotation and translation, according to the pose parameters of the scanners, and is given by Eq. (2).

$$\begin{bmatrix} x_2 \\ y_2 \\ z_2 \end{bmatrix} = R_{12} \cdot \begin{bmatrix} x_1 \\ y_1 \\ z_1 \end{bmatrix} + t_{12} \quad (2)$$

$$\text{where: } R_{12} = R_1 \cdot R_2^T \quad \text{and, } t_{12} = \begin{bmatrix} t_{1x} - t_{2x} \\ t_{1y} - t_{2y} \\ t_{1z} - t_{2z} \end{bmatrix} \cdot R_2$$

t_1, R_1, t_2, R_2 are the position and orientation matrices of the two scanners, respectively, and $[x_1, y_1, z_1]^T, [x_2, y_2, z_2]^T$ are the 3D coordinates in the individual scanners reference frames. Figure 5.c shows the analyzed scan, while Figure 5.b shows the same scan as transformed into the viewing point of the reference scan in Figure 5.a.

3.2 Detection of changes

When transformed, comparison between the scans can be reduced, with some adaptations, into a mere image subtraction. This image subtraction in the range panorama representation has some appealing properties: i) when a scan is transformed into the view point of the reference scan, occluded areas of the analyzed scan become "no-information" (or void) regions, as Figure 5.b shows, and therefore, have no "change-like" effect,

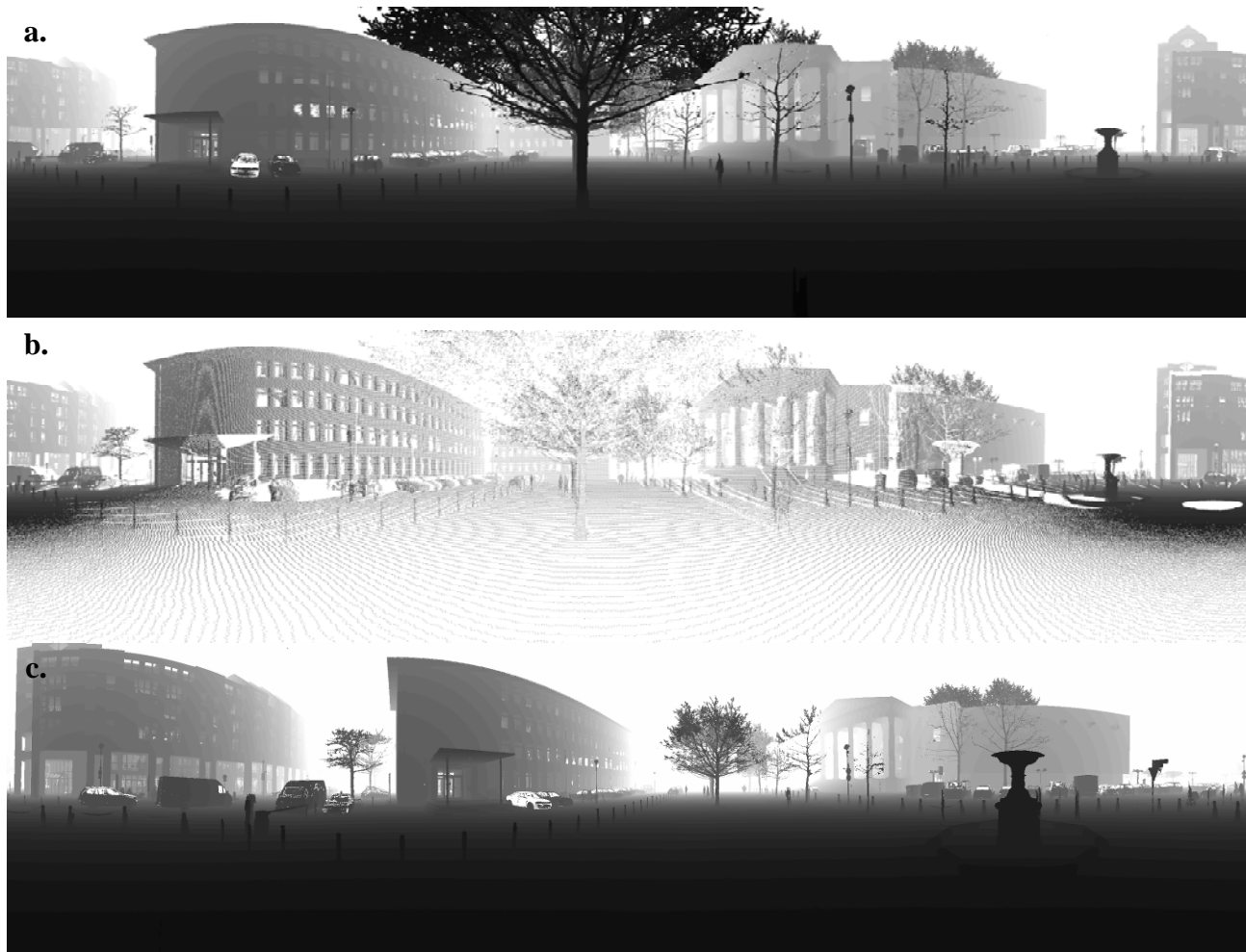


Figure 5. a. Reference scan. b. Analyzed scan transformed into the reference frame. c. Analyzed scan in its original local frame (not transformed).

ii) regions seen from the analyzed scan but not from the reference scan (occluded by the reference) will fall behind the occluding objects. As such, they will have bigger range values than those of the occluding objects and, therefore, a "no change" status, and iii) scale – since objects close to the scanner occupy more pixels and far objects occupy less, the need to characterize multi-scale comparison arises. However, as objects from the analyzed scan are transformed into the reference scan frame, object scale differences will be resolved in large.

For the detection of changes, we apply the following rule:

$$d_{i,j} = \begin{cases} \text{change} & R_{i,j} - A_{i,j} > \varepsilon \\ \text{no change} & |R_{i,j} - A_{i,j}| \leq \varepsilon \\ \text{occlusion (no change)} & R_{i,j} - A_{i,j} < -\varepsilon \end{cases} \quad (3)$$

with d_{ij} pixel in the difference image, R_{ij} pixel in the reference image, A_{ij} pixel in the analyzed one, and ε an accuracy threshold. As can be noticed, the change detection is directional, namely negative differences, which are due to occlusion, cannot be described as changes. Additionally, "no-data" (no-information) regions in the transformed scan cannot be interpreted as a change (for consistency with the above definition and for implementation purposes, we assign "max-range" values there). So, in order to assess the overall difference between two epochs, changes should be mutually detected between the different scans, with the comparison between the

reference scan and the analyzed scan telling what appears in the analyzed but not in the reference, and the reverse comparison telling what appears in the analyzed scan but not in the reference. Their union comprises the overall change; their exclusion reveals the static objects in the scene.

3.3 Pre and post processing

With the outline of the proposed differencing approach, we turn to discuss the pre- and post- processing phases that handle the additional scan characteristics that were pointed out, particularly no-return regions and ranging errors around corners and edges.

Correction for no-data regions – As Figures 5.a, c show, the range panorama has no-return regions due to reflecting surfaces or in open areas such as the skies. No-information regions have zero ranges there, and therefore will not be able to show changes (having negative distance and therefore considered occluded). To avoid this effect, no-reflectance regions in the reference scan are being filled by their neighboring values. These regions are detected by their "hole" appearance in the data (hole size is defined by a preset value). Figure 6 shows the filling effect, with Figure 6.a showing the raw laser data and highlighting two no-reflectance regions among many others that are seen around windows and car shields, and Figure 6.b showing the filling effect. For the background (skies etc.) regions, a "max-range" value is assigned. This way, not only no-reflectance regions are filled but also the different extent of both scans is handled.

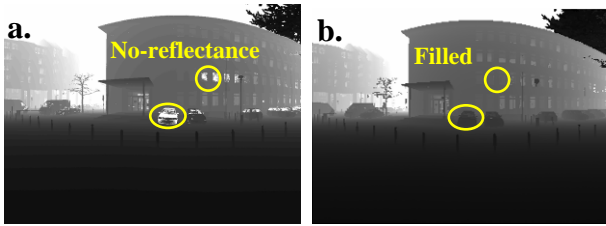


Figure 6. Filling no reflectance regions

Reduction of noise and edge effect – to eliminate the effect of edges and corners in the image that oftentimes result in noisy ranges, dilation-like operation is performed. The idea is to use a filter to locally dilate close object and erode its background. This way, we emphasize close objects and make the comparison between corresponding pixels more secure. Figure 7 shows the effect of the order filter operator.



Figure 7. Results of applying the order filter.

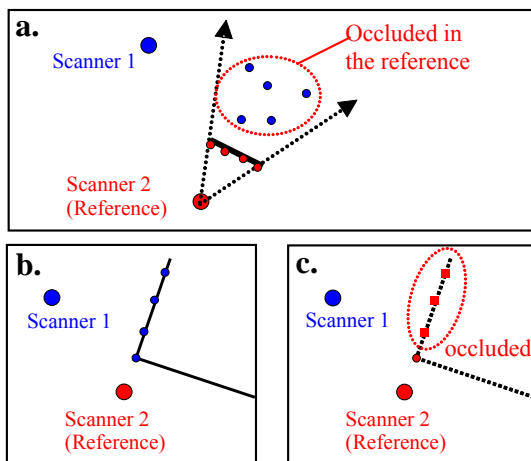


Figure 8. Occluded points and the effect of object co-aligned with the scanner

Multiple objects per viewing direction – one feature of the transformation into the reference scan coordinate system is that ranges in the analyzed frame that are co-aligned with the reference scanner viewing direction will all fall on the same image pixel. If those ranges are occluded this effect will go unnoticed (see Figure 8.a), however when they fall on a new

object in the scene, only a single point (the closest) that depict the object will be considered a change while the rest will be ignored (Figures 8.b, c illustrate this effect). Therefore, instead of assessing a single laser point, the complete sequence should be evaluated.

Post processing - Following the detection of changes, which we perform pixel/range-wise, regions are formed. Further than the elimination of small regions, the grouping, which is performed in image space, is indifferent to the depth variation of the points. Therefore, spurious changes that are not connected in 3D space should be detected and eliminated. For such elimination, we study the neighbors of each detected point in 3D space. Such evaluation is relatively simple to perform as it involves defining a window around the point in image space and then truncating ranges that are further to the point than a given distance. If within this box, the number of points with change status is smaller than a given value, the point is not considered a change. This way, spurious changes are eliminated. We point that a window around the point, which is a simple definition, offers in fact a scale aware definition of the surrounding.

4. RESULTS AND DISCUSSION

The application of the change detection model is demonstrated in Figure 9 on a complete scene (the analyzed scan is compared here with the reference). The detection threshold, ϵ , was set to 5cm. Due to space limitation, we do not extend this comparison into multiple scans, and point that the extension of this approach is fairly straightforward. Changes in this scene between the two epochs are mainly passerbys and parking vehicles. They indicate the level of detail that can be noticed at various ranges (consider again Figure 5). As an example, we point to the two sitting persons on the distant building with the neo-classical front. On a larger scale, in Figure 10.a a bus that crosses the scene can be noticed. Manual inspection of the scene in reference to the detected changes shows that all the actual changes between the two scenes were indeed detected. Considering the very different views from which the two scenes were acquired, the ability to detect walking persons shows the great potential of the proposed approach to detect changes of various size and within a cluttered natural environment. Since comparison is performed by image subtraction, the detection of difference is almost immediate, requiring mostly the transformation of the analyzed scan into the reference scene, and if the total change is sought, applying the same transformation in the reverse order.

The Figures show that a clutter of spurious changes has fallen on trees. The lack of structure in trees and the vegetation penetration property are some reasons for such changes to appear. Additionally, the ranging mode (first return or last

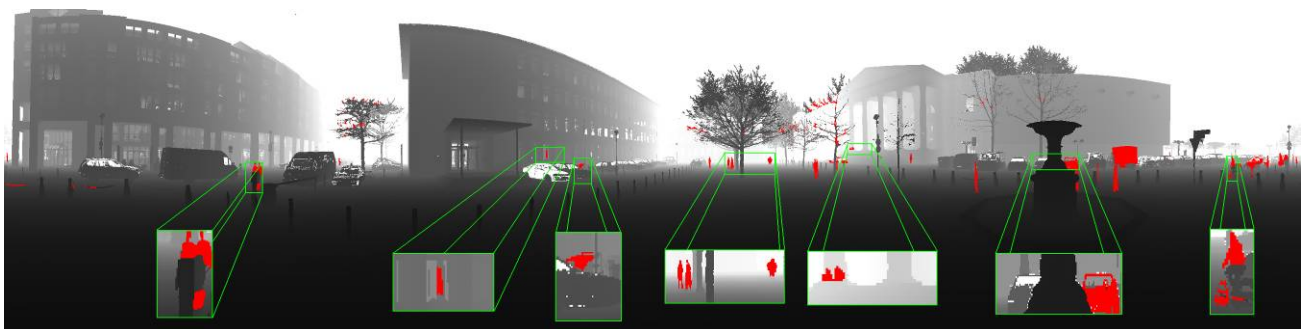


Figure 9. changes detected in the analyzed scan when compared to the reference one.

return) has an impact on non-solid objects and therefore affects the detection. The results indicate that for change detection applications, preferences for a first-return mode (namely, the closest object) are of reason and need. In terms of false alarms, chains between poles have also been detected as changes due to lack of information on them in the other scan, most likely for similar reason or due to noisy ranges that measurement of such objects is prone to.

While the differentiation between occluded areas and actual changes is a natural feature of the proposed model, it has interesting consequences regarding partially occluded objects. Being point-based, the comparison methodology holds no objects notion in it. Therefore, partially occluded objects will be partially marked as a change (see Figure 10.b and the bicycles highlighted in Figure 9). Linking (or reintegrating) such object parts can be performed via graph methods. We point out that adding object notion to the detection at the current stage when changes have been identified already is a more efficient (and to some degree natural) way than a comprehensive study of all objects in the scene, only as a means to identify which of them were changed.

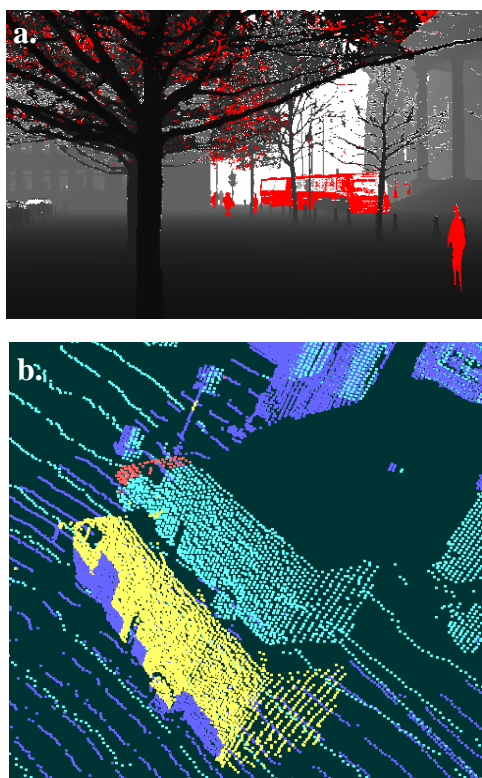


Figure 10. Detection of changes, **a.** large and small moving objects in the scene with false detection around trees. **b.** under occlusions (described in 3D); blue and cyan: two registered scans; yellow and red: changes detected in the two scans respectively.

5. CONCLUSIONS

This work has demonstrated the feasibility of change detection with no imposition of external constraints. It has shown that efficient solution to such complex features as varying scale across the scene, occlusion, and laser scanning artifacts exist. As was shown, the transformation of the data to the viewing setup of the reference scan, and the polar representation that was used, solve scale and occlusion problems in a natural way.

Additionally, morphologic operators that were applied on the range data managed solving such problems as ranging limits, noise and no reflectance regions. The range subtraction of the points in the organized angular space provided a multi-scale analysis, not affected by the scanner position and the varying scanning resolution. The results show that not only major changes are detected, but also minor ones like passerbys in different size.

Future work on this proposed methodology will focus on methods for the elimination of false detection, particularly around vegetated objects and on adding object notion into the detection process (so that no two parts of the same object will be defined as change while the rest of it not). However, the current state of the results makes such analyzes and extensions much narrowed and focused compared to a complete analysis of the whole scene.

6. ACKNOWLEDGEMENT

The authors would like to thank Dr. Claus Brenner for making the data used for our tests available.

7. REFERENCES

- Bitelli, G., Gusella, R. C., L. Mognol, A., 2004. Image Change Detection on Urban Area: The Earthquake Case. *International Archives of Photogrammetry and Remote Sensing*, 35(B5)
- Girardeau-Montaut, D., Roux, M., Marc, R., Thibault, G., 2005. Change detection on points cloud data acquired with a ground laser scanner. *International Archives of Photogrammetry, Remote Sensing*. 36(3/W19):30-35
- Gorte, B., Pfeifer, N., 2004. Structuring laser-scanned trees using 3D mathematical morphology. *International Archives of Photogrammetry and Remote Sensing*, 35 (B5), 929-933.
- Gosliga van R., Lindenbergh, R., Pfeifer, N., 2006. Deformation Analysis of a Bored Tunnel by Means of Terrestrial Laserscanning. *Image Engineering and Vision Metrology*, ISPRS Symposium, Dresden.
- Hofton, M., Blair, J., 2001. Laser pulse correlation: A method for detecting subtle topographic change using Lidar return waveforms. *International Archives of Photogrammetry and Remote Sensing*. Vol. 34(3/W4): 181-184.
- Hsiao, K. H., Yu, J., Tseng, Y. H., 2004. Change Detection of Landslide Terrains Using Ground-Based Lidar Data. *Int. Archives of Photogrammetry and Remote Sens.*, 35(B5)
- Lindenbergh, R., Pfeifer, N., 2005. A Statistical Deformation Analysis of Two Epochs of Terrestrial Laser Data of a Lock. *7th Conference on Optical 3-D measurement techniques*, Vienna.
- Murakami, H., Nakagawa, K., Hasegawa, H., Shibata, I., Iwanami, E., 1999. Change detection of buildings using an airborne laser scanner. *ISPRS Journal of Photogrammetry & Remote Sensing* 54 (1999) 148-152.
- Schäfer, T., T. W., Peter Kyrinovič, Miriam Zámečnicková, 2004. Deformation Measurement Using Terrestrial Laser Scanning at the Hydropower Station of Gabčíkovo. *INGEO 2004 and FIG Regional Central and Eastern European Conference on Engineering Surveying*. Bratislava, Slovakia
- Vogtle, T., Steinle, E., 2004. Detection and recognition of changes in buildings geometry derived from multitemporal laserscanning data. *International Archives of Photogrammetry and Remote Sensing*, 35(B3)
- Vu, T., Matsuoka, M., Yamazaki, F., 2004. Lidar-based change detection of buildings in dense urban areas. *Geoscience and Remote Sensing Symposium, 2004. IGARSS '04. Proceedings 2004 IEEE International*.

HIERARCHICAL WATERSHED SEGMENTATION OF CANOPY HEIGHT MODEL FOR MULTI-SCALE FOREST INVENTORY

Kaiguang Zhao *, Sorin Popescu

Spatial Sciences Lab., Dept. of Ecosystem Science and Management, Texas A&M University, College Station, TX 77840, USA - (zhaokg, s-popescu)@tamu.edu

KEY WORDS: LiDAR, CHM, Watershed segmentation, Scale, Crown delineation, Forest inventory

ABSTRACT:

Canopy Height Model (CHM) is a standard LiDAR-derived product for deriving relevant forest inventory information, among which individual tree identification is a crucial task. The watershed algorithm from markers is the typical procedure applied to CHMs for delineation of crowns. However, for low-quality CHMs or under certain canopy conditions, segmentation at individual tree level is not practical, e.g., due to grouped trees in dense forests. In this study, we investigated the feasibility of a hierarchical watershed transform (HWT) algorithm to segment CHMs at both individual tree levels and scales above that. As compared to the results by the variable-window filtering for individual trees, HWT allows more flexibilities in removing nontreetop maxima by referring to the "dynamic" attributes of the potential treetops (i.e., local maxima). It is also found that the choice of filters for smoothing CHM has significant influences on the detection of treetops. Beyond individual tree level, the segmentation by HWT was compared with a commercial package eCognition, and both give similar segmentation results, though with minor differences. Due to the lack of field-measured trees matched with LiDAR-detected ones, no quantitative evaluation of accuracy is provided in this study. Nevertheless, the results of this study reveal that HWT is a viable procedure that could be applied for multilevel segmentation of CHM.

1. INTRODUCTION

Reliable mapping of forest resources is a crucial task in many scientific and practical settings, e.g., regional estimate of biomass or fuel models as the input of fire behaviour modelling. For spatially-explicit forest inventory, LiDAR (Light Detection And Ranging) has become a well-established technique in terms of its capability of direct measurements on canopy structures (Hyypä, Inkinen, 1999; Næsset, 2002; Maltamo et al., 2004). Extensive research efforts have been focused on the use of airborne laser scanners for deriving forest information by employing various approaches at relevant analysis unit, i.e., grid, stand or individual tree level. A canopy height model (CHM), which represents the difference between the top canopy surface and the underlying ground topography, becomes a standard LiDAR product that can be effectively derived from LiDAR raw data through appropriate filtering of LiDAR point clouds for the separation of ground hits and canopy hits.

In practice, CHMs are available in raster formats and can be considered as 2D images where individual tree crowns are often visually noticeable. To automatically delineate tree crowns or detect individual trees from the CHM, a variety of algorithms or procedures have been devised or explored across various forest conditions, which include but are not limited to image segmentation, local maxima filtering, and template matching (Persson et al., 2002; Popescu et al., 2002; Koch et al., 2006; Chen et al., 2006; Falkowski et al., 2006). Furthermore, with individual trees identified, tree height and crown width also can be measured directly from CHM, and other tree dimension parameters such as stem diameters can be predicted from LiDAR-derived metrics by regression models (Pysalo and Hyypä, 2002; Popescu et al. 2003). These algorithms for tree identification often make the assumptions that treetops correspond to local maxima present in the CHM, or that tree

crown assumes certain types of geometry that could be evaluated against the templates used. Among the segmentation approaches, watershed transform is the most popular technique in segmenting a CHM because it is intuitively straightforward to treat each concave tree crown in the inverted CHM as a catchment basin. However, cautions should be exercised as to how to appropriately select local maxima as candidates of treetops. For example, within a single crown, there may be multiple local maxima that result primarily from the real irregularity of crowns or partly from random errors in the procedures of creating the CHM; therefore over-segmentation is usually observed in such situations. As remedies, common strategies are to pre-process the CHM using a smoothing filter, or to merge over-segmented regions ad hoc; but too strong a filter could possibly smear out small trees; as a result, smoothing filters with adaptive parameters are often desired to alleviate such situations. Koch et al. (2006) used a pouring-algorithm, which is similar in spirit to watershed segmentation, to delineate tree crowns over a temperate deciduous and mixed forest, where the authors applied a Gaussian filtering with a varying parameter adaptive to height classes, devised several schemes to deal with spurious regions, and also employed a Ray algorithm to trace the actual crown edge within each segment. On the other hand, in the local filtering for treetops, a smaller window tends to have larger commission errors while a larger window often leads to more omission errors. An improved version of local maxima filtering is demonstrated in Popescu et al. (2003) by using a circular window and adapting its size locally relative to height by referring to a pre-defined height-crown equation; this variable window filtering proves successful considering the fact that higher trees generally have larger crowns. In Chen et al. (2006), a further refinement of variable window size filtering is realized by taking into account the variability in the prediction of crown width from tree height. Falkowski et al. (2006) performed wavelet-transform on CHM

* Correspondence author

image using 2D Mexican Hat wavelet and identified local maxima in the resulting convolved image as potential treetops; their method is in essence a template-matching procedure.

Despite all these successes, difficulties or problems are often reported in previous studies on tree-level crown segmentation. These are often witnessed as the relative large error of missing or misidentifying trees, particularly over forests with high canopy closure and density. Ideally, in open forests where no overlapping or suppressed trees exist, all the aforementioned algorithms supposedly are able to find all trees if the shape of tree crowns is also well-defined. Generally, the difficulties in correct delineation may be attributed to the incapability of CHM to capture real canopy surfaces that may be caused by low quality of LiDAR data, improper resolution for rasterization of CHM, or ineffectiveness of procedures for generating CHM (e.g., methods of classifying raw returns, or interpolation algorithms); in most cases, the complexity of canopy surface itself prevents high accuracy in identifying trees. Although sophisticated algorithms tend to consider more aspects either in the phase of pre-processing or post-processing in attempt to reduce commission and omission errors, experiential evidences suggest that in some cases it is extremely difficult or even impossible to delineate individual tree crowns in CHMs even with one of the most sophisticated image processing tools such as the human vision system (Bortolot, 2005). To this end, some researchers, alternatively, went beyond individual tree levels to examine the usefulness of CHM. For example, Bortolot (2006) investigated the use of CHM for tree clusters that correspond to a group of tree crowns. van Aardt et al. (2006) used the eCognition package (Definiens Imaging GmbH, Munich, Germany) to segment CHM at stand levels and then assessed forest volume and biomass on a per-segment basis. In certain senses, the use of CHM at scales greater than individual tree levels circumvents the difficulties in crown segmentation and can accommodate the purposes of operational inventory at scales appropriate for forest management.

The objective of this study is to investigate segmentation of CHM for forest inventory at multiple scales by using a hierarchical watershed transform algorithm. The watershed algorithm used in this work is a marker-controlled morphological algorithm that has also been utilized for isolating individual trees in previous researches, e.g., Chen et al. (2006), among others. Its hierarchy characteristics result from the use of “dynamics” as criteria to select markers that are then used for growing basins at the corresponding scale. Specifically, first we rely on the “dynamics” attributes of local maxima for the selection of potential treetops in the delineation of tree crowns, and next we apply the hierarchical watershed transform (HWT) for CHM segmentation at both tree levels and scales greater than individual trees. The results were compared to those by the established variable window filtering at individual tree levels and those by eCognition at levels above individual trees, respectively.

2. MATERIALS

2.1 Study Area

A forested area of approximately 47 sq km, located in eastern Texas, USA, is chosen for this study. The airborne laser coverage consists of pine plantations in various developmental stages, old growth pine stands in the Sam Houston National

Forest, many of which with a natural pine stand structure, and upland and bottomland hardwoods. Much of the southern U.S. is covered by forest types similar to the ones included in our study area.

2.2 Airborne Laser Data and Canopy Height Model

Laser scanner data were acquired with a Leica-Geosystems ALS40 during the leaf-off season in March 2004 by M7 Visual Intelligence Inc. of Houston, Texas. The LiDAR system was operated to record two returns per pulse, i.e., the first and the last, with a reported accuracy of 20-30 cm and 15 cm for horizontal and vertical positioning, respectively, and was configured to scan ± 10 degrees from nadir. On average, the dataset has a point density of 2.6 hits per m^2 .

A Digital Surface Model (DSM) was created by first selecting the LiDAR point of maximum height within each 0.5m x 0.5m cell that contains at least one laser hits, and next interpolating the selected laser points into a regular grid with a spatial resolution of 0.5m by triangulation. A Digital Elevation Model (DEM) was derived using a proprietary package and was made available by the data vendor. Consequently, the CHM was generated through the pixelwise subtraction of DEM from DSM.

3. METHODS

3.1 Hierarchical Watershed Transform (HWT)

The idea of watershed transform (WS) is typically illustrated with respect to immersion simulation. In classical WS, holes are punched at local minima (to be more precise, regional minima) while a improved algorithm known as watershed from markers (WSM) punches the holes at the prescribed markers (Soille, 2003). Denote the WSM as follows,

$$R = WSM(I, M)$$

where I is the input image, i.e., the inverted CHM, M is the set of markers, and R is the set of segmented regions. Notice that the cardinalities of R and M (the number of elements in each set) are the same and there exists a one-to-one mapping between the two sets. Apparently, if all local minima are considered as markers, the WS and the WSM produce the same results. On the other hand, another algorithm, the Hierarchical watershed transform (HWT), is a multi-scale watershed approach that depends on the “dynamic” of local minima to create a set of nested partitions (Dougherty and Lotufo, 2003). The “dynamic” H_d of a minimum is defined as the height one has to climb up from the minimum in order to reach another minimum of lower value, as illustrated in Figure 1 (left) for the minimum point m which has a neighbouring minimum m' of lower height. In fact, H_d is the height extinction value of the corresponding valley in the h -minima operator; and it has two counterparts, i.e., “area-dynamic” A_d and “volume-dynamic” V_d , which can be defined similarly. For example, the “volume-dynamic” V_d of a minimum is the volume of water that has to be filled to reach another minimum of lower height (Figure 1c). An HWT at a given scale s is the WSM using only local minima with dynamics greater than or equal to s as markers. This can be expressed as,

$$R = WSM(I, M_s) = HWT(I, s)$$

with $M_s = \{m \in RMIN(I); DYN(m) \geq s\}$

where $RMIN(\cdot)$ is the operator to obtain local minima from the input image I (e.g., the inverted CHM) and $DYN(\cdot)$ is the operator to calculate the dynamic (or area- and volume-dynamics) of a local minimum. When s increases, fewer minima are selected as markers, and hence a coarser segmentation is obtained. Of particular note is that s has no direct correspondence to the scale commonly used for the spatial extents. The implementation of HWT used in this study is based on minimum-cost path algorithm as described in Lotufo and Falcao (2000), and it requires the discrete value of CHM. Thus, we digitized the float height values into integers using a 0.01m quantification interval. If $s = 1$, i.e., the finest scale, the HWT will produce the same segmentation as classical watershed transform (WS) because all the minima are selected.

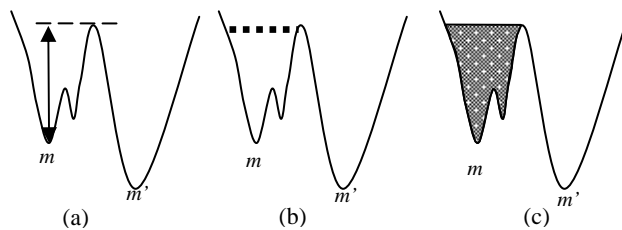


Figure 1. Illustration of the concept of “dynamic” for a local minimum m whose neighbouring minimum of lower height is m' ; for simplicity, a 1-D signal is used instead of 2D CHM surface. (a) the dynamic of m as indicated by the arrow, (b) the area-dynamic of m as indicated by the dashed line, (c) and the volume-dynamic of m as indicated by the hatched area.

3.2 Segmentation of CHM at Individual Tree Level

In the segmentation of CHM by watershed from markers, the number of delineated crowns is equal to the number of markers used. Therefore, careful selection of markers as treetops must be performed. It is also impractical to select all the local maxima as treetops due to over-segmentation. Previous researches employed different strategies to perform the subset selection of local maxima (Popescu et al., 2002, Popescu and Wynne, 2004; Chen et al., 2006; Koch et al., 2006). In this work, at least four attributes, i.e., the CHM height and three dynamic values, are tagged to each local minimum. Based on these four attributes directly or other indicators derived from them, a series of decision rules could be devised to help guide the selection of treetop minima in the inverted CHM as demonstrated by a few examples in the following:

(1) If the height of a minimum is lower than a threshold, i.e., 2.5 m for this study, it is labelled as nontreetop; however, more complicated schemes could adapt the height threshold locally. The intuition of this rule is that when a minimum’s height is too low, it is less likely to be a treetop.

(2) Given a local minimum with a height larger than a threshold, i.e., 15 m in this work, if the ratio of its dynamic to height is greater than a prescribed value (0.5), it will be identified as treetop; and if its area dynamic or volume-dynamic is below a threshold, it is deemed as a nontreetop. Otherwise, the status of the minimum remains undetermined. In case that the ratio and

area (volume)-dynamic criteria conflict, the latter takes priority as a conservative strategy to reduce over-segmentation. As with (1), the thresholds can also vary adaptively; for example, the threshold for area-dynamic can be the lower limit of predication interval based on a height vs. crown-area equation. The justification for the ratio criterion lies in that the dynamic indicates the depth of crown “valley”, thus, the deeper the valley is relative to the height of its minimum, the more likely it is to be a crown. However, if the “valley” is too narrow as indicated by a small value of area-dynamic, it is less possible to be a crown; this argument justifies the area-dynamic criteria.

(3) Besides within-crown spurious local minima, there may be nontreetop minima dangling along crown-ground borders that are caused by protruding branches, or in some cases, there exists non-tree features that produce isolated minima. It could be helpful to use $H_d \cdot A_d / V_d$ (the ratio of dynamic times area-dynamic to volume dynamic) as a initial criterion to identify these local minima; for example, if the ratio is near 1, the minimum more likely belongs to this category of nontreetop minima. In this study, the ratio threshold is set to be 0.95.

Other more detailed rules could be devised to remove spurious minima or keep treetops. In these rules, adaptive schemes should be preferred if prior knowledge is available, and it also will be advantageous to take into account all the four attributes attached to each minimum. For instance, when using variable-window filtering, in order not to miss too many treetops, it’s preferable to have a window size that is a little smaller (i.e., the lower limit of prediction interval of crown width) so as to incorporate the variability of crown width given a tree height; but this leads to a high risk of commission errors. A remedy to alleviate this situation is to refer to A_d or V_d as further guidance. As to the aforementioned rules, of particular note is that for certain local minima, two or more criteria may lead to conflicting judgments; whichever should take precedence is dependent on the degree of belief as to how the assumptions of each criterion approximate the real situations.

On the other hand, as another common strategy to reduce local height variations, we pre-processed the CHM by smoothing procedures before applying watershed segmentation. In addition to Gaussian filtering, we also used the wavelet-based filter to “de-noise” CHM. The use of wavelet for image analysis characterizes the adaptive basis functions for capturing local signal features as well as a multi-scale representation of the image (Matlab Online Help, Mathworks Inc. USA). Despite the availability of automatic “de-noising” wavelet algorithms with minimal prior input, in this study we adjusted the threshold parameters in wavelet filtering through a trial-and-error approach, as described later in this section.

3.3 Segmentation of CHM beyond individual tree levels

Segmentation beyond tree levels is an alternative to analyze CHM when the algorithms of individual tree crown cannot be appropriately applied. As in our case, trees in the CHM over certain forested areas are barely identifiable. To extend the HWT to deal with such cases, there are multiple options for procedures of selecting markers. Each of three types of dynamics, or their combinations could be used as criteria to choose markers from the minima for multi-scale segmentation. For example, in this study, we attempted to choose as markers those minima whose values of $H_d \cdot A_d$ are larger than a specified threshold; and the threshold plays a role like a scale

parameter. Alternatively, volume-dynamic could be directly used as criteria to select markers.

As with segmentation of individual trees, smoothing filters can be first applied to CHM for coarser segmentation. Furthermore, with multi-resolution decomposition of CHM by wavelet, we were able to perform segmentation on the wavelet-filtered coarse-level image.

In this study, we randomly selected 5 sample subsets of CHM over our study area, each with a size of 256m x 256 m, and applied segmentation to each subset at individual tree levels and above with the aforementioned procedures where we used symlet basis in the wavelet smoothing and decomposition, due to its near symmetry property and its resemblance to crown shape. The 5 selected subsets of CHM represent various growth stages, and all have relatively high canopy closures (e.g., unthinned pine plantations). For the Gaussian filtering, we set $\sigma = 2$ as argued in Chen et al. (2006), and used a window size of 1.5m. In the wavelet-based filtering, we first performed a 2-level decomposition of the CHM and then chose level-dependent thresholds for smoothing: at the first level, the threshold was selected as the 90% percentile of magnitudes of detailed coefficients, and at the second level the 70% percentile was used; the thresholds were determined empirically.

4. RESULTS AND DISCUSSION

A typical scenario of forested area of the study site was shown in Figure 2 where a portion of the smoothed CHMs respectively by Gaussian and wavelet filters is also displayed, as compared to the original CHM. When evaluated visually it became clear that in our case the Gaussian filtering has stronger smoothing effects than wavelet filter. For example, Gaussian filter can effectively fill the “holes” within crowns while a certain number of relatively large holes, though reduced, are still preserved in the wavelet-filtered CHM.

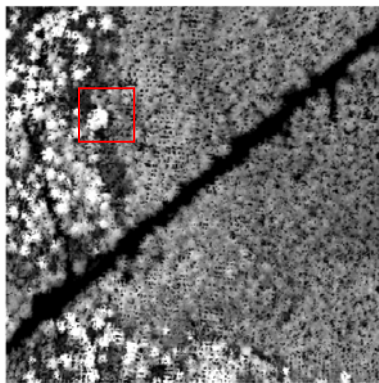


Figure 2. One selected subset of CHM for this study (above) together with a close-up of the area indicated by the red rectangles (below) where the left is the original CHM, the middle for the smoothed CHM by Gaussian filtering, and the

right for the smoothed CHM by wavelet filtering. It seems very difficult to recognize individual trees over parts of the CHM.

For the CHM in Figure 2, there are totally 14081 local maxima in the original CHM while the Gaussian filtered CHM only has 3230 maxima as compared to 5305 in the wavelet-filtered CHM. Out of these 14801 local maxima, the variable window filtering (VWF) as proposed in Popescu et al. (2002) identified 2660 of them as treetops. With the criteria using the dynamics properties, 2867 were selected as treetops from the original CHM; with the same dynamic criteria, 1325 local maxima were identified as treetops from the Gaussian filtered CHM, and 2263 from wavelet-filtered CHM. This suggested that the wavelet filter used in this study tends to preserve local features, thus resulting in more local maxima in comparison to Gaussian filtering, as also shown in Figure 2.

In all the five selected subsets of CHM, we have a limited number of field-sampled trees. But, unfortunately, for most of these trees, we failed to match them with LiDAR trees detected with the above algorithms. Also, we found it is not an easy endeavour to manually delineate trees out of CHM based on visual interpretation as shown in the close-up view of Figure 2. Therefore, no attempt is made in this study to report quantitatively the accuracy of tree identification due to the unavailability of reference data; and only comparisons between the methods were reported in terms of numbers of detected trees and mean tree height for all the 5 subsets as listed in Table 1. The numbers of detected trees are significantly different among methods ($p < 0.005$, ANOVA), but the differences in mean tree height are not statistically significant ($p = 0.76$, ANOVA). Both the two smoothing procedures significantly reduce the tree numbers ($p < 0.001$, paired-t tests) and the Gaussian filtering produces the least number of trees in all cases.

	Tree Number				Mean Tree height(m)			
	VWF	WS- Org	WS- Gau	WS- Wav	VWF	WS- Org	WS- Gau	WS- Wav
1	2660	2867	1325	2263	15.5	16.0	15.9	16.9
2	4468	3910	1587	2702	12.9	13.1	12.2	13.4
3	3583	3419	1504	2597	15.2	15.3	14.6	15.5
4	1416	2355	1302	2221	20.6	21.8	22.1	24.0
5	2572	2720	1229	2017	14.7	17.2	18.8	20.9

Table 1. Comparison of tree number and mean tree height between different methods where VWF stands for variable-window filtering in Popescu et al. (2002); and WS-org, WS-gau and WS-wav for watershed segmentation using the dynamic-based criteria applied respectively on original CHM, Gaussian-filtered CHM and Wavelet-filtered CHM.

In addition, qualitative evaluation is given over part of the CHM in Figure 2. It can be seen that no one method is superior to others according to visual examination as demonstrated in Figure 3. However, the smoothing, especially the Gaussian filtering, does help remove some, though not all, spurious local maxima. Also, the smoothing may produce inconsistent results over different parts of the CHM; for example, in Figure 3d there are more trees identified around the centre and fewer trees around the left corner as compared to Figure 3b. Overall, the result for the Gaussian-filtered CHM seems to offer a more satisfactory segmentation on this particular area than other

methods, although no optimal selection of filtering parameters σ and window size was performed.

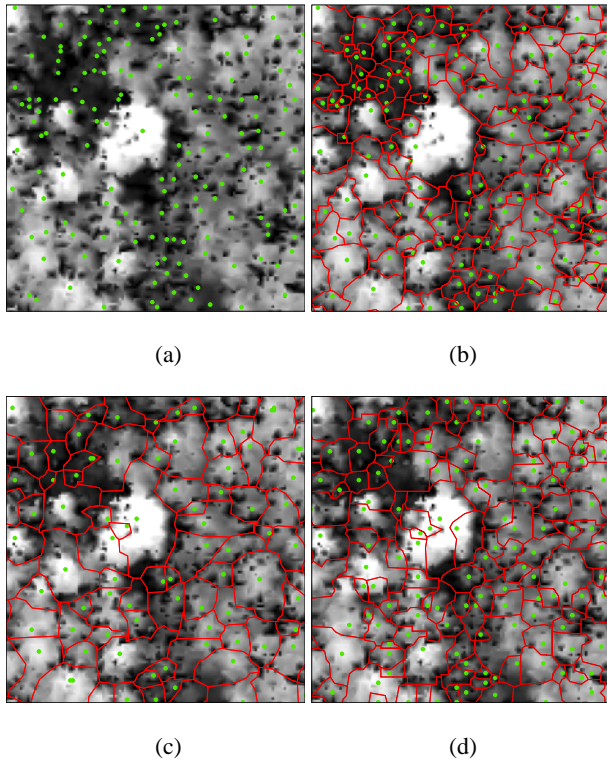


Figure 3. A visual comparison between different methods for tree identification: (a) Variable-window filtering, (b) WST on original CHM, (c) WST on Gaussian-filtered CHM, and (d) WST on the wavelet-filtered CHM. The dot points represent the treetops, and the polygons in (a)-(d) represent the segmented basins.

Above individual tree level, we thresholded the product of dynamics and area-dynamic ($H_d \cdot A_d$) to choose markers for the HWT. The segmentation is greatly influenced by the choice of indicators or the threshold value for the chosen indicator (scale parameter), and the scale parameters for different indicators have different interpretation; therefore, we only presented the results of different methods for the purpose of visual examination. Figure 4 depicts the segmentation results in four cases that include the eCognition and the HWT respectively applied on the original, the Gaussian-filtered, and the wavelet-filtered CHM. The eCognition segmentation used a scale parameter of 100 with a balance of 0.5 vs 0.5 between colour and shape, and 0.5 vs. 0.5 between compactness and smoothness; and for all the other three with HWT, the threshold for $H_d \cdot A_d$ is set to 15000 m². All the four cases tend to delineate the relatively homogeneous areas; however, no pair among the four is identical although they look similar. It also becomes clear that the smoothing, either Gaussian or wavelet filters, will also have minor effects on segmentation. A major difference between eCognition and the HWT is that the former delineated the road as a single object while the HWT divided forested areas along the “dam” built in the middle of the road, and this is obviously caused by the nature of algorithms. To be precise, the eCognition tends to aggregate the connected pixels that have similar values; on the other hand, the HWT builds the segment boundaries according to water flooding.

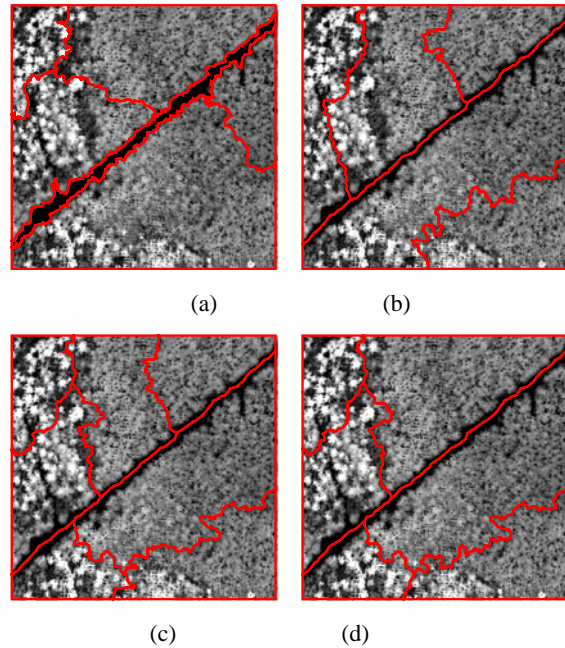


Figure 4: Comparison of segmentation results at stand levels: (a) eCognition, (b) HWT on original CHM, (c) HWT on Gaussian-filtered CHM and (d) HWT on the wavelet-filtered CHM

5. CONCLUSION

Hierarchical watershed segmentation of CHM is obtained by examining the “dynamics” properties of local maxima. The use of these dynamic attributes provides extra information as well as more flexibilities in devising rules to determine if a local maximum is treetop or not for individual tree detection. In this study, no sophisticated rules were explored; instead we simply used thresholds for the removal of nontreetop maxima. Further studies could investigate other possible criteria in determination of treetop maxima. Our results also suggested that smoothing plays an important role in suppressing spurious local maxima in CHM, and the Gaussian filter tends to produce stronger smoothing effects than wavelet-based procedures for dense forests of our study area; but neither of the two filters is consistently superior to the other. When it is difficult or infeasible to detect individual from a CHM, HWT is a practical choice to segment CHM at stand level or above. The segmentation of CHM by HWT beyond individual tree levels produces regions that are relatively homogeneous, although it does not generate exactly the same segments as the hierarchical segmentation approach of eCognition due to the disparity of algorithms themselves as well as the difference in parameters controlling scales. At such scales as those above individual-tree levels, one challenging issue remains as to how to develop methods for estimation of forest parameters since the analysis unit, not equal in area, prevent the direct use of a prediction model that are established assuming the uniform size of analysis unit (i.e., grid). Nevertheless, the results of this study show that HWT is a viable procedure in multi-level segmentation of LiDAR-derived CHM at scales appropriate for planned forestry management.

6. ACKNOWLEDGEMENTS

We gratefully acknowledge the support provided by the Texas Forest Service (award #: 02-DG-11083148-050); and we are very thankful for the help provided with the data collection and

processing by Curt Stripling, all forestry personnel with the Texas Forest Service, and by graduate students, Muge Mutlu and Alicia Griffin. Our special thanks are also due to the three anonymous reviewers for their constructive comments.

REFERENCES

- Bortolot, Z., 2005. A Tree Cluster Approach to Estimating Stand Parameters using Small Footprint LiDAR Data, Virginia Tech, <http://cears.fw.vt.edu/silviscan/presentations/author51.pdf> (accessed 28 Apr. 2007).
- Bortolot Z., 2006. Using Tree Clusters to Derive Forest Properties from Small Footprint Lidar Data. Photogram. Engineer. Remote Sensing 72:1389–1397.
- Chen, Q., Baldocchi, D.D., and Gong, P., 2006. Isolating individual trees in a savanna woodland using small footprint LiDAR data. Photogram. Engineer. Remote Sensing 72:923–932.
- Dougherty, E.R., and Lotufo, R.A., 2003. Hands-on Morphological Image Processing. SPIE Press.
- Falkowski, M.J., Smith, A.M.S., Hudak, A.T., Gessler, PE, Vierling, LA, Crookston, NL., 2006. Automated estimation of individual conifer tree height and crown diameter via two-dimensional spatial wavelet analysis of lidar data. Canadian Journal of Remote Sensing 32, 153–161.
- Hyypä, J. and Inkinen, M., 1999. Detecting and estimating attributes for single trees using laser scanner. The Photogrammetric Journal of Finland, 16(2), pp. 27-42.
- Koch, B., Heyder, U., Weinacker, H., 2006. Detection of individual tree crowns in airborne lidar data Photogram. Engineer. Remote Sensing 72: 357-363.
- Lotufo, R., and Falcao, A., 2000. The ordered queue and the optimality of the watershed approaches. In: Mathematical Morphology and its Application to Image and Signal Processing; J. Goutsias and L. Vincent and D. Bloomberg (editor). Kluwer Academic Publishers.
- Maltamo, M., Eerikäinen, K., Pitkänen, J., Hyypä, J., Vehmas, M., 2004. Estimation of timber volume and stem density based on scanning laser altimetry and expected tree size distribution functions. Rem Sens Environ 90:319–330
- Næsset, E., 2002. Predicting forest stand characteristics with airborne scanning laser using a practical two-stage procedure and field data. Remote Sens. Environ. 80: 88_99.
- Persson, Å., Holmgren, J., and Söderman, U., 2002. Detecting and measuring individual trees using airborne laser scanning. Photogrammetric Engineering and Remote Sensing, 68(9), 925-932.
- Popescu, S.C., and Wynne, R.H. 2004. Seeing the trees in the forest: using lidar and multispectral data fusion with local filtering and variable window size for estimating tree height. Photogrammetric Engineering & Remote Sensing, Vol. 70, pp. 589–604.
- Popescu, S.C., Wynne, R.H., and Nelson R.F. 2003. Measuring individual tree crown diameter with lidar and assessing its influence on estimating forest volume and biomass. Can. J. Remote 29: 564–577.
- Popescu, S.C., Wynne, R.H., Nelson, R.F., 2002. Estimating plot-level tree heights with lidar: local filtering with a canopyheight based variable window size. Computers and Electronics in Agriculture, 37, pp. 71-95.
- Pyysalo, U., and Hyypä, H., 2002. Reconstructing tree crowns from laser scanner data for feature extraction. In: ISPRS Commission III, Symposium 2002 September 9 -13, 2002, Graz, Austria, pp. B–218 ff.
- Soille, P., 2003. Morphological Image Analysis: Principles and Applications, 2nd edition, Springer-Verlag, Berlin, Germany.
- van Aardt, J.A.N., Wynne, R. H., and Oderwald, R., 2006. Forest Volume and Biomass Estimation Using Small-Footprint Lidar-Distributional Parameters on a Per-Segment Basis. Forest Science, 52 (6): 635-649.

Index of Authors

A				
Ahokas, E.	201	Chasmer, L.	96	190
Abramo, E.	26	Chauve, A.		102
Akca, D.	1	Chen, Y.		241
Akel, N. A.	119	Chen, R.		241
Andersen, H.-E	8 77	Cho, H.-K.		248
Andrei, C.-O.	241	Coops, N. C.	38	167
Arias, P.	56	Crosilla, F.		26
Armesto, J.	56	D		
Awaya, Y.	401	Dahlin, B.		227
B		Deseilligny, M. P.		102
Bae, K.-H.	14	Dold, C.		84
Barazzetti, L.	20	Doytsher, Y.		119
Barilotti, A.	26	Duong, H.		108
Barnea, S.	32	Durrieu, S.		102
Barr, A.	96	E		
Bater, C. W.	38 167	Ene, L.		114
Becker, S.	43	F		
Bienert, A.	50	Filin, S.	32	119 430
Biskup, K.	56	Fleck, S.		125
Black, A.	96	Forlani, G.		130
Boehl, J.	144	Frey, O.		294
Boesch, R.	144	Furuya, N.		401
Bollandsås, O. M.	62 300	G		
Boulaassal, H.	65	Gatziolis, D.		136
Boyd, D. S.	71	Geist, T.	195	221
Brauns, M.	125	Gergel, S. E.	38	167
Breidenbach, J.	8 77	Ginzler, C.		144
Brenner, C.	84	Glista, M.		424
Bretar, F.	102	Gobakken, T.	114	150
Briese, C.	311	Goepfert, J.		156
Brolly, G.	211	Gómez Lahoz, J.	162	338
Brovelli, M.	20	González Aguilera, D.	162	338
Bruun, E.	227	Goodwin, N. R.	38	167
Brzank, A.	90	Gorte, B.	173	221
Bücken, A.	350	Gruen, A.		1
C		Grussenmeyer, P.	65	407
Čapek, K.	241			

H				L			
Haala, N.			43	Landes, T.			65 407
Haapaniemi, F.			227	Lee, W.-K.			248
Haggrén, H.			241	Leuschner, C.			125
Hansen, von, W.			178	Liang, X.			258 253
Hanssen, K. H.			62	Lichti, D.			14
Haywood, A.			389	Lindenbergh, R.			108
Heipke, C.			90	Linkosalmi, M.			227
Hill, R. A.			71 184	Litkey, P.			201 258 355
Hirata, Y.			401	Lohani, B.			264
Honkasalo, J.			227	Lorenzo, H.			56
Honkavaara, E.			355	Loubser, D.			389
Hopkinson, C.			96 190	Lumme, J.			258
Hyypä, H.			241 355 201	M			
Hyypä, J.			201 234 241	Maas, H.-G.			373
			253 270	Mallet, C.			102
			280 355	Maltamo, M.			270 288
Höfle, B.			195 221	Marthiniussen, S.			62
I				Matikainen, L.			253 280
Ilvesniemi, S.			227	McCaughey, J. H.			96
J				McCaughey, R. J.			77
Jungkunst, H.			125	Mehtätalo, L.			288
K				Meier, E.			294
Kaartinen, H.			201 234 280	Melzer, T.			413
Kaasalainen, S.			201	Middelkoop, H.			395
Keane, E.			50	Mishra, R. K.			264
Khoshelham, K.			206	Mohan, F.			50
Kimberley, M. O.			389	Morsdorf, F.			294
Király, G.			211	Mustonen, J.			227
Kljun, N.			96	N			
Kobler, A.			216	Næsset, E.			114 150 300
Koch, B.			419				379 62
Kodde, M.			221	Nardinocchi, C.			130
Koetz, B.			294	North, P.			344
Korpela, I.			227	Nugent, C.			50
Kosonen, I.			234	O			
Koziol, K.			424	Obertreiber, N.			125
Krahwinkler, P.			350	Ogrinc, P.			216
Krzystek, P.			332	Ørka, H. O.			300
Kukko, A.			201 234 241	Oude Elberink, S.			305
Kuutti, V.			227	P			
Kwak, D.-A.			248	Packalén, P.			288 270
Kändler, G.			77	Pesonen, A.			270
				Peuhkurinen, J.			270

Pfeifer, N.	108	195	V	
	221	311	Virtanen, H.	227
Pierzchalski, M.		424	Vosselman, G.	108 305 320
Popescu, S.		436	W	
Pu, S.		320	Wagner, W.	413
Puech, W.		102	Wang, Y.	419
R			Waser, L. T.	144
Rehor, M.		326	Watt, P. J.	389
Reitberger, J.		332	Weinacker, H.	419
Reutebuch, S.		77	Wezyk, P.	424
Rodríguez González, P.	162	338	Z	
Roncat, A.		413	Zeibak, R.	430
Rosette, J.		344	Zhao, K.	436
Rossmann, J.		350		
Rutzinger, M.		195		
Rönnholm, P.	241	258 355		
S				
Sakai, A.		401		
Sakai, T.		401		
Salminen, V.-M.		241		
Salo, M.		227		
Samberg, A.		362		
Scaioni, M.		20		
Scheller, S.		50		
Schluse, M.		350		
Schmidt, I.		125		
Schneider, D.		373		
Schäfer, H.		227		
Sepic, F.		26		
Soergel, U.		156		
Solberg, S.		379		
Sotoodeh, S.		383		
Stephens, P. R.		389		
Stilla, U.		332		
Straatsma, M.		395		
Suárez, J.		344		
Suomi, O.		227		
Suvanto, A.		270		
T				
Takahashi, T.		401		
Tarsha-Kurdi, F.	65	407		
Treitz, P.		96		
U				
Ullrich, A.		413		

Index of Keywords

3D		350	Canopy projection		125
3D generalized Hough Transformation		206	Canopy structure	62 96	125
3D model		419	Carbon dioxide		96
3D modeling		320	Carbon models		389
3D modelling		56	Change detection	326	430
3D road reconstruction		305	CHM		436
3D surface		1	City modeling		119
A			Classification	90 130	195
Accuracy	65 156	270		280 300	326
Aerial image		280	Close-range photogrammetry		258
AHN		108	Clustering		383
Airborne	234	363	Comparison		326
Airborne laser scanner	114	150	Coniferous		71
Airborne laser scanners		253	Co-registration		1
Airborne laser scanning	195	221	Crevasses		221
	288	311	Crown delineation		436
Airborne lidar		96	Cultural heritage		162
Algorithm		65	Curved surfaces		119
Algorithms	32 130	178	D		
Allometry		227	Data Format		363
Analysis	413 300	332	Data fusion		305
ASPRS		363	DBH		424
Automatic methods		424	Decay class		38
Automation	50 130		Deciduous		71
	178	280	Decomposition		413
B			Deconvolution		413
Beer-Lambert		190	Defoliation		379
Biomass		8	Degree of composition		144
Broadleaf		184	DEM	216 221	326
Building	280	407	DEM/DTM	130	401
Building reconstruction	119	178	Dense digital surface model		20
Bundle adjustment		373	Detection	280	407
C			Diameters along thg stem		50
Calibration	14 227		Digital terrain model	20	311
	311	373	Disaster		326
Camera		373	Douglas-fir		136
Canopy		419	DTM	108 311	326
Canopy closure		144	Dynamic approaches		26
Canopy density		150	E		
Canopy height		150	Eddy covariance		96
Canopy height model	71	144	Education tool		264
			EMST		383

Evaluation		320	Laboratory measurements		201
Extraction		407			
F			L		
Facade Interpretation		44	LAI	248	379
Feature extraction	32	156 338	LAS		363
Features		305	Laser altimetry		108
First-last pulse		253	Laser Scanner	373	383
Floodplains		395	Laser scanner data	62	305
Flux footprint		96	Laser scanning	14	56 90
Forest	216	300		156	184 201
Forest biodiversity		38		206	234 241
Forest inventory	50	77 114		258	280 300
		136 288			350 355
		389 436	Laserscanning		363 401
Forest structure		38	Leaf area index	190	248 379
Forestry	8	211 270	Leaf-off		253 395
		332 344	LIDAR	8	20 26
		350 401		38	44 77
Free form		119		178	234 248
Full Waveform		108		311	326 332
Fuzzy logic	90	326		379	401 407
					413 436
G			Lidar	90	102 119
Gabriel graph		383		130	136 144
gap fraction		190		156	169 184
Generalized gaussian		102		190	216 270
Geometry		311		344	363 419
Georeferencing		1	Lidar intensity		71
GIS		350			
Glacier		221	M		
Glaciology		195	Manual methods		424
GPS		241	Mapping		227
			Matching		227
H			Mathematical Morphology		221
Herbaceous vegetation		395	Mixed-effects model		77
High resolution		300	Mobile mapping		241
HyMap		71	Modeling	227	338
			Modelling	44	102 211
I					270 407
ICESat		108	Modelling of sensor		264
IMU		241	Morphological analysis		26
Integration		355	Morphology		430
Intensity	190	195	Multiple surfaces		1
Intensity values		156	Multi-Scale		227
Interpolation		71			
Inventory	8	270	N		
	300	344	National Forest Inventory (NFI)		144
			nDSM		216
K			O		
Korf		288	Object recognition		206
Kyoto Protocol		389			

Old-growth forest	125	Satellite	344
Orientation	311	Scale	436
Orthophoto	20	Scots pine	288
Outlier detection	383	Segmentation	50 65 173
Overstorey	184		195 280 311
			326 332
			338 407
P			
Pacific northwest	136	Sensor registration	162
Panorama	373	Shipbuilding	56
Performance	178	Signal processing	102
Photogrammetry	162 211	Simulation	234
	338 355	Simulator	114 264
Photo-plot	227	Single tree	211
Photosynthesis	96	Single Tree Delineation	350
Photosynthetically Active Radiation	248	Site index	136
Planar targets	14	Snags	38
Point cloud	32 44 50	Software	264
	56 65 178	Software development	162 338
	195 206 383	Spatial DB	20
	413 419	Species identification	253
Point cloud density	216	Stand basal area	424
Point clouds	430	Stand volume	77
Point density	248	Standards	363
Pointcloud	1	Statistics	8
Positioning	241	Surface matching	1
Prediction	270	Systematic error	14
Processing	407		
Pulse density	150	T	
Pulse detection	413	Template	227
		Terrestrial	56 178
			234 363
Q			
Quality	234	Terrestrial laser scanning	32 50 84
Quality analysis	305		173 211 311
			320 424 430
		Terrestrial lidar	125
R		Three-dimensional	44 65
Radiometric calibration	201	TIN	320
Random effects	77	TLS	65
Range images	84 173	Topographic	305
Recognition	270	Traffic environment	241
Regeneration	62	Tree basal area	424
Region growing	26	Tree crown	419
Registration	32 84 178	Tree extraction	26
	311 355	Tree height	125
REIN algorithm	216	Tree identification	258
Relative orientation	84	True orthophoto	20
Remote Sensing	270 401	Trunk detection	258
Research tool	264		
Respiration	96	U	
RTK	241	Underbody	56
		Understorey	184
S		Understorey vegetation	169
Sampling	8 227 389		

Uneven-aged forest			62
Urban			44
V			
Validation			71
Variance component estimation			373
Vegetation	156	332	344
Vegetation cover			169
Vegetation density			395
Vegetation heigh			395
Vegetation Index			248
Vegetation indexes			26
Vertical structure			419
W			
Water			90
Watershed segmentation			436
Waveform	413	234	258
Waveform analysis			102
Weibull			288
Wildlife tree class			38
Woodland			184
Woody area			379